NASA Conference Publication 2071
AFGL-TR-79-0082

(NASA-CP-2071) SPACECRAFT CHARGING TECHNOLOGY, 1978 (NASA) 908 p HC A99/MF A01 CSCL 22B

N79-24001 THRU N79-24057 Unclas G3/18 22123

Spacecraft Charging Technology - 1978

A conference held at
U.S. Air Force Academy
Colorado Springs, Colorado
October 31 - November 2, 1978

NASA Conference Publication 2071
AFGL-TR-79-0082

Spacecraft Charging Technology - 1978

A conference sponsored by
U. S. Air Force Geophysics
Laboratory, Hanscom AFB
Massachusetts, and Lewis
Research Center, Cleveland
Ohio, and held at U.S. Air
Force Academy, Colorado
Springs, Colorado
October 31 - November 2, 1978

National Aeronautics and
Space Administration

**Scientific and Technical
Information Office**

1979

PREFACE

The second Spacecraft Charging Technology Conference was held at the U.S. Air Force Academy from October 31 to November 2, 1978. The first conference, held two years earlier, was so successful in bringing together experts from diverse areas of this technology to exchange results and viewpoints that it was believed another conference would be of substantial benefit.

The tenor of the presentations at this conference was gratifying. No longer are we working with first concepts and theories. We now have, in hand, space and ground test data that correlate well; analytical programs that can model the observed phenomena; and the imminent flight of the SCATHA spacecraft, which will extend our knowledge of the spacecraft charging environment. Although the technology is far from being complete, there was a feeling of confidence among the participants that we are beginning to develop a working knowledge of the problems and their potential remedies.

One session of this conference introduced a new area of general interest, environmental interactions with on-board, high-voltage spacecraft systems operating over a wide range of altitudes from low Earth orbit to geosynchronous orbit. These interactions must be considered during the initial design phases of future high-power space systems.

The proceedings includes 52 of the 54 papers presented at the conference. The panel discussion was recorded, has been transcribed and edited, and is included. The proceedings follows the conference session format. Four papers are printed at the end of the proceedings that were not presented at the conference.

Col. John E. Brooke, Assistant Director of Science and Technology, USAF Systems Command; and James J. Kramer, Associate Administrator for Aeronautics and Space Technology, National Aeronautics and Space Administration, approved and endorsed the conference. Col. Bernard S. Morgan, Jr., Commander of the USAF Geophysics Laboratory, USAF Systems Command, and Dr. John F. McCarthy, Jr., Director of the NASA Lewis Research Center, encouraged and supported the conference. Lt. Gen. K. L. Tallman, Superintendent of the USAF Academy, arranged accommodations, transportation, meals, and facilities. Capt. William Denton, Directorate of Conferences, USAF, gave outstanding support at the conference. The members of the Conference Program Committee were Maj. George Kuck, Capt. Henry Garrett, Dr. William Lehn, N. John Stevens, Dr. Elden Whipple, and Dr. Alan Rosen.

Robert C. Finke
NASA Lewis Research Center

Charles P. Pike
USAF Geophysics Laboratory

Cochairmen

CONTENTS

KEYNOTE ADDRESS

Floyd R. Stuart, Col., USAF
USAF Space and Missile Systems Organization

Good Morning - Both General Ward and Colonel Brooke asked me to convey their regrets for not being here due to the press of business.

I would like to welcome you to this, the second Spacecraft Charging Technology Conference. I am enthusiastic about this conference because I feel this is the best way to insure a maximum exchange of results. As you can see, we have an excellent turnout - about 150 attendees. There are representatives from U.S. industries and universities, from the European Space Agency and, quite naturally, since this is a joint DOD/NASA Technology Program, we have NASA as well as Army, Navy and Air Force participants.

This is the second conference. The first was a smashing success. There were over 225 attendees and 60 papers. From all indications, this conference will also be a success.

Technology involving spacecraft charging is one of the many interdependent research areas in aeronautics and astronautics that are coordinated by the AFSC/NASA Space Research and Technology Review Group. These interdependent technology programs have resulted from our awareness that many technical problems are common to both agencies and, also, from the fact that we both share budgetary constraints.

NASA and DOD strive to identify these common technical problems and then assign agency responsibility for providing the required technology. If one agency has the technical lead in an area, then we assign to it responsibility for developing the technology for both agencies. In some cases, an agency has cancelled its program and transferred funds to the responsible agency. Where both agencies have desired to maintain programs, the programs have been jointly managed and the technical responsibility has been clearly established.

The concept of interdependency has taken hold, and benefits are beginning to accrue. Interdependency allows us to stretch our limited research and development dollars, to reduce or eliminate duplication, and to maximize the technology return per dollar invested.

Spacecraft charging is a 5 year program between Air Force Systems Command and NASA's Office of Aeronautics and Space Technology. A steering committee incorporates NASA and DOD requirements into the investigation. The ultimate objective of the program is to protect our satellites from the harmful effects of high voltage arc-discharges. This objective is met by develop-

ing design criteria and test methods. Each element of the program is assigned to either NASA or the Air Force with well defined accountability. Contractual and in-house efforts are working on this program. Program success requires everyone involved to execute their portion successfully. Technology elements include development of analytical programs to define the environment and model the spacecraft interaction with this environment. There are experimental programs to develop ground facilities to simulate the environment, to determine the response of spacecraft materials to this environment, and to develop new or modified materials.

The spacecraft charging at high altitudes or "SCATHA" satellite managed by the SAMSO STP office will be used to define the environment, to measure charging and discharging characteristics of materials, to provide data for calibration of the analytical models, and to measure satellite contamination. The electrical potential of SCATHA will be actively controlled using an electron and ion beam system.

I see significant progress in the program and I will mention just a few of the accomplishments.

All SCATHA instrumentation has been delivered and integrated. Systems level testing is finished and launch is scheduled for early next year.

A rocket flight showed that electron and ion beams can control vehicle potential. Measurements on the ATS-5 and 6 satellites show the plasma neutralizer can control the surface potential over the spacecraft.

A baseline "Military Standard" for spacecraft charging has been written including a specification of the environment.

A "Design Guidelines Monograph" details techniques to minimize satellite charging.

Silica-fabric thermal control coatings have been developed for use in satellite charging control. Transparent conductive coatings for controlling charging on thermal blankets, on second surface mirrors, and on solar cell covers are now available.

A model of the internal charge buildup within insulators is operating and environmental simulation facilities are characterizing the charging of insulators.

The NASA Charging Analyzer Computer Program is being used to compute satellite voltage distributions.

In addition to these accomplishments, new programs have been initiated. One deals with investigating the effects of a systems generated electromagnetic pulse on an electrically charged satellite. Another investigates the charge buildup on a satellite, which occurs after a high altitude detonation, and the charge breakdown processes.

In conclusion, spacecraft charging is a successful cooperative effort. Your efforts have produced results that, today, are essential to the design of reliable and survivable space systems. As we move into the next era of space technology in which satellites will grow in size, power, complexity, and cost, you again will be called upon to develop the required technology to insure success.

We have a full agenda - so I don't want to take any more of your time. Again -- I welcome you to this - the second Spacecraft Charging Technology Conference.

Thank you.

DESCRIPTION OF THE SPACE TEST PROGRAM P78-2 SPACECRAFT AND PAYLOADS

Lt Col John C. Durrett
USAF Space & Missile Systems Organization

John R. Stevens
The Aerospace Corporation

INTRODUCTION

The USAF Space Test Program was designated in 1975 as the management agency for procurement of the Department of Defense spacecraft which supports the government USAF/NASA spacecraft charging at high altitude program. The spacecraft was designated the Space Test Program P78-2 spaceflight. Built by the Martin Marietta Corporation in Denver, Colorado, the spacecraft and its payloads are designed to measure the environment at near synchronous altitude and the interactions of the environment on the spacecraft.

SPACECRAFT

The P78-2 spacecraft is spin-stabilized and will be placed in a near synchronous, equatorial earth orbit from the Eastern Test Range by a Delta 2914 in January 1979. The spacecraft houses, protects, and supports several scientific and engineering payloads. It spins about an axis which lies in the orbit plane and is normal to the earth-sun line. On-orbit, the satellite will be controlled by the Air Force Satellite Control Facility (AFSCF) and will communicate directly with remote tracking stations in New Hampshire, the Indian Ocean, Guam, Hawaii, and at Vandenberg AFB. The mission is planned for a one-year duration but the spacecraft is provided with sufficient expendables for two years. Actual lifetime of the satellite will probably be limited by survival of electronic equipment in the ionizing radiation environment.

The body of the spacecraft has a cylindrical shape approximately 1.75 m in both length and diameter. Booms, antennae, and some instrument protrusions alter the basic cylindrical shape. Most of the spacecraft and payload equipment is mounted in the central portion of the cylinder. On orbit, seven experiment booms are deployed. The boom arrangement isolates sensitive instruments from spacecraft influences and provides clear fields of view for other instruments. Two solar arrays encircle the cylinder, one forward and one aft of the central portion. An apogee insertion motor is housed in the aft central portion of the spacecraft.

In addition to the usual spacecraft components, a transient pulse monitor has been incorporated as part of the spacecraft. This instrument obtains quantitative measurements of the electromagnetic pulse characteristics on the spacecraft. It measures the number of pulses, the positive and negative pulse amplitudes, and the positive and negative integral of the pulses.

Fabrication and assembly of the spacecraft have been completed. The spacecraft has been shipped from Denver to the Goddard Spaceflight Center where the magnetic and moment of inertia characteristics of the spacecraft are being measured. Next, the spacecraft will be shipped to the Eastern Test Range from which it will be launched in January 1979. The expected orbit parameters are listed below.

Apogee	42,250 km
Perigee	27,500 km
Inclination	8.5 deg

The final orbit will have an easterly drift rate of 6 deg/day for the satellite.

PAYLOADS

The payloads have been sponsored and produced by many different agencies. The attached table delineates the many participants. A brief description of each payload follows. A more detailed description of the spacecraft and its payloads was distributed as part of the registration material. Additional copies of the detailed payload descriptions entitled "Description of the Space Test Program P78-2 Spacecraft and Payloads" can be obtained by writing to:

HQ SAMSO/YCT
Attn: Lt Col J. C. Durrett
P. O. Box 92960
Worldway Postal Center
Los Angeles, CA 90009

ENGINEERING EXPERIMENTS SC1

One of the engineering experiments measures the profile of charging events on insulators, grounded insulators, and isolated conductors in conjunction with various environmental parameters measured on the same satellite. Surface potentials up to 20 kV are measured using an electrostatic voltmeter and also by measuring leakage currents.

Other experiments measure the power spectrum of very low frequency electromagnetic waves. Using a spectrum analyzer the spectrum from

400 Hz to 300,000 Hz is measured in eight frequency intervals. Spectrum measurements are also made in the RF region of the electromagnetic spectrum. Five measurements are made in the 2 to 30 MHz band. Objectives of these instruments are to measure characteristics of electromagnetic disturbances on the spacecraft and to measure the intensity and spectra of electromagnetic and electrostatic emissions caused by the energetic particles near the spacecraft.

A pulse shape analyzer measures the shape of electromagnetic pulses in the time domain from 7 nsec to 3.7 msec.

SHEATH ELECTRIC FIELDS SC2

This experiment is intended to provide the electron and ion distribution functions over a limited energy range, less than 20 keV, at three positions in the spacecraft plasma sheath. The experiment also measures the floating potential relative to the spacecraft ground of two biasable spherical probes. The aims of the experiment are to obtain insight into the characteristics of spacecraft sheath fields, to observe the effects of particles that comprise the energetic plasma near a spacecraft, and to observe the potential that a relatively simple geometrical shape attains in the plasma environment both in sunlight and in shadow.

The proton detector consists of a two-element solid-state telescope. Protons with energy between 17 and 717 keV are measured in six energy channels.

An ion detection system consists of a two-element solid-state telescope that is highly collimated and heavily shielded. Ions with energies greater than 90 keV/nucleon are detected.

HIGH ENERGY PARTICLE SPECTROMETER SC3

The instrument is a solid-state particle spectrometer consisting of four sensor elements. Various logic combinations of the four sensors in the instrument are used to determine the particle types and energy ranges. The various particle types and energy ranges are measured in several time-multiplexed modes of operation that are command-selectable. Electrons with energy between 50 keV and 5 MeV are analyzed as are protons with energy between 5 and 200 MeV.

SATELLITE ELECTRON AND ION BEAM SYSTEM SC4

The satellite electron beam system is to be used for the ejection of electrons from the P78-2 spacecraft. Instrument ground is connected by a low impedance path to the spacecraft ground, and thus ejection of electrons

from the electron gun will drive the potential of the spacecraft positive with respect to the ambient plasma. The payload will be used (1) to determine the electron current required to prevent charging of the spacecraft ground caused by in situ electrons and (2) to swing the vehicle to a positive potential relative to the ambient plasma.

The positive Ion Beam System payload is to be used on the P78-2 spacecraft for the ejection of charged particles: positive ions, electrons, or beams containing both positive ions and electrons. The payload is electrically connected to the P78-2 spacecraft ground through a low impedance path so that the ejection of charge will play a large role in determining the potential difference between spacecraft ground and the ambient plasma. The ion source is a Xenon discharge chamber. This instrument can be used to adjust the potential of the spacecraft with respect to the ambient plasma. The potential can be either negative or positive depending on how much electron neutralizer current is used.

RAPID SCAN PARTICLE DETECTOR SC5

This detector will measure the flux of electrons and ions incident to the spacecraft both perpendicular and parallel to the spin axis of the spacecraft. The number density, temperature, and bulk flow of the plasma and the relationship of these quantities to the occurrence of spacecraft charging will be determined. The instrument also monitors operation of the Electron and Ion Beam System.

The instrument consists of two sets of spectrometers mounted perpendicular and parallel to the spin axis of the satellite. Each set of spectrometers consists of eight sensors; four measure electrons and four measure ions. These sensors measure electron differential flux from 50 eV to 1.1 MeV and ion differential flux from 50 eV to 35 MeV.

THERMAL PLASMA ANALYZER SC6

This instrument is intended to measure the ambient thermal plasma and the electrostatic potential of the satellite with respect to the ambient plasma. The ion density is measured in the range 10^1 to 10^5 per cm^3. The particle temperature is measured from 0.5 eV to 100 eV. The satellite potential is measured in the range of -100 V to +100 V. In addition, the instrument mounted on the satellite body will measure the flux of photoelectrons from the satellite. The Thermal Plasma Analyzer consists of three identical planar particle traps which can be operated as retarding potential analyzers.

LIGHT ION MASS SPECTROMETER SC7

Three spectrometers are designed to measure the density, temperature, and composition of the low-energy ion plasma in the vicinity of the P78-2 spacecraft. In order to understand the complex plasma-satellite interaction, all important charged particle populations must be identified and measured. The cold plasma (E <100 eV) component is important at and near synchronous orbit altitudes and at times can be the dominant component in terms of density, exceeding 100 ions/cm^3.

This payload consists of three sensor heads and one central electronics package. Each sensor head consists of a retarding potential analyzer, ion mass spectrometer, and ion detector. The fluxes of oxygen, helium and hydrogen are measured for energies less than 100 eV.

ENERGETIC ION COMPOSITION EXPERIMENT SC8

This instrument is an energetic ion mass spectrometer containing three parallel analyzer units, each of which measures ions in a different energy region of the range from 0.1 to 32 keV. Each unit consists of a crossed electric and magnetic field velocity filter (Wein filter) in series with an electrostatic analyzer (ESA) and a channel electron multiplier sensor. Elements with mass from 1 to 160 AMU are analyzed with mass resolution of 1 to 20 AMU, respectively.

UCSD CHARGED PARTICLE EXPERIMENT SC9

The experiment measures charged particle fluxes as a function of energy, direction, and time. The charged particles that will be measured consist of environmental electrons and ions and also particles emitted from the spacecraft, such as photoelectrons, secondary electrons, and particles emitted by the Electron/Ion Beam System.

The experiment has five electrostatic charged particle detectors. Two detectors (one for negative and one for positive particles) are contained in each rotating detector assembly. Each rotating detector assembly can be rotated through a maximum of 220 deg. One rotating detector assembly rotates so that its detectors look in a plane tangent to the cylindrical side of the spacecraft. It is capable of measuring particles with energy from a few eV to 81 keV. The other rotating detector assembly looks in a plane that cuts across the forward face of the spacecraft, and is capable of measuring particles with energy from 0.2 eV to 1550 eV.

ELECTRIC FIELD DETECTOR SC10

This instrument is a double floating ensemble that will measure DC electric fields in the ambient plasma and also spacecraft charging events. The antenna is a dipole which is 100 M tip to tip. Both differential and common mode measurements can be made. The signal strength from DC to 200 Hz can be analyzed.

MAGNETIC FIELD MONITOR SC11

The instrument is a triaxial fluxgate magnetometer. Each axis has a range of approximately ±500 γ. The resolution of the magnetic field measurement is 0.3 γ. The spin axis component is analyzed through a spectrometer with a sensitivity of ~20 mγ for frequencies between 5 and 100 Hz.

SPACECRAFT CONTAMINATION ML12

This experiment is designed to determine if spacecraft charging contributes significantly to the rate of contamination arriving at exterior spacecraft surfaces. The contamination transport mode under investigation involves the ionization of molecules outgassed or released by the vehicle within the vehicle plasma sheath and their subsequent electrostatic attraction to the vehicle. One sensor is a combined retarding potential analyzer and temperature controlled quartz crystal microbalance. With it, distinction can be made between charged and uncharged arriving molecules. Information concerning the temperature dependence of contamination adsorption and desorption rates can be obtained. Another sensor, thermal control coating trays, exposes samples of different spacecraft surface materials to arriving contamination and continuously measures the temperature and hence solar absorptance of these materials.

TABLE I. PRINCIPAL INVESTIGATORS/SPONSORS

Experiment Number	Title	Principal Investigator/ Sponsor	Address
SC1	Engineering Experiments	Dr. H. C. Koons/ USAF/AFSC/SAMSO	The Aerospace Corporation P.O. Box 92957 Los Angeles, CA 90009
SC2	Spacecraft Sheath Electric Fields	Dr. J. F. Fennell/ USAF/AFSC/SAMSO	The Aerospace Corporation P.O. Box 92957 Los Angeles, CA 90009
SC3	High Energy Particle Spectrometer	Dr. J. B. Reagan Office of Naval Research	Lockheed Palo Alto Research Lab, 3251 Hanover Street Palo Alto, CA 94304
SC4	Satellite Electron and Positive Ion Beam System	Dr. H. A. Cohen/ USAF/AFSC/AFGL	Hanscom AFB/LKB Bedford, MA 01731
SC5	Rapid Scan Particle Detector	Lt. D. Hardy/ USAF/AFSC/AFGL	Hanscom AFB/PHE Bedford, MA 01731
SC6	Thermal Plasma Analyzer	Dr. R. C. Sagalyn/ USAF/AFSC/AFGL	Hanscom AFB/PHR Bedford, MA 01731
SC7	Light Ion Mass Spectrometer	Dr. D. L. Reasoner/ Office of Naval Research	NASA Marshall Space Flight Center, Code BS-23 Huntsville, AL 35815
SC8	Energetic Ion Composition Experiment	Dr. R. G. Johnson/ Office of Naval Research	Lockheed Palo Alto Research Lab, 3251 Hanover Street Palo Alto, CA 94304
SC9	UCSD Charged Particle Experiment	Dr. S. E. Deforest/ Office of Naval Research/USAF/AFSC/ SAMSO	University of California B019 Dept. of Physics La Jolla, CA 92093
SC10	Electric Field Detector	Dr. T. L. Aggson/ Office of Naval Research	NASA Goddard Space Flight Center, Code 625 Greenbelt, MD 20771
SC11	Magnetic Field Monitor	Dr. B. G. Ledley/ Office of Naval Research	NASA Goddard Space Flight Center, Code 625 Greenbelt, MD 20771
ML12	Spacecraft Contamination	Dr. D. F. Hall/ USAF/AFSC/AFML	The Aerospace Corporation P.O. Box 92957 Los Angeles, CA 90009

D2

N79-24003

MODELING OF THE GEOSYNCHRONOUS PLASMA ENVIRONMENT

H. B. Garrett
Air Force Geophysics Laboratory

SUMMARY

An analytic simulation of the geosynchronous environment in terms of local time and the daily A_p index is presented. The simulation is compared with actual statistical data from approximately 50 days of ATS-5 plasma data and 50 days of ATS-6 plasma data. At low levels of activity the model adequately simulates the local time variations of the plasma parameters. At high values of geomagnetic activity, the predicted magnitudes of the plasma parameters agree with the statistical results but the effects of multiple injections are evident in both the data and the simulation, biasing the local time variations.

INTRODUCTION

The geosynchronous environment is probably the harshest space environment from a spacecraft charging standpoint. As a result, the modeling of the geosynchronous plasma and of the associated potential variations is critical to a proper understanding of spacecraft charging. As this is also the region of primary communication satellite operation, it is doubly important to accurately model this region. In this paper we will discuss the efforts of the Air Force Geophysics Laboratory in defining the geosynchronous environment. The first section will present the types of models and data available from AFGL. These models will be compared and preliminary results discussed in subsequent sections.

DEFINITION OF MODELS

Philosophical Considerations

There are at least four types of magnetospheric models that are of concern to the spacecraft charging community. Briefly, the simplest (conceptually) is a statistical compendium or histogram of various parameters as a function of space and time. Such models have little theoretical input, being based on actual measurements. Consideration of basic physical principles makes possible the creation of simple analytic expressions capable of simulating the environment - the second type of model. Third, are static field models - that is, models which employ theory to predict the trajectories of charged particles

in static magnetospheric electric and magnetic fields. Finally, the most complete models from a theoretical standpoint are full, 3-dimensional time-dependent models capable of accounting for real time variations in the plasma environment. Considering the level of our current efforts in spacecraft charging, we will limit ourselves to the first two types of models - the latter two models are much too detailed for our present needs (see Garrett, 1978, for a review of current models in each of these categories).

Statistical Model

Statistical models, as defined here, are compendiums or histograms of various plasma parameters based on actual data. Basic examples of this type of model are the distribution functions of Chan et al. (1977) who generated an "average" spectrum in terms of energy and differential number flux for various magnetospheric and solar wind regions. Likewise, Su and Konradi (1977) have averaged a year of ATS-5 geosynchronous data to obtain average particle distribution functions and other statistical parameters. Although we have taken a somewhat similar course at AFGL, we have limited our analysis to the first four integral moments (c f., DeForest and McIlwain, 1971) of the distribution function.

The 4 moments are defined as follows:

$$\langle N_i \rangle = 4\pi \int_0^\infty (V^0)\, f_i\, V^2\, dV = n_i \tag{1}$$

$$\langle NF_i \rangle = \int_0^\infty (V^1)\, f_i\, V^2\, dV = \frac{n_i}{2} \left(\frac{2kT_i}{\pi m_i}\right)^{\frac{1}{2}} \tag{2}$$

$$\langle P_i \rangle = 4\pi\, (1/3\, m_i) \int_0^\infty (V^2)\, f_i\, V^2\, dV = n_i kT_i \tag{3}$$

$$\langle EF_i \rangle = (\tfrac{1}{2} m_i) \int_0^\infty (V^3)\, f_i\, V^2\, dV = \frac{m_i n_i}{2} \left(\frac{2kT_i}{\pi m_i}\right)^{3/2} \tag{4}$$

where

$\langle N_i \rangle$ = number density for species i (number/cm^3)

$\langle NF_i \rangle$ = number flux for species i (number/cm^{2}sec-sr)

$\langle P_i \rangle$ = pressure for species i (dynes/cm^2)

$\langle EF_i \rangle$ = energy flux for species i (ergs/cm^{2}sec-sr)

The integral results on the right are for a Maxwell-Boltzmann distribution:

$$f_i\,(V) = n_i \left(\frac{m_i}{2\pi\, kT_i}\right)^{3/2} e^{-mV_i^2/2kT_i} \tag{5}$$

where n_i = number density of species i

m_i = mass of species i

T_i = temperature of species i

V_i = velocity of species i

K = Boltzmann constant

$f_{...}$ = distribution in sec^3/km^6

The description of the plasma in terms of these quantities is quite useful as not only are they physically meaningful in their own right, but they can be used to derive a Maxwellian or 2-Maxwellian distribution of the environment (see Garrett and DeForest, 1978).

Su and Konradi (1977) have compiled statistics on the 4 moments for ATS-5 during 1970. Their data consist of 10 minute values for the distribution functions derived from scanning ATS-5 spectrograms. We have undertaken a similar study of approximately 50 days of ATS-5 data from 1969 and 1970 and 45 days of ATS-6 data from 1974 and 1976 (Johnson et al., 1978). In our study the original digital data were integrated to give the 4 moments of the distribution function for each satellite. The ATS-6 data were corrected for satellite potential and return currents (the ATS-5 satellite spectra begin at 50 ev precluding a correction except in extreme cases like eclipses). The 4 moments were combined to give 10 minute averages (note: the 4 moments can be properly averaged in a physical and mathematical sense, the temperature cannot). For ATS-5 we have the detector components both parallel and perpendicular to the satellite spin axis, for ATS-6 we have only the component parallel to the earth's spin axis. The tapes were then merged with geophysical and ephemeris data (Garrett et al., 1978).

The tapes were and are being analyzed by a variety of techniques. In response to a desire on the part of the spacecraft charging community, we have, as a first step, compiled tables of the characteristics of the electron and ion currents and temperatures. The occurrence frequencies (note: the ATS-6 data are still being reviewed and may be subject to revision) for these parameters are plotted in figure 1. Several features are apparent in this figure which will be discussed in detail later.

An important point in the derivation of figure 1 that must be considered is the estimation of the plasma temperature from the 4 moments of the distribution function. A single temperature cannot be defined if the plasma is not Maxwellian or in the case the plasma consists of two or more Maxwellian components - circumstances which are the norm at geosynchronous orbit. As a test of this effect, we have defined two "temperatures:"

$$T\ (AVG) = \frac{\langle P \rangle}{\langle N \rangle} \qquad (6)$$

$$T\ (RMS) = \frac{\langle EF \rangle}{2\ \langle NF \rangle} \tag{7}$$

These temperatures will be equal and have meaning as temperatures <u>if and only if</u> the plasma is a Maxwellian plasma (i.e., representable by equation 5). The marked difference between T(AVG) and T(RMS) in figure 1 is a direct result of the absence of a Maxwellian plasma at geosynchronous orbit.

If the plasma is considered to consist of 2 Maxwellian components, then we can define two temperatures and two densities as follows for species i:

$$f_{2i}\ (V_i) = n_{1i} \left(\frac{m_i}{2\pi kT_{1i}}\right)^{3/2} e^{-m_i V_i^2/2kT_{1i}} + n_{2i} \left(\frac{m_i}{2\pi kT_{2i}}\right)^{3/2} e^{-m_i V_i^2/2kT_{2i}} \tag{8}$$

n_{1i}, T_{1i}, n_{2i}, and T_{2i} can be derived directly from equations 1 through 4. T(AVG) and T(RMS) can be expressed in terms of these quantities:

$$T\ (AVG) = k\ \frac{n_1T_1 + n_2T_2}{n_1 + n_2} \tag{9}$$

$$T\ (RMS) = k\ \frac{n_1T_1^{3/2} + n_2T_2^{3/2}}{n_1T_1^{\frac{1}{2}} + n_2T_2^{\frac{1}{2}}} \tag{10}$$

For typical values we find:

<u>For Electrons</u>	<u>For Ions</u>
$n_1 = 1/cm^3$	$n_1 = 1/cm^3$
$T_1 = 500$ eV	$T_1 = 100$ eV
$n_2 = 0.2/cm^3$	$n_2 = 1/cm^3$
$T_2 = 6000$ eV	$T_2 = 9000$ eV
$T(AVG) \simeq 1400$ eV	$T(AVG) \simeq 4550$ eV
$T(RMS) \simeq 2750$ eV	$T(RMS) \simeq 8150$ eV

These values are very close to the median values for ATS-5 shown in figure 1 and, we believe, readily explain the differences between T(AVG) and T(RMS). It is also important to note that T_1 and T_2 are not necessarily valid temperatures. They are the result of a definite fitting process - their primary use being as scaling parameters in obtaining a 2-Maxwellian fit to the distribution function. A common problem is that when the plasma is close to Maxwellian, one of the temperatures will be unrealistically large even though the fitted distribution is quite close to the actual one.

Analytic Simulation Model

In the previous section we outlined the steps involved in deriving our statistical data base and indicated some of the problems we encountered in attempting to derive "temperatures." In this section we discuss a straightforward application of the 4 moments. Briefly, a major deficiency in the statistical model of the geosynchronous orbit is that it only gives average values and ranges for given parameters, no attempt being made to preserve the simultaneous time variations in different parameters (i.e., if A is large, how do we know if B is large or small?) In order to maintain the correlated variations in different parameters, we have made use of linear regression techniques. Three hour averages of the 4 moments of the electron and ion distribution functions for 10 carefully selected days* of ATS-5 data (see Table 1) were fit by linear regression techniques to an equation varying linearly in the geomagnetic index A_p and diurnally and semidiurnally in local time LT:

$$M(LT, A_p) = (a_o + a_1 A_p)\left\{b_o + b_1 \cos\left[\frac{\pi}{12}(LT + t_1)\right] + b_2 \cos\left[\frac{\pi}{6}(LT + t_2)\right]\right\}$$

where $M(LT, A_p)$ = predicted value of the moment M at local time LT and for activity level $A_p = \frac{\sum a_p}{8}$ (i.e., daily average of a_p)

$a_o, a_1, b_o, b_1, b_2, t_1, t_2$ = coefficiencts determined by the regression (see Table 1).

To use the model, one provides A_p and local time. The model then returns the 4 moments for the electrons and ion in the units given in Table 1. The reader is referred to Garrett (1977) for a detailed discussion of the uses and

* The days were carefully selected to correspond to periods when plasma was injected while the satellite was at midnight - periods when maximum spacecraft charging is believed to take place.

applications of the model and problems associated with it. Only a cursory description will be given here.

The analytic model has been found to adequately simulate variations in the geosynchronous environment following substorm injection when a satellite is at local midnight for A_p values of ~ 4 to ~ 48 (i.e., low to moderately high activity). Above ~ 48, the model properly simulates the environment but is biased toward the plasma parameters on the particular days of high activity that were studied, not average conditions. The parameters returned by the model show the peak in charging to shift from near midnight (as expected) to near noon for high levels of activity. This was traced to the actual data for which the plasma parameters clearly peak near noon for high activity (i.e. days 348, 1970; 217 and 223, 1972). As we were careful to select only days for which injections began when the ATS-5 satellite was near midnight, this may well be a common feature of the plasma conditions associated with high activity.

MODELING RESULTS

Figure 1 presented the results which form the basis of the AFGL Environmental Specification. Figure 2 is a plot of the average local time variations of T(AVG), T(RMS), and current for ATS-5 and ATS-6. Error bars have not been indicated but they are roughly 50% of the average value. Also shown are estimates of T(AVG), T(RMS), and current for an A_p value of 15 (or average geomagnetic activity) as derived from the AFGL simulation model. For ATS-5 the results for the statistical model and the simulation model are in excellent agreement confirming that the simulation adequately predicts average conditions.

Figure 3 indicates typical (A_p = 15) and active (A_p = 207) conditions as predicted by the simulation model (the average energy is the ratio of the energy density to number density and is equal to 3/2 T(AVG)). The results are in good agreement with DeForest and McIlwain (1971) for "typical" activity levels. Figure 4 gives the results for n_1, T_1, n_2, and T_2. Note in all cases that there is an approximately X10 change in the 4 moments for the electrons and X4 for the ions with geomagnetic activity (also, the current as current density is directly proportional to number flux), but little in energy (or temperature). This observation is also born out by the statistical model (see Garrett, et al. 1978), there being, at most, a doubling of temperature.

Although the differences between ATS-5 and ATS-6 as presented in figures 1 and 2 are likely due to the near-doubling in geomagnetic activity between the ATS-5 and ATS-6 data, the foregoing observations and differences preclude an unambiguous explanation at this time. Interestingly, there is significant qualitative agreement as to the local time variation between ATS-5 and ATS-6. T(RMS), for example, peaks near 1800 for electrons and ions while the current peaks near midnight. T(AVG) peaks near 2100 for the ions (the case is not clear for the electrons). Considering the varied data sources from which the results came, this agreement is quite surprising and deserves further analysis.

CONCLUSIONS

The Air Force Geophysics Laboratory has developed two simple models of the geosynchronous plasma environment. These models were specifically developed in response to the needs of the spacecraft charging community. In summary, a detailed model (i.e., the histograms and average values versus local time) was developed based on ATS-5 and ATS-6 data. Although this model provides information on the ranges of parameters, it does not simulate actual plasma changes in time. An analytic simulation model expressible in a particularly compact form was developed in response to this latter need. The two models were shown to be consistent for average conditions. The simulation is known to predict maximum spacecraft potentials near noon for high levels of geomagnetic activity as it is deliberately biased toward injection events beginning when the satellite is near midnight. Even so, it adequately predicts geosynchronous plasma variations under a variety of conditions.

A final point is the importance of the observation that T(AVG) ≠ T(RMS) most of the time. This means that only rarely (apparently primarily at midnight) is the low energy plasma representable by a Maxwellian distribution and, hence, a temperature in the classical sense of the word. Errors as great as a factor of 3 are common between T(AVG) and T(RMS). It is, therefore, strongly recommended that a 2-Maxwellian distribution be used where possible as a minimal representation of the plasma. This distribution is readily derived by a simple algebraic expression from the 4 moments of the distribution function (see Garrett, 1977). All data and computer programs are available from AFGL.

REFERENCES

1. Chan, K. W., D. M. Sawyer, and J. J. Vette: A Model of the Near-Earth Plasma Environment and Application to the ISEE-A an -B Orbit, NSSDC/WDC-A-R&S 77-01, July 1977.

2. DeForest, S. E., and C. E. McIlwain: Plasma Clouds in the Magnetosphere, J. Geophys. Res., 76, 3587-3611, 1971.

3. Garrett, H. B.: Modeling of the Geosynchronous Orbit Plasma Environment - Part I, AFGL-TR-77-0288, 1977.

4. Garrett, H. B.: Quantitative Models of the 0 to 100 KeV Mid-Magnetospheric Particle Environment, To appear in the Proceedings of the AGU Chapman Conference on Quantitative Models of the Magnetosphere, La Jolla, CA, 18-22 September 1978, edited by W. P. Olson, 1978.

5. Garrett, H. B., G. Mullen, E. Zemba, and S. E. DeForest: ATS-5 and ATS-6 Statistical Data Atlas-Temperature, Current, and Potential at Geosynchronous Orbit, To appear as AFGL In-House Report, 1978.

6. Johnson, B., J. Quinn, and S. DeForest: Spacecraft Charging on ATS-6, Proceedings of the Symposium "The Effect of the Ionosphere on Space Systems and Communications," Washington, D.C., 1978.

TABLE 1. MULTIPLE REGRESSION COEFFICIENTS*

I	C_0	C_1	C_2	C_3	C_4	C_5	C_6	C_7	C_8	C_9
1	.38 + 02	-.42 + 02	.22 + 02	-.21 + 01	-.23 + 02	.43 + 00	-.73 - 01	-.60 - 01	-.80 - 01	.44 - 01
2	.99 + 02	-.27 + 02	.23 + 01	-.28 + 01	-.33 + 01	.21 + 00	.98 - 02	-.35 - 01	-.48 - 01	.37 - 01
3	.52 + 01	-.10 + 02	.64 + 01	.26 + 01	-.48 + 01	.13 + 00	-.28 - 01	-.33 - 01	-.20 - 01	.23 - 02
4	.77 + 02	-.45 + 01	.16 + 02	-.81 + 00	-.31 + 01	.16 + 00	-.49 - 01	.42 - 01	-.64 - 01	.24 - 01
5	.36 + 02	-.74 + 02	.50 + 02	.21 + 02	-.11 + 02	.91 + 00	-.33 - 01	-.51 + 00	-.17 + 00	-.47 - 01
6	.19 + 02	-.52 + 00	.31 + 01	-.63 - 01	-.50 + 00	.38 - 01	-.12 - 01	.15 - 01	-.18 - 01	.34 - 02
7	.47 + 02	-.68 + 02	.38 + 02	.76 + 01	-.44 + 02	.81 + 00	-.24 + 00	-.45 - 01	-.11 + 00	.50 - 01
8	.62 + 01	-.95 + 00	.14 + 01	-.13 + 00	-.30 + 00	.15 - 01	-.34 - 02	.76 - 03	-.47 - 02	.25 - 02

where:

I = 1 n_e x 100 (number/cm^3) 5 EF_e x 100 (erg/cm^2-sec-ster)

2 n_I x 100 (number/cm^3) 6 EF_I x 100 (erg/cm^2-sec-ster)

3 P_e x 10^{10} (dynes/cm^2) 7 NF_e x 10^{-6} (number/cm^2-sec-ster)

4 P_I x 10^{10} (dynes/cm^2) 8 NF_I x 10^{-6} (number/cm^2-sec-ster)

such that:

$$M_I(A_p, Lt) = C_o + C_1 \cos\left(\frac{2\pi}{24} t\right) + C_2 \sin\left(\frac{2\pi}{24} t\right) + C_3 \cos\left(\frac{4\pi}{24} t\right) + C_4 \sin\left(\frac{4\pi}{24} t\right) + C_5 A'_p + C_6 A'_p \cos\left(\frac{2\pi}{24} t\right) + C_7 A'_p \sin\left(\frac{2\pi}{24} t\right) + C_8 A'_p \cos\left(\frac{4\pi}{24} t\right) + C_9 A'_p \sin\left(\frac{4\pi}{24} t\right)$$

$t = Lt + 6.5$ $\quad A'_p = 8 \cdot A_p$

*second number is power Lt = local time

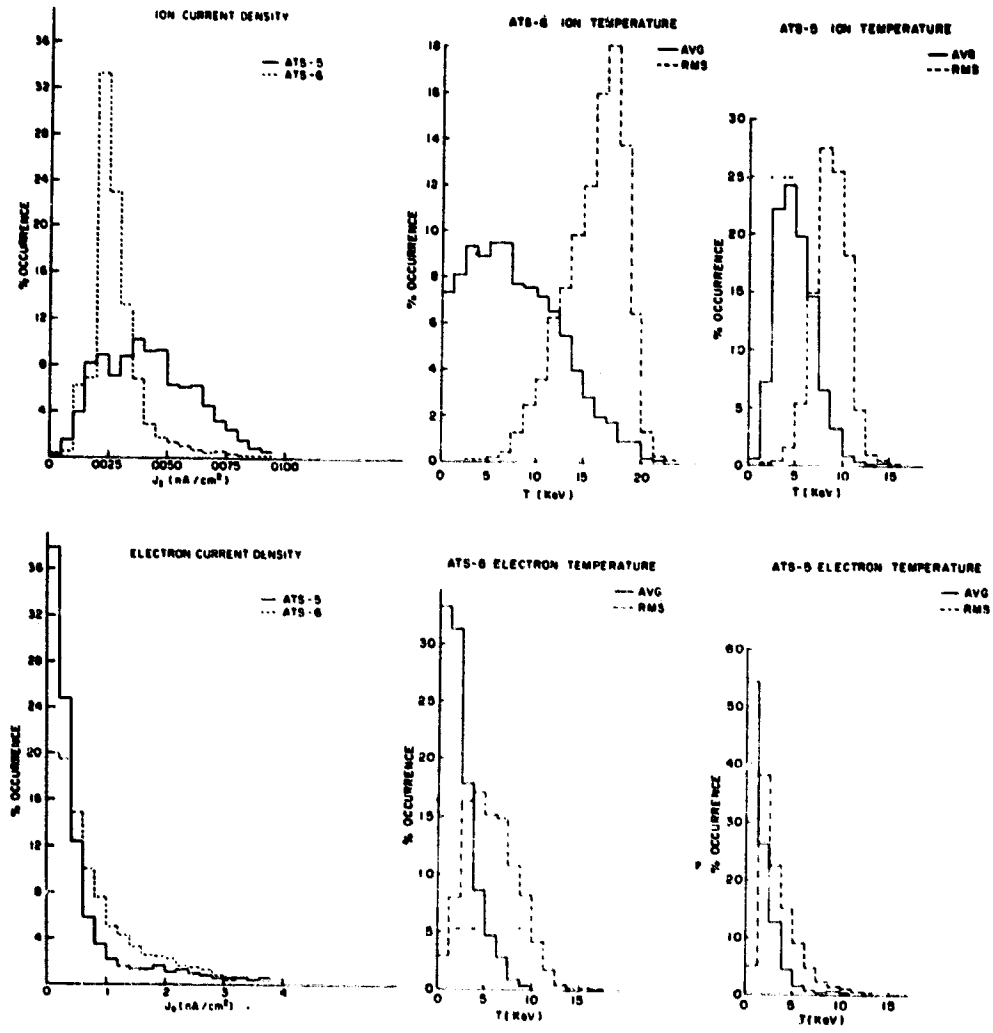

Figure 1. - Statistical occurrence frequencies of ATS-5 (1969 and 1970) and ATS-6 (1974 and 1976) electron and ion current densities, T(RMS), and T(AVG). ATS-6 values should be considered provisional.

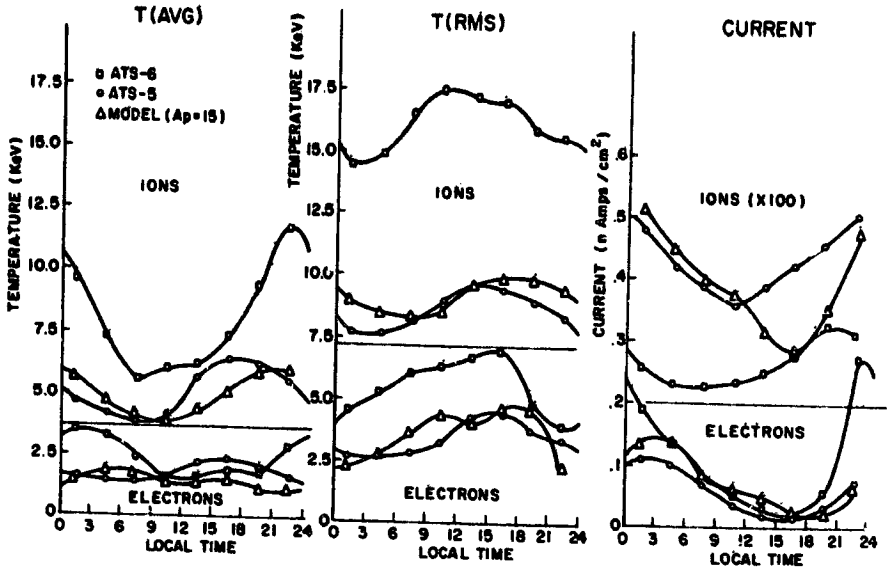

Figure 2. - Average values for current density, T(AVG) and T(RMS) for ATS-5 and ATS-6 data. Values for A_p = 15 are also plotted for simulation model. Error bars are not indicated but are approximately 50% of average value.

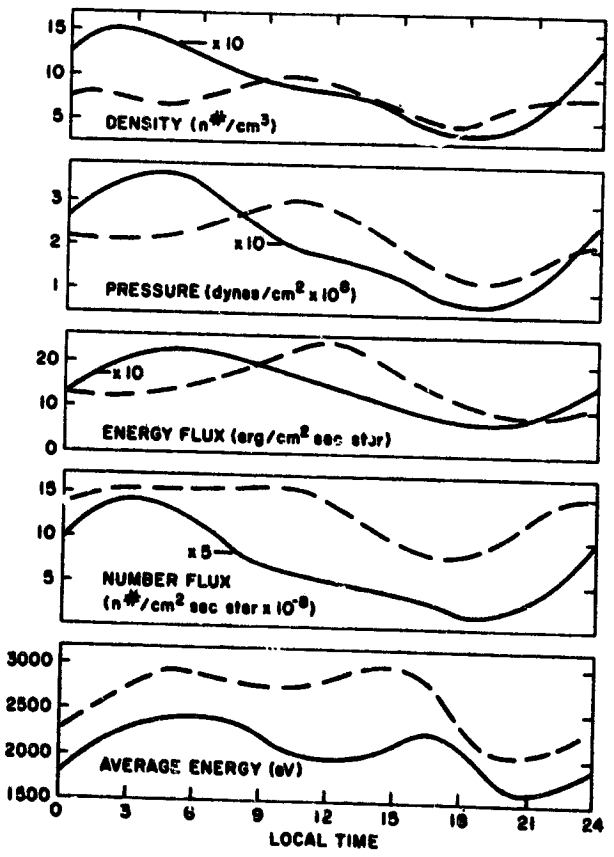

(a) Electrons.

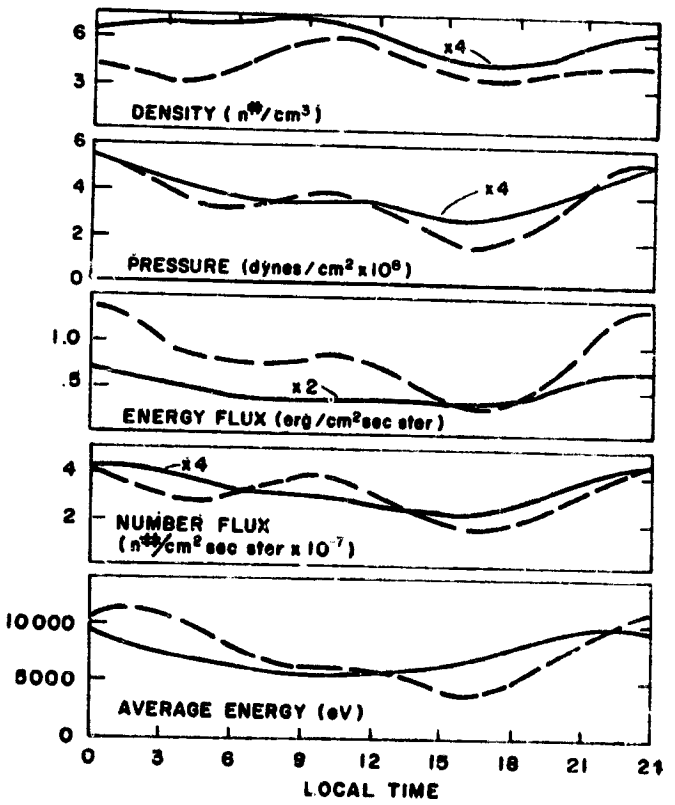

(b) Ions.

Figure 3. - Variations in 4 moments and mean energy according to AFGL simulation code for A_p = 15 (solid line) and A_p = 207 (dashed line).

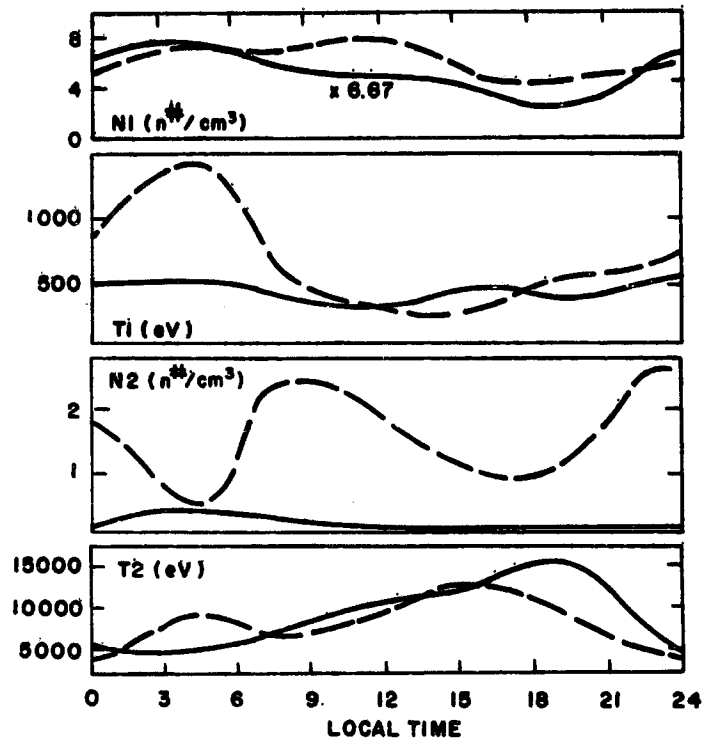

(a) Electrons.

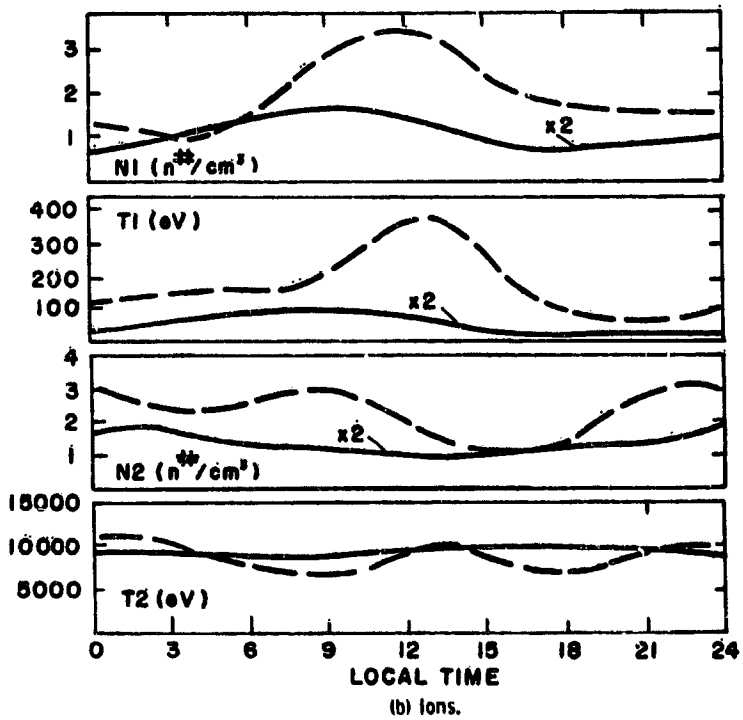

(b) Ions.

Figure 4. - Variations in N1, T1, N2, and T2 according to AFGL simulation code for A_p = 15 (solid line) and A_p = 207 (dashed line).

AVERAGE PLASMA ENVIRONMENT AT GEOSYNCHRONOUS ORBIT

S.-Y. Su
Lockheed Electronics Co., Inc.

A. Konradi
NASA Johnson Space Center

SUMMARY

The average plasma environment at geosynchronous orbit (GSO) is derived from a whole year's worth of plasma data obtained by the UCSD electrostatic electrometer on board ATS-5. The result is primarily intended for use as a general reference for engineers designing a large spacecraft to be flown at GSO. A simple mathematical formula using a 3rd order polynomial is found to be adequate for representing the yearly averaged particle energy spectrum from 70 to 41,000 eV under different geomagnetic conditions. Furthermore, correlation analyses with the geomagnetic planetary index Kp and with the auroral electrojet index AE were carried out in the hope that the ground observations of the geomagnetic field variations can be used to predict the plasma variations in space. Unfortunately, the results indicate that such forecasting is not feasible by use of these two popular geomagnetic parameters alone.

INTRODUCTION

A general introduction to the plasma environment near geosynchronous orbit (GSO) was given by S. E. DeForest (ref. 1) at last year's conference. It was understood that the dynamic behavior of the plasma environment near GSO is extremely complicated and that the observations made by a single spacecraft so far fail to resolve the temporal and spatial variations of the environment. Without complete knowledge of the physical processes of the environment, it is impossible to present any numerical model to quantify the plasma parameters that describe the complicated dynamic magnetosphere during the substorm period. However, long-term statistical averages of the plasma environment can be used as a ground-zero approach in defining the plasma environment at GSO. Such a model can be used by theoreticians as the steady-state solution in the particle-spacecraft interaction model. It also is a great asset to engineers in understanding the long-term dosage of the low radiation to be considered in the design of a large spacecraft.

Only a few spacecraft have carried detectors that are capable of measuring particles with a wide range of energies. The UCSD plasma experiment flown on ATS-5 at GSO measured plasma energy flux intensity for the energy range from 50 to 50,000 eV for both positive ions (assumed to be protons) and electrons. These particle data represent the typical plasma environment at GSO. They are available to the science community in the form of particle energy spectrograms plotted on microfilm, with differential energy flux intensities encoded into a range of gray scales. No example of such a spectrogram will be shown here because it is assumed that the audience is familiar

with the format of McIlwain's spectrogram (ref. 2). The data coverage was fairly complete at the beginning of experiment so that the year 1970 was chosen for long-term statistical analysis. The year 1970 is quite close to the sun-spot maximum of the 11-year solar cycle; thus, these plasma data should represent a moderately active radiation environment at GSO.

DATA REDUCTION

To obtain the numerical values of the particle energy spectrum for the present analysis, we first used the Boller and Chivens Photometric Data System's Microdensitometer to digitize the gray codings of the energy flux intensity in the spectrogram from the microfilm. In order to avoid edge-interference of the data on the microfilm during the process of digitization, the minimum and maximum energy limits are set at 70 eV and 41,000 eV, respectively. Forty-eight energy level steps between the minimum and maximum limits were chosen to cover approximately equal energy intervals on a logarithmic scale. The data were digitized at 10-minute spacings of universal time (UT). The numerical data of day 1 and day 2 of 1970 obtained by the digitization procedure were plotted to compare with the data published by DeForest and McIlwain (ref. 2). The digitized data were found to be accurate within a factor of 2 of the original data. The digitized particle energy flux intensities were converted to particle number flux intensities by dividing the energy flux intensities by the corresponding energy level measured in eV. The data for each 10-minute interval is then stored as a single data point in the computer's memory to create a large data bank for the analysis carried out in the next section.

Owing to the man-power shortage for digitizing the spectrogram on the microfilm, only the particle fluxes perpendicular to the local geomagnetic field lines were digitized. The pitch angle distributions of the particles are not available in the present analysis.

DATA ANALYSIS

The data are presented in local time (LT), instead of universal time (UT), to indicate the satellite location in the magnetosphere. The local time is related to universal time by the formula LT = UT-7. As mentioned before, the data are obtained at 10-minute intervals and are stored in the computer's memory bank. Three consecutive data points are then averaged into one half-hour data point. All available half-hour averages in 1970 were then averaged into 24 hourly averaged data points along the satellite's 24-hour period orbit. The results are shown in Figure 1. The electrons are seen to have higher flux intensities than the protons at all times. The shapes of the energy spectra for both protons and electrons change very little between two adjacent local-time observations. However, noticeable changes are evident in the flux intensities and in spectral shapes between widely separated local times (e.g., compare 00-01 LT and 12-13 LT). The reason for such differences is that the satellite detects large flux intensities in the night-side magnetosphere where the low energy plasmas are energized during substorms. As those newly energized plasmas begin to drift around the earth toward the day-side magnetosphere, they are subjected to various loss mechanisms and to particle

dispersion effects. Thus, they appear to be different in spectral shape and in intensity level when they are detected by the spacecraft on the day-side or on the night-side. The observation of a local minimum in both the proton and electron spectra for the energy range from 500 to 8000 eV, in the day-side magnetosphere, indicates that both particle species in that energy range have been greatly depleted due to a greater loss process operative on them.

The results of the averaged, energy-integrated number flux, energy flux, and energy density of low energy plasma particles observed in 1970 are listed in Tables 1 and 2 for protons and electrons, respectively. It is known from experience that protons and electrons with energies between 10,000 and 200,000 eV contribute substantially to energy flux intensity and energy density, but not to number flux intensity. Since the present study covers only particle energies up to 41,000 eV, to obtain estimates of the particle energy flux and the energy density at GSO we should multiply the values given in Tables 1 and 2 by factors of 2 to 5.

A frequency distribution of the occurrence of large integral flux levels along the satellite orbit is plotted in Figure 2. The criteria for selecting the critical flux levels for protons and electrons are set so that they represent flux intensities that are commonly observed during moderate substorms. The high electron flux intensities are primarily observed in the night-side magnetosphere, with the maximum frequency occurrence located between 01 and 02 LT. On the other hand, high proton flux intensities are observed at all local times although the peak frequency is still centered around 00 LT. The reason for such contrast in distribution is that the electrons are more readily precipitated into the upper atmosphere as they drift toward the day-side magnetosphere after they are injected in the night-side magnetosphere; thus, they rarely show high flux levels on the day-side. Protons, on the other hand, are more stable so that the level of flux intensity is more or less maintained along the drift paths after they were injected in the night-side magnetosphere.

Because the loss mechanism is not very operative for protons, the level of proton flux intensity along the GSO changes very little, indicating lesser dependence on geomagnetic conditions, while the electron flux intensity fluctuates drastically in accordance with geomagnetic activities. In other words, the maximum and minimum electron flux intensities can differ by about a factor of 750, yet the maximum and minimum proton flux intensities differ merely by a factor of 20.

One of the objectives of the present data analysis is to correlate the energy-integrated flux intensities observed at GSO with the geomagnetic activities represented by some types of ground observations. This is carried out in the hope that the total flux level in space can be predicted from observations of geomagnetic indices on the ground. Because of the different loss mechanisms operative upon protons and electrons at GSO, the measured electron flux intensities may fail to show any large flux variations in the day-side magnetosphere as seen in Figure 2. On the other hand, the newly injected protons may blend with the old residual proton fluxes and drift together around the earth to become indistinguishable from each other. The complicated temporal and spatial variations of the protons and electrons in space may limit the utility of the

correlation analysis. Nevertheless, a linear correlation analysis was carried out to determine the degree of the relationship between the particle flux intensities and the geomagnetic indices. The geomagnetic indices used for the analysis are the auroral electrojet (AE) index and the geomagnetic planetary (Kp) index. The AE index can, in principle, reveal substorm activity in the magnetosphere and is available in half-hour averages for the present study. On the other hand, the Kp index is only available in 3-hour averages so that correlation analysis with this index is carried out for supplementary purposes only. The linear correlation coefficients for the electron and proton fluxes with AE indices at various lag times are shown in Figure 3. The correlation analysis was carried out by using logarithmic values of the flux intensities and the AE values. Analyses with different combinations in the form of the flux intensities and the AE indices were also performed. No significant changes in linear correlation coefficients were noticed so that Figure 3 can be regarded as a typical result.

As was expected, a correlation between the particle flux intensity in space and the AE index observed on the ground exists, but is not as striking as one might anticipate. Although the correlation coefficient is barely larger than 0.2 as shown in Figure 3, the probability of having 15,000 random pairs of numbers for a correlation coefficient of 0.2 is much less than 0.0001 (Bevington, ref. 3). Therefore, a definite, causal relationship does exist between the observation of high particle flux intensity in space and recordings of the large AE values by ground stations. However, the low correlation coefficient also indicates that we cannot expect a one-to-one correspondence between the variations of the flux intensity and the AE index. In general, the correlation coefficients between the electron flux intensities and the AE indices are better than those between proton flux intensities and the AE indices, but still lack any striking significance. Since the particles are most likely to be energized in the night-side magnetosphere and therefore show high flux intensities during substorms, there may exist a better correlation between particle fluxes and the substorm indicator index AE during the 12-hour period each day when the satellite is in the night-side magnetosphere. Therefore, we have calculated another correlation coefficient between the electron flux variations and the AE indices in regions of local time from 20 LT through midnight to 08 LT. This coincides with the regions of high probability for observing large electron flux intensity as seen in Figure 2. The result is shown in Figure 4. The correlation coefficients are impressively high. The peak correlation occurs with the AE index shifted half an hour ahead in time of the observed electron flux intensity. The peak coefficient of 0.65 implies that there is probably a one-to-one correspondence between the peaks of the AE index and the electron flux intensity. With the best correlation being obtained by comparing the flux intensity with the AE index half an hour before the flux observation, we might think that we could forecast the arrival of a large electron flux at the spacecraft. However, the slow changes in the correlation coefficients around the peak value as seen in Figure 4 means that the prediction may be impractical because of the lack of definite cut-off criteria for selecting the peak.

The proton fluxes, on the other hand, fail to show an improved correlation with the AE index even when the satellite observation is limited to the night-side magnetosphere so that we did not plot the results in Figure 4.

Furthermore, neither proton nor electron fluxes show a good correlation with the Kp indices. Since the Kp index can now be forecasted on a real-time basis, as a reference to the expected values of the particle flux intensities at different Kp values, Table 3 lists the maximum particle flux intensities observed at various local times for different Kp values. The particle flux intensity, in general, increases as Kp increases. However, there are some flux intensities which are observed during very high Kp yet show smaller values than those observed at lower Kp as seen in Table 3. The reason for such a discrepancy is due to the fact that the number of observations made during high Kp is too small to yield a good statistical representation.

MATHEMATICAL MODEL

Another objective of the data analysis is to derive a mathematical model for particle flux intensities observed at GSO. The model can be used for simulation of particle encounters by a spacecraft at a certain local time with a specified geomagnetic condition. However, we should always remember that the dynamic behavior of the plasmas at GSO is so complicated that only the statistical averages of the particle fluxes can be predicted.

From inspection of Figure 1, we conclude that the particle energy spectrum cannot be fitted by a single Maxwellian distribution function, but a reasonably good fit may be obtained by a composite of several Maxwellian distributions. The search for correct components in the optimum set of the composite functions can become a very tedious and laborious process. Since the use of composite functions may bear no physical significance with respect to the actual particle flux distribution, we may as well use a polynomial curve to fit the particle flux intensity. We selected polynomials varying from 1st to 10th order to carry out the least-squares procedure for fitting all the flux intensities in Figure 1. The chi-square test is then applied to choose the best-fit polynomial. It was found that a 3rd order polynomial yields a consistently low value of chi-square. On this basis, we conclude that the 3rd order polynomial can best represent the flux intensities in Figure 1.

The result of the polynomial fit is given by...

$$\log_{10}(F) = A_1 + A_2(\log_{10} E) + A_3(\log_{10} E)^2 + A_4(\log_{10} E)^3 \qquad (1)$$

where F is the particle number flux intensity and E is the particle energy in eV. The coefficients A_1 through A_4 have also been evaluated for different local times and geomagnetic conditions. Tables 4 through 6 show values of these coefficients for the model applied at the given local time under a specific geomagnetic condition. The value of the particle flux intensity calculated from Equation (1) is of course valid only for the particle energy range from 70 to 41,000 eV.

REFERENCES

1. DeForest, S.E.: The Plasma Environment at Geosynchronous Orbit, Proceedings of the Spacecraft Charging Technology Conference, AFGL-TR-77-0051, 1977, pp. 37-52.
2. DeForest, S.E.; McIlwain, C.E.: Plasma Clouds in the Magnetosphere, Journal of Geophysical Research, 1971, pp. 3587-3611.
3. Bevington, P.R.: Data Reduction and Error Analysis for the Physical Sciences, McGraw-Hill Book Co., New York, 1969, pp. 119-163.

TABLE 1. Protons at Geostationary Altitude

Local Time	Flux Intensity protons/cm^2-sec-ster	Energy Density ergs/cm^3-ster	Energy Flux Intensity ergs/cm^2-sec-ster
00-01	1.14 E 7	1.48 E-9	0.278
01-02	1.08 E 7	1.40 E-9	0.268
02-03	1.34 E 7	1.45 E-9	0.268
03-04	1.45 E 7	1.54 E-9	0.291
04-05	1.00 E 7	1.17 E-9	0.222
05-06	9.01 E 6	1.12 E-9	0.215
06-07	8.47 E 6	1.09 E-9	0.212
07-08	7.83 E 6	1.03 E-9	0.203
08-09	7.39 E 6	9.96 E-10	0.200
09-10	7.08 E 6	9.88 E-10	0.203
10-11	7.13 E 6	1.02 E-9	0.210
11-12	7.29 E 6	1.06 E-9	0.218
12-13	7.55 E 6	1.12 E-9	0.231
13-14	8.12 E 6	1.21 E-9	0.249
14-15	8.60 E 6	1.28 E-9	0.259
15-16	9.16 E 6	1.37 E-9	0.278
16-17	1.00 E 7	1.45 E-9	0.290
17-18	1.10 E 7	1.59 E-9	0.316
18-19	1.10 E 7	1.59 E-9	0.315
19-20	1.10 E 7	1.57 E-9	0.310
20-21	1.14 E 7	1.61 E-9	0.315
21-22	1.15 E 7	1.61 E-9	0.315
22-23	1.17 E 7	1.61 E-9	0.312
23-24	1.16 E 7	1.55 E-9	0.295

TABLE 2. Electrons at Geostationary Altitude

Local Time	Flux Intensity electrons/cm^2-sec-ster	Energy Density ergs/cm^3-ster	Energy Flux Intensity ergs/cm^2-sec-ster
00-01	2.90 E 8	5.47 E-10	3.03
01-02	3.49 E 8	6.76 E-10	3.87
02-03	3.41 E 8	6.69 E-10	3.85
03-04	3.26 E 8	6.55 E-10	3.89
04-05	3.44 E 8	6.07 E-10	3.61
05-06	2.73 E 8	5.43 E-10	3.24
06-07	2.39 E 8	4.81 E-10	2.93
07-08	1.98 E 8	4.07 E-10	2.54
08-09	1.56 E 8	3.26 E-10	2.06
09-10	1.21 E 8	2.54 E-10	1.65
10-11	1.01 E 8	2.14 E-10	1.41
11-12	8.38 E 7	1.78 E-10	1.18
12-13	6.97 E 7	1.53 E-10	1.02
13-14	6.45 E 7	1.42 E-10	0.952
14-15	5.88 E 7	1.28 E-10	0.856
15-16	5.52 E 7	1.18 E-10	0.787
16-17	5.89 E 7	1.21 E-10	0.798
17-18	5.35 E 7	1.01 E-10	0.638
18-19	5.69 E 7	1.01 E-10	0.614
19-20	6.66 E 7	1.10 E-10	0.629
20-21	9.90 E 7	1.66 E-10	0.907
21-22	1.47 E 8	2.55 E-10	1.41
22-23	1.95 E 8	3.38 E-10	1.79
23-24	2.44 E 8	4.38 E-10	2.34

TABLE 3A. Maximum Proton Integral Fluxes
(Protons/cm^2-sec-ster)

K_p / UT*	0-2	2+-4	4+-6	6+-9
00-03	1.08E7	1.39E7	1.93E7	1.59E7
03-06	1.19E7	1.46E7	1.83E7	2.10E7
06-09	1.22E7	1.56E7	1.64E7	2.38E7
09-12	1.00E7	1.27E7	1.93E7	8.17E6
12-15	8.36E6	1.05E7	1.83E7	1.47E7
15-18	7.25E6	9.59E6	1.73E7	1.18E7
18-21	7.98E6	1.02E7	1.51E7	7.23E6
21-24	9.51E6	1.21E7	1.69E7	2.12E7

*LT = UT-7

TABLE 3B. Maximum Electron Integral Fluxes
(Electrons/cm^2-sec-ster)

K_p / UT*	0-2	2+-4	4+-6	6+-9
00-03	5.43E7	8.49E7	3.30E8	3.91E8
03-06	1.12E8	3.58E8	5.54E8	9.49E8
06-09	3.22E8	5.86E8	9.23E8	1.08E9
09-12	3.20E8	6.37E8	8.65E8	8.17E8
12-15	2.04E8	4.50E8	7.65E8	6.89E8
15-18	1.18E8	2.31E8	4.88E8	1.73E8
18-21	8.27E7	1.08E8	1.23E8	5.25E7
21-24	7.59E7	6.89E7	8.05E7	2.46E8

*LT = UT-7

TABLE 4. Coefficients of the polynomial fit to the yearly averaged fluxes

	LT	A_1	A_2	A_3	A_4
Protons	00-01	7.193	-3.491	-0.976	-0.099
	01-02	8.039	-4.177	1.148	-0.113
	02-03	7.216	-3.276	0.850	-0.082
	03-04	6.431	-2.465	0.572	-0.052
	04-05	6.103	-2.019	0.414	-0.035
	05-06	5.707	-1.500	0.222	-0.014
	06-07	5.554	-1.329	0.146	-0.004
	07-08	4.982	-0.705	-0.007	0.021
	08-09	3.763	0.519	-0.495	0.067
	09-10	3.641	0.869	-0.673	0.091
	10-11	3.748	0.782	-0.670	0.094
	11-12	5.008	-0.385	-0.349	0.067
	12-13	6.788	-2.108	0.161	0.019
	13-14	8.502	-3.954	0.758	-0.041
	14-15	10.529	-6.041	1.439	-0.112
	15-16	12.002	-7.589	1.953	-0.165
	16-17	11.561	-7.238	1.903	-0.167
	17-18	13.097	-8.940	2.486	-0.229
	18-19	13.565	-9.370	2.616	-0.241
	19-20	11.908	-7.944	2.220	-0.206
	20-21	12.424	-8.415	2.377	-0.223
	21-22	11.050	-7.099	1.986	-0.186
	22-23	10.313	-6.351	1.770	-0.167
	23-24	8.962	-5.202	1.475	-0.144
Electrons	00-01	9.789	-5.258	1.892	-0.237
	01-02	8.721	-3.981	1.446	-0.187
	02-03	9.550	-4.797	1.699	-0.212
	03-04	9.417	-4.599	1.595	-0.197
	04-05	9.470	-4.578	1.565	-0.193
	05-06	9.917	-4.899	1.631	-0.196
	06-07	10.353	-5.194	1.662	-0.194
	07-08	10.723	-5.411	1.670	-0.189
	08-09	11.157	-5.731	1.708	-0.187
	09-10	11.635	-6.232	1.828	-0.195
	10-11	12.432	-6.883	1.986	-0.207
	11-12	12.933	-7.362	2.107	-0.216
	12-13	12.472	-7.041	2.016	-0.207
	13-14	12.747	-7.435	2.146	-0.221
	14-15	12.353	-7.016	2.014	-0.208
	15-16	12.274	-6.935	1.972	-0.202
	16-17	11.252	-5.849	1.644	-0.172
	17-18	10.280	-4.844	1.316	-0.139
	18-19	9.204	-3.832	1.049	-0.118
	19-20	7.502	-2.188	0.574	-0.076
	20-21	7.902	-2.895	0.936	-0.125
	21-22	8.017	-3.029	1.019	-0.136
	22-23	9.655	-4.873	1.694	-0.213
	23-24	9.317	-4.750	1.728	-0.222

TABLE 5. Coefficients of the polynomial fit to the quiet-time averaged fluxes

	LT	A_1	A_2	A_3	A_4
Protons	00-01	7.320	-3.510	0.921	-0.088
	01-02	6.940	-3.024	0.754	-0.071
	02-03	5.870	-1.929	0.403	-0.036
	03-04	3.723	0.409	-0.407	0.052
	04-05	3.763	0.542	-0.489	0.064
	05-06	3.676	0.654	-0.559	0.074
	06-07	3.167	1.298	-0.796	0.101
	07-08	3.013	1.471	-0.863	0.109
	08-09	2.191	2.263	-1.146	0.141
	09-10	2.162	2.394	-1.241	0.156
	10-11	3.172	1.498	-0.982	0.133
	11-12	4.185	0.441	-0.652	0.101
	12-13	5.321	-0.638	-0.327	0.070
	13-14	5.823	-1.311	-0.076	0.042
	14-15	6.801	-2.259	0.224	0.012
	15-16	7.725	-3.214	0.538	-0.021
	16-17	8.908	-4.422	0.941	-0.064
	17-18	10.456	-6.376	1.652	-0.142
	18-19	14.759	-10.447	2.881	-0.261
	19-20	11.019	-7.066	1.917	-0.173
	20-21	11.142	-7.057	1.900	-0.171
	21-22	12.464	-8.400	2.340	-0.217
	22-23	11.186	-7.218	2.013	-0.189
	23-24	10.579	-6.717	1.902	-0.183
Electrons	00-01	7.792	-2.927	1.024	-0.143
	01-02	7.819	-2.909	1.034	-0.145
	02-03	10.128	-5.308	1.831	-0.229
	03-04	10.820	-5.921	1.980	-0.239
	04-05	9.844	-4.765	1.549	-0.190
	05-06	10.087	-4.889	1.526	-0.181
	06-07	10.351	-5.035	1.538	-0.179
	07-08	10.425	-5.123	1.552	-0.179
	08-09	11.407	-5.994	1.767	-0.195
	09-10	11.479	-6.077	1.784	-0.196
	10-11	10.982	-5.663	1.645	-0.181
	11-12	10.768	-5.423	1.566	-0.172
	12-13	10.198	-4.988	1.428	-0.157
	13-14	10.624	-5.414	1.576	-0.173
	14-15	9.485	-4.155	1.166	-0.132
	15-16	9.341	-3.959	1.083	-0.122
	16-17	8.841	-3.423	0.922	-0.107
	17-18	9.632	-4.334	1.197	-0.132
	18-19	9.672	-4.462	1.262	-0.148
	19-20	8.769	-3.624	1.003	-0.115
	20-21	7.385	-2.216	0.585	-0.076
	21-22	5.714	-0.358	-0.008	-0.018
	22-23	7.789	-2.598	0.771	-0.101
	23-24	7.198	-2.161	0.697	-0.101

Table 6. Coeff. of the polynomial fit to the disturbed-time averaged fluxes

	LT	A_1	A_2	A_3	A_4
Protons	00-01	3.998	-0.421	0.052	-0.009
	01-02	4.907	-1.069	0.192	-0.018
	02-03	5.124	-1.207	0.233	-0.023
	03-04	3.512	0.248	-0.186	0.016
	04-05	4.547	-0.683	0.080	-0.009
	05-06	4.925	-0.979	0.171	-0.019
	06-07	5.178	-1.293	0.265	-0.027
	07-08	4.270	-0.291	-0.096	0.013
	08-09	2.429	1.568	-0.689	0.074
	09-10	2.101	2.134	-0.960	0.110
	10-11	2.266	2.162	-1.042	0.126
	11-12	3.836	0.729	-0.655	0.094
	12-13	6.634	-2.135	0.232	0.008
	13-14	8.968	-4.543	0.996	-0.069
	14-15	10.930	-6.562	1.671	-0.140
	15-16	11.609	-7.407	1.991	-0.177
	16-17	10.488	-6.137	1.588	-0.138
	17-18	7.322	-3.516	0.915	-0.083
	18-19	9.508	-5.596	1.534	-0.142
	19-20	8.326	-4.552	1.249	-0.118
	20-21	10.809	-6.988	2.029	-0.198
	21-22	7.234	-3.520	0.950	-0.090
	22-23	7.188	-3.414	0.910	-0.086
	23-24	5.663	-2.035	0.542	-0.056
Electrons	00-01	7.743	-3.213	1.274	-0.174
	01-02	6.978	-2.325	0.989	-0.146
	02-03	7.317	-2.457	0.961	-0.136
	03-04	6.893	-1.933	0.767	-0.113
	04-05	6.600	-1.734	0.721	-0.110
	05-06	7.241	-2.227	0.826	-0.117
	06-07	8.379	-3.233	1.084	-0.137
	07-08	8.391	-3.087	0.991	-0.123
	08-09	7.775	-2.314	0.684	-0.087
	09-10	9.107	-3.580	1.016	-0.115
	10-11	11.298	-5.575	1.570	-0.163
	11-12	12.412	-6.722	1.883	-0.190
	12-13	13.674	-8.249	2.383	-0.240
	13-14	14.368	-9.004	2.618	-0.264
	14-15	13.778	-8.469	2.444	-0.246
	15-16	13.343	-8.103	2.339	-0.237
	16-17	10.763	-5.344	1.474	-0.153
	17-18	8.474	-3.035	0.841	-0.103
	18-19	8.656	-3.469	1.108	-0.144
	19-20	8.655	-3.546	1.204	-0.162
	20-21	9.633	-4.922	1.763	-0.226
	21-22	9.343	-4.568	1.624	-0.205
	22-23	10.996	-6.438	2.321	-0.287
	23-24	9.675	-5.245	1.976	-0.254

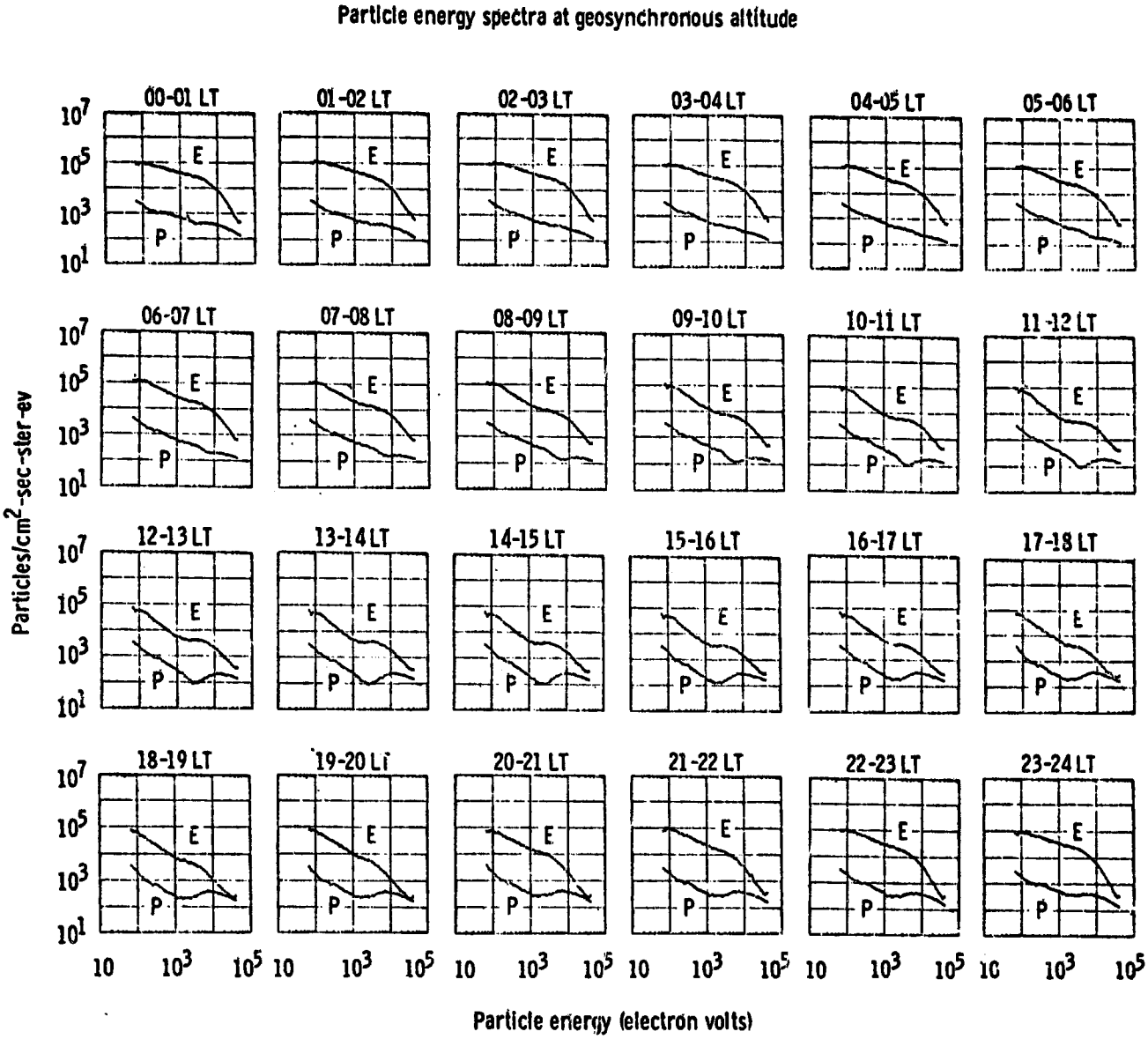

Figure 1: Hourly averages of the proton and electron fluxes observed by ATS-5 geostationary satellite in the year 1970. The upper curve in each frame is the electron flux intensity while the lower one is the proton flux intensity. Although the flux intensities between two adjacent local time observations are seen to be the same, great variations exists for flux intensities at widely separated locations.

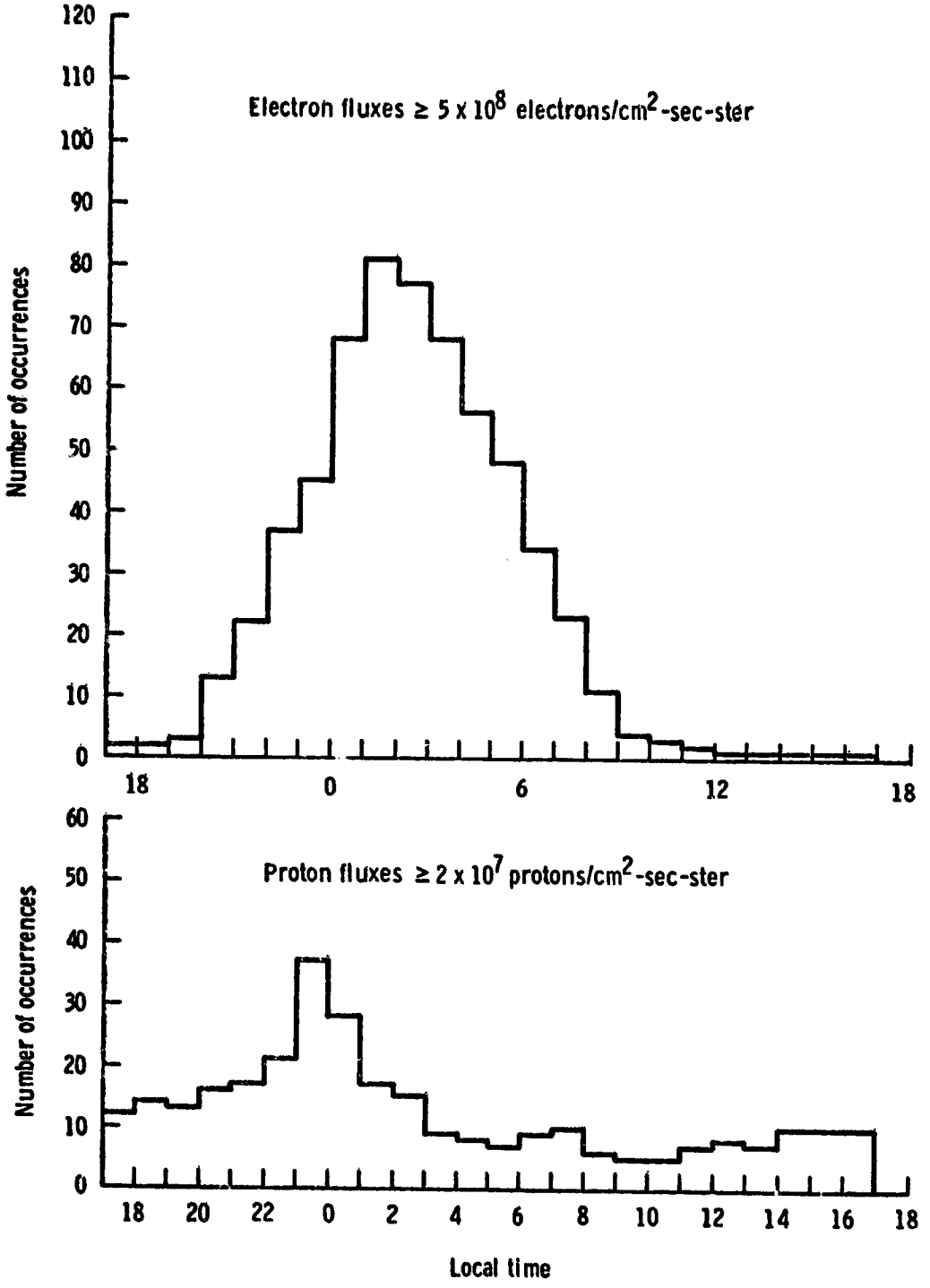

Figure 2: The frequency distribution of the occurrence of high flux intensities observed by ATS-5 in 1970. In general the high flux intensities were observed when the satellite was in the night-side magnetosphere.

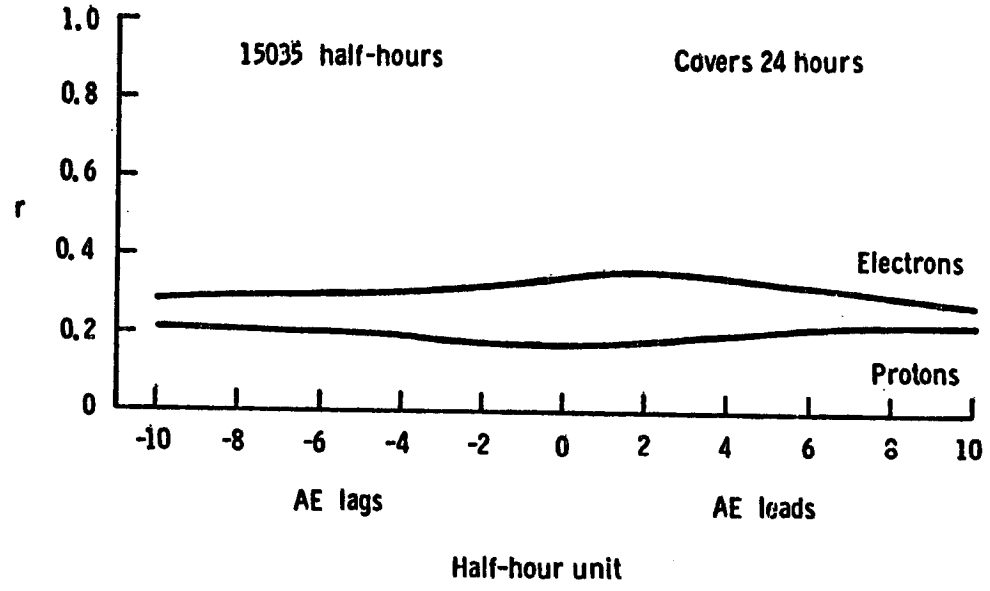

Figure 3: The linear correlation coefficients between the proton and electron flux intensities and the auroral electrojet (AE) indices at various lag times.

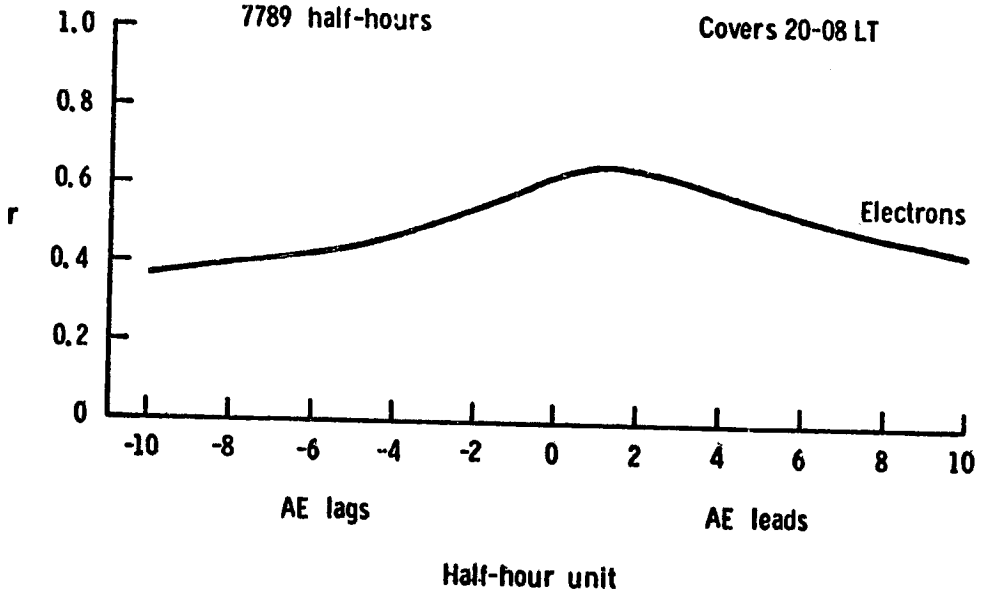

Figure 4: The linear correlation coefficients between the electron flux intensities observed by ATS-5 in the night-side magnetosphere and the AE indices at various lag times.

ATS-5 AND ATS-6 POTENTIALS DURING ECLIPSE

Allen G. Rubin and Henry B. Garrett
Air Force Geophysics Laboratory

SUMMARY

ATS-5 and ATS-6 data for spacecraft charging during eclipse conditions is analyzed. ATS-5 and ATS-6 charged to voltages greater than 100 volts for about 55% of the eclipse periods examined. The mean spacecraft potential during eclipse was 2 keV for ATS-5, and the highest potential measured was 10 kilovolts. For ATS-6, the mean potential during eclipse was 4 keV, the highest potential measured being 20 keV. The average measured spacecraft potentials for both ATS-5 and 6 depend approximately linearly upon K_p. This relationship is due mainly to the dependence of electron current density on K_p near midnight. Spacecraft potentials at geosynchronous orbit may, to a rough approximation, thus be inferred from ground-based measurements of K_p, the planetary 3-hour index.

INTRODUCTION

As the ATS-5 and ATS-6 spacecraft have been monitoring the plasma environment at synchronous orbit since 1969, the data provided by these satellites comprises the most extensive data base available of low-energy plasma conditions at geosynchronous orbit.

The present paper is a study of the statistics of charging events based on data from 157 eclipses from ATS-5 and 40 eclipses from ATS-6.

THE DISTRIBUTION OF CHARGING POTENTIALS

For these eclipse charging events, ten minute averages of the charging potentials were obtained. Figure 1 shows the distribution of charging potentials plotted separately for ATS-5 and ATS-6.

For ATS-5, 55% exhibit charging to negative potentials greater than 110 volts and 54% of the ATS-6 charging intervals are greater than 100 volts. This means that both ATS-5 and ATS-6 charge to substantial negative voltages in more than half of the eclipse intervals. The mean charging voltage of ATS-5 is 2 kilovolts for ATS-5 and 4 kilovolts for ATS-6. The highest observed potential is 10 kilovolts for ATS-5 and 20 kilovolts for ATS-6.

Figure 2 shows the distribution of K_p and the 3-hour planetary index

for the ATS-5 and ATS-6 data time periods. ATS-6 data was taken during a more active geomagnetic period than ATS-5, so that the mean value of K_p for the ATS-6 time period is considerably higher than that for the ATS-5 time period. The higher mean charging potential for ATS-6 is no doubt due to hotter injected plasmas for the ATS-6 time period.

CHARGING POTENTIALS VERSUS K_p

Eclipse potentials versus K_p are shown in Figure 3 for eclipse events on ATS-5 and ATS-6 for K_p values up to 6. The error bars shown are the standard deviations ($\pm$ 1 σ) of the data. The spacecraft potential rises linearly with K_p within the error.

Shown on this figure as well is a theoretical curve based on a current balance calculation in which secondary emission properties of ATS-5 and 6 materials have been accounted for in an approximate manner, using an average secondary emission coefficient. This theoretical curve is given by

$$qV_o = T_e \ln \left(\frac{J_e}{10\ J_i} \right)$$

where the factor 10 takes account of secondary emission properties (Garrett and Rubin, 1978).

R.M.S. electron temperature as a function of K_p is shown in Figure 4 for the time period 2100-300. The electron mean temperature varies from 2 to 4 keV. The variation of the ratio of electron to ion current densities with K_p is much greater, as shown in Figure 5. The theoretical prediction of spacecraft potential, as the product of T_e and $\ln (J_e/10\ J_i)$, shows that it is the dependence of the ratio of electron to ion current densities on the magnetic activity index, K_p, which is responsible for the strong dependence of charging potential on K_p. The mean R.M.S. electron temperature at a given K_p for the 2100-0300 time period, for the entire ATS-5 and ATS-6 data base, was employed for this calculation. The theoretical curve corresponds very well to observed potentials for K_p values up to 4, but is somewhat higher at larger K_p values.

The spacecraft potential is shown to be proportional to K_p for the 6-hour period around midnight. K_p is an easily accessible quantity, having long been used as an indicator of geomagnetic activity. Since K_p is calculated from ground-based magnetometer systems, it will be useful, to the accuracy of the error bars, as an indicator of the maximum potentials to be expected on a shadowed spacecraft surface at geosynchronous orbit. As ATS-5 and ATS-6 have radically different shapes, this result could be applicable for a variety of satellites (see Purvis et al., 1977, for a comparison between ATS-5 and ATS-6 potentials in eclipse).

REFERENCES

1. Garrett, H.B. and A.G. Rubin (1978):Spacecraft Charging at Geosynchronous Orbit-Generalized Solution for Eclipse Passage, Geophysical Res. Lett. (to be published).

2. Purvis, C.K., R.O. Bartlett, and S.E. DeForest: Active Control of Spacecraft Charging on ATS-5 and ATS-6, Proceedings of the Spacecraft Charging Technology Conference, edited by C.P. Pike and R.H. Lovell, AFGL-TR-770051/NASA TM 7350, p. 107-120 (1977).

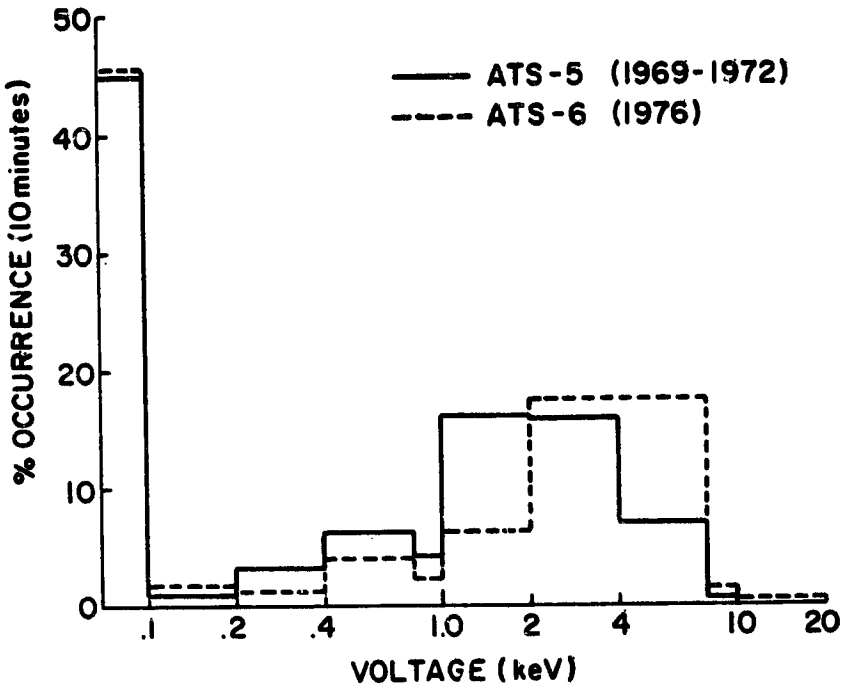

Figure 1. - Occurrence frequency of charging potentials on ATS-5 and ATS-6.

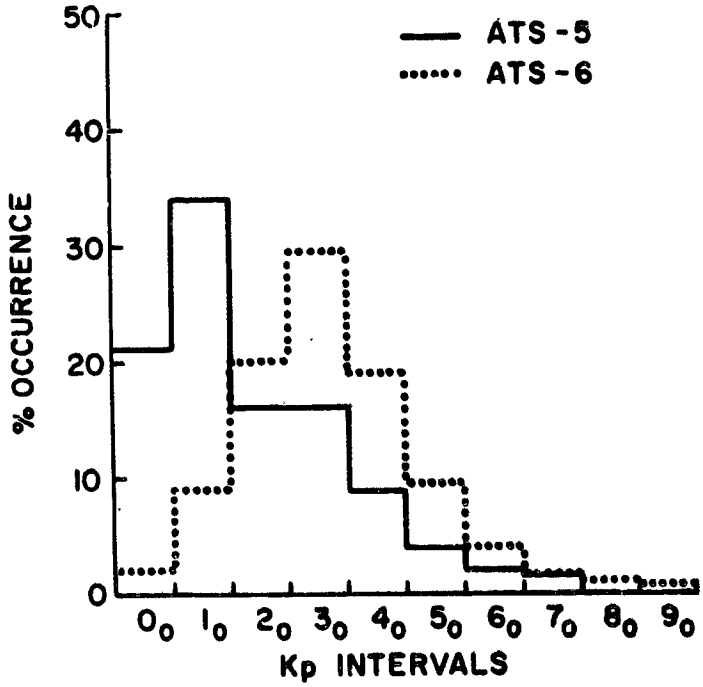

Figure 2. - Occurrence frequency of K_p for ATS-5 and ATS-6 time periods.

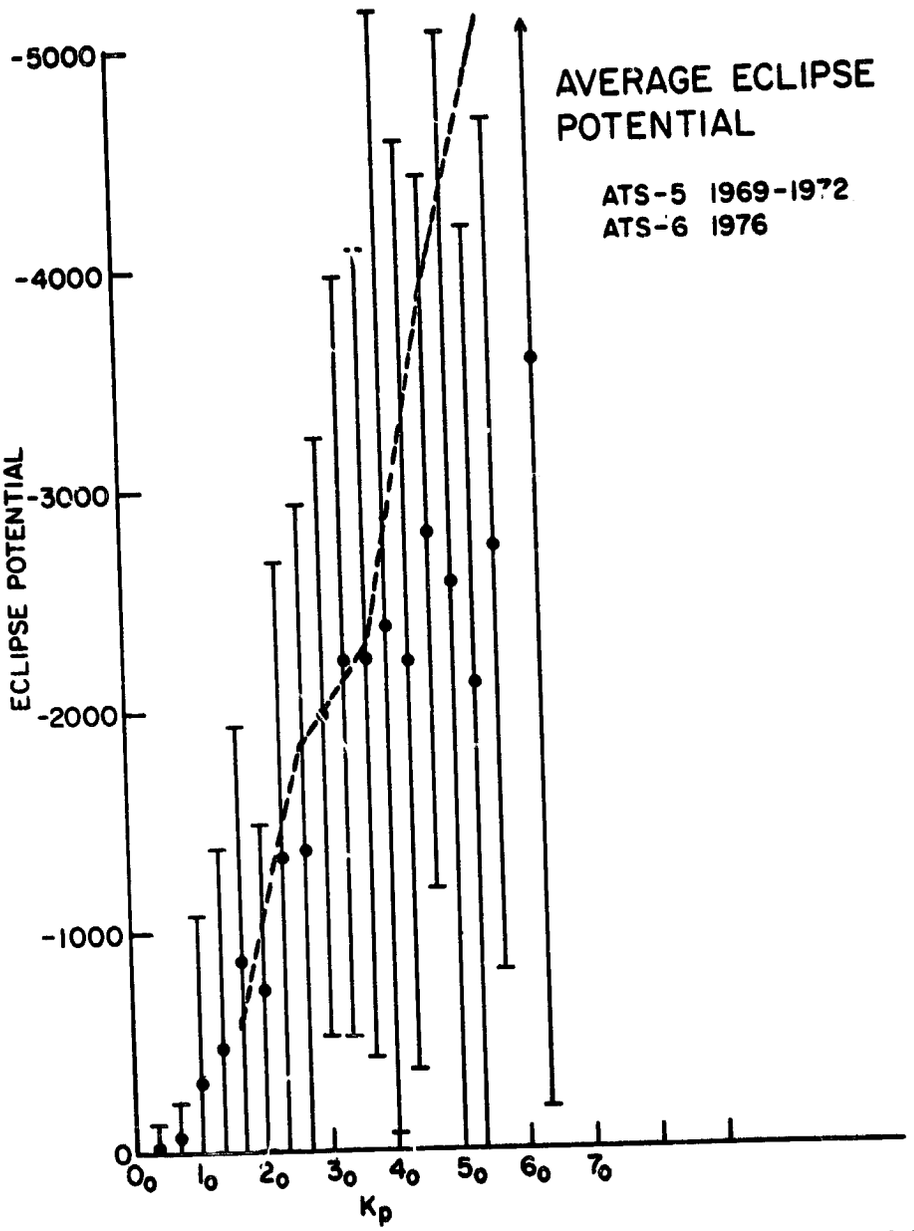

Figure 3. - Average eclipse potentials of ATS-5 and ATS-6 as function of K_p.

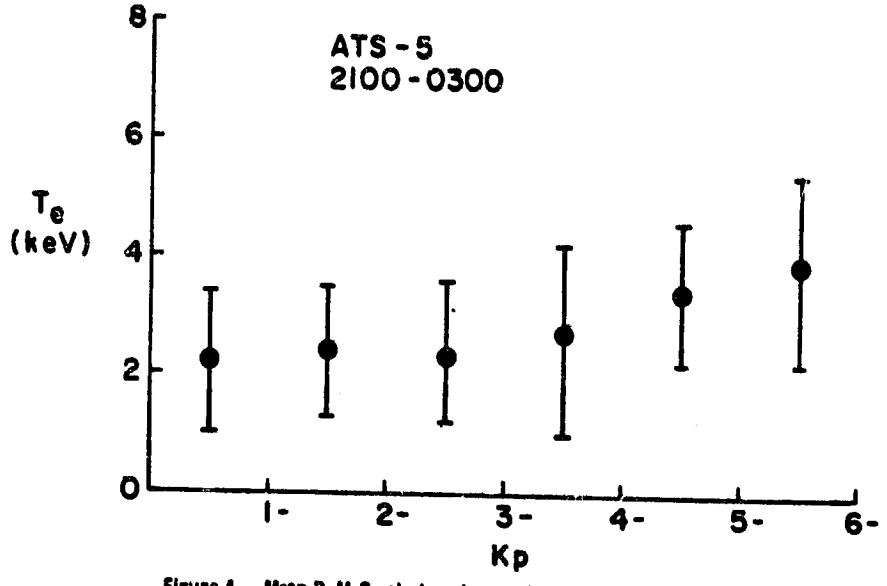

Figure 4. - Mean R. M. S. electron temperature as function of K_p for eclipses.

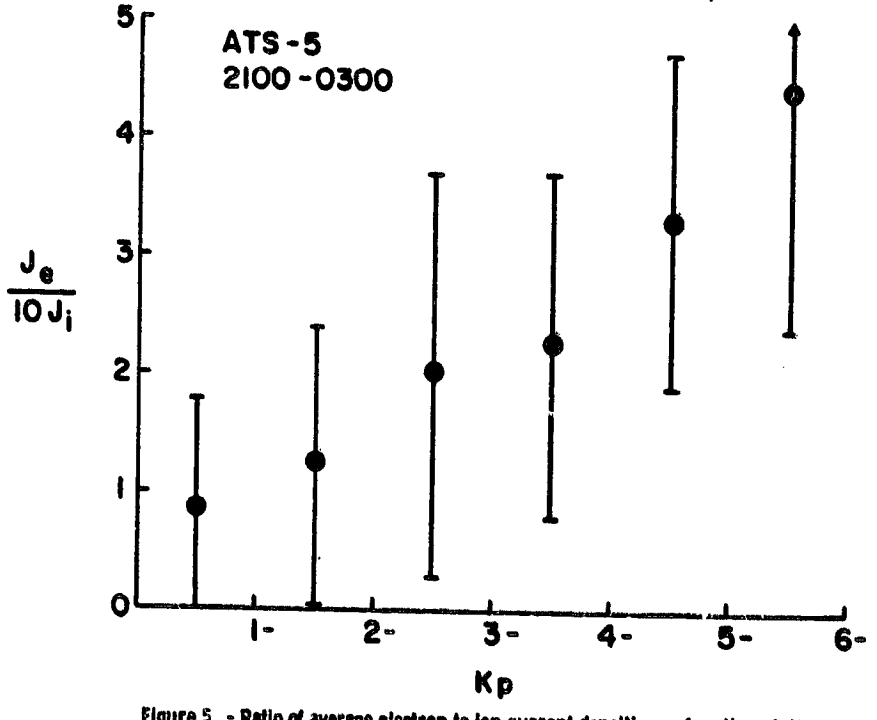

Figure 5. - Ratio of average electron to ion current densities as function of K_p for eclipses.

D5

* N79-24006

SUMMARY OF THE TWO YEAR NASA PROGRAM FOR ACTIVE CONTROL OF ATS-5/6 ENVIRONMENTAL CHARGING

Robert O. Bartlett
NASA Goddard Space Flight Center

Carolyn K. Purvis
NASA Lewis Research Center

SUMMARY

Over the past several years numerous experiments have been conducted on the ATS-5 and ATS-6 which have demonstrated the feasibility of modifying or clamping the environmentally induced potential of these spacecraft. This has been accomplished utilizing the ion engine experiments and monitoring their effects with the University of California, San Diego, Auroral Particles instruments on each spacecraft.

The results of these experiments have shown that a thermionic electron source is capable of replacing photo-emitted electrons during eclipse. However, the utility of this type of device is limited if its emission is suppressed by local electric fields. On the other hand, it has been shown that a plasma source will not only serve as a substitute for photo-emitted electrons but will also suppress differential charging of isolated elements of the spacecraft which would tend to suppress electron emission. This later device is therefore capable of clamping the potential of a spacecraft without special consideration of its coupling to the ambient plasma.

An overview of the experiments and a summary of their results are presented in this paper. Therefore, this paper serves as a "road map" to the spacecraft charging experiments conducted on ATS-5 and ATS-6.

INTRODUCTION

In May of 1976, the National Aeronautics and Space Administration (NASA) awarded a contract to the University of California, San Diego (UCSD) with the objective of studying active control of environmental charging on the Applications Technology Satellites (ATS) 5 and 6. This study was an element in the joint NASA/Air Force investigation of geosynchronous satellite charging (Lovell et al., 1976). The in-orbit experimental phase of this study has now been concluded. The contract report of the first year's activities is

now available, and the final report will be available in the near future. Initial results of this effort will be summarized here; however, further analysis is warranted, and it is the hope of the authors that this paper will provide sufficient stimulus to encourage additional investigation of these data.

The results of these experiments have provided 213 data sets from ATS-5 and 36 data sets from ATS-6. Several of these experiments were conducted simultaneously on the two satellites. During the course of these measurements, 111 instances of environmental charging to potentials in excess of 1000 volts have been observed. No anomalous effect has been associated with any of these charging events on either satellite.

The ATS-5 and the ATS-6 satellites each carried an Auroral Particles Experiment and a Cesium Ion Engine Experiment. These instruments were jointly utilized to conduct this investigation of actively controlling satellite charging. While neither instrument was developed with this application as an objective, the experimental results demonstrated the achievement of altered or clamped satellite potential. There are features of these experiments which raise questions which have not been conclusively answered. Instruments specifically designed to study active control of satellite charging will clearly yield more definitive results. However, it is felt that the experiments described here have added to the understanding of the environmental charging phenomenon and should complement the results of future experiments such as the USAF Space Test Program, P78-2 (Durrett et al., 1978).

DESCRIPTION OF ATS-5 AND ATS-6 INSTRUMENTATION

The details of the ATS-5 and ATS-6 spacecraft and their respective instruments have been previously presented (Bartlett et al., 1975; Purvis et al., 1976). In summary, Figures 1 and 2 depict the key features of each of these satellites including the relative locations of the Auroral Particles Experiment and the Cesium Ion Engine Experiment. The Auroral Particles Experiment on ATS-5 provided measurement of ion and electron flux in the 50 eV to 50 keV energy range at fixed instrument apertures. The ATS-6 Auroral Particles Experiment extended this range from 0.1 eV to 80 keV and incorporated a scanning aperture to provide angular resolution. The ATS-5 ion engines are of the contact ionization type utilizing a thermionic electron source (neutralizer). Alternately the ATS-6 ion engines are of the bombardment type utilizing a low energy cesium plasma as its neutralizer. When the cesium ion source is operated, the neutralizer serves as a ready source of electrons to maintain a net charge neutrality. The neutralizer can also be operated without the ion source. The ion sources and the neutralizers were utilized to alter the current balance of each spacecraft and thus actively control the spacecraft's potential. The Auroral Particles Experiments were utilized to measure this effect.

TEST CONDITIONS

Since geogynchronous spacecraft charging was first measured (DeForest, 1972), it was clear that the spacecraft normally dominates ambient plasma perturbation with a ready source of photo-emitted electrons. The obvious exception occurs during the vernal and autumnal eclipse of the Sun. The most recent study of ATS-5 and ATS-6 potentials during eclipse is reported by Rubin et al., 1978.

Neither ATS ion engine was designed to provide a bias of the neutralizer or ion source relative to spacecraft ground. Therefore, most of the potential control experiments have been conducted during eclipse when natural spacecraft charging events were likely. All of these eclipse tests have utilized only the neutralizers on the spacecraft. A few operations of the ATS-5 and ATS-6 ion sources have occurred during full Sun periods of the orbit. The design of each ion engine required that the neutralizer be operated when the ion source was operated.[1] This restriction has been eliminated and other features, such as biasing, have been incorporated into the ion/electron source to be flown on USAF Space Test Program mission P78-2 (Cohen et al., 1978).

A summary of the measurements relating to active control of the ATS-5 and ATS-6 potential is shown in Table 1. Various restrictions and problems precluded all combinations of instruments and test conditions. It is felt that the results of these measurements provide a basis for predicting the behavior of electron and ion sources as spacecraft potential control devices. The missing data sets therefore represent desirable but not essential experiments relative to the ATS-5 and ATS-6 spacecraft charging study.

ATS-5 EXPERIMENTAL RESULTS

While the ATS-5 ion engine was operated briefly as a thruster (DeForest et al., 1973), the far more interesting results were obtained from the operation of its thermionic neutralizer during eclipse. This is primarily due to the large spacecraft potentials encountered during eclipse which well exceeded the 50-eV minimum energy resolution of the UCSD Auroral Particles Experiment. Recent spectrogram data from day 87 of 1978 are presented in Figure 3 as typical of a spacecraft charging event which is modified by the operation of the thermionic neutralizer. The spectrogram is a time plot showing energy of arriving electron and ion fluxes. The density of the particle flux

---

[1] A special operation of the ATS-5 ion engine was conducted in 1973 commanding it off in an abnormal manner. This briefly produced an ion beam while the neutralizer was off. Limited data indicate that the spacecraft charged to a potential of about -3000 V (DeForest et al., 1973).

is indicated by the gray scale moving from dark (minimum) to light (maximum). At the onset of eclipse, denoted on Figure 3, the spacecraft charged to a potential of about -2000 volts. This can be seen in Figure 3 as the dense (light) band of ions rising in energy. As the spacecraft potential goes negative, low energy ions from the ambient are attracted to the spacecraft and their energy upon arrival would be that of the spacecraft's potential. It follows that no ions can have energy less than the spacecraft's potential. The apparent ion flux at energies less than the spacecraft potential is therefore instrument noise. Considering the nearly 9 years of orbital operation, this instrument remains remarkably sensitive.

The spectrogram primarily finds its utility in qualitative examinations of environmental flux features. By extracting the spacecraft's potential from the environmental data, the effect of the operation of the ion engine's thermionic neutralizer during day 87, 1978, eclipse is shown again in Figure 4. This linear plot more quantitatively demonstrates the effect of the neutralizer's operation. When the hot filament is first turned on, the spacecraft initially discharges to a potential below -130 volts. The time between the energy scans showing the spacecraft at -1500 volts and -130 volts is about 14 seconds. Subsequently, the spacecraft is charged to a potential of about 1000 volts. Following the turn-off of the neutralizer, the spacecraft charged to about -2500 volts.

The slow charging of the spacecraft while the neutralizer is on is believed to have resulted from the suppression of electron emission by differential charging between the spacecraft structure at neutralizer potential and the insulated thermal cover around the neutralizer. The hot neutralizer filament is mounted approximately 3 cm inboard of the spacecraft skin. The suppression of electron emission from the ion engine neutralizer in this geometry has been measured in the laboratory (Goldstein, 1976). Additionally, laboratory measurement of differential charging between conductive and nonconductive materials immersed in a high energy electron beam has been performed by Purvis (1978) which simulated the emission of electrons from the conductive element of the spacecraft. A charging of the insulated materials with a similar time constant to that measured in orbit was observed. The potential overshoot observed at the turn-off of the neutralizer (Figure 4) is also typical of numerous active charge control experiments. This phenomenon can also be explained as an effect of differential charging of the insulated spacecraft surfaces associated with the operation of the neutralizer. The artificially higher negative potential on these surfaces at neutralizer turn-off would alter the natural current balance with the ambience until all surfaces reached their equilibrium potentials.

An additional series of orbital tests was structured to further examine the effect of the neutralizer's operation on spacecraft potential. Simultaneous operation of both the ion engine neutralizers on ATS-5 was performed. Typical results of these experiments are presented in Figure 5. Three such data sets were obtained. The turn-on of the second neutralizer did not have a marked effect. However, when the first neutralizer was turned off, a slight decrease in the spacecraft potential was observed during all three tests. This phenomenon is not understood. When the second neutralizer was

turned off, the spacecraft potential rose in a fashion typical of single neutralizer operations.

In summary, the hot filament neutralizer has been shown to have a significant effect on the potential of ATS-5 during a spacecraft charging event. However, due to suppression of electron emission, the spacecraft was not clamped at plasma potential. Laboratory data support the likelihood that differential charging of insulated spacecraft surfaces is suppressing electron emission. This hypothesis is consistent with the transient behavior observed at the turn-on and turn-off of the neutralizer in orbit. Alternately, the suppression of electron emission by a plasma sheath around the spacecraft can not be ruled out. Measurements suggesting the presence of such a barrier around ATS-6 have been presented (Whipple, 1975). Additional consideration of these data seems well justified.

ATS-6 EXPERIMENT RESULTS

The results of the ATS-6 experiments complement those of ATS-5. Since the ATS-6 ion engine neutralizer utilized a low energy plasma as an electron source, the effects of a second-type neutralizer could be measured. Additionally, the ATS-6 Auroral Particles Experiment provided significantly enhanced energy resolution.

The effect of the operation of the ATS-6 ion engine as a thruster has been studied by Goldstein et al., (1976) and more recently by Olsen (1978). In this configuration the ion source and neutralizer are simultaneously operated. To summarize these tests, Figure 6 is presented. The data demonstrate that the potential of ATS-6 was clamped at about -4 volts throughout the 4-day operation of the Ion Engine Experiment.

The cesium vapor flow to the plasma neutralizer is regulated to control the potential of an anode probe in its discharge. The potential of the probe during the four-day operation of the ion engine was about +4.5 V relative to spacecraft ground as measured by telemetry. Since the neutralizer cathode potential is that of spacecraft ground, the potential of the anode probe is at or very near the potential of the ambient plasma. If the probe were operated at spacecraft potential and the cathode of the plasma neutralizer were operated with a negative bias, the spacecraft might well have been held at plasma potential. The ATS-6 Ion Engine Experiment had no such bias capability. It remains for this concept to be demonstrated.

Several other interesting features of the UCSD data were observed while the ion thruster and neutralizer were jointly operated. There are indications that differential charging on ATS-6 was suppressed during this operation and that the measurement of environmental data was enhanced by a constant spacecraft potential (Olsen, 1978). Although the UCSD particle detectors cannot distinguish between protons and other ions,

further analysis of the data may yield additional insight into the nature of particle flux to the ATS-6 while the Ion Engine Experiment was operating. Present indications are that variation in low energy ion flux appears to more nearly follow natural variations of the plasma rather than an ion flux originating from the ion engine itself (Olsen, 1978).

Of equal interest were the ATS-6 ion engine neutralizer tests that were conducted during eclipse. A spectrogram of such a test on day 97, 1977, is presented in Figure 7. The spacecraft potential from the same data is linearly plotted in Figure 8. These data demonstrate that the low energy plasma neutralizer is sufficient to discharge the spacecraft. Due to the absence of natural low energy ions during this test, the exact potential to which the spacecraft was clamped can not be measured with precision. Other experiments of this type have shown that the spacecraft potential is clamped to approximately -5 V by the neutralizer's operation. The operation of the plasma neutralizer has also been shown to reduce differential charging of the spacecraft, but not to the same extent as the operation of the ion thruster. This is most likely due to the larger density of free low energy ions associated with the ion thruster's operation.

Closer examination of the data presented in Figures 7 and 8 provides several interesting observations. The operation of the plasma neutralizer differs significantly from that of the thermionic neutralizer. To operate the thermionic neutralizer on ATS-5, power is simply applied to a tantalum filament by command, and the filament reaches its operating temperature in a fraction of a second. When the plasma neutralizer is commanded on, power is applied to a heater which warms a supply of cesium in order to deliver cesium vapor to the plasma neutralizer. When the density of the cesium vapor and the cesium surface coverage of the neutralizer cathode are sufficient, a plasma discharge strikes. Initially, this discharge operates from a relatively low cesium vapor flow rate and is referred to as the plume mode of operation because of its physical appearance. As the cesium supply continues to heat, the cesium vapor flow rate increases and the plasma transitions to a point discharge described as the spot mode of operation. As seen in Figure 8, the occurrence of neutralizer spot mode operation, which is telemetered, had no measurable effect on the spacecraft's potential. The occurrence of plume mode, which is not telemetered, seems to have provided an ample source of electrons to discharge the spacecraft with a time constant too short to be measured with the 16-second energy range scan of the UCSD instrument. As shown in Figures 7 and 8, the discharge of the spacecraft occurred toward the end of the predicted time when the neutralizer would strike based on ground test data. Due to a malfunction of the ion engine, the neutralizer vaporizer heater was operating at a slightly reduced power, so a longer start-up time for the neutralizer would be expected. To turn off the neutralizer, all power was removed from the experiment. This effectively meant that the neutralizer would instantaneously cease providing electrons and ions. Figures 7 and 8 indicate that the time constant associated with the spacecraft naturally recharging was significantly longer than that required to discharge the spacecraft with the neutralizer. Also note that natural charging and discharging time constants associated with the onset and exit from eclipse are similar to that associated with the

recharging of the spacecraft following the neutralizer operation. The conclusion drawn from these facts is that the ambient plasma currents on this day were overwhelmingly dominated by the operation of the neutralizer. This same conclusion was supported by all other ATS-6 active charge control experiments.

CONCLUSION

The generalized conclusions presented here are based on the results of all active spacecraft charge control experiments conducted on ATS-5 and ATS-6 rather than the limited data presented in this paper. In summary, these experiments have provided the first known measurements of the interaction of the natural plasma and an artificially produced plasma at geosynchronous altitude. The effects of these experiments on the potentials of ATS-5 and ATS-6 have been examined with the following observations:

- The thermionic electron source on ATS-5 provided electrons to replace photoemitted electrons in eclipse; however, charging of the insulated surface around this emitter suppressed electron current and prevented the spacecraft from being driven to plasma potential for all plasma conditions.

- The neutralizer plasma source on ATS-6 maintained the spacecraft potential within a few volts of the ambient potential for both positive and negative charging events for all observed plasma conditions.

- Based on these measurements, it seems likely that a spacecraft could be clamped at plasma potential by a low-energy plasma discharge which could be biased to compensate for the coupling to the ambient. This has not been demonstrated however.

- Operation of the ion engine on ATS-6 was shown to suppress differential charging and clamp the spacecraft potential at a fixed voltage relative to the ambient plasma.

- Active spacecraft potential control has not hindered, but has enhanced the ability to make environmental measurements at energies less than a few volts.

It has previously been shown that the environmental charging of ATS-5 and ATS-6 has produced nearly identical potentials when the two satellites were at similar longitudes (Purvis, 1976). This seems quite astonishing considering the marked difference between the two satellites as summarized in Table 2.

Based on this observation, it follows that the dominant factor controlling the equilibrium potential of a satellite is not the satellites' characteristics but the constituency of the ambient plasma. It is therefore felt that the above observations are generally valid and do not apply solely to the satellites upon which the measurements were made.

Lastly, the time constants associated with all observed natural charging and discharging events well exceeded the time constant associated with the discharging of the satellite by either of the two active control devices. It is therefore clear that these active control devices completely dominate all natural current sources during these experiments. Since no spacecraft anomaly on ATS-5 or ATS-6 has been associated with a natural charging event or an active control experiment, it follows that the task of insuring that a satellite is not sensitive to the electromagnetic interference (EMI) potentially associated with environmental charging is feasible. There is no question, however, that unique satellite design constraints may make the task of EMI sensitivity quite severe.

ACKNOWLEDGMENT

The two instruments utilized to conduct this study were independently conceived with individual experiment objectives. The authors wished to express their appreciation for the support and guidance in conducting these experiments from the principal investigators of the Auroral Particles Experiment, Dr. Carl E. McIlwain, UCSD, and of the Cesium Bombardment Ion Engine Experiment, Dr. Robert E. Hunter, GSFC, retired.

This investigation was conceived after launch, and both scheduling and operations support had to be arranged. The authors therefore wish to additionally acknowledge the contributions of the Orbiting Satellite Project staff and their contractors, GSFC, Dr. James E. Kupperian, Project Manager.

The authors finally wish to acknowledge the contributions of Dr. E. C. Whipple, Dr. S. E. DeForest, and Mr. R. C. Olsen of UCSD and Dr. R. Goldstein of JPL, all of whom have served as co-experimenters during this investigation.

REFERENCES

1. Bartlett, R. O.; DeForest, S. E.; and Goldstein, R.: Spacecraft Charging Control Demonstration at Geosynchronous Altitude. AIAA Paper 75-359, AIAA 11th Electric Propulsion Conference, New Orleans, Louisiana, (1975).

2. Cohen, H. A.; Sherman, C.; Mullen, E. G.; Huber, W. B.; Masek, T. D.; Sluder, R. B.; Mizera, P. F.; Schnauss, R.; Adamo, R. C.; Nanovich, J. E.; and Delorey, D. E., "Design Development, and Flight of a Spacecraft Charging Sounding Rocket Payload," USAF/NASA Spacecraft Charging Technology Conference, Colorado Springs, Colorado, (1978).

3. DeForest, S. E., and Goldstein, R., A Study of Electrostatic Charging of ATS-5 Satellite during Ion Thruster Operation, Final Technical Report, NAS JPL 953675, 1973, Jet Propulsion Lab, Pasadena, California.

4. Durrett, J.C., and Stevens, J.R., "Overview of the Space Test Program P78-2 Space Flight," USAF/NASA Spacecraft Charging Technology Conference, Colorado Springs, Colorado, (1978).

5. Goldstein, R.: Active Control of Potential of the Geosynchronous Satellite ATS-5 and ATS-6. Paper I-6, Spacecraft Charging Technology Conference, Colorado Springs, Colorado, (1976).

6. Goldstein, R., and DeForest, S.E.: Active Control of Spacecraft Potentials at Geosynchronous Orbit. Progress in Astronautics and Aeronautics, 47, 169, A. Rosen, ed., MIT Press, Cambridge, Massachusetts, (1976).

7. Lovell, R.R., Stevens, N.J., Sehober, W., Pike, C.P., and Lehn, W., "Spacecraft Charging Investigation: A Joint Research and Technology Program," AIAA Progress in Astronautics and Aeronautics, 47, 3, A. Rosen, ed., MIT Press, Cambridge, Massachusetts, (1976).

8. Olsen, R. C.: "Operation of the ATS-6 Ion Engine and Plasma Bridge Neutralizer at Geosynchronous Altitude," AIAA/DGLR 13th International Electric Propulsion Conference, San Diego, California, (1978).

9. Purvis, C. K., Staskus, J.V., Roche, J. C., and Berkopec, F.D., "Charging Rates of Metal/Dielectric Structures," USAF/NASA Spacecraft Charging Technology Conference, Colorado Springs, Colorado, (1978).

10. Purvis, C. K., Bartlett, R. O., and DeForest, S. E., "Active Control of Spacecraft Charging on ATS-5 and ATS-6," USAF/NASA Spacecraft Charging Technology Conference, Colorado Springs, Colorado, (1976).

11. Rubin, A. G., Garrett, H. B., and Rothwell, P. L., "ATS-5 and ATS-6 Potentials During Eclipse," USAF/NASA Spacecraft Charging Technology Conference, Colorado Springs, Colorado, (1978).

12. Whipple, E. C., Jr.: Observation of Photoelectrons and Secondary Electrons Reflected from a Potential Barrier in the Vicinity of ATS-6. Journal of Geophysical Research, 81, 715, (1976).

Table 1. - Summary of Test Conditions

Configuration	Satellite	
	ATS-5	ATS-6
Ion Source w/Neutralizer	Sunlite - 2 Eclipse - None	Sunlite - 2 Eclipse - None
Neutralizer Only*	Sunlite - 24 Eclipse - 217	Sunlite - 22 Eclipse - 14

*The ATS-5 neutralizer produces electrons only while the ATS-6 neutralizer produces both electrons and ions.

Table 2. - Spacecraft Characteristics Summary

Launch (technology)	ATS-5 1969	ATS-6 1974
Attitude control	Spin stabilized	3 axis stabilized
Exterior surface	Quartz, paint	Kapton, aluminum, quartz, silicon, paint
Characteristic dimension	2 m	10 m

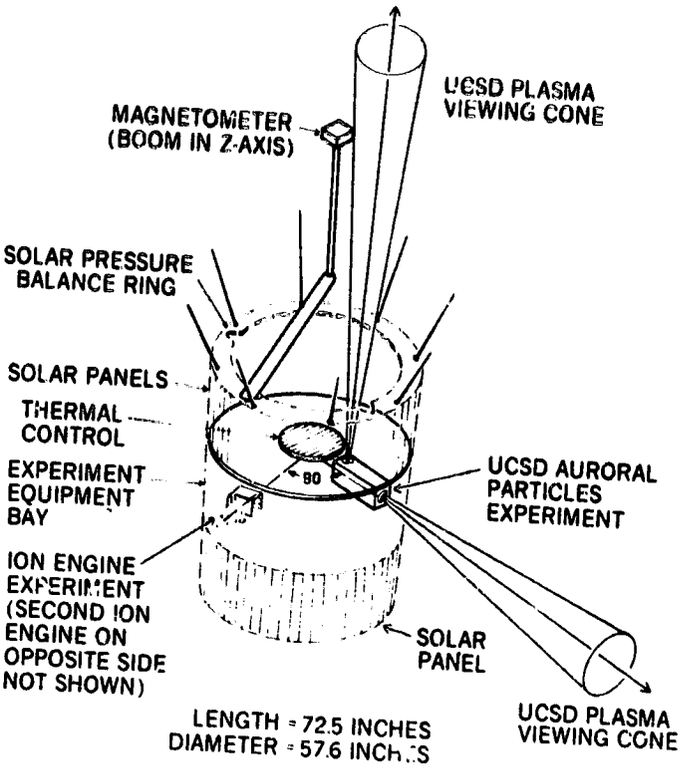

Figure 1. - ATS-5 Orbital Configuration

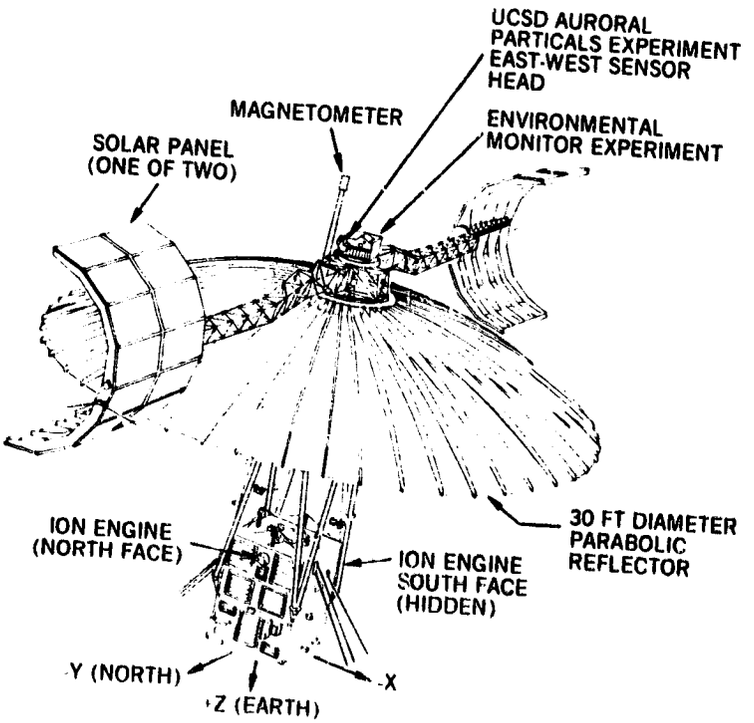

Figure 2. - ATS-6 Orbital Configuration

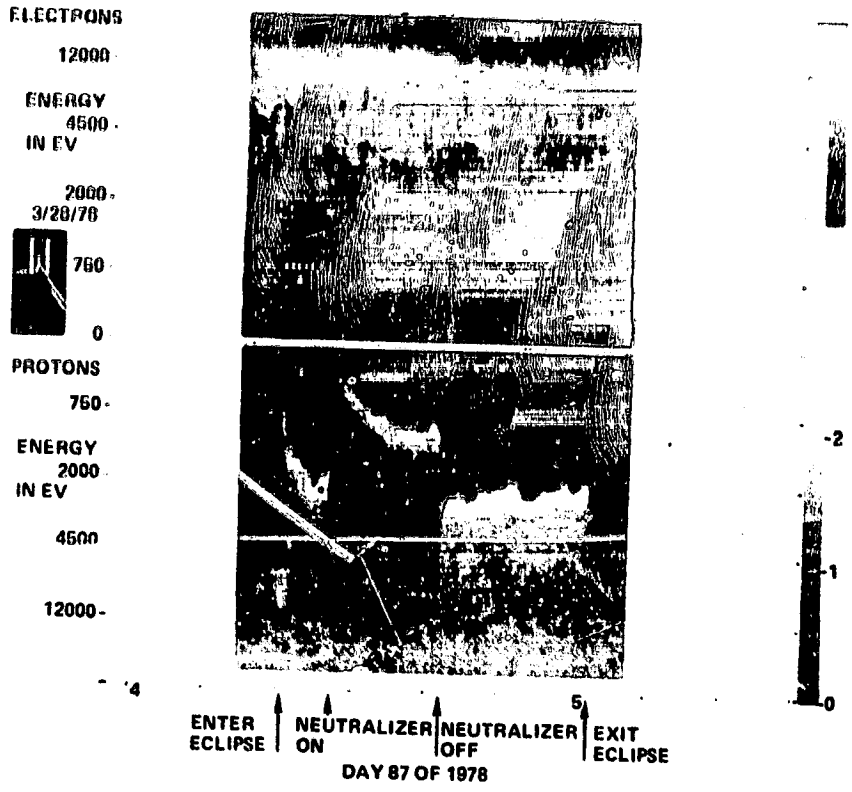

Figure 3. -ATS-5 Spectrogram (March 28, 1978 - Day 87)

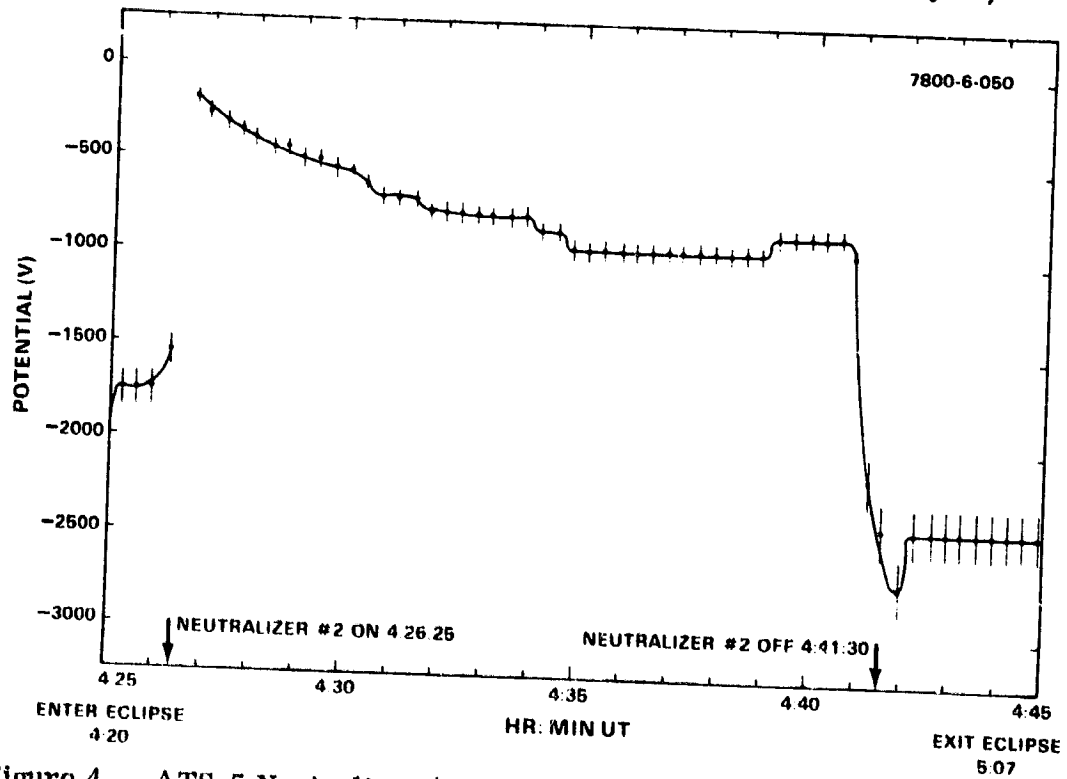

Figure 4. - ATS-5 Neutralizer/Eclipse Operation (March 28, 1978 - Day 87)

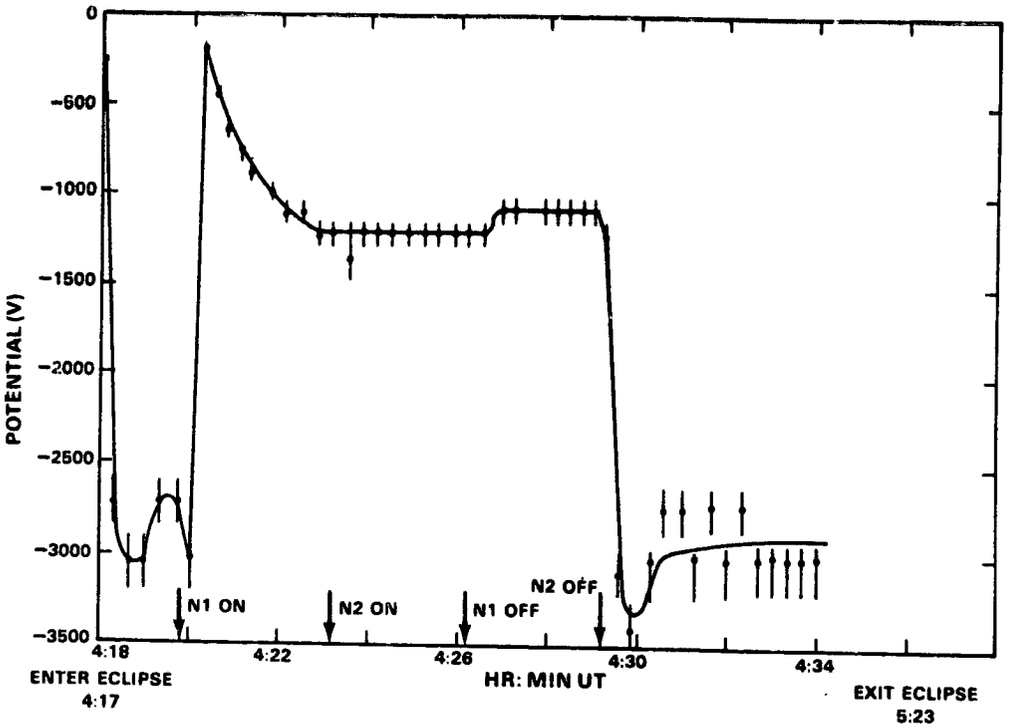

Figure 5. - ATS-5 Neutralizer/Eclipse Operation (February 28, 1978 - Day 59)

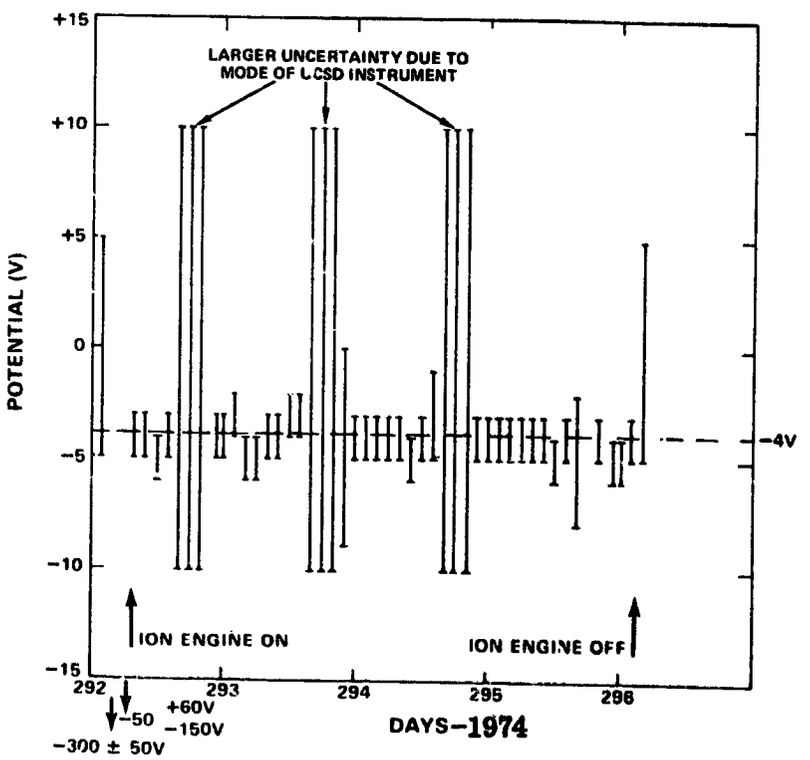

Figure 6. - ATS-6 Ion Engine Operation (No Eclipse)

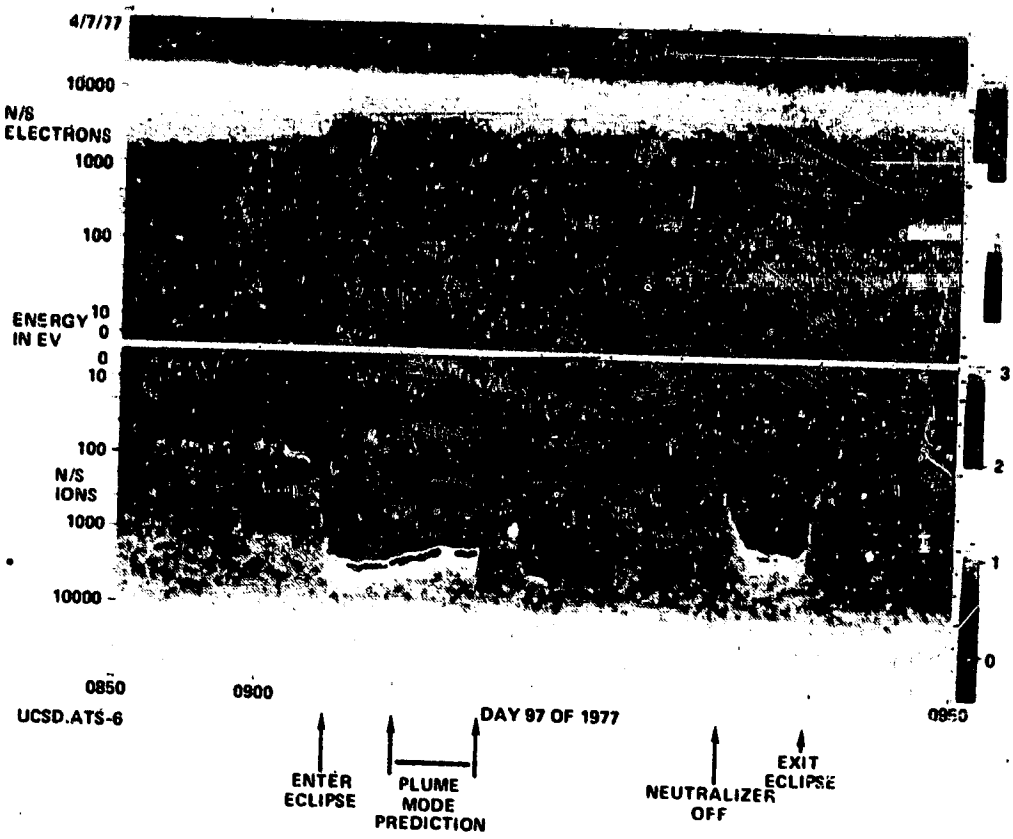

Figure 7.-ATS-6 Spectrogram (Day 97 of 1977)

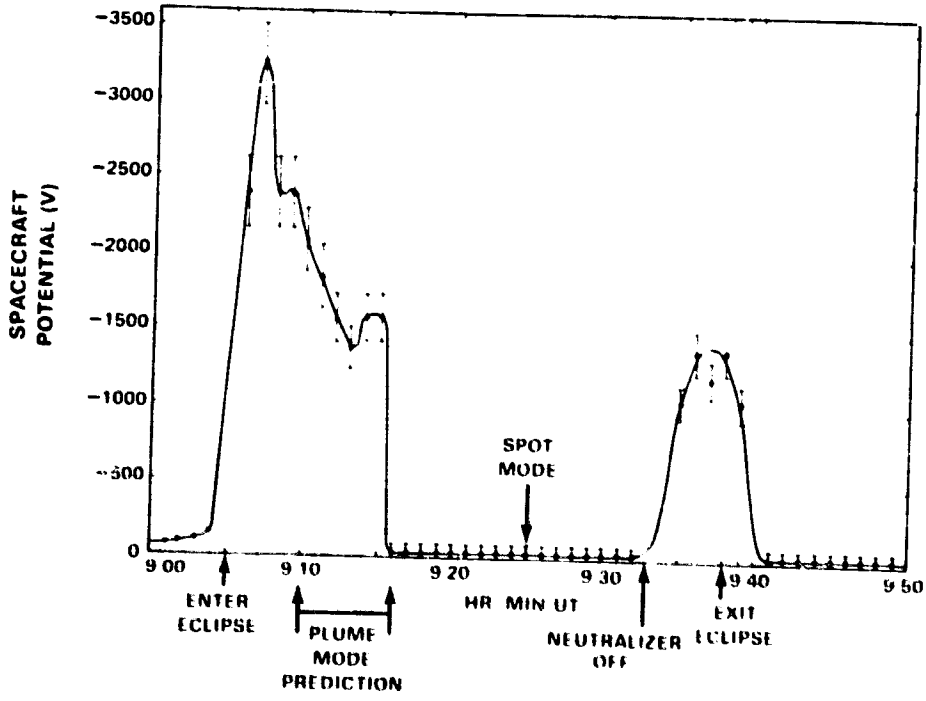

Figure 8.-ATS-6 Neutralizer/Eclipse Operation (Day 97 of 1977)

OPERATIONS OF THE ATS-6 ION ENGINE*

R. C. Olsen and E. C. Whipple
University of California, San Diego

ABSTRACT

The ion engine experiments on ATS-6 have been operated in daylight and eclipse. The effect on particle fluxes to the spacecraft was monitored with the UCSD Auroral Particles Experiment. These data also provide information on the potential of the spacecraft with respect to the ambient plasma and on the local electric fields caused by the charge distribution on the satellite.

Daylight operations of the plasma bridge neutralizer and the cesium thruster in fall, 1974, served to hold the spacecraft between -3 and -8 volts with respect to the ambient plasma. Neutralizer operation reduced differential charging effects, while operation of the thruster usually reduced the effects below the detectors sensitivity. Eclipse operations of the neutralizer reduced kilovolt negative potentials to a few volts. Operation of the thruster prevented possible charging of the satellite during substorms, making it possible to study low energy particle spectra which are at times obscured by charging during substorms.

INTRODUCTION

Applied Technology Satellite 6 carried two cesium ion thrusters up to geosynchronous altitude in 1974. Also on board was the UCSD Auroral Particles Experiment, designed to count electrons and ions in the 0-80 kev range. The ion engines were operated in 1974, and met most of their objectives. Unfortunately, neither engine could be restarted after their initial tests, but in 1976 and 1977 the plasma bridge neutralizers were successfully operated. These operations have been monitored with the UCSD instruments to determine the spacecraft potential and to try to understand the local electric fields.

ATS-5 and ATS-6 have experienced charging of several hundred volts in daylight, and potentials up to 18 kilovolts in eclipse. DeForest (1972) has reported on the former satellite. This charging accelerates ions into the spacecraft and repels electrons, degrading measurements of the environment. Differential charging is even more serious in its effect on data. (Grard, DeForest, and Whipple, 1977). Whipple (1976) has studied the trapping of photoelectrons by ATS-6. He shows that a barrier can be set up around the spacecraft, returning spacecraft generated electrons (primarily photoelectrons) to the spacecraft, and shutting out the ambient electrons.

*This work was supported by NASA Lewis Research Center Grant NSG 3150.

The ion engine operations are being studied as a means of controlling charging. Based on preliminary results from the 1974 operations, the neutralizers were operated with the objective of modifying large potentials. Goldstein and DeForest (1976) have reported on the engine operations and on some of the similar tests run on ATS-5. A report cataloguing the data up through 1976 was compiled by Olsen and Whipple (1977).

Following are more detailed descriptions of ATS-6, its ion engines, and the UCSD detectors. The electrostatic characteristics of the spacecraft will be emphasized. Following this is an analysis of the operations of the two engines in daylight and an operation of the plasma bridge neutralizer in eclipse with the spacecraft highly charged.

ATS-6

The satellite is a large (~ 15 meters) inhomogeneous array of materials (see figure 1). The UCSD experiment sits on top of the satellite in the environmental measurements package (EME). The exterior of the EME package is nominally conducting. It is flanked by solar arrays (insulators) which are on booms extending 25 feet on either side. Below the EME package is a parabolic antenna 9 meters in diameter. Its electrostatic properties are not well known. Constructed from dacron mesh, it is coated with copper, which is in turn covered by a lubricant (insulator) to aid deployment. Five meters below the antenna is the earth viewing module (EVM) which contains the ion engines. The surface of the EVM is conducting. In short, ATS-6 is a large electrostatically complicated satellite. Geometrically, the ion engines and the particle detectors are well separated.

ION ENGINES

The ion engines are cesium bombardment engines utilizing the magnetoelectrostatic containment concept (see figure 2). Two grids are used to extract and accelerate the plasma. Neutralizing electrons are supplied by a plasma bridge neutralizer. The neutralizer generates its own cesium plasma at the plasma probe potential. This plasma provides the necessary electrons to the ion beam. The neutralizer is the main link between the engine, beam, and the spacecraft mainframe. The main thruster is essentially floating. The beam is nominally .1 amp accelerated through 1.1 kv, with the outer grid at -560 volts. It produces 4.45 mN (1 millipound) of thrust (see Worlock, et al., 1975).

DETECTORS

The UCSD Auroral Particles Experiment consists of two sets of rotating detectors and one fixed detector. The rotating detectors are paired ion and electron detectors; the fixed detector measures only ions. All count particles as a function of energy (0-81 keV in 64 exponential steps, 16 sec.)

and angle (220° in 2 1/2 minutes). These instruments can be considered differential in angle, area, and energy (Mauk and McIlwain, 1975).

OPERATIONS

The ion engines were operated in two main experiments. The first lasted about one hour and was conducted in a low energy environment. The second operation lasted 92 hours, began during a fairly active period, and included a variety of environments.

Day 199/74

The first ATS-6 ion engine operation was on July 18, 1974. The data is presented in spectrogram form in figure 3. The spectrogram provides the count rate as a function of time (horizontal axis) and energy (vertical axis). The energy scales are logarithmic, with the ion scale inverted. Electrons are in the top band, ions in the lower. The intensity is proportional to the count rate. In these spectrograms, the intensity cycles, that is, it reaches a maximum lightness, and then cycles to black and starts over again. This occurs in figure 3 for the 10 eV ions. The pitch angle for this detector is plotted over the spectrogram, and is seen here cycling between 10° at the bottom and 150° at the top. The spectra varies as the detector rotates, showing the pitch angle distribution.

There is a band of low energy electrons from 0-50 electron volts visible in the spectrogram. The bottom few eV of the spectra are photoelectrons, the rest ambient plasma. There is no apparent differential charging. When the neutralizer ignites at 3:10, there is a change in the low energy spectra for electrons and ions. The decrease in intensity of the electrons is mirrored by an increase in the ion intensity. This and the absence of ions below 4 eV are interpreted as a shift in potential to about 4 volts negative. By comparison of the particle spectra before and after neutralizer ignition, we infer the spacecraft was 4 or 5 volts positive before the neutralizer ignited. After the potential shifts, the photoelectrons are repelled by the spacecraft.

The neutralizer arced off at 3:16, and both it and the ion engine turned on at 3:32. The spectra changes promptly at both transitions. The spacecraft then goes to -5 to -7 volts potential, and remains there until 4:03, when the engine and neutralizer flamed out. The engine reignites at 4:08, and stays on until 4:35, when the experiment ended. At each of these shutoffs the spectra resumes the form it had before the test. The ambient plasma can be considered constant over this time period.

These data show that operation of the plasma bridge neutralizer, with and without the engine, causes the spacecraft to shift from a small positive potential to a negative potential of a few volts. Simple current balance arguments show that in the neutralizer-only mode the neutralizer was emitting a net positive current, i.e., ions.

The second ion engine test was conducted under different environmental conditions, and lasted for a much longer period of time (92 hours). The engine ignited in the latter stages of a substorm. The spacecraft was charged to -50 volts, accompanied by a differential charging barrier of about 90 volts. These effects can be seen in figure 4, which shows the ignitions of the neutralizer and thruster. These transitions are at 7:44 and 8:05 respectively. The shorter time period of the spectrogram emphasizes the angular variations in the spectra. The effects of the differential charging before the engine ignites can be seen in the low energy band of electrons in the top half of figure 4. The sharp transition at low energies is the signature of this effect. It implies that some surface of the spacecraft is at least 100 volts negative with respect to the satellite mainframe and our instrument.

The potential of the mainframe is plotted in figure 5. The spacecraft potential was inferred from the first (lowest) energy channel of the detector containing an appreciable number of ions. We have assumed that we are not seeing any cesium ions from the engine. To add consistency to the data most of the data points were taken with the detector at $\approx 90^{\circ}$, which corresponds to looking straight out from the spacecraft. The detector was not pointed at 90° during the ignition of the neutralizer at 7:40 so two data points taken at 170° were included. It can be seen that the neutralizer quickly brings the spacecraft within a few volts of the ambient plasma. Uncertainties in the spacecraft potential are largely due to a lack of low energy particles at 90° thus making most of the points between 7:40 and 8:05 an upper bound on the magnitude of the potential. The potential leveled off at about -4 or -5 volts when the thruster stabilized.

The differential barrier around the spacecraft shows a more interesting variation. The value plotted in figure 6 is the energy of the transition from high to low counts. The error bars are basically plus or minus one energy channel. When the neutralizer ignites at 7:40 there is a sharp drop in this energy but it does not reach zero. The thruster comes on at 8:05, and by 8:10 the differential charging signature is gone. This behaviour could be explained by the need of negatively charged insulators for an extra ion source to discharge them. The neutralizer is not putting out enough ions to do the job. The thruster provides a source of charge exchange ions which could be diffusing around the spacecraft, drawn by the local fields.

This ignition process showed that a plasma bridge neutralizer is capable of discharging a negative satellite. In contrast to the previous operation, it is supplying a net negative current, i.e. emitting electrons. The spacecraft again attains an equilibrium potential of a few volts negative. This is effectively the coupling potential between the spacecraft (the neutralizer probe) and the ion beam. Differential charging is reduced by the neutralizer but is not completely eliminated until the thruster has been on for 3-5 minutes.

Days 292-296/74

The spacecraft was held at about -4 or -5 volts throughout the 92-hour operation. A number of magnetospheric substorms occurred during this time period. During similar storms outside this time period, the spacecraft charged several hundred volts negative and was accompanied by severe differential charging. Data from this time period are displayed in figure 7. The engine operation begins on day 292 at 8:00 and ends on day 296 at 04:00. The largely constant band of ions at 10 eV show the constancy of the potential. The potential is fluctuating before and after this operation, negative before (up to -300 V) and probably positive afterwards. The white blotches at the middle of the spectrogram, centered around hour 18 of each day, are due to an instrumental effect, and are effectively data dropouts in that energy region. The electron data is undisturbed by differential charging.

We see here an example of the improvement in the data when the spacecraft potential is controlled.

Day 98/77

If the spacecraft goes into eclipse, the absence of photoelectrons changes the balance of currents to the spacecraft. It is common for the spacecraft to be at equilibrium at a few volts negative in eclipse. When the plasma bridge neutralizer was operated under these conditions, there was little or no change in the spacecraft potential. However, if the environment is energetic, as in the aftermath of a geomagnetic substorm, spacecraft at geosynchronous orbit sometimes reach several kilovolts. On April 8, 1977 (day 98), ATS-6 reached -8 kV. The neutralizer was operated during the eclipse to modify the spacecraft potential. The data for this event are presented in figure 8. The solar array current is a function of the spacecraft illumination. The neutralizer probe voltage shows that the neutralizer is on, but the telemetry saturates at 15.7 volts. Ignition of the neutralizer (into "plume" mode), is recognized more sensitively by the spacecraft potential, the bottom graph. The break in the probe voltage curve at 9:22 is the neutralizer entering "spot" mode. Prior to eclipse, the spacecraft was at -50 V. Upon entering eclipse (9:05) it charges even higher and then discharges quickly when the neutralizer begins supplying electrons (9:12). When the neutralizer is turned off (9:30), the spacecraft promptly charges back up. Upon exiting eclipse (9:35) the spacecraft discharged again. This and other operations under similar conditions showed that the plasma bridge neutralizer is capable of discharging kilovolt potentials.

SUMMARY

ATS-6 ion engine operations from 1974 and a neutralizer operation from 1977 have been analyzed. These operations showed that the plasma bridge neutralizer operating alone could discharge a negatively charged spacecraft, or shift a positive spacecraft to slightly negative. The neutralizer reduced but did not eliminate differential charging. Operation of the main thruster

clamped the spacecraft at ≈ -5 volts, the potential difference between the spacecraft and the ion beam, and eliminated differential charging at the startup of the thruster.

To further understand these results, more work needs to be done in characterizing ion engines as particle sources, particularly in the low energy region, and as a function of time at ignition.

REFERENCES

1. DeForest, S. E.: Spacecraft Charging at Synchronous Orbit. J. Geophys. Res., vol. 77, p. 651, 1972.

2. Goldstein, R.; DeForest, S. E.: Active Control of Spacecraft Potentials at Geosynchronous Orbit, Spacecraft Charging by Magnetospheric Plasmas. Progress in Astronautics and Aeronautics, vol. 47, ed. A. Rosen, AIAA and MIT Press, Cambridge, Mass., 1976.

3. Grard, R. J. L.; DeForest, S. E.; Whipple, E. C., Jr.: Comment on Low Energy Electron Measurements in the Jovian Magnetosphere, Geophysical Research Letters, vol. 4, p. 247, 1977.

4. Mauk, B. H.; McIlwain, C. E.: UCSD Auroral Particles Experiment. IEEE Transactions on Aerospace and Electronic Systems, vol. AES-11, p. 1125, 1975.

5. Olsen, R. C.; Whipple, E. C.: Active Experiments in Modifying Spacecraft Potential: Results from ATS-5 and ATS-6. Final Report NAS 5-23481, Goddard Space Flight Center, May 1977.

6. Whipple, E. C.: Observation of Photoelectrons and Secondary Electrons Reflected from a Potential Barrier in the Vicinity of ATS-6. Journal of Geophysical Research, vol. 81, p. 715, 1976.

7. Worlock, R. M.; James, E. L.; Hunter, R. E.; Bartlett, R. O.: Cesium Bombardment Engine North-South Stationkeeping Experiment. IEEE Transactions on Aerospace and Electronic Systems, AES-11, p. 1176, 1975.

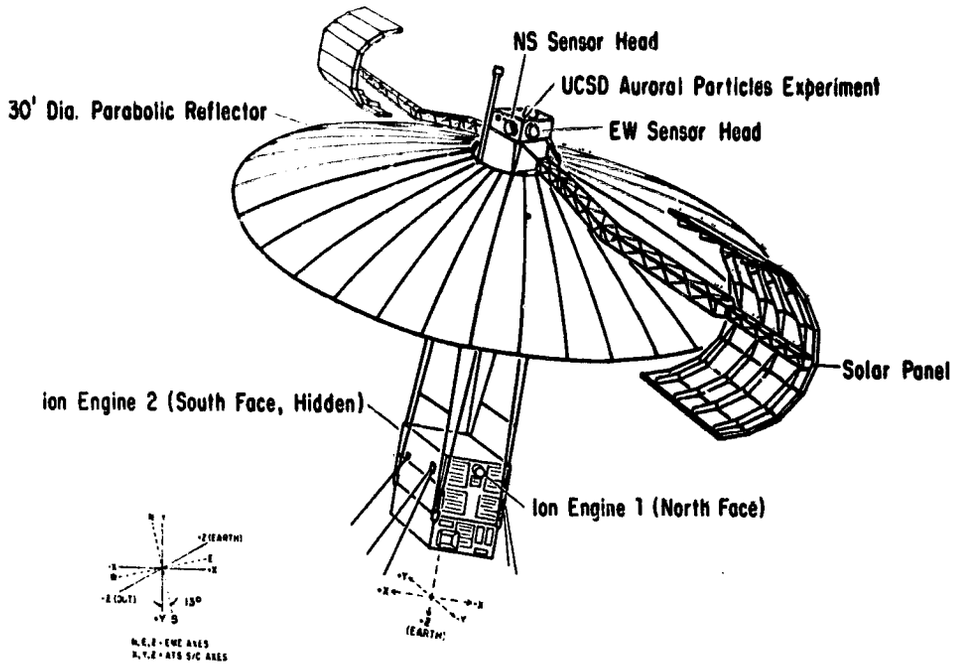

Figure 1. - ATS-6: Detectors and ion engines.

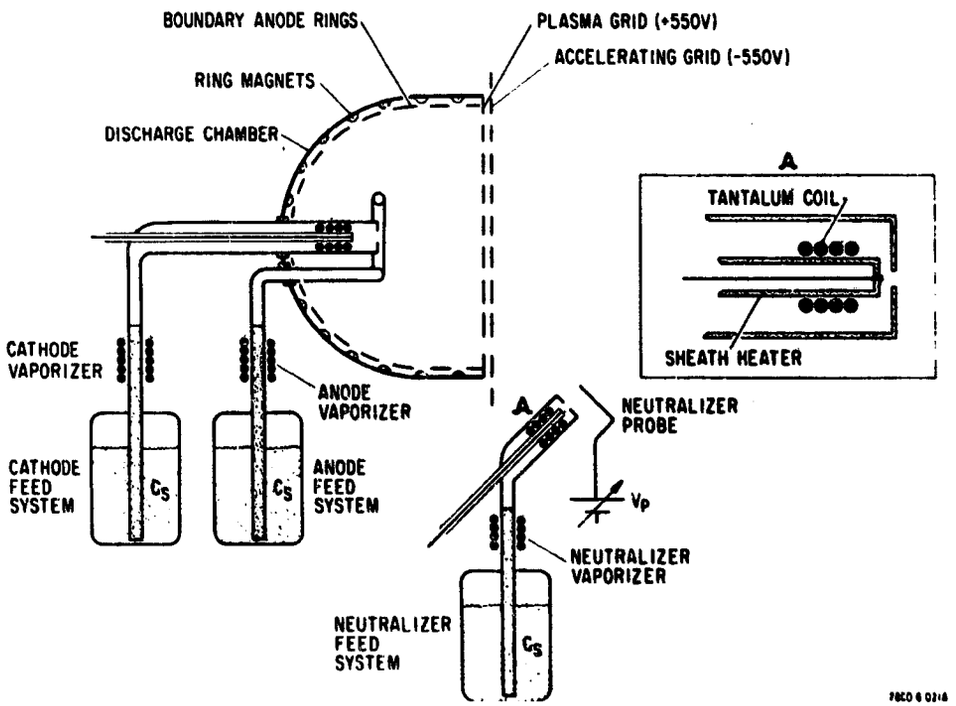

Figure 2. - ATS-6 ion engine.

Figure 3. - Day 199/74: Spectrogram for ion engine operation.

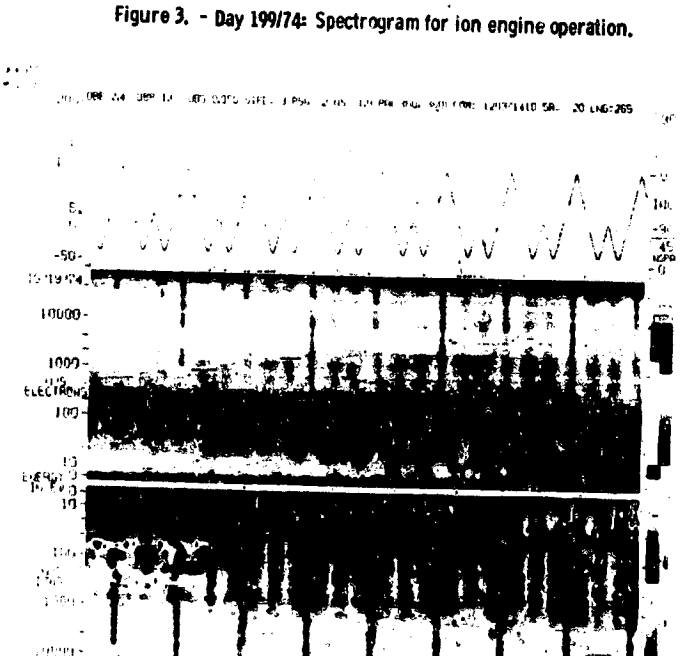

Figure 4. - Day 292/74: Spectrogram for ion engine operation.

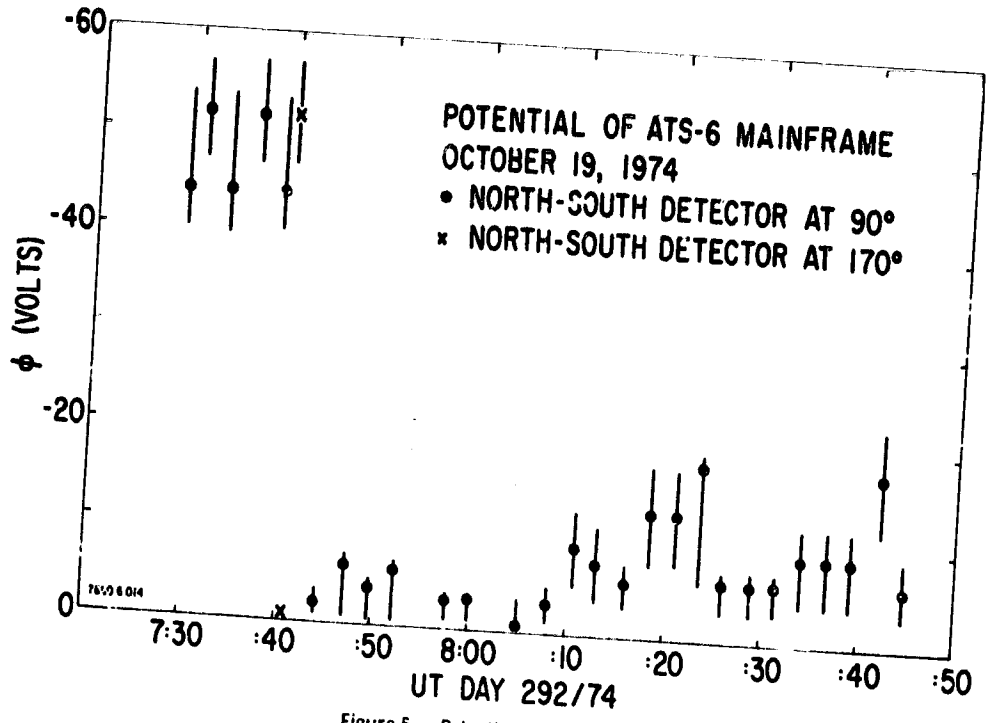

Figure 5. - Potential of ATS-6 mainframe.

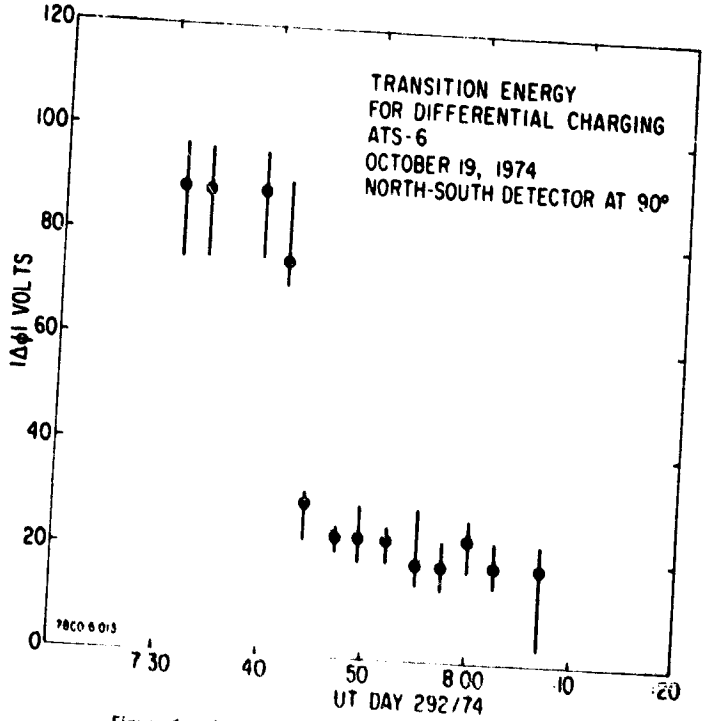

Figure 6. - Transition energy for differential charging.

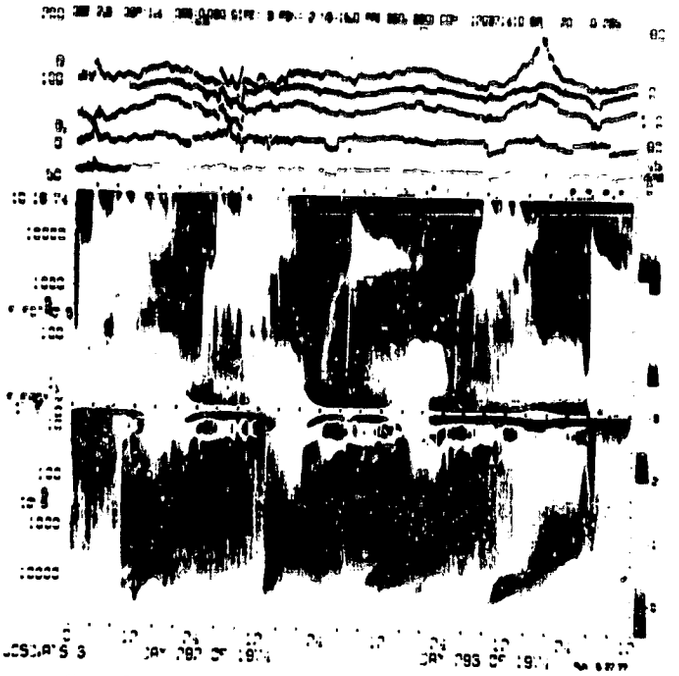

Figure 7. - Days 292-296/74: Spectrogram for ion engine operation.

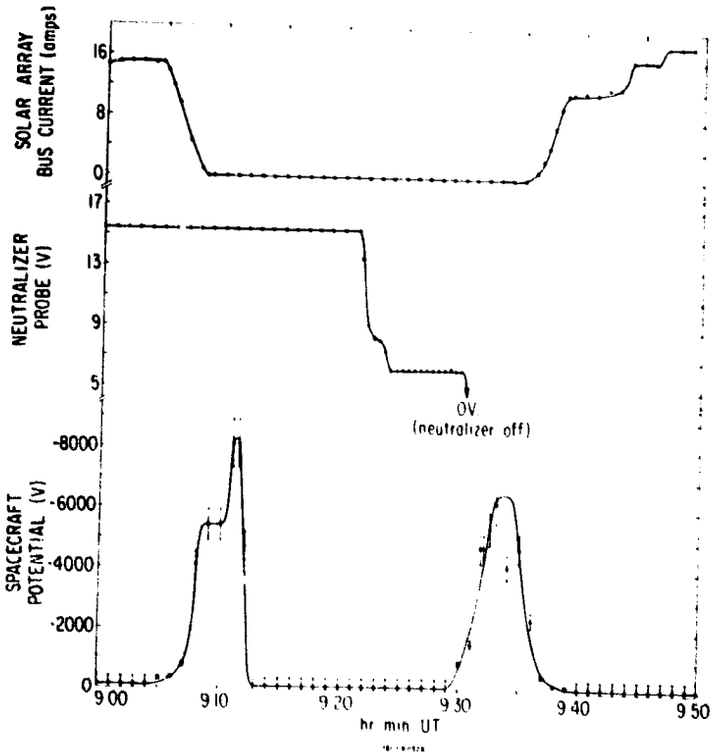

Figure 8. - Day 98/77: Spacecraft potential in eclipse.

N79-24008

CHARACTERISTICS OF DIFFERENTIAL CHARGING OF ATS-6*

Bruce Johnson and Elden Whipple
University of California, San Diego

Since the launch of the ATS-6 satellite into a geostationary orbit in June of 1974, the UCSD Auroral Particles Experiment has collected an enormous wealth of data. It was not surprising to find these data indicating the ATS-6 satellite was charging to negative potentials of hundreds of volts since ATS-5 charged to such values (DeForest, ref. 1). Since then it has been well established that spacecrafts of varying configurations can frequently charge to hundreds and sometimes thousands of negative volts (DeForest, ref. 2; Reasoner et al., ref. 5). Less well understood is the phenomena of differential charging. Differential charging is simply the charging of different parts of a spacecraft to different values. Clearly this could happen since a typical spacecraft has solar arrays, conducting surfaces, thermal blankets, etc., all of which have different charging properties; but the identification of differential charging as such is not as simple as the idea. Fortunately ATS-6 has some peculiarities in its data that lend well to a differential charging explanation, and that is the topic of this paper.

DESCRIPTION OF THE EXPERIMENT AND DATA

The UCSD Auroral Particles Experiment consists of five particle detectors. There are two rotating heads each containing a positive ion and electron detector. One head rotates in the north-south plane, while the other rotates in the east-west plane. The fifth particle detector is a fixed ion detector pointed eastward in the direction of the spacecraft motion. The rotating heads have a 220° range. Each detector can collect particles at 64 energy steps, ranging from 0 eV to 81 KeV, with the capability of dwelling at one particular energy step or scanning through all 64 steps in 16 seconds. The resolution of the particle analyzers is such that $\Delta E/E$ is approximately 20%. The angular resolution is approximately 2.5° by 6.4° for a flat spectrum. (A more detailed description of this instrument package is given in Mauk and McIlwain, ref. 4.)

Thirteen days of data were analyzed containing peculiarities in the electron data attributed to differential charging. On one of these days the satellite was eclipsed by the earth at local midnight. A useful visual aid for examining the data are spectrograms (fig. 1). A spectrogram plots universal time on the horizontal axis and energy in eV on the vertical axis. Particle count rates are represented by the intensity of the gray scale. The top half of the spectrogram is for electrons; the bottom half is for ions. The ion energy scale is inverted.

---

*This research was supported by NASA Lewis Research Center Grant NSG-3150.

DATA

Referring to figure 1, the particle detectors (i.e. spacecraft) are definitely charged negatively since ion count rates are zero up to a certain energy which defines the potential. Starting at about hour 10 the negative potential increases in magnitude to over 600 volts at about 10:30. Mirroring this ion behavior is the peculiar electron shadow up to a couple hundred eV. Along the boundary of this shadow just after the tenth hour is a 10 minute period of intense count rates. This shadow and intense band are apparently photoelectrons and secondary electrons emitted from the spacecraft and returned to the particle detectors. The electron shadow always appears with the charging event. Its peak energy increases as the charge on the detectors increases. Even when there is no charging there is always a low energy, less than 20 eV, band of electrons. It has been shown that these electrons are photoelectrons and secondary electrons emitted by the spacecraft (ref. 6, Whipple, E. C.). The particle spectra are Maxwellians having temperatures of < 10 eV and densities < 100 per CC. The particles could not be from the ambient plasma since the ambient density is changed by $e^{-V/kT}$ when measured by a negatively charged detector. V is the potential difference between the ambient plasma and the detector. kT is the temperature of the electrons. Even for modest charging of a few times kT, the ambient density would be well over 100/CC which is contrary to observations. Ambient densities are less than 10/CC. Thus the electrons are photo and secondary electrons from the spacecraft, and since they mirror a charging event, the shadow must tell something about the charging characteristics. Further evidence that these particles are photoelectrons comes from eclipse data. Figure 2 shows day 66 of 1976, during which the satellite went into eclipse at about 21:20. Eclipse removes the solar photon flux and thus any photoelectron currents. Removal of this electron current carrying charge away from the spacecraft requires more negative potentials to balance the ambient current to the spacecraft. Thus an increase in charging occurs, to about -10,000 volts. Notice the loss of the shadow when this happens, indicating the electrons are indeed photoelectrons.

But the existence of these peculiar photoelectrons does not necessarily imply differential charging. However, if the spacecraft were uniformly charged to a negative value, a potential barrier would have to exist to return the photo and secondary electrons. Whipple (ref. 6) found that the magnitude of the barrier needed to return tens of eV electrons was too large to be explained by a uniformly charged spacecraft. That the barrier must exist is evidenced by the outline of the photoelectron shadow. Electrons with energies less than the energy outline are barrier-returned photoelectrons, whereas at larger energies are the ambient electrons with enough energy to penetrate the barrier. The only other way to sensibly produce a barrier is differential charging. Information about this barrier can be obtained by analyzing the intense count rates along the boundary of the photoelectrons as seen in figures 1 and 2. These intense count rates are termed spots.

In analyzing the spots, the particle count rates measured need to be clarified. The UCSD particle detectors actually measure the count rate over

an energy range E to E + ΔE. This differential count rate for a Maxwellian shifted by a positive potential goes as $E^2 e^{-(E-V)/kT}$, where E is the detector energy. V is the potential difference and here taken to be >0. The peak in the differential count rate occurs at 2 kT, assuming the distribution function has not been shifted to energies greater than 2 kT. This is shown in figure 3. So for photoelectrons or secondary electrons originating on a more negatively charged source, the count rate will be enhanced by e(V/kT) for E > V, and the count rate will be zero for E < V.

As mentioned even with no significant charging, there are low energy (< 20 eV) photoelectrons typically having a kT of less than 10 eV, and so peaking at E < 20 eV. Nevertheless even during large charging events a peak in the counting rate at E < 20 eV can still be observed. Thus these electrons must originate on a source with a differential charge of not more than 20 eV. It normally appears that V is approximately 0, so these photoelectrons probably originate from the package on which the detectors are mounted. Conducting materials cover these parts and are connected, so they have the same potential. However, during charging events where the shadow boundary exceeds 80 eV, the electrons at the high energy values also have temperatures less than 10 eV usually, but their count rates are too large to come from a source with V approximately zero. A Maxwellian of kT = 10 eV, N = 100/CC produces only about 400 counts per sec at E = 100 eV. Count rates at 100 eV are often over 1000 counts/sec during charging events. This implies some differential charging. An even stronger indication of differential charging and a potential barrier are the spots.

The spots are generally large count rates, ranging from 300 to 20,000 counts per second, observed at energies from 80 to 150 eV. Seldom does the spot count rate spectrum ever show a peak, but usually shows decreasing count rates with increasing energy for a couple of detector energy steps. This implies that the 2 kT peak of the spot is less than the energy of the first detected spot electrons. This energy of the first detected spot electron is termed the spot energy. Normally kT was around 30 eV for the spots analyzed, with the spots occurring around 100 eV. Figure 4 shows the local time of occurrence of all the spots studied. The local time axis is in half hours, so 12 corresponds to hour 6 which is dawn. Hour 0 is local midnight. This is the same local time distribution reported by Reasoner et al. (ref. 5). Charging, and thus differential charging, occurs around local midnight due to the larger electron fluxes caused by particle injections. Large electron fluxes to the spacecraft imply a large negative current, requiring a negative potential for current balance. Thus the spots are a charging phenomena also, probably related to high electron fluxes. Figure 5 shows the percent number of spots detected at different NS detector positions. 0 implies north, and 90 corresponds to looking away from the earth. The spots appear to come at all different angles, not readily identifying a single source. Likewise the spots occurred over a large pitch angle range for both the NS and EW detectors, so the spots are not always magnetically returned particles. That is, they are not always particles emitted from their source and spiralled around the magnetic field into the detectors. Potential differences are needed to return the electrons, and the spot energies give some insight as to the magnitude of these differences.

Figure 6 shows the spot energy versus the negative potential of the detector; all energies are in eV. First, notice that detector potentials can be over 800 eV, but the spot energies do not exceed about 280 eV. Over 80% of the spots occurred at energies less than 150 eV. It is not unreasonable to assume that the potential difference between the spot source and the particle detectors, V, is equal to the spot energy. This is reasonable since the spots occur very abruptly with large count rates, a behavior typical of the spot energy equalling V as in figure 3. This assumption gives the maximum value V could have, and the actual V is probably not much less than this to produce such enhanced count rates. If this assumption is nearly correct, then the spot energy versus detector potential is bounded by a line of V = .35 (potential), or the spot source charge is 1.35 times the potential. The charging of this source continues up to a maximum of V = 280 eV so it appears that the source of the spots will charge up faster than the detector, and then level off and stay a fixed 280 eV more negative than the detector at higher potentials. Figures 7 and 8 show the spot energy versus the potential for some typical days. They have the same charge up characteristics. Since these spots are always found at the top boundary of the shadow, their source's potential could be the main contributor to developing a potential barrier that returns spacecraft emitted particles.

A detailed study of day 33 (fig. 7) showed that as the detector potential increased the spot energy increased. The count rates increased not only from V increasing, but the temperature of the spot electrons increased from 30 eV to 50 eV. If V was taken as the energy of the spot as before, the densities of the electrons were from 1 to 4 per CC. Also the source potential of the spot increased about two times as fast as the detector potential. Since the electron flux was changing during this time, the changing temperatures and densities along with changing V seem to indicate that spot electrons were secondary emitted electrons. Temperatures of over 30 eV are not characteristic of photoelectrons, and neither is the changing temperatures since the solar photon flux doesn't change. However, as shown in figure 8 the secondary yield of a material is energy dependent. Thus, changing temperatures and larger temperatures (> 10 eV) can be characteristic of secondary electrons (ref. 3, Knott). A strong candidate for the source is the Minnesota experiment which sits protected from the sun on the package containing the particle detectors. Not being able to emit photoelectrons, it could charge faster than the detectors as electron fluxes increased. Covered with a thermal protecting paint it may be ideal for charging and emitting different spectra of photoelectrons in response to changing fluxes. On day 236, 1974, the count rates of the spots were observed to change as the Minnesota experiment rotated into new positions. Only on this day was such an obvious correlation found, but it does indicate that it probably is involved. Being less than a meter from the detectors, this experiment could dominate the local potentials since it is the only insulator so close. Charging to larger negative potentials than the detectors or package, it could produce a barrier. Other possibilities are the solar panels, but they are over 7 meters away, and their effect would be expected to be less.

Further work needs to be done on determining the secondary electron spectrum of the spots. Equations in reference 6 for the yield as a function

of energy could be used to calculate temperatures and densities of different materials. Potentials as a function of ambient flux could be calculated to see if the potential of the source would behave as observed. If the calculated values agree with those measured here, the source of the spots will be better understood and simple electric fields could then be modelled around the spacecraft.

CONCLUSION

In conclusion, differential charging seems to be responsible for returning photoelectrons to the spacecraft up to a couple hundred eV, depending on the spacecraft charge. Potential differences of 200 eV can exist between parts of the spacecraft, enhancing the count rates of emitted particles. It is believed that the Minnesota experiment on ATS-6 is largely responsible for producing a potential barrier that returns particles and produces intense spots in the count rates.

REFERENCES

1. DeForest, S. E.: Electrostatic Potentials Developed by ATS-5. Photon and Particle Interactions with Surfaces in Space, Grard, R. J. L., ed.

2. DeForest, S. E.: Spacecraft Charging at Synchronous Orbit. J. Geophys. Res., 77, 4, 651, 1972.

3. Knott, K.: The Equilibrium Potential of a Magnetospheric Satellite in an Eclipse Situation. Planetary and Space Science 20, 1137, 1972.

4. Mauk, B. H. and McIlwain, C. E.: ATS-6 UCSD Auroral Particles Experiment. IEEE Trans. Aerospace and Electronic Systems, 11, 6, 1125, 1975.

5. Reasoner, D. L.; Lennartsson, Walter; and Chappell, C. R.: Relationship Between ATS-6 Spacecraft-Charging Occurrences and Warm Plasma Encounters. Spacecraft Charging by Magnetospheric Plasmas, Rosen, A., ed., AIAA, New York, N.Y.

6. Whipple, E. C.: Observation of Photoelectrons and Secondary Electrons Reflected from a Potential Barrier in the Vicinity of ATS-6. J. Geophys. Res., 81, 4, 715, 1976.

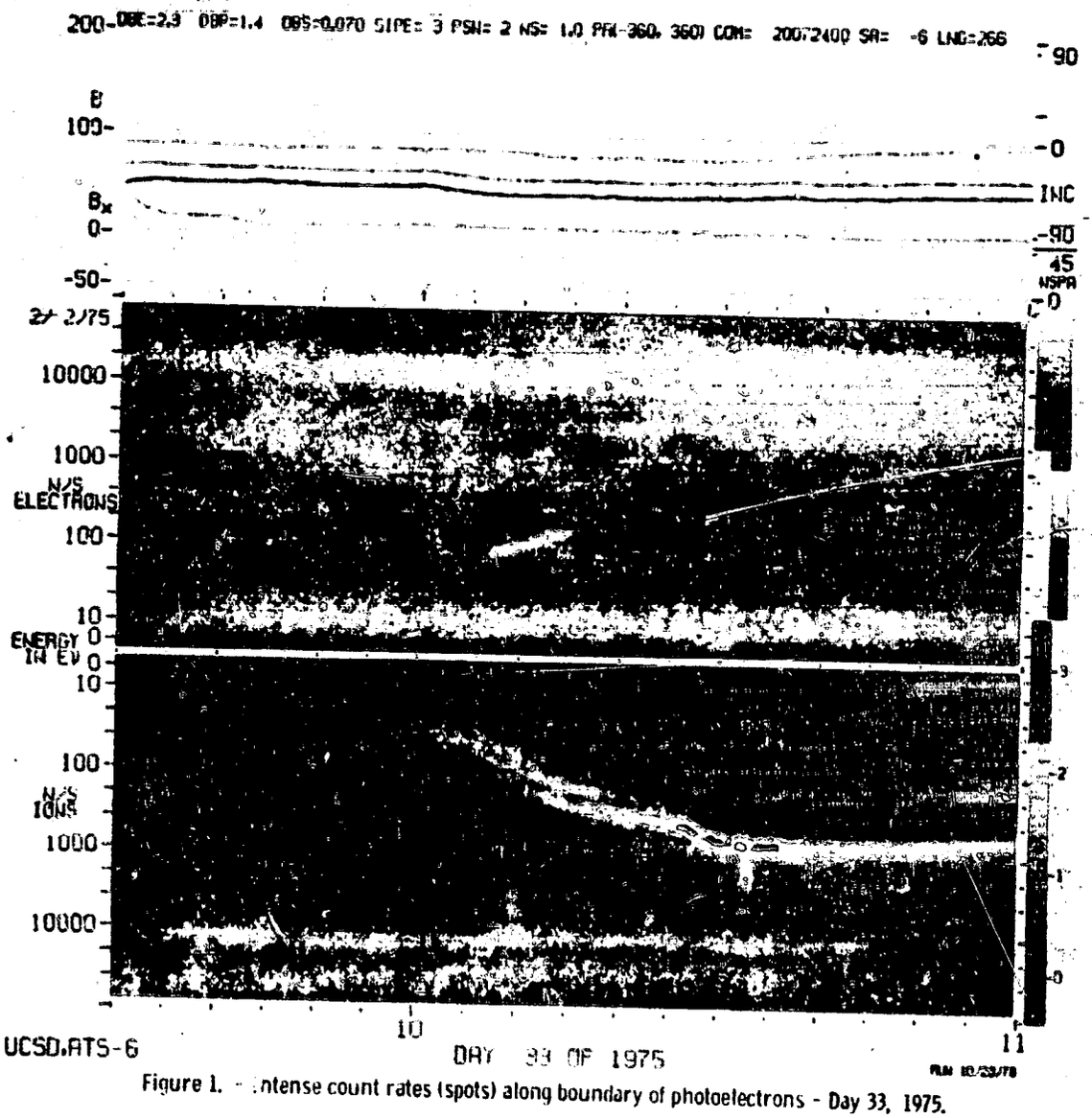

Figure 1. - Intense count rates (spots) along boundary of photoelectrons - Day 33, 1975.

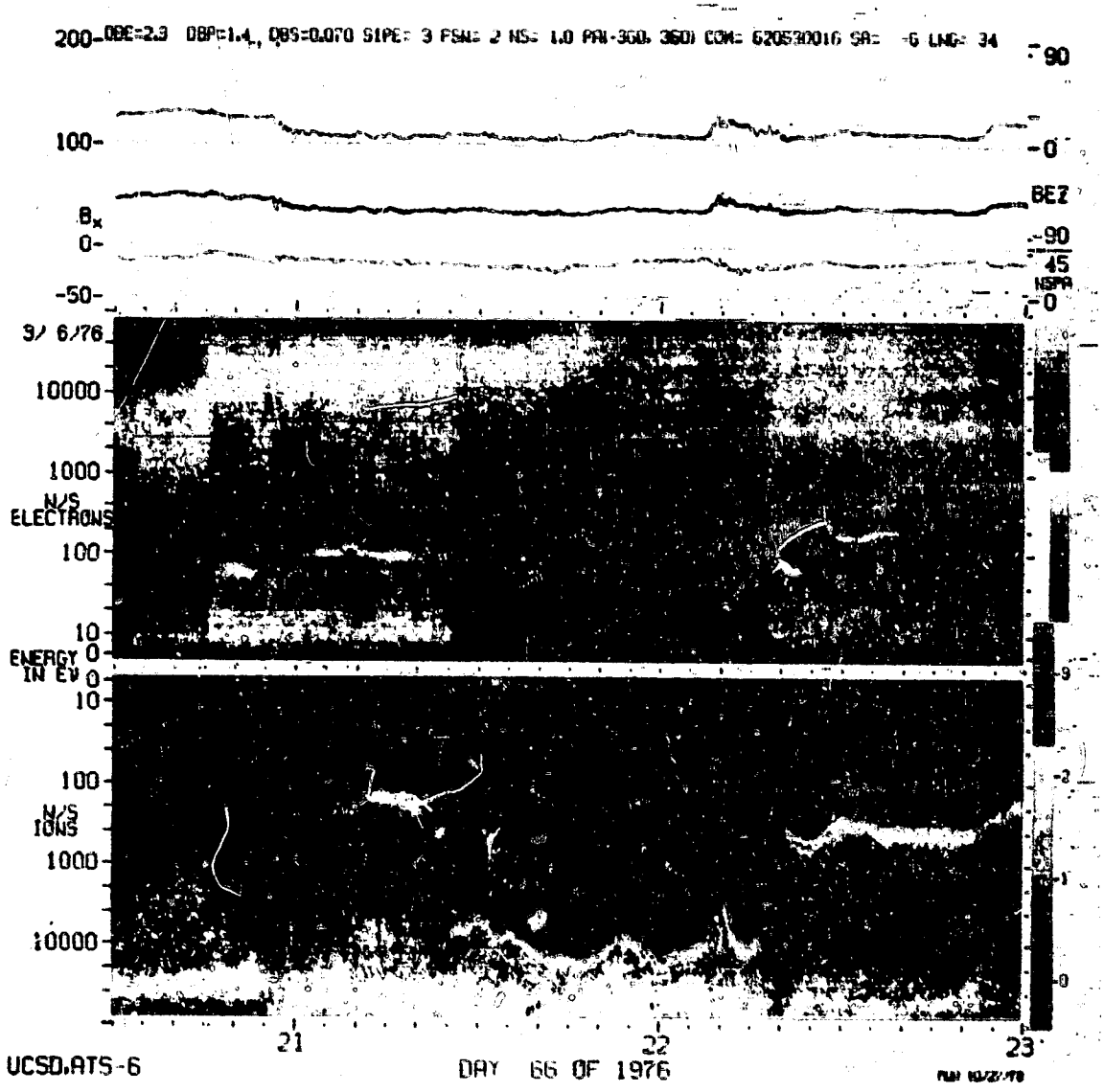

Figure 2. - Intense count rates (spots) along boundary of photoelectrons - Day 66, 1976.

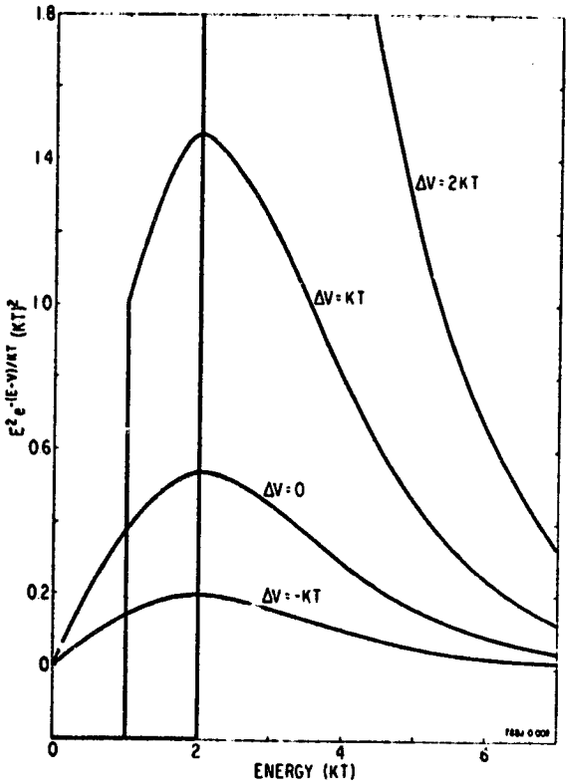

Figure 3. - Differential count rate of Maxwellian shifted by potential V.

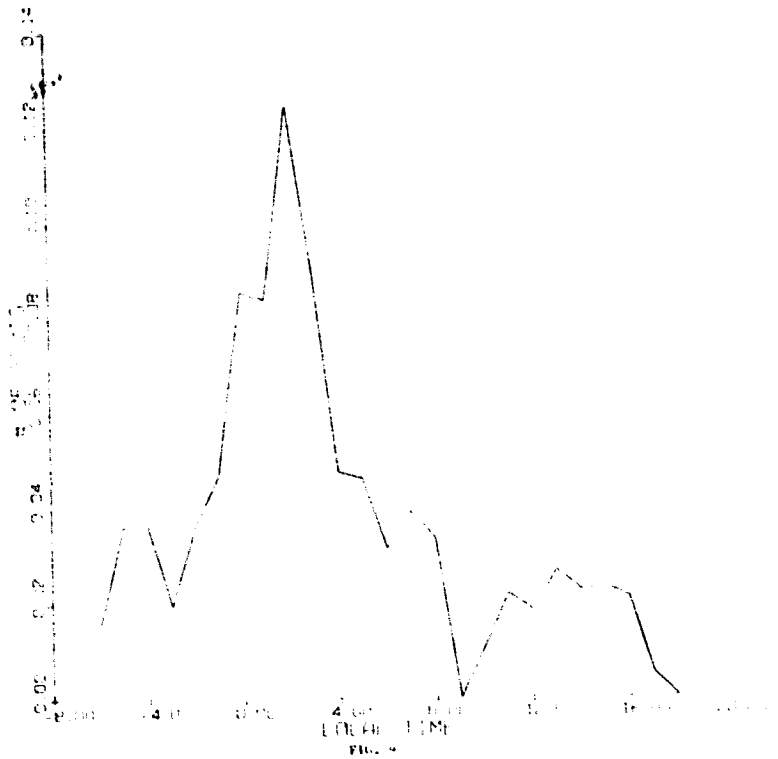

Figure 4. - Local time correspondence of spots.

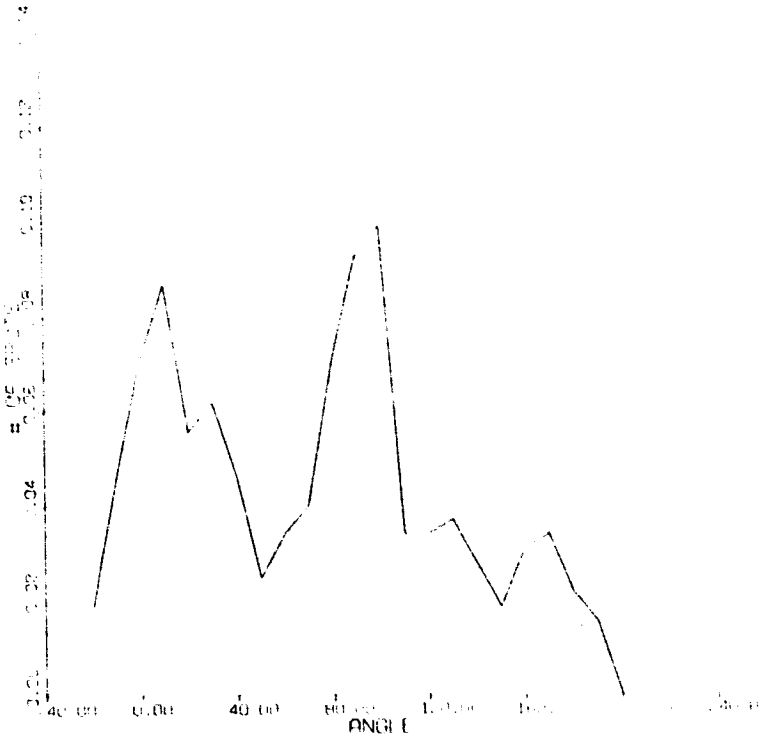

Figure 5. - Number of spots detected as function of angle.

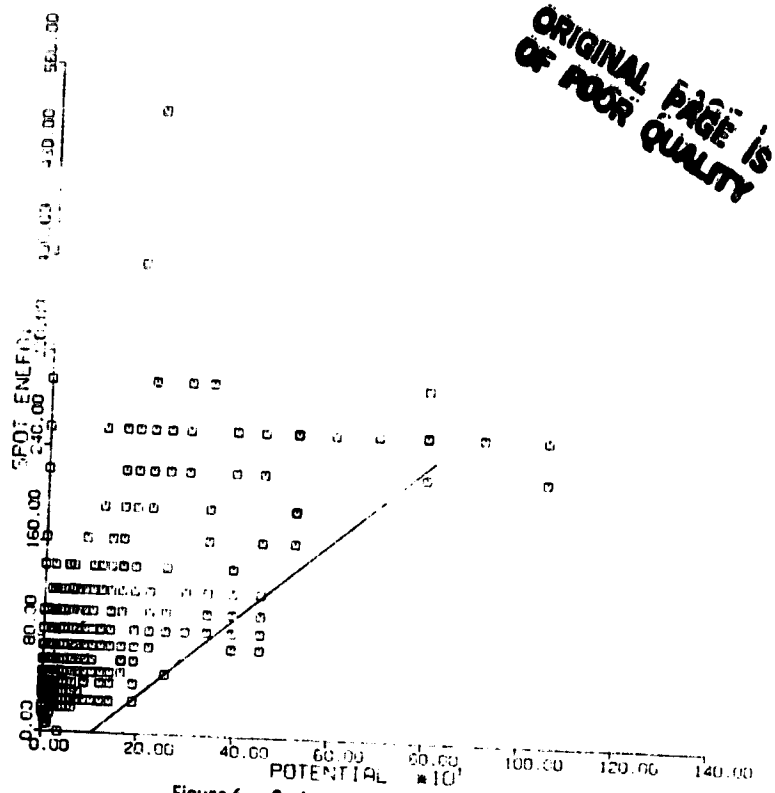

Figure 6. - Spot energy as function of potential.

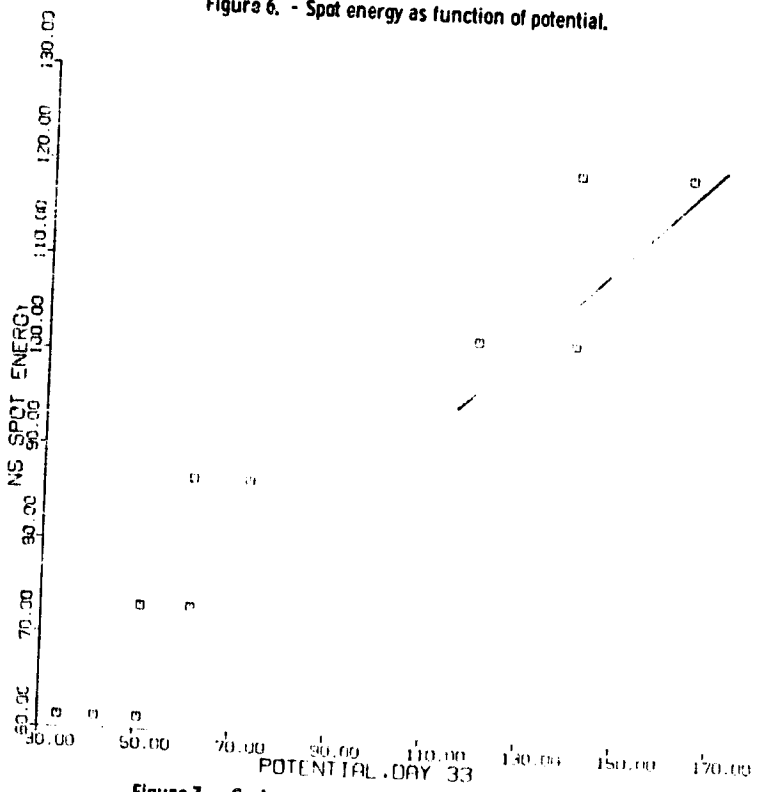

Figure 7. - Spot energy as function of potential - Day 33.

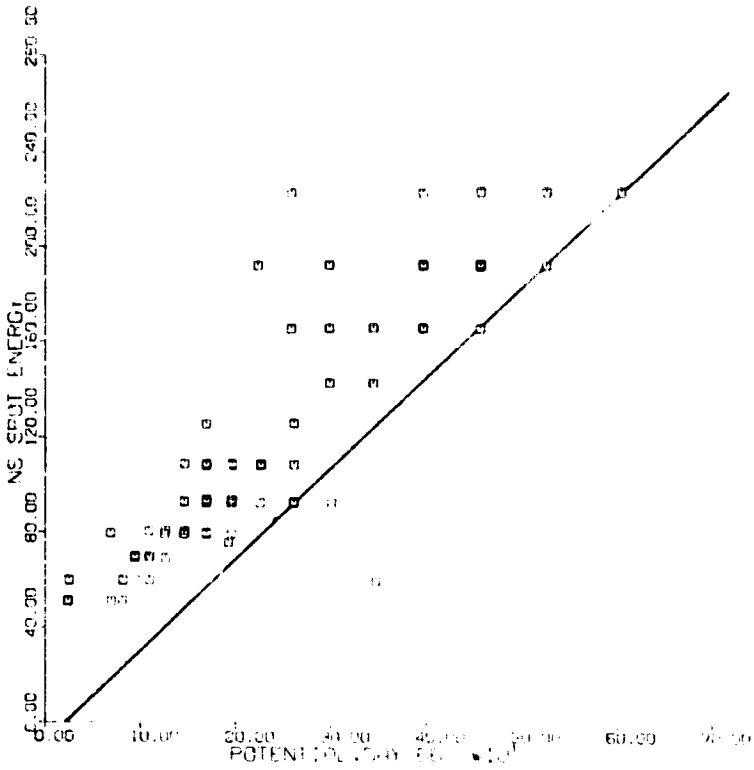

Figure 8. - Spot energy as function of potential - Day 66.

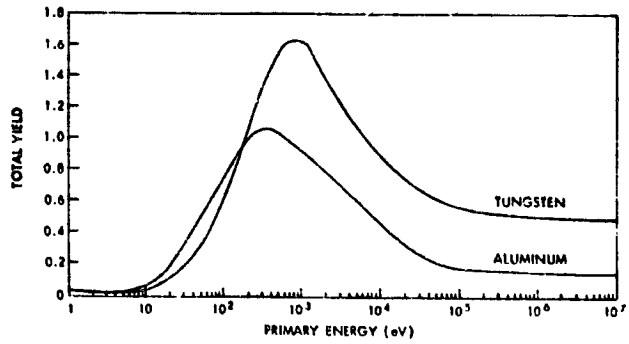

Figure 9. - Total secondary electron yield for tungsten and aluminum.

N79-24009

DESIGN, DEVELOPMENT, AND FLIGHT OF A SPACECRAFT CHARGING SOUNDING ROCKET PAYLOAD

H. A. Cohen, C. Sherman and E. G. Mullen
Air Force Geophysics Laboratory

W. B. Huber
Tri-Con Associates, Inc.

T. D. Masek
Hughes Research Laboratories

R. B. Sluder
PhotoMetrics, Inc.

P. F. Mizera and E.R. Schnauss
The Aerospace Corp.

R. C.Adamo and J. E. Nanovich
SRI International

D. E. Delorey
Boston College

INTRODUCTION

The ejection of charged particles from a space vehicle creates a difference in potential between the vehicle and the ambient plasma. For steady state this potential difference causes a return current flow to the vehicle equal to the ejected current. Although there have been a number of flights during which energetic electrons have been ejected from rocket payloads, a relationship to predict the vehicle to ambient plasma potential difference created by an ejected electron current is still unknown. In fact, questions still remain as to which environmental parameters are critical in determining this potential difference. There is even far less experimental data available from payload flights in which positive, rather than negative charge has been ejected. A primary purpose for the flight of the Spacecraft Charging Sounding Rocket Payload was to create charging on the payload by the emission of both positive ions and electrons, and to determine the relationship between environmental parameters and changes in vehicle potential during periods of emission.

The design and choice of instrumentation for this Spacecraft Charging Sounding Rocket Payload were also influenced by the desire to test prototypes of some of the SCATHA satellite payloads: the positive and negative charge ejection system - the Transient Pulse Monitor (TPM) and the Rocket Surface Potential Monitor (RSPM). Data were desired on not only the operation of these instruments, but on their mutual interactions during operation. The flight of

the Spacecraft Charging Sounding Rocket payload also permitted a comparison of measurements made with SCATHA payloads to measurements made with other more standard techniques not available for SCATHA use.

INSTRUMENTATION

The launch vehicle for this payload was an Astrobee F rocket. The payload was divided into two electrically isolated sections by a non-conducting disk. The payload forward section, a cylinder 254 cm in length and 38 cm in diameter, contained all the vehicle diagnostic instrumentation. The rear section, a cylinder 41 cm in length and 38 cm in diameter, contained the payload recovery parachute, and was electrically connected to the front payload section only through a bipolar voltmeter. The instrumentation, classified into four broad categories, is listed and briefly described in Table 1.

A major operational problem that had to be overcome for this flight was the starting of the satellite positive ion beam system (SPIBS). The usual starting procedure for the system during testing in laboratory vacuum chambers was to pump down the source for at least 24 hours before trying to ignite the discharge. The actual initial ignition following this pump down has taken from five minutes to a half hour, depending on the previous exposure of ion system's hollow cathode and expellant assembly line to air. With the system continuously under vacuum conditions once the ignition has been initially started, reignition can be achieved in periods from ten seconds to one minute. This initial starting period requirement, acceptable for satellite flights, was completely unacceptable for a limited duration sounding rocket flight. The ignition problem was solved by pumping down the ion beam system on the ground before launch, and starting a discharge in the ion beam system 1/2 hour before launch. Close to launch the system was sealed off with the gas still flowing into the ion source and with the discharge still on. At the proper altitude, the cap was opened and the ion beam system allowed to emit high energy positive ions.

Ambient Electron Density

Launch date and time were set so that there could be a low number density, and a wide dynamic range of number densities of electrons over the expected altitude range for particle ejection, 120 to 250 km. These two compatible criteria were best expected to be fulfilled several hours after sunset during periods of quiet geomagnetic activity. Geomagnetic values and 3 hour predictions were obtained during the course of the launch day from the Air Force Global Weather Central (AFGWC). Environmental conditions at the time of the flight are summarized in Table 2.

An ionosonde located at the White Sands Missile Range was used to take vertical incident ionograms at 1 minute intervals during the flight period. These ionograms show that a sporadic E layer (E_s) with a peak n_e of approximately 10^4 electrons/cm^3 existed at an altitude near 104 km throughout the flight.

This E_s layer prevented a direct measurement of the ionosphere in the 104 to 220 km region. The n_e above 220 km was determined by an ionogram inversion technique developed by A. K. Paul and J. W. Wright (1963). The region between 102 and 220 km was modeled to correspond to the relative shape of a mid-latitude, magnetically quiet ($K_p = 0$) electron density profile determined from ionogram analysis by Wakai (1967). The model values were iterated until they agreed with the average valley n_e of 3.84×10^3 electrons/cm^3 determined from the ionogram analysis. This technique of determining n_e in the valley region does not give any small scale structure, but is generally accurate to approximately ±20%. The n_e so determined is shown in Figure 3.

FLIGHT DESCRIPTION

The payload was launched from the White Sands Missile Range, New Mexico (lat 32°30'N, Long 106°30'W) on 21 January 1978 at 0900 UT (0200 LST). The flight trajectory is shown in Figure 1. The major flight events noted in Figure 1 are also listed in Table 3 in the sequence in which they occurred. Despin of the rocket produced a spin rate of approximately 1 rotation per 23 seconds for the data gathering interval (approximately 124 km on ascent to 111 km on descent). Separation of the payload from the rocket motor produced a tumbling of the payload through axial magnetic pitch angles ranging from approximately 5° to 180°.

With exceptions noted, all the instruments operated well; excellent data were obtained during the entire course of the flight with no telemetry losses. As planned, power to the payload charge ejection systems and sensing instrumentation was turned off at 111 km during descent. The payload parachute opened and operated successfully. During descent, into the lower atmosphere, the probe arm which was fully extended came off, and the gold plated surface material on the RSPM came off. On impact, the front disks of the ion beam source were broken. All the other equipment, specifically the camera and film, and the electronics of all the instrumentation were recovered in excellent reusable condition.

RESULTS

At launch plus 81 seconds when the RPA and TEP high voltage was turned on, high voltage arcing within the payload destroyed the electronic circuitry which controlled the RPA grid voltages. This caused the RPAs to function only as electrometers with the exception that RPA #1 had a +2 volt potential on the grid flush mounted with the payload skin. The arcing in the RPA, together with arcing produced later in the SPIBS, caused erratic behavior in the mode programmer throughout the flight, which in turn produced valuable unplanned, as well as the planned, SPIBS ejection modes. The arcing in SPIBS was first identified by characteristics on the output channels during laboratory tests. The times of arcing were corroborated during the flight by the Transient Pulse Monitor.

C-2

For a short time period after the SPIBS cap opening, a cathode to anode discharge was maintained in the ion source chamber. This permitted the ejection of 1.7 keV positive xenon ions at currents with values up to 370 μA. During the major portion of the flight, during ascent as well as descent, the cathode to anode discharge as the source of ions was replaced by the cathode to keeper discharge which resulted in ejected currents of 8 μA at .84 keV and 12 μA at 1.7 keV. A third unplanned SPIBS mode of 1 μA at 200 eV was also obtained. Electrons were emitted by the same ion beam system during the neutralizer filament bias mode. The ion beam system was operated from 125 km on ascent to 111 km on descent, a period of 350 seconds, and except for a short interval after the cap opening sequence, particles were emitted in a programmed cycle; the overall repetition rate was nominally six seconds, but some longer and shorter cycles were created due to SPIBS arcing. The electron beam system showed signs of cathode poisoning but did emit low currents of high energy electrons.

As shown in Figure 2, the sensors showed that the payload charged negatively and then positively with respect to the ambient plasma during the charge ejection of positive and negative particles respectively. As shown in Figure 3, the Thermal Emissive Probes, Bipolar-Intersegment Voltmeter, and Surface Potential Monitor responded to changes in vehicle potential in quite similar ways and had high negative correlations with ambient plasma density. All three sensor types gave repeatable results for ascent and descent. Figure 4 shows more clearly that although the sign and magnitude of potentials measured were the same, the actual values differed between the probes. These differences can be explained by the input impedance and time constants of the devices used to measure the voltages, the particle fluxes at the location of the probes, the magnitude of the voltages being measured, and the probe geometry. An analysis of these factors, using probe characteristics and load line diagrams, indicates in conformity with the majority of experimental results that at high voltages the Surface Potential Monitor should give the highest potential differences followed by the Bipolar Intersegment Voltmeter, and the Thermal Emissive Probes. The analysis shows that the probes should agree at lower voltages, and, in fact, at measured potentials less than 50 volts all three probe systems gave the same results.

The following is a summary of some of the results from the measurements of the probes during charged particle emission of the flight.

1. Unneutralized beams of positive and negatively charged particles can be emitted from a sounding rocket payload.

2. The payload can be charged either positively or negatively using charge ejection techniques.

3. There was excellent correlation between vehicle charging and ambient plasma density.

4. During periods of positive ion emission greater than 7 microamperes, vehicle charging levels were independent of vehicle pitch angle and ambient neutral particle density.

5. There was compatible and sometimes cooperative operation of the prototypes of instruments intended as SCATHA payloads.

REFERENCES

1. Paul, A. L., and Wright, J. W., J. Geophys. Res. 68, 5413-5420 (1963).

2. Wakai, N., J. Geophys. Res. 72, 4507-4517 (1967).

TABLE 1. - PAYLOAD INSTRUMENTATION

PURPOSE ....

Instrument

Method of Operation

I Charge Ejection

A. Electron Beam System

Electrons emitted from an indirectly heated oxide coated cathode maintained at negative potentials with respect to vehicle ground.

B. Satellite Positive Ion Beam System

Positively charged xenon ions extracted from a Penning discharge maintained at positive potentials with respect to vehicle ground. Electrons emitted from a heated filament kept at negative potentials with respect to vehicle ground.

II Measurement of the Payload Ground to Ambient Plasma Potential Difference

A. Thermal Emissive Probe

Coupled hot filament - passive probe mounted on an extendable boom. Outer shields of mounts driven to track probe voltages. A high impedance voltmeter measurement of probe to vehicle potential difference.

B. Bipolar Intersegment Voltmeter

A high impedance direct current equilibrium voltage measurement and a low impedance high frequency transient voltage measurement made between the isolated payload section and payload ground.

C. Surface Potential Monitor

Electrostatic measurement of the back surface potential of isolated kapton and gold surfaces. Also measurements of the current flow from the samples to vehicle ground.

D. Retarding Potential Analyzer

Measurement of the current to a collector placed behind a grid as a function of the retarding voltage applied to the grid.

III Vehicle Discharge Effects

A. Transient Pulse Monitor

TABLE 1. (Continued)

Radiation measurement of rate and amplitude of high frequency electric signals from discharges.

B. Camera-Arc Gap System

Photography of the dielectric surface gap between pairs of pointed conductors extended from the electrically isolated payload and the main payload sections.

C. Camera-Sheath Measurement System

Photography of a wedge of space adjacent to the payload skin.

IV Auxiliary Payload Measurements and Controls

A. Pitch Angle Measurement

B. Telemetry

C. Programmer

TABLE 2. - ENVIRONMENTAL FLIGHT CONDITIONS

Parameter	Condition
Magnetic Activity Index K_p	0 (Quiet)
10.7 cm Solar Flux	92
Wind	Light
Sky Visibility	Overcast
Solar Azimuth	71.3°
Solar Depression	64.9°
Lunar Azimuth	272.3°
Lunar Elevation	34.0°
Lunar Fraction Illuminated	92.2%

TABLE 3. - FLIGHT EVENTS SEQUENCE

TIME AFTER LAUNCH (Sec)	ALTITUDE (km)	EVENT
53	53	Motor Burnout
64	74	Despin
66	78	Motor Separation
69	83	Tip Blown
69	83	Boom Doors 1&2 Blown
69	83	Aerospace SSPM Door Blown
69	83	RPA #2 Door Blown
71	87	RPA #1 Door Blown
71	87	Camera Door Blown
81	105	TEP and RPA H.V. On
87	114	Electron Gun Cap Blown
94	125	Ion Gun Cap Blown
94	125	Camera On
95	127	500V TEP Boom Extended*
103	139	Ion Beam System On
157	205	Electron Beam System On
264	257.7	Apogee
443	111	Power Off

* 300V TEP Boom never fully extended. It may have remained totally inside the payload, or extended out to where the outer probe sphere was approximately 13 cm from the payload skin and the inner probe sphere was approximately 2.5 cm from the payload skin, or moved about somewhere between the limiting values.

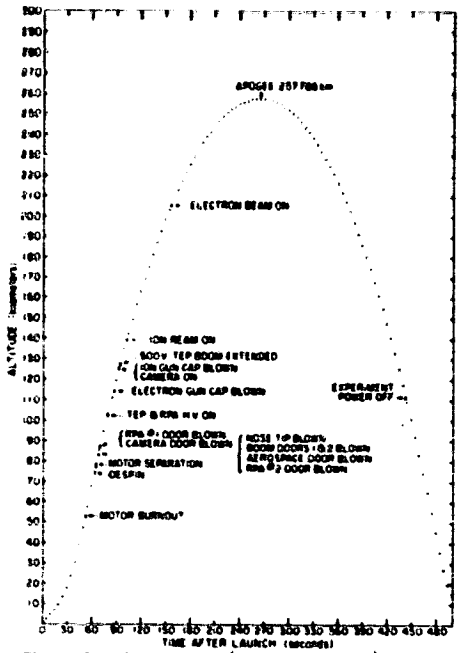

Figure 1. - Charging rocket A3L 603 flight sequence.

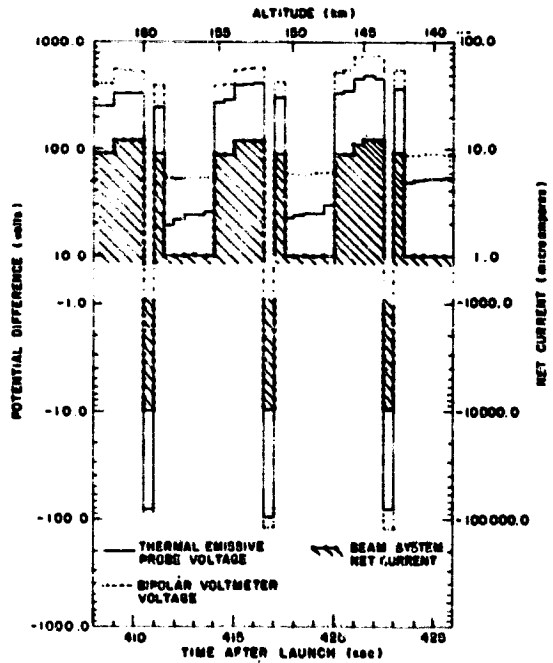

Figure 2. - Three program cycles.

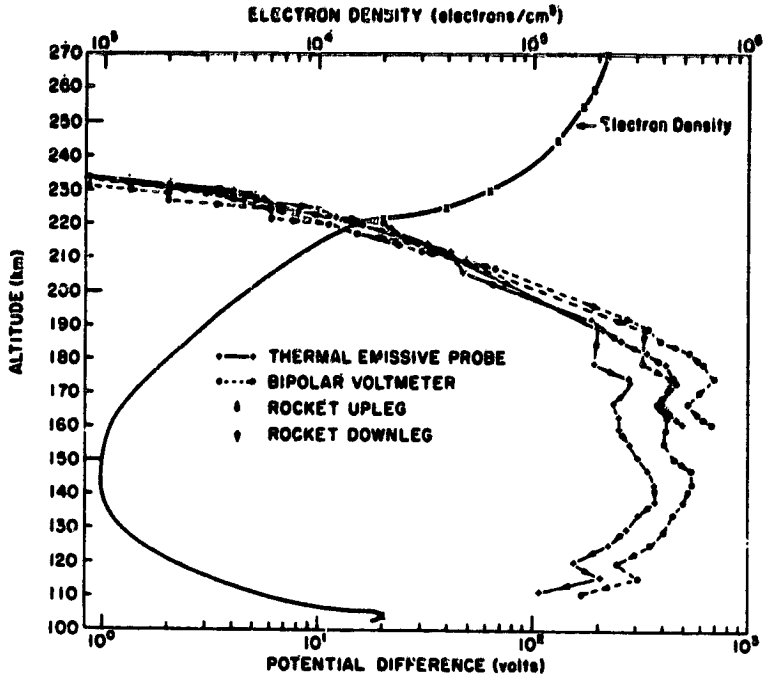

Figure 3. - Vehicle-to-ambient potential difference and electron density as function of altitude.

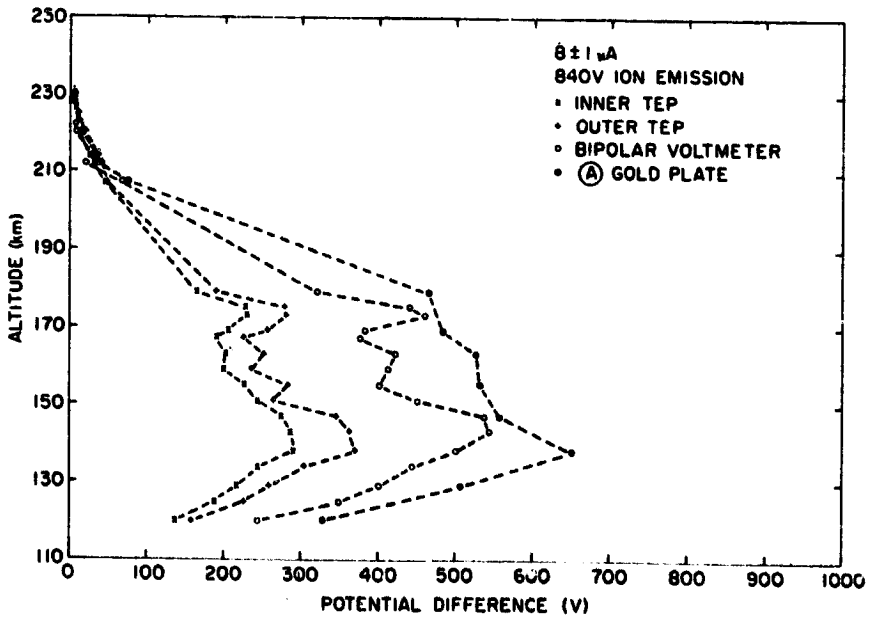

Figure 4. - Comparison of potential difference measurements.

DESCRIPTION AND CHARGING RESULTS FROM THE RSPM*

P. F. Mizera, E. R. Schnauss, and R. Vandre
The Aerospace Corporation

E. G. Mullen
Air Force Geophysics Laboratory

SUMMARY

Representative satellite materials, to be flown on STP-78-2 in 1979 on the SSPM instruments, were included as part of the AFGL Rocket payload flown from White Sands Missile Range on January 21, 1978. Potentials as high as ~ +1100 volts on the conductor and ~ +400 volts on the insulator were recorded by the RSPM near the minimum in the electron density vs altitude profile. In addition to the charging potentials measured during ion gun operation, sample charging currents also were recorded with time resolutions near 30 milliseconds. These results demonstrate the validity of the experiment concept of the SSPM on SCATHA.

INTRODUCTION

Spacecraft charging during natural and artificial events including solar eclipse will be studied in detail on the STP 78-2 (SCATHA) satellite. The charging of various thermal control materials [Al/kapton, OSR, Astroquartz, Ag/Teflon] will be measured by three Satellite-Surface-Potential-Monitors (SSPM), each capable of making measurements on up to four different samples. Specifically, each SSPM contains separate electronics to provide the back surface potential and associated bulk or induced currents of individual samples. The Rocket-Surface-Potential-Monitor (RSPM) is essentially one-half of an SSPM containing two samples, a gold plated magnesium conductor and an aluminized kapton insulator.

One of our primary purposes for including a modified version of the SSPM instrument on the AFGL rocket was to verify the concept of measuring back surface potentials to provide front surface values during artificial charging events. It was not feasible to directly measure the front surface potential of a sample material in space. The major design effort for the SSPM/RSPM was the development of a technique for measuring the rear surface potential of the samples so that the front surface potential could be derived.

---

*Work performed under USAF Contract F04701-78-C-0079

Physical Description

The RSPM is packaged in a rectangular, gold-plated, magnesium box, 33 cm by 16.5 cm by 5.1 cm and weighs 1.6 Kg (Fig. 1). The box, machined from a single piece of magnesium, contains four cells for housing circuitry, instrumentation and samples. Two adjacent cells on one side (each approximately 16 by 16 by 2.5 cm) contain potential and current measurement instrumentation and provide mounting for the samples. The signal conditioning circuitry, power supplies and interface hardware are behind the sample assemblies.

Sample Materials

The two samples used on the RSPM were a sheet of 5 mil kapton, aluminized on one surface, and a gold plated magnesium plate electrically isolated by a polycarbonate frame.

The aluminized back surface of the kapton sample was attached to a copper clad fiberglass sample board (Fig. 2) using conductive epoxy as an adhesive. The sample board contained a centrally located hole (.635 cm dia.) concentric with a circular area of the same size etched free of aluminum on the kapton sample. The Monroe electrostatic field sensor was mounted with its sensitive aperture centered under the hole in the sample board. This sensor was spaced about .25 mm from the back surface of the kapton sample. Surface charging on the kapton sample induced a corresponding potential on the back surface (cleared of aluminum) which was detected by the electrostatic sensor.

Bulk and induced currents, on the back side of the kapton sample, were collected by the rear surface electrode system (Fig. 3). They were conducted to ground through a sensitive electrometer.

The gold/magnesium sample plate was mounted in a Lexan 500 frame 2 mm above the Monroe sensor holder assembly. The plate, being an isolated conductor, allowed simple calibration by direct voltage stimulation of the front surface. The currents appearing in the sample board electrometer circuit were limited to capacitively induced currents since the sample was electrically isolated.

Signal Conditioning

The RSPM outputs were analog 0 to 5 volt DC signals. Since the SSPM outputs are digital, modification of the telemetery interface was required. A fresh approach was needed for the problem of a logarithmic current amplifier covering in excess of four decades of positive and negative current with the resulting output spanning zero to +5 volts DC (Fig. 4). The small temperature changes forecast allowed a simple diode feedback to be used for the logarithmic function. The second stage op-amp is driven to the rails by small current signals. Larger currents cause the drop across the feedback diodes to increase into the conduction region thereby reducing the voltage to the final amplifier. This results in an output at zero or +5 volt, depending on polarity, for zero input current. Larger currents cause the output to go toward +2.5 V. The positive and negative current curves cross each other at the 2.5 V line when the input is 5×10^{-7} A. (Fig. 5). This circuit provides a very sensitive indication of small currents, and allows sufficient dynamic range.

Temperature Measurements

Temperature measurements of each sample board were provided by a standard thermistor whose resistance was converted to a 0 to 5 volt output. Temperature ranged from ~16°C down to 6°C for kapton and remained relatively constant at ~18°C for the gold plate sample assembly.

Sample Calibration

The potential calibration was made using direct contact of an electrode on the front surface of the sample. The calibrating voltage was incremented in 100 volt steps between -3000 volts and +3000 volts (Fig. 6). A nonlinear calibration curve was used to provide more sensitivity to small potentials while still preserving the anticipated dynamic range requirement.

Current calibration was made by directly injecting a known current from a constant current source into the input of the electrometer circuit. The range for both positive and negative currents was 10^{-6} A to 10^{-10} A.

Temperature calibration was performed by taking numerous measurements after non-operating soaking periods at each temperature. The calibrated linear range was -10°C to +25°C.

RESULTS

The primary purpose for including the RSPM on the Air Force Geophysics Laboratory (AFGL) rocket was to test the feasibility of monitoring a conductor and an insulator with Monroe electrostatic sensors during gun operations. The flight also provided a qualification for the non-standard Monroe flight assembly on STP 78-2. In the previous paper given by Cohen et al., it was clearly shown that the upper stage of the rocket achieved negative potentials as high as 1000-1100 volts near electron densities of $10^3/cm^3$. These calculated densities were for altitudes near 150 km and corresponded to flight times near 111 sec and 418 sec.

For display purposes, we need to compare the RSPM measurements with a potential and a current monitor that describes the incident flux on the samples. The outer Thermal Emissive Probe (TEP) was used as a potential monitor and the Retarding Potential Analyzer (RPA) 2 was used as a current monitor.

Figure 7 shows these two measurements for the downleg low altitude portion of the flight. The top curve is the calculated electron density described in the previous presentation. RPA 2 is in units of nanoamperes and the TEP is in volts. The bottom two curves are the back-surface potentials of the gold plated magnesium sample and the aluminized kapton sample. During the time following ~395 seconds, the xenon ion source went through its pre-programed cycle that was discussed in the previous paper. In summary: ions are emitted at ~9 μamps with energy near 840 eV for 1 second, 12 μamps at

1.7 keV for 1.5 seconds, 80 eV electrons at approximate 10 milliamps for .5 seconds, ions at 840 eV at 9 μamps for .5 seconds followed by ≤200 volt ions at 1 μamp for 2.5 seconds to complete the cycle.

Both the conductor and insulator sample track the potential monitor throughout this time period. Average potentials are indicated. The time constants for the RSPM voltage sensors are much faster than the 0.5 sec averages shown in Fig. 7. The slow increase in voltage for the highest ion step (1.7 keV) is duplicated by the steady increase in RPA current. The most significant aspect of the potential profiles is when the ion gun cycles to low voltage for ~2.5 sec. The potential monitors (including the TEP) indicate a drop in potential of the rocket chassis. The sample potentials, measured by the RSPM remain at the initial value. If the potentials measured from the RSPM samples were due only to changes in the reference level in the circuitry, then the potential would drop when the chassis swings toward zero. The observations that the potentials remain up until a negative current is emitted from the gun (that drives the chassis positive to ~80 volts) is definitive proof that both the gold magnesium and kapton RSPM samples were charged during this flight. [A detailed description of the charging profiles has not been done at this time.]

Figure 8 shows the same measurements as the previous figure but for the upleg portion of the flight where the calculated density is a minimum. During the initial stages of the flight, the response to the ion gun was different. For example at T = 103 sec into the flight, the TEP measured values near 1000 volts with a collecting current in the RPA greater than 10 namps. As the gold magnesium conductor recorded values near 1100 volts, the kapton averaged ~300 volts. A thorough analysis of ion produced secondary electron production would have to be performed to compare with these numbers. Another interesting aspect of this data shows the first 0.5 sec average to be the highest value attained by the kapton back surface. While the gold sample continued to increase for the next second, the kapton potential decreased. This example will be addressed in more detail in Figure 9.

Another region of interest occurred near 108 sec. Negative current was recorded in the RPA between 10-30 namps for ~8 sec. The TEP monitor measured a negative potential change on the rocket chassis from -60 to -250 volts. The kapton potential changed from -3 to -15 volts. The gold plated magnesium sample, however, remained at -25 volts. A preliminary interpretation is that secondary electrons, produced by electron fluxes impinging on the sample, prevents significant charging. Laboratory measurements using electron beams show that significant charging on gold doesn't occur until electron energies greater than ~4 keV are reached.

One of the longest charging profiles in the entire flight occurs near 123 sec. The gold magnesium reached equilibrium in one second as does the TEP monitor. However, kapton continues to increase for several seconds.

Figure 9 shows the high resolution data from the RSPM. Each point is a 30 millisecond sample of the kapton potential and current on the left side and the gold plated magnesium voltage and induced current on the right side. This figure gives an indication of the time resolution of the RSPM to charging in space. For example the decay of the charging current on the gold sample falls by 1/e in less than 20 milliseconds. The rise time (1/e) of the kapton sample is approximately the sampling time. This example was shown in the previous figure and showed a drop in the kapton voltage after the initial 0.5 sec. or so. From the bulk current monitor on kapton, there is no obvious reason why the back surface voltage should decrease.

The final figure shows the RSPM instrument parameters. Based on our preliminary analysis, the major objectives were met with complete success. We would like to suggest that operational programs concerned with material charging in orbit should consider flying such a monitor for a direct in situ measurement. If the SSPM instruments on SCATHA perform as well as the RSPM instrument did then we can expect a wealth of useful material charging data in the coming year.

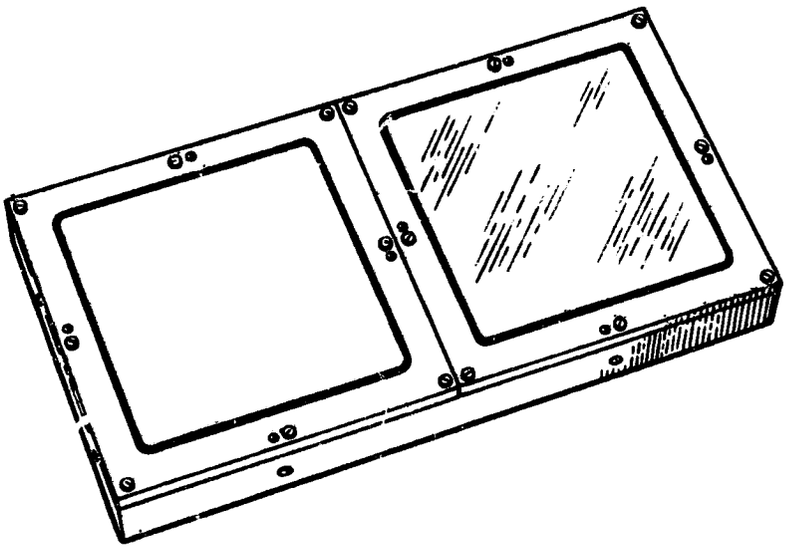

Figure 1 A sketch of the Rocket Surface Potential Monitor with aluminized kapton and gold plated magnesium samples

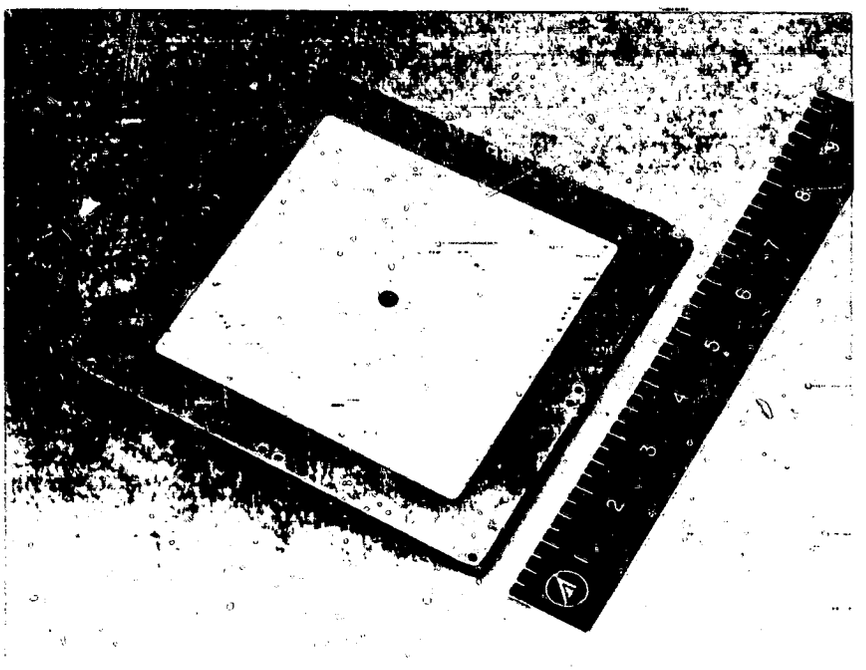

Figure 2 Typical SSPM sample board on which the RSPM kapton sample was mounted. Active current collecting area is approximately 5 inches square or ~ 160 cm^2.

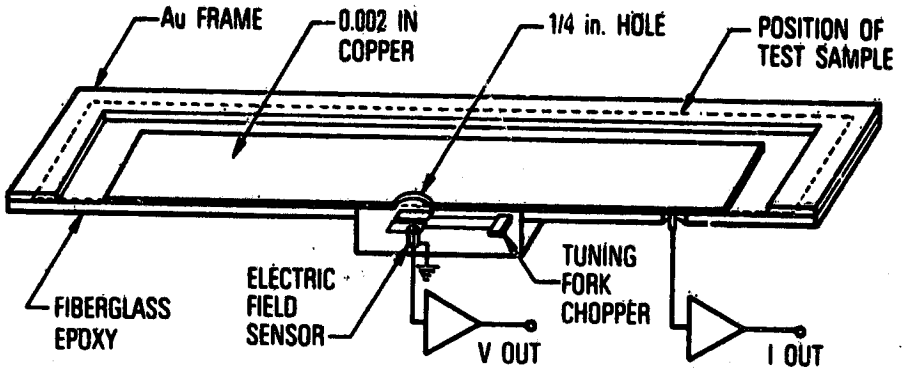

Figure 3 Schematic representation of the dielectric sample holder and associated sensors. The electric field sensor is positioned under the back surface of kapton with a 0.25 inch diameter aluminum etched region.

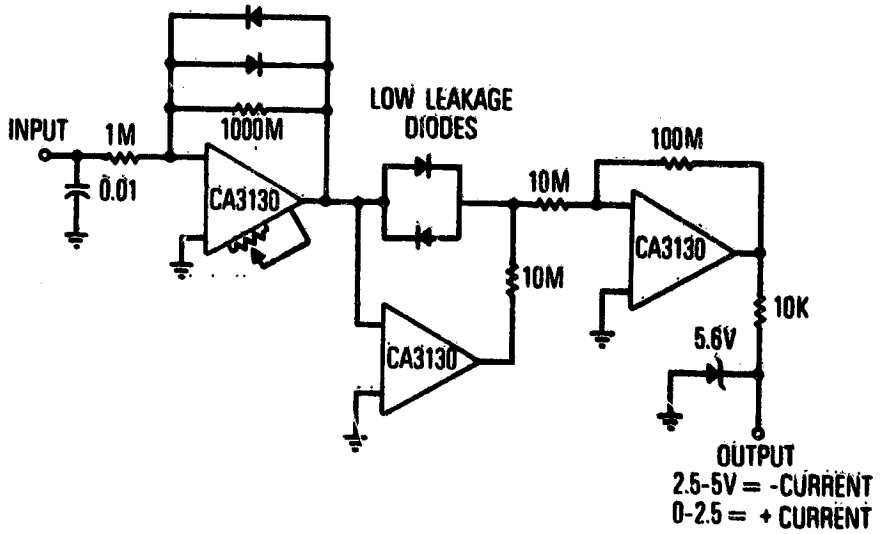

Figure 4 Schematic diagram of the logarithmic current amplifier designed for the RSPM that takes the digital electrometer outputs and converts them to analog T/M.

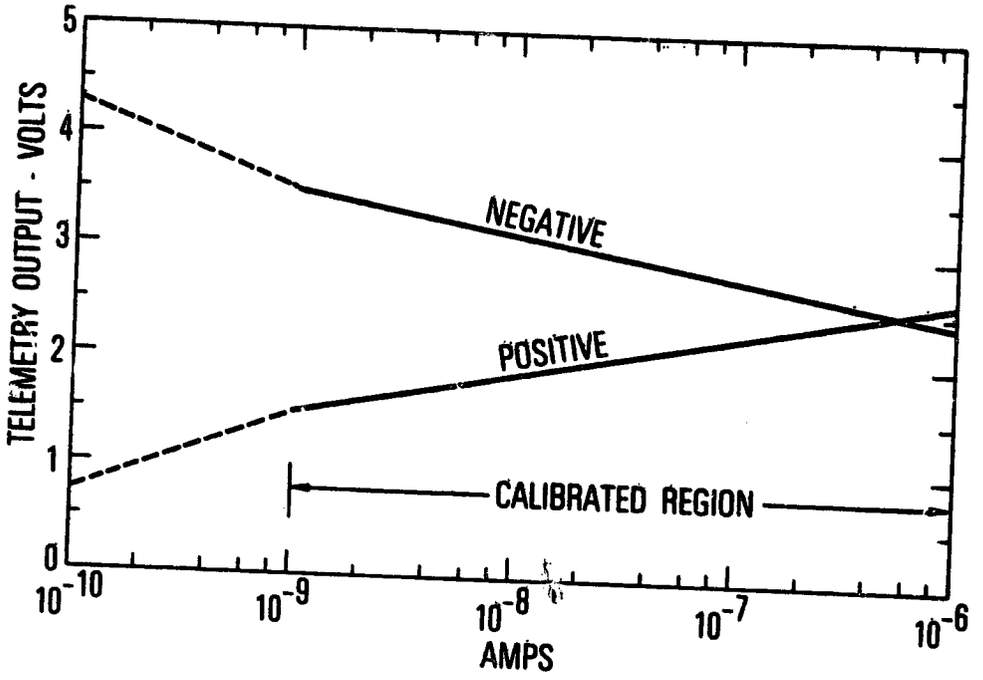

Figure 5. - RSPM current calibration.

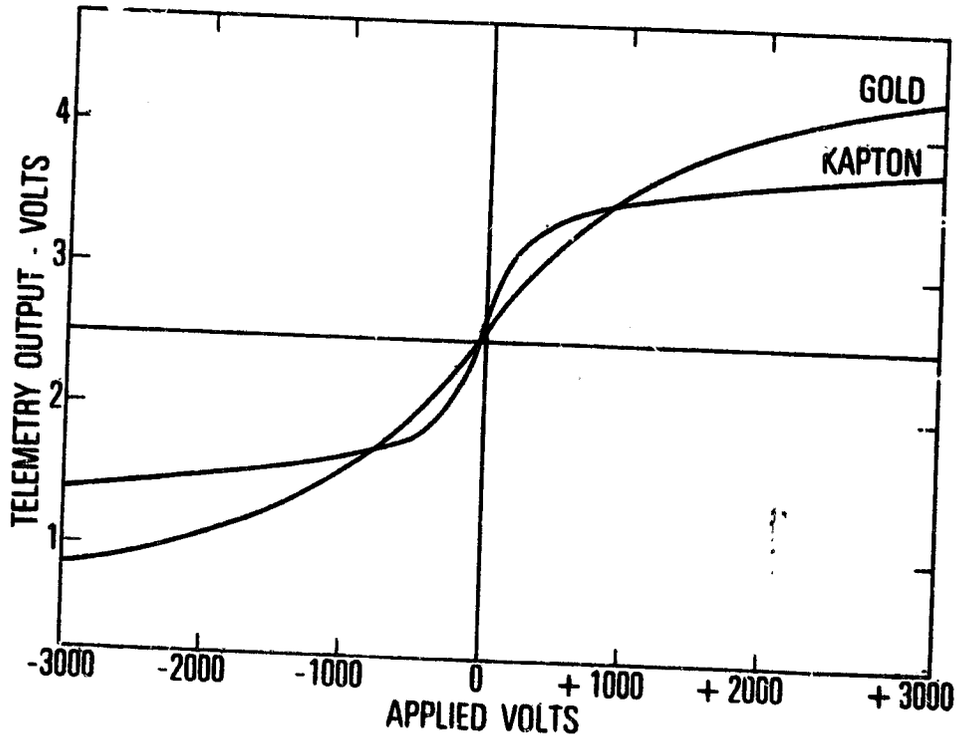

Figure 6. - RSPM voltage calibration.

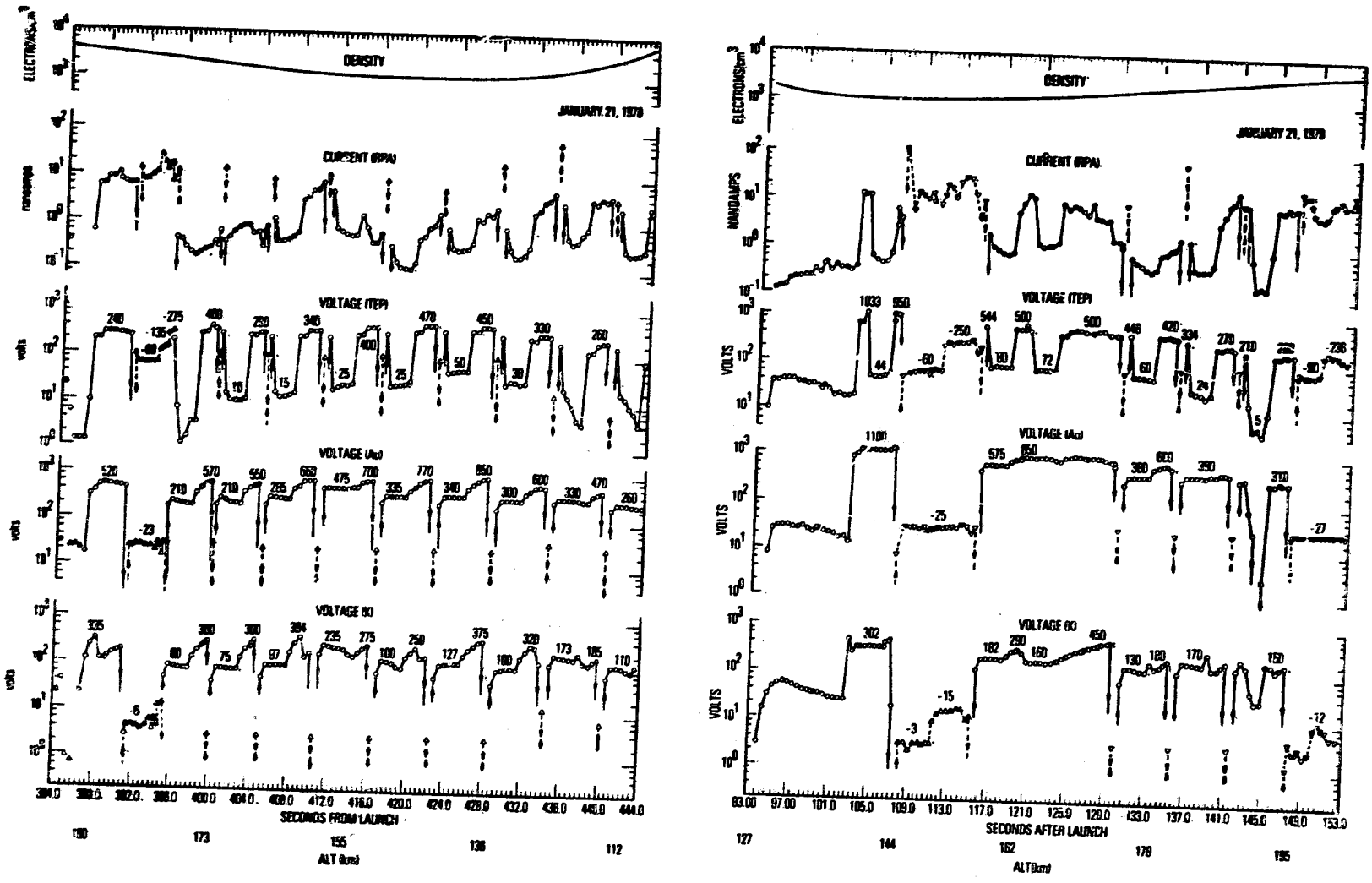

Downleg (Figure 7) and Upleg (Figure 3) charging results from the rocket flight showing estimated electron density at the top as a function of flight time and altitude. Return current to the rocket is measured by a Retarding Potential Analyzer (RPA) and the potential difference between the environment and the rocket chassis is provided by the Thermal Emissive Probe (TEP). Back surface voltages are shown for the gold sample and kapton sample from the RSPM.

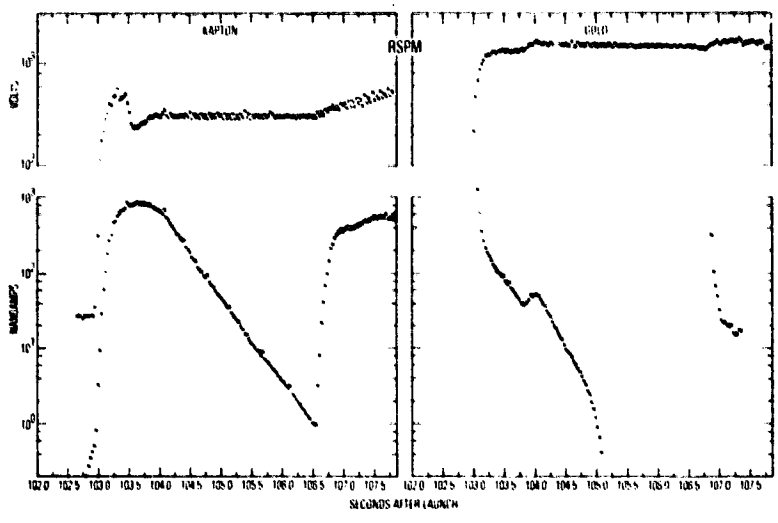

Figure 9 High resolution (~ 30 m sec/sample) data from potential and current outputs of the RSPM. The charging times of the kapton and the isolated gold plated conductor can be easily resolved.

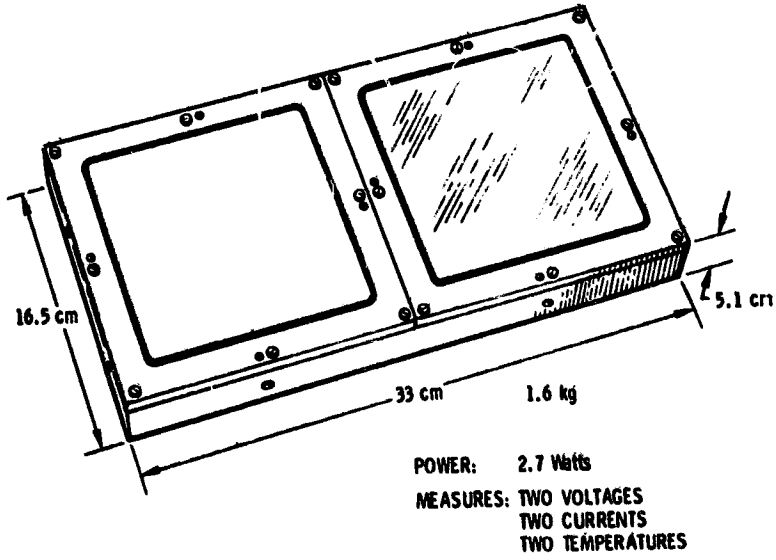

Figure 10 Characteristics of the RSPM.

D/6

N79-24011

THE CAPABILITIES OF THE NASA CHARGING ANALYZER PROGRAM*

I. Katz, J. J. Cassidy, M. J. Mandell,
G. W. Schnuelle, P. G. Steen
Systems, Science and Software

J. C. Roche
NASA Lewis Research Center

ABSTRACT

Desirable features in a spacecraft modeling code are enumerated. The NASCAP (NASA Charging Analyzer Program) is discussed in terms of its approach to the problem. Samples of problem setup and output are provided which demonstrate the ease with which the program can be used. A simple but interesting case of spacecraft charging is examined and other applications are discussed.

INTRODUCTION

The basic concerns of a computer spacecraft model can be broken down into five areas.

1. Features of the spacecraft itself
2. Features of the environment
3. The spacecraft-environment interaction
4. Man-hours to set up and computer time to run a calculation
5. A way to verify the model

In modeling the spacecraft itself, the point is to get in as much detail as can reasonably be included. This will vary depending on the type of model being used. The features desired (Whipple (ref. 1)) are first, some geometrical detail, such as the basic shape of the spacecraft body and any protrusions such as booms and antennae. Second, one would want to include which parts of the surface are bare conductor and which are dielectric coated. Third, it would be nice to have some representation of the electrical circuitry connecting parts of the spacecraft surface.

*This work supported by the National Aeronautics and Space Administration, Lewis Research Center, under Contract NAS3-21050.

It is also important to decide what approximations go into the environment surrounding the spacecraft. The most basic decision is how to model the ambient plasma. Can you include the region far from the spacecraft, and get a detailed look at the region close in? Can you specify normal and extreme conditions? Does the plasma charge in time? Other aspects of the environment that are of concern are the sun, the plasma sheath, and particle trajectories.

The spacecraft-environment interaction is mainly a matter of particle currents to and from the spacecraft surface. The important charging currents are

1. Incident electrons
2. Photocurrent
3. Incident protons
4. Secondary electrons from electron impact
5. Secondary electrons from proton impact
6. Electron backscatter

These processes vary around the spacecraft surface, depending on local potential, surface material, and solar illumination. An ideal model would take all this local information into consideration when calculating particle fluxes.

Computer time for spacecraft modeling can be prohibitive. A model that is general ends up solving a series of equations with hundreds or thousands of variables. An exact solution is enormously expensive, and it may be hard to get convergence from an iterative solution. Much care must be put into this aspect of the problem, lest an otherwise elegant modeling program start to impersonate an infinite loop.

The most expensive way to verify a modeling program is to build a spacecraft like the model and send it up. Other, more reasonable techniques, are to model ground experiments, to check answers for reasonableness, and to test the program on known problems.

NASCAP APPROACH

As we have seen, the physics which must be examined in order to model spacecraft charging presents a problem of formidable dimensions. It would be impractical to develop a computer code that was state of the art in every aspect of the problem. By placing restrictions on the class of problems to be examined we have been able to construct the NASA Charging Analyzer Program which provides useful information in those cases of most practical interest. It is most applicable to the high voltage charging caused by magnetospheric substorms.

Our approach has been to limit the range of ambient environments to those whose Debye lengths, λ_D, are large compared to object dimensions. For magnetospheric substorms this is definitely true.

$\theta_e \sim 10{,}000$ eV

$n_e \sim 1$ cm^{-3}

$\lambda_D \sim 0.7$ km

Only for the very largest conceivable spacecraft are object dimensions comparable to Debye lengths. For finite Debye lengths we have included ambient plasma screening approximations, albeit of modest applicability.

Overall, we have modeled all aspects of the problem except electromagnetic wave propagation. Our idea has been to use the best available analytical theories wherever possible and to minimize the brute force number crunching. By doing this we have been able to combine good treatments of ambient environment, sheath, complex object, and electrical and particle interactions into a single code. This is done by using known physics and developing approximate models where necessary. For example, NASCAP contains analytical approximations to electron backscatter as a function of electron energy and angle. While not as accurate as Monte Carlo transport results, these formulations do give reasonable yield estimates and can be evaluated quickly at hundreds of surface locations each timestep. Thus we obtain reasonable estimates in reasonable amounts of time as opposed to best estimates regardless of cost. This philosophy permeates the code. Where quasi-analytical models were necessary but unavailable, we have developed them.

The procedure followed in the code is to approximate the spacecraft in a 3-D Cartesian grid. Free space around the satellite is provided by nesting grids within grids where each grid has a linear dimension twice that of the grid it surrounds. There can be an arbitrary number of these nested grids. However, the more grids, the longer the computer time per calculation (fig. 1).

All parts of the spacecraft must remain in the innermost grid, except for booms which can extend into several grids. The object itself is composed of an assembly of cubes, sliced cubes, plane surfaces, and skinny cylinders, as shown in figure 2. Each surface can be of an independently specified material, with up to 15 different materials permitted (fig. 3). Certain classes of surfaces may be subdivided for higher resolution.

Object definition is by far the most complicated aspect of using a three-dimensional computer code. To make the program easy to use, NASCAP provides an extremely simple object definition

language. Complex three-dimensional spacecraft can be described with a minimum of effort. The satellite shown in figure 4 is a good example. The central structure is octagonal with a gold circumference and aluminum top and bottom surfaces. The two planar sheets represent solar cells with kapton covering the back surface. They are attached to the main body with kapton coated cylinders. This object was defined using 31 brief lines of input (fig. 5). The simple object definition commands are fully explained in the NASCAP User's Manual (ref. 2).

Once the object definition is complete, the program alternately calculates charge accumulations on surfaces and potentials caused by these charges. Due to the variety of timescales in the system, the algorithm used to advance the charge distribution in time is extremely complex, so complex that it uses a couple thousand element self-generated capacitor model as its own internal estimator.

NASCAP produces a variety of printed and graphical output. The fundamental idea is to help the user follow the progress of the calculation (figs. 6-14).

The first graphic output is a two-dimensional view of the spacecraft with surface cells shaded to show the material types. Each surface cell is individually classified by material, with up to 15 different material types allowed.

Next is a three-dimensional perspective view of the spacecraft without hidden line removal. This is helpful in tracking down object definition problems. It is followed by a view from the same perspective with surface cells outlined. In this surface cell plot, hidden lines are removed. The user gets a quick and accurate feeling for the defined object. The routine that generates these plots also calculates exposed surface areas for determining photoelectron emission.

These plots are generated at object definition time, before the actual satellite charging begins. The major outputs of the charging calculation are the flux breakdown printout and potential contours.

The flux breakdown printout shows, for any surface cell(s), the charging currents operating on that cell. Each individual surface cell requires a separate calculation. By requesting flux breakdown printouts, the user can closely follow the charging process at any point on the surface.

Contour plots are an efficient way to show what's happening to the electrostatic potential both near the spacecraft and far away. The user can look at the potential contour plots generated every time cycle and get a good feeling for global changes in the spacecraft sheath.

NASCAP detector routines plot flux density versus energy of particles reaching the detectors. Detectors can be placed, at the user's discretion, on any surface cell.

The emitter routines plot trajectories of particles emitted at various energies. These trajectories, along with potential contour plots, give a very good idea of fields surrounding the spacecraft or test tank object.

Finally, if local electric field stresses exceed some user specified threshold value, a message is printed and the code redistributes charge as if a discharge had occurred.

VALIDITY OF THE MODEL

With a model as broad in scope and as complex (over 400 subroutines) as NASCAP, the immediate question is "How do you know that it gets reasonable answers?" So that we have confidence in NASCAP results, testing and comparing to analytical results has been a major part of the development program. The accuracy of the various components have been examined in configurations simple enough to determine their inherent accuracy.

Since the capacitances of simple objects such as spheres, cubes and cylinders are known quite well, we have used these to determine how well the potential routines work. For all cases the NASCAP results were within 10 percent of analytical predictions, and for objects of more than a zone resolution and for booms of radius much less than the grid spacing, the NASCAP results were accurate to a few percent. The electric fields in space were of corresponding accuracy near the satellite and increasing accuracy away from the vehicle. The accuracy of the potentials are limited only by the ability of the finite element interpolation functions to represent the true solution. For complex objects, the NASCAP code uses the same algorithms and the accuracy should be comparable. Since NASCAP automatically takes into account mutual capacitances, it is a vast improvement over hand generated capacitor models for complex spacecraft.

NASCAP assumes that charge is accumulated on, as opposed to deposited within, dielectrics. Bulk conduction is included. We have performed detailed one-dimensional calculations of charge transport within dielectrics, and have found this to be a reasonable approximation for electrons of a few to tens of kilovolts in all but the thinnest of dielectrics. It is also an approximation that can easily be modified in the future if the need arises.

The charging currents are the algebraic sum of incident fluxes and backscattered, secondary, and photoemitted electrons. For spherical test cases we have compared NASCAP reverse

trajectory currents with spherical probe formulas (ref. 3). Depending on the number of trajectories sampled the results were in reasonable agreement, the largest errors due to the differences between numerical and analytical integrals over angle of the backscatter and secondary emission formulas. Thus the two basic requirements of a charging calculation, the potential and charge accumulation, are performed well by NASCAP.

The NASCAP material interaction models have been developed from literature results. Their predictions are being compared with laboratory experiments and are the subject of another paper in this session. It should be pointed out, however, that NASCAP accepts parameters for these models as input and that the models themselves are contained in very short, easily replaceable subroutines. Consequently, modifications and improvements in the formulations can be made very simply if needed.

The particle trajectory algorithms are second order accurate in particle timesteps insuring good conservation of energy and magnetic moment. Orbits are followed beyond the outermost grid boundaries by using an extrapolation of the monopole potential. This allows long excursions of emitted particles to see if they return to the spacecraft.

The algorithm employed to integrate charging currents over a timestep is quite complex to ensure physical results. Rather than describe the technique in detail, we present a calculation which illustrates how it works.

A simple example, which nevertheless displays some of NASCAP's usefulness as a model, is the case of a spherical object in sunlight. Since the photocurrent is larger than the incident electron current, a capacitor-current balance model would lead one to the conclusion that a sunlit surface will remain at a positive potential relative to the surrounding plasma. However, the NASCAP charging current integration routines recognize that space charge limiting prevents photoelectrons and secondary electrons from supporting a potential barrier of more than a few volts. This feature, combined with the multidimensional aspects of the potential leads to a very different equilibrium, one with the illuminated surfaces a kilovolt negative.

We ran NASCAP for the case of a teflon coated sphere in sunlight. The environment for this case is an isotropic, Maxwellian plasma with a temperature of 20 keV and a density $n_e = n_i = 1\ cm^{-3}$. Sunlight was incident on one side of the sphere (fig. 15).

Figures 16-22 show the time development of the electrostatic field. (The satellite-sun line lies in the plane of these figures. Dark and sunlit cells are differentiated by shading.) For the first $\sim$0.1 second the sphere charged uniformly. Over the next few seconds, the negative charge accumulated by the shaded

surfaces began to dominate the electrostatic field, causing a saddle point to appear in front of a sunlit surface. At about 10 seconds the potential at the saddle point became negative. The sunlit surface maintained a potential a few volts positive relative to the saddle point. Final steady state is reached with the sunlit surface at -1.0 kV and the shaded surface at -3.6 kV.

The final steady state potentials were reached at time $t \simeq 10^4$ sec. This involved some 30 timesteps, and used total computer time of about one-half hour. Thus in a reasonable amount of computer time NASCAP can provide good physical insight into charging phenomena, insight which is unobtainable using simpler computer models.

4. APPLICATIONS OF NASCAP

NASCAP is designed primarily to give engineering estimates of spacecraft potentials during magnetospheric substorms. It also can provide detailed particle spectra for a given environment and spacecraft potential configuration in order to aid in interpreting results of scientific experiments. As of this time the applications of NASCAP have been limited to the comparison with laboratory material charging test results and to the generation of models of a few scientific spacecraft. Comparisons have been done to validate the material properties portion of the code. A later paper in this section (Roche, et al.) will discuss the results of these studies.

One application of NASCAP which is of engineering importance is the study of active charging control. The operation of onboard charged particle beams has been proposed as a means of minimizing the effects of ambient environment spacecraft charging. NASCAP features an emitter algorithm that models the trajectories and charge transfer effects of such beams. For example, we have placed a one kilovolt, one milliampere electron emitter on a satellite precharged to -2.5 kV. The potentials on spacecraft ground and on an insulated surface as a function of time are shown on figure 23. Notice that the insulator will differentially charge to a substantial negative potential. Sample particle trajectory plots during the charging phase are shown in figure 24. By modeling such systems NASCAP can estimate their utility and point out any severe design problems, so that actual flight experiments have the best chance for success.

An important problem, particularly in the future, is the interactions of large space structures. While not specifically designed for this application, the finite Debye length sheath treatment in the NASCAP code will combine with the reverse trajectory particle flux routines to give good estimates of space charge limited charge collection. The present algorithm employs linear

Debye shielding (figs. 25, 26). In the future, models of the ambient plasma sheath more relevant to dense collisionless plasmas, will be implemented. The object definition routines can already handle objects of large size by decreasing the object resolution (fig. 27).

The most ambitious application to date is the generation of the SCATHA model. This model utilizes the full capabilities of the code. The model and some preliminary calculations are the subject of the following paper.

REFERENCES

1. Whipple, E., "Proceedings of the Spacecraft Charging Technology Conference," 24 February 1977, p. 889.

2. Cassidy, J. J., "NASCAP User's Manual – 1978," NASA CR-159417, 1978.

3. Katz, I.; Parks, D. E.; Mandell, M. J.; Harvey, J. M. Brownell, Jr., D. H.; Wang, S. S. and Rotenberg, M., "A Three Dimensional Dynamic Study of Electrostatic Charging in Materials, NASA CR-135256, August 1977.

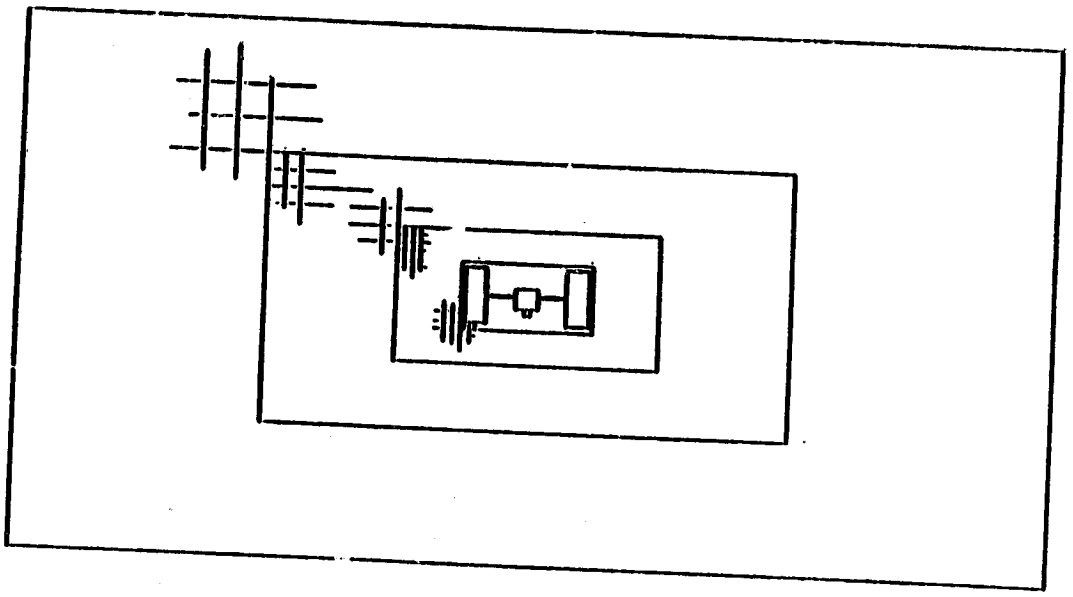

Figure 1. A two-dimensional view of the first four nested meshes. Each succeeding mesh increases the volume of calculation space by a factor of eight. Calculation time is roughly linear with the number of meshes.

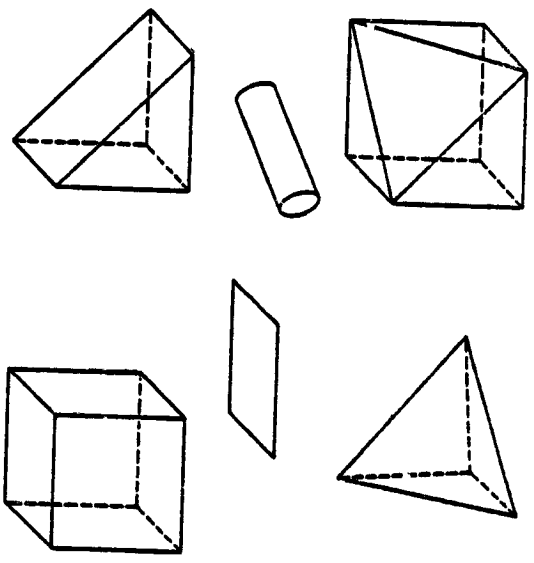

Figure 2. NASCAP can simulate virtually any object that can be built from these fundamental shapes – cube, three types of sliced cube, planar square, and thin cylinder.

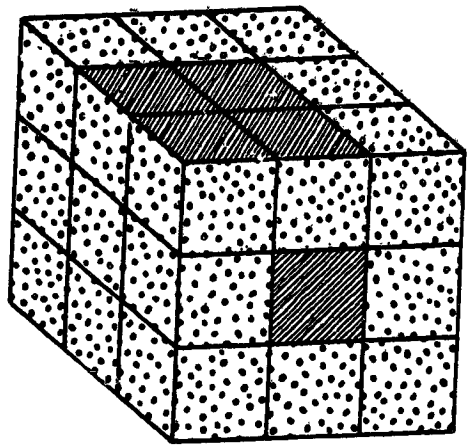

Figure 3. The spacecraft surface is made up of as many as 1200 surface cells. Each cell is assigned a material type and an underlying conductor. The surface cell may represent either bare conductor or dielectric layer.

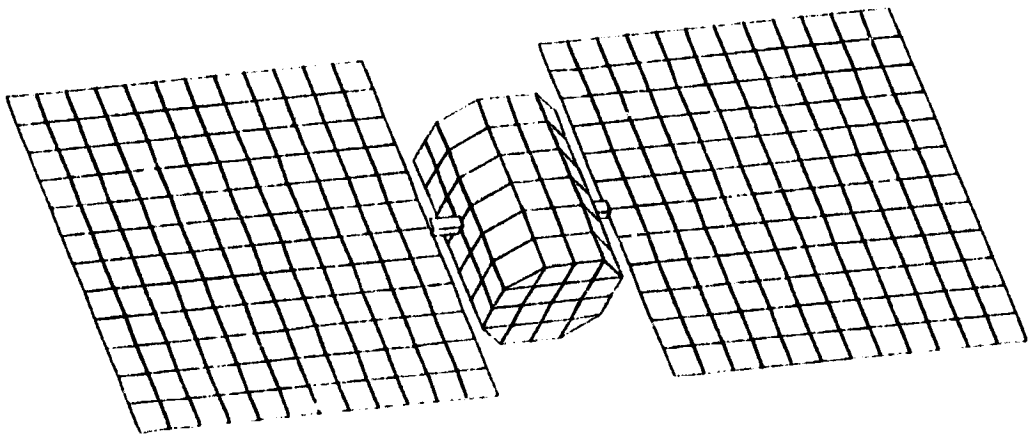

Figure 4. Paddle satellite. A geometrically complex object with four types of surface material.

```
[MATERIAL PROPERTIES DEFINITIONS]

OCTAGON
AXIS          -3    0    0          3    0    0
WIDTH          4
SIDE           2
SURFACE   -              ALUMINUM
SURFACE   C              GOLD
SURFACE   +              ALUMINUM
ENDOBJ
PLATE
CORNER        -6    0   -15
DELTAS        12    0    12
TOP       +Y             SIO2
BOTTOM    -Y             KAPTON
ENDOBJ
PLATE
CORNER        -6    0     3
DELTAS        12    0    12
TOP       +Y             SIO2
BOTTOM    -Y             KAPTON
ENDOBJ
BOOM
AXIS           0    0     2    1    0    0    3    1
RADIUS    0.2
SURFACE   KAPTON
ENDOBJ
BOOM
AXIS           0    0    -2    1    0    0   -3    1
RADIUS    0.2
SURFACE   KAPTON
ENDOBJ
ENDSAT
```

Figure 5. Object definition. The object in the preceding figure (paddle satellite) is defined by these commands.

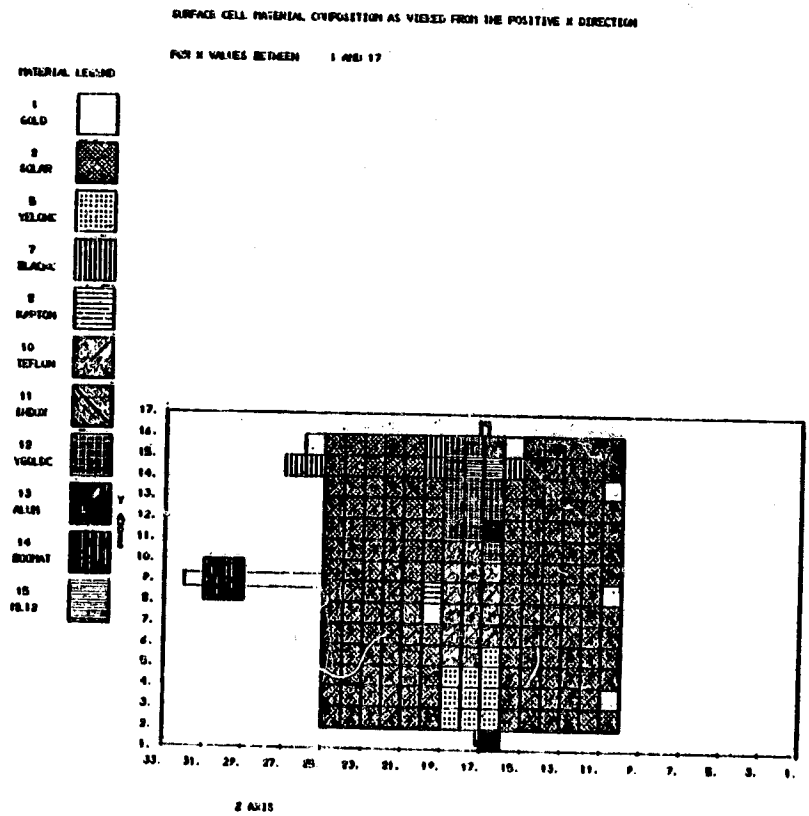

Figure 6. Satellite illustration plots show the material composition of each surface cell.

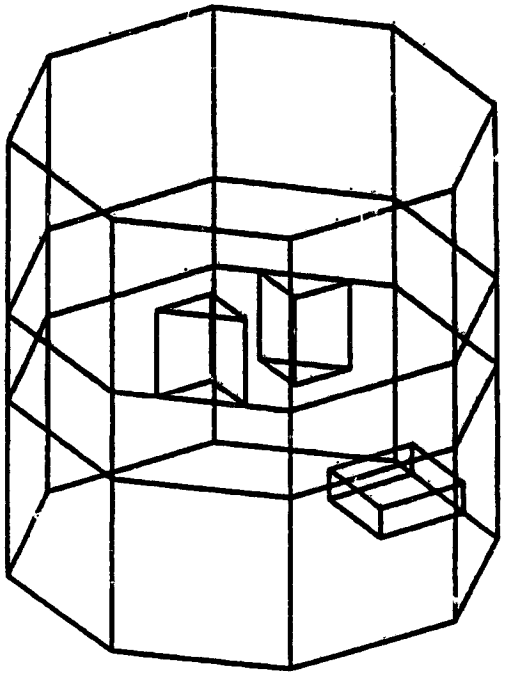

Figure 7. Object structural plots give a perspective view without hidden line removal.

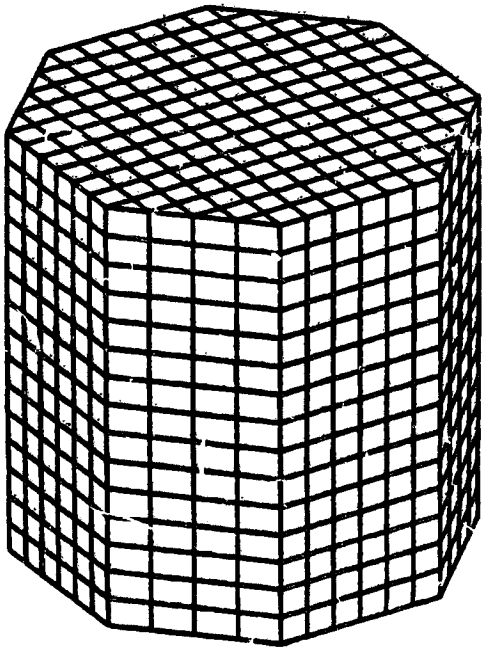

Figure 8. Surface cell hidden line plots give a clear idea of overall spacecraft structure.

```
SURFACE CELL NO.   15                                  CODE =       011112100702
                                                       LOCATION =    9 10  8
                                                       NORMAL =      0  1 -1
                                                       MATERIAL =   TEFLON

                          POTENTIAL =  -1.096+01 VOLTS
                          FIELD =    7.665-3 VOLTS/METER

FLUXES IN A/M**2
      INCIDENT ELECTRONS                                3.16-06
           RESULTING BACKSCATTER                        8.60-07
           RESULTING SECONDARIES                        1.32-06
      INCIDENT PROTONS                                  7.39-08
           RESULTING SECONDARIES                        7.17-07
      PHOTOCURRENT                                      0.00
                                                        - - - - - -
    NET FLUX                                           -1.96-07
```

Figure 9. A breakdown of charging currents can be requested for any surface cell. This information is given at each timestep.

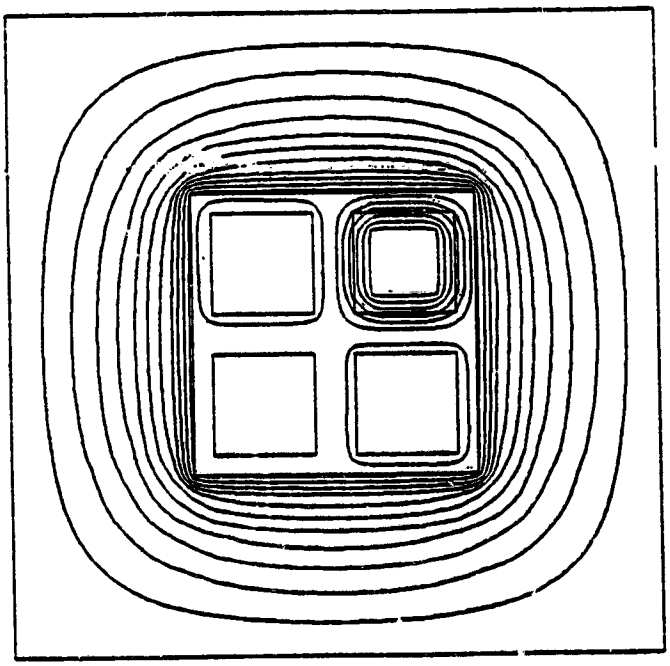

Figure 10. Two-dimensional potential contour plots give a clear picture of electrostatic potential at each timestep.

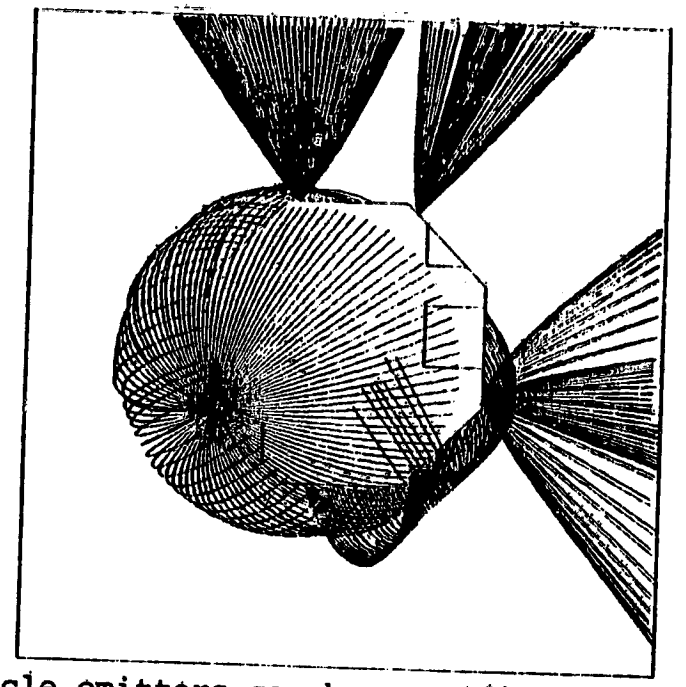

Figure 11. Particle emitters can be specified at any surface cell. This plot shows particles from five emitters for various angles of emission.

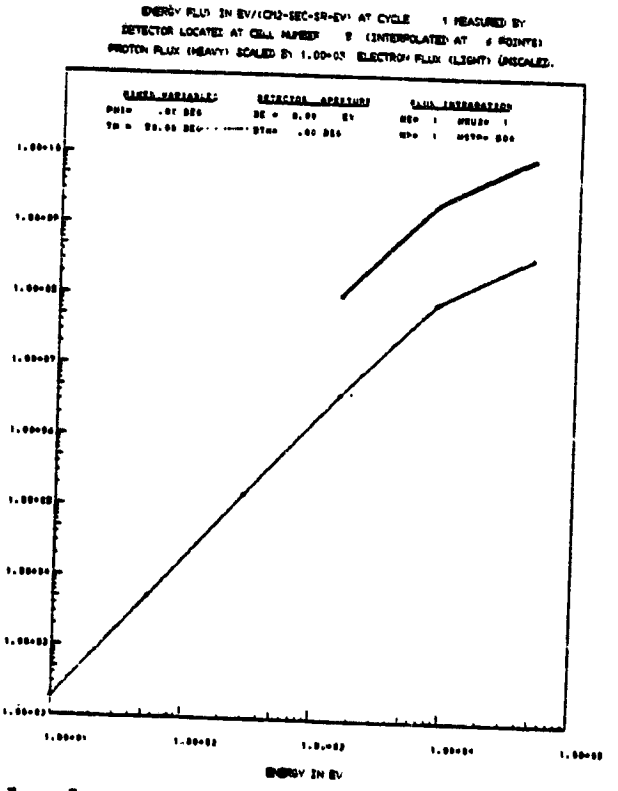

Figure 12. Particle detector plots show energy versus flux density. Detectors can also be located at any surface cell.

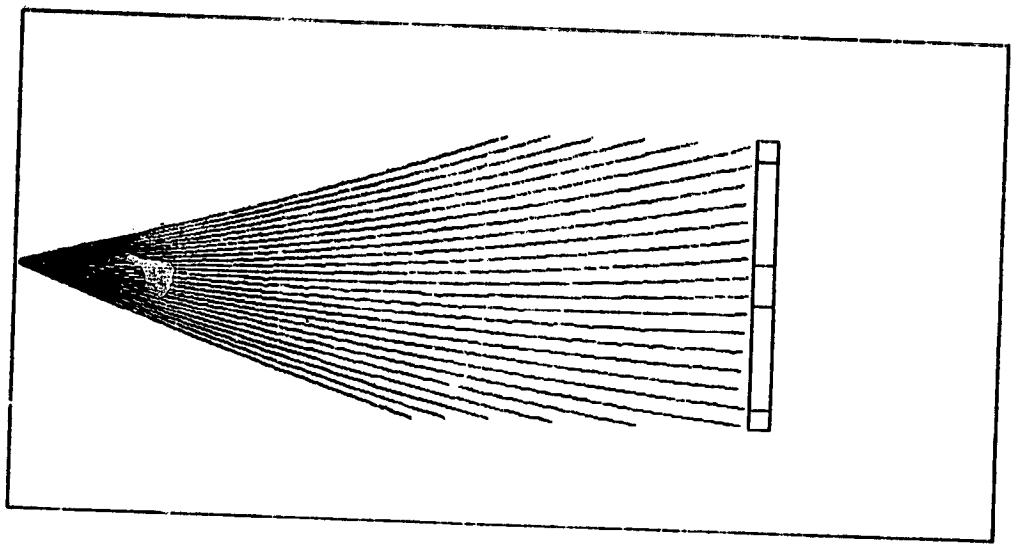

Figure 13. Graphic output for a test tank case includes trajectories of electrons from the source to the object.

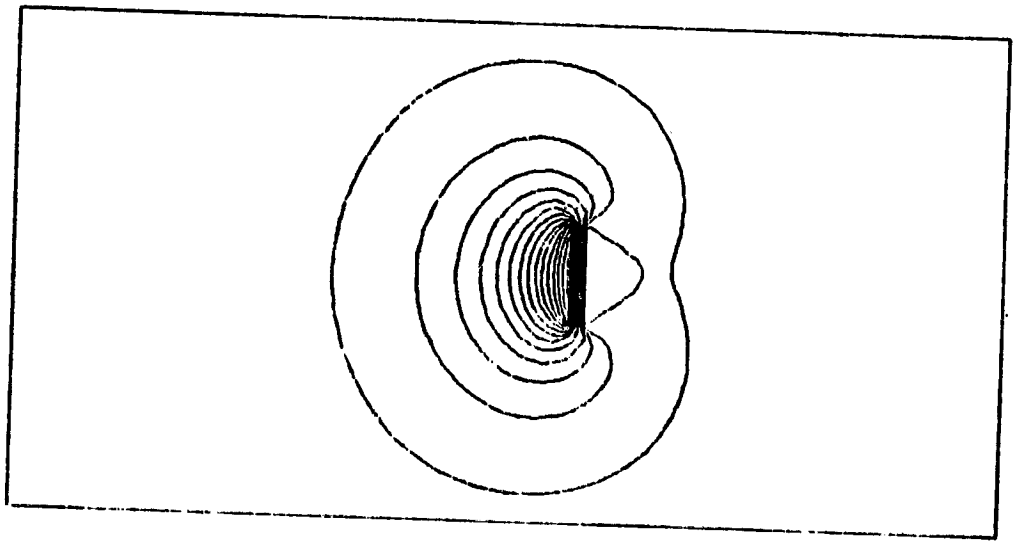

Figure 14. Potential contours around a fully charged teflon covered grounded plate in a ground test tank. An electron beam is coming from the left. Notice the fully formed potential saddle point to the right of the plate.

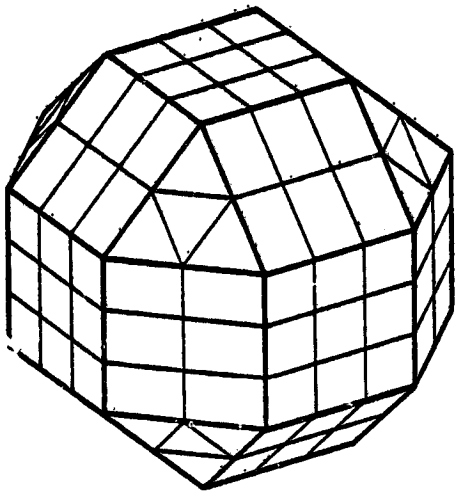

Figure 15. A NASCAP sphere – modeled as a twenty-six faceted object. This one is 3 meters in diameter with 158 surface cells and 144 surface nodes.

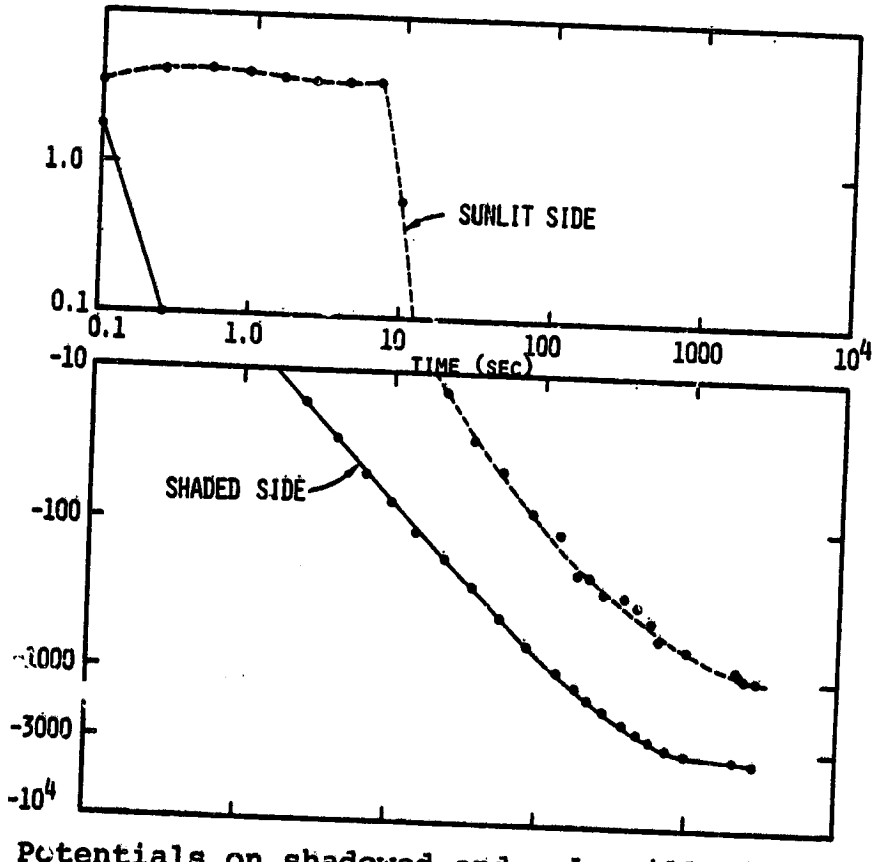

Figure 16. Potentials on shadowed and solar illuminated surfaces of a teflon sphere in a plasma ($N_e = 10^6/m^3$, θ = 20 keV).

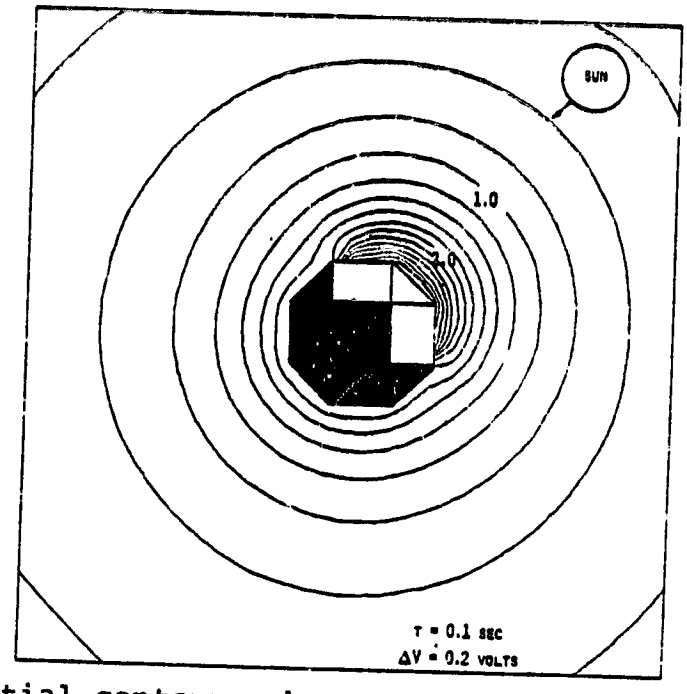

Figure 17. Potential contours about a sunlit sphere early in time.

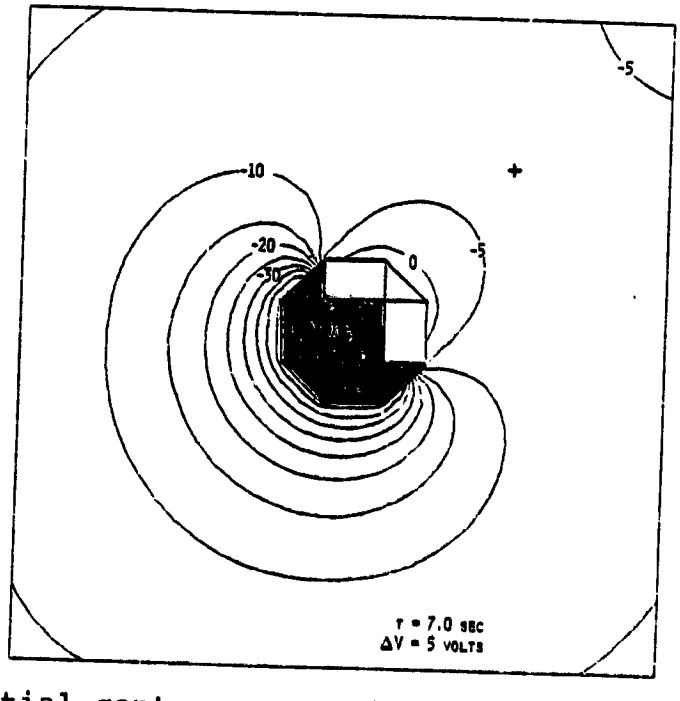

Figure 18. Potential contours around sunlit sphere showing early appearance of saddle point (+) at -5.6 volts.

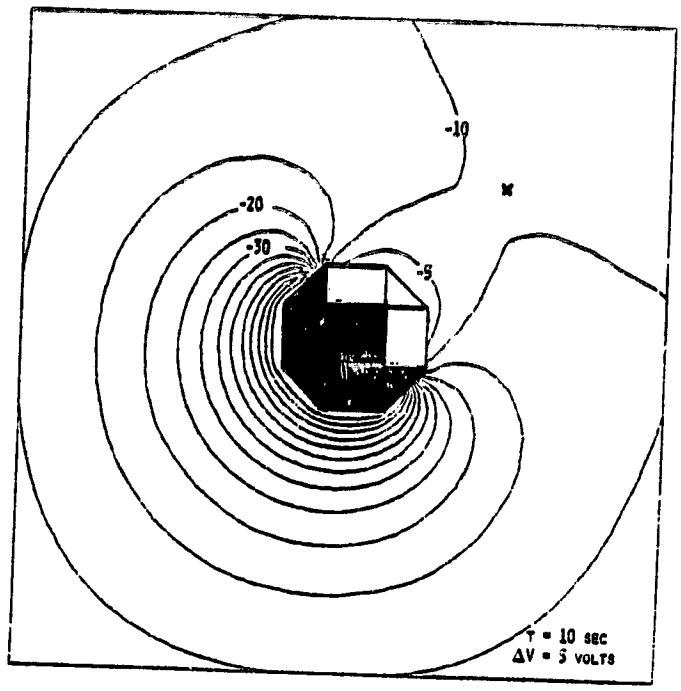

Figure 19. Potential contours around sunlit sphere showing fully formed saddle point at approximately -8 volts.

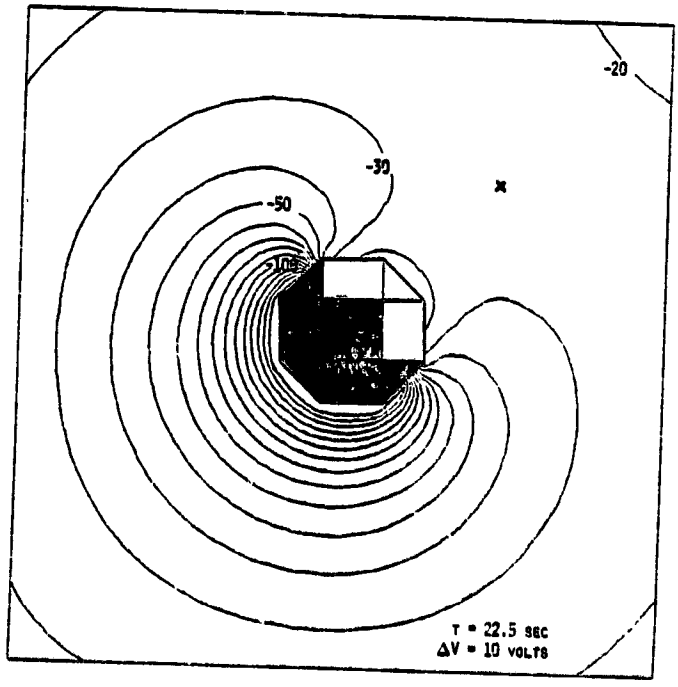

Figure 20. Potential contours about sunlit sphere showing saddle point at approximately -25 volts.

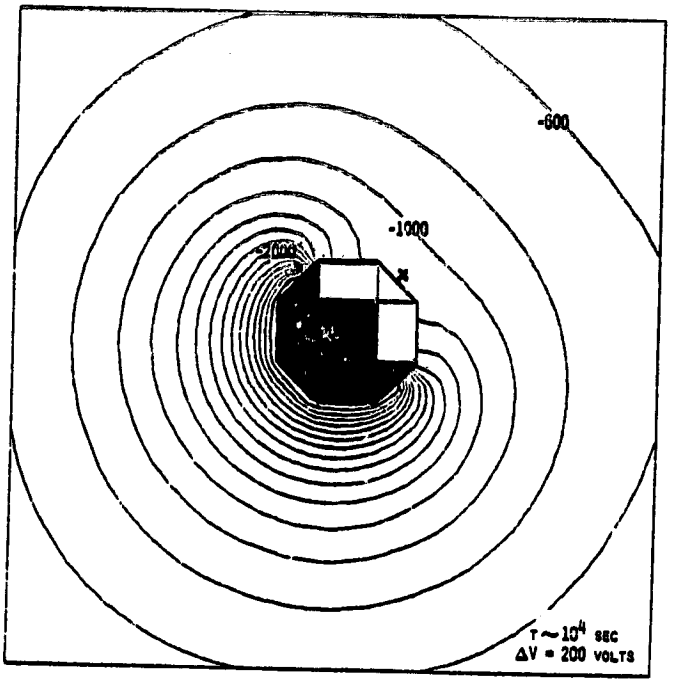

Figure 21. Steady state potential contours about sunlit sphere.

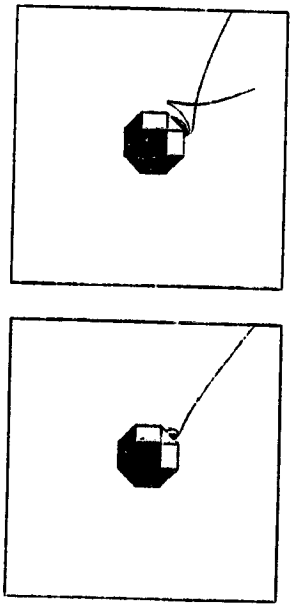

Figure 22. Trajectories of electrons emitted at various energies from fully charged sunlit sphere.

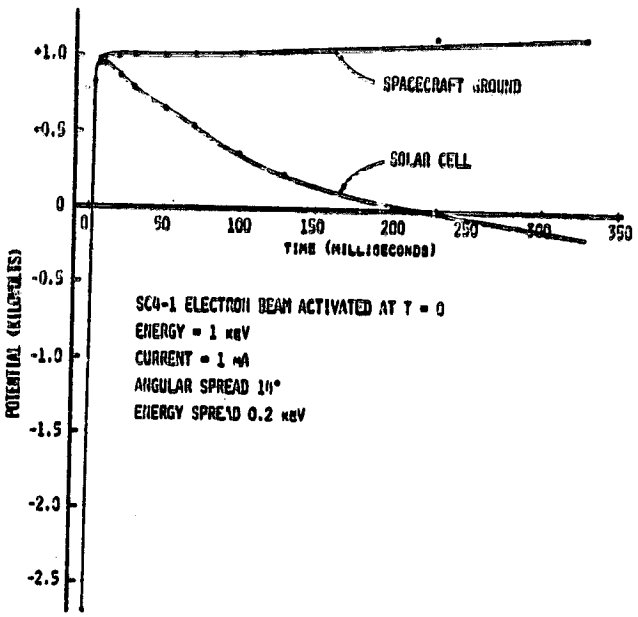

Figure 23. Active control simulation. A 1 mA particle emitter is activated with beam energy of 1 keV. The spacecraft goes from a negative 2.5 kV potential to positive 1.0 kV. Spacecraft ground remains at about that level while a solar cell on the surface falls back to a negative potential.

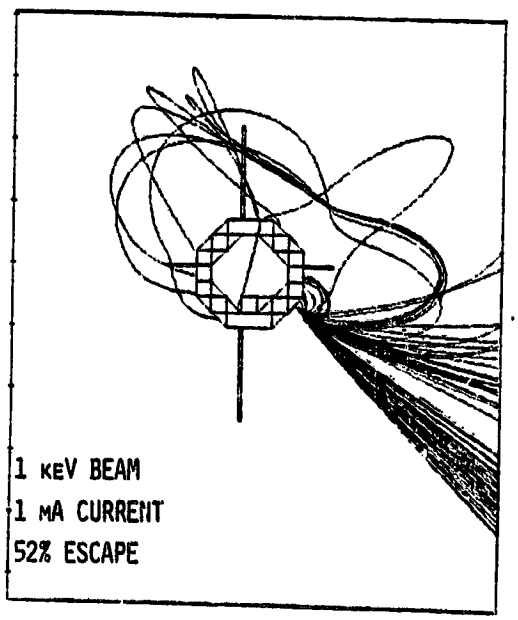

Figure 24. Particle emitter trajectory plot. Some of the emitted particles escape the spacecraft vicinity, while others return to various points on the surface.

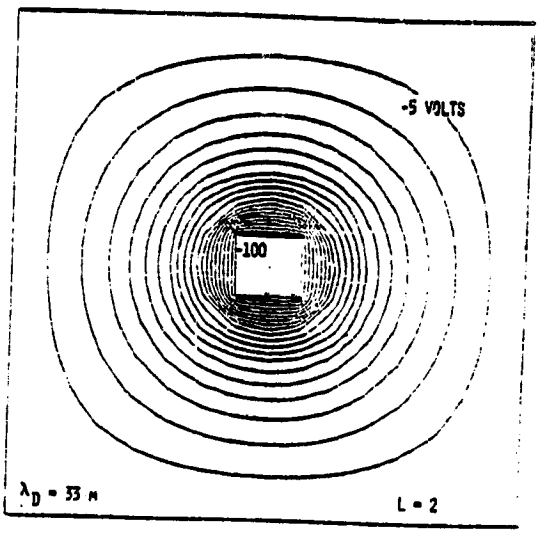

Figure 25. An approximate screening expression is employed to show shielding effects. Shown is a two meter cube charged to -100 V, in a plasma with Debye length of 33 meters.

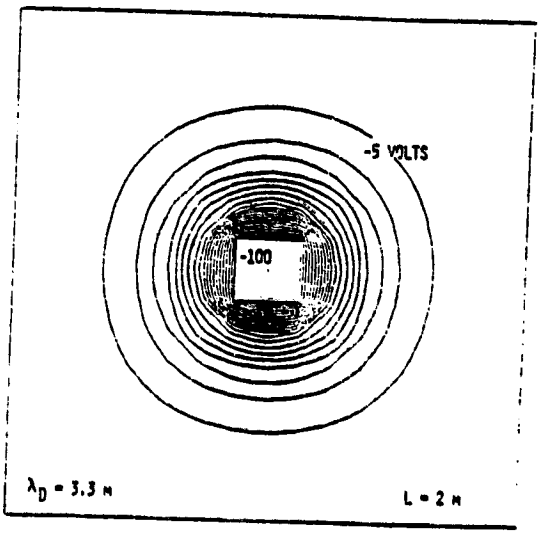

Figure 26. Here the same cube is charged once again to -100 V. This plasma has Debye length of 3.3 meters. The denser plasma leads to more significant shielding, and the potential falloff is steeper near the cube.

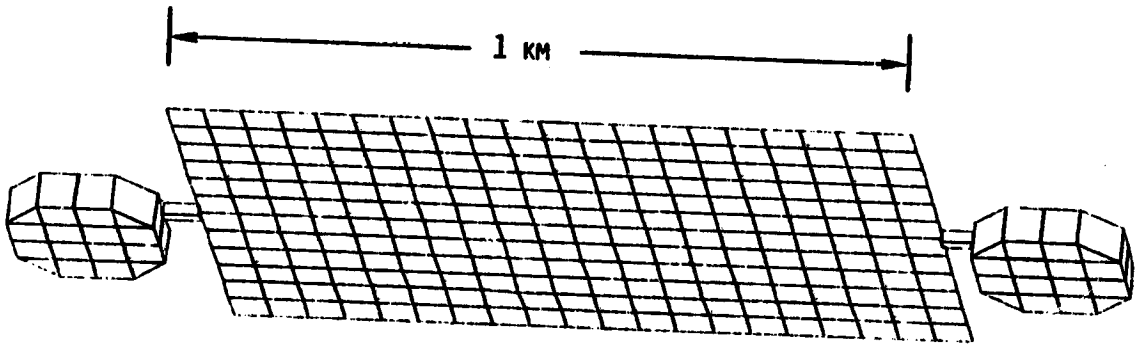

Figure 27. Solar power space station model.

N79-24012

CHARGING ANALYSIS OF THE SCATHA SATELLITE*

G. W. Schnuelle, D. E. Parks, I. Katz,
M. J. Mandell, P. G. Steen, J. J. Cassidy
Systems, Science and Software

A. Rubin
Air Force Geophysics Laboratory

ABSTRACT

We describe here a detailed model of the geometrical, material, and electrical properties of the SCATHA satellite for use with the NASA Charging Analyzer Program (NASCAP). Charging calculations in an intense magnetospheric substorm environment demonstrate that (1) long booms can significantly perturb the potentials near the spacecraft, and (2) discharging by sunlight or by active control can cause serious time-dependent differential charging problems.

INTRODUCTION

We have developed a detailed model of the SCATHA satellite for use with the NASA Charging Analyzer Program (NASCAP) (refs. 1 and 2). The model accounts for such geometrical complexities as booms, shadowing, and the presence of insulating materials over portions of the conducting ground of the space vehicle. The effects of photoemission and secondary emission caused by electron and ion impact, active control devices such as electron and ion beams, and surface and bulk conductivity are included in the model. To our knowledge, this model represents the most complete and realistic treatment of spacecraft charging attempted to date for any satellite.

Section 2 below describes the SCATHA model employed in NASCAP. A detailed shadowing study was performed for a geometrically more accurate SCATHA model; this work is described in Section 3. We have performed charging calculations for one environment using the present model, and the results of these calculations are described in Section 4. Preliminary conclusions of this study are summarized in Section 5.

*This work supported by the National Aeronautics and Space Administration, Lewis Research Center, under Contract NAS3-21050.

SCATHA MODEL DEVELOPMENT

The NASCAP program allows the specification of the geometrical, material, and electrical properties of a spacecraft in considerable detail. We have attempted to incorporate the most current and complete information available for SCATHA into our model. However, the present model is meant primarily to illustrate the intended level and scope of our study, rather than to provide the final word on a model specification. The NASCAP code allows model features to be easily altered to make our model a more faithful representation of the SCATHA satellite if the need arises.

Perspective views of our gridded model are shown in figures 1 and 2. The main body of the satellite is represented as a right octagonal cylinder, with the aft cavity visible in figure 2. The OMNI antenna and the SC9 cluster of experiments are visible on the forward surface of the satellite. Our model reproduces the actual SCATHA geometrical features extremely well, as shown in table 1. Note in particular that the treatment of booms in NASCAP allows the actual boom radii to be reproduced exactly in the model. The requirements in NASCAP that booms parallel coordinate axes and intercept mesh points in all grids effectively force any long booms to pass through the center of the innermost mesh. Therefore, our present model includes only the SC6, SC11, and the two SC2 booms, with the orientations fixed at right angles to one another.

Figure 3 illustrates the computational space in which NASCAP solves Poisson's equation for this model. Monopole boundary conditions are imposed on the edges of the outermost grid, which is a rectangular prism of dimensions 1.6 × 1.6 × 3.2 m. The zone size decreases by a factor of 2 in each of the four successive inner grids, so that the effective resolution is 11.5 cm near the satellite body. (Local mesh refinement techniques in NASCAP allow a resolution of 2.5 cm for selected zones on the satellite.)

Our model includes the specification of 15 distinct exposed surface materials, each of which is specified by the values of some 13 user-supplied parameters. The surface materials are described in table 2. We have attempted to find experimentally measured values for all parameters; where this has not been possible, suitable estimates based on the properties of similar materials have been used. Table 3 lists the values employed in the calculations reported here. The analytical expressions in which these parameters are used to evaluate net surface currents are described in detail in reference 5. The formulation of electron backscattering in NASCAP has been somewhat modified recently, and the newer treatment is described in appendix A. The exposed materials are illustrated in figure 4 in which the locations of several of the SCATHA experiments are also shown. Experiments at the ends of SCATHA booms are modeled as a single boom segment

whose radius is adjusted to match the exposed surface area of the actual experiment.

The model includes six distinct underlying conductors: spacecraft ground, the reference band, and the four experiments SC2-1, SC2-2, SC6-1 and SC6-2. Each of these underlying conductors is capacitively coupled to spacecraft ground, and each can be separately biased with respect to ground. A seventh conductor could be introduced to underlay the solar cells at an appropriate bias. In this study the reference band was allowed to float and all other conductors were biased to the ground potential.

NASCAP has extensive capabilities to model particle emitters and detectors located on the spacecraft body, as described previously (ref. 2). These features of NASCAP can be used in the analysis of the operation of, for example, the SCA1 experiments SC4, SC5, SC6, SC7, and SC9. Such studies should be particularly helpful in determining the influence of spacecraft fields on particles emitted during active control, and in determining the source of particles seen at detector sites.

SHADOWING STUDY

For the SCATHA shadowing study, we were required to generate percent shadowing tables for various experiments. We were able to generate accurate tables using relatively small amounts of computer time: less than 5 minutes Univac 1100/81 time was required for a table of 7560 entries.

Since the geometrical capabilities of the NASCAP shadowing routines are more general than the rest of the code, we were able to employ a SCATHA model for shadowing in which each experiment was treated geometrically in much finer detail than in the model described in Section 2. Figure 5 shows the level of detail in a perspective view of the ML12-7 experiments on the forward surface. Booms were placed at their actual locations on the satellite, and the experiments at the boom ends were given a great deal of geometrical complexity. Figure 6 shows the SC2-1, SC1-4, and SC6-1 booms as they were resolved in the shadowing study.

These detailed geometrical shapes were input to the usual NASCAP shadowing routines (HIDCEL) for table generation. The tables cover satellite rotation in 1° increments for the satellite plane deviations from the sun line of -5° to +5°.

CHARGING CALCULATIONS

The model was subjected to an extremely intense substorm described by a superposition of two Maxwellian plasmas with the following parameters:

$\theta_{e1} = 40{,}000$ eV

$\theta_{i1} = 20{,}000$ eV

$n_{e1} = 10\ cm^{-3}$

$n_{i1} = 10\ cm^{-3}$

$\theta_{e2} = 100$ eV

$\theta_{i2} = 100$ eV

$n_{e2} = 10\ cm^{-3}$

$n_{i2} = 10\ cm^{-3}$

The effects of ambient space charge were neglected in the solution of Poisson's equation here, since the mean satellite radius, r_s, is much smaller than the plasma Debye length, λ_D.

$r_s \sim 100$ cm

$\lambda_D \sim 700 \sqrt{\frac{\theta}{n_e}} \sim 2200$ cm

$r_s/\lambda_D \sim 0.05$

There was no sunlight present in the first calculation described below.

Potential contours during the initial overall charging phase ($\sim 10^{-3}$ seconds) are shown in figures 7 and 8. The question of whether booms have a significant effect on the sheath potentials is clearly answered by examining figure 9, which shows potential contours in a plane a half meter below the plane of the booms. Figure 10 shows similar contours in a calculation with the booms omitted; the distortion of contours by the booms is obvious. While the boom radii are small, ~ 2 cm, the effect on potentials is related to the boom capacitance, which varies only logarithmically with radius. This results in long range potential interactions from thin booms, where the characteristic decay distance is closer to the boom length than to the boom radius.

The rapid initial charging is followed by a much slower development of differential charging, as illustrated in figure 11. For this example the maximum differential developed after 22 seconds was 700 volts and the maximum field strength in a dielectric layer was 24,000 volts/cm. Figure 12 shows contours in the plane of the booms after 22 seconds; note the differential charging developed at the boom ends due to variations in the material properties between the experiments and the boom coatings.

The two-Maxwellian description of the plasma leads to a low overall charging voltage of only -7.3 keV despite the presence of a plasma component with an electron temperature of 40 keV. For the particular case we have studied here, low energy protons are being collected at an enormous rate and these, augmented by the secondary electrons they produce, balance the incident electron current. NASCAP uses a proton collection model in which the collection increases linearly with voltage, which is valid in the present case where r_s/λ_D is small, as discussed by Laframboise (ref. 4). Table 4 shows the detailed current balance near equilibrium for the boom surface material in the presence of the double Maxwellian environment described above. Also shown in table 4 is a similar breakdown for the same material subjected only to the high energy single Maxwellian component. The equilibrium potential is -32 keV in this case, indicating that the final potentials reached would have been much lower had we employed a single Maxwellian plasma model. For both plasma models, the final potentials reached will depend on the exact values employed for the proton and electron induced secondary yields. Great care should be exercised in the determination of the values and associated error estimates for parameters which affect the production of secondary electrons in these and similar calculations.

Finally, the atomic number dependence of backscatter coefficients tends to make high-Z materials charge less negatively than other elements. For SCATHA, this means that the magnitude of the boom potentials will be significantly lower than most other surfaces, since exposed platinum constitutes much of its surface area.

We have performed a similar calculation on this model in which the sunlight was turned on after 22 seconds of charging in eclipse. The photoemission results in strong differential charging ($\sim$3 keV) along the booms, as shown in figure 13. In our model the boom surfaces are very weakly capacitively coupled to the grounded cable shields which extend the length of the booms, while the experiments at the ends of the SC2 and SC6 booms are coupled closely to spacecraft ground. This weak coupling has the effect of allowing the booms to react rapidly to environmental perturbations compared to the rest of the satellite, leading to temporary conditions of high differential charging. We have observed similar effects when discharging the satellite with an electron gun.

The potentials near the satellite in sunlight are dominated by the monopole field of the spacecraft body. A photoemitting boom surface element can discharge only to the value of the local monopole potential, since further discharge is limited by immediate reflection of photoelectrons. This has the amazing consequence that the booms, strongly perturbing in eclipse, now seem to disappear in the potential contours near the satellite body. Note that significant differential charging in sunlight along the

SC2 booms will certainly persist at equilibrium due to large differences between the photoemission from surfaces on booms and on the SC2-1 and SC2-2 experiments. Our calculations neglect any effective surface conductivity parallel to the booms due to the presence of a photosheath. The surface conductivity features of NASCAP could easily be invoked to simulate this effect, which would reduce the magnitude of the differential charging observed here.

The calculations reported here were performed on the Univac 1100/81 computer at Systems, Science and Software. Each cycle of charging and solution of the potential equations required approximately 15 minutes CPU time during differential charging, and 5 minutes CPU time when no differential charging occurred. Approximately 10 cycles of each type were required for the calculations reported here. We have developed a second SCATHA model for testing purposes in which the zone size is twice that of the model presented here and the booms are shortened; computer times are reduced by roughly 80 percent for this model, and all of the results described above can be observed in calculations using the smaller model. The half-scale model will be useful whenever fine resolution on the satellite surfaces is not required.

CONCLUSIONS

We have completed the development of a detailed model of the SCATHA satellite. Preliminary results from calculations in one magnetospheric environment indicate that:

- The presence of a low energy component in a two-Maxwellian description of the magnetospheric environment reduces the maximum charging of a satellite relative to that found for a single Maxwellian.
- The booms have substantial impact on potentials near the spacecraft in eclipse.
- The use of high atomic number coatings, such as platinum on the booms, may increase the severity of differential charging.
- Discharging by sunlight or by active control may lead to transient increases in differential charging along the booms due to the weak coupling of the booms to spacecraft ground.

Our calculations demonstrate that the prediction of spacecraft potentials for SCATHA is an exceedingly complex problem, in which the full capabilities of the NASCAP treatment of geometrical features, material properties, and dynamic interaction with the environment are utilized. We plan to continue this study of

SCATHA using NASCAP with particular emphasis on boom perturbations and the effects of active control.

APPENDIX A. ELECTRON BACKSCATTER

Electron backscatter is modeled in NASCAP as a function of electron energy and mean atomic number of backscattering material. The formulation first used in NASCAP (ref. 5) was valid only for low-Z materials. To remove this restriction we have used a formula of Burke (ref. 6) to obtain the backscatter coefficient for isotropically incident electrons as

$$\eta_1 = 0.475\ Z^{0.177} - 0.40 \tag{A1}$$

The backscatter coefficient for normal incidence, η_o, is then found by solving the equation

$$\eta_1 = 2[1 - \eta_o(1-\ln \eta_o)]/(\ln \eta_o)^2 \tag{A2}$$

which comes from assuming the angular dependent backscatter coefficient (ref. 7) to be

$$\eta(\theta) = \eta_o \exp[-(\ln \eta_o)\ (1 - \cos\theta)] \tag{A3}$$

The energy dependence (ref. 4) is then taken to be

$$\eta_o(\varepsilon) = \gamma(\varepsilon)\ (\eta_o + 0.1 \exp(-\varepsilon/5)) \tag{A4}$$

$$\gamma(\varepsilon) = \begin{cases} 0 & \varepsilon < 50 \text{ eV} \\ \ln (20\ \varepsilon)/\ln 20 & 50 \text{ eV} < \varepsilon < 1 \text{ keV} \\ 1 & \varepsilon > 1 \text{ keV} \end{cases}$$

where ε is in keV.

The energy dependent η_o from (A4) is then used in (A2) or (A3) to calculate the relevant backscatter coefficient.

REFERENCES

1. Katz, I., Parks, D. E., Mandell, M. J., Harvey, J. M. and Wang, S. S., "NASCAP, A Three-Dimensional Charging Analyzer Program for Complex Spacecraft," IEEE Transactions on Nuclear Science, 6, 1977, p. 2276.

2. Katz, I., Cassidy, J. J., Mandell, M. J., Schnuelle, G. W., Steen, P. G. and Roche, J. C., "The Capabilities of the NASA Charging Analyzer Program," preceding paper at this conference.

3. Steen, P. G., "SCATHA Experiment Shadowing Study," Systems, Science and Software Topical Report SSS-R-78-3658, May 1978.

4. Laframboise, J. G., UTIAS Report No. 100, 1966.

5. Katz, I., Parks, D. E., Mandell, M. J., Harvey, J. M., Brownell, Jr., D. H., Wang, S. S. and Rotenberg, M., "A Three-Dimensional Dynamic Study of Electrostatic Charging in Materials," NASA CR-135256, August 1977.

6. Burke, E. A., "Soft X-ray Induced Electron Emission," IEEE Transactions on Nuclear Science, NS-24, 1977, pp. 2505-2509.

7. Darlington, E. H. and Cosslett, V. E., "Backscattering of 0.5-10 keV Electrons from Solid Targets," J. Phys. D5, 1972, p. 1969.

TABLE 1. COMPARISON OF ACTUAL SCATHA GEOMETRICAL FEATURES TO GRIDDED NASCAP MODEL

Zone Size = 4.54 in. (11.5 cm)

	SCATHA	MODEL
Radius	33.6 inches	32.0 inches
Height	68.7	68.0
Solar Array Height	29	27.2
Bellyband Height	11.3	13.6
SC9-1 Experiment	9.2 × 6 × 8	9.1 × 4.5 × 9.1
SC6-1 Boom	1.7 (radius) 118 (length)	1.7 113.2
Surface Area	2.16×10^4 sq. in.	2.11×10^4 sq. in.
Solar Array Area	1.23×10^4	1.15×10^4
Forward Surface Area	0.36×10^4	0.34×10^4

TABLE 2. EXPOSED SURFACE MATERIALS

GOLD:	gold plate
SOLAR:	solar cells, coated fused silica
WHITEN:	non-conducting white paint (STM K792)
SCREEN:	SC5 screen material, a conducting fictitious material which absorbs but does not emit charged particles
YELOWC:	conducting yellow paint
GOLDPD:	88 percent gold plate with 12 percent conductive black paint (STM K748) in a polka dot pattern
BLACKC:	conductive black paint (STM K748)
KAPTON:	kapton
SIO2:	SiO_2 fabric
TEFLON:	teflon
INDOX:	indium oxide
YGOLDC:	conducting yellow paint (50 percent) gold (50 percent)
ML12:	ML12-3 and ML12-4 surface, a fictitious material whose properties are an average of the properties of the several materials on the ML12 surfaces
ALUM:	aluminum plate
BOOMAT:	platinum banded kapton

TABLE 3. MATERIAL PROPERTIES FOR EXPOSED SURFACES[a]

Property[b]	GOLD	SOLAR	WHITEN	SCREEN	BLACKC YELOWC	GOLDPD	KAPTON
1	-	4.00+00	3.50+00	-	3.50+00	-	3.50+00
2	1.00-03	1.79-04	5.00-05	1.00-03	5.00-05	1.00-03	1.25-04
3	∞	1.00-14	5.90-14	∞	5.00-10	∞	1.00-14
4	7.90+01	1.00+01	5.00+00	1.00+00	5.00+00	7.01+01	5.00+00
5	8.80-01	4.10+00	2.10+00	0.00	2.10+00	1.03+00	2.10+00
6	8.00-01	4.10-01	1.50-01	1.00+00	1.50-01	7.20-01	1.50-01
7	8.30+01	-1.00+00	-1.00+00	1.00+01	-1.00+00	8.30+01	-1.00+00
8	1.63+00	0.00	0.00	1.50+00	0.00	1.63+00	0.00
9	3.46+01	2.30+00	1.05+00	0.00	1.05+00	3.46+01	1.42+00
10	7.00-01	2.08+01	9.80+00	1.00+00	9.80+00	7.00-01	9.80+00
11	4.00-01	1.36+00	1.40+00	0.00	1.40+00	4.00-01	1.40+00
12	5.00+01	4.00+01	7.00+01	1.00+00	7.00+01	5.00+01	7.00+01
13	2.90-05	2.00-05	2.00-05	0.00	2.00-05	2.90-05	2.00-05

	SIO2	TEFLON	INDOX	YGOLDC	ALUMIN	BOOMAT[c]	ML12
1	4.00+00	2.00+00	-	-	-	2.00+00	-
2	2.75-04	1.25-04	1.00-03	1.00-03	1.00-03	5.00-03	1.00-03
3	2.75-12	1.00-14	∞	∞	∞	1.00-10	∞
4	1.00+01	1.00+01	2.44+01	4.20+01	1.30+01	6.34+01	6.00+00
5	2.40+00	3.00+00	1.40+00	1.49+00	9.70-01	1.86+00	1.00+00
6	4.00-01	3.00-01	8.00-01	4.80-01	3.00-01	5.90-01	3.00-01
7	-1.00+00	-1.00+00	-1.00+00	-1.00+00	2.60+02	8.30+01	-1.00+00
8	0.00	0.00	0.00	0.00	1.30+00	1.63+00	0.00
9	1.02+00	2.00+00	7.18+00	1.02+01	2.40+02	3.46+01	2.00+00
10	2.00+01	1.67+01	5.55+01	4.20+01	1.73+00	7.00-01	1.20+01
11	1.40+00	1.40+00	1.36+00	1.00+00	1.36+00	4.00-01	1.40+00
12	7.00+01	7.00+01	4.00+01	6.00+01	4.00+01	5.00+01	7.00+01
13	2.00-05	2.00-05	3.20-05	2.40-05	4.00-05	2.72-05	2.10-05

TABLE 3. (Continued)

[a]The materials are described in Table 2.

[b]The thirteen properties are as follows (see Reference 4 and Appendix A for further details):

Property 1:	Relative dielectric constant for insulators (dimensionless).
Property 2:	Thickness of dielectric film or vacuum gap (meters).
Property 3:	Electrical conductivity (mho/m). The value ∞ indicates a vacuum gap over a conducting surface.
Property 4:	Atomic number (dimensionless).
Property 5:	Maximum secondary electron yield for electron impact at normal incidence (dimensionless).
Property 6:	Primary electron energy to produce maximum yield at normal incidence (keV).
Properties 7-10:	Range for incident electrons. Either: $\text{Range} = P_7 E^{P_8} + P_9 E^{P_{10}}$ where the range is in angstroms and for the energy in keV, or $P_7 = -1.$ to indicate use of an empirical range formula; P_9 = density (g/cm^3); P_{10} = mean atomic weight (dimensionless).
Property 11:	Secondary electron yield for normally incident 1 keV protons.
Property 12:	Proton energy to produce maximum secondary electron yield (keV).
Property 13:	Photoelectron yield for normally incident sunlight (A/m^2).

[c]The dielectric constant and thickness for the boom surfaces were chosen to reflect the effective capacitance to the underlying cable shield.

TABLE 4. COMPONENTS OF INCIDENT AND EMITTED CURRENTS (10^{-5} A/m^2) FOR BOOM SURFACE MATERIAL NEAR STEADY STATE.

	Double Maxwellian	Single Maxwellian
Potential	-7000 Volts	-32,000 Volts
Incident Electrons	-4.6	-2.3
Resulting Backscatter	2.7	1.4
Resulting Secondaries	.7	.4
Incident Protons	.6	.2
Resulting Secondaries	.6	.3

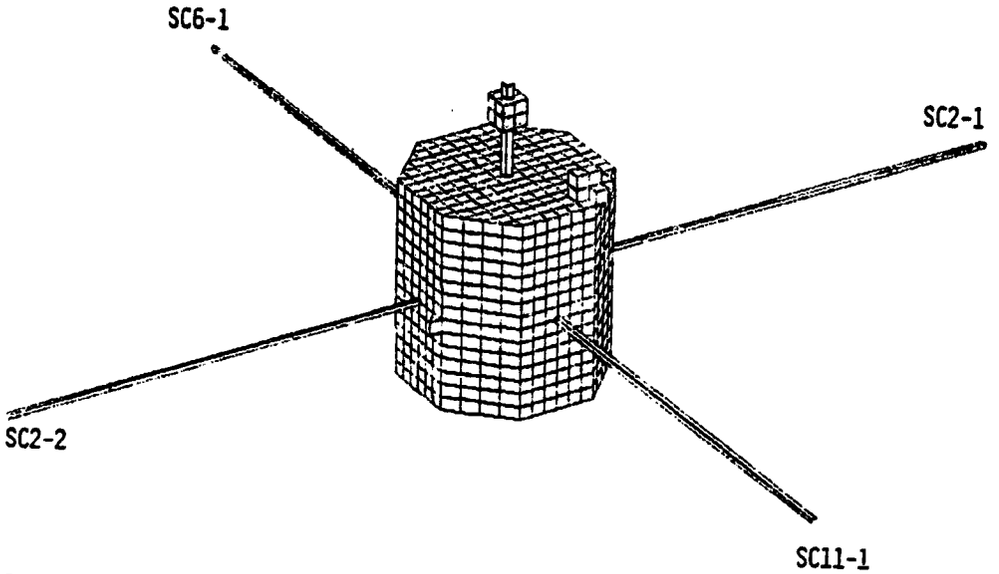

Figure 1. SCATHA model: side view. The 50 m antenna and the SC1-4 boom are not included in this model.

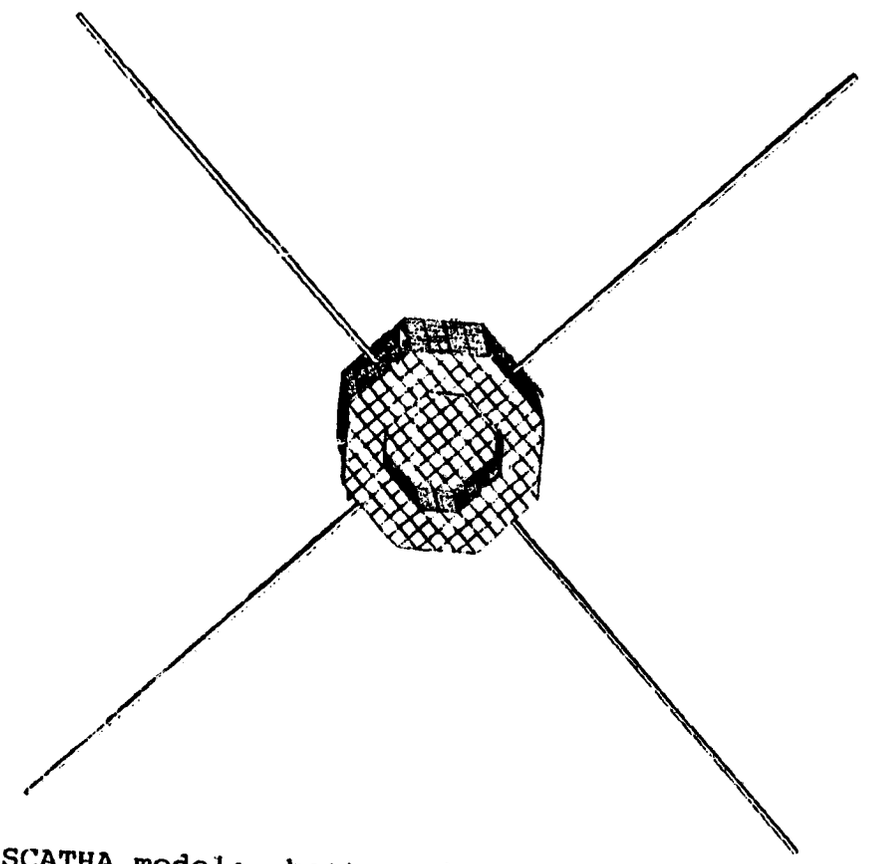

Figure 2. SCATHA model: bottom view with aft cavity visible.

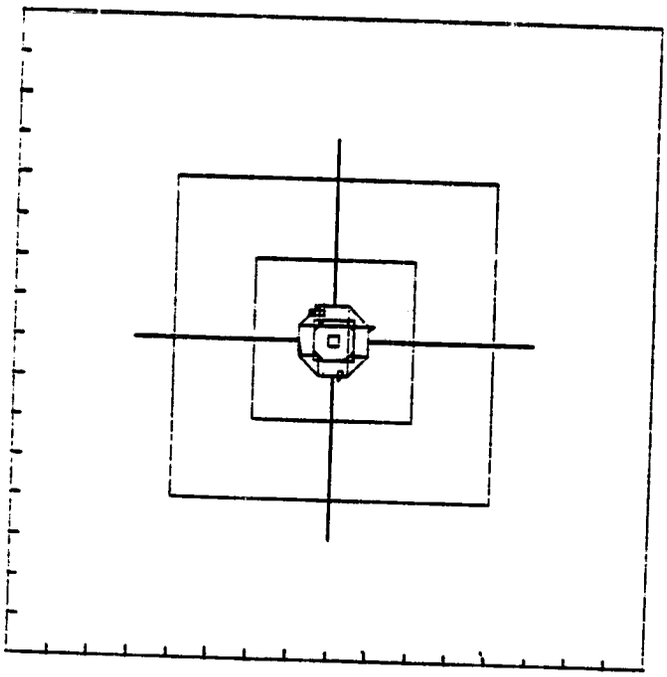

Figure 3. Computational space surrounding the SCATHA model, showing the nesting of the grids. The tic marks along the axes indicate the outer grid zone size; the zone size decreases by a factor of two in successive grids.

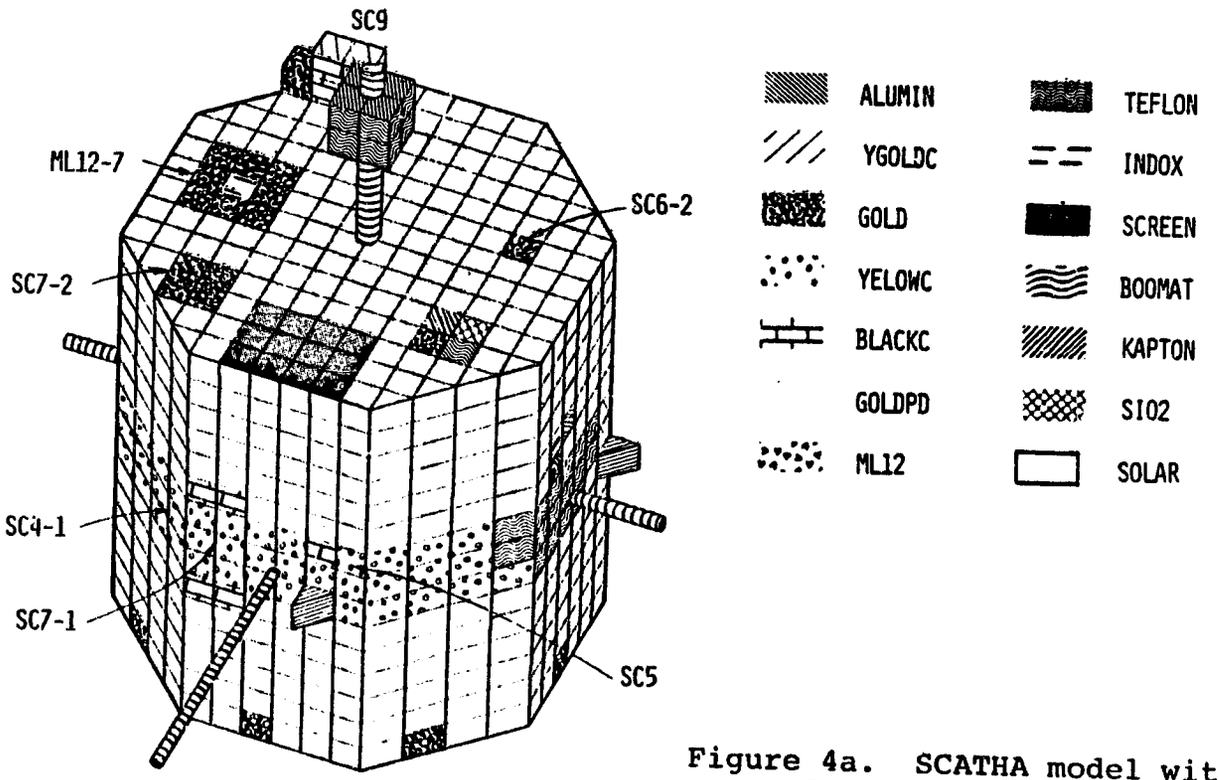

Figure 4a. SCATHA model with exposed surface materials illustrated.

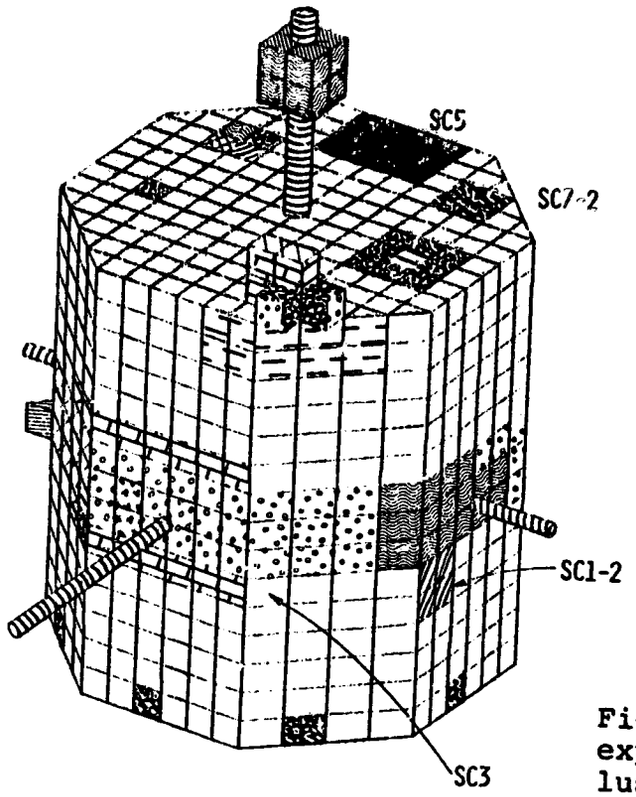

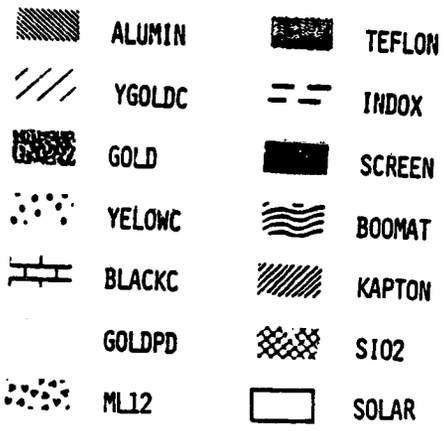

Figure 4b. SCATHA model with exposed surface materials illustrated.

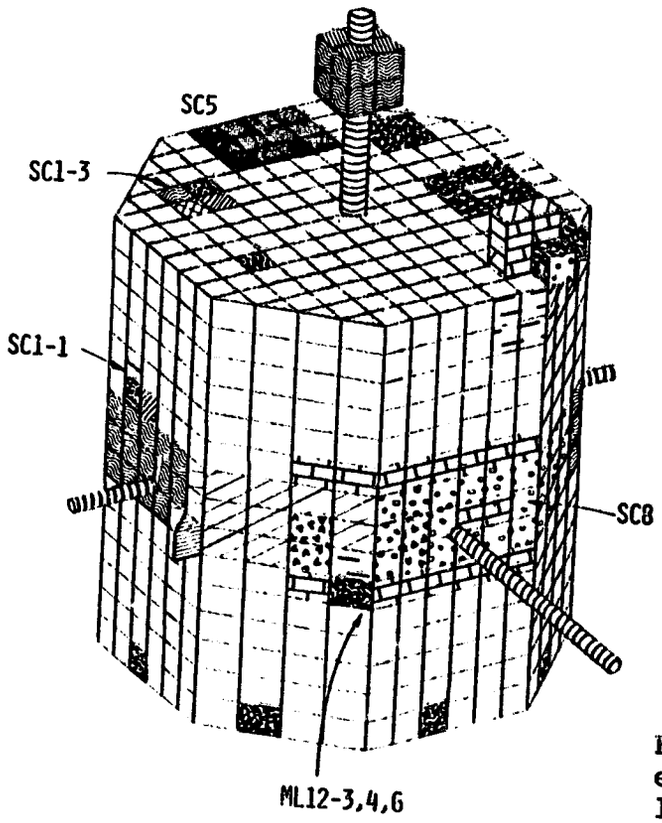

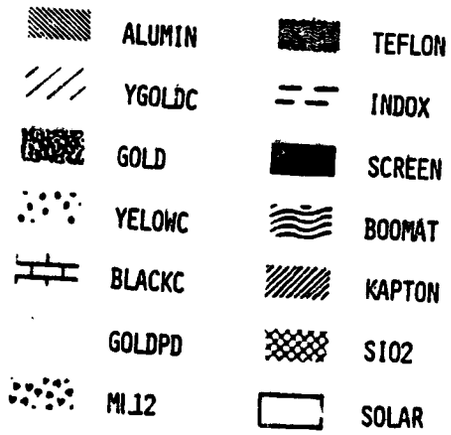

Figure 4c. SCATHA model with exposed surface materials illustrated.

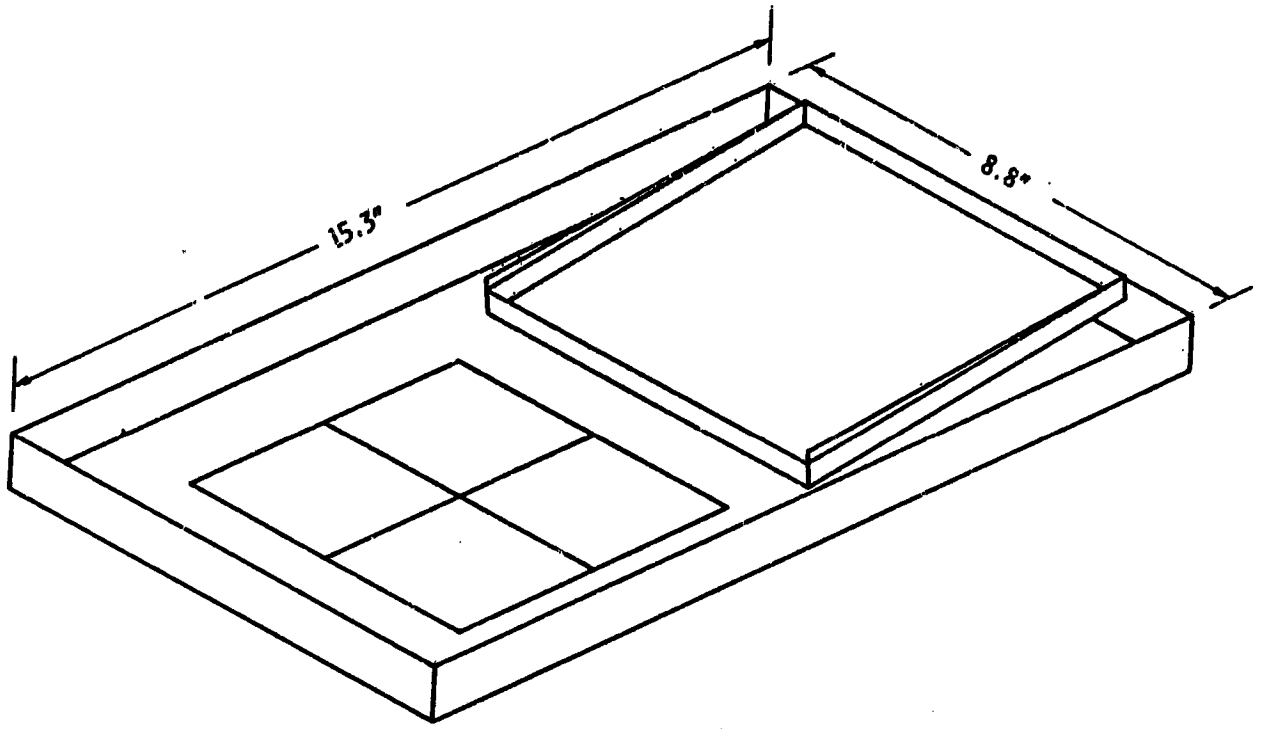

Figure 5. ML12-7 experiment as resolved for the SCATHA shadowing study.

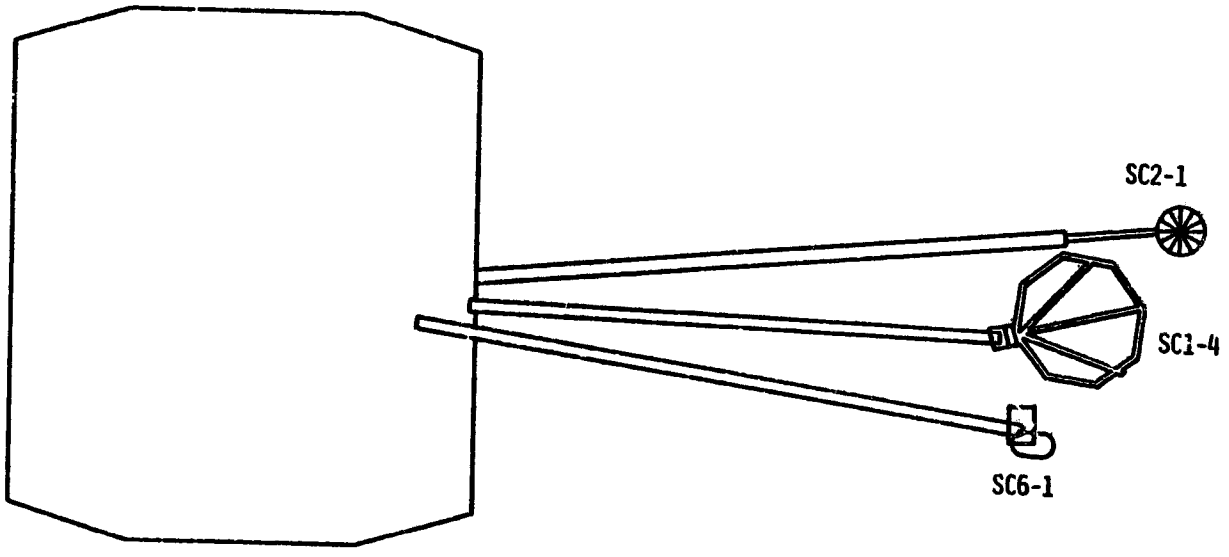

Figure 6. SCATHA booms as resolved in the shadowing study.

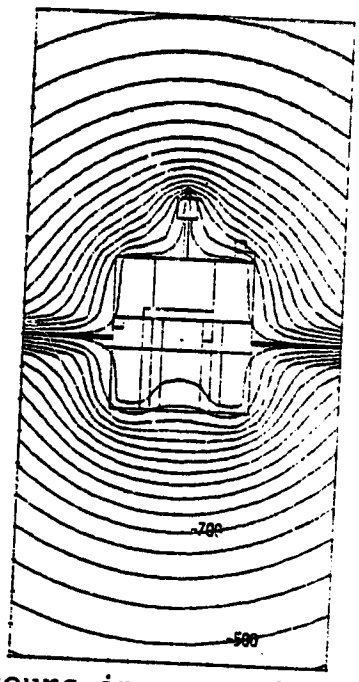

Figure 7. Potential contours in a vertical plane through SCATHA center (only two of the four grids are plotted). Note the contours extending into the aft cavity. Time $\sim 10^{-3}$ seconds. Contours from -450 to -1250 volts in 50 volt steps.

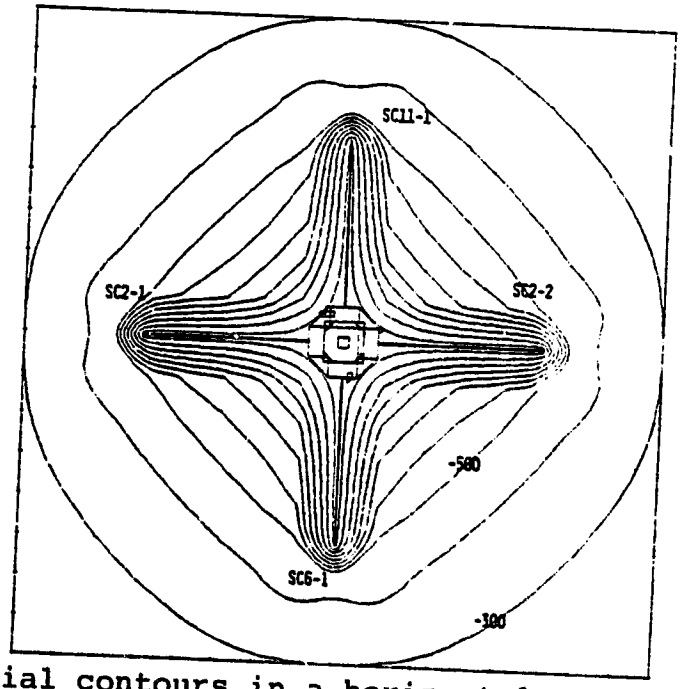

Figure 8. Potential contours in a horizontal plane through SCATHA center. Time $\sim 10^{-3}$ seconds. Contours from -300 to -1200 volts in 100 volt steps. The relative orientations of the booms is the same in later figures. The dimples in the potential contours near the boom ends are artifacts associated with an imperfect match of potential interpolation functions.

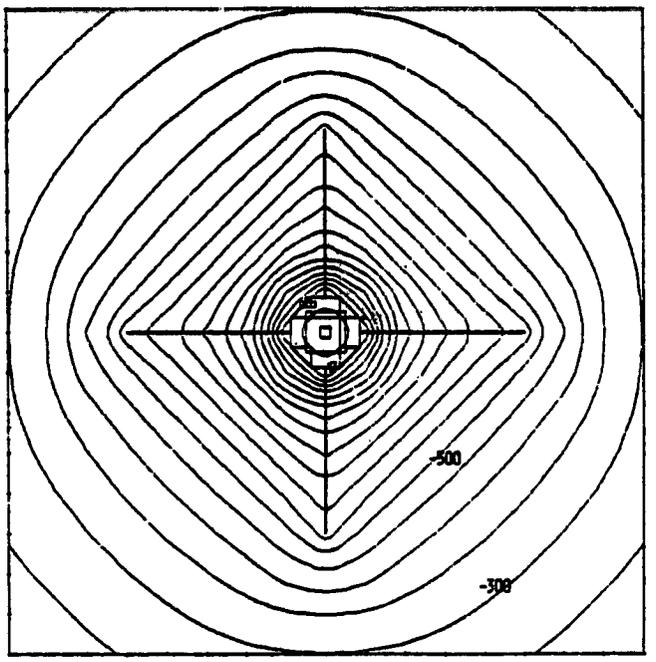

Figure 9. Potential contours in a horizontal plane 1 m below SCATHA center. Time $\sim 10^{-3}$ seconds. Contours from -250 to -1150 volts in 50 volt steps.

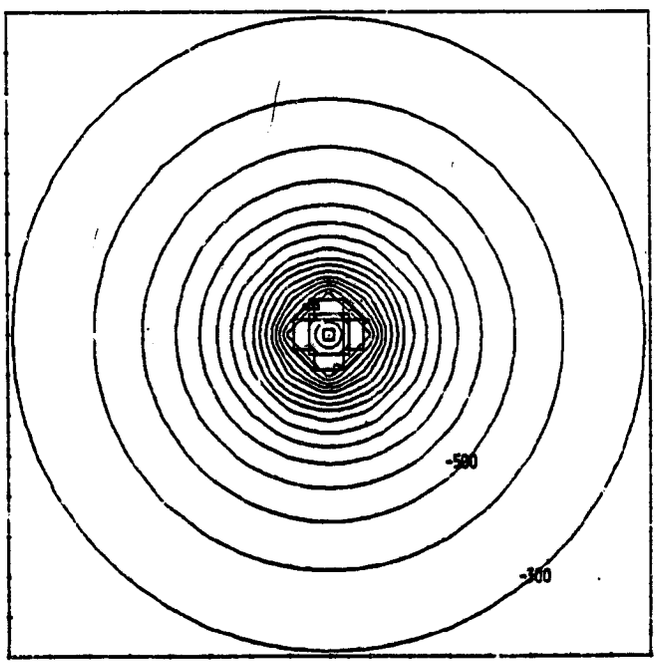

Figure 10. Potential contours in a horizontal plane 1 m below SCATHA center for a model in which the booms have been removed. Time $\sim 10^{-3}$ seconds. Contours from -300 to -1900 volts in 100 volt steps.

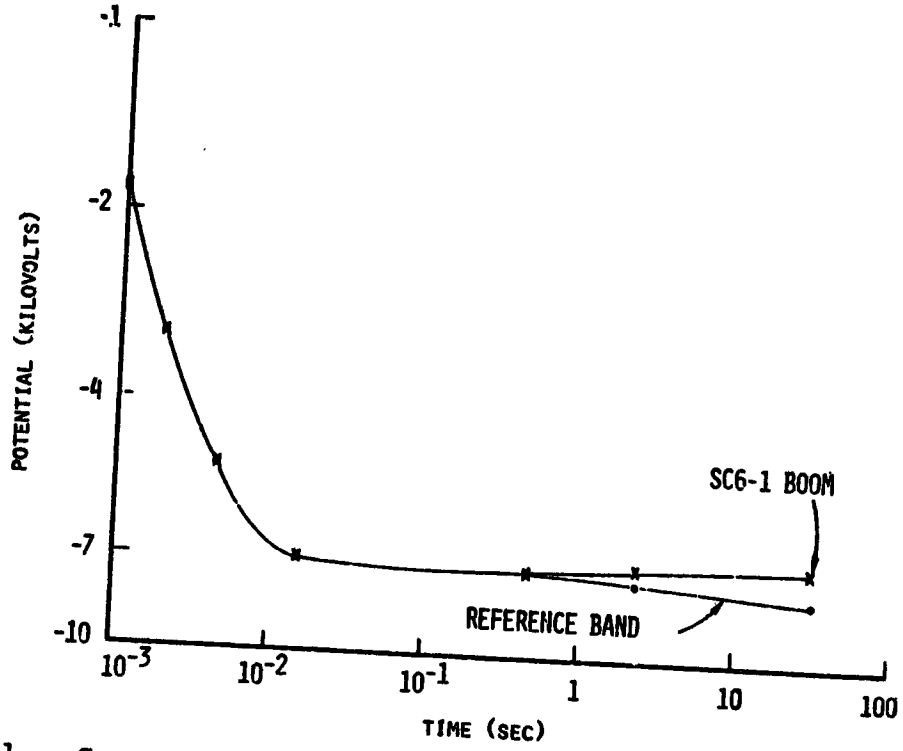

Figure 11. Spacecraft potential versus time for two points on SCATHA satellite.

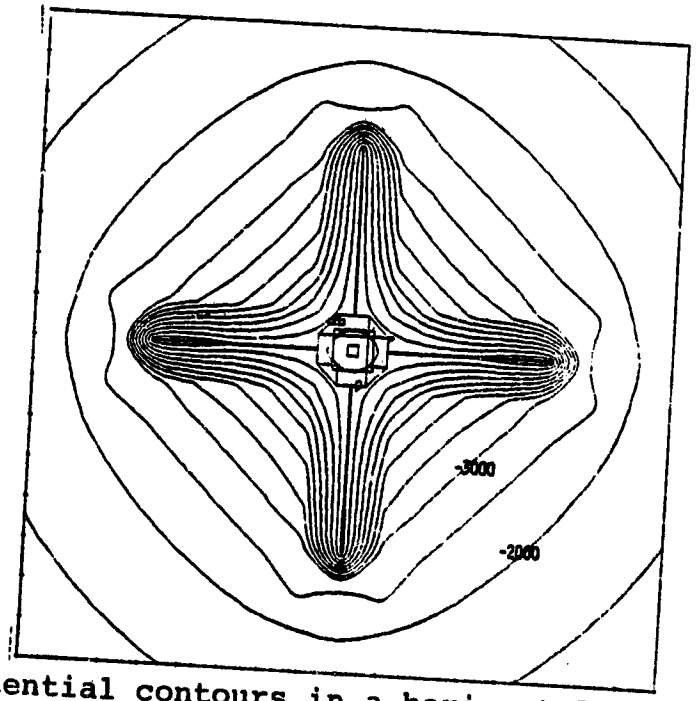

Figure 12. Potential contours in a horizontal plane through SCATHA center, with differential charging along booms. Time ∿22 seconds. Contours from -2000 to -7000 volts in 500 volt steps.

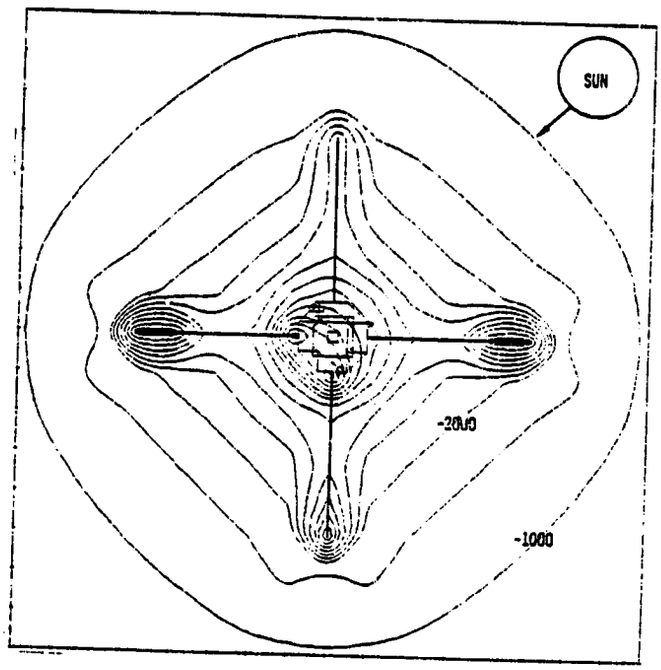

Figure 13. Potential contours for sunlit case in a horizontal plane through SCATHA center. Time ∿38 seconds. Contours from -1000 to -7500 volts in 500 volt steps.

D12

N79-24013

COMPARISON OF NASCAP PREDICTIONS WITH EXPERIMENTAL DATA

James C. Roche and Carolyn K. Purvis
NASA Lewis Research Center

SUMMARY

NASCAP (the NASA charging analyzer program) is a three-dimensional, finite-element computer code capable of simulating the electrostatic charging of an arbitrary body either in a ground test tank or in the space environment. The code incorporates surface property parameters needed to simulate insulating and conducting materials. These parameters are being updated as required to bring the NASCAP predictions into correspondence with data from ground tests conducted at the Lewis research Center. NASCAP predictions are also being compared with data from the ATS-5 spacecraft. The significance of these results is discussed.

INTRODUCTION

In the past few years the electrostatic charging of spacecraft by the charged-particle environment has become an area of concern to both spacecraft designers and space scientists. This concern arises from the statistical correlation between the occurrence of electronic switching anomalies on spacecraft and the detection of geomagnetic substorm conditions by ground stations (ref. 1). The hypothesis is that this higher-energy-particle environment charges spacecraft surfaces to a point where breakdown occurs. The resulting electromagnetic interference is picked up by the spacecraft electrical wiring and triggers logic circuits, thereby causing the anomaly. Experimental and theoretical investigations have been established to test this hypothesis.

As usual, there are problems with both approaches. It is impossible to simulate completely the space environment in ground facilities. The usual compromise is to use energetic electrons (2 to 20 keV). Purely theoretical methods have been restricted to simplified cases involving equilibrium conditions or symmetrical geometry. A generalized digital computer simulation has a different set of strengths and weaknesses and could be used to complement both experiment and theoretical analysis. Clearly an analytical tool is needed to aid in the understanding of electrostatic charging phenomena.

Generalized digital computer simulations have been used in the past to solve complex body interactions, for example, thermal and structural analyzer computer codes such as SINDA (ref. 2) and NASTRAN (ref. 3). The NASA charging analyzer program (NASCAP) is a fully three-dimensional, Cartesian finite-element code with no symmetry or equilibrium restrictions. By taking time steps in a quasi-static manner, it can simulate the charging history of a general object either in space or in a test tank. However, the primary weakness

of any finite-element approximation to a continuum is that fine-grain phenomena can occur between the finite number of lattice points into which the space is divided.

Accurate modeling of the surface interaction properties for the outer surface materials of an object is another problem that is common to both computer simulations and purely theoretical approaches. Near equilibrium, the net charging current to the object is the small difference between relatively large incoming and outgoing currents. The outgoing currents are due to such processes as backscattering, secondary emission, and photoemission. The models of these processes used in NASCAP were derived from the open literature. Parameter values for five common spacecraft surface materials (two conductors and three insulators) are included in the code.

This paper compares the NASCAP code computations with the results from a simple tank experiment. Also, by using a simulation of the ATS-5 spacecraft, comparisons are made between the predicted and actual potentials of the spacecraft structure. It is only through such comparisons that confidence can be built up in other, more complex, applications of the code.

NASCAP CODE DESCRIPTION

The NASCAP code is a finite-element spacecraft-charging simulation that is written in FORTRAN V and is currently operational on two computers: the Univac 1100 at the Lewis Research Center and the CDC 6600 at the Air Force Geophysics Laboratory. An overall description of the code and its capabilities is given in reference 4. A detailed discussion of its physical basis is given in reference 5. The structure of the software itself is described in detail in reference 6.

Program Elements

This description of the program elements is intended only as a brief survey to provide background information for this paper and is keyed to the flow chart in figure 1.

Environment definition. - One of two basic operating modes is specified: ground test tank or space. For the ground-test mode, the outer boundary of the computational grid is grounded and an electron beam of an arbitrary current-density pattern is aimed along the central axis. For the space mode, a plasma environment is specified at the outer boundary - either pure Maxwellian or an arbitrary distribution. For either case the direction and magnitude of the incident solar illumination is specified.

Object definition. - The object to be defined and the space immediately adjacent to it are divided into a number of volume cells (referred to as the inner grid) from 16x16x16 to 16x16x32. The object is modeled by using cubical cells and such portions of these cells as can be constructed by sectioning

cubes (fig. 2). There can be as many as 1000 surface cells, each of which can either be covered with an insulating film or left bare. The number of nested grids (fig. 3) is then specified, each of which has twice the size and half the resolution of the next inner grid. For example, an inner grid plus two nested grids would contain from 13 000 to 26 000 computational points.

Trajectory calculations. - Starting from a known particle flux at the outer boundary and an assumed initial potential, the incident flux to each surface cell is computed.

Shadowing. - Starting from the known solar vector, the percentage of illumination that falls on each surface cell is computed.

Surface interactions. - Starting from known particle and photon fluxes on each surface cell, the backscattering secondary emission and photoemission are computed. Surface materials and their interaction processes are modeled by using the following list of parameters (table I):

(1) Relative dielectric constant

(2) Thickness of dielectric film

(3) Electrical conductivity

(4) Atomic number

(5) Maximum secondary-electron yield for electron impact at normal incidence

(6) Primary-electron energy to produce maximum yield at normal incidence

(7-10) Four empirical parameters for use in a double-exponential model of penetration depth of incident electrons (range)

(11) Secondary-electron yield for normally incident 1-keV protons

(12) Proton energy to produce maximum secondary-electron yield

(13) Photoelectron yield for normally incident sunlight

The atomic number is used in the computation of back-scattered electrons and also, if required, in the Feldman range formula (table I, footnote c). The range is used in the computation of secondaries due to primary electrons. The values of all these parameters for five materials as initially incorporated into the NASCAP code are given in reference 6 and are repeated here in table I.

Charge accumulation. - The net current to each surface cell is determined and assumed to hold constant over one time increment. This results in an updated charge pattern over the surface of the test object.

Potential solver. - Given the updated charge pattern on the surface of the object, the potential solver uses a conjugate gradient iteration method to compute the potentials at each grid point. These new potentials can now be used to compute new fluxes to each cell for the next time step.

OPERATING CONDITIONS

A few words are in order regarding the computer running time for these simulations. The tank model, for example, has 22 000 grid points and required about 13 seconds of computer time for each potential iteration. NASCAP prints out a numerical measure of convergence, and it is possible to inspect this parameter and judge the appropriate number of iterations for each time step. A method for automatically adjusting the number of iterations so that the potential converges to within some specified accuracy is being incorporated into the code. The length of the time step and the accuracy could then be selected according to the physical situation with the knowledge that the number of potential iterations will adjust itself to meet these constraints.

For space-mode calculations the current version of NASCAP is capable of handling spacecraft that are three-axis stabilized or slowly spinning. A rapidly spinning spacecraft in sunlight is difficult to simulate. This case is discussed in more detail in the section Summary of ATS-5 Comparison. A method of applying average levels of illumination to the appropriate cells on a constant basis will be incorporated into the code to handle rapidly spinning spacecraft in sunlight.

COMPARISON OF NASCAP PREDICTIONS WITH GROUND-TEST DATA

In ground-test-tank experiments, material specimens are exposed to the flux from an electron gun. Therefore only those properties of the material that are related to electron impact, such as backscattered electrons and secondary-electron emission, are relevant. Comparing NASCAP predictions with test data would then verify the electron-impact material parameters. This leaves the parameters related to proton impact yet to be evaluated. This could be accomplished by space flight data comparisons.

Procedure

The test-tank experiments used for comparison with NASCAP predictions were conducted in a 2-meter-diameter vacuum chamber at the Lewis Research Center. Flat test specimens were irradiated with an electron beam, and their surface voltages were monitored with a field-sensing probe that scans across the surface at regular intervals at a distance of 3 millimeters. Before each experiment, the surface of the specimen was discharged with a plasma source. This facility and its instrumentation are described in detail in reference 7.

The NASCAP model of this facility is shown in figure 3. The cylindrical tank is modeled by the square cross-section of the third and outer grid, which is truncated at each end to the correct length. There are a total of approximately 22 000 grid points in this relatively simple model. The test specimen has a cross-section of 15 centimeters by 20 centimeters and is located, as shown, in the inner grid. The resolution in the test specimen is 2.5 centimeters. The electron beam is aimed along the central axis of the tank. Since NASCAP is capable of modeling an arbitrary current-density pattern, data from an electron gun calibration were inserted into the code. After a slight beam curvature - caused by the magnetic field of the Earth - is allowed for, the gun current-flux profile is taken to be that which would produce the measured current-density pattern in the plane of the test specimen before any charging. As the specimen charges, the current-density pattern spreads, but the flux profile at the gun remains constant.

Tests were conducted on the following types of specimens: bare aluminum baseplate, silvered Teflon (0.127 mm thick), two types of thermal blanket, and a solar-array-segment module. The thermal blankets both consisted of a surface layer of Kapton (0.127 mm thick) over multiple layers of silvered Mylar that were grounded to the baseplate. The blankets differed only in the technique used for grounding the Mylar layers. The aluminum baseplate was grounded for all tests except the first, in which it was left bare and ungrounded so that its floating potential could be measured. Each specimen was irradiated with a beam having a nominal central density of 1 nA/cm^2 as measured with a Faraday cup. The beam accelerating voltage was set at 5, 8, 10, and 12 keV for each specimen.

The silvered Teflon was modeled as a plain, 0.127-millimeter-thick layer of Teflon since it was bonded to the baseplate with the silvered side against the plate. Both thermal blankets were modeled as a 0.127-millimeter-thick layer of Kapton since this was the composition of the top layer of both blankets and the metallized layers underneath were grounded. The solar-array-segment module was modeled as a 0.203-millimeter-thick layer of silica.

Summary of Ground-Test Comparisons

Surface voltage profiles for the test samples, resulting from electron bombardment, were compared with the NASCAP predictions by using the available literature values for electron-impact material parameters (table I). The results are summarized here.

Aluminum. - The NASCAP comparison indicated that the aluminum test surface was, in reality, an aluminum oxide surface. Using literature values for the material properties of aluminum oxide instead of pure aluminum resulted in excellent agreement (fig. 4). Since no special precautions were taken to prevent oxidation of the aluminum, it is reasonable to assume that the test surface was aluminum oxide.

Only the steady-state potentials were compared for this specimen. To compare transient surface voltages, the NASCAP code requires a value for the

capacitance between the electrically floating aluminum plate and ground. This capacitance value was not available.

Silvered Teflon. - The steady-state NASCAP predictions for silvered Teflon are in excellent agreement with the test data (fig. 5). The transient voltage predictions are in fair agreement but seem to lag consistently behind the experimental charging data.

Aluminized Kapton. - Both the steady-state and transient predictions for aluminized Kapton are in good agreement with the limited test data (fig. 6).

Solar-array segments. - There are significant discrepancies between the predictions and the test data for solar-array (silicon dioxide) segments (fig. 7). The difficulty here could be similar to that which was experienced with the bare aluminum plate. The solar-array cover slide that was tested had a coating of an antireflective compound, but the parameters in table I were derived for pure silica. This case is still under investigation, and parameter adjustments will be made when additional data are available.

COMPARISON OF NASCAP PREDICTIONS WITH ATS-5 DATA

The spacecraft that was selected for comparison with the NASCAP code was the ATS-5. This spacecraft carries a particle analyzer, and thus there is a large amount of information available concerning its charged-particle environment. Information on the spacecraft itself and its instruments is given in reference 8. Data from its particle analyzer have been reduced and fitted to a double Maxwellian model (ref. 9).

Procedure

The NASCAP model of the ATS-5 is shown in figure 8. The cylindrical outer surface of the spacecraft is modeled as an octagon with a central region covered with Teflon and end regions covered with silica to simulate the solar array. The cavities at each end are covered with Teflon. Since about 10 percent of the solar-array area consists of exposed metallic interconnects, 10 percent of the surface cells in the solar-array regions have been left as exposed aluminum. There are 880 surface cells in this model. The environment was simulated by a single Maxwellian approximation with a density of 1 particle per cubic centimeter and a temperature of 5 keV for both species. These values are typical of much of the actual data.

Summary of ATS-5 Comparison

First, eclipse conditions were simulated by using parameters from table I. This resulted in a spacecraft ground potential of approximately -2300 volts, which did not agree with the flight data. However, the simple expedient of halving the secondary yields due to ion impact on the Teflon and the silica

(which are not well-known values) produced a spacecraft ground potential of -3800 volts, a figure that was actually measured on the spacecraft several times under similar environmental conditions. Figure 9 shows potential contours in the charged condition (spacecraft ground at -3800 V).

The ATS-5 rotated at 76 revolutions per minute. As noted earlier, a rapid spin rate presents a practical simulation problem. NASCAP models the rotation by changing the Sun angle and recomputing the shadow pattern at each time step. For this to be a realistic simulation, there should be at least 10 time steps per revolution, or approximately 80-millisecond time steps. Although absolute charging occurs in a matter of seconds, it takes many minutes for the differential charging pattern to fully develop. This would lead to a prohibitive number of time steps.

If the spin rate is reduced so that larger time steps can be taken, another problem is encountered: saddle-point formation (ref. 10). This saddle-point formation results from a field distribution around the satellite that effectively reduces photocurrents from the illuminated surfaces. This limits the NASCAP treatment of rapidly spinning spacecraft. This constraint will be alleviated in future modifications of the code.

A simulation of a stationary ATS-5 model in the sunlight was run for qualitative comparison only. The resulting potential contours are shown in figure 10 and seem to be reasonable. The simulation indicated a ground potential from -400 to -500 volts. Flight data from the spinning ATS-5 have shown ground potentials near zero volts in the sunlight. Therefore, it seems plausible that a stationary ATS-5 that is having a fraction of its electron emission suppressed by a saddle point on its sunlit side would develop such negative potentials.

CONCLUDING REMARKS

The work described herein demonstrates that the NASCAP code generates results that are in reasonable agreement with available ground-test and spacecraft data. Ground-test results reveal that better material-property values are needed for the five common materials currently implemented in the code. Altering the values of the code parameters is a simple task, and the code is structured so that even the models of the processes could be changed without disrupting other areas of the code. Also, a methodical system for altering the values of the code parameters in response to experimental data is clearly needed.

REFERENCES

1. McPherson, D. A.; Cauffman, D. P.; and Schober, W.: Spacecraft Charging at High Altitudes - The SCATHA Satellite Program. AIAA Paper 75-92, Jan. 1975.

2. Smith, J. P.: Systems Improved Numerical Differencing Analyzer (SINDA): User's Manual. TRW-14690-H001-R0-00, TRW Systems Group, 1971.

3. The NASTRAN User's Manual (Level 16.0 Supplement). NASA SP-222(03), 1976.

4. Katz, I.; et al.: The Capabilities of the NASA Charging Analyzer Program. Spacecraft Charging Technology - 1978. NASA CP-2071, 1979.

5. Katz, I.; et al.: A Three Dimensional Dynamic Study of Electrostatic Charging in Materials. (SSS-R-77-3367, Systems Science and Software; NASA Contract NAS3-20119.) NASA CR-135256, 1977.

6. Mandell, M. J.; Harvey, J. M.; and Katz, I.: NASCAP User's Manual. (SSS-R-77-3368, Systems Science and Software, NASA Contract NAS3-20119.) NASA CR-135259, 1977.

7. Berkopec, F. D.; Stevens, N. J.; and Sturman, J. C.: The Lewis Research Center Geomagnetic Substorm Simulation Facility. NASA TM X-73602, 1976.

8. Goldstein, R.; and DeForest, S. E.: Active Control of Spacecraft Potentials at Geosynchronous Orbit. Spacecraft Charging by Magnetospheric Plasmas, Progress in Astronautics and Aeronautics, Vol. 47, A. Rosen, ed., American Institute of Aeronautics and Astronautics, 1976, pp. 169-181.

9. Garrett, H. B.: Modeling of the Geosynchronous Orbit Plasma Environment - Part I. AFGL-TR-77-0288, Pt. 1, Air Force Geophysics Laboratory, 1977.

10. Mandell, M. J.; et al.: The Decrease in Effective Photocurrents due to Saddlepoints in Electrostatic Potentials near Differentially Charged Spacecraft. Presented at the 1978 IEEE Annual Conference on Nuclear and Space Radiation Effects, Albuquerque, N. Mex., July 18-21, 1978, Session C-4.

TABLE I. - MATERIAL-PARAMETER VALUES

Parameter	Description	Material				
		Aluminum	Magnesium	Teflon	Kapton	Silica
1	Relative dielectric constant (dimensionless)	1.0	1.0	2.0	3.5	4.0
2	Thickness of dielectric film, m	(a)	(a)	(a)	(a)	(a)
3	Electrical conductivity, mho/m	$^{b}-1$	$^{b}-1$	10^{-14}	10^{-14}	10^{-14}
4	Atomic number (dimensionless)	13	12	10	5	10
5	Maximum secondary-electron yield for electron impact at normal incidence (dimensionless)	0.97	0.92	3.00	2.10	2.40
6	Primary-electron energy to produce maximum yield at normal incidence, keV	0.30	0.25	0.30	0.15	0.40
7-10	Parameters used in double-exponential model: dimensionless	26	$^{c}-1$	$^{c}-1$	$^{c}-1$	25
	----------	1.30	----	----	----	0.12
	dimensionless	24	(1.74)	(2.00)	(1.42)	36
	----------	1.73	(24.3)	(16.7)	(9.8)	1.63
11	Secondary-electron yield for normally incident 1-keV protons (dimensionless)	1.36	1.36	1.40	1.40	1.40
12	Proton energy to produce maximum secondary-electron yield, keV	40	40	70	70	70
13	Photoelectron yield for normally incident sunlight	$4x10^{-5}$	$2x10^{-5}$	$2x10^{-5}$	$2x10^{-5}$	$2x10^{-5}$

[a]As required.

[b]A flag indicating a vacuum gap over a bare conductor.

[c]A flag indicating the use of Feldman's range formula (ref. 1, appendix F.2). After receipt of this flag, the eighth parameter is ignored, the ninth parameter is specific gravity, and the tenth parameter is mean atomic weight.

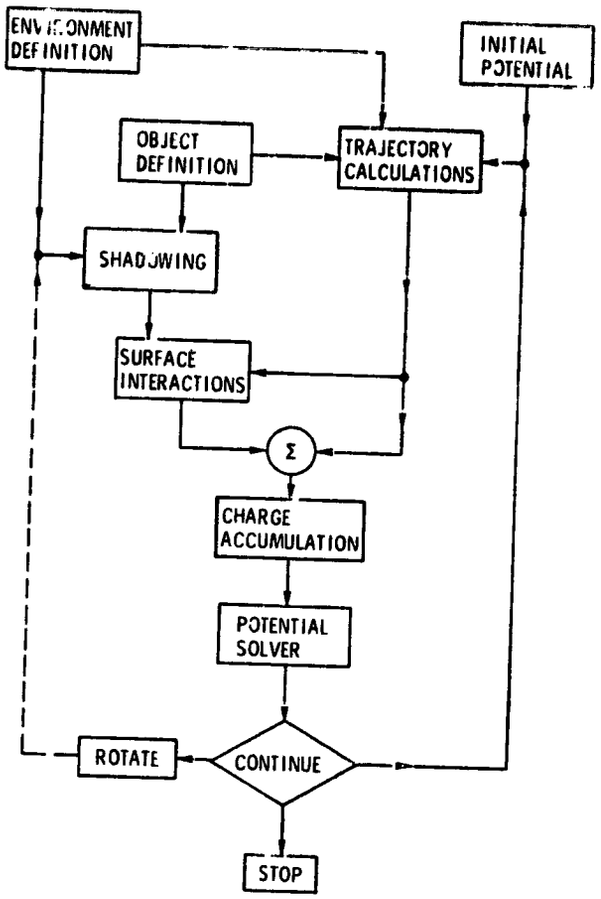

Figure 1. - NASCAP flow chart.

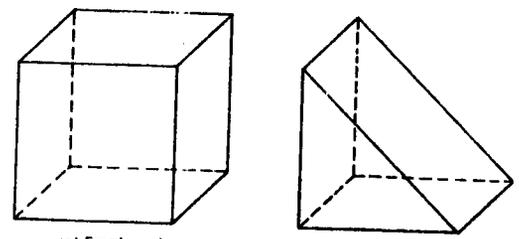

(a) Empty cube.

(b) Wedge-shaped cell with 110 surface.

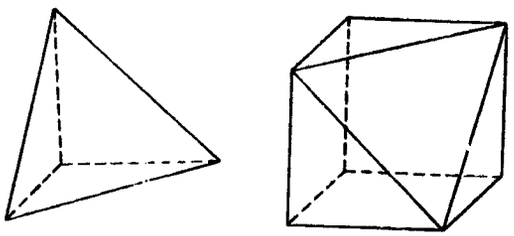

(c) Tetrahedron with 111 surface.

(d) Truncated cube with 111 surface.

Figure 2. - Four shapes of volume cells considered by NASCAP code.

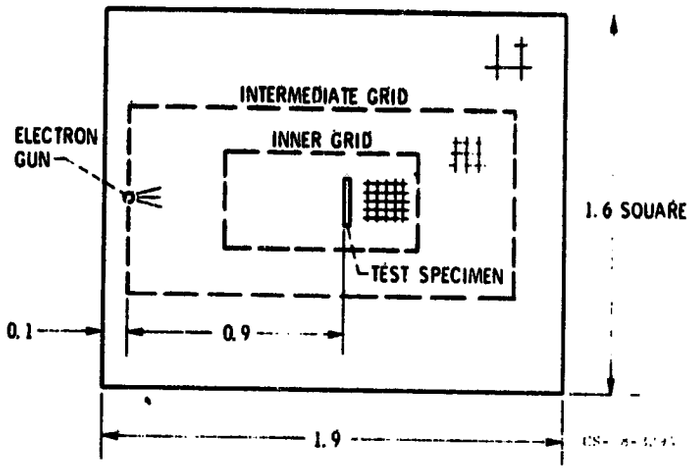

Figure 3. - Test-tank model. (Dimensions are in meters.)

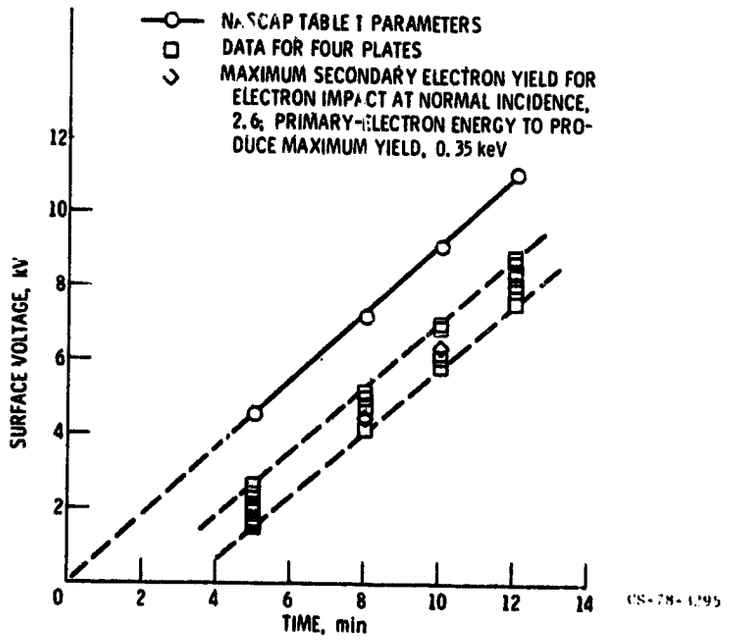

Figure 4. - Surface voltage profile for aluminum.

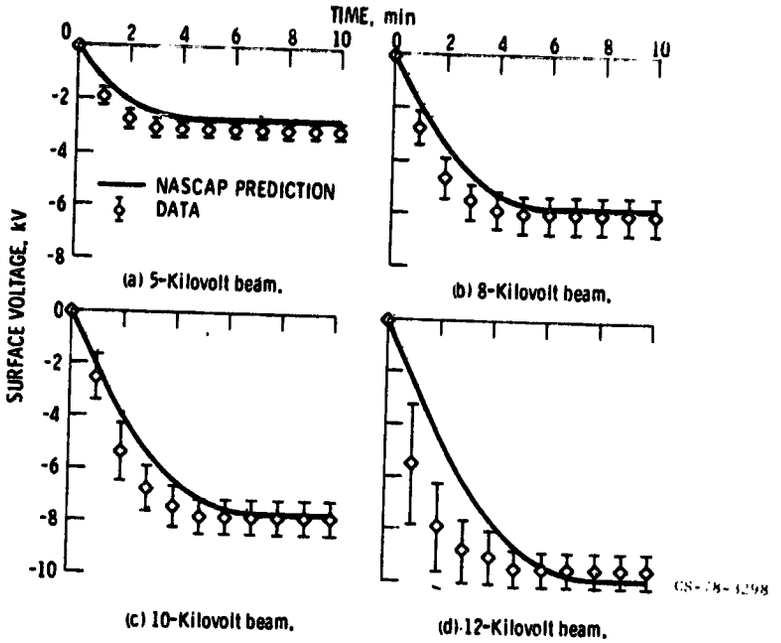

Figure 5. - Surface voltage profiles for silvered Teflon.

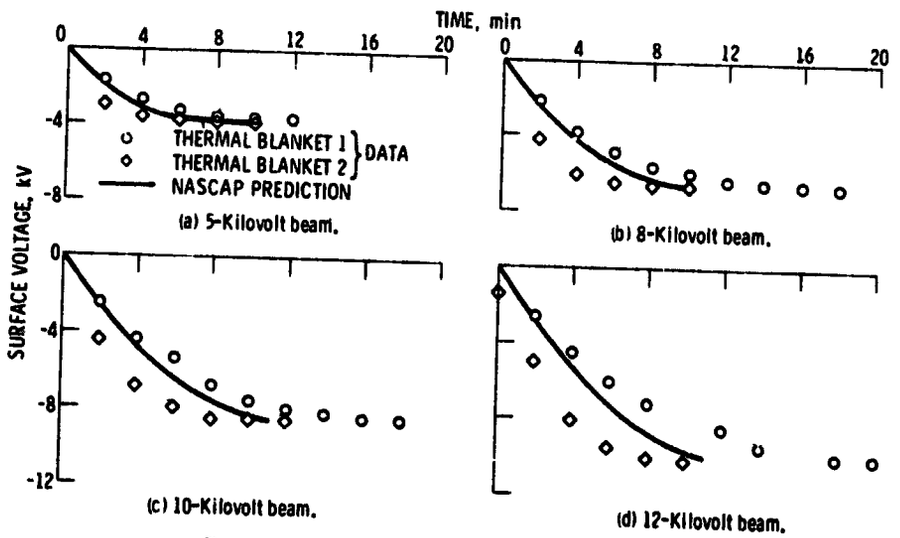

Figure 6. - Surface voltage profiles for aluminized Kapton.

CS-78-1299

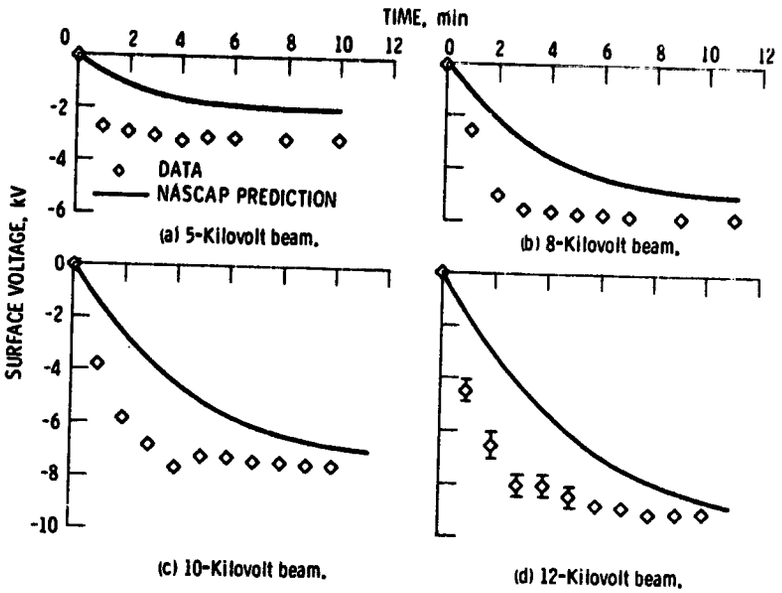

Figure 7. - Surface voltage profiles for solar-array (silicon dioxide) segments.

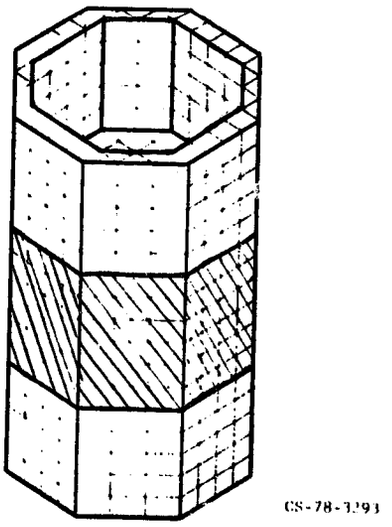

Figure 8. - NASCAP model of ATS-5.

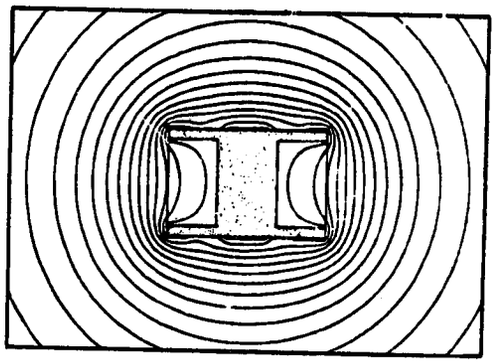

Figure 9. - Simulation of potential contours of ATS-5 in charged condition in eclipse.

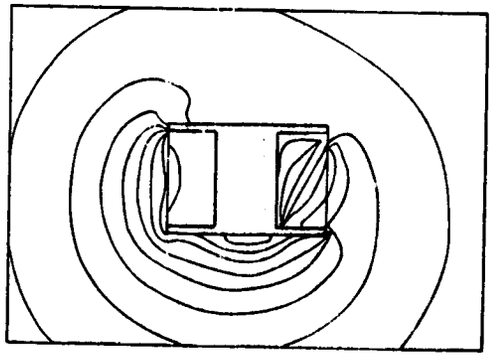

Figure 10. - Simulation of potential contours of ATS-5 in sunlight.

D13

N79-24014

SPACECRAFT CHARGING RESULTS FOR THE DSCS-III SATELLITE

Michael J. Massaro and Dale Ling
General Electric Space Division

ABSTRACT

Spacecraft charging results are presented for the DSCS-III satellite for a severe geomagnetic substorm. Spacecraft charging results were obtained by the use of the Electrostatic Charging Analysis Program (ESCAP). The ESCAP computer code which can determine both the transient or steady-state differential charging potentials is an engineering design tool that utilizes a circuit theory approach to spacecraft charging. Using the ESCAP code, the steady-state (static) differential potentials of the outer spacecraft surfaces and metallic structure were obtained for the DSCS-III satellite when under the influence of a severe geomagnetic substorm during the local midnight-to-dawn quadrant of its geosynchronous orbital path. The results obtained indicate that, in the steady-state, most of the DSCS-III outer surface materials will not achieve differential potentials large enough to produce an electrostatic discharge (ESD). Recent changes to the ESCAP code to improve execution time are discussed as well as model improvements for future development.

INTRODUCTION

The main purpose of this paper is to present the results of a spacecraft charging analysis of the DSCS-III satellite. (DSCS-III is the third generation satellite of the Defense Satellite Communication System.) In addition, a discussion of an approach to determine the probabilistic rate of electrostatic discharge (ESD) of dielectric materials is presented. Spacecraft charging refers to that phenomenon whereby the outer materials of spacecraft attain surface charges produced by the bombardment of energetic charged particles. During a geomagnetic substorm the outer dielectric surfaces can achieve differential potentials at which electrostatic discharge (ESD) can occur. ESD can cause degradation of the thermal properties of materials, state changes of operational circuitry, and RF interference to receivers. Thus, it is important to determine if any of the outer dielectric materials, will be a source of ESD.

Spacecraft charging results were obtained by using the Electrostatic Charging Analysis Program (ESCAP) which was developed by the General Electric Space Division under an internally funded research program. The ESCAP code can determine both the transient and steady-state differential potentials; however, at present, only the steady-state solutions can be obtained with a

reasonable amount of computer time (20-30 minutes of main-frame computer time for 1 to 3 minutes of transient results versus 5-10 seconds of main-frame time for a complete steady-state solution). The ESCAP code utilizes a circuit theory approach to spacecraft charging. The spacecraft-to-environment interaction is determined by representing the charged particle environment as equivalent current source functions and by representing the spacecraft by its electrically equivalent circuit with respect to the plasma charging phenomenon. The charging model includes a sun/earth/spacecraft orbit model that simulates the sun illumination conditions of the spacecraft outer surfaces throughout the geosynchronous orbit.

Recent changes to decrease the computer time needed to execute a steady-state solution are discussed as well as improvements in the plasma current source representation. In addition, the variation of S/C charging differential potentials as a function of the secondary electron emission coefficient is presented.

The paper is organized as follows. First, a brief description of ESCAP is given. The S/C charging results for the DSCS-III satellite are presented along with a description of its material and geometric configuration and the pertinent plasma and emission parameters used in the analysis. Next, ESD probabilities of occurrence are derived and lastly, the ESCAP code improvements are discussed.

SPACECRAFT CHARGING MODEL

The spacecraft charging model can best be described in terms of the flow chart shown in figure 1. The ESCAP code consists of four separate models: a plasma model, an electrical model, a S/C geometrical model; and a solar/earth/orbital model. The plasma model represents the charging and discharging mechanism of the ambient plasma with respect to the spacecraft by equivalent current sources. The current sources, which are dependent on the particle energy distribution functions, constitute the forcing functions of the charging model equations. At present, the plasma generated current sources are assumed to have a single, omnidirectional Maxwellian energy distribution with time-independent parameters for the duration of the subsystem. However, the model can be easily modified to consider a "two- Maxwellian" energy distribution plasma representation as well as field-aligned fluxes. The approach to accomplish this is discussed in a later section.

The electrical model defines the lumped element equivalent circuit representation of the spacecraft surfaces with respect to the electrostatic charging phenomenon. The plasma model and electrical model are combined to form the non-linear spacecraft charging equations. The spacecraft geometrical model defines the spacecraft outer surfaces in terms of approximate planar surfaces and curved surface projections and defines the vertices of all planar and curved surfaces in terms of a spacecraft reference coordinate system. The solar/earth/orbital model determines the location of the spacecraft with respect to the sun and the earth. The geometrical model and the

solar/earth/orbital model are combined to determine the variation of the sun-illumination conditions of the outer surfaces with respect to orbital position.

To complete the modeling, the surface material properties and configuration are defined. The surface material properties that are most important in a spacecraft charging analysis are the relative dielectric constant; the variation of the surface resistivity with respect to electrical stress level; and the variation of the bulk resistivity with respect to electrical stress level. The material configuration definition describes the location of the various thermal blanket and surface coating materials.

A more detailed description of the program is given in reference 1.

MATERIAL AND GEOMETRIC CONFIGURATION

DSCS-III is a three-axis stabilized spacecraft operating in a geosynchronous orbit. The spacecraft has two nineteen beam transmit multiple beam antennas, a sixty-one beam receive multiple beam antenna, two earth coverage receive antennas, two earth coverage transmit antennas, a gimballed dish transmit antenna (GDA), and a receive antenna and a transmit antenna for the Single Channel Transponder (SCT). The main body of the spacecraft is almost cube shaped with the approximate dimensions shown in figure 2. Also shown in figure 2 is the outer thermal blanket material and coating configuration. A summary of the thermal blanket material properties and locations is given in table 1. To prevent the fiberglass structural parts of the SCT antennas from becoming a source of ESD, the fiberglass surfaces were coated with conductive Indium Tin Oxide (ITO). The thickness of the conductive coating was chosen to promote a gradual depletion of the surface charge to the structure with minimal effect on the RF performance of the SCT antennas. From similar coating processes it has been found that a minimum total surface resistance of 500 K Ω can be expected for ITO. The bulk resistivity values listed in table 1 are the values measured at a low voltage level; however, the actual bulk resistivity characteristics, i.e., bulk resistivity as a function of the potential across the material, were employed in the analysis. A summary of the areas of the outer thermal blanket materials and coatings is given in table 2. The amount of exposed structural metal is also listed as well as those surfaces that are never exposed to direct radiation from the sun, i.e., the "permanently shadowed" areas.

PLASMA PARAMETERS AND SPACECRAFT CHARGING EQUATIONS

Recently there has been considerable effort to refine and expand the plasma substorm environmental data base, that is, the diurnal variation of the parameters that characterize the plasma substorm particle density and energy distributions. In particular, the Air Force Geophysical Laboratories (AFGL) has established a computer based plasma substorm parameter data file (ref. 2)

which contains parameters for a "one" Maxwellian or "two" Maxwellian approximation to the actual measured plasma distribution. AFGL supplied the Space Division with a representative range of plasma substorm parameter values. Part of the information supplied was a single Maxwellian distribution function approximation of the actual measured particle density and energy distributions. The single Maxwellian distribution approximation parameters were used in the ESCAP program. The range of plasma particle temperatures and current densitites supplied by AFGL and the range of secondary and photoemission parameters obtained from the literature are presented in table 3.

Also shown in table 3 are the parameter values selected for use in the ESCAP program. Three levels of substorm activity were established: mild, moderate, and severe. Since the electron particles have the greatest influence on spacecraft charging, the electron current density and energy values were used to classify the substorm. Spacecraft charging results were obtained for all three levels of substorms; however, only the results for the severe substorm will be presented herein.

The equivalent plasma and photoemission generated current sources were derived in reference 1 and are based on a "single Maxwellian" approximation to the actual plasma particle energy distribution functions. Incident protons and electrons as well as secondary electrons and photoelectrons were considered in the plasma model. For a large dielectric surface, the current forcing function will have the general form (see ref. 1)

$$I_D(V) = \left[\left(J_{po}e^{-V/T_p}\right)\left(1 + f_{pd}e^{-V/T_s}\right) + \left(J_{pho}\right)_d (\cos\alpha)e^{-V/T_{ph}} + \left(J_{eo}e^{V/T_e}\right)\left(f_{ed}e^{-V/T_s} - 1\right)\right] \cdot A \qquad (1)$$

where I_D is the total positive current into a large dielectric surface, A is the area of the surface, J_{eo} is the average ambient electron current density incident to a neutral surface, J_{po} is the average ambient proton current density incident to a neutral surface, $(J_{pho})_d$ is the average photoelectron current density emitted from an illuminated neutral dielectric surface, V is the absolute potential of the dielectric surface, T_e is the equivalent temperature, expressed in volts, of the Maxwell-Boltzmann (M-B) distribution approximating the plasma electron energy distribution, T_p is the equivalent temperature of the M-B distribution approximating the plasma proton energy distribution and is expressed in volts, T_s is the equivalent temperature of the M-B distribution representing the energy distribution of the secondary emission electrons and is expressed in volts, T_{ph} is the equivalent temperature of the M-B distribution representing the energy distribution of the photoelectrons expressed in volts, f_{ed} is the secondary electron emission coefficient for electrons incident to a dielectric surface, f_{pd} is the secondary electron emission

coefficient for protons incident to a dielectric surface, and α is the sun aspect angle for the dielectric surface.

The above equation must satisfy the following condition

$$e^{sV/X} = \begin{cases} 1 \text{ if } s = +1 \text{ and } V > 0; \text{ otherwise leave unchanged} \\ \\ 1 \text{ if } s = -1 \text{ and } V \leq 0; \text{ otherwise leave unchanged} \end{cases}$$

The sun aspect angle, α, is the angle between the sun-line and the surface normal vector and

$$\cos \alpha = \begin{cases} \cos \alpha & \text{for } |\alpha| < \pi/2 \\ 0 & \text{for } |\alpha| \geq \pi/2 \quad \text{(self-shadowing conditions)} \end{cases} \tag{3}$$

The positive current flowing into the metallic structure is (see ref. 1)

$$I_M(V) = A_{MT}J_{po}(1 + V/T_p)e^{-V/T_p}\left(1 + f_{pm}e^{-V/T_s}\right) + A_{MT}J_{eo}e^{V/T_e}\left(f_{em}e^{-V/T_s} - 1\right)(1 + |V/T_e|) + \sum_{i=1}^{m} A_{Mi}(J_{pho})_m (\cos \alpha_i)e^{-V/T_{ph}} \tag{4}$$

where equations (2) and (3) hold for the above equation and A_{MT} is the total exposed metallic area, A_{Mi} is the exposed area of the i^{th} metallic surface, m is the total number of exposed metallic surfaces, α_i is the sun aspect angle for the i^{th} metallic surface, f_{pm} is the secondary electron emission coefficient for protons incident to a surface, metallic f_{em} is the secondary electron emission coefficient for electrons incident to a metallic surface, and the following holds for the small area correction terms

$$(1 + V/T_p) = \begin{cases} (1 + V/T_p) \text{ for } V \geq 0 \\ 1 \text{ for } V < 0 \end{cases} \quad (5)$$

$$(1 + |V/T_e|) = \begin{cases} (1 + |V/T_e|) \text{ for } V \leq 0 \\ 1 \text{ for } V > 0 \end{cases} \quad (6)$$

The lumped element, equivalent electrical circuit representation of the spacecraft outer surfaces with respect to the electrostatic charging phenomenon was derived in reference 1 and is shown in figure 3. The steady-state spacecraft charging equations for the simplified circuit of figure 3 are given by

$$\frac{V_1 - V_o}{R_1 (V_1 - V_o)} = I_1 (V_1) \quad (7)$$

$$\vdots \qquad \vdots$$

$$\frac{V_n - V_o}{R_n (V_n - V_o)} = I_n (V_n) \quad (8)$$

$$\sum_{i=0}^{n} I_i = 0$$

It has been assumed that there are n outer surfaces. The i^{th} surface has an absolute potential of V_i volts and each surface, or node, has a corresponding plasma and photoemission generated current source, I_i, having the general form of equation (1). The spacecraft structure has an absolute potential of V_o volts and I_o is the plasma and photoemission generated current source into the exposed metallic surfaces and is given by equation (4). Equations (7) and (8) in general, will be non-linear since the leakage resistances are non-linear functions of stress level $(V_i - V_o)$ and the plasma currents are non-linear functions of stress level also, i.e., voltage dependent current sources.

The number of equations, n, is a function of both the number of surfaces with different materials and with different sun illumination conditions, i.e., the number of surfaces with different orientations with respect to the spacecraft reference coordinate system. The solution of this set of n simultaneous nonlinear equations is discussed in a later section.

SPACECRAFT CHARGING RESULTS

Spacecraft charging results were obtained for the peak of the winter-solstice and fall-equinox orbital periods for a severe substorm. It was assumed that the plasma substorm had a duration of nine hours starting at 23:00 LT and ending at 8:00 LT. The extremes of spacecraft response are obtained during these two orbital periods. For example, during equinox the spacecraft will experience eclipse conditions (total-shadowing) and the spacecraft structure achieves its highest negative potential; whereas during winter-solstice the spacecraft structure achieves its lowest negative potential. The latter condition results from the fact that the South Panel has more exposed metal than the North Panel and that during winter-solstice the South Panel is illuminated by the sun. The OSR coverglass material exhibited the greatest steady-state potential difference, i.e., the potential difference between the outer surface and the spacecraft structure. The steady-state potential differences of the above material as well as the absolute potential of the spacecraft structure during a severe substorm are listed in tables 4 and 5, for fall-equinox and winter-solstice, respectively. It can be seeen from these tables that the spacecraft structure achieves a maximum negative absolute potential of -14 kV during eclipse and a minimum negative absolute potential of -170 V during winter-solstice. The OSR coverglass material achieves its greatest potential difference during winter-solstice. The steady-state absolute potentials of all of the spacecraft outer surfaces for a severe substorm are shown in figures 4 and 5 for fall-equinox and winter-solstice at 8:00 LT, respectively.

A summary of the maximum steady-state potential differences achieved by all of the outer surfaces during the fall-equinox and winter-solstice orbital periods is listed in table 6. It can be seen from table 6 that the OSR coverglass achieved the highest steady-state potential difference, 5200 volts. Because of the potential differences attained by the OSR coverglass, this material may be a possible source of ESD and the OSR coverglass material will be the only steady-state source of ESD during a severe substorm. Electron bombardment tests of this material have indicated that low-level, observable discharges will occur at potential differences on the order of 7 kV. In order to assess the effects of the ESD produced by the OSR coverglass on the performance of the DSCS-III system both the radiated ESD field levels and the rate of ESD had to be determined. Measured values of the magnitude of radiated ESD fields are presented in reference 3 and an estimate of the probabilistic occurrence rate of ESD is derived in the following section.

Finally, it should be mentioned that the above spacecraft charging analysis considered only the steady-state potential differences. It is possible for the solar array coverglass to produce ESD because of transient potential differences between the coverglass and the spacecraft metallic structure. However, these discharges, if any, will be produced only during severe substorms and only when the spacecraft enters and exits eclipse.

ESD PROBABILITIES OF OCCURRENCE

In order to determine the probabilities of occurrence of ESD from OSR coverglass, a sample of the material was subjected to electron bombardment tests to simulate a severe substorm environment. The OSR Glass was bombarded with electrons having an accelerating potential of 20KeV and a density of $1.5na/cm^2$. This current density value is about twice the maximum electron current density of any plasma substorm that has been measured up to the present time. Discharges were observed at the rate of about one every twenty seconds. Since there are twenty separate sections of OSR glass on DSCS III (each section consisting of hundreds of cells of OSR glass) and since each section can discharge independently, a binomial probability density function was used to characterize the statistical occurrence of ESD from OSR coverglass. Thus, the probability of k discharges in Δt seconds is

$$P(k) = \binom{n}{k} p^k q^{n-k} \tag{9}$$

where P(k) is the probability of k discharges in Δt seconds, n is the number of sections of OSR glass, 20, p is the probability of a discharge occurring in Δt seconds and q is the probability of no discharge in Δt seconds. For the OSR cover glass there results

$$p = \frac{\Delta t}{T}$$

$$q = \overline{p} = (1-p) \tag{10}$$

where T is the periodicity of a discharge for one section of OSR glass and is equal to about 20 seconds for the simulated substorm. The probability of m-or-more discharges occurring in one second is the complement of the probability of (m-1)-or-less discharges occurring and from equation (7) is given by

$$\text{Pr(m-or-more discharges)} = 1-\text{Pr((m-1)-or-less discharges)} = 1-\sum_{k=0}^{m-1} P(k) \tag{11}$$

Using equation (11), the ESD probabilities of occurrence were computed for one-or-more up to ten-or-more discharges occurring randomly in one second and the results are presented in table 7. It can be seen from table 7 that the probability of ten-or-more discharges occurring per second is extremely

remote; whereas, there is a high probability that at least one discharge will occur each second.

In the above formulation it has been assumed that each section of OSR glass, independent of the number of cells per section, will have the same discharge rate as the nine cell sample that was tested. This assumption is valid if there is a tendency for most of the cells to be affected by the discharge process.

Variation of Differential Potential with Secondary Emission

In the simplified spacecraft charging approach presented herein, the secondary electron emission coefficients were assumed to be a constant value, .5 for metals and .75 for dielectrics. To determine the sensitivity of the steady-state solutions with respect to the secondary emission coefficient, steady-state charging solutions for OSR coverglass were obtained for secondary emission coefficients ranging from .5 to .95. The results for eclipse and at winter-solstice, 8:00LT are shown in figure 6 along with the absolute potential of the spacecraft structure for the winter-solstice orbital period at 8:00 LT. It can be seen in figure 6 that for eclipse as the secondary emission coefficient increases the coverglass becomes increasingly more positive with respect to the S/C structure. This is to be expected since as the secondary coefficient increases there is more net positive current flow (less negative current flow) into the dielectric materials than into the metallic structure which has an assumed secondary emission coefficient of .5. Whereas, during winter-solstice at 8:00 LT as the coefficient decreases, the coverglass, which is self-shadowed, becomes increasingly negative with respect to the structure. As the coefficient decreases there is less net positive current flow (more negative current flow) to the OSR coverglass. The structural potential also becomes more negative as the secondary coefficient decreases; however, it is strongly affected by the photoemission currents both directly and indirectly.

ESCAP Code Improvements

Recent improvements have been incorporated in the ESCAP code to decrease the comuter time needed to execute a steady-state solution. From equations (7) and (8) the steady-state equations can be written as

$$\left[I_i - \frac{V_i - V_o}{R_i (V_i - V_o)} \right] = 0 \qquad (10)$$

for $1 \leq i \leq n$, and

$$\sum_{i=0}^{m} I_i = 0 \qquad (11)$$

The solution to this system of equations can be viewed as an optimization problem where equation (11), which represents a current balance condition, must be minimized while simultaneously satisfying the set of n nonlinear equations (10) which can be considered as constraint equations on the current balance condition. If the structural potential, V_o, is considered as an independent variable and the n surface potentials as dependent variables, then for a given value of V_s (structural absolute potential), a of each of the n variables V_i, for $1 \leq i \leq n$, can be found from (10) and the validity of the current balance value can be determined from (11). Since all of the terms of the left side of (10) are well-behaved, monotonic functions, a unimodal single variable sequential search technique (ref. 4) can be used to solve (10) for V_i when given a value of V_o, i.e., that value of V_i which minimizes (10) for a given value of V_o is the desired solution. Since (11) as a function of V_o represents the sum of monotonically decreasing or increasing functions, it also will be a unimodal function of V_o. Consequently, a single variable search technique can also be used to find that value of V_o which minimizes (11). This value of V_o represents the desired solution.

The Fibonacci sequential single variable search technique (ref. 4) was employed to minimize (solve) equations (10) and (11). The total range of possible surface potential values was divided into two regions and the search was conducted in one of these two possible regions for each surface. For surfaces with a positive or low negative potential, the range of potential values from +10V to -200V was iteratively searched. Within only twenty-two iterations the interval of uncertainty was reduced to .007 (a factor of 3×10^{-5}). For surfaces with a high negative potential the range of potential values from -200V to -40,000V was iteratively searched. Within only twenty iterations the interval of uncertainty was reduced to 3.5V (a factor of 10^{-4}). In the process of solving equations (10) and (11) by this approach it was found that the final net current incident to the total outside surface was a factor of 10^5 less than the initial net current flow to the spacecraft. It should also be noted that the search process produced the same solution after starting the search at a number of different initial starting points; this confirmed the unimodality assumption. In addition, the code has been programmed such that it can automatically determine which of the two regions should be searched for a particular surface, and the polarity of that surface.

Recently it has been proposed in reference 2 that the actual plasma particle current densities and energies could be adequately represented by a sum of two or more Maxwellian distributions. As can be seen from the S/C charging equations given previously, the form of the equations can readily accommodate two or more Maxwellian distributions and associated parameters. In addition, field-aligned fluxes can be included by simply altering the current sources to the particular surfaces of the S/C that are affected by the field aligned flux. The modified spacecraft charging equations would then have the form

$$
\begin{aligned}
\frac{V_1 - V_o}{R_1(V_1 - V_o)} &= \sum_j I_{1j} \\
&\vdots \qquad\qquad \vdots \\
\frac{V_i - V_o}{R_i(V_i - V_o)} &= \sum_j I_{ij} + I_{f_i} \\
&\vdots \qquad\qquad \vdots \\
\frac{V_k - V_o}{R_k(V_k - V_o)} &= \sum_j I_{kj} + I_{f_k} \\
&\vdots \qquad\qquad \vdots \\
\frac{V_n - V_o}{R_n(V_n - V_o)} &= \sum_j I_{nj}
\end{aligned}
\tag{12}
$$

where the plasma generated net current flow to a surface is represented by a sum of j Maxwellian distributions and the i^{th} through k^{th} surfaces are affected by field aligned fluxes represented by an I_f equivalent current source. The above modifications to the spacecraft charging equations represent possible future improvements in the ESCAP code.

CONCLUSIONS

This paper has presented steady-state spacecraft charging results for the DSCS-III satellite during the equinox and winter-solstice orbital periods for a severe geomagnetic substorm. It was shown that only one of the outer dielectric surface materials, the OSR coverglass, could be a possible source of ESD in the steady-state. Conductive coatings have been used to control ESD on the dielectric structural parts of antennas operating at low frequencies. Silica cloth materials and blankets have been used to control ESD on most of the surfaces of the spacecraft. It was found that the steady-state solutions were strongly dependent on the value of the secondary electron emission coefficient.

At present, the computer model uses a single Maxwellian approximation to the actual plasma distribution and the substorm is assumed to be time-independent for the duration of the substorm. However, the spacecraft charging equations can easily accommodate a "two Maxwellian" approximation to the actual plasma distribution as well as field-aligned particle fluxes. Once the geometrical, electrical, and material configurations of a spacecraft have been defined and entered into the code, the steady-state solutions can be obtained at every hour over the orbital period from 23:00 LT to 8:00 LT with a small amount of computer execution time (typically 3-5 minutes).

REFERENCES

1. Massaro, M. J., Green, T., and Ling, D., "A Charging Model for Three-Axis Stabilized Spacecraft", Proc. of the S/C Charging Technology Conference, Feb., 1977, AFGL-TR-77-0051, NASA TMX-73537.

2. Garrett, H.B., "Modeling of the Geosynchronous Orbit Plasma Model - Part I," Dec., 1977, AFGL-TR-77-0288, Air Force Surveys in Geophysics, No. 380.

3. Condon, G. P., "Design Development of S/C Shielding Protection Against EMI from S/C Charging/Discharging Products", GE TIS No. 76SDS053, Dec., 1976.

4. Wilde, D. J., "Optimum Seeking Methods: Prentice-Hall, N.J., 1964.

Table 1. DSCS-III Material Parameter Summary

Surface	Material	Relative Dielectric Constant	Bulk Resistivity (Ω - cm)	Thickness (cm)	Capacitance (pf/cm^2)	Resistance ($\Omega-cm^2$)
1. Back-side	No. 527 silica cloth blanket	1.7	10^{15}	.030	5.0	3×10^{13}
2. West Panel	No. 527 silica cloth blanket	1.7	10^{15}	.030	5.0	3×10^{13}
3A. North Panel	No. 527 silica cloth blanket	1.7	10^{15}	.030	5.0	3×10^{13}
3B. N.P. Window	OSR glass	4.5	7.6×10^{15}*	.020	20.0	1.5×10^{14}
4A. South Panel	No. 527 silica cloth	1.7	10^{15}	.030	5.0	3×10^{13}
4B. S.P. Window	OSR glass	4.5	7.6×10^{15}*	020	20.0	1.5×10^{14}
5. East Panel	No. 527 silica cloth blanket	1.7	10^{15}	.030	5.0	3×10^{13}
6. Earth Side						
6A. MBA-RX 6B. MBA-TX1, TX2	No. 570/550/581 silica cloth composite	1.12	10^{16}	0.605	0.20	6.05×10^{15}
6C. GDA-TX 6D. E.C. - TX1, TX2 6E. E.C - RX1, RX2	No. 570 silica cloth	1.9	10^{16}	0.068	2.5	6.8×10^{14}
6F. S.P. Edge 6G. N.P. Edge	No. 527 silica cloth blanket	1.7	10^{15}	.030	5.0	3×10^{13}
6H. SCT-RX	Fiberglass with conductive ITO Coating	2.4		0.152	1.4	500KΩ+
6I. SCT-TX	Fiberglass with conductive ITO Coating	2.4		0.305	0.70	500KΩ+
7A. Solar Array - sunside	Solar array coverglass	7.0	4.8×10^{16}	.0152	40.8	7.3×10^{14}
7B. Solar Array - darkside	Chemglaze	2.1	3.3×10^{15}	0.005	37.2	1.65×10^{13}
7C. Solar Array Yoke - sunside	No. 527 silica cloth blanket	1.7	10^{15}	.030	5.0	3×10^{13}
7D. Solar Array Yoke - sunside	Chemglaze	2.1	3.3×10^{15}	0.005	37.2	1.65×10^{13}
7E. S.A. Yoke Window - Darkside	No. 527 silica cloth	1.7	10^{15}	.030	5.0	3×10^{13}
7F. Solar Array Yoke - Darkside	Chemglaze	2.1	3.3×10^{15}	0.005	37.2	1.65×10^{13}

* Includes both bulk and surface resistivities

\+ Total surface resistance

Table 2. Surface Area Summary

SURFACE IDENTIFICATION	MATERIAL	AREA (CM^2)
1. BACKSIDE	#527 SILICA BLK.	52,075
	EXPOSED METAL	709
2. WEST PANEL	#527 SILICA BLK.	33,264
	EXPOSED METAL	842
3. NORTH PANEL	#527 SILICA BLK.	26,411
	OSR GLASS	19,286
	EXPOSED METAL	2,486
4. SOUTH PANEL	#527 SILICA BLK.	48,174
	OSR GLASS	7,200
	EXPOSED METAL	2,713
5. EAST PANEL	#527 SILICA BLK.	33,337
	EXPOSED METAL	1 118
6. EARTH SIDE	#527 SILICA BLK.	18,766
	#570 SILICA CLOTH	6 453
	#570/550/581 CLOTH COMPOSITE	23,596
	FIBERGLASS WITH ITO	37
	EXPOSED METAL	3,958
7. & SOLAR ARRAY SUN SIDE 9.	SOLAR ARRAY COMPOSITE	116,968
	#527 SILICA CLOTH (YOKE)	4,843
8. & SOLAR ARRAY DARK-SIDE 10.	CHEMGLAZE (INCLUDING YOKE)	122,649
11. PERMANENTLY SHADOWED AREAS	#527 SILICA BLK.	8,860
	FIBERGLASS WITH ITO	289
	EXPOSED METAL	10,681

Table 3. Photoemission, Secondary Emission and Omnidirectional Plasma Parameters

PARAMETER	TYPICAL RANGE	VALUE SELECTED
T_{ph}	$1\ V \leq T_{ph} \leq 3V$	2 V
T_e	$2\ V \leq T_e \leq 4\ V$	2 V
f_{em}	$0 \leq f_{em} \leq 1$	0.6
f_{ed}	$0 \leq f_{ed} \leq 1$	0.75
f_{pm}	$0 \leq f_{pm} \leq 1$	0.6
f_{pd}	$0 \leq f_{pd} \leq 1$	0.75
T_o	$1KV \leq T_o^* \leq 7.0KV$	2.2KV (MILD SUBSTORM) 5.3KV (MODERATE SUBSTORM) 7.0KV (SEVERE SUBSTORM)
T_p	$2.5KV \leq T_p^* \leq 10.4KV$	3.0 KV (MILD SUBSTORM) 5.8 KV (MODERATE SUBSTORM) 8.8 KV (SEVERE SUBSTORM)
J_{ph_o}	$0.82\ na/cm^2 \leq J_{ph_o} \leq 4\ na/cm^2$	3 na/cm^2 (METALS) 0.9 na/cm^2 (DIELECTRICS)
J_{e_o}	$0.004na/cm^2 \leq J_{e_o}^* \leq 0.8\ na/cm^2$	1.0na/cm^2 (MILD SUBSTORM) 0.5na/cm^2 (MODERATE SUBSTORM) 0.5na/cm^2 (SEVERE SUBSTORM)
J_{p_o}	$2pa/cm^2 \leq J_{p_o}^* \leq 28\ pa/cm^2$	18.5pa/cm^2 (MILD SUBSTORM) 10pa/cm^2 (MODERATE SUBSTORM) 10pa/cm^2 (SEVERE SUBSTORM)

* THESE PARAMETERS REPRESENT A SINGLE MAXWELLIAN DISTRIBUTION APPROXIMATION TO THE ACTUAL MEASURED PARTICLE DENSITY AND ENERGY DISTRIBUTIONS. PARAMETER VALUES WERE SUPPLIED BY THE AIR FORCE GEOPHYSICAL LABORATORY, HANSCOM AFB, MASS.

Table 4. Summary of Steady-State Results For A Severe Substorm During Fall-Equinox

LOCAL TIME	MATERIAL WITH THE MAXIMUM POTENTIAL DIFFERENCE OSR GLASS ON NORTH AND SOUTH PANELS	ABSOLUTE POTENTIAL OF S/C STRUCTURE (VOLTS)
23:00	- 5160	- 240
24:00 (ECLIPSE)	160	- 14160
1:00	- 5160	- 235
2:00	- 5165	- 210
3:00	- 5165	- 205
4:00	- 5165	- 210
5:00	- 5165	- 220
6:00	- 4780	- 1490
7:00	- 5165	- 220
8:00	- 5170	- 200

Table 5. Summary of Steady-State Results for a Severe Substorm During Winter-Solstice

LOCAL TIME	MATERIAL WITH THE MAXIMUM POTENTIAL DIFFERENCE (VOLTS)	ABSOLUTE POTENTIAL OF S/C STRUCTURE (VOLTS)
	OSR GLASS ON NORTH PANEL	
23.00	- 5175	- 175
24:00	- 5170	- 190
1:00	- 5175	- 175
2:00	- 5200	- 170
3:00	- 5175	- 175
4:00	- 5170	- 180
5:00	- 5170	- 180
6:00	- 5170	- 200
7:00	- 5170	- 180
8:00	- 5175	- 175

Table 6. Summary of Maximum Potential Differences of Outer Surfaces During a Severe Geomagnetic Substorm

	MAXIMUM POTENTIAL DIFFERENCE BETWEEN SURFACE AND S/C STRUCTURE (VOLTS)
1. BACK-SIDE NO. 527 SILICA CLOTH BLANKET	-220
2. WEST PANEL, NO. 527 SILICA CLOTH BLANKET	±170
3. NORTH PANEL, NO. 527 SILICA CLOTH BLANKET	-170
4. NORTH PANEL, OSR GLASS COMPOSITE	-5200
5. SOUTH PANEL NO. 527 SILICA CLOTH BLANKET	190
6. SOUTH PANEL, OSR GLASS COMPOSITE	-5200
7. EAST PANEL, NO. 527 SILICA CLOTH BLANKET	230
8. EARTH SIDE, NO. 527 SILICA CLOTH BLANKET	225
9. EARTH SIDE, NO. 570 SILICA CLOTH	240
10. EARTH-SIDE, NO. 570/550/581 SILICA CLOTH COMPOSITE	-270
11. EARTH-SIDE, CONDUCTIVELY COATED FIBERGLASS	-2
12. SOLAR ARRAY, SOLAR ARRAY COVER GLASS	1500
13. SOLAR ARRAY, CHEMGLAZE PAINT	-1370
14. PERMANENTLY SHADOWED, CONDUCTIVELY COATED FIBERGLASS	-2
15. PERMANENTLY SHADOWED, NO. 527 SILICA CLOTH	-160

Table 7. ESD Probabilities of Occurrence For the OSR Glass Composite Material During A Severe Substorm*

NO. OF ESD DISCHARGES OCCURRING AT RANDOM TIMES IN ONE SECOND	PROBABILITY OF OCCURRENCE
≥ 1	0.642
≥ 2	0.264
≥ 3	0.0755
≥ 4	0.016
≥ 5	2.6×10^{-3}
≥ 6	3.3×10^{-4}
≥ 7	3.4×10^{-5}
≥ 8	3×10^{-6}
≥ 9	2×10^{-7}
≥ 10	1×10^{-8}

* THE SEVERE SUBSTORM WAS SIMULATED BY BOMBARDING THE OSR GLASS MATERIAL SAMPLE WITH 20 KeV ELECTRONS HAVING A CURRENT DENSITY OF 1.5 NA/CM^2

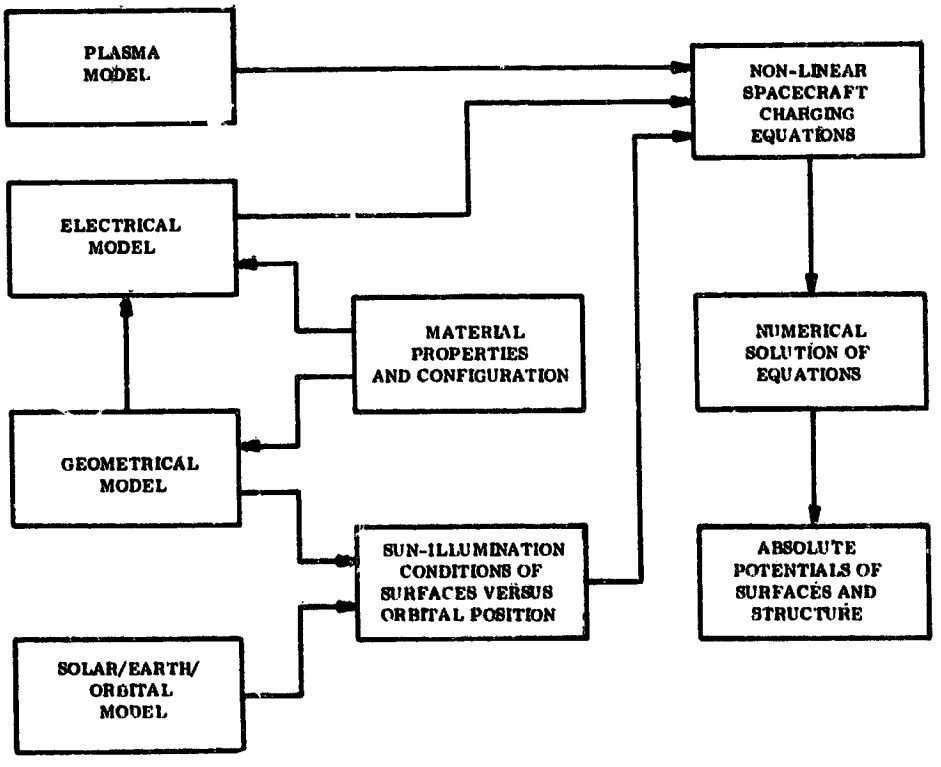

Figure 1. Spacecraft Charging Model Flow Chart.

C-3

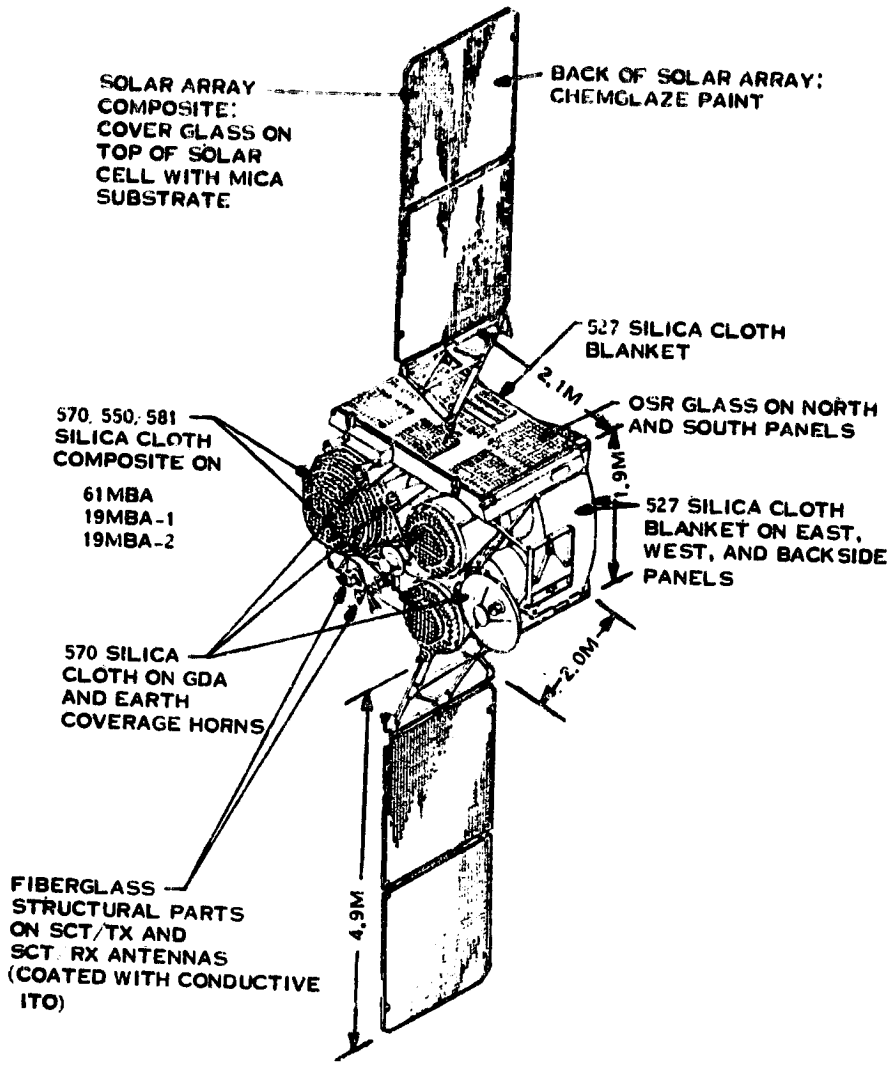

Figure 2. DSCS-III Material Configuration.

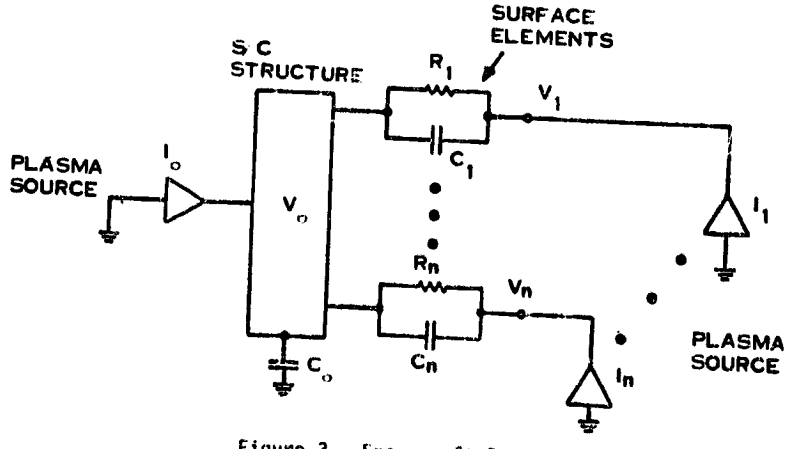

Figure 3. Spacecraft Equivalent Circuit

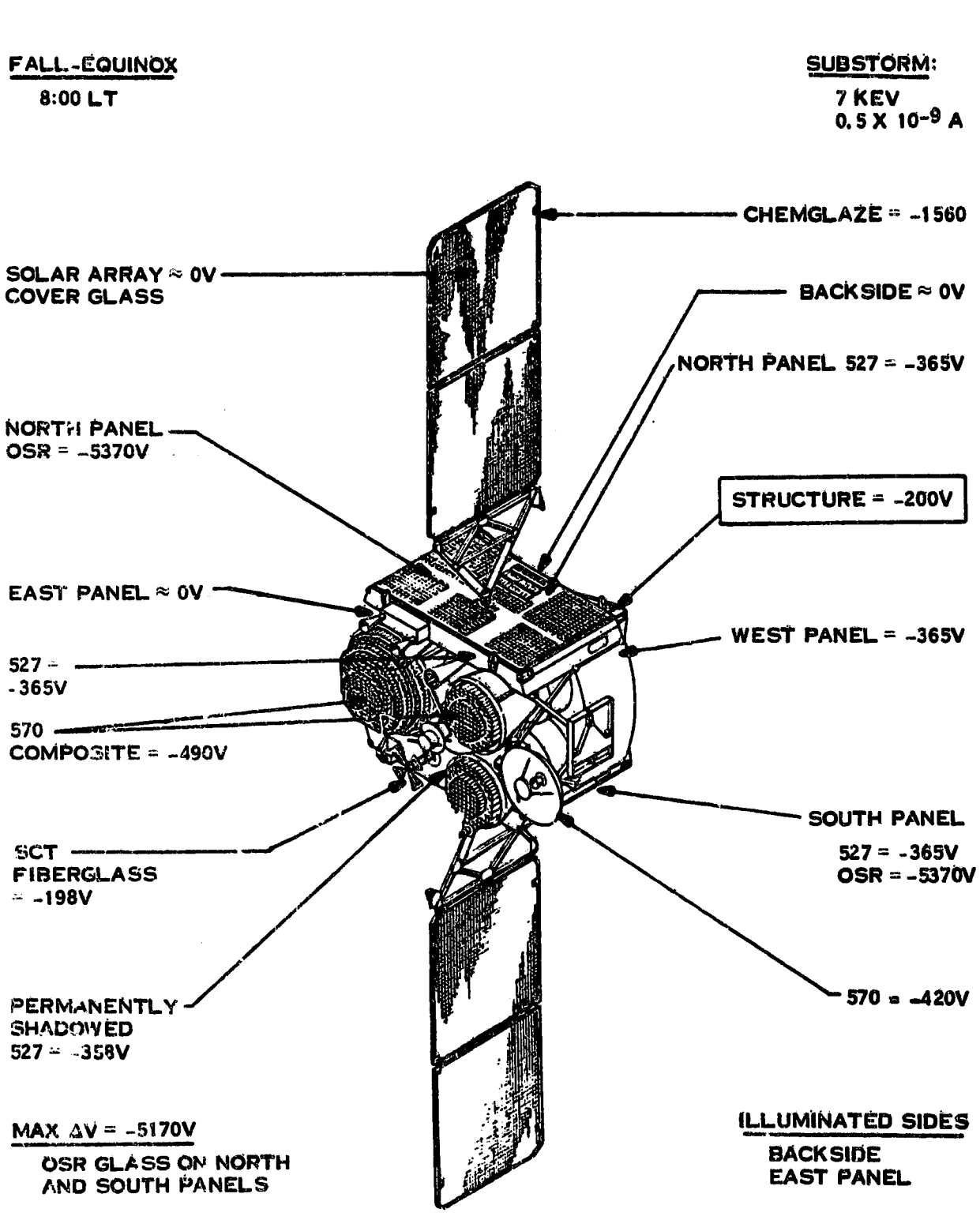

Figure 4. Steady-State Absolute Potentials of DSCS-III at 8:00 L.T. (Fall-Equinox) For A Severe Substorm

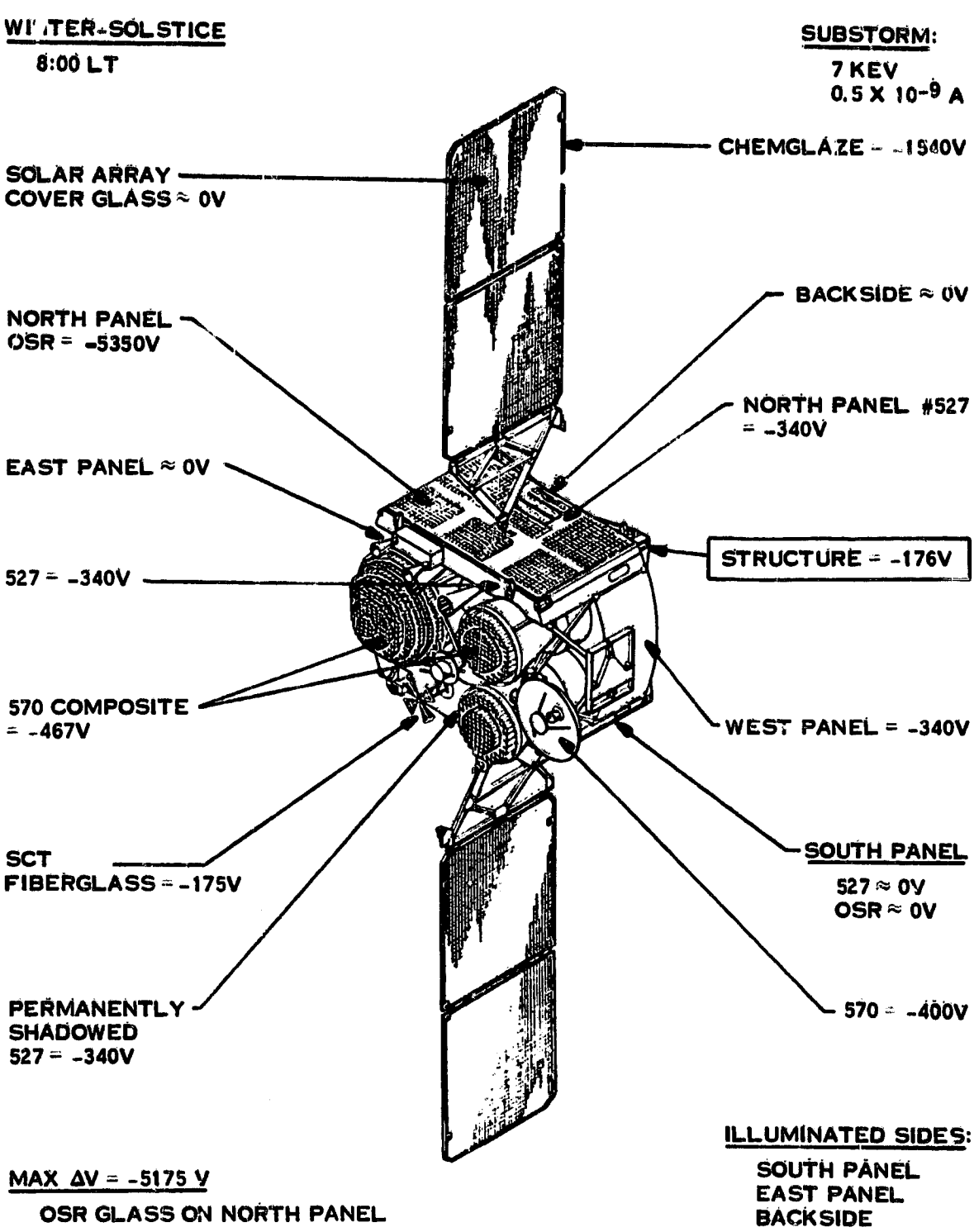

Figure 5. Steady-State Absolute Potentials of DSCS-III at 8:00 L.T. (Winter-Solstice) During A Severe Substorm.

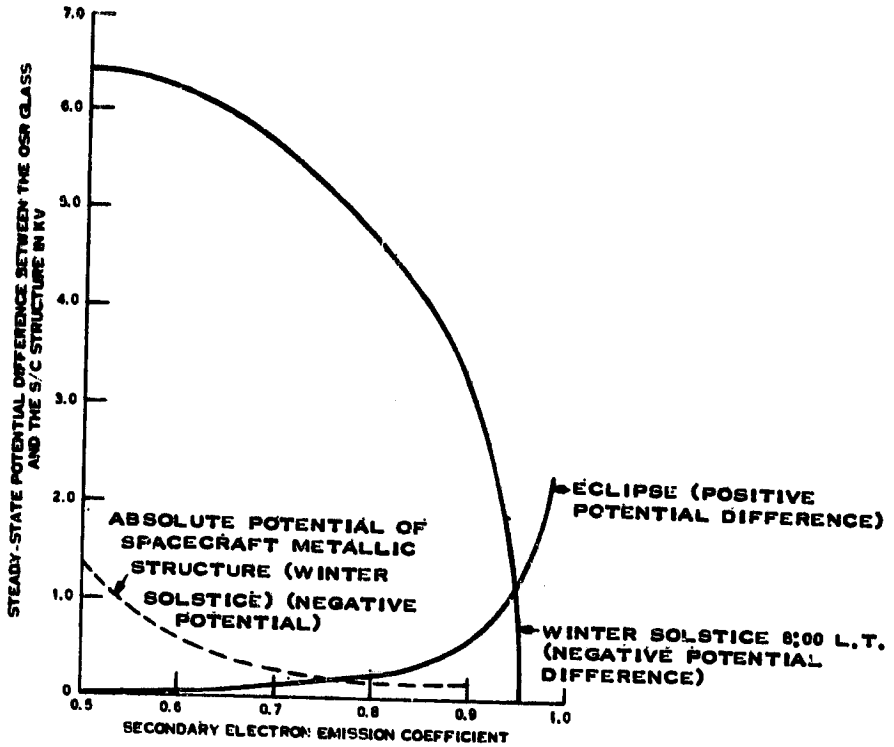

Figure 6. Variation of Steady-State Differential Potential As A Function of Secondary Electron Emission Coefficient

PREDICTION OF ION DRIFT EFFECTS ON SPACECRAFT FLOATING POTENTIALS*

Jen-Shih Chang, S.M.L. Prokopenko, R. Goard and J.G. Laframboise
Centre for Research in Experimental Space Science and Physics Department
York University

ABSTRACT

The plasma environment of high-altitude spacecraft has been observed to involve ion drift velocities which sometimes become comparable to ion mean thermal speeds. Such drifts may cause an electrically isolated spacecraft surface to float at a substantially increased negative potential if it is simultaneously shaded and downstream relative to the drift direction. We present a calculation of upper and lower bounds on such potentials for a spherical spacecraft, based on the fact that ion collection on the spacecraft at its downstream point is bounded above by the corresponding current which would be collected if the spacecraft were an equipotential (i.e. were more attractive for ions elsewhere on its surface than it is in reality) and bounded below by the corresponding result for a sphere at space potential. The results show that (1) the ion speed ratio at which drift effects become "important" (i.e. change the floating potential by at least 10%) can be as low as 0.1, and may be decreased if the ambient electrons are non-Maxwellian; (2) the effects of ion speed ratio increase with increasing ion-to-electron temperature ratio; (3) negative floating potentials for drifting Maxwellian ion velocity distributions with speed ratio unity are typically about twice as large as the corresponding potentials for nondrifting conditions.

INTRODUCTION

If a spacecraft is exposed to ambient ions whose drift velocity U is comparable to or larger than their most probable thermal speed [ion speed ratio $S_i = U/(2kT_i/m_i)^{\frac{1}{2}} \gtrsim 1$, where k is Boltzmann's constant and m_i and T_i are ion mass and assumed ion temperature], a large decrease in ion flux J_i to downstream surfaces will occur. Unless such surfaces are able to expel surplus incident electron fluxes, e.g. by photoemission, their floating potentials will become substantially more negative as a result. If the ambient electron temperature T_e is simultaneously large or more generally the ambient electron energy distribution has a significant high-energy component, then large absolute increases in negative floating potentials will occur, with correspondingly increased arcing hazards. Even if T_e is relatively small, such effects may influence surface potentials enough to disturb particle and field measurements. S_i values of order unity may be reached in the Earth's outer magnetosphere (Mauk 1975; DeForest 1977, Figs. 6 and 8); larger values are likely in the outer Jovian magnetosphere and magnetosheath (Goldstein and Divine 1977), and in the solar wind (Dessler 1967, Axford 1968, Manka 1973). In both outer

*work supported by the U.S. Air Force Office of Scientific Research under grant number AFOSR-76-2962.

magnetospheres, electron distributions having substantial high-energy components have been observed (DeForest and McIlwain 1971, Goldstein and Divine 1977).

A calculation of ion drift effects on the floating potential of the lunar surface has been done by Manka (1973), using a local-current-balance formation. Parker (1978) has done exact numerical calculations of floating surface potentials for nonconductive finite cylindrical objects, including photoemission due to illumination of one end and ion drift parallel to the axis of symmetry.

In this paper, we have done an approximate calculation of ion drift effects on the floating potential of a shaded, downstream, electrically isolated surface element on a spherical spacecraft (Fig. 1), using a local-current-balance formulation which yields upper and lower bounds on such potentials. This formulation is an adaptation of that of Prokopenko and Laframboise (1977). The basis of the calculation is as follows: if one compares, on one hand, a situation wherein the entire spacecraft is at the same potential as the surface element in question, with, on the other hand, a more realistic situation wherein the rest of the spacecraft is at a less negative potential (Fig. 2), then in the latter case, the potential well surrounding the surface element will be steeper and less spatially extended, and the ion collection will in general be decreased. When $S_i \neq 0$, this argument is subject to qualifications not present in the nondrifting case, for which it is rigorously true in a wide range of conditions (Laframboise and Parker 1973, Laframboise and Godard 1974). In particular, one can envision hypothetical asymmetric sheath potentials which would cause a high-speed-ratio ambient ion distribution to be focused onto the downstream point. We exclude such cases in what follows.

The most extreme example of steepening would be a potential profile which was equal to space potential almost to the spacecraft surface, then fell discontinuously to surface potential. In this limit, the surface element in question would collect just the downstream space-potential current corresponding to the given ion speed ratio. The downstream-point current-density values corresponding to a unipotential sphere at, respectively, the potential of the surface element and space potential may therefore be regarded as upper and lower bounds on the actual current collection at that potential, the upper bound being subject to the above-mentioned qualifications. The resulting values of local floating surface potential may correspondingly be regarded as upper and lower bounds on more realistic values of this quantity. The above-mentioned upper and lower bounds on current correspond, respectively, to the "three-dimensional" and "one-dimensional" velocity-space cutoffs considered by Prokopenko and Laframboise (1977) for nondrifting situations.

THEORY OF LOCAL ION COLLECTION ON A UNIPOTENTIAL SPHERE

We assume a collisionless plasma with a drifting Maxwellian ion velocity distribution and negligible magnetic field, containing a fully charge-absorbing, unipotential, spherical electrode. We assume that Debye length $\lambda_D \gg$ electrode radius r_s. In the resulting spherically symmetric Laplace potential $\varphi(r) = \varphi_s r_s/r$, the nondimensional ion current density at the electrode surface is (Godard 1975, p. 31)

$$j_i = \int_{\max(0,\chi_s)}^{\infty} \int_{0}^{\beta-\chi_s} \exp(-\beta - 2S_i\beta^{\frac{1}{2}} \cos\mu\cos\theta - S_i^2) I_o(2S_i\beta^{\frac{1}{2}}\sin\mu\sin\theta)\, d\Omega\, d\beta \tag{2.1}$$

where $\chi_s = q\varphi_s/kT$, $\beta = E/kT$, $\Omega = L^2/(2mr_s^2\,kT)$, $j = J/[N_\infty q(kT/2\pi m)^{\frac{1}{2}}]$, I_o is the modified Bessel function of zero order, N_∞ is number density far from the electrode, μ is angular surface position coordinate measured from the upstream direction, θ is change in direction of the radius vector of a particle as it moves from infinity to radial distance r_s, and θ is related to particle energy E, angular momentum L, charge q and the potential profile $\varphi(r)$ by the following expression (Goldstein 1950, Ch.3):

$$\theta = \int_{r_s}^{\infty} L\,dr/\{r^2[2mE - 2mq\varphi(r) - L^2/r^2]\}^{\frac{1}{2}} \tag{2.2}$$

We have computed j_i by integrating Eq. (2.1) numerically. For the given Laplace potential, Eq. (2.2) can be integrated analytically. We obtain

$$\theta = \sin^{-1}[(2\Omega + \chi_s)/(\chi_s^2 + 4\beta\Omega)^{\frac{1}{2}}] - \sin^{-1}[\chi_s/(\chi_s^2 + 4\beta\Omega)^{\frac{1}{2}}] \tag{2.3}$$

For space potential ($\chi_s = 0$), Eq. (2.1) can be integrated analytically. The result is (Tsien 1946)

$$j_i = \pi^{\frac{1}{2}} S_i \cos\mu\,[1 + \mathrm{erf}(S_i\cos\mu)] + \exp(-S_i^2\cos^2\mu) \tag{2.4}$$

Figure 3 shows results obtained for the ion current density $j_{i\pi}$ at the downstream point $\mu = \pi$, as a function of S_i, with χ_s as a parameter, where $\chi_s = e\varphi_s/kT_i \leq 0$ and $e \equiv q_i$. As expected, $j_{i\pi}$ decreases with increasing S_i and increases with increasing $|\chi_s|$. In Fig. 4, the same results are graphed logarithmically as functions of χ_s. Figure 4 shows that these results may be approximated with an error $\lesssim 5\%$ by power-law relations of the form

$$j_{i\pi}(\chi_s) = j_{i\pi}(\chi_s = 0) + A_\pi|\chi_s|^{\alpha_\pi} \quad \ldots \leq 0 \tag{2.5}$$

The resulting S_i dependence of the coefficients A_π, α_π and $B_\pi \equiv j_{i\pi}(\chi_s = 0)$ is shown in Fig.5.

RESULTS AND DISCUSSION

Upper and lower bounds on negative downstream-point floating potentials for a shaded, isolated surface element, obtained by numerical solution of the equation $J_i + J_e = 0$, are shown in Fig. 6 for various ion-to-electron temperature ratios $\epsilon = T_i/T_e$. Here we have assumed that ambient electrons are Maxwellian, and that J_i is given alternatively by Eq. (2.5) with Fig. 5, and by Eq. (2.4), yielding upper and lower bounds on ion current, corresponding respectively to "three-dimensional" and "one-dimensional" ion velocity-space cutoffs (Sec. 1). We have also assumed that secondary, backscattered, and photoemitted electron currents are zero. The lower-bound results are subject to the qualifications noted in Sec. 1. The dashed lines in Fig. 6 represent floating potentials for the nondrifting case $S_i = 0$. At ion speed ratios larger than those shown, the situation becomes complicated by electron speed ratio effects, especially at larger values of ϵ. In Fig. 6 we see that at larger values of ϵ, effects of S_i

become important at smaller S_i values.

In Fig. 7, upper and lower bounds are shown which are similar to those of Fig. 6, except that instead of Maxwellian electron velocity distributions, we have used the "quiet" and "disturbed" electron distributions measured by Shield and Frank (1970) and DeForest and McIlwain (1971) respectively in the Earth's outer magnetosphere, and approximated by Knott (1972), as described by Prokopenko and Laframboise (1977) and Laframboise and Prokopenko (1978). The ion temperatures used are 111.6 eV and 2.43 keV, respectively. These values were obtained by integrating the electron velocity distributions to find $N_{e\infty}$, equating $N_{i\infty}$ to the result, then assuming that the ions were Maxwellian and that the ratio of ion to electron random fluxes was 0.025. This procedure differs from that used by Knott (1972) and Prokopenko and Laframboise (1977), in which an ion-to-electron random flux ratio of 0.025 and an ion temperature of 1 keV were assumed simultaneously, thereby violating ambient charge neutrality in general. The corresponding electron mean energies are 270 eV and 8.78 keV. The method used for calculating electron currents is described in Prokopenko and Laframboise (1977). We see that S_i effects become important at smaller S_i values in "quiet" magnetospheric conditions. The ratio of ion to electron mean energies implied by the above data is also larger in "quiet" conditions, corresponding to the dependence of S_i effects on ϵ noted in Fig. 6. The "quiet" and "disturbed" distributions also differ substantially in shape (Knott, 1972, Figs. 1 and 2b). The onset of "significant" drift effects (i.e. floating potential changes $\gtrsim 10\%$) is seen to occur at S_i values as low as 0.1, depending on conditions. It occurs at lower S_i values in the presence of the "quiet" distribution than in any of the other cases shown in Figs. 6 and 7. In Figs. 6 and 7, negative floating potentials for $S_i = 1$ are in most cases about twice as large as the corresponding potentials for nondrifting situations.

REFERENCES

Axford, W.I. (1968), Observations of the interplanetary plasma, Space Sci. Rev. 8, 331-365.

DeForest, S.E. (1977), The plasma environment at geosynchronous orbit. In: Proc. USAF-NASA Spacecraft Charging Technology Conference, C.P. Pike and R.R. Lovell, Editors, Report No. AFGL-TR-77-0051,Air Force Geophysics Laboratory, Hanscom AFB, Massachusetts/NASA TMX-73537, Lewis Research Center, Cleveland,Ohio, pp. 37-52.

DeForest, S.E., and McIlwain, C.E. (1971), Plasma clouds in the magnetosphere, J. Geophys. Res. 76, 3587-3611.

Dessler, A.J. (1967), Solar wind and interplanetary magnetic field, Rev. Geophys. 5, 1-41.

Godard, R. (1975), A symmetrical model for cylindrical and spherical collectors in a flowing collisionless plasma, Ph.D. Thesis, York University, Toronto.

Goldstein, H. (1950), Classical Mechanics, Addison-Wesley Pub. Co., Reading, Massachusetts.

Goldstein, R. and Divine, N. (1977), Plasma distribution and spacecraft charging modeling near Jupiter. In: Proc. USAF-NASA Spacecraft Charging

Technology Conference, C.P. Pike and R.R. Lovell, Editors, Report No. AFGL-TR-77-0051, Air Force Geophysics Laboratory, Hanscom AFB, Massachusetts /NASA TMX-73537, Lewis Research Center, Cleveland, Ohio, pp. 131-141.

Knott, K. (1972), The equilibrium potential of a magnetospheric satellite in an eclipse situation, Planet. Space Sci. 20, 1137-1146.

Laframboise, J.G., and Godard, R. (1974), Perturbation of an electrostatic probe by a spacecraft at small speed ratios, Planet. Space Sci. 22, 1145-1155.

Laframboise, J.G., and Parker, L.W. (1973), Probe design for orbit-limited current collection, Phys. Fluids 16, 629-636.

Laframboise, J.G., and Prokopenko, S.M.L. (1978), Predictions of high-voltage differential charging on geostationary spacecraft, Paper 4.4, 1978 Ionospheric Effects Symposium, Arlington, January 1978 (proceedings in press).

Manka, R.H. (1973), Plasma and potential at the lunar surface. In: Photon and Particle Interactions with Surfaces in Space, R.J.L. Grard, Editor, D. Reidel Pub. Co., Dordrecht, Holland, pp. 347-361.

Mauk, B. (1975), Magnetospheric substorm pitch angle distribution, EOS 56, 423.

Parker, L.W. (1978), Potential barriers and asymmetric sheaths due to differential charging of nonconducting spacecraft. Report No. AFGL-TR-78-0045, Air Force Geophysics Laboratory, Hanscom AFB, Massachusetts.

Prokopenko, S.M.L., and Laframboise, J.G. (1977), Prediction of large negative shaded-side spacecraft potentials. In: Proc. USAF-NASA Spacecraft Charging Technology Conference, C.P.Pike and R.R. Lovell, Editors, Report No. AFGL-TR-77-0051, Air Force Geophysics Laboratory, Hanscom AFB, Massachusetts/NASA TMX-73537, Lewis Research Center, Cleveland, Ohio, pp. 369-387.

Shield, M.A., and Frank, L.A. (1970), Electron observations between the inner edge of the plasma sheet and the magnetosphere, J. Geophys. Res. 75, 5401-5414.

Tsien, H.S. (1946), Superaerodynamics, mechanics of rarefied gases, J. Aero. Sci. 13, 653-664.

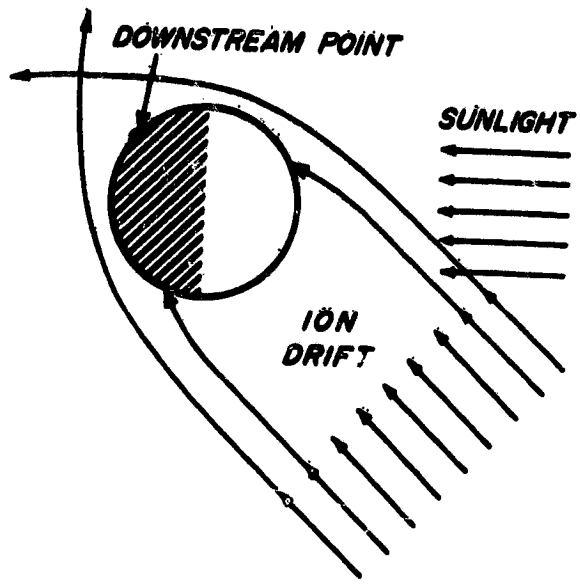

Figure 1. Spherical spacecraft with downstream point (relative to ion drift direction) shaded.

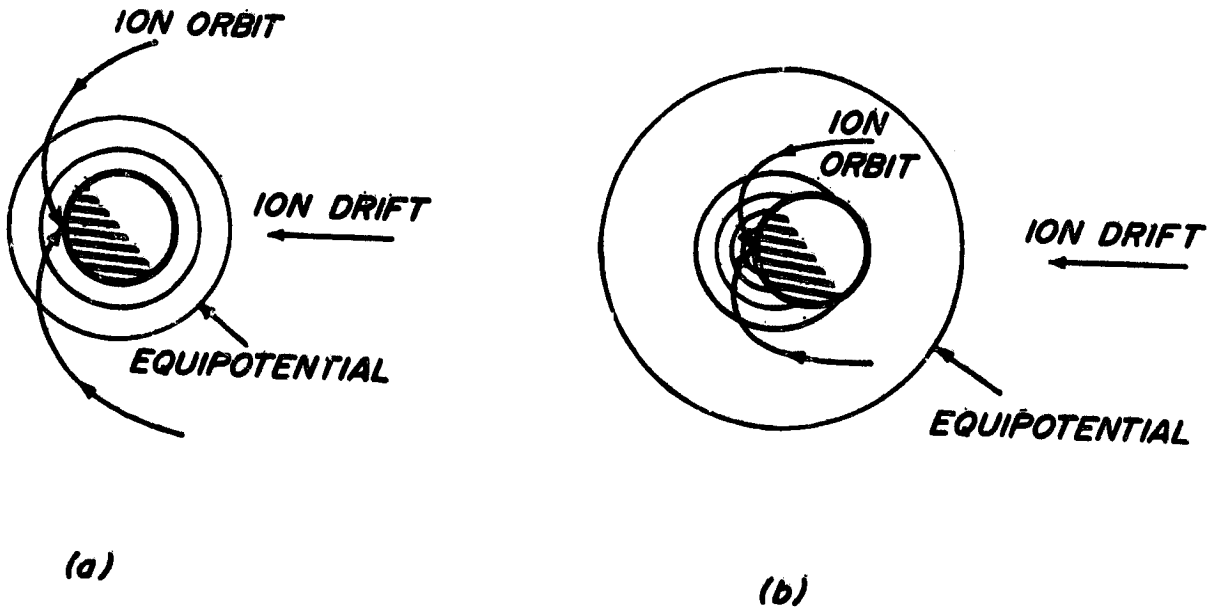

Figure 2.(a) Hypothetical symmetric equipotentials around a spherical spacecraft (b) nonsymmetric equipotentials around the same spacecraft.

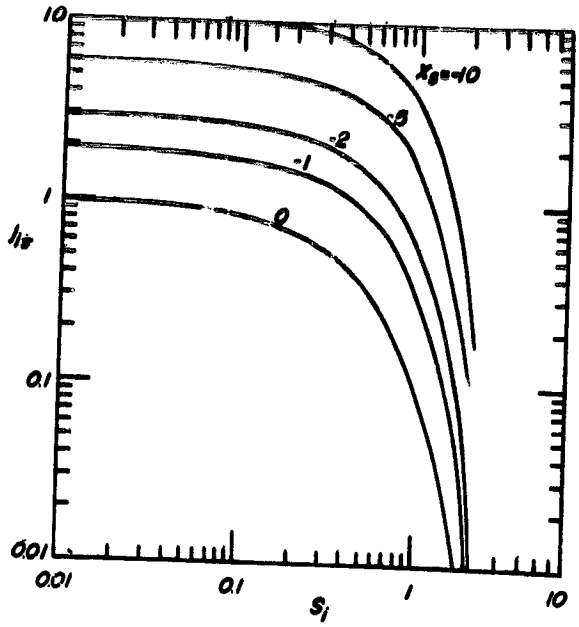

Figure 3. Nondimensional downstream-point ion current density $j_{i\pi} = J_{i\pi}/[N_\infty e(kT_i/2\pi m_i)^{\frac{1}{2}}]$ as a function of ion speed ratio $S_i = U/(2kT_i/m_i)^{\frac{1}{2}}$ for various nondimensional surface potentials $\chi_s = e\varphi_s/kT_i$, assuming spherical geometry, zero magnetic field, uniform surface potential, collisionless large-Debye-length conditions, and drifting Maxwellian ions. For $S_i \to 0$, $j_{i\pi} \to 1 + |\chi_s|$ when $\chi_s < 0$.

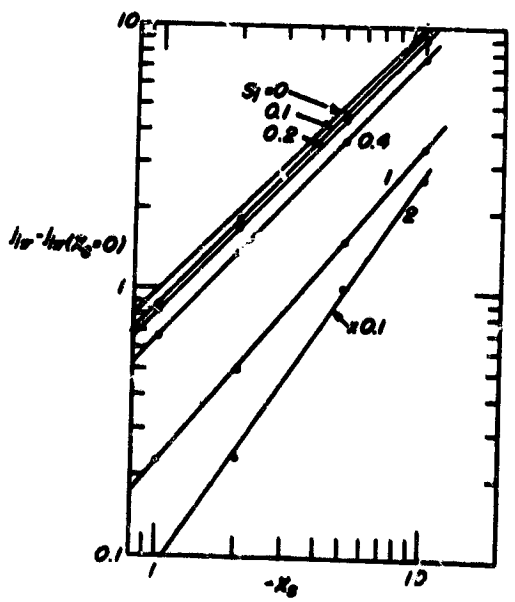

Figure 4. Nondimensional downstream-point ion current density $j_{i\pi}$ as a function of surface potential χ_s for various ion speed ratios S_i, for the same conditions as in Fig. 3. The straight lines shown are power-law approximations.

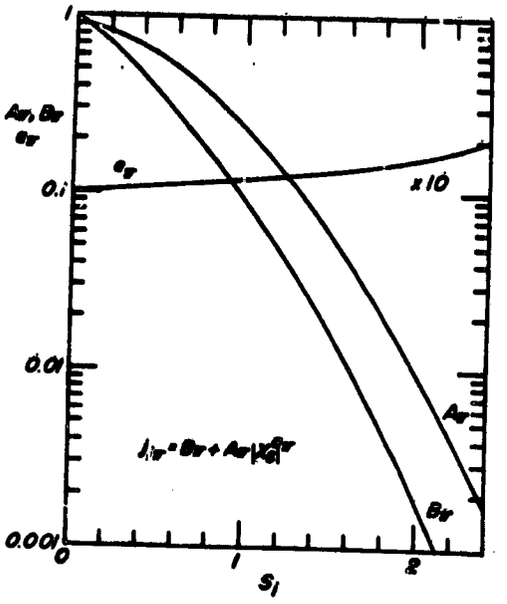

Figure 5. Dependence of the power-law coefficients A_π, B_π and α_π on ion speed ratio S_i.

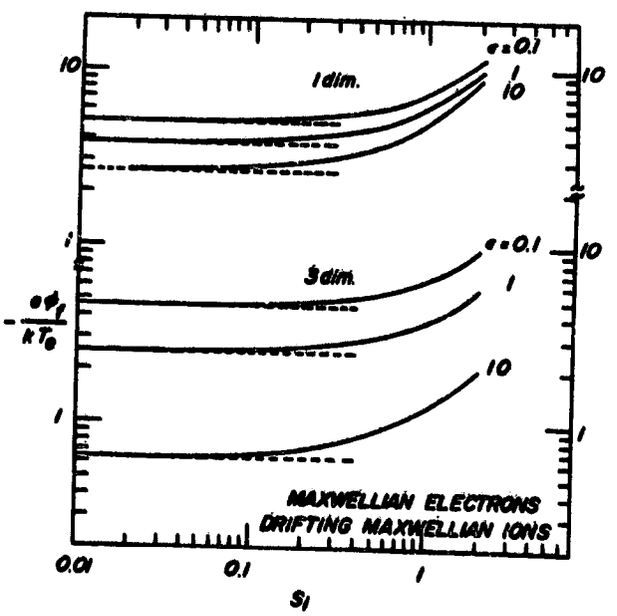

Figure 6. Upper and lower bounds on floating potential φ_f at shaded downstream point of spacecraft, as a function of ion speed ratio S_i for various ion-to-electron temperature ratios ϵ, for Maxwellian electrons and drifting Maxwellian ions, for 1-dimensional and 3-dimensional ion velocity space cutoffs.

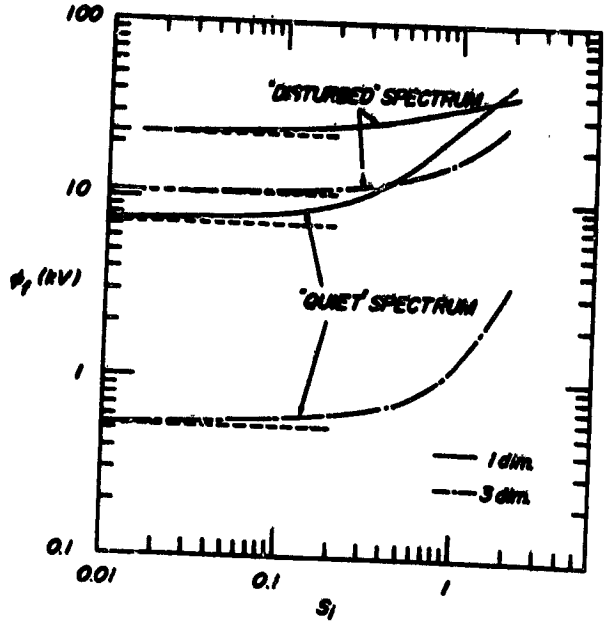

Figure 7. Upper and lower bounds on floating potential φ_s at shaded downstream point of spacecraft, as a function of ion speed ratio S_i for "disturbed" and "quiet" electron velocity spectra representing geostationary orbit conditions, for 1-dimensional and 3-dimensional ion velocity space cutoffs.

D15

N79-24016

NUMERICAL CALCULATIONS OF HIGH-ALTITUDE DIFFERENTIAL CHARGING:* PRELIMINARY RESULTS

J.G. Laframboise, R. Godard and S.M.L. Prokopenko
Physics Department, York University

ABSTRACT

A two-dimensional simulation program has been constructed in order to obtain theoretical predictions of floating potential distributions on geostationary spacecraft. The geometry used is infinite-cylindrical with angle dependence. Effects of finite spacecraft length on sheath potential profiles can be included in an approximate way. The program can treat either steady-state conditions or slowly time-varying situations involving external time scales much larger than particle transit times. Approximate, locally dependent expressions are used to provide space-charge density profiles, but numerical orbit-following is used to calculate surface currents. Ambient velocity distributions are assumed to be isotropic, beam-like, or some superposition of these. Preliminary results are presented which demonstrate the readiness of the program to play a useful role in spacecraft charging studies.

INTRODUCTION

A numerical simulation program has been constructed having the following features:

(1) infinite circular cylindrical geometry with angle-dependence
(2) floating surface potential distribution found using "quasistatic iteration" (Laframboise and Prokopenko, 1977) in which sheath potential changes during particle transit times are ignored
(3) calculation of all incident currents by numerical orbit-following, including iterative determination of velocity-space cutoff boundaries for all particle species
(4) use of simplified charge density expressions, rather than numerical orbit-following, in solving Poisson's equation for sheath potentials
(5) incident particle velocity distributions isotropic or beam-like (monokinetic), or some superposition of these
(6) input formats as flexible as possible with regard to inclusion of
    (a) velocity distributions of incident particles, photoelectrons, secondary electrons, backscattered electrons, and gun emissions
    (b) internal current pathways including surface conductive layers
    (c) surface capacitances.

Detailed rationales for the above features have been given by Laframboise and Prokopenko (1977). Effects of finite spacecraft length on sheath potential

* Work supported by the U.S. Air Force Office of Scientific Research under grant no. AFOSR-76-2962.

profiles can be included in either of two approximate ways which lead to modifications of the two-dimensional Poisson equation to be solved. We include here a brief description of these methods, although neither has been used in obtaining the preliminary results presented in Sec. 2. The first method is derived by pretending that the circular inner boundary of the computation grid, which represents the spacecraft surface, is no longer a cross-section of an infinite cylinder, but rather is a cross-section through the equatorial plane of a prolate spheroid of polar-to-equatorial axis ratio $L \geq 1$. We also assume that the sheath potential is (for some unspecified reason) independent of the latitude coordinate perpendicular to this plane. This leads to a modified Poisson equation of the form

$$\tanh^2 \xi \frac{\partial^2 \chi}{\partial \xi^2} + \tanh \xi \frac{\partial \chi}{\partial \xi} + \frac{\partial^2 \chi}{\partial \theta^2} = \frac{\sinh^2 \xi}{\sinh^2 \xi_s} \left(\frac{R_s}{\lambda_D} \right)^2 (n_e - n_i) \qquad (1.1)$$

where $\chi = e\phi/kT_e$, ξ is a radial coordinate in the equatorial plane and is related to nondimensional radius $r = R/R_s$, defined in the same plane, by the relation

$r = (L^2 - 1)^{\frac{1}{2}} \sinh \xi$, $\xi_s = \frac{1}{2} \ell n \, [(L+1)/(L-1)]$, θ is angular coordinate in the same plane, R_s is spacecraft radius, λ_D is Debye length, and n_e and n_i are the nondimensional electron and ion densities $N_e/N_{e\infty}$ and $N_i/N_{i\infty}$, where N_∞ is ambient density of either species. Use of Eq. (1.1) in place of the usual polar-coordinate Poisson equation would result in sheath potential profiles which became increasingly steeper as L decreased, thus allowing for approximate estimates of sheath potentials around finite cylinders. The limiting case $L = 1$ would correspond to an assumed spherical geometry without latitude dependence; the limit $L \to \infty$ leads to recovery of infinite cylindrical geometry.

The transformation $s = \ell n \coth \frac{1}{2}\xi$ leads to the alternative form

$$\frac{1}{\cosh^2 \xi} \frac{\partial^2 \chi}{\partial s^2} + \frac{\partial^2 \chi}{\partial \theta^2} = \frac{\sinh^2 \xi}{\sinh^2 \xi_s} \left(\frac{R_s}{\lambda_D} \right)^2 (n_e - n_i) \qquad (1.2)$$

which contains no first-order terms. For small ξ, s varies logarithmically with r; for large ξ, s varies as r^{-1}.

The second method is derived by first writing the nondimensional Poisson equation for cylindrical coordinates, which has the form

$$\frac{\partial^2 \chi}{\partial r^2} + \frac{1}{r} \frac{\partial \chi}{\partial r} + \frac{1}{r^2} \frac{\partial^2 \chi}{\partial \theta^2} + \frac{\partial^2 \chi}{\partial z^2} = \left(\frac{R_s}{\lambda_D} \right)^2 (n_e - n_i) \qquad (1.3)$$

We then assume that $\chi(r,\theta,z)$ is periodic in z, such that values of χ repeat after nondimensional distance 2ℓ parallel to the z axis. In particular, we assume that $\chi(r,\theta,\pm\ell)$ = some given dependence $\chi_\ell(r,\theta)$, and that $\chi(r,\theta,0) = \chi_0(r,\theta)$ to be found. We further assume that $\partial\chi/\partial z = 0$ at $z = 0$, $z = \pm\ell$, $z = \pm 2\ell$, etc, and that only the lowest Fourier component of the z dependence of χ is present. Then

$$\chi(r,\theta,z) = \tfrac{1}{2}[\chi_0(r,\theta) + \chi_\ell(r,\theta)] + \tfrac{1}{2}[\chi_0(r,\theta) - \chi_\ell(r,\theta)] \cos\left(\frac{\pi z}{\ell} \right) \qquad (1.4)$$

and, at $z = 0$, we have

$$\frac{\partial^2 \chi_0}{\partial z^2} = \tfrac{1}{2} \left(\frac{\pi}{\ell} \right)^2 [\chi_\ell(r,\theta) - \chi_0(r,\theta)] \qquad (1.5)$$

The Poisson equation for $\chi_0(r,\theta)$ now becomes

$$\frac{\partial^2 \chi_0}{\partial r^2} + \frac{1}{r}\frac{\partial \chi_0}{\partial r} + \frac{1}{r^2}\frac{\partial^2 \chi_0}{\partial \theta^2} - \tfrac{1}{2}\left(\frac{\pi}{\ell}\right)^2 \chi_0 = \left(\frac{R_s}{\lambda_D}\right)^2 (n_e - n_i) - \tfrac{1}{2}\left(\frac{\pi}{\ell}\right)^2 \chi_\ell(r,\theta) \quad (1.6)$$

We see that in this Poisson equation, effects of z-dependence are represented by a homogeneous "Helmholtz" term and a fictitious space charge contribution. The z-dependence incorporated into this equation could represent approximately the effects on sheath potentials of finite spacecraft length and/or features such as conductive circumferential bands. Equations (1.2) and (1.6) are both solvable by standard methods; both are linear. Both contain only two (radius and angle) independent variables.

Other numerical simulations of the high-altitude spacecraft charging problem include those of Katz et al. (1977) for a wide variety of three-dimensional geometries, Parker (1978a) for finite circular cylindrical geometry with azimuthal symmetry, and Parker (1978b) for the three-dimensional disturbed region around a thin rectangular plate. All of these treatments use quasistatic iteration. Among older treatments, that of Soop (1972) is noteworthy because it is two-dimensional and fully time-dependent. The treatments of Schröder (1973), Rothwell et al. (1976), Whipple (1976) and Lafon (1976) involve self-consistent calculations of space charge densities but assume that sheath potentials have radial symmetry. The latter is a serious limitation because of the inherently angle-dependent nature of the problem.

RESULTS AND DISCUSSION

Figures 1 - 3 show equipotential contours surrounding an infinite cylindrical spacecraft surface having two independently floating conductive sectors, the smaller of which is shaded in all three cases, and subtends angles of 90°, 45° and 22½°, respectively. In obtaining these results and also those in Figs. 4 and 5, an eight-level discretization in velocity space has been used for each particle species involved (ambient electrons, ambient ions, photoelectrons, and, in Fig. 5, secondary and backscattered electrons). In Figs. 1 - 6, T_{ph} is assumed photoelectron temperature. The calculation was judged to have converged sufficiently when the magnitude of the total unbalanced current to each sector was < 0.01 times the total current of ambient electrons to the same sector. In Figs. 1 and 5, this criterion is unsatisfied on the larger sector and on both sectors, respectively. The resulting floating surface potentials in Figs. 1 - 5 are accurate to within approximately 50 V or better. A noteworthy feature of Figs. 1 - 3 concerns the dependence of the shaded-sector potential on sector angle. The indicated values of -2956V, -2956V and -2969V respectively, provide an indication that ion collection is orbit-limited for sector angles of 90° and 45°, but orbit-limitation has (just) broken down for a sector angle of 22½°. This result is consistent with a prediction by Prokopenko and Laframboise (1977) that the potential well configuration around a sufficiently small shaded electrically isolated surface element can produce breakdown of orbit-limited ion collection on it, driving its floating potential more negative than otherwise.

Figure 4 shows a situation identical to that of Fig. 3 except that the spacecraft has been rotated counterclockwise by 90°, bringing the smaller sector partly into sunlight. As a result, its potential has risen, as expected. At the same time the larger sector, which now has a smaller proportion of its total area sunlit, has become more negative.

Figure 5 shows a situation identical to that of Fig. 3 except that currents due to electron backscattering and also secondary emission caused by electron impact have been included. In comparison with Fig. 3, both sector potentials have risen substantially because of the inclusion of these currents. A barrier of negative potential is now evident on the sunlit side of the spacecraft (Fahleson, 1970; Prokopenko and Laframboise, 1977). In this case, the shaded-sector potential has been influenced more strongly by breakdown of orbit-limited ion collection than in Fig. 3. If such breakdown had not occurred, the shaded-sector potential would have been -1985V. The omission of secondary emission due to ion impact in this calculation causes the floating potentials shown to be slightly more negative than would otherwise be the case.

Figure 6 differs from Figs. 1 - 5 in that the situation shown is for an insulating spacecraft surface, for which a floating condition requires local current balance to exist at every point. It also differs in being not a converged result, but a "guess field" (first-iterate) potential distribution based on a local current balance calculation in which attracted-species currents were assumed orbit-limited everywhere, and all emitted photoelectrons were assumed to escape. The latter assumption is clearly wrong in view of the barrier of negative potential which exists on the sunlit side of the spacecraft. Excess electron collection will therefore occur on sunlit surfaces, driving their potentials more negative. Attempts to converge onto a floating condition have provided qualitative confirmation of such behavior, but successful convergence had not yet been achieved when this was written. The reason appears to involve the fact that on a curved surface, photoemission current decreases continuously as a function of distance from the subsolar point. A point (whose location is not known in advance) will therefore exist at which photoemission becomes insufficient to hold the surface close to space potential. Beyond this point, surface potential will decrease rapidly as a function of position. The surface potential profile will therefore contain a "shoulder" whose location evolves as the calculation proceeds. Combination of this situation with truncation errors in the photocurrent calculation appears to be responsible for the observed lack of convergence. A variety of approaches are presently being explored in an effort to overcome this difficulty, including the construction of a surface-current model for photoemission which includes production-gradient as well as potential-gradient effects.

CONCLUSIONS

We have presented results from a two-dimensional numerical simulation of the high-altitude differential charging problem. Although these results are preliminary, they provide verification of a prediction by Prokopenko and Laframboise (1977) that breakdown of orbit-limited ion collection can occur on a sufficiently small shaded isolated surface element, driving its floating potential more negative than otherwise. The results also verify another prediction (Fahleson, 1973; Prokopenko and Laframboise, 1977) that barriers of negative potential can form on the sunlit side of a differentially charged spacecraft in the absence of space-charge effects. A variety of other phenomena, including effects of time-dependent external conditions, effects of surface material properties including those of "multiple-root" materials (Prokopenko and Laframboise, 1977), and effects of gun emissions remain to be investigated. The results obtained so far provide evidence that the simulation

program is ready to play a useful role in studies of high-altitude spacecraft charging problems.

REFERENCES

Fahleson, U. (1973) Plasma-vehicle interactions in space: some aspects of present knowledge and future development. In: Photon and Particle Interactions with Surfaces in Space, R.J.L. Grard, Editor, D. Reidel Pub. Co., Dordrecht, Holland, pp. 563-569.

Katz, I., Parks, D.E., Wang, S., and Wilson, A. (1977), Dynamic modeling of spacecraft in a collisionless plasma. In: Proc. USAF-NASA Spacecraft Charging Technology Conference, C.P. Pike and R.R. Lovell, Editors, Report No. AFGL-TR-77-0051, Air Force Geophysics Laboratory, Hanscom AFB, Massachusetts/NASA TMX-73537, Lewis Research Center, Cleveland, Ohio, pp. 319-330.

Lafon, J.-P.J. (1976), On the sheath surrounding a conductor emitting photoelectrons in an isotropic collisionless plasma, Radio Sci. 11, pp. 483-493.

Laframboise, J.G., and Prokopenko, S.M.L. (1977), Numerical simulation of spacecraft charging phenomena. In: Proc. USAF-NASA Spacecraft Charging Technology Conference, C.P. Pike and R.R. Lovell, Editors, Report No. AFGL-TR-77-0051, Air Force Geophysics Laboratory, Hanscom AFB, Massachusetts/NASA TMX-73537, Lewis Research Center, Cleveland, Ohio, pp. 309-318.

Laframboise, J.G., and Prokopenko, S.M.L. (1978), Predictions of high-voltage differential charging on geostationary spacecraft, Paper 4.4, 1978 Ionospheric Effects Symposium, Arlington, January 1978 (proceedings in press).

Parker, L.W. (1978), Potential barriers and asymmetric sheaths due to differential charging of nonconducting spacecraft. Report No. AFGL-TR-78-0045, Air Force Geophysics Laboratory, Hanscom AFB, Massachusetts.

Parker, L.W. (1978), Plasma sheath effects on equilibrium voltage distributions of large high-power satellite solar arrays. Paper III-4, 2nd USAF-NASA Spacecraft Charging Technology Conference, Colorado Springs, October 1978.

Prokopenko, S.M.L., and Laframboise, J.G., (1977), Prediction of large negative shaded-side spacecraft potentials. In: Proc. USAF-NASA Spacecraft Charging Technology Conference, C.P.Pike and R.R. Lovell, Editors, Report No. AFGL-TR-77-0051, Air Force Geophysics Laboratory, Hanscom AFB, Massachusetts /NASA TMX-73537, Lewis Research Center, Cleveland, Ohio, pp. 369-387.

Rothwell, P.L., Rubin, A.G., Pavel, A.L., and Katz, L. (1976), Simulation of the plasma sheath surrounding a charged spacecraft. In: Spacecraft Charging by Magnetospheric Plasmas, A. Rosen, Editor, AIAA, New York, and MIT Press, Cambridge, Massachusetts, pp. 121-133.

Schröder, H. (1973), Spherically symmetric model of the photoelectron sheath for moderately large plasma Debye lengths. In: Photon and Particle Interactions with Surfaces in Space, R.J.L. Grard, Editor, D. Reidel Pub. Co., Dordrecht, Holland, pp. 51-58.

Soop, M. (1972), Report on photo-sheath calculations for the satellite GEOS, Planet.Space Sci. 20, pp. 859-870.

Whipple, E.C., Jr. (1976), Theory of the spherically symmetric photoelectron sheath: a thick sheath approximation and comparison with the ATS 6 observation of a potential barrier. J. Geophys. Res. 81, pp. 601-607.

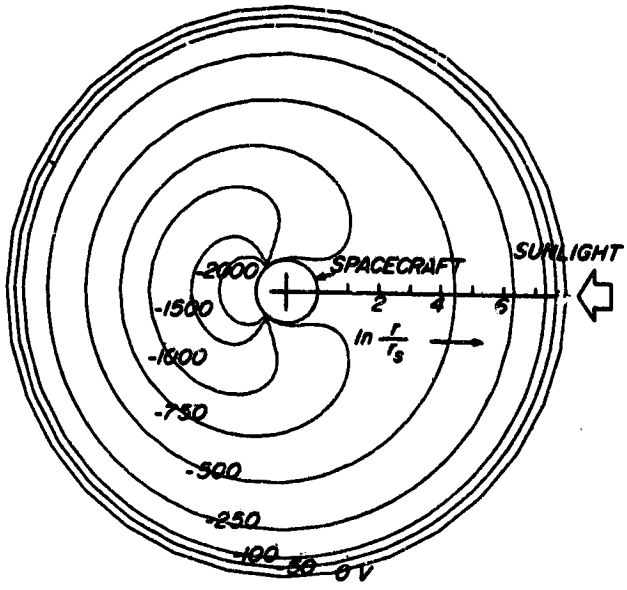

Figure 1. Equipotential contours around an infinite cylindrical spacecraft with two conductive sectors having angles of 270° and 90°. Sector potentials are -735V and -2956V, respectively. Residual sector currents are -0.0066 and -0.0060 times sector electron random currents, respectively. $T_i = T_e =$ 1keV, $T_{ph} =$ 1eV, $N_{e\infty} = 50$ cm^{-3}. Assumed photoemission flux J_{ph} is 42×10^{-6} A/m^2 at normal sunlight incidence (i.e. that for aluminum). Secondary and backscattered fluxes are assumed zero. Computation grid contains 34 x 16 intervals. Space charge is neglected.

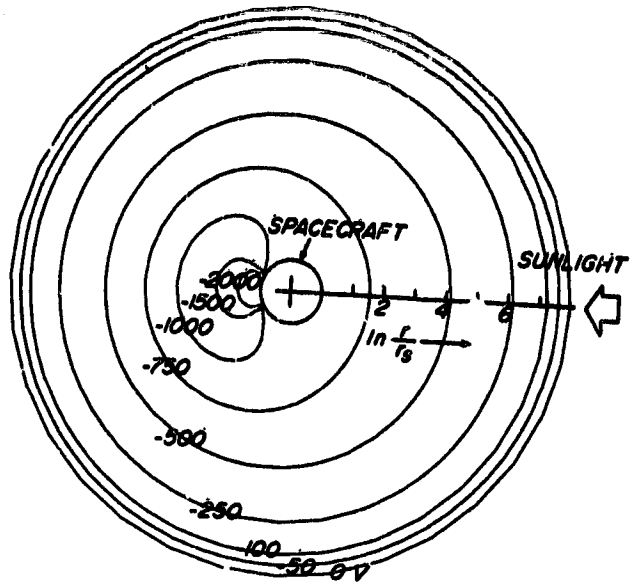

Figure 2. Equipotential contours around an infinite cylindrical spacecraft with two conductive sectors having angles of 315° and 45°. Sector potentials are -856V and -2956V, respectively. Residual sector currents are -0.0038 and -9.0×10^{-7} times sector electron random currents, respectively. Other data are same as for Fig. 1.

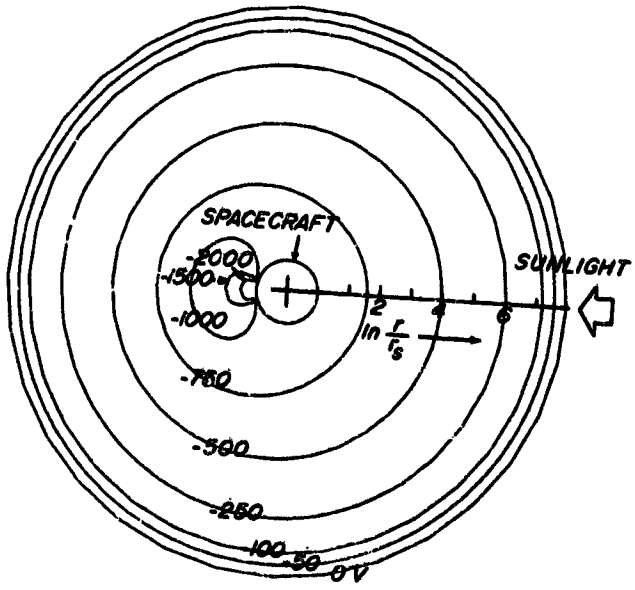

Figure 3. Equipotential contours around an infinite cylindrical spacecraft with two conductive sectors having angles of 337½° and 22½°. Sector potentials are -893V and -2969V, respectively. Residual sector currents are -0.0032 and 2.2×10^{-4} times sector electron random currents, respectively. Other data are same as for Fig. 1.

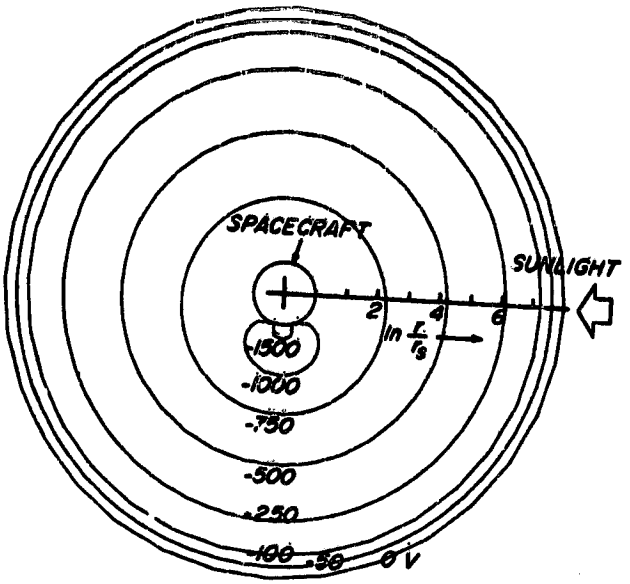

Figure 4. Same as Fig. 3 except rotated by 90° with respect to sunward direction. Sector angles are 337½° and 22½°. Sector potentials are -998V and -1964V, respectively. Residual sector currents are -0.0071 and -7.5×10^{-4} times sector electron random currents, respectively.

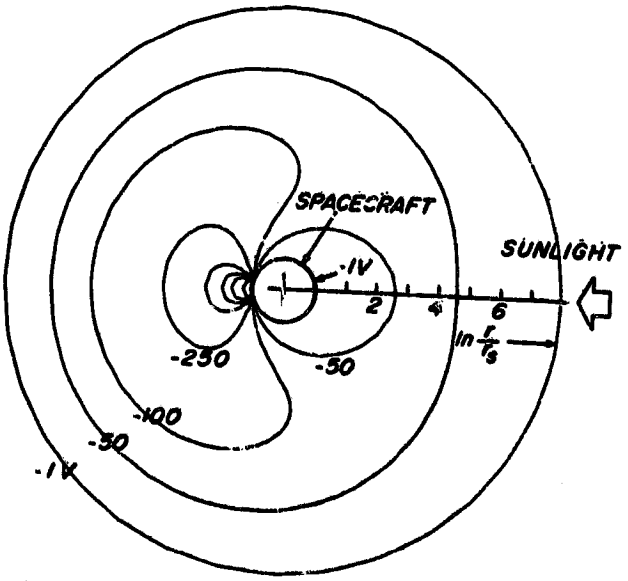

Figure 5. Same as Fig. 3 except that secondary and backscattered currents due to electron impact are included. Sector angles are 337½° and 22½°. Sector potentials are 0.124V and -2126V, respectively. Residual sector currents are -0.042 and 0.021 times sector electron random currents, respectively. Secondary and backscatter data used [illegible] ose given for aluminum by Laframboise and Prokopenko (1978). [illegible] ials on unlabeled contours are -500, -750, -1000, -1500 and -2000V.

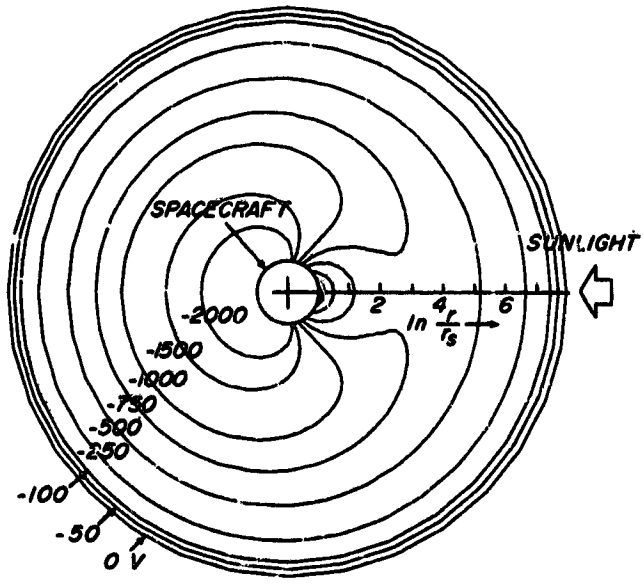

Figure 6. Equipotential contours around an infinite cylindrical spacecraft having an insulating surface, corresponding to a "guess field" surface potential distribution determined using local current balance considerations, with all potential barrier effects ignored. Maximum and minimum surface potentials are 5.42×10^{-3} V and -2956V, respectively. Assumed values of T_i, T_e, $N_{e\infty}$, T_{ph} and J_{ph} are the same as for Fig. 1. Secondary and backscattered fluxes are assumed zero. Computation grid contains 34 x 16 intervals. Space charge is neglected.

D16

N79-24017

ANALYTICAL STUDY OF THE TIME DEPENDENT SPACECRAFT-PLASMA INTERACTION*

J. W. Cipolla, Jr. and M. B. Silevitch
Northeastern University

SUMMARY

A study of the time dependent interaction of an initially uniform equilibrium plasma with a plane conducting surface has been made in order to achieve a more complete understanding of the dynamics of the charging process and of the approach to the floating potential on the surface. Numerical solutions of the cold ion equations of motion in conjunction with equilibrium electrons and Poisson's equation show the formation of an ion-rich sheath near the surface and the coupling of the non-neutral region to the undisturbed plasma through a quasineutral rarefaction. Analytical treatment of the quasineutral region shows excellent agreement (within 1%) with the numerical results.

INTRODUCTION AND FORMULATION OF EQUATIONS

Observations of anomalous behavior in synchronous orbit satellites and the attribution of these effects to the charging of spacecraft by energetic electrons has led to the need for more complete understanding of the dynamic interaction of solid bodies with plasmas. In this work a mathematical model of this time dependent interaction is presented. Previous analytical work on time dependent plasma boundary value problems has been restricted to time dependent probe theory, in which the sheath development and plasma response to a known variation of probe potential is sought (ref. 1-6), to plasma expansion into vacuum (ref. 7-9), and to ion acceleration in a steep density gradient (ref. 10). It is essential to note, however, that in our work (in contrast to these earlier treatments) both the probe potential and plasma response are unknown and linked through the self-consistent set of equations to be set down in further detail below.

Consider a planar conducting slab of arbitrary thickness initially uncharged and in equilibrium with a collisionless neutral stationary plasma (fig. 1). At time $t = 0$ the slab begins to absorb all charge incident upon it but remains non-emitting. This non-emitting catalytic wall assumption is introduced solely for simplicity; the effects of partial absorption and recombination of electrons and ions respectively and of such emissions as photoemission, secondary emission, etc. can be included as adjustments in the boundary conditions of the problem. This physical situation could describe either a planar laboratory probe, a nonplanar laboratory system in contact with a small

*This work was supported by AFOSR contract F19628-76-C-0246 and grant 78-3731.

Debye length plasma, or planar portions of a satellite in contact with the earth's plasma environment. For many conditions of interest, the electron to ion temperature ratio T_e/T_i is equal to or greater than unity, so that the random thermal electron flux initially dominates the ion flux to the boundary, resulting in the buildup of a negative surface charge on both exposed surfaces while the condition of zero electric field is maintained in the slab interior. Since all subsequent development occurs symmetrically, attention is focused on the half space $x > 0$ with the right face of the slab located in the plane $x = 0$, keeping in mind, however, that within one skin depth of the surface the electric field is uniformly zero. It is clear that the initial acquisition of negative surface charge leaves an ion rich layer immediately adjacent to the slab, in which a negative potential and electric field are established due to the initial charge separation. These self-consistent fields then act to decelerate electrons and accelerate ions until a balance between their fluxes is achieved (at least for singly ionized plasmas), at which point no net current flows to the boundary and the process achieves a steady state.

In our further discussion and analytical development it is convenient to make the following assumptions:

1. Plasma electrons, with thermal energy kT_e, are to be treated as always in a quasistatic equilibrium state relative to the ions. Thus the nondimensional electron number density and flux are given by

$$n_e(\psi) = e^{-\psi}\left(1 - \frac{1}{2}\,\mathrm{erfc}\sqrt{\psi_w - \psi}\right)\left(1 - \frac{1}{2}\,\mathrm{erfc}\sqrt{\psi_w}\right)^{-1} \tag{1a}$$

$$j_e(\psi) = -\left(\frac{m_i}{2\pi m_e}\right)^{1/2} e^{-\psi_w}\left(1 - \frac{1}{2}\,\mathrm{erfc}\sqrt{\psi_w}\right)^{-1} \tag{1b}$$

where the dimensional (with tildes) density, flux, potential, and wall potential, respectively, are defined by

$$\tilde{n}_e = n_e n_o\,, \quad \tilde{j}_e = j_e n_o c\,, \quad -\tilde{\phi} = (kT_e/|e|)\psi\,, \quad -\tilde{\phi}(o,t) = (kT_e/|e|)\psi_w$$

where n_o is the density of the undisturbed plasma and $c = (kT_e/m_i)^{1/2}$ is the ion acoustic speed. The complementary error function reflects the halfrange nature of the electron distribution function due to the absorbing boundary and has been discussed in detail by Hu and Zeiring in reference 11. Equations (1a) and (1b) are reasonable since the charging dynamics are expected to scale as the ion plasma period

$$\omega_{pi}^{-1} = (\varepsilon_o m_i/n_o e^2)^{1/2}$$

whereas the equipartition time for electrons can be expected to scale as

$$\omega_{pe}^{-1} = (m_e/m_i)^{1/2}\omega_{pi}^{-1}$$

This argument is standard and should not predict unphysical results.

2. The ion thermal motion is negligible compared to the electrons ($T_e >> T_i$) so that ion dynamics are governed solely by the self-consistent electric field in the cold ion approximation to the equations of motion.

Thus we may write as the complete system of equations

$$\frac{\partial n}{\partial t} + \frac{\partial}{\partial x}(nu) = 0 \tag{2}$$

$$\frac{\partial u}{\partial t} + u\frac{\partial u}{\partial x} = \frac{\partial \psi}{\partial x} \tag{3}$$

$$\frac{\partial^2 \psi}{\partial x^2} = n - n_e(\psi) \tag{4}$$

where n and u represent the ion density and velocity scaled with respect to the undisturbed plasma density n_o and the ion acoustic speed c. In addition, t is time measured in ion plasma periods ω_{pi}^{-1} and x is distance in electron Debye lengths λ_{De} with $\lambda_{De}\,\omega_{pi} = c$. Asymptotic conditions satisfied in the undisturbed plasma are given by

$$u,\ \psi,\ \frac{d\psi}{dx} \to 0\ , \quad n \to 1 \quad \text{as } x \to \infty \tag{5}$$

The catalytic wall boundary condition links the dynamic behavior of the non-neutral sheath region with the continuing accumulation of charge on the wall. Using Gauss' law on a thin control volume surrounding the surface then gives

$$\frac{\partial E}{\partial t} = j_e(\psi_w) - nu \quad \text{at } x = 0 \tag{6}$$

and the boundary condition on ψ is then

$$\frac{d\psi}{dx} = E \quad \text{at } x = 0 \tag{7}$$

NUMERICAL RESULTS

We have integrated eqs. (2)-(4) numerically using a scheme similar to that of Widner et al. (ref. 12). First Poisson's equation is solved using a relaxation method with a variable convergence factor. The derivative boundary condition at $x = 0$ is incorporated into the relaxation using an image point technique and the asymptotic condition is satisfied by setting $\psi = 0$ at some x location sufficiently far into the plasma ($\psi = 0$ and $x = 80$ in the calculations presented here). The ion density and velocity are then advanced in time by numerically integrating the finite difference form of the continuity and momentum equations using the potential and electric field previously obtained. These updated n and u are then used to advance the electric field at

the wall through eq. (6) which then serves to update the boundary condition (eq. 7) for the next iteration of Poisson's equation which now also includes an updated ion density. This procedure is then repeated until a steady state is reached. To start the calculation we assume the initial surface electric field to be caused by absorption of the random thermal electron flux through a matrix of stationary, uniform ions during an initial period of one electron plasma period. Poisson's equation was then solved with this initial field at $x = 0$ and the resulting potential and electron density distribution then served as "initial" conditions for the subsequent calculations. The distance and time spacings used were $\Delta x = .2$ and $\Delta t = .01$, with the x-axis divided into 400 intervals.

Figures (2 a) and (3 a) show plots of density and potential vs. x during the initial stage of charging for $t = 0$, 1, and 2. Figures (2 b) and (3 b) show the final stages of the approach to a steady state. The development of a non-neutral sheath region is clearly shown in these later times, with the sheath edge ($n \approx n_e$) moving into a quasineutral region of the plasma which has been pre-accelerated by an advancing ion acoustic disturbance. We note that neither the field nor potential vanishes at the sheath edge ($x_s \approx 15$ for $t = 72$) although the field is gradually diminishing in time. Furthermore, the wall potential ψ_w is within 3% of its floating value of 3.81 after only $10\ \omega_{pi}^{-1}$, although the electric field and ion flux at the wall take somewhat longer to approach their steady values of $E_w = -.716$ and $n_w u_w = -.382$, respectively.

In order to place the qualitative behavior of the sheath and plasma into better focus, consider the x-t diagram of fig. (4). The curve $x = \xi(t)$ represents the sheath edge, defined as the locus of points where $n \approx n_e$. Andrews (ref. 3) has shown that as long as $\dot{\xi}(t) > c$, no disturbance from the sheath and wall region may propagate into the undisturbed plasma. However, as the sheath edge decelerates through the point P_1 at which $\dot{\xi}(t_1) = c$, an ion acoustic rarefaction propagates into the plasma. As the sheath approaches the asymptotic steady state (shown for convenience at P_3), the constantly emitted rarefaction waves accelerate ions until at P_3 and beyond the sheath has reached a stable position, and the ions reach a steady final velocity entering the sheath, shown below to be the ion acoustic speed.

ANALYTICAL TREATMENT OF QUASINEUTRAL PLASMA

This composite picture of sheath development may be made quantitative by considering the equations of motion in the quasineutral region. Setting

$$n = n_e = e^{-\psi} \tag{8}$$

in eqs. (2) and (3) and neglecting Poisson's equation yields

$$\frac{\partial \ln n}{\partial t} + \frac{\partial u}{\partial x} + u \frac{\partial \ln n}{\partial x} = 0 \tag{9}$$

$$\frac{\partial u}{\partial t} + u \frac{\partial u}{\partial x} + \frac{\partial \ell n\, n}{\partial x} = 0 \tag{10}$$

The use of the equilibrium Boltzmann density for electrons (eq. 8) instead of the correct density as given by eq. (1a) is accurate to within about 1% for $t > 10$. The correct halfrange behavior should be retained only during the early stages of charging while the wall potential is still relatively small. Adding and subtracting these equations then gives the characteristic forms

$$\frac{D^{\pm}}{Dt} J^{\pm} = 0 \tag{11}$$

where

$$J^{\pm} = u \pm \ell n\, n \tag{12}$$

$$\frac{D^{\pm}}{Dt} = \frac{\partial}{\partial t} + (u \pm 1) \frac{\partial}{\partial x} \tag{13}$$

The solution to these equations is then

$$J^{\pm} = \text{const} \tag{14}$$

on the characteristics $f^{\pm}$ defined by

$$\frac{dx}{dt} = u \pm 1 \tag{15}$$

At this point several comments may be made about the resulting quasineutral plasma flow.

(i) The region beyond $\xi(t)$ is called a simple wave region since the $f^{\pm}$ characteristics are all straight lines. This may be seen by noting that at any point in the plasma

$$u = \frac{1}{2} (J^{+} + J^{-}) \tag{16}$$

Now consider two adjacent points P' and P" on the characteristic f_2^{+} in fig. 4. It is clear from eq. (14) that $J^{+}(P') = J^{+}(P")$. Furthermore, the quantity J^{-} is not only invariant along a given characteristic but, since all f^{-} characteristics originate in a region of constant state with $u = 0$ and $n = 1$, J^{-} is also the same on different f^{-} characteristics; therefore

$$J^{-}(P') = J^{-}(P") = 0 \tag{17}$$

where J^{-} has been evaluated in the undisturbed plasma. Consequently, $u' = u"$ and

$$\left.\frac{dx}{dt}\right|_{p'} = u' + 1 = u'' + 1 = \left.\frac{dx}{dt}\right|_{p''} \tag{18}$$

so that the slope of each f^+ characteristic is constant. Therefore, the f^+ characteristics represent lines of constant u and therefore also lines of constant $\ell n\ n$.

(ii) It is clear that along the characteristic f_1^+

$$\left.\frac{dx}{dt}\right|_1 = u_1 + 1 = 1 \tag{19}$$

since $u_1 = 0$. Furthermore, in order for the dynamical quantities to achieve steady values at the sheath edge, the asymptotic characteristic (shown for convenience as f_3) must be horizontal. Therefore,

$$\left.\frac{dx}{dt}\right|_3 = u_3 + 1 = 0 \tag{20}$$

or

$$u_3 = -1 \tag{21}$$

Consequently, the rarefaction consists of a fan of straight line characteristics varying in slope from 1 to 0, which has the effect of accelerating the stationary ions to precisely the ion acoustic speed before appreciable charge separation may occur in the sheath.

Using eqs. (12), (14), (16), and (17) gives for point P'

$$u' = \frac{1}{2}(J^+ + J^-) = \frac{1}{2}[u_s + \ell n\ n_s] \tag{22}$$

where u_s and n_s are the ion velocity and number at point P_2 on the sheath edge. Since u is constant on f_2^+

$$u' = u_s = \frac{1}{2}u_s + \frac{1}{2}\ell n\ n_s \tag{23}$$

or

$$u_s = \ell n\ n_s = -\psi_s \tag{24}$$

so that the f^+ characteristics are also lines of constant potential. Since $u_s < 0$, it is seen that $n_s < 1$ and $\psi_s > 0$.

This effectively solves the complete gas dynamic problem in the plasma region. However, to construct the solution explicitly requires knowledge of data along the sheath edge, which can only come in this self-consistent charging problem from using the relevant dynamical equations in the sheath itself obtained in the numerical solution.

We may, however, now completely describe the steady state sheath values and use these to check our numerical results. Using $u_s = -1$ as the steady ion velocity at the sheath edge then gives

$$u_s = -1 , \quad \psi_s = 1 , \quad n_s = e^{-1}$$

Now using the steady continuity and momentum equations for ions gives

$$n_w u_w = n_s u_s = -e^{-1}$$

$$u_w^2 - 2\psi_w = u_s^2 - 2\psi_s = -1$$

and the balance of ion and electron currents to the wall gives

$$-e^{-1} = n_w u_w = j_e(\psi_w) = -\left(\frac{m_i}{2\pi m_e}\right)^{1/2} e^{-\psi_w}$$

where we have again neglected the halfrange character of the electron distribution. The floating potential may then be found as

$$\psi_w = 1 + \frac{1}{2} \ln \frac{m_i}{2\pi m_e} = 3.84$$

and the ion velocity at $x = 0$ as

$$u_w = -\sqrt{2\psi_w - 1} = -2.60$$

An examination of the numerical solution then shows the floating potential (3.81) and the ion velocity at the wall (-2.61) are correctly computed to within 1% of the exact values found using the method of characteristics.

REFERENCES

1. Sander, K.F., J. Plasma Phys., 3, 353 (1969).
2. J.E. Allen and J.G. Andrews, J. Plasma Phys., 4, 187 (1970).
3. J.G. Andrews, J. Plasma Phys., 4, 603 (1970).
4. J.G. Andrews and R.H. Varey, Phys. Fluids, 14, 339 (1971).
5. C.H. Shih and E. Levi, AIAA Journal, 10, 104 (1972).
6. M.M. Widner and J.W. Poukey, Phys. Fluids, 19, 1838 (1976).
7. A.V. Gurevich, L.V. Pariiskaya, and L.P. Pitaevskiĭ, Zh. Eksp. Teor. Fiz. 49, 647 (1965) [Sov. Phys. - JETP 22, 449 (1966)]; Zh. Eksp. Teor. Fiz. 63, 516 (1972) [Sov. Phys. - JETP 36, 274 (1973)].

8. J.E. Crow, P.L. Auer, and J.E. Allen, J. Plasma Phys., 14, 65 (1975).
9. M. Widner, I. Alexeff, and W.D. Jones, Phys. Fluids, 14, 795 (1971).
10. F.S. Felber and R. Decoste, Phys. Fluids, 21, 520 (1978).
11. P.N. Hu and S. Ziering, Phys. Fluids, 9, 2168 (1966).
12. M. Widner, I. Alexeff, W.D. Jones, and K.E. Lonngren, Phys. Fluids, 13, 2532 (1970).

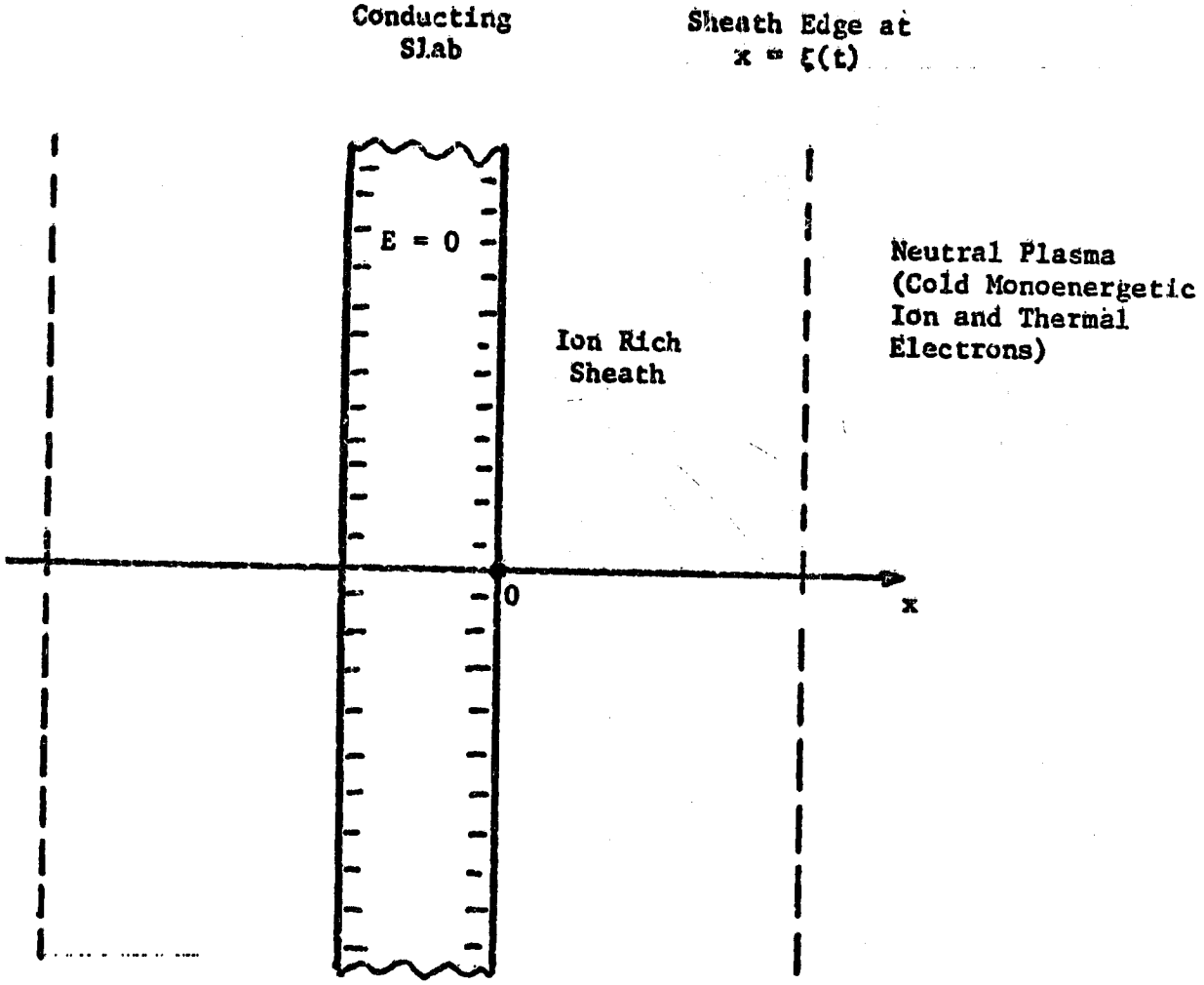

Figure 1. - Geometry.

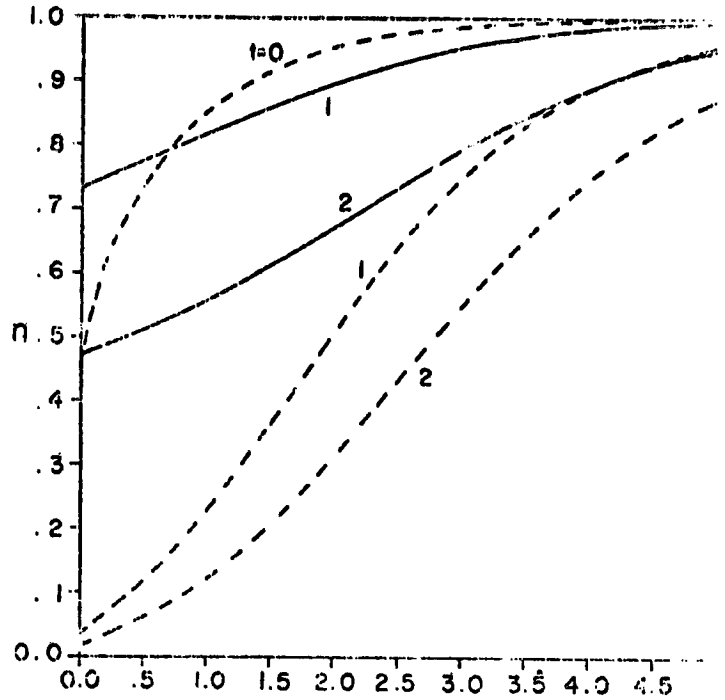

(a) Initial stage of charging.

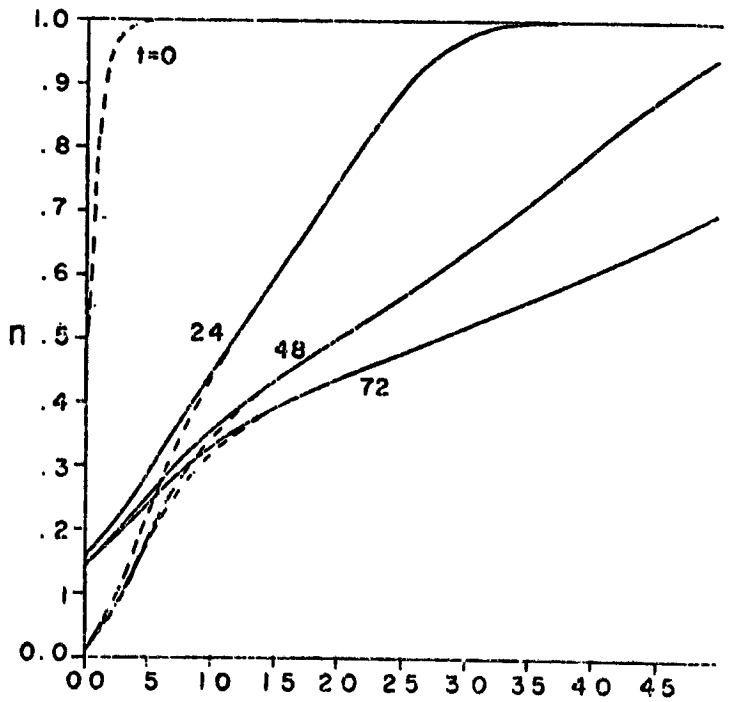

(b) Final stage of charging.

Figure 2. - Ion and electron densities as function of distance for several times in ω_{pi}^{-1} units. Electron densities are shown dotted.

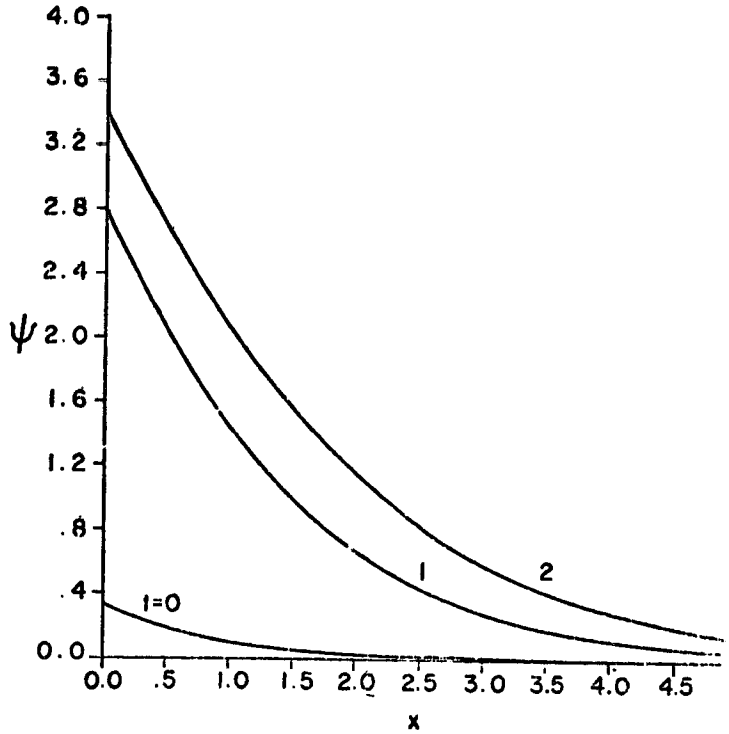

(a) Initial stage of charging.

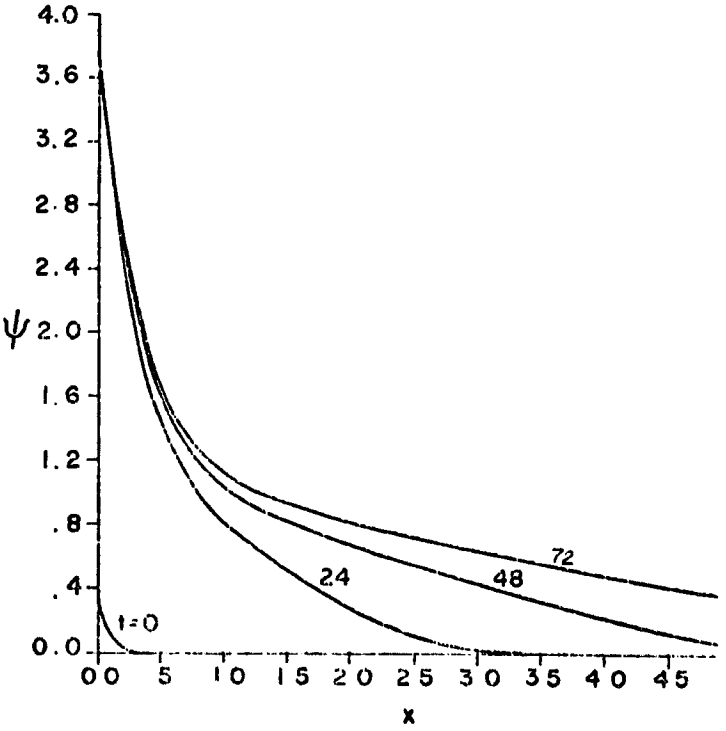

(b) Final stage of charging.

Figure 3. - Normalized potential as function of distance in Debye lengths for several times in ω_{pi}^{-1} units.

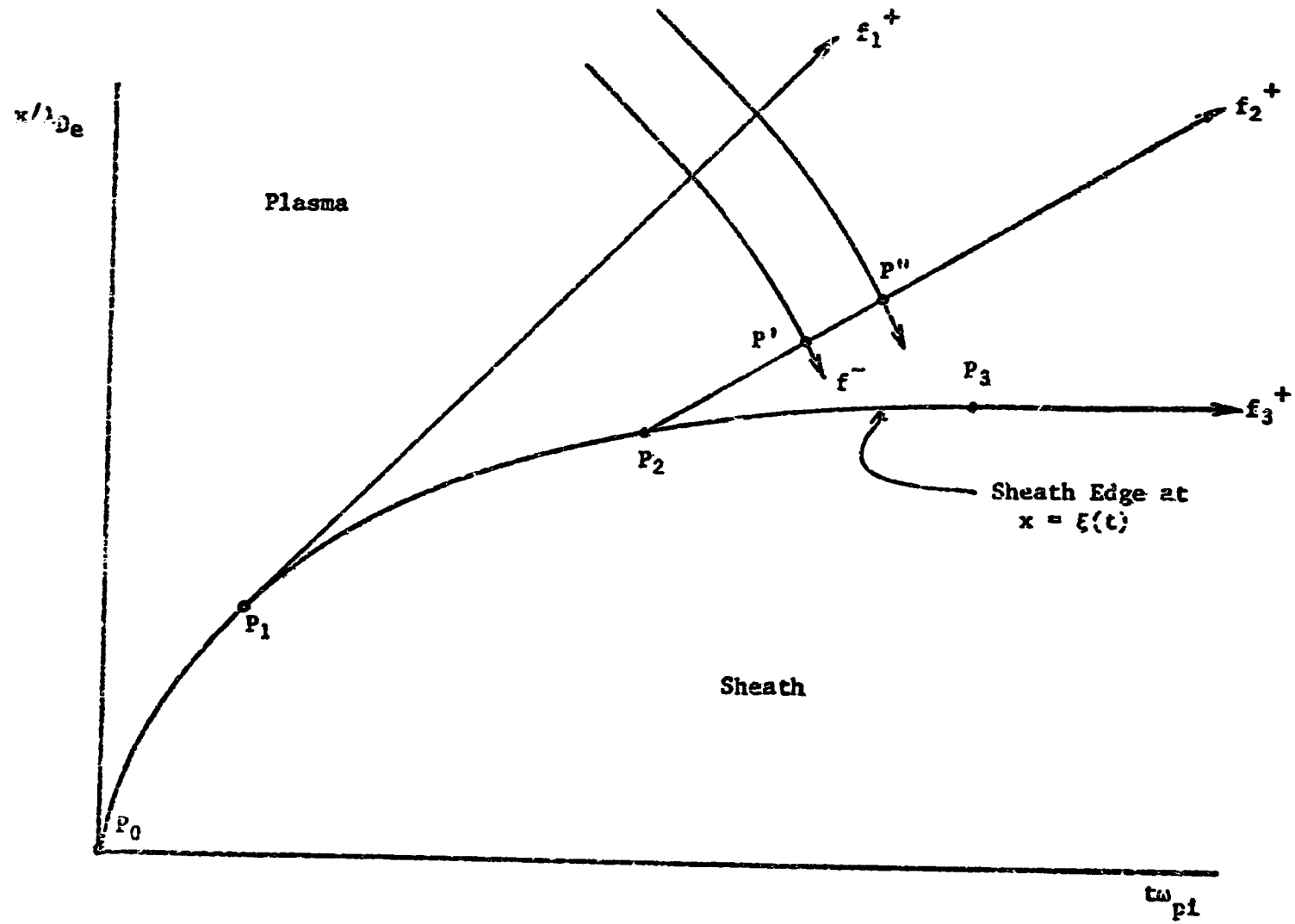

Figure 4 - Characteristic diagram for sheath edge motion.

ELECTRON TRANSPORT MODEL OF DIELECTRIC CHARGING*

Brian L. Beers, Hsing-chow Hwang,
Dong L. Lin, and Vernon W. Pine
SCIENCE APPLICATIONS, INC.

SUMMARY

A computer code (SCCPOEM) has been assembled to describe the charging of dielectrics due to irradiation by electrons. The primary purpose for developing the code was to make available a convenient tool for studying the internal fields and charge densities in electron-irradiated dielectrics. The code, which is based on the primary electron transport code POEM (ref. 1), is applicable to arbitrary dielectrics, source spectra, and current time histories. The code calculations are illustrated by a series of semi-analytical solutions. Calculations to date suggest that the front face electric field is insufficient to cause breakdown, but that bulk breakdown fields can easily be exceeded.

INTRODUCTION

One of the major concerns generated by the spacecraft charging problem is the possibility of catastrophic breakdown and discharge of dielectrically stored charge. By this time, ample experimental evidence is available to indicate that such discharges do occur both in space (see, e.g., refs. 2-3) and in laboratory simulations (see, e.g., refs. 4-12) of the electron charging environment. While it is generally acknowledged that an understanding of these events requires a knowledge of the internal fields and charge densities in the dielectric, very little work on this problem has been reported in the spacecraft charging literature, the notable exceptions being the paper of Meulenberg (ref. 12) and certain estimates reported in the NASCAP code documentation (ref. 13). It is the purpose of this paper to describe our initial research in developing tools for quantitatively understanding these important internal quantities.

*This work was sponsored, in part, by the COMMUNICATIONS RESEARCH CENTRE of Canada.

The general subject of charge trapping, charge storage, and current flow in dielectrics is an exceedingly complex area of research (see, e.g., refs. 14-16). Our approach to this problem for the situations of interest to satellite charging has been to develop a computer model (SCCPOEM) (ref. 17) of the dielectric charging process which

- isolates the essential features of the charging process which depend on the dielectric
- is sufficiently general to permit comparison to laboratory simulation data
- is sufficiently general to permit easy application to arbitrary dielectrics, electron source spectra, and current time histories
- incorporates in a detailed quantitative fashion all those features of the charging process which are believed to be well-known
- has the flexibility to add modular units which may be necessary to describe additional physics
- is inexpensive enough to run to permit parametric studies

To achieve these goals, we have restricted the model to one-dimensional geometry and have coupled the existing SAI Monte Carlo electron transport code POEM (ref. 1) with various standard algorithms for computing the internal charge and field evolution. The existing code configuration relies on macroscopic phenomenological descriptions of some of the important dielectric processes (e.g., bulk conduction is treated with an empirically determined conductivity model). Work is currently underway to include a detailed carrier statistics package into the code description of the trapping.

After introducing the basic features of the model, code results are illustrated by a series of special case analytical solutions which rely on the basic transport calculations. The presentation utilizes the method of successive complication, i.e., the results proceed from the simplest to the most complicated by the successive relaxation of constraints. Because dielectric phenomena are generally so complicated, we believe this method to be essential for isolating those ingredients of the model which are critical. Future research may then focus on these critical areas.

The analytical results are followed by completely numerical computations for cases which are too difficult to handle analytically. All of the sample calculations suggest that the front face electric field arising from the charge separation of the deposited electrons and the secondary emission electron depletion region is well below expected breakdown fields. As these results are not in keeping with the Meulenberg discharge hypothesis (ref. 12),

we pinpoint the assumptions which give rise to our results, discuss limitations of the calculations, and suggest experiments which may be useful in determining the range of validity of our predictions.

ONE-DIMENSIONAL MODEL

Shown in figure 1 is the basic one-dimensional model which is assumed throughout this paper. We have chosen this model for several reasons. Our primary concern is with the conditions which occur internal to the dielectric. The indicated dielectric geometry provides the simplest configuration which can be investigated. This geometry has the advantage of isolating the physical effects occurring within the dielectric from complicated multi-dimensional effects due to transverse currents and fields. Additionally, it is expected that a one-dimensional treatment of the dielectric is an excellent approximation over most of the dielectric area. That is, away from edges, corners, holes, etc., the external conditions vary slowly transverse to the surface compared to variations through the sample (variations in mils or less). Relating the incident spectrum and primary current J_I to the source spectrum and current J_∞ in one dimension is not generally justified. For a realistic satellite configuration, this relationship can only be extracted by using a three-dimensional code of the NASCAP type (ref. 13). Recognizing this, we have established our computational algorithm so that it will accept an incident spectrum and current from other sources. The specific relationship implied by figure 1, however, is itself useful. Most laboratory simulation arrangements attempt to achieve this simple configuration to some degree. The computed results may be directly compared to the data from these configurations to obtain meaningful information. The additional merit of the configuration is that complicated multi-dimensional effects do not obscure the attempt to understand the basic charging process.

Several additional simplifications should be noted. It is assumed that the beam energy and current density and the model dimensions are such that

(1) the potential does not change significantly during an electron transit time, and

(2) that space charge effects in the vacuum are negligible.

For laboratory applications in the regimes of interest to spacecraft charging, these assumptions are true to a very high degree of accuracy. Under these conditions, the current density is constant throughout the vacuum region. We also assume that the source current is constant in time throughout this paper. While there are undoubtedly interesting effects which may be studied by modulating the beam current, we felt it best to initiate our studies with the customary laboratory condition of constant current. The code version of the model, SCCPOEM, easily accepts time-dependent currents. We do, however, explicitly consider two separate time histories for the source spectrum. We arbitrarily designate these as the "normal" and "feedback" cases. The "normal"

case corresponds to the typical experimental circumstances in which the source spectrum is constant. The "feedback" case is distinguished by having an incident spectrum that is constant. Experimentally, this would correspond to applying an additional accelerating voltage to the source spectrum which exactly cancels the retarding potential of the charged surface. From an analytical point of view, this condition has the merit of maintaining constant source terms. Experimentally, this configuration could be useful for studying the dependence of important charging quantities (backscatter and secondary currents, for example) on the sample voltage and charging history.

Our notation for a number of the primary quantities, and our choice of spatial coordinate system is given in Figure 1. The capacitance (per unit area) of the dielectric surface to the left hand plate (∞) C_o is related to the distance to the surface L by $C_o = \epsilon_o/L$, while the sample capacitance C_D is related to the sample thickness δ by $C_D = \epsilon/\delta$ (ϵ_o and ϵ are the permittivities of the vacuum and dielectric, respectively). For laboratory conditions C_o (capacitance to tank) is normally determined by a dimension somewhat smaller than the distance to the electron source. Generally, however, the condition $C_o << C_D$ holds. We still often find it convenient to eliminate the dependence of the solution on this laboratory dimension, and will take $C_o = 0$ (with appropriate limits). The equations describing the basic charging process are well known and have been documented elsewhere (ref. 17) for the model presented here. They are presented as needed in the course of the text.

THICK SAMPLES — EXTERIOR CHARGING VARIABLES

The external charging process may be characterized by a simple circuit model. The equations of the model are

$$C_o \frac{dV_o}{dt} = \bar{J}_o - \bar{J} \tag{1}$$

$$C_D \frac{dV_D}{dt} = \bar{J}_D - \bar{J} \tag{2}$$

where V_o is the potential drop from the left hand plate to the surface, V_D is the drop from the surface to the right hand plate, and the other symbols have the meanings noted above. Equations (1) and (2) are a rigorous consequence of the Maxwell equations. During the normal laboratory charging operation, the sample plate is connected to ground using a low value resistor, so that effective short circuit boundary conditions are the rule ($V_o + V_D = 0$). We consider this case exclusively throughout. Under these conditions, the external (short-circuit) current $\bar{J}$* is given by

*To avoid repetition, we refer to current densities as currents, with the area implied.

$$\bar{J} = \frac{C_D}{C}\bar{J}_o + \frac{C_o}{C}\bar{J}_D \tag{3}$$

where $C = C_o + C_D$ is the total capacitance (parallel) of the sample surface to ground. The charging rate of the surface potential (V_o) is then determined by

$$C\frac{dV_o}{dt} = \bar{J}_o - \bar{J}_D \tag{4}$$

which is the equation previously used by Purvis, et al. (ref. 18).

Internal to the dielectric the electric field satisfies the one-dimensional equation of Poisson:

$$\frac{dE}{dx} = \rho/\varepsilon \tag{5}$$

where ρ is charge density in the dielectric. Let Q be the total charge (per unit area) in the dielectric. Integration of equation (5) yields the result

$$Q = \frac{\varepsilon(1 + \delta/L)}{(\delta - \bar{x})} V_o \tag{6}$$

where $\bar{x}$ is the mean depth of the charge in the dielectric,

$$\bar{x} = \frac{\int_o^\delta \rho(x)x\,dx}{Q} \tag{7}$$

If the inequality $\bar{x} << \delta$ holds throughout the charging, then $\bar{x}$ may be neglected — the voltage is determined by the geometric capacitance of the surface. Under these circumstances, the electric field is uniform throughout most of the sample, and a bulk conductivity may be used to characterize the conduction current through the volume. Thus, the conduction current J_D in equation (4) may be replaced by GV_o, where G is the conductance per unit area. These observations have been made numerous times and represent the standard approximation for use in higher dimensional codes of the NASCAP variety (ref. 13).

The point of this rather obvious exercise is that for thick samples ($\bar{x} << \delta$) the quantities normally measured in charging experiments are effectively decoupled from the charge distribution which determines the electric field in the deposition region. This means that these measurements are unlikely to provide direct information about how the charge and fields are distributed in the surface layer.

Shown in figure 2 are the range and mean penetration of normally incident electrons in Teflon. Assuming that the electrons are trapped upon deposition in the material (which is true for small enough charge densities), we can see that even for 20 keV (3.2×10^{-15} joules) electrons, the mean penetration of 2 microns (2×10^{-6} m) is significantly smaller than the thickness of most spacecraft dielectrics (25 - 125 μm). If significant rearrangement of the charge does not occur via very low energy transport processes, then we may expect that this simple circuit model of the charging should adequately represent the internal charging measurements. This is the approach which was previously pursued by Purvis, et al. (ref. 18).

Let us assume that the secondary and backscatter yields from the dielectric do not depend on the surface voltage or charging history of the sample, but are a function only of the incident electron energy spectrum. Then the spatial current $\bar{J}_o$ is a function only of the source energy spectrum and the sample voltage. From above, the dielectric current $\bar{J}_D$ equals GV_o, where, in general, the conductance G is a function of V_o. The solution in this case may be reduced to quadrature:

$$\frac{t}{C} = \int_o^{V_o} \frac{dV'}{(\bar{J}_o(V') - GV')} \tag{8}$$

The relation implied by equation (8) must be inverted to provide the voltage as a function of time. Because the integral is not normally expressible in terms of tabulated functions, the direct numerical solution of equation (4) as performed by Purvis, et al. (ref. 18) is usually preferable.

Several simply expressible cases are worth noting. They are not unrealistic and provide excellent checks on numerical solutions. Let the conductance be independent of field strength, and let $\bar{J}_o$ be constant ("feedback" case). In this case V_o is given by

$$V_o = \frac{\bar{J}_o}{G}\left(1 - \exp(-\frac{G}{C}t)\right) \tag{9}$$

Shown in figure 3 is the backscatter yield Y_{BS} from Teflon as computed by SCCPOEM. It is reasonable to choose this quantity to be constant over the range of interest (2 - 20 keV)($3.2 - 32 \times 10^{-15}$ J). Also shown in figure 3 are two representations of the secondary yield curve for normally incident electrons on Teflon as compiled by Wall, et al. (ref. 19), one using the Sternglass fit (ref. 20), and the other using a power law fit of Burke, et al. (ref. 21). An intermediate representation which varies inversely with electron energy is also sketched. If we use this very crude intermediate representation of the secondary yield for a constant conductivity dielectric, then the integral in equation (8) may easily be resolved for the "normal" case of monoenergetic electrons. Let the secondary yield Y_s have the form $Y_s = A/E_I$,

where E_I is the incident electron energy. The time history of the charging is described by the equation

$$2\frac{G}{C}t = \left(\frac{E_+ + E_-}{E_+ - E_-}\right) \ell n \left[\frac{(E + eV_o - E_-)(E - E_+)}{(E + eV_o - E_+)(E - E_-)}\right]$$

$$- \ell n \left[\frac{(E + eV_o - E_-)(E + eV_o - E_+)}{(E - E_+)(E - E_-)}\right] \qquad (10)$$

where

$$E_\pm = (2G)^{-1} \left\{GE - e(1 - Y_{BS})\, J_\infty \right.$$

$$\left. \pm \left[\left(GE - e(1 - Y_{BS})\, J_\infty\right)^2 + 4eGAJ_\infty\right]^{1/2} \right\} \qquad (11)$$

e is the electronic charge, E the source energy, and Y_{BS} the backscatter coefficient.

The potential to which the sample will charge is obtained by setting the charging current to zero, i.e.,

$$\overline{J}_o = GV \qquad (12)$$

which is a special case of the charging equation which has been traditionally used in the spacecraft charging community. The equation is, in general, a transcendental equation which may be solved by standard relaxation techniques. For the "feedback" current source the solution is simplest. Shown in figure 4 is the final voltage for the "normal" case of normally incident monoenergetic electrons on Teflon, assuming a constant bulk conductivity of 3.3×10^{-16} mho/m (S/M). Note that the solution depends only on the ratio $(\sigma/\delta J_\infty)$, so solutions for other values of σ may be obtained by scaling. The solution shown in figure 4 assumes the correct power law fit of figure 3 for the secondary yield. For small currents, the charging is stopped by leakage currents while for large source currents, the charging is stopped by secondary emission.

INTERNAL FIELDS — MONOENERGETIC NORMALLY INCIDENT SOURCES

We have seen above that for thick samples the external variables are effectively decoupled from the internal variables. It is our primary interest to understand the internal fields in the thin surface layer in which the charge deposition takes place. In this section we give expressions for these fields under various special circumstances for monoenergetic normally incident source electrons, the customary laboratory configuration. It will be assumed throughout that secondary emission occurs from a layer which is much thinner ($\sim 10^{-9}$ m) than the primary deposition layer (at least 10^{-7} m). The positive depletion region will appear as a surface charge.

Shown in figures 5 and 6 are the charge deposition and dose profiles calculated by SCCPOEM for normally incident monoenergetic electrons on Teflon. Note the significant spread in both of these quantities. We will assume throughout this section that these primary electrons are trapped in the spatial region where they thermalize and that all charge relaxation occurs via conduction mechanisms. Carrier dynamics will be discussed in future work.

NON-CHARGING BEAM

Assume that the primary beam energy is such that the secondary plus backscatter current equals the incident current ($E \sim 2.5$ keV) (4×10^{-16} J). Under these circumstances, the surface potential remains identically zero, while $J_o = \dot{J} = 0$. The current in the dielectric is given by $J_p(x) + \sigma(x)E$, where J_p is the current due to the incident electrons, and $\sigma(x)$ is the local conductivity (which we assume may depend on x, but not E). The internal electric field E is given by

$$E(x,t) = -\frac{J_p(x)}{\sigma(x)}\left(1 - \exp\left(-\frac{\sigma(x)}{\varepsilon}t\right)\right) \tag{13}$$

The primary current J_p is proportional to the incident current $J_p(x) = Y(x)J_I$, where Y(x) is the current profile. Suppose that $\sigma(x)$ is the ambient conductivity. Under these conditions, the asymptotic field will scale with J_I, indicating that breakdown would always occur if the beam current were large enough. In the regions of interest, however, dielectric conductivity is dominated by the radiation induced conductivity (driven by the primary electrons) in the primary deposition region. This conductivity has the empirical form (ref. 22):

$$\frac{\sigma}{\varepsilon} = K_p \dot{D}^{\Delta} \tag{14}$$

where K_p and Δ are empirically determined constants, and $\dot{D}$ is the dose rate in the medium. Experimentally, Δ is found to be in the range $1/2 \leq \Delta \leq 1$, with contemporary opinion favoring unity as the correct value. Since the dose rate

is proportional to the incident current, for any value of Δ less than unity, larger and larger fields may be driven in the dielectric by using larger and larger current densities. For Δ equal to unity, the asymptotic field is independent of J_I, and is given by

$$E = \frac{Y(x)}{\varepsilon K_p R(x)} \tag{15}$$

where R(x) is the dose profile in the medium.

The spatial dependences of the field and charge density are shown for Teflon in Figure 7 using a value of $K_p = 1.68 \times 10^{-5}$ $(Rads)^{-1}$ (1.68×10^{-3} $(Gy)^{-1}$) (ref. 23). The field scales inversely with K_p. The peak field appears at the front face of the dielectric. The potential drop ΔV across this charge separation region is obtained by integrating equation (15). It is related to the mean field $\bar{E}$ by $\bar{E} = (\Delta V)d$, where d is the thickness of the charge trapping region. Clearly, within this model, the value of the conductivity constant is critical in determining whether the fields become sufficiently high for breakdown to occur. Using the range of values quoted by Wall, et al. (ref. 19), we have computed the expected range of fields in this layer for Mylar, Kapton, and Teflon. These results are shown in Table 1.

With the possible exception of the maximum field for Kapton ($\sim 10^8$ V/m), these fields are nowhere near breakdown fields. One mil samples of the three materials have very similar breakdown strengths of about 3×10^8 V/m. Further, this strength increases with decreasing thickness. In particular, for the 1000 Å (10^{-7} m) charging depth of this problem, the maximum potential drop of only six volts would make it appear very unlikely that breakdown can occur for any of these materials under the given irradiation condition.

The time required to reach this saturation field depends on the incident current. For Teflon, with a 1 nA/cm^2 (10^{-5} A/m^2) beam, $K_p = 1.68 \times 10^{-5}$ $(Rads)^{-1}$ (1.68×10^{-3} $(Gy)^{-1}$) (ref. 23), the dielectric relaxation time $\tau = \varepsilon/\sigma$ has a value of 7.7 sec. This quantity scales inversely with beam current and dielectric conductivity coefficient. Thus, the smaller value of K_p quoted in the literature (ref. 19) (e.g., Mylar) could have relaxation times as long as 125 sec at a beam current of 1 nA/cm^2 (10^{-5} A/m^2). None of these times is especially long compared to laboratory irradiation times.

"FEEDBACK" CONTROLLED CHARGING BEAM

For this case, the incident beam energy and current are constant. A reasonable assumption is that the secondary and backscatter emission are also constant, so that J_o is likewise constant. (Note that this type of experiment would be ideal for checking this assumption.) The primary dose and charge deposition profiles will also be constant in time. These simplifications make the problem analytically tractable. If we assume that the conductivity is independent of electric field, then an exact solution may be given. The method of solution requires the application of LaPlace transforms, a method we have used elsewhere (ref. 24) for a similar problem. This solution is extremely

unwieldy and will not be detailed herein. Instead, we note that if $C_o = 0$, then further simplification occurs. Corrections to the solution for finite C_o are of order C_o/C_D, so that the approximate solution is an excellent representation of reality for most laboratory configurations. With these assumptions, we find the following expression for E:

$$E(x,t) = \frac{[\bar{J}_o - J_p(x)]}{\sigma(x)} [1 - \exp(-\frac{\sigma(x)}{\epsilon} t)] \tag{16}$$

Note that this solution does not depend on the thick sample assumption. If we consider the primary deposition region only ($J_p \neq 0$), then the solution is identical to that given previously, except that $(\bar{J}_o - J_p)$ is the current profile of interest. Note that the electric field profile now changes sign as was first pointed out by Meulenberg (ref. 12). For incident energies such that $|\bar{J}_o - J_p(0)| > |\bar{J}_o|$, the peak electric field can occur at the front face while for the reverse inequality, the peak field is always in the bulk. In the bulk, the electric field is given by J_o/σ_o, where σ_o is the bulk conductivity, so that E_{BULK} may be made arbitrarily large by increasing the incident current.

At the front face $J_p(0) = (1 - Y_{BS})J_I$ and $\bar{J}_o = (1 - Y_S - Y_{BS})J_I$, where Y_S, Y_{BS} are the secondary and backscatter yields, respectively. Thus, at saturation, the front face field E_{FF} is given by

$$E_{FF} = -\frac{Y_S J_I}{\sigma(0)} \tag{17}$$

For sufficiently large currents ($>10^{-8}$ A/m^2), the radiation-induced conductivity completely dominates the ambient conductivity, so that $\sigma(0)$ takes the radiation-induced value. With a conductivity of the form of equation (14), we again note that E_{FF} may take on arbitrarily large values for sufficiently large currents if $\Delta < 1$. For the case that Δ has the value unity, the value of the front face field is independent of the current. Moreover, if we use the fit of Burke, et al. (ref. 21) to the secondary emission yield shown in figure 3, we find that E_{FF} is also independent of the primary beam energy. This occurrence will be discussed in further detail below. The maximum value of the front face electric field for Teflon, Mylar, and Kapton may be obtained from the maximum values given in Table 1. These occur for the minimum value of K_p. A use of the Sternglass fit (ref. 20) to the secondary yield shown in Figure 3 would result in smaller fields.

GROUNDED FRONT FACE

Another case of interest occurs when the front face of the dielectric is coated with a thin layer (compared to an electron range) of conductor, and the conductor is grounded to the sample backside. This situation also effectively occurs when sunlight is present on the sample, so that a plethora of photoelectrons are available to keep the sample from charging. The general solution

for the time dependence of this problem has been given by us elsewhere (ref. 24). It involves LaPlace transforms and is rather complicated, so it will not be repeated here. The saturation field, however, has a simple form, given by

$$E = \frac{\bar{J} - J_p(x)}{\sigma(x)} \tag{18}$$

where

$$\bar{J} = \frac{\int_0^\delta dx \, \frac{J_p(x)}{\sigma(x)}}{\int_0^\delta dx \, \frac{1}{\sigma(x)}} \tag{19}$$

and $J_p(x)$ is the primary current profile in the medium. From equation (19), we can see that the short circuit current $\bar{J}$ is of order $\bar{J}_p(\bar{x}/\delta)$, where $\bar{x}$ is the mean penetration. Thus, for thick samples $\bar{J}$ is small compared to J_p. The largest front face field occurs for $\bar{J} = 0$ and has the value $-(J_p(0) \div \sigma(0))$. Specializing to the case where conductivity is proportional to dose rate (our above remarks hold for $\Delta < 1$), this field is again independent of current. Shown in figure 8 is the stopping power for electrons in Teflon as a function of energy. For normally incident electrons, the surface dose also has this shape, decreasing for increasing energy. Because the backscatter yield is essentially constant in this regime (figure 3), $J_p(0)$ is essentially constant. This means that the front face electric field is an increasing function of the primary beam energy. This is illustrated in figure 9 for Teflon, Mylar, and Kapton using the minimum values of K_p quoted in Table 1. A comparison of these values with those given above, and in sections below, shows that grounding the face has made the front face field larger. Of course, the bulk fields are severely reduced.

"NORMAL" CHARGING BEAM

The case considered in this section represents the conventional laboratory charging condition of a monoenergetic normally incident source for which the source energy is constant in time. As the sample charges, the incident electron energy decreases, and the dose and charge deposition profiles vary as illustrated in figures 5 and 6. This situation appears too complicated for analytical attack. We illustrate the numerical solution given by SCCPOEM for 5 mil (1.27×10^{-4} m) Teflon. The secondary yield algorithm used takes the yield proportional to the dose as suggested by Burke, et al. (ref. 21). For normally incident electrons, this reproduces the power law fit given in figure 3. The bulk conductivity was taken from the data of Adamo and Nanevicz (ref. 25). The transient conductivity was taken proportional to the dose rate, with a coefficient of $K_p = 1.68 \times 10^{-5}$ (Rads)$^{-1}$ (1.68×10^{-3} (Gy)$^{-1}$) (ref. 23).

With these inputs, it is found that the surface charges to the voltage given in figure 4. The time dependence of the voltage and current histories are qualitatively similar to the data presented by Purvis, et al. (ref. 18). Quantitatively, the calculations show a slower charging than the data, and the calculated saturation current is far less than measured. As noted by Purvis, et al. (ref. 18), these discrepancies are probably due to capacitive fringing effects and surface leakage current. Artificially decreasing the capacitance and increasing the bulk conductivity gives solutions which adequately represent the data.

Shown in figure 10 is the time dependence of the electric field profile for a 12 keV (1.92×10^{-15} J) 1 nA/cm^2 (10^{-5} A/m^2) charging beam. It should be noticed that the front face field is already at its saturation value at the first time plot (t = 50 sec). The bulk field evolves to its final value as V/δ, where V is given by the external charging variables. Shown in figure 11 is the saturation field in Teflon as a function of the primary beam energy. Note that the field near the front face is identical for all the charging energies, while the magnitude of the bulk field reflects the equilibrium voltage shown in figure 4.

It certainly makes sense that the fields near the front face are identical, because as external saturation is reached, the incident electrons take on very nearly the same energy. For later time, this corresponds to constant J_o, dose and charge deposition profiles. The solution is then easy to demonstrate explicitly by using the internal equilibrium condition $\bar{J} = J$ but will not be pursued further here. What may perhaps be more surprising to the reader is that the value of the front face field shown in these figures is, in fact, a much more general result. This will be shown below after discussing several further examples.

INTERNAL FIELDS — OTHER SOURCES

The charging conditions which can occur are more general than those discussed above. These include the complications due to angular dependence in the source spectrum, as well as energetically distributed sources. While our charging geometry is much less realistic for these more general source configurations, it is instructive to briefly indicate these effects.

MONOENERGETIC ISOTROPIC SOURCE

Shown in figure 12 are the voltage time histories of 5 mil (1.27×10^{-4} m) Teflon subjected to normally incident and isotropically incident 20 keV (3.2×10^{-15} J) electrons. The saturation electric fields are compared in figure 13. The isotropic source charges much more slowly and reaches a significantly smaller voltage. This result occurs because both the backscatter and secondary yields are significantly higher for the isotropic source. Internally, the fields close to the front face evolve slowly (following the voltage curve of figure 12). Note that the front face field for the isotropic source is identical to the front face field for normally incident sources.

ISOTROPIC MAXWELLIAN SOURCE

We have computed the electron transport for a 10 keV (1.6×10^{-15} J) isotropic Maxwellian distribution. The backscatter yield was determined to be 0.34, while the secondary yield was determined to be 1.55. Thus, it is expected that the Teflon will charge positively. The code is not equipped to handle this possibility. The plethora of secondaries mean that the sample will charge to a few volts positive in a very short time, the exact value of the voltage depending on the secondary electron distribution. The voltage will adjust to make the net current to the surface zero. So far as the internal fields are concerned, this is precisely the case described above as the "non-charging" beam (similarly, the grounded front face situation). Thus, the internal electric field is given by equation (13). Our numerical results indicate a broad positive charge layer ($\sim$1 μm) near the front surface and a deeply buried negative charge. We are still investigating the correctness of this pecularity.

GENERAL FRONT FACE FIELD

The appearance of a single value for the front face field under a number of circumstances suggests a universality of this value within our computational model. This is indeed the case. The following considerations hold for charging conditions which result in a negative voltage (not artificially grounded). The field at the surface satisfies...

$$\frac{\partial E}{\partial t}(o,t) = \frac{\bar{J} - J(o,t)}{\varepsilon} \tag{20}$$

For the case of vanishing tank capacitance ($C_o = 0$), $\bar{J} = \bar{J}_o$. The current in the dielectric consists of the primary current J_p and the conduction current σE. At the surface $\bar{J}_o - J_p(o) = -J_{BS}$, so that equation (20) becomes

$$\frac{dE}{dt}(o,t) + \frac{\sigma(o)}{\varepsilon} E(o,t) = -J_{BS}(t) \tag{21}$$

The primary assumption of the computational model is that the backscatter current is proportional to the surface dose rate ($-J_{BS} = \alpha\dot{D}$) and the conductivity is proportional to dose rate ($\sigma = \varepsilon K_p \dot{D}$). With these two assumptions, the surface field solution is

$$E(o,t) = \left(\frac{\alpha}{\varepsilon K_p}\right)\left(1 - \exp[-K_p D(t)]\right) \tag{22}$$

Thus, the field takes on a value determined only by the dose and saturates to a universal material dependent value ($\alpha/\varepsilon K_p$). This value is that given in Table 1 and is independent of the charging spectrum and time history.

FIELD DEPENDENT PRIMARY TRANSPORT

For completeness, we have performed the primary electron transport, including the effect of the internal electric fields on the electron motion. The effect was found to be completely negligible. A glance at figure 8 makes this easy to understand. The minimum value of the stopping power [for 20 keV (3.2×10^{-15} J) electrons] (in electric field units) is 2×10^9 V/m. Since the maximum fields encountered in these calculations are a few times 10^8 V/m, the fields have, at most, a 10% effect. For "normal" charging conditions, the effect is far less than this maximum, because of the sharp rise in stopping power for lower electron energies and the small value of the front face field.

CONCLUSIONS

We have presented a detailed model of the charging of dielectrics due to incident electrons. The computer model (SCCPOEM) as currently configured does not include the following effects:

- sunlight effects
- thermal effects
- ionic effects
- multi-dimensional effects
- field and charging history dependent secondary emission effects
- detailed carrier statistics effects, and
- very long time effects

The first four of these limit the applicability of the code to specialized charging situations but do not constitute limitations of principle.

The code presently chooses the secondary emission coefficient to be proportional to the computed surface dose as suggested by Burke, et al. (ref. 21). While this algorithm may fail at low energy [below a kilovolt (1.6×10^{-16} J)], it appears consistent with the experimental data above this energy. It is possible, however, that the secondary emission depends on the surface fields and charge profile which develops [see, e.g., Dekker (ref. 26)]. Some evidence is being accumulated by Robinson (ref. 27) that this effect occurs under the conditions of interest. Should the effect be demonstrated to be important, it can readily be incorporated into the code. This is true because the secondary emission primarily affects the external charging algorithm and enters the internal calculations as a boundary condition.

The major matters of principle not currently handled by the code are the details of the carrier statistics and migration. Empirical models are being utilized for both the bulk conductivity and the radiation induced conductivity. This shortcoming is currently being rectified. A version of the code which incorporates a carrier kinetics description of the conduction process is being developed. In defense of our present treatment, however, it must be mentioned

that a model utilizing direct empirical data has a major advantage over a more fundamental approach. Typically, the quantities which are required for a kinetic approach are very poorly known. The empirical conductivity data, while reflecting all these more fundamental quantities, has the advantage of being a direct measure of the relaxation phenomena. If used in the proper domain, the only uncertainties are the direct uncertainty in the conductivity measurement itself. The major uncertainty of principle is the domain of applicability. A good way to determine this domain is to use the model, make predictions, and compare to experiment. We have chosen this path. Indications are that the model is satisfactory for reasonably thick samples with fields not too near breakdown.

Dielectrics subject to electrical stresses undergo persistent change over very long periods of time (many years). This type of effect is completely beyond the scope of our present model.

Within the above constraints, the model provides a simple and effective tool for computing internal fields and charge densities in electron-irradiated dielectrics. Our computations to date indicate the following:

- At low charging currents, the final voltage is limited by bulk conduction, while at high currents, the voltage is limited by secondary emission.
- Normal charging gives rise to a field reversal layer as suggested by Meulenberg (ref. 12) but does not appear to give breakdown level fields at the surface.
- Charging with normally incident electrons under conditions in which the voltage is secondary limited gives rise to similar field profiles near the front face independent of charging energy.
- Secondary limited charging gives rise to a "universal" material dependent front face field.
- Grounded coatings on the front face decrease the bulk field but give rise to enhanced fields at the front face.
- Strong internal fields can arise even in low voltage positive charging environments.
- Angular distributions of monoenergetic electrons give less severe internal fields than normally incident electrons.

The key assumptions which give rise to the above conclusions are

- The independence of the secondary yield on charging conditions (dependence on only the incident electron spectrum).
- The proportionality of the secondary emission current to the dose rate.
- The use of the empirical conductivity model of equation (14) with $\Delta = 1$.
- The value of the empirical transient conductivity constant K_p.

We note some experiments which may be performed to test our conclusions and some of the assumptions:

- "Feedback" controlled experiments can be used to check the constancy of the secondary emission current.
- High current "non-charging" beams may be used to check the linearity of the transient conductivity with dose rate.
- Charge density interrogation experiments of the type suggested by Sessler, et al. (ref. 28) may be performed to directly compare to predicted charge densities.
- Grounded front face experiments may be performed to compare to short-circuit current predictions and check for breakdown.
- Very thin sample experiments can be performed with conventional measurements to check the influence of internal charge location on external variables.

We believe experiments of the above type, coupled with a detailed investigation of carrier kinetics restrictions, should lead to further understanding of the dielectric charging process.

We are indebted to Dr. J. V. Gore for numerous discussions, as well as certain of the calculations which appear herein.

REFERENCES

1. Chadsey, W. L.: POEM, AFCRL Technical Report, TR-75-0324, 1975.

2. Nanevicz, J. E.; Adamo, R. C.; and Scharfman, W. E.: SRI International, final report, Contract No. F04701-71-C-0130, P. O. 126192, Project 2611, 1974.

3. Stevens, N. J.; Lovell, R. R.; and Klinect: Preliminary Report on the CTS Transient Event Counter Performance through the 1976 Spring Eclipse Season, in "Proceedings of the Spacecraft Charging Technology Conference," C. P. Pike and R. R. Lovell, editors, Air Force Surveys in Geophysics, No. 364, AFGL-TR-77-0051, NASA TMX-73537, 24 February 1977, p. 81.

4. Stevens, N. J., Berkopec, F. D.; Staskus, J. V.; Blech, R. A.; and S. J. Narcisco: Testing of Typical Spacecraft Materials in a Simulated Substorm Environment, ibid., p. 431.

5. Bogus, K. P.: Investigation of a CTS Solar Cell Test Patch Under Simulated Geomagnetic Substorm Charging Conditions, ibid., p. 487.

6. Robinson, J. W.: Charge Distributions Near Metal-Dielectric Interfaces Before and After Dielectric Surface Flashover, ibid., p. 503.

7. Balmain, K. G.; Cuchanski, M.; and Kremer, P. C.: Surface Micro-discharges on Spacecraft Dielectrics, ibid., p. 519.

8. Hoffmaster, D. K.; Inouye, G. T.; and Sellen, J. M., Jr.: Surge Current and Electron Swarm Tunnel Tests of Thermal Blanket and Ground Strap Materials, ibid., p. 527.

9. Amore, L. J. and Eagles, A. E.: Materials and Techniques for Spacecraft Static Charge Control, ibid., p. 621.

10. Nanevicz, J. E. and Adamo, R. C.: Spacecraft Charging Studies of Voltage Breakdown Processes on Spacecraft Thermal Control Mirrors, in Spacecraft Charging by Magnetospheric Plasmas, Vol. 47, Progress in Astronautics and Aeronautics, A. Rosen, editor, 1976, p. 225.

11. Yadlowky, E. J.; Hazelton, R. C.; and Churchhill: Characterization of Electrical Discharges on Teflon Dielectrics Used as Spacecraft Thermal Control Surfaces, paper V-2, this proceedings.

12. Meulenberg, A., Jr.: Evidence for a New Discharge Mechanism for Dielectrics in a Plasma, ref. 10, idem, p. 237.

13. Katz, I.; Parks, D. E.; Mandell, M. J.; Harvey, J. M.; Brownell, D. H., Jr.; Wang, S. S.; and Rotenberg, M.: A Three Dimensional Dynamic Study of Electrostatic Charging in Materials, NASA CR-135256, NASA Lewis Research Center, Cleveland, Ohio, 1977.

14. O'Dwyer, J. J.: The Theory of Electrical Conduction and Breakdown in Solid Dielectrics, Clarendon Press, Oxford, 1973.

15. Moh, N. F. and Davis, E. A.: Electronic Processes in Non-Crystalline Materials, Clarendon Press, Oxford, 1971.

16. Lampert, M. A. and Mark, P.: Current Injection in Solids, Academic Press, New York, 1970.

17. Beers, B. L. and Pine, V. W.: Electron Transport Model of Dielectric Charging, Interim Report, SAI-102-78-002, for Communications Research Centre, Ottowa, Ontario, Canada, Science Applications, Inc., 8330 Old Courthouse Road, Vienna, Virginia, 1978.

18. Purvis, C. K.; Stevens, N. J.; and Oglebay, J. C.: Charging Characteristics of Materials: Comparison of Experimental Results with Simple Analytical Models, ref. 3, idem, p. 459.

19. Wall, J. A.; Burke, E. A.; and Frederickson, A. R.: Results of Literature Search on Dielectric Properties and Electron Interaction Phenomena Related to Spacecraft Charging, ref. 3, idem, p. 569.

20. Sternglass, E. J.: Phys. Rev. 80, 1950, p. 925.

21. Burke, E. A.; Wall, J. A.; and Frederickson, A. R.: Radiation-Induced Low Energy Electron Emission from Metals, IEEE Trans. Nuc. Sci., NS-19, 1972 p. 193.

22. Fowler, J. F.: Proc. Roy. Soc. London, Ser. A236, 1956, p. 464.

23. Weingart, R. C.; Barlett, R. H.; Lee, R. S.; and Hofer, W.: X-Ray Induced Photoconductivity in Dielectric Films, IEEE Trans. Nuc. Sci., NS-19, 1972, p. 15.

24. Beers, B.: Radiation-Induced Signals in Cables - II, IEEE Trans. Nuc. Sci., NS-24, 1977, p. 2429.

25. Adamo, R. C.; Nanevicz, J. E.; and Grier, N.: Conductivity Effects in High-Voltage Spacecraft Insulating Materials, ref. 3, idem, p. 669.

26. Dekker, A. J.: Secondary Electron Emission, Solid State Physics 6, 1958, p. 251.

27. Robinson, J. W.: Stable Dielectric Charge Distributions from Field Enhancement of Secondary Emission, paper V-8, this proceedings.

28. Sessler, G. M.; West, J. E.: Berkley, D. A.; and Morgenstern, G.: Determination of Spatial Distribution of Charges in Thin Dielectrics, Phys. Rev. Lett. 38, 1977, p. 368.

TABLE 1. RANGE OF VALUES OF PEAK ELECTRIC FIELD FOR NON-CHARGING BEAM

Range reflects spread in quoted values of the Transient Dielectric Conductivity Coefficient K_p (ref. 19).

MATERIAL	PEAK ELECTRIC FIELD ($\times 10^6$ V/m)	MEAN ELECTRIC FIELD ($\times 10^6$ V/m)	POTENTIAL DROP (volts)
TEFLON	0.11 - 5.5	0.06 - 2.9	0.007 - 0.372
MYLAR	52. - 61.	28. - 32.	3.5 - 4.1
KAPTON	1.8 - 92.	1.0 - 49.	0.1 - 6.2

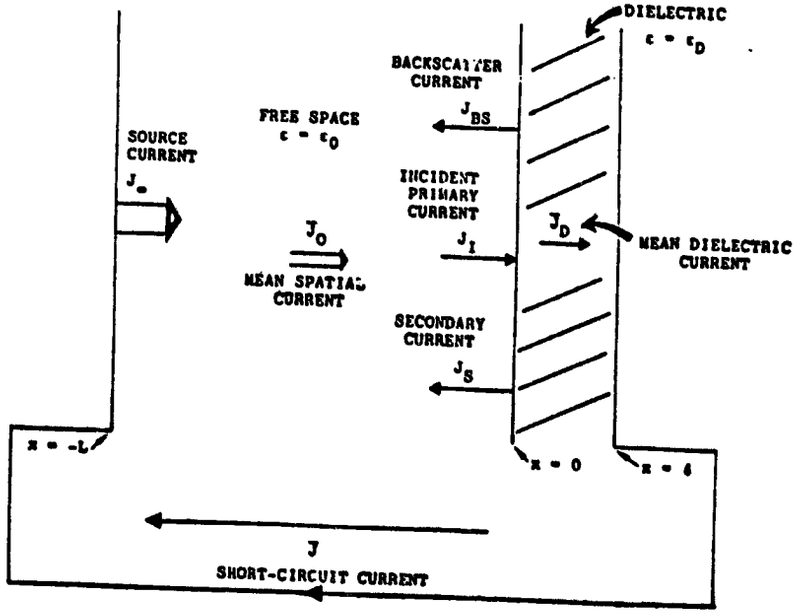

FIGURE 1. ONE-DIMENSIONAL CHARGING MODEL

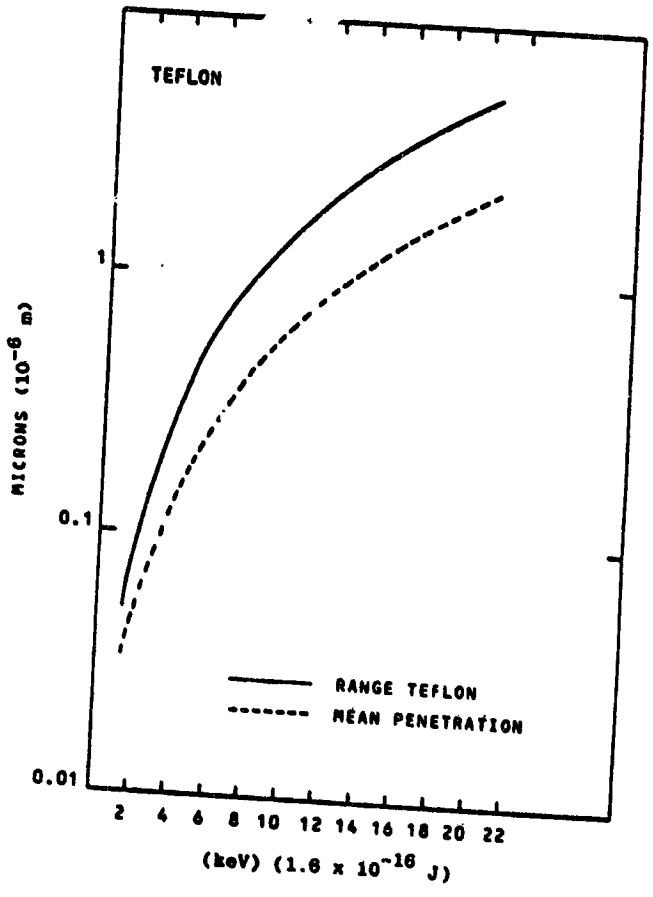

FIGURE 2. RANGE AND MEAN PENETRATION FOR NORMALLY INCIDENT ELECTRONS IN TEFLON

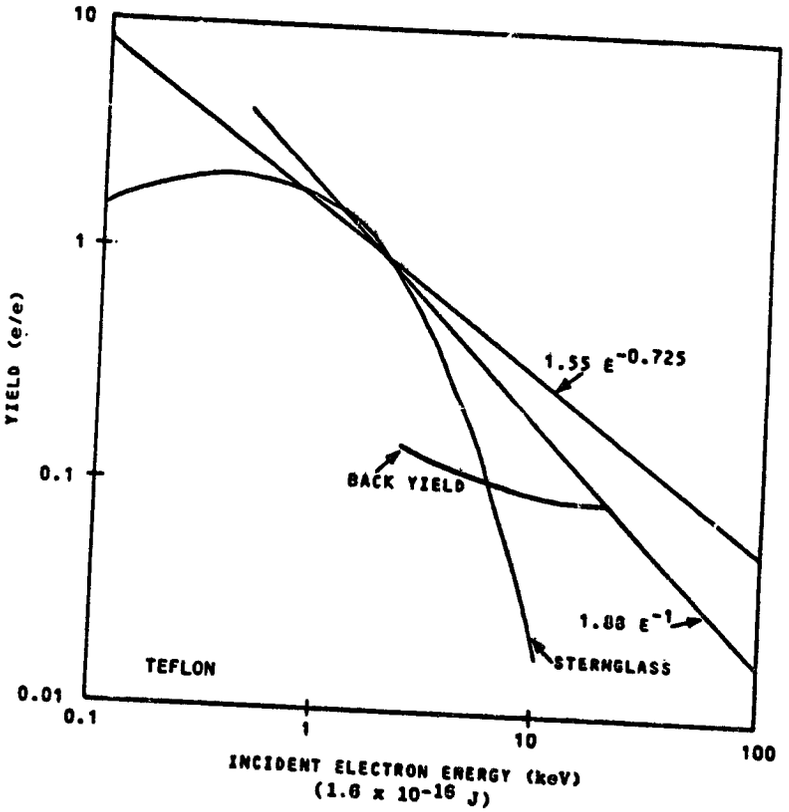

FIGURE 3. BACKSCATTER AND SECONDARY YIELDS FOR NORMALLY INCIDENT ELECTRONS ON TEFLON

SOURCES ARE CITED IN THE TEXT.

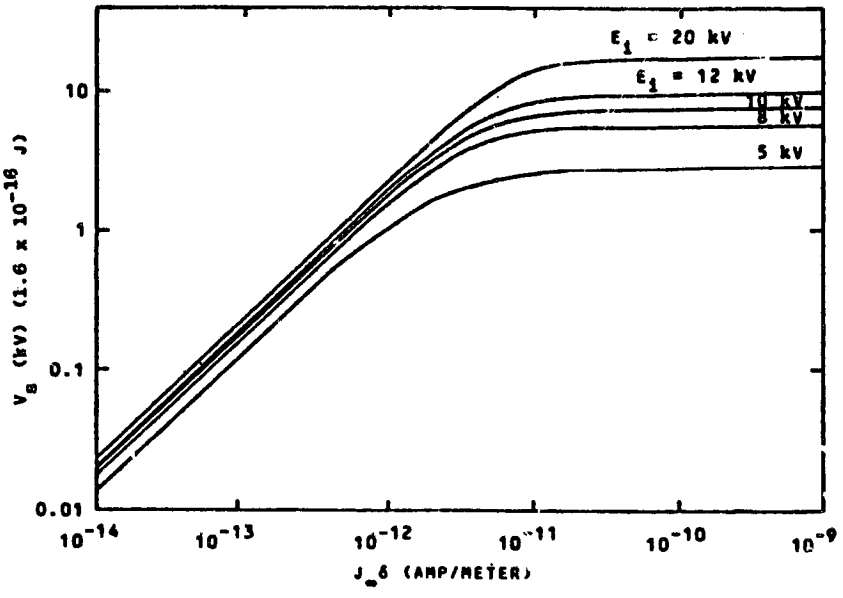

FIGURE 4. SATURATION CHARGING VOLTAGE FOR NORMALLY INCIDENT ELECTRONS ON TEFLON AS A FUNCTION OF THE CHARGING CURRENT DENSITY TIMES THE DIELECTRIC THICKNESS

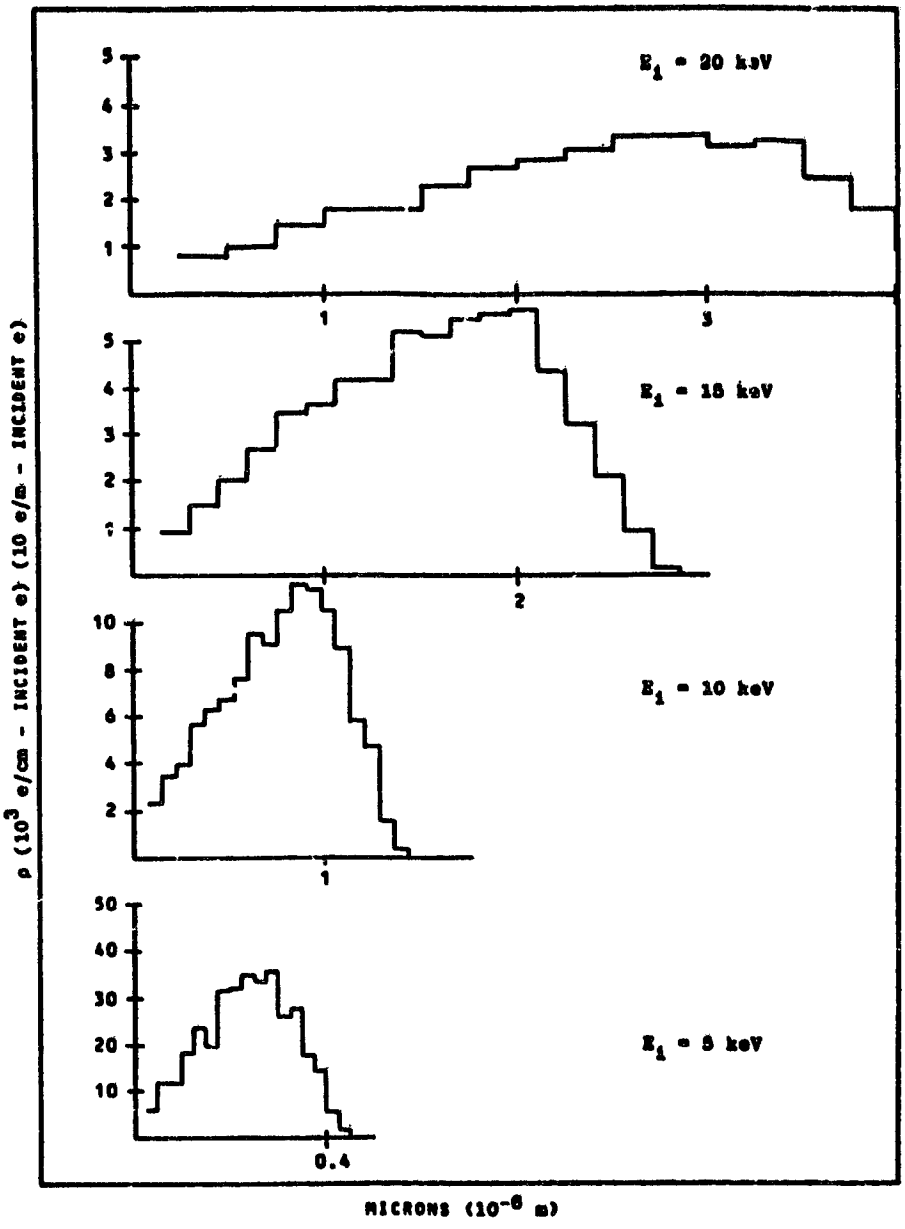

FIGURE 5. CHARGE DEPOSITION PROFILE IN TEFLON FOR NORMALLY INCIDENT ELECTRONS

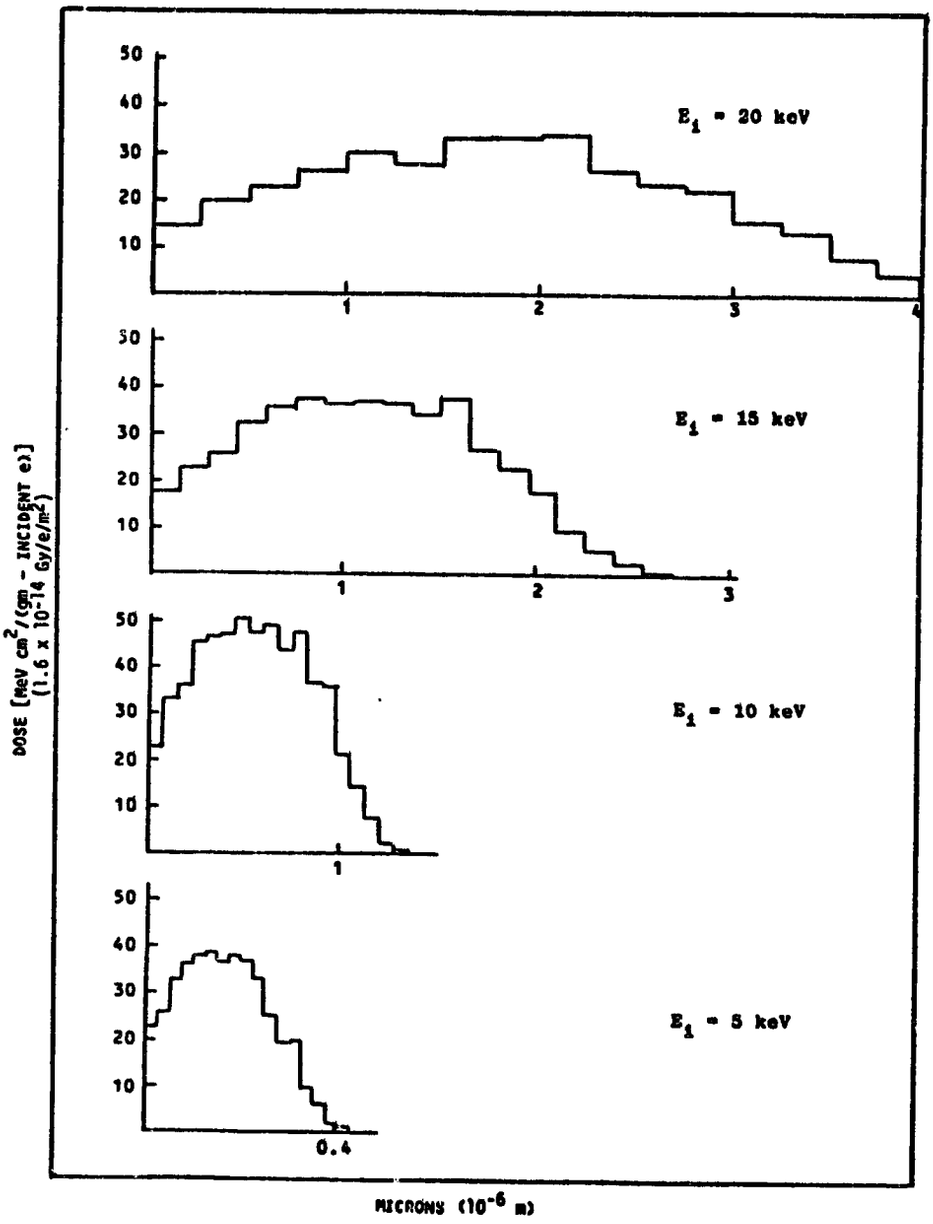

FIGURE 6. DOSE PROFILE IN TEFLON FOR NORMALLY INCIDENT ELECTRONS

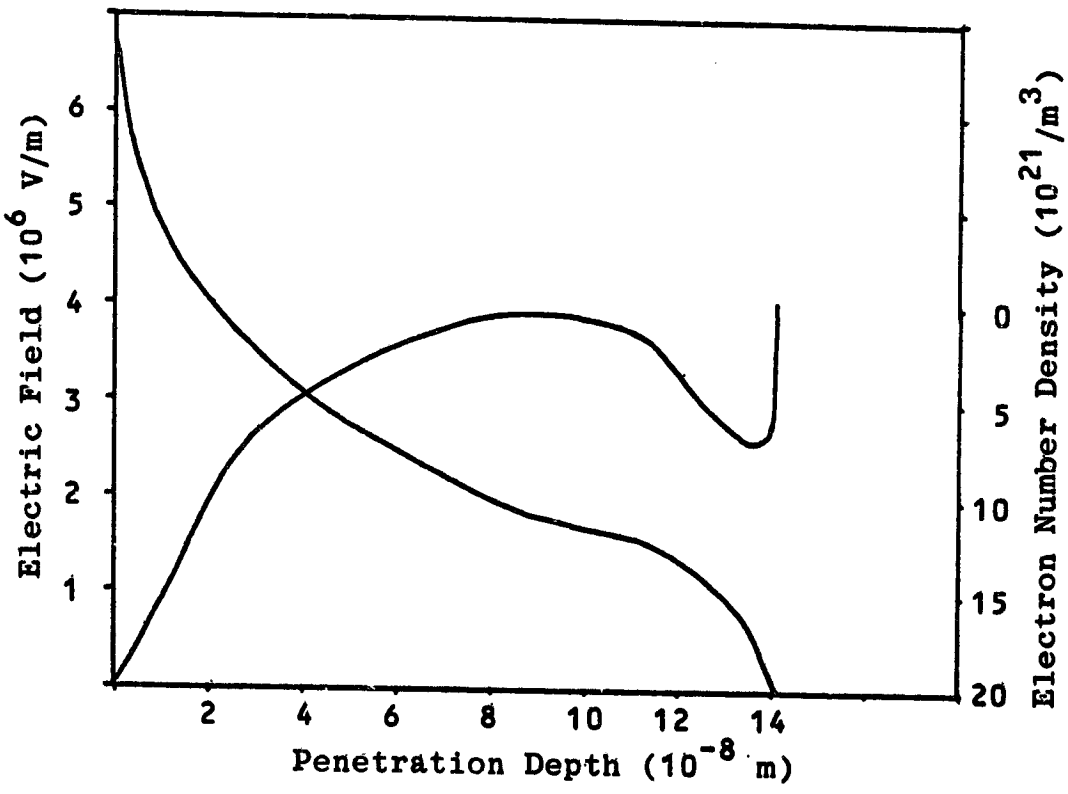

FIGURE 7. SATURATION ELECTRIC FIELD IN TEFLON FOR NON-CHARGING NORMALLY INCIDENT BEAM

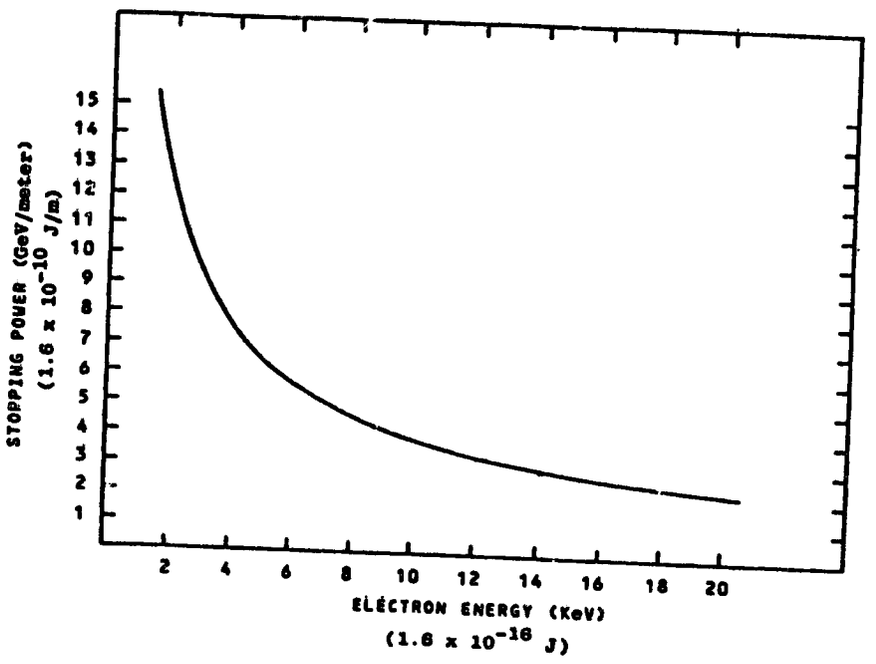

FIGURE 8. ELECTRONIC STOPPING POWER OF TEFLON

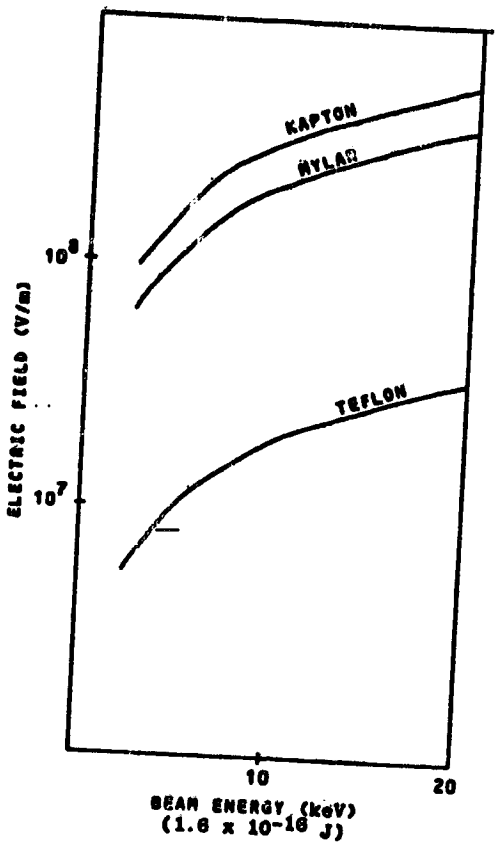

FIGURE 9. FRONT SURFACE SATURATION FIELD FOR GROUNDED FRONT-FACE - NORMALLY INCIDENT ELECTRONS - MINIMUM VALUE OF K_p

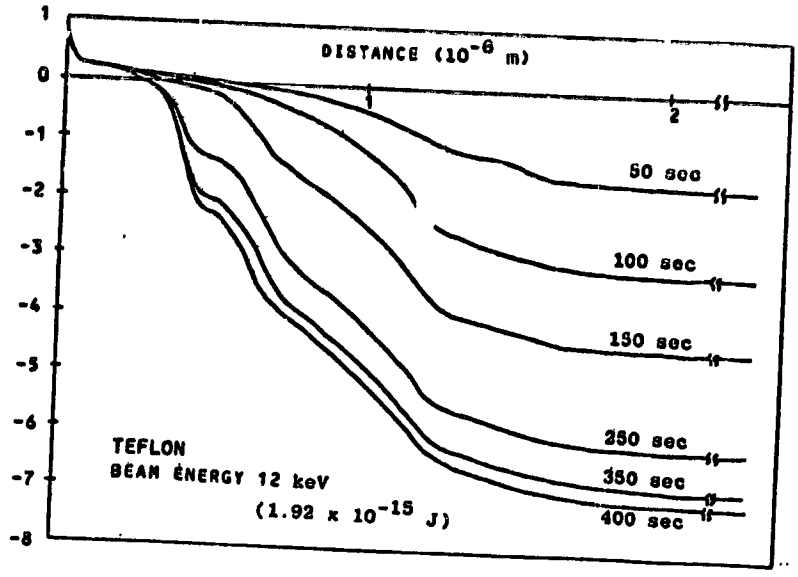

FIGURE 10. TIME HISTORY OF THE ELECTRIC FIELD PROFILE IN TEFLON - NORMALLY INCIDENT 12 keV ELECTRONS

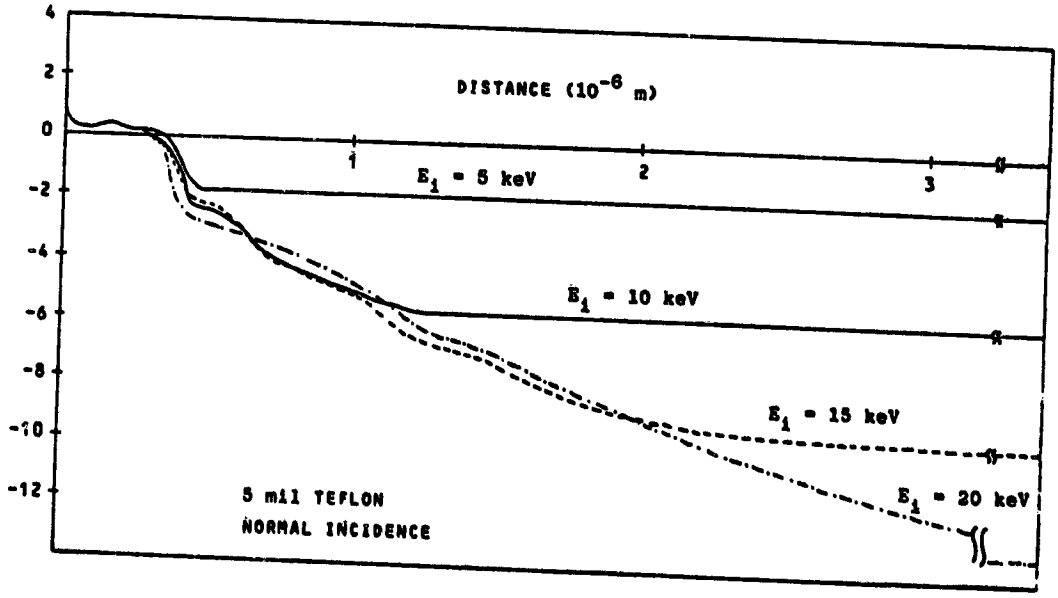

FIGURE 11. SATURATION ELECTRIC FIELD PROFILES IN 5 mil (1.27×10^{-4} m) TEFLON - NORMALLY INCIDENT ELECTRONS

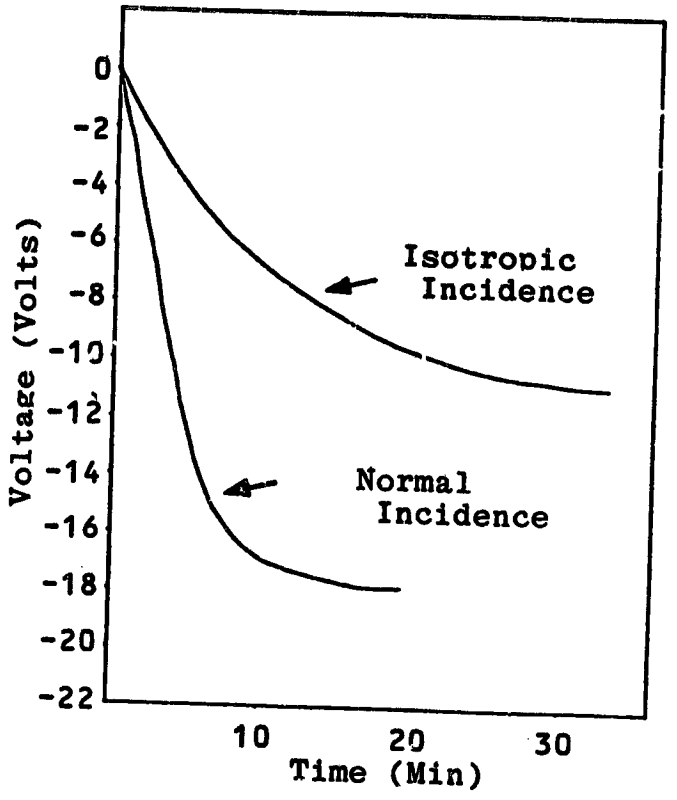

FIGURE 12. CHARGING VOLTAGE TIME HISTORIES FOR NORMALLY INCIDENT AND ISOTROPIC 20 keV ELECTRONS ON 5 mil TEFLON

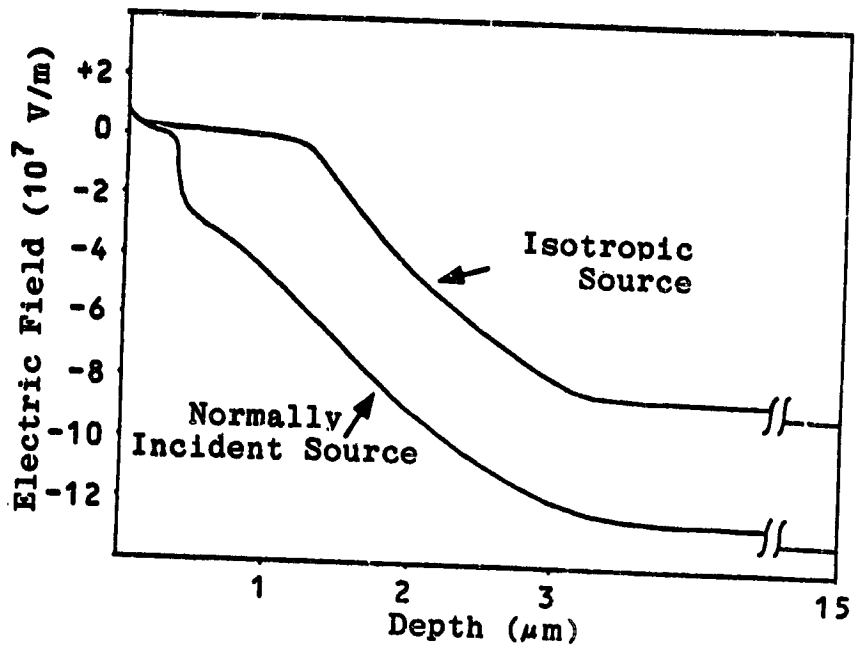

FIGURE 13. COMPARISON OF SATURATION ELECTRIC FIELD PROFILES FOR NORMALLY INCIDENT AND ISOTROPIC 20 keV CHARGING SOURCE — 5 mil TEFLON —

THE CALCULATION OF SPACECRAFT POTENTIAL - COMPARISON BETWEEN THEORY AND OBSERVATION

H. B. Garrett
Air Force Geophysics Laboratory

SUMMARY

A simple charge balance model based on the work of DeForest has been adapted for the calculation of spacecraft potentials. The model is calibrated with ATS-5 plasma data from the University of California plasma experiments. Once calibrated, the model is used to calculate the time-varying potential that is observed as a spacecraft passes in and out of eclipse. Errors on the order of ±800 volts are observed over a range of 0 to -10,000 volts. Possible applications of the model to large space structures are discussed. Of special interest is the unique use of eclipse observations to test the spacecraft charging model.

INTRODUCTION

The calculation of the potential on a satellite immersed in a plasma is, at best, a difficult problem. In particular, the accurate prediction of the potential on a spacecraft in the space environment requires the simultaneous calculation of the paths of all charged particles in the vicinity of the spacecraft. In principle this is possible, in practice it is not feasible and a variety of techniques have been developed to simplify the problem (see, for example, Whipple, 1965 (ref. 1); Rothwell et al., 1977 (ref. 2); Laframboise and Prokopenko, 1977 (ref. 3); Parker, 1977 (ref. 4) and references therein). Although capable of an accurate treatment both in time and space, these models are limited in usefulness as they require large amounts of computer time or do not include all of the various current sources necessary to simulate the charging phenomenon. This paper describes an approximate solution to the problem that yields spacecraft potentials by making assumptions which are equivalent to the "thick sheath" probe solution for a sphere. Though similar models have been developed by Rosen (1975) (ref. 5); Massaro et al. (1977) (ref. 6); Inouye (1976) (ref. 7), and Purvis et al. (1977) (ref. 8), none have included the actual measured spectra in their calculations. The model to be described in this paper uses actual ATS-5 data and is adapted from methods originally developed by Whipple (1965) (ref. 1) and DeForest (1972) (ref. 9). The model, limited somewhat in its range of applicability to potentials of -10,000 volts and plasma temperatures between 50 eV and 30 keV, results in significant savings in computer time over more complicated models.

In the first part of this paper the model will be formulated. The individual current sources are presented and approximations as a function of satellite potential developed. The model is calibrated using actual ATS-5 observations of the potential. Two examples will be discussed in which the model is used to study the effects of the time-varying geosynchronous environment and of a time-varying photoelectron flux on spacecraft potential. Applications of the model will be briefly discussed.

MODEL FORMULATION

In solving the spacecraft charging problem, we are concerned with finding the spacecraft potential $\emptyset$ such that

$$J_e - (J_I + J_{se} + J_{sI} + J_{BSe} + J_{ph}) = 0 \qquad (1)$$

where J_e = Incident electron current

J_I = Incident ion current

J_{se} = Secondary emitted electron current due to J_e

J_{sI} = Secondary emitted electron current due to J_I

J_{BSe} = Back scattered electron current due to J_e

J_{ph} = Photoelectron emission

Given the incident ion and electron particle spectra, the currents J_e, J_I, J_{se}, J_{sI}, and J_{BSe} are found and adjusted by varying the potential on the spacecraft until equation (1) holds. This is the basic problem and in subsequent sections we will outline methods of calculating the currents as a function of potential.

ELECTRON AND ION INCIDENT CURRENT

The ATS-5 satellite employs electrostatic analyzers and, instead of the distribution function f (V) as a function of velocity V which is normally used in current calculations, these detectors return the differential energy flux, $\frac{d\,(EF)}{dE}$. Thus, it is convenient to express the integrals necessary to obtain the various currents in terms of the energy E and $\frac{d(EF)}{dE}$ rather than f(V) and V.

The conversion from f to $\frac{d(EF)}{dE}$ is given by

$$f = \frac{d\,(EF)}{dE} \quad \frac{\frac{1}{2}\,m^2}{E2} \tag{2}$$

where the conversion factors (K_e and K_I) are, if f is given in sec^3/km^6, $\frac{d(EF)}{dE}$ in $ergs/cm^2$ sec ster eV, and E in eV:

$$K_e = .1617 \text{ for electrons} \tag{3}$$

$$K_I = 5.45 \times 10^5 \text{ for ions} \tag{4}$$

As $\langle NF \rangle = \int_0^\infty V^3 f(V)\, dV$

This gives

$$\langle NF_e \rangle = K_e \int_0^\infty \frac{d(EF)}{dE}\Big|_e \frac{dE}{E} \tag{5}$$

$$\langle NF_I \rangle = K_I \int_0^\infty \frac{d(EF)}{dE}\Big|_I \frac{dE}{E}$$

where the results are left in terms of the number flux rather than actual current density J ($J = \pi q \langle NF \rangle$, where q is the charge on a particle). The values of $\frac{d(EF)}{dE}$ must be shifted by an energy equal to the desired potential before the integration (see Garrett, 1978 (ref. 10) for details). In the actual case an interpolation is necessary as the desired value of $\frac{d(EF)}{dE}$ for the shifted spectrum usually does not correspond to an observed value of $\frac{d(EF)}{dE}$. Further, as the ATS-5 data correspond to discrete energy bands for the range 51 eV to 51 keV, the integrals become sums (dE becomes ΔE) over this range. Results indicate that these approximations are adequate for a range of 50 eV to 30 keV in temperature and 0 V to -10,000 V in potential.

SECONDARY EMISSION CURRENTS

Electrons and ions striking the satellite surface are either scattered off the surface or cause the emission of low energy, secondary electrons.

Secondary emission is usually given in terms of the incident differential current density, $\frac{dJ_i}{dE}$. $\frac{dJ_i}{dE}$ is related to $\frac{d(EF)}{dE}$ by

$$\frac{dJ_i}{dE} = \frac{q\pi}{E} \frac{d(EF)}{dE} \tag{6}$$

(the $q\pi$ factor will be dropped in future discussions).

For secondary emission, the amount of secondary current emitted for a given incident flux is expressed as a ratio $\delta(E)$:

$$\delta(E) = \frac{dJ_s(E)}{dJ_i(E)} \tag{7}$$

where $\delta(E)$ = the secondary electron yield function

$\frac{dJ_s}{dE}$ = differential secondary current density

$\frac{dJ_i}{dE}$ = differential incident current density

From equations 6 and 7

$$\frac{d J_s(E)}{dE} = \delta(E) \frac{dJ_i}{dE}(E) = \frac{\delta(E)}{E} \frac{d(EF)}{dE} \tag{8}$$

The normalized differential current spectrum, $g(E')$, of the secondary electrons is approximately independent of the incident particle energy and, for aluminum, given in figure 1. Multiplying $g(E')$ by the secondary current density $J_s(E)$ gives the differential current density of secondary electrons due to particles of energy E as

$$\frac{dJ(E', E)}{dE'} = g(E') J_s(E) \tag{9}$$

This implies that the total current density is given by

$$J_{TS} = \int_0^\infty dE' \int_0^\infty dE \frac{d^2 J(E', E)}{dE' dE}$$

$$= \int_0^\infty g(E')\, dE' \int_0^\infty \delta(E) \left[\frac{d(EF)}{dE}\right] \frac{dE}{E} \qquad (10)$$

$g(E')$ peaks sharply at ~ 2 eV and thus for ions and electrons is ~ 0 if the potential is greater than +2 volts (all the secondary electrons are attracted). Thus, to the order of accuracy of these calculations $g(E')\, dE'$ will be assumed = 0 for $\phi > 0$ and = 1 for $\phi \leq 0$. $\delta(E)$ is approximated for electrons impacting on aluminum by the curve shown in figure 2 (Whipple, 1965 (ref. 1)). $\delta(E)$ is not well known for ions impacting on aluminum but a fit to data as presented by Whipple (1965) (ref. 1)) for H^+ over the energy range of interest is presented in figure 3.

$\delta(E)$ for the incident ions and electrons is substituted into equation (10) and integrated using the appropriate shifted values for $\frac{d(EF)}{dE}$ to obtain the secondary emission currents due to the electrons and ions. Typically, the secondary emission due to electrons results in a current of approximately 25-50% that of the incident electron current while the secondary emission due to ions results in an electron current approximately 2-3 times that of the incident ions. As will be discussed shortly, it was necessary to adjust these values to obtain accurate estimates of the potential.

BACKSCATTERED ELECTRON CURRENT

Some incident electrons are reflected and give rise to the backscattered electron current (the backscattered current due to ions is very small and ignored). Although simple theories of collisional scattering such as those of Everhart (1960) (ref. 12) are useful in predicting the net current, experimental curves for backscattered emission from aluminum are also available. DeForest (1972) (ref. 9) has adapted the experimental results of Sternglass (1954) (ref. 12) to the ATS-5 data. His development, which will be presented here, is similar to that given for secondary electrons.

The basic equation for backscattering is

$$J_{BSe} = \int_0^\infty dE' \int_{E'}^\infty B(E', E) \frac{dJ_i(E)}{dE} dE \qquad (11)$$

where E' = energy of backscattered particles ($E' \leq E$)

E = energy of incident particles

$B(E',E)$ = percentage of electrons scattered at a given energy E' as a result of an incident electron at energy E

$J_i(E)$ = incident current (electrons in this case)

From Sternglass (1954) (ref. 12)

$$B(E',E) = \frac{G(E'/E)}{E} \tag{12}$$

G is given as a function of $K = E'/E$ (DeForest, private communication) in figure 4 for aluminum.

Continuing, equation 11 becomes

$$J_{BSe} = \int_0^{\infty} \frac{dE'}{E'} \int_{E'}^{\infty} \left[\frac{E'}{E} G\left(\frac{E'}{E}\right)\right] \left|\frac{d(EF)}{dE}\right|_e \frac{dE}{E} \tag{13}$$

Substituting the proper values of $\left|\frac{d(EF)}{dE}\right|_e$ in equation (13) and performing the integration gives the total current due to backscattered electrons. For aluminum, a ratio of ~25% for the backscattered current to incident current is obtained in agreement with other estimates. Unlike the secondary electron current, though, the backscattered current is a gradual function of positive spacecraft potential. For positive potentials, the 0 integral limit in equation (13) is replaced by $|q\phi|$, the energy shift due to the spacecraft potential.

PHOTOELECTRON EMISSION

Light, particularly in the ultraviolet, falling on the spacecraft causes the emission of photoelectrons. Although the characteristics of the emitted particles and the processes involved are well known, the actual photoelectron emission from a spacecraft is poorly known. The reason is the variety of materials on the typical spacecraft surface and the lack of precise knowledge of the solar spectrum and its interaction with various materials. Grard et al. (1973) (ref. 13) and Whipple (1965) (ref. 1) have combined the solar spectrum with the emission characteristics of various substances to give the photo-

electron current as a function of energy. DeForest (private communication) has developed an algorithm that approximates their results. It gives the photoelectron current as a function of positive spacecraft potential (for negative potential all of the photoelectron current leaves the spacecraft). It is

$$J_{ph} = \frac{J_{po}}{(\phi/.7+1)^2} \tag{14}$$

Values for J_{po} are given in Table 1. From this table it is clear that estimates of J_{po} range over an order of magnitude. Fortunately, most examples of charging that we will be concerned with involve shadowed surfaces, in which case $J_{po} = 0$. The charging model will, however, in conjunction with actual data, be used in a later section to estimate the value of J_{po} appropriate to ATS-5.

COMPARISON WITH DATA

The ultimate check of any model is how well the predicted results compare with actual measurements. The basic set of data will be spectra from ATS-5 for periods immediately before and after entry into the earth's shadow. These periods were selected as they can be used not only to study large potential variations (on the order of ~6 keV) but also to calibrate the photoelectron flux. Table 2 lists the eclipses studied and the potentials observed during the eclipses.

ATS-5 does not consist of a single material nor can it be said to be spherical in shape (a tacit assumption in the preceding analysis). However, keeping to the spirit of a "simple" charging model, the satellite was approximated as an aluminum sphere. Figure 5 shows the results of these calculations. The discrepancies between observed and predicted potentials have been corrected by adjusting the magnitudes of the secondary emission terms by multiplying each one by a constant correction factor to give a best fit in a least squares sense (the backscattered flux is directly proportional to the incident electron flux so that determining its coefficient is somewhat difficult as it may reflect slight errors in the actual measurement of J_e). For correction factors of 1.3 (J_{se}), .55 (J_{sI}), and .4 (J_{BSe}), the results have a standard deviation of +800 volts. It should be kept in mind, though, that the model is based on several assumptions and, considering these, this agreement is quite good.

MODEL APPLICATION

The model has been developed for two purposes. First, combined with the geosynchronous plasma model developed by Garrett (1977) (ref. 14), it can be used to predict potentials on spacecraft as a function of the geomagnetic index

A_p and LT, the satellite local time. It also is employed to calculate the potential on a spacecraft as it passes into and out of the earth's shadow.

Figure 6 plots the potential variations predicted by the model for the geosynchronous simulation model of Garrett (ref. 14) (1977) for moderate geomagnetic activity (A_p = 15) and high geomagnetic activity (A_p = 207). That simulation gives a "2 Maxwellian fit" to the plasma such that the distribution functions are for electrons.

$$f_e(E) = 27.2\left[N_e\left(\frac{T1_e}{1000}\right)^{-3/2} e^{-E/T1_e} + N2_e\left(\frac{T2_e}{1000}\right)^{-3/2} e^{-E/T2_e}\right] \quad (15)$$

and for ions

$$f_I(E) = 2.14\times10^6\left[N1_I\left(\frac{T1_I}{1000}\right)^{-3/2} e^{-E/T1_I} + N^2{}_I\left(\frac{T2_I}{1000}\right)^{-3/2} e^{-E/T2_I}\right] \quad (16)$$

where $N1_e$, $N2_e$ = electron number densities (n/cm^3)

$T1_e$, $T2_e$ = electron temperatures (eV)

$N1_I$, $N2_I$ = ion number densities (n/cm^3)

$T1_I$, $T2_I$ = ion temperatures (eV)

The distribution functions are converted to differential energy spectra using equation (2). The spectra are inserted into the program and, assuming no photoelectron current, the potential calculated. These potentials are the maximum that would be expected for a shadowed, electrically isolated surface as a result of the ambient environment.

Another use of the model is in the determination of the potential as a spacecraft passes into the earth's shadow. The eclipse data described earlier are used in conjunction with the model to determine the current necessary to give the observed potential variations as ATS-5 passed into and out of the

earth's shadow. Presumably, this residual current is the photoelectron current. By varying the amplitude of an appropriate model of atmospheric attenuation to fit this residual (or photoelectron) current, J_{po} was found. The results for ATS-5 for 2 atmospheric models are illustrated in figure 7. The resulting J_{po} value was determined to be .4 n Amps/cm^2 for the best atmospheric model which is in agreement with the lower values in Table 2. The reader is referred to Garrett (1978) (ref. 15) for details of this procedure.

Figure 8 shows the observed and predicted potentials as ATS-5 passes into and out of eclipse on days 260 and 292, 1970. In figure 9 are similar results for ATS-6 on days 59 and 66, 1976. The results of the predictions are adequate and within the $\pm$800 V error but their deviations from the observed values at low potential may indicate either a need to include sheath effects or that the thick sheath, spherical probe approximation is inaccurate for low ($\lesssim$ 100 V) potentials. In any event, this method of testing, by comparing the observed and predicted potentials as the photoelectron flux is varied, should prove to be a powerful tool for comparison with other spacecraft charging models in the future.

Given that the model is valid, it can be employed in a variety of simu-
identical with an electron beam, the model can test the effects of charged beams on satellites. Likewise, the data employed in calibrating the model can be used to test other models of beam phenomena. Although the scaling of our results to large structures may be somewhat dubious quantitatively, it is clear that the model can also estimate possible effects on large structures. For example, if we approximate a large structure by nodes which must meet equation (1), then the model can be used to predict the potential at each point on the surface of a large structure as it enters eclipse. When this is done, it turns out that rather large time varying potential gradients due solely to different photoelectron emission rates on a structure can be generated - a clear threat to future missions.

CONCLUSION

A simple model based on the work of Whipple (1965) (ref. 1) and DeForest (1972) (ref. 9) has been developed. The model was calibrated with ATS-5 plasma data. The model predictions for the potential on a satellite as it passed into eclipse were compared with actual observations. The results indicate agreement between the predicted and observed values. The model is used in conjunction with a model simulation of the geosynchronous environment to predict spacecraft potentials under different geomagnetic and local time conditions. The model, after being calibrated, successfully predicts potentials with $\pm$800 V accuracy over a range of 10,000 V. It includes relevant current terms and is efficient in comparison with other complex models taking $\sim$2 sec per potential calculation. FORTRAN programs are available from AFGL.

REFERENCES

1. Whipple, E. C. (1965): The Equilibrium Electric Potential of a Body in the Upper Atmosphere, NASA X-615-65-296.

2. Rothwell, P. L., Rubin, A. G., and Yates, G. K. (1977): A Simulation Model of Time-Dependent Plasma-Spacecraft Interactions, Proc. of the Spacecraft Charging Conference, AFGL-TR-77-0051/NASA TMX-73537.

3. Laframboise, J. G., and Prokopenko, S.M.L. (1977): Numerical Simulation of Spacecraft Charging Phenomena, Proc. of the Spacecraft Charging Conference, AFGL-TR-77-0051/NASA TMX-73537.

4. Parker, L. W. (1977): Calculation of a Sheath and Wake Structure About a Pill Box-Shaped Spacecraft in a Flowing Plasma, Proc. of the Spacecraft Charging Conference, AFGL-TR-77-0051/NASA TMX-73537.

5. Rosen, A. (1975): Spacecraft Charging: Environment Induced Anomalies, Paper 75-91, AIAA 13th Aerospace Sciences Meeting, 1975.

6. Massaro, M. J., Green, T., and Ling, D. (1977): A Charging Model for Three-Axis Stabilized Spacecraft, Proc. of the Spacecraft Charging Conference, AFGL-TR-77-0051/NASA TMX-73537.

7. Inouye, G. T. (1976): Spacecraft Potentials in a Substorm Environment, Spacecraft Charging by Magnetospheric Plasma, AIAA Progress in Astronautics and Aeronautics Series, Vol 42, Rosen (Editor).

8. Purvis, C. K., Stevens, N. J., and Oglebay, J. C. (1977): Charging Characteristics of Materials: Comparison of Experimental Results with Simple Analytical Models, Proc. of the Spacecraft Charging Conference, AFGL-TR-77-0051/NASA TMX-73537.

9. DeForest, S. E. (1972): Spacecraft Charging at Synchronous Orbit, J. Geophys. Res., 77: (No. 4): 651.

10. Garrett, H. B. (1978): Spacecraft Potential Calculations - A Model, AFGL-TR-78-0116.

11. Everhart, T. E. (1960): Simple Theory Concerning the Reflection of Electrons from Solids, Journal of Appl. Phys., 31: (No. 8): 1483.

12. Sternglass, E. J. (1954): Backscattering of Kilovolt Electrons from Solids, Phys. Rev., 95: 345.

13. Grard, R.J.L., Knott, K. and Pedersen, A. (1973): The Influence of Photoelectron and Secondary Electron Emission on Electric Field Measurements in the Magnetosphere and Solar Wind, Photon and Particle Interactions with Surfaces in Space, R.J.C. Grard (Ed.) D. Reidel Publishing Co., Dordrecht, Holland, pp. 163-189.

14. Garrett, H.B. (1977): Modeling of the Geosynchronous Orbit Plasma Environment, Part I, AFGL-TR-77-0288.

15. Garrett, H.B. (1978): Effects of a Time-Varying Photoelectron Flux on Spacecraft Potential, AFGL-TR-78-0119.

TABLE 1

Author	Saturation Current (n Amps/cm^2)	
Grard et al. (1973)[13]	4.20	(Aluminum oxide)
	3.00	(Indium oxide)
	.40	(Graphite)
DeForest (1972)[9]	.82	(ATS-5)
Whipple (1965)[1]	3.00	(Rocket-aluminum)

TABLE 2

Date	UT	Potential
1969 22 Sep	0629	-3400
	0731	-3810
16 Oct	0627	-5360
	0711	-3810
1970 12 Sep	0631	-2420
	0718	-1730
15 Sep	0626	-877
	0721	-1540
17 Sep	0623	-5380
	0723	-3040
19 Sep	0620	-2720
	0724	-1940
26 Sep	0724	-2170
17 Oct	0630	-1230
	0659	-2170
18 Oct	0633	-397
	0650	-316
19 Oct	0640	-396
	0648	-558

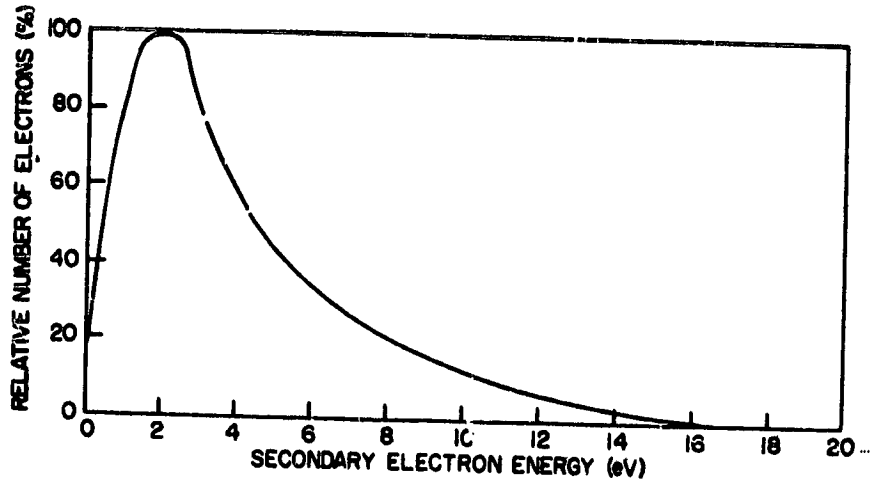

Figure 1. - Relative number of emitted secondary electrons as function of energy. (From Whipple (1965), ref. 1.)

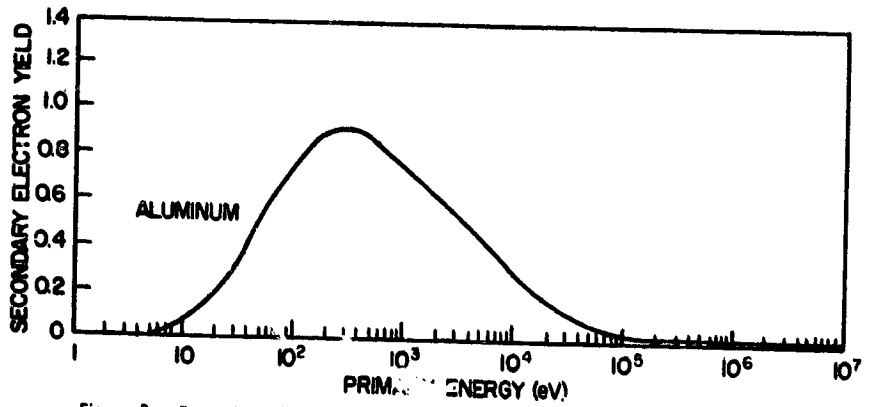

Figure 2. - Secondary electron yield for electron impact on aluminum as function of energy. (From Whipple (1965), ref. 1.)

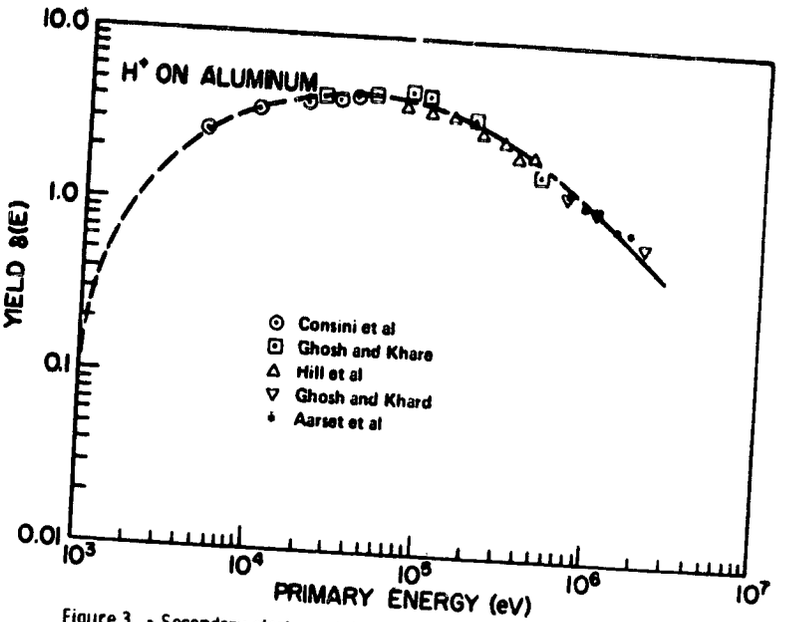

Figure 3. - Secondary electron yield for ion (H^+) impact on aluminum as function of energy. (From Whipple (1965), ref. 1.)

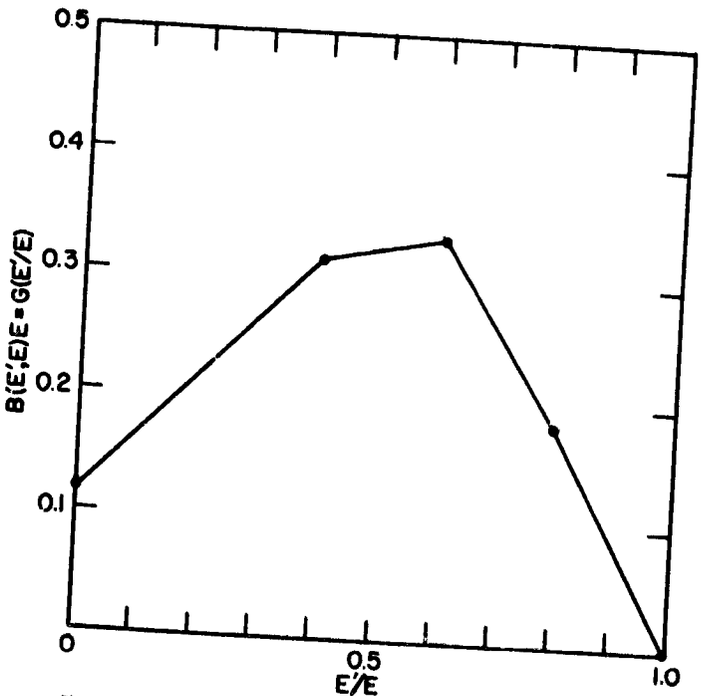

Figure 4. - B(E', E) · E as function of (E'/E) where B(E', E) is approximately the percentage of electrons scattered at a given energy E' as a result of a particle at an incident energy E. (From Sternglass (1954), ref. 12.)

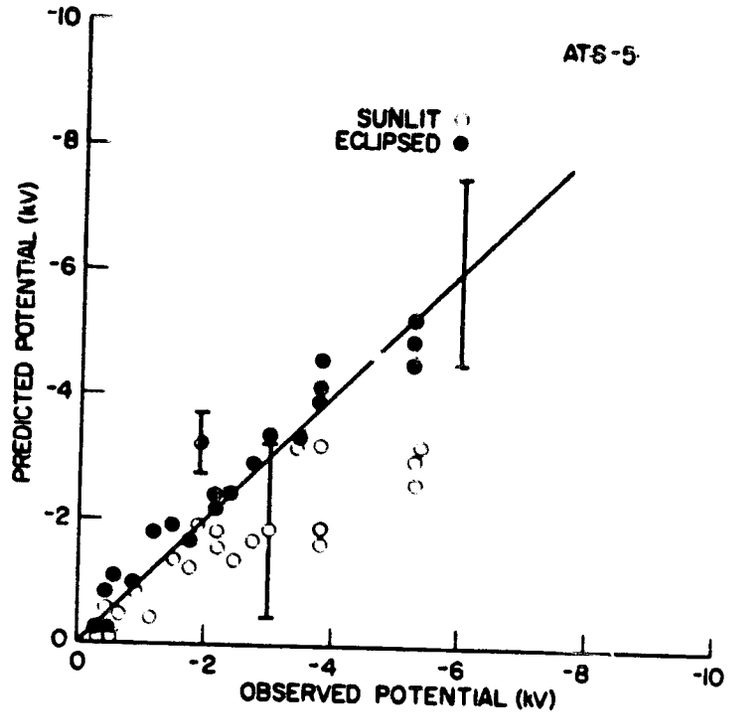

Figure 5. - Predicted potential as function of observed potential. (Results are for spectra when satellite was illuminated (sunlit) and when it was shadowed (eclipsed).)

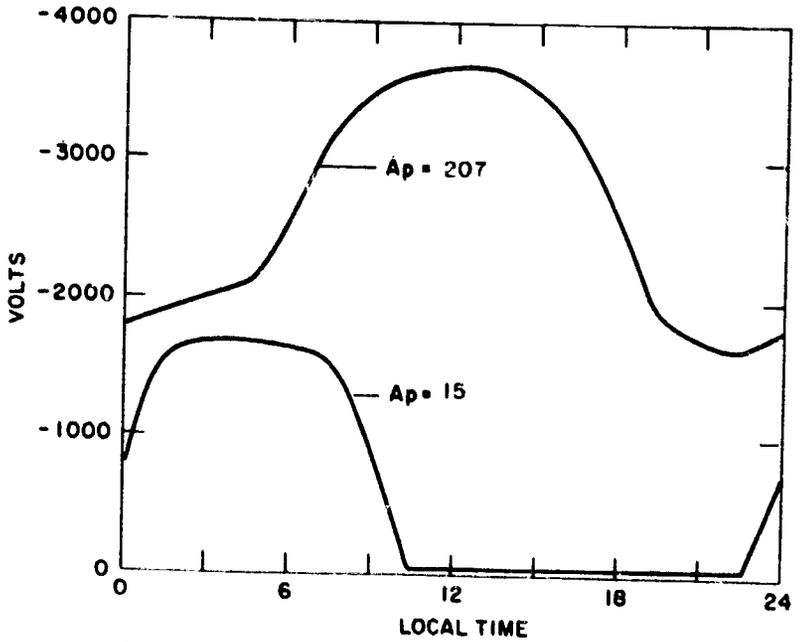

Figure 6. - Predicted potential of a shadowed, electrically isolated surface as function of time.

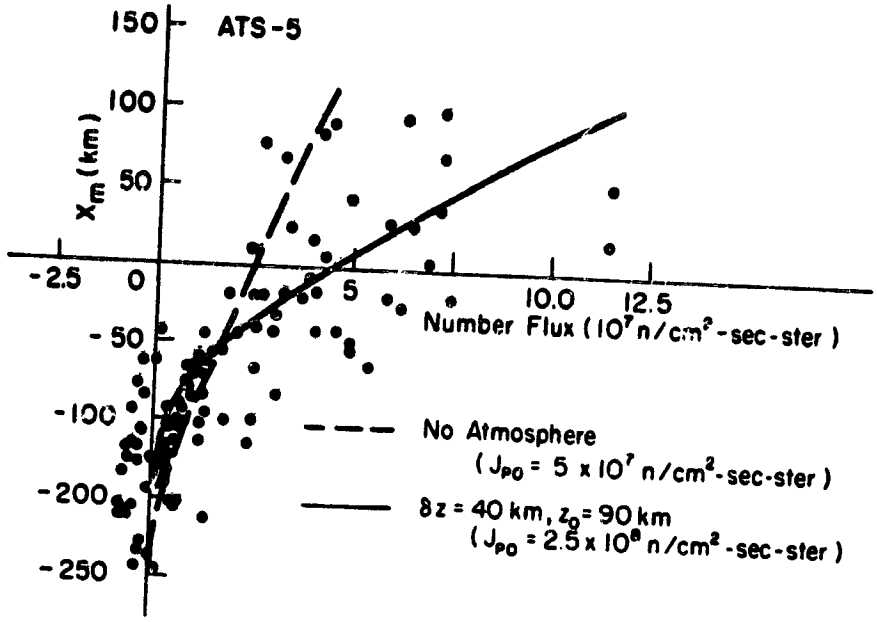

Figure 7. - Residual (photoelectron) current estimated for 21 ATS-5 eclipse passages. (This is the current necessary to explain the observed satellite potential after all ambient and secondary currents have been substracted. Two atmospheric attenuation profiles are also plotted.)

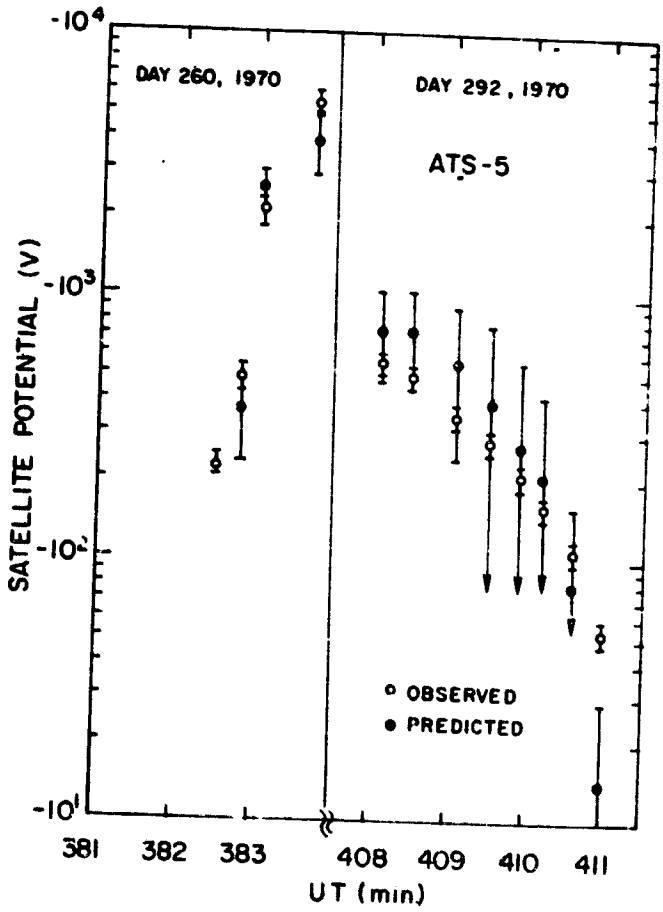

Figure 8. - Observed and predicted (average of sunlit and eclipsed spectra) potentials for eclipse entry of ATS-5 on day 260, 1970, and for eclipse exit on day 292, 1970.

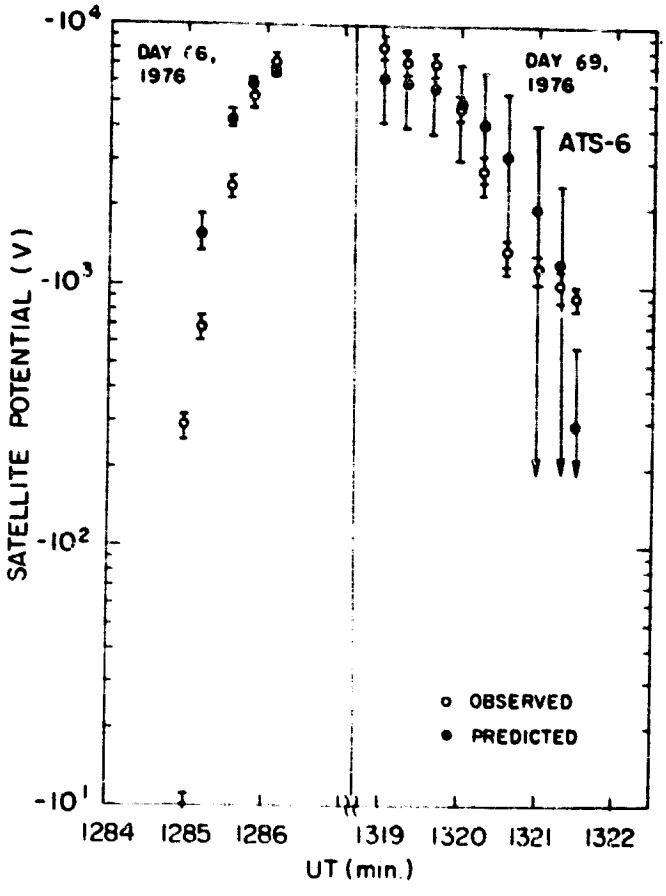

Figure 9. - Observed and predicted taverage of sunlit and eclipsed spectral potentials for eclipse entry of ATS-6 on day 66, 1976, and eclipse exit on day 69, 1976.

D19

N79-24020

SPACECRAFT POTENTIAL CONTROL ON ISEE-1

A. Gonfalone and A. Pedersen
European Space Agency

U.V. Fahleson and C-G. Fälthammar
Royal Institute of Technology

F.S. Mozer and R.B. Torbert
University of California, Berkeley

ABSTRACT

The paper reports on the active control of the potential of the ISEE-1 satellite by the use of electron guns. The electron guns contain a special cathode capable of emitting an electron current selectable between 10^{-8} and 10^{-3}A at energies from approximately.6 to 41 eV.

Results obtained during flight show that the satellite potential can be stabilized at a value more positive than the normally positive floating potential. The electron guns also reduce the spin modulation of the spacecraft potential which is due to the aspect dependent photoemission of the long booms. Plasma parameters like electron temperature and density can be deduced from the variation of the spacecraft potential as a function of the gun current. The effects of electron beam emission on other experiments is briefly mentioned.

INTRODUCTION

The prime purpose of the electron guns mounted on the ISEE-1 spacecraft was to improve double probe electric field measurements. The scientific aim of the electric field experiment is to measure quasi-static fields in a range of about .1 to 200 mV/m (ref. 1). The spin plane component of the field is obtained from the spin modulation of the potential difference between a pair of 8 cm diameter vitreous carbon spheres separated by 73.5 m. The emission of beam of electrons parallel to the spin axis should have reduced the asymmetry in the potential produced by the photoelectrons. Several on orbit tests have shown that the electron guns have no significant influence on the electric field experiment. The interpretation of this unexpected result is that even without the electron beams the electric dipole moment of the photoelectron cloud is small enough for its effect on the double probe measurement to be negligible (ref. 2). The cloud symmetry is more favourable than expected from simplified model calculations (ref. 3).

The operation of the gun can still be a tool for the study of phenomena induced by the injection of a charged particle beam into a natural plasma. The intensity of the beam is far below intensities usually considered for

active experiments (ref. 4) but can be sufficient to investigate active potential control of a body immersed in a plasma, plasma-beam instabilities, and waves.

Control of the spacecraft potential may also be a prerequisite for electric fields and low energy particle measurements in the vicinity of Jupiter (ref. 5) where the photoemission rate is 30 times less than at the Earth orbit or even at geosynchronous orbit to avoid negative charging during eclipses (ref. 6). Previous experiments have shown that thermoionic electron emission from a thruster could be used to reduce negative charging (ref. 7). It is shown in this paper that electron guns can be used to clamp the potential of a conductive spacecraft a few volts positive with respect to the plasma potential.

SYMBOLS

I	current
V	voltage
I_e	electron current collected by a conductive body in a plasma
I_o	value of I_e at the plasma potential
I_{pe}	photo electron current collected by a conductive body in sunlight
I_g	electron gun current
V_{sc}	potential of the spacecraft
V_{pl}	plasma potential
V_k	accelerating voltage of gun electrons with respect to the spacecraft potential

EXPERIMENTAL TECHNIQUE

Figure 1 illustrates the structure of the electron gun (ref. 8). The primary concern was in this case to reduce as much as possible the weight and the power needed for the emission of the electron beam. The cathode used in the gun is a tungsten impregnated cathode developed by Philips (ref. 9) from which a current of 500 μA at an energy of 41 eV could be drawn. Risks of contamination of the cathode were carefully studied and the following measures resulted in the safe operation of the guns. The two guns were opened at 600 km altitude where the concentration of oxygen is low, 15 days had elapsed since the launch so that the outgassing of the spacecraft was reduced, the opening system described in reference 8 was clean and finally a reactivating program was incorporated in the electronics of the experiment.

Tests were conducted before launch to simulate the effects of beam emission on spacecraft potential. The electron guns were attached to a metallic structure which could be biased (potential of the structure during the simulation is called V_{sc}) with respect to the walls (potential called V_{pl}) of a vacuum chamber (diameter 3 m, length 7 m). Figure 2 which summarizes the results shows that the beam current falls off with a slope of about 20 μA per volt and that at low energies ($V_k < 20$ V) spacecharge effects reduce the efficiency of the gun. The mechanism of formation of a virtual cathode in front of the gun at low energies may be invoked to explain the reduction in efficiency: at low energies the emission of electrons from the virtual cathode back to the anode of the gun is greater than the emission to the walls of the chamber at larger distances.

The configuration of the ISEE-1 spacecraft is illustrated in figure 3. In order to minimize potential disturbances originating at the spacecraft or in its vicinity an electrostatic cleanliness specification on the spacecraft surface was implemented at an early stage in the project with the result that the skin is essentially an equipotential surface (surface conductivity approximately $10^5 \Omega / \square$). Potentials can be measured between the satellite body and the probes at the end of the booms; the body of the spacecraft, as will be shown in the last section, can be considered as a large collecting probe.

On board, 13 instruments measure electron and ion populations, magnetic field, plasma waves and other plasma parameters (ref. 10). The orbit is highly elliptic with an apogee of 22.6 Earth radii and a perigee at about 300 km so that the plasmapause, the magnetopause and the bow shock are crossed successively. The measurements presented here were obtained on the 7th November 1977, starting at 17.00 hrs 49 min 40 sec UT when the spacecraft was in the solar wind at a distance of about 17.6 RE.

MEASUREMENTS

The current collection of a conductive body immersed in a space plasma is represented qualitatively as a function of potential in figure 4: the voltage reference is that of the undisturbed plasma at large distances from the body; I_e represents the current collected in shadow or when the photoemission rate is low, I_{pe} represents the contribution of the photoelectron current.

Plasma Potential Measurements

The vitreous carbon probes at the end of the wire booms can be used as conventional Langmuir probes with the difference that their current is swept rather than their voltage. The passage of the probe through the plasma potential has a clear signature indicated by a sudden change in the photoelectron current emitted by the probe. Biasing the probe with a negative current of about -60 nA maintains it within a fraction of a volt of the plasma potential for the data considered here.

Spacecraft Potential Control

The spacecraft potential is measured between the satellite body and one probe biased to be slightly positive relative to the plasma potential. Figure 5 a, b and c show the variations of the spacecraft potential and the electric field signals for 3 different values of the emitted gun current, as a function of the energy of the beam. The accelerating beam voltage V_k is maximum at the left of the figure and is stepped down automatically by steps of 1.6 Volt from 40.8 V to .58 V. The time necessary to step from one level of energy to the next may vary and the arrows indicate the times when the beam energy is equal to 8.6 eV and can be used as reference points. As mentioned earlier the sinusoidal signal representing the electric field is not affected by changes in beam energy or in gun current. (The spikes appearing regularly are due to the sudden change in potential of the probes as they pass in the shadow of the spacecraft).

When the gun current is set at 120 μA (fig. 5 a) the spacecraft potential follows closely the beam energy down to an energy of 8.6 eV where the gun looses its control of the potential. At this energy and lower, space charge effects limit the emission of the gun as was observed during the tests, and as is shown in figure 2 for $V_k < 20$ V. A detailed examination of the voltages indeed shows that decreasing the beam energy from 40 eV to 15 eV changes the spacecraft potential by only 23 V giving a ratio of .92 for V_{sc}/V_k. As will be shown in figure 6 this is due to the fact that beam electrons are not monoenergetic but have a spread in energy around a mean value. When the gun current is set at 60 μA (fig. 5 b) a modulation of the spacecraft potential at twice the spin frequency appears for high values of the beam energy; the modulation disappears betwen 24 V and 8.6 V where the modulation appears again. When the beam current is set at 30 μA the range where the control occurs is limited between 14 V and 8.6 V.
The modulation of the potential at twice the spin frequency is due to the changing photoemission of the shields of the long booms as they spin with the spacecraft. In the particular case of figure 5, the shields were biased at the potential of the probes minus 4 V which means that they are more negative than the plasma and consequently they are a source of photoelectrons. To compensate the changing photoelectron current of the booms the spacecraft potential adjusts to values where incoming and outgoing currents are equal.

The explanation for this behaviour is illustrated in figure 6 which shows current-voltage characteristics of the gun and of the spacecraft including the booms. The dotted line represents the emitted gun current at various energies, the fall off of the beam current has been assumed to be similar to the measured value of 20 μA/V (as shown in figure 2). The continuous lines represent the current collected by the spacecraft (similar to the current collected by a positive conductive body as was shown in the first quadrant of figure 4). The thick line corresponds to the minimum photoemission from the booms, the thinner line to the maximum photo emission. These two curves have been constructed from the data shown in figure 5 where the potential of the spacecraft can be measured for different values of the gun current.

The modulation of the spacecraft potential at twice the spin frequency occurs when the curve representing the current collected by the body cuts the gun current curve on the plateau, control of potential occurs when the gun current is larger than the current collected by the spacecraft body, the amount of gun current emitted into space is equal to the collected current. At voltages less than 8.6 V the modulation reappears with a smaller amplitude because the gun current ceases and the potential oscillates between 10 V and 5 V as is shown in fig. 6; as the slope of the collected current curves is larger at low energies the potential modulation decreases with the spacecraft potential.

DISCUSSION

As was shown in the previous section, the satellite potential can be stabilized at a specified value positive with respect to the plasma potential by operating electron guns at appropriate energies. The guns can be used to compensate for small variations in spacecraft potential due to the aspect dependent photoemission of the long booms which, in the case considered, were biased negatively and thus were a source of photoelectrons. Limited possibilities to measure the ambient temperature exist in the experiment complement on board ISEE-1. In the following a method to determine the plasma density and temperature from the gun measurements is outlined. A simple model for electron collection is assumed $I_e = I_o\ (1 + V_{sc}/V_e)$ where $I_o = n\ e\ v\ S/4$ with n the density, e the electron charge, v the thermal speed ($eVe = mV^2/2$) and S the collecting surface of the entire spacecraft, approximately 10 m^2. The value of I_o is obtained by extrapolating towards low voltages the curve representing the electron saturation current. As an indication the values obtained from figure 6 are $n = 30\ cm^{-3}$ and $V_e = 14.6$ V.

When the control of the spacecraft potential by the electron gun is effective a fraction of the gun current returns to the spacecraft. As noted by the particle experimenters on ISEE-1 this return flux increases considerably the countrate of particle detectors in the vicinity of the return area. The beam also excites plasma instabilities which have been observed in a frequency range around 20 kHz and detected by the other electric antenna on the spacecraft.

It therefore appears that in spite of their low electron beam intensities, some fundamental plasma physics phenomena can be investigated with the electron guns on board ISEE-1 in the future.

REFERENCES

1. Mozer, F.S.: A proposal to measure quasi static electric fields on the Mother/Daughter Satellites, Space Sciences Laboratory, University of California, Berkeley, Calif., Rept. 454, 1972.

2. Mozer, F.S., Torbert, R.B., Fahleson, U.V., Fälthammar, G.G., Gonfalone, A. Pedersen, A. : Measurements of quasi static and low frequency electric fields with spherical double probes on the ISEE-1 Spacecraft, IEEE transactions on Geoscience Electronics, Vol. GE-16, no. 3, July 1978.

3. Grard, R.J.L., Knott, K., and Pedersen, A. : The Influence of Photo-Electron and Secondary Electron Emission on Electric Field Measurements in the Magnetosphere and Solar Wind. Photon and Particle Interactions with Surfaces in Space, edited by R.J.L. Grard, Reidel Publishing Co., Dordrecht, Holland, 1973, pp. 163-189.

4. Winckler, J.R.: A summary of recent results under the ECHO program for the study of the magnetosphere by artificial electron beams. Univ. of Minnesota, Cosmic Physics, Technical Report ## 168, 1 Sep 1976, Minneapolis, Minn. 55455.

5. Grard, R.J.L., Gonfalone A., and Pedersen A.: Spacecraft potential control with electron emitters, in Spacecraft Charging by Magnetospheric Plasmas, Alan Rosen, editor, vol. 47, Progress in Astronautics and Aeronautics, 1976, pp 159-168.

6. DeForest, S.E., Spacecraft Charging at Synchronous Orbit. Journal of Geophysical Research, Vol. 77, Feb. 1972, pp. 651-659.

7. Goldstein, R. and DeForest S. E.: Active control of spacecraft Potentials at Geosynchronous Orbit, in Spacecraft Charging by Magnetospheric Plasmas, Alan Rosen, editor, vol. 47, Progress in Astronautics and Aeronautics, 1976. pp. 169-181.

8. Arends, H.J., Gonfalone, A.: Mechanical opening system for vacuum tubes in space environment. Review of Scientific Instruments, Vol. 47, no. 1, January 1976, pp. 153-155.

9. Zalm, P., van Stratum, A.J.A.: Osmium Dispenser Cathodes, Philips Technical Review, Vol. 27, no. 314, 1966, pp. 69-75.

10. Ogilvie, K., Von Rosenvinge, T. and Durney, A.: "International Sun Earth Explorer: A Three Spacecraft Program," Science , vol. 198, 1977, pp. 131-148.

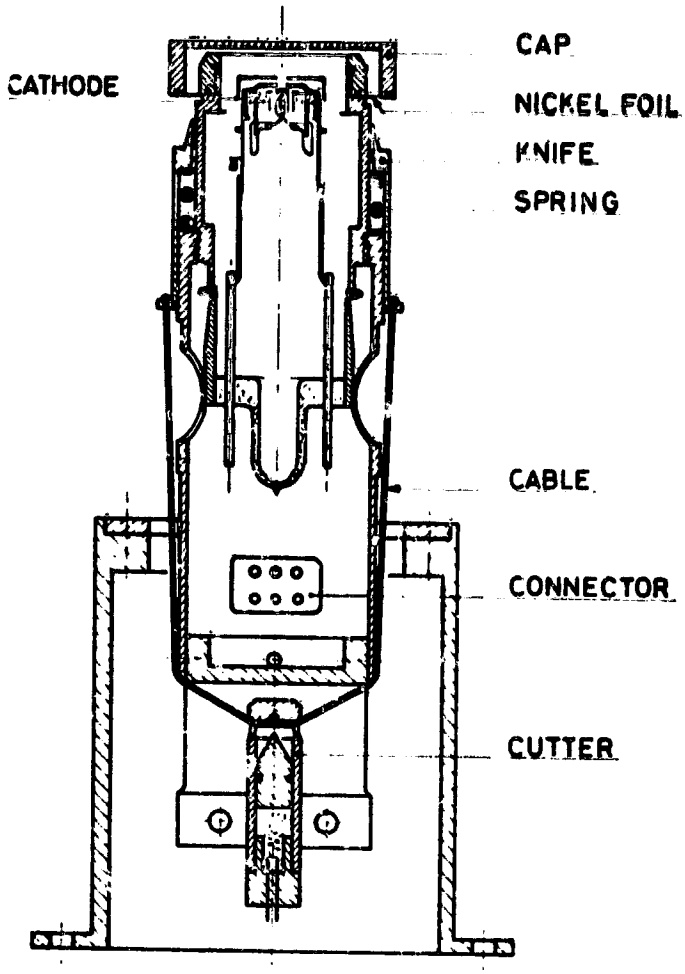

FIG.1 ELECTRON GUN STRUCTURE

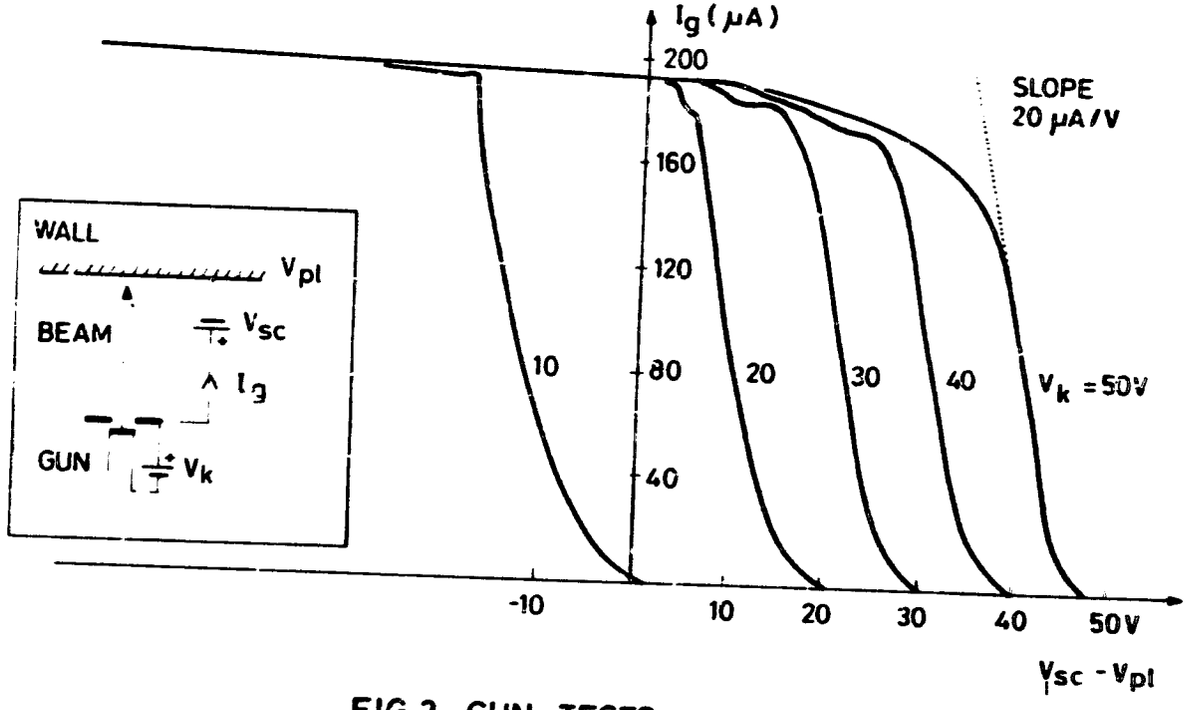

FIG.2 GUN TESTS

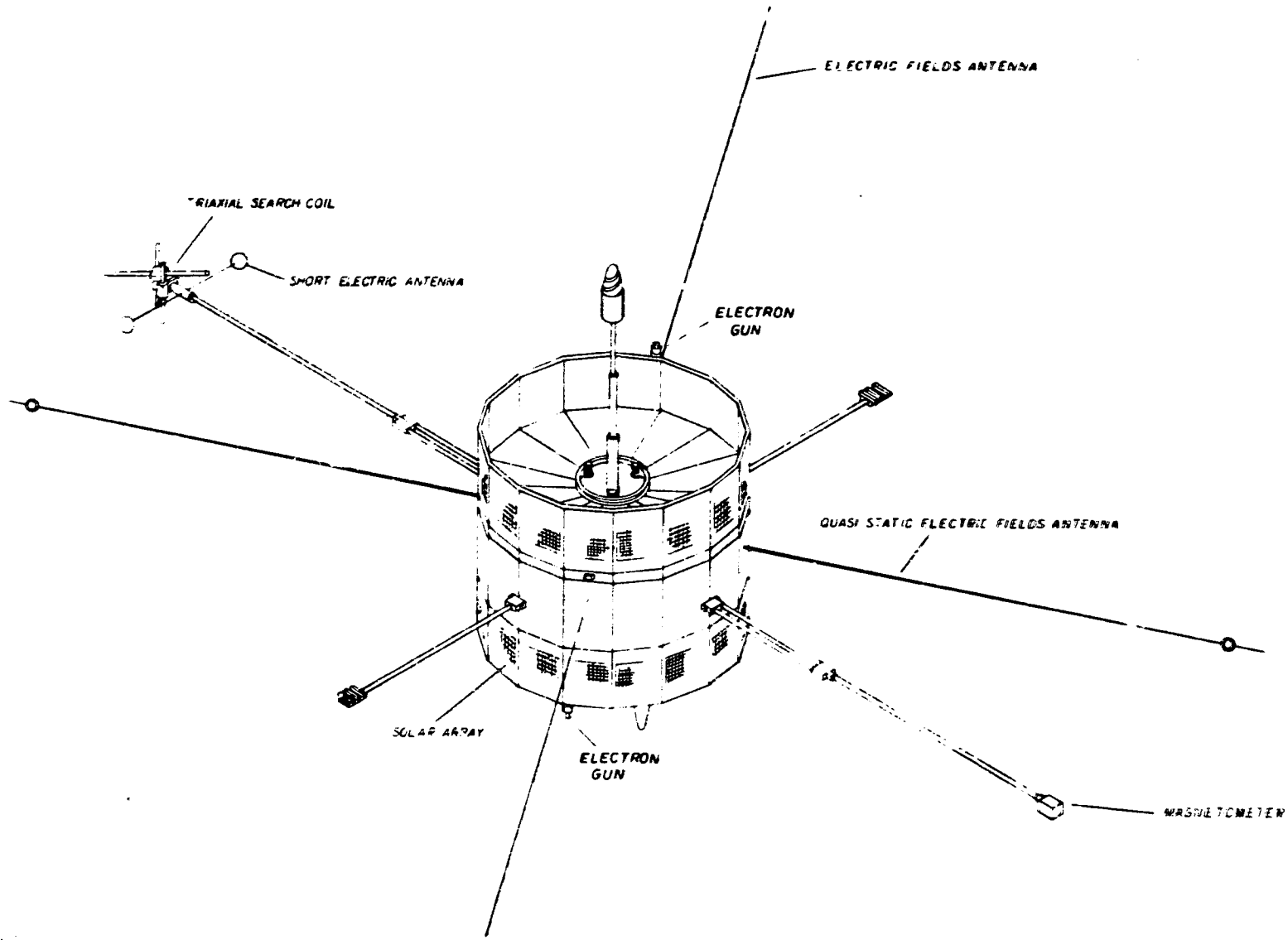

FIG. 3 ISEE-1 SPACECRAFT CONFIGURATION

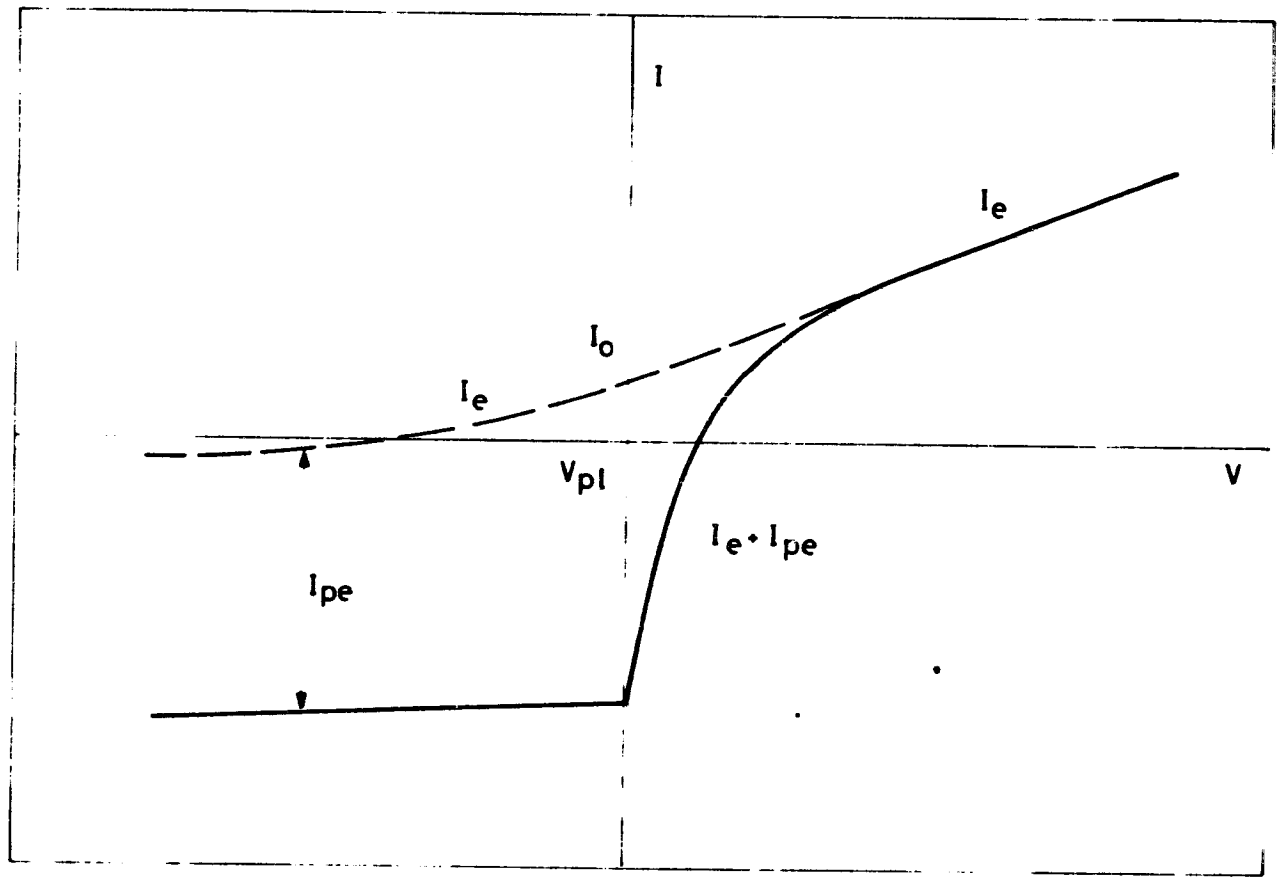

FIG.4 CURRENT-VOLTAGE CHARACTERISTIC OF A CONDUCTIVE BODY IN A SPACE PLASMA

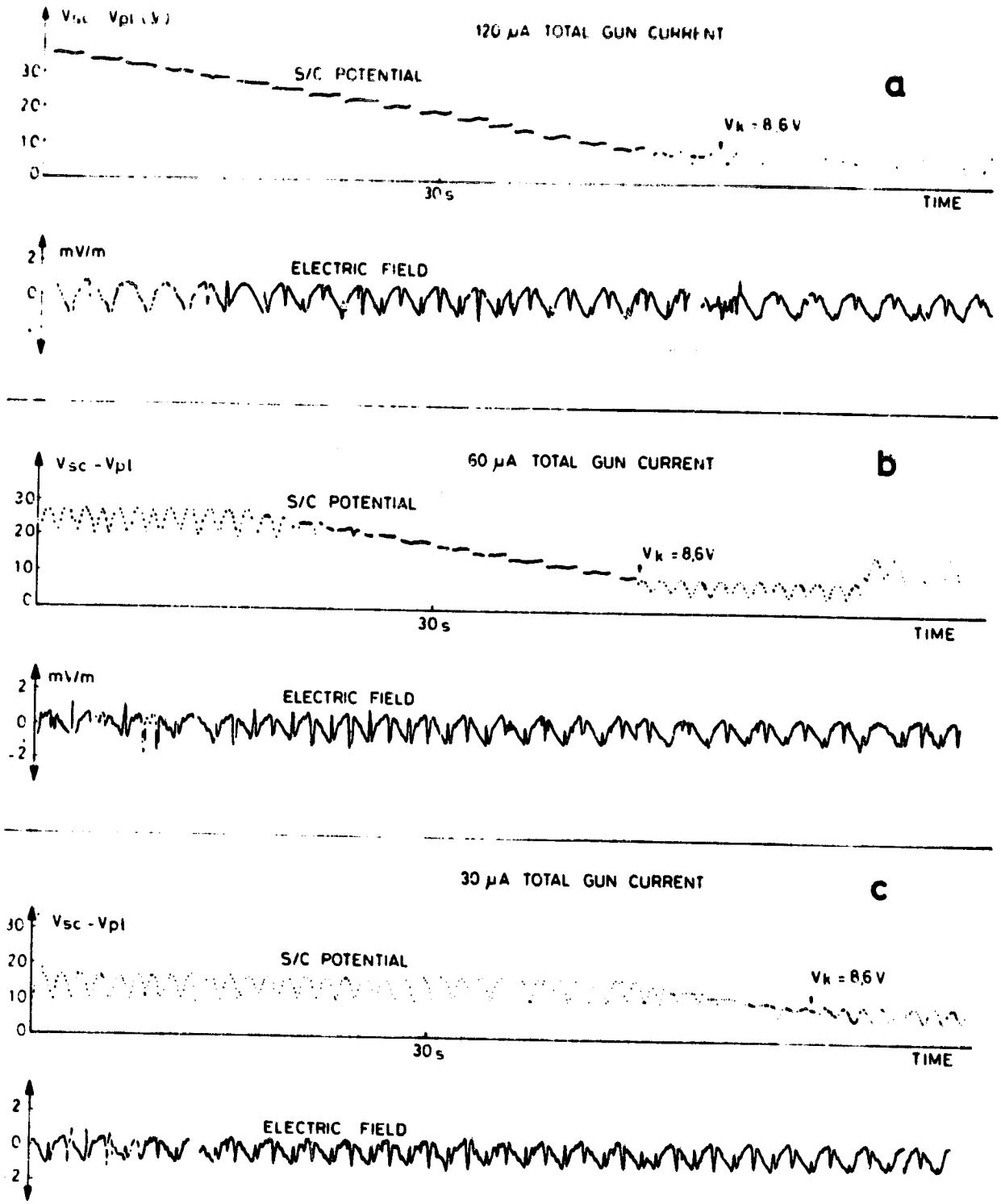

FIG.5 SPACECRAFT POTENTIAL AND ELECTRIC FIELD

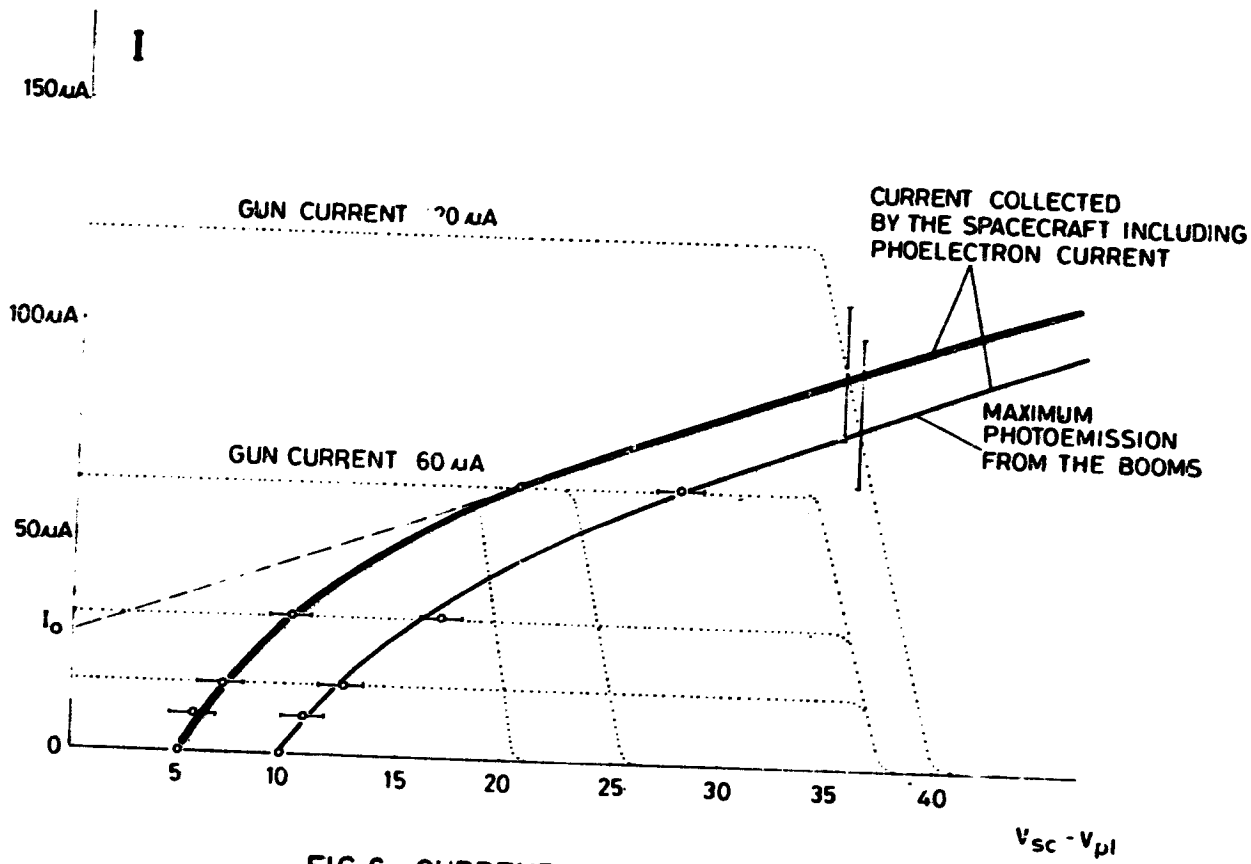

FIG. 6 CURRENT - VOLTAGE CURVES

INTERACTIONS BETWEEN SPACECRAFT AND THE CHARGED-PARTICLE ENVIRONMENT

N. John Stevens
NASA Lewis Research Center

SUMMARY

Spacecraft-environment interactions are defined as the responses of a spacecraft surface to a charged-particle environment. This response can influence spacecraft system performance. Interactions can be divided into two broad categories: spacecraft passive, in which the environment acts on the spacecraft; and spacecraft active, in which the spacecraft causes the interaction. Passive interactions include the spacecraft-charging phenomenon. Active interactions include the relatively new interactions arising from the use of very large spacecraft and space power systems in future missions. In this category the concern is both for the effect the environment can have on spacecraft systems and for the effect the large spacecraft can have on the environment. To illustrate active interactions, a large power system operating at elevated voltages is considered. Possible interactions are described, available experimental data are reviewed, and the effect on power system performance is estimated.

INTRODUCTION

Spacecraft have traditionally been designed to fit within launch vehicle capabilities and shroud dimensions. At times, the ingenuity of designers has been severely taxed to include all systems within these constraints. As a result, spacecraft typically have been cylinders (or at least packaged as cylinders) 150 to 300 centimeters in diameter, with deployables as required. Now, with the advent of the shuttle space transportation system, these limits have changed. Very large spacecraft can be accommodated for future missions. Studies are being conducted on spacecraft to be used for such diverse activities as manufacturing, scientific exploration, power generation, and human habitation in locations ranging from low Earth orbits (250 to 400 km) to geosynchronous altitude and beyond (refs. 1 to 8). Structures proposed for these missions range in size from 200 meters for a large structure-assembly demonstration in the mid-1980's (ref. 9) to several kilometers for the Solar Power Satellite (SPS) (ref. 3). These large structures are being designed with relatively lightweight materials to achieve the required low densities.

These spacecraft must function in the space environment. Anomalous behavior of geosynchronous satellite systems has shown that the space environment is not completely benign. Interactions between the charged-particle environment and spacecraft exterior surfaces (i.e., spacecraft charging) can disrupt spacecraft systems (refs. 10 and 11). The size of the new generation of spacecraft will be approximately the plasma Debye length in the geosynchronous

environment. This can result in increased interactions between the insulators and quasi-conductors and the charged-particle environment. The large size of these new spacecraft raises concern about charging effects on them in low Earth orbits. In this environment the spacecraft moving through the Earth's magnetic field can induce electromagnetic stresses that should be considered in the design. The spacecraft physical dimensions are also of real concern for their effect on the environment.

Proposed large, high-power systems ranging from tens of kilowatts to gigawatts have given rise to another aspect of environmental interactions. One means of improving electrical efficiency and reducing weight for these power systems is to operate at voltages higher than those currently being used. The SPS design calls for the generation of 15 gigawatts to 40 kilovolts. To date, the highest operating voltage used in space is the 100-volt system in Skylab. At this voltage, interactions with the environment are negligible (ref. 12). Operation at higher voltages in a plasma environment, however, can influence system performance.

For these reasons, spacecraft-environment interactions are associated with future space programs. These interactions must be understood, evaluated, and neutralized, if necessary, in the design phases of the programs. In this paper, categories of spacecraft-environment interactions are defined and briefly described. The primary emphasis is on interactions between the environment and large space power systems operating at elevated voltages. Available experimental data on high-voltage surface-plasma interactions are reviewed and, based on this information, the effect of these interactions on power system performance is estimated.

SPACECRAFT-ENVIRONMENT INTERACTION CATEGORIES

In this paper, spacecraft-environment interactions are defined as the responses of a spacecraft surface to the charged-particle environment of space. Spacecraft surfaces will respond to the environment at all altitudes. However, the interaction is of concern only where it influences system performance.

Interactions of concern between a spacecraft and the environment are illustrated in figure 1. A large spacecraft configuration with a large, high-power solar array is illustrated. There are two broad categories of interactions: category 1, spacecraft passive, where the charged-particle environment acts on the spacecraft surfaces; and category 2, spacecraft active, where the spacecraft causes the interaction. Each of these categories is described in the following paragraphs.

Category 1 - Spacecraft Passive Interactions

The principal spacecraft passive interaction of concern is spacecraft charging. This interaction occurs primarily at geosynchronous altitudes when kilovolt energy particles from geosynchronous substorms electrostatically

charge shadowed insulating surfaces to high negative voltages. If the voltage stress on an insulator exceeds its breakdown threshold at an edge or an imperfection (ref. 13), discharges can occur. Energy from this discharge can couple into the spacecraft electrical harness, upset low-level logic circuits, and disrupt system performance. In addition, discharges can deteriorate thermal control surfaces and thus increase spacecraft temperatures. The differential charging of spacecraft surfaces can also ionize neutral gas molecules and enhance surface contamination by attracting charged particles back to the spacecraft surfaces (ref. 14). It can also disrupt scientific instrument measurements. Since there are many references available on this subject (e.g., see refs. 10 and 11), it is not discussed further in this paper.

Other aspects of this category of interactions, such as the possibility of charging by high-energy environmental particles and sputtered atoms, have not been fully investigated. It has been suggested that in a high-energy interaction such particles could charge the wires within a satellite by penetrating the exterior and depositing on wire insulation (ref. 15). Another possible interaction involving high-energy particles could occur if particles are deposited within the exterior surface of a satellite while the exterior surface is neutralized by the thermal plasma (low-energy components of the environment). This could build up an electrostatic bilayer, similar to that suggested in reference 16, which could discharge. This phenomenon would be more likely to occur where the charged-particle environment is more energetic, on spacecraft in the Earth's radiation belts or in the Jovian environment. In the sputtered-atom interaction, sputtered particles could become charged and, as such, they would be an additional current to be considered and an additional source of contamination particles. Specifically excluded from consideration in spacecraft passive interaction is radiation damage to solar cells and electronic components. This has been studied in detail by others.

Category 2 - Spacecraft Active Interactions

In spacecraft active interactions the spacecraft itself or a system on the spacecraft causes the interaction with the environment. These interactions are of concern at all altitudes in space. Spacecraft active interactions include those involving the motion of very large spacecraft proposed for future missions. The orbital velocity of spacecraft through the Earth's magnetic field can induce electric fields within the structure. The differential voltages induced by a large spacecraft can be significant and can give rise to electromagnetically induced forces that can cause distortions within the structure (ref. 17). These induced forces and any subsequent interaction with the environment must be accommodated in the design of large space structures. These interactions are discussed in more detail in references 18 and 19. Very large structures in space can also modify the environment by sweeping out charged particles (ref. 17). Such structures can drastically change the charged-particle environment and cause further interactions with themselves. These problems must be resolved before large space structures are launched.

The principal interaction of concern in this paper is the coupling between the thermal or low-energy plasma environment and a space power system

operating at elevated voltages. This interaction, illustrated as the parasitic current loop in figure 1, is discussed in more detail later in this paper. The thermal plasma environment in equatorial orbit (fig. 2) ranges from about a million particles per cubic centimeter in low Earth orbits to about 10 particles per cubic centimeter at geosynchronous altitude. The thermal energy of these particles is less than 5 eV. This environment can interact with exposed portions of high-voltage systems, and these interactions must be considered in system designs. Interactions that must be evaluated are plasma coupling currents between the high-voltage system and the environment, effects of charge stored in or on the insulator surface, and plasma-initiated discharges (refs. 20 and 21). These interactions are described as functions of operating voltages, time in orbit, plasma properties, and insulator properties. The effect of these interactions on power system performance is illustrated in the next section.

INTERACTIONS WITH LARGE SPACE POWER SYSTEMS

The concept of a large space power system is used to illustrate the rationale for operating at elevated voltages and to estimate the influence of environmental interactions on system performance. Since some effects are configuration dependent and plasma interactions are complex, simplifying assumptions are made in this illustrative example. More sophisticated computer programs are being developed to investigate these interactions in more detail (refs. 22 to 25).

Power System Characteristics

The concept of a large space power system assumed to illustrate interactions with the environment is shown in figure 3. This system is composed of 5-kilowatt solar-array modules connected to give the desired total power output. These modules are each 5 meters by 10 meters and have operating line voltage and current, V_L and I_l as shown in figure 4. The modules are arranged in pairs on two wings. Power is generated with all modules at the same specified voltage and is brought into a central load region on a pair of transmission lines on each wing. Power is converted to the required voltages within the central body. With this arrangement the modules on each wing form parallel electrical circuits: All are on the same voltage V_L with the load current increasing in equal amounts in the transmission line as modules are added. Power systems capable of generating 20 to 500 kilowatts (in increments of 20 kW) can be conveniently studied.

The first consideration is to determine the operating voltage for the system. As shown in figure 4, voltages for a 5-kilowatt module could vary over a wide range from the commonly used 30 volts to 5000 volts. The advantage of higher voltages is usually a reduction in power loss and weight. This advantage can be demonstrated by simple computations of the power loss and weight of the transmission lines alone as the power level increases.

In these computations the transmission line is assumed to be aluminum, based on the results given in reference 26. The cross-sectional area of each line is assumed to be constant at 1 square centimeter. The power lost in the four main transmission lines, expressed as a fraction of the total power generated, can be calculated from

$$\frac{P_L}{P_T} = \frac{4}{P_T}\left(I_1^2R_1 + I_2^2R_2 + I_3^2R_3 + \ldots + I_n^2R_n\right) = \frac{4\rho}{P_T A}\sum_{i=1}^{n} I_i l_i \qquad (1)$$

where

P_L power lost in transmission lines, W

P_T total power generated, W

I_i load current in line at each module, A

R_i resistance in line at each module, ohms

ρ electrical resistivity of aluminum, 2.8×10^{-6} ohm-cm

A cross-sectional area of transmission line, 1 cm^2

l_i characteristic line length for each module, cm

n number of 10-kW module sets on one wing

Since the modules are considered to be added in pairs on each wing in parallel electrical circuits, the load current is computed on the basis of 10-kilowatt module sets at a specified operating voltage. As module sets are added to increase power output conditions, the load current increases by equal amounts. The characteristic line lengths have been assumed to be the distance to the center of each module set. For the first module set this is the distance from the central load section (assumed to be 10 m). Line lengths for subsequent module sets are assumed to be 5.5 meters.

Results of computations based on equation (1) are shown in figure 5. It is apparent from this figure that any power system, with the assumptions used here, would dissipate nearly all its power in the lines if 500 kilowatts were generated at 100 volts. For large space power systems, operational voltage levels must be increased to reduce line losses.

The assumption of constant cross-sectional area for the transmission line is poor because of thermal considerations. A 1-square-centimeter cross-sectional line would probably vaporize at the currents indicated for 100-volt operation. A trade-off must be made between power loss and the weight gained by increasing the line cross-sectional area. Such a trade-off can be approximated for the power system considered here. The line weight in grams is

$$W_L = 4\gamma A \sum_{i=1}^{n} l_i \qquad (2)$$

where γ is the density of aluminum (2.7 g/cm^3). Thus, the line weight required to maintain a 5-percent power loss in the transmission line is computed. This weight is compared with a total system weight based on a design goal of 10 kg/kW. Combining equations (1) and (2) to eliminate the cross-sectional area and expressing the result as the desired weight fraction results in

$$\frac{W_L}{W_T} = \frac{16\gamma\rho}{W_T P_L}\left(\sum_{i=1}^{n} I_i^2 l_i\right)\left(\sum_{i=1}^{n} l_i\right)$$

where W_T is the total system weight in kilograms. Since it is assumed that $P_L = 0.05\ P_T$ and $W_T = 10\ P_T$, then

$$\frac{W_L}{W_T} = \frac{32\gamma\rho}{W_T P_L}\left(\sum_{i=1}^{n} I_i^2 l_i\right)\left(\sum_{i=1}^{n} l_i\right) \qquad (3)$$

The results of equation (3) are shown in figure 6. Here again a 500-kilowatt system operating at 100 volts with a 5-percent power loss in the transmission lines would have a line weight approximately equal to the desired total system weight. Hence, operating voltages must be increased to make large power systems feasible. The method of computation used here totally neglects any effects within the 5-kilowatt modules. If these effects are considered, there could be additional line losses that would be minimized by higher voltage operation.

Other power system design concepts - such as a single, very large solar array and modular designs with multiple transmission lines (a pair for each module) - have been subjected to similar reviews. The results are similar: Power losses and weight can be significantly reduced by operating at higher voltage levels.

In the example described here, operating voltage levels are allowed to vary from 100 to 5000 volts. In an actual system, high-voltage components would be needed for switching and other operations. Although these high-voltage components do not now exist, the technology for developing them is being pursued (ref. 26). Although large power systems should use high operating voltages to minimize power losses and weight, a high-voltage system exposed to space could interact with the charged-particle environment. This interaction could influence system performance. These possible interactions and their effect on system performance are discussed in the following paragraphs.

Background. - The spacecraft-system - charged-particle-environment interaction considered here was briefly described in the definition of category 2 interactions. In this section, the description of this interaction is expanded.

Consider a solar-array power system as shown in figure 7. In the standard construction of this array, cover slides do not completely cover the metallic interconnections between solar cells. These cell interconnections are at various voltages, depending on their location in the array circuits. Because the array is exposed to space plasma, the interconnections act as biased probes, attracting or repelling charged particles. At some location on the array, the generated voltage is equal to the space plasma potential. Cell interconnections that are at voltages V_+ above the space potential will attract an electron current that depends on the number density and energy of the electrons in the environment and on the voltage difference between the interconnections and space. Those interconnections that are at voltages V_- below the space plasma potential will repel electrons and attract an ion current. The voltage distribution in the interconnections relative to space must be such that electron and ion currents are equal. This flow of electrons and ions can be considered as plasma coupling currents that form a current loop in parallel with the spacecraft electrical load. The loop is parasitic and represents a power loss. This interaction should be more pronounced in low Earth orbits because of the high number density of the low-energy thermal plasma (fig. 2).

Experimental results. - To assess the impact of space plasma on solar-array performance, it is necessary to estimate the current collection (i.e., the plasma coupling current) of an array that has small, biased conductor areas surrounded by large areas of insulation. This estimate is based on results of experiments conducted on biased solar-array segments in plasma environments. Such experiments (refs. 27 to 30) have been conducted ever since an interesting enhancement effect was first reported 10 years ago (ref. 31). The results presented here are based primarily on tests made at the Lewis Research Center (ref. 12). All other results are in substantial agreement with these.

A small solar-array segment of twenty-four 2-centimeter-by-2-centimeter cells mounted in series on a Kapton sheet and a fiberglass board was tested in Lewis' geomagnetic substorm simulation facility. This segment had standard mesh interconnections between the cells. Bias voltages V_A were applied to the segment by laboratory power supplies to determine both positive and negative voltage interactions. The test facility was housed in a 1.8-meter-diameter by 1.8-meter-long vacuum chamber capable of operating in the 10^{-6}-torr range. A plasma environment was generated by ionizing nitrogen gas. Both plasma coupling currents and surface voltages on the array segment were measured during the tests, which were conducted at plasma densities of about 10^4 and 10^3 per cubic centimeter (ref. 32).

Surface voltage profiles for part of the segment are shown in figure 8. For low, positive applied potentials ($\leq$100 V), the quartz cover slide assumes a small negative voltage in order to maintain electron and ion currents to that surface (fig. 8(a)). This voltage is measured about 3 millimeters above the quartz surface by a noncontacting, capacitively coupled surface voltage probe.

Negative voltage on the quartz cover slides appears to suppress the voltage in the plasma above the interconnections to less than 10 percent of the applied voltage. As positive potentials are increased above 100 volts, a transition occurs in surface voltage profiles (fig. 8(b)): The surface voltage of the quartz cover slides approaches that of the interconnections. It is as if the voltage sheaths have "snapped over" or expanded to encompass the cover slides. A voltage sheath is the distance required for the voltage to decay to plasma potential through the rearrangement of plasma particles. Snap-over seems to occur when the sheath approaches solar-cell dimensions. Effective surface voltage after snap-over is 50 volts less than the applied voltage.

Results for negative applied voltages are shown in figures 8(c) and (d). The quartz cover slides again assume slightly negative voltages. Electric fields in the plasma due to the biased interconnections are suppressed and confined by the quartz surface voltage. Instead of a snap-over phenomenon, this confinement remains until the field builds up to a point where discharge occurs. The voltage at which breakdown (discharge) occurs depends on the plasma density. For these tests, breakdown occurred at about -600 volts at densities of about 10^4 per cubic centimeter and about -750 volts at densities of about 10^3 per cubic centimeter. Other tests have indicated that breakdown can occur at densities corresponding to geosynchronous altitudes when the negative bias voltage magnitudes are greater than 5000 volts (ref. 28).

Plasma coupling currents for the small segment are shown in figure 9. The current collection phenomenon agrees with the trends indicated by the surface voltage data. For low, positive applied potentials (<100 V), plasma currents in amperes can be approximated by an empirical relationship that depends on the measured or suppressed voltage in the plasma and the interconnections:

$$I_e = j_{eo} \frac{A_i}{4} \left(1 + \frac{V_m}{E_e}\right) \qquad \text{for } V_A < 100 \text{ V} \tag{4}$$

where

j_{eo} electron thermal current density, A/cm^2

A_i total interconnection area, 4.8 cm^2

V_m measured voltage in plasma at interconnection, V

E_e electron temperature in plasma, eV

V_A applied bias voltage, V

The measured voltage V_m has been found to be about 10 percent of the applied voltage V_A.

For positive applied potentials greater than 100 volts, the current collection in amperes can be approximated by what appears to be space-charge-limited current collection based on a reduced voltage and the panel area:

$$I_e = j_{eo} \frac{A_p}{4} \left(1 + \frac{V_A - 50}{E_e}\right)^{0.8} \qquad \text{for } V_A > 100 \text{ V} \tag{5}$$

where A_p is the total fiberglass panel area (180 cm^2). In the transition region (≈100 V), no expression has been found to fit the current data.

Plasma coupling current collection at negative voltages seems to fit a relationship similar to equation (4), where ion thermal current density and temperature j_{io} and E_i are substituted for j_{eo} and E_e to the point where there is a transition to discharge. No relationship has been developed to predict the onset of discharge at various plasma densities.

Modern solar-array technology seems to favor a wraparound interconnection over the conventional mesh interconnection (fig. 10). Wraparound interconnection construction eliminates the expansion bend of the conventional interconnection, and this conceivably might influence plasma interactions. A sample of 2-centimeter-by-4-centimeter solar cells, with wraparound interconnections, mounted on a Kapton sheet was tested to evaluate the interaction (ref. 12). Surface voltage profiles for tests in plasma densities of 10^5 per cubic centimeter at positive applied voltage are shown in figure 11. Here snap-over occurred at a slightly higher voltage (190 V), possibly because of the large solar-cell size. When negative voltages were applied, the discharge phenomenon was again observed. Onset of breakdown for this sample was about -700 volts. In this test, the discharges were photographed (fig. 12) and are seen to occur at the cell edges, as would be expected from surface voltage profiles.

High-voltage operation may cause long-term degradation of solar-array performance even if plasma coupling currents can be neglected. The only test conducted to date to evaluate this condition is a 114-hour test of a 100-square-centimeter solar-array segment. The segment was biased to 4 kilovolts and the plasma environment was controlled so that the coupling current was kept at 10 microamperes (ref. 28). (From short-term tests this coupling current was considered to be too low to cause detrimental effects.) After the test, however, the interconnections had obviously darkened and the cover slides appeared to be coated. Voltage-current curves of the array segment made before and after the test indicated a 7-percent decrease in short-circuit current (fig. 13). This contamination may have been due to facility effects, and additional testing is required to evaluate possible enhanced contamination effects.

A solution to interaction problems would be to cover all biased conductors. This would work only if there are no penetrations in the covering. Experimental results obtained when a small pinhole (0.038 cm diam) was made in a Kapton insulating film over a biased conductor are shown in figure 14. Such holes in insulators can result in disproportionally large electron currents. Furthermore, tests have indicated that collection currents can be proportional to the total insulator area (ref. 28). The mechanism for this pinhole current collection phenomenon appears to be an interaction between electric fields from the pinhole expanding into the plasma and along the insulator surface. This effect can be seen from results of tests with a biased metal disk placed on a Kapton insulator (ref. 32). At low, positive applied potentials the Kapton

surface assumed a slightly negative voltage (fig. 15). As the applied voltage exceeded 100 volts, the surface voltage on the Kapton changed: It became more and more positive until the whole surface was strongly positive. It is believed that plasma electrons are accelerated into the Kapton and generate secondaries that are collected by the disk and increase the measured currents. For negative applied potentials, the electric fields remained in the region of the disk and no increased currents were found.

The experimental results reported here were obtained on relatively small solar-array and insulator-pinhole samples. The effects obtained with these small samples have been verified in space by the Plasma Interaction Experiment (PIX) flight results (ref. 33). Tests with larger samples (10 m by 1 m) to evaluate increased area effects have recently been started (ref. 34). The small-sample tests indicate that there can be significant interaction effects that could influence space power system performance. The initial indications from the large-sample tests seem to verify the results of the small sample tests. These results are summarized in figure 16. For those areas of the array that are positive with respect to the space plasma potential, there will be electron collection interactions. At low, positive voltages these interactions will depend on biased interconnection areas and a suppressed voltage. As voltages increase, there will be a transition to whole-panel current collection that probably will depend on space-charge-limited current collection. At negative voltages, ions will collect at the interconnections at suppressed voltages. As the array voltage becomes more strongly negative, discharges or arcing will disrupt the power generation.

The influence of these experimentally determined interaction effects on the performance of large, high-voltage space power systems is considered in the next section.

Interaction Effects on Large Power Systems

By using information gained from experimental results, we can estimate the influence of environmental interactions on a large space power system like that shown in figure 3. Such a power system will float electrically at some voltage relative to the space plasma potential so that equal electron and ion currents will be collected. Since electrons are more mobile than ions, the array will be predominantly negative with respect to space potential. Absolute ground reference is the space plasma potential and not the spacecraft. Those areas of the array that are positive V_+ with respect to the space plasma potential will collect electrons as in the positive applied potential experiments. Those areas of the array that are negative V_- with respect to the space plasma potential will collect ions as in negative applied potential experiments. System operating line voltage V_L will be the sum of the absolute values of the positive and negative voltages (i.e., $V_L = |V_+| + |V_-|$).

To determine the floating potential of this power system, electron and ion currents have to be computed as a function of environmental parameters, system geometry, and voltage differences between the array and space. The method of current collection of large panels is not completely understood at this time.

Several papers on this phenomenon have been given at this conference (refs. 22 to 25). However, to illustrate the environmental interaction effects, experimental results given in the previous section are extrapolated here to large systems.

Based on experimental results, the following charged-particle interactions should occur in a large space power system:

(1) Those portions of the array that are at positive voltages less than 100 volts will collect electron current proportional to the interconnection area and to a voltage that is about 10 percent of the actual voltage at the interconnections (eq. (4)).

(2) Those portions of the array that are at positive voltages greater than 100 volts will collect electron currents proportional to the panel area and to a voltage that is 50 volts less than the actual voltage at the interconnections (eq. (5)).

(3) Those portions of the array that are at negative voltages will collect ion currents proportional to the interconnection area and to a voltage that is about 10 percent of the actual voltage at the interconnections (ion current version of eq. (4)).

(4) Discharges will occur in low Earth orbits in those portions of the array that are between -500 and -1000 volts, and at geosynchronous altitudes in those portions of the array that are greater than -5000 volts.

The second interaction states, in other words, that higher-positive-voltage portions of the array will collect electron current proportional to the 0.8 power of the voltage. Another model for current collection at these voltages has been proposed (ref. 12). This model assumes that current collection can be computed as the electron flux to an expanded sheath. The sheath is curved at the panel edges, with the radius of curvature determined from the Child-Langmuir relationship, and flat across the central portion of the array. In this model the radius is proportional to the 0.75 power of the voltage. So the functional dependence of both models is similar.

Since environmental interactions between a space power system at various voltages and the space charged-particle environment should be more pronounced in low Earth orbits, this environment is used in this illustrative example. Pertinent environmental parameters for 400-kilometer orbital conditions are given in table I (ref. 35). The magnitude of plasma coupling current interactions at geosynchronous altitudes can be assumed to be orders of magnitude less than those in low Earth orbits since the thermal plasma density is less.

Under equilibrium conditions, the voltage distribution on the interconnections will assume values such that the total electron current I_e collected from the plasma (electron plasma coupling current) will equal the ion current I_i collected. Since electrons are more mobile than ions, areas A_+ of the array that are at positive voltages will be smaller than areas A_- that are at negative voltages. Furthermore, it can be expected that the positive voltage

V_+ of the electron collection areas (relative to the space plasma potential) will be less than the negative voltage V_-. These conditions can be written as

$$I_e = I_i$$

or

$$j_{eo} \frac{A_+}{4} \left(1 + \frac{0.1\ V_+}{E_e}\right) = j_{io} \frac{A_-}{4} \left(1 + \frac{0.1\ V_-}{E_e}\right) \qquad \text{for } V_+ \leq 100\ V$$

and

$$j_{eo} \frac{A'_+}{4} \left(1 + \frac{V_+ - 50}{E_e}\right)^{0.8} = j_{io} \frac{A_-}{4} \left(1 + \frac{0.1\ V_-}{E_e}\right) \qquad \text{for } V_+ > 100\ V$$

where

$$|V_+| + |V_-| = V_L$$

and

A'_+ panel area at positive voltage

j_{eo}, j_{io}, E_e, and E_i plasma properties (table I)

The total interconnection area is assumed to be 5 percent of the total array area.

To solve these equations, a relationship between collection areas and voltages above and below space plasma potentials is needed. Since all array modules have been assumed to be at the same operating line voltage V_L and voltage distributions within the module have been neglected, many combinations of voltage and area are possible. For this example, it is assumed that positive portions of the array are at 10 percent of operating voltage (i.e., $V_+ = 0.1\ V_L$ and $V_- = 0.9\ V_L$). The array will probably not be significantly more positive than this, so the example is valid for illustrative purposes.

Plasma coupling currents can now be computed for large power systems at various operating voltages. These parasitic currents can then be compared with the operating current to evaluate the influence of the loss through the environment. Since a fixed percentage was used for the positive and negative voltages relative to the space plasma potential and since the array size is proportional to the power generated, the ratio of coupling current to operating current has turned out to be independent of power level. Results, as a function of operating voltage, are shown in figure 17. These results are in reasonable agreement with those given in reference 12.

The results of this exercise indicate that plasma coupling current losses at operating voltages less than 500 volts are not serious in low Earth orbits and, therefore, are definitely not a problem at geosynchronous altitudes. The limitation in going to higher operating voltages appears to be the arcing in the negative portions of the array. This arcing also will be a problem at geosynchronous altitudes but at negative voltages greater than 5000 volts. If this arcing is truly an electric-field-confinement effect, a technological investigation should lead to practical methods of overcoming this limitation. Once arcing is eliminated, operation of power systems, in the kilovolt range, without detrimental plasma interactions should be possible at all altitudes.

There is a possibility that ion thrusters will be used with large space power systems (ref. 3). If ion thrusters are used, additional current flows must be considered. Since the thruster neutralizer produces electrons in response to electric fields surrounding it, it can maintain the structure at space plasma potential. The array, then, will be at a positive voltage (relative to the space plasma potential) that approaches the operating voltage. Under these conditions, a large electron current can be collected that can influence array performance. In addition, electron collection may be enhanced through a charge-exchange plasma from the thrusters. This interaction has been reported in references 36 and 37 and is described further in a paper for this conference (ref. 38).

It is recognized that the computations presented here are simplistic. A considerable number of factors have been neglected: for example, the motion of the system through space producing ram and wake effects, material secondary and photoemission characteristics, effects due to voltage distributions within the array, and magnetic field effects. Even so, it is believed that the general conclusions indicated by this example are valid.

A considerable amount of work still has to be done in a technological investigation to improve the accuracy of analytical models, to verify ground test results in space, and to analyze complex geometries used in large space power systems. The questions of long-term interaction and enhanced contamination effects still have to be addressed. However, significant benefits to power systems can be achieved if high-voltage operation can be shown to be feasible.

CONCLUDING REMARKS

Very large spacecraft with dimensions ranging to kilometers have been proposed for future space missions. These spacecraft will incorporate relatively lightweight materials (composites and insulators) to achieve the required low densities. The spacecraft charging investigation has shown that such materials can be charged by environmental fluxes and that these interactions cannot be ignored. Similar spacecraft - charged-particle-environment interactions can be expected for these new, large spacecraft. Large space power systems are also being considered for future missions. Powers to multikilowatt levels are proposed. At these power levels, it is advantageous to use operating voltages higher than those presently being used in order to reduce transmission-line

weights and losses. This elevated-voltage operation could cause interactions with the space charged-particle environment. Therefore, there is a need to expand technological investigations of such interactions.

Two broad categories of spacecraft environmental interactions have been defined: spacecraft passive, where the environment acts on the spacecraft; and spacecraft active, where a system on the spacecraft causes the interaction. The principal interaction in the first category is spacecraft-charging phenomena. Considerable progress has been made in understanding this interaction, but the study is not yet complete.

Spacecraft active interactions present relatively new interaction concepts. As an example of these interactions, a large space power system in low Earth orbit operating over a wide range of voltages is considered. Based on the available experimental data, it appears that the environmental interactions are negligible for operating voltages to 500 volts in Earth orbits above 400 kilometers. The limiting factor in going to even higher voltages is the tendency to discharge in the portions of the array that are strongly negative relative to space (-500 to -1000 V in low Earth orbits and -500 to -10 000 V at geosynchronous altitudes). This tendency to discharge appears to be due to the confinement of electric fields at the interconnections between solar cells. A comprehensive technological investigation should lead to a means for controlling this discharge characteristic.

Large systems will interact with the environment to produce effects within the spacecraft, and the converse can also occur: Large spacecraft can affect the environment by sweeping up the charged particles to cause as yet unknown repercussions. This emphasizes the need to understand and evaluate all possible interactions with the environment before proposed large spacecraft are launched, to safeguard both the spacecraft systems and the environment.

REFERENCES

1. Outlook for Space. NASA SP-286, 1976.

2. Johnson, R. D.; and Holbrow, C., eds.: Space Settlements, A Design Study. NASA SP-413, 1977.

3. Woodcock, G. R.: Solar Satellites, Space Key to Our Future. Astronaut. Aeronaut., vol. 15, no. 7/8, July/Aug. 1977, pp. 30-43.

4. Satellite Power Systems (SPS) Feasibility Study. (SD76-SA-0239-1, Rockwell International Corp.; NASA Contract NAS8-32161.) NASA CR-150439, 1976.

5. Systems Definition on Space-Based Power Conversion Systems. (D180-20309-1, Boeing Aerospace Co.; NASA Contract NAS8-31628.) NASA CR-150209, 1977.

6. Poeschel, R. L.; and Hawthorne, E. J.: Extended Performance Solar Electric Propulsion Thrust System Study. Vol. 2 - Baseline Thrust System. (Hughes Research Labs.; NASA Contract NAS3-20395.) NASA CR-135281, 1977.

7. Friedman, L. D.; et al.: Solar Sailing - The Concept Made Realistic. AIAA Paper 78-82, Jan. 1978.

8. AIAA Conference on Large Space Platforms: Future Needs and Capabilities. Hyatt House Hotel, Los Angeles, California, Sept. 27-29, 1978.

9. Covault, Craig: Structure Assembly Demonstration Slated for Large Space Structures in Low Orbit. Avia. Week Space Technol., vol. 108, June 12, 1978, pp. 49-53.

10. Rosen, Alan, ed.: Spacecraft Charging by Magnetospheric Plasmas. Progress in Astronautics and Aeronautics, vol. 47, American Institute of Aeronautics and Astronautics, Inc., 1976.

11. Pike, C. P.; and Lovell, R. R., eds.: Proceedings of the Spacecraft Charging Technology Conference. Air Force Geophysics Laboratory AFGL-TR-0051 and NASA TM X-73537, 1977.

12. Purvis, C. K.; Stevens, N. J.; and Berkopec, F. D.: Interaction of Large, High Power Systems with Operational Orbit Charged Particle Environment. NASA TM-73867, 1977.

13. Stevens, N. J.; Purvis, C. K.; and Staskus, J. V.: Insulator Edge Voltage Gradient Effects in Spacecraft Charging Phenomena. NASA TM-78988, 1978.

14. Hall, David F.; et al.: Experiment to Measure Enhancement of Spacecraft Contamination by Spacecraft Charging. Eighth Conference in Space Simulation. NASA SP-379, 1975, pp. 89-107.

15. Wenaas, E. P.: Spacecraft Charging Effects by the High-Energy Natural Environment. IEEE Trans. Nucl. Sci., vol. NS-24, no. 6, Dec. 1977, pp. 2281-2284.

16. Meulenberg, A., Jr.: Evidence for New Discharge Mechanisms for Dielectrics in a Plasma. Spacecraft Charging by Magnetospheric Plasmas, A. Rosen, ed., Progress in Astronautics and Aeronautics, vol. 47, American Institute of Aeronautics and Astronautics, Inc., 1976, pp. 237-246.

17. Rosen, A., Chairman: Workshop on Environmental Interactions with Large Orbital Power Systems. Future Orbital Power Systems Technology Requirements. NASA CP-2058, 1978, pp. 309-312.

18. Miller, E.; et al.: Environmental Interaction Implications for Large Space Systems. Spacecraft Charging Technology - 1978. NASA CP-2071, 1979.

19. Stevens, N. John: Space Environmental Interactions with Spacecraft Surfaces. AIAA Paper 79-0386, Jan. 1979.

20. Knauer, W.; et al.: High Voltage Solar Array Study. (Hughes Research Labs.; NASA Contract NAS3-11535.) NASA CR-72675, 1970.

21. Springgate, W. F.; and Oman, H.: High Voltage Solar Array Study. (D2-121734-1, Boeing Co.; NASA Contract NAS3-11534.) NASA CR-72674, 1969.

22. Parker, L. W.: Plasma Sheath Effects on Equilibrium Voltage Distributions of Large High Power Satellite Solar Arrays. Spacecraft Charging Technology - 1978. NASA CP-2071, 1979.

23. Parker, L. W.: Magnetic Shielding of Large High Power Satellite Solar Arrays Using Internal Currents. Spacecraft Charging Technology - 1978. NASA CP-2071, 1979.

24. Domitz, S.; and Kolecki, J. C.: Effect of Parasitic Plasma Currents on Solar-Array Power Output. Spacecraft Charging Technology - 1978. NASA CP-2071, 1979.

25. Freeman, J. W.; and Reiff, P. H.: Environmental Protection for the Solar Power Satellite. Spacecraft Charging Technology - 1978. NASA CP-2071, 1979.

26. Finke, R. C.; et al.: Power Management and Control For Space Systems. Future Orbital Power System Technology Requirements. NASA CP-2058, 1978, pp. 195-207.

27. Herron, B. G.; Bayless, J. R.; and Worden, J. D.: High Voltage Solar Array Technology. AIAA Paper 72-443, Apr. 1972.

28. Kennerud, K. L.: High Voltage Solar Array Experiments. (Boeing Aerospace Co.; NASA Contract NAS3-14364.) NASA CR-121280, 1974.

29. Domitz, S.; and Grier, N. T.: The Interaction of Spacecraft High Voltage Power Systems with the Space Plasma Environment. Power Electronics Specialists Conference, Institute of Electrical and Electronics Engineers, Inc., 1974, pp. 62-69.

30. Stevens, N. John: Solar Array Experiments on the SPHINX Satellite. NASA TM X-71458, 1973.

31. Cole, R. K.; Ogawa, H. S.; and Sellen, J. M., Jr.: Operation of Solar Cell Arrays in Dilute Streaming Plasmas. (TRW-09357-6006-R000, TRW Systems; NASA Contract NAS3-10612.) NASA CR-72376, 1968.

32. Stevens, N. J.; et al.: Investigation of High Voltage Spacecraft System Interactions with Plasma Environments. AIAA Paper 78-672, Apr. 1978.

33. Grier, N. T.; and Stevens, N. J.: Plasma Interaction Experiment (PIX) Satellite Results. Spacecraft Charging Technology - 1978. NASA CP-2071, 1979.

34. McCoy, J. E.; and Konradi, A.: Sheath Effects Observed on a 10-Meter-High Voltage Panel in a Simulated Low-Earth-Orbit Plasma. Spacecraft Charging Technology - 1978. NASA CP-2071.

35. Liemohn, H. B.: Electrical Charging of Shuttle Orbiter. IEEE Trans. Plasma Sci., vol. PS-4, Dec. 1976, pp. 229-240.

36. Kaufman, H. R.; Isaacson, G. C.; and Domitz, S.: The Interactions of Solar Arrays with Electrical Thrusters. AIAA Paper 76-1051, Nov. 1976.

37. Parks, D. E.; and Katz, I.: Spacecraft-Generated Plasma Interaction with High Voltage Solar Array. AIAA Paper 78-673, Apr. 1978.

38. Liemohn, H. B.: Plasma Particle Trajectories Around Spacecraft Propelled by Ion Thrusters. Spacecraft Charging Technology - 1978. NASA CP-2071, 1979.

TABLE I. - ENVIRONMENTAL PARAMETERS

[Orbit, 400 km; O_{16}^{+} ions.]

Electron number density, n_e, cm^{-3}	2×10^{5}
Electron temperature, E_e, eV	0.22
Electron current density, j_{eo}, A/cm^2	2.4×10^{-7}
Ion number density, n_i, cm^{-3}	2×10^{5}
Ion temperature, E_i, eV	0.09
Ion current density, j_{io}, A/cm^2	9.4×10^{-10}

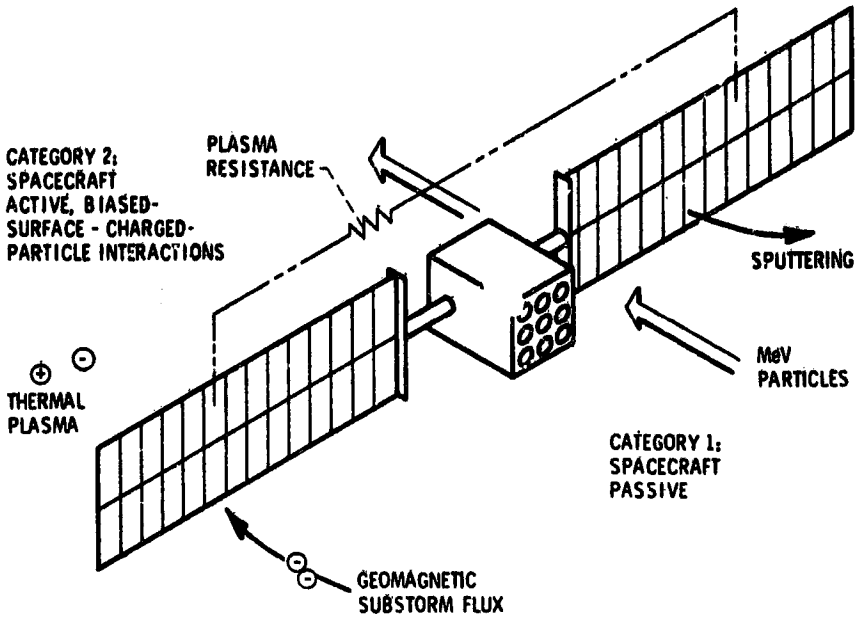

Figure 1. - Spacecraft-environment interactions.

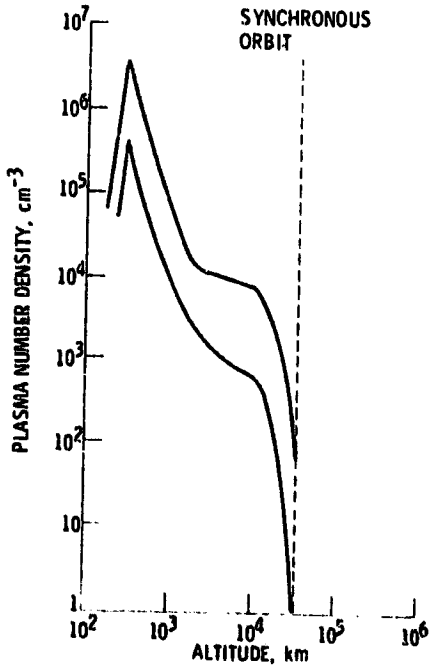

Figure 2. - Plasma number density as function of altitude in equatorial orbit. (From ref. 32.)

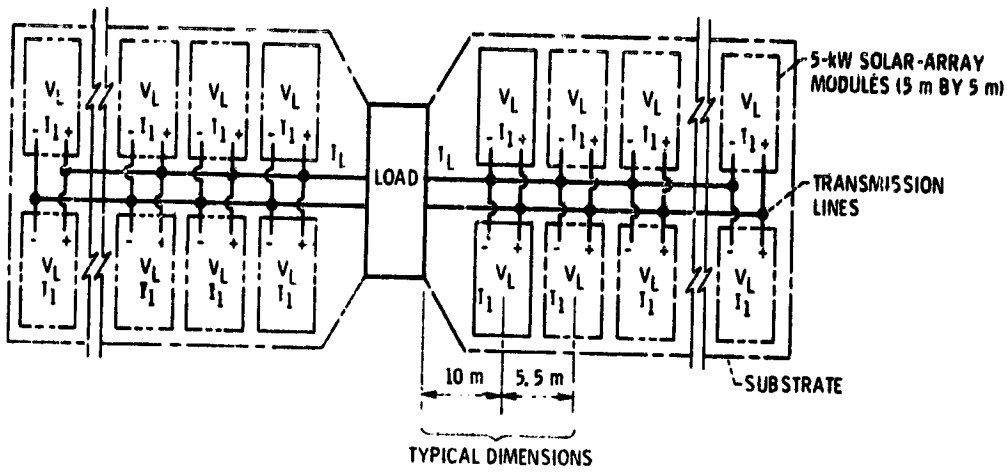

Figure 3. - Conceptual model of large space power system.

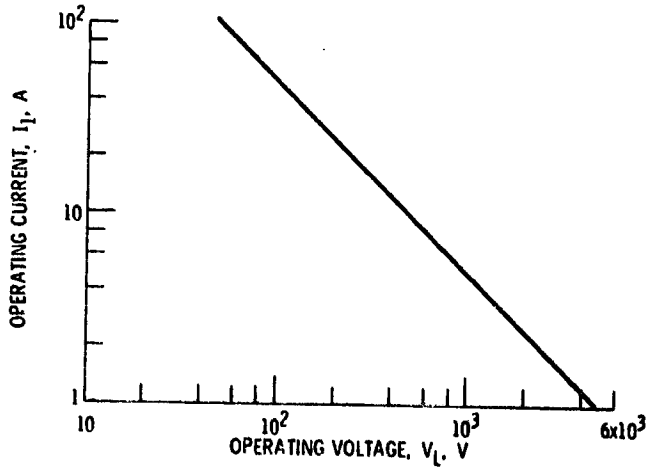

Figure 4. - Load characteristics for 5-kilowatt module.

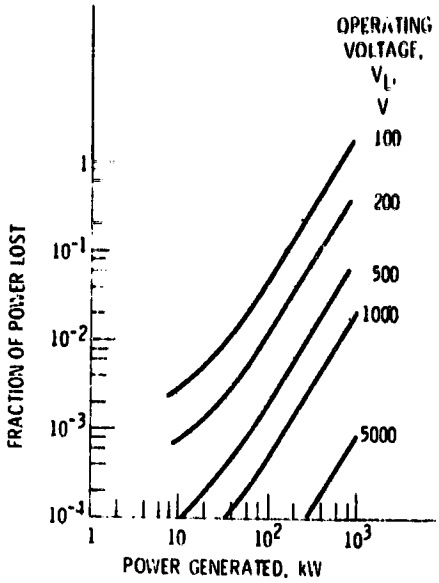

Figure 5. - Fraction of power lost in aluminum distribution lines with 1-square-centimeter cross-sectional area.

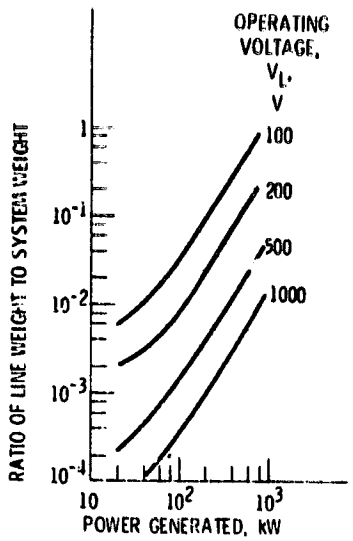

Figure 6. - Ratio of transmission line weight to design goal system weight for 5-percent power loss. Design goal, 10 kg/kW.

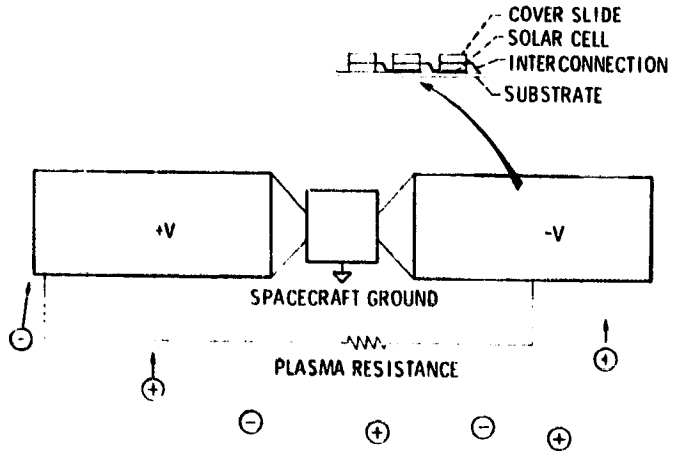

Figure 7. - Spacecraft higher-voltage-system - environment interactions.

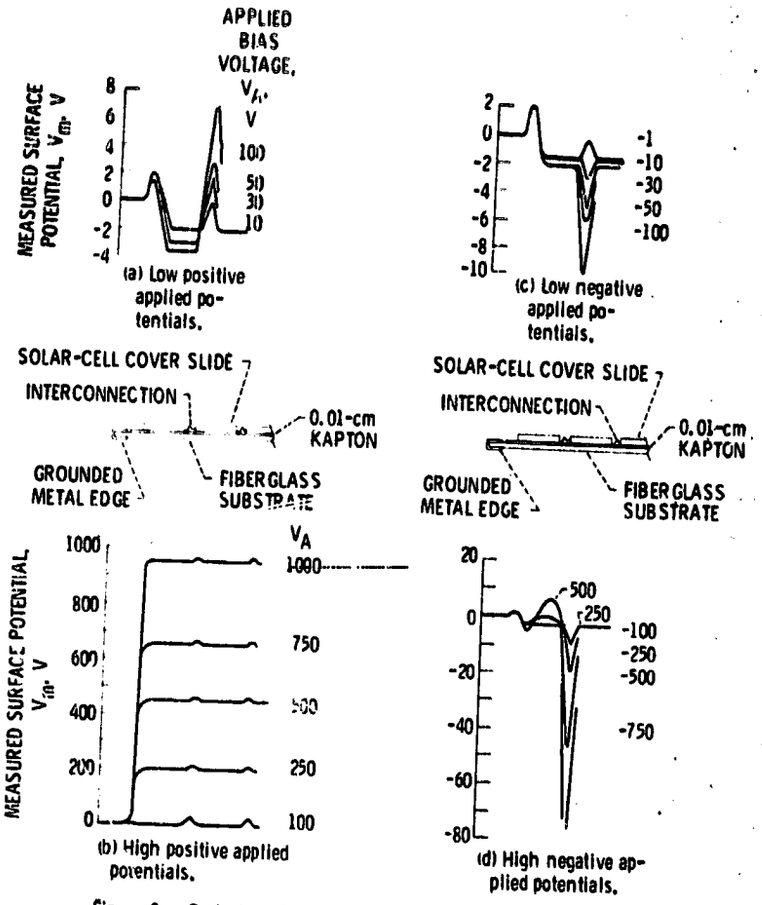

Figure 8. - Typical surface voltage profiles for a solar-array segment. (From ref. 32.)

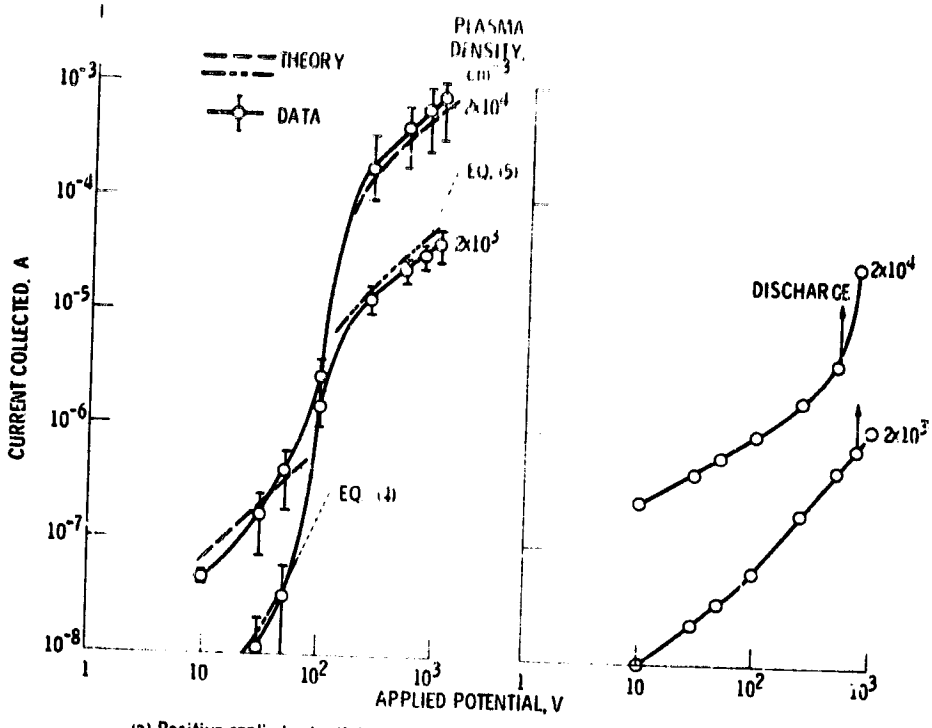

(a) Positive applied potentials.

(b) Negative applied potentials.

Figure 9. - Plasma coupling currents for solar-array experiment. (From ref. 32.)

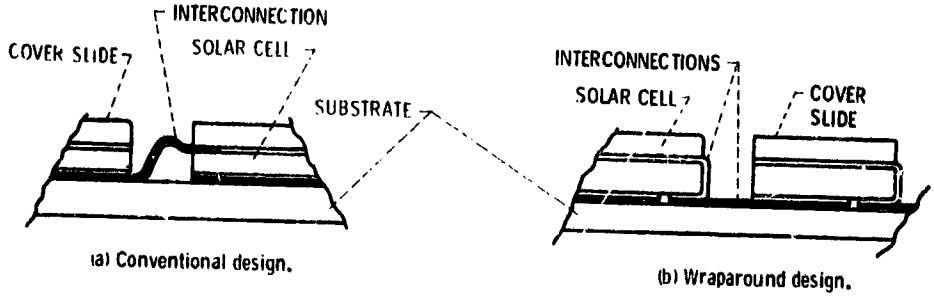

(a) Conventional design.

(b) Wraparound design.

Figure 10. - Solar-array interconnection configurations.

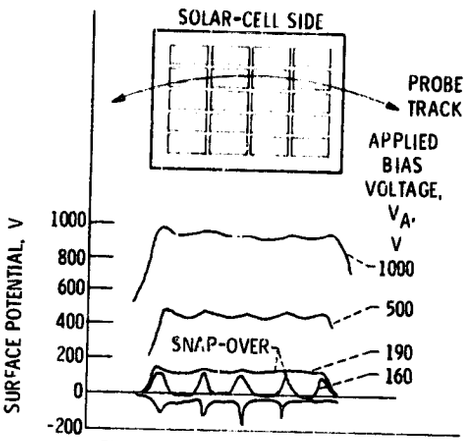

Figure 11. - Surface voltage profiles with wraparound interconnects. (From ref. 12.)

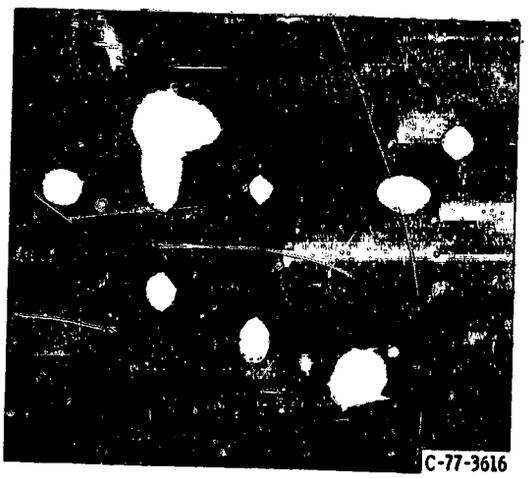

Figure 12. - Arcing on solar-cell array sample (cell side). Two-centimeter-by-4-centimeter wraparound cells on Kapton. (From ref. 32.)

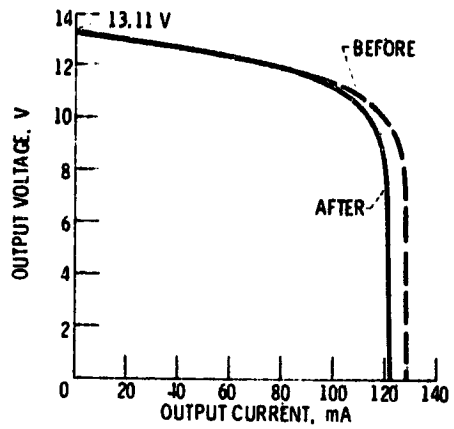

Figure 13. - Degradation in solar-array segment performance after 114-hour test at 4 kilovolts. Solar-array segment area, 100 cm^2; cell temperature, 49° C; light intensity, 135.3 mW/cm^2. (From ref. 28.)

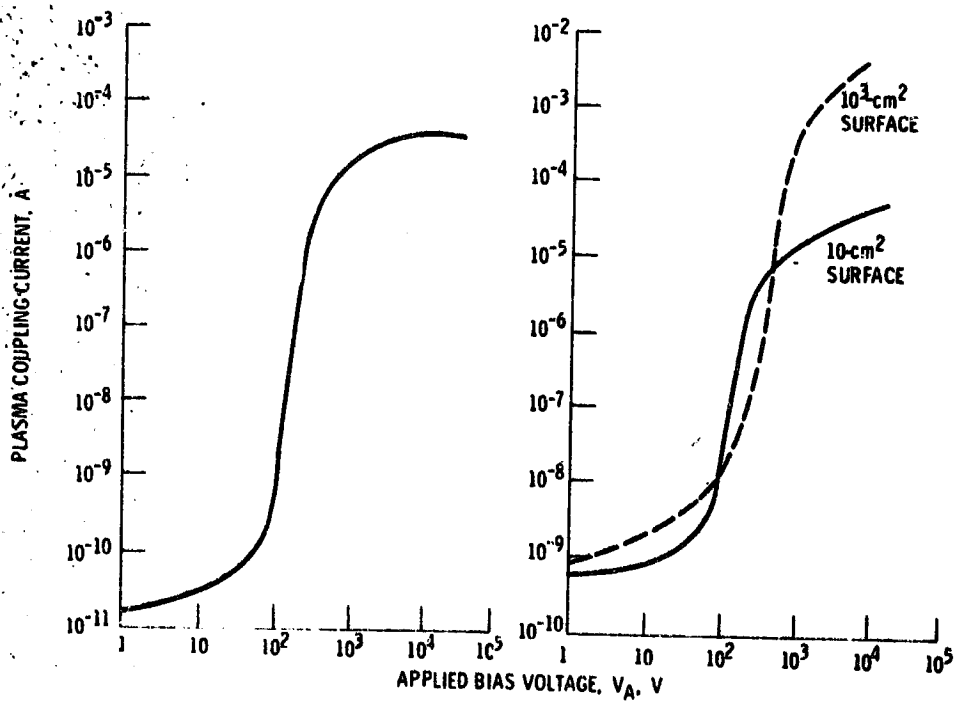

Figure 14. - Current collection phenomenon with pinhole in Kapton film. Plasma density, 1.7×10^4 cm^{-3}. Pinhole diameter, 0.038 cm.

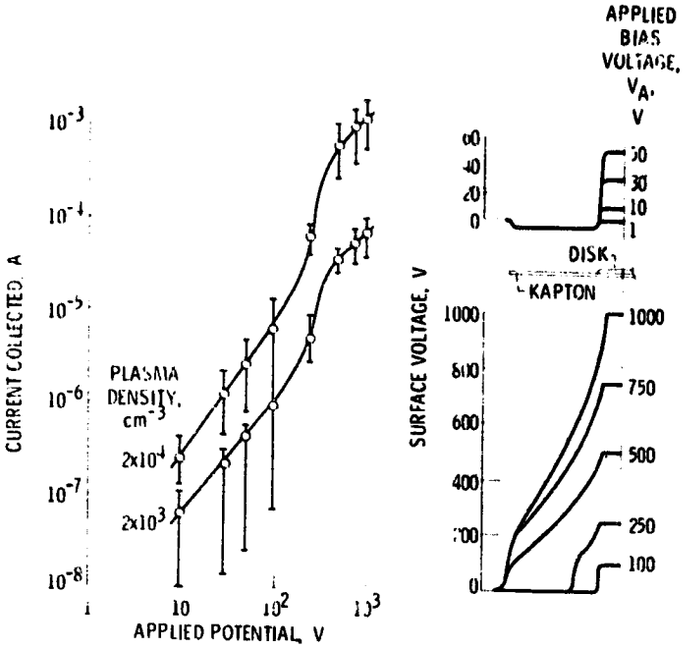

(a-1) Plasma coupling currents.

(a-2) Typical surface voltage profile.

(a) Positive applied potentials.

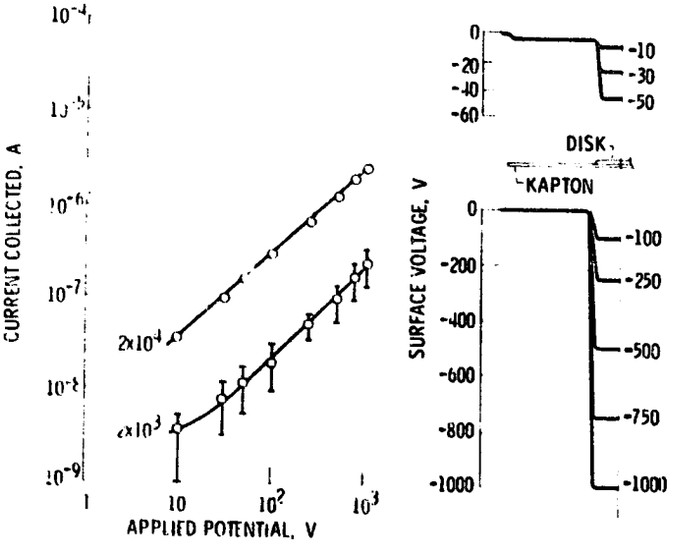

(b-1) Plasma coupling currents.

(b-2) Typical surface voltage profiles.

(b) Negative applied potential.

Figure 15. - Plasma interactions with metal disk on Kapton surface. (From ref. 32.)

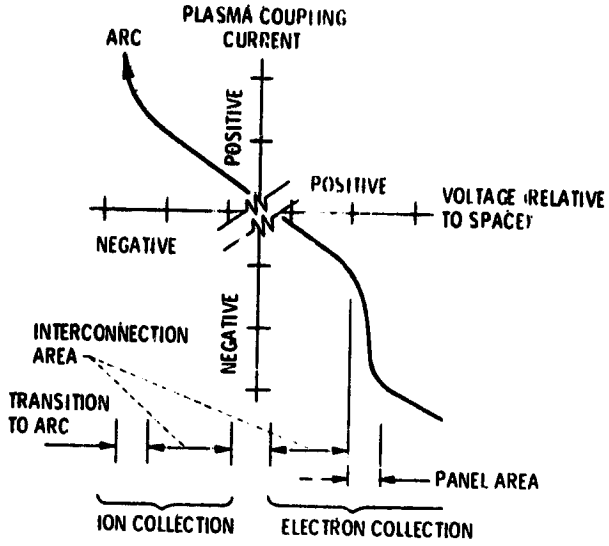

Figure 16. - Solar-array - charged-particle-environment interactions summary.

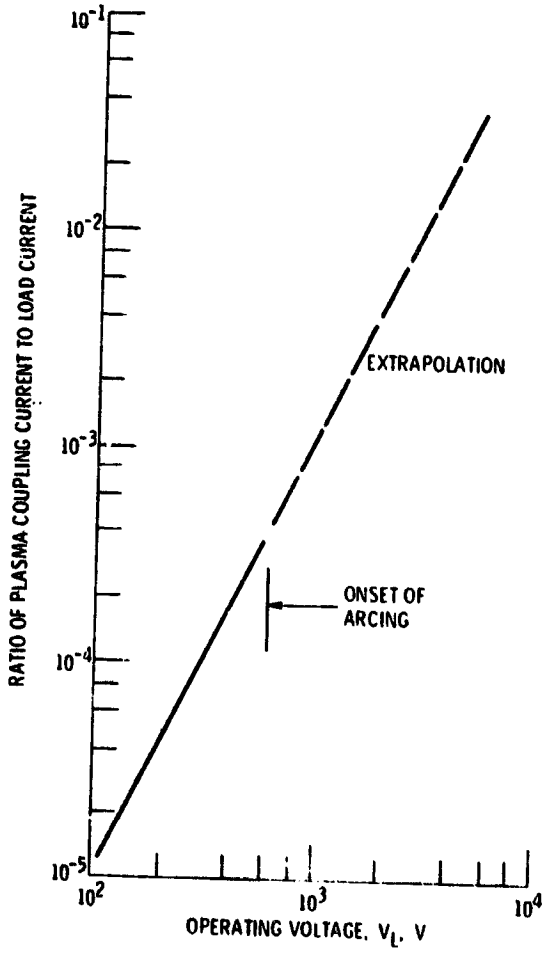

Figure 17. - Plasma coupling losses. All power levels; 400-km orbit. ($V_+ = 0.1\ V_L$; $V_- = 0.9\ V_L$.)

N79-24022

PLASMA INTERACTION EXPERIMENT (PIX) FLIGHT RESULTS

Norman T. Grier and N. John Stevens
NASA Lewis Research Center

SUMMARY

An auxiliary payload package called PIX (plasma interaction experiment) was launched on March 5, 1978, on the Landsat 3 launch vehicle to study interactions between the space charged-particle environment and surfaces at high applied positive and negative voltages (±1 kV). Three experimental surfaces were used in this package: a plain disk to act as a control, a disk on a Kapton sheet to determine the effect of surrounding insulation on current collection, and a small solar-array segment to evaluate the effect of distributing biased surfaces among an array of insulators. The package remained with the Delta second stage in a 920-kilometer polar orbit. Because of the constraint of real-time data acquisition, only half of the results from the 4 hours of PIX operations were recovered. The results did verify effects found in ground simulation testing: namely, that insulation can suppress electron current collection at voltages less than 250 volts and enhance it above 500 volts, that ion currents to a disk are not influenced by surrounding insulation, and that solar-array segments arc at negative bias voltages greater than -750 volts. The results of this experiment are discussed in detail in this paper.

INTRODUCTION

The design of space power systems has traditionally been conservative. These systems usually are constructed to generate power at 28 to 32 volts. For special applications, systems operating at 50 to 100 volts have been built and flown (e.g., refs. 1 to 3). This design philosophy is viable for the moderate power levels presently used (i.e., kilowatt levels), but trends for the future are toward larger and larger powers (refs. 4 to 6). If operating voltages for these larger systems are not increased, load currents will rise to a value where distribution losses could become prohibitive (ref. 7).

Increasing operating voltage levels above those currently used requires careful consideration. All space power systems have exposed conductors that are at some voltage level. These systems operate in a low-energy, charged-particle environment that ranges from about a million particles per cubic centimeter at low Earth orbit to about 10 particles per cubic centimeter at geosynchronous altitudes. Simple plasma probe theory (ref. 8) indicates that, in this type of environment, an exposed biased conductor will interact by collecting particles. At low operating voltages, particle collection will be negligible. However, as the voltage is increased, the particle collection can become significant and the effect should be considered (refs. 9 and 10).

High-voltage-surface - charged-particle environmental interactions have been studied for the past several years. Ground simulation studies conducted to determine the basic interactions (refs. 11 to 15) show that interactions can be strongly influenced by the presence of insulators around the biased conductors. When a positive bias voltage of a few hundred volts is applied to solar-array segments, the electron current collection is enhanced by orders of magnitude. When a negative bias voltage of a few hundred volts is applied, arcing occurs. In addition to these collection phenomena, there are unknown effects of long-term deposition of charge on insulators and of electrostatically enhanced contamination. All these factors will influence the performance of large space power systems and should be understood and accounted for in the early system-design phases.

The ground simulation results that supported the concern over these interactions usually were criticized as being influenced by facility effects. It has been suggested that tank walls could influence the interactions and that both the ambient-pressure and plasma-environment simulations do not correspond to actual space conditions. If tank-wall effects are dominant, such interactions might not exist in space. The first flight experiment to investigate these interactions in space was a free-flying satellite called SPHINX, an acronym for space plasma - high-voltage interaction experiment (ref. 16). The satellite was built and qualified but was lost when the Titan-Centaur proof flight failed to place the payload into orbit in February 1974.

The investigation of the interactions continued, but no opportunities to obtain flight experiments arose until recently. An auxiliary payload experiment was proposed and accepted for the Landsat 3 mission. This package was called PIX, an acronym standing for plasma interaction experiment. On the Landsat 3 mission, PIX was permanently attached to the Delta second stage so that the experiment was conducted in the 900-kilometer polar orbit of that stage. The experiment was automatically sequenced, starting just after the Landsat separated and ending at the depletion of the batteries. The Delta telemetry system was used to transmit the data to Earth, but only with real-time data recovery. The mission was launched and the PIX operated on March 5, 1978. It was known that this experiment would result only in relatively short-time interaction data in a limited range of plasma densities. However, it was believed that these first space results would provide sufficient data for a meaningful comparison to ground simulation results and would verify the existence of the interactions.

In this paper the PIX package is briefly described and the flight results are presented and discussed. The correlation between the flight data and the ground simulation data is also given.

DESCRIPTION OF PIX

The plasma interaction experiment was designed to determine the biased-conductor current collection from space environments when the conductor is surrounded by insulators and to obtain space data to compare with results of

ground simulation tests. The resulting package and its mounting on the Delta second stage are shown in figure 1. A block diagram of PIX is shown in figure 2.

The PIX consisted of two main parts: the electronics enclosure and the experiment plate. These parts were mounted 90° apart on the Delta second stage. The electronics enclosure housed the bias power supply, three electrically floating current sensors, the switches, the battery, the power conditioner, and the sequencer. The sequencer acted as the experiment controller and as the interface with the Delta telemetry system. These components are described in detail in reference 17.

Three experimental surfaces were used on PIX: a plain disk, a disk on Kapton, and a solar-array segment. The plain-disk experiment, consisted of a gold-plated metal disk 3 centimeters in diameter (area, ~10 cm^2) mounted on, but electrically isolated from, the grounded exterior of the electronics enclosure. This experiment was to act as a control. Because of the auxiliary payload nature of PIX, components had to be minimized and deployables were forbidden. Plasma diagnostic devices to measure environmental conditions, therefore, had to be minimized. It was anticipated that the plain disk would behave well. This would allow comparative measurements to the other surfaces with insulating surroundings and provide, at least, an indicator of plasma conditions.

The other two surfaces were mounted on, but electrically isolated from, the experiment plate. The disk-on-Kapton experiment consisted of a gold-plated metal disk, identical to the plain disk, mounted on a 20-centimeter-diameter (area, ~325 cm^2), 5-mil-thick Kapton sheet. By comparing the data from this experiment with the plain-disk results, the influence of the Kapton sheet on current collection could be determined. The solar-array experiment consisted of a series string of twenty-four 2-centimeter-by-2-centimeter, 10-ohm-centimeter silicon solar cells with fused silica cover glass (area, ~100 cm^2) mounted on a fiberglass board. Conventional bar interconnections (area, ~5 cm^2) were used in this array. These interconnections were connected to the bias power supply and formed the current collection area. By comparing the data from this experiment with the plain-disk results, the effect of distributing a biased conductor among insulating surfaces could be determined.

Each experiment was connected to a separate current sensor that was biased by the power supply (fig. 2). Both positive and negative voltage steps from 0 to 1000 volts could be selected. The plain-disk experiment was constantly biased. Either the disk-on-Kapton or the solar-array segment was also biased. When one of these two experiments was connected to the power supply, the other current sensor was switched to a known resistor to calibrate that sensor. The separation distance between the plain disk and the other experiments on the experiment plate was sufficient to ensure that there would be no interaction between the two operating experiments at the anticipated plasma densities.

The PIX experimental surfaces were subjected to testing in ground simulation facilities before launch (ref. 18). In addition, the flight package was tested in a plasma environment to verify that the experiments would function properly and to obtain additional data for comparison with flight results.

PIX FLIGHT OPERATIONS

The PIX was carried into orbit on March 5, 1978, on the Landsat 3 launch vehicle. The orbital parameters achieved for the Delta second stage and PIX were

Altitude, km	920±15
Inclination, deg	99
Period, min	103

The experimental sequence started 20 seconds after Landsat separation, or at 19:08:47 universal time (UT). The operational sequence used for PIX is shown in figure 3. Phase 1 of the experiment required the bias power supply to be at 526 volts for 12 minutes. This total time was divided into 2-minute intervals during which first the solar-array segment was biased and then the disk-on-Kapton experiment. Unfortunately, during this phase the Delta was maneuvering to release a second auxiliary payload, Oscar, and then reorienting to meet the PIX requirement that the experiment plate be shadowed.

Phase 2 of the experiment started at 19:20 UT and continued for about 4 hours, after which time the telemetry system on the Delta no longer functioned. The cycle consisted of 1-minute positive voltage steps of 120, 256, 526, and 1004 volts, first with the disk-on-Kapton experiment biased and then with the solar-array experiment biased. The power supply was then held at 0 volt for 1 minute for an internal calibration of all three current sensors. Then, 1-minute negative voltage steps of -120, -256, -526, -734, and -1004 volts were applied first to the solar-array experiment and then to the disk-on-Kapton experiment. Calibration was then repeated. The total cycle time was 20 minutes, and 12 cycles were known to have been completed. The data from PIX were obtained only when the Delta was in range of either Air Force or NASA ground stations. Approximately half of the data were retrieved by these stations. The telemetry coverage for the PIX is shown in figure 3.

FLIGHT RESULTS

All the flight data under equilibrium current collection conditions, obtained for phase 2, are given in figure 4 as plasma coupling current as a function of applied voltage. The telemetry frame rate for all the PIX data was one frame per second. Sixty data points were received at each voltage level during phase 2. One-hundred-and-twenty data points were received before each experiment was switched during phase 1. The transient data showed that the coupling current reached equilibrium within a few seconds after the voltage was applied. The 1-minute hold time at each voltage level was demonstrated to be more than adequate. The latitudes of PIX for the particular cycle are also given in figure 4. Data for cycles 4 and 9 and part of cycle 10 were obtained when PIX was in the Earth's shadow.

For phase 1 operation, where the voltage was held constant at 526 volts, the equilibrium currents were the following:

Disk-on-Kapton current, A	3×10^{-4} to 7×10^{-4}
Solar-array-segment current, A	6×10^{-4} to 9×10^{-4}
Plain-disk current, A	$<1\times10^{-7}$

The very low current for the plain-disk experiment was probably caused by the plain disk being partially in the satellite wake and the spacecraft ground becoming negatively biased. This effect is explained in detail in the section DISCUSSION.

Sun angle data obtained for the Delta indicated that the proper attitude was achieved approximately 3 minutes into phase 2 of PIX operations. This attitude placed the electronic enclosure box, the plain-disk experiment, and part of the back of the experiment plate in direct sunlight. Sun positions and velocity vectors for phase 1 operations and cycles 1 and 2 of phase 2 operations are shown in figure 5. Since the Delta's attitude control battery was depleted 42 minutes after PIX was activated, attitude and velocity data were received only through part of cycle 2. However, from the temperature data, it is known that the electronic enclosure box cover was 20 to 30 degrees F hotter than the experiment plate during the sunlit portion of PIX's orbit. Since this temperature trend continued throughout the operating life, PIX's attitude relative to the Sun probably remained fixed beyond the 42 minutes.

DISCUSSION

Phase 2 results are discussed first, since understanding these data leads to an explanation of phase 1 data. Phase 2 data are presented in figure 4 in the order received: namely, disk on Kapton positively biased, solar-array segment positively biased, solar-array segment negatively biased, and disk on Kapton negatively biased for each cycle (fig. 3). The phase 2 data for each experiment are discussed separately.

Phase 2 Operations

Plain-disk experiment (positive bias). - A plain disk surrounded by spacecraft ground was chosen to serve as a control. This configuration was expected to have a predictable current-voltage behavior. However, from figure 4, it is evident that for positive bias the plain disk exhibited unanticipated behavior at the 500- and 1000-volt levels. With the exception of cycle 11, where the disk-on-Kapton current was low, the plain-disk current at the 500- and 1000-volt levels either decreased drastically (cycles 6B, 10B, and 12A) or decreased gradually (cycles 2, 7, 11, and 12B). The power supply had an output of at least 3 milliamperes, so the decreases were probably not caused by power supply limitations. The calibration modes in the electrometer always indicated that the current sensors were working properly. Therefore, it was concluded that the whole spacecraft became negatively charged and hindered electron collection.

However, for most of the cycles the current measured at the 120- and 256-volt levels was in the range expected. From these date the average plasma density was estimated to be ~2.0×10^4 electrons/cm^3 (for the literature value of temperature, 2000 K).

The electron current collected by the positively biased experimental surfaces had to be balanced by the ion current collected by the rest of the spacecraft's grounded surfaces. However, there was only limited exposed grounded metal area on the Delta second stage and the PIX satellite packages (experiment plate and enclosure box cover) to act as ion collectors. When positive voltages of 500 and 1000 volts were applied to the experimental surfaces, the exposed grounded structure was not large enough to collect sufficient ions to balance the electron current and still remain at zero potential. So, the spacecraft ground floated negatively with respect to the plasma. This retarded the electron collection and enhanced the ion collection to balance the currents. The plain disk, being relatively small with a large surrounding grounded surface, experienced a larger reduction in electron current than either the solar-array-segment or the disk-on-Kapton experiments.

To determine the decrease in the electron collection caused by a negative voltage on the PIX experiment plate and electronic enclosure box cover, the engineering model of these surfaces was placed in a ground simulation facility at Lewis and tested with the structures negatively biased. The current to the samples was measured for various negative potentials on the structure. The plasma density used in this test was approximately 3×10^4 electrons/cm^3. The results are shown in figure 6. The ordinate is the ratio of the measured current to the current with the structure at zero potential I/I_0. This ratio is presented as a function of structure negative bias voltage, with several positive bias voltages given on the samples.

Figure 6(a) can be used to estimate the negative floating voltage for the grounded surfaces on PIX and the Delta second stage for those cycles that showed a gradual decrease in electron current. It must be assumed first that the flight current readings for 120 and 256 volts are correct. The slope found at these two voltages is used to extrapolate the flight current data to 1000 volts. These extrapolated currents for 500 and 1000 volts are used for I_0 at these two voltages and the actual flight data are used for I to form the ratio I/I_0 for use in figure 6(a) to determine the spacecraft potential. The results are given in table I and show that PIX floated as high as 30 volts negative.

Data from cycle 7 were chosen for comparison with ground-simulation data. For this cycle, data points were obtained for each voltage level and, except for the gradual decrease in electron current, no other unusual behavior was noticed. Figure 7(a) shows the flight-adjusted coupling current and the preflight ground simulation current for the plain disk as a function of applied voltage. The agreement is within a factor of 2, which is within the uncertainty of the measurement. The ground simulation data were obtained with a plasma density of approximately 2×10^4 electrons/cm^3.

This explanation for the gradual decrease in electron current for positive bias leads to a possible explanation for the steep drop in the plain-disk electron current shown for cycles 6B, 10B, and 12A in figure 4. Ground tests on the engineering model of the PIX electronic enclosure were performed with the plasma density decreased by an order of magnitude to $\sim 2\times10^4$ electrons/cm^3. The enclosure was negatively biased while the disk was positively biased to 1000 volts. The electron current to the disk was measured. The results are shown in figure 8. A negative bias of -15 volts completely cut off the electron current for all positive voltages to 1000 volts. Similar tests performed at this plasma density on the experiment-plate engineering model showed that the current to the disk-on-Kapton and the solar-array-segment experiments was lower than in the higher density test but was not completely cut off. The results given in references 19 and 20 indicated that, in the wake of a satellite, the plasma density may be a factor of 10 or more lower than at other positions around the satellite. Therefore, if during these cycles the plain disk were in the spacecraft wake, the combination of lower plasma density and a ground potential of greater than -15 volts would cause the current to the disk to be cut off.

Plain-disk experiment (negative bias). - The results for negative bias on the plain disk shown in figure 4 were as anticipated. The current varied approximately linearly in each cycle. Figure 9(a) shows the cycle 6 data and the preflight ground simulation results. The preflight ground test results are for a plasma density of approximately 2×10^4 electrons/cm^3. Cycle 6 data were chosen for comparison because they are typical of the flight results. In addition, they were taken at a time nearest to cycle 7, which was used in the positive-bias comparison. The same ground simulation with the same plasma number density could thus be used in the comparisons.

Disk-on-Kapton experiment (positive bias). - The purpose of the disk-on-Kapton experiment was to determine whether or not the Kapton insulator enhanced electron collection in space, as has been observed in ground tests. With the exception of cycle 10, the flight data showed a large increase in current at the 500- and 1000-volt levels. In cycles 1 and 2, the 1000-volt current was high enough to trip the power supply. From these results, it appears that Kapton does enhance the electron collection at the higher voltage levels tested.

The positive-bias flight test data for the disk-on-Kapton experiment also showed the influence due to the negative bias on the spacecraft at the 500- and 1000-volt levels. The currents were lower than expected for these voltage levels. However, the currents can be adjusted for this by using table I and figure 6(c). This was done for cycle 7 (fig. 7(b)). Figure 7(b) also shows the preflight ground simulation results for a plasma density of 2×10^4 electrons/cm^3. The adjusted electron current and the preflight results are within a factor of 2 throughout the voltage range. This is within the uncertainty of the measurements.

For all cycles except 10 and 12, the plain-disk current was larger than the disk-on-Kapton current at the 100- and 256-volt levels (fig. 4). This difference was also observed in all the ground simulations. This implies that Kapton suppresses electron collection at low voltages but enhances it at high

voltages. In ground simulations the transition from suppression to enhancement always occurred below 1000 volts (ref. 18). The flight results agree with this transition.

The dip in electron current observed in cycles 10 and 11 is not understood at this time. Current sensor checks made before and after these tests indicated that sensors were performing properly.

Disk-on-Kapton experiment (negative bias). - It was expected that the Kapton insulator would have no effect on the ion current at negative voltages. The flight currents obtained from this surface were close to those of the plain disk. The ground simulation ion current, as a function of negative voltage, is from one-half to one-third less than the flight data for cycle 6. Nitrogen ions were used as the plasma ions in the ground simulation. In flight the ions are O^+, He^+, and H^+. Because of this and the uncertainty of the flight experiments' positions relative to the ram or wake, the agreement is believed to be within the uncertainty of the experimental measurements.

Solar-array-segment experiment (positive bias). - The solar-array-segment experiment was designed to determine the effect of a distribution of insulators and electrodes on the current. Ground simulations have shown (ref. 18) that a solar array should collect charges from a plasma in a manner similar to the disk-on-Kapton experiment. Figure 4 substantiates these ground simulation results. In each positive-bias cycle, the electron current was low (suppressed) at the 120- and 256-volt levels and increased sharply (enhanced) at the higher voltages. However, in cycle 6 the current decreased at the 1000-volt level from its value at the 526-volt level. Also, some other cycles had lower-than-expected currents at 1000 volts. Both phenomena are believed to be caused by the spacecraft's ground surfaces becoming negatively biased, as explained earlier.

Figure 7(c) shows the solar-array current for cycle 7 after it was adjusted for the negative bias on the spacecraft ground. Also shown are the preflight ground simulation results for the solar array with a plasma density of $\sim 2 \times 10^4$ electrons/cm^3. The largest discrepancy occurs at the two lowest voltages, where the difference is between a factor of 4 and 7. However, no conclusion can be drawn from this since the amount of suppression at the low voltages can be random. This was observed in ground data and can also be seen in the flight data given in figure 4.

Solar-array experiment (negative bias). - In all the negatively biased flight cycles, the solar array arced at the -1000-volt setting and tripped off the power supply. This agrees with preflight ground simulation results in that arcs always tripped the power supply at the -1000-volt level. In some ground simulations, arcing was preceded by a larger-than-normal increase in ion current at the previous lower voltage. This phenomenon was observed in the flight data from cycle 6, where a much larger-than-expected rise in current occurred at -500 volts.

Cycle 6 ion current data and the preflight data taken at plasma density of $\sim 2 \times 10^4$ electrons/cm^3 are shown in figure 9(c). The preflight data are one-

third lower than the flight data at the lower voltages. This is within the expected range for these voltage levels. In this particular preflight simulation, arcing occurred at the -734-volt level and tripped off the power supply.

Phase 1 Discussion

The data obtained for phase 1 operation can now be understood more clearly. The plain-disk current was very low, and the disk-on-Kapton and solar-array-segment currents were normal. During phase 1 operations, the experiment plate with the disk-on-Kapton and solar-array-segment experiments faced in the velocity ram direction of the spacecraft, and the electronic enclosure box with the plain-disk experiment was partially in the wake. The low current collected by the plain disk was probably caused by the whole spacecraft's grounded surfaces floating negatively, in addition to the low-density environment around the plain disk.

CONCLUSIONS

The plasma interaction experiment (PIX) operated successfully for 4 hours in a nearly circular polar orbit at an altitude of about 920 kilometers. All the electronic packages on board operated for at least 4 hours. The following conclusions concerning spacecraft-plasma interactions were drawn from the results of the PIX experiments:

1. An insulator surrounding a positively biased electrode suppresses electron collection at voltages below 256 volts and enhances electron collection at voltages above 500 volts.

2. Ion currents to negatively biased electrodes are not influenced by surrounding insulation. The ion current depends only on the size of the electrodes, the bias voltage, the spacecraft velocity, and the plasma properties.

3. A solar-array segment, when biased to negative voltages greater than -700 volts, discharges and generates currents greater than 3 milliamperes. The normal current level expected at these voltages is less than 10 microamperes.

4. A large metal surface biased at a relative low negative voltage ($<$-30 V) surrounding a relatively high positively biased (500 to 1000 V) small electrode can drastically reduce the electron current to the electrode and may at times completely cut off the electron current. The reduction is proportional to the ratio of electrode area to surrounding metal surface area.

These phenomena occurred in space and agree with those observed in ground simulation facilities. For these sample sizes, voltage ranges, and plasma densities, the ground-simulation-facility results reproduce the flight data. Therefore, detailed studies can be conducted in ground simulation facilities and the results used confidently in space applications. However, caution must

be exercised in extending ground data to larger samples and higher voltages than reported herein. As samples get larger or voltages get higher, the sheaths may extend to the walls in ground facilities, limiting current collection and influencing test results. Large samples and higher bias-voltage effects still must be determined in space to develop scaling laws for very large systems.

The PIX operated over a much shorter time than the multiyear lifetime of proposed satellites. Long-term effects may change the surface characteristic and reduce the arcing for negatively biased arrays or change the suppression-enhancement characteristic for positively biased arrays and electrodes. These effects should be evaluated in ground facilities and verified by space flight tests.

REFERENCES

1. Siegert, Clifford E.: Development History and Flight Performance of Sert II Solar Array. NASA TM X-2246, 1971.

2. Raine, H. R.: The Communications Technology Satellite Flight Performance. IAF Paper 76-223, Oct. 1976.

3. Woosely, A. P.; Smith, O. B.; and Nassen, H. S.: Skylab Technology Electrical Power System. AAS Paper 74-129, Aug. 1974.

4. Woodcock, G. R.: Solar Satellites, Space Key to Our Future. Astronaut. Aeronaut., vol. 15, no. 7/8, July-Aug. 1977, pp. 30-43.

5. Satellite Power System (SPS) Feasibility Study. (SD76-SA-0239-1, Rockwell International Corp.; NASA Contract NAS8-32161.) NASA CR-150439, 1976.

6. Systems Definition on Space-Based Power Conversion Systems. (D180-20309-1, Boeing Aerospace Co.; NASA Contract NAS8-31628.) NASA CR-150209, 1977.

7. Stevens, N. John: Spacecraft - Charged-Particle Environmental Interactions. Spacecraft Charging Technology - 1978. NASA CP-2071, 1979.

8. Chen, F. F.: Electric Probes. Plasma Diagnostic Techniques, R. H. Huddlestone and S. L. Leonard, eds., Pure and Applied Physics, Vol. 21, Academic Press, Inc., 1965, pp. 113-200.

9. Knauer, W.; et al.: High Voltage Solar Array Study. (Hughes Research Labs.; NASA Contract NA33-11535.) NASA CR-72675, 1970.

10. Springgate, W. F.; and Oman, H.: High Voltage Solar Array Study. (D2-121734-1, Boeing Co.; NASA Contract NAS3-11534.) NASA CR-72674, 1969.

11. Cole, Robert K.; Ogawa, H. S.; and Sellen, J. M., Jr.: Operation of Solar Cell Arrays in Dilute Streaming Plasmas. (TRW-09357-6006-R000, TRW Systems; NASA Contract NAS3-10612.) NASA CR-72376, 1968.

12. Herron, B. G.; Bayless, J. R.; and Worden, J. D.: High Voltage Solar Array Technology. AIAA Paper 72-443, Apr. 1972.

13. Kennerud, K. L.: High Voltage Solar Array Experiments. (Boeing Co.; NASA Contract NAS3-14364.) NASA CR-121280, 1974.

14. Domitz, Stanley; and Grier, Norman T.: The Interaction of Spacecraft High Voltage Power Systems with the Space Plasma Environment. Power Electronics Specialists Conference, Institute of Electrical Engineers, Inc., 1974, pp. 62-69.

15. Grier, Norman T.; and Domitz, Stanley: Current From a Dilute Plasma Measured Through Holes in Insulators. NASA TN D-8111, 1975.

16. Stevens, N. John: Solar Array Experiments on the SPHINX Satellite. NASA TM X-71458, 1973.

17. Ignaczak, L. R.; et al.: The Plasma Interaction Experiment (PIX) Description and Test Program - Electrometers. NASA TM-78863, 1978.

18. Stevens, N. J.; et al.: Investigation of High Voltage Spacecraft System Interactions with Plasma Environments. AIAA Paper 78-672, Apr. 1978.

19. Samir, U.; and Wrenn, G. L.: The Dependence of Charge and Potential Distribution Around a Spacecraft on Ionic Composition. Planet. Space Sci., vol. 17, Apr. 1969, pp. 693-706.

20. Samir, Uri: A Possible Explanation of a Order of Magnitude Discrepancy in Electron-Wake Measurements. J. Geophys. Res., vol. 75, Feb. 1, 1970, pp. 855-858.

TABLE I. - CALCULATED SPACECRAFT

FLOATING POTENTIALS

Cycle	Experiments active[a]	PIX power supply voltage, V	Spacecraft potential, V
2	D/K and PD	500	-7.5
	SA and PD	500	-13
	SA and PD	1000	-22
7	D/K and PD	500	-13
	D/K and PD	1000	-23
	SA and PD	500	-15
	SA and PD	1000	-30
11	SA and PD	500	-9
	SA and PD	1000	-26
12	SA and PD	500	-9
	SA and PD	1000	-23

[a]D/K denotes disk-on-Kapton experiment; PD denotes plain-disk experiment; SA denotes solar-array-segment experiment.

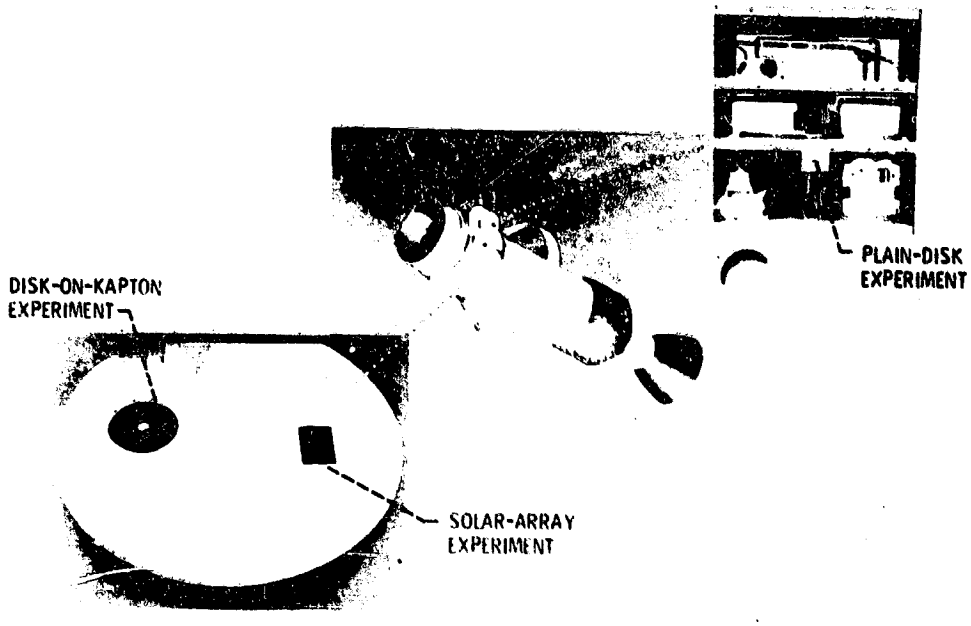

Figure 1. - Plasma interaction experiment (PIX).

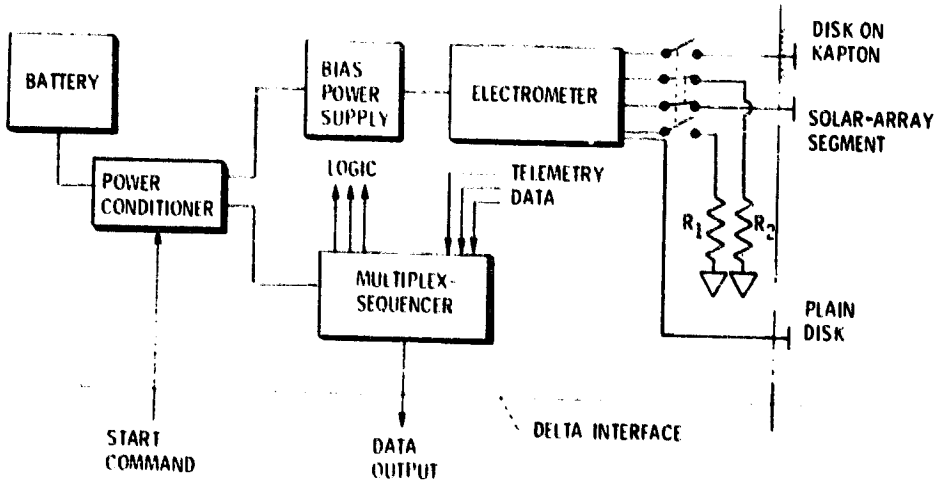

Figure 2. - Schematic diagram of plasma interaction experiment.

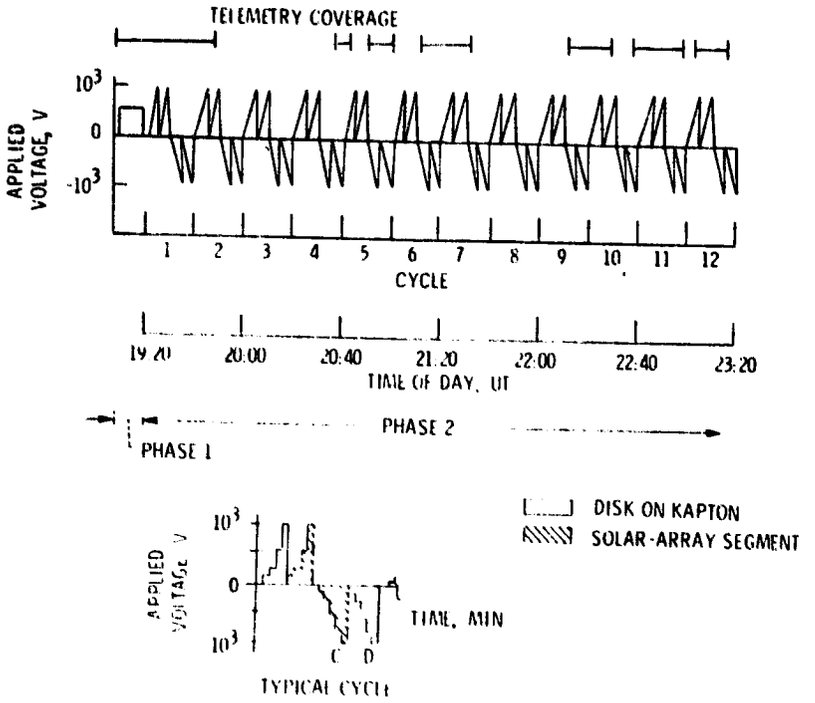

Figure 3. Operational sequence of plasma interaction experiment.

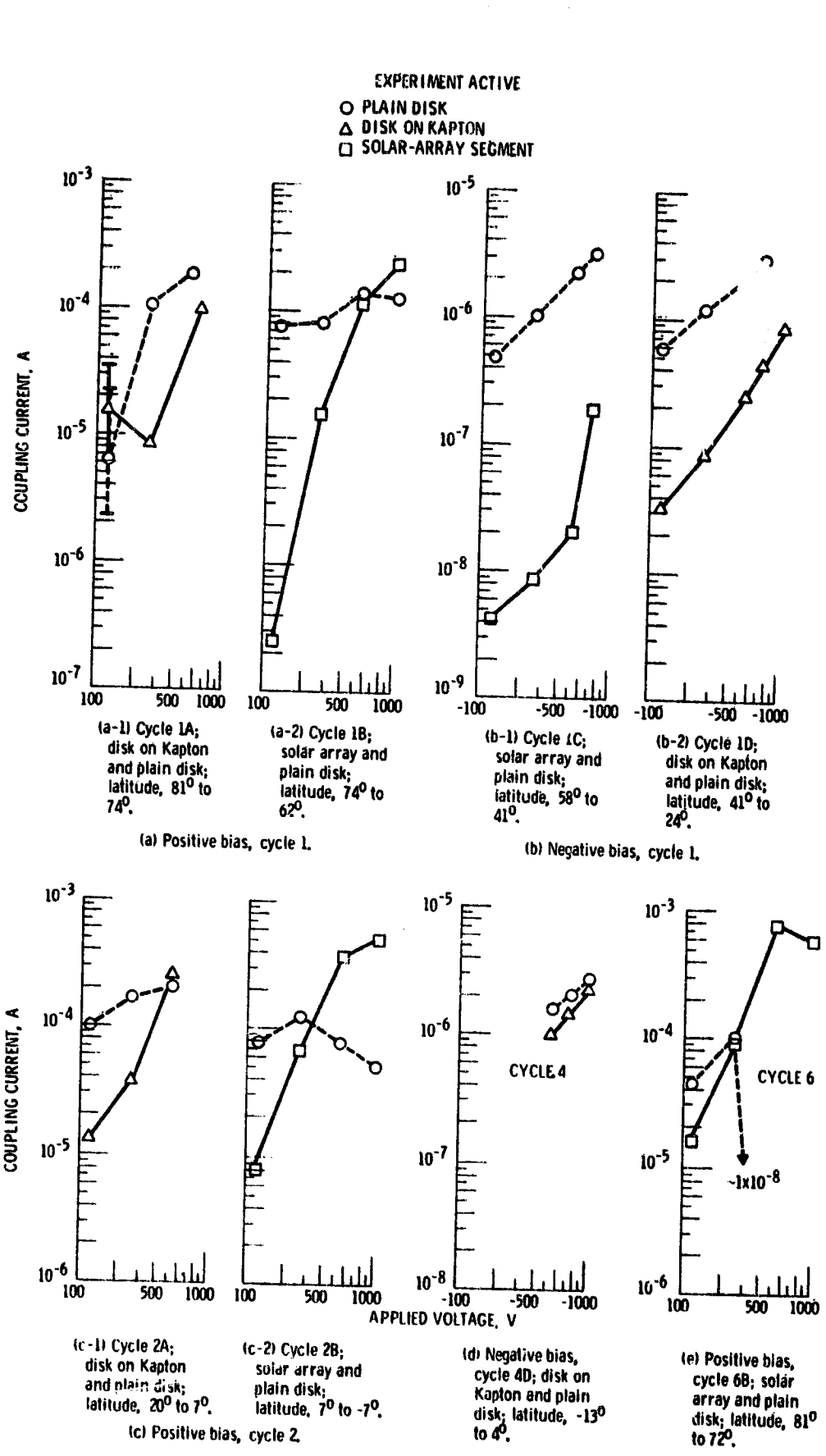

(a-1) Cycle 1A; disk on Kapton and plain disk; latitude, 81° to 74°.

(a-2) Cycle 1B; solar array and plain disk; latitude, 74° to 62°.

(a) Positive bias, cycle 1.

(b-1) Cycle 1C; solar array and plain disk; latitude, 58° to 41°.

(b-2) Cycle 1D; disk on Kapton and plain disk; latitude, 41° to 24°.

(b) Negative bias, cycle 1.

(c-1) Cycle 2A; disk on Kapton and plain disk; latitude, 20° to 7°.

(c-2) Cycle 2B; solar array and plain disk; latitude, 7° to -7°.

(c) Positive bias, cycle 2.

(d) Negative bias, cycle 4D; disk on Kapton and plain disk; latitude, -13° to 4°.

(e) Positive bias, cycle 6B; solar array and plain disk; latitude, 81° to 72°.

Figure 4. - Coupling current for PIX experiments as function of applied voltage at all voltage cycles received.

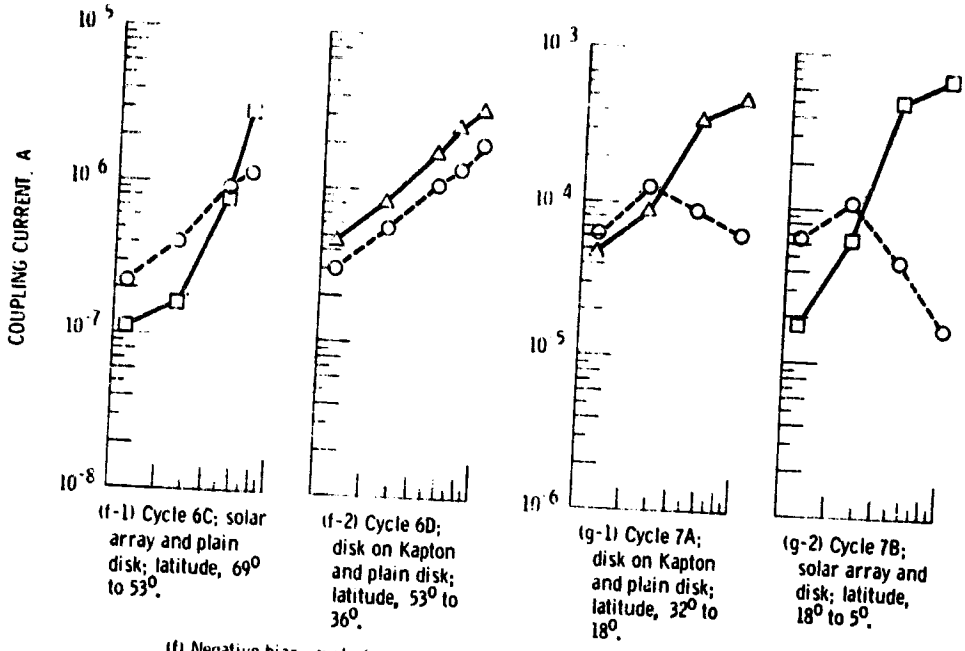

(f-1) Cycle 6C; solar array and plain disk; latitude, 69° to 53°.

(f-2) Cycle 6D; disk on Kapton and plain disk; latitude, 53° to 36°.

(f) Negative bias, cycle 6.

(g-1) Cycle 7A; disk on Kapton and plain disk; latitude, 32° to 18°.

(g-2) Cycle 7B; solar array and disk; latitude, 18° to 5°.

(g) Positive bias, cycle 7.

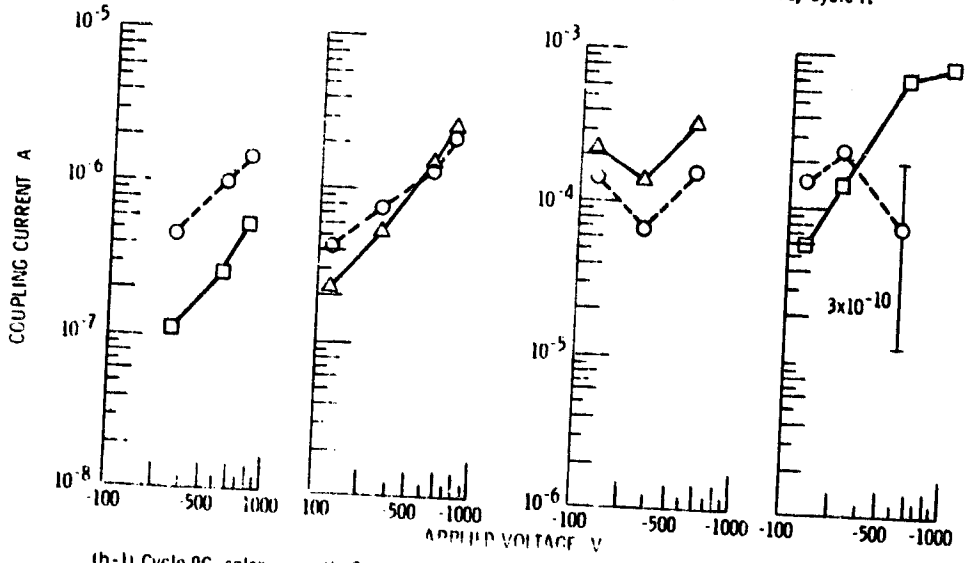

(h-1) Cycle 9C; solar array and plain disk; latitude, -41° to -24°.

(h-2) Cycle 9D; disk on Kapton and plain disk; latitude, -24° to -7°.

(h) Negative bias, cycle 9.

(i-1) Cycle 10A; disk on Kapton and plain disk; latitude, 4° to 10°.

(i-2) Cycle 10B; solar array and disk; latitude, 10° to 24°.

(i) Positive bias, cycle 10.

Figure 4. - Continued.

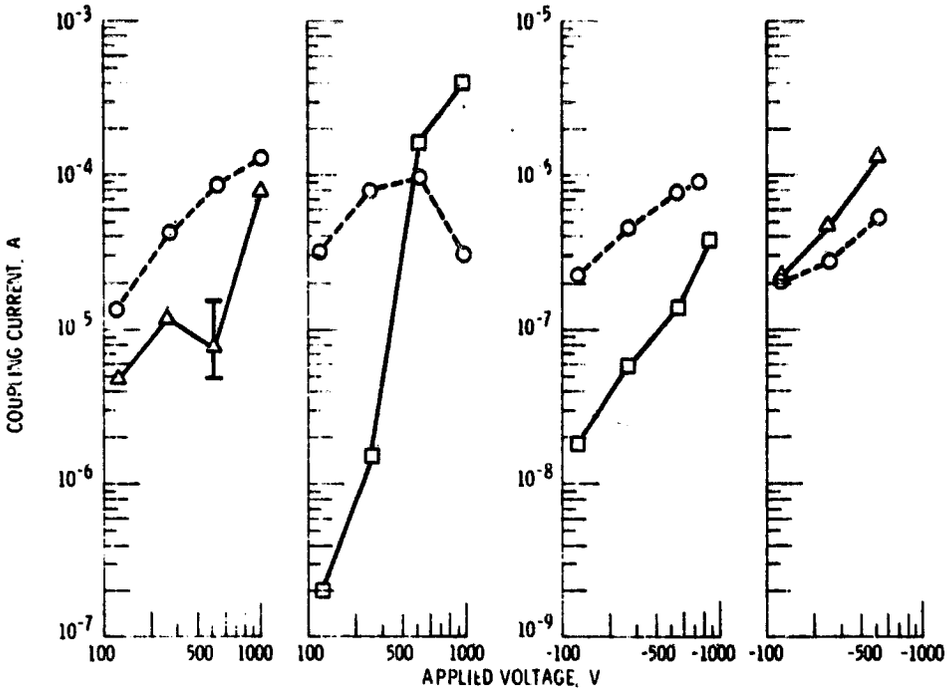

(j-1) Cycle 11A; disk on Kapton and plain disk; latitude, 65° to 77°.

(j-2) Cycle 11B; solar array and plain disk; latitude, 77° to 80°.

(j) Positive bias, cycle 11.

(k-1) Cycle 11C; solar array and plain disk; latitude, 78° to 64°.

(k-2) Cycle 11D; disk on Kapton and plain disk; latitude, 64° to 47°.

(k) Negative bias, cycle 11.

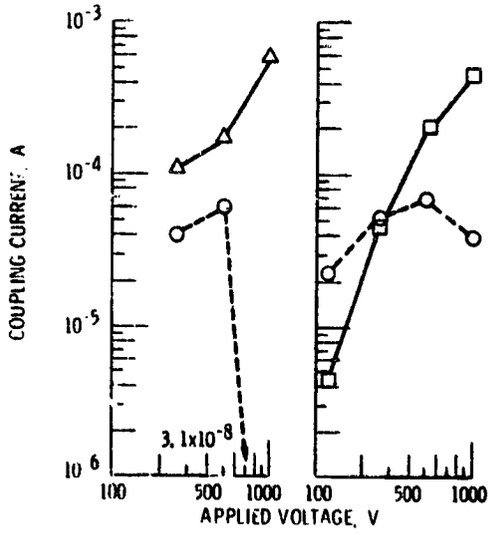

(ℓ-1) Cycle 12; disk on Kapton and plain disk; latitude, 44° to 27°.

(ℓ-2) Cycle 12; solar array and plain disk; latitude, 27° to 16°.

(ℓ) Positive bias, cycle 12.

Figure 4. - Concluded.

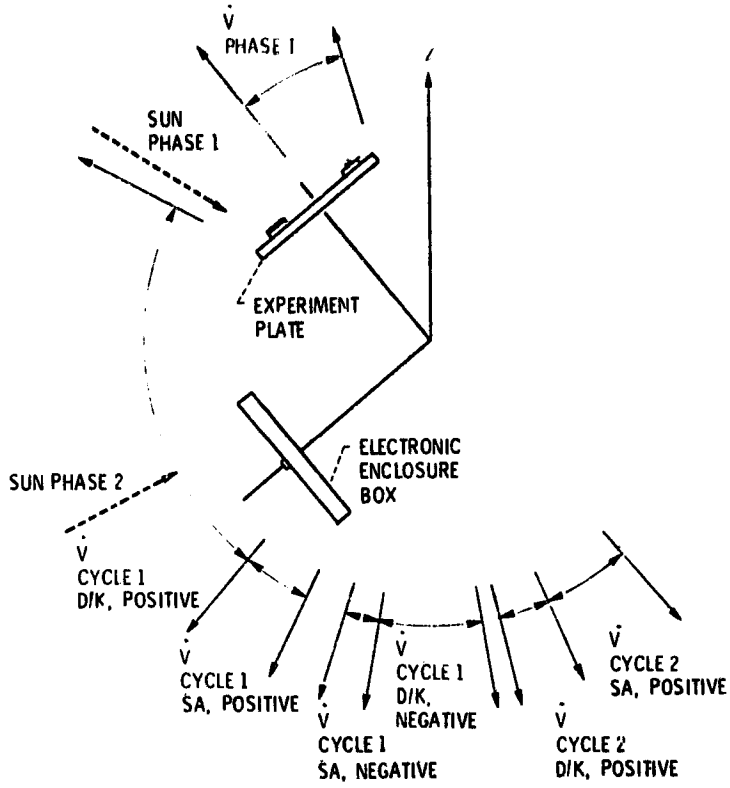

Figure 5. - Sun and velocity-vector angular positions during initial 42 minutes of PIX flight, where D/K denotes disk-on-Kapton experiment and SA denotes solar-array experiment.

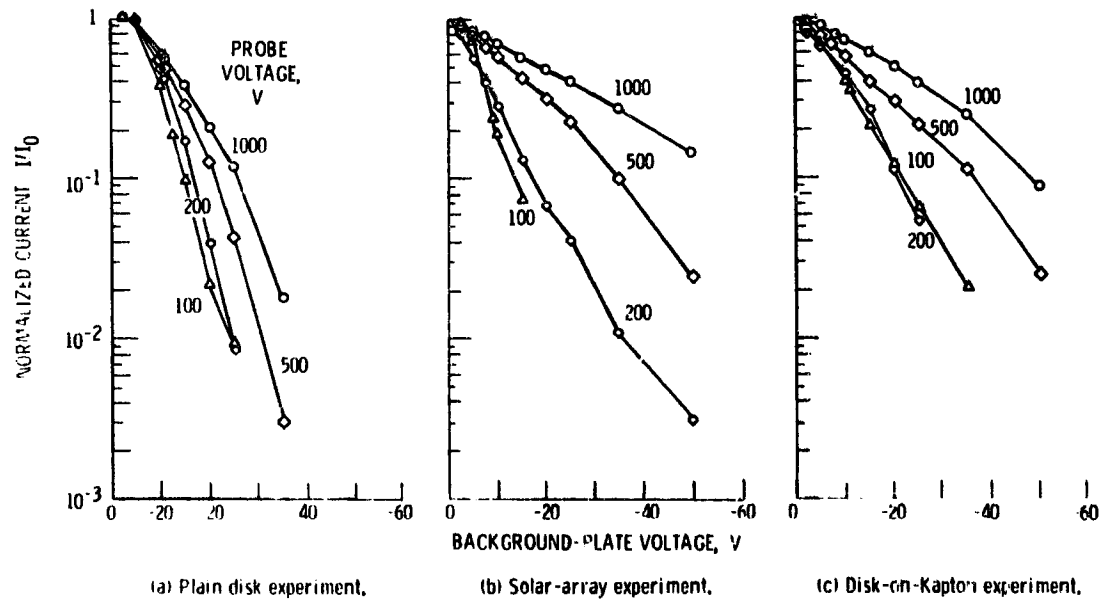

(a) Plain disk experiment. (b) Solar-array experiment. (c) Disk-on-Kapton experiment.

Figure 6. - Normalized current as function of background plate voltage for all experiments - ground simulation tests. Plasma density, 3×10^4 electrons/cm^3.

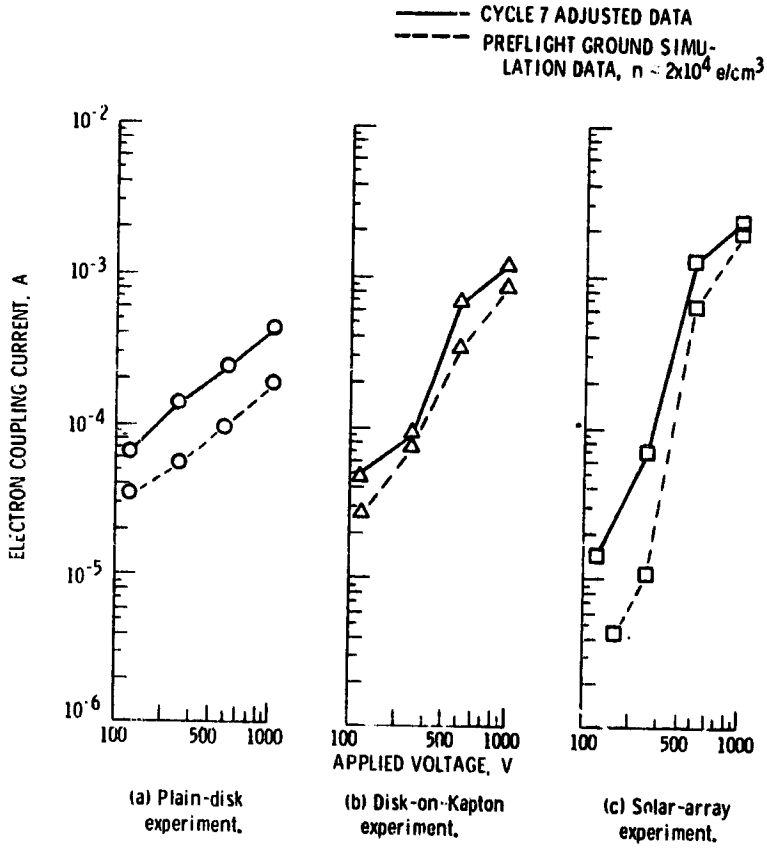

Figure 7. - Adjusted flight current for cycle 7 and preflight ground simulation current as function of applied voltage.

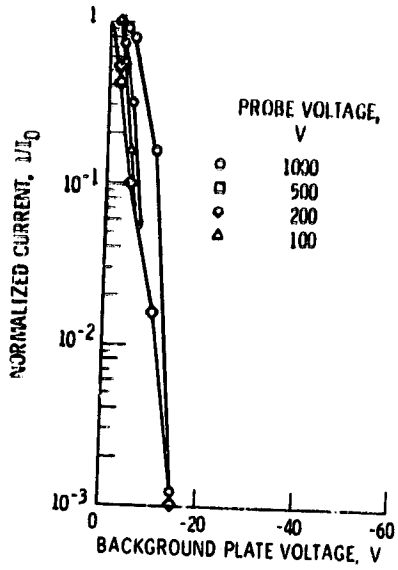

Figure 8. - Normalized current as function of background-plate voltage for plain-disk experiment - ground simulation tests. Plasma density, 2×10^3 electrons/cm^3.

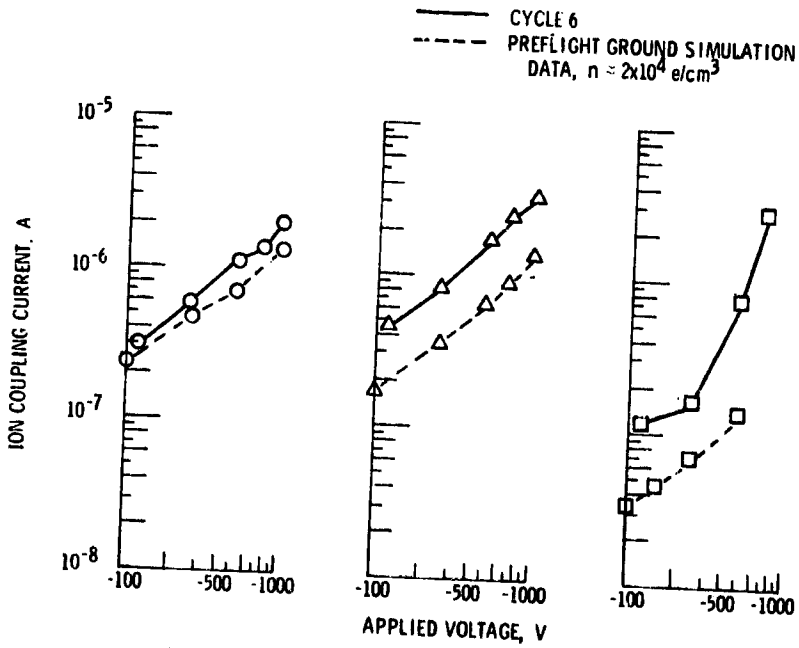

Figure 9. - Flight ion current for cycle 6 and preflight ground simulation current as function of applied voltage.

D-22

N79-24023

SHEATH EFFECTS OBSERVED ON A 10 METER HIGH VOLTAGE PANEL IN SIMULATED LOW EARTH ORBIT PLASMA

James E. McCoy and Andrei Konradi
NASA Johnson Space Center

SUMMARY

A large (1m x 10m) flat surface of conductive material was biased to high voltage (±3000 V) to simulate the behavior of a large solar array in low earth orbit. The model "array" was operated in a plasma environment of 10^3-10^6/cm^3, with sufficient free space around it for the resulting plasma sheaths to develop unimpeded for 5-10 meters into the surrounding plasma. Measurements of the resulting sheath thickness as a function of plasma density and applied voltage were obtained. The observed thickness varied approximately as $V^{3/4}$ and $N^{1/2}$ as would be expected for space charge limited flow between large plane surfaces with a constant source current density. This effect appears to limit total current leakage from the test "array" until sheath dimensions exceed about 1 meter.

Total leakage current was also measured with the "array" biased 0-4 kV from end to end, floating in equilibrium with the ambient plasma. The positive end of the array was observed to float at +93 V, with a total current leakage through the plasma slightly under 2 mA/m^2, or 0.7 watt/ft^2.

INTRODUCTION

Hardware and techniques have recently been developed to adapt the large thermal vacuum test chamber at NASA Johnson Space Center to simulate the ionospheric plasma environment characteristic of low earth orbit (LEO). Plasma density, flow direction and magnetic field strength were controllable for test purposes within the 20 meter diameter chamber. Plasma simulation and testing on this large scale is expected to become of increasing value as requirements to operate large systems at high voltage increase. We report here the initial results obtained in tests of a 1 meter by 10 meters simulated high voltage solar array, typical of development tests which will require this type of facility.

The test model used consists of roughly one square meter of actual solar cells at the top of the panel, with the remaining 9 meters simulated by a panel of conductive plastic material of sufficient internal resistance to be biased at several kilovolts end-to-end. The resulting panel surface potential varies in an approximately linear manner, the same as would be obtained from a string of very many solar cells connected in the simplest series configuration to give the same high voltage output end-to-end. Copper strips

are placed across the panel every five feet to provide good electrical contact for the bias voltage power supplies, or for monitoring of intermediate surface voltage and current values. Three moveable probes are located in front of the panel as it hangs in the test chamber, used to locate the outer boundary of the high voltage "sheaths" expected to form around the panel and control its equilibrium interaction with the surrounding plasma.

LEO PLASMA CURRENT LEAKAGE

Although space is a very good vacuum, it is not absolute and the very thin residual "gases" present are capable of causing significant electrical interactions under certain conditions. This has been noticed particularly by various satellites in geosynchronous orbit (GEO), which are observed to charge up to surface potentials of several kilovolts under solar eclipse/geomagnetic "storm" conditions. The ambient plasma is too thin to effectively bleed off the charge acquired from "storm" radiation absorbed by the satellites (refs. 1 and 2).

In LEO, the denser plasma easily overcomes any radiation charge build-up. This should eliminate the problems with unwanted charge build-ups observed in GEO but results in a new problem for large high power solar arrays due to the exact inverse of the GEO problem. In LEO, even necessary high voltages may be bled off by the dense ambient plasma.

Feasibility studies of the SPS concept have identified this as a potential problem in attempting to operate the large solar arrays at high voltages. Reference 3 in particular observed that current leakage to space (per unit area) would increase at high voltage by orders of magnitude over that experienced by present day low voltage systems, based on extensive laboratory test and analysis using small (1-20 cm) surfaces at high voltages. Assuming certain scaling laws observed to be approximately true on the 1-20 cm scale (in effect, assuming some constant sheath conductance per unit area between the array and the plasma), they calculated the power losses due to these parasitic currents shown in figure 1. The projected loss for the 15 kw array would exceed solar cell output for voltages exceeding +2 kV or -16 kV for a typical Shuttle orbit near the F2 ionospheric maximum.

An alternative theoretical analysis indicates that quite different scaling relations should be expected to apply. By this analysis, current collection by large solar arrays should be controlled by (plasma) charge separation fields, which should form space charge limited "sheaths" that confine the current collecting voltages on the arrays within these sheaths. Distinct outer boundaries to the current collecting sheaths surrounding a high voltage surface should be expected to reach a limiting size of the order of 1 meter/kilovolt, nearly independent of the size of the high voltage surface. When the assumptions in this analysis are valid, total current collected depends only on the outer surface area of sheath available to intercept ambient (drift) currents existing in the undisturbed plasma outside the objects' sheath. The resulting current multiplication factor at any voltage would be the ratio of outer sheath surface area to object surface areas, as illustrated by figure 2. (In effect, sheath

"conductance" per unit area becomes a function of both voltage and size, rather than a constant as in some oversimplified lumped circuit element analogies.) For illustration, we assume plasma parameters such that the resulting sheath thickness grows from 10 cm at ±100 V to 10 meters at ±10 kV. This sheath becomes very large compared to the 10 cm sphere, the total current collected increasing by nearly 10^4 (a very high "conductance" sheath). The same plasma sheath, around a 1 km "SPS" array, has a very small ratio of sheath to object size. The total current collected should increase by only a few percent, a very low sheath "conductance" which becomes even lower with increased voltage.

Operating in the large chamber at JSC, it is possible to observe the growth of these sheaths around a 1x10 meter object with 0.1-10 kV applied. This permits a test of their behavior in "free space" without the inevitable wall effects due to sheath growth in smaller chambers.

TEST SET-UP FOR SHEATH STUDIES

The performance of an actual test on the scale of 10 meters available in the large chamber was needed to determine which (if either) scaling relations are applicable to large solar arrays. Figure 3 shows the layout of the basic configuration used for most tests. The high voltage panel ("SPS") was hung near the center of the chamber, with 7-10 meters of free space available in all directions for unobstructed development of the high voltage plasma sheaths. The expected extent of sheath development is illustrated for an SPS model in series connected configuration, with high voltage at top and bottom at ground, for two typical sheath thicknesses of 1 meter and 3 meters. The three probes labeled 22-24 can be moved horizontally from outside the sheath to locate the outer sheath boundary (point of first observed change in plasma conditions). The sheath and associated effects could also be observed visually using low light TV cameras at the first and third floor levels. Large solenoid coils around the chamber provided control of the vertical magnetic field from 0-1.5 gauss. Plasma density and electron temperature measurements were obtained from 15 half inch spherical Langmuir probes located at various points around the chamber.

Plasma Generation

Plasma generation was available from three devices. A 30 cm Kaufman thruster borrowed from LeRC was used with argon gas to generate flowing plasma densities of 10^4 to 10^6 (cm^{-3}), directed either horizontally (across the magnetic field) from the third level into the face of the panel or vertically from the center of the floor (along the magnetic field) along the length of the panel. Plasma electron temperatures varied from 0.5-2 ev, being typically 1 ev. Ion temperatures and flow velocity were not directly measured, flow energy is estimated to have varied from 15-25 ev. Predominately (monatomic) Ar^+ ions were observed in the chamber, however significant numbers of N_2^+, H_2O^+, and HO^+ and some other species were observed. These may constitute a significant (thermal?) population of charge exchange or other secondary ions in the plasma, created from the residual gas.

A 6 inch Kaufman thruster device was fabricated at JSC to provide a lower density source, using H_2, N_2, and He as well as argon as the input gas. Plasma densities of 10^2 to 10^4 (cm^{-3}) were observed, either flowing vertically from center floor or diffused from a horizontal flow across the one meter level above the floor. Electron temperature was typically slightly less than 1 eV.

The third source of plasma employed was a large 5 meter loop antenna, driven at 1-5 MHz to excite an irregular plasma from the residual neutral chamber gases. Properties of this plasma were quite different, densities estimated at 10^3-10^5 (cm^{-3}) with electron temperature about 2-4 eV (based on 1/2" spherical Langmuir probe currents).

SPS Model for Test

Figure 4 shows the physical dimensions of the "SPS" model as tested, as well as location and identification of available test connections to the copper contact strips. The actual dimensions differed slightly from the nominal 1x10 meter design for ease of fabrication. For test purposes, the array was operated in each of three electrical configurations shown. The "series connected (floating)" configuration is the actual case which would be obtained in space; with currents closing from the positive voltage (V_+) end of the array, through the conducting plasma, to the negative portion of the array. The chamber walls and lab ground are not involved in the circuit at all (except in determining the roughly uniform "plasma potential" outside the sheaths). The relative potential of the entire test array and floating power supply will adjust itself relative to the plasma potential so that the total electron current collected along the positive voltage portion of the array exactly equals the total ion current collected along the negative portion. The location of the point along the array which is at "plasma ground" potential will be inversely proportional to the relative ambient current densities of ions and electrons in the free plasma. For typical conditions, this will result in the array "floating" 97-99% negative with respect to plasma potential.

Since operation in the fully floating configuration was physically awkward, most "series connected" testing was done with the power supply and one end of the array grounded to the chamber walls. This was equivalent to testing the negative or positive portions of a floating array individually, with the return current path closing through the chamber wall (via the plasma). In either case, all voltage drops from array surface potential to plasma potential are contained within the sheath. The outer surface of the sheath is at plasma potential. The plasma is effectively a perfectly conducting medium with constant internal potential (within a factor of kT).

A third configuration frequently employed, for maximum simplicity of operation and data analysis, was "constant HV" with the entire surface of the array at the same potential and all current returning through the plasma to the chamber walls.

This test object was designed to produce the extreme values of current leakage possible from a large solar array or other high voltage surface. To eliminate confusion from attempting a correct treatment of the effect of relative surface area and configuration of conductive and insulated portions of the surface of an array, the entire front surface (except the actual solar cell section) was made conductive. The "SPS" model should therefore generate the large scale (outer) sheath configuration believed to be of primary importance in determining its equilibrium interaction with an ambient plasma. The currents collected will not be reduced by any insulation factor.

Test Objectives

In order to test the validity of the proposed approach to scaling calculations of plasma current leakage based on relative sheath to object size, three primary topics were identified for investigation:

(1) Existence, sharpness and size of the expected outer sheath boundary

(2) Equilibrium floating potential of a large panel (array) with fixed voltage differential along its length

(3) Magnitude of leakage currents induced to/from large surfaces as a function of voltage (actually, sheath size)

A secondary topic was the possible existence and behavior of transient current pulses (electrical breakdown or "arcs" to the plasma) reported to occur in smaller scale experiments (refs. 3 and 4).

EXPERIMENTAL RESULTS

The fundamental result achieved was direct observation of the existence, form and dimensions of the plasma sheaths formed about the high voltage panel. Leakage currents between the panel and the surrounding plasma, through the observed sheaths, were recorded for comparison with the theoretically expected current transmission capacities of the sheaths. The existence and form of the sheaths was observed by two independent means, both of which detect the location and "sharpness" of the outer boundary with minimum disturbance of its configuration by physical intrusion of hardware.

Sheath Observation by LLTV

Figure 5 shows a typical LLTV image of the series connected sheath, with surface potential on the SPS increasing from 0 at the bottom end to 1 KV near the top (actually about the center of the panel) of the picture. The sheath is the dark area, seen to increase approximately linearly in thickness from 0 at 0 volts to perhaps 1-2 meters at 1 KV. The outer boundary is generally rather sharply defined in the LLTV image, as expected from the space charge limited thickness hypothesis.

The sheath is frequently visible on LLTV, as a dark region in front of the panel which expands or contracts as a function of voltage on the panel face, when viewed under sufficiently high plasma density conditions against a dark background. We believe the sheath region is dark because with electrons (or ions) excluded, little of the ambient plasma recombination/de-excitation leading to photon emission occurs. In any case, acceleration of ions (or electrons) in the sheath leads to a reduction in number density by more than an order of magnitude. The sheath becomes unobservable when the outer boundary becomes large and curved, not parallel to the line of sight, or viewed against a bright background (such as the aluminized mylar toward the top of fig. 5).

Sheath Detection by Probes

The second method involved watching for an alteration in the observed I vs. V current collection characteristic of a moveable Langmuir probe as it approaches and enters the outer boundary of the sheath from the external plasma (or equivalently, as the sheath expands to envelope the probe as the surface voltage of the panel is increased). After some experimentation, a satisfactory operational technique was developed for recording this information. A series of log I vs. voltage curves were recorded for electron collection from the zero current voltage up to +100 volts, as surface voltage on the panel was increased in steps from zero until the probe (at a particular location) was deep inside the panel's sheath. A representative set of curves is shown in fig. 6. The undisturbed plasma at this point was about 10^6/cc with an electron temperature (T_e) slightly less than 1 eV as deduced from the initial curve recorded with 0 V on the panel. The linear increase in current from (thermal current density) about 1×10^{-5} amp at +6 V to 9.5×10^{-4} amp at +100 V is consistent with normal orbit limited electron collection in such a plasma.

As voltage is applied to the panel, no effect is seen at the probe location (still outside the growing panel sheath) until the applied voltage (V_{op}) reaches -800V, when a slight displacement of the curve at higher probe voltages is first detectable. Increasing V_{op} by 100v to -900v causes a clearly noticeable reduction in probe current at +100v bias, more than resulted from the previous 800 volt change. There is as yet no change below the linear portion of the curve. We interpret this as indicating the probe is still (just) outside the panel's sheath boundary but near enough for the probe's expanding effective radius of electron collection (about 5 inches for a ½ inch probe at +100v) to partially contact the region of sheath disturbed ambient electron currents. (A partial "shadowing" of the probe location by the growing plasma absorbing sheath may also be expected, particularly when the panel is located between the probe and the plasma source.) The sheath has probably just passed the location of the probe when -1,000v is applied to the panel, the current zero-crossing voltage has shifted. As the panel voltage is increased further, moving the location of the sheath edge further beyond the probe location, even greater positive voltages are required on the probe before its electron attracting field is strong enough to reach beyond the electron depleted sheath boundary to an undisturbed plasma region containing electrons which it can then draw to its surface. When

panel voltage has increased to -1500v, the probe is so deep inside the panel's ion sheath that +100v on the probe is able to draw less than 0.1% of the electron current available outside the sheath (+70v is required to attract any measurable electrons at all into this electron depleted region).

A set of curves similar in appearance is obtained for positive (electron collecting) sheaths. The causes are probably quite different, since there are electrons present to be collected inside this sheath. The probe current zero crossing voltage will still shift to progressively higher positive voltages as the sheath is entered, since the probe will repel electrons until it exceeds the local (positive) potential inside the sheath. The current collected will then be reduced due to the combined lower density and higher energy of the available electrons, and their essentially unidirectional velocity distribution.

Sheath Size

The test results show a distinct limitation to sheath growth, as a function of voltage and (ambient plasma) current density. Within present limits of experimental error, the observed sheath thicknesses follow the $V^{3/4} \div n^{1/2}$ dependence expected for space charge limited current flow with d (sheath thickness) the free variable. Figure 7 shows the applied voltage required at various plasma densities for the outer sheath surface to reach a Langmuir probe (#23 in Fig. 3) located 1 meter from the surface of the array. The reference line is the theoretical thickness calculated for a one-dimensional planar geometry case (Appendix A) with an effective electron or ion "temperature" of 1 eV. Notice the electron sheath (shown as ⊕) is about the same size as the ion collection sheaths (shown as ○).

Sheath Current Leakage vs. Voltage

The resultant leakage current multiplication factor was observed to be much lower than observed on previous small scale tests. Figure 8 shows current leakage from "SPS" to the plasma observed from -10 to -3000 volts in four ambient plasma densities ranging from 10^4 to 10^6 per cubic centimeter. The observed rate of increase in leakage current with voltage is seen to increase as the resulting sheaths become large compared to panel width, as expected from figure 2. The regions of sheath size shown are rough estimates, based on the calculation in figure 20 normalized to an actual measurement for each data set.

Floating Potential

Recalling the requirement that total current flowing to an electrically isolated panel in series connected configuration be zero for voltage equilibrium with the ambient plasma to exist, we expect values of V- and V+ relative to the plasma shift so that (fig. 9)

$$J_{oi} A_- = -J_{oe} A+ \qquad (1)$$

where j_{oi} and j_{oe} are the ambient ion and electron current densities across the outer sheath boundaries, and A- and A+ are the effective surface areas of the negative and positive potential sheaths. We neglect current contributions from other sources such as secondaries, and the area (± a few kT) immediately around the V = 0 (w.r.t. Vp) point along the panel. For reasonably thin sheaths, relative to panel dimensions, we can use the approximation

$$\frac{A-}{A+} = \frac{L(-)}{L(+)} = \frac{V-}{V+} \tag{2}$$

where L(-), L(+) are the lengths of the panel sections floating negative, positive with respect to plasma potential. $\Delta V/\Delta L$ along the panel is assumed constant. (We note the assumption j_{oi}, j_{oe} constant along the sheaths does not require j_i, j_e constant along the panel. Current density along the panel should vary due to focusing effects, without affecting our assumptions so long as the relative geometric shapes of A- and A+ are the same. This should be true for thermal velocity distributions and approximately valid for ion streaming velocities oriented perpendicular to the face of the panel. For other orientations, more careful account must be made for both the effective intercept cross-section (A-) and effective reduction in j_{oi} due to screening by both the panel and the positive (A+) sheath.)

In the case of thermal electron currents and directional streaming of ions with mean energy

$$E_i = \frac{1}{2} m_i v_i^2 \tag{3}$$

We can use (1-D calculation)

$$j_e = n_e q_e \bar{V}_e = -n_e e \sqrt{\frac{kT_e}{m_e}} \tag{4}$$

$$j_i = n_i q_i \bar{V}_i = +n_i e \sqrt{2E_i/m_i} \tag{5}$$

Therefore

$$\frac{-j_e}{j_i} = \sqrt{\frac{m_i}{m_e}} \sqrt{\frac{kT_e}{2E_i}} \tag{6}$$

For an Ar+ plasma, $\sqrt{m_i/m_e} = 270$. Typical values for electron temperature of lev and ion beam energy of 20 ev give

$$\frac{-j_e}{j_i} \approx 43 \tag{7}$$

Using (7) in (1) and (2)

$$\frac{-J_e}{J_i} = \frac{A-}{A+} = \frac{L_{(-)}}{L_{(+)}} = 43 = \frac{V-}{V+} \qquad (8)$$

We therefore expect the panel to float about 2.3% positive, the remainder (97.7% of L, V_{op}) negative under these conditions. Representative current density and voltage values expected along an array are shown in fig. 10(a).

Comparison with Observation
(Ion flow perpendicular to panel face)

This was verified experimentally. The 30 cm thruster was operated from the third level catwalk, aimed horizontal directly into the face of the panel. Average plasma density along the panel is estimated to exceed $10^6/cm^3$, based on supply current of 21 mA at V_{op} = 2000 V compared to 15 mA (at -2000 V) observed earlier when probe measurements indicated densities decreasing from $1.1x10^6$ at the bottom to $2.2x10^5$ at the top of the panel. The experiment configuration was series connected (floating) as shown in fig. 4. Using a pair of electrically isolated power supplies in series, voltages (V_{op}) from 500 to 5500 V were applied to the panel while monitoring the voltage at lead #8 using a DVM referenced to lab ground. (The plasma potential was +5 - 10 V referenced to lab ground.) As long as the panel floated more than 90% negative wrt ground, the DVM at #8 would read -0.167 V_{op} less V+. Readings of V+ directly at lead #10 were also recorded at V_{op} = -3 kV and -4 kV. Values observed are plotted in fig. 11. $V+/V_{op}$ at 3-4 kV is 2.6-2.3%, very nearly the expected value.

The behavior of V at lead #8 indicates this is probably true at lower values of V_{op}, but the high leakage currents cause a loading down of the resistive panel such that $\Delta V/\Delta L$ is no longer constant and a large fraction of the panel surface between #8 and #10 is in effect left out of the circuit at V_{op} = 500 - 1000 V. At these voltages the entire current supplied at the ends of the panel is carried part of the length entirely through the plasma, leaving zero current in the panel. Therefore $\Delta V/\Delta L$ = 0 in this section, which floats slightly negative so as to repel (97%) of the electrons and draw no net current from the plasma. This is illustrated in fig. 10(b).

Power Loss

Total current supplied to the panel was recorded for each voltage. This allowed calculation of current leakage estimates and the resultant power lost to the plasma as a function of V_{op}. The calculated current leakage values were obtained under assumptions which may be in error ±25%. These errors cancel in further calculation of total power lost. Results are shown in Table 1. The 56 watts estimated lost in driving plasma currents at V_{op} = 4,000V is significant, but well under the roughly 1 kilowatt available from a solar array this size.

This result is plotted in fig. 12 for comparison with the earlier estimates in ref. 3 using constant leakage per unit area and reducing the

total by 90% to allow for relative insulator/conductor areas. The "error bars" show our estimated uncertainty in plasma conditions and possible reduction in total currents due to 90% insulation (our measurements were for a 100% conductive surface).

Arcing to Plasma

Arcing, defined here as any sharp and transient increase in current drain to the plasma was frequently observed. Most measurements of current loss vs. voltage were limited to voltages less than 2-3 KV because arc induced transients became so severe that useful meter readings could not be made. Although some arcs were "small" and did not affect the rest of the panel except for small pulses in the current meter, many resulted in complete discharge of the panel voltage, which required 1-5 seconds to rebuild. This was visible both in the collapse of the sheaths to much smaller dimensions (observed both in the LLTV dark image, see fig. 13, and with any Langmuir probe located inside the sheath, see fig. 14) and as a voltage drop indicated by the power supply meter. The time and electrical power required to restore the sheath could be appreciable (estimate typically 2 seconds and 50 joules). This collapse of the entire sheath was observed, by LLTV, to occur even in cases where the discharge was observed to come from an insulator surface located 1-2 meters out in the sheath and having no contact with the conductive panel surface other than the plasma (fig. 15).

The arcs were observed to occur at positive voltages over +400V, and negative voltages over -1,000V. There appears to be no particular dependence between plasma density and minimum voltage for the onset of arcing. At any given density, arcing would occur at -1KV on some days and then not occur at voltages up to -3 KV the next day. The appearance of the arcs, as observed by LLTV, varied greatly. However, arcs occurring at negative voltage tended to appear as point discharges, even when occurring from an extensive flat surface. Positive voltage arcs more often would involve most or all of a large surface in a sudden (less than 1/30 sec) bright discharge.

A very interesting finding is that every arc observed by the LLTV system to date occurred from an insulator surface. We have not yet observed a single instance of a visible arc occurring from the conductive surface area of the panel. It would appear that the arcs are the result of a local charge build-up due to sheath currents impinging on a nonconductor in their path in a process similar to that occurring with satellites in GEO during substorms. Most of the resulting current drain from the panel biasing power supplies must be due to large scale currents within the collapsing (space charge) sheath, not directly due to the small area of visible flash region currents.

Surface Glow: Ion Focusing

A very noticeable effect occurs at negative panel voltages, where a distinct surface glow pattern is observed by LLTV to form along the face of the panel (see fig. 16). This pattern has a shape suggestive of a flow along the panel and was originally thought to be due to secondary electrons cascading

along the surface voltage gradient. This was ruled out when the voltage gradients were found not necessary for formation of the pattern. The pattern is observed to become brighter and narrower as panel voltage increases (fig. 17). We now believe it is due to focusing of the incoming ions by the plasma sheath, which acts as a large cylindrical lens in front of the panel. As the size and curvature of the sheath potential surfaces increase with voltage, the degree of focusing also increases as illustrated in fig. 18. This focusing effect is present at both ends of the panel when operated in constant high voltage configuration (see figs. 16 and 17) but vanishes at the grounded end (fig. 19) for a series connected panel. This is probably due to the sheath size there flattening out to zero.

CONCLUSIONS

We conclude that estimates based on calculations of space charge limited sheath dimensions provide a promising working model for calculating design estimates of high voltage plasma current leakage from large solar arrays and similar objects. It would appear necessary that all such estimates be verified by a carefully developed sequence of plasma-vacuum tests progressing from small lab chambers to full scale flight tests, due to large differences in applicable scaling relations which are observed to result from subtle differences in assumed conditions. Large scale tests of the sort described here, together with adequate math models to provide continuity between different design or test details, will be an important element in any development test sequence for systems involving large surfaces or high voltages.

The present results are preliminary, based on exploratory measurements intended to determine the feasibility of this type of investigation and order of magnitude of the experimental quantities to be measured. Detailed verification and extension of these results is the first objective of our next series of tests. Development of math models to include the space charge effects is needed. Detailed cross-checking of the predictions of such models with actual measurements within the 1-5 meter sheaths during tests in the large chamber should be very useful to aid further development of both models and tests.

The present results indicate that equilibrium high voltage leakage currents to the plasma should be much less than some earlier predictions had indicated, particularly for very large solar arrays. The power loss, and other effects, due to the observed arcing phenomena threatens to be much more significant unless adequate means are developed to understand and control it. More detailed and complete study of the large scale high voltage sheaths around a solar array appears basic to an adequate treatment of both problems. While the dense plasma present in LEO will bleed off any natural charge build-up from passive surfaces, the plasma sheath formed around any high voltage surface envelopes all surrounding structure in an environment very similar to that at GEO during intense storm conditions. Within the sheath, strong flows of the collected species of charge are accelerated to kilovolt energies while most charge of the opposite sign is excluded from the sheath area and cannot act to bleed off areas of surface charge build-up and prevent eventual arcing.

APPENDIX A

CALCULATION OF SHEATH THICKNESS

The size of the sheaths is expected to vary in such a manner that space charge limited flow conditions prevail. The calculation is somewhat different from the usual case considered, in that the current density available across the virtual "electrode" formed by the outer sheath surface is considered as fixed (by the ambient thermal motion or orbital velocity current flow across that boundary) while the separation of the two "electrode" surfaces (the outer sheath boundary and the panel face) is freely variable. For example, we calculate the expected sheath thickness, d, for the case of planar geometry by equating the random thermal current of the attracted particle species (electron or ion)

$$J_o = 1/4\ N_o q\ \sqrt{\frac{8kT}{\pi m}} \tag{1}$$

or for directed (1-D) flow

$$J_o = N_o q \sqrt{\frac{kT}{m}} \tag{1a}$$

to the Langmuir-Child Law expression for planar diode space charge limited current

$$J_{sc} = \frac{4\epsilon_o}{9}\sqrt{\frac{2q}{m}}\ \ \frac{V^{3/2}}{d^2} \tag{2}$$

Therefore, defining kT = E (expressed in electron volts) and k* to incorporate the appropriate velocity distribution function in a general expression for

$$J_o = k^* N_o\ q \sqrt{\frac{kT}{m}}$$

We obtain

$$d = \frac{5.89 \times 10^3}{\sqrt{k^*}}\ \ \frac{|V|^{3/4}}{N_o^{1/2}\ E^{1/4}} \tag{3}$$

Where $\sqrt{k^*} = 1.0$ for 1D flow and $\sqrt{k^*} = .63$ for Maxwell distribution. In most cases of interest, k* is probably close to 1. Even the thermal electrons must have their velocity distribution altered significantly from Maxwellian near the sheath boundary, as there exists flow in but none out.

Notice that the particle mass (m) does not appear in (3). For a given plasma density (singly ionized), the electron sheath will be the same size as the opposite polarity ion sheath if their temperatures are the same. The current

densities across the sheath outer boundaries will be higher for electrons in the ratio

$$\frac{j_{oe}}{j_{oi}} = \sqrt{\frac{T_e m_i}{T_i m_e}} \tag{4}$$

For the case of streaming flow velocities greater than mean thermal velocity (usually the case for ions in low earth orbit) it is necessary to use a carefully selected equivalent temperature, or the direct expression

$$j_{oi} = Nq \langle v \rangle \cos\theta \tag{5}$$

where $\langle v \rangle$ is the average velocity (i.e., orbital velocity or velocity of thruster beam energy) and θ is the angle between flow vector and sheath normal.

The resulting relation between plasma density and voltage required to cause a given sheath thickness d is plotted in fig. 20 for several values of d. The calculation should be reasonably good for $d \ll 1$ meter. For $d \approx 1$ meter and $d \gg 1$ meter, similar expressions can be obtained for cylindrical and spherical geometry respectively, using

cylindrical
$$j_{oe} = \frac{4\epsilon_o}{9}\sqrt{\frac{2q}{m}}\frac{V^{3/2}}{1a\beta^2} \tag{6}$$

spherical
$$j_{os} = \frac{4\epsilon_o}{9}\sqrt{\frac{2q}{m}}\frac{V^{3/2}}{r^2x^2} \tag{7}$$

where α^2 and β^2 are quantities tabulated by Langmuir (refs. 5 and 6). For thick sheaths we use an approximation from ref. 3:

$$x^2 \approx 1.16 \left(\frac{r_o}{a}\right)^{3/2} \tag{8}$$

where r_o = outer radius of sheath, a = probe radius. Therefore (3) becomes

$$(d + a) = r_o = 137 \frac{(aV)^{3/7}}{N_o^{2/7} E^{1/7}} \tag{9}$$

The result for $d = 3m$ (with $a = \frac{1}{2}m$, $E = 1ev$) is also plotted on fig. 20 for comparison with the planar calculation at 10 ft. The actual, roughly cylindrical geometry, value should lie somewhere between these extremes.

REFERENCES

1. Rosen, A. (ed.) Spacecraft Charging by Magnetospheric Plasmas, Progress in Astronautics & Aeronautics, Vol. 47, MIT Press, Cambridge, MA, 1976.

2. Pike, C.P. and Lovell, R.R. (eds), Proceedings of the Spacecraft Charging Technology Conference, Air Force Geophysics Laboratory, AFGL-TR-0051, 1977 (also NASA TMX-73537).

3. Kennerud, K.L., "High Voltage Solar Array Experiments," NASA CR-121280, 1974.

4. Stevens, N.J., et al., "Investigation of high voltage spacecraft system interactions with plasma environments", AIAA Paper 78-672, April 1978.

5. Langmuir and Blodgett, "Currents limited by space charge between coaxial cylinders", Phys. Rev. 22, 347-356 (1923).

6. Langmuir and Blodgett, "Currents limited by space charge between concentric spheres", Phys. Rev. 23, 49, 1924.

TABLE I. - POWER LOSS WITH OPERATING VOLTAGE

[Series-connected, 9-m^2 floating array; no insulation; $N_o > 10^6/cm^3$.]

V_{op}	I_{supply}	$I_{leakage}$	Power Leakage
500	6 ma	4 ma	1.3 watts
1000	12	7.5	5
1500	15	7	7
2000	21	10.5	14
3000	31	15	30
3500	36	17	40
4000	41	21	56
-4000	44	24	64

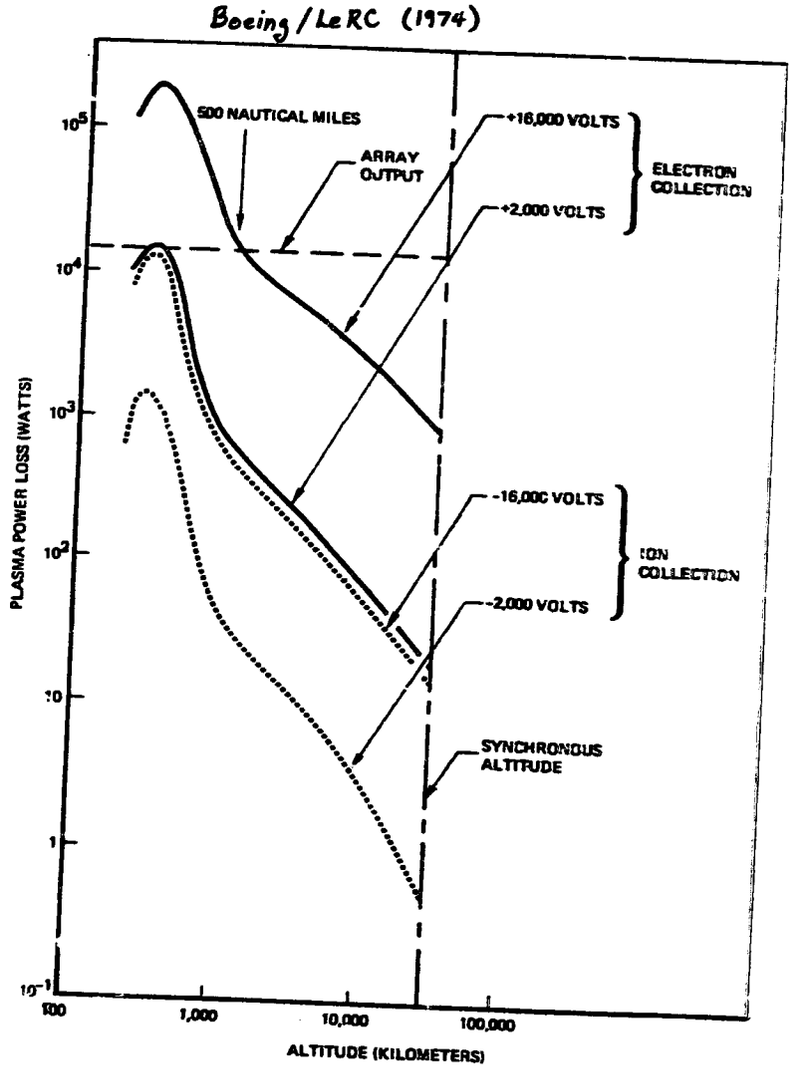

Fig. 1 - Plasma power losses of biased, 15-kilowatt solar array with 90% insulating surface. (From ref. 3.)

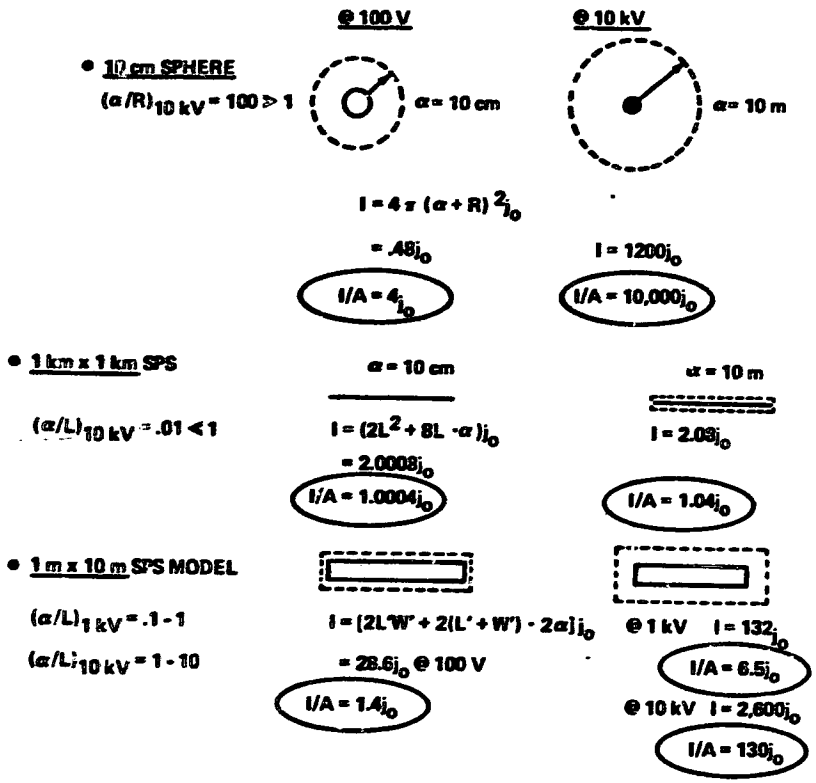

CURRENT VS VOLTAGE VS α/L

- α/L = RATIO OF PLASMA SHEATH THICKNESS TO OBJECT SIZE
- CURRENT CROSSING OUTER SURFACE OF SHEATH COLLECTED/ CONCENTRATED TO SURFACE AREA A CF OBJECT

Fig. 2a - Effect of sheath size relative to object size on plasma current collection.

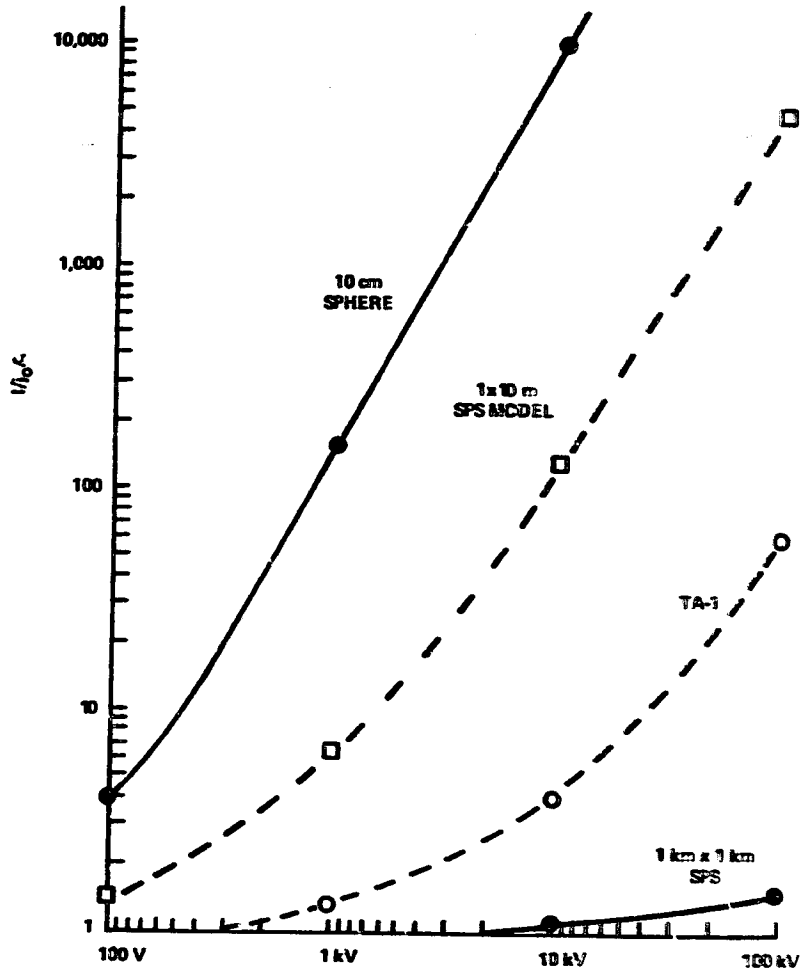

Fig. 2b - Limitation of current multiplication ratio vs voltage expected for collecting objects of increasing size, assuming sheath size limited.

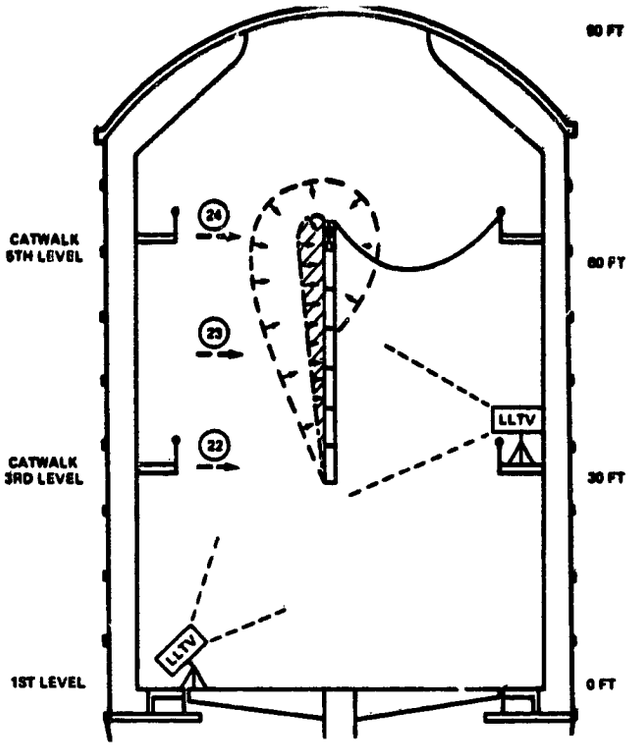

Fig. 3 - High Voltage "array" test lay-out in Chamber A

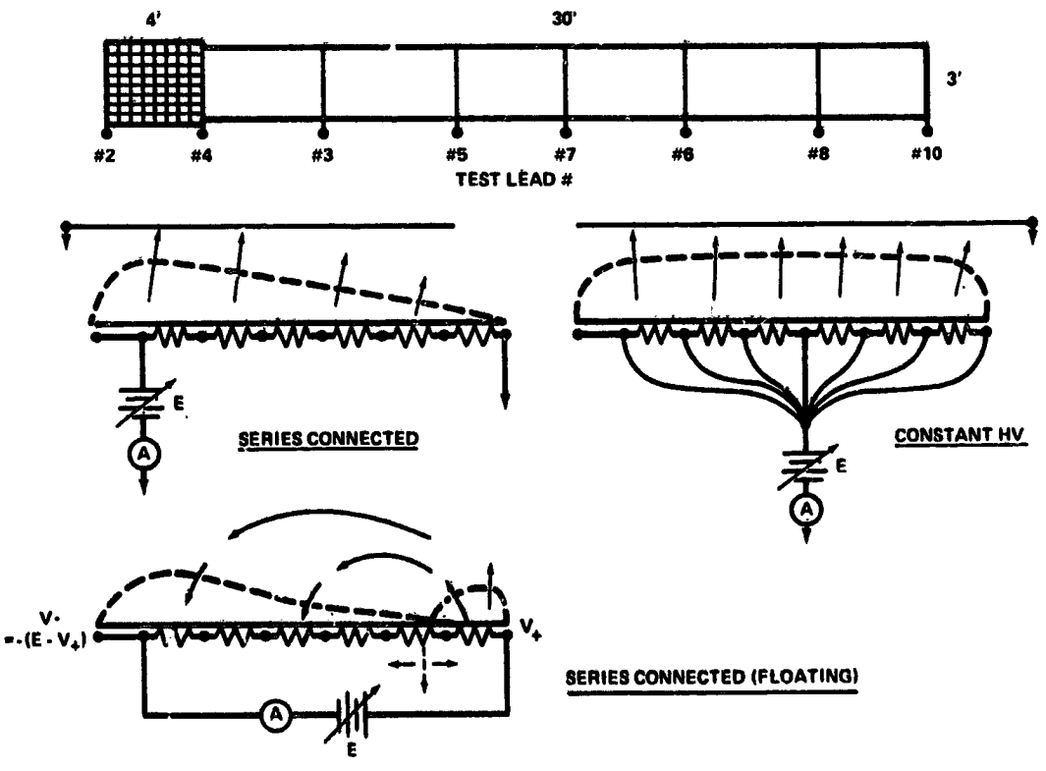

Fig. 4 - Simulated high voltage array electrical configurations (SPL-1; 1977).

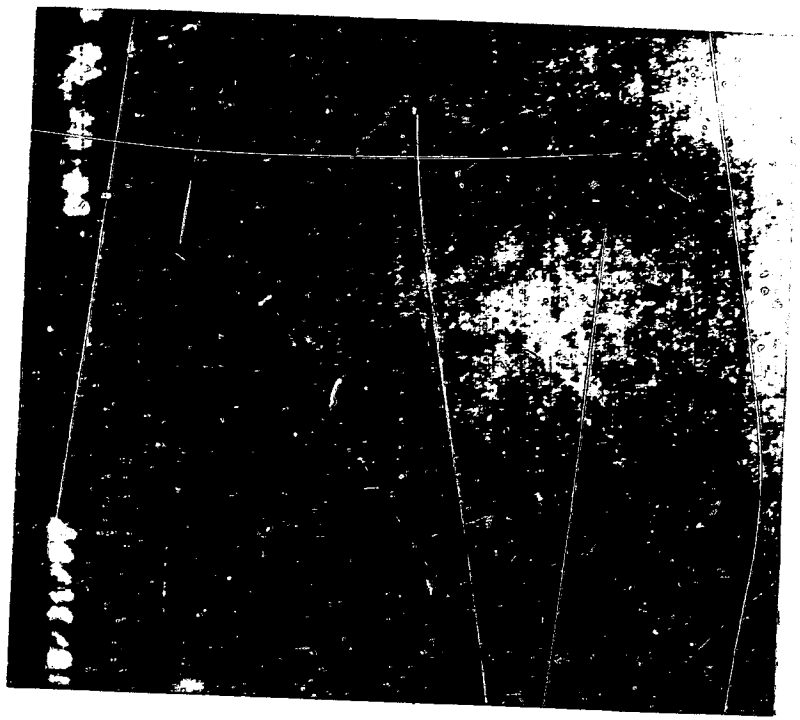

Fig. 5 - LLTV image of HV plasma sheath.
"SPS" edge-on, series connected.

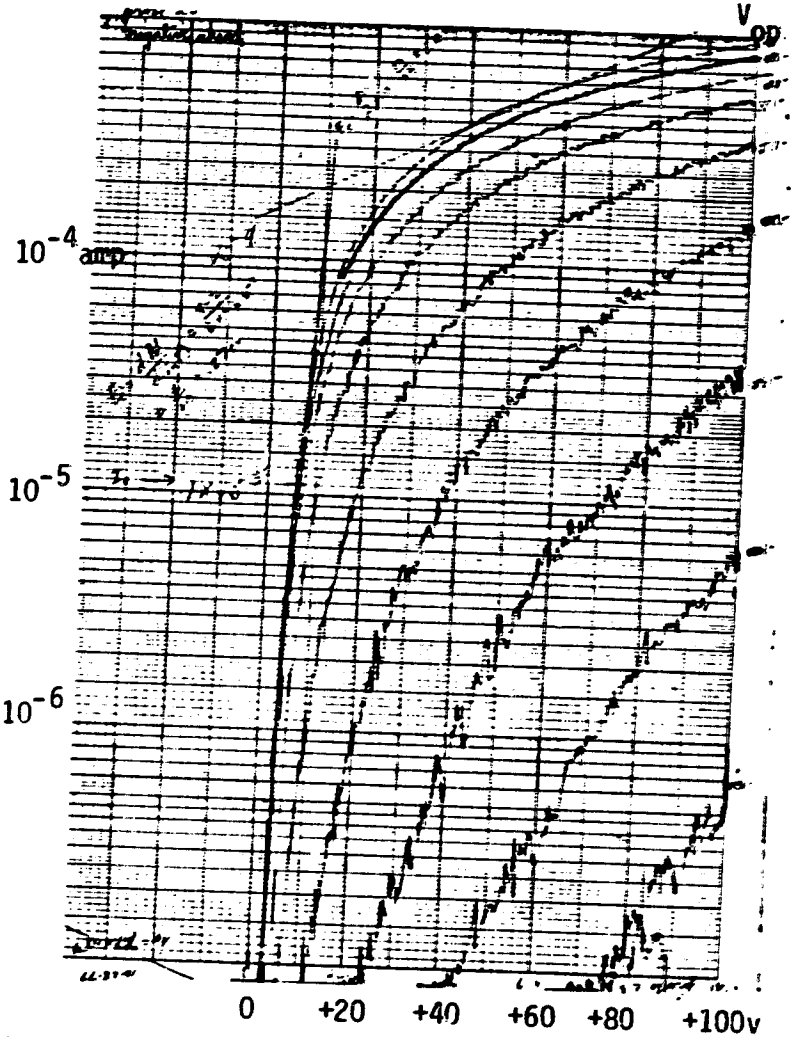

Fig. 6 PROBE BIAS VOLTAGE vs Log I
Change with V_{op} as sheath expands past probe.

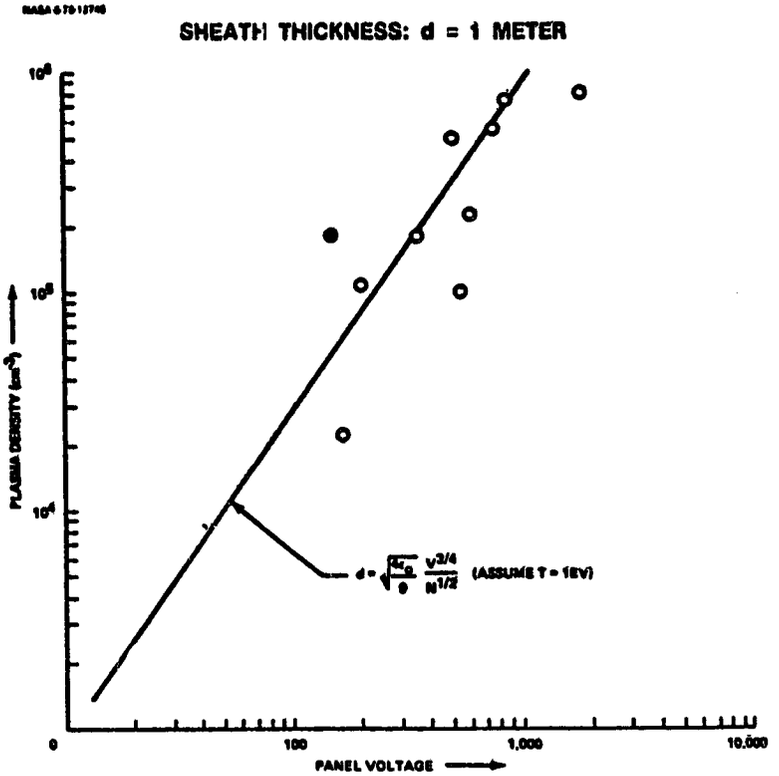

Fig. 7 - Applied voltage required for outer sheath surface to reach Langmuir probe located 1 meter from surface of array.

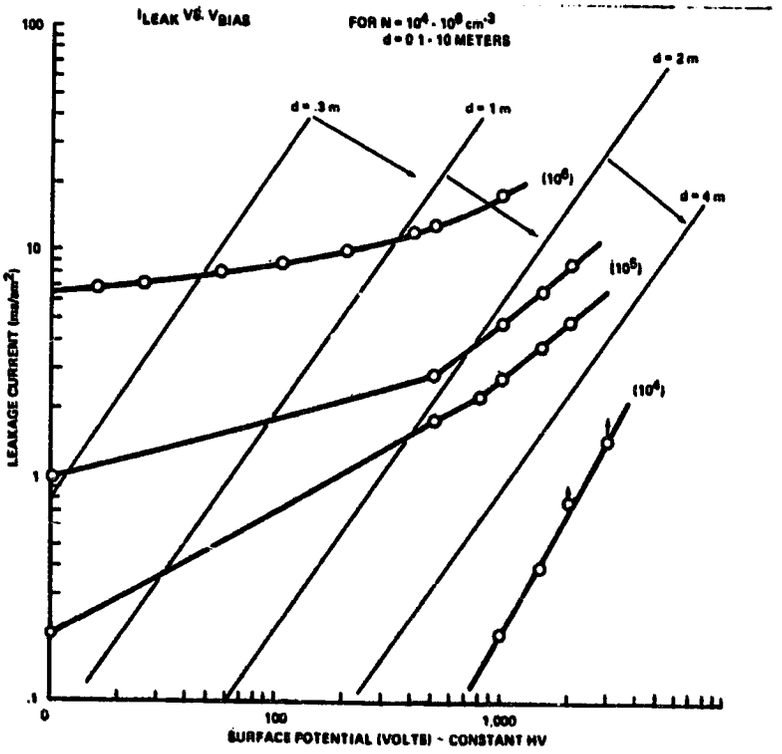

Fig. 8 - Current leakage from SPS to plasma.

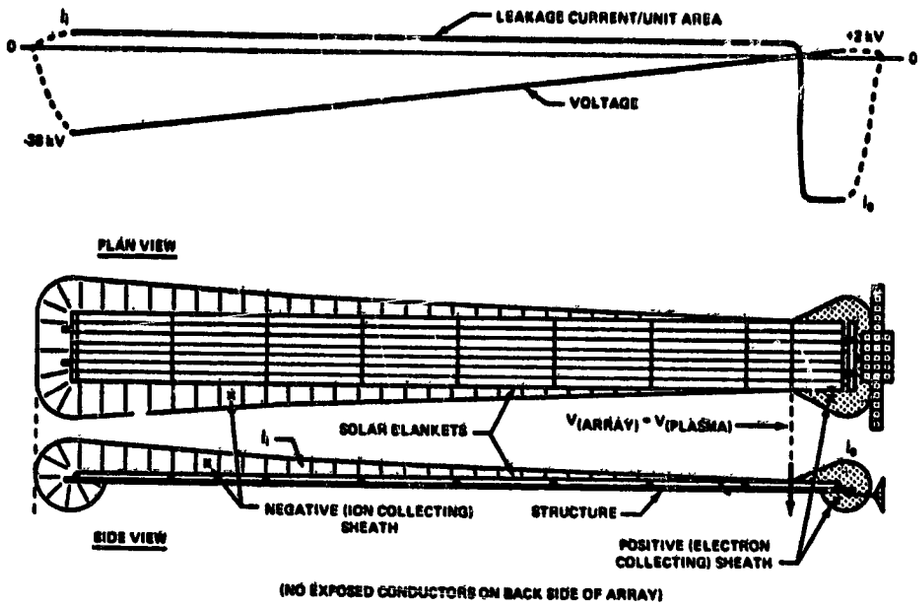

Fig. 9 - Preliminary model of expected space charge limited sheath development around a 10 Mw solar array in LEO. Voltage, with respect to plasma potential, along the array must shift so as to balance ion current against electrons.

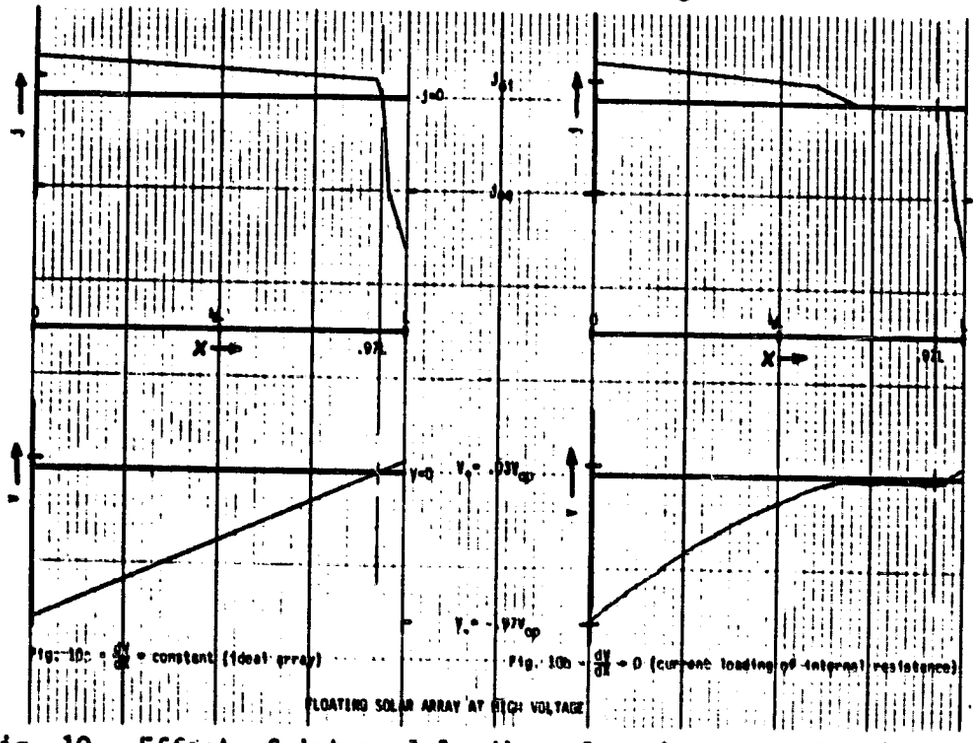

Fig. 10 - Effect of internal loading of series connected (floating) high voltage array due to plasma leakage currents.

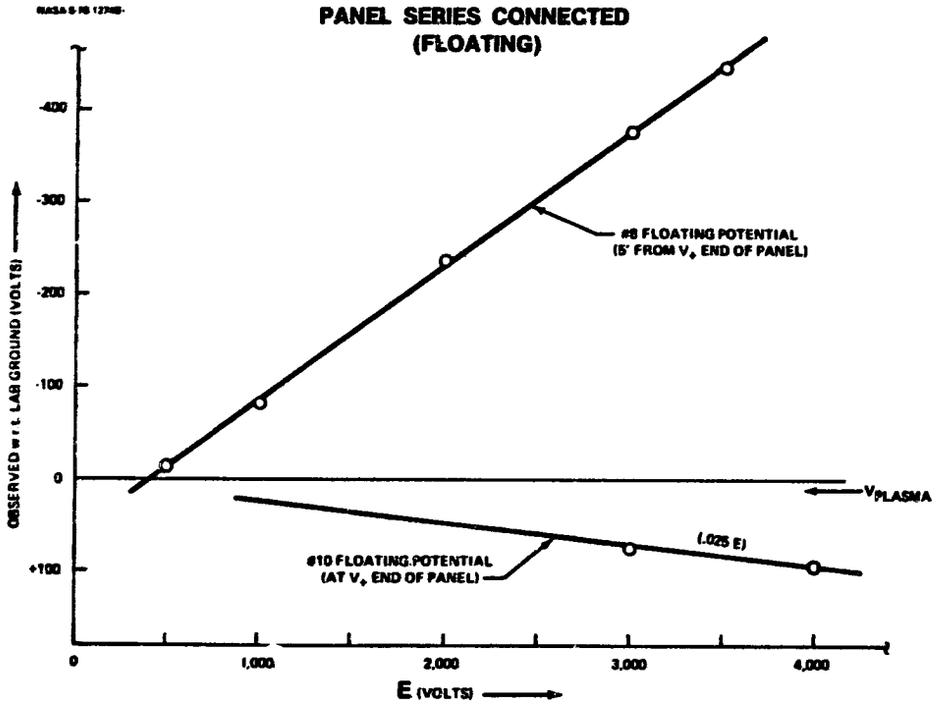

Fig. 11 - Equilibrium floating potential of positive end of simulated high voltage solar array .

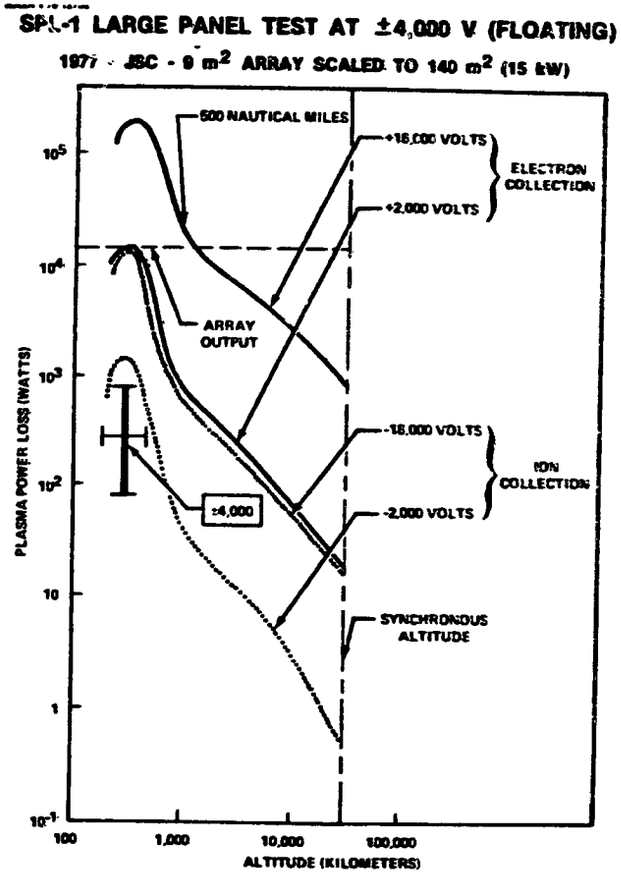

Fig. 12 - Power loss due to plasma leakage currents observed at ± 4000V, from an uninsulated 1 x 10 meter simulated solar array, plotted for comparison with estimated curves shown in fig. 1.

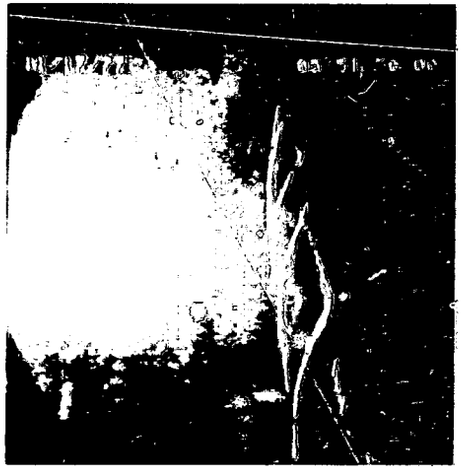

(13a) sheath before arc

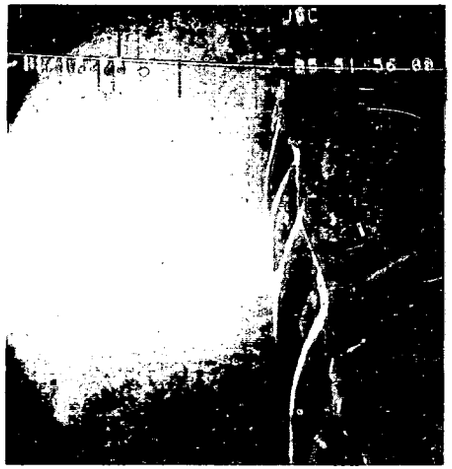

(13b) 1/30 sec after arc

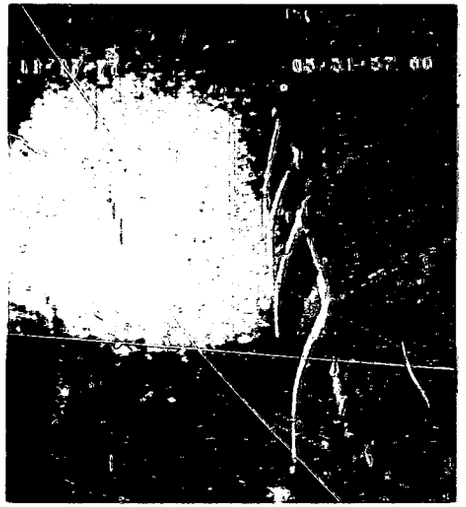

(13c) 1/2 sec after arc

(13d) 1 sec after arc

Fig. 13 - LLTV sequence showing sheath collapse and slow recovery following "arc" discharge.

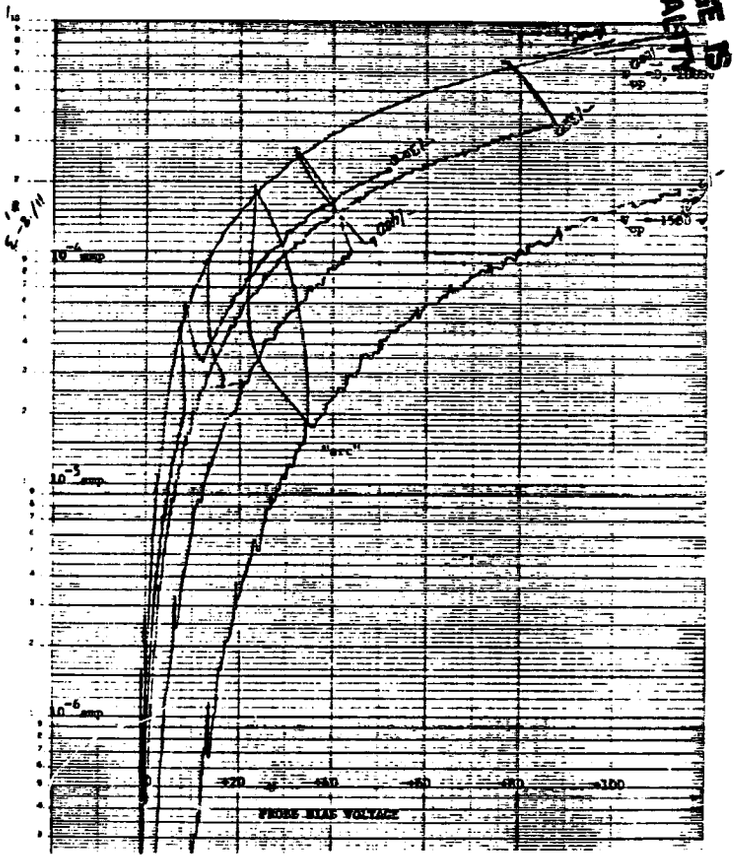

Fig.14 - Set of log I vs V curves showing several arcs with sheath collapse. Probe recorded value I(V) following arc shifts from point along "inside the sheath" curve to a value along original "outside the sheath" curve, then slowly returns to its pre-arc I(V) conditions.

Fig.15a - Arc from mylar tape holding teflon insulated rod to plastic brace, located (arrow) 1-2m in front of "SPS" (@-3000V), inside ion sheath. Edge-on view shows simultaneous collapse of sheath, with no bright glow.

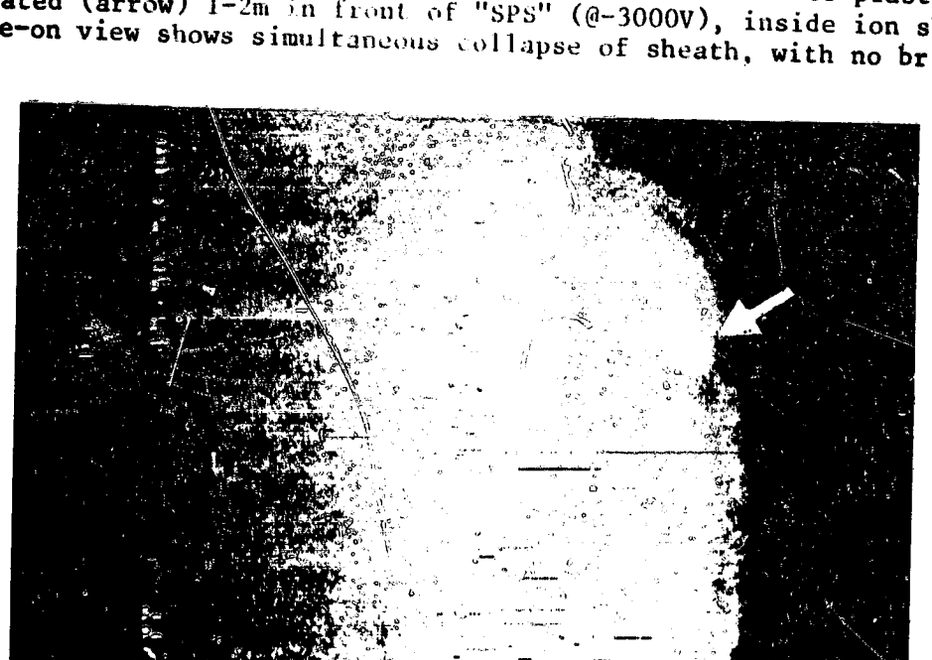

Fig.15b - Arc from teflon insulated/mylar wrapped wire, at point 5m along the wire, 1m behind "SPS" panel (edge on, @-3000V); inside thick electron sheath. Note greatly brighter emission from surrounding region.

Fig. 16 - Surface Glow (Ion Focusing) on face of "SPS" panel. Constant 1.0 kV.

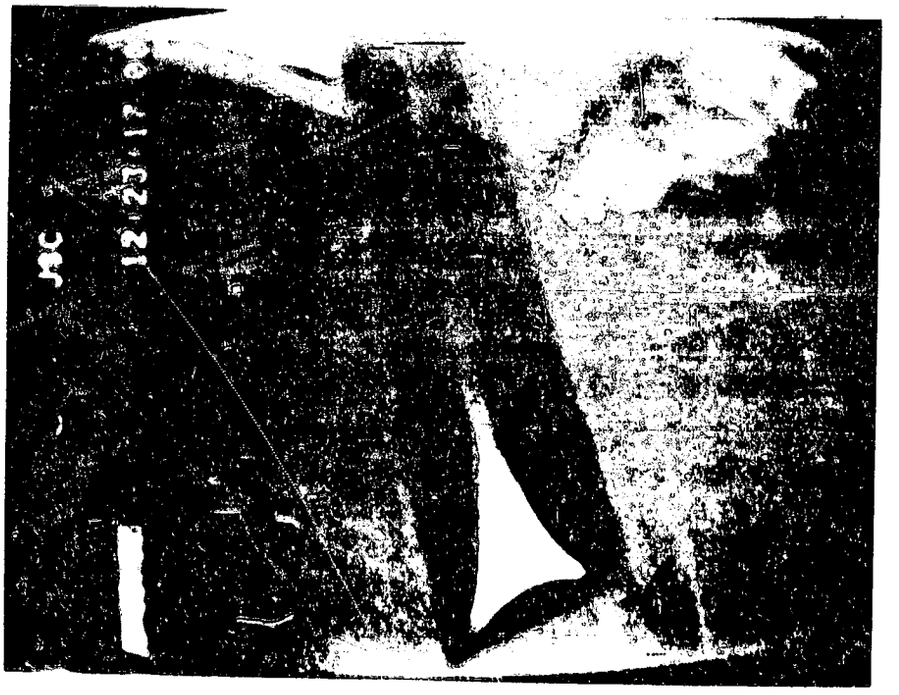

Fig. 17 - Surface Glow (Ion Focusing) on face of "SPS" panel. Constant 2.5kV.

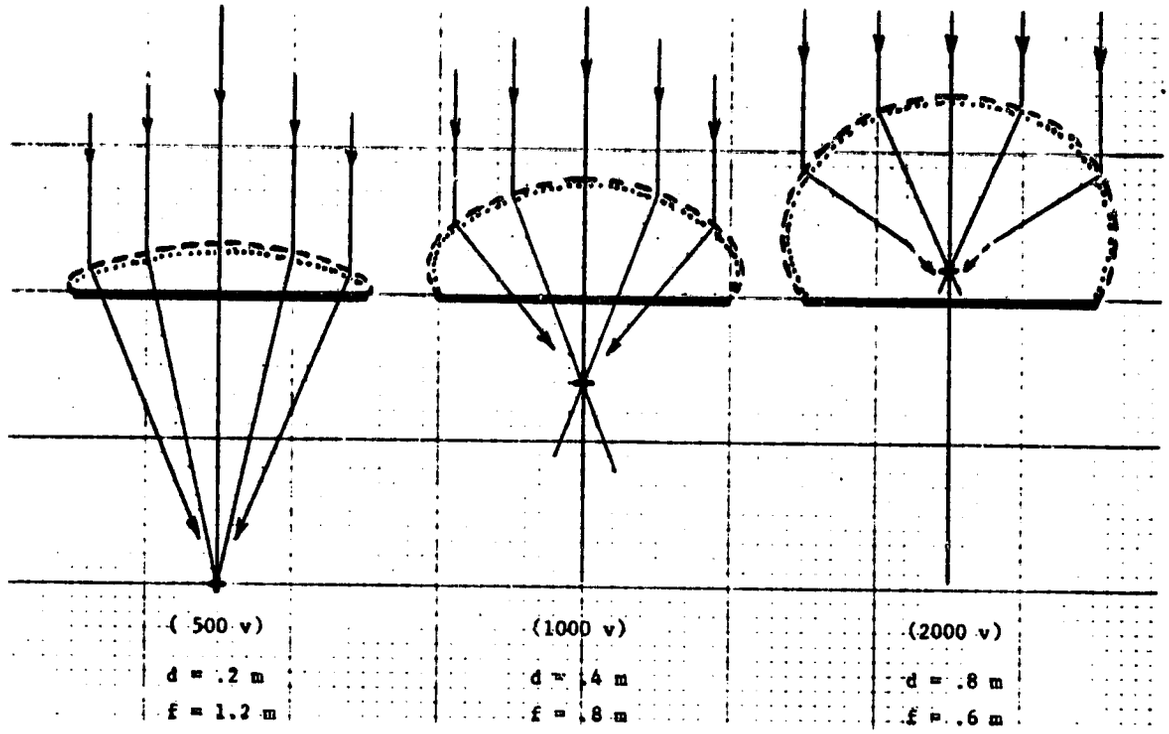

Fig.18 - Ion focusing onto panel by cylindrical lens effect of space charge sheath. Model is qualitative, to illustrate relative behavior to be expected as sheath expands (with increased V, or reduced density).

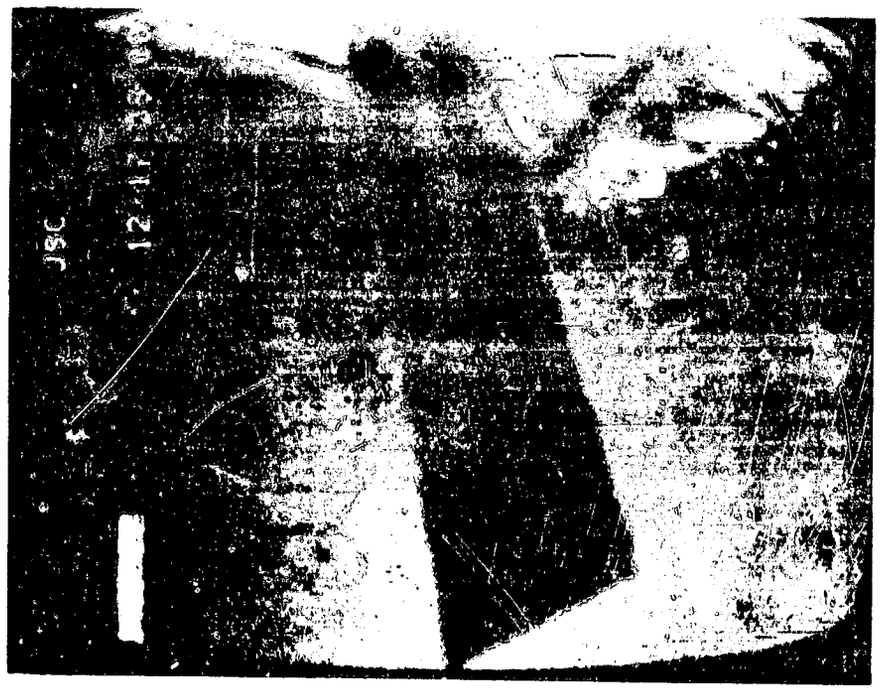

Fig. 19 - Surface Glow (Ion Focusing) at grounded end of panel (sheath thickness flattens to zero as voltage decreases to ground).

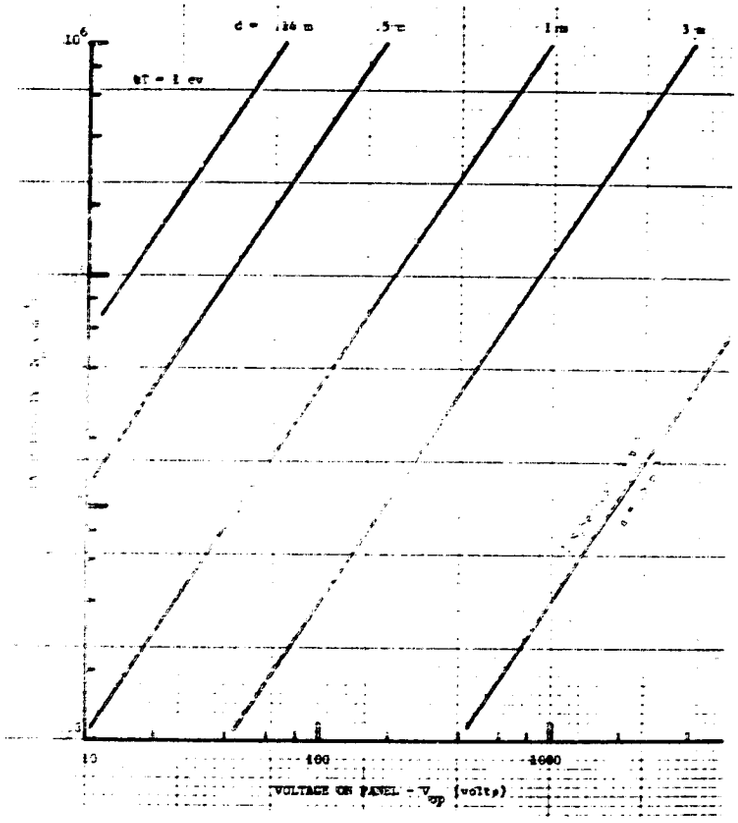

Fig. 20 - Planar space charge limited sheaths, ion or electron collecting. Thickness d vs N_o, V_{op}.

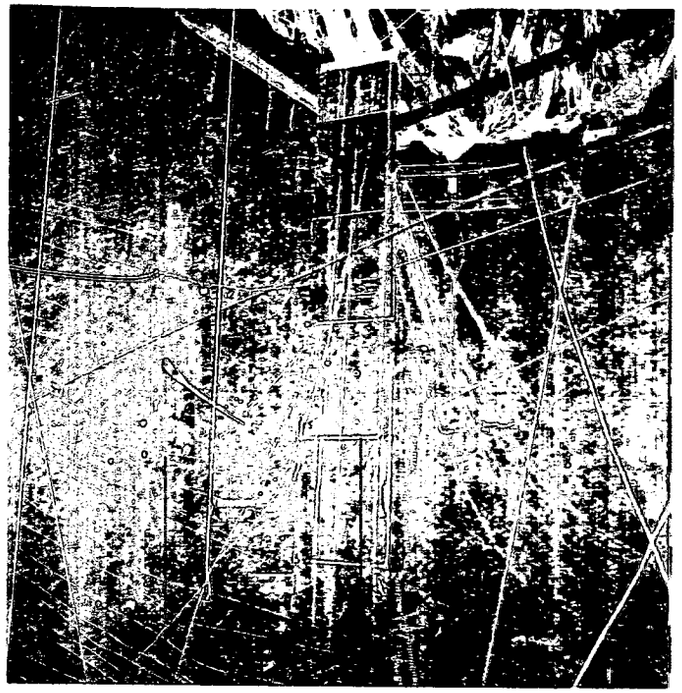

Fig. 21 - "SPS" installed in chamber A for SPL-1 tests. Note movable probes in front.

N79-24024

PLASMA SHEATH EFFECTS AND VOLTAGE DISTRIBUTIONS OF LARGE HIGH-POWER SATELLITE SOLAR ARRAYS

Lee W. Parker
Lee W. Parker, Inc.

SUMMARY

Knowledge of the floating voltage configuration of a large array in orbit is needed in order to estimate various plasma-interaction effects. The equilibrium configuration of array voltages relative to space depends on the sheath structure. The latter dependence for an exposed array is examined in the light of two finite-sheath effects neglected in previous analyses which have assumed the planar approximation based on the thin-sheath limit. One effect is that electron currents may be seriously underestimated. The other is that a potential barrier for electrons can occur, restricting electron currents. The problem is not a priori a thin-sheath problem either with respect to plasma electrons or with respect to wake effects. A conducting surface is assumed on the basis of a conductivity argument. Finite-sheath effects are investigated using the thick-sheath limit. The results of assuming thin-sheath and thick-sheath limits on the floating configuration of a linearly connected array are studied, under conditions appropriate to both LEO and GEO. Sheath thickness and parasitic power leakage are estimated analytically. Numerically computed fields using a 3-D code are displayed in the thick-sheath limit. Potential barriers appear in the cases of (a) a linearly connected array in GEO, and (b) an "overlapping sheath" interaction problem involving adjacent strips with large voltage jumps between them.

INTRODUCTION

High-power solar arrays for satellite power systems are presently being planned with dimensions of kilometers and with tens of kilovolts distributed over their surfaces. This paper is concerned with the "floating potential" of an array with exposed interconnects, that is, with the equilibrium voltage configuration under the conditions of (a) overall current balance, and (b) fixed relative voltages along the array between the positive and negative terminals. Knowledge of the floating configuration is needed for estimating a number of plasma-interaction effects, in both low earth orbit (LEO) and geosynchronous orbit (GEO). Among these are (a) parasitic power leakage due to ambient plasma currents, (b) power leakage due to ion thruster currents, (c) sputtering and erosion, (d) secondary-electron emission and cascade, (e) velocity wake effects, and (f) differential charging effects. The array will float so that a part of it is positive and the remainder is negative.

Two effects have been neglected in previous analyses. One of these is that the positive section may be smaller than the sheath thickness and may require a more general treatment than the usual planar approximation based on the thin-sheath limit. One result is that more electron current may be collected than may be expected on the basis of a thin sheath; this shortens the positive section further. Another effect is the possible appearance of a potential barrier for electrons (the array has a net negative charge); this tends to reduce electron currents, thus lengthening the positive section. The question can be decided only by self-consistent calculations including space charge. The problem is not really a thin-sheath problem a priori; the size of the positive section depends on the solution. Also, the thin-sheath concept must break down when the array is looking into its own wake.

In this paper we assume two limits, those of a thin sheath and a thick sheath, and calculate analytically the associated floating voltage configurations of a linear 40-kv array with exposed interconnects. The thick-sheath limit is useful for investigating finite-sheath effects. The true self-consistent solution may lie between the two limits. Potential barrier effects on the array voltages are neglected. The floating configurations can be determined more precisely including the effects of potential barriers by self-consistent numerical solutions (cf. ref. 1). Magnetic fields are neglected, as well as voltage drops due to internal currents.

Formulas and results obtained by analytical approximations for sheath thickness, and for parasitic power leakage in the two limits, are presented for both LEO and GEO. The structure of the sheath is computed using a 3-D computer code called PANEL (ref. 2), where a flat rectangular plate with a nonuniform distribution of surface voltage serves as a model for a flat high-voltage solar array. In the thick-sheath limit the field solution shows that the potential barrier for electrons has a height of 2 kv for a 40-kv array. Thus, for electrons with temperatures below 2 kev, the electron current would be reduced, and the positive section of the array would increase in size. The appearance of a potential barrier is typical in differential charging situations (refs. 1 and 3). PANEL was used also to compute fields for various finite sheath thicknesses, using a linearized space-charge model. The results (not shown here) indicate that the barrier decreases in height and approaches the edge of the array as the Debye length decreases.

Also examined is the "overlapping-sheath" question of current collection by adjacent areas with a large potential jump between them. (This could apply for example to exposed terminals on the back of an array.) The model consists of alternating strips at 0 and 1000 volts (assumed relative to space). The plasma currents are calculated using the "inside-out" method (ref. 4) of reversed trajectories. The high-voltage areas tend, through creation of potential barriers, to prevent the plasma particles repelled by them from reaching their low-voltage neighbor areas, thus controlling the current-voltage characteristics of the low-voltage areas.

CONDUCTIVITY OF INSULATED SURFACES

We assume here that the array has a conducting surface (interconnects exposed to the plasma). It should be noted that the alternative option of insulating the entire array from the plasma by a thin perfectly non-conducting dielectric coating is unfeasible, for the following reason. An insulated array would tend to float with all surface points equilibrated to a potential of the order of the plasma temperature (or of the photoelectron energy where photoemission is dominant). With large voltages (tens of kilovolts) existing on the array surfaces under the dielectric layer, a thin dielectric layer of the order of 20 microns thick can be subjected to electric fields E of the order of 10^7 v/cm, well above nominal breakdown thresholds. Hence breakdown is likely for very good insulators.

A small but finite dielectric conductivity, on the other hand, can change the problem essentially from that of an insulating surface to that of a conducting surface. To estimate the "cross-over" critical conductivity, we compare the rates of (a) surface discharging by conduction through the dielectric, and of (b) surface charging by plasma currents. The ratio of these rates may be approximated by $\sigma E/j$, where σ, E, and j denote the conductivity, internal electric field, and charging current density, respectively. This ratio should be greater than unity to avoid breakdown and effectively to provide conducting surfaces. Assuming $j=10^{-10}$ amp/cm^2 as typical of GEO conditions, and $E=10^6$ v/cm as a maximum allowed value, we obtain $\sigma E/j=10^{16}\ \sigma$(mho/cm). Hence $\sigma=10^{-16}$ mho/cm is the critical conductivity. A change in σ of a half of an order of magnitude in one direction or the other will make the layer essentially conducting or essentially nonconducting. Typical spacecraft insulating materials such as quartz, Kapton and Teflon have lower conductivities than this in the dark but higher conductivities than this in sunlight (ref. 5). Hence at least in sunlight a quartz- or Teflon-coated front surface may be considered conducting, and the analysis of this paper applies. (However, the Kapton backing presently contemplated for the back surfaces of the array is a good insulator in the dark and runs the hazard of incurring breakdowns.)

In the next section we treat sheath thickness, for the case where the sheath is due to the ambient plasma. Photoemitted or secondary-electron contributions should also be considered since in GEO they may contribute significantly not only to fluxes but also to space charge and reduced sheath thickness. Strong photoemission contributions are treated, for example, by Parker (ref. 6) and by Soop and by Schröder (see ref. 7). Their effects are also discussed briefly in the present paper.

SHEATH THICKNESS

We assume the solar array is a flat rectangular plate, with the voltage distribution on its surface varying linearly along one of the dimensions, and constant along the other dimension. The surface is assumed to be conducting (that is, the solar-cell interconnects are assumed to be exposed to the plasma). Figure 1 shows schematically how the sheath might look in a side view of the panel, with the floating voltages distributed from left to right. The negative

section on the left is relatively long, of length L_1. The positive section on the right is relatively short, of length L_2. The dividing point between the two sections is at space potential. The sheaths of the two sections are shown to thicken as the voltage relative to space increases in magnitude. The negative section (L_1) collects mostly ion current, while the positive section (L_2) collects mostly electron current. The linear voltage variation on the surface is shown in the lower part of the figure, going from negative V_1 at the most negative end to positive V_2 at the most positive end.

Sheath structures generally require self-consistent numerical solutions (e.g., refs. 1, 8-9). When the sheath is thin relative to the body dimensions, however, and consists essentially only of attracted ambient-plasma particles, an analytical approximation is available based on a "space-charge-limited" diode model, the so-called Child (or Child-Langmuir) model (ref. 10). This is a unipolar sheath model wherein the attracted charged particles are accelerated in a beam toward the collecting plate, starting with zero energy. If e and m denote the particle charge and mass, V denotes the voltage, j denotes the current density, and S denotes the diode plate separation, then the sheath thickness may be estimated from the Child law relating V, j, and S. In c.g.s. units, this is

$$S = (2e/m)^{1/4} \cdot V^{3/4}/(9\pi j)^{1/2} \tag{1}$$

where the sheath thickness is identified with the plate separation. In sheath thickness estimations, it is customary to replace j by the random thermal current density at the sheath edge, $j_o = en_o (kT/2\pi m)^{\frac{1}{2}}$, where n_o is the particle density and T is the temperature of the Maxwellian distribution. If there is also a significant drift velocity v_o (as in the case of O^+ ions in LEO) toward the panel, j_o may be replaced by $[\exp(-M^2) + \sqrt{\pi}\, M(1 + \text{erf } M)]\, j_o$, where M is the ion Mach number $M=(mv_o^2/2kT)^{\frac{1}{2}}$. Thus, in practical units, taking into account both thermal and drift (ion "ram") currents at the sheath edge, the planar equation (1) may be written

$$S(\text{meters}) = 9.33 \frac{V^{3/4}(\text{volts})}{n_o^{\frac{1}{2}}(\text{cm}^{-3}) \cdot T^{\frac{1}{4}}(\text{ev}) \cdot (\text{RAM})^{\frac{1}{2}}} \tag{2}$$

where

$$\text{RAM} = \exp(-M^2) + \sqrt{\pi} M (1 + \text{erf} M) \tag{3}$$

Equation 2 cannot be used when S is comparable with or exceeds the body dimensions. Corrections for non-planarity are frequently made using the analogous spherical diode model, where the particles move radially inward from an outer emitter to an inner spherical collector, with no angular momentum. Langmuir and Blodgett (ref. 11) give a table of factors which may be used in conjunction with equation (2). It should be noted that equation (2) assumes that the panel is looking into the ram direction and is invalid if the panel looks into the wake.

FLOATING CONFIGURATION BASED ON THIN SHEATH LIMIT

In the thin sheath limit, referring to figure 1 and assuming only attracted-particle contributions to the array currents (because of the large voltages compared with particle energies), and because in this limit the currents are constant over the two sections of the array, we may express the current balance condition as

$$RAM \cdot j_{io} \cdot L_1 = j_{eo} \cdot L_2 \tag{4}$$

where L_1 and L_2 denote, respectively, the lengths of the negative (left) and positive (right) sections; j_{io} and j_{eo} are the random thermal currents of ions and electrons, respectively; and RAM is defined by equation (3). If the array looks into the ram direction, RAM can be greater than unity for the ions. For equal ion and electron temperatures, equation (4) yields the ratio of the positive to negative lengths:

$$\frac{L_2}{L_1} = \sqrt{\frac{m_e}{m_i}} \cdot (RAM) \tag{5}$$

where m_e and m_i denote the electron and ion masses, respectively. Results for LEO and GEO are shown in table 1, under the columns labelled "THIN LEO" and "THIN GEO".

For LEO we assume oxygen ions with Mach number M=6.4 (ref. 12), which yields RAM=22.7. From equation (5) we obtain $L_2/L_1=0.132$, so that $L_2=117$ m is the length of the positive section of a one-kilometer array. Thus the positive end of a 40-kv array floats at $V_2=+4700$v. The negative section length and end voltage are $L_1=883$m and $V_1=-35300$v, respectively. These values of L_2, L_1, V_2, and V_1 are shown in the "THIN LEO" column of table 1. From equation (2), assuming in addition $n_o=10^5$ cm^{-3} and T=0.1 ev, we obtain sheath thicknesses $S_2=30$m and $S_1=28$m, as shown in table 1. Thus, the sheath is thin compared with the lengths of both the positive and negative sections. Hence the thin-sheath limit seems valid for LEO. However, it should be noted that we are neglecting edge effects and velocity-flow wake effects.

For GEO we assume hydrogen ions, with Mach number zero (i.e., RAM=1). From equation (5), we obtain $L_2/L_1=0.0233$. Hence the positive-section length and end-voltage of a one-kilometer 40-kv array are $L_2=23$m and $V_2=+900$v, respectively. The length and end-voltage of the negative section are $L_1=977$m and $V_1=-39100$v, respectively. These lengths and voltages are shown in the "thin sheath" diagram of figure 2. From equation (2), assuming $n_o=1$ cm^{-3} and T=10000ev, we obtain sheath thicknesses $S_2=150$m, that is, large compared with L_2; and $S_1=2600$m, that is, large compared with L_1. (See table 1.) Hence, the sheaths of both sections are thick rather than thin (even when the Langmuir-Blodgett spherical correction factors are applied), and the thin-sheath assumption in the absence and secondary and photoelectron contributions is invalid for GEO. However, since photoelectron and secondary-electron contributions are important in GEO, the sheath will be of finite thickness and its structure must be calculated

self-consistently (refs. 6 and 7). Nevertheless, the thick-sheath limit is useful for investigating finite-sheath effects.

FLOATING CONFIGURATION IN GEO BASED ON THICK SHEATH LIMIT

In the thick-sheath (Laplacian) limit, a sphere collects attracted-particle current density in accord with the well-known orbit-limited ideal Langmuir formula

$$j = \left(1 + c\frac{eV}{kT}\right) \cdot j_o \qquad (6)$$

where j_o is the random thermal current density and c is equal to unity. Other 3-dimensional shapes as well can collect orbit-limited current in accord with equation (6) with c=1 (ref. 13). A flat circular surface (such as the end of a cylinder) has a linear current-voltage characteristic describable by equation (6) with c less than unity (ref. 14). We assume here that all points of the (conducting) solar-array surface collect current density proportional to j_oV. This implies that (a) the voltage everywhere is large such that eV/kT is large compared with unity, (b) only attracted particles contribute, (c) the coefficient c is the same for all points, and (d) there are no potential barriers. Then, since V=V(x) and j=j(x) are linear functions of position x on the panel surface, we must integrate j(x) over x to compute the total currents collected by the negative and positive sections. The current balance condition can be shown to yield

$$\frac{L_2}{L_1} = \left(\frac{m_e}{m_i}\right)^{1/4} \cdot (RAM)^{1/2} \qquad (7)$$

for the ratio of lengths, independent of the coefficient c. That is, the thick-sheath ratio L_2/L_1 is the square root of the corresponding thin-sheath ratio in equation (5).

Results for GEO are shown in the last column of table 1, labelled "THICK GEO." The positive and negative sections of a one-kilometer array are L_2=132m and L_1=868m, respectively. The corresponding positive and negative end-voltages are V_2=+5300v and V_1=-34700v, respectively. These lengths and voltages are shown in the "THICK SHEATH" diagram of figure 2.

POWER LEAKAGE IN LEO AND GEO

We may estimate power losses to the plasma in a similar manner to that in which we estimated floating voltages above. For the thin-sheath limit, the current density is constant over the (positive or negative) section, and the voltage varies linearly. Hence the power density varies linearly. The average power loss per unit area may be shown to be given by

$$\bar{P}_{(\text{thin sheath})} = \frac{V/2}{\left[\frac{1}{j_{eo}} + \frac{1}{RAM \cdot j_{io}}\right]} \tag{8}$$

where V is the total voltage differential V_2-V_1 across the array and the other symbols have been defined above. In practical units, assuming Maxwellian distributions with equal ion and electron temperatures, the current density may be written

$$j_0(\text{amp/m}^2) = 2.68 \times 10^{-8}\, n_0(\text{cm}^{-3})\, \sqrt{T(\text{ev})/m(m_e)} \tag{9}$$

where $m(m_e)$ denotes the particle mass in units of the electron mass; and $\bar{P}$ becomes

$$\bar{P}_{(\text{thin sheath})}\left(\frac{\text{watt}}{\text{m}^2}\right) = 1.34 \times 10^{-8}\, \frac{V(\text{volts}) \cdot n_0(\text{cm}^{-3}) \cdot \sqrt{T(\text{ev})}}{[1 + \sqrt{m_i/m_e} \,/\, RAM]} \tag{10}$$

Again, the array is assumed to be looking into the ram direction in collecting ion currents, where RAM can be greater than unity. In LEO, assuming m_i/m_e= 29380, with values of n_0, T, and RAM given in table 1, and taking V=40000 volts, we obtain $\bar{P}$≈2 watt/m^2. This value does not seem to represent a serious loss effect. It should be remembered, however, that the sheath could thicken, and power leakage could increase, near the edges and when the array looks into its own wake. In addition, we chose n_0=10^5 cm^{-3}; this value could go as high as 10^6 cm^{-3} in the F-region.

For the thick-sheath limit, the current density may be assumed to vary linearly, as was done for the floating configuration. Hence the power density varies quadratically. The average power loss per unit area may be shown to be given by

$$\bar{P}_{(\text{thick sheath})} = \frac{(cV/3) \cdot (eV/kT)}{\left[\frac{1}{\sqrt{j_{eo}}} + \frac{1}{\sqrt{RAM \cdot j_{io}}}\right]^2} \tag{11}$$

where c is the coefficient in equation (6). In practical units, $\bar{P}$ becomes

$$\bar{P}_{(\text{thick sheath})}\left(\frac{\text{watt}}{\text{m}^2}\right) = 0.89 \times 10^{-8}\, \frac{cV^2(\text{volts}) \cdot n_0(\text{cm}^{-3}) / \sqrt{T(\text{ev})}}{[1 + (m_i/m_e)^{1/4} \,/\, RAM^{1/2}]^2} \tag{12}$$

In GEO, assuming c=1, m_i/m_e=1836, the values of n_0, T, and RAM given in table 1, and taking V=40000 volts, we obtain $\bar{P}$≈0.0025 watt/m^2, which seems inconsequential compared with about 100 watt/m^2 nominally deliverable by the solar cells.

On the other hand, if the array is in LEO and is looking into its own wake, so that the sheath is thick rather than thin, equation (12) yields $\bar{P}$=22700 watt/m^2, indicating that catastrophic power losses can occur. (We took c=1 and RAM=1 but used the other parameter values listed in the "THIN LEO" column of table 1.)

In both equations (10) and (12), the dominant contribution is made by the smaller of the two currents, ion and electron. In both LEO and GEO the second term in the denominator is dominant because the ion current is the smaller of the two.

It should be noted that if we had included photoelectron contributions:

(a) the photoelectrons (of energy of the order of volts) would readily escape from the negative section but not from the positive section, and

(b) the photoelectron current density escaping from the negative section can be comparable in magnitude with the plasma electron current density on the positive section.

Hence the array would float with roughly equal positive and negative sections. Moreover, the sheath would be thin rather than thick because of the photoelectrons. Thus, the average power loss in GEO (without wake effects) would be of the order of $j_{eo}V$, or 0.1 watt/m^2.

STRUCTURE OF SHEATH IN GEO.

NUMERICAL RESULTS OF COMPUTER CODE "PANEL"

In this section we adopt the linear surface voltage distribution given analytically by the thick-sheath limit (the "THICK SHEATH" diagram in figure 2), and describe the computational approach used and results obtained by the computer code PANEL. Thus, the panel appears as in figure 3, namely, a rectangular plate, with the voltage varying linearly in one direction and constant in the other direction. The voltage runs from -34.7 kv at the negative end to +5.3 kv at the positive end. The 0-kv position is at 0.868 of the panel length. (Since the field is a solution of Laplace's equation, all lengths scale with the length of the panel.)

While the panel voltage configuration has been chosen on the basis of an approximate analysis, the calculation of the field structure requires a numerical technique. A grid method is used, whereby the panel is discretized by a collection of grid points, at which the panel potentials are defined.

Figure 4 shows the panel defined as a section of the x-y plane, in 3-dimensional cartesian x-y-z space. Grid intervals Δx and Δy are chosen, as shown in the figure, but not necessarily uniform. Particle fluxes are calculated at points on the panel by computationally following reversed trajectories to determine their origin. (This "inside-out" method was developed in 1964

(ref. 4) for efficient calculations in steady-state 3-dimensional sheath problems.) Figure 4 shows schematically two possible types of trajectory contributions to a point on the panel; in one example the trajectory comes from the ambient plasma at infinity, while in the other the trajectory comes from another point on the panel (e.g., a secondary or photoelectron). The type of trajectory which actually occurs, for a given incident velocity vector, can only be determined by numerical computation.

In a self-consistent calculation of the floating configuration, the fluxes of ions and electrons at the array points are computed, and the array potentials are adjusted (maintaining fixed relative potential differences) until there is global current balance. Power leakage is calculated by integrating the product of local net current density times local potential over the surface of the array.

The field in the space around the panel is represented by a large grid in 3-dimensional x-y-z space. This is used to calculate forces along trajectories by interpolation between grid points where the potentials are defined. In figure 5 the coarsest possible grid is shown, with only 32 grid points. The panel is represented by the shaded area between 4 grid points. In an actual problem orders of magnitude more points are used, both in space and on the panel. For example, the panel in figure 4 is represented by a 6x7 surface grid of 42 points. This should be embedded in a spatial grid of 1000 to 10000 grid points. About 3000 points were used to obtain the results discussed below.

The numerical field solution is obtained by replacing Laplace's equation by a set of linear algebraic equations, one for each unknown potential. One of the boundary conditions is that the potentials satisfy the prescribed panel surface-potential distribution (shown in figure 3 resulting from the thick-sheath analysis). The other condition is that the potential vanish at infinity. On the outer boundaries of the grid the potential satisfies a suitable relationship between its value and its gradient. The above procedures are outlined in reference 2 and are implemented, for example, in reference 8 for a spacecraft model in r-z geometry.

Linear Voltage Distribution

The field solution for a linearly distributed array in a hydrogen plasma is displayed in figure 6 in the form of a set of equipotential contours. The equipotentials are divided into negative and positive sets, with the zero-potential (space potential) contour tightly enclosing the positive end. Thus, all the positive contours are contained within this small contour. The negative contours have expanded to the right, "engulfing" the positive set and creating a negative saddle point (potential barrier for electrons) at about an array length L to the right of the right end of the array. This happens because the array has a net negative charge. The barrier, of height 2.1 kv, will exclude all electrons with energies less than this. Hence, if the electron temperature is less than 2 kev, the position of zero potential is moved to the left, toward the midpoint (at L/2). If the zero potential were at the midpoint, the negative and positive contours would be symmetric and the potential distribution would be dipole-like.

The solution displayed in figure 6 is the Laplace field. Solutions were also obtained for finite sheath thickness by the assumption of linearized space charge. This leads to a Helmholtz equation with a Debye-length-like parameter (refs. 15-16), whose solutions are 3-D generalizations of the well-known Debye potential. This parameter was assigned successively smaller values, representing a set of solutions (not shown) for diminishing Debye length. With decreasing Debye length, the above potential barrier becomes smaller and is "pulled in" toward the edge of the array.

Alternating Voltages - Overlapping Sheaths

Figure 7 illustrates a panel with alternating strips of zero volts and one kilovolt. This case can represent exposed connections on the backside of an array. It was run to determine the effects of "overlapping sheaths," that is, the effect on the current-voltage characteristic at a point on the surface due to a different potential maintained nearby. For one-volt ions and electrons, it was found that on the zero-volt surfaces the low-energy ions (repelled particles) were excluded (by potential barriers) because of the adjacent +1-kv surfaces, while the electron fluxes (attracted particles) had essentially their random-thermal values. On the 1-kv surfaces, the ion and electron fluxes were essentially the same as for a flat surface entirely at 1 kv, namely, slightly less than half of the ideal Langmuir value due to excluded trajectories for the electrons and the Boltzmann factor for the ions.

Figure 8 displays the equipotential contours for the field solution corresponding to the alternating strips of figure 7, including three saddle points associated with each of the three zero-volt strips. The figure is symmetric about the panel center and is drawn only for the right half. The sizes of the potential barriers, 320 volts and 93 volts, show why the repelled low-energy particles were excluded from the zero-volt strips. If there were infinitely many strips, periodically spaced, the saddle points would also be periodically spaced and centered above the zero-potential strips.

The alternating voltage configuration on the array was assumed. Its floating configuration was not determined. This would require a numerical self-consistent solution because of the potential barriers.

This paper has benefited from the author's discussions with James G. Laframboise.

REFERENCES

1. Parker, L.W.: Differential Charging and Sheath Asymmetry of Nonconducting Spacecraft Due to Plasma Flows. J. Geophys. Res., vol. 83, no. A10, Oct. 1978, p. 4873.

2. Parker, L.W.: Power Loss Calculation for High-Voltage Solar Arrays. Computer Method in Three-Dimensional Space (PANEL). Lee W. Parker, Inc. Report, Feb. 1977.

3. Whipple, E.C., Jr.: Observation of Photoelectrons and Secondary Electrons Reflected from a Potential Barrier in the Vicinity of ATS 6. J. Geophys. Res., vol. 81, 1976, p. 715.

4. Parker, L.W.: Numerical Methods for Computing the Density of a Rarefied Gas About a Moving Object. Allied Res. Assoc. Report AFCRL-64-193, Mar. 1964.

5. Adamo, R.C.; and Nanevicz, J.E.: Effects of Illumination on the Conductivity Properties of Spacecraft Insulating Materials. Stanford Res. Inst. Report NASA CR-135201, July 1977; Coffey, H.T.; Nanevicz, J.E.; and Adamo, R.C.: Photoconductivity of High-Voltage Space Insulating Materials. Stanford Res. Inst. Report, Oct. 1975.

6. Parker, L.W.: Theory of Electron Emission Effects in Symmetric Probe and Spacecraft Sheaths. Lee W. Parker, Inc. Report AFGL-TR-76-0294, Sept. 1976.

7. Grard, R.J.L. (Ed.): Photon and Particle Interactions with Surfaces in Space. D. Reidel, Hingham, Mass., 1973.

8. Parker, L.W.: Calculation of Sheath and Wake Structure About a Pillbox-Shaped Spacecraft in a Flowing Plasma, in Proceedings of the Spacecraft Charging Technology Conference, Report AFGL-TR-77-0051/NASA TMX-73537, Pike, C.P. and Lovell, R.R., Eds., Feb. 1977, p. 331.

9. Parker, L.W.; and Whipple, E.C., Jr.: Theory of a Satellite Electrostatic Probe. Ann. Phys., vol. 44, no. 1, 1967, p. 126.

10. Child, C.D.: Phys. Rev., vol. 32, 1911, p. 492; (see Cobine, J.D.: Gaseous Conductors. Dover, New York, 1958, Eq. 6.9); Langmuir, I.: Phys. Rev., vol. 2, 1913, p. 450 (see ref. 11).

11. Langmuir, I.; and Blodgett, K.B.: Currents Limited by Space Charge Between Concentric Spheres. Phys. Rev., vol. 24, 1924, p. 49.

12. Liemohn, H.B.: Electrical Charging of Shuttle Orbiter. IEEE Trans. Plasma Sci., vol. PS-4, no. 4, Dec. 1976, p. 229.

13. Laframboise, J.G.; and Parker, L.W.: Probe Design for Orbit-Limited Current Collection. Phys. Fluids, vol. 16, no. 5, 1973, p. 629.

14. Parker, L.W.; and Laframboise, J.G.: Multi-Electrode Plasma Probe for Orbit-Limited-Current Measurements. II. Numerical Verification. Phys. Fluids, vol. 21, no. 4, 1978, p. 588.

15. Parker, L.W.: Computation of Ion Collection by a Large Rocket-Mounted Mass-Spectrometer Plate at a Large Drawing-In Potential. Mt. Auburn Res. Assoc. Report AFCRL-72-0524, Sept. 1972.

16. Parker, L.W.: Computer Solutions in Electrostatic Probe Theory, Part II. Two-Electrode Systems in r,z Geometry. Mt. Auburn Res. Assoc. Report AFAL-TR-72-222, Apr. 1973.

Table 1.

SHEATH THICKNESS, LENGTHS, AND VOLTAGES OF POSITIVE AND NEGATIVE SECTIONS OF A 40-kv ARRAY OF LENGTH 1 km

	THIN LEO (O^+ ions)	THIN GEO (H^+ ions)	THICK GEO (H^+ ions)
M = ion Mach number	6.4	0	0
RAM = ram current factor	23	1	1
L_2(m) = length of positive section	117	23	132
L_1(m) = length of negative section	883	977	868
V_2(v) = positive-end voltage	+4700	+900	+5300
V_1(v) = negative-end voltage	-35300	-39100	-34700
$n_0(cm^{-3})$ = ambient plasma density	10^5	1	1
T(ev) = ambient plasma temperature	0.1	10^4	10^4
S_2(m) = sheath thickness at positive end	30	150	∞
S_1(m) = sheath thickness at negative end	28	2600	∞

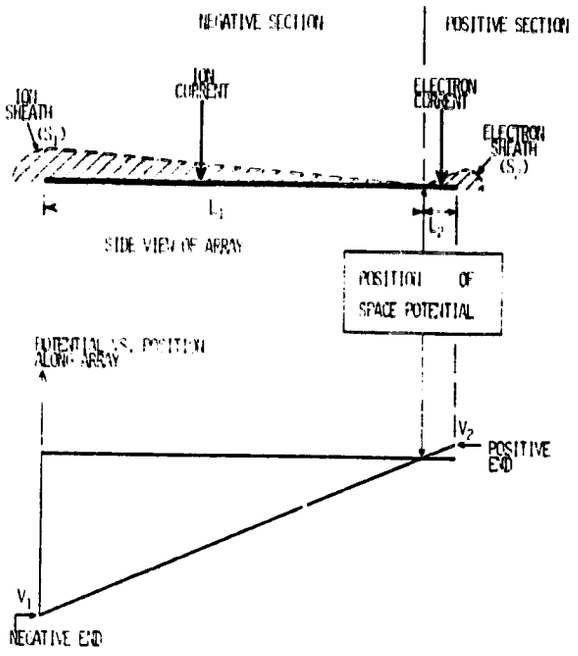

Figure 1. - Linear voltage variations in rectangular sheath panels.

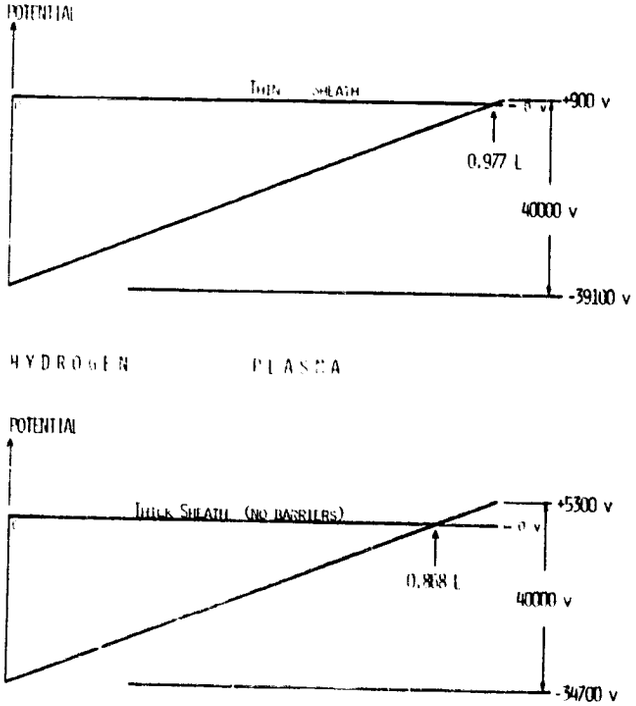

Figure 2. - Linear floating voltage configurations - thin- and thick-sheath limits in hydrogen plasma.

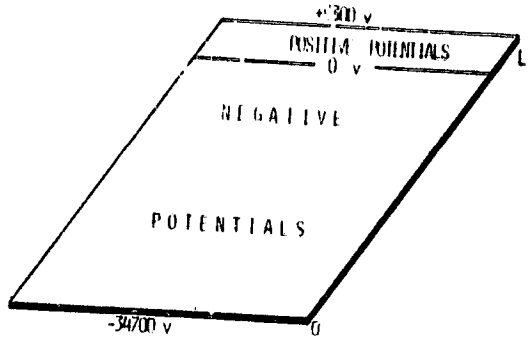

Figure 3. - Model for array sheath calculation - thick-sheath limit in hydrogen plasma.

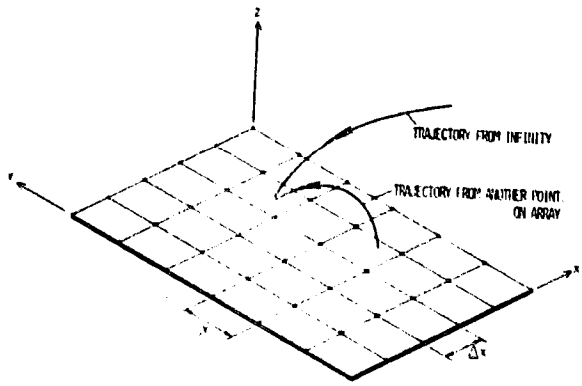

Figure 4. - Computational model for array panel.

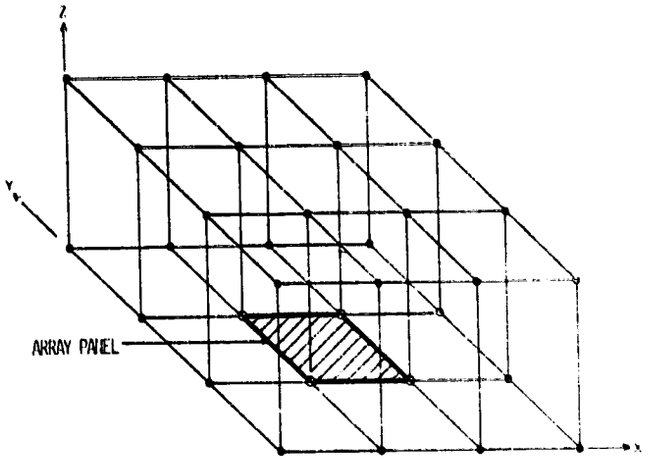

Figure 5. - Computational grid for array sheath calculation.

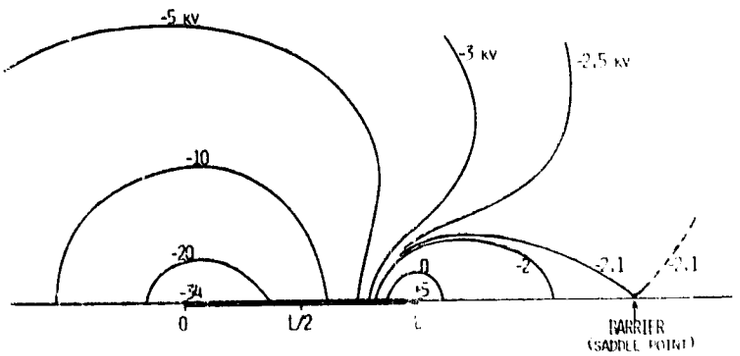

Figure 6. - Equipotential contours (in kilovolts) for sheath of floating linear array.

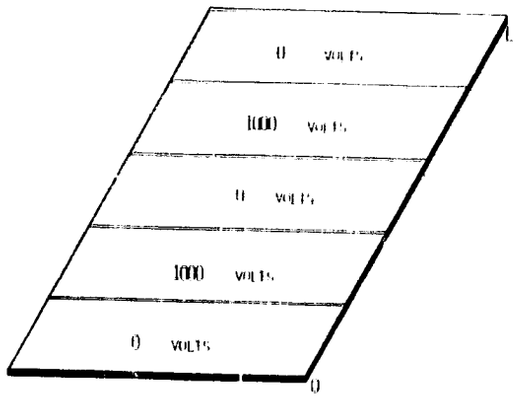

Figure 7. - Model for overlapping sheaths of alternating high- and low-voltage areas.

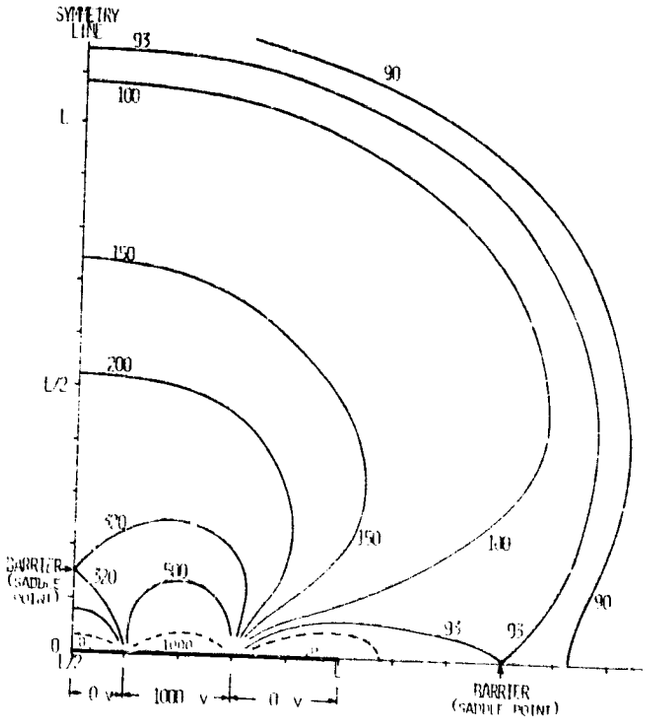

Figure 8. - Equipotential contours (in volts) for overlapping sheaths of alternating high- and low-voltage areas.

N79-24025

EFFECT OF PARASITIC PLASMA CURRENTS ON SOLAR-ARRAY POWER OUTPUT

Stanley Domitz and Joseph C. Kolecki
NASA Lewis Research Center

SUMMARY

Solar-array voltage-current curves are calculated by assuming the existence of parasitic loads that consist of local currents of charged particles collected by the array. Three cases of interest are calculated to demonstrate how the distribution and magnitude of parasitic currents affect output. Solar-array performance degradation became significant when the total parasitic current plus the load current exceeded the short-circuit current. Approximate graphical methods were useful for many applications. Power loss, which was calculated by summing the product of parasitic current and the local potential, underestimated the loss in maximum power.

INTRODUCTION

Higher powered spacecraft now being considered for future mission requirements may have solar arrays of much higher voltage output than those used in the past. The interaction of high-voltage solar arrays with a charged-particle environment has been the subject of previous study (refs. 1 to 5). The problem considered here is the effect of a parasitic load on the voltage-current output curve of the solar array itself. The parasitic load, which is actually the external collection of ambient charged particles falling on exposed conductors of the solar array, degrades useful array power output.

The collection of charged particles can arise from (1) interaction between the solar array and the ambient space plasma and (2) interaction between the array and the low-energy plasma emitted from an onboard ion source, such as an electric thruster.

The overall effect on the solar array of parasitic-current collection is to change the effective operating point of the array: For a given required load current the solar array will operate at a lower voltage and therefore at a lower power output. The current at each individual solar cell is the sum of the normal load current, which passes equally through all the cells in a series string, and the parasitic current, which varies at each cell. The parasitic current is, in general, a function of the cell potential, its position on the solar array, and the ambient plasma conditions. If the individual solar-cell current is known, its voltage can be calculated from the characteristic voltage-current curve for the type of solar cell used. The total array voltage is then the sum of the individual cell voltages. A computer program was written to

perform these summations and thus to obtain the full solar-array voltage-current curve for various conditions of interest.

Solar-array voltage-current curves were calculated for three cases of interest, representing three mechanisms for parasitic current collection:

(1) Parasitic current collected uniformly over the entire array - This one-dimensional model simplifies calculations since the parasitic current at each cell is a constant and is not affected by cell potential or array geometry. The physical situation is that the plasma sheath is small in relation to the solar-array dimensions.

(2) Parasitic current collected as a function of distance from a fixed source - The local source in this case is the charge-exchange plasma emanating from an electric thruster.

(3) Parasitic current as a function of potential - This corresponds to the infinite-sheath case, where the collected current depends on the local solar-cell potential.

The problem of parasitic currents arises normally only for high-voltage arrays such as those being considered for high-power operation. At the usual array voltages (<100 V), the parasitic current is a small fraction of the array current and is therefore not observed. For voltages in the multikilovolt range, there is a compound voltage effect - the addition of parasitic current in long series strings and the enhancement of collected current through growth of the collecting plasma sheath.

SYMBOLS

A	cell area
I	current out of string (load current)
I_L	load current, A
$I_{p,N}$	total parasitic flux falling on array, mA
i	current in solar cell, mA
i_{mp}	current at maximum power, mA
i_o	reverse saturation current, mA
i_p	parasitic flux, mA/cm^2
i_{pc}	parasitic flux, i_pA, mA/cell
i_{sc}	short-circuit current, 125 mA (assumed)

N	number of cells in series
V	voltage across string (load voltage), V
ΔV	local potential of solar cell measured from zero reference
v	voltage across solar cell, V
v_{mp}	voltage at maximum power, V
v_{oc}	open-circuit voltage (0.6 V assumed for one solar cell)

GENERAL CALCULATIONAL SCHEME

Computer Calculations

For the general case of N solar cells in a series connection ($C_1, C_2, \ldots, C_m, \ldots, C_N$), the load current I_L passes through each cell and through the load (fig. 1(a)). The parasitic currents $i_{pc,1}, i_{pc,2}, i_{pc,3}, \ldots, i_{pc,n}$ are collected externally by each cell, as shown in figure 1. The currents are additive so that each cell carries the sum of the parasitic currents collected from the cells ahead of it in the string. The total current is

$$I_L + \sum_{\zeta=1}^{m} i_{pc,\zeta}$$

at the m^{th} cell and increases until, at some point in the string, short-circuit current is reached. At short-circuit current, the solar-cell voltage drops to zero. The remainder of the cells in the string are also at zero voltage, and they act merely as a current-carrying wire.

The potential of each solar cell is computed as a function of the current passing through it. For the calculations in this paper a simple diode type of expression is used (ref. 6):

$$v = K[\ln(i_{sc} + i_o - i) - \ln i_o] \tag{1}$$

where v is the solar-cell potential, i is the solar-cell current (load current plus parasitic current), i_o is reverse saturation current, and K is a constant. The basic cell used in this paper is 2 centimeters by 2 centimeters with an open-circuit voltage of 0.6 volt and a short-circuit current of 0.125 ampere. In practical applications, equation (1) can be replaced by a more complicated expression involving temperature, or the solar-cell curve can be represented by a set of experimental data points. In either case the individual

solar-cell potential is obtained as a function of current and the total array potential is found by summing individual cell voltages:

$$V = \sum_{K=1}^{N} v_K$$

Therefore, to solve for the solar-array voltage-current curve, the required inputs are

(1) The array geometry - the number of solar cells in series and in parallel

(2) The distribution of parasitic current collected on the array

(3) The voltage-current curve for an individual cell

The most difficult problem is to obtain the distribution of parasitic current. In this paper only simple forms for parasitic current are used, but in general the current collected will be a complicated function of cell potential and array geometry. The method of computer calculation is described in more detail in appendix A of this paper.

Analytical Method

It is possible to obtain an analytical solution under certain conditions. For a solar-cell voltage-current curve of the form given in equation (1) and for an equal distribution of parasitic current over the array, the total array potential can be given as follows (ref. 2)

$$V = \frac{K}{i_{pc}} (A \ln A - B \ln B - Ni_{pc}) - KN \ln i_o$$

where

$$A = i_{sc} + i_o - i$$

$$B = i_{sc} + i_o - i - Ni_{pc}$$

Graphical Method

In addition to computer calculations, a graphical method can be used for most cases of interest. The graphical solution is based on a simple approximation. It is assumed that each solar cell is either "on" at some average constant voltage or "off" at zero voltage in a saturated state. This requires a rectangular solar-cell voltage-current curve. Determining the total array voltage becomes a matter of determining how many cells are generating power

and choosing an average potential for each cell. The graphical method is discussed further in appendix B of this paper.

Floating Array

The calculations for positively and negatively biased arrays are identical except that, in general, the current collection density will be smaller for the negatively biased arrays that are collecting ions. The floating condition for a solar array requires that the zero potential point of the array adjust itself so that no net current is collected; that is, the collection of ions equals the collection of electrons. To meet the floating requirement, an iterative procedure can be used to equalize the total flux of positive and negative currents. In balancing currents, the spacecraft conducting-area must be taken into account. For the floating array, those cells driven to short-circuit saturation are grouped together on the solar array at the location of floating potential, rather than at the endpoint of the array (fig. 1(b)).

RESULTS

Case 1 - Parasitic Currents Distributed Uniformly over Solar Array

The voltage-current curves of the array calculated with the methods described in the preceding section are shown in figure 2. Parasitic flux per cell i_{pc} is a parameter. The upper set of curves in figure 2 represents a series string of 40 000 cells; the lower set of curves represents a string of 4000 cells. Increasing the number of solar cells in series with constant parasitic flux decreases the fraction of useful array power because of the additive effect of the collected current. An interesting feature of figure 2 is that the right sides of the curves are almost straight lines emanating from $I = i_{sc}$. The reason for this is that in this region, cells are going into short-circuit condition at a linear rate as load current is increased, dropping the overall potential monotonically.

In figure 2 the parametric curves are given as parasitic current per cell. Relating this number to local plasma conditions would require consideration of a large number of variables such as the possibility of front and back current collection, local plasma density, ram and wake effects, magnetic field effects, and the influence of many factors on the location of the array floating point. Such factors have not been considered here; instead, the emphasis is on finding the reaction of the solar array to a given parasitic current distribution.

In figure 2 the solar-array current given represents that for a single string of cells. For a number of strings in parallel the current is proportional to the number of parallel strings. For example, with 100 parallel cells the labeled currents in figure 3 are multiplied by 100, but the array potentials remain the same.

The ratio of maximum power with parasitic current to maximum power without parasitic current is shown in figure 3 as a function of the number of cells in series with constant flux as a parameter. Essentially, the maximum-power points are replotted from data like those shown in figure 2. As expected, for a given parasitic current, the maximum-power ratio decreases with increasing string length. For a floating array, figure 3 represents the number of cells in a series string that could be either positive (collecting electrons) or negative (collecting ions). Figure 3 shows that for calculations where parasitic currents are collected in a thin sheath, the drop in maximum power is small for a floating array (where the array is primarily negatively biased) even in the ionosphere.

The voltage-current curve for a case 1 problem obtained by the graphical method is shown in figure 4. On the original solar-array curve a current $I_{p,N}$, the total parasitic flux falling on the array, is marked off on the abscissa from $I = i_{sc}$ toward the origin. A straight line is drawn from i_{sc} to the point where the original curve crosses $i_{sc} - I_{p,N}$. The graphical method is explained in more detail in appendix B of this paper.

Case 2 - Current Collection from Local Source

For the calculation of current collection from a local source, the source of charged particles is the charge-exchange plasma from an electric thruster exhaust beam (ref. 7). Charge-exchange ions drift away from the beam to create a bridge that enables electrons to be collected by the solar array. A directly coupled array is always at positive polarity. Since the volume of charged-particle production is small and distances to the array are large, the current flux to the array falls off rapidly with distance, as shown in figure 5.

The solar-array power is 25 kilowatts, divided into two equal wings of 12.5 kilowatts each, 4.2 meters wide and 26.8 meters long. The maximum potential is 1200 volts, directly coupled to the thruster. The solar cells are arranged so that the zero-voltage point is inboard and the maximum voltage is at the outboard tip of the arrays. One wing consists of 200 000 cells, 2000 cells in series and 100 cells in parallel.

For calculation purposes, the array is divided into 10 equal sections, as shown in figure 5. The parasitic current to each segment is obtained from the data of reference 7 and is considered to be constant in the section. Within each section, the calculation of the total section voltage proceeds as in case 1. The overall potential is obtained by adding voltages of the 10 sections.

Figure 6 shows the resulting voltage-current curve. The total collected parasitic current is approximately 25 percent of the solar-array current, and the decrease in maximum-power point is about 18 percent, as shown in figure 6. Because most of the parasitic current is collected at low voltage for this configuration, the effect on the array is minimized. The parasitic current distribution, however, is sensitive to the model chosen for charge-exchange

ion flow. At the present time, the details of such flow for a cluster of electric thrusters have not been fully investigated.

A graphical method can again be used. Within each solar-array segment, the parasitic flux is considered to be constant. The voltage-current curve of each segment is obtained graphically in the same manner as in case 1. The resultant graph is made up of a series of straight-line segments that can be replaced with a smooth curve that approximates the true voltage-current curve.

Case 3 - Parasitic Current as Function of Potential

For the two previous cases the collected current was considered to be one-dimensional, consisting of the ambient particle flux falling on the solar array. There was no enhancement of current collected due to the effect of the local potential. To study the effect of voltage-enhanced currents on the solar-array power output, the collected currents were assumed to be of the form

$$i_{pc} = i_p A\left(1 + \frac{V}{V_{th}}\right) \tag{2}$$

Equation (2) represents the infinite-sheath case, or "orbit limited" current collection for a spherical probe. Equation (2) is approximately correct for a plain-disk probe. It is not strictly correct for large surfaces because of the intersection of particle trajectories with the array; however, trajectory calculations agree with exact calculations within a factor of 2.

The resultant voltage-current curves are shown in figure 7. Equation (2) is used to represent parasitic current for an array of 4000 cells in series with flux density as a parameter. In figure 7 the right slopes of the curves are no longer straight lines because of the nonlinear parasitic current collection. For a given parasitic flux the loss in power is much greater than for the thin-sheath case. This is due to the multiplying factor of solar-cell potential in this case. Since parasitic current for this example is proportional to voltage, the calculated power used in collecting current is proportional to voltage squared.

The next logical example to consider would be the thick-sheath case, where the effect of space charge has been taken into account. Such a computation has not been attempted because of the lack of an easily manipulated model of current collection at individual cell locations. Approximate space-charge-limited current models have been attempted (refs. 1, 6, and 8) by using geometrical figures such as flat plates, spheres, and cylinders. But for our calculations it is necessary to determine exactly where the current is collected. Another complicating factor of the finite-sheath case is that the collection of current does not increase linearly with solar-array area, and therefore the results would not be in the form of a generalized voltage-current curve.

Approximate graphical methods apply to voltage-enhanced currents also. Again the solar array is divided into segments, each with an average voltage. If the current collection is known as a function of voltage, each section can

be drawn in the same manner as in case 2. The total curve again is obtained by connecting the line segments.

DISCUSSION OF RESULTS

If the parasitic current distribution on the solar array is known, whether or not to proceed with voltage-current curve calculation depends on the particular problem. One reason for generating the voltage-current curve is to find the operating point on the curve and to determine the power available more accurately. For example, it is often necessary to know the power at the maximum-power point. The power lost to parasitic currents is usually defined as the summation over the array of the product of the parasitic currents and the potential at which they are collected. Although this is a useful number, it can be misleading. For example, in figure 4, the calculated power loss for the thin-sheath case is equal to the cross-hatched area (areas under the curve represent power). Under parasitic load the new maximum power is at point B; the original maximum power of the array is at point A. The power lost is therefore the power at A - minus the power at B, or about twice the calculated value. The reason for this discrepancy can be seen by examining figure 4. Because of the degradation in the shape of the voltage-current curve, maximum power - which is represented by the rectangle of greatest area that can be drawn under the curve - is reduced more than anticipated. There is a further reduction in power if the array must be operated at a voltage or current other than the maximum power point. Thus the "true" power-loss determination depends on requirements for the overall system.

Another interesting example concerning power loss is the case 2 result, interaction with an onboard electric thruster. Here, because of the distribution of charge-exchange ions, parasitic currents are largest at the inboard sections of the solar array (fig. 5). If the total flux to the array is increased, the power loss does not increase linearly. The reason for this is that once the lower potential cells saturate and drop to zero voltage an increase in parasitic flux has no effect on those particular cells. Although no general rule has been found to relate the calculated power loss to the "actual power loss," the calculated power loss is usually lower. If this value is unacceptable, there is little reason for going through the full array calculations.

Another measure of solar-array degradation due to parasitic currents is the sum of the total currents involved, the load current plus the total parasitic current. If this sum is greater than the solar-array short-circuit current, some degradation must be present. The reason for this is that total current, the sum of load current and total parasitic current, must pass through the last cell in the string of cells shown in figure 1. When the total current exceeds the short-circuit current of that cell, the cell is driven to zero potential. Further increase in current drives more cells into saturation and the array voltage begins to drop rapidly. An approximate way to arrive at the total array potential is to consider the array of N cells to consist of m

solar cells "on" at some average voltage v_{av} and n cells "off" at zero voltage. The array total voltage is

$$V = mv_{av}$$

This method is used when

$$I_L + \sum_{\zeta=1}^{N} i_{pc,\zeta} \geq i_{sc}$$

The graphical method discussed earlier is based on this idea and is discussed further in appendix B of this paper.

The following simple examples illustrate the use of this idea:

(1) Positively biased array (electron flux, 10^{-6} A/cm^2, an ionospheric condition; solar-cell short circuit, 0.30 A/cm^2) - If I_L is 27 milliamperes, $i_{sc} - I_L = 3$ milliamperes. Thus, 3 milliamperes is the margin that can be used up before the last cell in a string saturates, a margin of 3000 cells in series. If there were 4000 cells in series at these conditions, 1000 cells would be saturated at zero potential and 3000 cells would be at v_{av}. The total array voltage would then be 3000 v_{av}.

(2) Floating array with 10 000 cells in series - a good approximation is to assume that the array is entirely negative. If the ion flux is 10^{-8} ampere per cell, the load current is 27 milliamperes, and the margin is 3 milliamperes, the total parasitic current is 0.1 milliampere, not enough to saturate any cells. Therefore there is little effect on array potential.

For a floating array the assumption used in the preceding example, that the voltage-current curve of the negative portion of the array can be used as the entire array curve is a convenient starting point. Accurate calculation requires the addition of two curves, one for the positively biased section and one for the negatively biased section. However, iteration is required because the floating point shifts in the process and greatly increases the amount of computation required.

An unusual effect occurs when some of the solar cells on a floating array are driven into saturation. In this case, there is a group of cells at zero potential located at the floating point. As the array orientation changes the floating point, and consequently the group of saturated cells moves about in response to the changing external conditions, the effect is similar to shadowing of a solar array by a spacecraft protrusion such as an extended boom.

CONCLUDING REMARKS

The solar-array voltage-current curve can be calculated if the parasitic current distribution on the array is known and the individual solar-cell oper-

ating curve is given. The most difficult task at present is to formulate the current distributions.

The justification for calculating the array voltage-current curve is to obtain the operating point and power output of the array more accurately. The calculated power loss $\sum i_{pc} \Delta V$ is usually less than the actual power loss and may differ by a factor of 2 or more, depending on the operating point.

If the sum of array load current plus total parasitic current is greater than the array short-circuit current, array performance will noticeably degrade and further calculation is indicated.

An approximate solar-array voltage-current curve can be drawn by dividing the array into sections and constructing the curve from straight-line segments. The total array voltage at any load current is found from $V = mV_{av}$, where m is the number of active solar cells.

For a floating array with large enough parasitic currents, a group of cells on the array will be at zero potential and will move about as a result of changing conditions. The phenomenon is similar to array shadowing.

APPENDIX A

METHOD OF COMPUTER CALCULATION

The case of N solar cells in series with parasitic currents is shown in figure 8, where all currents are taken to be electron currents. In this figure, V is the load voltage and I is the load current. Let $i_{pc,\zeta}$ be the parasitic flux falling on the ζ^{th} solar cell. The current $i_{pc,\zeta}$ may be regarded as a function of voltage and current. The equation relating these currents is

$$I = I_{tot} - \sum_{\zeta=1}^{N} i_{pc,\zeta} \tag{A1}$$

where I_{tot} is the current flowing between the array and the ground. The equation for V involves the sum of the individual solar-cell voltages v_ζ and is

$$V = \sum_{\zeta=1}^{N} v_\zeta \tag{A2}$$

where

$$v_\zeta = K_1 \ln(i_{sc} - i_\zeta + i_o) + K_2 \ln i_o \tag{A3}$$

The term i_ζ in equation (A3) is the current flowing into the ζ^{th} solar cell and is given by

$$i_\zeta = I + \sum_{\lambda=1}^{\zeta-1} i_{pc,\lambda} \tag{A4}$$

The complete voltage-current characteristic is obtained by solving these equations. The calculations are done in two groups, each group yielding a portion of the total voltage-current curve. The first group of calculations apply to the case where some number of cells in the series string are in saturation. In this case $I_{tot} = i_{sc}$ and the term N in equations (A1) and (A2) is replaced by a variable n representing the number of active cells in the string. The variable n varies in the interval $0 \leq n < N$. The second group of calculations applies to the case where all the cells in the string are active. In this case $n = N = \text{Constant}$, and I_{tot} becomes a variable and varies in the interval $0 \leq I_{tot} < i_{sc}$. This grouping of calculations arises out of the peculiar physics of this situation. The contribution of each group of calculations to the total voltage-current curve is shown in figure 8.

APPENDIX B

GRAPHICAL CONSTRUCTION OF VOLTAGE-CURRENT CURVE WITH PARASITICS

It is initially assumed that the voltage-current characteristics of a single solar cell can be approximated by a square curve, as shown in figure 9. The voltage v^* shown in the figure as the intercept of the voltage-current characteristic with the voltage axis is defined to be a suitably chosen voltage near to the voltage at maximum power. If $I = i_{sc}$, then $V = 0$. If $0 \leq I < i_{sc}$ then $V = v^*$. If N identical solar cells are connected in series, then, for $0 \leq I < i_{sc}$, $V = Nv^*$.

The concept of parasitic currents can be introduced at this point. Suppose that parasitic current is uniform per cell; that is, suppose that $i_{pc} = \text{Constant}$. If M cells are in saturation ($I = i_{sc}$ and $V = 0$) from the effect of this parasitic, $V = (N - M)v^*$. Since M is a variable, for the portion of the curve corresponding to the case of cells in saturation, V is a linear function of M. For the case of no cells in saturation, the remainder of the curve is given by $V = Nv^*$. The characteristic is drawn so that the current intercept is at short-circuit current i_{sc}.

The graphical method of constructing the voltage-current characteristic of N cells in series with $i_{pc} = \text{Constant}$ can now be developed. The voltage-current curve without parasitics is taken as the starting point. This curve is a rectangle with current intercept i_{sc} and voltage intercept Nv^*.

A threshold current i_{co} is introduced such that, if $0 \leq I < i_{co}$, then N cells are active and, if $i_{co} < I < i_{sc}$, then some number $M \leq N$ of cells is in saturation because of the presence of the parasitic i_{pc}.

For any current I in the interval $i_{co} < I \leq i_{sc}$, the number M is found as follows: The requirement is set that $I + (N - M)i_{pc} = i_{sc}$. Then $(N - M) = 1/i_{pc}(i_{sc} - I)$. But when I is in the interval $i_{co} < I \leq i_{sc}$, the voltage V is given by $V = (N - M)v^*$. Thus, in this interval

$$V = \frac{1}{i_{pc}} (i_{sc} - I)v^*$$

that is, V varies linearly with I.

Since for any current I in the interval $0 \leq I \leq i_{co}$ the voltage is $V = Nv^*$, an approximate curve can now be drawn. This curve is shown in figure 10. It is useful to find the current i_{co}. In the case of the approximation being discussed, the solution for i_{co} is quite simple. The equation $N - M = 1/i_{pc}(i_{sc} - I)$ is used at the instant $I = i_{co}$. At this instant, $M = 0$ and $i_{co} = i_{sc} - Ni_{pc}$. Thus, given a rectangular solar-array voltage-current curve, the curve with parasitic $i_{pc} = \text{Constant}$ can be constructed by drawing a straight line $V = Nv^*$. In practice, greater accuracy is obtained if the straight line drawn from i_{sc} (fig. 10) is allowed to intercept the original voltage-current curve, as shown in figure 4.

REFERENCES

1. Knauer, W., et al.: High Voltage Solar Array Study. (Hughes Research Laboratories; NASA Contract NAS3-11535.) NASA CR-72675, 1970.

2. Springgate, W. F.; and Oman, H.: High Voltage Solar Array Study. (D2-121734-I, Boeing Aerospace Co.; NASA Contract NAS3-11534.) NASA CR-72674, 1969.

3. Kennerud, K. L.: High Voltage Solar Array Experiments. (Boeing Aerospace Co.; NASA Contract NAS3-14364.) NASA CR-121280, 1974.

4. Domitz, S.; and Grier, N. T.: The Interaction of Spacecraft High Voltage Power Systems with the Space Plasma Environment. Power Electronics Specialists Conference, Institute of Electrical and Electronics Engineers Inc., 1974, pp. 62-69.

5. Herron, B. G.; Bayless, J. R.; and Worden, J. D.: High Voltage Solar Array Technology. AIAA Paper 72-443, Apr. 1972.

6. Purvis, C.; Stevens, N. J.; and Berkopec, F. D.: Interaction of Large, High Power Systems with Operational Orbit Charged Particle Environments. NASA TM-73867, 1977.

7. Solar Cell Array Design Handbook, Vol. 1. (JPL SP43-38, Jet Propulsion Laboratory; NASA Contract NAS7-100 and JPL-953913.) 1976.

8. Kaufman, H. R.; Isaacson, G. C.; and Domitz, S.: The Interaction of Solar Arrays with Electric Thrusters. AIAA Paper 76-1051, Nov. 1976.

9. Parks, D. E.; and Katz, I.: Solar Electric Propulsion Thruster Interactions with Solar Arrays. (SSS-R-78-3420, Systems Science and Software; NASA Contract NAS3-20119.) NASA CR-135257, 1977.

10. Parker, L. W.: Sheath Interaction Between an Orbiting High-Voltage Solar Array and the Space Plasma. Trans. Am. Geophys. Union, vol. 58, no. 12, Dec. 1977, Abstract p. 1215.

11. Parks, D. E.; and Katz, I.: Spacecraft-Generated Plasma Interaction with High Voltage Solar Array. AIAA Paper 78-673, Apr. 1978.

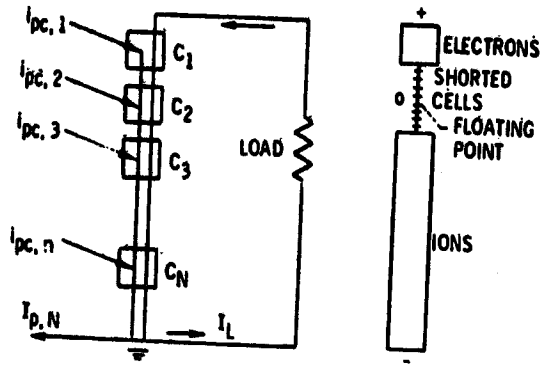

(a) Current circuits. (b) Floating array.

CS-78-1364

Figure 1. - Schematic of current systems.

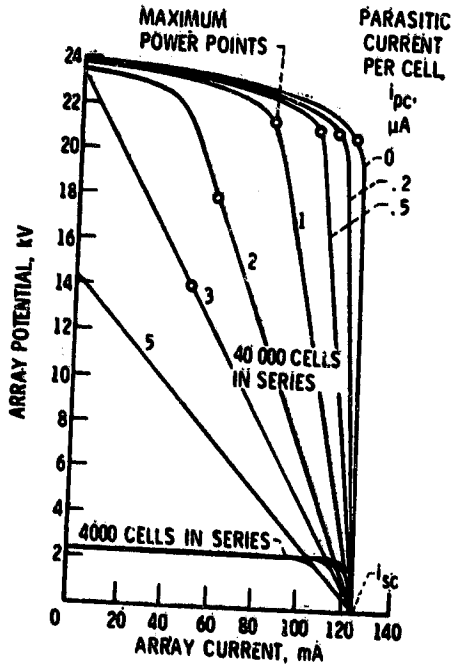

CS-78-1366

Figure 2. - Solar-array voltage-current curve with parasitic flux as parameter.

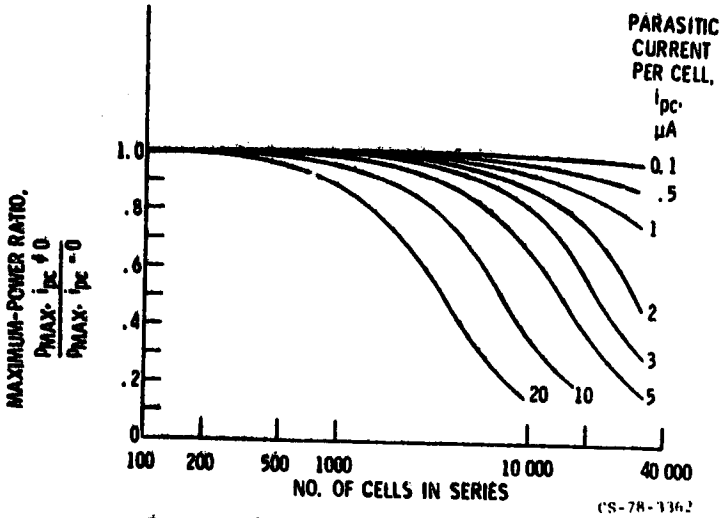

Figure 3. - Maximum-power ratio as function of number of cells in series for constant parasitic flux (thin sheath).

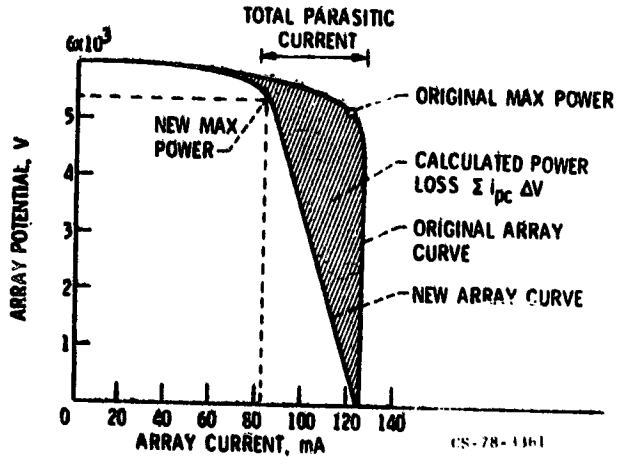

Figure 4. - Graphical construction for thin-sheath case.

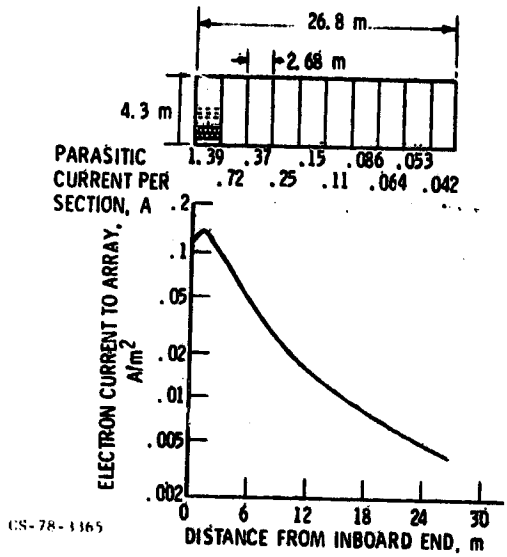

Figure 5. - Solar-array layout and parasitic flux.

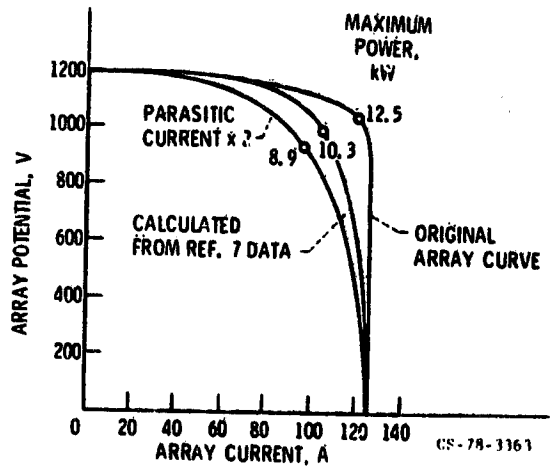

Figure 6. - Voltage-current curve for solar array - thruster integration.

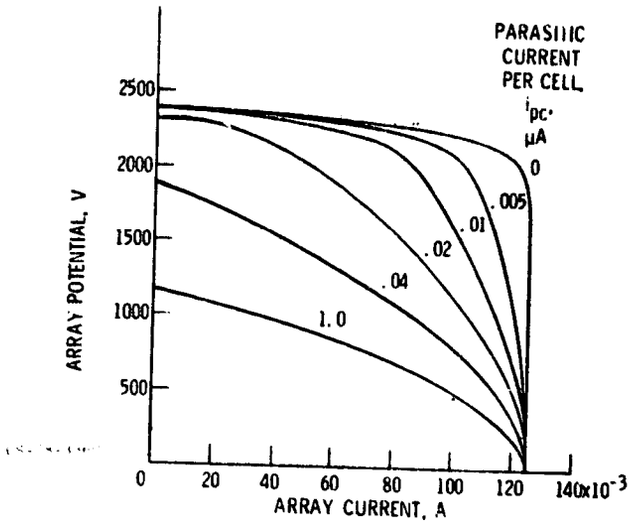

Figure 7. - Voltage-current curve for voltage-dependent current collection - 4000 cells in series.

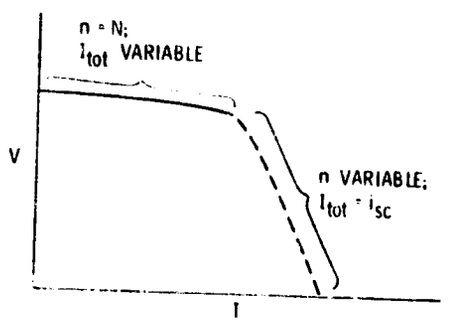

Figure 8. - Contribution of each group of calculations to total voltage-current characteristic.

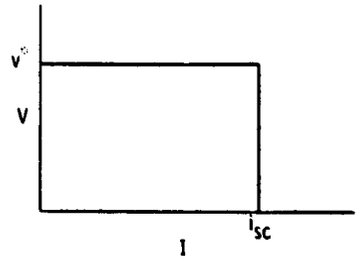

Figure 9. - Square approximation to solar-cell voltage-current characteristic.

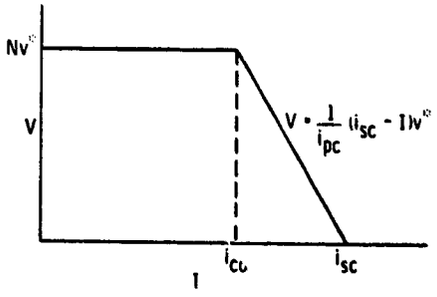

Figure 10. - Approximate voltage-current curve with parasitic flux i_{pc} constant.

D25

N79-24026

MAGNETIC SHIELDING OF LARGE HIGH-POWER-SATELLITE SOLAR ARRAYS USING INTERNAL CURRENTS

Lee W. Parker
Lee W. Parker, Inc.

William A. Oran
NASA Marshall Space Flight Center

SUMMARY

Present concepts for solar power satellites involve dimensions up to tens of kilometers and operating internal currents up to hundreds of kiloamperes. The question addressed here is whether the local magnetic fields generated by these strong currents during normal operation (effectively providing the array with its own "magnetosphere") can shield the array against impacts by plasma ions and electrons (and from thruster plasmas) which can cause possible losses such as power leakage and surface erosion. An affirmative answer is indicated by approximate solution of the inherently 3-D problem.

In the present work one of several prototype concepts has been modeled by a long narrow rectangular panel 2 km wide and 20 km long. The currents flow in parallel across the narrow dimension (sheet current) and along the edges (wire currents). The wire currents accumulate from zero to 100 kiloamp and are the dominant sources. The magnetic field is approximated analytically as due to separate sheet and locally constant wire currents. The equations of motion for charged particles in this magnetic field are analyzed using conservation of canonical momentum to find dynamical limits of the motion, that is, regions inaccessible to the particles. The ion and electron fluxes at points on the surface are represented analytically for monoenergetic distributions and are evaluated by Parker's quadrature technique for Maxwellian particle velocity distributions. Sample numerical results for electrons and protons correlate well with the ratios of (a) the particle gyroradius to the array width and (b) the particle momentum to the critical momentum $e\mu I$, where e is the particle charge, μ is the magnetic permeability, and I is the wire current. The field will prevent kilovolt protons and mev electrons from reaching significant fractions of the surface.

The analysis is applicable to both low earth orbit and geosynchronous orbit, when appropriate particle masses and temperatures are substituted. It suggests that the current distribution may be designed so as to optimize the shielding and that the solar cell lifetime in orbit may be prolonged by a possible factor of 5.

INTRODUCTION

For the purposes of the present analysis of magnetic shielding, we assume a model suggested by a Rockwell International study (ref. 1 and fig. 1). It is represented in the simplified manner shown in figure 2. Here we have a flat panel, lying in the x-y plane, made up of strips of photovoltaic cells. Each strip is of length 2X and consists of photovoltaic cells connected in series along the x-direction. The strips of cells are stacked in the y-direction and are electrically connected in parallel at their ends to end-bus wires at positions x = +X and x = -X. The array extends from y=0 to y=L. Electric fields are neglected, which should be valid for thin sheaths.

This arrangement yields a current-flow distribution as follows. The cross-current flows from bus to bus in the +x direction, and the currents accumulate along the bus wires. Therefore, we have essentially two kinds of currents as sources for magnetic fields:

(1) a surface current density (a "sheet current") in the plane of the panel, directed in the +x direction, with the current per unit length (K) independent of x and y, and

(2) a "wire current" (I) due to flow in the bus wires, directed in the +y and -y directions, which accumulates from zero amps at y=0 to 10^5 amps at y=L. The variation can be assumed to be linear in y, although this assumption is not essential.

For the purpose of calculating magnetic fields, these assumptions allow us to establish the current sources as K=5 amp/meter and $I=I_0 \cdot (y/L)$ amp, where L is 20 km in figure 2 and I_0 is 10^5 amp. We assume further that, except near the ends of the array, the magnetic field in the vicinity of the array is the superposition of two contributions: One is due to a current strip-sheet, of finite width 2X, lying in the x-y plane (between -X and +X in figure 2b), infinitely long in the y-direction, consisting of a constant current/length K. The other is the bifilar circuit due to two infinitely long parallel wires, at $x=\pm X$, carrying constant current I. Thus, end effects are neglected, which may be reasonable for most points along a long, narrow array with a slow variation of currents with y.

MAGNETIC FIELD

These assumptions allow us to approximate the magnetic field at any point as due to current sources which are constant in the y-direction and extend to positive and negative infinity in the y-direction. Thus, they produce a magnetic field independent of y. The sheet current affects only the y-component of the field, while the wire currents affect only the x and z components. Hence, we may superimpose the two independent magnetic field systems, expressed in c.g.s. units, as follows:

$$B_x = 2\mu I z \left[\frac{1}{(x+X)^2 + z^2} - \frac{1}{(x-X)^2 + z^2}\right] \quad (1)$$

$$B_z = 2\mu I \left[\frac{x-X}{(x-X)^2 + z^2} - \frac{x+X}{(x+X)^2 + z^2}\right] \quad (2)$$

$$B_y = 2\mu K \left[\arctan\left(\frac{x-X}{z}\right) - \arctan\left(\frac{x+X}{z}\right)\right] \quad (3)$$

where B_x and B_z are produced by the wire currents and B_y is produced by the strip-sheet current; μ is the magnetic permeability. This field distribution is illustrated in figure 3. Note that the magnetic field due to the wire current inhibits particle motion in the y-direction, while the magnetic field due to the sheet current inhibits particle motion in the x-z plane. These expressions may be used to estimate magnetic intensities. The magnetic field intensity on the surface of the panel due to the wires is given by equation (2) evaluated at z=0, namely,

$$B_z = -\frac{4\mu I}{X} \cdot \frac{1}{1-(x/X)^2} = -0.4 \text{ gauss} \cdot \frac{1}{1-(x/X)^2} \quad (4)$$

for I = 100 kiloamp and X = 1 km

The magnetic field intensity on the surface of the panel due to the sheet current is given by equation (3) evaluated at z=0, namely,

$$B_y = -2\pi\mu K = -0.0314 \text{ gauss} \quad (5)$$

for $K = 10^5$ amp/20 km = 5 amp/meter

Thus, the field due to the wires is an order of magnitude stronger than the field due to the sheet current, over most of the length of the panel.

CONSERVATION OF CANONICAL MOMENTUM. DYNAMICAL LIMITS OF THE MOTION

Using equations (1)-(3) and some manipulation, the equations of motion, neglecting electric forces, can be written

$$\ddot{x} = -\frac{2e\mu K}{m}\psi\dot{z} - \frac{1}{2}\frac{\partial}{\partial x}\dot{y}^2 \quad (6)$$

$$\ddot{z} = +\frac{2e\mu K}{m}\psi\dot{x} - \frac{1}{2}\frac{\partial}{\partial z}\dot{y}^2 \quad (7)$$

$$\dot{y} = \frac{e\mu I}{m}(\phi - \phi_o) + \dot{y}_o \quad (8)$$

where

$$\psi \equiv \arctan\left(\frac{x+X}{z}\right) - \arctan\left(\frac{x-X}{z}\right) \tag{9}$$

$$\phi \equiv \ln\left[\frac{(x-X)^2 + z^2}{(x+X)^2 + z^2}\right] \tag{10}$$

and the subscripts "o" denote initial conditions. The quantities m and e denote the particle mass and charge, respectively. We have an integral of the motion in y, and $\dot{y}^2/2$ represents an effective potential function of x and z, whose gradient represents an effective electric field. From conservation of energy we have

$$\dot{x}^2 + \dot{y}^2 + \dot{z}^2 = v^2 = \text{constant} \tag{11}$$

so that

$$\dot{x}^2 + \dot{z}^2 = v^2 - \dot{y}^2 = v^2 - \left(\dot{y}_o + \frac{e\mu I}{m}(\phi - \phi_o)\right)^2 \geq 0 \tag{12}$$

The region in x-z space where equation (12) is satisfied represents a region of physically allowed motion; the rest of x-z space is dynamically forbidden. A dynamical analysis along similar lines was applied to current collection by a charged satellite in the LEO geomagnetic field by Parker and Murphy in reference 2. Clearly, ϕ is constant on a circle whose center is on the x-axis.

From analysis of equations (10) and (12) it can be shown that an electron or ion with a given energy may reach a point x on the surface with angles of incidence such that (for positive x)

$$-1 \leq \dot{y}/(\dot{x}^2 + \dot{y}^2 + \dot{z}^2)^{1/2} \leq 1 - P/Q \tag{13}$$

where

$$P \equiv \ln\left[\frac{(x+X)^2}{(x-X)^2}\right] \tag{14}$$

(X is the position of the wire)

and

$$Q \equiv \frac{p(E)}{e\mu I} \quad \left(= 1445\frac{\sqrt{E(ev)}}{I(amp)} \text{ for protons; } = 33.7\,\frac{\sqrt{E(ev)}}{I(amp)}\sqrt{1+E(mev)} \text{ for electrons}\right) \tag{15}$$

where p(E) denotes the particle momentum as a function of energy E. The quantity Q is the ratio of particle momentum to the "magnetic" scale momentum $e\mu I$. p(E) is $\sqrt{2mE}$ for nonrelativistic particles. The additional square-root factor for electrons is [illegible] lativistic correction.

Note that

(a) particles of all energies coming from infinity can reach x=0 (the mid-line of the panel), and

(b) particles coming from infinity with energy E cannot hit beyond $x=x_{max}$

where

$$\frac{x_{max}}{X} = \tanh\left(\frac{Q}{2}\right) \tag{16}$$

(The latter derives from the condition that P/Q in equation (13) cannot exceed 2.) Thus, no particles with finite energy can hit the wire.

The magnetic scale of momentum, $e\mu I$, is 1.6×10^{-16} gm-cm/sec when I is 100 kiloamp. (It is proportionally lower as I decreases along the array.) Electrons with this momentum (Q=1) are relativistic, with energy E=2.5 mev. In geosynchronous orbit we may assume that the ions are protons. They would have the magnetic scale of momentum if their energy were E=4.8 kev. In low-earth orbit, assuming oxygen ions, the corresponding energy is 300 ev. This implies a simple criterion based on the magnitude of Q. If Q is small, the particles cannot penetrate. Assuming that the particle temperatures in geosynchronous orbit may at times be 1 ev ("cold" particles) and at other times be 10 kev ("hot" particles), we infer that electrons of both temperatures, whose values of Q are 3.37×10^{-4} and 3.37×10^{-2}, respectively, are easily excluded from most of the array surface. Similarly, the cold protons, with Q=0.0144, are also excluded. The 10-kev protons, however, with Q=1.445, may penetrate to the surface. In low-earth orbit, where the particle temperatures are of the order of 0.1 ev, both ions and electrons are easily excluded. The above Q-values are obtained assuming I=100 kiloamp, i.e., they are appropriate for the high-current end of the array. It should be noted that Q is related to the gyro-radius R_g, evaluated at the mid-line of the array, based on the magnitude of B_z from equation (4); namely, the gyronumber R_g/X is equal to Q/4.

FLUXES

The dynamical limits represented by equations (13)-(15) may be used to compute particle fluxes at the surface. For a monoenergetic isotropic particle velocity distribution, the number of particles hitting unit area on the surface in unit time, at a distance x from the center-line, may be shown to be given by

$$F_{mono}(E) = \frac{n_o}{4}\sqrt{\frac{2E}{m}}\left\{1 - \frac{1}{\pi}\cos^{-1}A + \frac{A}{\pi}\sqrt{1 - A^2}\right\} \tag{17}$$

where $A = 1 - P/Q$,

n_0 is the particle number density at infinity, E and m are the particle energy and mass, and P and Q are given by equations (14) and (15). Thus, the factor in brackets becomes unity as P/Q becomes small. It vanishes if P/Q exceeds 2 (see equation (16)). If Q is small, P must also remain small, which means that surface impacts are confined to the vicinity of the center-line (x=0). Also, the flux distribution is symmetric about the center-line.

The flux due to a Maxwellian velocity distribution may be computed by integrating equation (17) over the energy distribution. This must be done numerically, by quadratures. Using Parker's quadrature method (ref. 3), dimensionless flux-profile data were computed, for electrons and protons, for temperatures T=10 kev and T=1 ev, typical values in geosynchronous orbit. The profiles (positive x only), are shown in tables 1-3, for y-values along the panel from 20 km down to zero, in steps of 2 km. The current I is assumed to be proportionally reduced as y decreases. The x-values range from zero to 1 km in steps of 0.1 km. The second column, labelled "x_{max}", shows how close to the wire (at x=1) particles of energy equal to the temperature can get (equation (16)).

Table 1 shows 10-kev proton profiles. The profiles are fairly well spread out over the surface, but with a sharp dropoff to zero at x=1 km, as expected. As y decreases the coverage of the surface becomes greater as the wire current decreases. The data of the table indicates that the proton gyroradius R_g at E=10 kev and B=0.4 gauss (midway between the currents at y=20 km - see equation (4)) is 2.3 km, a size comparable with the width of the array. E_{scale}=4.8 kev is the magnetic scale energy, and the thermal energy 10 kev is larger than this. Hence there is consistency between the lack of shielding of 10-kev ions and the sizes of E_{scale} and R_g. Note that the density is unity (ambient value) along the axis (x=0), and along the last row, for y=0 (where the current and magnetic field vanish). Recalling that these results represent dynamical limits, it is evident that the "ridge" of unit density along the axis (middle of panel) should actually be significantly lower due to the inhibition of motion in the x-z plane by the sheet-current magnetic field.

Table 2 shows 1-ev proton profiles. Here, there is essentially no coverage of the surface (except very near x=0. See the x_{max} column). Hence the shielding is very effective. This is also consistent with the thermal energy of 1 ev being much less than E_{scale}=4.8 kev, as well as with R_g=23 m at 0.4 gauss being much less than 1 km.

Table 3 shows 10-kev electron profiles. Here, the penetration is slightly greater, particularly near y=0. However, the panel may be considered effectively shielded. Calculations were also done for 1-ev electrons, but results are not shown here, since, as may be expected, the penetration is completely negligible, much less than in table 3. For the 10-kev and 1-ev electrons, R_g has the values 53 meters and 53 cm, respectively.

These numerical-integration results are consistent with expectations based on the simple criterion of Q compared with unity, where E is set equal to kT.

POSSIBLE INCREASE OF SOLAR CELL LIFETIME

It is estimated that 80 percent of the radiation damage to solar cells would be due to the trapped Van Allen belt electrons with energies up to 5 mev (E. G. Stassinopoulos, private communication, 1978), against which magnetic shielding is possible. (The remaining 20 percent is due mostly to cosmic rays which are not presently shieldable.) From the simple criterion of this paper that Q be less than unity, we see from equation (15) that electrons up to several mev in energy are prevented from reaching a large fraction of the array surface in the vicinity of the 100-kiloamp currents. In particular, from equations (15) and (16), with E=5 mev and I(y) represented by 5000y amp, with y in km, the area shielded against up-to-5-mev electrons lies between x(km)=tanh [0.923x20/y(km)] and x(km)=1.0. At y=20 km, this range of positions is from 730 m to 1000 m. Hence the range of protected positions is 270 m, within which the solar cell lifetime would be prolonged by a possible factor of 5.

We would like to thank James G. Laframboise for his helpful comments.

REFERENCES

1. Rockwell International Report, Satellite Power System (SPS) Feasibility Study, SD76-SA-0239-2, 1976.

2. Parker, L. W.; and Murphy, B. L.: Potential Buildup on an Electron-Emitting Ionospheric Satellite. J. Geophys. Res., vol. 72, 1967, p. 1631.

3. Parker, L. W.: Calculation of Sheath and Wake Structure about a Pillbox-Shaped Spacecraft in a Flowing Plasma. Proceedings of the Spacecraft Charging Technology Conference, C. P. Pike and R. R. Lovell, Eds., Report AFGL-TR-77-0051/NASA TMX-73537, Feb. 1977, p. 331.

Table 1.

DYNAMICAL LIMITS
MAGNETICALLY SHIELDED FLUX PROFILES
10 kev IONS

2 km x 20 km
100000 amps
E_{scale} = 4.8 kev
R_g = 2.3 km*

		x(km) →										
y(km)	x_{max}	0.	.1	.2	.3	.4	.5	.6	.7	.8	.9	1.0
20	.62	1.00	.92	.80	.66	.51	.36	.23	.12	.04	.00	0.
18	.67	1.00	.94	.83	.70	.56	.42	.29	.17	.07	.01	0.
16	.72	1.00	.95	.85	.74	.62	.49	.35	.23	.11	.03	0.
14	.77	1.00	.95	.88	.78	.67	.56	.43	.30	.17	.06	0.
12	.83	1.00	.96	.90	.82	.73	.63	.51	.39	.25	.11	0.
10	.89	1.00	.97	.92	.86	.79	.70	.61	.49	.36	.20	0.
8	.95	1.00	.98	.94	.90	.84	.78	.70	.61	.49	.32	0.
6	.98	1.00	.99	.96	.93	.89	.85	.79	.72	.63	.48	0.
4	1.00†	1.00	.99	.98	.96	.94	.91	.88	.84	.78	.68	0.
2	1.00†	1.00	1.00	.99	.99	.98	.97	.96	.94	.91	.87	0.
0	1.00	1.00	1.00	1.00	1.00	1.00	1.00	1.00	1.00	1.00	1.00	0.

*Ion gyroradius based on B = 0.4 gauss midway between wire currents at 100000 amp. Note: R_g is larger than array width of 2 km.

†Very close to but less than unity.

Table 2.

DYNAMICAL LIMITS
MAGNETICALLY SHIELDED FLUX PROFILES
1 ev IONS

2 km x 20 km
100000 amps
E_{scale} = 4.8 kev
R_g = 23 m*

		x(km) →										
y(km)	x_{max}	0.	.1	.2	.3	.4	.5	.6	.7	.8	.9	1.0
20	.01	1.00	0.	0.	0.	0.	0.	0.	0.	0.	0.	0.
18	.01	1.00	0.	0.	0.	0.	0.	0.	0.	0.	0.	0.
16	.01	1.00	0.	0.	0.	0.	0.	0.	0.	0.	0.	0.
14	.01	1.00	0.	0.	0.	0.	0.	0.	0.	0.	0.	0.
12	.01	1.00	0.	0.	0.	0.	0.	0.	0.	0.	0.	0.
10	.01	1.00	0.	0.	0.	0.	0.	0.	0.	0.	0.	0.
8	.02	1.00	0.	0.	0.	0.	0.	0.	0.	0.	0.	0.
6	.02	1.00	0.	0.	0.	0.	0.	0.	0.	0.	0.	0.
4	.04	1.00	0.	0.	0.	0.	0.	0.	0.	0.	0.	0.
2	.07	1.00	.07	0.	0.	0.	0.	0.	0.	0.	0.	0.
0	1.00	1.00	1.00	1.00	1.00	1.00	1.00	1.00	1.00	1.00	1.00	0.

*Ion gyroradius based on B = 0.4 gauss midway between wire currents at 100000 amp. Note: R_g is small compared with array width of 2 km.

Table 3.

DYNAMICAL LIMITS
MAGNETICALLY SHIELDED FLUX PROFILES
10 kev ELECTRONS

2 km x 20 km
100000 amps
E_{scale} = 2.5 mev
R_g = 53 m*

		x(km) →										
y(km)	x_{max}	0.	.1	.2	.3	.4	.5	.6	.7	.8	.9	1.0
20	.02	1.00	0.	0.	0.	0.	0.	0.	0.	0.	0.	0.
18	.02	1.00	0.	0.	0.	0.	0.	0.	0.	0.	0.	0.
16	.02	1.00	0.	0.	0.	0.	0.	0.	0.	0.	0.	0.
14	.02	1.00	0.	0.	0.	0.	0.	0.	0.	0.	0.	0.
12	.03	1.00	0.	0.	0.	0.	0.	0.	0.	0.	0.	0.
10	.03	1.00	0.	0.	0.	0.	0.	0.	0.	0.	0.	0.
8	.04	1.00	.00	0.	0.	0.	0.	0.	0.	0.	0.	0.
6	.06	1.00	.02	0.	0.	0.	0.	0.	0.	0.	0.	0.
4	.08	1.00	.12	.00	0.	0.	0.	0.	0.	0.	0.	0.
2	.17	1.00	.50	.12	.01	.00	0.	0.	0.	0.	0.	0.
0	1.00	1.00	1.00	1.00	1.00	1.00	1.00	1.00	1.00	1.00	1.00	1.00

*Electron gyroradius based on B = 0.4 gauss midway between wire currents at 100000 amp. Note: R_g is small compared with array width of 2 km.

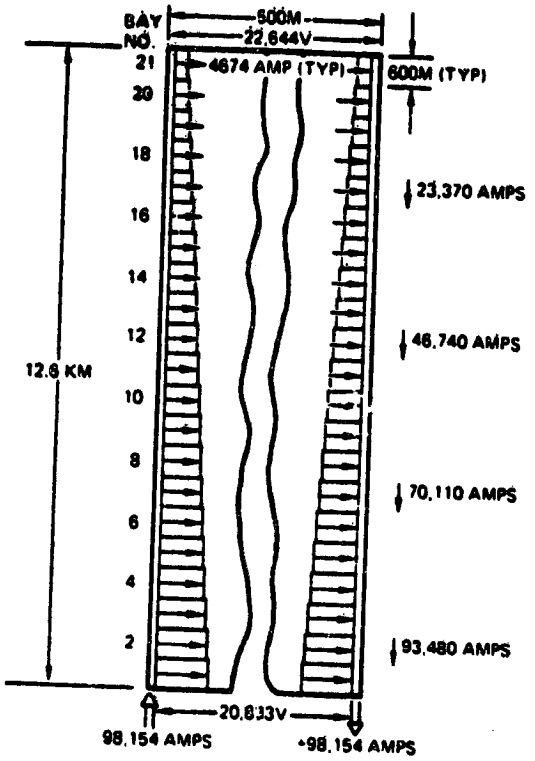

Figure 1. - Sample design configuration (Rockwell).

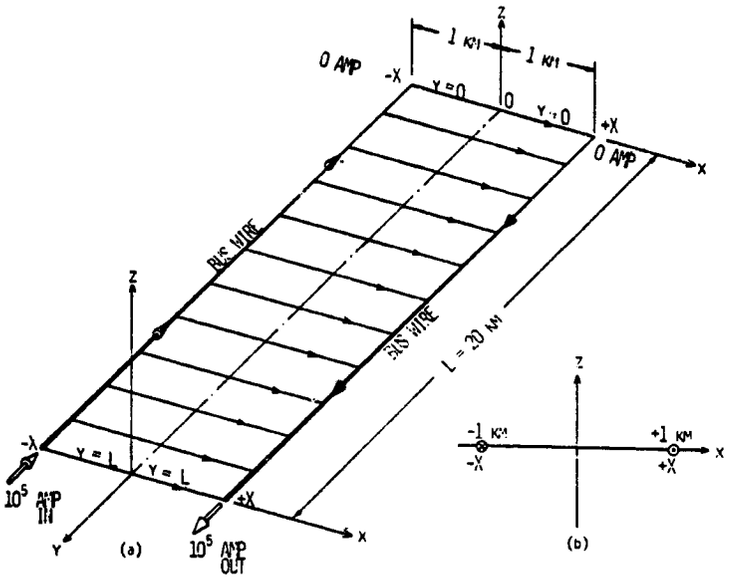

Figure 2. - Current distributions in solar array panel analytical model.

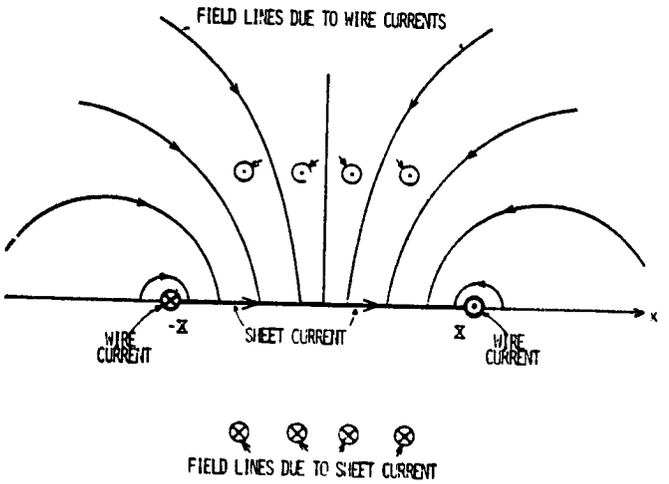

Figure 3. - Magnetic field systems in solar array panel analytical model.

D16

N79-24027

ENVIRONMENTAL INTERACTION IMPLICATIONS FOR LARGE SPACE SYSTEMS

E. Miller, W. Fischbein, M. Stauber, P. Suh
Grumman Aerospace Corporation

ABSTRACT

Large Space Systems (LSS) comprise a new class of spacecraft, the design and performance of which may be seriously affected by a variety of environmental interactions.

In addition to dimensions which are orders of a magnitude larger than those of conventional spacecraft, most LSS are characterized by low density structures, extensive dielectric surfaces and composite structural elements. Many LSS also require multikilowatt or megawatt power systems, which might operate at multikilovolt levels. Perhaps most significant is that most of these advanced systems must operate efficiently for 10 to 30 years with little or no maintenance.

This paper addresses the special concerns associated with spacecraft charging and plasma interactions from the LSS designer's viewpoint. Survivability of these systems under combined solar U.V., particle radiation and repeated electrical discharges is of primary importance. Additional questions regard the character of electrical discharges over very large areas, the effects of high current/voltage systems and magnitude of induced structural disturbances.

Incorporation of large scale charge controls and complicated electrical and structural interactions could impose difficult design requirements and have a major impact on LSS costs. Worst-case estimates are made, and possible design/performance impacts assessed for LSS environmental interactions of major concern.

A concept is described for a large scale experiment platform which utilizes space structure demonstration articles presently under study by the Air Force and NASA. These platforms could provide several thousand square meters of test area, with maximum dimensions up to one kilometer.

Accelerated charge/discharge, induced avalanche and plasma power loss experiments might be configured for low earth orbit, and the free-flyer test platform retrieved after several months for analysis of combined environmental effects. Additional instrumentation could be installed, the platform boosted to geosynchronous orbit to measure large scale plasma characteristics and spacecraft interactions, and test samples retrieved with a manned orbit transfer vehicle after long-term exposure.

INTRODUCTION

The Space Shuttle will open a new era of space transportation in the early 1980's. A multitude of long duration, complex, multifunction missions will be possible with the unique capabilities of the Space Transportation System (STS). Many of the advanced missions considered for the next two decades will require a new generation of spacecraft, called Large Space Systems (LSS).

Some of the LSS concepts, devised for a variety of applications, are illustrated in Figure 1. The LSS of the 1980's will be orders of magnitude larger than anything launched to date. Most will be constructed in space using materials and support machinery transported by the STS. By the 1990's, much larger Solar Power System demonstration articles, second or third generation LSS, might be flown.

Although designed for a wide variety of missions, the basic characteristics of most unmanned LSS are quite similar. Spaceborne radars, communication and scientific platforms and solar power demonstration articles are large, low density structures which generally make extensive use of dielectric and composite materials. Exposed surface areas for these systems range from thousands to millions of square meters. Also, several missions require multikilowatt to megawatt electrical power sources and could operate at multikilovolt levels.

Numerous analytical, manufacturing and test methods must be developed to deal with these huge structures, high power and voltage levels and novel construction and deployment techniques. One of the greatest challenges facing the LSS designer, however, is to achieve a reliable, efficient system which can survive the space environment, with little or no maintenance for 10 to 30 years.

The need for long-term environmental effects data on LSS candidate materials is well known. Some laboratory tests have already begun and flight experiments (SCATHA, LDEF) are scheduled for the near future. The compounding effects of electrostatic charging and repeated electrical discharges on materials and components and structural and electrical interactions with the space plasma could have a serious impact on the design, performance and economic viability of many LSS.

A program was initiated by Grumman last year to assess the impact of environmental interactions on the LSS under study. This combined engineering/research effort includes modeling of coupling mechanisms, identification of most probable trouble spots, nominal and worst-case estimates of environmental effects and alternate design approaches to minimize or eliminate damaging effects. Some of the results of these studies are described below.

DESCRIPTION OF TYPICAL LARGE SPACE SYSTEMS

Several LSS programs have been conducted by Grumman during the past few years. Conceptual and preliminary designs have been developed for solar power satellites, space stations, space-based radars, multifunction communication and surveillance platforms, space construction platforms and large space structure demonstration articles. Two such systems, designed for widely different missions, are the Space Based Radar (SBR) and Solar Power Satellite (SPS) Demonstration Article.

SBR

The general arrangement of a typical SBR is shown in Figure 2. This system emplcys a unique, deployable wire wheel antenna which can be stowed in and deployed from the shuttle in diameters up to 300 meters.

The antenna is attached to and supported by a drum that is the basic structure at the lower end. This drum also provides mounting surfaces for communications antennas, the lower systems package (LSP), the lower attitude control thrusters and the mast canister. Attached to the upper end of a deployable mast is the upper systems package (USP) which provides mounting surfaces for the antenna feed, upper thrusters and solar or nuclear power source.

The phased-array antenna is supported by a graphite/epoxy compression rim assembly which, in turn, is supported by spring-tensioned fore and aft stays (graphite/epoxy strips). The phased-array antenna is made of gore panel assemblies that lie in the plane of the rim and are spring-tensioned between the rim and drum. The compression rim assembly is a polygon composed of thinwall tubes; the number and length depends on the deployed diameter.

The triangular antenna array gore assemblies, shown in Figure 3, are made in sections and spliced together by circumferential mini-hinged beams that provide the required interlayer spacing. For the space-fed phased array, the triple layer panels consist of ground-side and feed-side antenna planes located one quarter wave-length from the ground plane.

The antenna planes consist of frame-mounted subarrays shown in Figure 4. The frames are assembled edge-to-edge in an axisymmetric array of rows and columns within the bounds of the gore section. Each frame is a square structure made of 2.5 mil aluminum. The sub-arrays, dipoles and feed lines are made of 0.25 mil copper, on 1 mil H-film substrate.

The ground plane consists of a 2.5 mil pierced aluminum sheet. The resulting mesh sections are bounded by radial edge tapes and reinforced with transverse aluminum battens.

Solid state RF amplifiers and digital electronics are mounted on the ground plane. These are powered from upper and lower antenna planes at -180 vdc and -10 vdc respectively. The electrical network, distributed throughout the antenna, carries about 90% of the total generated power to several hundred thousand electronic modules.

All antenna and ground plane surfaces may be covered with a thermal control coating to minimize temperature gradients throughout the array. Electrically conductive coatings could be used on the ground plane, but non-conductive coatings would be used on the antenna planes to permit proper operation of the dipoles.

The LSP drum is fabricated of aluminum alloy in a thin skin, cylindrical configuration. The USP is also fabricated of aluminum alloy. The nuclear reactor mast or solar array support structure (with drive motors) mounts to the upper frame of the USP. Up to 100 kilowatts of power is provided to the subsystems and phased array modules.

Depending on system size, jet or ion thrusters are used for attitude control. Thrusters mounted on the LSP provide stationkeeping, roll control, and

part of the pitch and yaw control. Additional thrusters are mounted on the USP to complete pitch and yaw control.

Active or passive versions of the deployable wire wheel antenna can be used for many different missions. Grumman has emphasized the phased array approach for SBR, and detailed lightweight gore designs and models have been developed for these systems. Reflector and bootlace lens antennas have also been designed for radiometry and communications systems.

SPS Demonstration Article

Feasibility and conceptual design studies conducted over the past few years have shown that the SPS is an attractive power source alternative for the twenty first century. Further technology development is being encouraged, and it is likely that some form of SPS technology verification spacecraft will be flown in the 1990's.

The relative scales of these SPS test articles can be appreciated from Figure 5. Here, some of the growth possibilities leading to the full-scale SPS are illustrated. Note that even modestly sized demonstrations systems are from ten to several hundred times larger than the largest photovoltaic system presently being considered for the early 1980's - - a 50 kilowatt array for the LEO power module.

Several photovoltaic SPS concepts are being studied including planar and concentrator arrays, silicon, gallium arsenide and other solar cells. The structural arrangement of a typical concentrator SPS is shown in Figure 6. Solar cell blanket and concentrator support trusses are of aluminum or composite material, constructed from smaller, one-meter beams which are automatically fabricated in space. The slotted waveguide antenna is made of aluminum or metallized composites and includes thousands or millions or DC-RF converters.

Cross sections of advanced solar cell blankets which might be used for the SPS are shown in Figure 7. Compared to current technology, SPS solar cell blankets will be much thinner and lighter. Glass or plastics might be used for substrates or continuous cell covers. Solar cells are interconnected via very thin wraparound contacts and bus conductors, and, if klystrons are used for RF power conversion, series cell strings could operate at voltages up to 47.5 kilovolts.

Many solar-powered LSS in the mid to late 1980's will likely use solar cell blankets similar to these SPS candidates but will probably operate at voltages no higher than a few hundred volts.

The reference SPS demonstration article used for Grumman environmental interaction studies is shown in Figure 8. The basic planar array configuration is similar to that from a recent NASA/Boeing study, sized to provide 100 megawatts of rectified power on the ground. Structure, antenna and solar cell blankets are similar to those described above. Electrical distribution and

control networks are integrated throughout the array; power is transmitted to the antenna via slip rings. Attitude control and stationkeeping is provided by thrusters. The effective density of the spacecraft, including all subsystems is about 3×10^{-3} kg/m^3.

One of many possible electrical configurations is shown in the figure. In general, solar cell strings are arranged with opposing current flow to minimize magnetic torques on the spacecraft. In this example, 16 strings each generate 250 amps at 41 to 45 kilovolts. Positive and negative busses are located at the center and ends of the array. These connect to the main power busses which run the length of the array and terminate at the slip rings. A total of 4000 amps is delivered to the RF converters at 40 kilovolts.

ENVIRONMENTAL INTERACTIONS AND EFFECTS

The study of LSS environmental interactions was initiated by identifying those charge/discharge effects and plasma interactions that might have an impact on the design, performance or cost of these spacecraft. Initial concerns for the SBR and SPS demonstration article are summarized in Tables 1 and 2. The potential interactions, sites and effects listed in these tables are common to most LSS using advanced solar cell arrays or phased array antennas.

Degradation of dielectric structures, optical materials and surfaces can result from repeated electrical discharges as described in the literature. Numerous dielectric-metal interfaces exist throughout the SBR and SPS, specifically at the antenna dipoles and solar cell edges, which are potentially susceptible to discharge-induced damage. Discharges on metallized dielectric delay lines and waveguides could also erode these critical elements.

Damage or disruption of the electrical distribution network, while a concern for all LSS, may be especially severe with large, distributed power systems as on SBR and SPS type spacecraft. Interactions with very high, distributed voltages and numerous RF converters and waveguide antennas are of particular importance for the SPS.

The lightweight, flexible LSS structures will distort under electrostatic forces, on-board, geomagnetic and VXB field interaction, plasma coupling currents and induced differential heating. Surface distortions and plane separation variations could have a significant effect on antenna gain, efficiency and pointing accuracy. Plasma-induced forces will also affect attitude control and stationkeeping requirements. The trusters used for these functions may also contribute to spacecraft contamination, differential charging and power loss in multikilovolt systems.

ANALYSES OF LSS ENVIRONMENTAL INTERACTIONS

Preliminary analyses and engineering estimates were made to assess the possible magnitude of some of the effects of plasma interactions and other environmental factors on LSS performance. These analyses emphasized the SPS demonstration article, as it can be expected to experience such effects with

greater severity than, for example the SBR, due to its larger currents, voltages, and size.

Specifically, analyses were made of the potential distribution on the cover of a 47 KV solar array under substorm conditions and of the magnetic shielding against charging currents provided by the on-board current distributions on a 100 MW SPS demonstration article. Other estimates performed include plasma leakage currents, erosion rates due to proton scattering, torques from on-board current coupling to B_{GEO}, and solar array performance loss due to radiation damage.

In analyzing the charging potential distribution on the 47 KV solar array an array length of 700 m was assumed, with the solar cell interconnected such as to provide a constant impressed voltage gradient along, and a constant voltage across, the array.

Without solar illumination and without the effect of solar cell cover slides, magnetic substorm charging currents would float this potential distribution so as to make most of the array length negative with respect to the plasma (based on a simple plasma particle drift approximation).

The inclusion of sun-illumination ($Jpe(V_s=0) = 3\ nA/cm^2$) and of the effect of dielectric cover material in a self-consistent (thick sheath) analysis leads to substantially different results for the surface potential distribution on the array. The specific analyses employed the following approach: A local value of the array potential V_p is assumed and the potential V_s on the overlying surface point is calculated selfconsistently, subject to the equilibrium voltage conditions $\Sigma J_i(V_s) = 0$, where the J_i represent the current density elements shown in Fig. 9. The current balance includes the leakage current J_ℓ through the dielectric cover for an appropriate value of the cover bulk resistance. The calculation is repeated for a series of equally spaced V_p values on both sides of the point where the leakage current reverses direction as a result of a change in the sign of (V_s-V_p). The location on the array where Vp changes sign, relative to either end of the array is then determined by the condition

$$\int_{A_{in}} (J_\ell)_{in}\, dA = \int_{A_{out}} (J_\ell)_{out}\, dA$$

This also determines the parasitic current in the circuit formed through the dielectric cover, the array, and the plasma.

Two cases were analyzed, for bulk resistance values of 10^{14} and 10^{13} ohm-cm^2, respectively. For the higher resistance, the surface potential V_s is positive but very low (a few volts), as shown in Fig. 10a. The integrated leakage current value for a 95 m wide array section is .038 amp. For the lower resistance value (10^{13} ohm-cm^2) the surface potential becomes at least partly dependent on the array potential V_p. Namely, V_s becomes strongly positive for positive V_p values, while for negative V_p it remains at a few volts positive. (Fig. 10b.). The integrated leakage current here is .19 amps for the array section. Since the full array has 16 such sections the total leakage current

is 0.6 amp for the 10^{14} ohm-cm^2 array cover and 3.1 amp for the 10^{13} ohm-cm^2 cover. In either case this is an insignificant fraction of the 4000 amp full array current.

The SPS will produce significant magnetic fields as a result of the large array currents. These fields could act to shield the array from plasma particles, at least locally.

The effectiveness of this shielding was estimated for the 100 MW SPS demonstration article (under neglect of electrostatic forces), with current sources and current busses arranged as shown in Fig. 11. This arrangement consists of 16 sheet current sources of dimensions 190 by 377.5 meters and 14 line current sources corresponding to the current busses. Each sheet source carries a current of 250 amps, while bus currents range from 250 to 3000 amps. For this current distribution the magnetic field over the array was determined. Fig. 12 shows the component of the magnetic field B_{11}, lying in the plane parallel to and one meter above the array surface.[11] The B-field mapping provided the basis for estimating the minimum energy needed by particles to reach the array. For this estimate the particles were assumed to be normally incident on the array surface, and the minimum energy, E_c, was determined from the minimum normal momentum necessary for penetration to the distance of a gyro radius from the array surface. Values of E_c for electrons are shown in Fig. 12 at various locations on the array. For example, above the midpoint of the 3000 amp bus the array is screened from normally incident electrons of up to 32 keV. However, away from the busses, and particularly at the interfaces between opposing current sheets the electron cutoff energies for normal incidence become very low. This indicates that an arrangement of array currents, such as shown in Fig. 11, although favorable for minimizing induced torques, may promote differential charging by electrons. For protons, the cutoff energies are 1/1836 of those for electrons, hence, the magnetic fields considered here will not shield against protons above a few tens of electron volts. For example, the maximum proton cutoff energy, obtained above the 3000 amp bus, is 17 eV.

Another estimate concerned the torques induced from the coupling of the array currents to the ambient geomagnetic field, taken as 0.001 gauss. The array was assumed to be oriented so as to have the main current bus aligned with the field; the torques would therefore arise from forces on the secondary busses running at right angles to the main bus. A maximum torque of 18 Newton-meters (13 ft-lb) about the array center-line is estimated; the resultant increment in ΔV requirements for attitude control is insignificant.

An estimate was also made of the added thrust capability required for station keeping if all the substorm particles were incident on only one side of the array. The combined pressure from an electron flux of 6.10^9 e/cm^2/sec

and a proton flux of $1.4 \cdot 10^8$ p/cm^2/sec is found to be $7.8 \cdot 10^{-11}$ newtons/m^2 ($1.6 \cdot 10^{-8}$ lb/ft^2). This represents about 1/6 of the solar pressure on the array.

In view of the frequently encountered concern with ion sputtering as a mechanism for surface erosion and contaminant production, a worst case assessment of proton sputtering on SiO_2 was made. A continuous substorm proton flux of $1.4 \cdot 10^8$ p/cm^2/sec at kT = 15 keV was assumed, together with a spectrum-integrated sputtering yield of 10^{-2}. This leads to a mass removal rate of $1.4 \cdot 10^{-9}$ g/cm^2/year (or $6.3 \cdot 10^{-2}$ Å/year), which per se is insignificant; however, the optical performance of solar cell covers may be degraded in the process. The associated contaminant production rate is 0.09 g/day for the 100-MW demonstration article, which is compared with a mass release of 1×10^5 g/day from hydrazine thrusters or 2×10^4 g/day from cesium thrusters for station keeping.

Therefore, the development of a solar blanket in which radiation damage can be removed by on-site annealing appears to be essential for SPS. A design concept for a heat-annealable solar cell is shown in Fig. 7.

The importance of radiation damage in degrading the performance of solar arrays is well recognized. For example, radiation darkening in solar cell cover glass is expected to produce a transmission loss of $\sim$ 4% over a 30 year SPS life-time; here the darkening tends to be limited by concurrent ultraviolet annealing. (Note that a 4% performance loss represents a 2.5% increase in SPS program costs.) By comparison, solar cell degradation by radiation is much more severe in GEO. This degradation is equivalent to that produced by a yearly fluence of 1 to 2 x 10^{14} 1-MeV electrons (including the contributions from solar flares). A 16% efficient cell will degrade 20 to 30% over 10 years in GEO, primarily due to solar flare proton damage.

LARGE SCALE ENVIRONMENTAL INTERACTION EXPERIMENT PLATFORM

Air Force and NASA studies are now defining test articles and flight programs which will demonstrate on-orbit construction of large space structures. These demonstrations will be the first LSS-related activities in space, and according to current plans, will occur by 1984. One of the concepts for such a demonstration article is shown in Figure 13. This utility platform is constructed while attached to the Shuttle, utilizing one-meter beams which are fabricated by the automatic beam builder located in the Shuttle payload bay. A simple gravity-gradient stabilized platform is shown in the figure which supports several earth-pointing experiments. Electrical power and other subsystems have also been added to provide long-term, free flyer capability.

The same platform could carry a variety of material, component and subsystem segments as depicted in Figure 14. In this example, several different material, solar cell blanket and antenna gore samples, in various sizes and configurations, are mounted over almost all of the available 900 square meter test surface. Temperature and illumination sensors, particle and electromagnetic pulse (EMP) detectors are distributed throughout the test samples.

Integrators, recorders and other equipment are located in an experiment support package. The platform is powered by radioisotope thermoelectric generator (RTG) to eliminate plasma disturbances and orientation requirements associated with solar cell arrays.

Low Earth Orbit (LEO) Tests

The platform can be left in LEO for extended periods and periodically revisited by the Shuttle. Test samples and on-board data can be retrieved, and new samples added if desired.

Since LEO plasma characteristics are significantly different from those in geosynchronous orbit (GEO), relatively few LEO test results will extrapolate to GEO. However, charge/discharge effects, passive charge controls and space environment synergisms could be evaluated, and size/configuration relationships established for large area elements. Also, since most LSS programs include construction and operation of demonstration systems in LEO, these tests will provide valuable design/performance data for these systems.

Other tests which might be used to verify analytical models and ground test results are

- Materials response-plasma dynamics
- Transient-induced differential charging
- Discharge avalanche
- Electric/magnetic field-induced forces
- Voltage/leakage current scaling

High Altitude Tests

With the addition of a propulsion stage, the platform could be placed in elliptical orbit or in GEO where the majority of LSS will eventually operate. A conceptual design of the largest test platform which could be boosted to high altitude from LEO is shown in Figure 15. This article is constructed in a manner identical to that described above, with its maximum dimensions nearly 100 meters. A cluster of three IUS (Interim Upper Stage) engines are used to propel the 6800 kilogram spacecraft. A total of 4800 square meters of platform area is available for test samples. Instrumentation and experiment support equipment is distributed throughout the platform, and an RTG used for electrical power as with the LEO platform. One or more retractable plasma probes can be added as shown to measure plasma characteristics at various distances from the spacecraft. Motor-driven boom designs are available for probe extensions up to one kilometer.

A test platform of this type in GEO could provide definitive environmental interaction data to guide the design of future LSS. The following types of

tests could be performed, in additon to those listed above, for a nearly complete characterization of physical processes and coupling mechnisms:

- Electric field acceleration
- Magnetic field deflection/focusing
- Plasma-induced heating
- Geometrical particle shadowing
- Plasma sheath formation
- Plasma instability non-linear effects
- Spacecraft geomagnetic wake
- Active charge controls
- Large scale performance verification

This LSS test platform could be constructed and placed in GEO by the mid-1980's. Real-time data could be recorded shortly after orbit insertion. Data can be sampled over long intervals to evaluate effects of environment variations and long-term material property changes.

An advanced orbit transfer vehicle (OTV), which might be available around 1990, could visit the LSS test platform in GEO. Test samples could be inspected, retrieved for ground tests and replaced with new or different samples for additional space testing. If accelerated materials ground tests cannot be properly developed, or prove too costly, long-term GEO experiments of this type may be the only way to derive the design data and confidence levels needed before committing to development of a complex, costly LSS.

Much research and engineering analysis must yet be done to estimate LSS environmental interactions and effects. Many plasma-related interactions and long-term materials effects will most likely require large test articles of the type described above; the opportunity to fly these experiments will be here shortly. A program should be formulated now to define the research and analyses to be performed, the types of experiments to be flown, and to begin preliminary designs of the large scale experiment platform.

TABLE 1 POTENTIAL CHARGE/DISCHARGE EFFECTS ON LSS

EFFECT	SBR	SPS DEMO
• DIELECTRIC CRAZING/DARKENING	• SOLAR CELL COVERS & THERMAL CONTROL SURFACES	
• DIELECTRIC EMBRITTLEMENT	• SOLAR ARRAY SUBSTRATE & COMPOSITE/GLASS STRUCTURAL ELEMENTS	
• CONTAMINANT DEPOSITION	• SOLAR CELL COVERS, THERMAL CONTROL SURFACES • ACCELERATED ELECTRICAL DISCHARGES	
• METAL EROSION/VAPORIZATION	• SOLAR CELL INTERCONNECTS & THERMAL BLANKETS	
	• ANTENNA DIPOLES/DELAY LINES/ELECTRONIC MODULE CONTACTS	• METAL/COMPOSITE WAVEGUIDES
• INSULATION BURNTHROUGH	• DC POWER DISTRIBUTION	
		• RF CONVERTER FEEDS
• EMI/VOLTAGE TRANSIENTS	• SUBSYSTEM WIRING/ELECTRONICS	
	• ANTENNA POWER DISTRIBUTION & ELECTRONICS	• POWER DISTRIBUTION NETWORK
• ELECTROSTATIC FORCES-STRUCTURAL DISTORTIONS	• PRIMARY/SECONDARY STRUCTURE	
	• ANTENNA/GROUND PLANES	

TABLE 2 POTENTIAL PLASMA INTERACTIONS WITH LSS

INTERACTION	SBR	SPS DEMO
• PLASMA PARTICLE ACCELERATION BY CHARGED SURFACES	• INCREASED RADIATION DAMAGE • ORBIT/ATTITUDE DISTURBANCE FORCES	
• PLASMA/LSS COUPLING CURRENTS	• EXAGGERATED ECLIPSE/LOAD TRANSIENTS • DISTORTING FORCES/TORQUES	
• MAGNETIC FIELD FOCUSING/DEFLECTION	• INCREASED DIFFERENTIAL CHARGING	
	• ANTENNA POWER DISTRIB.	• POWER DISTRIB. NETWORK
• ELECTRIC FIELD ACCELERATION		• AVALANCHE BREAKDOWN
• PLASMA LEAKAGE CURRENTS		• HIGH VOLTAGE POWER LOSS
• ELECTRIC/MAGNETIC FIELDS – ELECTRON BEAMS		• RF CONVERTER BEAM DEFOCUSING
• MULTIPACTOR DISCHARGE		• WAVEGUIDE BREAKDOWN
• ION THRUSTER EXCHANGE CURRENTS	• INCREASED DIFFERENTIAL CHARGING	
		• INCREASED POWER LOSS

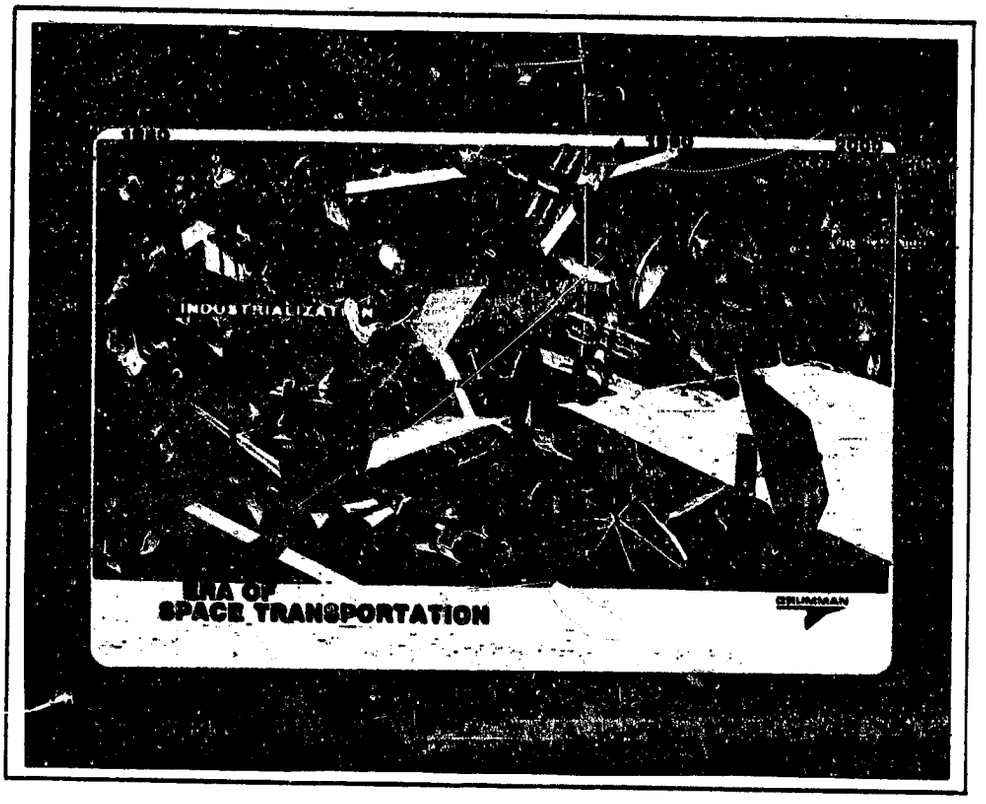

Figure 1. Era of Space Transportation

Figure 2 Space Based Radar Configuration

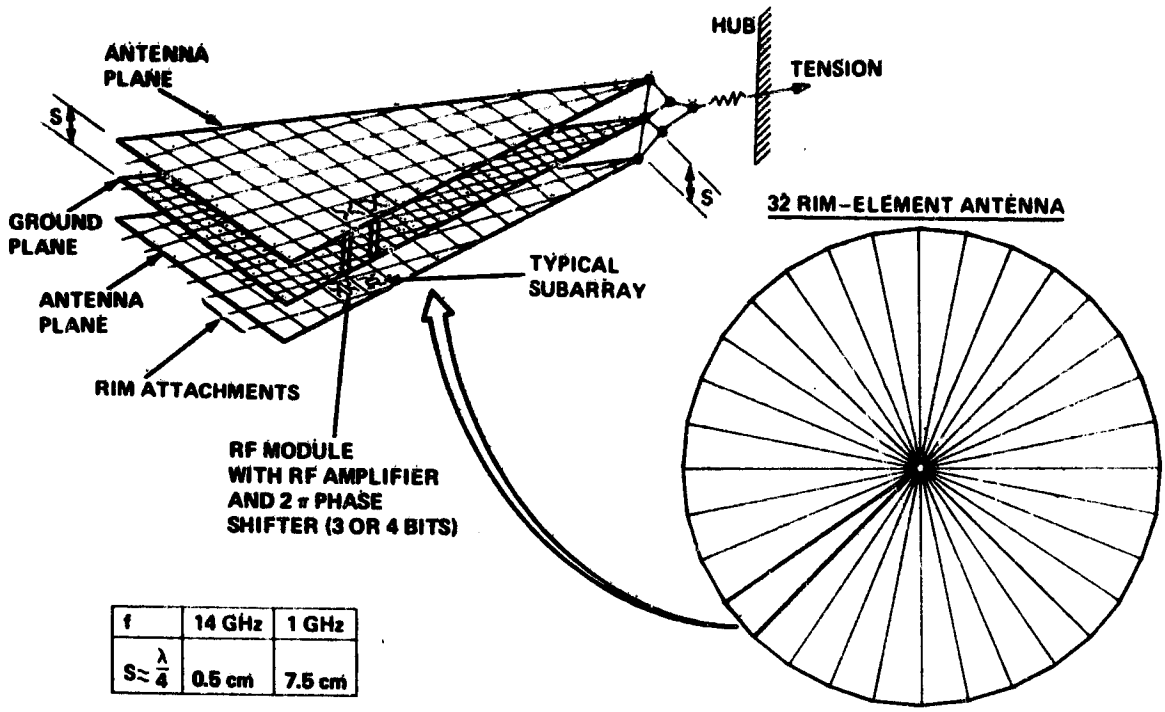

f	14 GHz	1 GHz
$S \simeq \frac{\lambda}{4}$	0.5 cm	7.5 cm

Figure 3. Phased Array (Active)

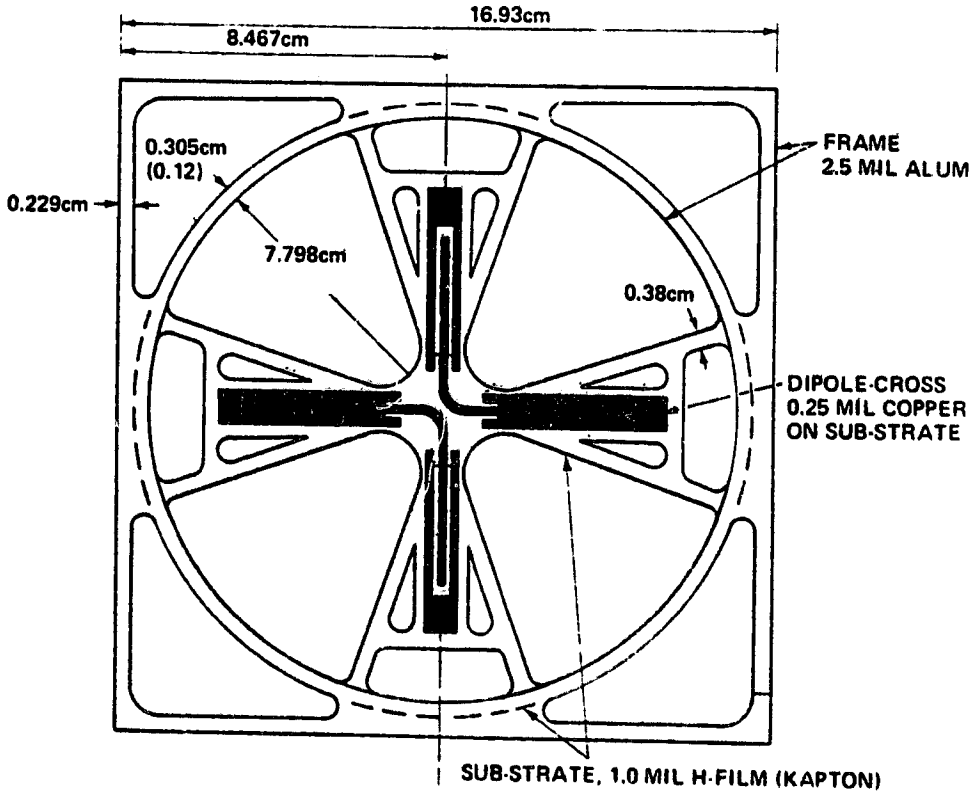

Figure 4. Subarray Structural Arrangement

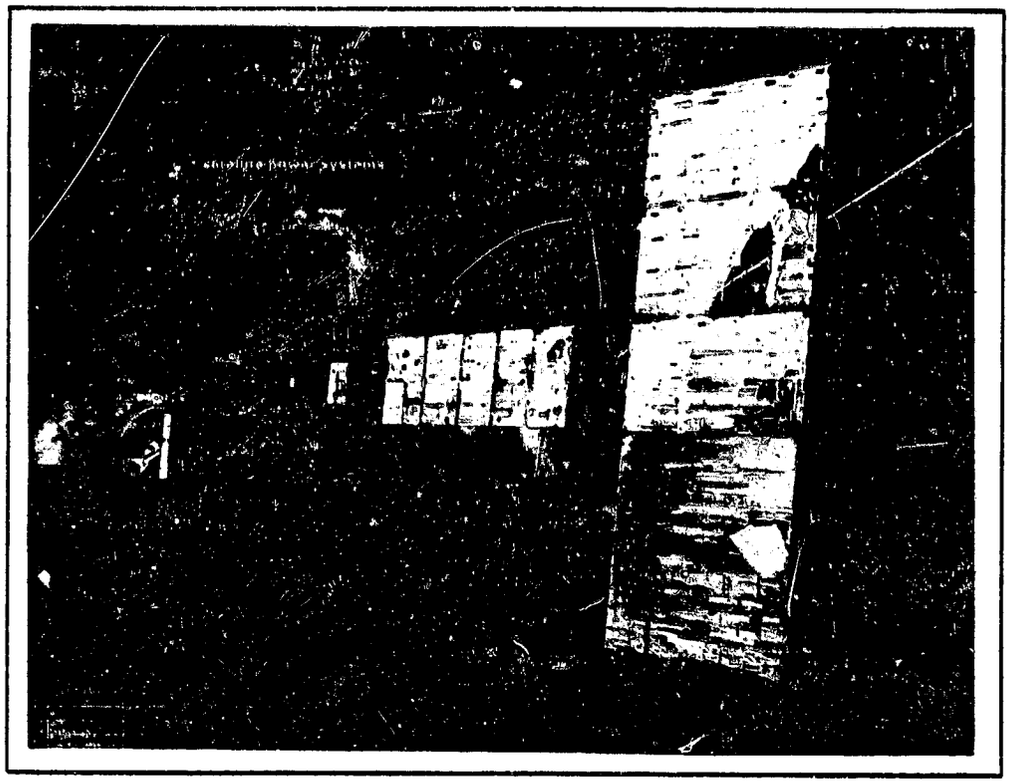

Figure 5. Evolution of Solar Satellite Power Systems

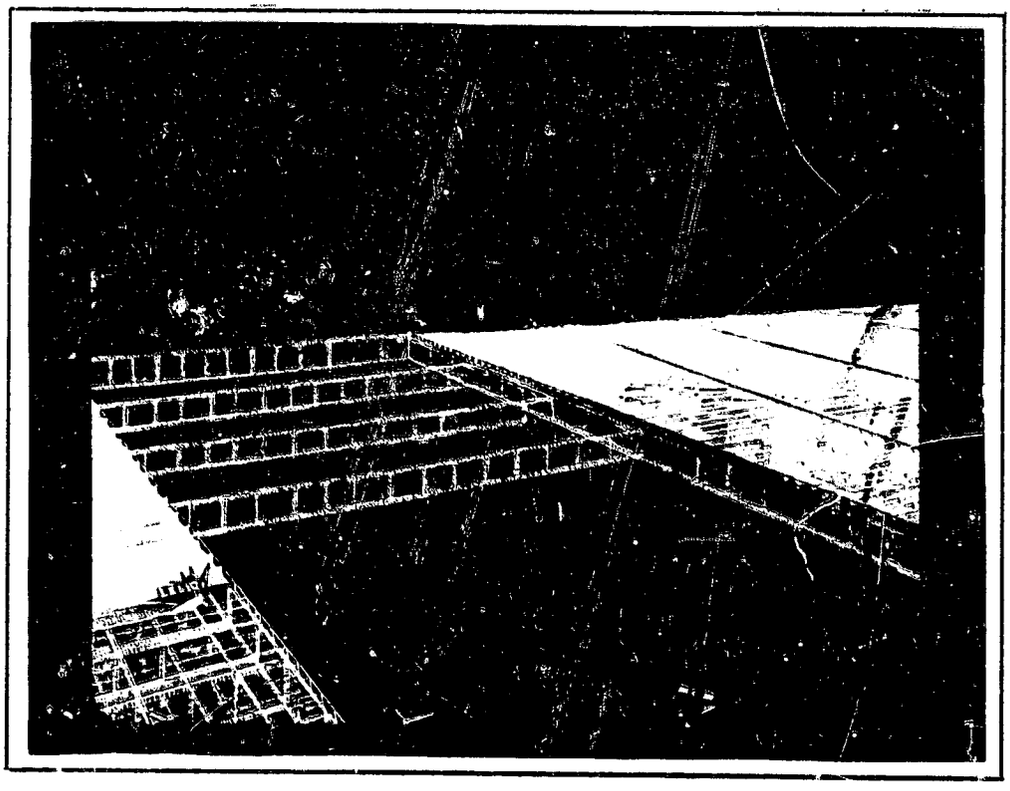

Figure 6. SPS Construction (Antenna Proximity)

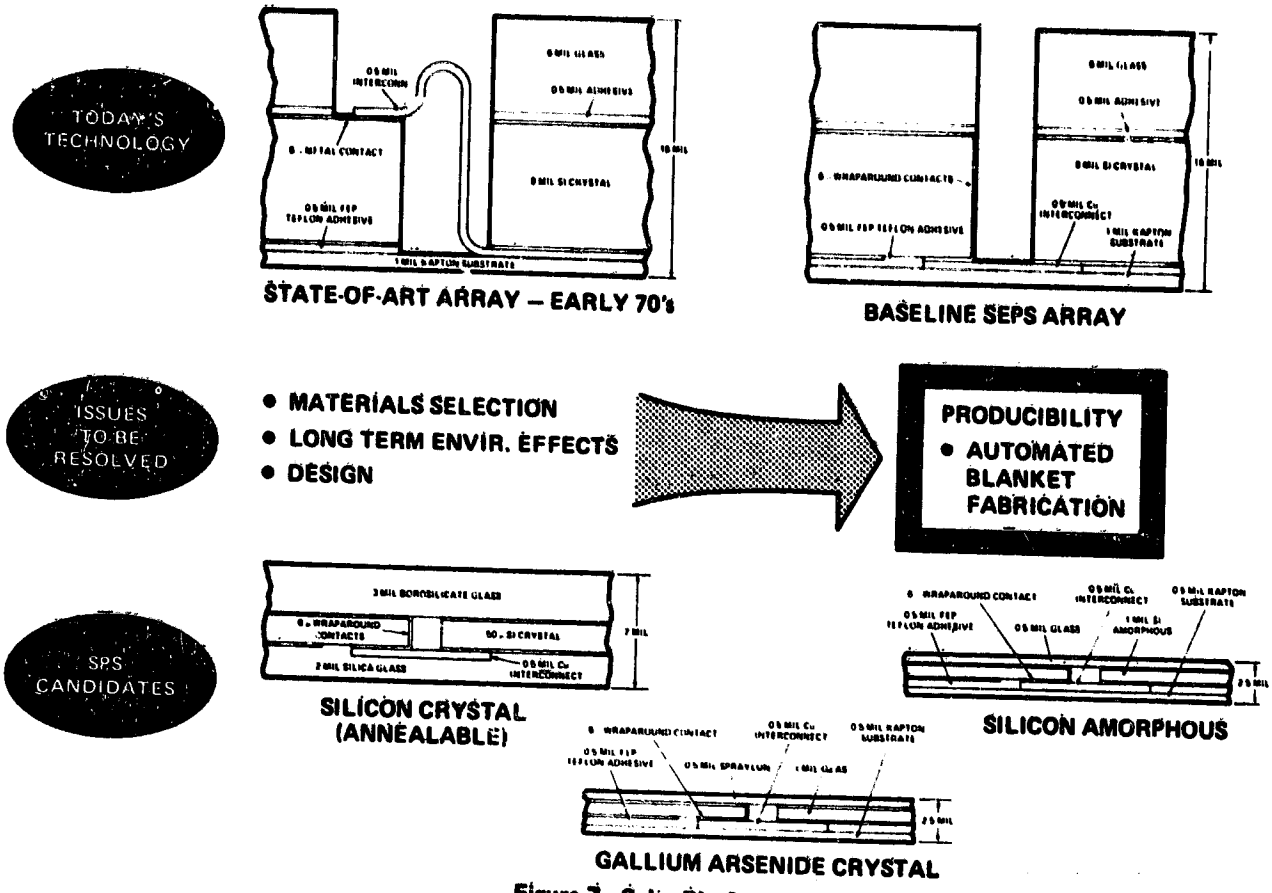

Figure 7. Solar Blanket

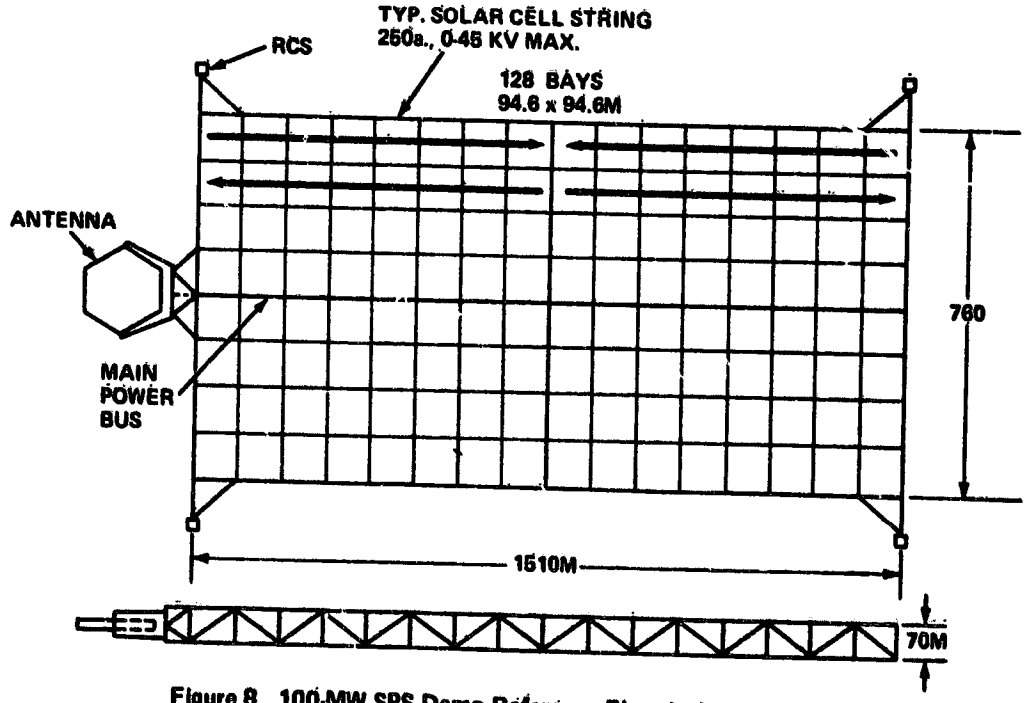

Figure 8. 100-MW SPS Demo Reference Electrical Configuration

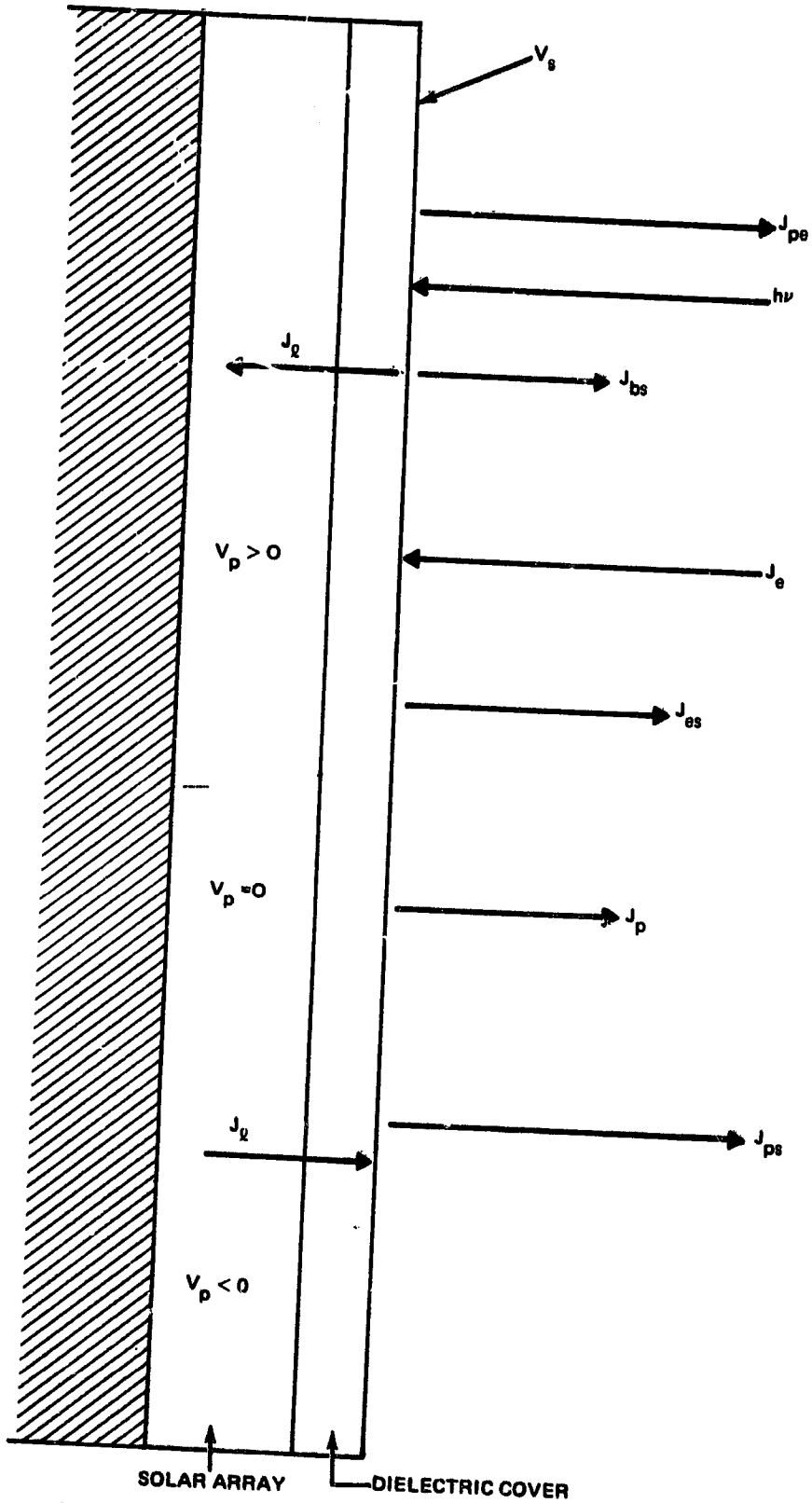

Fig. 9 Charging Currents on Solar Array with Dielectric Cover

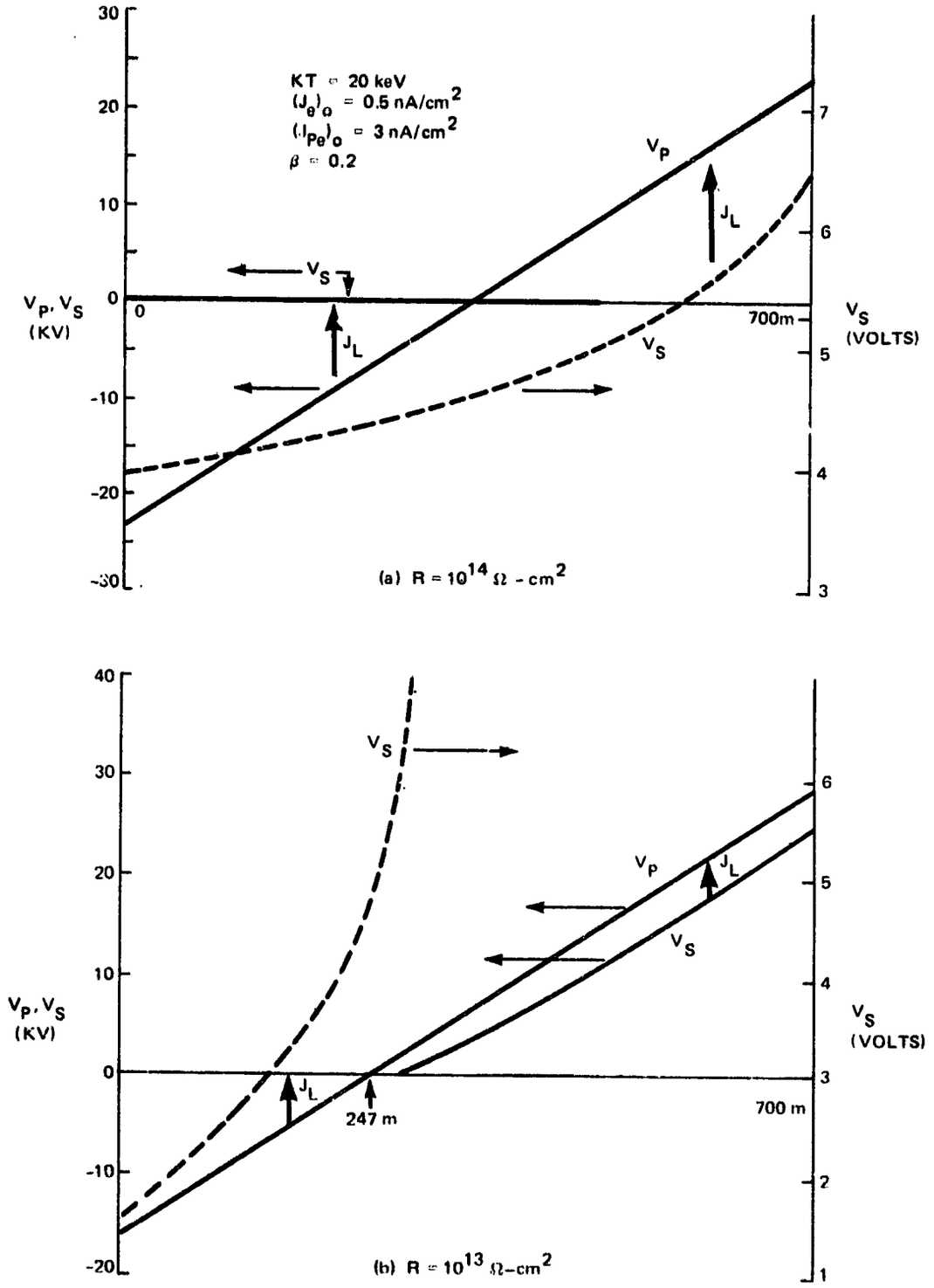

Fig. 10 Surface Potential (V_S) and Solar Cell Floating Potential (V_P) for 47-KV Solar Array with Cover

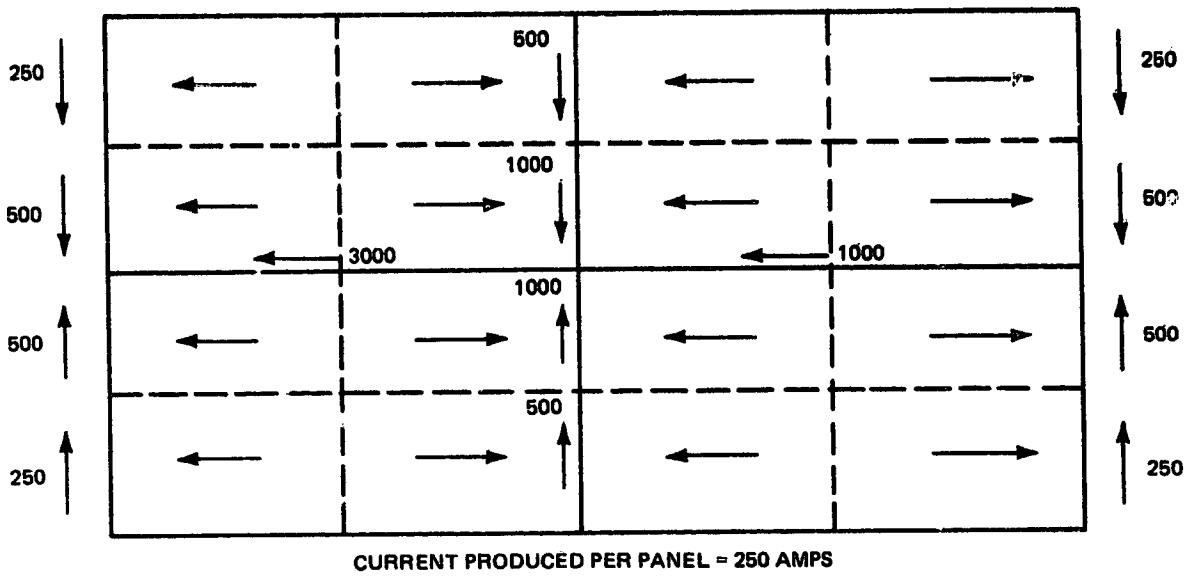

Figure 11. SPS Current Flow

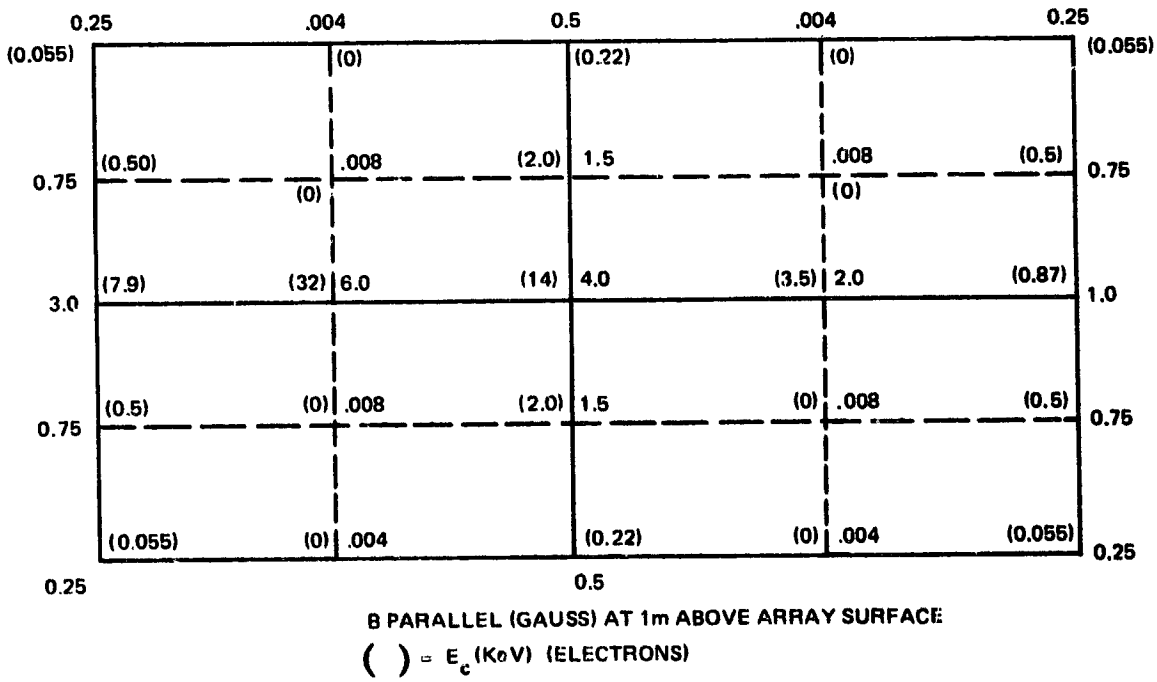

Figure 12. SPS Magnetic Shielding

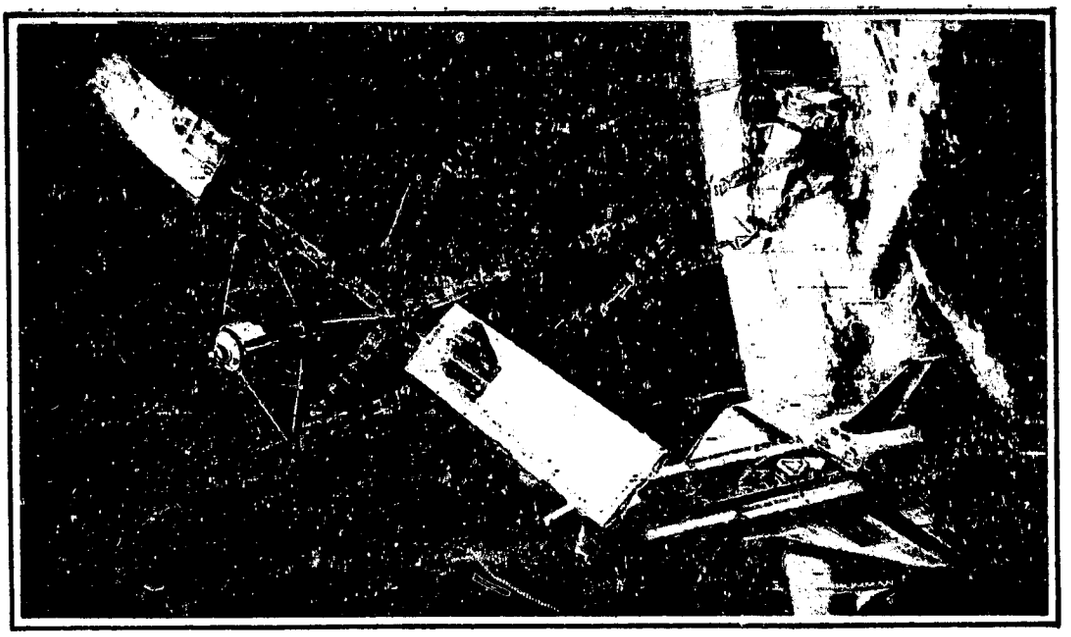

Figure 13. Utility Platform Constructed by Shuttle-Based Beam Builder

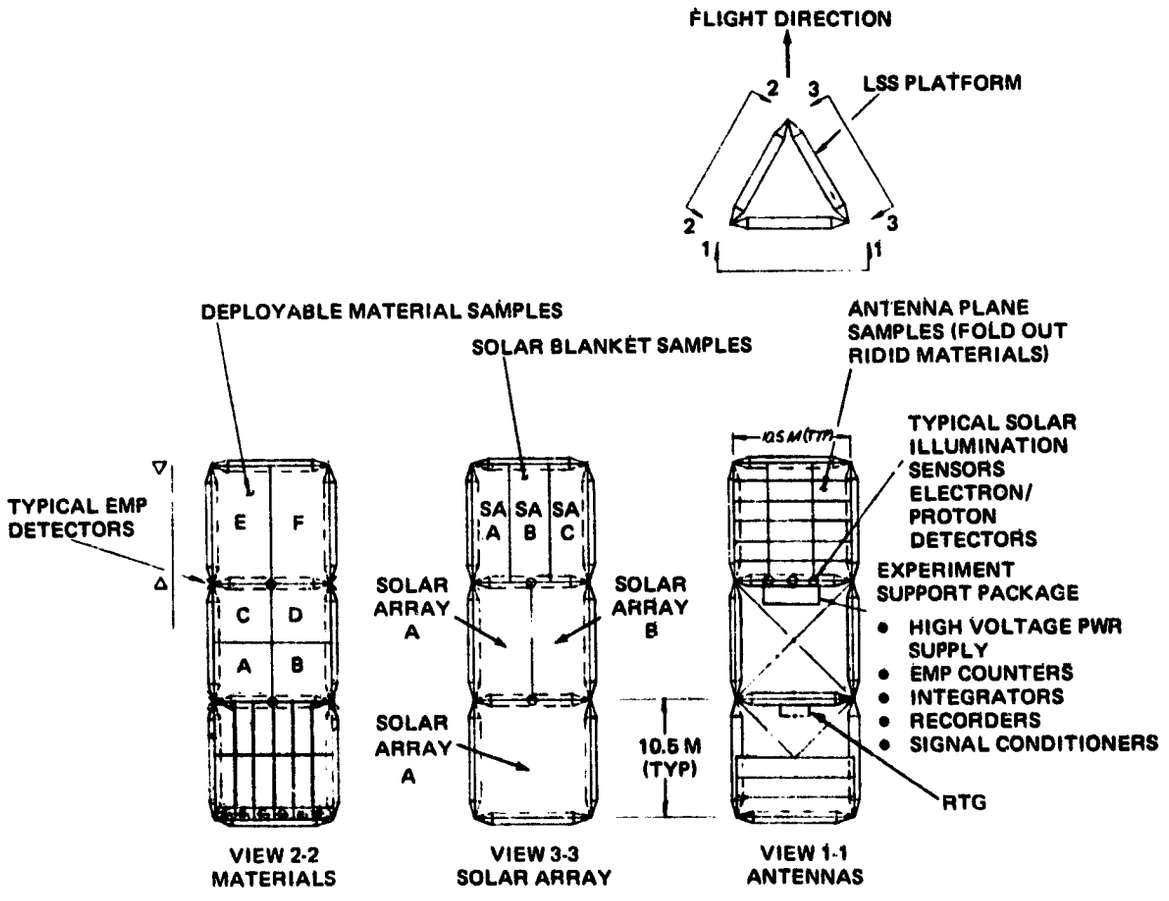

Figure 14. Materials Exposure/Plasma Charging Experiment

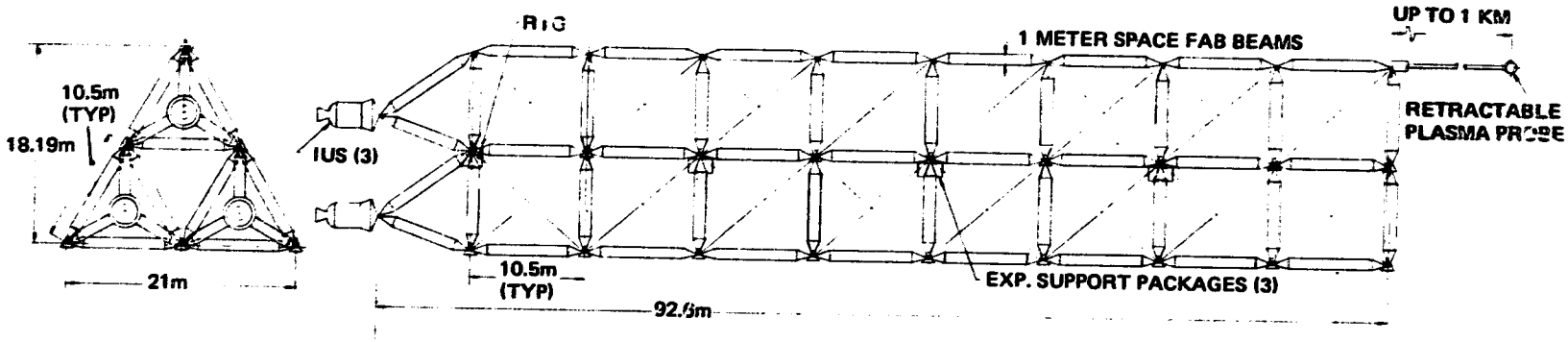

Figure 15. Large Scale GEO Exp. Platform

SPACE ENVIRONMENTAL EFFECTS AND THE SOLAR POWER SATELLITE

John W. Freeman, David Cooke, and Patricia Reiff
Department of Space Physics and Astronomy
Rice University

ABSTRACT

This report summarizes some preliminary findings regarding the interactions between the space plasma at GEO and the Marshall Space Flight Center January 1978 baseline SPS design. These include the following:

1. The parasitic load will be dominated by photoelectrons and will amount to about 34 MW.

2. Material of higher conductivity than kapton should be used for the solar reflector substrate and the solar cell blanket support material.

3. The satellite structure and solar reflector should be tied electrically to midpoint voltage of each solar cell array.

4. Tests should be run on the proposed solar cell cover glass material (synthetic sapphire) to determine if breakdown is expected.

INTRODUCTION

Figure 1 illustrates the basic concept of the solar power satellite. A large area solar cell array converts sunlight into D.C. electricity. This is in turn converted to microwaves via klystrons. The 1 km diameter microwave antenna directs the beam from the geosynchronous orbit satellite to a receiving antenna on the ground. The receiving antenna (called a rectenna) consists of a large array of dipoles, rectifying diodes and filters whose output is D.C. electricity suitable for conversion to A. C. distrbution to a power grid.

The area of the solar cell array is about 50 km^2 for a 5GW output satellite. If solar concentrating reflectors are used the solar cell surface area may be reduced.

The Rice University study is concerned with the NASA Marshall Space Flight Center SPS baseline design as of January

1978. The purpose of the study is to investigate and make design recommendations regarding satellite charging due to geostationary orbit ambient plasmas.

The study involves the following steps:

1. Define the "worst case" plasma environment.
2. Calculate probable voltages at critical points on the satellite.
3. Identify vulnerable areas.
4. Suggest design changes where necessary.
5. Calculate the probable new voltages after design changes.
6. Calculate the parasitic current loads.

Based on a search of the literature and data we have selected the following "worst case" conditions for the plasma sheet at geosynchronous orbit:

$$kT \text{ (electrons)} = 5 \text{ kev}$$

$$kT \text{ (protons)} = 10 \text{ kev}$$

$$n_e = n_p = 2 \text{ cm}^{-3}$$

These are not the absolute worst case conditions found but they are typical of a severe substorm and should be adequate to indicate out trouble spots in the spacecraft design.

Figure 2 illustrates the MSFC baseline design used in our study. This design employs solar reflectors to concentrate the sunlight on the solar cells. The concentration ratio is 2. The solar reflectors are the sides of the troughs shown in arrays of three at each end of the satellite. The solar cell blankets are suspended by cables at the floor of each of the troughs in a trampoline fashion. The solar cells are connected in parallel across the trough and in series along the trough so that each pair of blankets puts out about 6000 amps at 45.5KV. There are six such pairs on each of the six troughs.

CURRENTS

Our first task was to compute the plasma thermal currents and photoelectron currents to the solar cell array. In treating

the plasma electron and ion currents we assumed a thin sheath approximation, ie. that the collecting area was the area of solar cell array (front and back) and that positive ions would be attracted to the negative portion of the array and electrons to the positive. We assumed that the photoelectron current from the negative array would be the expected photoelectron current density times the array area. The photoelectron current density was obtained by integrating the product of the photoelectron yield function for synthetic sapphire and the solar spectrum. The resulting photocurrent density is 3×10^{-9} amp/cm^2. For the positive array, we assumed that the solar reflectors would supply a bath of photoelectrons which would be attracted to the positive array. Since the subtended area of the solar reflector adjacent to the solar array is about the same as that of the array the photoelectron current is taken to be the current density times the array area. Figure 3 illustrates the photoelectron paths and gives the current densities. The photoelectron current is found to dominate the thermal ion and electron currents both of which are given by

$$J = \frac{ne}{4}\sqrt{\frac{8kT}{\pi m}}$$

where n, T and m are the number density, temperature and mass of the ions or electrons, and k and e are the Boltzman constant and electron charge, respectively. The resulting parasitic current, Ip, mostly photoelectrons, is about 3000 amps. Assuming the midpoint of the solar array is grounded to the solar reflector, the average voltage above and below ground $\bar{V}$ is 11,375 volts. The parasitic load is therefore

$$P_p = I_p \bar{V} = 34 \text{ MW}$$

This is about 0.7% of the 5 GW output.

SOLAR CELL SURFACE VOLTAGES

Turning to the voltages developed on the satellite, we decided at the outset that the solar cells were probably the single most vulnerable item on the satellite because they are exposed solid state devices. Figure 4 shows the design of the GaAlAs Solar Cell being considered for the MSFC Baseline design. This cell is an inverted design with synthetic sapphire forming both the cover glass and substrate. The sapphire is 20 micrometers thick. The cell is supported by a 25 micrometer kapton blanket.

For our purposes the cell is idealized as a sapphire, active region, Kapton sandwich (see Figure 5). The voltages across the sapphire and Kapton dielectrics are then the IR drops resulting from the photoelectron and plasma thermal currents times the resistance of the dielectrics. These voltages are shown in Figure 5. The assumed resistivities of sapphire and kapton are 10^{12} ohm-cm and 10^{16} ohm-cm respectively. The largest voltage is that across the kapton blanket on the positive array. This may exceed the breakdown voltage for kapton, 2×10^6 V/cm.

THE OPTIMUM GROUNDING POINT

To calculate the floating potential for the solar cell array (defined as the point on the series voltage string closest to the plasma potential) we require that, at equilbrium, the sum of all currents between the satellite and the plasma be zero. We calculate this sum by adding the currents to the positive and negative areas of the array, A^+ and A^-

$$A^-(J_{phe} + 2J_i) = A^+(J_{phe} + 2J_e)$$

ignoring the metallic solar reflectors. Here J_{phe}, J_i and J_e are the photoelectron, ion and electron current densities. This yields

$$\frac{A^-}{A^+} = 1.17$$

Ideally, the negative area (and hence voltage string) should be 17% larger than the positive surface. We do not consider the calculation to have 17% precision, however. We recommend grounding the midpoint of each voltage string to the satellite structure and the solar reflectors.

It might be argued that the photoelectrons, J_{phe}, are not part of the spacecraft-magnetospheric plasma current loop and therefore should not be included in the current balance equation. We believe that a substantial fraction of the photoelectrons will escape to space and that their inclusion is therefore appropriate. In calculating the electric potentials of bodies in space it is accepted practice to include the photoelectron currents (eg. Whipple, 1965; Manka, 1973). Moreover, estimates of the electric potential of the lunar surface can only be made to agree with the experimental values when photoelectron emission is included (Freeman and Ibrahim, 1975; Freeman, Fenner and Hills, 1975).

The floating potential will change with time but will probably tend to equilibrate about the midpoint on the voltage string so this is probably a good choice as a practical matter (L.W. Parker, private communication).

VOLTAGES ON PASSIVE SURFACES

We estimate the voltage, ϕ, on the darkside passive (unbiased) surfaces of the satellite using Chopra's equation (Chopra, 1961) . .

$$\phi \equiv - \frac{kT_e}{2e} \ln \left[\frac{M_i T_e}{M_e T_i} \right]$$

For the sunlit surfaces, the potential is several times the mean photoelectron energy. Thus, we expect +10 to +100 volts for the sunlit surfaces and -10,000 to -20,000 volts for the darkside surfaces. The backside of the solar reflectors are 1/2 mil kapton whose breakdown voltage should be less than 2500 volts. Thus, arcing is to be expected on the backside of the solar reflectors. Figure 6 summarizes these voltages at various points on the satellite.

THE SHEATH THICKNESS

Because of the high voltage biases produced by the solar cells the appropriate sheath is a Child-Langmuir sheath given by (Langmuir, 1914)

$$J = \frac{1}{9\pi} \left(\frac{2e}{m_e} \right)^{1/2} \frac{V^{3/2}}{d^2}$$

If we take J to be the plasma electron thermal current given by

$$J = \frac{en}{4} \left(\frac{8kT}{\pi m} \right)^{1/2}$$

we have for the sheath thickness

$$d = 933 \, n^{-1/2} \, (kt)^{-1/4} \, V^{3/4}$$

d is in cm; n, electrons cm^{-3}; kt in eV and V in volts. This is the expression given by Parker (this volume) except for the deletion of his term which corrects for a significant ram current. The ram current due to satellite motion through the medium is negligible because the thermal plasma and the satellite both co-rotate at the same velocity. Plasma flows from the geomagnetic tail are ignored here.

Figure 7 is a sketch showing the dimensions of the Child-Langmuir sheath. Note that it is of the order of the width but not length dimensions of the satellite. Our earlier thin sheath approximation is valid only to within factors of unity.

CONCLUSIONS

At this point in the study, our conclusions are as follows:

1. Voltage breakdown will occur on the solar reflector backsides and probably on the solar cell kapton support blanket.

2. The parasitic load will be dominated by photoelectrons and will amount to about 34 MW (for GEO only).

3. The optimum ground point to the structure and solar reflectors is the middle of each solar cell voltage string ie. we want +22.75KV to -22.75KV.

4. Tests should be run on the solar cell front face in a substorm test facility to see if conductive cover glasses should be used.

ACKNOWLEDGEMENTS

We would like to acknowledge helpful discussions with Dr. L.W. Parker. This research was supported by the Marshall Space Flight Center and The Brown Foundation.

REFERENCES

1. Chopra, K.P., Rev. Mod. Phys., 33, 153, 1961.

2. Freeman, J.W. and M. IBrahim, Lunar Electric Fields, Surface Potential and Associated Plasma Sheaths, the Moon, 14, 103-114, 1975.

3. Freeman, J.W., M.A. Fenner, and H.K. Hills, Electric Potential of the Moon in the Solar Wind, J. Geo. Phys. Res., 78, 4560, 1973.

4. Manka, R.H., Plasma and Potential at the Lunar Surface, Proceedings of the ESLAB Symposium on Photon and Particle Interactions with Surfaces in Space, D. Reidel Publishing Co., 1973.

5. Whipple, Elden Cole, Jr., The Equilbrium Electric Potential of a Body in the Upper Atmosphere and Interplanetary Space. Ph.D. Thesis George Washington University, 1965.

6. Langmuir, Irving, Phys. Rev., 2, 450, 1913; Phys. Lets., 15, 348, 516, 1914.

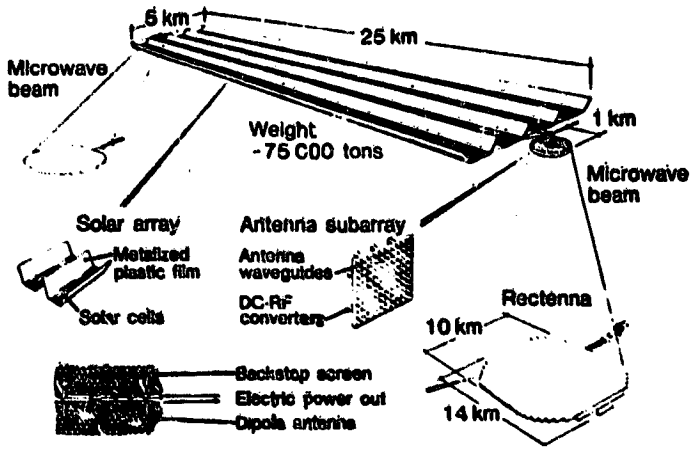

Figure 1. - Typical SPS configuration (2x5000 MW output).

NASA-S-77-15022

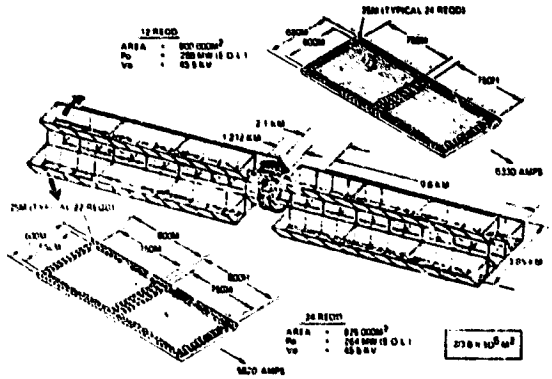

Figure 2. - Marshall Space Flight Center baseline design.

THE VARIOUS CURRENT DENSITIES ARE:

J_{PHE} = 5×10^{-9} AMP/CM^2 (FOR SAPPHIRE)

J_i (PLASMA) = 3×10^{-10} AMP/CM^2

J_i (PLASMA) = 1×10^{-11} AMP/CM^2

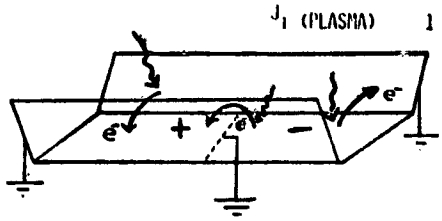

PHOTOELECTRON FLOW DIRECTIONS

TOTAL PARASITIC CURRENT:

$I_p \cong$ 3000 AMPS

V = 11,375 V

THE PARASITIC POWER IS:

$P_p \cong$ 34 MW

(0.7% OF OUTPUT POWER)

Figure 3. - Photoelectron paths and current densities.

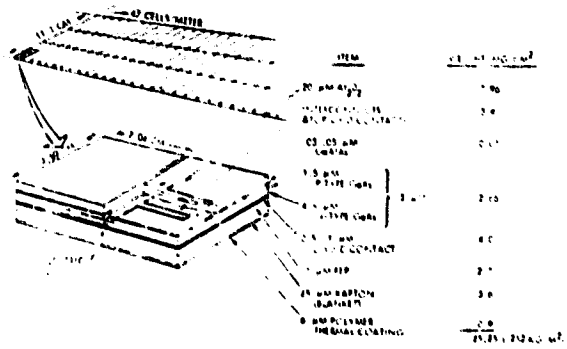

Figure 4. - Cross section of GaAlAs solar cell blanket.

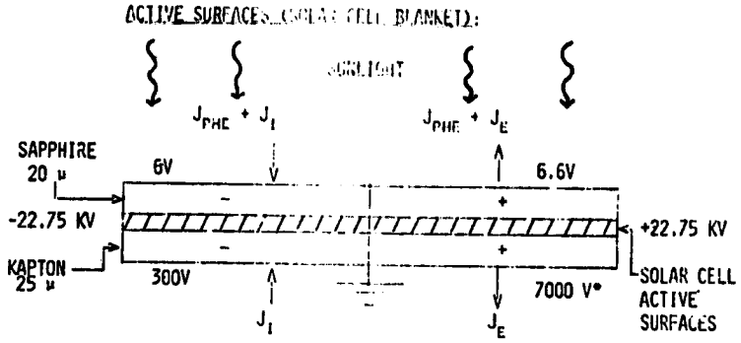

VOLTAGES SHOWN ARE RELATIVE TO THE LOCAL SOLAR CELL VOLTAGE. THEY REPRESENT THE IR DROP ACROSS THE COVER GLASS OR KAPTON BLANKET.

* THE KAPTON BREAKDOWN VOLTAGE IS ~ 5000 V

Figure 5. - Schematic of solar cell.

SUMMARY OF VOLTAGES:

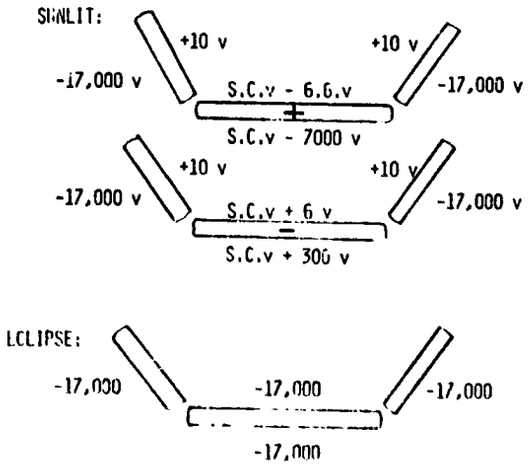

Figure 6. - Summary of voltages on satellite passive surfaces.

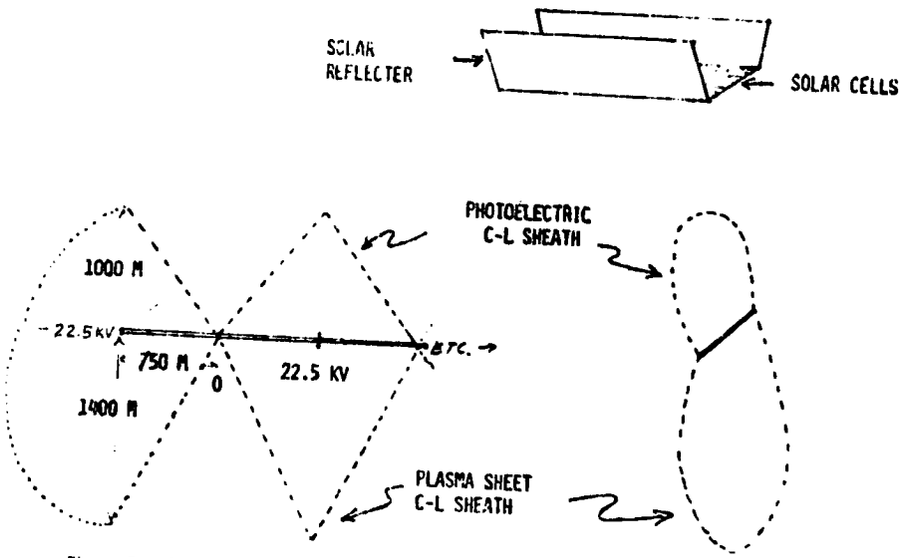

Figure 7. - One-dimmensional Child-Langmuir sheath shape for one trough in MSFC SPC design.

PLASMA PARTICLE TRAJECTORIES AROUND SPACECRAFT PROPELLED BY ION THRUSTERS

H. B. Liemohn, R. L. Copeland, and W. M. Leavens
Boeing Aerospace Company

ABSTRACT

Ion thrusters are being considered for propulsion of future spacecraft due to their relatively low fuel mass to thrust ratio and easy access to solar power for long duration missions. Operation of such thrusters requires high spacecraft potentials, and their local electric fields can draw return current from the thruster plasmas, reducing system efficiency. In this paper, the thruster plasma is assumed to be described by a collimated energetic beam (∿10 keV) and a cloud of ionized thermal propellant (∿10 eV) produced by charge-exchange. A simple adiabatic model is used to describe the expansion of these neutral plasmas away from the source. As the pressure falls, shielding currents dissipate, and the geomagnetic field takes control of the particles. In low earth orbit, it is concluded that the vehicle easily outruns its thruster plasma. At geosynchronous altitude, the local electric fields around high voltage surfaces collect return current from the thermal plasma that appears to be limited only by the available space charge. Results appropriate to proposed electric propulsion missions and the solar power satellite are presented and operational considerations are discussed.

INTRODUCTION

Spacecraft requirements for long-duration missions and minimum vehicle weight have enhanced interest in ion thrusters that operate from solar energy. Although these propulsion systems have low thrust, their low mass to overall thrust during prolonged missions makes them strong candidates for interplanetary explorations to comets and asteroids and as a means of station keeping for geosynchronous payloads. They are also attractive for orbit-transfer propulsion when time is not a primary limitation.

A number of small thrusters have been built and tested in space and the laboratory (e.g., refs. 1-4). Somewhat larger propulsion modules have been conceived for future large-scale applications (refs. 5,6). All of these thrusters generate a thermal plasma in a chamber and accelerate the ions across closely spaced grids. The high grid voltage collimates the ion beam, and an adjacent electron source provides immediate neutralization. A secondary source of plasma at the outlet occurs by charge exchange between the beam ions and escaping neutral atoms. Approximately 15% of the beam charge is transferred to these thermals which represent a significant source of local current. Some operational characteristics of these thrusters are summarized in table I.

TABLE I. NOMINAL ION THRUSTER CHARACTERISTICS
(refs. 5-7 and D. Grim, private communication)

Source Grid Diameter (cm)	30	100
Propellant Gas	Hg	A
Beam Current (A)	2	80
Acceleration Voltage (kV)	1.1	10*
Exit Plane Beam Density (ions/cm^3)	$\sim 5 \times 10^9$	
Exit Plane Thermal Density (ions/cm^3)	$\sim 10^{11}$	
Thermal Ion Current (A)	0.2	~8
Efficiency (%)	70	80
Thrust (N)	0.13	6

*Solar power satellite station keeping operation at geosynchronous altitude.

The plasma environs around the spacecraft consist of both thruster exhaust and natural background. Some characteristics of these plasmas that are needed in the following analysis are presented in table II. Only operations in low earth orbit (LEO) around 400 km altitude and geosynchronous earth orbit (GEO) at 6.6 earth radii geocentric are considered here to demonstrate the effects. The spacecraft is assumed to be following a circular trajectory so that its speed relative to the background magnetoplasma is 7.7 km/sec at LEO and nearly zero at GEO. At LEO the natural plasma density is adequate to shield the spacecraft fields from the thruster plasma. However, the tenuous conditions at GEO allow fields to extend well beyond the vehicle dimensions.

TABLE II. PLASMA ENVIRONMENT PARAMETERS
(refs. 7-8)

	LEO at 400 km	GEO at 36,000 km		
		Natural Plasma	Argon Thruster Plasma	
			Beam	Thermal
Ion Density (m^{-3})	LEO	$10^{11} - 10^{12}$	-	-
	GEO	$10^6 - 10^7$	-	-
Ion Thermal Energy (eV)	LEO	0.1		
	GEO	1 - 10	10	10
Ion Mean Free Path (km)	LEO	~ 10	$\sim 10^2$	10
	GEO	$\sim 10^6$	$\sim 10^7$	10^3
Ion Larmor Radii (km)	LEO	1	2	0.5
	GEO	1,000	500	60
Debye Length (cm)	LEO	~0.8	0.03	0.007
	GEO	~800	(at exit plane)	

For ion propulsion to operate efficiently from solar energy, a high voltage solar array is required to avoid the extra weight of power converters. The local electric fields around these panels can attract the thruster plasma if Debye shielding by the ambient plasma is inadequate. Additionally, as the thruster plasma disperses, the geomagnetic field eventually takes control of the particles, and some geometries permit orbits to fold back on the vehicle surface. Such return current diminishes the effectiveness of the overall system by inhibiting propulsion and/or leaking power from the solar energy collectors.

The purpose of this paper is to investigate the interaction of the thruster plasma with its parent power source. The intention is to understand the plasma behavior qualitatively and make quantitative assessments where return current may be significant. The goal is to identify modes where there are negligible system losses, determine characteristics of modes where return current levels impact the system efficiency, and explore ways to modify inefficient configurations. In the following section a model is developed for the expansion characteristics of the energetic beam and thermal plasma. The next section describes the role of the geomagnetic field. The spacecraft field effects are treated in the last section.

THRUSTER PLASMA EXPANSION

Rather than solve the nonlinear MHD fluid equations numerically for equilibrium conditions, a less complicated approach is presented in which the trajectory equation for the average plasma column radius with time is derived analytically from conservation of energy and adiabatic constraint equations. The adiabatic fluid equations are used because they are often a valid approximation for collisionless systems. The only requirement is that the third moment of the distribution function around the mean expansion speed must be small. This, along with conservation of particles, yields an equation for the average plasma density with time. It is solved only for the ion motion, assuming that there exists a charge neutralizing background of electrons that follow the ions.

From conservation of energy,

$$1/2\ M\ \bar{v}^2 = k(T_o - T) \tag{1}$$

where M is the ion mass, v is the local mean ion velocity, k is Boltzmann's constant, T_o is the thermal ion temperature at the source, and T is the local ion temperature along the beam. The adiabatic constraint equation is

$$T/N_\ell^{\gamma-1} = T_o/N_o^{\gamma-1} \tag{2}$$

where N_ℓ is the line plasma density, N_o is the source density, and γ is the ratio of specific heats which has the value 5/3 here.

Since the divergence angle of ion trajectories exiting the accelerating diode is small, and the axial ion speed greatly exceeds the rocket speed, a line source plasma model with radial adiabatic expansion can approximate the beam plasma expansion. Assuming no end losses, conservation of particles requires

$$N_\ell / N_o = (r_o/r)^2 \tag{3}$$

where r_o and r are the column radii at the thruster and along the beam. Integrating the differential equation resulting from eqs. (1), (2), and (3), gives an implicit expression for r(t),

$$\bar{v}_o\, t = \left(\frac{3}{4}\right) r_o \left[\left(\frac{r}{r_o}\right)^{2/3} \left[\left(\frac{r}{r_o}\right)^{4/3} - 1\right]^{1/2} + \log\left[\left(\frac{r}{r_o}\right)^{2/3} + \left(\frac{r}{r_o}\right)^{4/3} - 1\right)^{1/2}\right]\right] \tag{4}$$

where $\bar{v}_o$ is the initial plasma thermal velocity. Equation (4) may be solved numerically. From eqs. (1) to (3) one can easily obtain $N_\ell(t)$, $T(t)$, $\bar{v}(t)$, and $z = ut$, where u is the directed beam speed.

A Gaussian angular distribution is assumed to account for beam divergence at the source. Combining these results leads to an expression for the beam envelope,

$$N(\theta, z) = N_\ell(z)\; e^{-|\theta/\theta_o|^2} \tag{5}$$

where N_ℓ is the axial density calculated as above, θ is the angle with respect to the z axis, and θ_o is typically 3°. Figure 1 shows beam plasma density contours for a one meter argon 100 cm thruster at two different times

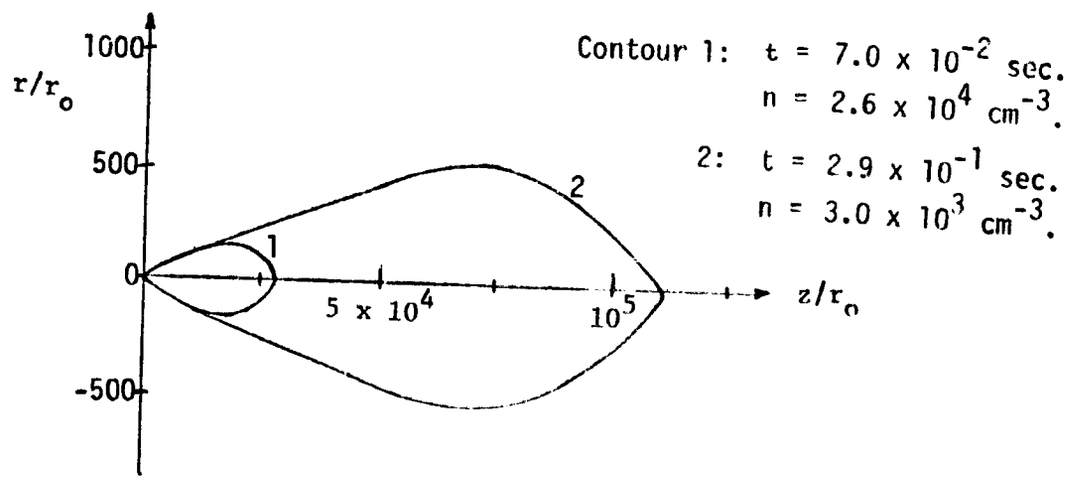

Figure 1. - Beam plasma density contours for argon SPS thruster.

Thermal Plasma

Charge transfer within the beam, between the slow neutrals and the fast ions, produces a relatively high density cool plasma which remains in the neighborhood of the thruster. The source characteristics of this plasma plume depend upon the charge transfer production rate and the subsequent motion of the slow ions which are described in the Appendix. The latter step is considerably more complicated, because the ion dynamics are dominated by the electrostatic potential structure in the charge transfer region, which in turn is determined by the beam neutralization process.

Here, the adiabatic model is assumed to adequately describe the motion of the thermal plasma away from the source. However, the isotropic motion of neutrals suggests hemispherical expansion so that conservation of particles now has the form

$$n_s/n_o = (r_o/\rho)^3 \tag{6}$$

where n is density and ρ is radial distance. Following the same analysis as before, yields an explicit equation for $\rho(t)$,

$$\frac{\rho}{r_o} = \left[1 + \left(\frac{v_o t}{r_o}\right)^2\right]^{1/2} \tag{7}$$

where $\bar{v}_o$ is the mean velocity in the source region. Similarly, expressions for $n_s(t)$, $T(t)$, and $\bar{v}(t)$ may be obtained. The initial density distribution of neutrals is assumed to have a cos θ angular distribution (ref. 7). Consequently, the thermal density envelope has the form

$$n(\theta,\rho) = n_s(\rho) \cos\theta \tag{8}$$

Figure 2 shows density contours of the thermal plasma from the argon thruster for two different times. Note that the density levels for the contours in both figures 1 and 2 are the same. Also, it is important to note that the beam plasma escapes the spacecraft region easily while the slower thermal plasma remains in the vicinity of the spacecraft.

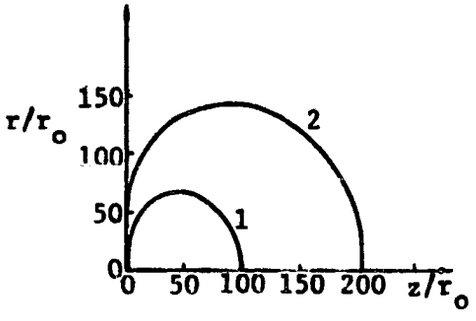

Contour 1: $t = 8.7 \times 10^{-3}$ sec, $n = 2.6 \times 10^{4}$ cm^{-3}

Contour 2: $t = 1.7 \times 10^{-2}$ sec, $n = 3 \times 10^{3}$ cm^{-3}

Figure 2. - Thermal plasma density contours for argon SPS thruster.

GEOMAGNETIC FIELD EFFECTS

The thruster plasma is sufficiently dense in the vicinity of its exit plane (see table I) to generate its own currents that buck out the geomagnetic field. As the beam and thermal plasmas expand however, these currents are dispersed, and the geomagnetic field eventually takes control of the individual particles. An exact treatment of this transition process is extremely complex and beyond the scope of this paper. A simple pressure balance criterion is used instead, since the exact transition process does not appear to affect the conclusions. The motion of the particles is described by conventional adiabatic theory (e.g., refs. 10, 11) ac the local geomagnetic field is fairly uniform locally. The effect of spacecraft electric fields is treated in the next section.

Due to the large ion Larmor radii and mean free paths compared to characteristic plasma dimensions (see table II), a continuous transition from the plasma fluid to single particle orbits probably extends over an appreciable fraction of the thermal and beam plasma plumes. The pressure balance expression

$$\frac{1}{2} NM \bar{v}^2 = B^2/8\pi \tag{9}$$

where B is the geomagnetic field, is recognized as a gross approximation. However, it serves a useful purpose as the estimated locations of the transitions are found to be relatively close to the source. Injection velocities for ions into the geomagnetic field are assumed to be those of the free expansion, since the Larmor radii are large. These assumptions provide a reasonably consistent model for estimating geomagnetic effects.

Beam Plasma

From the beam qualities described by eq. (5) and displayed in fig. 1, it is evident that these energetic ions are well collimated. Substituting these density envelopes into eq. (9) and evaluating at LEO and GEO gives the transition values shown in table III. Comparison of these results with those in table II confirms the assumption regarding the lack of geomagnetic distortion through the transition.

TABLE III. THRUSTER PLASMA FLUID TO PARTICLE ORBIT TRANSITION LOCATION

	B (gauss)	Density N or n_3 (ions/cm^3)	Beam z/r_o	Beam r/r_o	Thermal ρ/r_o
LEO (400 km)	0.31	2.4×10^8	63	2.9	4.8
GEO (36,000 km)	0.0011	2.9×10^3	40,000	400	208

The ion-beam directed velocity is substantially greater than that of the spacecraft at LEO as well as at GEO. Consequently, these ions enter the geomagnetic field with their beam speed. Since their thermal motion is small as well, their pitch angle relative to the geomagnetic field is nearly equal to the angle between the thruster direction and the field. These ions follow well known first-order adiabatic orbits along geomagnetic flux tubes (e.g., refs. 10, 11). Depending on their mirror altitude, they may be trapped for an extended period (possibly years above LEO).

Most applications at LEO involve accelerating spacecraft to attain higher altitude and the ion beam is directed at a large angle to the field. The tilt of the geomagnetic axis relative to the earth's axis and appreciable trajectory inclinations can produce angles as small as 30° or less, however. If the beam is directed toward the atmosphere, the particles are completely absorbed in the spacecraft hemisphere; if the beam is directed upward it travels to the opposite hemisphere, where it is deposited.

At GEO the spacecraft is usually stationary in the geomagnetic field, and the ion beam may be directed at any angle with respect to the field depending upon its purpose. Generally the beam ions are injected into trapped orbits of long duration. Their longitudinal drift motion and subsequent dispersion is expected to eliminate any appreciable return current to the spacecraft. However, some caution is advised to avoid those rare conditions around the geomagnetic equator that create particle mirror locations close to the vehicle which could cause bursts of return current. At the opposite extreme, beams injected nearly parallel to the field (within the loss cone) follow the flux tube down to the atmosphere where they are absorbed. Due to the variety of possible operating conditions, no attempt is made to provide quantitative results here, although they are readily calculable.

Thermal Plasma

Due to its hemispherical expansion, the thermal plasma density falls much faster than that of the beam. Consequently, its transition location is very close to the vehicle as indicated by the values in table III. Furthermore, the thermal plasma does not function as independently of the spacecraft as the beam can; the plume stays close to the vehicle until the field takes control. Thus, these ions cause concern as a possible return current source.

The motion of the thermal ions is most easily perceived in the rest frame of the spacecraft as a continuum of expanding spheres, which is depicted schematically in figure 3. As the plume density drops to the transition threshold defined by eq. (9), the rearward hemisphere acts as a source surface for injection into the geomagnetic field. Alternatively, in the laboratory frame the ion motion is perceived as a vector sum of the spacecraft velocity and radial expansion vector as shown in figure 4. This vector diagram is valid for all times of interest since the expansion motion is radial at nearly constant speed and the Larmor radii are large compared with the plume dimensions (table II). At the outer boundary the mean thermal expansion is 6.9 km/sec compared to the spacecraft speed of 7.7 km/sec at LEO.

At LEO it is evident from figure 4 that the plume cannot "catch up" to the spacecraft (when local electric fields are omitted from consideration), because thermal speed is directed into the hemisphere away from the vehicle. Even those ions in the energetic Maxwellian tail of the thermal plasma move away due to lack of collisions back toward the vehicle. A typical cluster of thermal ion orbits is shown in figure 5 for the case where the spacecraft is being propelled normal to the local geomagnetic field.

The thermal ions emanating from a geosynchronous satellite thruster would follow geomagnetic orbits like those in figure 5 assuming no electric fields were present; however, the scale is now 300 times larger (see Larmor radii in table II). Those ions injected nearly orthogonal to the local geomagnetic field can return to the spacecraft after one gyration if their velocity components satisfy the inequality

$$v_{\parallel}/v < \ell_{\parallel}\,(\mathrm{km})/60\pi \qquad (10)$$

where $v_{\parallel}$ is the velocity component parallel to the field, v is total ion speed, and $\ell_{\parallel}$ is the dimension of the spacecraft parallel to the field. For a typical 100 m extension less than 0.0005 of the thermal ion charge would be collected directly; the rest enter trapped orbits.

All the other ions travel away along geomagnetic flux tubes until they mirror and return past the plane of the spacecraft. From adiabatic theory for geomagnetically trapped particles (e.g., refs. 10, 11), the time to return to the spacecraft is on the order of $2\,R_e/\bar{v}$, where R_e is the geocentric distance to the spacecraft. For argon ions at 10 eV, this bounce time is $\sim 1.2 \times 10^4$ secs. During this time they drift in longitude at the rate of about 3×10^{-8} rad/sec, which corresponds to an equatorial transit distance of 1500 km, well away from the spacecraft.

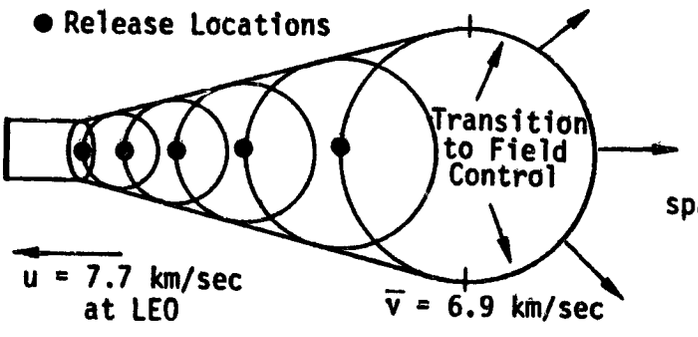

Figure 3. - Thermal ion plume expansion (spacecraft frame).

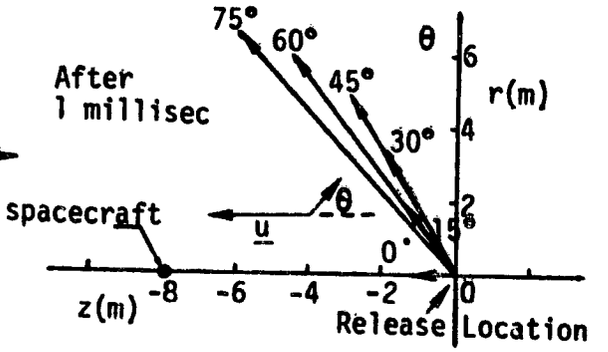

Figure 4. - Thermal ion trajectories at LEO (laboratory frame).

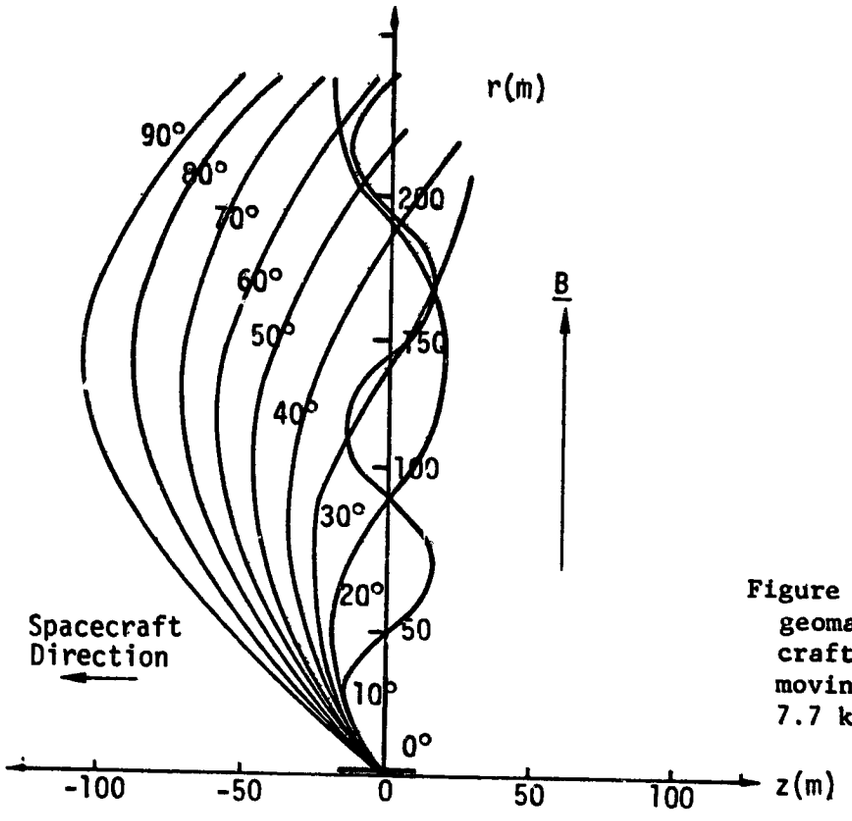

Figure 5. - Thermal ion geomagnetic orbits (spacecraft thruster at LEO moving across $\underline{B}$ at 7.7 km/sec).

SPACECRAFT FIELD EFFECTS

Spacecraft that employ ion thrusters for propulsion will probably use solar arrays to generate their electrical power. Since significant propulsion can only be achieved with high power levels, the array will undoubtedly operate at high voltages to reduce conduction losses. Such potentials on exterior spacecraft surfaces produce regions of high electric field which can dramatically alter the thruster plasma. Since the thermal plasma cloud lingers in the vicinity of the spacecraft, the ions and electrons are easily attracted back to the vehicle by these fields. If the surface is insulated, space charge can build up to neutralize the applied fields. If there is access to non-insulated conductors, as, for example, exposed solar cell connectors, the return current shortcircuits the system, lowering efficiency. Presumably the main thruster beam operates at such an energy and distance from these field sources that it remains unaffected.

A spacecraft driven internally to high voltages behaves like a floating double probe (refs. 12, 13). Its potential distribution is biased negative due to the higher mobility of electrons. Experience has shown that a double probe in an ionospheric plasma with an impressed voltage V has its positive end at about 0.1 V above the plasma potential and its negative end around 0.9 V below plasma potential (ref. 14). This large negative field region attracts the thermal ions from the thruster, and their rate of collection limits the return current to the vehicle.

Return Current Theory

The range of spacecraft generated electric fields determines the volume of plasma that can supply return current. The electric field around a naturally charged spacecraft extends outward only a few Debye lengths (see table II) because of shielding by the ambient plasma. For high voltage solar arrays, however, the shielding length is larger, and it is necessary to determine the scaling with array voltage.

When the applied potential energy eV is much greater than the thermal kinetic energy kT, the ions are pulled from the plasma with nearly zero energy (kT), and the electron space charge becomes exponentially small just a few Debye lengths from the plasma edge. Under these conditions the Langmuir-Childs space-charge analysis applies (refs. 15, 16). The ion current density flowing from the background plasma to a negative satellite surface is

$$j_{L.C.} = \frac{(2e/M)^{1/2} V^{3/2}}{9\pi\beta^2 x^2} \tag{11}$$

where β^2 is a geometry factor and x is the distance between the source plasma and the collector. The ion current j_i collected by the surface is limited to that available from the surrounding environment, including the ambient plasma ions and ram current on forward surfaces (due to spacecraft motion), as well as ion thruster sources.

The separation x is determined by limiting $j_{L.C.}$ to the available j_i that can be drawn from the surrounding region. For the geosynchronous situation where $j_i = ne\bar{v}$, equation (11) has the solution

$$\beta x = \left[\frac{8\pi^{1/2}}{9}\right]^{1/2} \left[\frac{eV}{kT}\right]^{3/4} \left[\frac{kT}{4\pi ne^2}\right]^{1/2} \tag{12}$$

Note that βx is independent of particle mass, and thus applies to ion- or electron-collecting sheaths. The factor β is unity for plane-parallel geometry (or any curved surfaces with βx much less than a typical dimension) but may vary substantially for other geometries (ref. 16).

For the conditions of geostationary orbit, a plane electrode at 10 kV would have a shielding length of ∿7 km. Thermal plasma bubbles produced by ion thrusters on booms even one kilometer away would be within the range of the electric fields from the spacecraft.

Solar Power Satellite Applications

As an illustration of the space charge limit on return current, consider station keeping of the solar power satellite (SPS) at GEO. One version of the SPS system (ref. 6) has 25 control thrusters located on a 0.5 km boom extending from each corner of the solar array rectangle. Operating

characteristics are those of the 100 cm argon thruster listed in table I. The solar panel is designed to operate at 40 kV so that its central power mains are around 4 kV positive and 36 kV negative with respect to the external plasma. At the edge of the array near the boom the panel potential is midway between the mains.

Consider first the case where the coaxial power line to the thrusters is unshielded with its exterior surface at the negative potential. The thermal ions are attracted to the cable by its external fields. The amount of current that this cable can collect has been estimated using the methods developed by Langmuir (refs. 15, 16) and treating the cable as a rectangular strip of length L and width πa. The running integral of the charge limited current starting from the end of strip away from the source and stopping at the thruster cluster radius r_o is given by the expression

$$I(>z) = \frac{4\pi\varepsilon_o a}{L}\left(\frac{2e}{M}\right)^{1/2} V^{3/2}\left[\frac{\cos\theta}{(1-\cos\theta)} + \ell n\ (1-\cos\theta)\right] \qquad (13)$$

where $$\theta = \sin^{-1}(z/L) \qquad r_o \leq z \leq L \qquad (14)$$

The plot of $I(>z)$ in figure 6 demonstrates the concentration of current density near the thruster. The SPS thruster cluster at the end of the boom produces about 200 A of thermal plasma, and the integral $I(r_o)$ over the 500 m boom reveals that about 300 A could be collected on a 1 m coaxial cable.

This current collection can be eliminated by suitable insulation around the conducting surfaces. But the high voltage solar panels provide an alternate sink for thermal ions. The space-charge limited current capacity of such surfaces is described by equation (13) as well, and the current density has a profile similar to that in fig. 6. A schematic diagram of the current flow to SPS is shown in fig. 7. Most of the charge would be collected in the corner region where the boom attaches to the main structure. The enormous dimensions of the collecting surface imply that all of the thermal ion current would be collected by the exposed solar cell interconnects.

Insulating the entire solar panel surface would eliminate this return current path. However, this insulation membrane must be able to withstand high voltages that are created by charge collection on the outer surface. Laboratory experiments with plastic materials such as Kapton have been performed (ref. 17), and the material suffered breakdown and pinhole formation at the edges of conducting elements. Development of new materials or somewhat thicker membranes presumably will be needed to withstand the electric fields. Thus, to avoid solar panel breakdown, collection of thermal return currents on bare coaxial cable appears to be a more desirable procedure.

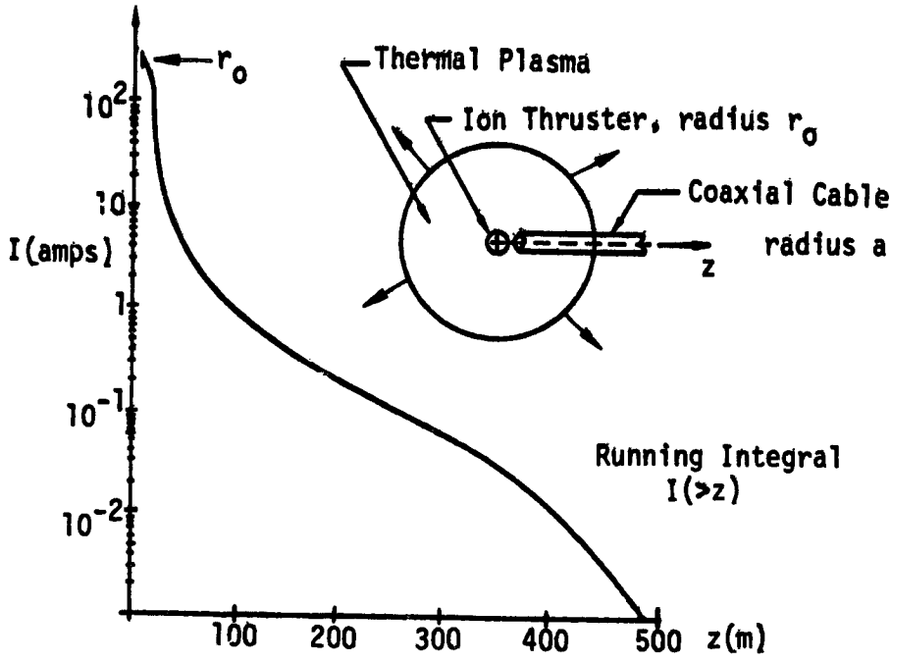

Figure 6. - Space-charge-limited current collected by exposed boom cable to thruster cluster on SPS.

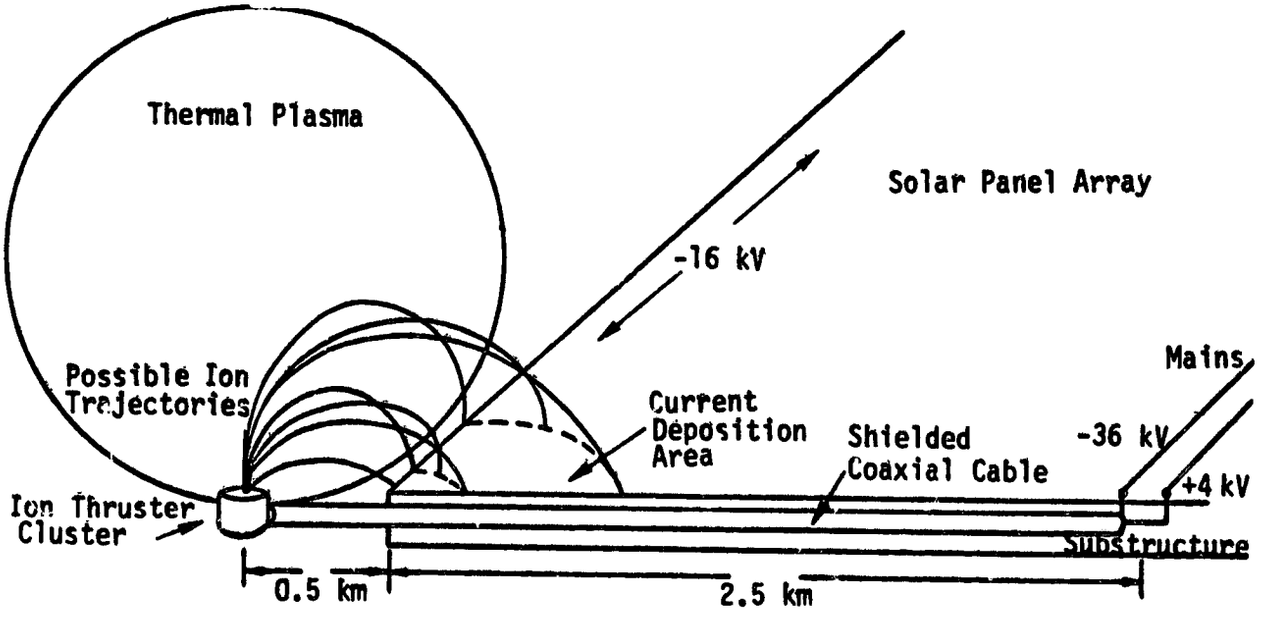

Figure 7. - Thermal ion current collected by unshielded solar cell interconnects on SPS panels.

APPENDIX. THERMAL ION GENERATION

Charge-Transfer Plasma

The slow neutrals are assumed to expand spherically as if they originated at a point a distance r_o behind the accelerating mesh. The fast ions are assumed to flow in a constant radius cylinder over the range where the neutral density is high enough to support charge transfer. Because a significant fraction of the original ion beam undergoes charge transfer, it is necessary to solve the coupled equations for the densities of fast and slow ions.

Momentum transfer during charge transfer collisions can be neglected. However, we also neglect the effects of momentum changing collisions, which is not entirely justified and would have a significant effect on the thermal plasma expansion. In the expansion calculations, we have used spherical expansion rather than cylindrical expansion (as implied by the potential model) as a crude way of accounting for the typical forward motion of the thermal particles acquired in elastic collisions with beam particles.

Slow ion creation and loss:

$$\frac{dn_s^+}{dt} = \nabla \cdot j_s^+ = \frac{\sigma(v_f - v_s)}{v_f\, v_s} (j_f^+ j_s - j_s^+ j_f) \tag{1}$$

where

$$j_s^+ = n_s^+ v_s \text{ etc., and}$$

$$j_f = j_f^+ + j_f^o \; ; \; j_s = j_s^+ + j_s^o \, ,$$

and σ is the charge transfer cross-section.

Fast ion creation and loss:

$$\frac{dn_f^+}{dt} = -\nabla \cdot j_f^+ = \frac{\sigma(v_f - v_s)}{v_f\, v_s} (j_s^+ j_f - j_f^+ j_s) \tag{2}$$

$$-\frac{dn_f^+}{dt} = \frac{dn_s^+}{dt} \tag{3}$$

Taking Z = 0 at the effective center of spherical expansion for the slow particles, and letting

$$j_s = I_o/Z^2 \quad , \quad j_s^+ = I_o^+/Z^2 \tag{4}$$

we have

$$\nabla \cdot j_s = \frac{1}{Z^2} \frac{\partial}{\partial Z} (Z^2 j_s) \text{ when operating} \tag{5}$$

on j_s , j_s^+ , j_s^o , and

$$\nabla \cdot j_f = \frac{\partial}{\partial Z} j_f \tag{6}$$

Combining (4) and (5) and defining slow fluences $\bar{v}_s$, $\bar{v}_s^+$ by

$$j_s = \bar{v}_s/Z^2 \ , \ j_s^+ = \bar{v}_s^+ (Z)/Z^2 \tag{7}$$

we obtain a differential equation for the slow ion fluence,

$$\frac{\partial^2 j_s^+}{\partial Z^2} + \left(\frac{j_s}{KZ^2} + \frac{j_f}{K}\right) \frac{\partial j_s^+}{\partial Z} = 0 \tag{8}$$

where

$$K = \frac{v_f \, v_s}{\sigma(v_f - v_s)} \tag{9}$$

The solution of equation (8) is

$$\frac{\partial j_s^+}{\partial Z} = a \, e^{-p(Z)} \tag{10}$$

when

$$p(Z) = \frac{j_s}{K} \left(\frac{1}{Z_o} - \frac{1}{Z}\right) + \frac{j_f}{K} (Z - Z_o) \tag{11}$$

where Z_o is the thruster exit position, i.e., $Z_o \approx r_o$, the exit radius. Since $p(Z_o) = 0$, the constant a is given by the initial value of the charge transfer rate,

$$a = \frac{j_f \, j_s}{K \, Z_o^2} \tag{12}$$

Thus the slow ion source distribution is

$$\frac{\partial j_s^+}{\partial Z} = \frac{j_f \, j_s}{K \, Z_o^2} \, e^{-p(Z)} \tag{13}$$

and the net slow ion current is

$$j_s^+(Z) = \frac{j_f \, j_s}{KZ_o^2} \int_{Z_o}^{Z} e^{-p(Z)} \, dZ \tag{14}$$

Thermal Ion Acceleration

The thruster beam is emitted over an area A_o with average density n_b and speed v_b such that

$$I_b = e\, n_b\, v_b\, A_o \tag{1}$$

where

$$\frac{1}{2} M v_b^2 = eV_b - eV_n \tag{2}$$

where M is the ion mass, V_b is the beam accelerating voltage, and V_n is any ion retarding potential which builds up between the outer accelerating grid (vehicle skin) and the beam in order to pull in sufficient electrons from the neutralizer to balance the ion space charge.

The region near the vehicle skin where the drop V_n occurs is assumed to be small compared to the charge transfer mean free path, and we will also assume that relatively few slow charge transfer ions move backward to the grid (both of these approximations are substantiated by the results). Then the total positive charge density near the exit grid is $e\, n_b$. Overall space charge neutrality requires that

$$n_e = n_b \tag{3}$$

The electrons are supplied by a plasma source mounted on one side of the thruster. The open area of the plasma source is much smaller than A_o. The outer structure of the neutralizing plasma source is grounded to the outer structure of the thruster. This plasma can be assumed to have an electron temperature of $\sim$1 eV and an ion temperature of perhaps 0.1 eV. Since the net current emitted by the vehicle must be zero, the neutral plasma must be the source of a current, I_e.

Drawing this current from the plasma to the beam requires the voltage V_n, i.e.,

$$I_e\,(V_n) = -I_b \tag{4}$$

The functional form for the neutralization current is the Langmuir-Childs equation (ref. 15):

$$I_e = A\, j_{L.C.} = \frac{(2e/m)^{1/2}\, V_n^{3/2}}{9\pi\beta^2 \ell^2} A_n \tag{5}$$

where m is the electron mass, ℓ is the separation between the beam and the thruster plasma, β is the appropriate geometrical factor, and A_n is the emitting area of the neutralizing plasma. Equations (4) and (5) determine V_n, the difference between the potential at the center of the beam and the vehicle skin potential,

$$V_n = \left\{ \frac{9}{\sqrt{\frac{2e}{m}}} \left[\frac{\pi(\beta\ell)^2}{A_n} \right] I_b \right\}^{2/3} \tag{6}$$

Evaluating the constants

$$V_n = 5.7 \times 10^3 \left[\frac{I_b (\beta\ell)^2}{A_n} \right]^{2/3} \text{ (Volts)} \tag{6a}$$

we se that $\beta\ell$ must be very small or A_n must be large in order to explain the observed drops of just a few tens of volts between the beam center and the surrounding space.

It is impossible to obtain a large emitting area, with the small emitter presently in use and the low ion temperatures characteristic of these plasma generators.

The gap, however, can be quite small. We shall see below that the charge transfer plasma density is approximately 2.6×10^{10} cm^{-3}. The space charge shielding length for these ions, assuming a temperature of 1000°K, is $\lambda_t \simeq 7(T_t/n_{th})^{1/2}$. The expression for the voltage required to emit I_b across a gap determined by a shielding plasma is

$$V_n = 7.7 \times 10^4 \left[\frac{I_b T_o}{A_n n_t} \right]^{1/2} \tag{7}$$

For a current of 80 amps and the above plasma characteristics, equation (7) gives

$$V_n = 15.4 \text{ volts}$$

Without the charge transfer plasma, V_n would be much larger.

REFERENCES

1. Worlock, R.; Trump, G.; Sellen, J. M., Jr.; and Kemp, R. F.: Title Unavailable. AIAA Paper 73-1101, 1973.

2. Bartlett, R. O.; DeForest, S. E.; and Goldstein, R.: Spacecraft Charging Control Demonstration at Geosynchronous Altitude. AIAA Paper 75-359, March 1975.

3. Komatsu, G. K.; Sellen, J. M., Jr.; and Zafran, S.: Ion Beam Plume and E-Flux Measurements of an 8 cm Mercury Ion Thruster. To be published in J. Spacecraft and Rockets.

4. Kaufman, H. R.; and Isaacson, G. C.: The Interactions of Solar Arrays with Electric Thrusters. AIAA Paper 76-105, 1976.

5. Austin, R. E.; Dod, R. E.; and Grim, D.: Solar Electric Propulsion for the Halley's Comet Rendezvous Mission: Foundation for Future Missions. AIAA Paper 78-83, Jan. 1978.

6. Solar Power Satellite System Definition Study Part III, Preferred Concept System Definition. G. R. Woodcock, Mr., Boeing Rpt. D180-24071-1, NAS-15196, DRL T-1346, DRD MA-664T, March 1978.

7. Staggs, J. F.; Gula, W. P., and Kerslake, W. R.: Distribution of Neutral Atoms and Charge-Exchange Ions Downstream of an Ion Thruster, J. Spacecraft 5, Feb. 1968, pp. 159-164.

8. Liemohn, H. B.: Electrical Charging of Shuttle Orbiter, IEEE Trans. Plasma Science, PS-4, Dec. 1976, pp. 229-240.

9. McPherson, D. A.; Cauffman, D. P.; and Schober, W. R.: Spacecraft Charging at High Altitudes: SCATHA Satellite Program. J. Spacecraft 12, Oct. 1975.

10. Rossi, B.; and Olbert, S.: Introduction to the Physics of Space, McGraw-Hill, 1970, pp. 157-187.

11. Liemohn, H. B.: Radiation Belt Particle Orbits, Boeing Rpt. D1-82-0116, June 1961.

12. Chen, F. F.: Electric Probes, in Plasma Diagnostic Techniques. Huddlestone, R. H.; and Leonard, S. L.; editors. Academic Press, 1965, pp. 113-200.

13. Swift, J. D.; and Schwar, M.J.R.: Electrical Probes for Plasma Diagnostics. American Elsevier, 1970, pp. 137-155.

14. Stevens, N. J.; Spacecraft-Charged-Particle Environment Interactions. (Paper 3-1) Proc. Spacecraft Charging Technology Conference, C. P. Pike and R. C. Finke, editors, 1979.

15. Langmuir, I.; and Blodgett, K.: Currents Limited by Space Charge Between Coaxial Cylinders. Phys. Rev. 21, 1923, pp. 347-356.

16. Cobine, J. D.: Gaseous Conductors: Theory and Applications. Dover Publications, New York, 1958, pp. 123-128.

17. Kennerud, K. L.: High Voltage Solar Array Experiments. Boeing Rpt. to NASA/LeRC, GR 12180, Mar. 1974.

D29

N79-24030

STATUS OF MATERIALS CHARACTERIZATION STUDIES

Carolyn K. Purvis
NASA Lewis Research Center

SUMMARY

In the context of the spacecraft charging technology investigation, studies have been made to characterize the response of typical spacecraft surface materials to the charging environment. The objective is to obtain an understanding of the charging and discharging behavior of such materials for the reliable prediction of spacecraft response to charging environments and as a guide for the design of future spacecraft. Materials have been characterized in terms of such basic properties as resistivity and secondary emission and in terms of charging and discharging behavior in simulated charging environments. Both types of information are required to develop adequate predictive capabilities. This paper summarizes the results obtained to date, assesses the present understanding of charging and discharging behavior, and identifies areas in need of further study.

INTRODUCTION

The spacecraft charging technology investigation is being conducted to provide design guidelines and test standards for the control of absolute and differential charging of geosynchronous spacecraft (ref. 1). Attainment of this objective requires development of the capability to predict spacecraft response to charging environments. The phenomenology of spacecraft charging response consists basically of the electrostatic charging of spacecraft surfaces by the environment and the arc discharging of differentially charged spacecraft surfaces, including the coupling of the discharge energy into spacecraft electrical systems. During these processes, the spacecraft's surface materials interact with the environment, with each other, and with the spacecraft's structure and electrical systems - largely through the absorption, emission, and conduction of charge. The response of a given area of surface material depends on the environment, the properties of the material (resistivity, secondary yields, dielectric strength, etc.), and its configuration (i.e., its geometrical and electrical relationships to other portions of the spacecraft). Reliable prediction of spacecraft charging response thus requires accounting for the effects of both the basic properties of spacecraft materials and their configurations on their charging and arc discharging behavior.

Materials are characterized for spacecraft charging by identifying and describing their particular traits or features, in configurations typical of spacecraft construction, that determine a spacecraft's charging response in a given environment. Materials characterization studies have three objectives:

(1) to support model development by providing insights into the mechanisms that determine charging responses, (2) to identify the values of material property parameters that are needed as inputs to models, and (3) to provide the data required to validate models.

Three approaches have been taken: Literature reviews have been made to locate relevant information. Experiments have been performed in which samples of spacecraft materials in various configurations were exposed to charging environments (in general, to electron beams). Parametric studies have exercised models of the charging phenomena to identify the importance of various parameters in determining charging response.

For purposes of materials characterization, the spacecraft charging phenomena can be divided into two classes, charging and discharging. Charging characteristics are those that determine a surface's equilibrium potential in a specified environment and its charging rate. Discharging characteristics are those that determine the conditions causing an arc discharge to occur and the features of the discharge. Coupling of discharge energy into spacecraft systems depends on the features of the discharge and on spacecraft design. From the materials characterization standpoint, coupling does not constitute a separate area of investigation, but rather defines a requirement for an arc description in terms of the arc's electromagnetic signature. Both the charging and the discharging responses are affected by the properties of the materials, by their configurations, and by the environment. Identifying the roles of these effects and their relative importance in determining charging and discharging responses is an essential part of materials characterization.

The present paper summarizes the status of materials characterization studies in terms of progress toward attaining the three objectives for the two classes of response.

CHARGING RESPONSE

Mechanisms

Charging is the response by which a surface comes into equilibrium with its environment. The environment of interest consists of charged particles and photons incident on the surface. The surface interacts with this environment by absorbing, emitting, and conducting charge and thereby acquiring a potential relative to the environment such that, in equilibrium, the net current to the surface is zero. This must be true at each point on an insulating surface.

The mechanism by which orbiting spacecraft acquire nonzero potentials was known well before spacecraft charging became recognized as an operational hazard (ref. 2). The observed charging of geosynchronous spacecraft to negative kilovolt potentials is attributed to the same current-balance mechanism operating in the geomagnetic substorm environment, in which the plasmas are characterized by kilovolt temperatures (refs. 3 and 4). Charging-response models vary widely in the sophistication of techniques used to calculate incident,

emitted, and conducted fluxes to surface elements but have in common the condition of zero net current to all surface elements in equilibrium (refs. 5 to 8). The time required to attain equilibrium depends on the net currents to various surfaces and the capacitances in the system (refs. 8 and 9).

The problem of determining charging response thus reduces to calculating net currents to surfaces. The net current to a particular surface element is simply the sum of incident, emitted, and conducted currents. These currents depend on the environment, the properties and potential of the surface element, and the effects of its surroundings.

Material Properties

The simplest case to consider is that of an isolated slab of insulation. In this case, a surface element interacts with the external environment and, if it is an insulator, with the metal structure directly beneath it. Current densities to a surface element of such an insulator are illustrated in figure 1. The current densities depicted are those considered significant for charging response in the geosynchronous substorm environment, in which electron and ion distributions are expected to have temperatures in the kilovolt range (refs. 2, 8, and 10).

In this simple case, current densities of incident ions and electrons (j_i and j_e, respectively) depend on the undisturbed environment and on the surface potential φ_S. All other current densities depend on the properties of the surface material as well as on environmental input (incident ions, electrons, and photons). The material properties required are evidently those that describe the yields of emitted electrons as functions of the energy and angle of incident particle impact and the bulk conductivity of the insulator.

Environmental effects on surface charging are illustrated in figure 2. Figure 2(a) depicts local effects of two adjacent surface elements at different potentials. If φ_2 is more negative than φ_1 (as illustrated), the resulting fields affect the trajectories of incoming electrons (and ions) so that the energy and angle distributions of environmental particles incident on each surface element depend on both φ_1 and φ_2. Trajectories of emitted electrons are also affected by these fields, so low-energy electrons emitted by surface 2 (at φ_2) can be collected by the more positive surface (at φ_1). These collected electrons then represent an additional source of incident current to surface 1. In addition, surface currents can flow between the two surface elements j_{s1}.

Figure 2(b) depicts a similar, but more global, effect in which a potential barrier results in the exclusion of low-energy environmental electrons from the distribution arriving at surface 1 (at φ_1) and in trapping of secondary electrons emitted by this surface. Such trapping reduces the effective secondary yield of surface 1. Formation of potential barriers can result from differences in the properties of surface materials (as depicted) or from anisotropies in the environment. The most obvious environmental anisotropy is solar illumination; formation of potential barriers due to illumination of one side

of a spacecraft is expected (refs. 11 and 12). The ATS-6 data indicate that such potential barriers do develop in space (ref. 13).

In terms of material properties, the effects of surroundings indicate a need to know the surface conductivity and the energy and angle distributions of emitted electrons.

The material properties needed to calculate charging response then are basically the yields and distributions of electrons for electron, ion, and photon impact and conductivities. These yields and distributions in turn depend on physical and chemical properties and can also be functions of applied field, temperature, etc. Charging modelers have used methods to calculate the energy and angle dependence of electron yields that differ in the specific parameters required. Table I lists material properties commonly used in charging models. Specifically included in the table are properties required by the NASA charging analyzer program (NASCAP) code (refs. 8 and 14), which gives the most detailed treatment of material properties. Two of the listed properties, radiation-induced conductivity σ_R and dielectric strength E_D, are of more interest for discharging response than for charging response but are included in table I for completeness.

The materials whose properties are needed are those used for spacecraft surfaces. These include pure metals and alloys; polymer films; quartz; and a host of paints, coatings, composites, and fabrics developed particularly for space applications. The extent to which property information is available for these materials varies widely. In general, fairly complete characterizations are possible for pure metals, and many characteristics of quartz and of polymer films (Teflon, Kapton, and Mylar) have been measured. By contrast, very little is known about the properties of alloys and other spacecraft-specific materials.

To date, a comprehensive compilation of required material property information has not been made. A literature survey (ref. 15) has indicated that dielectric and electron interaction data are available for polymers. Conducting studies have been made for polymer films and quartz (refs. 16 to 18) and for some other spacecraft materials (refs. 19 to 21). Photoelectron emission has been measured for some spacecraft materials (ref. 22). Modelers of charging have compiled property data on materials of specific interest to their studies (refs. 2, 7, 8, and 23). Secondary-electron yield due to ion (H^+) impact appears to be the least available property for all materials of interest.

Thus, although material property information required to model the charging of spacecraft surfaces is available, it is both incomplete and scattered. An effort to compile the available information and to identify specific areas of deficiency is needed. Information on the influences of temperature, illumination-applied fields, surface condition, aging, etc., on the various properties should be included in such a compilation. Once specific areas of deficiency are identified, experimental programs to obtain the missing information can be devised.

Experimental Results

Ground studies of the charging of spacecraft surface materials have been reported by several investigators (refs. 24 to 31). Such tests generally involve exposing the surface of interest to normally incident monoenergetic electron beams in vacuum chambers. Two types of sample have been investigated: samples of single materials (polymer, paint, etc.) and samples in a "spacecraft configuration" (solar-a ray segments, thermal blankets, etc.). The single-material samples have generally been mounted on metal substrates that were electrically grounded to the facility. The spacecraft-configuration samples have generally been tested with their metallic portions grounded to the facility. Data reported include current in the ground line and surface potentials. A "typical data set" (fig. 1 of ref. 24) is reproduced in figure 3.

The most common method of summarizing charging test results is by plotting surface potential at equilibrium as a function of electron beam voltage, as illustrated in figure 4. The figure shows two types of response for insulators. Linear behavior is interpreted to indicate that the material's resistivity is large enough for leakage currents to be negligible. In this case the equilibrium potential is determined by surface emission characteristics (secondary-electron current due to electron impact j_{se} and backscattered electron current j_{bs}). Behavior in which the surface potential reaches a plateau beyond some beam voltage is interpreted to indicate that the equilibrium potential is determined by leakage current in the plateau region. The type of behavior observed depended on material thickness and beam current density as well as on resistivity and electron emission characteristics. This complicates comparison of results from different investigators, since the beam current densities used vary from one to another. With 1-nA/cm^2 beam current densities, 0.01-centimeter-thick Teflon and Kapton samples exhibited emission-dominated behavior to beam voltages of 12 and 14 kilovolts, respectively; in these tests, arcing occurred at higher beam voltages (ref. 24). Leakage-dominated equilibrium has been reported for thin ($<$0.0025 cm thick) Kapton and Mylar (ref. 29) and for S-13GLO paint (ref. 24) with 1-nA/cm^2 beams, and for 0.005-centimeter-thick Kapton at slightly higher current densities (ref. 28).

Equilibrium potential profiles of several surface-material samples exhibit irregularities that are probably due to configuration effects such as those illustrated in figure 2 (beam deflection, trapping of secondaries, etc.) (refs. 9, 24, and 29). Irregularities in equilibrium surface potential caused by the presence of small gaps between sections of a single type of insulation (e.g., solar-cell cover slides or strips of Teflon tape) were also observed. These became more pronounced for larger samples, apparently as a result of increased beam deflection by the larger samples (ref. 30).

Efforts to validate the NASCAP code by comparing its predictions with experimental data have begun (refs. 9 and 14). Agreement between prediction and experiment is generally very good when both material properties and test data are available (e.g., Teflon and Kapton). Additional experimental data for single-material samples are needed, since it is preferable to validate the models for individual materials before adding the complexity of surroundings effects.

Since experiments have been performed with normally incident monoenergetic electron beams, the data presently available do not permit models to be calibrated for the effects of distributed (in energy and angle) electron fluxes or for electron emission due to ion or photon impact. Experiments incorporating these additional environmental factors are needed, since the space environment consists of distributed fluxes of ions, electrons, and photons.

Ground testing of complex objects (spacecraft models), with concurrent modeling, is required to ensure that configuration effects are modeled adequately.

Parametric Studies

The two preceding sections identified the need for experimental efforts to obtain material properties and to provide model validation data for a variety of materials. The test matrix to examine each material in each environment, even without considering experiments to study configuration effects or discharge characteristics, is prohibitively large. Since charging models that incorporate material, configuration, and environmental factors are available, one approach to reducing the number of tests required is to conduct parametric studies. Such studies can be used to identify those material properties and configuration characteristics that are most important in determining charging response to various environments and how accurately the properties must be known for a given prediction accuracy.

As an example, effects of changing secondary-electron yields on predicted charging response to ground test and space environments are illustrated in figure 5. Figure 5(a) shows NASCAP predictions of the charging response of a metal plate in a 10-keV electron beam for three sets of secondary-electron-yield parameters. The metal plate is electrically floating and has a capacitance to its surroundings of 200 picofarads. No illumination or ions are present, so the currents to the plate are due to the beam and the emission of backscattered and secondary electrons by the plate. As shown in the figure, changing either the maximum yield δ_m or the energy for maximum yield E_m affects both the final plate potential and the rate at which charging occurs. From these curves, changing δ_m has a stronger effect on equilibrium potential than changing E_m: Using the middle curve ($\delta_m = 2.6$, $E_m = 300$) as a base and reducing δ_m by 63 percent (to 0.97) increase the final potential by 38 percent. Increasing E_m by 33 percent (to 400) decreases the final potential by only 9 percent. The dependence of final potential on beam voltage is linear, as shown in reference 14.

Figure 5(b) shows NASCAP predictions of the charging response of an ATS-5 model object (ref. 14) in a 5-keV, 1-particle/cm^3 Maxwellian "space environment." On the time scale of figure 5(b), differential charging is negligible, so the entire object is at the potential shown. The curves reflect effects of halving the secondary-electron yield for 1-keV proton impact δ_p for all surface materials. "Standard" δ_p's are those in the current version of NASCAP for Teflon, silicon dioxide, and aluminum, which are the surface materials of the ATS-5 object (ref. 14). With the curve for standard δ_p's as a base, a

50 percent reduction in δ_p's has resulted in a 58-percent increase in potential.

Secondary electron yield is expected to be an important factor in determining final potential in space substorm conditions, because secondary yields for protons with impact energies of tens of kilovolts are expected to be greater than unity and these effectively add to the proton fluxes (refs. 2 and 32). Figure 5 suggests that ion-generated secondary electrons are an important determinant of absolute spacecraft potential. Obviously, the information presented in figure 5 is insufficient to determine whether the relationships are linear and over what range of material and environmental parameters they are appropriate. It does, however, indicate the usefulness of parametric studies.

Although no comprehensive parametric studies of material property influences have been reported to date, some work has been done (ref. 33) and further results are expected (refs. 34 to 36). Such studies should be expanded to include configuration effects; it has been suggested (ref. 9) that the relative areas of different surface materials are an important consideration in determining charging rates and levels.

DISCHARGE RESPONSE

Mechanisms

Although charging response is adequately understood in terms of current balances, quantitative discharge mechanism models have yet to be devised. To attain a predictive capability it is necessary to identify the mechanisms responsible for initiation and propagation of arc discharges and to describe arcs in terms of their electromagnetic signatures.

Discharges of concern for spacecraft charging are those that can occur on dielectric surfaces charged by exposure to fluxes of kilovolt particles. The dielectric surface exposed to this environment is supposed to be charged negatively with respect to the underlying spacecraft structure. It thus acts as a cathode in a discharge. The situation differs from voltage breakdown of a dielectric between metal plates in that there is no dielectric-metal interface at the cathode, there is a limited supply of charge at the cathode, and the electric field in the dielectric is created by charges that are removed when discharge occurs. Little information on this type of discharge has been reported in the literature (ref. 15).

For calculating charging response it is sufficient to consider the absorption, emission, and conduction of charge to occur at material surfaces (since the depth of penetration of kilovolt particles is much less than the thickness of spacecraft surface materials). However, such a description is probably inadequate for considering discharge-response mechanisms.

Kilovolt electrons incident on a dielectric surface penetrate a distance of micrometers. Secondary electrons are emitted from a region within a few

tens of angstroms from the surface. This results in a charge distribution inside the dielectric in which negative charge accumulates in some layer below the surface. The situation is sketched schematically in figure 6 for a dielectric slab mounted on a grounded metal substrate. Electrons are emitted from a region near the surface; incident electrons penetrate further into the dielectric, and a region of radiation-enhanced conductivity is formed; a distribution of negative charge (fig. 6) inside the dielectric results. The detailed shape of this distribution depends on material properties (bulk conductivity σ_B, radiation-induced conductivity σ_R, electron range R_E, and emission yields), on the distribution of incident electrons, and on irradiation time. Models now exist that describe such charge deposition profiles (refs. 8, 37, and 38), and techniques have been devised for their measurement (ref. 39).

Although no quantitative models of discharge mechanisms have yet been developed, mechanisms involving charge propagation in the radiation-enhanced region (refs. 40 and 41) and arc propagation by secondary emission (refs. 27 and 42) have been suggested. Such mechanisms have yet to be evaluated.

Experimental Results

In the absence of quantitative theoretical models for discharges, experiments must be relied on to provide both insights into discharge mechanisms and a data base from which empirical models can be constructed.

Investigations of the discharge response of electron-irradiated spacecraft dielectrics have been reported by a number of workers (refs. 24, 27, 28, 30, 41, and 43 to 47). For the most part, such investigations have involved exposure to monoenergetic electron beams of insulator samples mounted on grounded substrates or spacecraft-configuration samples (solar-array segments, thermal blankets, etc.) mounted with their metal portions grounded. Data taken include current in the ground line and surface potentials. In some experiments a scanning electron microscope has been used as both the electron source and the diagnostic (refs. 41 and 45). Typical current-to-ground and voltage-versus-time results are illustrated in figure 7. When a sample is exposed to an electron beam, charge and voltage build up on the dielectric surface and a corresponding current flows in the ground line. When a discharge occurs, a fast current pulse is observed (denoted by the arrow in fig. 7) that signifies net negative charge leaving the surface: The surface potential drops and charging resumes.

Charges transferred and a fast current pulse (return or reverse current pulse) observed during a discharge are illustrated in figure 8. In figure 8(a), charges are shown emanating from a trigger site. Charges Q_1 and Q_2 are transferred to the substrate, where they cancel with their image charges. The net charge Q_I leaves the surface and couples through the external circuit, which includes the vacuum facility and associated structures. Current flows in the ground line (meter I) and reflects the transfer Q_I (which is a negative charge). The horizontal arrows in figure 8(a) represent charge transferred on or near the surface to the trigger site, that is, arc propagation or a charge release mechanism.

A return current pulse is illustrated in figure 8(b), and Q_I is just the time integral of this current pulse. Such pulses exhibit a wide variety of detailed shapes (see, e.g., ref. 30) and may reflect multiple rather than truly single events. They are most easily characterized in terms of parameters such as peak current I_p, duration Δt, net charge $Q_I \equiv \int_{\Delta t} I_p \, dt$, and rise time $dI/dt|_i$. Results reported vary widely and depend on sample size and instrumentation as well as on sample material and configuration. The values of I_p, Q_I, and Δt all increase with increasing sample area for small samples (ref. 46); recent results indicate limitations on how large an area is affected in a single discharge (ref. 30). As an example, values given for samples of a few hundred square centimeters in area are Δt ~500 nanoseconds, I_p ~20 to 100 amperes, and Q_I ~20 to 60 μC for silvered-Teflon samples (ref. 24).

A critical aspect of instrumentation that must be considered in investigating return current pulses is the impedance to ground in the experimental setup. Typical surface potentials at discharge are about 10 kilovolts, and peak currents are about 100 amperes. Thus, a 50-ohm termination does not approximate a short circuit in this case, and test results may depend strongly on this impedance (ref. 30). This is of particular concern for application of results to the spacecraft situation.

In addition to descriptions of return current pulses, estimates have been made of the energy in a discharge, the charge transferred, and the area discharged (refs. 24 and 30). To date, no data have been reported on the radiated electromagnetic signature of such arcs. This information is important to calculations of electromagnetic interference (EMI) resulting from discharges. It is lacking because none of the experiments reported to date have been conducted in anechoic chambers so that facility resonances have made EMI measurements impossible.

The trigger mechanism for discharges is not understood, but data indicate that the observed discharges begin at gaps, holes, or edges and do not represent bulk dielectric breakdown (refs. 24, 27, 30, 43, and 44). Thus, discharges are observed at electric field stresses signficicantly less than the dielectric strengths of the insulators under study when gaps or edges are present. Some threshold condition, probably configuration dependent, other than insulator dielectric strength must be quantitatively defined for accurate arc prediction.

Experimental evidence to date indicates that discharges begin at gaps in insulation; that charge is removed from an area much larger than the trigger site; that a net negative charge is ejected from a surface during discharge; and that this charge ejection results in significant currents flowing in ground lines. Yet to be investigated are the EMI due to discharges and effects on discharge response of such environmental factors as distributed fluxes of electrons and the presence of ions. Experiments in which solar-array segments with flexible substrates of Kapton-fiberglass laminates have been illuminated during exposure to electron beams have indicated that arcing on such structures is greatly reduced during illumination, probably because of photoconductivity and the thermal enhancement of Kapton conductivity (refs. 24 and 46).

CONCLUDING REMARKS

The charging response of surfaces exposed to charged-particle and photon fluxes is understood in terms of current-density balance mechanisms. Models of charging response are available and predictions agree well with experimental results for cases in which material properties are adequately known. Material property information now available should be compiled to identify specific areas and materials for which data are lacking and to provide property values for use in prediction. A cursory examination of the information available indicates that the least well-known property for most materials of interest is secondary-electron yield due to ion impact and that the most poorly characterized materials are those that have been developed specifically for space applications. Also poorly known are property changes with time due to exposure, repeated arcing, etc. The experimentation required to determine material properties adequately for charging-response predictions can be significantly reduced by using parametric studies to identify those properties most important for determining charging response and how accurately these properties must be known for a specified prediction accuracy.

Data on charging response of spacecraft surface materials under monoenergetic electron irradiation are available for many, though not all, materials of interest. Data on the effects of additional environmental factors are needed. Of particular concern is information on the response to ion impact since this is expected to be an important determinant of spacecraft response. Effects of more complex geometries also need investigation to ensure that the modeling is adequate.

The mechanisms for initiation and propagation of arc discharges are not yet understood, although a number of their characteristics have been experimentally identified. The initiation mechanism is apparently configuration dependent: Arcs occur preferentially at gaps, seams, and edges. A net negative charge is emitted during discharges. Its measured magnitude depends on system instrumentation as well as on sample material and area. These dependencies are of particular interest in modeling arc propagation as well as in extrapolating ground test data to space conditions. Models of charge deposition and transport in electron-irradiated dielectrics have been devised, and they provide a necessary first step toward developing discharge mechanism models.

This paper has summarized the present status of materials characterization studies. Efforts are being made to develop empirical models for discharge pulses. Data on a wider variety of materials and configurations are needed to support this activity as well as mechanism model development. There is a growing data base on characteristics of return current pulses. Yet to be investigated are the electromagnetic interference spectra from arc discharges and the effects of such environmental factors as distributed fluxes of electrons and ions and temperature on discharge response.

REFERENCES

1. Lovell, R. R.; et al.: Spacecraft Charging Investigation: A Joint Research and Technology Program. Spacecraft Charging by Magnetospheric Plasmas, A. Rosen, ed., Progress in Astronautics and Aeronautics, vol. 47, American Institute of Aeronautics and Astronautics, Inc., 1976, pp. 3-14.

2. Whipple, Elden C., Jr.: The Equilibrium Electric Potential of a Body in the Upper Atmosphere and in Interplanetary Space. Ph.D. Thesis, George Washington Univ., 1965.

3. DeForest, Sherman E.: Spacecraft Charging at Geosynchronous Orbit. J. Geophys. Res., vol. 77, no. 4, Feb. 1, 1972, pp. 651-659.

4. Bartlett, R. D.; DeForest, S. E.; and Goldstein, R.: Spacecraft-Charging Control Demonstration at Geosynchronous Altitude. AIAA Paper 75-359, Mar. 1975.

5. Whipple, Elden C., Jr.: Modeling of Spacecraft Charging. Proceedings of the Spacecraft Charging Technology Conference, C. P. Pike and R. R. Lovell, eds., AFGL-TR-77-0051, NASA TM X-73537, 1977, pp. 225-235.

6. Inouye, G. T.: Spacecraft Charging Model. AIAA Paper 75-255, Jan. 1975.

7. Laframboise, J. G.; and Prokopenko, S. M. L.: Numerical Simulation of Spacecraft Charging Phenomena. Proceedings of the Spacecraft Charging Technology Conference, C. P. Pike and R. R. Lovell, eds., AFGL-TR-77-0051, NASA TM X-73537, 1977, pp. 309-318.

8. Katz, I.; et al.: A Three-Dimensional Dynamic Study of Electrostatic Charging in Materials. (SSS-R-77-3367, Systems Science and Software; NASA Contract NAS3-20119.) NASA CR-135256, 1977.

9. Purvis, C. K.; et al.: Charging Rates of Metal-Dielectric Structures. Spacecraft Charging Technology - 1978, NASA CP-2071, 1979.

10. Garrett, Henry B.: Spacecraft Potential Calculations - A Model. AFGL-TR-78-0116, Air Force Geophysical Lab., 1978.

11. Prokopenko, S. M. L.; and Laframboise, J. G.: Prediction of Large Negative Shaded-Side Spacecraft Potentials. Proceedings of the Spacecraft Charging Technology Conference, C. P. Pike and R. R. Lovell, eds., AFGL-TR-77-0051, NASA TM X-73537, 1977, pp. 369-387.

12. Mandell, M. J.; et al.: The Decrease in Effective Photocurrents due to Saddle Points in Electrostatic Potentials Near Differently Charged Spacecraft. Presented at 1978 IEEE Annual Conference on Nuclear and Space Radiation Effects, Albuquerque, N. Mex., July 18-21, 1978, Session C-4.

13. Whipple, E. C., Jr.: Observation of Photoelectrons and Secondary Electrons Reflected from a Potential Barrier in the Vicinity of ATS-6. J. Geophys. Res., vol. 81, Feb. 1, 1976, pp. 715-719.

14. Roche, J. C.; and Purvis, C. K.: Comparison of NASCAP Predictions with Experimental Data. Spacecraft Charging Technology - 1978, NASA CP-2071, 1979.

15. Wall, J. A.; Burke, E. A.; and Frederickson, A. R.: Results of Literature Search on Dielectric Properties and Electron Interaction Phenomena Related to Spacecraft Charging. Proceedings of the Spacecraft Charging Technology Conference, C. P. Pike and R. R. Lovell, eds., AFGL-TR-77-0051, NASA TM X-73537, 1977, pp. 569-591.

16. Coffey, H. T.; Nanevicz, J. E.; and Adamo, R. C.: Photoconductivity of High-Voltage Space Insulating Materials. (Stanford Research Inst.; NASA Contract NAS3-18912.) NASA CR-134995, 1975.

17. Adamo, R. C.; and Nanevicz, J. E.: Effects of Illumination on the Conductivity Properties of Spacecraft Insulating Materials. (Stanford Research Inst.; NASA Contract NAS3-20080.) NASA CR-135201, 1977.

18. Adamo, Richard C.; Nanevicz, Joseph E.; and Grier, Norman: Conductivity Effects in High Voltage Spacecraft Insulating Materials. Proceedings of the Spacecraft Charging Technology Conference, C. P. Pike and R. R. Lovell, eds., AFGL-TR-0051, NASA TM X-73537, 1977, pp. 669-686.

19. Gilligan, J. E.; Wolf, R. E.; and Ray C.: Electrically Conductive Paints for Satellites. Proceedings of the Spacecraft Charging Technology Conference, C P. Pike and R. R. Lovell, eds., AFGL-TR-77-0051, NASA TM X-73537, 1977, pp. 593-611.

20. Belanger, V. J.; and Eagles, A. E.: Secondary Emission Conductivity of High Purity Silica Fabric. Proceedings of the Spacecraft Charging Technology Conference, C. P. Pike and R. R. Lovell, eds., AFGL-TR-77-0031, NASA TM X-73537, 1977, pp. 655-668.

21. Viehmann, W.; Shai, C. M.; and Sanford, E. L.: Investigation of Conductive Thermal Control Coatings by a Contactless Method in Vacuo. Proceedings of the Spacecraft Charging Technology Conference, C. P. Pike and R. R. Lovell, eds., AFGL-TR-77-0051, NASA TM X-73537, 1977, pp. 687-698.

22. Feuerbacher, B.; and Fitton, B.: Experimental Investigation of Photoemission from Satellite Surface Materials. J. Appl. Phys., vol. 43, no. 4, 1972, pp. 1563-1572.

23. Grard, R. J. L.; Knott, K.; and Pedersen, A.: The Influence of Photoelectron and Secondary Electron Emission on Electric Field Measurements in the Magnetosphere and Solar Wind. Photon and Particle Interactions with Surfaces in Space. R. J. L. Grard, ed., D. Reidel Publishing Co., (Dordrecht) 1973, pp. 163-189.

24. Stevens, N. John; et al.: Testing of Typical Spacecraft Materials in a Simulated Substorm Environment. Proceedings of the Spacecraft Charging Technology Conference, C. P. Pike and R. R. Lovell, eds., AFGL-TR-77-0051, NASA TM X-73537, 1977, pp. 431-457.

25. Stevens, N. John; Klinect, Vernon W.; and Berkopec, Frank D.: Environmental Charging of Spacecraft Surfaces - Tests of Thermal Control Materials for Use on the Global Positioning System Flight Space Vehicle - Part 1: Specimens 1 to 5. NASA TM X-73467, 1976.

26. Stevens, N. John; Berkopec, Frank D.; and Blech, Richard A.: Environmental Charging of Spacecraft Surfaces - Tests of Thermal Control Materials for Use on the Global Positioning System Flight Space Vehicle - Part 2: Specimens 6 to 9. NASA TM X-73485, 1976.

27. Robinson, James W.: Charge Distributions near Metal-Dielectric Interfaces before and after Dielectric Surface Flashover. Proceedings of the Spacecraft Charging Technology Conference, C. P. Pike and R. R. Lovell, eds., AFGL-TR-77-0051, NASA TM X-73537, 1977, pp. 503-515.

28. Robinson, P. A., Jr.: The Behavior of Partially Metallized Kapton for Spacecraft Charging Control. AIAA Paper 78-675, Apr. 1978.

29. Staskus, J. V.; and Berkopec, F. D.: Charging Test Results for Flexible Insulators and Composites. Spacecraft Charging Technology - 1978. NASA CP-2071, 1979.

30. Aron, P. R.; and Staskus, J. V.: Area Scaling Investigations of Charging Phenomenon. Spacecraft Charging Technology - 1978. NASA CP-2071, 1979.

31. Purvis, C. K.; Stevens, N. J.; and Oglebay, J. C.: Charging Characteristics of Materials: Comparison of Experimental Results with Simple Analytical Models. Proceedings of the Spacecraft Charging Technology Conference, C. P. Pike and R. R. Lovell, eds., AFGL-TR-77-0051, NASA TM X-73537, 1977, pp. 459-486.

32. Kaminsky, Manfred: Atomic and Ionic Impact Phenomena on Metal Surfaces. Academic Press, 1965.

33. Rubin, A. G.; Rothwell, P. L.; and Yates, G. K.: Reduction of Spacecraft Charging Using Highly Emissive Surface Materials. Presented at the 1978 Symposium on the Effect of the Ionosphere on Space and Terrestrial Systems, Naval Research Lab. and Office of Naval Research, Wash., D.C., Jan. 24-26, 1978, Session IV, Paper 4-7.

34. Suh, P. K.; and Stauber, M. C.: Material Parameter Dependence of Equilibrium Charging Potentials. Spacecraft Charging Technology - 1978. NASA CP-2071, 1979.

35. Sanders, N. L.; and Inouye, G. T.: Secondary Emission Effects on Spacecraft Charging Energy Distribution Considerations. Spacecraft Charging Technology - 1978. NASA CP-2071, 1979.

36. Haffner, J. W.: Secondary Electron Effects on Spacecraft Charging. Spacecraft Charging Technology - 1978. NASA CP-2071, 1979.

37. Beers, B. L.; Pine, V. W.; and Gore, J. V.: Electron Transport Model of Dielectric Charging. Spacecraft Charging Technology - 1978. NASA CP-2071, 1979.

38. Monteith, L. K.; and Hauser, J. R.: Space Charge Effects in Insulators Resulting from Electron Irradiation. J. Appl. Phys., vol. 38, no. 13, Dec. 1967, pp. 5355-5365.

39. Sessler, G. M.; West, J. E.; and Berkley, D. A.: Determination of Spatial Distribution of Charges in Thin Dielectrics. Phys. Rev. Lett., vol. 38, no. 7, Feb. 14, 1977, pp. 368-371.

40. Meulenberg, A., Jr.: Evidence for a New Discharge Mechanism for Dielectrics in a Plasma. Spacecraft Charging by Magnetospheric Plasmas, Progress in Astronautics and Aeronautics, vol. 47, A. Rosen, ed., American Institute of Aeronautics and Astronautics, 1976, pp. 237-246.

41. Balmain, K. G.; Orszag, M.; and Kremer, P.: Surface Discharges or Spacecraft Dielectrics in a Scanning Electron Microscope. Spacecraft Charging by Magnetospheric Plasmas, Progress in Astronautics and Aeronautics, vol. 47, A. Rosen, ed., American Institute of Aeronautics and Astronautics, 1976, pp. 213-223.

42. Inouye, G. T.; and Sellen, J. M.: A Proposed Mechanism for the Initiation and Propagation of Dielectric Surface Discharges. Presented at the 1978 Symposium on the Effect of the Ionosphere on Space and Terrestrial Systems, Naval Research Lab. and Office of Naval Research, Wash., D.C., Jan. 24-26, 1978, Session IV, Paper 4-8.

43. Adamo, R. C.; and Nanevicz, J. E.: Spacecraft Charging Studies of Voltage Breakdown Processes on Spacecraft Thermal Control Mirrors. Spacecraft Charging by Magnetospheric Plasmas, Progress in Astronautics and Aeronautics, vol. 47, A. Rosen, ed., American Institute of Aeronautics and Astronautics, 1976, pp. 225-235.

44. Yadlowsky, E. J.; Hazelton, R. C.; and Churchill, R. J.: Puncture Discharges in Surface Dielectrics as Contaminant Sources in Spacecraft Environments. (Colorado State Univ.; NASA Contract NSG-3145.) NASA CR-157105, 1978.

45. Balmain, K. G.; Kremer, P. C.; and Cuchanski, M.: Charged-Area Effects on Spacecraft Dielectric Arc Discharges. Presented at the 1978 Symposium on the Effect of the Ionosphere on Space and Terrestrial Systems, Naval

Research Lab. and Office of Naval Research, Wash., D.C., Jan. 24-26, 1978, Session IV, Paper 4-5.

46. Bogus, K. P.: Investigation of a CTS Solar Cell Test Patch under Simulated Geomagnetic Substorm Charging Conditions. Proceedings of the Spacecraft Charging Technology Conference, C. P. Pike and R. R. Lovell, eds., AFGL-TR-77-0051, NASA TM X-73537, 1977, pp. 487-501.

47. Hoffmaster, D. K.; Inouye, G. T.; and Sellen, J. M., Jr.: Surge Current and Electron Swarm Tunnel Tests of Thermal Blanket and Ground Strap Materials. Proceedings of the Spacecraft Charging Technology Conference, C. P. Pike and R. R. Lovell, eds., AFGL-TR-77-0051, NASA TM X-73537, 1977, pp. 527-547.

TABLE I. - MATERIAL PROPERTIES

Type of property	Property	Symbol
Physical and chemical	Density	ρ
	Chemical composition	CC
	Atomic number	A
	Atomic weight	Z
Electrical	Dielectric constant	ϵ
	Bulk conductivity	σ_B
	Surface conductivity	σ_S
	Radiation-induced conductivity	σ_R
	Dielectric strength	E_D
Particle penetration	Electron range	R_e
	Ion range	R_i
	Rate of energy loss for electrons	dE_e/dx
	Rate of energy loss for ions	dE_i/dx
Electron emission	Photoelectron yield	$\delta_{PHO}(E_{ph},\theta)$
	Secondary-electron yield due to electron impact:	$\delta_{se}(E_e,\theta)$
	Maximum yield	δ_m
	Energy for maximum yield	E_m
	Backscatter coefficient	$\eta(E_e,\theta)$
	Secondary-electron yield due to ion impact:	$\delta_{si}(E_i,\theta)$
	Yield at E_i = 1 keV (protons)	δ_p
	Energy for maximum yield (protons)	E_p
	Work function	W
	Distribution of emitted photoelectrons	$f_{PHO}(E,\theta)$
	Distribution of secondary electrons from electron impact	$f_{se}(E,\theta)$
	Distribution of secondary electrons from ion impact	$f_{si}(E,\theta)$

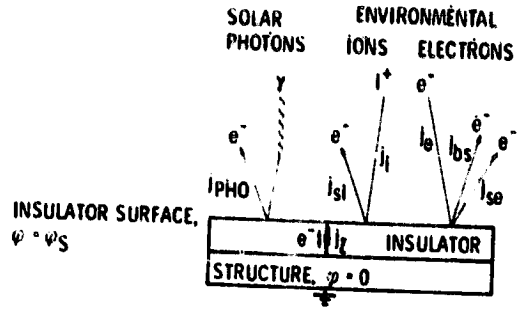

CURRENT DENSITY DUE TO-

j_e	ENVIRONMENTAL ELECTRONS
j_i	ENVIRONMENTAL IONS
j_{PHO}	PHOTOELECTRON YIELD
j_{se}	SECONDARY ELECTRONS DUE TO ELECTRON IMPACT
j_{bs}	BACKSCATTERED ELECTRONS
j_{si}	SECONDARY ELECTRONS DUE TO ION IMPACT
j_l	LEAKAGE THROUGH INSULATOR

EQUILIBRIUM CONDITION:

$$j_{net} = \sum_n j_n = 0$$

CS-78-1418

Figure 1. - Charging response - simple case (current densities to insulating surface element).

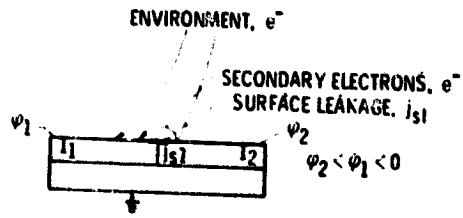

(a) Local effects.

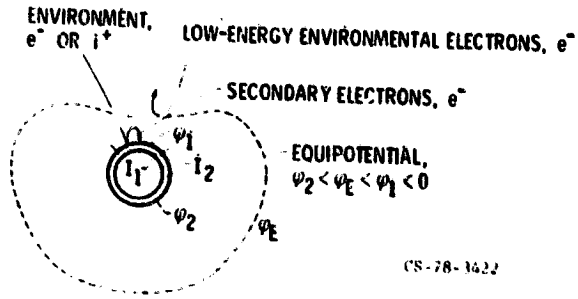

CS-78-1422

(b) Global effects.

Figure 2. - Charging response - configuration effects.

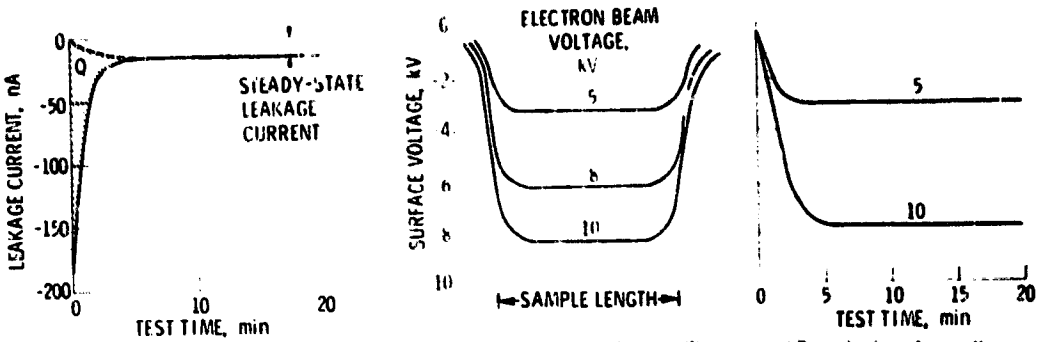

(a) Transient leakage current. (b) Steady-state voltage profiles. (c) Transient surface voltage.

Figure 3. - Typical data set from materials characterization tests - charging data.

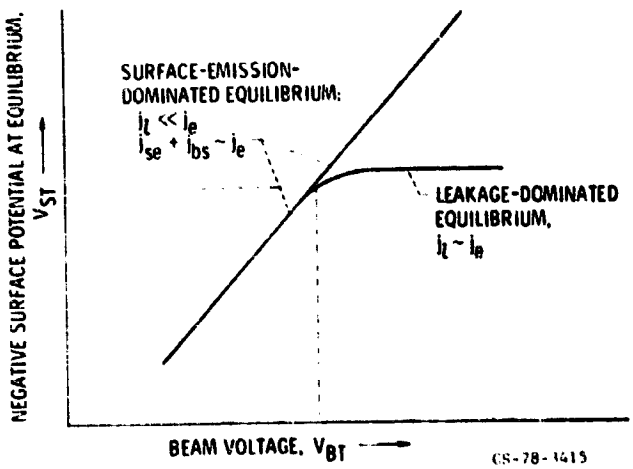

Figure 4. - Charging response - typical equilibrium surface voltage as function of beam voltage characteristics for insulators.

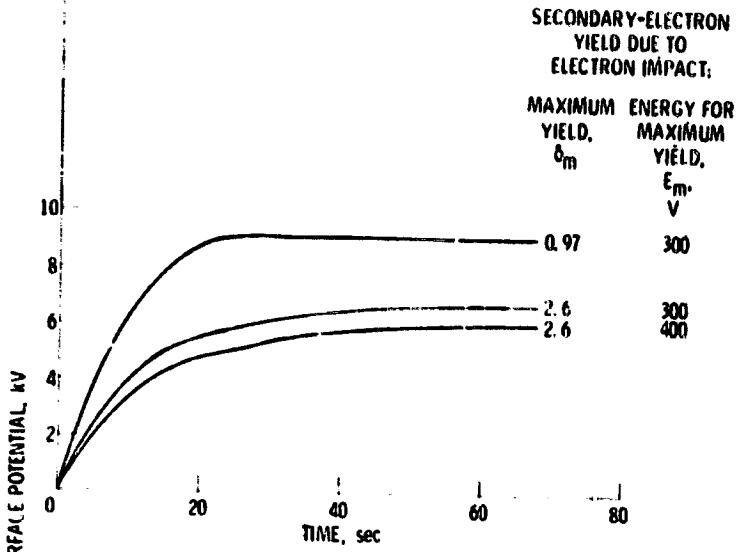

(a) NASCAP: tank mode; 10-kV electron beam; metal-plate capacitance, 200 pF.

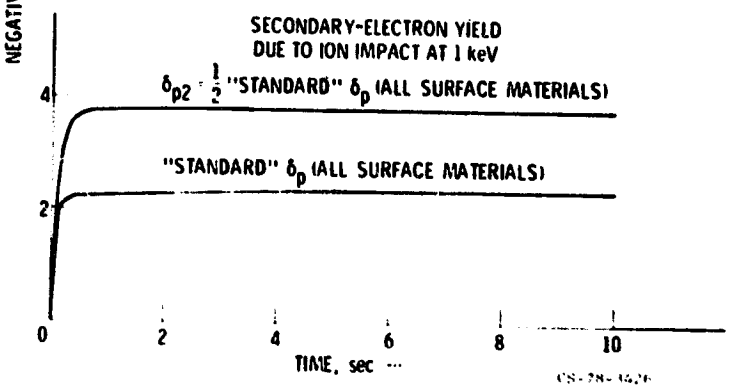

(b) NASCAP: space mode (5 keV, 1 particle/cm^3); ATS-5 model object.

Figure 5. - Charging response - effects of changing secondary-electron-yield parameters.

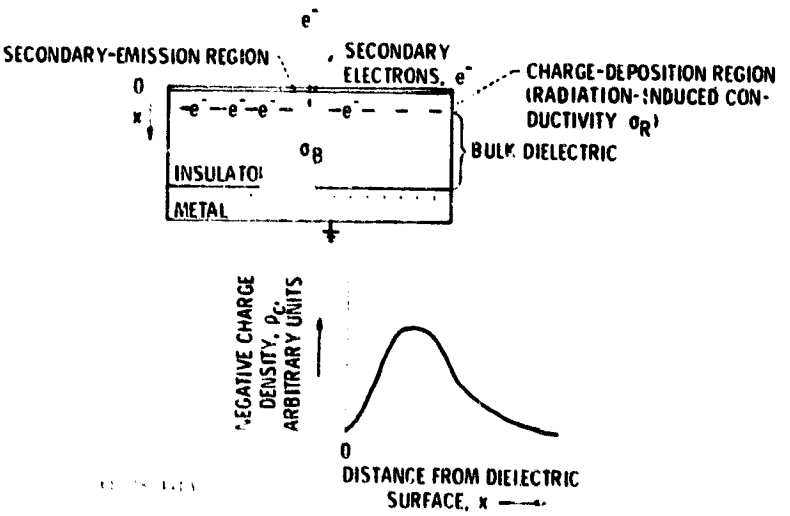

Figure 6. - Charge deposition.

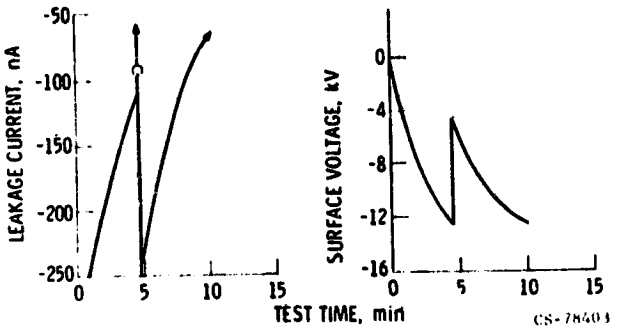

Figure 7. - Typical data set from materials characterization tests - discharging data.

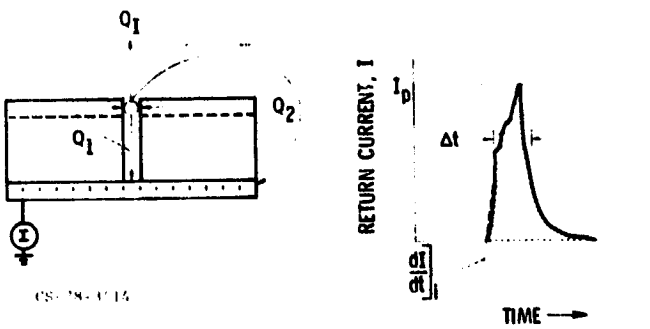

(a) Charges transferred during discharge.

(b) Return curren. pulse.

Figure 8. - Discharge response.

TEST RESULTS FOR ELECTRON BEAM CHARGING OF FLEXIBLE INSULATORS AND COMPOSITES

John V. Staskus and Frank C. Berkopec
NASA Lewis Research Center

SUMMARY

This paper discusses the results of materials tests conducted in the Lewis Research Center's geomagnetic-substorm-environment simulation facility. The materials tested were flexible solar-array substrates, graphite-fiber/epoxy - aluminum honeycomb panels, and thin dielectric films. The tests consisted of exposing the samples to monoenergetic electron beams ranging in energy from 2 to 20 keV. Surface potentials, dc currents, and surface discharges were the primary data.

Four solar-array substrate samples were tested. These samples consisted of Kapton sheet reinforced with fabrics of woven glass or carbon fibers. They represented different construction techniques that might be used to reduce the charge accumulation on the array back surface.

Five honeycomb-panel samples were tested, two of which were representative of Voyager antenna materials and had either conductive or nonconductive painted surfaces. A third sample was of Navstar solar-array substrate material. The other two samples were of materials proposed for use on Intelsat V. All the honeycomb-panel samples had graphite-fiber/epoxy composite face sheets.

The thin dielectric films were 2.54-micrometer-thick Mylar and 7.62-micrometer-thick Kapton.

INTRODUCTION

Many geosynchronous satellites have experienced behavior anomalies in electronics systems at some time during their lifetimes (refs. 1 and 2). These anomalies are believed to result from discharges that take place on various satellite surfaces after differential charging by the geomagnetic substorm environment (ref. 3). The Lewis Research Center has undertaken investigations of the charging behavior of various materials in its geomagnetic-substorm-environment simulation facility (ref. 4). Thermal control materials and some solar-array segments have undergone considerable testing (refs. 5 to 7). Concern about the behavior of materials proposed for use on future satellites led to the testing of several flexible insulator and composite samples.

Flexible-substrate solar arrays used on some communications satellites present a large insulator area that can be charged by the environment. The

first such array was designed and built for the Canadian-American Communications Technology Satellite (CTS) before spacecraft charging effects were understood. However, there was sufficient concern for the possible charging of this array that a charging investigation was conducted (ref. 8). The CTS has survived environmental charging since its launch in January 1976 but has suffered a power loss possibly because of a charging event (ref. 9).

When a similar solar array was proposed for use on the latest Comsat satellite, Intelsat V, several modifications to the substrate were suggested to minimize the charging of the dielectric surface. The Kapton-fiberglass substrate was changed to include woven carbon-fiber fabrics, or conductive surface coatings, or both. The fabric and coatings would be electrically grounded. These "quasi-conductive" dielectric substrates required testing to evaluate their effectiveness in controlling surface charging. Four solar-array segments with different carbon-fabric weaves and surface coatings were prepared by AEG-Telefunken and Comsat Corp. These segments are part of the samples tested and reported on herein.

Five graphite-fiber/epoxy - aluminum honeycomb panels (samples of materials for the Navstar, Voyager, and Intelsat V satellites) were also tested. They are representative of solar-array substrates, antenna materials, and structural panels used on these satellites. The two antenna-panel samples were painted, one with a conductive paint and the other with a nonconductive paint.

Two thin-film materials, 2.54-micrometer-thick aluminized Mylar and 7.62-micrometer-thick Kapton, were also tested.

The flexible-substrate solar-array samples and the Intelsat V honeycomb-panel samples were furnished by the Comsat Corp. The Navstar honeycomb-panel sample was provided by the Rockwell International Corp. And the Voyager honeycomb-panel samples were supplied by the Jet Propulsion Laboratory.

DESCRIPTIONS OF SAMPLES

Flexible-Substrate Solar-Array Samples

The four flexible-substrate solar-array samples were nominally 10 centimeters by 11 centimeters in area. The substrates were made of 12.5-micrometer-thick Kapton sheet (density, 19 g/m^2) that was reinforced with either a woven carbon-fiber material or a woven glass-fiber material bonded to one surface. A silver-filled polyester strip bonded to the back surface along each 10-centimeter edge provided electrical contact to the reinforcing and/or charge-control material. The front surface of each sample held 2-centimeter-by-4-centimeter solar cells of 10-ohm-centimeter resistivity.

Sample 1 (fig. 1) had 66-g/m^2 woven carbon-fiber material bonded to the back surface for reinforcing and charge control. The fabric elements were approximately 0.15 centimeter wide and were spaced 5 per centimeter, resulting in a bare Kapton area of about 6 percent. The conductive polyester edge-strips

were spaced 10 centimeters apart with 50 carbon-fabric elements connecting them. The woven material contained 48 carbon-fabric elements crossing the sample parallel to the polyester edge-strips. A short piece of Kapton-insulated wire was bonded into each polyester strip for making circuit connections. The resistance across the back of the substrate was 3.6 ohms. Eight 2-centimeter-by-4-centimeter solar cells were mounted on the bare Kapton front surface of the substrate in two parallel strings of four cells in series. The 0.01-centimeter-thick cerium-doped cover slides were applied with DC 9350 adhesive and were similar to those used on the Communications Technology Satellite (ref. 8).

Sample 2 (fig. 1) had 45-g/m^2 woven carbon-fiber reinforcing and charge-control material bonded to the back surface. The fabric elements were about 0.1 centimeter wide and were spaced approximately 3½ per centimeter, resulting in a bare Kapton area of about 42 percent. The conductive edge-strips were 9.8 centimeters apart and were joined by 34 carbon-fabric elements. Thirty-two carbon-fabric elements crossed the substrate parallel to the conductive edge-strips. The resistance of the substrate between the strips was 3.9 ohms. Circuit connections to the strips were made through a short piece of silver mesh bonded into each strip. Four 2-centimeter-by-4-centimeter solar cells connected in series were attached to the bare Kapton surface of the substrate. The long dimensions of the substrate and the cells were parallel. The 0.015-centimeter-thick cerium-doped cover slides had a magnesium fluoride antireflection coating.

Sample 3 (fig. 1) was like sample 2 except that a film of soot-bearing adhesive was spread over the woven carbon-fabric material to cover the bare Kapton and to improve the conductivity of the back surface. Thirty-three strands of the carbon-fabric material crossed the sample perpendicular to the conductive edge-strips, which were 9.9 centimeters apart. Thirty-two strands of material crossed the substrate parallel to the conductive edge-strips. Substrate resistance between the conductive edge-strips was 2 ohms.

Sample 4 (fig. 1) had 27-g/m^2-dense woven glass-fiber material applied to the front surface of the substrate for reinforcing. The weave density of about 24 strands per centimeter allowed very little, if any, bare Kapton to be exposed. Soot-bearing adhesive, as used on sample 3, was applied to the bare Kapton on the back surface. Two conductive polyester edge-strips were placed 9.9 centimeters apart on top of the soot-bearing adhesive. The resistance of the substrate between the strips was 5.3 kilohms. Table I summarizes the sample characteristics.

Graphite-Fiber/Epoxy - Aluminum Honeycomb Samples

Five honeycomb-panel samples were tested. All five had aluminum honeycomb cores with graphite-fiber/epoxy face sheets. Two of the samples were painted, one with a conductive paint and the other with a nonconductive paint. The remaining three samples had bare graphite-fiber/epoxy face sheets. The largest specimen (sample 5) was a sample of the Navstar satellite solar-array substrate. It was 30.8 centimeters by 29 centimeters by 1.59 centimeters thick.

Its 0.03-centimeter-thick face sheets were wrapped around two opposite edges of the core and were joined, making a loop around the core. A gap in the graphite-fiber material ran halfway around the loop across one face of the sample. The epoxy content was higher along this stripe than over the rest of the face sheet.

The two painted samples (6 and 7) were Voyager satellite antenna materials. The nonconductive painted sample was 38 centimeters by 6 centimeters by 1.6 centimeters thick with PV100 (titanium oxide in silicone alkyd) paint on one surface. The sample with conductive paint (7) was 14 centimeters by 14 centimeters by 2.5 centimeters thick with Goddard Space Flight Center paint designated NS43C on both sides.

The remaining two honeycomb-panel specimens (8 and 9) were samples of materials proposed for use on the Intelsat V satellite. Both specimens were 15 centimeters square. Sample 8 had 0.01-centimeter-thick woven graphite-fiber/epoxy face sheets bonded to a 1.8-centimeter-thick aluminum honeycomb core with 0.005 centimeter of unsupported epoxy. Sample 9 had 0.04-centimeter-thick unidirectional graphite-fiber/epoxy face sheets bonded to a 0.86-centimeter-thick aluminum honeycomb core. Both samples had a hole drilled through one corner. An aluminum block was cemented in the hole with conductive adhesive. The block provided a point for mounting and for making electrical connections.

Thin-Film Samples

The thin-film materials tested were

(1) Kapton polyimide film - type H, 127 micrometers thick and with a vapor-deposited aluminum film on one side

(2) Kapton polyimide film - type H, 7.62 micrometers thick and uncoated

(3) Mylar polyester film, 2.54 micrometers thick and with a vapor-deposited aluminum film on one side

The two thinner films were tested both totally isolated from ground and mounted on a grounded substrate. The thickest material was tested only while mounted on a grounded substrate.

The aluminum substrates were 17.1 centimeters by 20.3 centimeters with leads attached for measuring charging and leakage current. The two aluminized films were mounted with the aluminized sides in contact with the substrates. The two thinner films were mounted by wrapping the film around the substrate edges and taping it to the substrate back.

DISCUSSION OF TESTS AND RESULTS

Flexible-Substrate Solar-Array Samples

The testing of the flexible-substrate solar-array samples consisted of three parts. In the first part, the front surfaces were exposed to monoenergetic electron beams of 2 to 20 keV while in total darkness. In the second part, the back surfaces were exposed to monoenergetic electron beams while in total darkness. In the third part, the front surfaces were simultaneously exposed to a 20-keV electron beam and simulated solar illumination. The intensity of the illumination at the experiment surface was approximately 0.6 times the solar intensity at 1 AU. Nominal electron flux was 1 nA/cm^2 for all tests.

Each test was begun with the sample surface neutral. A gaseous-nitrogen ion source was used between tests to discharge this surface. During the tests, electron current collected by the solar cells and that collected by the substrate were monitored separately. The sample's surface potential was monitored with a noncontact, field-nulling, electrostatic voltmeter whose probe could be swept across the surface at a separation of about 0.2 centimeter. Discharge activity was monitored with a 15-centimeter-diameter loop antenna centered about 38 centimeters from the sample center.

The first series of tests - run for 20 to 30 minutes at beam voltages of 2, 5, 8, 10, 12, 14, 16, 18, and 20 kilovolts - were conducted to survey the response of the substrate front surface and the solar-cell cover slides. The second series of tests - run for 20 to 30 minutes at beam voltages of 2, 8, 12, 16, and 20 kilovolts - were conducted to survey the response of the back surface. The test results were compared to determine the most effective technique for controlling charge buildup on the back surfaces. In the third series of tests, the front surface of each sample was irradiated with a 1-nA/cm^2, 20-keV electron flux for 2 hours. The first 1/2 hour of the test was like the initial front-surface tests except that the sample temperature was lowered to about -18° C. During the second 1/2 hour the sample was illuminated by a solar simulator that produced about 0.6 times 1-AU solar intensity at the sample plane. During the third 1/2 hour the sample was again in darkness, and during the fourth 1/2 hour it was again illuminated. Throughout the test the temperature, substrate collection current, cell-circuit collection current, and surface potential profile were recorded each minute. During the illuminated portions of the test, the array-segment short-circuit current and open-circuit voltage was also recorded each minute.

The test results for sample 2 are shown in figures 2 to 5. Figure 2 shows typical surface potential profiles for the front and back surfaces of the sample taken while the surfaces were being bombarded in darkness. Figures 2(a) and (b) are equilibrium profiles of the front surface under exposure to 5-keV (low energy) and 20-keV (high energy) beams, respectively. The low-energy beam charges the Kapton border to a significantly higher potential than the solar-cell cover slide. The high-energy beam charges the cover slide and the Kapton border to comparable potentials. Figures 2(c) and (d) show the back surface in a high-energy beam early in the test and at equilibrium. The

approximately 0.1-centimeter-wide carbon-fiber threads and the intervening 0.2-centimeter squares of Kapton are resolvable as the alternating potential peaks and valleys. The conductive strips on the sample edges show up as high potential peaks. The most significant observation to be made is that the small open areas of Kapton on the back surface become charged to nearly the same potential as the broad open Kapton borders on the front surface.

Figure 3 shows the range of potentials occupied by the various surface materials of the sample for exposure to 2- to 20-keV electron beams. Figure 4 shows the equilibrium electron currents to the conductive substrate and solar-cell circuits in 2- to 20-keV electron beams. The current collected by the solar-cell circuit during electron irradiation of the back surface is not shown since it was more than an order of magnitude less than the current collected during front-surface irradiation.

The test conducted with the solar simulator is summarized in figure 5. Figures 5(a) and (b) show the surface potentials on the cover slides and the Kapton substrate border. Under illumination of only 0.6 Sun intensity, the surface potentials are reduced by an order of magnitude from the values reached during electron irradiation in total darkness possibly because of the photoconductivity of Kapton (ref. 10). Figure 5(c) shows sample temperature as a function of time. The thermocouple used to monitor the temperature was located in the center of the substrate's back surface. Because of its location it probably indicated the true temperature of all the sample surfaces only during the first 1/2 hour of testing. During this time, there were no thermal inputs to the sample and a steady state had been achieved. Figure 5(d) is a cumulative record of the discharge activity that took place during the test. The three counters connected to the loop antenna were operating with thresholds of 1, 2, and 5 volts. The top curve shows the discharges that generated pulses greater than 1 volt in the antenna. The bottom curve shows discharges that induced pulses greater than 2 volts. No discharges generating 5 volts were observed during the 2-hour test of sample 2. Discharge activity was greatest during the first 1/2 hour when the sample was cold and in darkness. The discharge rate was reduced after illumination of the sample but increased during the second 1/2 hour of darkness. The discharge rate during the second dark period was somewhat less than the rate during the first dark period possibly because of higher sample temperature.

The test results obtained with sample 3 are shown in figures 6 to 9. Figure 6 shows typical potential profiles for this sample. Sample 3 was identical to sample 2 except for the addition of the soot-bearing adhesive charge-control material to the back surface. The cover-slide and Kapton-border potential profile for low-energy (5-keV) electron beam irradiation (fig. 6(a)) is very similar to that for sample 2 (fig. 2(a)). The profile for high-energy (20-keV) electron beam irradiation (fig. 6(b)) shows that the Kapton border became less highly charged probably because of the additional soot-bearing adhesive charge-control material. The most dramatic improvement is shown in figure 6(c), the profile of the back surface exposed to a 20-keV electron beam. The maximum potential is two orders of magnitude less than that of the sample without the adhesive-soot material (sample 2). Figures 7 to 9 show surface potential as a function of beam energy, collected electron current as a function of beam

energy, and the curves summarizing the 2-hour test in which the sample was illuminated by simulated solar radiation.

The test results for sample 4 are summarized in figures 10 to 13. Figure 10(a) shows the potential profile of the front surface under exposure to a low-energy (5-keV) electron beam. The cover slide and the fiberglass-over-Kapton border became charged to approximately the same potentials as the cover slides and Kapton borders of samples 2 and 3. The potential profile of the front surface under exposure to a high-energy (20-keV) electron beam is shown in figure 10(b). Exposure of the back surface to a 20-keV beam produced the potential profile shown in figure 10(c). Recall that the back surface has the soot-bearing charge-control material applied to plain Kapton without any woven carbon-fiber material. Comparison with figure 6(c) shows that the adhesive-soot material alone is nearly as effective as the combined woven-carbon-fiber and adhesive-soot material in reducing charge accumulation. Figures 11 to 13 show surface potential as a function of beam energy, collected electron current as a function of beam energy, and the curves summarizing the 2-hour test of the sample subjected to alternating periods of darkness and simulated solar illumination.

The test results for sample 1 are summarized in figures 14 to 17. This sample was a better simulation of a proposed flight array in that the exposed area of the substrate on the solar-cell side was a small fraction of the total sample area. Figure 14(a) shows the two deep potential wells due to charge accumulation on the narrow Kapton borders. The potentials reached by the surfaces in the low-energy (5-keV) electron beam were much the same as the levels reached by similar surfaces on the other three samples. The voltage probe crossed four solar-cell cover slides as it traversed the sample, and evidence of these is barely discernible in figure 14(a). Figure 14(b) is a typical surface potential profile of sample 1 in a high-energy (20-keV) electron beam. The cover slides are more easily seen. The potential profile of the back surface in a 20-keV electron beam is shown in figure 14(c). The back surface of this sample looks much like the back surface of sample 2, except that the carbon-fiber material is more densely woven. Comparing figure 14(c) with figure 2(c) shows that the closer weave eliminated the numerous highly charged regions evident on the back-surface profile of sample 2. Although an improvement over the behavior of sample 2 was realized, the closer weave was not as effective in reducing charge accumulation as the adhesive-soot material applied to samples 3 and 4 (figs. 6(c) and 10(c)). Figures 15 to 17 show surface potential as a function of beam energy, sample current as a function of beam energy, and the curves summarizing the 2-hour test with periods of solar simulation.

Sample 1 experienced significantly more discharge activity on the front surface than did the other three samples. This may be due to the larger number of solar cells, whose cover slides could become charged and independently discharge to the solar-cell interconnections. Comparing figures 5(d), 9(d), 13(d), and 17(d) shows that illumination of the front surface significantly reduced or eliminated discharge activity on all samples, possibly because of the photoconductivity of Kapton (ref. 10). The data indicate that the densely woven carbon-fiber fabric alone or the less-dense carbon-fiber fabric with the

adhesive-soot material added were most effective in preventing discharge activity when the back surface was irradiated in darkness.

Graphite-Fiber/Epoxy - Aluminum Honeycomb Samples

The five honeycomb-panel samples were tested to determine, in each case, the degree to which the surfaces of interest became charged in monoenergetic electron beams of 2 to 20 keV.

The Navstar sample (5) was mounted with its back surface against a 27.3-centimeter-by-29.3-centimeter aluminum plate to which a lead was attached to measure electron current to the sample. Typical surface potential profiles are shown in figure 18(a). The ragged profile is probably a result of variation in the concentration of epoxy and graphite fibers at the surface. Note the prominent potential spike at the discontinuity in the graphite-fiber sheet. The general surface potential across the sample is shown in figure 18(b) as a function of beam energy. For energies greater than 5 keV, the potential increases only slightly if at all. The nominal current density at the center of the sample was 1 nA/cm^2 before each test, as read by the Faraday cup. The sample current recorded for each test was nearly 1 microampere, indicating an average flux over the 893-square-centimeter sample of about 1 nA/cm^2. No discharges were recorded by the loop antenna located near the sample or by the time-exposure camera.

The Voyager antenna samples (6 and 7) were exposed to electron beams of 2 to 20 keV and flux densities of 1 and 3 nA/cm^2. The dependence of the surface potential on beam energy and flux density is shown in figures 19(a) and (b). The dependence on beam energy disappears or is much reduced above 10 keV for both samples. The surface potential of the conductive-paint sample is about two orders of magnitude lower than that of the nonconductive-paint sample for the same beam conditions. Data from earlier tests of another nonconductive paint (S-13GLO) is shown in figure 19(c) for comparison.

The sample 8 and 9 honeycomb-panel surfaces were also exposed to 2- to 20-keV electron beams of 1- to 3-nA/cm^2 flux density. The samples were tested simultaneously, side by side. The tests were conducted with the samples at -40° C to better simulate the environment of the materials in use on Intelsat V. Typical surface potential profiles are shown in figure 20(a). The results of these tests, including the Navstar test data for comparison, are shown in figure 20(b). The ragged appearance of sample 8's profiles is similar to the Navstar profiles and is probably due to the varying epoxy concentration across the surface. Sample 9's profiles appear more uniform, with two prominent potential spikes at the locations of significant epoxy bleed through the carbon fibers. Though the loop antenna did not record any discharge activity, the sample current record and the time-exposure photographs show evidence of activity on sample 8.

The sample current records (fig. 21(a)) were quite noisy. The pulses on sample 9's current record may have been a response to what was happening on the other sample. The time-exposure photographs (fig. 22) show a faint glow out-

lining the graphite-fiber pattern of sample 8 but show no evidence of discharges from sample 9. Also, the surface potential of sample 8 appeared different with each sweep of the probe (fig. 21(b)), but sample 9's profile appeared nearly constant.

Thin-Film Samples

The first test specimen of Mylar was about 28 centimeters square and was isolated from ground, with the bare surface facing the electron source. An electron beam of nominally 1 nA/cm^2, at its center, in the plane of the specimen was stepped through various energies from 2½ to 20 keV. The potential of the Mylar surface was monitored by the electrostatic voltmeter.

The response of surface potential of the Mylar film to the varying beam energy is shown in figure 23. With the specimen isolated from ground and in total darkness, thus eliminating bulk conduction and photoemission currents, the equilibrium surface potential was a function of beam energy and the material secondary emission properties. Although no temperature-measuring devices were mounted on the specimen, it was estimated that the specimen was at 10° C, as were other structures within the chamber.

The surface potential response of the 7.62-micrometer-thick Kapton film to varying beam energy, with the specimen totally isolated from ground, is shown in figure 24. In this configuration, the surface potential is about the same as that of the Mylar film mounted similarly and exposed to the same-energy electron beam. The surface potentials are compared in figure 25 as a function of beam energy for both materials in the totally isolated and grounded substrate mounting configurations. The test data and calculated values of resistance and resistivity are contained in table II.

The data from the testing of the 127-micrometer-thick Kapton film show that the surface potential increased linearly with beam energy to about 12 keV. Beyond this level, discharges began to take place on the surface. The data taken were not sufficient to tell whether the discharges were characterized by charge transport from the front surface to the back surface at the edges or by charge emission from the surface to other structures within the chamber.

CONCLUSIONS

Four flexible-substrate solar-array segments, five graphite-fiber/epoxy - aluminum honeycomb panels, and two thin dielectric films were exposed to monoenergetic electron beams in the Lewis Research Center's geomagnetic-substorm-environment simulation facility. The array segments represented different approaches to making the dielectric back surface "quasi-conductive" and thus minimizing surface charge accumulation. The tests showed, as expected, that the more nearly continuous the quasi-conductive surface treatment, the lower the surface potential. The tests of the honeycomb-panel samples are evidence that strong, lightweight, nonmetallic structural materials are available that

have acceptable spacecraft-charging properties. If the surfaces have a sufficiently high and uniform concentration of conductive medium with a conductive path to ground, surface potentials well below those at which discharges occur can be maintained. Finally, thin dielectric films charge to high surface potentials when they are isolated from ground. However, when the films are placed over a conductive substrate at ground potential, surface potentials of less than 2½ kilovolts can be maintained even when the films are irradiated with 20-keV electrons.

REFERENCES

1. Fredricks, R. W.; and Scarf, F. L.: Observation of Spacecraft Charging Effects in Energetic Plasma Regions. Photon & Particle Interactions with Surfaces in Space, R. J. L. Grard, ed., D. Reidel Publ. Co., 1973, pp. 277-308.

2. McPherson, D. A.; Cauffman, D. P.; and Schober, W. R.: Spacecraft Charging at High Altitudes: The SCATHA Satellite Program. AIAA Paper 75-92, Jan. 1975.

3. Rosen, A.: Spacecraft Charging - Environment Induced Anomalies - Magnetic Substorm Effects. AIAA Paper 75-91, Jan. 1975.

4. Berkopec, Frank D.; Stevens, N. John; and Sturman, John C.: The Lewis Research Center Geomagnetic Substorm Simulation Facility. NASA TM X-73602, 1976.

5. Stevens, N. John; Klinect, Vernon W.; and Berkopec, Frank D.: Environmental Charging of Spacecraft Surfaces: Tests of Thermal Control Materials for Use on the Global Positioning System Flight Space Vehicle, Part 1: Specimens 1-5. NASA TM X-73467, 1976.

6. Stevens, N. John; Berkopec, Frank D.; and Blech, Richard A.: Environmental Charging of Spacecraft Surfaces: Tests of Thermal Control Materials for Use on the Global Positioning System Flight Space Vehicle, Part 2: Specimens 6-9. NASA TM X-73436, 1976.

7. Stevens, N. John; et al.: Testing of Typical Spacecraft Materials in a Simulated Substorm Environment. NASA TM X-73603, 1976.

8. Stevens, N. John; Lovell, Robert R.; and Gore, J. Victor: Spacecraft Charging Investigation for the CTS Project. NASA TM X-71795, 1975.

9. Stevens, N. John; Klinect, Vernon W.; and Gore, J. Victor: Summary of CTS Transient Event Counter Data After One Year of Operation. NASA TM X-73710, 1977.

10. Coffey, H. T.; Jenevicz, J. E.; and Adamo, R. C.: Photoconductivity of High-Voltage Space Insulating Materials. (SRI Proj. 3545, Stanford Res. Inst.; NASA Contract NAS3-18912.) NASA CR-134995, 1975.

TABLE I. - SAMPLE SUBSTRATE CHARACTERISTICS

Sample	Materials[a]	Element	Substrate without anticharging	Dimensions, mm	Anticharging represented by-	Resistance between conductive edge-stripe[a] kΩ
		Density, g/m^2				
1	Kapton (12.5 μm) CFC[b] CY 209 plus hardener HT 972	19 66 66	155	100 × 110	CFC[b]	0.0036
2	Kapton (12.5 μm) CFC[b] DuPont 46971 plus hardener RC 805	19 45 31	95	100 × 110	CFC[b]	0.0039
3	Kapton (12.5 μm) CFC[b] DuPont 46971 plus hardener RC 805	19 45 40	104	100 × 110	CFC,[b] DuPont 46971, hardener, and soot	0.0020
4	Kapton (12.5 μm) Fiberglass 90001 DuPont 46971 plus hardener RC 805	19 27 13	59	100 × 110	DuPont 46971, hardener, and soot	5.297

[a]All the samples had two strips of silver-filled polyester bonded to the back surface so that the back surface could be grounded.

[b]Carbon-fiber composite.

TABLE II. - TEST DATA AND CALCULATED RESISTANCE FOR THIN PLASTIC FILMS

Sample	Beam energy, keV	Surface potential, kV	Beam voltage minus surface voltage, kV	Sample current, μA	Sample current divided by area, nA/cm^2	Effective bulk resistance, Ω	Effective bulk resistivity, Ω-cm
127-μm-thick Kapton	2.5	1.64	0.86	0.011	0.032	0.149×10^{12}	0.409×10^{16}
	5	4.15	.85	.005	.014	$.83\times10^{12}$	2.277×10^{16}
	8	7	1	.006	.017	1.167×10^{12}	3.201×10^{16}
	10	9.0	1	.005	.015	1.8×10^{12}	4.938×10^{16}
	12	10.8	1.2	.007	.020	1.543×10^{12}	4.232×10^{16}
	[a]15	12.8	2.2	.008	.023	1.6×10^{12}	4.389×10^{16}
	[a]18	12.8	5.2	.012	.035	1.067×10^{12}	2.927×10^{16}
	[a]20	13.0	7	.013	.037	1×10^{12}	2.743×10^{16}
7.62-μm-thick Kapton	2.5	1.63	0.87	0.028	0.08	5.82×10^{10}	2.662×10^{16}
	5	2.12	2.88	.229	.657	$.926\times10^{10}$	$.423\times10^{16}$
	8	2.10	5.90	.278	.798	$.755\times10^{10}$	$.345\times10^{16}$
	10	1.96	8.04	.298	.823	$.658\times10^{10}$	$.300\times10^{16}$
	15	1.20	13.8	.579	1.66	$.207\times10^{10}$	$.094\times10^{16}$
	20	.50	19.5	.340	.978	$.147\times10^{10}$	$.067\times10^{16}$
2.54-μm-thick Mylar	2.5	1.1	1.4	0.09	0.259	1.222×10^{10}	1.676×10^{16}
	5	.925	4.075	.191	.548	$.484\times10^{10}$	$.664\times10^{16}$
	10	.32	9.68	.322	.924	$.099\times10^{10}$	$.136\times10^{16}$
	20	.039	19.961	.380	1.11	$.01\times10^{10}$	$.014\times10^{16}$

[a]Surface discharges occur; surface potential not truly in equilibrium; all samples 17.04 cm by 20.32 cm.

Figure 1. - Flexible-substrate solar-array samples.

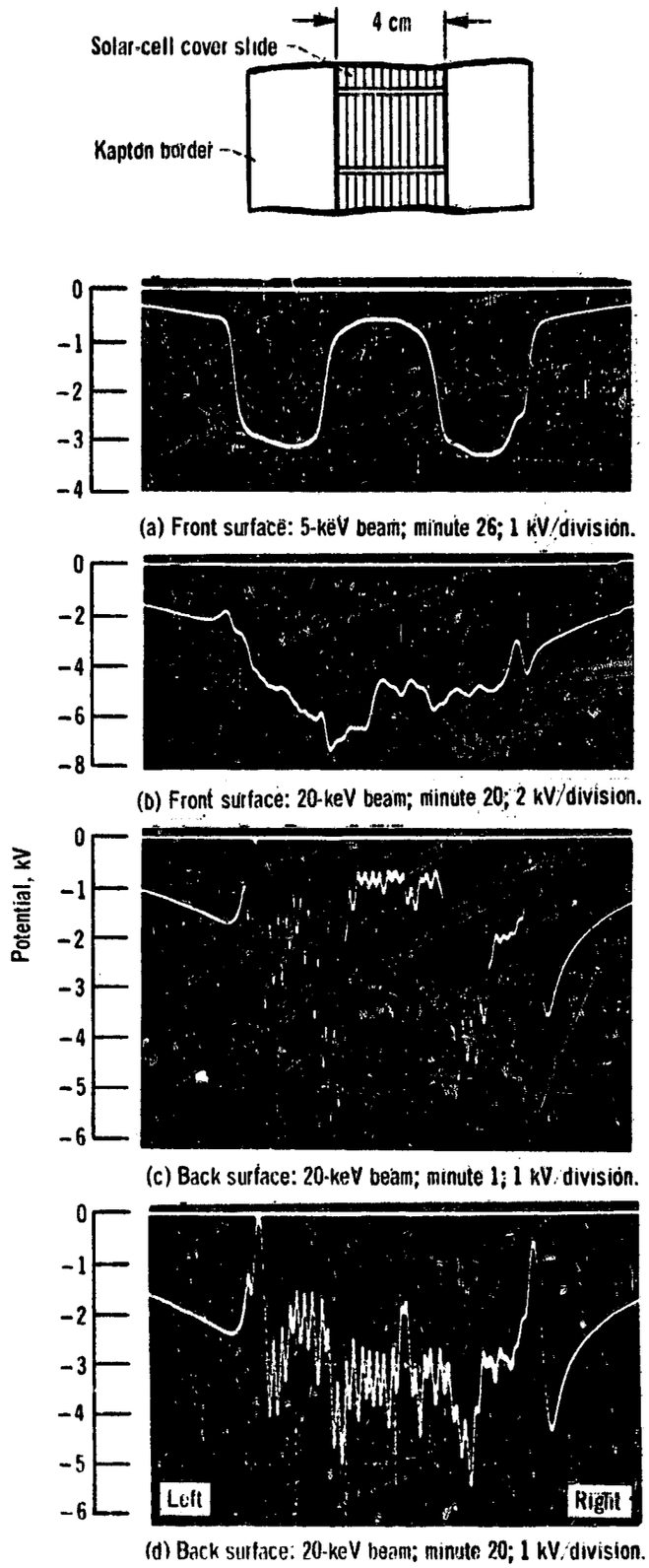

(a) Front surface: 5-keV beam; minute 26; 1 kV/division.

(b) Front surface: 20-keV beam; minute 20; 2 kV/division.

(c) Back surface: 20-keV beam; minute 1; 1 kV/division.

(d) Back surface: 20-keV beam; minute 20; 1 kV/division.

Figure 2. - Typical surface potential profiles of sample 2.

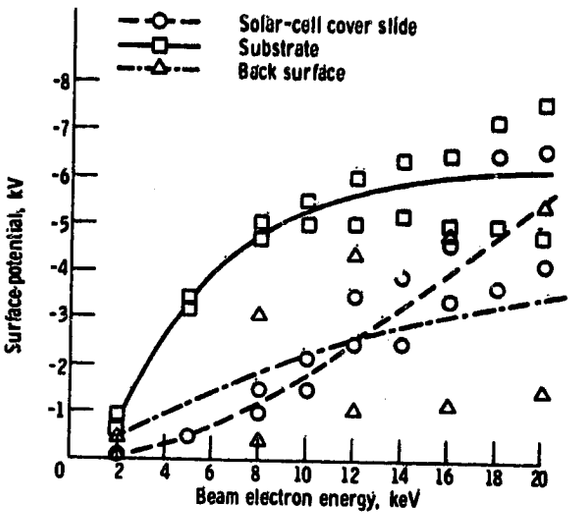

Figure 3. - Surface potential as function of beam energy for sample 2.

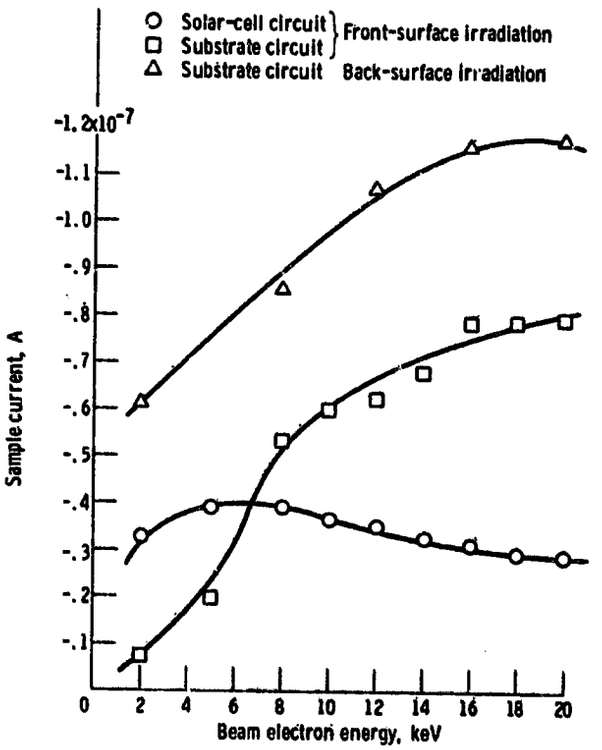

Figure 4. - Collected current as function of beam energy for sample 2.

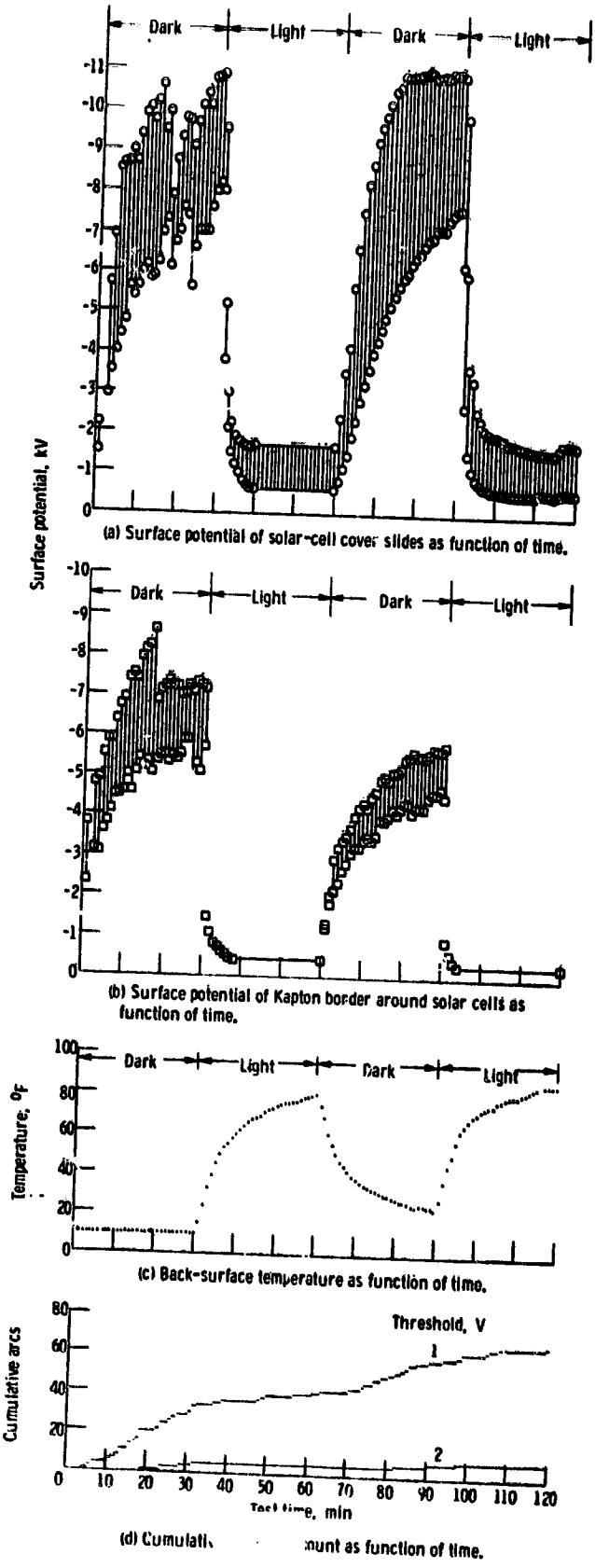

Figure 5. - Results of solar simulation test of sample 2.

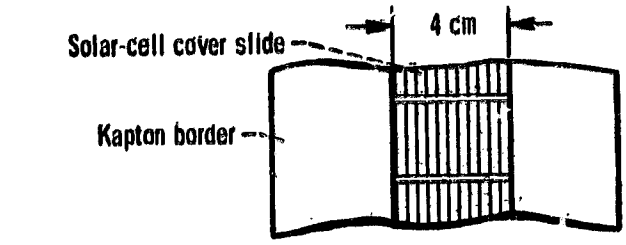

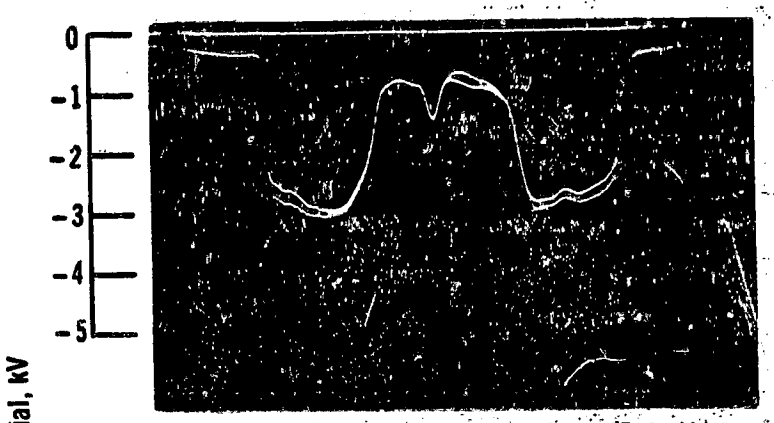

(a) Front surface: 5-keV beam; minutes 20 and 27; 1 kV/division.

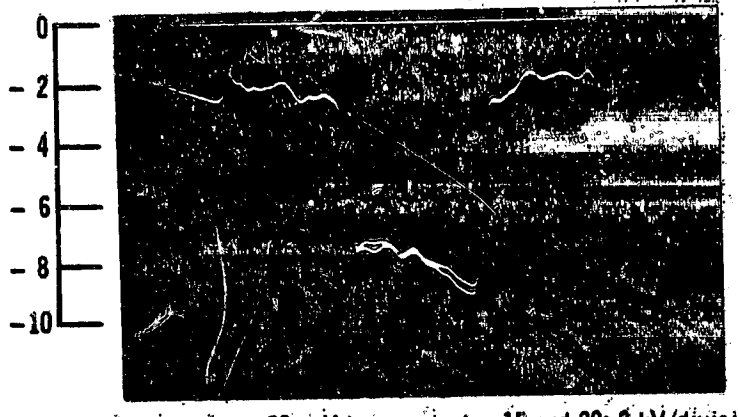

(b) Front surface: 20-keV beam; minutes 15 and 20; 2 kV/division.

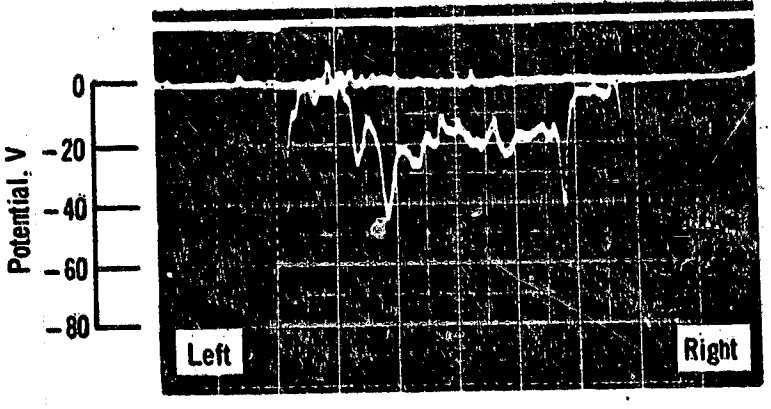

(c) Back surface: 20-keV beam; minute 20; 20 V/division.

Figure 6. - Typical surface potential profiles of sample 3.

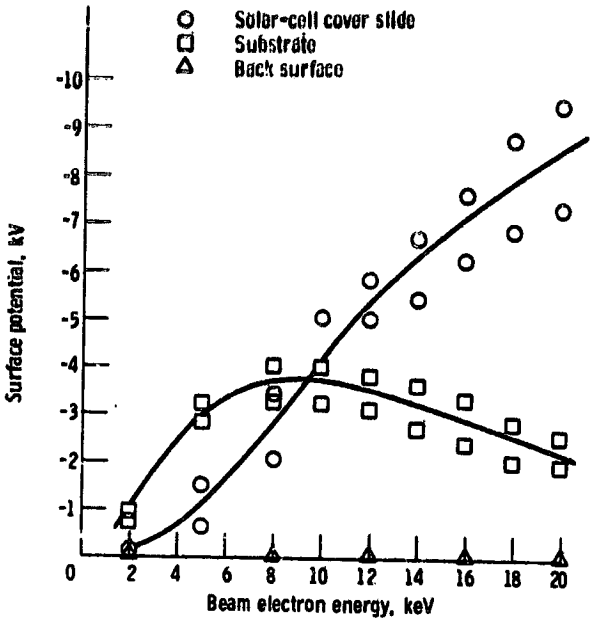

Figure 7. - Surface potential as function of beam energy for sample 3.

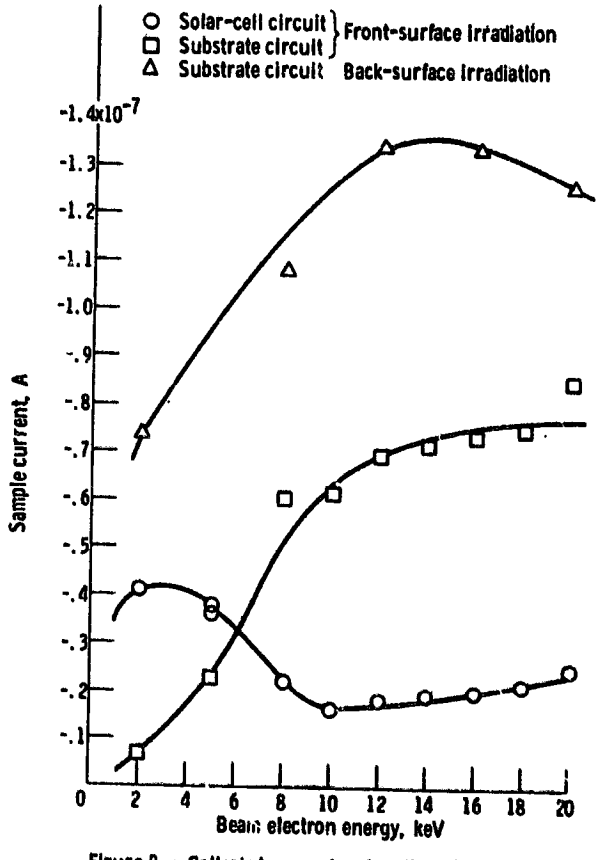

Figure 8. - Collected current as function of beam energy for sample 3.

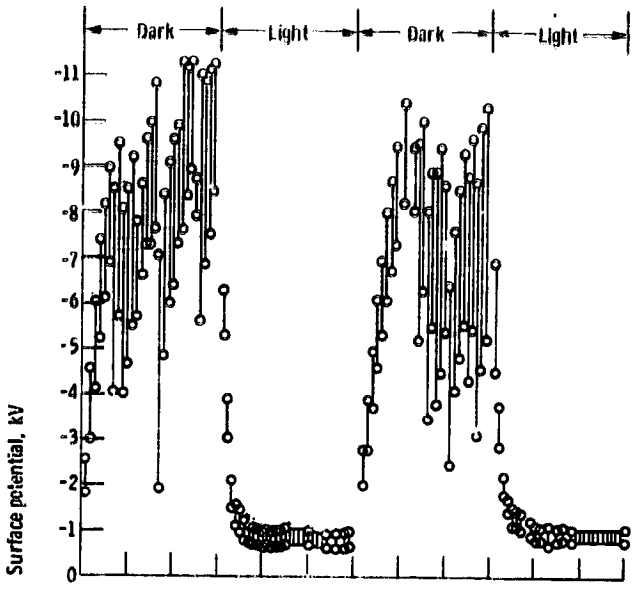

(a) Surface potential of solar-cell cover slides as function of time.

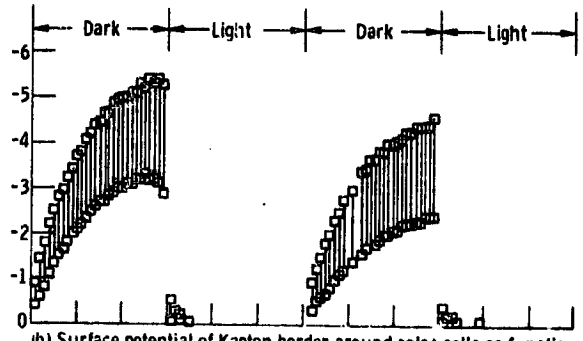

(b) Surface potential of Kapton border around solar cells as function of time.

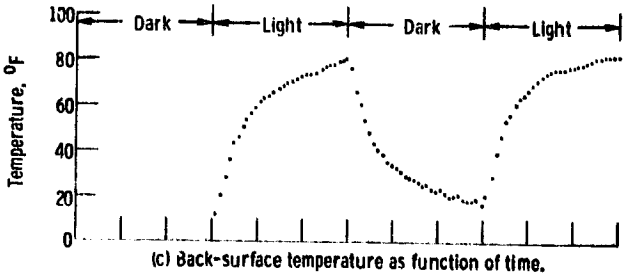

(c) Back-surface temperature as function of time.

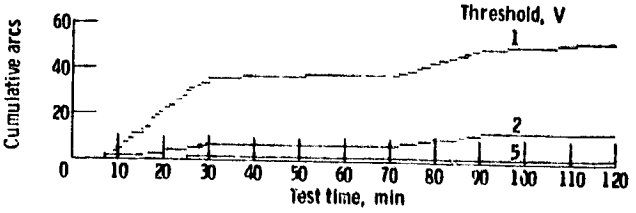

(d) Cumulative discharge count as function of time.

Figure 9. - Results of solar simulation test of sample 3.

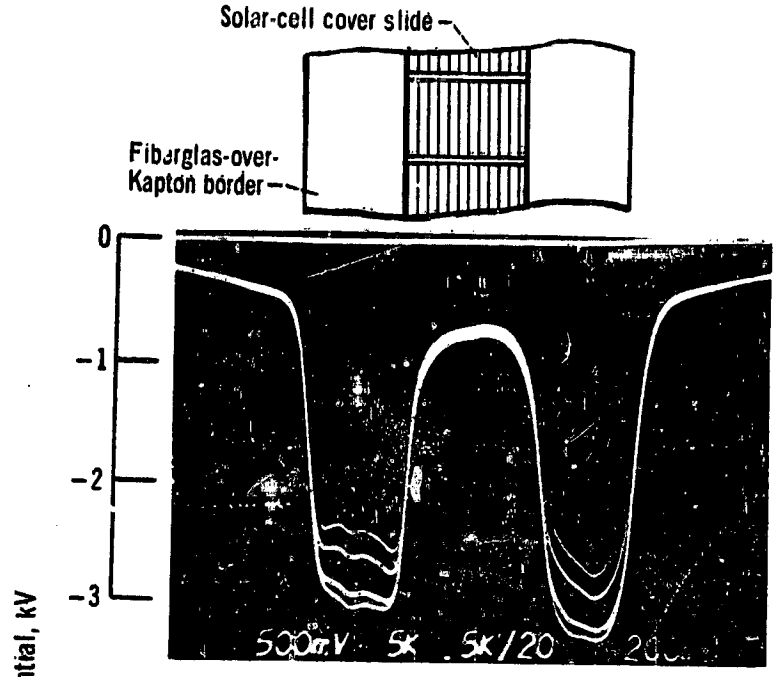

(a) Front surface: 5-keV beam; minutes 12, 14, 18, and 20; 500 V/division.

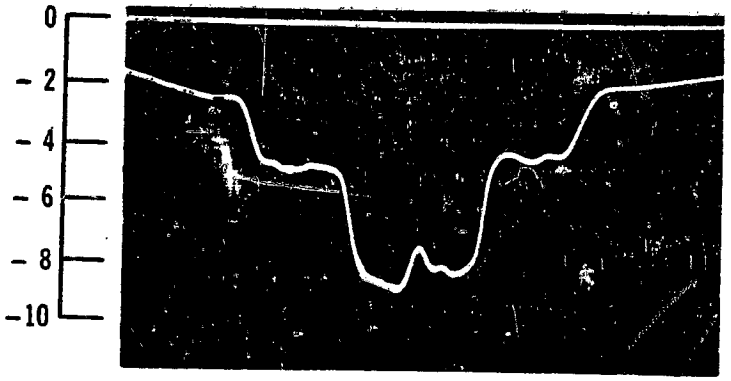

(b) Front surface: 20 keV/beam; minute 20; 2 kV/division.

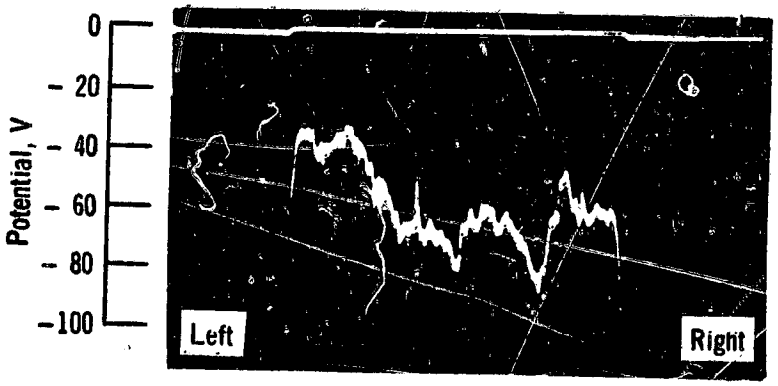

(c) Back surface: 20-keV beam; minute 22; 20 V/division.

Figure 10. - Typical surface potential profiles of sample 4.

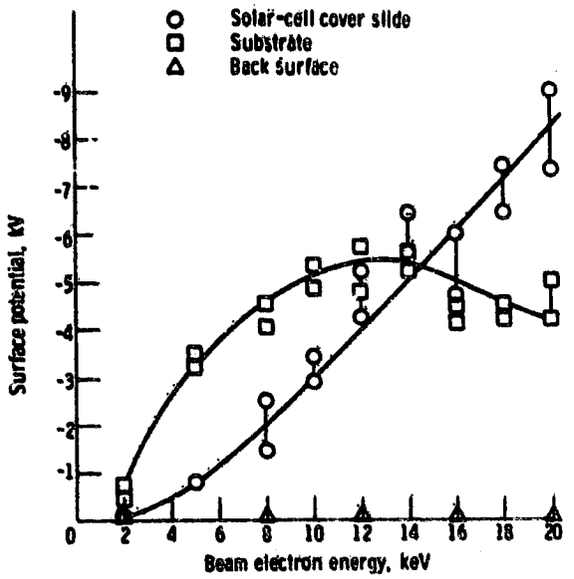

Figure 11. - Surface potential as function of beam energy for sample 4.

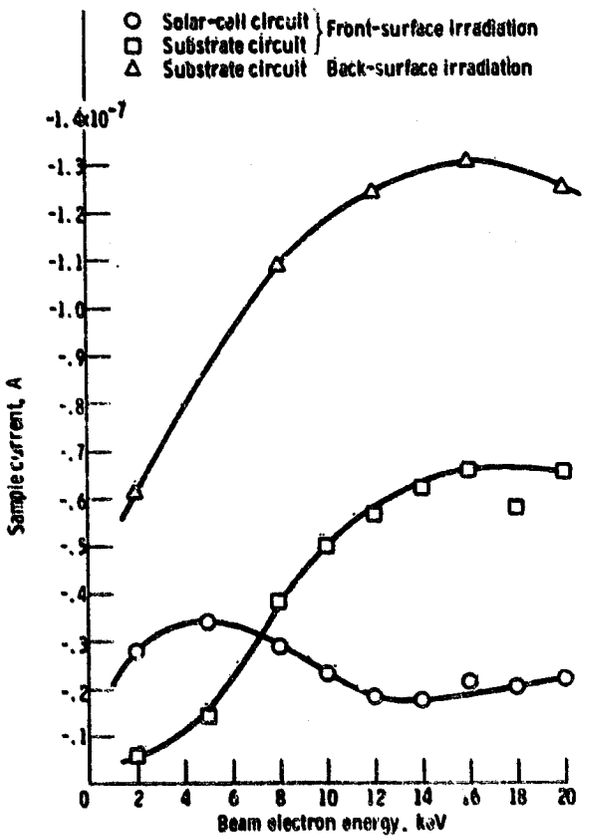

Figure 12. - Collected current as function of beam energy for sample 4.

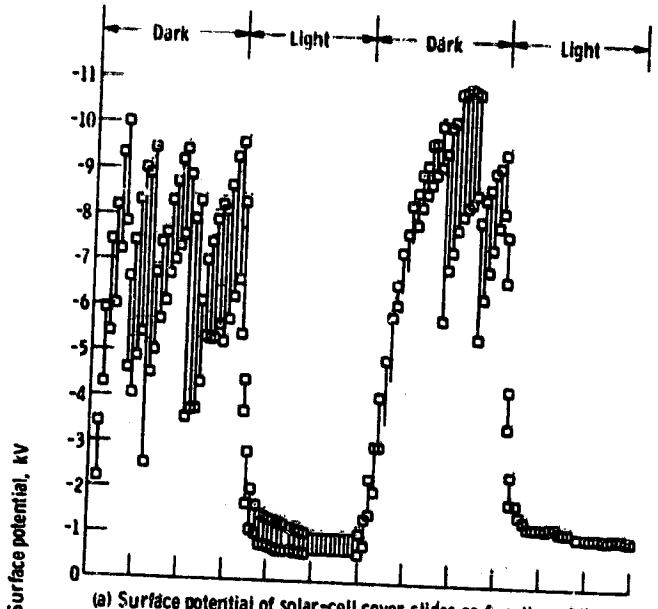

(a) Surface potential of solar-cell cover slides as function of time.

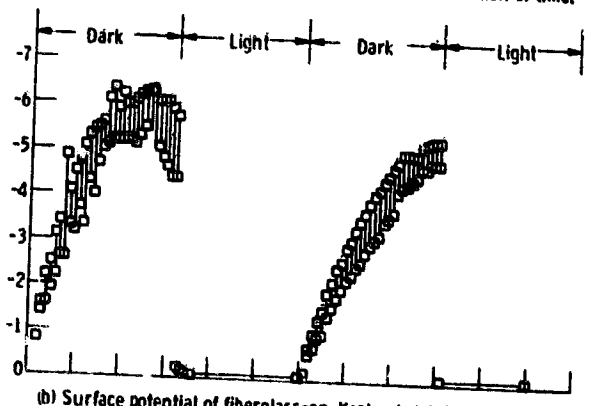

(b) Surface potential of fiberglass-on-Kapton border around solar cells as function of time.

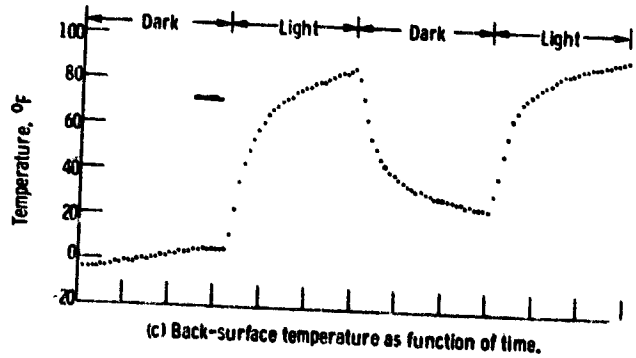

(c) Back-surface temperature as function of time.

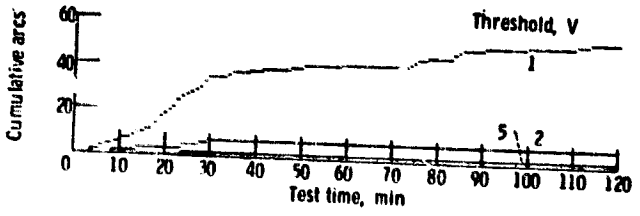

(d) Cumulative discharge count as function of time.

Figure 13. - Results of solar simulation test of sample 4.

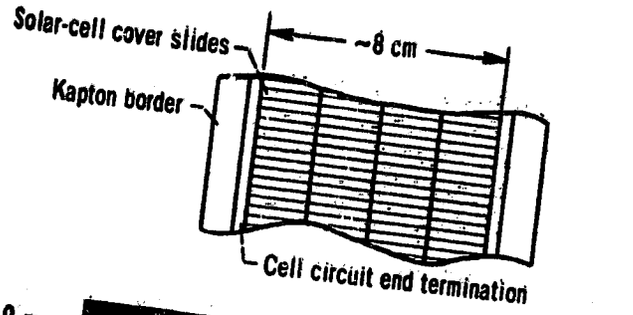

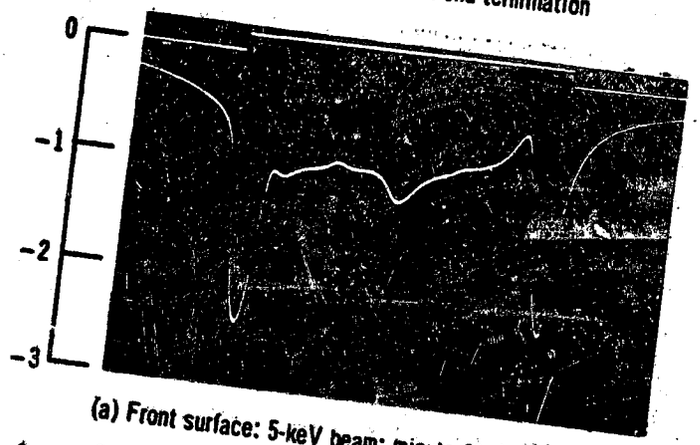

(a) Front surface: 5-keV beam; minute 21; 500 V/division.

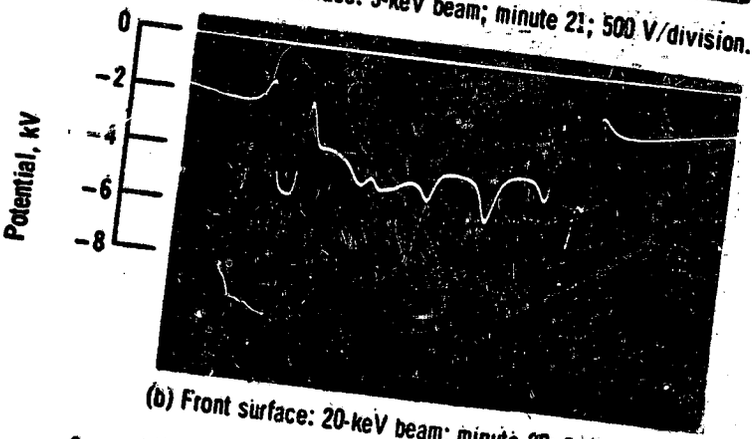

(b) Front surface: 20-keV beam; minute 20; 2 kV/division.

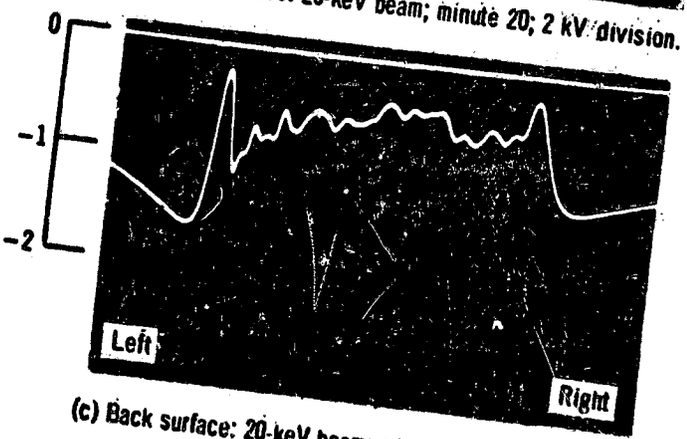

(c) Back surface: 20-keV beam; minute 30; 500 V/division.

Figure 14.- Typical surface potential profiles of sample 1.

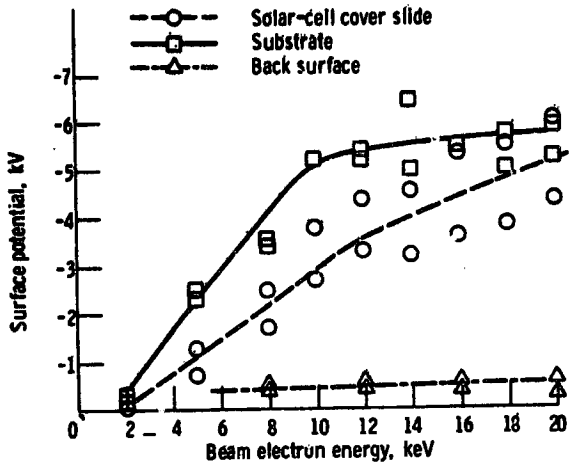

Figure 15. - Surface potential as function of beam energy for sample 1.

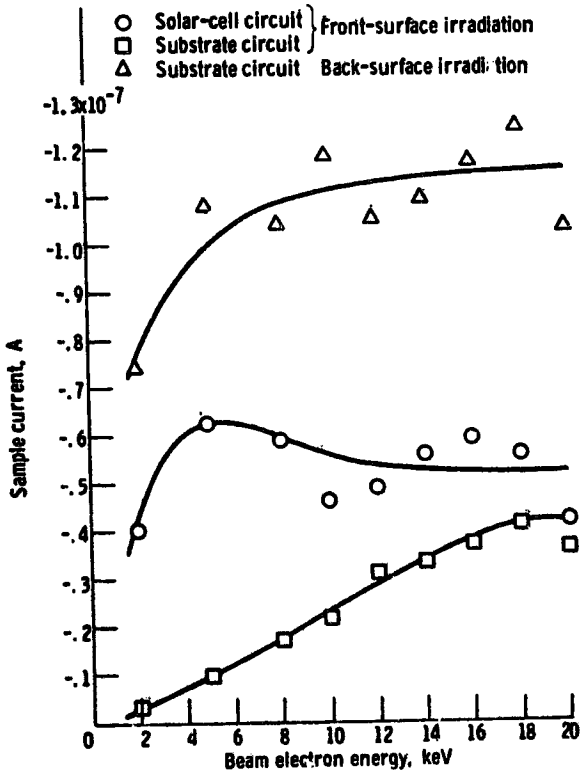

Figure 16. - Collected current as function of beam energy for sample 1.

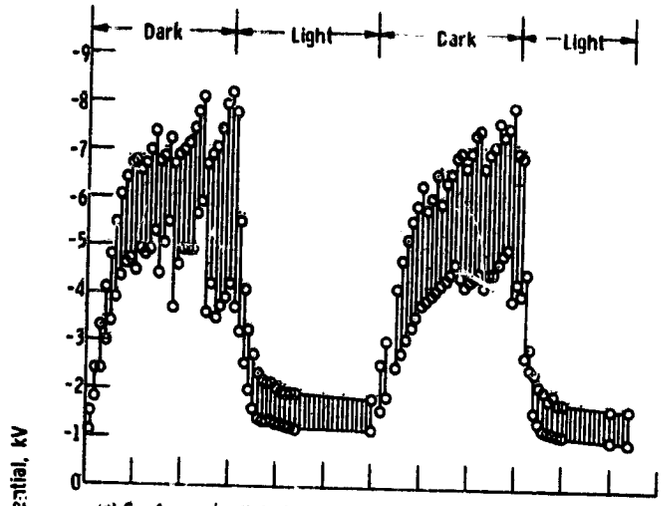

(a) Surface potential of solar-cell cover slides as function of time.

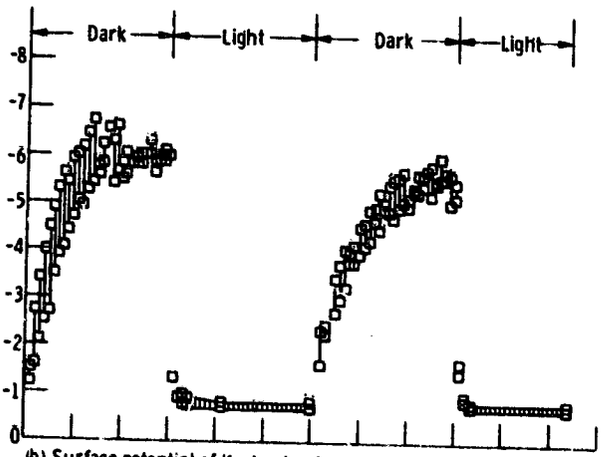

(b) Surface potential of Kapton border around solar cells as function of time.

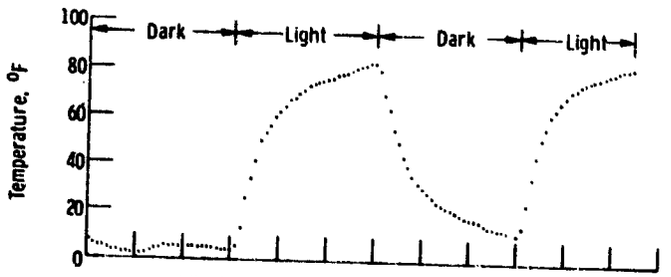

(c) Back-surface temperature as function of time.

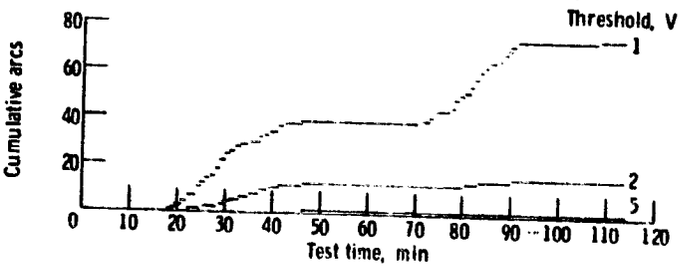

(d) Cumulative discharge count as function of time.

Figure 17. - Results of solar simulation test of sample 1.

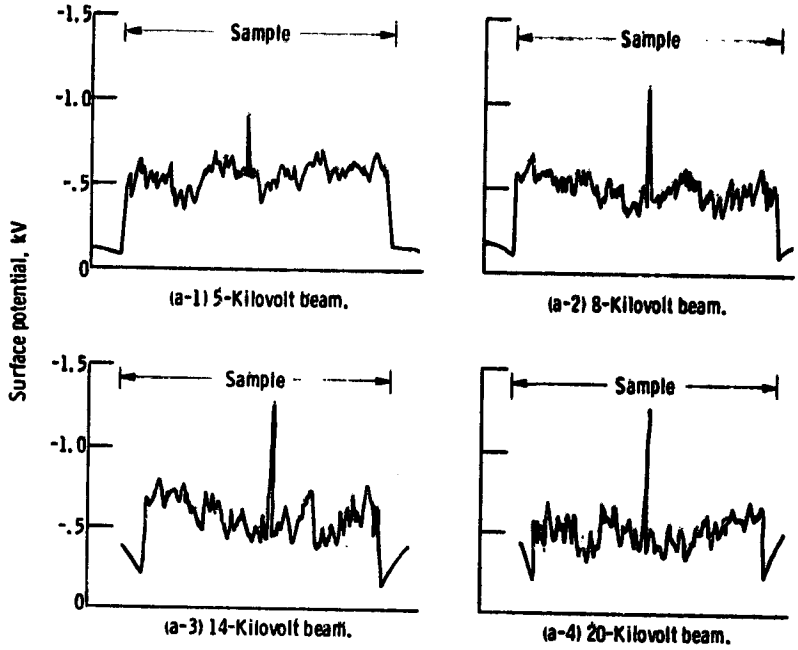

(a) Typical surface potential profiles.

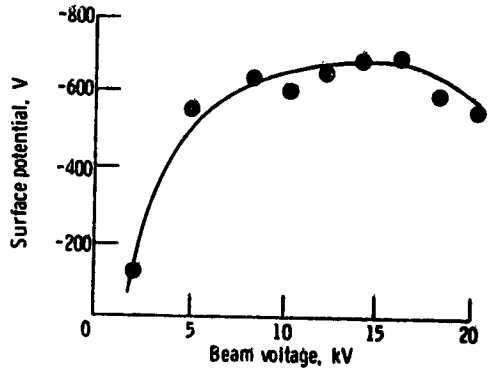

(b) Equilibrium surface potentials in 1-nA/cm^2-current-density electron beam.

Figure 18. - Results of Navstar solar-array substrate (sample 5) charging test.

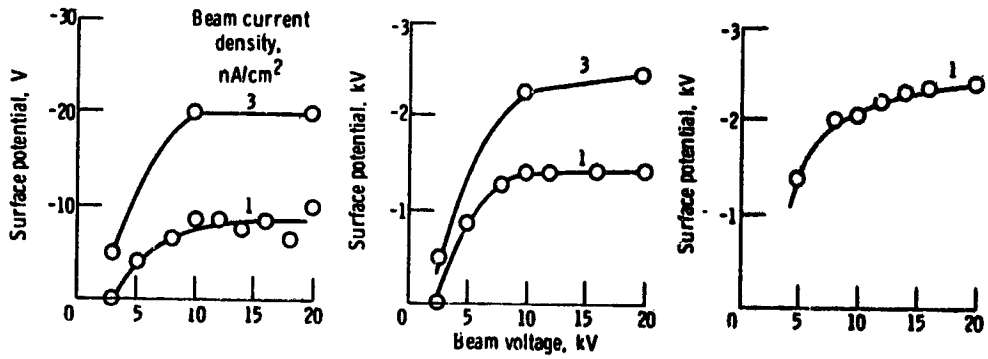

(a) Voyager antenna honeycomb panel with GSFC NS43C conductive paint (sample 6).

(b) Voyager antenna honeycomb panel with PV100 nonconductive paint (sample 7).

(c) Nonconductive paint (S-13GLO) on grounded metal substrate for comparison.

Figure 19. - Results of Voyager antenna honeycomb-panel charging test.

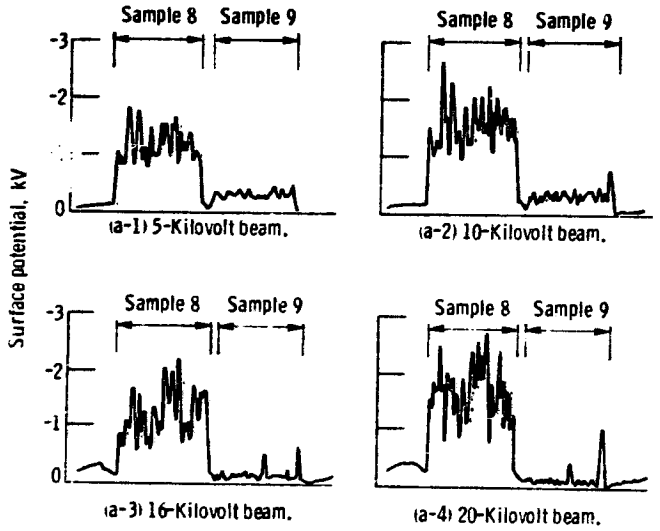

(a) Typical surface potential profiles.

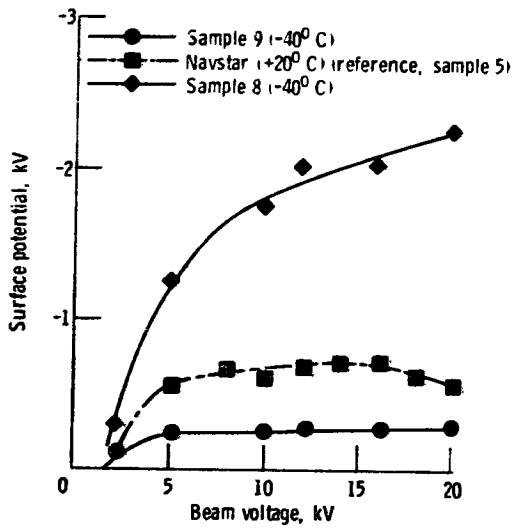

(b) Equilibrium surface potentials for 1- and 3-nA/cm^2-current-density electron beams.

Figure 20. - Results of honeycomb-panel samples (8 and 9) charging tests.

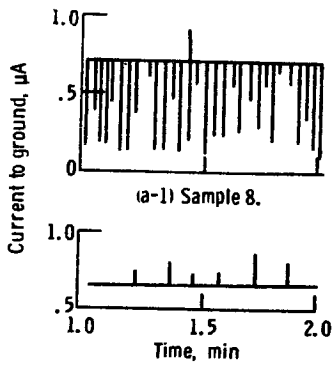

(a-1) Sample 8.

(a-2) Sample 9.

(a) Sample current traces in 16-keV electron beam.

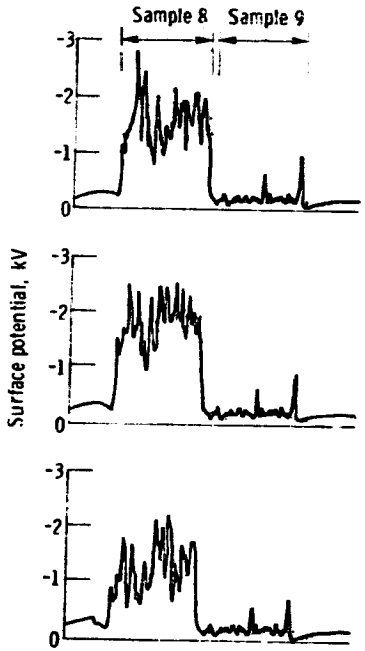

(b) Surface potential profiles in 16-keV electron beam.

Figure 21. - Transient behavior of honeycomb-panel samples (8 and 9).

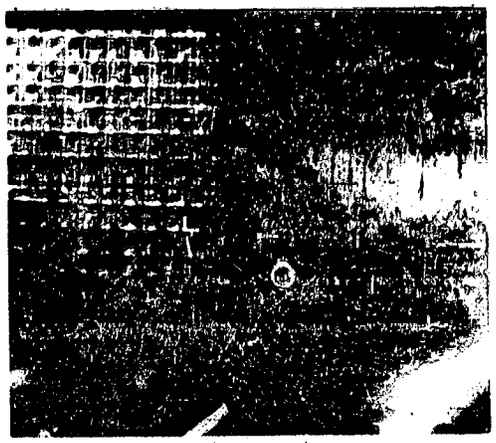

(a) 63-Minute time exposure at 16 keV; 1-nA/cm^2 electron beam.

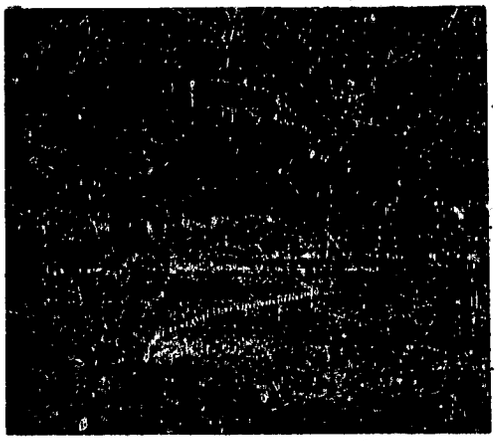

(b) 10-Minute time exposure at 16 keV; 1-nA/cm^2 electron beam.

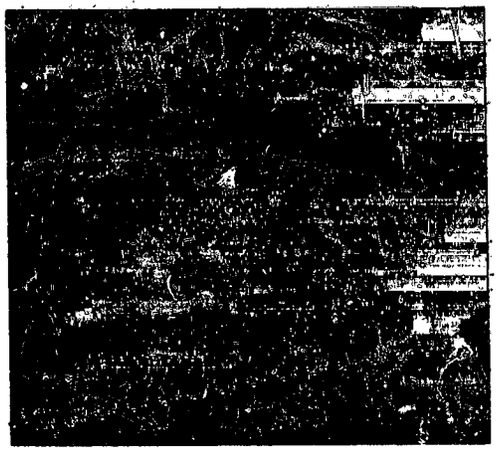

(c) Control time-exposure filament on, accelerating potential off.

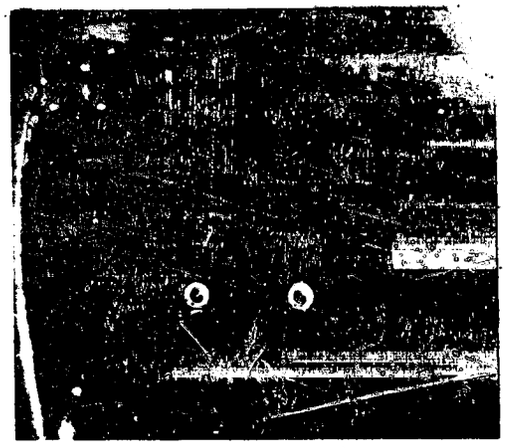

(d) Surface voltage probe sweeping across top of sample 8.

Figure 22. - Time-exposure photographs of honeycomb panels (samples 8 and 9).

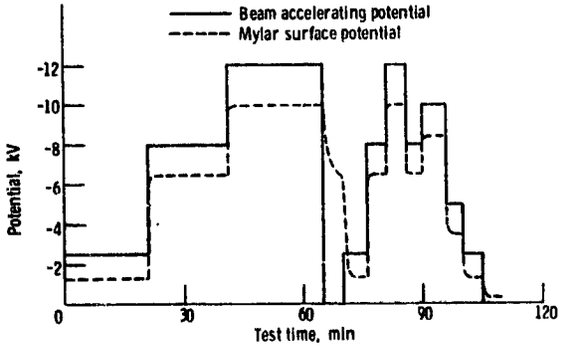

Figure 23. - Response of 2.54-micrometer-thick Mylar surface potential to varying electron beam energy. (Mylar isolated from ground.)

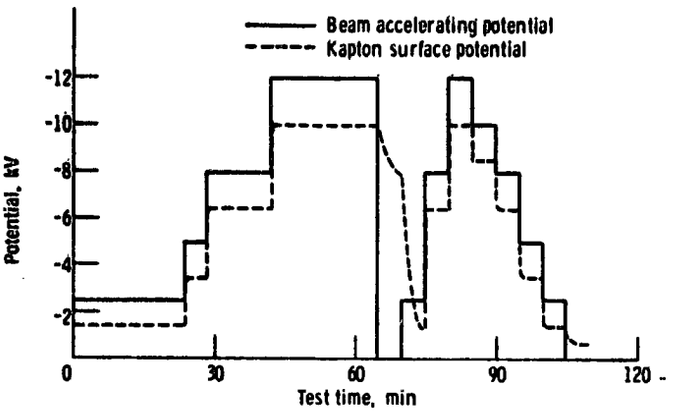

Figure 24. - Response of 7.62-micrometer-thick Kapton surface potential to varying electron beam energy. (Kapton isolated from ground.)

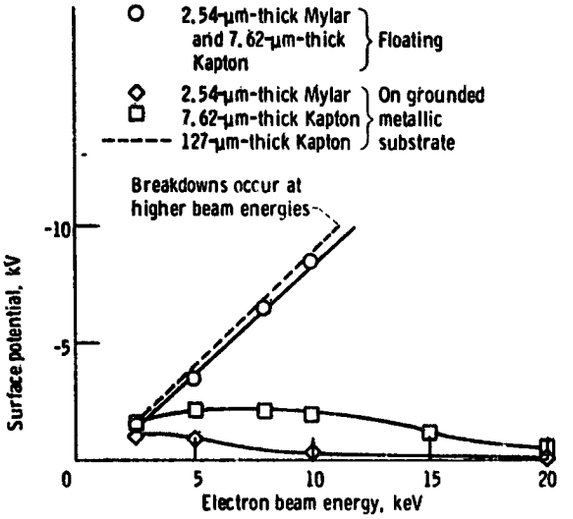

Figure 25. - Thin-film surface potential as function of electron beam energy.

D31

N79-24032

AREA SCALING INVESTIGATIONS OF CHARGING PHENOMENA

Paul R. Aron and John V. Staskus
NASA Lewis Research Center

SUMMARY

The charging and discharging behavior of square, planar samples of silvered, fluorinated ethylene-propylene (FEP) Teflon thermal control tape was measured. The equilibrium voltage profiles scaled with the width of the sample. A wide range of discharge pulse characteristics was observed, and the area dependences of the peak current, charge, and pulse widths are described. The observed scaling of the peak currents with area was weaker than that previously reported. The discharge parameters were observed to depend strongly on the grounding impedance and the beam voltage. Preliminary results suggest that measuring only the return-current-pulse characteristics is not adequate to describe the spacecraft discharging behavior of this material. The seams between strips of tape appear to play a fundamental role in determining the discharging behavior. An approximate propagation velocity for the charge cleanoff was extracted from the data. The samples - 232, 1265, and 5058 square centimeters in area - were exposed at ambient temperature to a 1- to 2-nA/cm^2 electron beam at energies of 10, 15, and 20 kilovolts in a 19-meter-long by 4.6-meter-diameter simulation facility at the Lewis Research Center.

INTRODUCTION

It has been clear from the beginning of the spacecraft charging investigation that an understanding of the geometric scaling laws that describe charging phenomena is of fundamental importance. Larger systems are being built, and even larger ones are being seriously proposed for future missions. Worse-case calculations and extrapolations from existing data have a limited reliability and utility. Therefore, experimental studies must be undertaken with larger areas of engineering material than previously tested. There is also an inadequate theoretical understanding of the discharge process. An experimental study of the variation with area of the parameters that describe the discharge process should provide important clues to guide the mathematical modeling effort. Some significant experimental measurements of area effects have been reported in the literature (refs. 1 and 2). Balmain (ref. 1) has systematically investigated area effects in a variety of spacecraft materials. His work was confined to areas of less than 100 square centimeters, but it did give the first clear experimental observation of the scaling of discharge pulse characteristics with area. Bogus (ref. 2) has also reported measurements of area scaling for large samples (3800 cm^2); however, his work has been confined to solar arrays.

At Lewis, an effort has begun to study systematically the area and geometry dependence of the charging and discharging parameters for a variety of spacecraft materials. Because of previous experience with silvered-Teflon thermal control tape, it was chosen as the first material to be tested in this investigation. The large size of the Lewis simulation facility has made it possible to study Teflon samples that are more than an order of magnitude larger than those previously reported.

MATERIALS, APPARATUS, AND PROCEDURE

Materials

The samples consisted of strips of 5-centimeter-wide, silvered, fluorinated ethylene-propylene (FEP) Teflon thermal control tape. The tape is a composite that consists of a 0.011-centimeter-thick sheet of Teflon with, first, a layer of vapor-deposited silver and, second, a layer of vapor-deposited Inconel 600. These layers were followed by a third, a 0.03-millimeter-thick layer of conductive adhesive. The adhesive was two parts GE SR525 silicone rubber mixed with one part silver powder (by weight). The tape was applied to a clean 0.313-centimeter-thick, square aluminum plate in strips extending the full length of the plate. The strips were butted edge to edge. The edges and the back of the plate were not covered. However, no part of the bare plate was exposed to the direct electron beam. The tape was applied with finger pressure and was tested in vacuum to have a resistance from the silver layer to the plate of approximately 60 ohms for a 1-square-centimeter area. Three sample assemblies were prepared - with areas of 232, 1265, and 5058 square centimeters.

Apparatus

Figure 1 shows the interior of the vacuum tank and the experimental arrangement. The 1265-square-centimeter sample is shown in place. It is fixed to the sample carriage, a vertical bar that can be moved remotely up to 1.1 meters horizontally, perpendicular to the tank axis. To the right of the sample is a stainless-steel beam shield. Behind the sample and, therefore, not visible in the figure is a 10-square-centimeter Faraday cup. Below and to the left of the sample is the arm on which are fixed the heads of two TREK model 340 HV electrostatic voltmeters. The spacing between the heads is adjustable and they are swept in a vertical arc across the sample surface. The probes were typically spaced 2 millimeters from the sample.

The sample assembly was grounded in one of two ways. In the first configuration, which is referred to as the 50-ohm configuration, the aluminum plate was insulated from the carriage and the tank structure. A 50-ohm coaxial lead approximately 10 meters long was brought from the sample out through the tank wall. The shield was grounded at the tank wall. The center conductor passed through the core of a Pearson model 110 current transformer. The lead was then brought to a switch that could ground it through a 50-ohm resistor or

apply it to the input of an electrometer. This configuration is shown in figure 2 as a solid line. In the second configuration, which is referred to as the low-impedance configuration, the insulator between the sample and the carriage was replaced by an 8-centimeter-long aluminum post threading the core of the Pearson current transformer. This configuration is shown in figure 2 as the dashed line. It was conceived to minimize the sample impedance to ground.

The current transformer is useful for signals with rise times greater than 50 nanoseconds. The transformer output was monitored with both a Tectronix model 7834 storage oscilloscope and a Biomation model 8100 waveform recorder. The waveform recorder was used in the pretrigger mode. In this mode it stores the output voltage of the Pearson transformer as a function of time over a selected interval (usually 20 μsec). This time interval includes a selectable time interval before the trigger. This capability is particularly useful for transient phenomenon as it eliminates the question about what happened before the trigger point. The signal was played back slowly through an integrator, and it and its time integral were recorded on a two-channel strip-chart recorder.

The output of the electrostatic voltmeters and their time integrals were recorded along with the various electrometer currents, position readouts, etc., on a multichannel strip-chart recorder. The electron flux (1 to 2 nA/cm^2) was generated by two Lewis electron guns (ref. 3). The guns were mounted next to one another, on either side of the tank axis, approximately 10 meters from the sample plane. The current distribution in this plane was measured by an array of current collection disks. The flux varied ±30 percent over the largest sample area. The electron trajectories were minimally affected by the Earth's magnetic field since the mild steel in the outer wall of the vacuum tank reduced the field by about a factor of 10.

A loop antenna feeding a three-level radiofrequency transient-event counter was located near the sample and served to count discharges and sort them by amplitude. Also located near the sample and visible in figure 1 in the upper right corner was a gaseous-nitrogen plasma source that was used to neutralize the surface charge on the sample.

The vacuum tank is a horizontal steel cylinder 19 meters long and 4.6 meters in diameter pumped by 20 liquid-nitrogen-baffled 91-centimeter-diameter oil diffusion pumps. It was comfortably operated at approximately 2.7×10^{-8} N/m^2 (2×10^{-6} torr) for these tests and has a no-load pressure of approximately 1.3×10^{-9} N/m^2 (10^{-7} torr).

Test Procedure

In the 50-ohm configuration the samples were exposed sequentially to 10-, 15-, and 20-kilovolt beams. The imbedded charge was neutralized with the plasma source between exposures. The sample was irradiated at each voltage for a short time (15 to 60 sec), and the surface voltage profiles were measured over the entire sample area at the end of each interval. At 10-kilovolt exposure the three samples were charged to equilibrium (fig. 3) with the sample ground

completed through the electrometer (fig. 2). At 15- and 20-kilovolt exposures the samples did not charge to equilibrium but began exhibiting breakdowns when the maximum surface voltage was as low as 8.5 kilovolts. With the ground switched from the electrometer to the 50-ohm termination, the return-current pulses were recorded until a representative group had been assembled. As the last procedure in the run, the electron beam was turned off just before the next predicted breakdown and the surface voltage profiles were measured. The beam was then turned back on until the next discharge and then immediately turned off and the surface resurveyed. These data give the total charge on the surface before and after a discharge.

After this sequence of measurements was made for the three samples, they were remounted in the low-impedance configuration, and their discharge behavior was remeasured at both 15- and 20-kilovolt electron fluxes.

RESULTS

Charging

Figure 3 is a typical time history of the charge buildup on a 232-square-centimeter sample in a 10-kilovolt electron beam. The voltage profiles were taken with the probes passing across approximately the middle of the sample. The individual strips of tape are revealed by the sharp dips on the surface voltage at the seams, where the tape strips are butted.

During the initial stages of charging, the distribution of charge on the surface should mirror the actual flux distribution (assuming, of course, that the surface properties are uniform over the sample). The observed variation of the surface voltage with the position of the 232- and 1265-square-centimeter samples is consistent with the measured ±30 percent variation of the beam flux over the sample plane. The largest sample (5058 cm^2) shows a somewhat wider variation, the origin of which is undetermined. All three samples at equilibrium exhibit a uniform profile except for the gaps and a characteristic falloff at the edges.

The equilibrium voltages at the center were 8.0, 7.2, and 7.6 kilovolts for the 232-, 1265-, and 5058-square-centimeter samples, respectively. The voltage profiles at equilibrium, in all three cases, do not exhibit complete bilateral symmetry. All are skewed in the same way, suggesting a lack of symmetry in the experimental arrangement as the cause.

Figure 4 shows the normalized voltage profiles, where the distance x is scaled by the half-width w of the sample and the voltage V by the maximum voltage V_m. In these reduced coordinates the three samples are, to first order, identical if the seams are ignored. This observed scaling with sample width is inconsistent with the model proposed by Parks and Mandell (September 1976 Monthly Progress Report on NASA Contract NAS3-20119, Systems, Science, and Software) and used by Stevens, et al. (ref. 4) to fit their edge-gradient data. Their model considers surface and bulk resistance along with a one-dimensional current-balance description (ref. 5) to predict the edge profiles. The in-

ability of the Parks-Mandell model to predict something as fundamental as the observed scaling indicates that the dominant physical mechanism that controls the edge profile has not been incorporated. Multidimensional effects are the most obvious possibilities. In particular, the spreading of the beam due to the finite width of the sample should be considered. The deflection of the incoming particles will certainly be greater for larger samples.

Discharging

Discharge phenomenon in these samples were studied at beam voltages of 15 and 20 kilovolts. Discharging seemed to begin when the maximum sample voltage was as low as 8.5 kilovolts. These early discharges were characterized by their small size relative to the more typical breakdowns. Figure 5 is a time history of the breakdown behavior of the 232-square-centimeter sample, which is typical. The voltage profiles were taken acros approximately the center of the sample and transverse to the tape direction.

The seams are apparent in figure 5(a) as two small dips. The probe sweeps over a 4-kilovolt calibration bar at the end of its travel. Figure 5(a) shows the profile after 215 seconds of charging with a 15-kilovolt electron beam. Figure 5(b) shows the same profile just after the first breakdown and 270 seconds after the start of charging. The breakdown is evident as a charge-depleted region around the left tape seam. The extent of this charge-depleted region along the seam direction is shown in figure 6. The only two sweeps that show depletion are figures 6(c) and (d), demonstrating that the length of the depleted region is no more than 768 centimeters long and is away from the ends of the sample. Figure 5(c) shows the profile after further charging; no breakdowns were observed on the arc counter or the current monitors. The overall voltage level is higher than in figure 5(b) and the charge-depleted region is filling in. Figure 5(d) shows the profile taken after 370 seconds of charging and immediately after the second observed breakdown. This profile, when compared with figure 5(c), indicates that both seams broke down. Figure 5(e) shows the same profile after 600 seconds of charging and before the next breakdown which occurred at 665 seconds. The results of that breakdown are shown in figure 5(f). Before this breakdown, the maximum surface voltage increased over that in figures 5(c) and (d) and almost total charge cleanoff resulted. Almost total charge cleanoff is typical of the behavior of this size sample for most of the subsequent breakdowns.

Qualitatively, the preceding sequence of events is analogous to the behavior seen commonly on high-voltage insulators when they are initially brought up to their working voltage. In this case, gaps that before breakdown have the largest voltage gradients (electric fields) break down initially at low voltages and, by depleting the charge near them, reduce the locally high electric field. The regions away from the gaps can then charge to even higher voltage until the next most sensitive high-electric-field-region breaks down. This allows the sample voltage to go even higher. This process continues until there are many sites similarly sensitive and quasi-repetitive behavior sets in.

Figure 7 shows three examples of the more typical return-current pulses I resulting from the discharge of the 232-square-centimeter sample. Figures 7(a)

and (b) show data taken with the 50-ohm grounding configuration at 15 and 20 kilovolts, respectively. Figure 7(c) shows a typical pulse with the low-impedance grounding configuration. The vertical gain is a factor of 2 smaller than in figures 7(a) and (b). A most distinctive characteristic of this sample when tested in the low-impedance configuration is the appearance of a positive precursor. That is, there is an initial downward spike that represents a positive current leaving the sample. Here, and in all the return-current-pulse data shown, a signal greater than zero represents a current of negative charge leaving the surface (ref. 6). Only this sample, in this configuration, exhibited a positive precurser and it always did. However, the net charge leaving the surface was always negative, as in the other samples. This positive precurser may be related to the positive charge bursts reported by Yadlowsky (ref. 7). He observed both positive and negative charge bursts with different time evolutions in breakdowns in bulk Teflon. This would suggest that such currents of both positive and negative particles are contributing to give the result reported here.

Figure 8 shows some typical return-current pulses from the 1265-square-centimeter sample. They have been chosen to demonstrate the range of sizes and shapes observed. The nonrepeatability of the shape, the wide variety of sizes, and the general lumpy quality of the pulses suggests that they are composites of many small breakdowns. The low-impedance pulses (figs. 8(c), (d), and (e)), though similar in overall shape, have higher frequency noise components than the 50-ohm pulses. Figure 9 shows some pulses from the 5058-square-centimeter sample. The same comments concerning the variability of size and shape that were made about the 1265-square-centimeter sample are appropriate here.

For the purpose of discussing area effects the individual return-current pulses are described by three parameters: the maximum current I, the total charge Q, and the time Δt, where Δt is defined as the width of the pulse at $I/2$. Except for the first few discharges that were described earlier, there was no evident systematic dependence of these parameters on the discharge history. A distribution function for these parameters was constructed by choosing a narrow interval of the variable and plotting the fractional number of events occurring in the interval. A smooth curve was then drawn through the point.

Figure 10 is an example of such a distribution function for the peak value I of the return-current pulses observed with the 1265-square-centimeter sample at 20 kilovolts with the low-impedance grounding configuration. The horizontal bar indicates the current interval.

These distributions were characterized by three parameters: the largest value of the parameter observed, denoted by the subscript M; the value of the parameter at the peak of the distribution function, which can be thought of as the most probable value, denoted by the subscript MP; and, finally, the width Δ of the distribution function at $1/2$ the MP value. Table I contains the reduced data arranged by area, beam voltage, and grounding configuration. The last two columns give the total number N_T of discharge pulses recorded and analyzed for both grounding configurations. The small number of pulses studied in the low-impedance, 15-kilovolt, 232-square-centimeter case resulted from a reluctance of the sample to break down under these conditions.

Figure 11 shows the data for the maximum current I_M observed as a function of area for the two grounding configurations and beam voltages. It was expected that the area dependence of this current would be of interest because it is a worst-case parameter. Where it seemed appropriate, a least-squares fit was drawn through the three points. The 20-kilovolt, 50-ohm data fit an $I_M = 14.3\ (A)^{0.25}$ line, where A denotes area. The low-impedance data at either beam voltage does not lend itself to a single-term power-law description, and straight lines are used to connect the points. The area scaling exhibited by the 20-kilovolt, 50-ohm data is weaker than the $(A)^{0.575}$ reported by Balmain (ref. 1) for smaller samples. It is difficult, however, to compare his work directly with that reported here since his grounding was different, his statistical treatment of the data was not the same, and his current density was three orders of magnitude larger. However, his data do extrapolate in close agreement with the low-impedance, 20-kilovolt, 232-square-centimeter point.

Two qualitative observations should be made about the maximum-current data in figure 11. First, in agreement with A. Rosen of TRW (private communication), the grounding configuration had a significant effect on the behavior. For example, at 20 kilovolts significantly larger currents were observed with the low-impedance ground than with the 50-ohm ground. However, 15 kilovolts the opposite is true. Second, both the 50-ohm and low-impedance data exhibit a weaker area dependence with a 15-kilovolt beam than with a 20-kilovolt beam.

Figure 12 shows the most probable peak current I_{MP} as a function of sample area in the same format as in the previous figure. The same strong dependence of the behavior of this parameter at 15 kilovolts on the nature of the grounding is observed. At 20 kilovolts the area dependence of I_{MP} is clearly much weaker than that exhibited by I_M. In fact, it would seem that to a first approximation, I_{MP} is independent of the area.

Figure 13 shows the maximum charge Q_M in the same format as in the two previous figures. At 20 kilovolts both grounding configurations show good least-squares fits to $Q_M = K(A)^{0.78}$, where K is a constant. The low-impedance configuration gave a somewhat larger value of K (0.38) than the 50-ohm configuration (0.30). The 15-kilovolt, 50-ohm data (fig. 13(b)) are fit (rather poorly) by $Q_M = 0.75\ (A)^{0.65}$, which is weaker than the 20-kilovolt scaling. But, given the quality of the fit, no conclusion can be drawn concerning the beam-voltage dependence of the exponent.

Figure 14 shows the most probable charge Q_{MP} as a function of area. At 20 kilovolts the dependence of this parameter on area is significantly weaker than that of Q_M, but at 15 kilovolts its behavior is similar to that of its Q_M counterpart. Both the Q_M and Q_{MP} data show the same sensitivity to the grounding configuration as does I_M in that, at 20 kilovolts, a low-impedance ground increases the charge over the 50-ohm value but at 15 kilovolts it decreases it.

Figure 15 shows the maximum discharge time Δt_M as a function of area. All four sets of data fit $\Delta t_M = K(A)^x$ very well. The values of K and x for the four cases are given on the figure. The 50-ohm data for both voltages

show that Δt_M scales approximately as the first power of the area, but the low-impedance data exhibit significantly weaker scaling.

Figure 16 shows the data for the most probable discharge time Δt_{MP}. The 20-kilovolt data in both grounding configurations fit $\Delta t_{MP} = K(A)^x$ in a convincing way, but with values of x significantly smaller than in the Δt_M cases. It appears that Δt_{MP} scales approximately as the square root of the area. This dependence suggests that a characteristic linear dimension may control the breakdown behavior. If it is assumed that the most probably breakdown starts somewhere in a seam, propagates along it at constant velocity, and is limited by the length of a single seam, the coefficient K can be interpreted as $1/2fv$, where v is the propagation velocity. The factor 2 is approximate and is inserted because the most probable pulse would start somewhere near the middle and propagate in both directions, f is a correction that would convert Δt to the total time the pulse propagates down the gap. A model of the discharge process that could predict the return-current-pulse shape is required to accurately evaluate f. Such a model does not exist, but f is assumed to be near 2. Within the limit of this crude description, the propagation velocity v is approximately 1.5×10^7 cm/sec for the 50-ohm data.

Discharge Phenomenology

A consideration of the basic physics of the discharge process in the geometry being studied here immediately calls to question the meaning of the pulse-current measurements described in this paper. Figure 17 schematically describes the experimental situation. In the figure, Q_{before} and Q_{after} are the net charge in the surface of the sample just before and just after the breakdown, respectively; Q_{pulse} is that part of the charge that goes to the baseplate in such a way as to go through the meter; and Q_{short} is that part of the charge that goes to the baseplate without going through the meter. Two contributions to Q_{short} are shown. The lower one corresponds to charge going around the edge of the sample and the upper one, which may be the largest part, corresponds to charge going down the seam to the baseplate.

There is no way, given the present limited understanding of the breakdown process, to predict the relative sizes of Q_{pulse} and Q_{short}. Their ratio should be governed by the details of the experimental geometry, materials, etc. Further, there is reason to expect that their characteristic time evolutions (Δt, e.g.) would be different since the characteristic impedance of the two paths is not likely to be the same. Since Q_{short} would probably have the lower impedance path, its Δt may be significantly smaller than the Δt corresponding to Q_{pulse}. In this experimental arrangement there is no way to determine directly the current-time signature corresponding to Q_{short}, but its magnitude was determined by applying the charge conservation equation shown in figure 17. Any conclusions drawn from these data must be considered to be tentative since only one pulse for each area and beam voltage was considered and only the 50-ohm grounding configuration was used.

The total charge on the surface before the pulse Q_{before} and the charge after the pulse Q_{after} were determined by integrating the surface voltage

profiles over the sample area and from the known ratio of capacitance to area ($0.17\ \mu F/m^2$). The sample was treated as a parallel-plate capacitance with the surface of the Teflon as one plate and the silver the other.

Figure 18 summarizes the data for the three charges - Q_{after}, Q_{pulse}, and Q_{short} - as a function of area for the two beam voltages. The charges are expressed as a fraction of Q_{before}. The data in figure 18(a) demonstrate that almost complete charge cleanoff occurs for the 232-square-centimeter sample, but the larger samples show that there is a tendency to saturation at a Q_{after}/Q_{before} of about 0.3. The fraction in the observed pulse Q_{pulse}/Q_{before} seems to drop from about 0.4 for the smallest area to about 0.3 at the largest area. The fraction in the unobserved pulse Q_{short}/Q_{before} starts at about 0.5 and drops to 0.3 or 0.4 at the largest area. Most importantly, it is certainly of the same order as Q_{pulse}/Q_{before} at all areas studied. This result clearly demonstrates that the experimental characterization of discharge behavior in ground tests such as are described in this paper must be done in a manner that considers the contribution of Q_{short} if results useful for extrapolation to spacecraft behavior are to be obtained.

CONCLUDING REMARKS

The charging and discharging characteristics of large-area samples of silvered Teflon tape presented herein demonstrate a complex behavior. These results are preliminary. There is much work to be done and many avenues to explore before an unambiguous picture can emerge. Even at this stage of the investigation, however, some definite conclusions can be drawn.

The 10-kilovolt charging data demonstrate that the edge-voltage profiles scale with the width of the sample. This implies that the existing one-dimensional model, which invokes bulk and surface currents, is incomplete and that multidimensional effects such as beam spreading must be included in any realistic model of insulator charging.

The discharge pulse data demonstrate that the grounding configuration is of real significance. It modifies both the magnitudes of the discharge parameters and in most cases their apparent scaling with area. The same statement can be made about the effect of beam voltage. This is a clear warning that tests with distributed fluxes and spacecraft-like configurations may be mandatory for a realistic simulation of spacecraft materials discharging behavior.

The first few discharges always take place at seams, in the high-voltage region of the sample. However, the role of seams in typical breakdowns is not completely clear. (This study does not distinguish clearly between seam-length effects and area effects since, for these samples, the seam length scales to a first approximation directly as the area.) This ambiguity can and should be resolved by measurements with solid insulator films.

The charge-balance results demonstrate that measuring only the return-current-pulse characteristics does not adequately define the behavior of these

materials for spacecraft applications. Consideration must be given to the magnitude and time evolution of Q_{short}. The time evolution of Q_{short} may not be related in any simple way to the observed time evolution of the return-current pulse.

Although the maximum peak currents continue to increase with area ($I \sim A^{0.4}$), the observation that the most-probable peak currents seem to be nearly independent of area suggests that there may be some limiting sample area that contributes to a pulse. Very large areas may also exhibit peak currents that appear area independent since the highest current pulse may continue to scale, but the probability of a high pulse being observed may decrease.

The discharge propagation velocity of 1.5×10^7 cm/sec extracted from these data could provide a clue to the nature of the dominant physical phenomenon controlling the discharge process.

REFERENCES

1. Balmain, K. G.; Kremer, P. C.; and Cuchanski, M.: Charged Area Effects on Spacecraft Dielectric Arc Discharges. Proceedings of 1978 Symposium on the Effect of the Ionosphere on Space and Terrestrial Systems. Office of Naval Research and Naval Research Laboratory, 1978, Session IV, pages 4-5.

2. Bogus, K. P.. Electrostatic Charging Effects on Deployable Solar Arrays. Presented at the Workshop on Space Technology, (DERTS, Toulouse, France), July 1977.

3. Berkopek, F. D.; Stevens, N. J.; and Sturman, J. C.: The Lewis Research Center Geomagnetic Substorm Simulation Facility. Proceedings of the Spacecraft Charging Technology Conference. C. Pike and R. K. Lovell, eds., AFGL-TR-77-0051 and NASA TM X-73537, 1977, pp. 423-430.

4. Stevens, N. J.; Purvis, C. K.; and Staskus, J. V.: Insulator Edge Voltage Gradient Effects in Spacecraft Charging Phonomena. NASA TM-78988, 1978.

5. Purvis, C. K.; Stevens, N. J.; and Oglebay, J. C.: Charging Characteristics of Materials. Comparison of Experimental Results and Simple Analytical Models. C. Pike and R. K. Lovell, eds., AFGL-77-0051 and NASA TM X-73537, 1977, pp. 459-486.

6. Adams, R. C.; and Nanevicz, J. E.. Spacecraft Charging Studies of Voltage Breakdown Processes on Spacecraft Thermal Control Mirrors. Spacecraft Charging by Magnetospheric Plasmas, A. Rosen, ed. Progress in Astronautics and Aeronautics, vol. 47, 1975, pp. 225-235.

7. Yadlowsky, E. J.; Hazelton, R. C.; and Churchill, R. J.. Puncture Discharges in Surface Dielectrics as Contaminant Sources in Spacecraft Environments. (Colorado State Univ.; NASA Contract NSG-3145.) NASA CR-157105, 1978.

TABLE I. - REDUCED DATA ON INDIVIDUAL RETURN-CURRENT PULSES

Sample area, cm^2	Beam voltage, kV	Grounding configuration[a]																			
		50 Ω	LI	50 Ω	LI	50 Ω	LI	50 Ω	LI	50 Ω	LI	50 Ω	LI	50 Ω	LI	50 Ω	LI	50 Ω	LI	50 Ω	LI
		Maximum current, I_M, A		Most probable current, I_{MP}, A		Most-probable-current interval, ΔI_{MP}, A		Maximum total charge, Q_M, μC		Most probable total charge, Q_{MP}, μC		Most-probable-total-charge interval, ΔQ_{MP}, μC		Maximum discharge time, Δt_M, μsec		Most probable width of pulse at I/2, Δt_{MP}, μsec		Most-probable-width interval, $\Delta(\Delta t_{MP})$, μsec		Total number of discharge pulses recorded and analyzed, N_T	
5058	20	240	330	52	63	125	250	260	340	30	135	130	130	3.6	2.7	1	1	0.7	1	36	25
	15	128	32	108	20	80	25	225	75	155	25	80	65	3.5	4	1.4	1.4	.25	.9	38	16
1265	20	110	138	63	50	50	100	68	80	50	50	65	100	1.1	1.3	.6	.6	.4	.4	15	26
	15	73	45	60	20	40	25	50	65	38	20	25	35	1	2.1	.5	.7	.4	.4	11	25
232	20	62	140	55	135	30	25	23	30	13	30	25	25	.25	.4	.22	.28	.02	.1	12	22
	15	60	23	58	22	2	2	32	7	25	5	10	5	.2	.95	.2	.85	0	.2	10	2

[a]50 Ω denotes 50-ohm grounding configuration (fig. 2); LI denotes low-impedance grounding configuration (fig. 2).

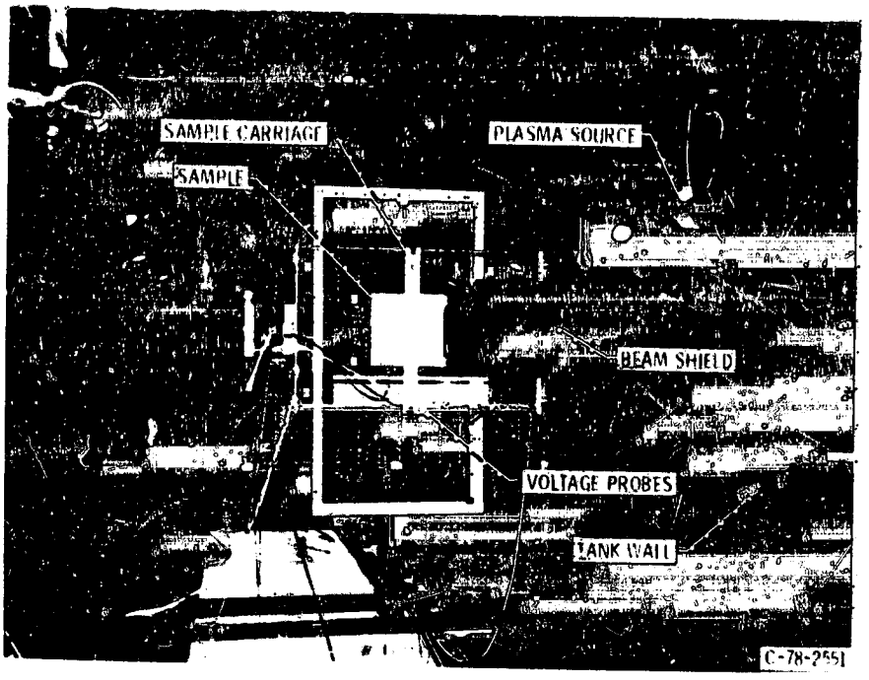

Figure 1. - Vacuum-tank interior and experimental arrangement.

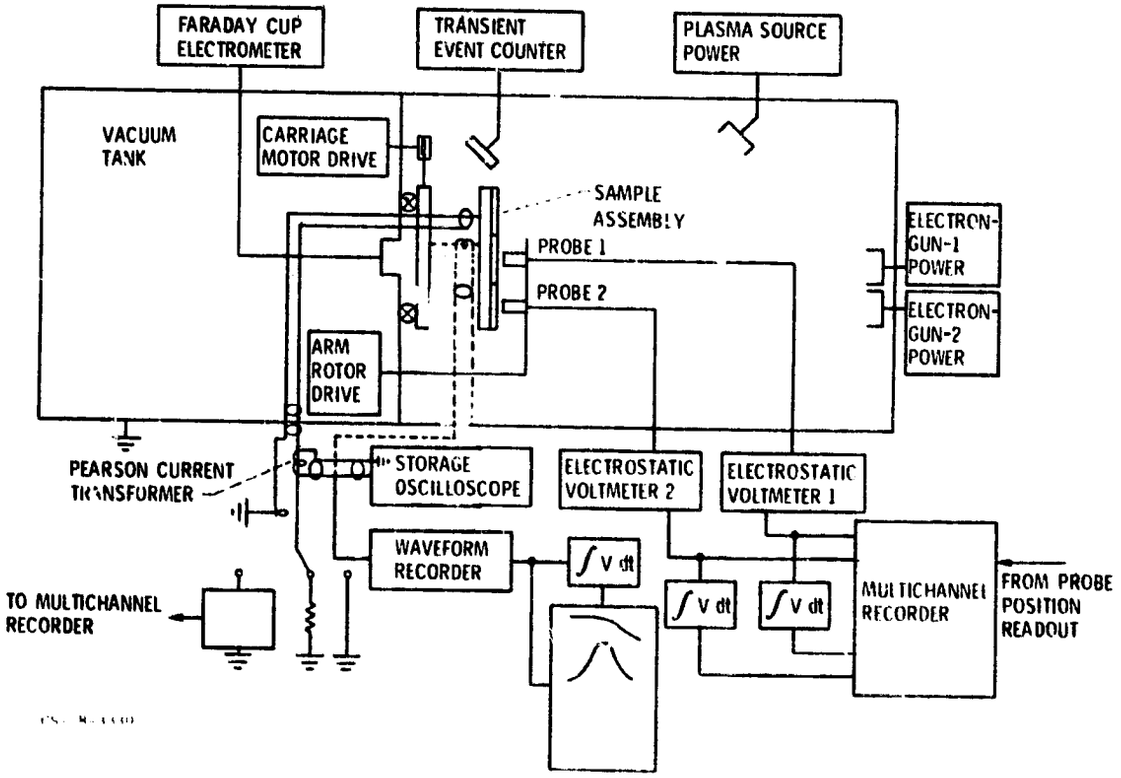

Figure 2. - Area-effects test facility.

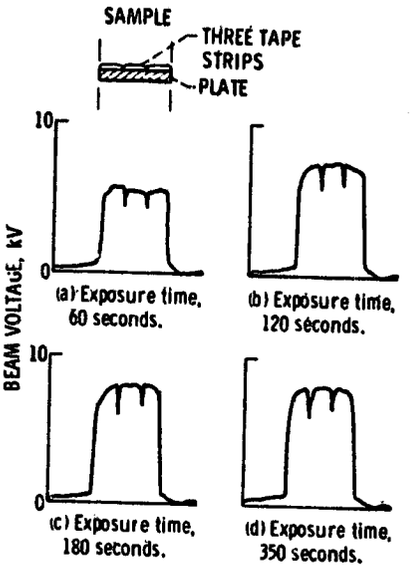

Figure 3. - Voltage profiles for 232-square-centimeter sample and 10-kilovolt beam.

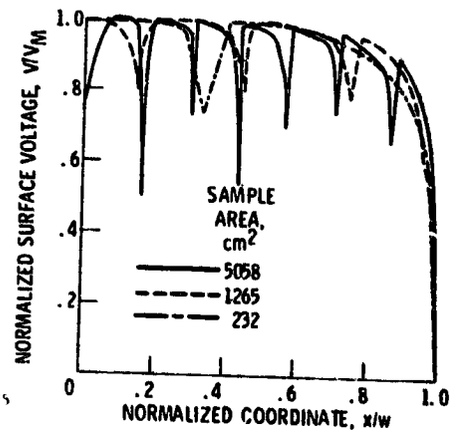

GS-78-3125

Figure 4. - Equilibrium surface-voltage profiles - normalized.

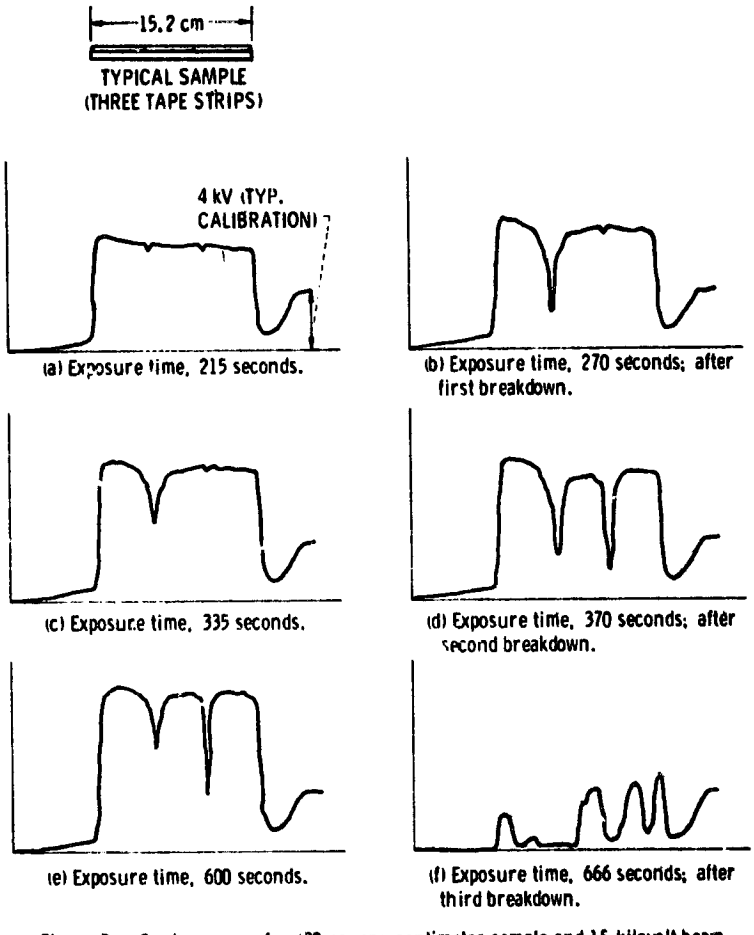

(a) Exposure time, 215 seconds.

(b) Exposure time, 270 seconds; after first breakdown.

(c) Exposure time, 335 seconds.

(d) Exposure time, 370 seconds; after second breakdown.

(e) Exposure time, 600 seconds.

(f) Exposure time, 666 seconds; after third breakdown.

Figure 5. - Center sweeps for .32-square-centimeter sample and 15-kilovolt beam.

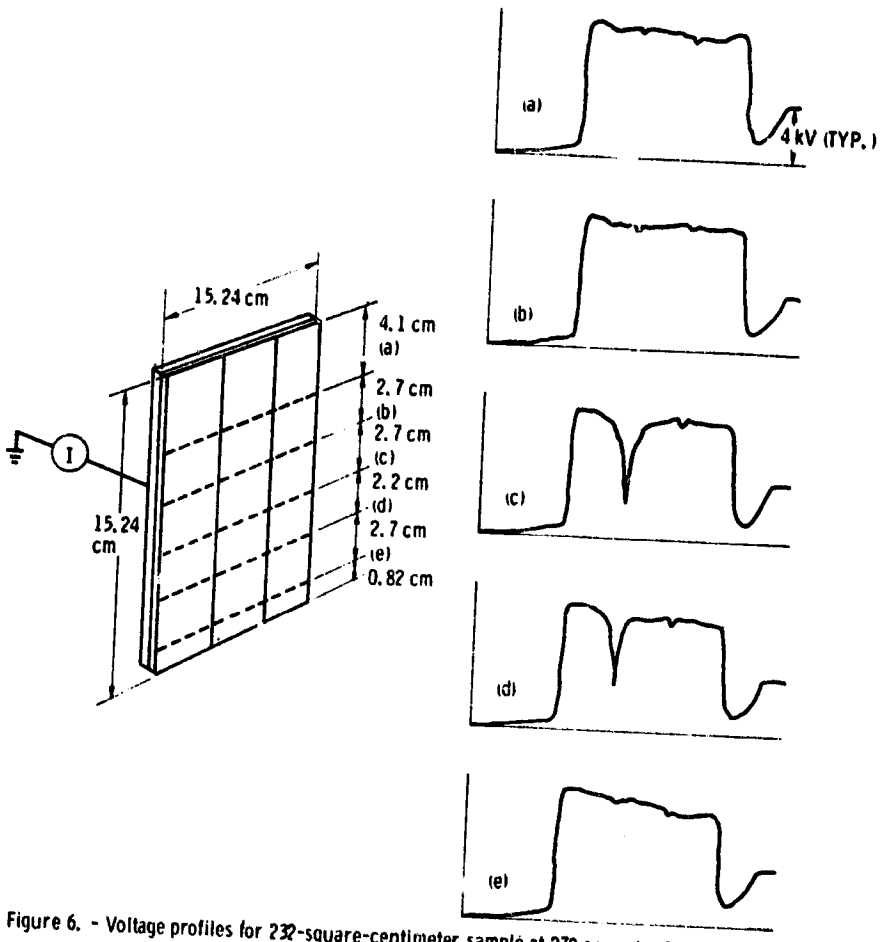

Figure 6. - Voltage profiles for 232-square-centimeter sample at 270 seconds of charging.

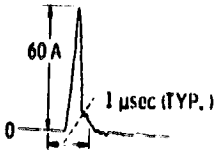

(a) 50-Ohm grounding configuration; 15-kilovolt beam.

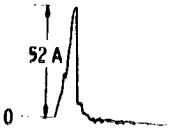

(b) 50-Ohm grounding configuration; 20-kilovolt beam.

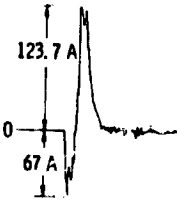

(c) Low-impedance grounding configuration; 20-kilovolt beam.

Figure 7. - Return-current pulses for 232-square-centimeter sample.

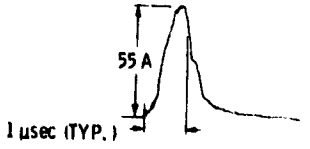

(a) 50-Ohm grounding configuration; 15-kilovolt beam.

(b) 50-Ohm grounding configuration; 20-kilovolt beam.

(c) Low-impedance grounding configuration; 15-kilovolt beam.

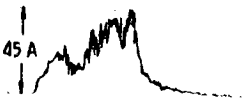

(d) Low-impedance grounding configuration; 15-kilovolt beam.

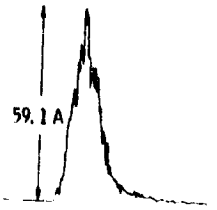

(d) Low-impedance grounding configuration; 20-kilovolt beam.

Figure 8. - Return-current pulses for 1265-square-centimeter sample.

(a) 50-Ohm grounding configuration; 15-kilovolt beam.

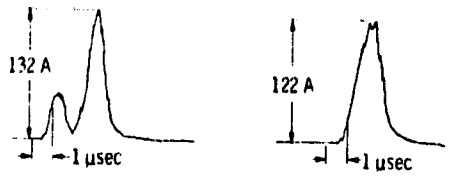

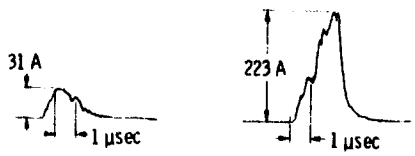

(b) 50-Ohm grounding configuration; 20-kilovolt beam.

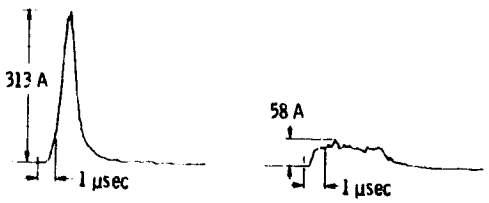

(c) Low-impedance grounding configuration; 20-kilovolt beam.

Figure 9. - Return-current pulses for 5058-square-centimeter sample.

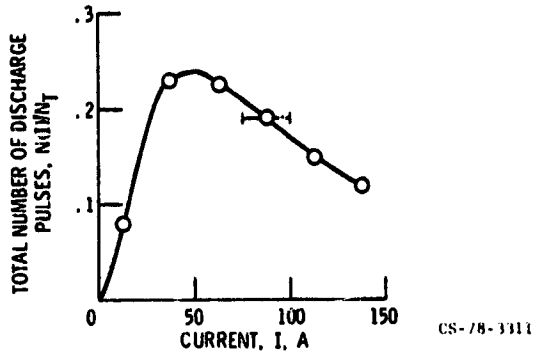

Figure 10. - Current distribution function for 1265-square-centimeter sample in 20-kilovolt beam.

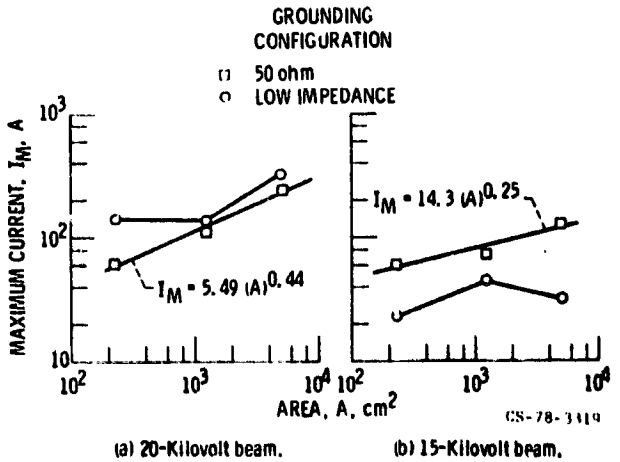

(a) 20-Kilovolt beam. (b) 15-Kilovolt beam.

Figure 11. - Maximum return current as function of area.

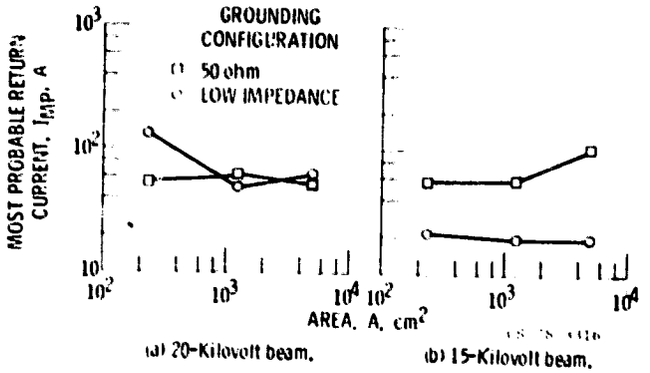

(a) 20-Kilovolt beam. (b) 15-Kilovolt beam.

Figure 12. - Most probable return current as function of area.

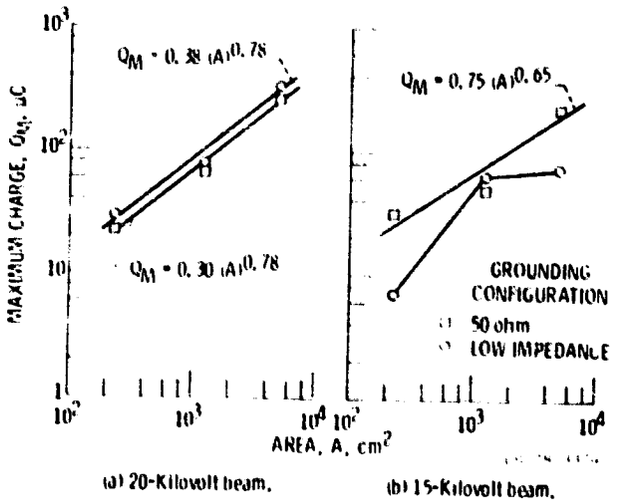

(a) 20-Kilovolt beam. (b) 15-Kilovolt beam.

Figure 13. - Maximum charge as function of area.

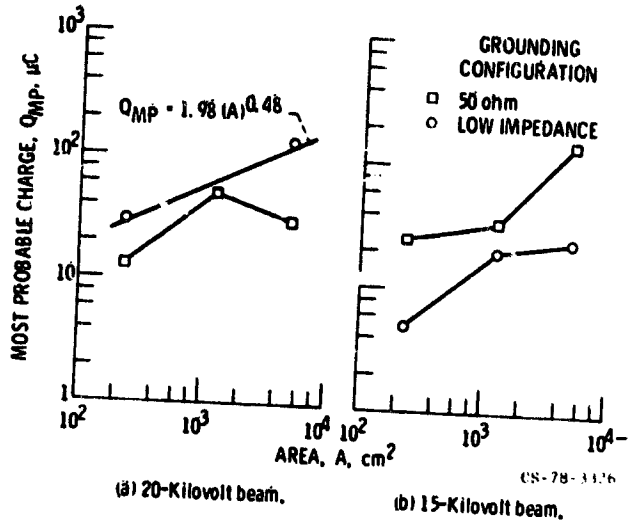

(a) 20-Kilovolt beam. (b) 15-Kilovolt beam.

Figure 14. - Most probable charge as function of area.

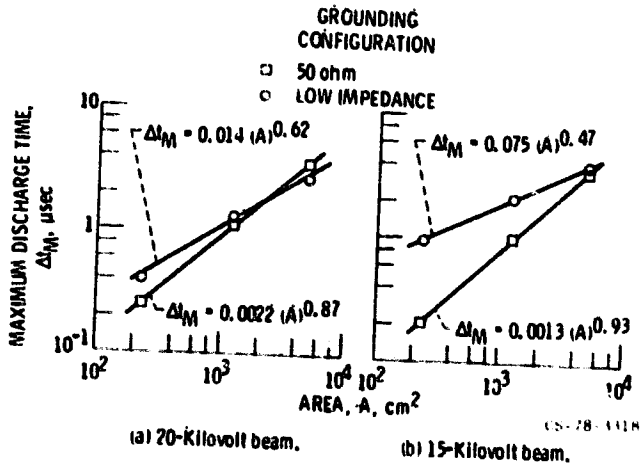

(a) 20-Kilovolt beam. (b) 15-Kilovolt beam.

Figure 15. - Maximum discharge time as function of area.

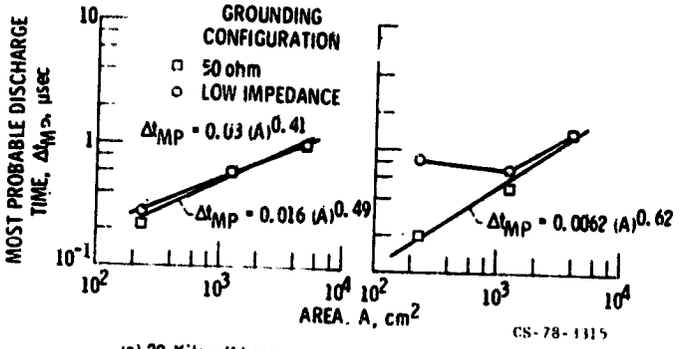

(a) 20-Kilovolt beam. (b) 15-Kilovolt beam.

Figure 16. - Most probable discharge time as function of area.

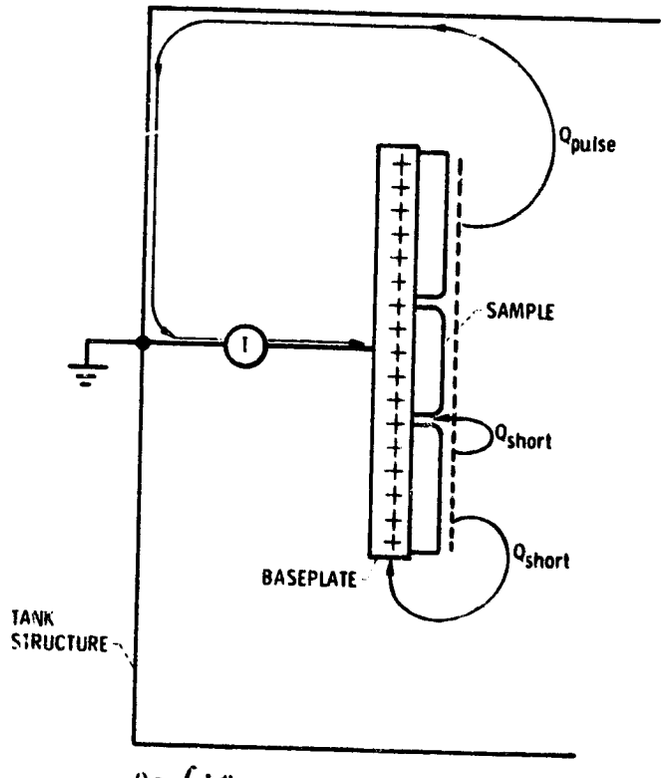

$Q = \int I\,dt$

$Q_{before} = Q_{after} + Q_{pulse} + Q_{short}$

Figure 17. - Breakdown charge distribution.

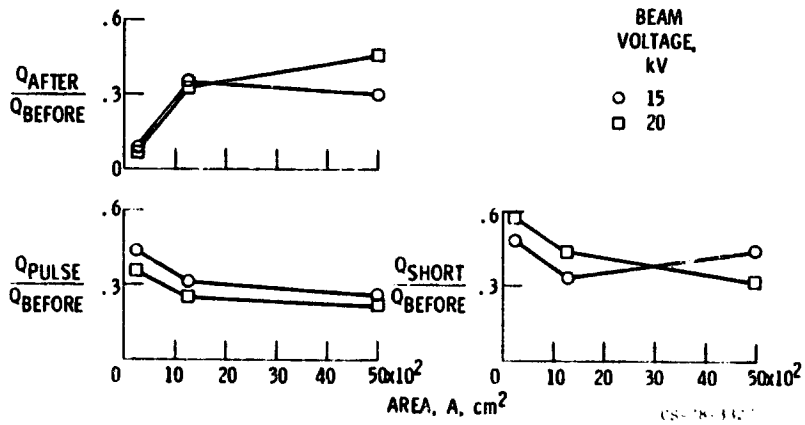

Figure 18. - Postbreakdown charge distribution.

D32

N79-24033

CHARGING RATES OF METAL-DIELECTRIC STRUCTURES

Carolyn K. Purvis, John V. Staskus, James C. Roche, and
Frank D. Berkopec
NASA Lewis Research Center

SUMMARY

Metal plates partially covered by 0.01-centimeter-thick fluorinated ethylene-propylene (FEP) Teflon were charged in the Lewis Research Center's geomagnetic substorm simulation facility using 5-, 8-, 10-, and 12-kilovolt electron beams. Surface voltage as a function of time was measured for various initial conditions (Teflon discharged or precharged) with the metal plate grounded or floating. Results indicate that both the charging rates and the levels to which the samples become charged are influenced by the geometry and initial charge state of the insulating surfaces.

The experiments are described and the results are presented and discussed. NASA charging analyzer program (NASCAP) models of the experiments have been generated, and the predictions obtained are described. Implications of the study results for spacecraft are discussed.

INTRODUCTION

Anomalous behavior of geosynchronous spacecraft has been attributed to the arc discharging of differentially charged spacecraft surfaces (ref. 1). In examining the response of a spacecraft to the charging environment, it is of interest to identify both the potentials to which various spacecraft surfaces charge and the rates at which these potentials vary in response to environmental changes. Of particular interest are the magnitudes and rates of change of the potential differences between various spacecraft surfaces.

It has been reported that the potentials (with respect to space plasma potential) of the ATS-5 and ATS-6 spacecraft structures can change rapidly by kilovolts in response to changes in the plasma environment, entry into and exit from eclipse, or the turning on or off of particle emitters (refs. 2 and 3). This is not surprising since the capacitance of these spacecraft with respect to the environment is small. The question of interest here is the effect of such changes on potential differences between spacecraft structures and insulating surface materials. Ground studies have shown that insulating films mounted on grounded substrates and subjected to bombardment by monoenergetic electron beams with current densities typical of the geosynchronous substorm environment require several minutes to reach equilibrium (refs. 4 and 5). Calculations with one-dimensional models indicate that even longer times may be

required to develop equilibrium differential charges in the actual space environment (ref. 5).

The study described in this paper was undertaken to investigate charging rates and final potentials of insulating surfaces and underlying metal portions of composite metal-dielectric structures. It is an extension of work previously reported (ref. 5). Ideas touched on in the earlier study are refined and revised on the basis of the data presented here. This paper describes the composite samples, the experiments, and their results. Predictions of the NASCAP code (ref. 6) for some of the experiments are presented and compared with the data. Implications of the results for spacecraft are discussed.

EXPERIMENT DESCRIPTION

The experiments were performed in the Lewis Research Center's geomagnetic substorm simulation facility (ref. 7). Samples were bombarded with beams of 5-, 8-, 10-, and 12-kilovolt electrons at a current density of 1 nA/cm^2. All tests were performed in the dark.

Samples Tested

Samples consisted of metal plates of aluminum alloy partially covered by strips of 0.01-centimeter-thick silvered FEP Teflon tape in several configurations. The tape was applied to the plates, silver side down, with conductive adhesive. The plates were mounted on 6.3-centimeter-long ceramic posts to provide electrical isolation. Coaxial cable leads from the plates were brought outside the tank so that the plates could be grounded to the tank structure or allowed to float electrically.

Tests were performed on samples with four different patterns of Teflon tape, shown in figure 1. All the plates were 15.2 centimeters by 20.6 centimeters and the Teflon tape was 5 centimeters wide. In the figure, crosshatched areas (labeled M) represent exposed metal and plain areas (labeled T) represent Teflon. The Teflon area is one-third the total for configuration 1, two-thirds the total for configurations 2 and 3, and the entire surface area for configuration 4.

Test Sequences

Two series of tests were run: The first used one sample of configuration 1 and one of configuration 2, and the second used one sample each of configurations 2, 3, and 4. Test sequences and quantities measured were the same for both series of tests, but diagnostic capabilities were increased for the second series.

In the first series of tests, surface voltage data were taken with a TREK Model 340 and a surface voltage probe that was mounted on a radial arm and

swept across the samples at a distance of 2 to 3 millimeters from the surface. The probe was positioned to pass across the center of the sample (series 1 probe track in fig. 1). The probe could also be stopped at any point in its sweep. Time histories of sample charging were taken both with the probe sweeping back and forth across the sample surface and with the probe stopped over the exposed metal plates. The stopped positions were chosen so that the probe's 0.95-centimeter-diameter head did not shield the Teflon from the beam.

In the second series, two TREK Model 340 HV surface voltage probes were mounted on the same swinging arm, again 2 to 3 millimeters from the surface. These probes were positioned so that the upper probe passed across the vertical centerline 4.8 centimeters above the sample center and the lower probe passed across the vertical centerline 6.6 centimeters below the sample center (series 2 probe tracks in fig. 1). Stopping the double-probe system over the exposed metal plate shielded some of the Teflon from the beam. Therefore, high-voltage leads from the plates were brought outside the tank, and a third probe arrangement was set up to monitor the plate voltages during charging. This probe monitored the plate voltages during charging both with the double probes sweeping and with them stopped well away from the sample.

All voltage data were recorded on a multichannel strip-chart recorder. The probe-arm sweep rate was set so that the probes crossed the sample in about 7 seconds. Data read from the strip chart were accurate to about ±5 percent, with a minimum error in resolution of about ±100 volts. The configuration 2 sample was tested in both test series so that effects due to differences in instrumentation could be identified.

The test sequence for each sample at each beam voltage was begun with the sample surface at zero potential (measured by the probes). The sequence consisted of the following steps:

(1) With the metal plate electrically floating, the sample was exposed to the beam and allowed to charge to equilibrium.

(2) With the beam still on, the metal plate was then grounded externally and the Teflon was allowed to charge until its surface potential reached equilibrium.

(3) Then the metal plate was electrically floated and the system allowed to charge until equilibrium was again reached.

This sequence was repeated at least twice with each sample in each series so that data could be taken with the probes sweeping and with the probes stopped. In addition, some tests were run in which fully charged floating samples were shielded from the beam during the grounding of the plates.

During the testing, particularly during the third step of the sequence, some effects were observed that were traced to nonuniformities in the electron beam or to interactions of the probes with the samples. To the extent possible, such instrumentation-related effects have been eliminated from the data reported.

EXPERIMENTAL RESULTS

In this section, test results are described and illustrated with the 5- and 8-kilovolt beam data. First, important general features of the samples' responses during the test sequence are identified in the 5-kilovolt data. Then sample responses to each step of the test sequence are considered in more detail and illustrated with the 8-kilovolt data. Except as noted, responses to the 10- and 12-kilovolt beams were qualitatively the same as those at lower beam voltages. Data points for Teflon represent probe readings at the centers of the Teflon strips. Where data from two probes were available, readings were averaged; error bars are used to indicated scatter in the data where appropriate.

The charging responses of the four test samples during the test sequence with the 5-kilovolt beam are shown in figure 2. To present the charging histories on the same time scale for comparison, the "ground plate" and "float plate" points have been plotted at 240 and 540 seconds, respectively. However, since the samples were all very nearly in equilibrium in these time frames, the illustrative value of setting the time scales equal was felt to be more important than preserving their details here.

The figure indicates several noteworthy general features of the samples' responses. First, in every instance in which rapid changes of potential occurred, the potential of the plate and that of the Teflon surface changed at nearly the same rate. That is, although absolute charging (changes in potential of the whole sample) can occur rapidly, differential charging (changes of the relative potentials of the Teflon surface and the underlying plate) takes place more slowly. This is in agreement with the concept that the rate of differential charging is controlled by the capacitance between the Teflon surface and the plate, whereas the rate of absolute charging depends on the much smaller capacitance between the sample as a whole and its surroundings. Thus, when the samples were exposed to the beam at the beginning of the sequence, the Teflon surfaces and the plates changed potential at the same rate for about the first 15 seconds. Then differential potentials began to develop. When the plates were grounded (at 240 sec in fig. 2), the differential potentials between the Teflon surfaces and the plates were maintained. The Teflon surface subsequently charged back to its equilibrium potential at a rate controlled by its capacitance to the plate. Again, when the plates were floated with the Teflon surfaces precharged (at 540 sec, in fig. 2), the initial change in plate potential was reflected in an equal change in the Teflon surface potential. In this case the Teflon surface became more negative than its equilibrium potential (overshot) and began to discharge to reestablish its equilibrium with the beam.

The second general point evident from figure 2 is that the plates charged more slowly with the Teflon precharged than with it initially uncharged. The charging rate of the plates with the Teflon precharged was affected by the relative areas of Teflon and metal exposed to the beam and, to a lesser degree, by the arrangement of the Teflon strips. Thus, the configuration 1 sample

plate charged most rapidly and the configuration 4 sample plate most slowly in the third step of the test sequence.

Finally, the Teflon surfaces in these tests always took on more negative potential than did the plates. This is consistent with observations of the charging of Teflon surfaces and bare metal plates (refs. 5 and 8). It means that the polarity of differential charging studied is one in which the insulation has a more negative equilibrium potential than does the metal "structure."

In the following sections, sample responses to the three steps of the test sequence are considered individually; the 8-kilovolt beam data are used to illustrate the behavior.

Step 1

In this step, the samples were charged from an "all zero" initial condition. The Teflon surfaces and the four sample plates responded as shown in figures 3(a) and (b), respectively. During the initial 15 seconds of charging, the plates and the Teflon surfaces of each configuration charged at nearly the same rate. Furthermore, all four configurations charged at the same rate. This is not surprising since the capacitances of the samples to their surroundings were nearly equal (measured to be 200±30 pF); the rate of absolute charging is dominated by this capacity.

The time histories of charging for the Teflon surfaces of the four configurations are very similar (fig. 3(a)). All are monotonic. The equilibrium potentials of the surfaces were all about -6 kilovolts, consistent with other measurements of Teflon samples (refs. 4 and 5).

Differences among the four configurations are shown by time histories of plate charging (fig. 3(b)). The data indicate that, after 20 to 40 seconds of charging, the configuration 1 plate was the least negative, the configuration 4 plate was the most negative, and the configuration 2 and 3 plates were at the same (intermediate) potential. The configuration 4 plate remained the most negative and, at equilibrium, had a potential only slightly less negative than the overlying Teflon surface and more negative than equilibrium potentials reported for bare plates (ref. 8). Although the charging of the configuration 1, 2, and 4 plates appeared monotonic, the configuration 3 plate reached a maximum negative potential at 20 to 40 seconds. It then decayed by about 500 volts to equilibrium.

These responses can be understood qualitatively by considering the currents to each sample as a whole and to its individual components (Teflon surfaces and metal) individually and the "capacitors" being charged by these currents. Initially, each sample charged as a whole at a rate that was determined by the total current it collected and its capacitance to its surroundings. Differential potentials between the Teflon surfaces and the plates result from charging the capacitors made up of these surfaces and requires currents to each side of these capacitors. The magnitude of the current available to charge the Teflon-to-plate capacitor must depend on the relative areas of Teflon and metal

exposed to the beam, on the differences between the secondary emission properties of the two materials, and on fields that can deflect the electrons.

In configuration 4, the plate had no direct access to the beam. The potential of the whole sample was driven by the net current to the Teflon surface. Because the plate could only collect "stray" currents (e.g., secondaries from the Teflon or beam electrons deflected by fields around the sample), there was essentially no current available to cause differential charging, and thus only a very small differential potential developed.

In configuration 3, the Teflon area was twice that of the metal plate exposed to the beam. Evidently, the Teflon area dominated the charging of the sample during the first 20 to 40 seconds of charging and caused the plate to "overshoot" (i.e., become more negative than) its equilibrium potential. At this point, the plate emitted more secondaries than it received primaries. This resulted in a net positive current to the plate, so that the negative potential of the plate was reduced.

If this description of the behavior of the configuration 3 sample plate is correct, it must be supposed that the configuration 2 sample plate also "overshoots" its individual equilibrium potential during the first 20 to 40 seconds of charging (since the relative areas of Teflon and exposed metal are the same for these two configurations). The fact that the configuration 2 plate does not discharge must then be due to the difference between the geometrical arrangements of the Teflon strips on the two samples. The exposed metal of configuration 2 was between the two Teflon strips, but the exposed metal of configuration 3 was on the edges of the sample. Since the Teflon surfaces were more negative than the plate, a potential barrier that prevented the secondary electrons from the plate from escaping existed in configuration 2. This implies that the final potential reached by the plate in this configuration was more negative than the "equilibrium potential" that this plate would have reached had it been exposed to the beam with no Teflon on it.

Step 2

In this step of the test sequence, the metal plates of fully charged samples (i.e., both the plates and Teflon surfaces charged as at the end of step 1) were grounded, and the Teflon was allowed to charge. Some tests were run in which the metal plates were grounded with the samples exposed to the beam, and some with the samples shielded from the beam. Shielded samples were grounded during probe sweeps and with the probes stopped away from the sample. (Sweeps were made before and after the grounding of the plates to determine the potentials.) Samples exposed to the beam were generally grounded during probe sweeps so that the Teflon surface potential could be observed as charging of the Teflon with the plate grounded began. Results are illustrated in figure 4 for a sample of configuration 3. In the figure, V_T represents the potential of the Teflon surface and V_M that of the plate before the plate is grounded. The crosshatched areas show the differential between the Teflon surface and the plate. The sample is sketched in along the abscissas to indicate its location. Figure 4(a) depicts probe traces (voltage readings across

the sample) taken before and after the plate was grounded and with the sample shielded from the beam. Figures 4(b) and (c) depict traces during which the plate was grounded and with the sample shielded from and exposed to the beam, respectively. In all cases, when the plate was grounded, the differential between the Teflon surface and the underlying plate was maintained, at least on the time scale of milliseconds required for the probes to sense and adjust to the change in potential. Grounding the plate is equivalent to grounding one side of a capacitor, with the other side (in this case, the Teflon surface) open circuited; the voltage across the capacitor does not change. Even if the beam is left on during the grounding of the plate, the current to the Teflon surface is too small to change the potential across the Teflon-plate capacitor noticeably in milliseconds. As shown in figure 4(c), the Teflon surface exposed to the beam began to charge after the plate was grounded, at a rate characteristic of the Teflon-plate capacitor. Charging of the Teflon surfaces with the plates grounded proceeded as in previously reported (ref. 5) charging tests of Teflon on grounded substrates.

Step 3

In this step, the plates were allowed to float electrically (by opening the ground connection) with the Teflon surface initially charged to its equilibrium potential. As has been noted (fig. 2), the plate charged negatively, causing the Teflon surface to become more negative than its equilibrium potential. Net current to the Teflon surface became positive (electrons out) so that the Teflon-to-plate capacitor was discharging while the plate-to-surroundings capacitor was charging. That is, the differential potential between the Teflon and the plate was being reduced by net electron emission current from the Teflon while the potential of the plate with respect to its surroundings was being made more negative by net electron current to the plate.

The samples' responses to step 3 of the test sequence with the 8-kilovolt beam are illustrated in figure 5. Evidently, the most important factor in determining the rate at which each sample plate charges is the area of metal exposed to the beam (fig. 5(a)). The configuration 1 plate charged most rapidly and the configuration 4 plate most slowly at every beam voltage tested. The rate at which the plate charged, in turn, determined how large an excursion from its equilibrium potential the Teflon surface made. This can be seen from 5-kilovolt data shown in figure 2; it is demonstrated more dramatically by the 8-kilovolt data shown in figure 5(b). With an 8-kilovolt beam (and also with the 10- and 12-kV beams) the potential of the configuration 1 plate changed rapidly during the first few seconds of charging. Its potential exceeded (in magnitude) the difference between the Teflon surface potential and the beam voltage (~-2 kV) before the differential between the plate and the Teflon surface had time to change. The net result was that the Teflon surface potential exceeded the beam voltage. When this happened, the electrons from the beam no longer reached the Teflon surface and the "capacitor plate," which is the Teflon surface, was effectively open circuited. The differential between the Teflon surface and the plate was maintained during the plate's charging. Probe measurements made 15 to 30 minutes later in the test sequences showed no change in this situation. The same results were obtained for this sample with the

probe sweeping across the surface and with it stationary. Clearly, this behavior cannot be expected in space, where ions and higher energy electrons preclude the possibility of a true "open circuit" situation. However, it does indicate that insulating surfaces can be driven far more negative with respect to the environment than their equilibrium potentials.

At the opposite extreme, the configuration 4 sample charged so slowly that with an 8-kilovolt beam (and also the 10- and 12-kV beams), the Teflon surface did not depart noticeably from its equilibrium potential (i.e., had maximum excursions of <100 V).

Charging rates for the plates of configuration 2 and 3 samples were intermediate between those of configurations 1 and 4. As shown in figure 5(a), the configuration 2 sample plate charged slightly faster than did the configuration 3 plate with the 8-kilovolt beam. The difference in charging rates of these two sample plates is more marked with the 5-kilovolt beam (fig. 2) but appears to decrease with increasing beam voltage (i.e., for the 10- and 12-kV beams). One can argue that the configuration 2 sample plate was expected to charge more quickly than the configuration 3 plate because of the trapping of the secondaries emitted by the plate in the configuration 2 sample. The reason for the decrease in the difference between charging rates of these two sample plates with increasing beam voltage is not clear. It might be due to the secondary yield decreasing with increasing impact energies for kilovolt primaries. This would reduce the number of secondaries available to be trapped and consequently reduce the difference between the currents to the plates in the two configurations. ...

The Teflon surfaces on the configuration 2 and 3 samples behaved in a similar fashion at all beam voltages tested. In each case the initial rise in plate potential caused the Teflon surface to become more negative than its equilibrium potential, and it proceeded to discharge slowly back to equilibrium as the plate charged. The plates for these samples charged slowly enough that the Teflon surface potential remained less (in magnitude) than the beam voltage by at least several hundred volts and was therefore able to discharge toward equilibrium.

NASCAP MODELS

The NASA charging analyzer program (NASCAP) is a computer code developed to calculate the charging of objects in three dimensions. The code and its capabilities are described elsewhere (refs. 6, 8, and 9). For this study, objects were defined in the code to represent the configuration 2 and 3 samples tested. Grid spacing was chosen to reflect the relative sizes of the samples and the test chamber, with the minimum number of grid points that gave a reasonable resolution on the sample. This choice and that of the time stepping option used were made to minimize computer time (rather than to maximize simulation accuracy). Simulations were run according to the "test tank" mode of code operation.

NASCAP Objects

Three objects were defined in the code for this study; they are illustrated in figure 6. Each object is composed of two metal plates that are one mesh unit thick and have one-mesh-unit spacing between them (fig. 6(a)). The "back" plate (i.e., the one farther from the electron gun) was held at ground potential during the simulation. Capacitance between the two plates was set at 200 picofarads to simulate the measured 200±30-picofarad capacity of the actual samples to their surroundings. The "front" plates that were exposed to the beam were defined to represent a bare metal plate (object 1, fig. 6(b)), and the configuration 2 and 3 samples (objects 2 and 3, figs. 6(c) and (d), respectively) described earlier. Each plate was six by eight surface cells in area and one cell thick. The grid points were 2.54 centimeters apart in the innermost mesh in the code. Thus the objects modeled were 15.2 centimeters by 20.3 centimeters, but the actual samples were 15.2 centimeters by 20.6 centimeters. The small difference in actual and modeled size should have had very little impact on the results. The bare metal plate was used to compare the behavior of plates with and without surface insulation. Teflon surface cells labeled "X" in figures 6(c) and (d) are those cells for which current and voltage information was printed during simulations. Figures 7 and 9 show the average values for these cells.

For the simulations in this study, standard NASCAP properties were used for the Teflon. The metal plates were modeled as aluminum, but with a secondary-electron emission coefficient of 2.6 and primary-electron energy to produce maximum secondary-electron yield for normal incidence of 350 electron volts to describe the yield of true secondary electrons. These choices are based on the results of a study in which the predicted and measured charging behaviors of materials were compared (ref. 8).

NASCAP runs were made to simulate the test sequences (steps 1, 2, and 3 in the section EXPERIMENT DESCRIPTION) for the configuration 2 and 3 samples with 8- and 10-kilovolt beams.

Simulation Results and Comparison with Data

Results of the NASCAP simulations of step 1 of the test sequence are shown in figure 7 for the 8-kilovolt beam case for objects 2 and 3. Data for configuration 2 and 3 samples are included for comparison. The code predicted that samples charge somewhat more slowly than the data indicate. However, overall agreement seems rather good. In particular, the potential of the object 3 plate was predicted to reach a maximum negative value and then decline in magnitude, as is observed in the data. The potential of the object 2 plate does not decline, again in agreement with observation. The code output indicates that this is due to suppression of the secondary electron emission from the plate by local fields in the case of object 2, as was surmised earlier. It was also speculated earlier that the plate may have "overshot" its equilibrium potential for these two sample configurations. This speculation is supported by the predicted charging histories of the metal plates of three objects shown in figure 8. Plates of objects 2 and 3 reached their maximum negative potentials

about 600 volts larger in magnitude than their equilibrium values. Object 3 plate discharged to equilibrium potential after about 8 minutes total charging time; object 2 plate remained "too negative" as a result of trapping of secondaries. This illustrates the kind of insights into charging behavior that NASCAP can provide.

At the beginning of the simulation of step 2, the plate was grounded and the potentials were recalculated "immediately" afterwards (actually the code takes a 0.001-sec time step). Again, predictions are in accord with the data: Differential potential between the Teflon surface and the plate was maintained. Charging of the Teflon back to equilibrium proceeded as expected. Again, the code predicted charging to occur more slowly than was observed, but the discrepancy was not great.

Predictions for step 3 of the test sequence are much less satisfactory; the predicted rate of charging in this step was much less than the observed rate. This is illustrated in figure 9 for object 2 (configuration 2 data) with a 10-kilovolt beam. The reasons for this are not presently understood. It may be that simulation inaccuracies due to choices of grid size and time stepping option are increased by the presence of large fields due to the precharged Teflon surfaces. Another possibility is that portions of the physics not modeled in the code are more important in this step of the test sequence than in others.

Despite the discrepancy between observed and predicted charging rates with the Teflon precharged, the code does predict the general features of the data, that is, that the initial charging of the plate causes the Teflon surface to become more negative than its equilibrium potential and subsequently to discharge toward this potential as the plate charges.

SUMMARY OF RESULTS AND CONCLUSIONS

The charging response of composite metal-dielectric structures has been investigated experimentally and simulated with the NASCAP code. Overall, the code's predictions were in good agreement with the data, particularly considering the uncertainties in the material properties used as input (ref. 8). Discrepancies in the time response do indicate, however, that caution should be used in predicting behavior of objects with large differential potentials between adjacent surface grid points. The code's predictions can be used to provide insight into charging response. Several features of the charging response of the composite samples have interesting implications for the charging behavior of spacecraft.

Although potentials on an entire object can change rapidly in response to changes in its environment, differential potentials across thin insulators change much more slowly. The rate of absolute charging depends on the capacitance of the entire object to its environment and the net current it receives from the environment. The rate of differential charging between an insulating surface and the structure beneath it depends on the capacitance between them and the net difference in currents to the two "plates" of this capacitor. The

currents available to charge these various "capacitors" depend on the relative surface areas of materials available to collect current from the environment, on the properties of these materials (such as secondary emission and resistivity) and their electrical interconnection, on local fields that can trap low-energy emitted particles, and on any "artificial" sources such as particle emitters. Factors that determine these currents affect both the rates at which the various "capacitors" charge and the potentials at which equilibrium with the environment is attained.

The capacitance of the spacecraft to its environment depends on its overall size, but the capacitances of various parts of the spacecraft to one another depend on the spacecraft's construction. In general, the spacecraft-to-environment capacitance is usually orders of magnitude less than the surface-to-surface capacitances. This means that sudden changes in the potential of a spacecraft do not result in sudden large changes in potentials across thin insulation. Thus, such operations as activating an electron emitter do not present an immediate arcing hazard to thin insulation. However, if there are insulating structures on the spacecraft that have small capacitances to the structure, these will charge back to their equilibrium potentials much more quickly than the thin insulators with large capacitances to the structure. This gives rise to the possibility of generating large differential potentials between different insulating surfaces after a sudden change in spacecraft potential. Finally, forcing the structure to remain at a fixed potential relative to the environment (by emitting electrons, for example) will allow large differential potentials to build up across thin insulators on time scales of minutes or tens of minutes.

Another consequence of the disparity in charging rates in the possibility of "overshoot"; that is, surfaces can acquire potentials significantly more negative (with respect to their environment) than equilibrium calculations would indicate. This is expected when there is an abrupt change in the environment of a precharged spacecraft. From an operational point of view, this effect should only be hazardous if the absolute spacecraft potential is of concern; for example, if two spacecraft are attempting to rendezvous.

From the point of view of the experimenter seeking to measure the plasma environment, both absolute and differential charging complicate the task of data interpretation. Effects of both types of charging on particle data from the ATS-5 and ATS-6 spacecraft have been reported (refs. 2, 10, and 11). Results of the present study indicate that shifts in reference potential (absolute charging) should occur relatively quickly in response to environmental changes but that changes in local fields around the spacecraft due to differential charging should occur relatively slowly. The latter effects are more subtle and thus should be more difficult to identify and eliminate in data analysis. Care should be used in locating such experiments on spacecraft and in designing scientific spacecraft to minimize charging effects.

REFERENCES

1. Rosen, A.: Spacecraft Charging: Environment-Induced Anomalies. AIAA Paper 75-91, Jan. 1975.

2. DeForest, S. E.: Spacecraft Charging at Geosynchronous Orbit. J. Geophys. Res., vol. 77, no. 4, Feb. 1, 1972, pp. 651-659.

3. Purvis, C. K.; Bartlett, R. O.; and DeForest, S. E.: Active Control of Spacecraft Charging on ATS-5 and ATS-6. Proceedings of the Spacecraft Charging Technology Conference. C. P. Pike and R. R. Lovell, eds., NASA TM X-73537, 1977, pp. 107-120.

4. Stevens, N. J.; et al.: Testing of Typical Spacecraft Materials in a Simulated Substorm Environment. Proceedings of the Spacecraft Charging Technology Conference, C. P. Pike and R. R. Lovell, eds., NASA TM X-73537, 1977, pp. 431-457.

5. Purvis, Carolyn K.; Steven, N. John; and Oglebay, Jon C.: Charging Characteristics of Materials: Comparison of Experiment Results with Simple Analytical Models. Proceedings of the Spacecraft Charging Technology Conference, C. P. Pike and R. R. Lovell, eds., NASA TM X-73537, 1977, pp. 459-486.

6. Katz, I.; et al.: The Capabilities of the NASA Charging Analyzer Program. Spacecraft Charging Technology - 1978. NASA CP-2071, 1979.

7. Berkopec, F. D.; Stevens, N. J.; and Sturman, J. C.: The Lewis Research Center Geomagnetic Substorm Simulation Facility. Proceedings of the Spacecraft Charging Technology Conference, C. P. Pike and R. R. Lovell, eds., NASA TM X-73537, 1977, pp. 423-430.

8. Roche, James C.; and Purvis, Carolyn K.: Comparison of NASCAP Predictions with Experimental Data. Spacecraft Charging Technology - 1978. NASA CP-2071, 1979.

9. Katz, I.; et al.: A Three-Dimensional Dynamic Study of Electrostatic Charging in Materials. (SSS-R-77-3367, Systems Science and Software; NASA Contract NAS3-20119.) NASA CR-135256, 1977.

10. DeForest, S. E.: Electrostatic Potentials Developed by ATS-5. Photon and Particle Interactions with Surfaces in Space, R. J. L. Grard, ed., D. Reidel Publishing Co. (Dordrecht), 1973, pp. 263-276.

11. Whipple, E. C., Jr.: Observation of Spacecraft Generated Electrostatic Fields in the Vicinity of the ATS-6 Satellite. AAS Paper 75-220, Aug. 1975.

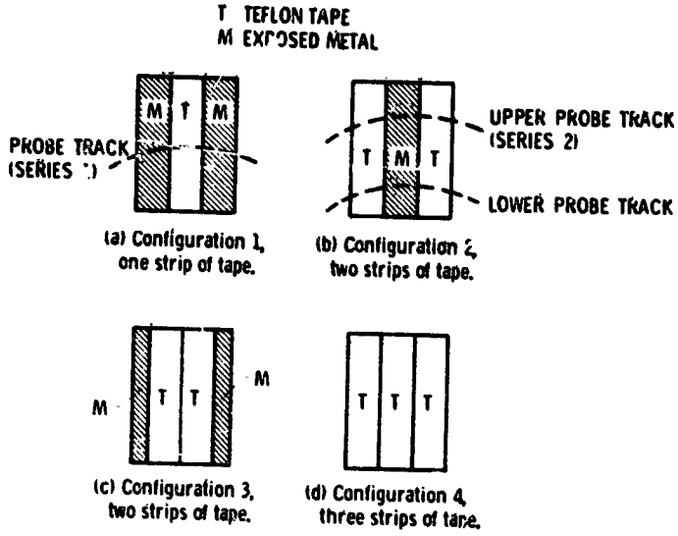

Figure 1. - Sample configurations.

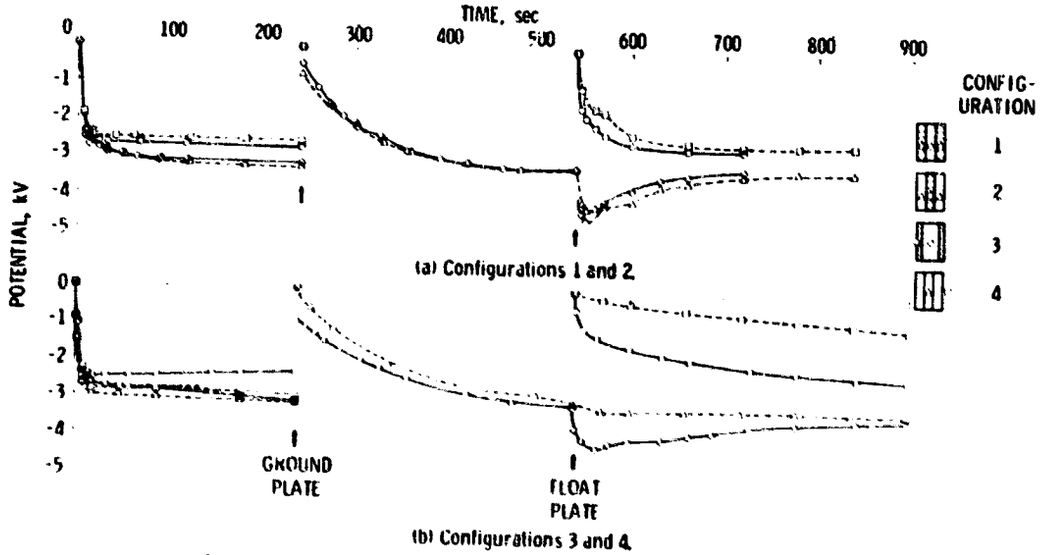

Figure 2. - Charging response of samples to test sequence - 5-kilovolt beam.

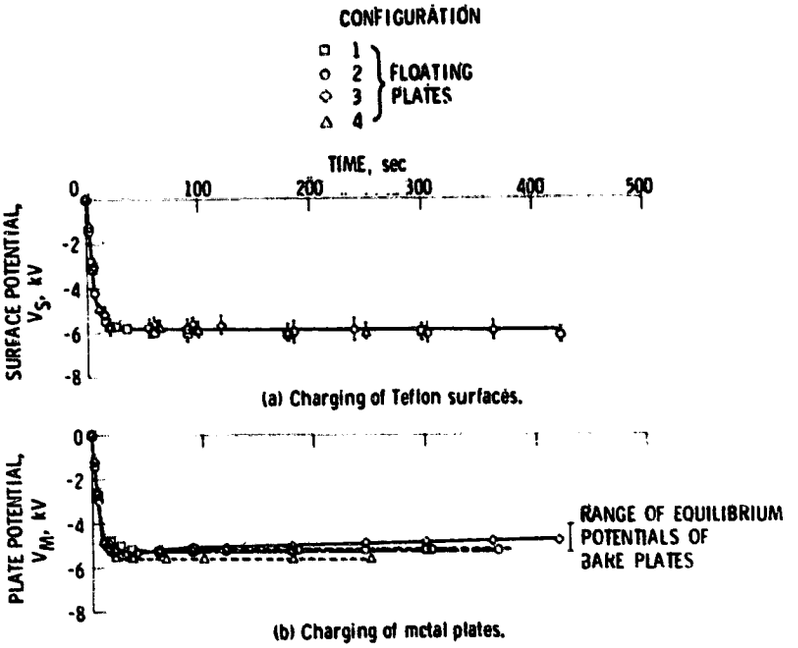

(a) Charging of Teflon surfaces.

(b) Charging of metal plates.

Figure 3. - Charging response of samples, sequence step 1 - 8-kilovolt beam.

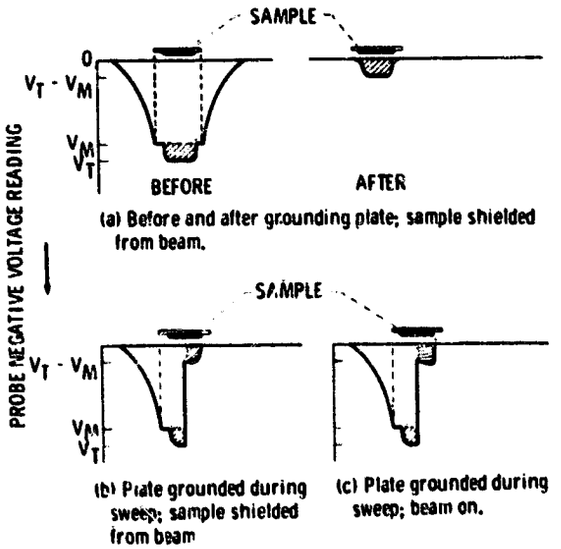

(a) Before and after grounding plate; sample shielded from beam.

(b) Plate grounded during sweep; sample shielded from beam

(c) Plate grounded during sweep; beam on.

Figure 4. - Grounding of plates. Typical probe traces.

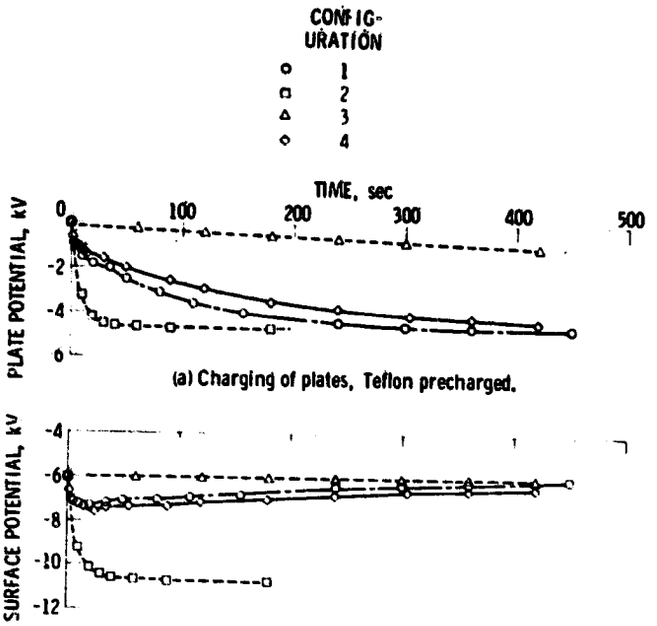

(a) Charging of plates, Teflon precharged.

(b) Charging of precharged Teflon on floating plates.

Figure 5. - Charging response of samples, sequence step 3 - 8-kilovolt beam.

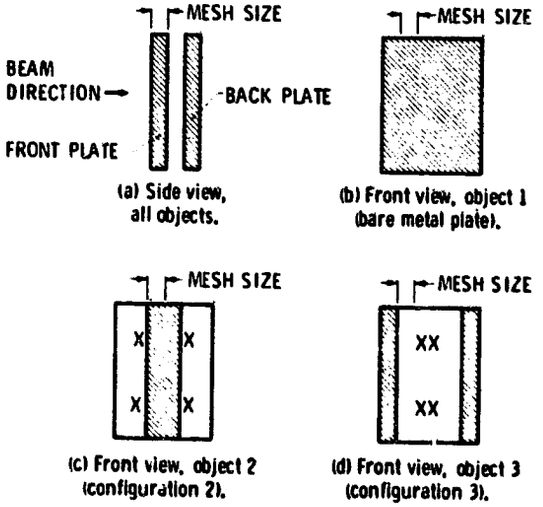

(a) Side view, all objects.

(b) Front view, object 1 (bare metal plate).

(c) Front view, object 2 (configuration 2).

(d) Front view, object 3 (configuration 3).

Figure 6. - NASCAP objects.

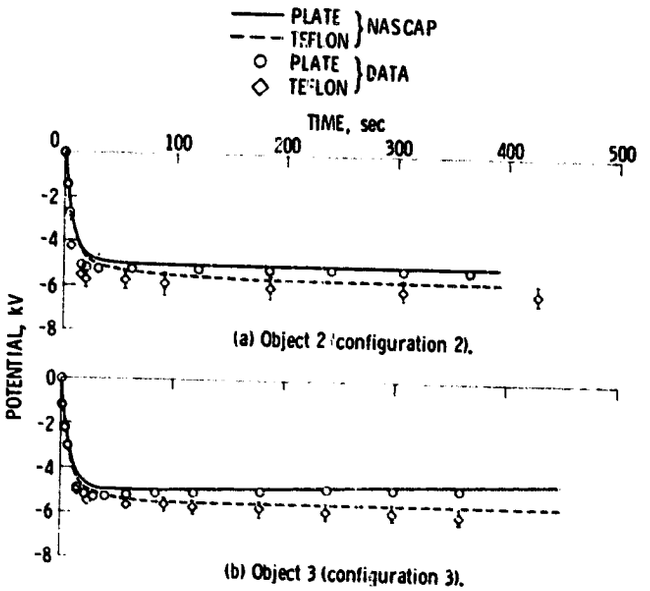

Figure 7. - Comparison of predictions with data - 8-kilovolt beam; all samples initially at zero potential.

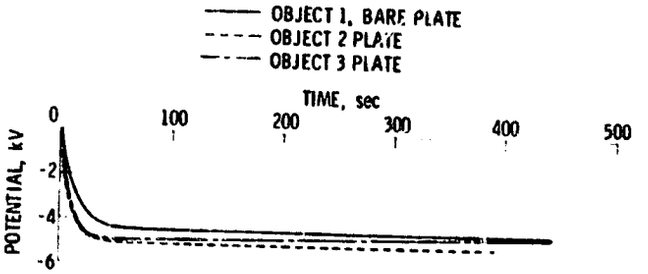

Figure 8. - NASCAP predictions, charging of metal plates - 8-kilovolt beam.

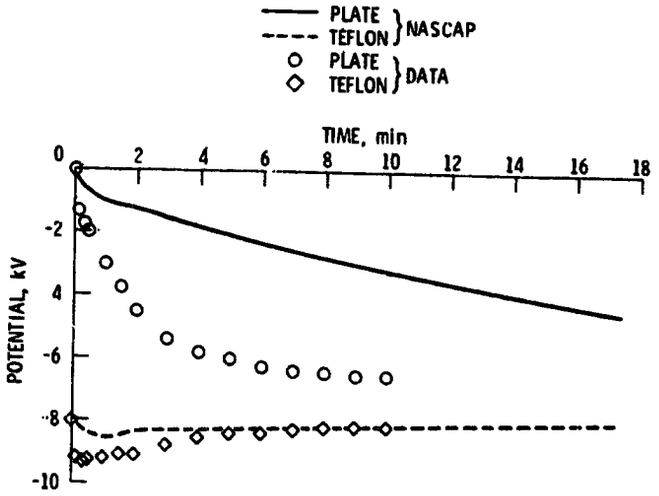

Figure 9. - Charging with Teflon precharged - 10-kilovolt beam, configuration 2.

D33

N79-24034

MATERIALS AND TECHNIQUES FOR SPACECRAFT STATIC CHARGE CONTROL II*

R. E. Schmidt and A. E. Eagles
General Electric Company
Space Division

Results of exploratory development on the design, fabrication and testing of transparent conductive coatings, conductive bulk materials and grounding techniques for application to high resistivity spacecraft dielectric materials to obtain control of static charge buildup are presented.

Deposition techniques for application of indium oxide, indium/tin oxide and other metal oxide thin films on Kapton, FEP Teflon, OSR and solar cell coverglasses are discussed. The techniques include RF and Magnetron sputtering and vapor deposition. Development, fabrication and testing of conductive glass tiles for OSR and solar cell coverglass applications is discussed.

Several grounding techniques for rapid charge dissipation from the conductively coated polymer and glass dielectrics which have been developed and tested in thermal cycled and electron plasma environments are described.

Results of the optical and electrical characterization and aging effects of these coatings, bulk materials and grounding techniques are discussed as they apply to the performance of their design functions in a geosynchronous orbit environment.

INTRODUCTION

Passive temperature control of spacecraft equilibrium temperature is accomplished by a controlled mix of solar reflective and infrared emissive properties of the materials on the spacecraft's external surfaces. High dielectric insulating materials are commonly used for this passive control because of their high solar reflectance in second surface mirror configurations and inherent high emittance. This class of materials includes back surface aluminized Kapton films, silvered FEP Teflon films and high purity silica glass with a back surface silver coating for use as Optical Solar Reflectors (OSR's), all of which are used as thermal control materials.

In geosynchronous orbit these dielectric materials are directly exposed to high energy electron plasmas which are particularly severe during geomagnetic substorm activity. As high dielectric insulating materials these materials will collect and support electric charge buildup until the dielectric strength is exceeded and electrical discharge or arcing occurs to areas or components with lower potential energy. These discharges result

* This work was supported by the Air Force Materials Laboratory under Contracts F33615-76-C-5075 and F33615-76-C-5258.

in degradation of the thermo-optical and mechanical properties and interference with low level logic commands to and from the spacecraft due to the radio frequency noise generated by the arc. Furthermore, the degradation of the thermal control surfaces by vaporization of the material itself or their second surface metalized coatings may interfere with other sensor systems by condensation of these volatiles on detector or radiator surfaces.

The purpose of this paper is to describe the development of materials and techniques to prevent and/or control the electrostatic charge buildup on several materials most commonly found on the external surfaces of geosynchronous orbiting satellites. It represents the progress made during the last eighteen months of a materials development and test program on developing transparent conductive coatings and materials for application to dielectric materials including

(1) Uncoated and silvered FEP Teflon thin films (2-5 mil) used for solar reflecting second surface mirrors with high emittance for thermal control coatings

(2) Uncoated and aluminized (back surface) Kapton type H film (2-3 mil) commonly used as a top layer for multilayer insulation blankets

(3) Optical Solar Reflecting (OSR) tiles (typically 8 mil) of fused silica with a back surface coating of silver and Inconel for second surface mirror applications requiring high thermal emittance surfaces (similar to the performance of the silvered FEP Teflon coating)

(4) Glass slides of fused silica and borosilicate (or microsheet) which are used for cover slides on silicon solar cells

APPROACH TO THE PROBLEM

Transparent Conductive Coatings

Conductive transparent coatings from semiconductor - metal oxides represent one possible means of controlling electrostatic charge buildup while having a minimal effect on the α and ϵ properties of the spacecraft materials. The most commonly used thin oxide films for transparent and conductive coatings have been combinations of indium oxide and tin oxide. The conductivity of these oxide coatings, first developed as resistance heaters on glass surfaces, is critically dependent on the creation of a proper oxygen-metal balance during the deposition to provide sufficient conduction electrons in the coating. The properties of these and other metal oxide coatings have been found to be strongly dependent on the conditions of the substrate and the deposition process.

Thin films of 90% indium oxide and 10% tin oxide have been deposited

onto 3 mil Kapton, 5 mil FEP Teflon sheets and OSR and coverglass tiles of fused silica and borosilicate using Magnetron, DC and RF sputtering and resistive heating vapor deposition techniques. Deposition has been demonstrated both reactively by Magnetron and DC sputtering and by resistive heating from In/Sn metal targets in an oxygen and argon atmosphere and non-reactively by RF sputtering from a dielectric indium/tin oxide target.

Visible absorptance and infrared emittance measurements of indium-tin oxide (ITO) reactively sputtered onto FEP Teflon films as conductive coatings in thicknesses up to 900 Å show a definite dependence upon thickness. Emittance, solar absorptance and transmittance in the visible region are shown in Figure 1 as a function of the coating thickness. As shown, the effect of the coating thickness is more pronounced in the visible spectrum than in the infrared.

Indium oxide and aluminum oxide coatings have been deposited in thicknesses down to 100 Å by resistive heating vapor deposition onto FEP Teflon and Kapton films and microsheet tiles. The films that were formed after the deposition were slightly dark due to oxygen deficiencies in the coatings. However, after heating in air at about 220°C for a period of 15 minutes the coatings were highly transparent with sheet resistances in the 10^8 ohm/square range. The results of these coatings are shown in Table I. Optical measurements between 0.27 and 2.7 μm show that heat treating at 200°C had no affect on the transmission of the Teflon film.

Reproduction of conductive transparent coatings was found to be strongly dependent upon the deposition technique and preparation parameters such as substrate temperature, vacuum, background of carrier gas and ratio of carrier to reactive gas, power levels and geometry of sample to source. Heat treatment of the coatings following the deposition as described above in some instances was found necessary to improve the transmittance of the thin film coatings. Table 2 shows some of the control variables which have been considered in depositing ITO by Magnetron sputtering.

The effect of post deposition heat treatment in air is most evident as a marked improvement in the optical transmission of the films deposited in both reactive and non-reactive deposition techniques. It has been found that the addition of an RF field to the planetary fixture during the magnetron sputtering relieves the requirements for this post-deposition heat treatment. The additional RF activation was found to have its most pronounced effect on the optical and electrical properties of the film when used during the deposition, while use following the deposition seemed to have little to no effect.

Other oxides of antimony, bismuth, lead, zinc, cadmium, titanium and silicon were also evaluated using resistive heating vapor deposition. All of the oxides showed reasonably high transmission on microsheet after post-deposition heat treatment but in general, showed high resistance insulator qualities or had surface resistances which varied considerably from batch to batch.

In general, most conductive and reproducible transparent coatings

were produced reactively by magnetron sputtering of indium-tin oxide from a 90% indium/10% tin target in a closely controlled oxygen/argon atmosphere with an in situ RF field applied to the planetary. The resulting ITO coatings had surface resistances predominantly in the low kilohms/square range in addition to a very low change in the absorptance of the substrate. Figure 2 shows a typical spectral response curve for 300 Å coating on a 5 mil FEP Teflon film and 10 mil borosilicate substrate.

Conductive Glass Development

A lithium borosilicate glass developed by GE several years ago under AFML contract F 33615-71-C-1656 with the designation GE-1TL was considered as a substitute glass material to prevent static charge buildup because of its good transmission and resistance to high energy electron (beta) radiation. A solid 11.4 cm diameter sample of the modified lithium borosilicate glass was cast in a shallow graphite mold, annealed and finally polished to a 0.14 cm (55 mil) thickness. A comparison of the transmittance of this glass with fused silica and borosilicate is shown in Figure 3A. A 1" x 1" x 1.8" block of the lithium borosilicate glass shown in Figure 3b was poured, annealed, cut and polished into 1" square wafers about 0.25 mm (10 mil) thick. These slides were then coated on one side with a 0.2 μm coating of silver to simulate an actual OSR configuration. Figure 3c is a plot of the solar reflectance and thermal emittance at 100°F of the GE 1TL glass tiles. The spectral weighted average of these curves give a value of R = 0.88 and α = 0.12 with ϵ = 0.86. Bulk resistance measurements of the 0.14 cm (55 mil) thick glass according to ASTM-D257 showed the modified lithium borosilicate resistance to be of the order of 10^{11} ohms.

Conductive Adhesive

Optical Solar Reflectors (OSR's) of fused silica and borosilicate (Corning 0211 microsheet) tiles have been coated with indium oxide, indium tin oxide and other metal oxides for evaluation during this program. Typically, three inch square matrices of one inch and three quarter inch square tiles have been mounted to aluminum plates as shown in Figure 4a for testing. A conductive, low outgassing, graphite loaded adhesive has been developed to bond the OSR's and provide a conductive path for charge dissipation to the spacecraft structure. The adhesive composition consisted of RTV 566 or 560 filled with 13% by weight of Hercules ¼ mm chopped graphite fibers. The RTV 566/HMS fiber formulation produced a resistivity of about 7.5×10^4 ohm-cm. The conductive adhesive in combination with the ITO or IO coated OSR's as shown in Figure 4b has been shown to provide a space stable adhesive system which provides a reliable conductive path between the coating and the metal support surface.

Chamfering

A major concern in using conductive coatings on OSR's and solar cell coverglasses is achieving a durable and continuous coating around the front

surface to the sides of the glass for a conductive path to the metal support structure. Chamfering of the glass edges in order to deposit a reliable hard and continuous conductive coating on the front and sides of the glass coupon was demonstrated as an alternate to the currently used method of welding conductive leads to contact points on each tile. The capillary action of the conductive adhesive between the tiles when they are pressed into position then provided the necessary conductive link between the coating and the metal frame, as illustrated in Figure 4c. Glass tiles of fused silica and microsheet have been successfully chamfered at a 45° angle using 600 grit emory polishing paper, as shown in Figure 5a under 3X magnification where each division is 0.127 mm (5 mils). A final OSR configuration with ITC coated chamfered 2 cm square microsheet tiles is shown in Figure 5b.

Solar Cell Coverglasses

Active solar cells in typically 2 cm by 4 cm size were used in fabricating, testing and evaluating the conductive transparent coatings and grounding techniques. Coverglasses of fused silica, microsheet and Cerium doped microsheet were bonded to the solar cells using Sylgard 182 or RTV 142. Typically, arrays were fabricated for testing in two series sets of 4 parallel cells as shown in Figure 6. The solar cells were then bonded to 3 mil Kapton substrates with Sylgard 182 and then mounted to an aluminum plate. Resistance measurements between the transparent conductively coated coverglasses and the solar cell circuit after mounting showed a high resistance of the order of 10^{11} ohms on a majority of the coated coverglasses. This high resistance is a result of the lack of a reliable conductive path between the coverglass coating and the solar cell bus electrode. Coating the coverglass after it had been mounted to the solar cell did not significantly improve the probability of creating a conductive path between the top of the coverglass the solar cell electrode. To improve the conductivity of this charge leakage path a silver loaded epoxy 1109S from Electroscience Labs was applied to the junction of the coverglass and solar cell bus electrode as shown in Figure 7a. After applying this conductive epoxy diluted with 3:1 mixture of Xylene along the edge of the glass and curing in air at 100° C for 90 minutes, the resistance between the solar cell electrode and the IO coated coverglasses, as shown in Figure 7b, was reduced to the order of 10^5 ohms for all the coverglasses.

Ground Bond Development

Several grounding techniques were evaluated to provide connections between conductive coatings on the Kapton and FEP Teflon films and the spacecraft structure. The objective was to provide integral metal to polymer film laminates with high peel and shear strengths which could withstand the thermal and electrical cycling environment of geosynchronous orbit. Four design configurations evaluated were

1. Adhesive bonded metal to polymer and overcoated with conductive oxide

2. Heat sealed metal to polymer bonds

3. Adhesive bonded metal to conductively coated polymer

4. Mechanical clamp to the conductively coated polymer

One mil thick thermo setting DuPont Pyralux adhesive was used to bond 1 mil thick copper foil to coated and uncoated substrates of 3 mil Kapton. The composite shown in figure 8a was formed between two heated plates (175°C) under about 1.34 x 10^6 Pascals (200 psi) for 2 minutes. A 500 Å coating of indium oxide over the entire Kapton sample including the ground tab provided a solderable joint with a resistance of 10^7 ohms to anywhere on the film surface. No success was obtained in trying to bond copper foil directly to the FEP Teflon using the Pyralux adhesive without any surface treatment. A direct heat sealing of the copper foil to the FEP Teflon was also attempted. However, the heat required to bond the FEP to the copper foil resulted in severe surface distortion and the Teflon to foil sealing edge was very susceptible to cracking. Application of an etching solution of Tetra Etch to the FEP Teflon improved the surface adhesion so that application of Pyralux sheet adhesive and copper foil as described above provided a strong solderable bond.

Adhesive bonding of the grounding electrode to the conductive oxide coated polymer films was also evaluated. Conductive tapes and epoxies were considered for application to the ITO coated polymers for attaching a solderable metal foil to the conductive coating. Table 3 summarizes the various ground bond configurations tested. For this application 3M's conductive copper tape X1181 showed much greater adhesion to the ITO coated Teflon and Kapton films than Eccobond's silver loaded epoxy. It was found that application of the Pyralux to the coated FEP surface required etching the coating from the FEP before a strong adhesive bond could be obtained. Thermal cycling tests were performed in air between -65° and +100°C on these bonds to evaluate their stability. Resistance measurements between the ground tabs and the ITO coatings during the thermal cycling are summarized in Table 4. The variation in a typical run is illustrated in Figure 9. These test results indicate that all the configurations were electrically stable during the three cycle test.

STATIC CHARGE TESTING

Test Facility

The electrostatic charging and control facility is shown schematically in Figure 10. The facility is designed to irradiate flat samples up to 4.5 inches in diameter at electron energies up to 30 KeV in a vacuum system which is initially in the mid 10^{-7} Torr range. The design of the gun includes a three element electrostatic lens to obtain uniform beam density across the sample area and allow adjustment in flux density. Current measuring electrodes are connected to the rear of the aluminum back plate sample holder for bulk leakage currents and to the annular sample retaining ring for surface leakage current monitoring.

A secondary electron collector cylinder is also part of the system which can be swung in place around the sample during irradiation to monitor charged particles leaving the surface of the sample. A Monroe model 144-1009s non-contacting electrostatic voltmeter probe is mounted on a rotable arm which can be swept across the sample surface when the secondary cylinder is not in place. During irradiation the probe may be swung completely out of the way of the beam or may be used to measure surface potentials during irradiation.

Coating Charge Control

Indium oxide (IO) and indium tin oxide conductively coated FEP Teflon and Kapton films were tested in the charging control facility. Bulk (I_D) and surface (I_R) conduction currents were recorded for beam potentials between 2KV and 20KV for the first several minutes of irradiation and also following shut off of the electron beam. Initial maxima and steady state values for the IO and ITO coated 3 mil Kapton and 5 mil FEP Teflon are shown in Tables 5 and 6. Surface potential measurements using the Monroe electrostatic voltmeter following irradiation at beam potentials of 10KV, 15KV and 20KV showed surface potentials of less than 5 volts for all four materials tested.

The typical line shape of the conduction currents I_D and I_R as the electron beam was turned on and off for the Kapton and Teflon materials is shown in Figure 11. Integration of the current over the transient portion of the current curves show that most of the charge deposited in the film below the coating was quickly dissipated when the beam was turned off as shown in Table 7.

Electron irradiation tests were also conducted on the ITO coated Kapton and Teflon samples for several hours over a period of six months. Between these tests the samples were stored in a dust free environment at room temperature. Following this series of tests no visible sample degradation was observed and the surface resistance measurements on the sample were in the $4\text{-}10\text{x}10^6$ ohm/square range before and after the irradiations.

Ground Bond Tests

The copper foil grounding connection on Kapton using Pyralux adhesive and overcoated with conductive transparent indium oxide, shown in Figure 8 was tested under electron irradiation. The surface current electrode was isolated from the perimeter of the sample except at the ground tab. The bulk and surface leakage currents were similar in character to those reported in Table 6.

Ground bonds soldered to conductive copper tape or copper tab/conductive epoxy and bonded to ITO coated films of Teflon and Kapton were also irradiated by 2KeV to 20KeV electrons. Figures 12a and 12b shows the general test configuration for the two bonding methods. Figure 12c shows the detail of the copper tab/Eccobond 56C/ITO ground connector on the Teflon. Bulk, surface and secondary collector currents were similar to those reported above. However, surface potentials up to -100V were

measured on samples shown in Figures 12b and c when irradiated at 20KV. These surface potentials were centered around the solder joints on the ground tabs and examination after the test revealed that traces of solder flux on the leads was responsible for the small charge accumulation.

OSR Matrix Testing

Table 8 shows a summary of the OSR configurations tested under electron irradiation. The effective conductivity or charge control of the graphite loaded RTV 566 was measured under electron irradiation to provide a baseline for future OSR matrix tests using the conductive adhesive. Table 9 summarizes the measured currents through the material (I_g) and the secondary electron collector. The surface potentials measured following irradiation show that the material charged nominally to between -90 and -160 volts.

Uncoated OSR Matrix

A three inch square matrix of nine square tiles of fused silica without any conductive coating was exposed to monoenergetic electron beams between 2KeV and 20KeV at nearly 10nA/cm^2 for several minutes. The glasses were mounted using the conductive adhesive. Currents measured through the backplate, around the perimeter and from the secondary collector are shown in Table 10. The maximum surface potential exceeded the range of the Monroe voltmeter following irradiation in a 4KeV beam but did not show electrostatic discharging until irradiated in a 15KeV beam. Reducing the beam density to below 4nA/cm^2 reduced the discharge rate but not proportionally. A similar set of measurements and observations were made on a 3 inch square matrix of uncoated OSR tiles of microsheet. Similar currents and potentials were also measured on an OSR matrix covering the entire 4.5" diameter sample area. Decay of the surface potential following irradiation at 6KV followed an exponential decay very closely with a 12.5 minute time constant and an initial potential of about -2100 volts.

An uncoated three inch square matrix of 16 chamfered 10 mil thick microsheet tiles using the conductive RTV was also tested under electron bombardment. Although similar current and surface potentials were measured as before for the other uncoated tiles and discharging was observed during the 15KeV beam irradiation, the discharge rates were not as regular as before. Figure 13 shows the variation of surface potential with electron beam energy for this uncoated OSR up to 6KeV irradiation.

Conductively Coated OSR Matrices

An OSR mosaic of 16 ITO coated 2 cm microsheet tiles mounted with conductive adhesive to an aluminum plate was irradiated in an electron beam with energies up to 20 KeV. The peak and steady state bulk leakage and secondary collector currents are listed in Table 11. Note that in contrast to the uncoated sample currents, the initial peak is much smaller, indicating a much smaller subsurface charge deposit than in the uncoated materials. Surface potential measurements with the capacitively coupled probe gave maximum surface voltages of 37V, 46V, and 45V after

irradiation by 10KeV, 15KeV and 20KeV electrons, respectively.

A 16 tile matrix of ITO coated chamfered 2 cm square microsheet tiles with conductive adhesive bonding was also tested. The test results, shown in Table 12, indicate the successful charge control demonstrated by the coated tiles. Measurement of the negligible surface potential and the lack of a subsurface charging peak on the bulk leakage current indicate a negligible charge buildup on this sample.

Conductive Glass OSR

Electron irradiation tests on a 3 inch square matrix of 0.38 mm (15 mil) thick one inch square tiles of modified lithium borosilicate (GE-iTL) glass with a silvered back surface between beam energies of 2 to 20 KeV showed no significant charge buildup on the glass surface. Bulk leakage and secondary collector currents are given in Table 13 for an average beam density of about 10nA/cm^2. No surface electrode was used on these samples because the relative conductance of the glass prevented any surface charge buildup.

Solar Cell Arrays

Four solar cell arrays were tested under irradiation by electron plasmas with energies up to 20 KeV. They were fabricated with varying degrees of charge control solutions. All of the arrays tested were fabricated in an active 2 cell by 4 cell arrangement with two series sets of 4 parallel cells. The two cm by four cm cell array thus formed a 7.6 cm (3 inch) square array. The array was tested in an active mode with a 10 ohm load resistor across the array leads. A beam aperture adaptor with a three-inch diameter similar to the one used for testing the OSR matrices was attached to the secondary collector approximately one-inch in front of the test fixture in order to restrict the electron beam to the solar cell area of the sample test fixture.

The initial configuration tested was an uncoated array. Unusually low potentials were recorded at all beam energies and no severe discharging was observed. Surface potentials of 360V, 830V, 1KV and 1.2KV were recorded after exposure to beam energies of 5, 10, 15 and 20KeV respectively. The low surface potentials for this uncoated sample was attributed to the small current output of the electron gun of about 0.2nA/cm^2 during this set of measurements.

An array was next tested whose coverglasses had been coated with indium oxide. The first set of measurements were made on the coated solar array without any conductive epoxy applied to the coverglass/solar cell bus area. Measurements were terminated after observing severe discharging while being irradiated in a 5KeV beam with a current density of 5nA/cm^2. The arcing and discharging disappeared after the solar cell bus/coverglass junction was overlaid with a coating of Electroscience 1109S conductive epoxy and retested in an electron

beam at energies up to 20KeV with beam densities up to 5nA/cm^2.

The next cell array tested used IO coated chamfered coverglasses with conductive epoxy applied along the chamfered edge and the cell electrode. Low surface potentials of 170, 275, 335, 365 and 390V at 4, 6, 10, 15 and 20KeV beam potentials indicate that no significant charge build up was occurring on the solar cell coverglasses. The IV performance of this array, before and after the irradiation is shown in Figure 14 and indicates a slight decrease in the power output of the cell. However the same magnitude decrease in power output was also observed on the uncoated array after electron irradiation.

A four by two solar cell array with Cerium doped microsheet coverglasses from Pelkington P.E. (PPE) was also tested in the ESD facility with energies up to 10KeV. The surface potentials measured with the Monoroe probe were nearly up to -2000V after irradiation in a 6KeV beam in contrast to the low potentials measured on the IO coated coverglasses. Due to high surface charge accumulation on the cerium doped coverglasses it is evident that the doping is insufficient to control the electrostatic charge buildup and further tests were terminated in order not to destroy the cells. The same type of decrease in power output was observed in these cells, shown in Figure 15, as was observed in the coated cell as a result of the irradiation tests.

Electron/UV Exposure

Six Teflon sample configurations were exposed to 1000 hours of combined electrons and the equivalent of one UV sun. The 5 mil thick samples which were tested were 1) Virgin FEP Teflon; 2) FEP Teflon which had been heat treated at 200°C for 30 minutes; 3) FEP Teflon with a 200 MΩ conductive coating of indium oxide which had been heat treated as in No. 2 and, 4-6) three samples with conductive coatings of indium oxide of different thicknesses and a thin flash overcoating of chrome oxide. The IO and chrome oxide coatings were deposited with the resistance heating at 1x10^{-4} Torr O_2 partial pressure. The indium was deposited in thicknesses of 350, 500, and 750 Å. Table 14 summarizes the average transmittance weighted over the solar spectrum from measurements in air before and after the exposure. Addition of the flash coating of the chromium oxide seems to retard the degradation of the coating.

CONCLUSION

Thin films of indium oxide and indium tin oxide have been successfully and reproducibly deposited as conductive transparent coatings onto glass, Kapton and FEP Teflon sheets as large as one foot square. Deposition by Magnetron sputtering has produced the most consistent and uniform coatings with no need for post deposition heat treatment resulting in coatings typically with a $\Delta\alpha$ of 0.02 from the uncoated substrates.

A modified lithium borosilicate glass developed by GE under another program has been fabricated in 0.38 mm (15 mil) OSR tiles. Tests under a simulated substorm environment have shown its ability to dissipate the incident charge flux and prevent any charge accumulation. The effective conductivity of the OSR bonding adhesive has been increased by the addition of graphite fiber to provide a conductive path between the transparent conductive coated OSR or conductive glass and the spacecraft grounding structure. The chamfering of the OSR tiles has been demonstrated along with the conductive coatings to provide a highly reliable conductive path from the front surface to the conductive adhesive.

Several grounding techniques have been evaluated for their ability to drain the charge buildup from the conductively coated surfaces of Teflon and Kapton films. The bonds have been thermally cycled and tested under electron irradiation in a simulated environment and have been shown to provide a stable conductive path between the conductive coating and spacecraft ground.

These conductive coatings, materials, and grounding techniques are now being further evaluated to determine the best coating thickness and processing techniques to provide the minimum optical interference to the substrate and still have a charge control material. Further development will evaluate the scale up of these processes for large samples and their behavior in larger and combined environments.

Table 1. Summary of Vacuum Vapor Deposited Transparent Conductive Oxide Films

MATERIAL	DEPOSITION RATE	BACKGROUND OXYGEN PRESSURE	TAPE (2) TEST	HEAT AT 425°F/ 15 MIN.	TRANSPARENCY	SURFACE RESISTIVITY (3) Ω/□	SUBSTRATE
Al_2O_3	25A/MIN.	5×10^{-5} TORR	P(1)	YES	NO DETECTABLE INCREASE IN TRANSMISSION BEFORE AND AFTER TESTING	5×10^{7} TO 5×10^{8}	KAPTON
In_2O_3	25A/MIN.	1×10^{-4} TORR	P	YES		5×10^{7} TO 5×10^{8}	KAPTON
In_2O_3	25A/MIN.	1×10^{-4} TORR	P	YES		5×10^{7} TO 5×10^{8}	FEP
Al_2O_3	250Å/MIN	5×10^{-5} TORR	P	YES		5×10^{7} TO 5×10^{8}	MICROSHEET
In_2O_3	250Å/MIN	1×10^{-4} TORR	P	YES		5×10^{7} TO 5×10^{8}	MICROSHEET
In_2O_3	250Å/MIN.	1×10^{-4} TORR	P	YES		5×10^{7} TO 5×10^{-8}	MICROSHEET

Table 2. Magnetron Coated FEP and Kapton

Material	Run	O_2 Partial Pressure Torr	Process Temp (°C)	Evaporation Rate Å/MIN	Thickness Å	Surface Resistivity Ω/□	Δ Transmission %
Kapton	24	3.8×10^{-4}	121	22	100	37K	.03
Kapton	25	4.4×10^{-4}	150	16	100	7.9K	.05
FEP	25	4.4×10^{-4}	150	16	100	7.9K	.10
Kapton	26	5.5×10^{-4}	121	2*	100	5×10^{8}	0
FEP	26	5.5×10^{-4}	121	2*	100	∞	0
Kapton	27	3.5×10^{-4}	100	20	300	12.5K	.10
FEP	27	3.5×10^{-4}	100	20	300	6.5K**	.16
Kapton	28	6×10^{-4}	100	22	300	350	.07
FEP	28	6×10^{-4}	100	22	300	1300	.10
FEP	28	6×10^{-4}	100	22	300	15000	.10
Kapton	29	4.9×10^{-4}	100	10	300	75K	.02

* Slow rate of evaporation enables more complete oxidation of ITO; increasing resistance and insulating properties of film.

** Post bake at 368°F for 4 hours reduced surface resistance to 1300 Ω/□.

Table 3. Copper Ground Bond Adhesion Strength

Substrate	Coating	Coating Etch	Substrate Etch	Adhesive	Shear Strength (psi)	Peel Strength (oz/in)
FEP Tefon	None		None	Pyralux	N/A	N/A
"	"		"	EA956*	5.6	N/A
"	"		"	Cu tape**	1.8	6.8
"	"		Tetra Etch	Pyralux	18.4	>32.0[a]
"	"		"	EA956	18.6	9.6
"	"		"	Cu tape	>21.6	36.0
"	ITO	None	None	Pyralux	18.6	8.3
"	"	"	"	EA956	19.2	7.7
"	"	"	"	56C	18.2	3.8
"	"	"	"	Cu tape	18.0	38.4
"	"	10% HC1	Tetra Etch	Pyralux	17.0	16.0
"	"	"	"	EA956	18.6	10.9
"	"	$10\%H_2SO_4$	"	Pyralux	19.0	21.1
"	"	"	"	EA956	17.8	12.8
"	"	$10\%NH_4F$ HF	"	Pyralux	18.2	8.3
"	"	"	"	EA956	19.6	11.5
Kapton	None		None	Pyralux	84.0	115.2
"	"		"	EA956	95*	11.2
"	"		"	Cu tape	59.0	46.4
"	ITO	None	"	Pyralux	91.0	120.0
"	"	"	"	EA956	80.0	16.0
"	"	"	"	56C	40.0	11.2
"	"	"	"	Cu tape	56.0	35.2
"	"	10% HC1	"	Pyralux	93.0	144.0
"	"	"	"	EA956	84[a]	3.2
"	"	$10\%H_2SO_4$	"	Pyralux	95[a]	a
"	"	"	"	EA956	87[a]	6.4
"	"	$10\%NH_4F$ HF	"	Pyralux	>100	128.0
"	"	"	"	EA956	72[a]	4.8
Aluminum	None	None	"	Cu tape	57	94.4

N/A - no measurable adhesion
a - substrate tore
* - Hysol adhesive EA956
** - 3M brand conductive tape #1181

Table 4. Extreme Values of Surface Resistance During Thermal Cycle Tests

Configuration	Minimum Resistance ($10^5\ \Omega$)	Maximum Resistance ($10^5\ \Omega$)
Copper Tape on ITO FEP Teflon	0.240	1.57
Copper Tape on ITO Kapton	0.114	0.472
Mechanical Clamp on ITO Kapton	0.032	0.078
Mechanical Clamp on ITO FEP Teflon	0.285	3.64
Copper Tab/EA 956/ITO Kapton	0.036	0.040
Copper Tab/Pyrolux/ITO Kapton	0.033	0.037
Copper Tab/56C/ITO FEP Teflon	0.645	1.52
Copper Tab/56C/ITO Kapton	0.133	0.257

Table 5. Summary of Current Measurements of IO and ITO FEP Teflon[a]

	IO FEP Teflon (Sample No. 44)					ITO FEP Teflon (Sample No. 37)				
Beam Potential (kV)	I_D[c] Max.	I_D[c] S.S.[b]	I_R Max.	I_R S.S.	I_S S.S.	I_D Max.	I_D S.S.[b]	I_R Max.	I_R S.S.	I_S S.S.
2	0.05	0.03	11	11	180	0.8	0.05	99	26	240
6	0.1	0.02	220	150	90	2.2	0.05	270	150	125
10	0.25	0.02	360	200	75	2.6	0.05	280	200	90
15	0.4	0.02	300	200	55	3.5	0.05	450	310	55
20	0.65	0.02	300	200	45	4.5	0.05	470	340	85

[a] All currents in units of nanoamperes

[b] Steady State

[c] I_D bulk conduction current

I_R surface conduction current

I_S secondary collector current

Table 6. Summary of Current Measurements of IO and ITO KAPTON[a]

Beam Potential (kV)	IO-Kapton (Sample No. 40)					ITO-Kapton (Sample No. 36)				
	I_D[b]		I_R		I_S	I_D		I_R		I_S
	Max	S. S.[d]	Max	S. S.	S. S.[c]	Max	S. S.	Max	S. S.	S. S.
2	0.2		150	120	280	nm[d]	nm	nm	nm	nm
6	1.4	0.03	540	330	100	21	0.1	630	420	160
10	3.4	nm	570	340	90	4.3	0.05	630	450	nm
15	8.1	0.02	600	360	70	9.9	0.05	750	460	nm
20	12.6	0.02	500	360	60	6.0	0.05	690	570	nm

[a] All currents in units of nanoamperes.

[b] I_D = bulk conduction current
I_R = surface conduction current
I_S = secondary collector current

[c] Steady state.

[d] Not measured.

Table 7. Stored and Drained Charge From IO Coated FEP Teflon

Beam Pot. (kV)	Charge Stored	Charge Leaked
10	1.21×10^{-9} C	0.53×10^{-9} C
15	1.47×10^{-9} C	0.80×10^{-9} C
20	1.89×10^{-9} C	0.84×10^{-9} C

Table 8. Conductive OSR Development Test Matrix

OSR MATERIAL	TILE SIZE	TILE MODIFICATION	TEST SAMPLE SIZE	ADHESIVE	COATING FRONT	COATING BACK	SAMPLE ID #
Fused Silica (Corning 7940)	1" Square	None	3" x 3"	Cond.RTV	--	Ag	#52
" "	4.5" diam	Solid disc	4.5" diam	--	--	--	#46
Microsheet (Corning 0211)	1" Square	None	3" x 3"	Cond.RTV	--	Ag	53
" "	1" "	None	4.5" diam.	Cond.RTV	--	Ag	57
" "	1" "	None	3" x 3"	Cond.RTV	ITO	Ag	86
" "	2 cm "	None	3" x 3"	Sylgard 182	--	Ag	34
" "	2 cm "	None	3" x 3"	Cond.RTV	--	Ag	70
" "	2 cm "	None	3" x 3"	Cond.RTV	ITO	Ag	38
" "	2 cm "	None	3" x 3"	Cond.RTV	GE-1TL frit	Ag	39
" "	2 cm "	Chamfered	3" x 3"	Cond.RTV	--	Ag	71
" "	2 cm "	Chamfered	3" x 3"	Cond.RTV	IO	Ag	72
" "	2 cm "	Chamfered	3" x 3"	Cond.RTV	ITO	Ag	85
GE-1TL	1" "	None	3" x 3"	Cond.RTV	--	Ag	64
" "	4.5" diam	Solid disc	4.5" diam	--	--	--	42
--	--	--	4.5" diam	Cond.RTV	--	--	33

Table 9. Summary of Currents in RTV With Graphite Filler

Beam Potential (kV)	I_D Steady State (nA)	I_S Steady State (nA)	Surface Potential (kV)
2	200	100	.09
4	250	80	.16
6	300	80	.16
8	350	80	.16
10	370	85	.15
15	480	100	.12
20	490	90	.09

Table 10. Summary of Currents of Uncoated Fused Silica Square OSR Mosaic

Beam Potential (kV)	I_D		I_R		I_S	Max. Surface Potential (V)
	Peak (nA)	S.S.[b] (nA)	Peak (nA)	S.S. (nA)	S.S. (nA)	
2	--	31	--	83	295	-400
4	90	38	13	19	290	-2240
6	> 100	50	8	23	275	
10	190	55	8	29	260	
15	> 200	90	--	26	220	

Table 11. Summary of Currents in ITO Coated Microsheet OSR Mosaic

Beam Potential (KV)	I_D		I_S		I_D/I_S
	Peak (nA)	S.S.[b] (nA)	Peak (nA)	S.S. (nA)	S.S.
10	260	200	-	30	6.6
	80	80	31	15	5.3
15	140	110	-	16	6.8
	40	40	7	5	8.0
20	110	80	17	12	6.6

Table 12. Summary of Currents in ITO Coated Chamfered 16 Tile Microsheet (2 cm square) OSR Matrix

Beam Potential (kV)	I_D		I_S		I_R	Surface Potential (V)
	Initial (nA)	S.S (nA)	Initial (nA)	S.S (nA)	S.S (rA)	
2	100	100	100	90	70	0
5	140	180	70	45	25	3
10		200	30	25	15	8
15	230	250	45	40	14	-
20	220	240	35	35	14	12

Table 13. Summary of Current and Surface Potential on GE-1TL OSR Mosaic

Beam Potential (kV)	I_D (nA)	I_S (nA)	$I_D/(I_S+I_D)$	Surface Potential (V)
2	65	550	.10	7
5	270	250	.52	8
10	350	190	.64	9
15	430	210	.67	9
20	450	220	.67	9

Table 14. Average Transmittance for Coated and Uncoated FEP Telfon Under Electron/UV Exposure

Sample	Pre Test Transmittance (%)	Post Test Transmittance (%)
FEP Teflon	90.3	87.0
FEP-Teflon (Heat-treated)	89.5	87.5
FEP/IO (200 MΩ)	84.6	79.6
FEP/IO + CO[a] (2 KMΩ)	35.0	82.0
FEP/IO + CO (200 MΩ)	84.4	81.7
FEP/IO + CO (2 MΩ)	81.8	78.9

[a] CO - Chromium Oxide

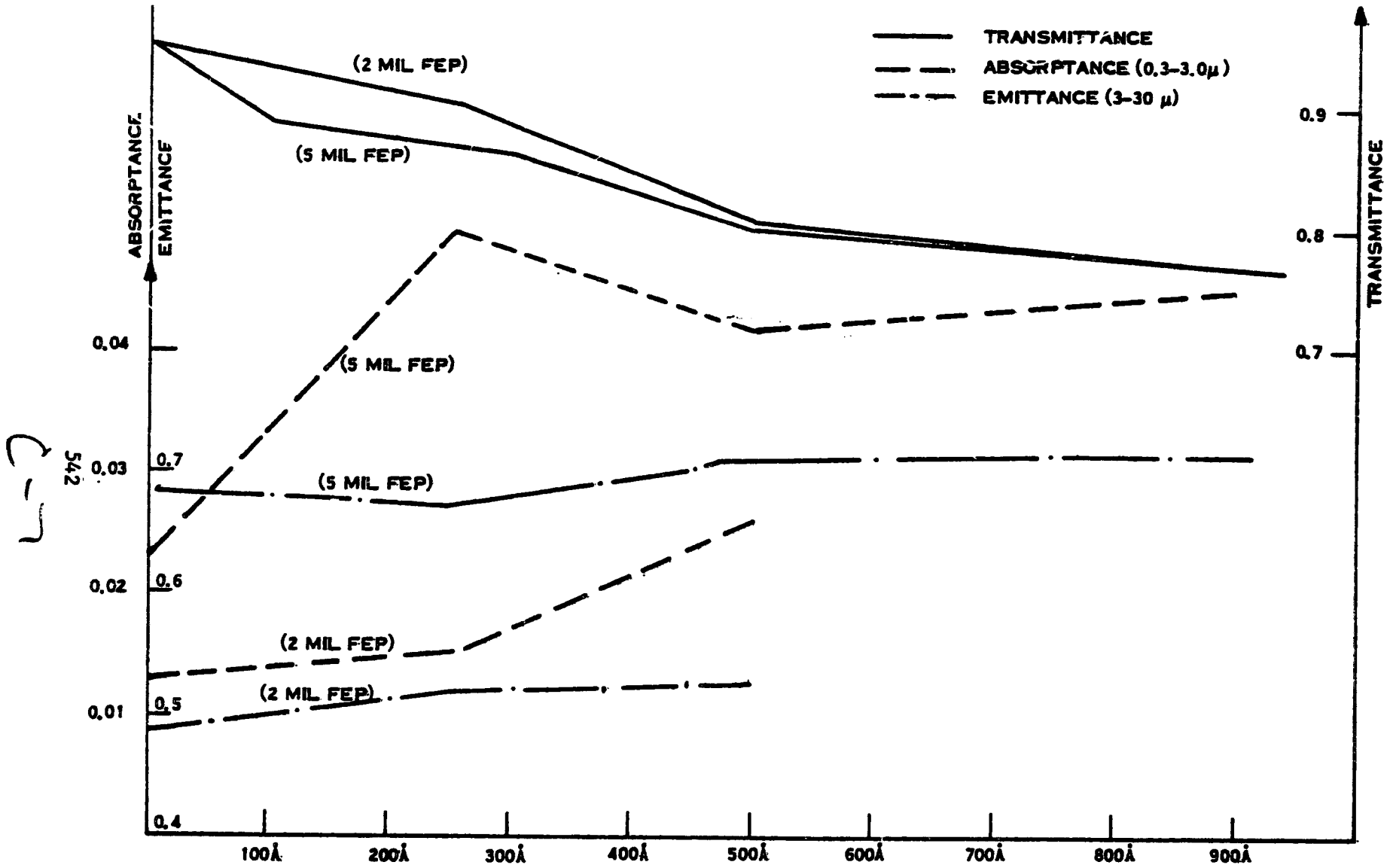

Figure 1. Optical Characterization of ITO Coating Thickness Dependence

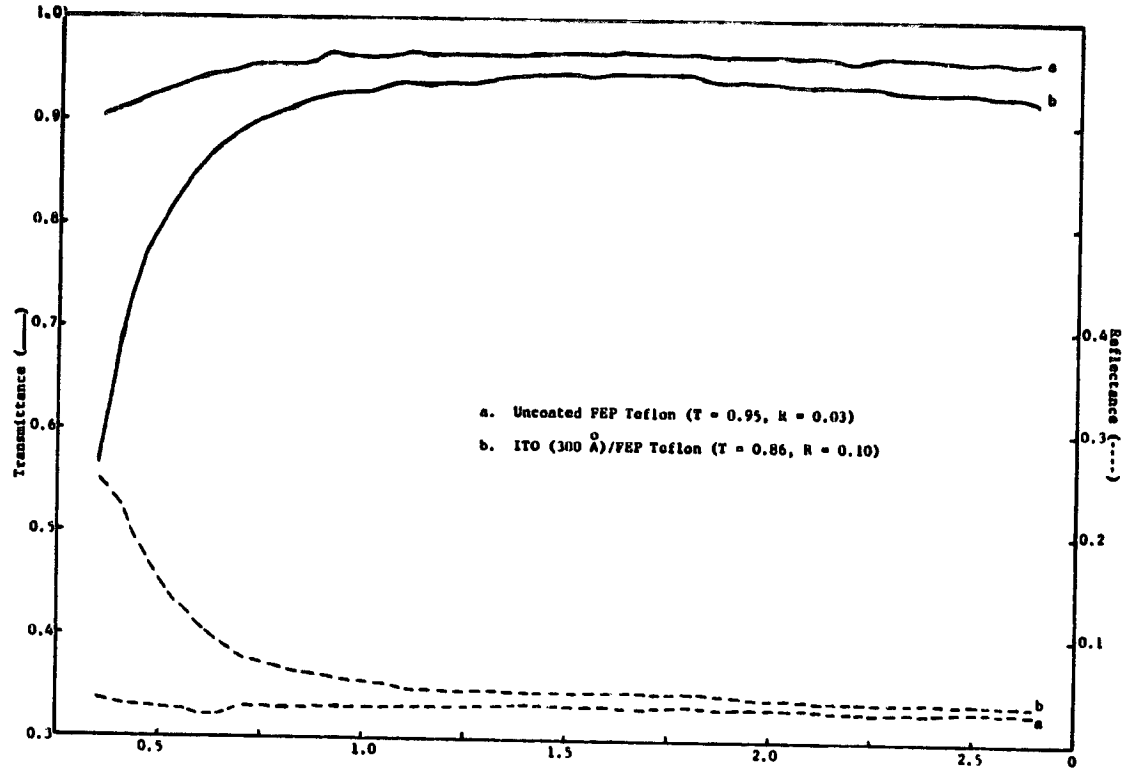

Figure 2a. Transmittance and Reflectance of ITO Coated FEP Teflon

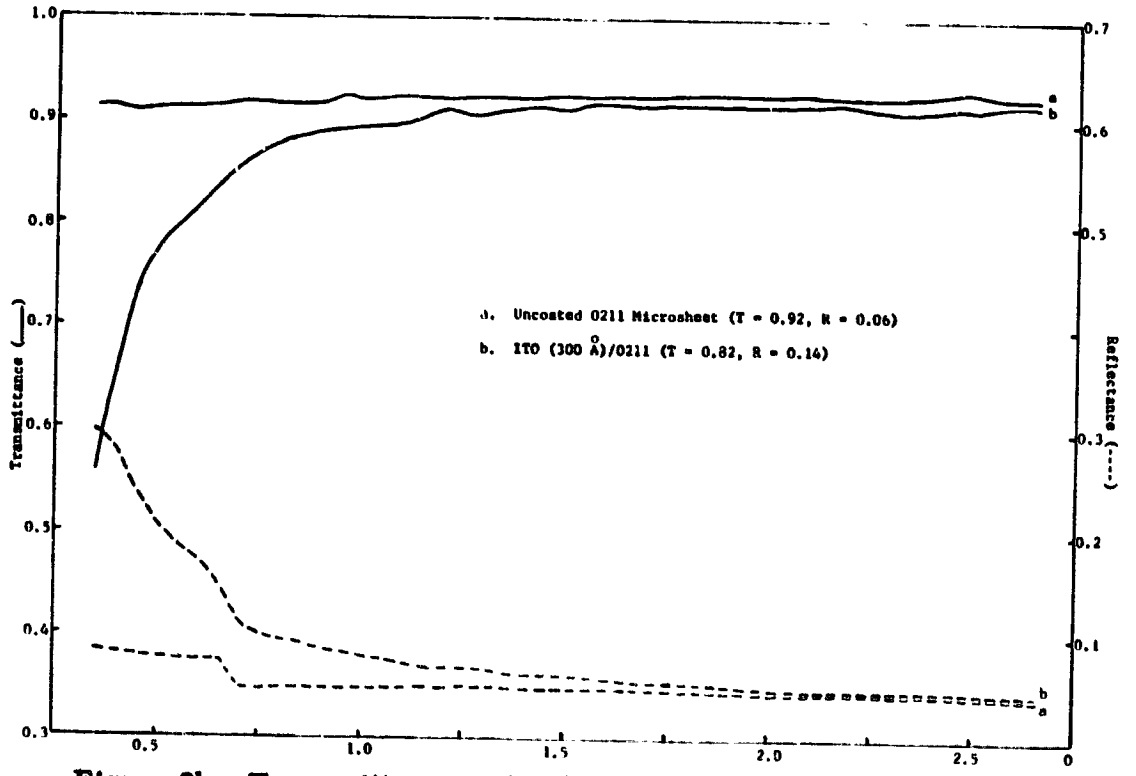

Figure 2b. Transmittance and Reflectance of ITO Coated Microsheet

Figure 3b. Block of GE-1TL Glass

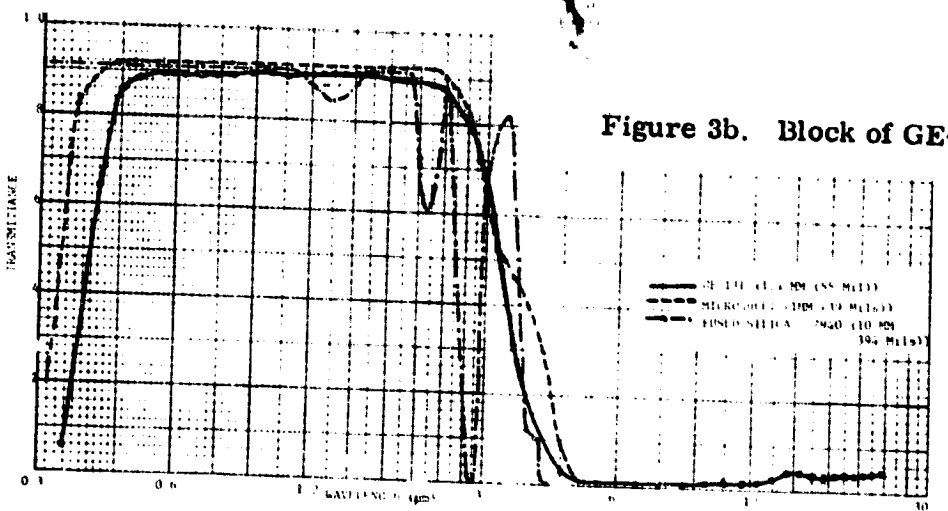

Figure 3a. Transmittance of Fused Silica, Borosilicate and GE-1TL Glass

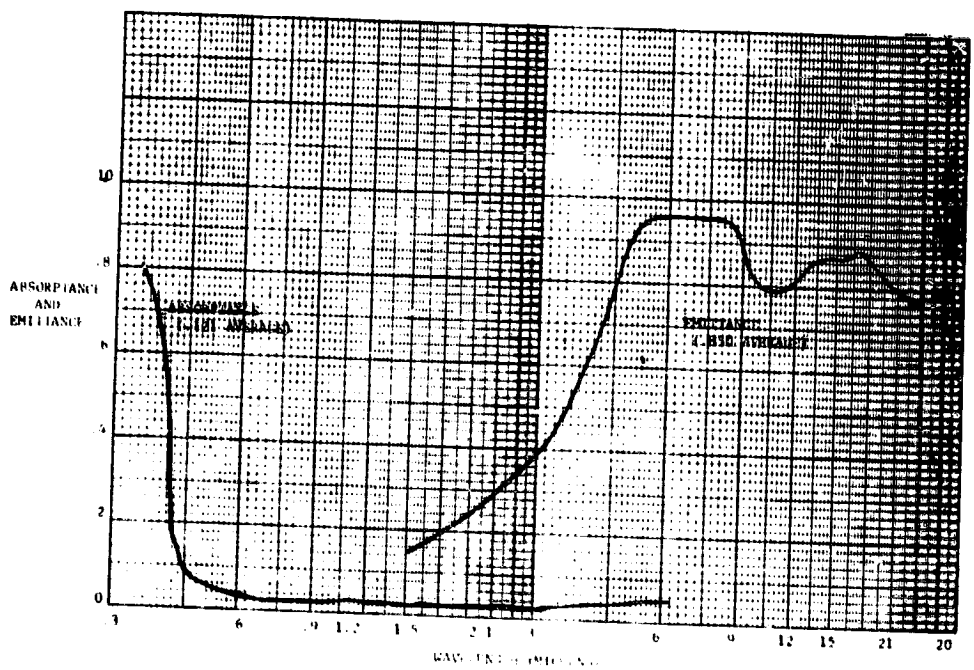

Figure 3c. Solar Absorptance and IR Emittance of GE-1TL Glass (10 Mil)

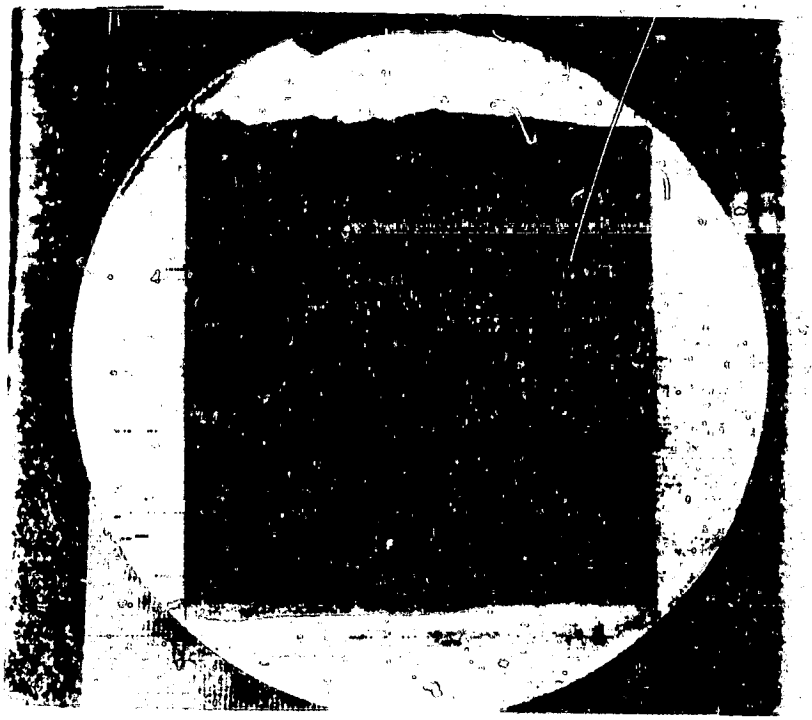

Figure 4a. OSR Configuration of ITO Coated One-Inch Square Microsheet

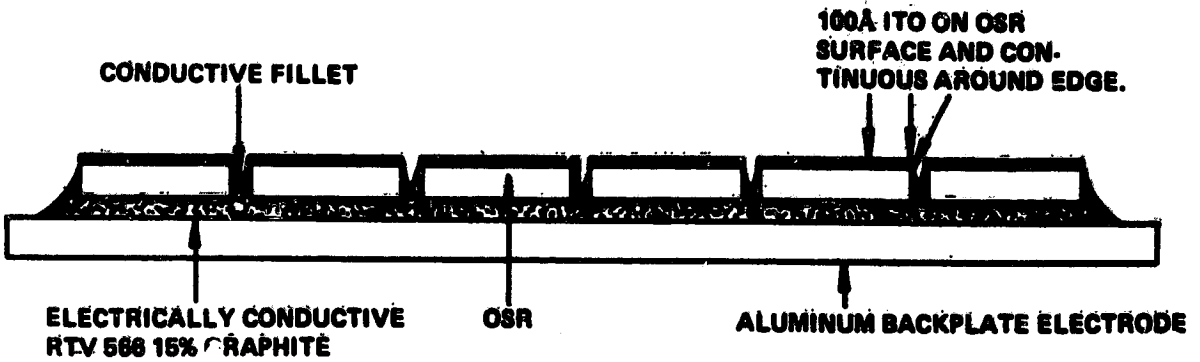

Figure 4b. Continuous Antistatic Grounded OSR Configuration

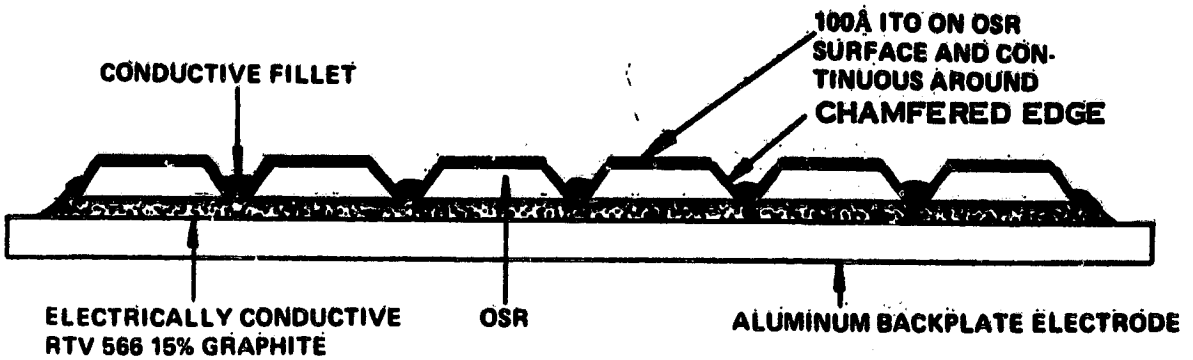

Figure 4c. Continuous Antistatic Grounded Chamfered OSR Configuration

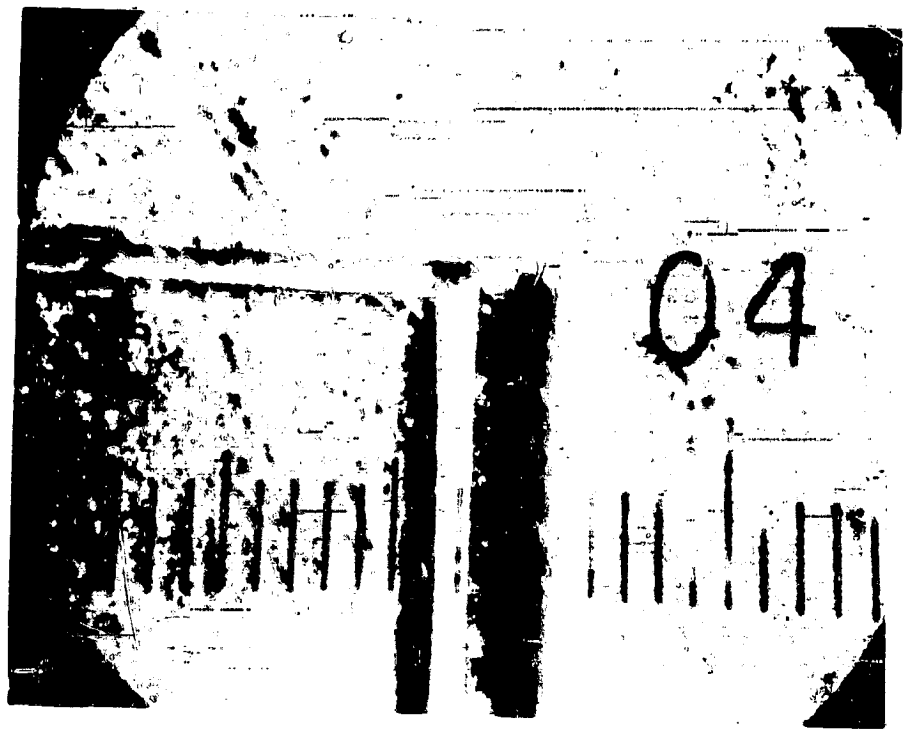

Figure 5a. Chamfered Edges of 10 Mil Thick Fused Silica

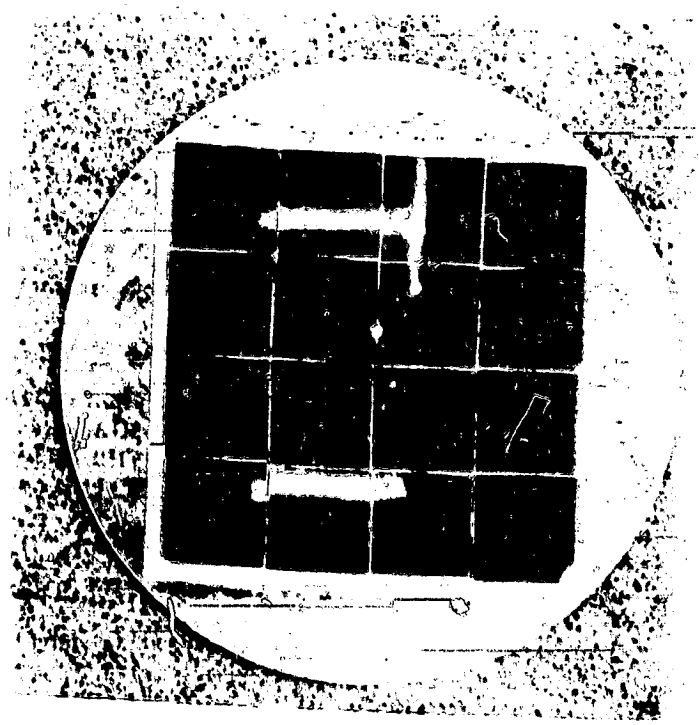

Figure 5b. ITO Coated OSR Matrix of Chamfered 2 cm Square Microsheet

Figure 6. Active Solar Cell Array with Uncoated Microsheet Coverglass

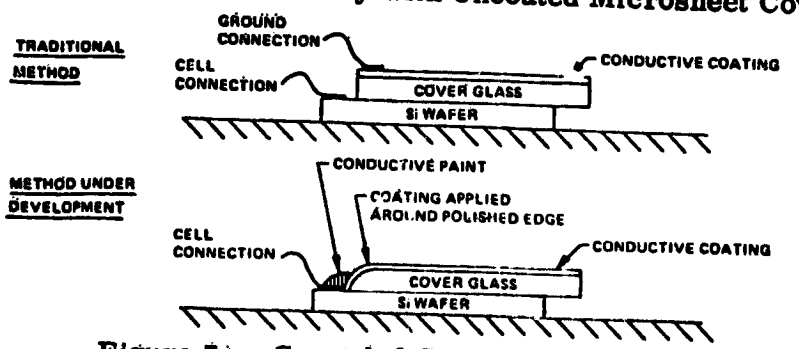

Figure 7a. Grounded Coverglass Design

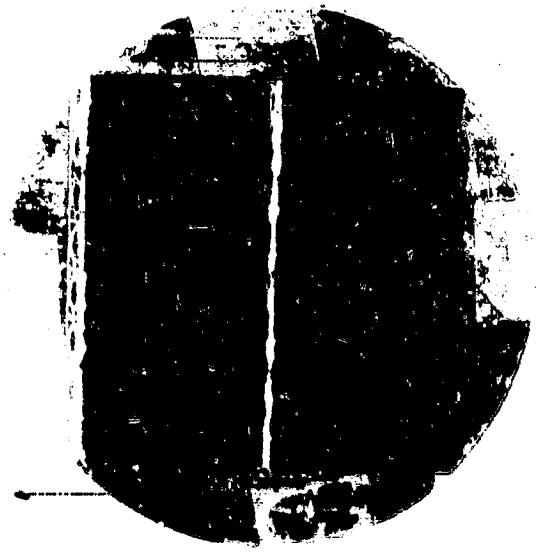

Figure 7b. Active IO Coated Solar Cell Array with 1109S Conductive Epoxy Ground Strip

Figure 8. Copper Foil Grounding Connection on Kapton Using Pyralux Adhesive

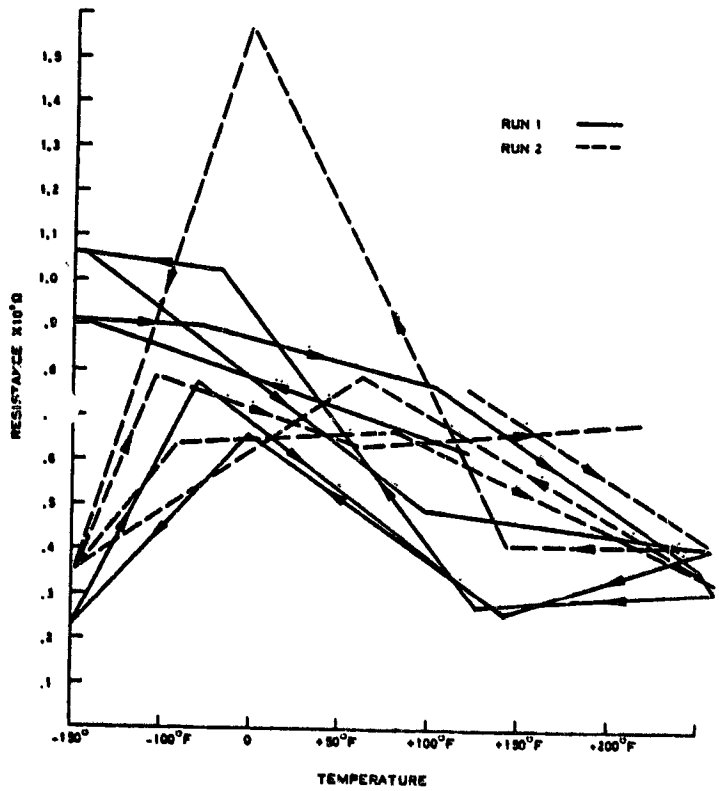

Figure 9. Resistance Cycling of Conductive Copper Tape Ground Strap on ITO and FEP Teflon (10 μA Current)

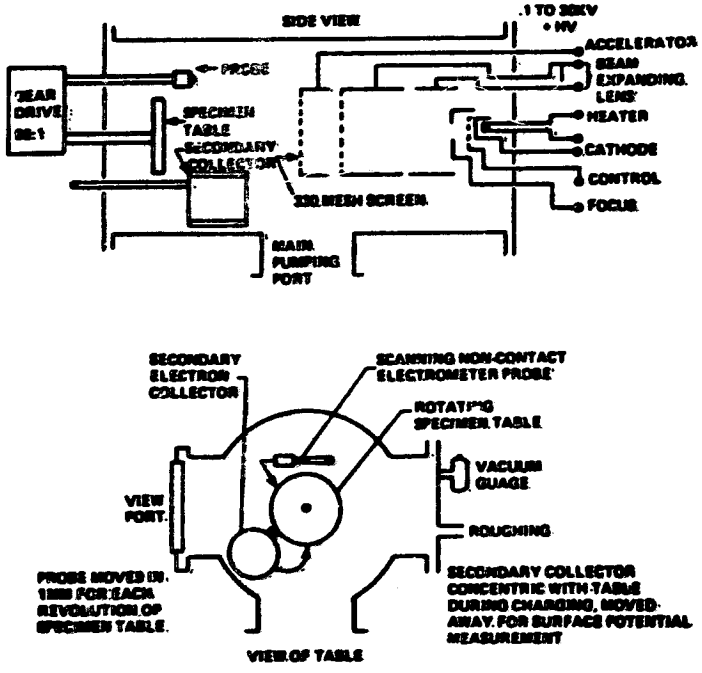

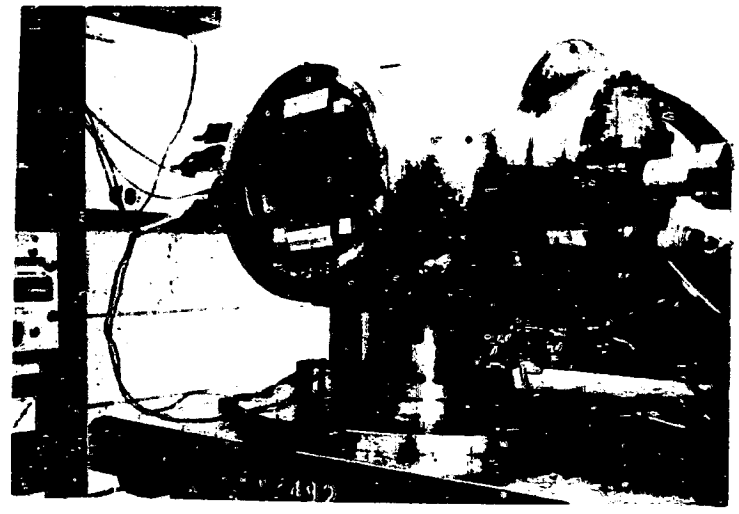

Figure 10. EST Test Facility

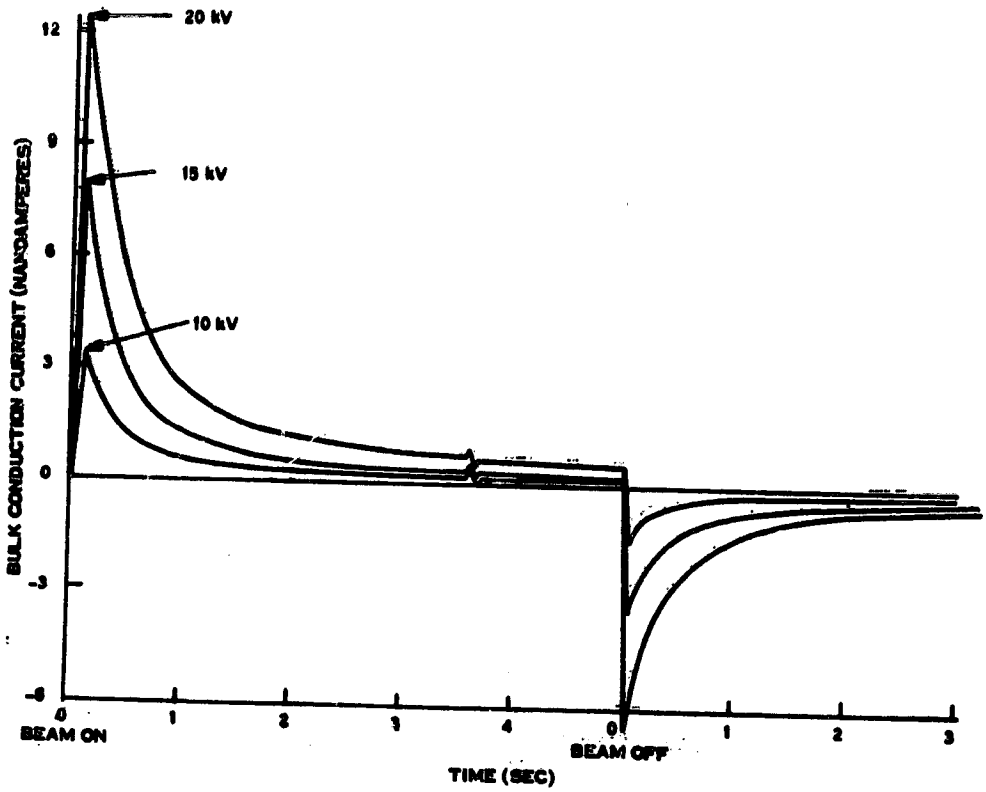

Figure 11. Bulk Conduction Currents for IO Kapton

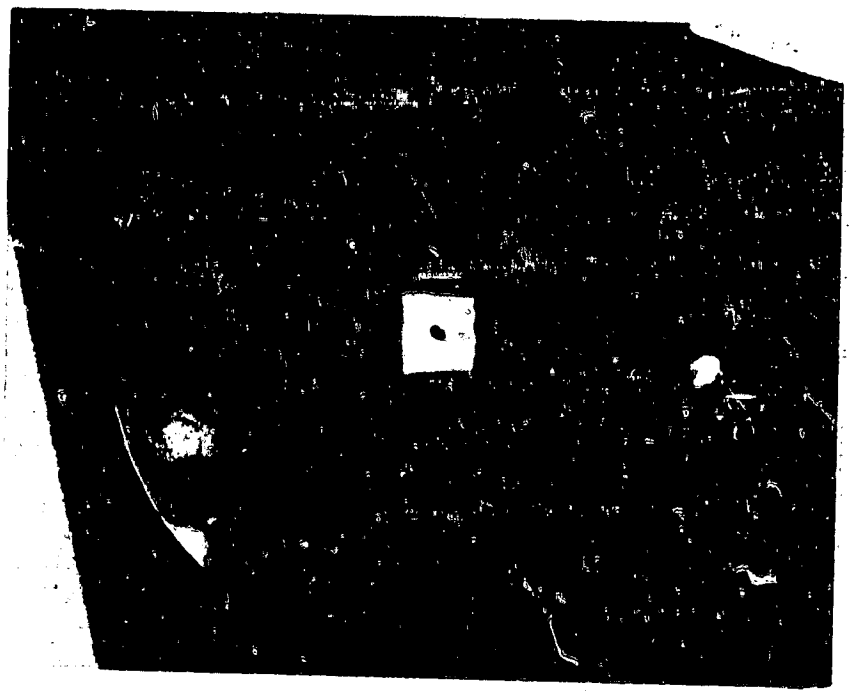

Figure 12a. ESD Test Configuration for Copper Tab Bonded to ITO Coated Kapton with Eccobond 56C

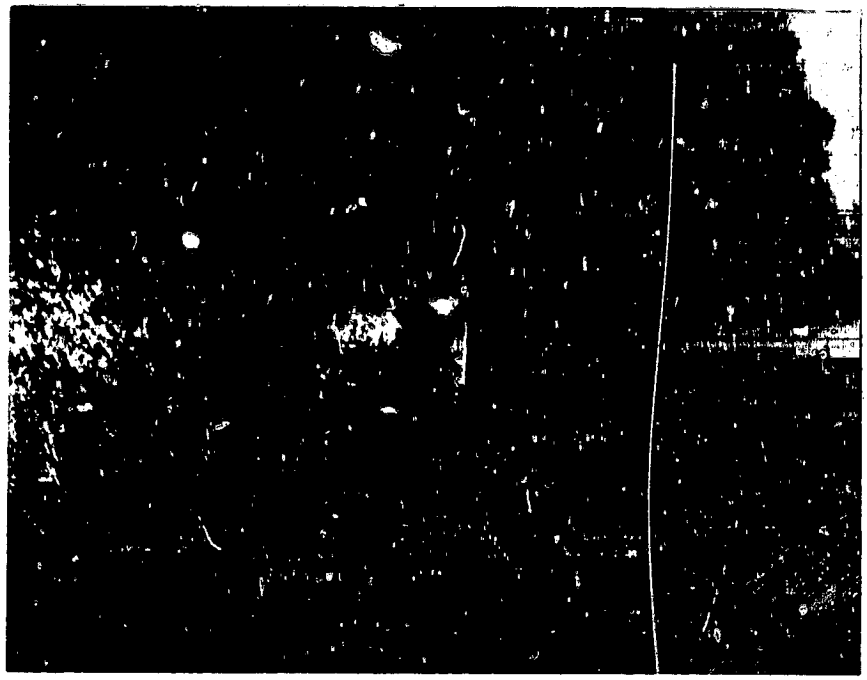

Figure 12b. 1/2" x 1/2" Conductive Copper Tape Ground Bond to ITO Coated FEP Teflon

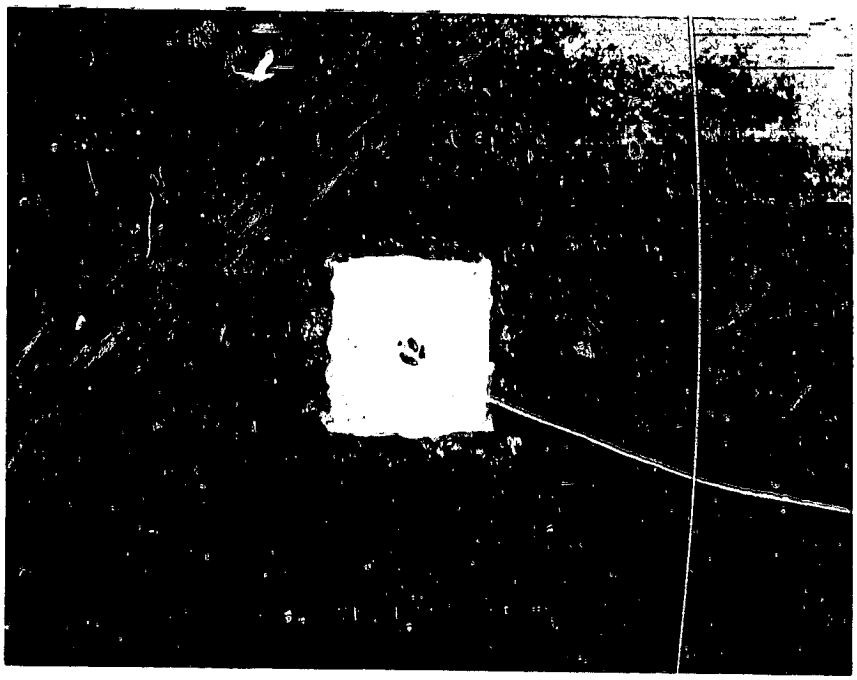

Figure 12c. 1/2" x 1/2" Copper Ground Tab Bonded to ITO Coated FEP Teflon with Eccobond 56C Conductive Cement

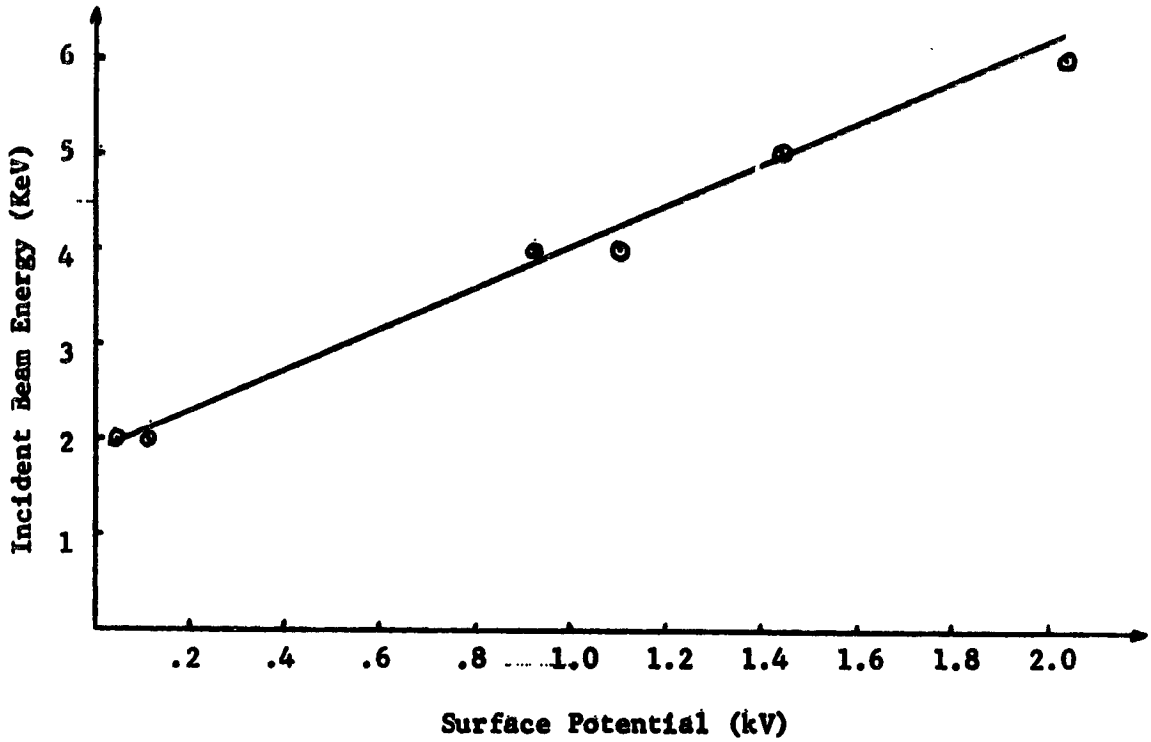

Figure 13. Surface Potential of Uncoated OSR Matrix in Electron Beam

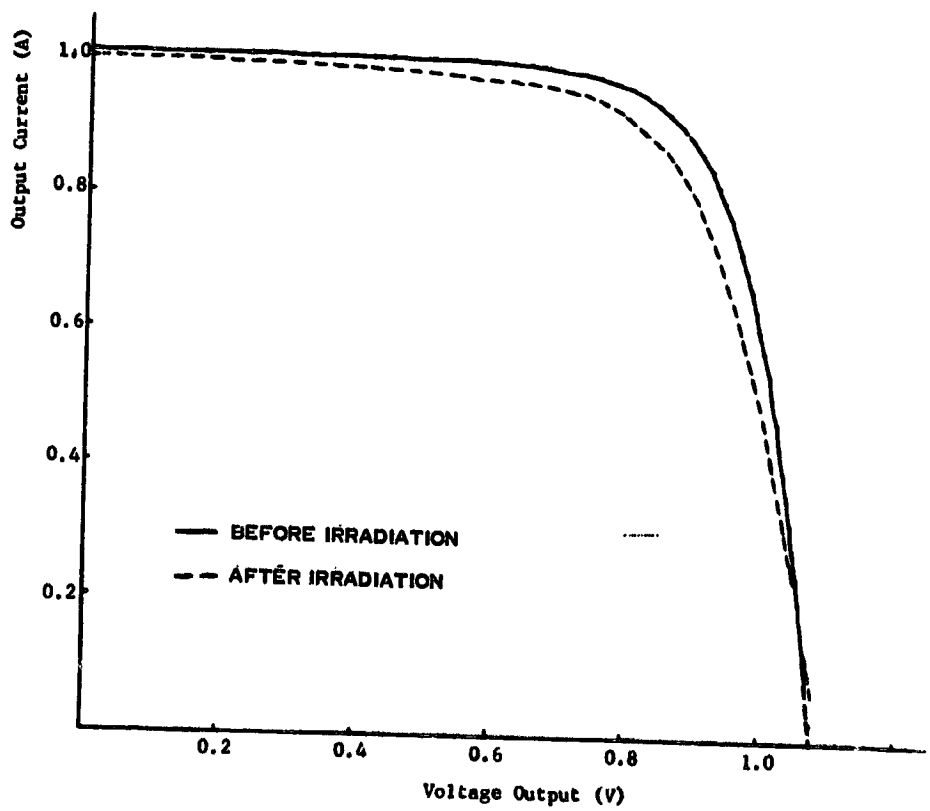

Figure 14. 2 x 4 IO Coated Solar Cell Array Performance After Electron Irradiation

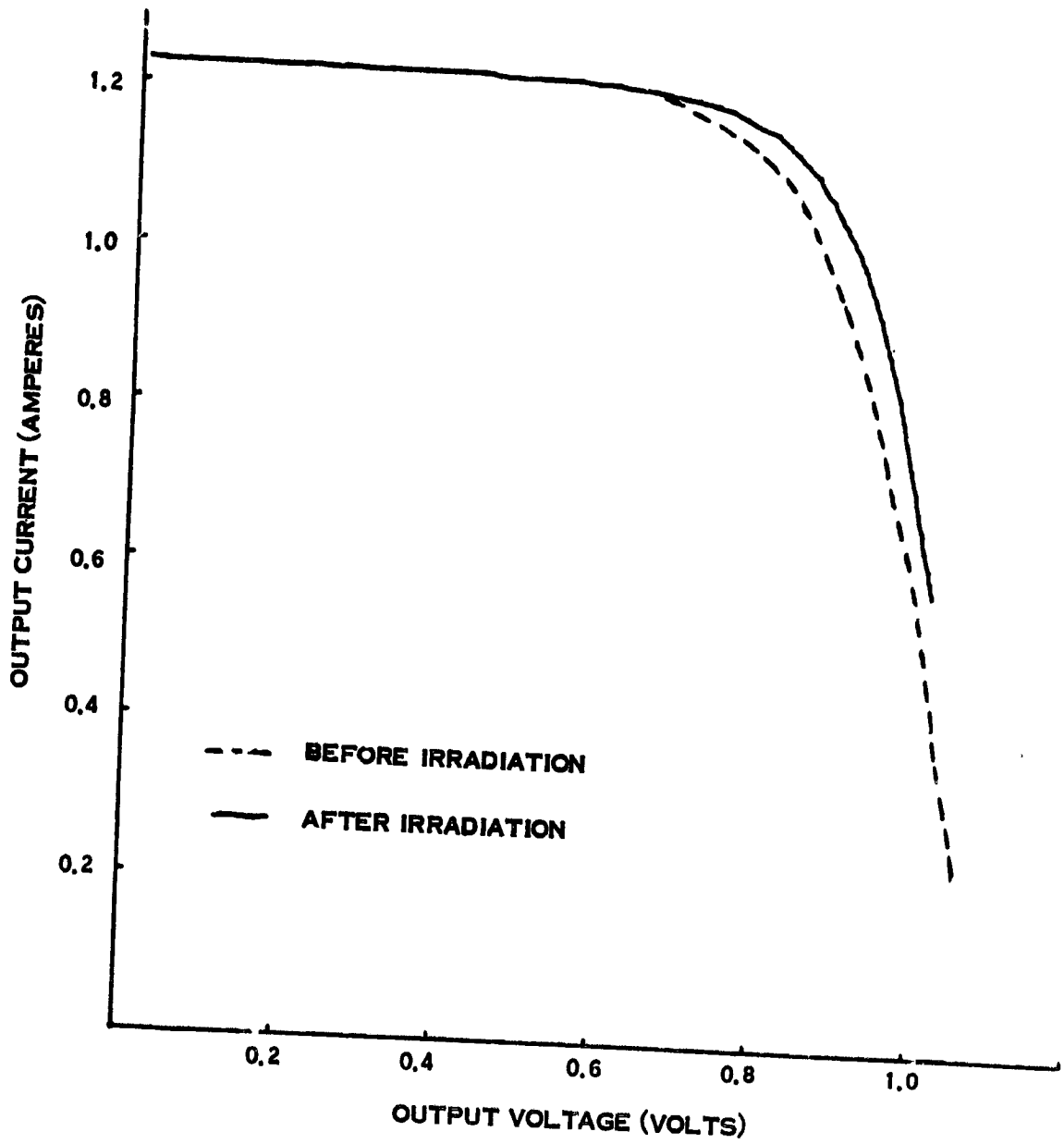

Figure 15. 2 x 4 Array With PPE Glass Without Conductive Coating After Electron Irradiation

D34

N79-24035

ELECTRIC FIELDS IN IRRADIATED DIELECTRICS

A. R. Frederickson
Rome Air Development Center

ABSTRACT

An existing model for quantitatively predicting electric field build-up in dielectrics is used to demonstrate the importance of material parameters. Results indicate that electron irradiation will produce 10^6 V/cm in important materials. Parameters which can alter this build-up are discussed. Comparison to known irradiation induced dielectric charging experiments is discussed.

INTRODUCTION

We wish to discuss the situation where space radiation penetrates a dielectric surface producing internal charge densities, fields, and possible breakdown effects. There are negligible transient magnetic field effects under typical space irradiation which corresponds to the classical dielectric work under low intensity laboratory irradiations. It has long been known that dielectrics can be made to spontaneously breakdown (discharge) under such irradiations (refs. 1,2) and that breakdown may occur during or hours after cessation of the irradiation (ref. 3). The Lichtenberg figures (ref. 1) which often result from such discharges are clear indications that internal bulk processes are fundamentally involved in the discharges. Work with samples which have not discharged indicates that very large (10^6 V/cm) fields are often generated in irradiated dielectrics (refs. 4 to 6). We will apply recently developed (refs. 7,8) methodology to calculate the internal electric fields, charge densities and current densities for irradiated dielectrics under such laboratory irradiations. In principle the method can be used for space radiations but the necessary set of parameters has not yet been quantitatively evaluated for space radiation.

The Lichtenberg figure effect is so dramatic that it has long been of interest and results of work on the effect may be helpful to the spacecraft charging area. The effect is usually reported for electron irradiations above 100 keV but has also been seen for X-rays. The figures are often associated with a large physical flaw in the sample introduced either prior to or after the irradiation. Discharges in materials do not always produce figures. Samples with initial figures can produce further Lichtenberg figures upon subsequent additional irradiations. We therefore deduce that spacecraft dielectrics may discharge spontaneously under irradiation especially in regions of high flaw density and that dielectrics charged up by irradiation can be discharged by micrometeorite impact at a later time.

Early work on discharges in irradiated dielectrics related the discharge to the sample material, the nature and quantum energy of the radiation, and the total exposure required to induce discharge. Empirical guidelines have been used by persons wishing to make Lichtenberg figures based on what worked in the past. A change in the radiation beam energy or the sample size or shape often resulted in no discharges but explanations for such effects were not quantitatively investigated. Only recently has some basic data and modelling become available to quantitatively predict the generation of intense electric fields in irradiated dielectrics (refs. 7-9).

From work in the various subfields of radiation transport (photon, proton, ion, electron, and neutron) we can predict the spatially dependent flux and current of charged particles at high energies (>100 eV) in the dielectric (ref. 10). Thus we can predict the spatial distribution of charge deposited by the high energy radiations. This distribution of charge can then be used to predict the electric fields internal to the dielectric.

Simultaneously, the problem of electric conduction in irradiated dielectrics has been theoretically (ref. 11) and experimentally (ref. 12) investigated. Results from these investigations allow us to calculate the conduction currents and the relaxation currents arising from the space charge fields in the dielectrics. It turns out theoretically, as we see below, that the conduction processes can either cause or prevent the development of breakdown fields. Information (ref. 13) and discrepancies (ref. 12) in the literature indicate that a great amount of uncertainty accompanies the evaluation of dielectric conductivity. However enough data exist that we can use it either as first guesses in our calculations or as worst case extremum in calculations for engineering application.

We can apply the radiation transport data and the dielectric conductivity data to Maxwell's equations and predict the transient or steady state response of a system of conductors and dielectrics. It is particularly simple in one dimension (ref. 14) although I believe we are constrained to numerical solutions on the computer in any case. We perform such a one-dimensional (1-D) calculation in this paper to illustrate the generic effects and the important parameters which relate to the bulk dielectric breakdown problem.

The particular example we choose to look at is dictated by availability of data on radiation transport, availability and ease of experimental comparison, possible application to spacecraft situations, and clarity of illustration. We irradiate thick (0.1 to 0.4 cm) sheets of Teflon with 1 MeV electrons while both sides of the sheet are at ground potential.

MODEL

The sample and irradiation geometry are shown in figure 1. The front and rear electrodes are assumed to not perturb the radiation transport in the dielectric; the amount of perturbation can be calculated and is truly negligible in this arrangement with electrons (ref. 15). The front electrode must be very

thin relative to an electron range and the rear electrode must be similar in atomic number to the dielectric. If the electrodes violate these constraints it is possible to correct "exactly" for the effect by use of electron transport codes but that involves extra work not related to the problem at hand.

For most of the calculations presented below, the Teflon was 0.3 cm thick. It has sometimes been found that breakdown occurs more readily in samples between one and two electron ranges thick and thus the choice of 0.3 cm. Results for other thicknesses are also given to show that theory similarly predicts such a thickness dependence.

The irradiation intensity may be high for spacecraft purposes but is chosen to correspond to easily realizable experimental conditions. Calculations have been made for various intensities, and nonlinearities which are due to dark conductivity effects do not become important until the intensity is reduced by 10^3 or more. For purposes of demonstration only we wish to avoid these effects.

Grounding or fixing the bias on both electrodes makes an immediately tractable situation. If we allowed the front surface to float, the calculation would become more complicated without improving our understanding. Because of (a) secondary emission effects, (b) the simultaneous presence of positive and negative charge plasma around the satellite, and (c) photoelectron emission, it seems that usually a dielectric surface will not charge beyond 10^4 volts relative to the rear electrode (body of the satellite). It is clear from the results that 10^4 volts on the surface will not significantly alter the large internal fields generated in the dielectric. Thus, grounding both electrodes is not expected to deviate from the situation seen on real satellites within the dielectric except in unusual cases.

The equations and numerical techniques have been completely described elsewhere (ref. 7). The dielectric is initially net charge neutral. The irradiation begins at time $t = 0$ and continues uninterrupted. As electrons accumulate in the dielectric, electric fields build up resulting in the generation of significant conduction current. The conduction current also causes charge to be moved around and deposited in the dielectric. This is a dynamic process which continues to change dramatically as the irradiation progresses in time.

At selected times we can use the computer print-out to monitor the spatial charge density, electric field, net current density (sum of incident electron beam current and conduction current) and meter current. The meter current is mathematically determined by integrating the net current density over the thickness of the dielectric: it can be thought of as the image current flowing to the rear electrode so that the electrode remains at ground potential. As we watch the various quantities change during the irradiation we can understand the physics of the process.

It is instructive to vary the parameters which describe the dielectric or the radiation and see the resulting changes. This provides further insight into the complex physical processes which take place. As in all numerical

solution techniques it is difficult to pick out the parameters, a-priori, that are critical to our situation. However, with a few runs given below we can see that certain parameters are important to the spacecraft charging problem.

RESULTS

The Calculation

Figure 2 describes the current directly attributable to the motion of the incident electrons as they scatter and lose energy in the dielectric; notice they are all stopped before penetrating 0.25 cm. This curve is an approximate fit to Monte Carlo data (ref. 17) using the function $A \exp(1 - \exp Bx^n)$ and is open to argument since very little data is available. However the shape is essentially correct and should serve our purposes well.

We calculate the rate of charge deposited by this high energy electron current from the continuity equation

$$-\frac{\partial \rho}{\partial t} = \frac{d\bar{J}}{dx} \tag{1}$$

in one dimension where ρ is the charge density, J is the current density, and x is the depth in the dielectric. We then determine $\rho(t)$ from

$$\rho(t) = \rho(t = 0) + \int_0^t \frac{\partial \rho}{\partial t'}\, dt' \tag{2}$$

Figure 3 shows the result for $t = 6$ seconds.

We can use several methods (Gauss' law is sufficient) to determine the electric field resulting from such a space density. The electric field resulting from the space charge density at $t = 6$ seconds is shown in figure 4. Note that peak fields are rapidly approaching 10^5 V/cm. Such large fields must result in some conduction current.

There are many many models we can use to estimate the conduction currents (ref. 13). Our purpose is not to validate conduction models but to investigate the parameters controlling field build-up in irradiated dielectrics. We choose to use a popular expression for conductivity (refs. 12,13)

$$\sigma = k\dot{D} + \sigma_0 \tag{3}$$

where σ is conductivity, k is a coefficient empirically determined (ref. 12), $\dot{D}$ is dose rate supplied by the high energy radiation, and σ_0 is the conductivity under no irradiation. Of course there are many other conductivity effects (field dependence, trap effects, total dose effects) which could be put easily into the computer but they do not help clarify the basic picture. Figure 5 is a plot of equation (3) for the particular case at hand (ref. 18); the

conductivity is a strongly varying function of depth in the dielectric.

Using the conductivity and electric field data we calculate the conduction current

$$\bar{J}_c(x) = \sigma(x)\bar{E}(x) \tag{4}$$

and assuming the high energy electron current, J_0, remains constant we determine the net current in the dielectric, J, from

$$\bar{J}(x,t) = \bar{J}_c(x,t) + \bar{J}_0(x) \tag{5}$$

Equations (1) and (2) are recalculated at time t using equation (5) to determine the electric field which results in a changed J_c and the process is continued, self consistently, using small time steps on the computer.

Data

Figure 6 shows the evolution of $J(x)$ from $t = 0$ to $t = 100$ seconds; there is quite a change occurring in $J_c(x)$ over this time span as a result of the build-up of spacecharge. Figure 7 shows the spacecharge density from $t = 0$ to $t = 100$ seconds. The increase in magnitude of ρ as the irradiation progresses is a natural result of the deposition of high energy electrons. The drastic change of shape between $\rho(x,t = 10)$ and $\rho(x,t = 100)$ curves is a dramatic demonstration of the importance of conduction currents. Figure 8 shows the evolution of $E(x)$ from $t = 0$ to $t = 100$ seconds. Notice that $E(x)$ is approaching maximum values of 10^6 V/cm which may cause breakdown.

Figure 9 describes the net current density, $J(x)$, for times from 100 to 500 seconds. Notice that as time progresses, the current density is tending towards a "flat" function. If $J(x)$ were constant then $\partial\rho/\partial t$ would be zero. It is postulated here that <u>usually</u> the build-up of conduction current occurs in such a way that $J(x)$ becomes, ultimately, a constant and final equilibrium is obtained. However irradiation and geometrical conditions might be obtainable so that oscillatory equilibrium occurs (for example analogous to the Gunn effect (ref. 19)).

Also notice in figure 9 that the "peak" is continually moving to the right. This has important implications for the electric field build-up near the rear electrode. The motion of this "peak" is very dependent on the assumed initial current distribution, $J_0(x)$, especially in the region of large x. It should be noted that in this region of x, $J_0(x)$ is sometimes called the straggling tail of the electron penetration distribution and is a subject of current controversy; the exact shape of the curve for $J_0(x)$ at large x is uncertain and yet may have importance in this dielectric area. At late times in the irradiation, only electrons in this straggling tail region penetrate the dielectric beyond the centroid of the spacecharge distribution and contribute to a continuing change in the spacecharge density. MeV electrons which do not penetrate to the "peak" at late times are exactly cancelled by conduction processes at these shallower depths.

Figure 10 plots the spacecharge density $\rho(x)$, at times from 100 to 1000 seconds. Notice that the peak in electron density constantly moves to larger depths as the electrons in the straggling tail become caught between the repulsive force of the charge distribution centroid and the "impenetrable" region of low conductivity near the rear electrode. An important concept results from this: If a region of negligible conductivity exists, the $J_0(x)$ distribution may cause continued spacecharge build-up until the spacecharge fields are comparable to the free electron stopping power of the medium which usually exceeds 10^7 V/cm - a field definitely in the breakdown category.

Also notice in figure 10 the important result that a positive spacecharge density develops in the region of $x = 0.12$ cm. This is similar to a result experimentally observed by Evdokimov and Tubalov (ref. 20) and theoretically predicted by Matsuoka et al. (ref. 9) by a similar calculation. The positive spacecharge has important implications for the spacecraft charging problems. The process which generates the positive spacecharge might be described as follows:

(a) A large negative spacecharge occurs near the extrapolated range depth of the incident electrons.

(b) The resulting electric field drives carriers through the conducting regions, such carriers then pile up at the borders of the less-conductive regions.

(c) In this case, "holes" are driven from the region of high dose rate (where they are generated) towards the negative charge centroid. Before they reach the negative charge region they are "stopped" by the significantly lowered conductivity (at approximately 0.15 cm) near the negative charge centroid. (This argument is for qualitative purposes and is not meant to imply that either holes or electrons are the dominant conduction mechanism.)

Figures 11 and 12 show how the net current density continues to decrease on average, continues to "flatten out" and how the electrons in the straggling tail continue to add electrons deep in the dielectric. The curves have not been computed for $t > 5\times10^4$ seconds but it is obvious that straggling electrons will continue to add charge until the conduction through the unirradiated region, $J_c(x = 0.3\text{ cm})$, equals the net current at the front surface $J(x = 0)$.

Figure 13 describes the space charge density as time progresses out to 5×10^4 seconds. The trends evident in prior figures continue but we are now approaching equilibrium. Another important fact becomes obvious for electron irradiated dielectrics: For fully penetrating radiations such as thin dielectrics or gamma rays equilibrium is reached at total doses typically 10^5 rads or less (ref. 12) but for nonpenetrating radiations the straggling effect can substantially increase the "dose to equilibrium," in this case to greater than 10^7 rads.[1] It should be noted that Teflon seriously degrades at 10^6 rads while most other dielectrics require 10^8 or more for degradation.

[1] $(5\times10^4 \text{ seconds})\ (2\times10^2 \text{ rads/sec}) = 10^7$ rads.

Figure 14 is a plot of the electric field at late times. Notice that the field $E(x = 0,t)$ has stabilized while at $x > 0.1$ it has not stabilized. The electric field is the most important parameter since we are interested in predicting breakdown. There are three maxima in the field; at the front surface, at the rear surface, and at approximately 0.18 cm. In one dimension the front and rear surface fields are derivable from the zeroth and first moments of the charge distribution (i.e., from the net total charge and the position of the centroid of the charge) but the fields interior to the dielectric are calculable only from the full distribution. At late times the field interior to the dielectric (related to the positive space charge region) becomes larger than the front surface field and also of sufficient magnitude to produce breakdown.

It should be remembered that the positive space charge region resulted from the conductivity gradient. We can generalize this result to say that any dielectric structure with a conductivity gradient is likely to internally charge up to produce large electric fields in regions adjacent to the gradient while under external irradiation. If one constructs a dielectric of layers (even of the same material from different batches) one is introducing another mechanism whereby dielectric breakdown under irradiation might occur. Conductivity gradients can be introduced by many factors (heat and light, for example) and should be avoided in spacecraft dielectrics.

Figure 15 is a plot of the three maxima in the electric field as a function of time. Of course these results are peculiar to the particular conditions chosen for this exercise. The relative magnitudes of the maxima (peaks) could change severely with changes in sample thickness, beam energy, dark conductivity, or coefficient of induced conductivity k (see eq. (3)). Other terms such as delayed conductivity, field dependent conductivity, and radiation damage would also be important. Never-the-less this figure vividly demonstrates that breakdown fields can occur with greatest likelihood near the surfaces or in interior regions of modulated conductivity.

The dark conductivity σ_0 assumed in the calculations was 10^{-20} ohm^{-1} cm^{-1}, probably an extreme for "Teflon." Similar calculations were also run for $\sigma_0 = 10^{-17}$ ohm^{-1} cm^{-1}, the other extreme, with almost identical results. The main difference is obvious in figure 15: the interior and rear surface field strengths do not become quite as large and reach equilibrium sooner.

Teflon has a coefficient of induced conductivity k greater than most dielectrics of interest. If we decrease k then the equilibrium electric fields will increase and thus other dielectrics are more likely than "Teflon" to breakdown. They may easily build up fields 10 times higher than Teflon in some irradiation conditions.

We can vary the coefficient of radiation induced conductivity by a factor of 10 or more and still be within the range of values reported in the literature. Table 1 describes the results for one particular case. Notice that the coefficient of induced conductivity acts nearly as a dark conductivity term at the front surface, that is, the electric field is nearly linearly dependent on resistivity, but at the center and rear the fields are not linearly dependent on the coefficient. This nonlinearity is strong when the radiation is nonpene-

trating. With fully penetrating radiation the equilibrium electric fields are always nearly linearly dependent on the coefficient of radiation induced conductivity.

It is interesting to vary the dielectric thickness and see how the three maximum (peak) field strengths vary. Table 2 shows the results for 1 MeV electron irradiation. In general, fully penetrating radiation is likely to produce smaller fields than nonpenetrating radiation and Bernhard Gross reports experiments on electron irradiations where breakdowns indeed occur most readily in samples with thicknesses between one and two electron ranges. However, by no means are breakdowns exclusive to this thickness range.

COMPARISON WITH EXPERIMENT

Our calculations produce one easy observable - the meter current. Figure 16 shows the meter current as a function of time during the irradiation. We have not been able to do the experiment prior to this conference but a similar experiment and calculation has been reported (ref. 9) with excellent agreement. Considering all the variables and their uncertainties, I would not expect good agreement in general. For several years we have been performing similar experiments with γ and X-rays without obtaining (meter current) excellent agreement, but we have created large fields routinely - it is a shocking experience to handle an irradiated dielectric.

This experiment has been performed once since the conference with poor comparison with the theory. The meter current was two orders of magnitude lower than expected at early time so we raised the beam current intensity to 4×10^{-4} A/m^2. The current slowly rose in time starting at 2×10^{-8} A and 3000 seconds later was 2.7×10^{-7} A declining to 1.3×10^{-7} A by 10^4 seconds. After 3000 seconds the meter began violent, sometimes full scale pulsing reflecting some sort of breakdown process which grew throughout the remaining irradiation. This irradiation was significantly more intense than the calculations above, but such an effect would not be predicted by the model.[2]

There are methods for investigating the trapped charge distribution in the dielectric such as thermally stimulated discharge and others (ref. 20), but the methods are indirect and may contain weak assumptions. This area seems to be more popular in the recent literature. I hope further work in this area will prove helpful to us. We would like to do similar calculations for a broad spectrum of irradiations but it will be hard work to put together a dose profile for 1 keV to 10 MeV electrons from the literature; it will be impossible to find data to construct the high energy electron current profile for that energy range. The best we could do is to make a guess or to get "someone" to do a Monte-Carlo run for a specific spectra of interest. Based on experience from several tens of calculations (refs. 7,12) for a variety of materials under a variety of irradiations I believe that for any given spectrum with quanta above

[2]Immediately prior to publication a lower intensity experiment was performed and gave agreement with the model at early times. The reason for the above discrepancies is not yet clear.

10 keV large fields will be generated in most "good" dielectrics and that given a particular dielectric geometry it is the unusual spectra which would not substantially charge dielectrics. I think it would be unlikely to find a spectra which would not charge a dielectric to $>10^5$ V/cm; further work is required to prove or disprove this statement (ref. 21).

It is here proposed that the following experiment be done because it is central to spacecraft charging. The theory described above can predict values for radiation induced conductivity and dark conductivity which would significantly reduce the maximum electric fields. We know that nonpenetrating high energy electrons are as troublesome as any radiations so we could alter samples to increase k and σ_0 and use electrons to test their charge-up response. It may be possible to formulate dielectrics with the proper spacecraft properties (optical, thermal, mechanical as well as conductive) without the danger of field build-up.

It is clear that effects such as field dependent conductivity, dose related damage, radiation induced traps, contacts, etc., can be important. They all impact the generation of fields through the conductivity term in our model. Their quantitative evaluation is very variable for materials of interest. At this time, such effects seem to be relatively small compared to the radiation induced conductivity term. But, it might be profitable to consider these effects with an eye to increasing the conductivity under irradiation and through the unirradiated region, if any exists. Experiments on these effects would be helpful.

SUMMARY

We have described a model which predicts currents and fields in irradiated dielectrics; we find some weak empirical agreement in the literature and in our own experiments. It turns out that the parameters which describe the conduction mechanisms in the dielectric may be critical for spacecraft purposes since they seem to be the handle by which we can prevent excessive electric field build-up. A nonuniform conductivity profile in the dielectric is shown to be potentially important: we should avoid such profiles. In general the higher energy quanta (>10 keV) are probably more important because they penetrate deeper and deposit greater electric potential energy in the dielectric causing more energetic breakdown discharges.

Several suggestions are made concerning the search for usable dielectrics which will not substantially charge up; increasing the bulk conductivity offers the greatest potential for eliminating discharges and decreasing differential charging.

REFERENCES

1. Furuta, J., Hiraoka, E., and Okamoto, S., J. Appl. Phys. 37, 1873 (1966).

2. Vorob'ev, A. A., Zavadovskaya, E. K., Starodubtsev, V. A., and Fedorov, B. V., Soviet Physics Journal, 1977, Plenum Press, translator, p. 171. (UDC 53.043:537.224).

3. Brown, R. G., J. Appl. Phys. 38, 3904 (1967).

4. Evdokimov, O. B., Kononov, B. A., and Yagushkin, N. I., Soviet Physics Journal 1978 (Plenum Press translation), p. 1339.

5. Zavadovskaya, E. K., Annenkov, Yu. M., Starodubtsev, V. A., Vakhromeev, V. G., and Malofienko, G. M., Soviet Physics Journal (Plenum Press translation) 1974, p. 144.

6. Gross, B., Dow, J., and Nablo, S. V., J. Appl. Phys. 44, 2459 (1973).

7. Frederickson, A. R., AFCRL-TR-74-0582, 1974 (Available NTIS); IEEE Trans. Nuc. Sci. NS22, 2556 (1975).

8. Pigneret, J., and Strobak, H., IEEE Trans. Nuc. Sci. NS23, 1886 (1976).

9. Matsuoka, Shingo, et al., IEEE Trans. Nuc. Sci. NS23, 1447 (1976).

10. High energy radiation transport modeling has steadily improved since 1950 with the widespread use of nuclear energy. For example, data for the calculations below was obtained from work by Martin Berger of NBS during the 1960's and from work by John Halbleib et al. of Sandia Labs. during the 1970's. Many other sources for such data are now available in the literature.

11. No single reference is helpful here. To appreciate the diversity of this field, one must review a large number of works and the following brief list of authors is a beginning point: Albert Rose (book), Richard H. Bube (book), J. F. Fowler, H. J. Wintle, Bernhard Gross, Thomas J. Ahrens, L. K. Monteith, and H. E. Boesch.

12. For a reasonably complete up to date listing of references see A. R. Frederickson, IEEE Trans. Nuc. Sci. NS24, 2532 (1977). For a list of parameters for various dielectrics see T. J. Ahrens and F. Wooten, IEEE Trans. Nuc. Sci. NS23, 1268 (1976), and R. C. Weingart et al., IEEE Trans. Nuc. Sci. NS19, 15 (1972).

13. Wintle, H. J., IEEE Trans. Electrical Insulation, EI-12, 97-113 (1977). Also contains extensive references.

14. For an example of the increased complexity of modeling in 3-D see I. Katz et al., NASA CR-135256, "A Three Dimensional Dynamic Study of Electrostatic Charging in Materials" (Aug. 1977).

15. However if we were using X-ray irradiation, the choice of electrodes could severely distort the results as is shown in references 7, 8, and 16.

16. Chadsey, W. L., IEEE Trans. Nuc. Sci. NS21, 235-42 (1974).

17. Perkins, J. F., Phys. Rev. 126, 1781-4 (1962).

18. For examples of dose depth data see: G. J. Lockwood, G. H. Miller, and J. A. Halbleib, IEEE Trans. Nuc. Sci. NS20, 326 (1973); Harvey Eisen, "Electron Depth-Dose Distribution Measurements in Metals and Two Layer Slabs" Thesis, Univ. Maryland, Dec. 6, 1971; M. J. Berger and S. M. Seltzer, Protection Against Space Radiation, NASA SP-169, p. 285 (1967).

19. Private communication, Jacques E. Ludman, 1978.

20. Evdokimov, O. B., and Tubalov, N. P., Sov. Phys. Solid State 15, 1869 (March 1974, A.I.P. Translation).

21. Similar calculations for ∿10 keV electrons are reported by Beers and Pine at this conference and their results seem to be in agreement with these comments.

TABLE 1. - PEAK ELECTRIC FIELDS AT EQUILIBRIUM FOR 0.24-cm-THICK TEFLON UNDER 1-MeV ELECTRONS FOR THREE ASSUMED VALUES OF k
[10^{-5} A/m^2; $\sigma_0 = 10^{-17}$ ohm^{-1}cm^{-1}.]

k (see eq.(3)) sec/ohm meter rad	Equilibrium Electric Field Intensity, V/cm		
	Front	Center	Rear
10^{-14}	.056	.047	.52
10^{-15}	.545	.40	2.78
10^{-16}	4.81	2.42	10.2

TABLE 2. - PEAK ELECTRIC FIELD INTENSITIES AS FUNCTION OF "TEFLON" THICKNESS FOR ASSUMED VALUE OF DARK CONDUCTIVITY
[$\sigma_0 = 10^{-17}$ ohm^{-1}cm^{-1}; k = 10^{-15}.]

Dielectric Thickness	Equilibrium Field, 10^6 V/cm		
	Front	Center	Rear
.10 cm	.069	not defined	.108
.15 cm	.221	not defined	.639
.18 cm	.375	(.12)	1.71
.20 cm	.466	.20	2.76
.22 cm	.521	.31	3.34
.24 cm	.545	.40	2.78
.30 cm	.559	.50	1.04

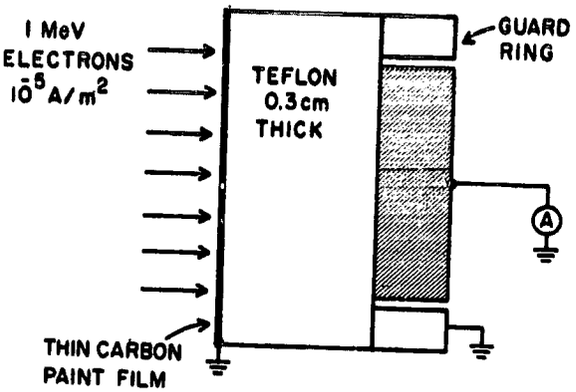

Fig. 1. The apparatus being modeled in the calculations and constructed for experimental comparison.

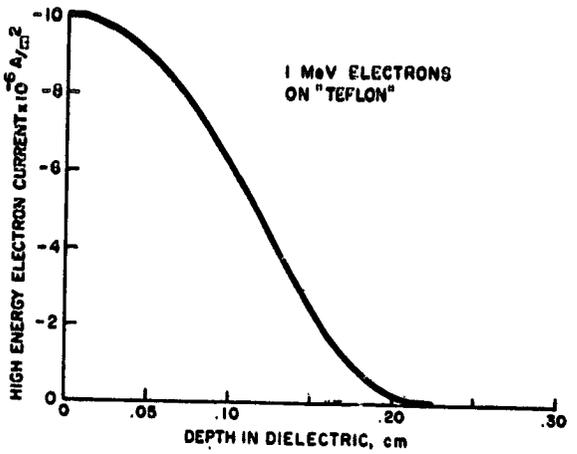

Fig. 2. The electric current due directly to the incident high energy electrons.

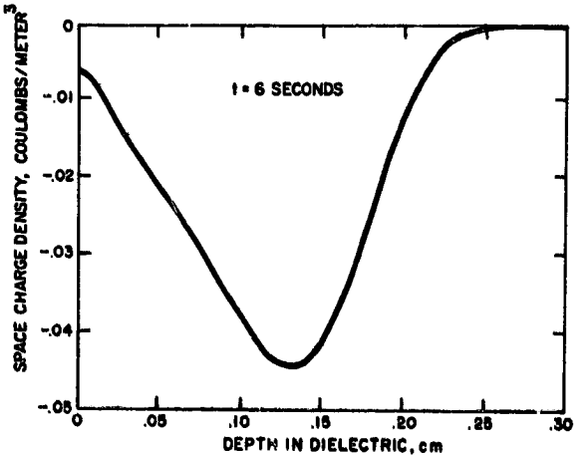

Fig. 3. The charge deposited in the dielectric by the current profile in figure 2 after six seconds irradiation.

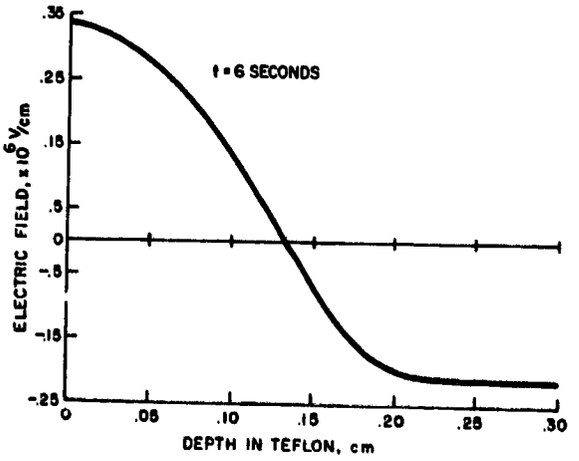

Fig. 4. The electric field due to the space charge shown in figure 3.

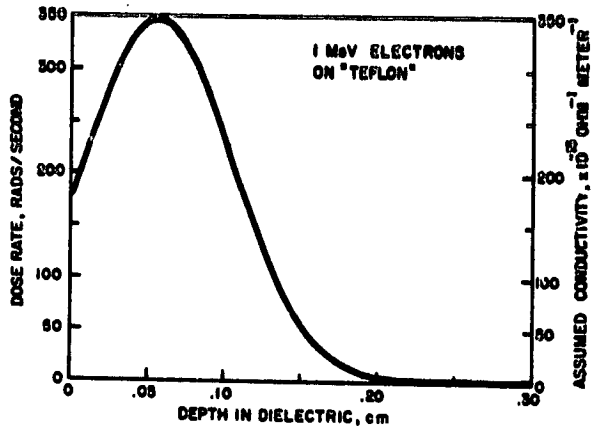

Fig. 5. The dose profile due to the irradiation. The conductivity profile is obtained from equation (3) using values for k obtained from reference 12.

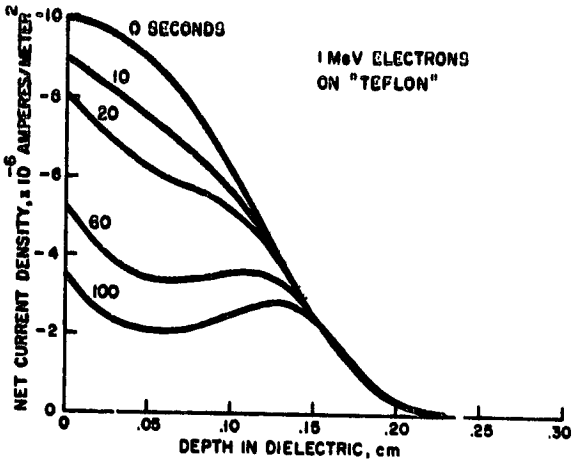

Fig. 6. The evolution of net current density (eq. (5)) at early times.

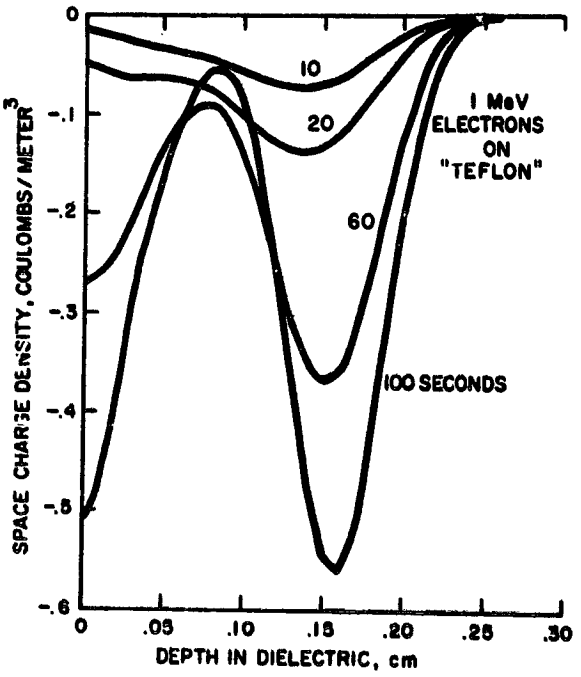

Fig. 7. The evolution of space charge density (eq. (2)) at early times.

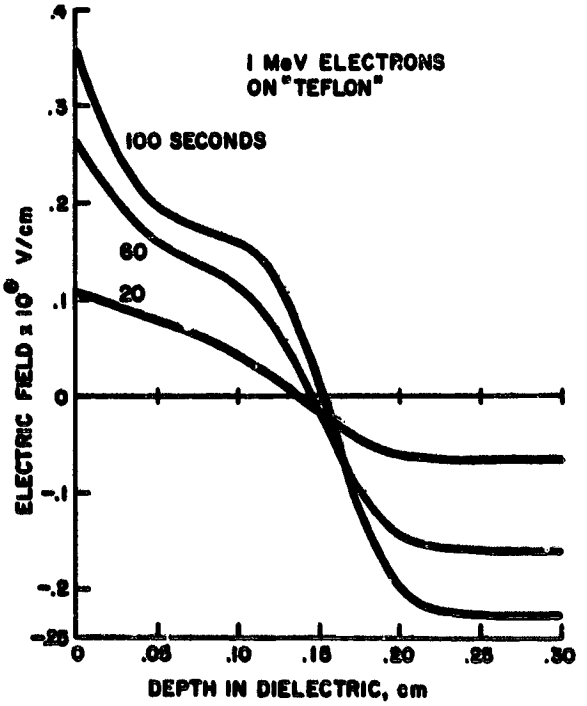

Fig. 8. The evolution of electric fields at early times.

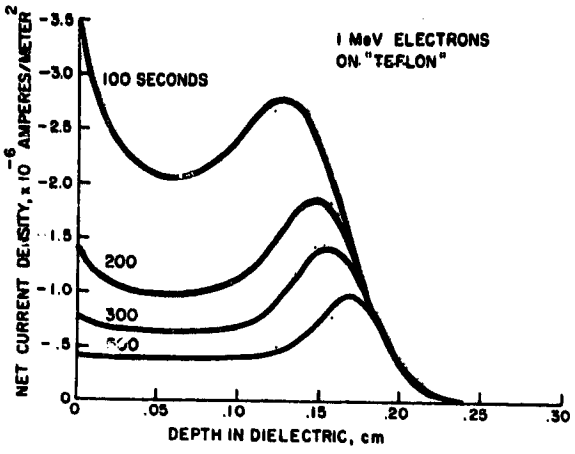

Fig. 9. The evolution of net current density at later times, 100 to 500 seconds.

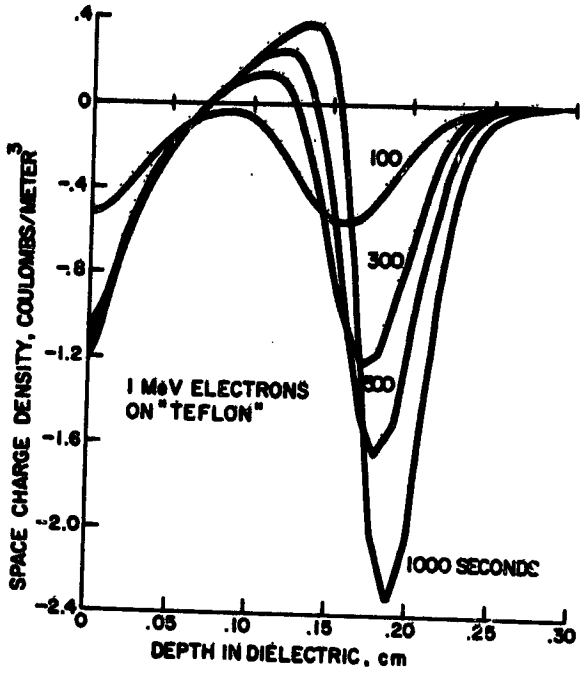

Fig. 10. Space charge density at times from 100 to 1000 seconds.

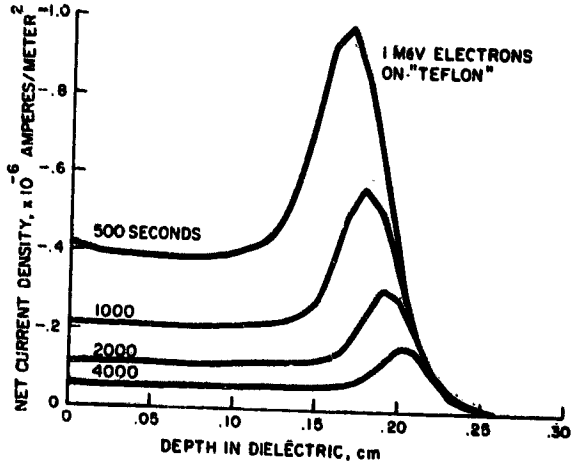

Fig. 11. Net current density at times from 500 to 4000 seconds.

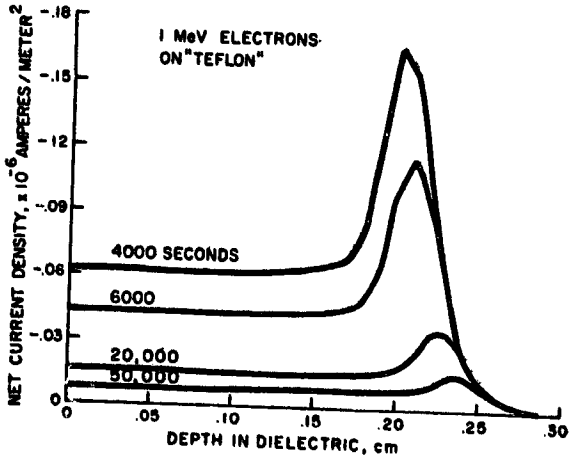

Fig. 12. Net current density at times 4000 to 50,000 seconds.

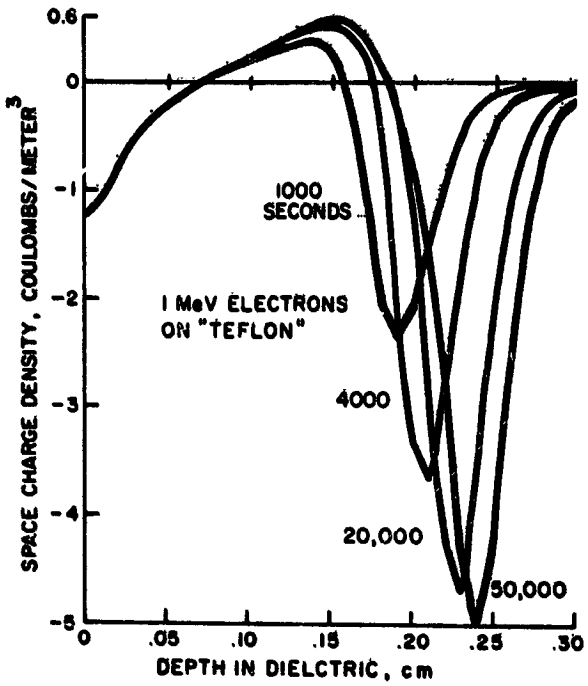

Fig. 13. Space charge density at times from 1,000 to 50,000 seconds.

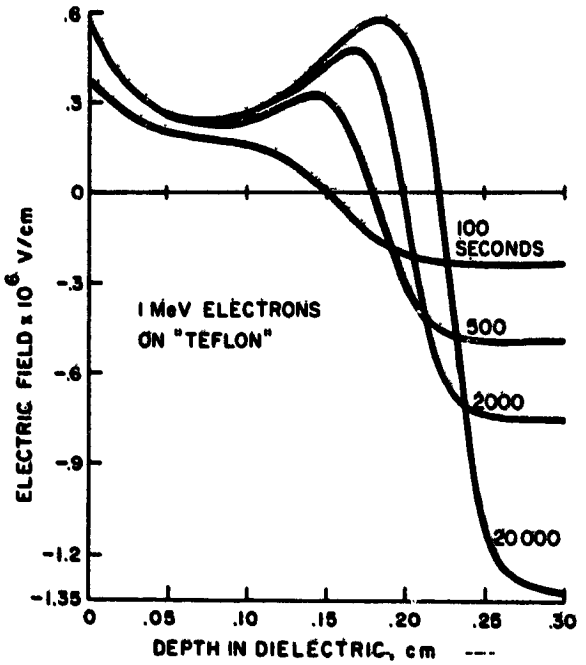

Fig. 14. Electric field at late times, 100 to 20,000 seconds.

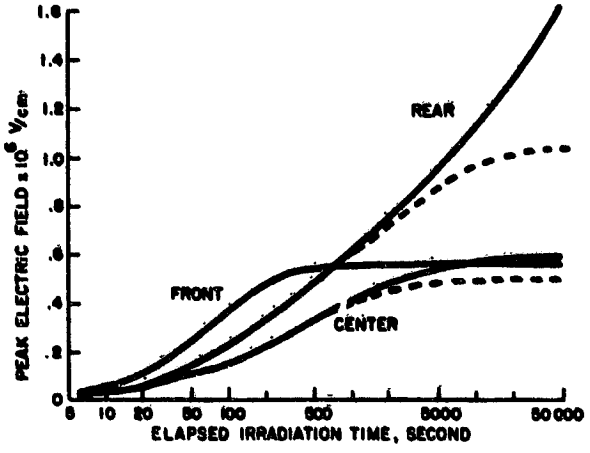

Fig. 15. Electric field intensity maxima for the three peaks evident in figure 14. The solid lines are for dark conductivity $\sigma_0 \cdot 10^{-20}$ohm^{-1}cm^{-1}, the dashed lines for $\sigma_0 \cdot 10^{-17}$ohm^{-1}cm^{-1}.

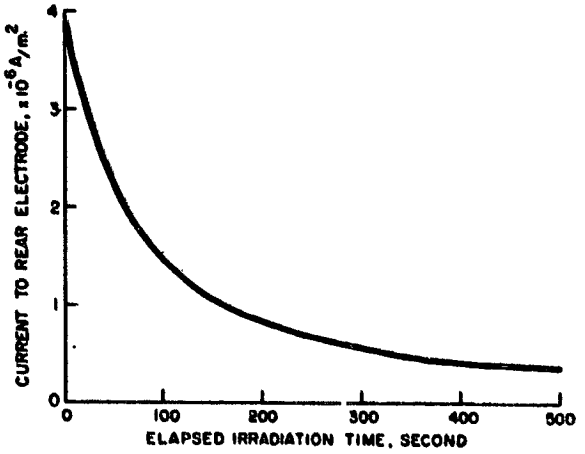

Fig. 16. Ammeter current as a function of time: see figure 1.

D35

N79-24036

EFFECTS OF ELECTRON IRRADIATION ON LARGE INSULATING SURFACES USED FOR EUROPEAN COMMUNICATIONS SATELLITES

J. Reddy and B. E. Serene
European Space Agency

INTRODUCTION

The Orbital Test Satellite (OTS) and its derivatives ECS (European Communications Satellite) and MARECS (Maritime ECS) make extensive use of aluminised kapton for passive thermal control.

The satellites are three axis stabilised and in geostationary orbit (OTS at 10°E). The external configuration is such that the kapton is in contact with the plasma and is able to charge electrostatically.

Some time ago a test programme was initiated to establish the maximum charging potentials of these surfaces and to give some indication of the discharge characteristics (Ref. 1). The results of this work, together with results obtained by others (Ref. 2, 3) led us to believe that the discharge characteristics and the consequent material degradation would be related to the size of the charging surface. In view of the large exposed insulating surfaces on OTS it was decided to perform a series of measurements on large samples ($\simeq 0.5\ m^2$) in order to establish the discharge rates and characteristics and observe any material degradation.

TEST SAMPLES AND PREPARATION

The largest exposed surfaces which present an insulating surface to the plasma are the VHF Shield Assembly and the Antenna Dish.

The VHF Shield Assembly is shown schematically in Fig. 1. The outer layer of aluminised kapton is separated from a relatively thick sheet of aluminium foil by a thin (6 μ) layer of kapton. The thick aluminium foil is connected electrically to the satellite structure and provides a continuous ground plane for the VHF Antennas on the satellite. The complete assembly is held together by means of adhesive kapton tape. In addition to this, and in order to provide a nominal electrical connection between the vacuum deposited aluminium and the main aluminium foil, a small rivet and washer assembly is used, shown in Fig. 2. For their assembly the central kapton layer is perforated allowing the aluminium to squeeze through and so provide el. trical continuity.

The VHF Shield Assembly is completed by a number of venting holes shown in Fig. 3.

The second item under test was a sample of the structure used for the main antenna dish. A schematic of this structure is shown in Fig. 4. This antenna comprises an aluminium honeycomb on which is mounted a carbon fibre sheet which is painted with white paint, type S13 GLO. It was not certain if this paint was conductive, and even so, the electrical continuity between the carbon fibre and the honeycomb was not assured.

Samples measuring 0.7 m x 0.7 m of these assemblies were prepared and mounted on an aluminium frame. The conductive rear surfaces of the samples were connected electrically to the frame which could then be used to provide a reference point for the measurements.

TEST CONFIGURATION AND CONDITIONS

The tests were performed under an Estec contract and financial and technical management by the Deutsche Forshungs und Versuchsanstalt für Luft und Raumfahrt (DFVLR) at Porz Wahn in Germany (Ref. 6). The chamber is shown in Fig. 5 and has a conventional commercial electron gun as a source. This is followed by a scattering foil (2 μ thick) in order to achieve reasonable homogeneity over the sample area. The scattering foil details are described in Ref. 4. The beam homogeneity was measured using three simple sensors traversing the chamber in the plane of the test object.

With the incident electron beam of 25 keV (before the scattering foil) the homogeneity obtained in the plane of the test sample was approximately 30 %. The flux profile is shown in Fig. 6.

The mounted samples were suspended in the chamber and isolated from it (Fig. 7). The frame was connected by means of a dedicated wire to a ground reference point external to the chamber. This allowed measurement of the leakage current and the discharge current. The incident flux was monitored by means of a fixed sensor in the plane of the test sample. A thermistor was mounted on the rear surface of the sample to measure temperature.

In addition to the above, a commercial field mill was installed on the scanning mechanism with the intention of measuring the sample surface potential. Unfortunately, due to the flexibility of the samples the mutual attraction of the field mill and sample precluded such measurements.

The discharge current was measured using a current probe type P6022 connected to a Biomation 8000 transient recorder. A schematic diagram of the electrical configuration is shown in Fig. 8.

The samples were irradiated for eight hours at two temperatures - room temperature (approx 20°) and liquid nitrogen temperature (-173°C) under a vacuum of 10^{-6}torr.

The effects of illumination of the surfaces on charging were simulated by illuminating the test samples with a simple 500 watt lamp mounted outside the chamber.

The incident flux was 10 n ampères.cm^{-2}. The electron beam energy after scattering was not measured directly but has been calculated to have the profile shown i Fig. 9. (Ref. 5 also.)

TEST RESULTS

The test results will be presented as follows:

a) —Visual observations during irradiation by electrons

b) Measurements made of leakage current and discharge characteristics

c) Observations of material degradation after irradiation is completed

VISUAL OBSERVATIONS

VHF Shield Assembly

The most immediate observation made during the irradiation of the VHF Shield Assembly was that it appeared as it the entire surface discharged with the major part of the illumination being around the venting holes and the central rivet (Fig. 10). In fact two distinct forms of discharge were observed. The first already described and also smaller point discharges apparently located randomly on the sample.

Antenna Structure

The visual observations here were limited to discharges observed at a particular point on the surface. The intensity of the discharges was so low that photography was not possible.

In addition to the discharges it was observed that the painted surfaces fluoresced with a yellow-green colour at room temperature but with a blue-violet colour at liquid nitrogen temperature. The explanation for this is not obvious.

ELECTRICAL MEASUREMENTS

VHF Shield Assembly

A plot of the leakage current versus time is shown in Fig. 11 showing the charging characteristics and the discharges. The rate of discharges is shown in Table 1 where it can be seen that the discharges became less frequent as the test proceeded.

During illumination with the lamp no discharges were observed at all.

Typical discharge currents are shown in Figs. 12 and 13. Unfortunately, equipment limitations did not allow an absolute measurement of the maximum amplitude. However, it can be seen that the amplitude may be in excess of 400 ampères with a rise time faster than one hundred nanoseconds and a pulse width of four microseconds. We should also note that the measurements were made on a ground connection several metres long which suggests that the actual maximum could be even higher.

Antenna Structure

A plot of the leakage current versus time in the antenna structure is shown in Fig 14. The rate of discharges is shown in Table 2, and here it can be seen that the rate of discharges stays constant and are only observed at liquid nitrogen temperatures.

Illumination with the lamp resulted in no change in the discharge characteristics indicating that there is little photo-emmission from this paint.

The discharge current was measured and is shown in Figs 15 and 16. It can be seen that the maximum current is considerably less than one ampère. In addition there is a pronounced 'ringing' associated with the length of the ground connection.

MATERIAL DEGRADATION

VHF Shield Assembly

The degradation of the vacuum deposited aluminium (VDA) is shown in Figs 17 - 20. As can be seen there has been considerable evaporation of the VDA in the regions surrounding the venting holes and the rivet. The evaporation of the VDA surrounding the rivet was sufficient to isolate the rivet from the VDA itself. In addition to the damage around the holes, damage was observed in the regions associated with small indentations in the VDA.

Further investigations showed that there was no degradation in the kapton itself even in those areas where VDA was evaporated.

In one instance the rear aluminium foil was actually punctured, apparently by the force of the aluminium evaporating. The area of VDA which was evaporated is estimated to be 0.3 % of the total surface area.

Antenna Structure

The only observable effect on the antenna structure surface was some discolouration of the paint in the region where discharges were observed. Closer inspection showed that the paint finish at this point was not very good and the possibility is that this defect promoted the discharges and subsequent degradation.

CONCLUSIONS

From the foregoing results it is clear that although it is capable of charging to a reasonably high potential, the effects of discharges on material property and EMI for the antenna structure are relatively insignificant.

For the VHF Shield Assembly the opposite is true. Here we have seen considerable damage to the VDA and associated with this are very large transient currents which could severely affect the system electronics.

It is difficult to assess the effects of the loss of VDA on the overall thermal design; however, a simple solution to this problem is to make the aluminum layer much thicker. This solution has been tried and the results are reported in Ref. 3. Furthermore, the need to reduce edges to a minimum by the exclusion of holes and rivets is also obvious.

With regard to the current transients solutions are somewhat less immediate. We have seen on smaller examples (0.1 m x 0.1 m) current transients of the order of thirty ampères. For samples described here we have currents of the order of several hundred ampères. Clearly there is a limit to the maximum amplitude which may be seen regardless of surface dimensions. However, it is certain that the energy dissipated in the discharge will continue to increase. The test results given here indicate a maximum discharge energy of the order of tens of joules. Such energy flowing in the satellite structure is almost certain to result in anomalous electronic behaviour.

With the present external satellite design 'frozen' with regard to thermally acceptable materials the only solution to this problem would appear to be desensitisation of all susceptible electronic circuitry.

Finally, it must be emphasised that any attempts to evaluate the charging and more importantly the discharging behaviour of materials must be made on samples which reflect accurately the mechanical configuration and more importantly the actual operational dimensions.

REFERENCES

1. Levy, L: Irradiations par electrons de revêtements de contrôle thermique. DERTS final report no 4050

2. Balmain, K G: Charging of spacecraft materials simulated in a scanning electron microscope. Electronics Letters 9 No 23

3. Stevens, N J, Lovell, R R, Gore, V: Spacecraft charging investigation for the CTS Project. NASA TMX 71795

4. Serene, B E, Reddy, J: Qualification of a large electron irradiation facility for telecommunication satellite differential charging simulation. 1978 Spacecraft Charging Conference

5. Levy, L, Sarrail, D: Evaluation de l'énergie d'un faisceau d'électrons au moyen d'un dispositif simple. DERTS report no NT/04/5

6. Feibig, W, Görler, G P, Klein, G: Electron irradiation experiments on two types of surface blankets of the satellite OTS. DFVLR final report IB 353 77/14

Table 1 Rate of discharges of the VHF Shield Assembly

Time	Number of discharges Room temperature	LiN_2
First hour	16	18
Second hour	17	14
Third hour	7	8
Fourth hour	2	0
Fifth hour	12	2
Sixth hour	14	2
Seventh hour	1	0
Eighth hour	4	4

Table 2 Rate of discharges of Antenna Structure

Time	Number of discharges Room temperature	LiN_2
First hour	zero	≈130
Second hour	zero	constant
Third hour	zero	constant
Fourth hour	zero	constant
Fifth hour	zero	constant
Sixth hour	zero	constant
Seventh hour	zero	constant
Eighth hour	zero	constant

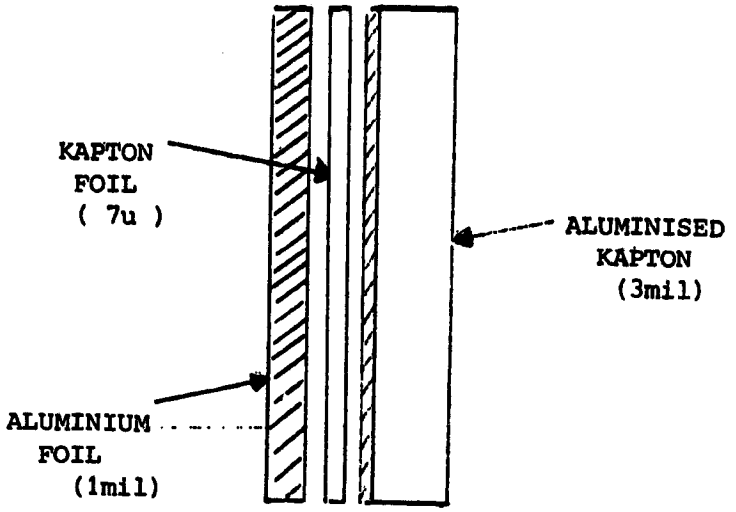

Fig 1: VHF Shield Assembly schematic

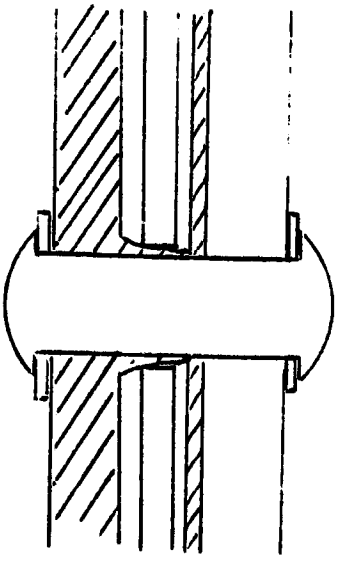

Fig 2: Rivet Assembly

Fig 3: Overall blanket view

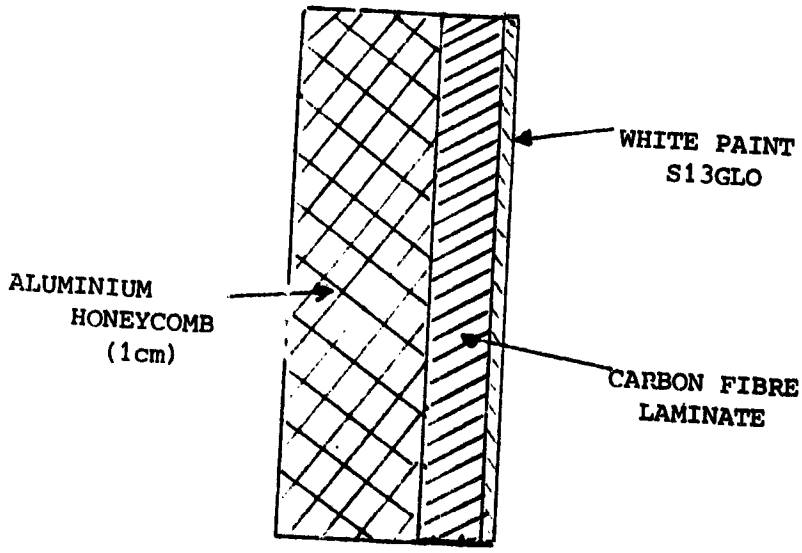

Fig 4: Antenna Structure schematic

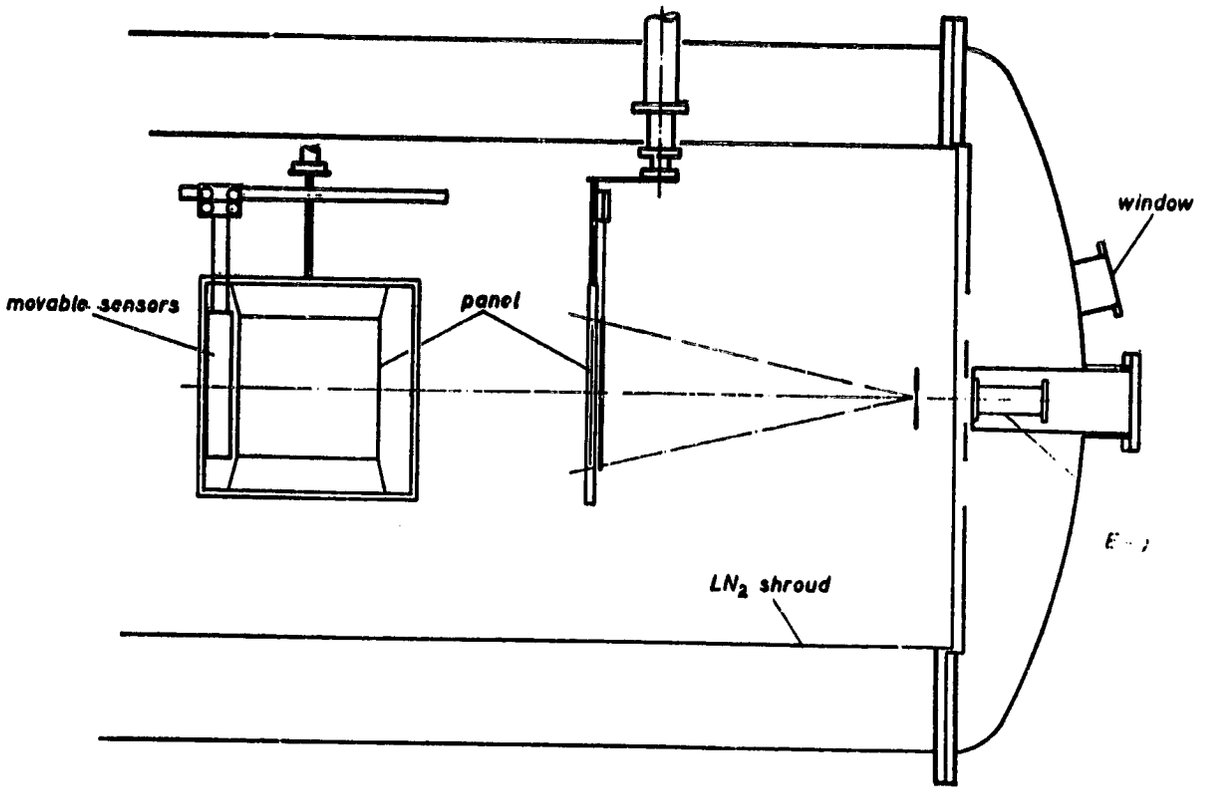

Fig 5: Vacuum chamber

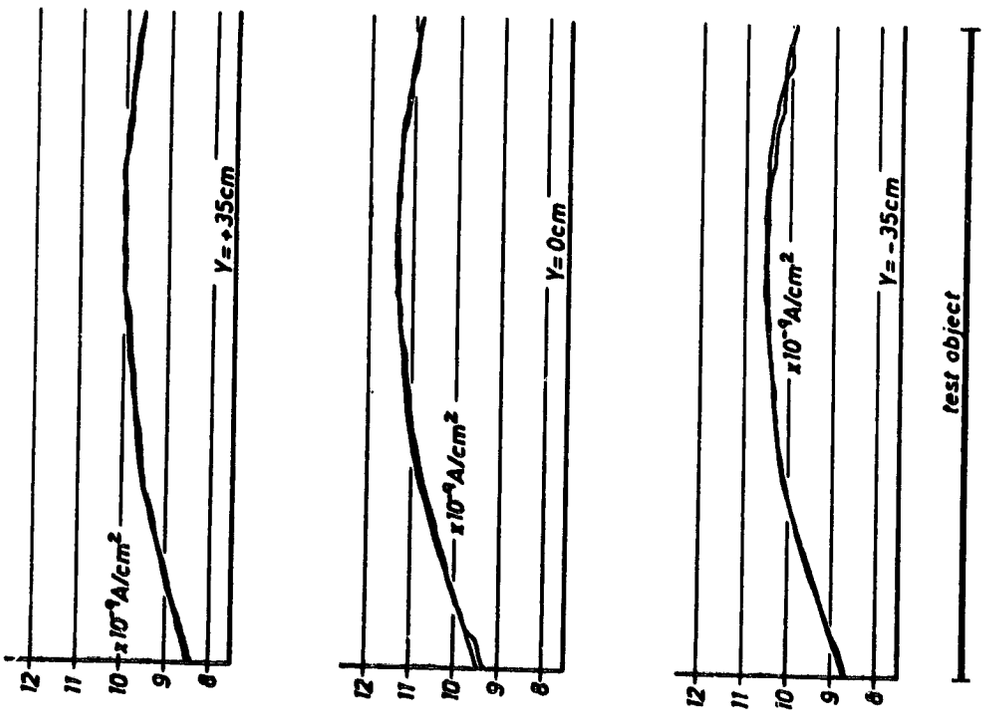

Fig 6: Flux profile

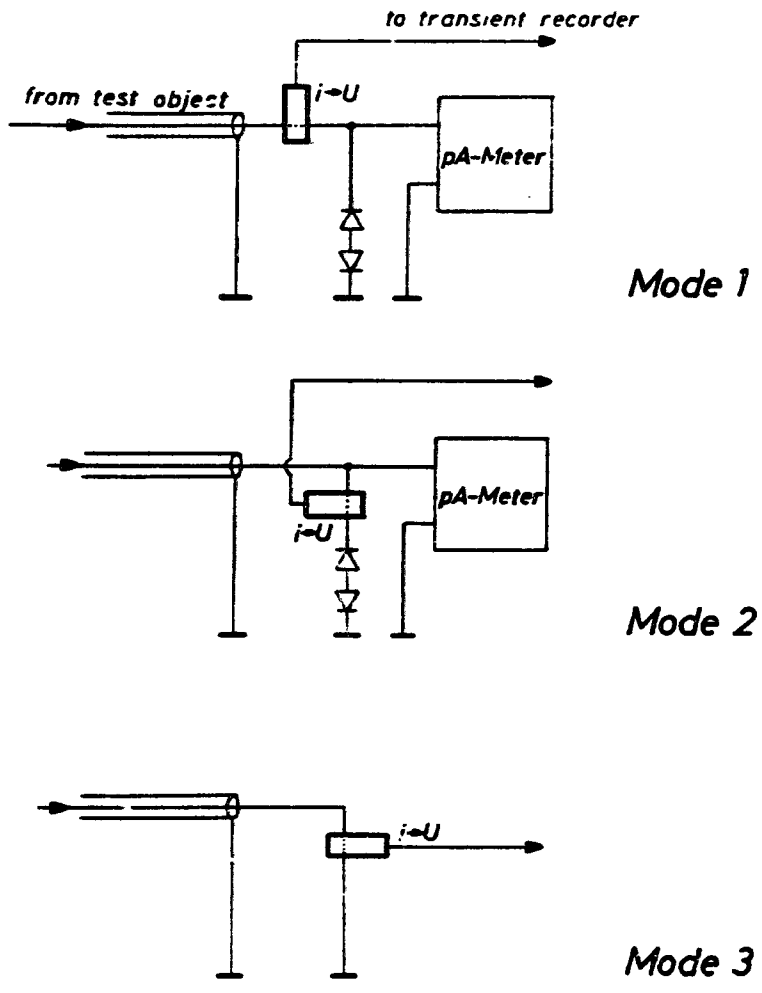

Fig 8: Electrical schematic

Fig 7: Sample mounting

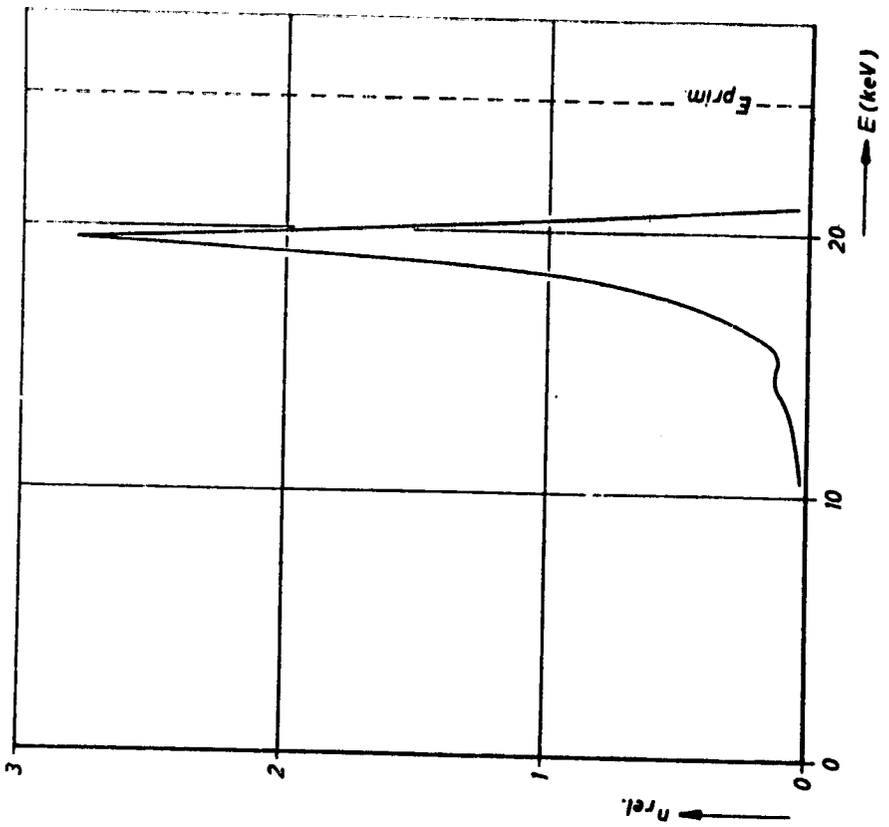

Fig 9: Electron energy profile

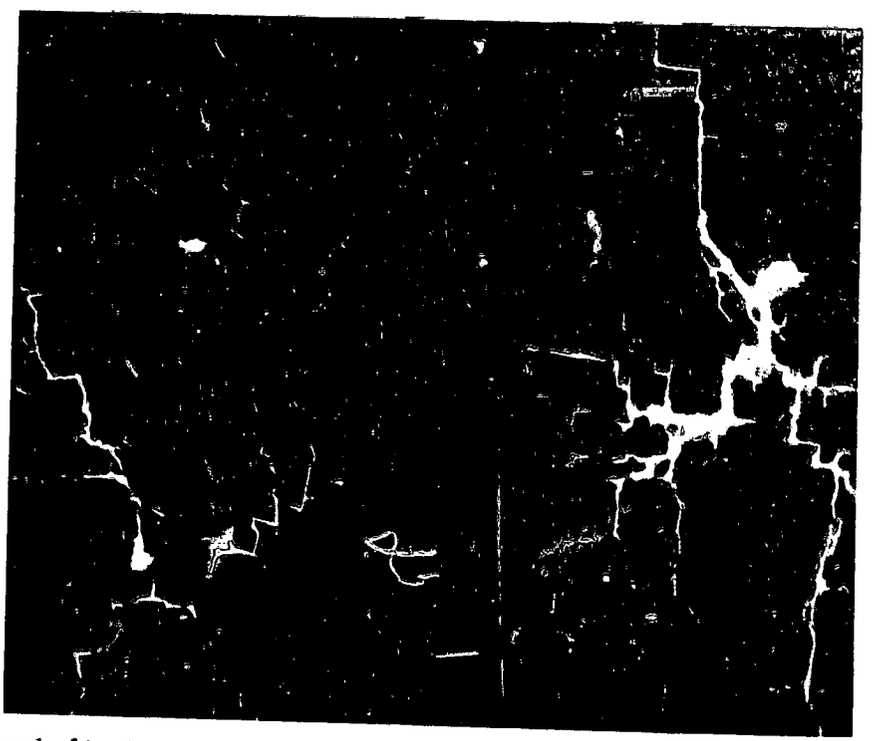

Fig 10: Typical discharge

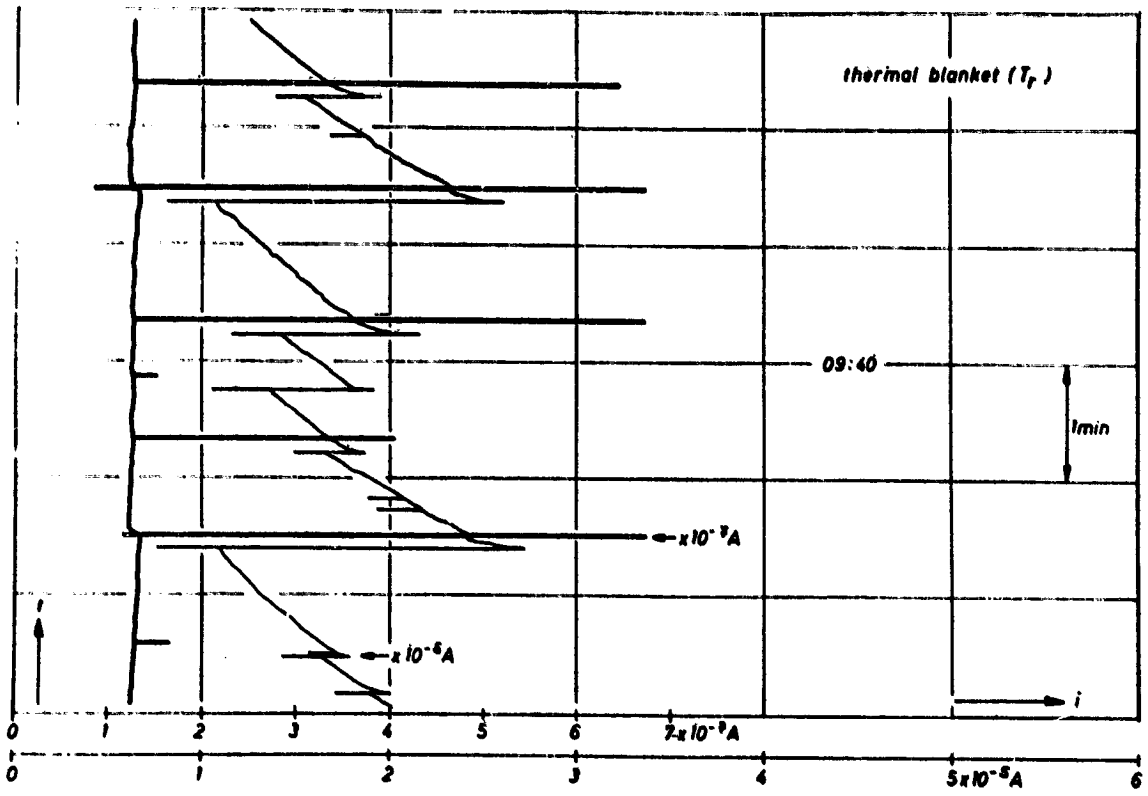

Fig 11: Leakage current - VHF Shield Assembly

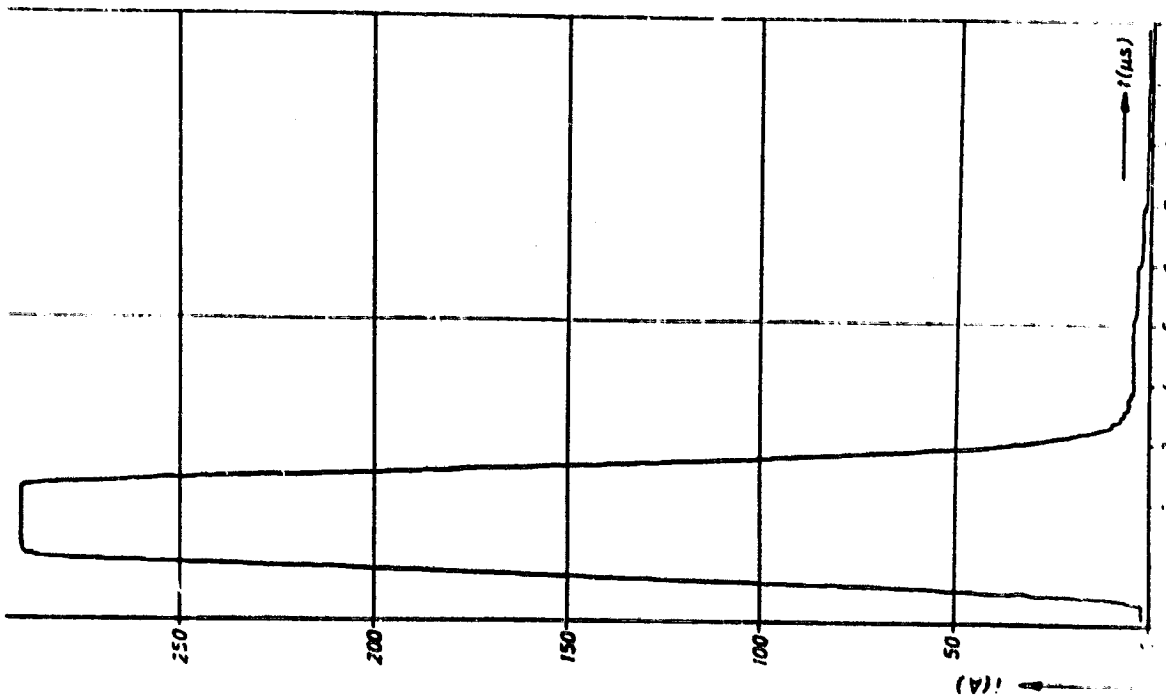

Fig 12: Current discharge-VHF Shield Assembly

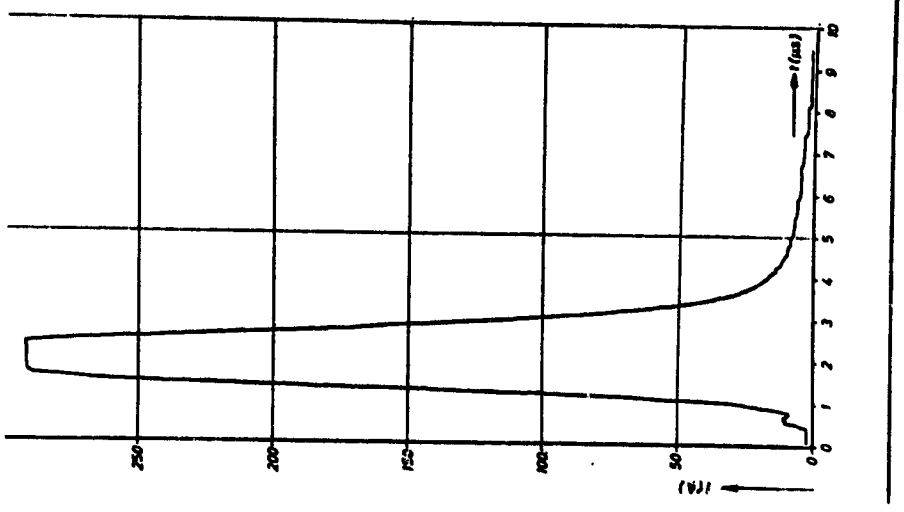

Fig 13: Discharge current - VHF Shield Assembly

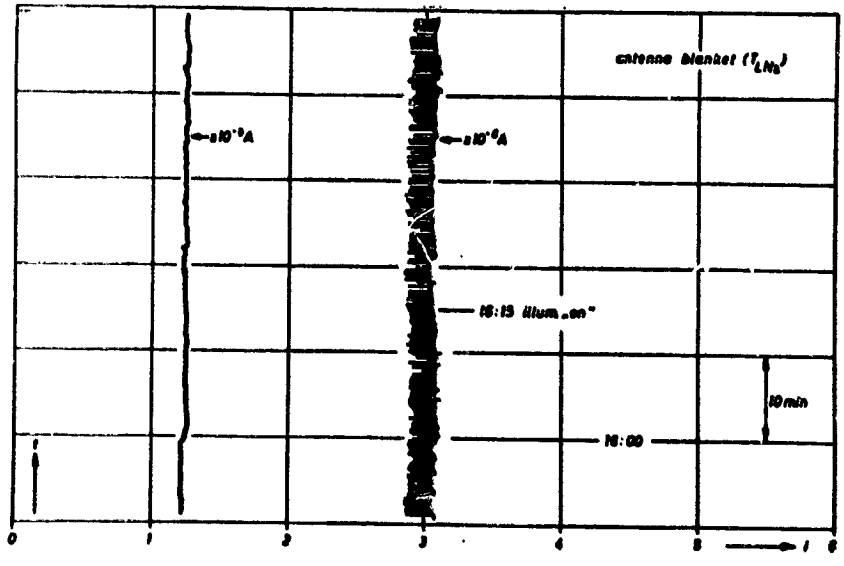

Fig 14: Leakage current - Antenna Structure

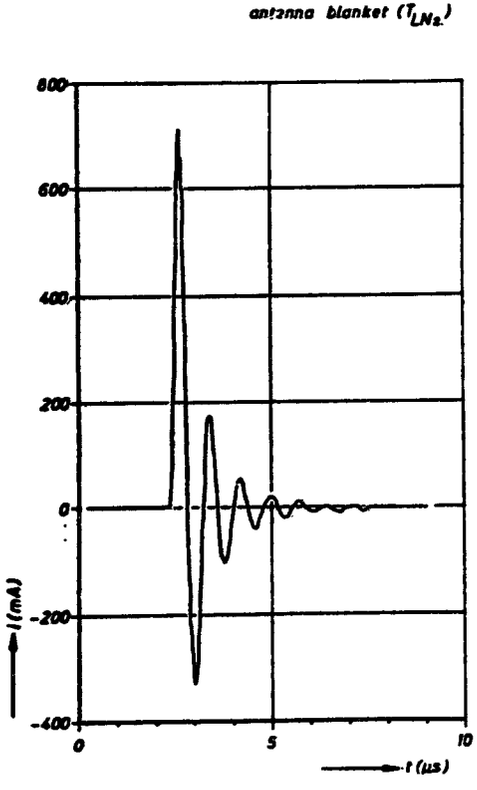

Fig 16: Discharge current - Antenna Structure

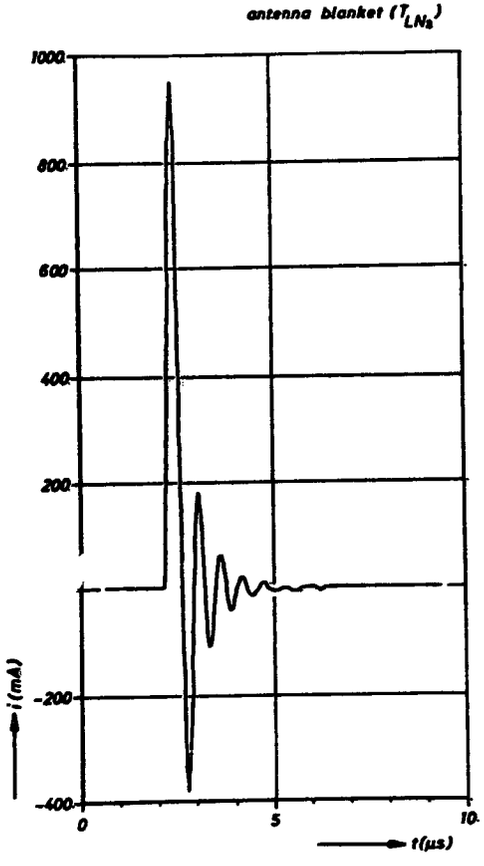

Fig 15: Discharge current - Antenna Structure

Fig 17: VHF Shield Assembly degradation

Fig 18: VHF Shield Assembly degradation

Fig 19: VHF Shield Assembly degradation

Fig 20: VHF Shield Assembly degradation

D36

N79-24037

SKYNET SATELLITE ELECTRON PRECHARGING EXPERIMENTS*

Victor A. J. van Lint, David A. Fromme, Roger Stettner
Mission Research Corporation

ABSTRACT

Large surface areas ($\sim 1\ m^2$) of the Skynet I Qualification Model (SQM) satellite were exposed to the environments of a) a flux of monoenergetic electrons and b) pulsed high-intensity X-ray photons from an exploding-wire-radiator (EWR) source, separately and simultaneously. Experiments were performed with both the cylindrical solar-cell panels and the end thermal blanket exposed to these environments. The satellite was instrumented with fiber-optics isolated fast-response sensors capable of sensing and recording the time-varying electric fields and surface currents on the satellite. Spontaneous discharges of the two surfaces were characterized prior to measurements of the interaction of the System-Generated Electromagnetic Pulse (SGEMP) from the X-ray photon burst with the electron precharged surfaces.

Spontaneous discharges of thermal blankets and of solar cells differed in several respects. Solar-cell discharges resulted in much larger changes in average satellite potential, with a net satellite charge loss of $\sim 10^{-6}$ coulombs being measured. Thermal blanket discharges, however, were smaller in magnitude, with the net loss of charge less than 5×10^{-8} coulombs. During the solar-cell panel experiments, at a precharge potential well below the threshold for spontaneous discharge, a discharge which was apparently triggered by an X-ray photon pulse was observed. This triggered discharge was similar to spontaneous discharges recorded for solar panel illuminations.

A two-dimensional self-consistent finite difference computer code (SEMP) was used to predict the currents on the Skynet both with and without precharging of the thermal blanket. These calculations, which used an estimated thermal-blanket voltage profile, predicted a factor of 2 increase in satellite exterior axial currents. Measured precharged enhancement factors for peak current density varied between a factor of 2 and 5 in good agreement with the predictions. The enhancement is probably due to the effect of the tangential electric fields rather than the normal field on the photo-electron orbits. A late-time current (> 100 nsec) was observed in the measurements but not in the predictions. This current may be due to secondary electrons repelled by the surface potential.

*Work supported by Defense Nuclear Agency under Contract DNA001-77-C-0009.

INTRODUCTION

Electron charging and spontaneous discharge characterizations have been performed on a variety of materials in the form of small samples (area $\leq 10^3$ cm^2) (References 1-7). The potential profiles on insulators, as a function of electron energy, current density and time have been measured. The frequency of discharge and some characteristics of the discharge process (replacement current -- etc.) have been determined. The importance of geometric effects near the insulator-metal interface has been established. The present experiments were designed to measure the effect of precharging on the SGEMP (System-Generated Electromagnetic Pulse) response produced by an exploding-wire radiator on a large scale sample of typical satellite configuration. As a necessary prerequisite some spontaneous discharge measurements were performed.

EXPERIMENTAL DETAILS

The Skynet Qualification Model (SQM) was provided by Ford Aerospace and Communications Corporation in conjunction with a series of SGEMP investigations and was chosen as the test object. The exterior geometry of the Skynet satellite is illustrated in Figure 1. In orbit it spins around its axis, exposing to the sun the solar cell panels around the periphery. The 2 x 2 cm silicon solar cells are covered with .014 cm thick x 2 x 2 cm cover glasses. They are mounted on eight honeycomb panels comprising two fiberglass sheets around an aluminum core. The solar cells are interconnected and are electrically connected to the satellite's metal structure by the primary power wiring only. The honeycomb cores are individually electrically insulated. The top and bottom surfaces of the thermal blanket are covered with a .01 cm layer of thermal paint (white on the top shield and black on the bottom). The thermal blanket is composed of a fiberglass layer .01 cm thick over several layers of aluminized mylar .007 cm thick supported by a 1.2 cm nylon fiber honeycomb sandwiched between two .005 cm aluminum plates. The aluminum sheets are electrically connected to the satellite's metal structure. On top of the satellite a small microwave reflector is mounted on a despun motor assembly. On the spinning section this is surrounded by a grounded metal ring. In the SQM the despun assembly was replaced by a metal plate during these experiments.

Results from sensors on the inside of the SQM and from internal wiring have been reported previously (Reference 8).

The SQM was placed inside a 4 m diameter x 6 m long vacuum chamber (furnished by Air Force Weapons Laboratory) attached to the OWL II EWR source (furnished by Physics International Company) as illustrated in Figure 2. A diffuse electron gun was mounted on the front face of the chamber, exposing the surface at an angle of $\sim 30^\circ$ with respect to the EWR source. The accelerating voltage in the gun was varied between 3 and 15 keV. The current density at the sample could be adjusted up to 100 μA/m^2. The geometry and properties of the electron gun produced a nonuniformity in the current density at the irradiated surface of approximately a factor of two. The vacuum chamber was provided with a LN_2-cooled

annular cold plate surrounding the aperture in the front, which maintained the vacuum near 1×10^{-5} Torr. The chamber was provided with an electromagnetic damper in the form of two cylindrical 200-Ohm sheets at .8 and .94 tank radii and a single sheet near the back wall. Pulsed electrical measurements indicate that the resultant damping times of the tank electrical modes are less than 20 ns.

The satellite metallic structure was grounded to the tank structure through a 50 kΩ string of resistors. This provided less than 5 volt structure potentials during charging at currents up to 10^{-4} A/m^2.

The structure was nevertheless isolated during discharges and photon pulses, both of which have durations significantly less than the 10 μsec time constant of the satellite and resistor chain.

Measurements were performed using a series of EG&G CMLX3B (Reference 9) surface current sensors on the exterior of the satellite as noted in Figure 1. All of the data was acquired via fiber-optic data links (Reference 10), recorded on Tektronix 7912 transient digitizers, and processed on a PDP 11/40 computer.

The characteristics of the photon source output have been discussed in References 11 and 12. The peak emission currents from surfaces of the satellite was ~ 300 A/m^2.

The electrostatic voltage was measured at one location on the top thermal cover .15 m from the outer edge and in the middle of a solar cell cover .15 m from the top edge with Trek electrostatic voltage probes. These measurements were qualitative only, since the irregular surfaces precluded scanning the probe head and it was left in place during electron spraying. Therefore the voltage achieved by the nearby surface may have been affected by the presence of the probe. The measured potentials remained essentially constant after the electron beam was turned off as long as the chamber pressure was below 2×10^{-5} Torr.

The time derivative of the electric field was monitored on the front thermal blanket opposite the position of the electrostatic voltmeter. Two $\dot{B}$ loops were also mounted $\sim$.2 m in the front of the front thermal blanket.

CALCULATION METHODS

The calculations were not designed to predict the details of the SGEMP response but to indicate the magnitude of the effect of precharging and explore the mechanisms of triggered discharges.

Calculations were based on the hypothesis that the interaction between precharging and SGEMP response was solely the effect of the pre-existing electric fields on the photoelectron orbits. The objective of the calculations was to compare SGEMP skin currents and fields with and without precharge; no discharge model was included in the simulations. The simulations were performed with a particle follower Maxwell solver SGEMP code. The effect of the SGEMP exposure on the electric field distribution was calculated to evaluate the hypothesis that

a discharge can be triggered by an SGEMP-induced increase in local electric stress.

The potential was measured at only one point in the experiment so that a measured potential profile was not used in the code simulation. Instead, a physically reasonable profile was used which incorporated the one data point. Figure 3 shows the model used in the simulation. The experimentally measured point showed a voltage difference between the dielectric surface and substrate of 3 kV. The prescribed profile was taken to be 3 kV between dielectric and substrate out to 60 cm from the center line, for the last 10 centimeters the potential difference dropped linearly to zero.

The cell size in the simulation, 2.5 cm is much larger than the actual dielectric thickness (2×10^{-2} cm) but smaller than all other physical dimensions. Physically we wish the potential difference to reflect the change in the real charge density on the surface, σ_R, as photoelectrons are emitted. To accomplish this we can prescribe the dielectric constant in the simulation. The relationship between voltage V and real charge density for a thin flat dielectric of thickness d is given by $\sigma_R = \varepsilon V/d$. The code value of ε, ε_c is given by $\varepsilon_c = \varepsilon \Delta z/d$, where ε is the actual dielectric constant in the experiment (about 4), d is the actual dielectric thickness, and Δz is equal to the grid size in the code.

The simulations with precharge were made by first slowly placing charge on the grid elements in the computer code SEMP. During the photon pulse simulation particles were emitted from the dielectric surface using a typical time history chosen from several individual shot records and a peak emission current of 1.8×10^{-2} amp/cm^2. A linear times exponential energy distribution having an average energy of 1.6 keV was used together with a cosine angular distribution with respect to the normal. This distribution represents adequately the emitted spectrum and distribution caused by the exploding wire photon source. Simulations were made both with and without precharging using the same time history and spectrum.

The effect of the SGEMP exposure on the electric field distribution was also calculated to evaluate the hypothesis that a discharge can be triggered by an SGEMP-induced increase in local electric stress.

SPONTANEOUS DISCHARGE - THERMAL BLANKET

The nature of the spontaneous discharges observed visually on the thermal blanket and the solar cells were significantly different.

The thermal blanket discharges appeared as several small pin-points. The points were irregularly located, often near but not limited to the perimeter and mounting screws of the thermal blanket. Visually, many of these points would appear at approximately the same time.

The results from a $\dot{B}$ loop mounted in front of the front thermal blanket are shown in Figure 4. The trace shows fairly clear evidence of multiple exci-

tations over a time frame of ~ 600 nsec. Both the visual observations and the $\dot{B}$ traces shown were taken during a test period when the electron beam energy was near the threshold for breakdown and discharges occurred at a rate of 1-2 per minute as measured on the electrostatic voltage probe at a beam current of 9×10^{-5} A/c

The electrostatic voltmeter trace (Figure 5) provides a record of a typical thermal blanket charging/discharging sequence. The initial charging is typical of a charging capacitor and has been studied in detail on small samples, with movable voltage probes which provide a better measure of the surface potential distribution. There are two significant features of the discharges, indicated by slight vertical deflections in Figure 5. The first is that the discharge did not occur below a certain threshold beam energy, which corresponds to a threshold potential. The second feature is that a discharge seems to represent a minor perturbation of the surface potential at the probe location. The probe is at a fixed point and the discharges could be remote (~ .5 m) from the probe. Nevertheless, the discharges do not seem to involve the entire area (or even a large fraction of the area) since the voltage does not drop significantly.

The $\dot{E}$ probe, located 180° opposite the electrostatic voltage probe, provided time resolution of the voltage change during a discharge. The traces shown in Figure 6 present the output from this probe for several of the spontaneous discharges. A feature of this $\dot{E}$ trace is the precursor (noted by the arrow in Figure 6). The precursor corresponds to an increase in the potential (less negative) over a period of ~ 200 nsec prior to the sudden onset of the main discharge lasting ~ 100 nsec.

The area of the $\dot{E}$ probe trace is approximately zero indicating the electric field (and charge) near the probe fluctuates during a thermal blanket discharge but undergoes no significant net change. This agrees with the TREK probe measurements at another location.

A second feature that should be noted is the high frequency oscillations present in the main discharge time frame. The response of the satellite structure to thermal blanket discharges was described in a previous paper (Reference 8). The satellite response when compared to previous electrical and photon tests (References 8 and 13) suggests that 1) the discharge process consists of a number of discrete fast events, 2) the discharge was far from axially symmetric, and 3) secondary excitations occur in the ~ 600 nsec time frame.

All of these results agree with the external sensor results presented in this paper.

SPONTANEOUS DISCHARGES - SOLAR CELLS

The typical solar cell discharge appeared visually as a localized line spark along the edge of one or a few solar cell cover glasses, rather than the several light spots noted on thermal blanket discharges.

Portions of the trace from the electrostatic voltmeter during a charging/discharging sequence of the solar cells is given in Figure 7. Several important features should be noted. The discharges occur above a certain threshold potential as in the thermal blanket discharges. The absolute magnitude of this threshold in these measurements is biased by the fact that the voltage probe could not move and shadows the immediate area of the measurements. The second feature (obvious in several of the discharges) is the magnitude of the voltage change. In one particular case (Figure 7b) the potential fell almost to zero volts, corresponding to a clean wipe-off of the charge on the solar cell being monitored.

The final feature (Figure 7a & 7c) is an increase in the potential of the solar cell being monitored. This occurred on several occasions and corresponds to a transfer of electrons from a surrounding solar cell to the cell being monitored.

Replacement current, measured on the 50 kΩ resistor chain (Figure 8), consistently indicated that ~ 1000 nC of electrons were transported from the model to the tank walls during solar cell discharges. This amount of charge would raise the average potential of the solar cell covers to near ground, after which electrons would no longer be accelerated to the tank walls. This amount of charge also corresponds approximately to the amount of charge stored on a single solar cell cover calculated from the measured surface potential. Figure 8b also includes an example of a second high frequency excitation ~ 600 nsec after the initial discharge.

The rise time of the replacement current is determined by the time history of the electrons leaving the model and their transit times to the tank wall. The expected electron energy at the tank wall corresponds to the average potential of the satellite. The average potential experienced by the electron will be significantly less than this due to the decrease in satellite potential (from charge emission) and to the spatial distribution of the potential. An average potential of 1 kV produces an electron transit time of several hundred nanoseconds, in reasonable agreement with Figure 8, and indicates a discharge emission time less than 100 nanoseconds. Results from sensors on the satellite presented in a previous paper (Reference 8) indicated that solar cell discharges excited external surface currents much larger than thermal blanket discharges. This agrees with the net charge loss measurements.

SGEMP RESPONSE OF PRECHARGED SATELLITE

The SQM was exposed to a series of EWR irradiations in an uncharged state and after a 10 minute exposure at 3×10^{-5} A/m^2 of electrons from the gun at 10 kV potential. The thermal cover was exposed four times (twice without charge and twice precharged). The solar cells were exposed four times (once without charge and three times precharged).

The external axial current density for thermal blanket irradiation is compared in Figure 9 with the results of the computer predictions. Both the calcu-

lations and measurements exhibit an increase in peak current compared to the uncharged response.

This peak current increase due to precharging is probably due to the modification of electron orbits by the tangential electric field. The static normal field due to charging is $\sim 10^4$ V/m and is small compared to the measured space charge fields of 10^5 V/m (Reference 14). A previous experiment and calculations with a metal disk charged to -10 kV indicated less than a 30% change in SGEMP response due to a field which is normal to the surface at all points. The differential charging of a dielectric above a grounded substrate can lead to significant potential gradients on the satellite and gives rise to transverse fields that affect every electron.

The broadening of the pulse shape noted in computer predictions cannot be confirmed by the measurement since the two photon pulses did differ in pulse shape in the 0-40 nsec range. The oscillations which produce the peak at 80 nsec in the predictions and at approximately 40 nsec and 60 nsec in the measurements are due to the interaction of the interior of the satellite with the external current through the gaps between the thermal blanket and the solar panel. The late time current (> 100 nsec) noted in the measurement is not due to this difference in pulse shape and is not present in the computer simulation. The late time current may be due to secondary electrons emitted from the surface which would normally be forced back to the surface by the space charge field. In the precharged case these electrons are repelled by the surface charge and may contribute to the net current from the top to the side of the satellite. Since the code does not produce or propagate secondary electrons they do not appear in the code.

Larger peak values and broadening of the pulse shape were typical of most of the sensors on the surface and in the interior of the satellite (Reference 8).

The external axial surface current density for a solar panel illumination with and without precharging is compared in Figure 10. The peak current density increase of a factor of 2-5 was comparable to that noted on the thermal blanket measurements.

Figure 11 represents the time histories for the axial current sensor, azimuthal current sensor and an axial surface current sensor on the inside of the solar panel during one of three solar panel precharged shots. The time of the photon excitation is noted by an arrow. An intense excitation on both of the axial current sensors occurs approximately 65 nsec after the photon pulse. The threshold for spontaneous discharges on the solar panel corresponded to a beam voltage of 14 kV during the previous electron exposures. No spontaneous discharges occurred at 10 kV, which was the beam voltage used for the charging prior to the photon irradiation. Thus it is likely that the discharge observed was triggered by the photon irradiation. The response of sensors near the illuminated solar panel was much larger than those further away as expected. The characteristics of the triggered discharge are similar to the spontaneous solar cell discharge characteristics discussed earlier as far as the instrumentation and analysis available thus far would determine.

The two-dimensional code described earlier was used to investigate possible mechanisms for triggering discharges. The simplest assumption regarding the triggering mechanism for either spontaneous or triggered discharges is to assume an electric field threshold exists above which a discharge occurs. The simulation was run for a model of the thermal blanket shown schematically in Figure 12a. A potential profile consistent with the single measured potential and graded linearly to the edge of the dielectric was assumed. The solid line in Figure 12b is a histogram of the electric fields normal to the surface at positions just above the surface resulting from this linear potential. The solid lines (0 nsec) represent the field just prior to the photon pulse. The dotted and dashed lines represent the field strengths at 15 & 30 nsec after the photon pulse. The normal fields above the surface (at 15 nsec and 30 nsec) are significantly higher than the uncharged photon response and higher than the initial field due to charging. The tangential field at Position 7 is increased also. As expected near the center of the dielectric there is very little change in the electric fields within the dielectric. Near the edge (Position 4) the field within the dielectric is increased but only slightly. The radial electric field in this simulation achieves its highest value both within and above the dielectric, prior to the photon pulse; the photons merely cause a relaxation of the radial fields at the positions investigated. The magnitude of the increases predicted by this simulation are not valid estimates due to cell size limitations.

The above simulation was run for a model of the thermal blanket. The geometry of a solar cell, which has a metal tab extending beyond the dielectric, would probably enhance the effects seen on this computer model. The simulation could not contain enough detail to treat the solar cell case.

Two major points, however, can be made from the simulation. Fields in excess of those due to the initial charging can be produced by the rearrangement of charge on a dielectric during a photon pulse, and this rearrangement of charge from the pulse lasts beyond the end of the pulse. The latter could be critical in terms of providing time for a discharge to begin. Research on vacuum dielectric breakdown has indicated that short pulse voltage thresholds are higher than the threshold for long pulses.

The triggered discharge may have very serious consequences for satellite design. The existing evidence indicates that solar-panel spontaneous discharges are limited to one or a few cover glasses. If a large number of cover glasses were charged to near their spontaneous discharge threshold, an intense photon pulse could trigger a simultaneous discharge of many of them, resulting in an electrical stress to the electronics much more severe than normally encountered.

SUMMARY

Spontaneous discharges on the large area thermal blanket material differed significantly from those on the solar panels covered with 2 x 2 cm solar cells. This is to be expected since the materials are quite different (paint and quartz) with quite different surfaces which affect the secondary electron emission.

Thermal blanket discharges: (1) appeared as multiple pin points, (2) seemed to consist of multiple high frequency discrete events, and (3) corresponded to small average satellite potential changes (small net charge loss < 50 nC). Solar panel spontaneous discharges: (1) appeared to be single line discharges near the edge of one or more solar cells, (2) corresponded to large average satellite potential changes (net charge loss ~ 1000 nC), (3) sometimes represent total discharge of at least one solar cell, and (4) seem to be limited to one or a few solar cells.

The magnitude of the modification of the SGEMP surface current response for thermal blanket illumination was in good agreement with the computer simulation. Thus the modification of the electron orbits by the transverse electric field seems to explain the enhancement of the SGEMP response to first order. A late time (> 100 nsec) current was noted experimentally but not in the code predictions. This may be due to secondary electrons not in the code.

A discharge which was very probably triggered by a photon pulse was observed on the solar cells. Its characteristics were similar to a spontaneous solar cell discharge. The possibility of triggering many solar cells simultaneously could pose a serious threat to electronics. A code simulation has indicated that an increase of surface potential gradients due to charge rearrangement during a photon pulse on a precharged surface could be the mechanism for triggering a discharge at potentials below the threshold.

Many thanks to John Rutherford and IRT Corporation, San Diego for support in designing and operating the electron gun; Harry Diamond Laboratories, Nasa Lewis Research and Spire Corporation for instrumentation support.

REFERENCES

1. USAF/NASA Spacecraft Charging Technology Conference, Colorado Springs, October 27-29, 1976.

2. Hoffmaster, D. K., and J. M. Sellen, Jr., Progress in Astron. and Aeron. 47, 185 (1975).

3. Purvis, C. K., N. J. Stevens and J. C. Oglebay, NASA Technical Memorandum, NASA TM X-73606 (1976).

4. Stevens, N. J., R. R. Lovell and V. Gore, Progress in Astron. and Aeron. 47, 263 (1975).

5. Stevens, N. J., V. W. Klinect and F. D. Berkopec; NASA Technical Memorandum, NASA TM X-73467 (1976).

6. Stevens, N. J., F. D. Berkopec and R. A. Blech, NASA Technical Memorandum, NASA TM X-73436 (1976).

7. Stevens, N. J., F. D. Berkopec, J. V. Staskus, R. A. Blech and S. J. Narcisco, NASA Technical Memorandum, NASA TM X-73603 (1976).

8. van Lint, V. A. J., D. A. Fromme, and John A. Rutherford, "Spontaneous Discharges and the Effect of Electron Charging on Skynet SGEMP Response," IEEE Trans. on Nucl. Sci., NS-25, December 1978.

9. Olsen, S. , D. Pabst, and G. D. Sauer "CML-X3A(R) B-dot Sensor," (EMP Sensor Handbook SH), 15 June 1976.

10. Blackburn, J. C. and A. Brombersky, IEEE Trans. on Nucl. Sci., NS-24, 2495 (1977).

11. Bernstein, A. J., IEEE Trans. on Nucl. Sci., NS-24, 2512 (1977).

12. Fromme, D. A., V. A. J. van Lint, R. G. Stettner and C. E. Mallon, IEEE Trans. on Nucl. Sci., NS-24, 2527 (1977).

13. Fromme, D. A., V. A. J. van Lint, R. Stettner, and B. M. Goldstein, "Exploding-Wire Photon Testing of Skynet Satellite," IEEE Trans. Nuclear Sci., NS-25, December 1978.

14. Fromme, D. A., R. G. Stettner, V. A. J. van Lint, C. L. Longmire, and R. Leadon, "SGEMP Response Investigations with Exploding-Wire Photons," IEEE Trans. Nucl. Sci., NS-24, 2371 (1977).

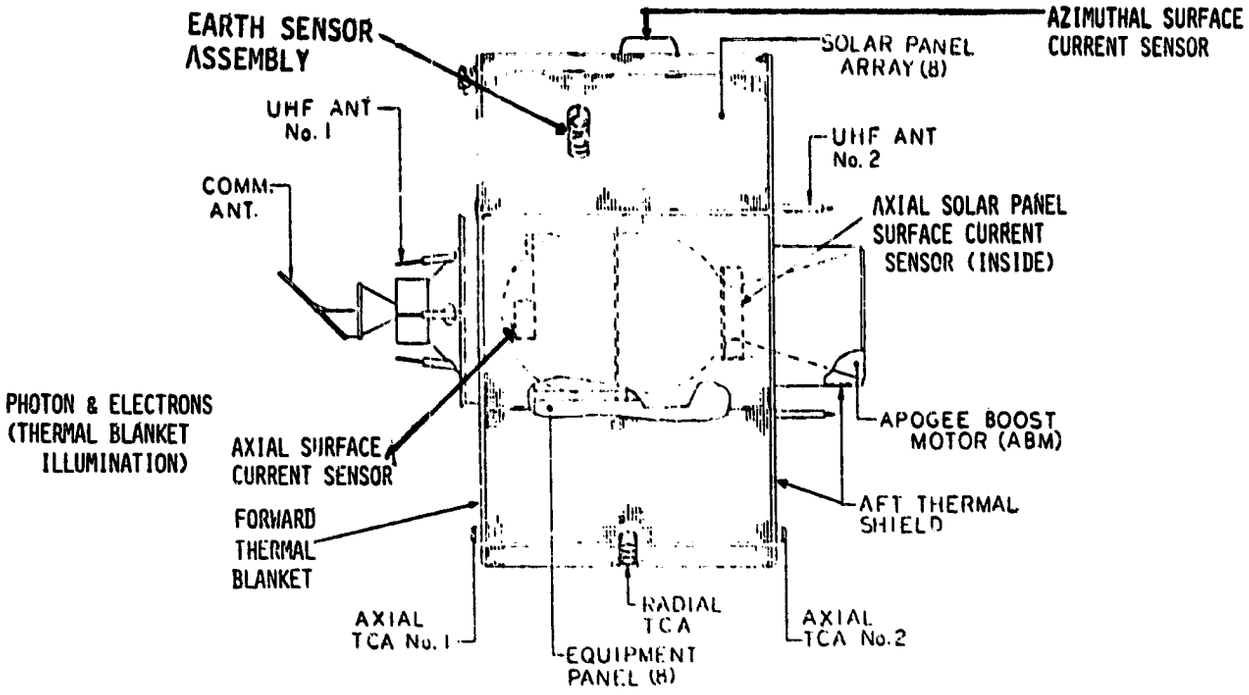

Figure 1. Skynet I satellite (side view).

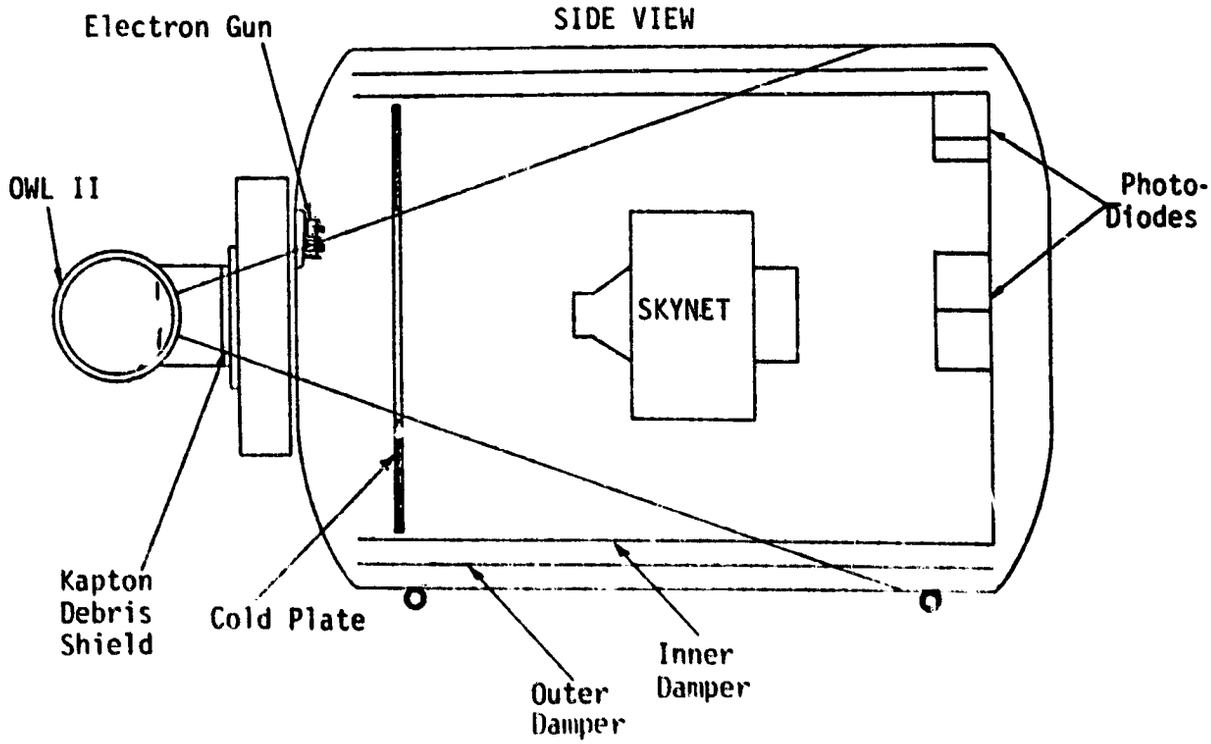

Figure 2. Skynet test setup.

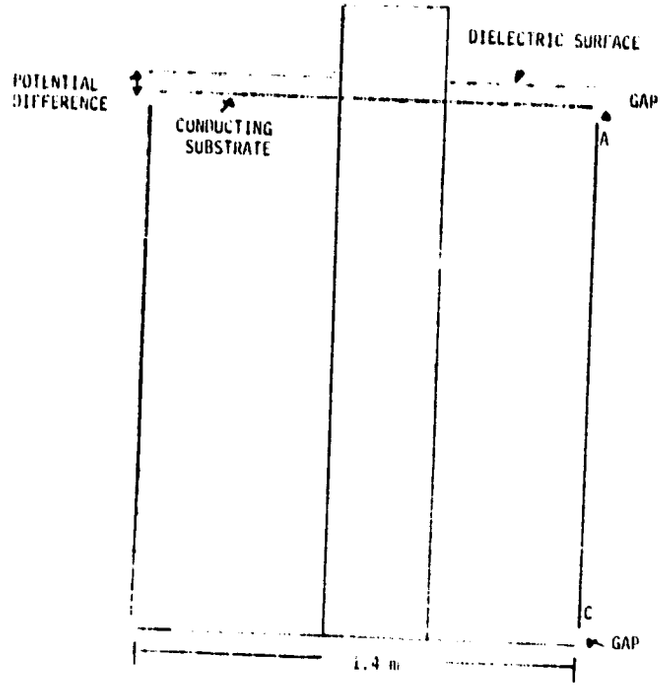

Figure 3. Cross section of computer simulation model.

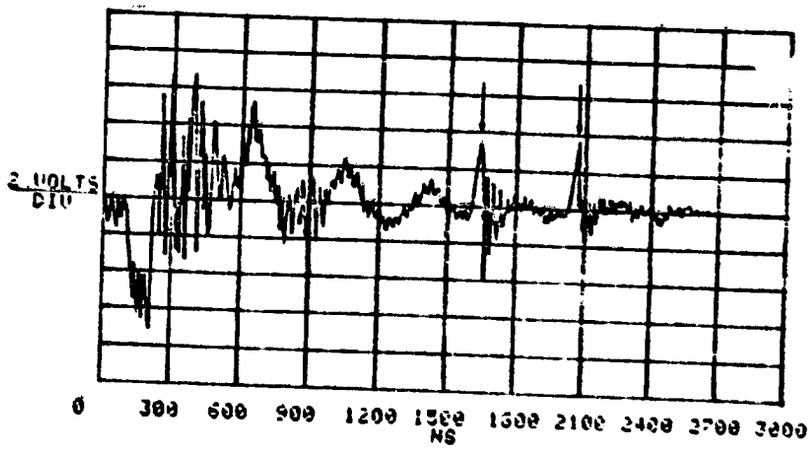

Figure 4. B time history showing multiple excitations (arrows).

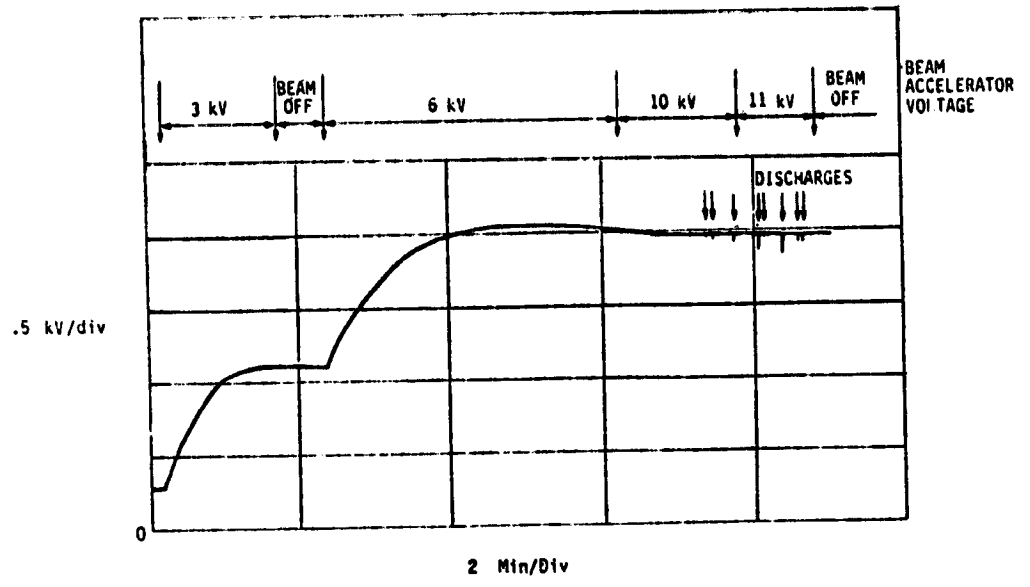

Figure 5. Electrostatic voltmeter trace of charging/discharging sequence of thermal blanket (charging rate 3×10^{-5} A/m^2).

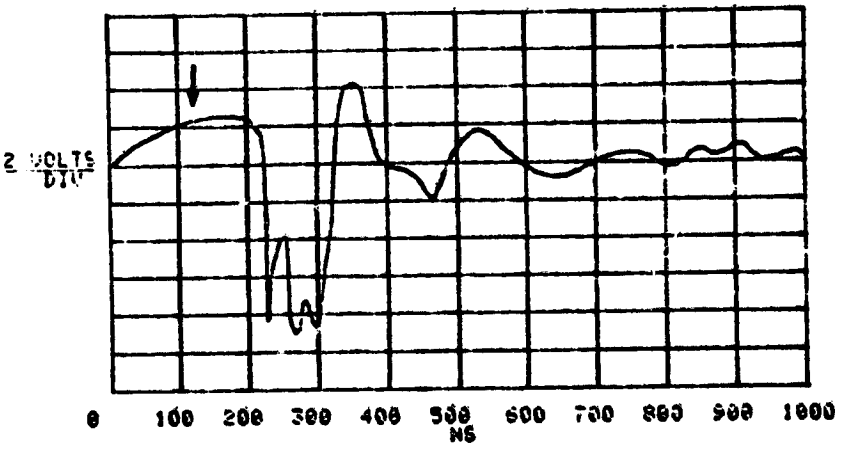

Figure 6a. Typical E dot time history.

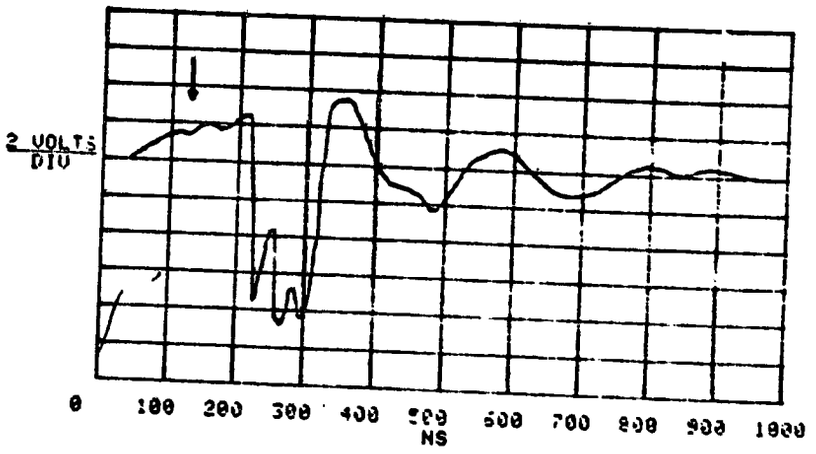

Figure 6b. Typical $\dot{E}$ time history.

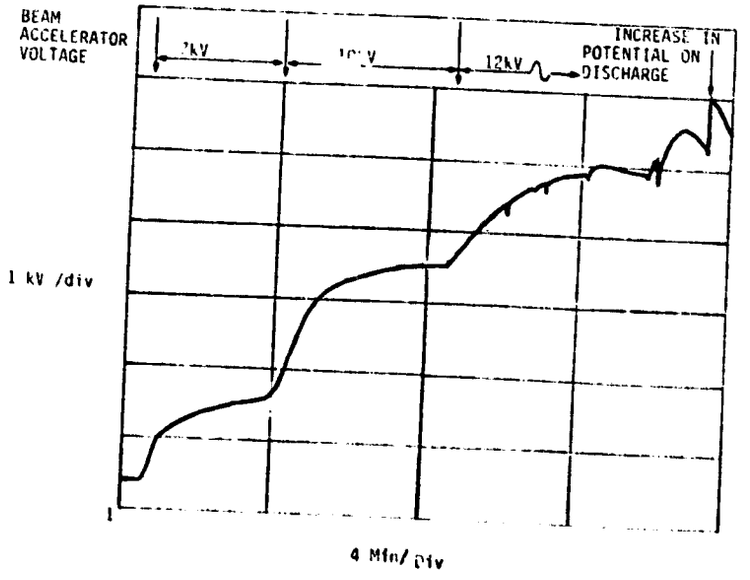

Figure 7a. Electrostatic voltmeter trace of solar cell charging time history (charging rate = 9x10-5 A/m^2).

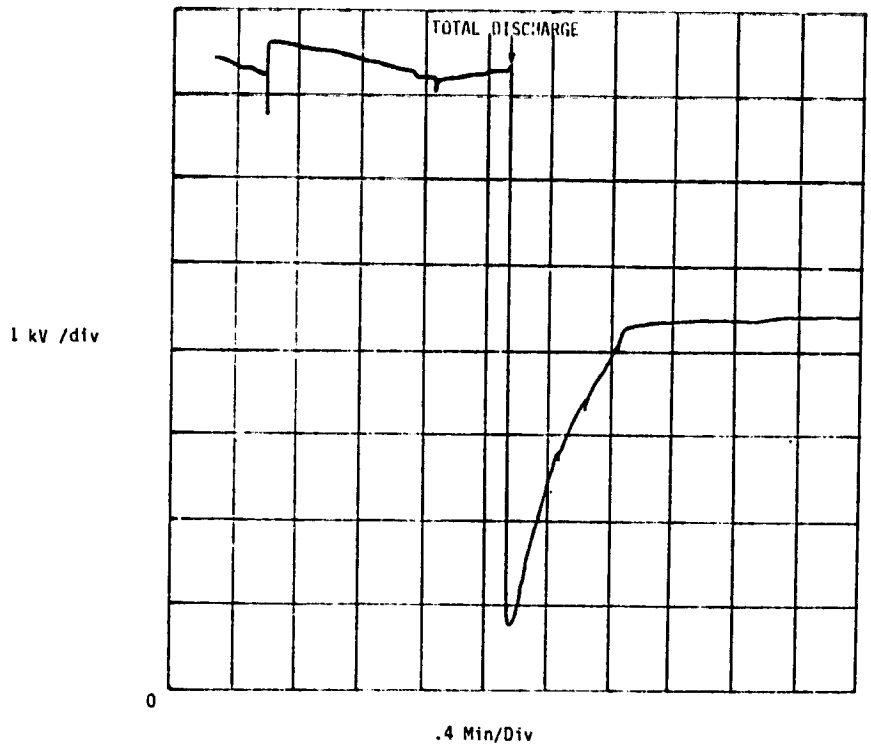

Figure 7b. Electrostatic voltmeter trace of solar cell charging time history (charging rate = 3×10^{-5} A/m^2).

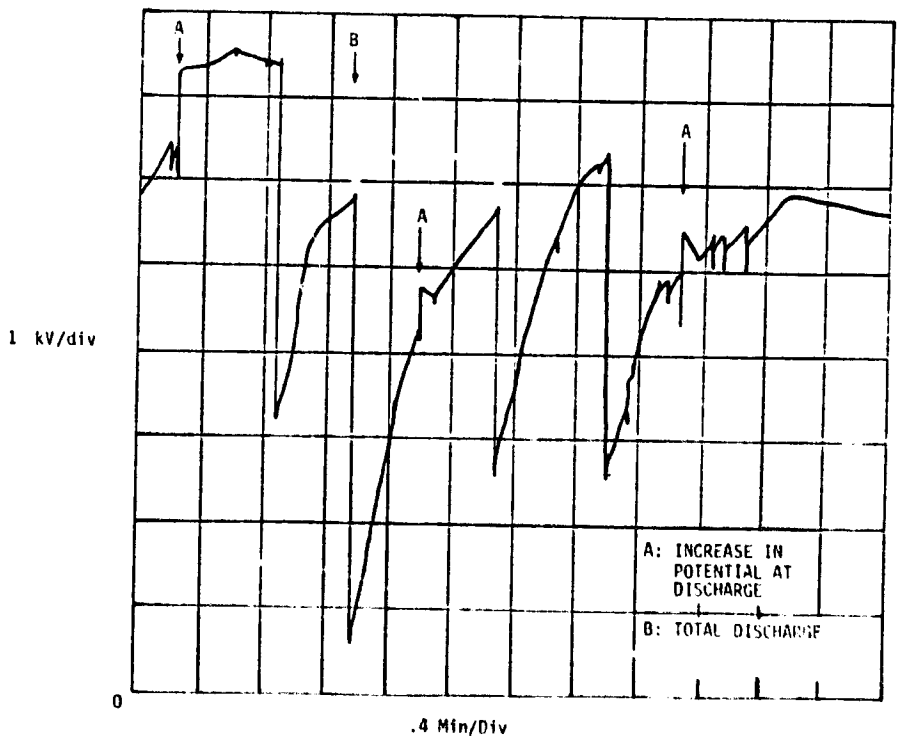

Figure 7c. Electrostatic voltmeter trace of solar cell charging time history (charging rate = 3×10^{-5} A/m^2).

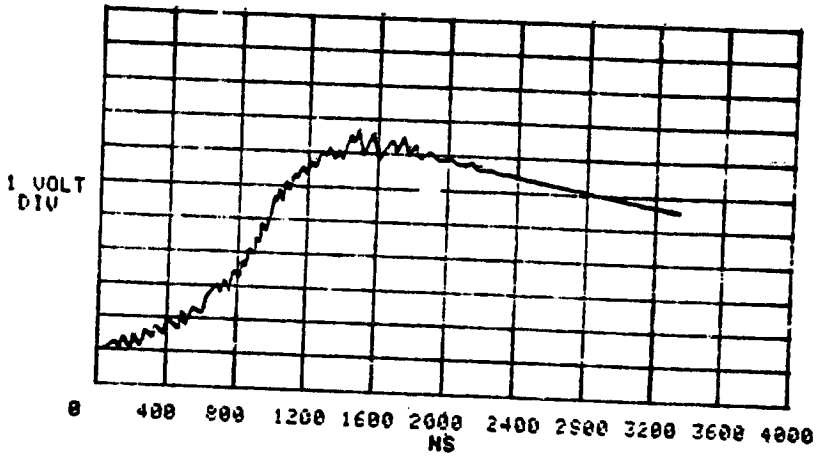

Figure 8a. Return current for solar cell illumination.

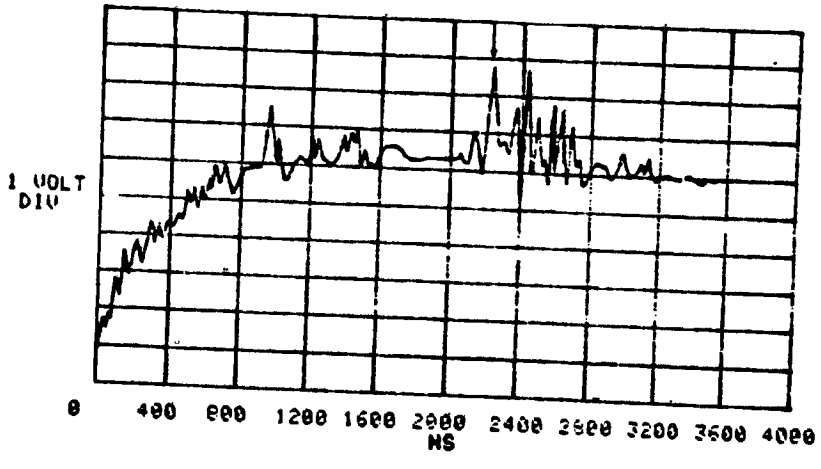

Figure 8b. Return current for solar cell illumination (arrow to second high frequency excitation).

·····Theoretical Predictions
—— Experimental Results

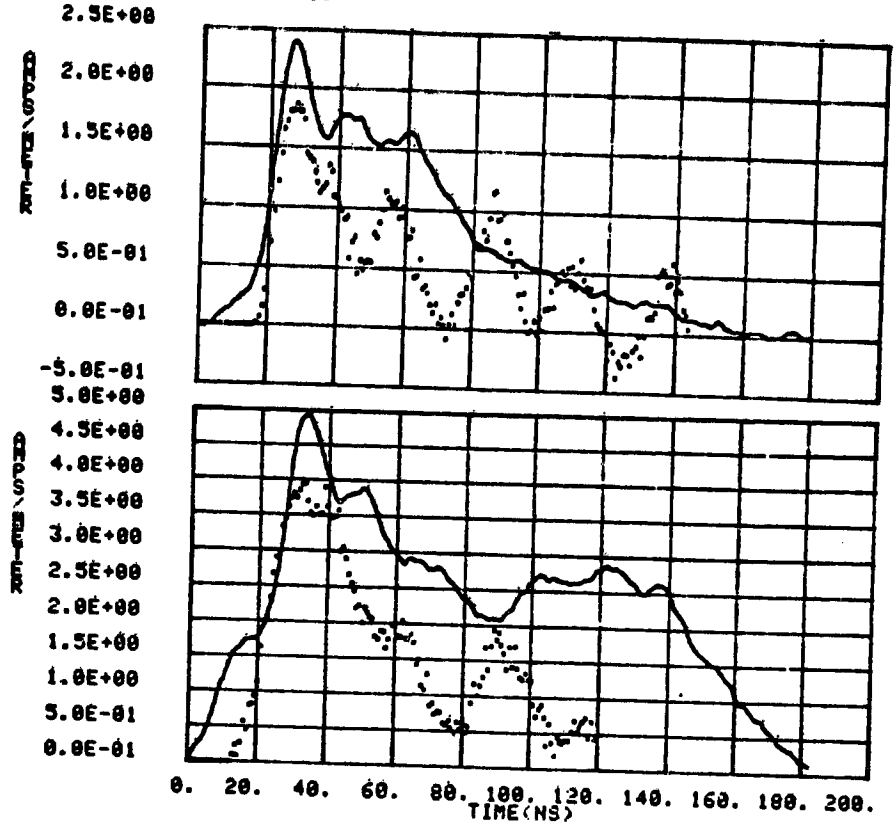

a) Without Precharging

b) With Precharging

Figure 9. External axial current density, thermal cover illumination.

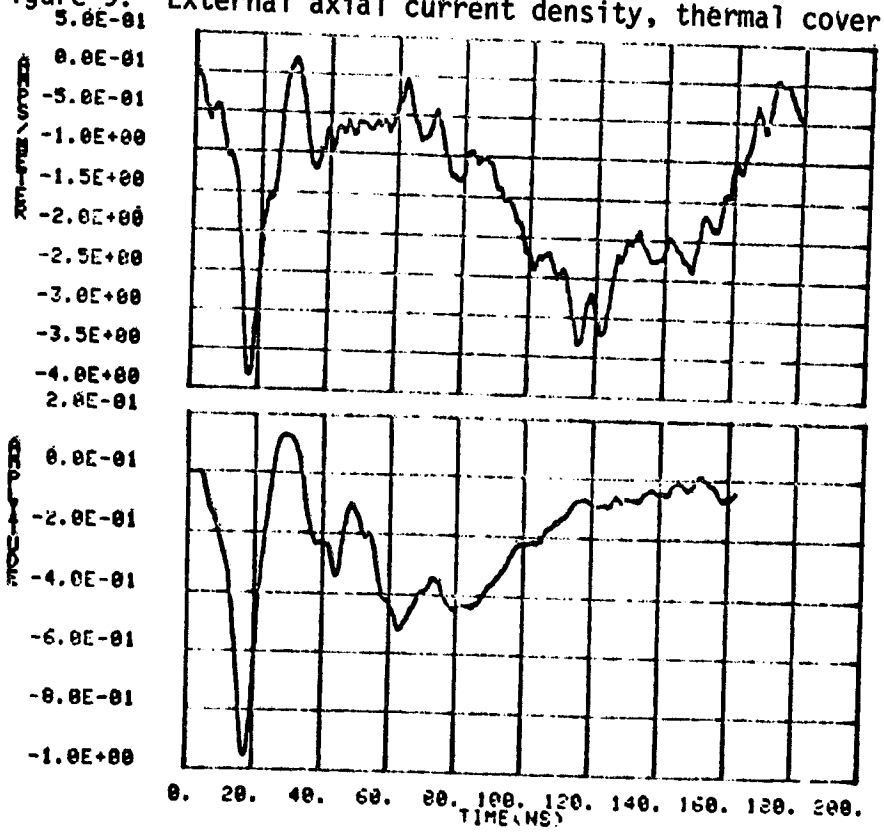

a) With Precharging

b) Without Precharging

Figure 10. External axial surface current density, solar panel illumination.

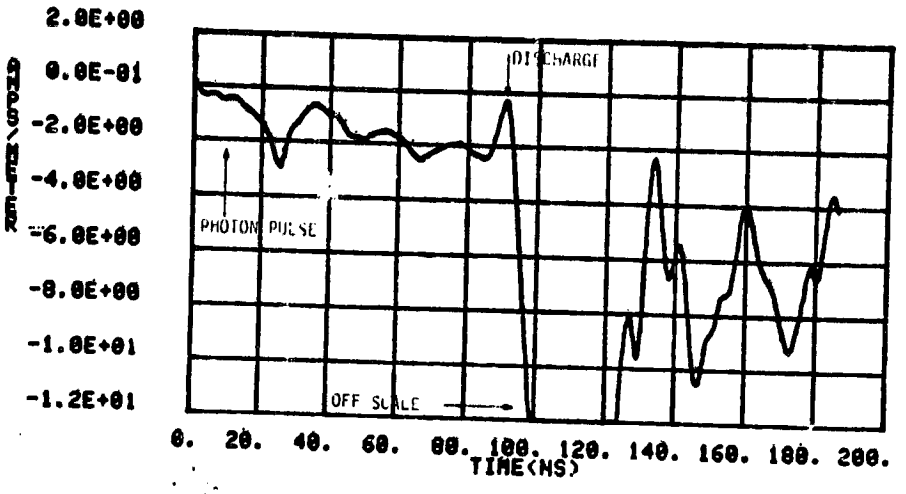

a) External Axial Surface Current Densit

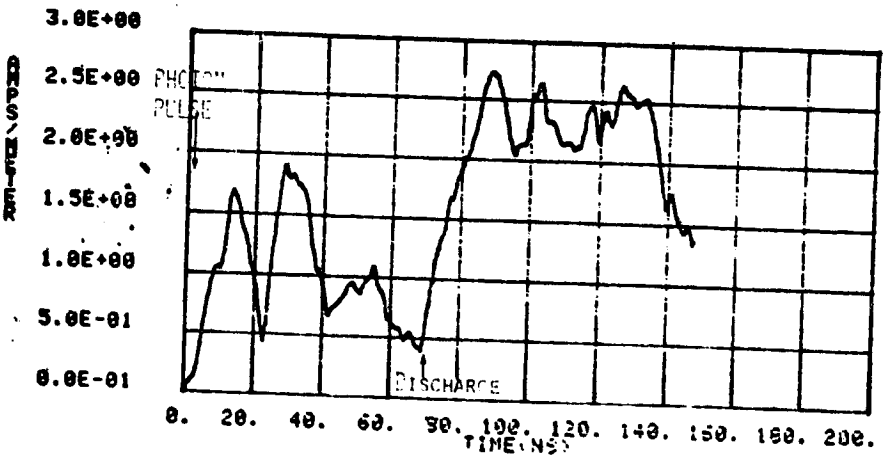

b) External Azimuthal Surface Current Density

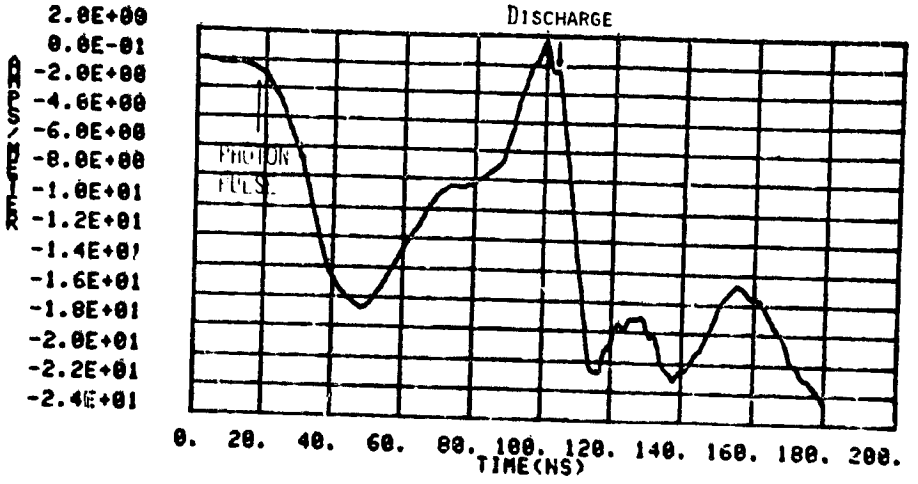

c) Surface Current Density Inside Solar Panel

Figure 11. Triggered Discharge

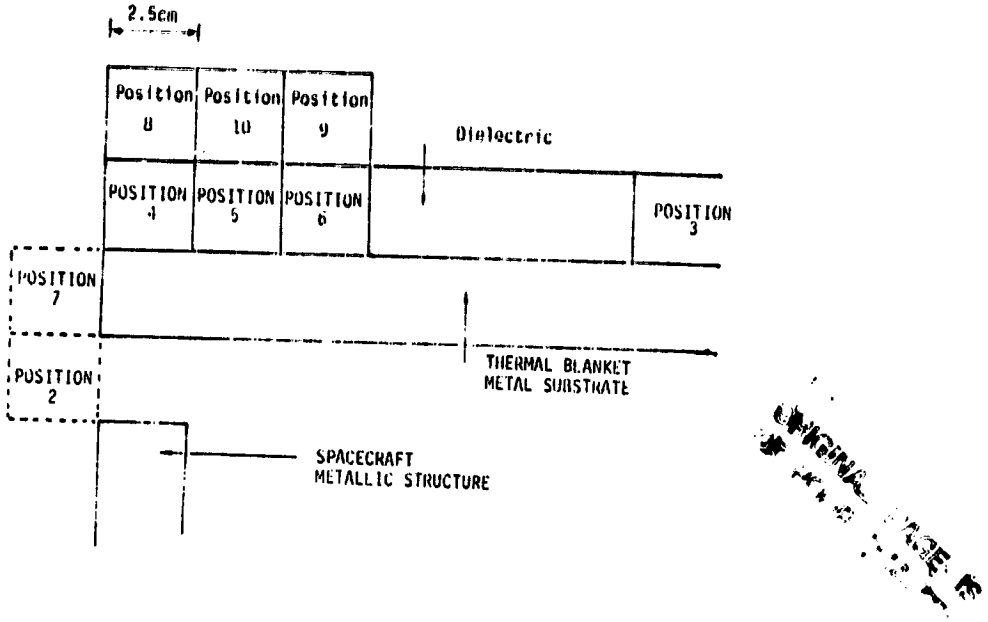

Figure 12a. Detail of computer model.

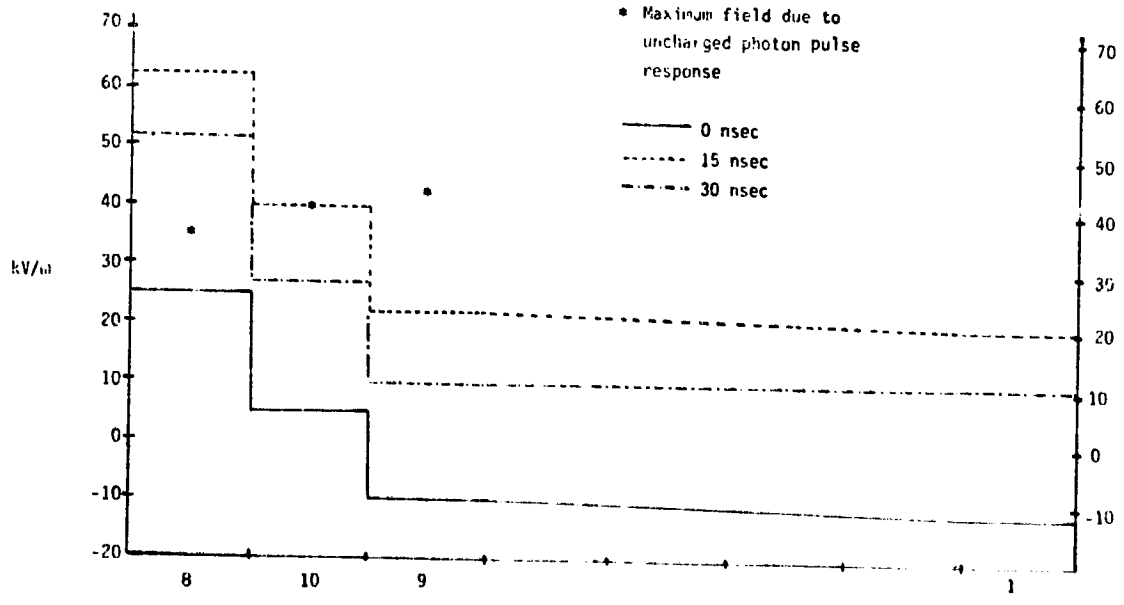

Figure 12b. Normal electric fields above the dielectric surface.

D37

N79-24038

POTENTIAL MAPPING WITH CHARGED-PARTICLE BEAMS*

James W. Robinson
David G. Tilley
The Pennsylvania State University

SUMMARY

Spacecraft charging produces electric fields near the structures being tested. The calculation of the fields is often difficult because of a complex geometry or a lack of data for dielectric surface potentials. This work seeks experimental methods of mapping the equipotential surfaces near some structure of interest. Such measurements can verify or supplement calculations. The two methods described rely on the detection of charged particles which have traversed the regions of interest and are detected remotely. Whereas techques have been developed previously for use with rotationally symmetric systems, no such restriction is applied in this work. One method is the measurement of ion energies for ions created at a point of interest and expelled from the region by the fields. The ion energy at the detector in eV corresponds to the potential where the ion was created. An ionizing beam forms the ions from background neutrals. The other method is to inject charged particles into the region of interest and to locate their exit points. A set of several trajectories becomes a data base for a systematic mapping technique. An iterative solution of a boundary value problem establishes concepts and limitations pertaining to the mapping problem.

INTRODUCTION

Measurements of electrical potential ultimately depend upon making an observation of a charged particle in the region of interest. Often some mechanical device is also inserted into the region but ideally one would use the smallest charge, the electron, by itself. Then the perturbing effect of the measurement would be at a minimum. This paper describes two approaches for making potential measurements in vacuum where nearby surface charges create the potentials to be measured. The methods both strive to keep the density of test charges to a minimum. All detection equipment is kept out of the region being measured.

The first of these two methods uses the neutral atoms or molecules always present. A collimated ionizing beam of electrons or photons passes through the region and the ions formed are collected and analyzed as they drift out of the region. Typically the pressure will be 10^{-5} Torr and ions will be

*This work was supported by The National Aeronautics and Space Administration under grant number NSG-3166.

detected with a continuous-dynode avalanche detector. The field must be oriented to expel ions for this method to be useable.

The other method requires no background neutrals and it is usable with fields of either polarity. Low-current particle beams are injected into the region of interest with known velocities and entry positions. Exit points are measured. The data from many trajectories may be combined in a iterative calculation that generates a map of the potential in the region probed by the beams.

These two methods have similar purposes but they differ sufficiently in technique that they are described separately in the two major sections of this report. Work is in progress for both methods so that directions of effort are indicated where appropriate.

IONIZATION OF NEUTRALS

This method of measuring potential is simple in concept. If a neutral molecule is located at some point of interest and is ionized by some process, then it will be accelerated by the electric fields and strike a properly positioned detector at reference potential. If the detector can measure the energy of the particle, then that energy (in eV) can be equated to the potential at the original point. A series of measurements point by point provides a map of the region of interest. Several variations of this method are possible but several constraints need to be recognized.

Resolution

The first quantity for which resolution is important is the position of the source point. Ions are generated in some neighborhood having radius a and centered at point r_o. If the potential function to be measured is $\phi(r)$ then its value will be in the range

$$\phi(r) = \phi(r_o) \pm \frac{\partial \phi}{\partial r} (\Delta r + a) \pm \phi_T \qquad (1)$$

where ϕ_T represents a random spread in the ion energies. In most situations, say for $\phi(r) > 1V$, randomness in ion energies may be neglected. However the spread of electron energies may be much higher. Hence ions are the preferred species in many situations but then the gradients must be such as to drive ions toward the detector. The randomness arises from the thermal energy of the neutrals being ionized and from energy imparted by the ionizing agent. The quantity a depends on the width of the particle beam or photon beam which is employed to ionize atoms. This parameter can be made very small by the use of focussed electron beams while with either photons or electrons the required fluxes are small enough that a pair of pin holes will emit a sufficient beam having a diameter of a few millimeters at the point of interest. Finally the effects of beam steering must be considered. Any beam is directed no more accurately than permitted by the reproducibility of

mechanical settings. However this feature should not set a significant limit. Rather the alignment of a system is the critical feature. Also an ionizing electron beam can be deflected by magnetic fields or electrostatic fields so that Δr can be unacceptably large. Increasing electron velocity to decrease Δr is only moderately helpful because above 100 eV, ionization cross sections decrease. When the preceding factors are weighed, the optimum choice for an ionizing agent often will be a collimated beam of photons.

The second quantity to be measured is energy of the ions being detected. After the ions enter the orifice of the detector they must be subjected to some selection process. Either some theshold condition may be imposed such that only those ions with energy exceeding the theshold are recorded, or some system such as a curved-plate analyzer may select particles with energies in a specified band. A threshold device we have used is recommended as it is capable of resolving to within 2% whereas a typical curved-plate system resolves at 7% (ref. 1).

Restrictions

Because of the desire to minimize the effects on the system being measured, one should observe several precautions. First the ionizing beam itself should not strike any surfaces. Otherwise it would modify the surface charge and the potentials at points of interest. Ideally the beam would pass by the structure creating the potential distribution and be absorbed in a dump on the other side from the source.

Another beam effect less easily dismissed is the drifting of electrons to the structure. These electrons are released along with ions at the point of interest. If ions are repelled from the structure, the electrons will be attracted. When neutral gas pressure is uniform throughout the vacuum chamber, ions and electrons are released from all points along the ionizing beam path, yet they are needed only at the one point. Conceivably the neutrals could be concentrated at the region of interest by pumping the chamber to a substantially lower pressure while injecting gas through an appropriately directed nozzle. Then, a beam of neutral atoms would cross paths with the ionizing beam. Use of a sensitive detector is necessary to minimize the charged-particle perturbations. The ionizing beam should be only as intense as needed for observing the response.

When an electron ionizing beam is used, the beam itself perturbs the potentials being measured. If a beam having radius a carries current I where acceleration is through voltage V, then the line charge density, using mks, is

$$\rho_\ell = I\sqrt{\frac{m}{2eV}} \tag{2}$$

The potential at a relative to some reference radius r_o is

$$V(a) - V(r_o) = \frac{\rho_\ell}{2\pi\epsilon_o} \ln (r_o/a) \tag{3}$$

For a typical beam of 1 mm, 10^{-6}A, and 100 V, where we let the reference r_o

correspond to separation between beam and structure (say 0.1 m) we find that $V(a) - V(r_o) = 0.0138V$. This can be ignored.

Electron Beam Experiments

An electron beam source and ion detector were built by David Ross as described in reference 2. These systems are described here and some results are given.

The electron gun consisted of a hot tungsten wire placed behind a pair of apertures. The outer aperture had a diameter of 1.1 mm and it was placed 19.6 mm from the inner aperture having a diameter of 1.4 mm. The apertures were grounded and the filament was biased at -150V to produce a current. As a fine wire probe was moved through the path of the beam, it showed a beam divergence of 2.6° such that at a typical working distance of 10 cm, the beam width was 4.5 mm. Currents, approximately 10^{-8}A, detected by the 1-mm probe wire provided more than adequate ionization.

The test configuration was a conducting right-dihedral angle biased typically at 70V relative to the detector located near the ground plane. Figure 1 shows computed equipotential contours and particle trajectories for the test configuration. The detector moved along the x-axis. The ion source was mounted with two degrees of freedom along the x and y axes and projected a beam more or less parallel to the apex of the wedge. The experiment was essentially two-dimensional.

The basic detector design is illustrated in figure 2. It provides four functions, a measure of beam position at the detector plane, a measure of beam angle, a measure of ion energy, and a means of detecting particles. The detector element was a continous-dynode electron multiplier operated in a pulse-generating mode so that it would indicate the impact of an ion on its input cone. It was followed with a two-stage 10-X amplifier, an oscilloscope which showed pulses, and a counter. For ions to reach the input cone they had to pass through a set of three apertures and a repeller electrode which provided the various types of discrimination. All elements of the system were rigidly mounted in a metal can which could be translated and rotated by mechanical linkages.

The two outer apertures provided the measure of location and angle. Only when both were positioned to correspond with incoming ions would ions enter the inner chamber. The apertures were 12.7 mm apart, the outer had a diameter of 0.76 mm, and the inner, 0.38 mm. The response as a function of angle had a measured half-width of 3°.

The second aperture, the third aperture, and the cylindrical repeller provided the energy discrimination. The repeller was biased positively and created a saddle-point potential between apertures. When particles had sufficient energy to pass over the saddle-point, they continued through the third aperture and were detected. The hole in the third aperture was somewhat larger than the others; this was to avoid loss of particles deflected as they passed over the saddle-point. Figure 3 shows response as a function of bias

voltage on the repeller. Particles at 19.3 eV were repelled by voltages on the tube exceeding 24.1V. The ratio 0.80 of these values corresponds well to 0.79 calculated for the drift-tube, radius-length ratio of 0.45. The drift-tube length was 2.8 cm.

The sample trajectories shown in figure 1 are computer simulations obtained by injecting ions at the detector plane with velocities more or less opposite to those measured. The source point is found to be a very sensitive function of angle, so sensitive that the measure of angle is practically useless. If the position angle measurements were sufficiently accurate, they could be used to corroborate the locations of the source points as determined by the aiming of the electron gun. However our experience has shown that the detector is useful only as an energy measuring instrument. The measure of angles is further complicated by the effects of the magnetic field which causes trajectories to curve.

Our experiences with an electron beam system have suggested two changes in technique. The ionizing beam should consist of photons so that it won't be deflected and the detector should have less angle resolving capability so that the ion beam can be more easily located. However the energy resolution should be maintained.

X-Ray Beam Experiments

A preliminary study of an X-ray beam system has been completed. The electron beam system was adapted to this purpose for a demonstration of concept and now a better X-ray system is being constructed.

For the demonstration of concept the electron source was replaced with an X-ray source which however did not fit well into the available space and could not be steered precisely. Nevertheless a beam was produced and ions were detected. Figure 4 shows detection response for two different orientations of the X-ray beam. Of interest here is the design of the X-ray source. A steel pin biased at +600V drew 0.8 mA of current from a nearby grounded tungsten filament. Soft X-rays emanating from the pin were collimated by a pair of apertures to form a beam which in this case had a radius of 1 cm in the working region.

Under construction are a source having much smaller apertures and a detector having wide-angle response. This combination is expected to provide better resolution.

POTENTIAL MAPPING FROM PARTICLE TRAJECTORIES

Various instances of using beam trajectories to map a rotationally symmetric potential profile have been reported (refs. 3,4) and a general mapping technique has been described where a reasonably dense plasma and magnetic field are required (ref. 5). This work seeks methods of generating potential maps where Laplace's equation is valid and magnetic field is

insignificant. Data characterizing the region of interest are obtained by injecting charged particles (or low-current beams) with known velocities and observing their exit points. A preliminary study of a boundary value problem has provided a useful frame of reference for studies of mapping techniques.

Boundary Value Problem

The analysis of data in the general mapping problem is equivalent, when charge density is low, to solving Laplace's equation. The data set will always be finite, i.e., a finite number of particle trajectories will have been observed, and the map will consequently be approximate. The analyst must decide upon the level of detail he requires and select a data set sufficient for his purposes. He must be cautious not to misuse his data in a manner represented by the function $y = \cos x$ which provides a perfect fit to the set of points ($y_i = 1$, $x_i = 2\pi i$).

The need to solve Laplace's equation led to a preliminary study of a boundary value problem in a context that could be extended to the mapping problem of interest. Being sought was an iterative technique which would converge toward a solution as precise as boundary specifications would justify. Convergence was accomplished by comparing the approximate solution with boundary constraints and then perturbing the solution to improve the match. The procedure was developed for boundary conditions specified as values of potential on a set of points spaced more or less uniformly on the boundary.

The key to the method is the choice of perturbing function. Let the estimated solution ϕ_e be of a functional form known to satisfy Laplace's equation. Also let some perturbation ϕ_d be a solution of Laplace's equation which decreases with distance from some singular point. Then the sum $\phi = \phi_e + \phi_d$ must be a solution because of the superposition principle. When ϕ_d is properly chosen, ϕ will match the boundary conditions more closely than ϕ_e does and a convergent process can be developed. The perturbation must be localized to a small portion of the boundary so that when an improvement is made in the match for that portion, the other portions will not be changed much. Also the singularity must be located outside of the region of interest. Consequently the singularity will be placed outside of but near to the boundary where matching is to be improved. The perturbation can be that of a single charge, a dipole, or a higher order pole but we have chosen to work exclusively with dipoles. They are reasonably localized without being overly difficult to manipulate.

With respect to some location and preferred direction, we may describe a dipole as

$$\phi_d = \mu \, (\cos\alpha)/\rho^2 \qquad (4)$$

where μ is the strength, α is the orientation of the field point, and ρ is the distance of the field point. This is the potential function in 3 dimensions for a dipole consisting of plus and minus point charges closely spaced.

However for 2-dimensional work the choice should be

$$\phi_d = \mu\ (\cos\alpha)/\rho \tag{5}$$

which represents the potential for plus and minus line charges. In either case the separation between charges is small compared with ρ and the dipole is a singularity. When a 2-dimensional dipole is located at (x_d,y_d) and a field point at (x,y), then ϕ_d is given by

$$\phi_d = \frac{\mu \cos\beta\,(x-x_d) + \mu \sin\beta\,(y-y_d)}{(x-x_d)^2 + (y-y_d)^2} \tag{6}$$

where β is the orientation of the dipole measured relative to the x-direction. Though we need not restrict β, we find it convenient to choose $\cos\beta = -x_d/r_d$ and $\sin\beta = -y_d/r_d$ where r_d is the displacement of the dipole from the origin. Thus when μ is positive, the positive side of the dipole faces the origin and ϕ_d is given by

$$\phi_d = -\frac{\mu}{r_d}\left(\frac{x_d(x-x_d) + y_d(y-y_d)}{(x-x_d)^2 + (y-y_d)^2}\right) \tag{7}$$

The dipole is placed so as to produce a desired perturbation in ϕ_e. Let the origin be at the centroid of a closed boundary curve (2-dimensions) whose radius is a single-valued function of angle. Assume that for some boundary point (R,θ) the discrepancy between ϕ_e and the specified boundary condition is largest of all discrepancies and then place the dipole on the same radius θ at $r_d > R$. See figure 5. At (R,θ), equation (7) reduces to

$$\phi_d(R,\theta) = \mu/(r_d-R) \tag{8}$$

and we are assured that the largest perturbation on the boundary will occur at (R,θ), at least if the radius of the boundary does not change greatly from one point to the next. If ϕ_b represents the specified boundary condition we require that

$$\phi_b(R,\theta) = \phi_e(R,\theta) + \mu/(r_d-R) \tag{9}$$

and then we calculate ϕ at all points of interest in the region. Even with β previously specified, we must exercise a choice of either r_d or μ.

When the dipole is placed far from the boundary its strength must also be large and its influence extends to a large portion of the bounded region. In the limit as r_d and μ approach infinity, the dipole affects all points equally and in fact shifts all points by a constant. At the other extreme, that of close placement, the effect of the dipole is very localized. The choice of position represents compromises between speed and accuracy of the solution. When boundary conditions are specified as a set of points, they can be satisfied easily by placing a small dipole very near to each point. However this solution is not desirable because it will bear little resemblance to the relatively smooth boundary function likely to have been implied by the set of boundary points. Furthermore various solutions may be obtained

as different choices of μ and r_d are made. When a minimum distance r_d-R is specified, a given dipole can be forced to influence several boundary points and the boundary function will be smooth. A solution will still not be unique but various solutions will differ only in small amounts. We have found practically that r_d-R should be at least as large as the distance between neighboring boundary points. A useful criterion expressed in terms of the number of boundary points n is that

$$r_d - R = RG/n \tag{10}$$

where typically $G \geq 2\pi$.

Convergence can be obtained by specifying that all dipoles will be a given distance from the boundary. In this case the number of dipoles is equal to the number of boundary points though a given dipole strength may be the sum of contributions from several iterations. However convergence may be faster if some criterion in introduced for picking distance. Figure 5 illustrates two situations in terms of discrepancies indicated by each point where we define discrepancy at the ith point by

$$d_i = \phi_{bi} - \phi_{ei} \tag{11}$$

When several adjacent points have discrepancies of the same sign, the dipole should be far enough away that it will perturb all of those points. On the other hand, when discrepancies alternate in sign, the dipole should be close. Noting that (R,θ) locates the point of absolute maximum discrepancy, we let (R',θ') represent the nearest point for which the discrepancy is of the opposite sign. Letting d_a be the average absolute discrepancy and T be some constant $0 < T < 1$, we can select r_d so that

$$\phi_d(R',\theta') = \pm T\, d_a \tag{12}$$

The sign is chosen to be the same as for $\phi_d(R,\theta)$. This requirement on $\phi_d(R',\theta')$ forces a choice of r_d that is sensitive to the polarities of nearby discrepancies, but retrictions are necessary. When T is specified as being small, the value of r_d may not satisfy equation (10) which must be given priority. When T is large the convergence will be slow and perhaps nonexistent. The benefits of introducing equation (12) are relatively minor.

Though, in concept, dipole perturbation alone should suffice for finding a solution, some auxiliary operations have been found to be useful. These are rotating, shifting, and scaling of the estimated potential function. As an initial estimated potential one may simply assume that $\phi = x$. However if say potential increases more or less as y, then a preliminary rotation of 90° is appropriate. One might subsequently replace ϕ_e by $\phi_e' = \phi_e + b$ where b represents a shift. In terms of discrepancies b is calculated from

$$b = -\sum_i d_i/n$$

When shifting has been done the average potential is

$$\phi_a = \sum_i \phi'_{ei}/n = \sum_i \phi_{bi}/n \qquad (14)$$

Finally a scaling factor can be determined:

$$c = \sum_i |\phi_{bi}-\phi_a| \; / \; \sum_i |\phi'_{ei}-\phi_a| \qquad (15)$$

The potential ϕ' is replaced by a scaled potential:

$$\phi'' = c\,(\phi'-\phi_a) + \phi_a \qquad (16)$$

For our work, each dipole addition has been preceded with both shifting and scaling operations.

Details of the method have been explained for the 2-dimensional case, though no assumptions have been introduced which would limit the method from being applied in 3 dimensions. The number of boundary points would be larger and correspondingly more dipoles would be required.

Potential has been found at points inside of a square by the method of dipole perturbations. The test problem is specified in figure 6 which shows 20 boundary points uniformly distributed in angle. All points on the bottom side of the square were assigned a potential of 0 and the others a potential of 10. Potentials were calculated for boundary points and for an array of internal points layed out in polar coordinates. Equipotential contours were then plotted as shown in figure 7. Points on the equipotentials were found by linearly interpolating along a straight line between array points; some of the irregularities noted in the figure may be attributed to the approximation made in the interpolation. Potential intervals between curves are 0.25V. This example required 214 dipoles where the convergence criterion was that $\Sigma|d_i| < 0.00001$, though a much less stringent criterion could have been used.

Potential Mapping

The transition from the boundary value problem to the particle-trajectory problem is accomplished by using trajectory data in place of boundary data when synthesizing the potential function. The general approach is to sum contributions of numerous dipoles placed outside the region of interest such that simulated particle trajectories in the region match the observed trajectories. As in the boundary value problem, the solution is not unique and the data must not be overextended.

The problem has been defined in two dimensions with reference to a line along which both beam source and detector move. A beam is injected into the space above the line, repelled, and returned to the line where its exit position is monitored. Measurements are of entrance position, entrance velocity, and exit position for as many selected beams as required by the application. The beam can be of either electrons or ions. A computer simulation uses a known potential distribution that can be produced experimentally with a set of parallel fins as illustrated in figure 8. The base line is at ground potential, all fins are equally biased, and equipotential,

lines have been computed for the configuration. Shown in the figure are several simulated particle trajectories. The potential ϕ can be found with a conformal mapping from a flat plane given by

$$\phi = \text{Imag}\,[\sin^{-1}(e^{c})] - \text{Imag}\,[\sin^{-1}(e^{w})],\ w = (c-y) + ix \quad (17)$$

The zero potential line does not exactly match the x-axis but the error is small enough to be ignored if c exceeds 2. The fin spacing is π.

Experimental trajectory data are being sought to test the procedure but they can also be simulated with a trajectory tracing program. In fact the simulation will permit an assessment of what experimental errors can be tolerated. Both for providing simulated data and for use in the potential mapping procedure, a tracing routine developed by DeVogelaere (ref. 6) has been programmed. The routine requires fields to be calculated at specific points on the trajectory and when potential is specified on a discrete set of points, Newton's interpolation procedure (ref. 7) is used.

The scenario of the simulation follows three steps. First the potential illustrated in figure 8 is calculated for a square array of points. The simulated particles are injected into the array, trajectories are traced, and exit points are recorded. Finally these simulated trajectories are used as a basis for generating various potential maps which can be compared with the original array to assess the effectiveness of the mapping procedure.

The map is constructed by placing dipoles above the region being mapped. Let the vertical placement y_d exceed the maximum range of the map so that the singularity does not fall in that range. There is a requirement that the reference plane have a fixed potential so that a dipole placed at (x_d,y_d) must be balanced with its image at $(x_d,-y_d)$. An original estimated potential function $\phi = ay$ is then perturbed by the placement of dipoles in pairs until some convergence criterion is met.

Work in progress presently deals with the process of selecting dipoles. Shown in figure 9 is a map which has partially converged after the placement of 8 relatively weak dipoles. The convergence is quite slow and subject to instabilities if it is speeded up. For this particular map, each dipole selection was based on the trajectory which deviated most from the desired exit point. This approach, analogous to the correction of the worst point in the boundary value problem, has some basic flaws which are best overcome by considering several neighboring trajectories in making the choice of a dipole. For example if two trajectories at different x-values have deviations of opposite sign then a dipole might be placed at some x_d intermediate between them. Choice of y_d is related to how many trajectories are to be substantially modified by the dipole. In any case dipoles are to be kept at least as far above the boundary as the trajectories are spaced from each other.

CONCLUDING REMARKS

Measurements show that a beam of electrons or photons can ionize enough neutrals at 10^{-5} Torr that they can be detected by a continuous-dynode electron multiplier behind collimating pinholes. The energy of the ions when detected is a direct measure of the potential where they were created. The photon beam has the advantage that it can be directed to the desired spot along a straight line whereas an electron beam curves in the electric and magnetic fields usually present. Though the ion detector was designed to provide spacial and angular resolution of the ion trajectories, it need only resolve energy.

A method of solving Laplace's equation is described where the final solution is the sum of some initial estimate and the contributions of selected dipoles placed outside the region of interest. A preliminary calculation is based upon the specification of potentials on a discrete set of boundary points. This result is then extended to the use of particle trajectory data in place of boundary potentials. Work in progress seeks to identify efficient schemes of picking dipoles from an analysis of trajectory data so that potential maps may be generated.

REFERENCES

1. Green, D. W. and Whalen, B. A.: Ionospheric Ion Flow Velocities From Measurements of the Ion Distribution Function Technique. Journal of Geophysical Research 79, pp. 2829-30, July 1, 1974.

2. Ross, David P.: Ion Tracking in an Electrostatic Potential Distribution. The Pennsylvania State University, NASA CR-156983, May 1978.

3. Stallings, C. H.: Journal of Applied Physics 42, p. 2831, 1971.

4. Black, W. M. and Robinson, J. W.: Measuring Rotationally Symmetric Potential Profiles with an Electron-Beam Probe. Journal of Applied Physics 45:6 pp. 2497-2501, June 1974.

5. Reinovsky, R. E. et al: Performance of a Feedback Controlled Electrostatic Analyzer for Use with an Ion Beam Probe Diagnostic System. IEEE Trans. on Plasma Science PS-3, 194-200, December 1975.

6. Booth, Andrew D.: Numerical Methods, Butterworths 1966, 3rd ed., p. 71.

7. Steffensen, J. F.: Interpolation, Williams and Wilkins 1927, pp. 14-34, 203-224.

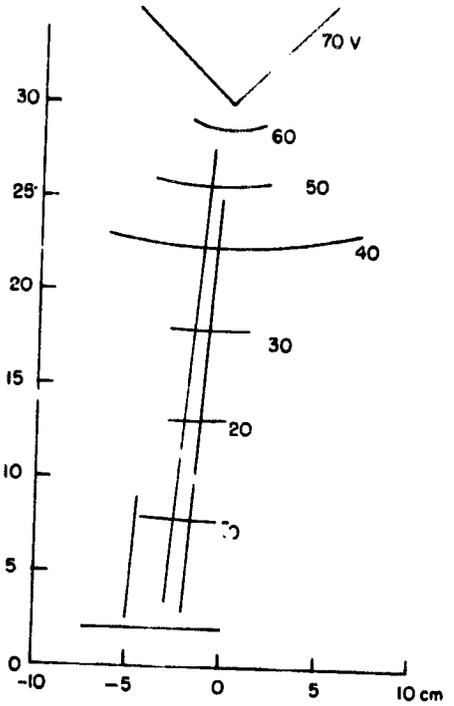

Figure 1. - Simulated trajectories for ionizing electron beam experiment.

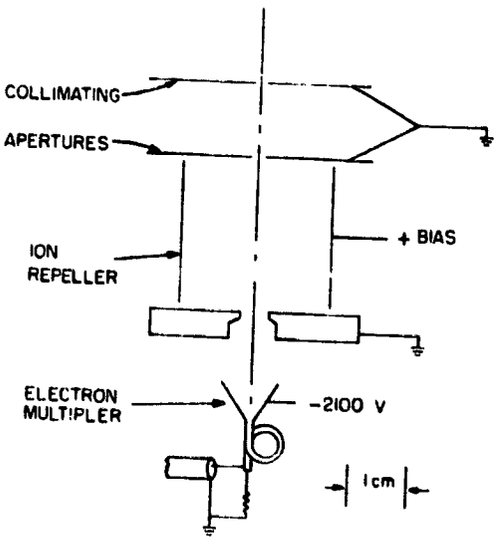

Figure 2. - Ion detection system.

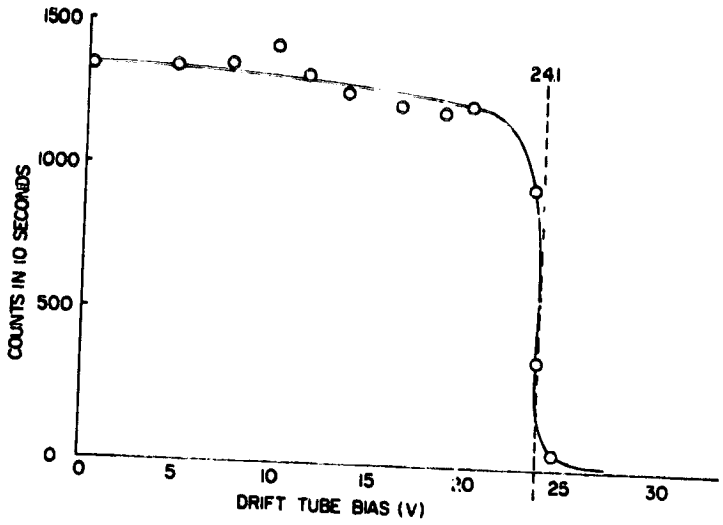

Figure 3. - Detector response to 19.3-eV ions.

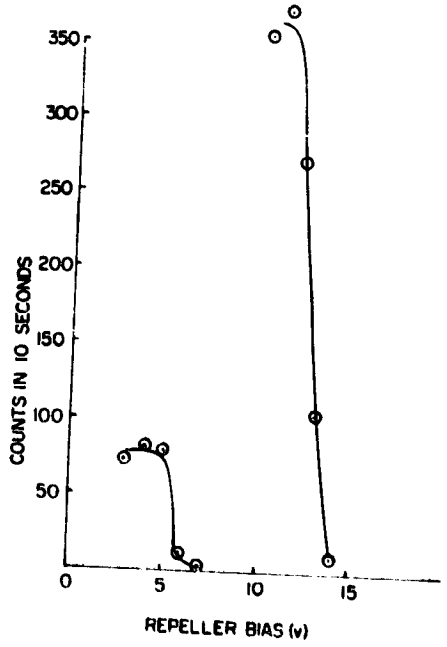

Figure 4. - Detector responses for two X-ray beam positions.

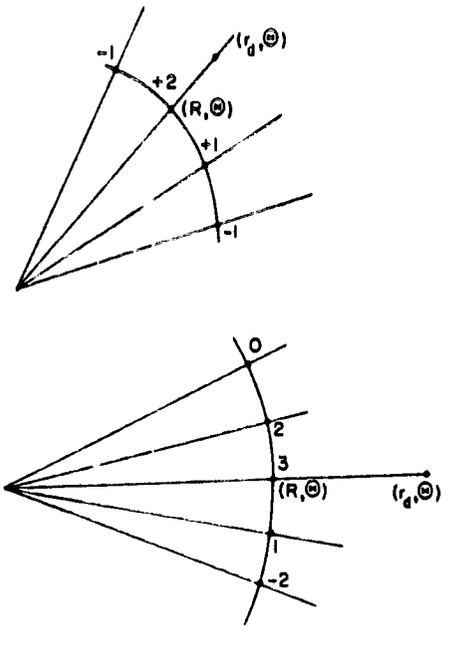

Figure 5. - Dipole placement, with numerals showing discrepancies.

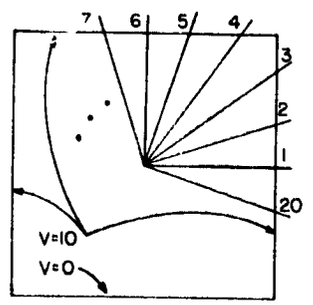

Figure 6. - Assignment of boundary conditions at 20 points.

Figure 7. - Equipotential lines for boundary value problem.

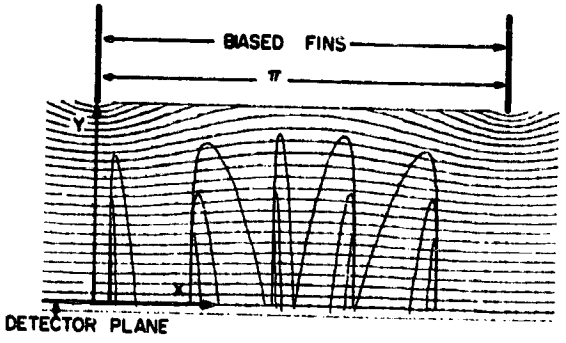

Figure 8. - Test potential and simulated trajectories.

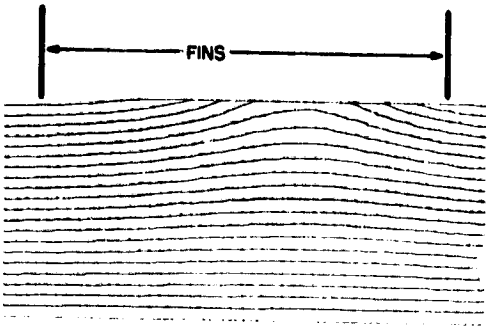

Figure 9. - Partially converged potential map based on trajectory data.

ELECTROSTATIC DISCHARGE PROPERTIES OF SELECTED VOYAGER SPACECRAFT MATERIALS*

J. B. Barengoltz
Jet Propulsion Laboratory
California Institute of Technology

R. B. Greegor II, L. B. Fogdall and S. S. Cannaday
Boeing Aerospace Company

ABSTRACT

As a part of an extensive program to assess and ameliorate the electrostatic discharge hazard to the Voyager spacecraft posed by passage through the charged particle environment near Jupiter, a testing activity to characterize the behavior of selected Voyager materials was undertaken. A series of twelve material and component samples were exposed to an electron beam in order to measure the time history and amplitude of resultant electrostatic discharges. These tests were conducted at a Boeing Aerospace Company combined radiation effects test chamber.

The typical experimental design was to mount the test article with its dielectric surface facing the beam and its conductive portion isolated from ground except by way of a shielded cable on which a discharge pulse could be observed. The behavior of the sample was then observed at bombarding energies from 20 to 100 keV in increasing 20 keV increments and then 90 to 30 keV in decreasing 20 keV increments. Observations were made at each energy for nominally two hours at an electron flux of 4×10^9 $cm^{-2}s^{-1}$.

INTRODUCTION

The differential electrical charging of spacecraft surfaces in a charged particle environment is a recognized subject of interest to spacecraft designers. This effect was originally a matter for the scientific instruments such as charged particle spectrometers where the measured spectrum would be offset. However, the observed correlation between anomalous effects in the electronics of geosynchronous satellites and magnetic substorms is a strong indication of differential charging and subsequent electrical discharges (Ref. 1).

The Voyager Project established an extensive program (Ref. 2) to assess and minimize this electrostatic discharge (ESD) hazard for the two Voyager spacecraft which will encounter the radiation environment near Jupiter. This

*This work presents the results of one phase of research carried out at the Jet Propulsion Laboratory, California Institute of Technology, under contract No. NAS7-100, sponsored by the National Aeronautics & Space Administration.

program's objective was to design the spacecraft so as to eliminate the hazard and to demonstrate through testing and analysis that the goal had been met. Components of this program included analyses of the differential charging, due to electrons, protons, and the photoelectric effect, of the Voyager spacecraft (performed by Sanders, et al. of TRW (Ref. 3)), a systematic design process to eliminate wherever possible exposed dielectrics from the spacecraft, simulated ESD tests of the spacecraft, and the computer code Systems Electromagnetic Analysis Program (SEMCAP) (TRW). The work described in this paper was intended to characterize the remaining suspect materials (from an ESD viewpoint) and to provide values for the magnitude of possible discharges. This data was required to ensure that the simulated ESD tests were adequately severe, and as input to SEMCAP, which was used to predict potential adverse subsystem responses and verify that corrective measures were appropriate.

Procedure

A series of twelve material and component samples from the Voyager spacecraft were exposed to an electron beam in order to measure the time history and amplitude of resultant electrostatic discharges. The test articles were FEP teflon, a section of magnetometer boom longeron with a piece of bare cable braid mounted on it, a section of longeron with a piece of jacketed cable mounted on it, a piece of the magnetometer cable (alone), a flight Brewster plate, a piece of plume shield, a section of the high gain antenna, a piece of the frequency selective subreflector, a separation connector, a piece of thermal blanket, a sample of the radioisotopic thermoelectric generator (RTG) case coating, and an end dome of an RTG case (Table 1). In general, these test articles can be categorized as follows: (1) planar dielectric/conductor structures (teflon, Brewster plate, high gain antenna); (2) non-planar dielectric/conductor structures (magnetometer boom longeron, frequency selective subreflector, separation connector); and (3) structures of unknown dielectric tendencies.

The samples were exposed in one of two Boeing combined radiation effects test chambers (CRETC) (Fig. 1). These systems are clean vacuum systems with fluidless pumping and glass, ceramic, and metal seals and with provisions for the simultaneous exposure of a sample to electrons, protons and ultraviolet. In these tests only the electron source was employed, at energies ranging from 20 to 100 keV and a flux of 4×10^9 $cm^{-2}s^{-1}$.

The electron energy was calculated from the known electron gun cathode potential with a loss in the aluminum scattering foil based on range-energy tables. A rotatable Faraday cup was employed to measure the electron beam profile after the spreading by the foil. A second, fixed Faraday cup was standarized for the flux at sample center and then used to monitor the electron beam during the exposure of a sample.

The test articles were mounted so that the dielectric surface, i.e., the exposed surface in spacecraft use, was facing the electron beam (Fig. 2, 3, & 4). The conductive part of the test article was isolated from ground except by way of a shielded cable on which a discharge pulse could be observed. This signal cable was connected to ground through a 50 Ω resistor for impedance

matching. The discharge pulses were measured by a fast rise-time current probe on the ground wire or the voltage across the resistor. The measured pulses were displayed on a wide bandwidth 7000 series Tektronix scope with fast writing speed (2cm ns^{-1}) and recorded by a Polaroid camera. A simple loop antenna was also located in the chamber to count all events, including those too small to trigger the pulse measurement circuit.

The general test procedure was to expose the sample to electrons at energies from 20 to 100 keV in 20 keV increments and then 90 to 30 keV in 20 keV decrements. At each energy observations were made for about two hours.

Test Results

A summary of the test results is provided in Table 2. Without exception, all of the samples known to be dielectric/conductor structures exhibited single pulse discharge-like events (See, e.g. Fig. 5). These samples are the teflon, magnetometer boom longeron (with cable or cable braid), Brewster plate, high gain antenna, frequency selective subreflector and the separation connector. Conversely all of the samples whose exposed dielectric surfaces had been modified during the Voyager ESD program to enhance conductivity and confer ESD immunity exhibited only atypical events. The signal from an atypical event was similar to a damped oscillation with a fast frequency (0.25 to 0.50 ns^{-1}) and a decay period of 50 to 200 ns. These samples were the magnetometer cable (alone) and the thermal blanket. The teflon outer insulation of the cable had been replaced by a wrap of "conductive" teflon tape. Similarly the outer Kapton surface of the thermal blanket had been painted with a "conductive" Sheldahl paint.

Of the doubtful dielectrics, the plume shield produced three single-pulse signals during its entire exposure and a larger number of atypical events. The sample exposed had a black, low-conductivity surface as supplied (perhaps an oxide layer). The two different sized samples of RTG case were observed to yield only atypical signals, however (Fig. 6, 7 & 8). There is some uncertainty about the resistivity of the iron titanate (in a borosilicate matrix) coating involved, but it is much less than all materials except the "conductive" teflon and Sheldahl.

DISCUSSION

The teflon results lend themselves to analysis because of the planar geometry and the known breakdown voltage of the material. In addition, the special sample holder employed (Fig. 2) drastically reduced edge effects by beam masking. Thus one expects a total surface charge of 11.6μC from the calculated capacitance and a breakdown voltage of 17.5 kV. The charge observed in the largest single discharge (determined by integration of the current pulse) was in fact 12μC(Fig. 5).

This result contrasts to some extent with the findings of Stevens, et al. (Ref. 4) of a "replacement" charge of 15μC (measured as in this work) for a measured discharge of 50 to 60μC in 127μm (5 mil) FEP teflon. Stevens, et al. determined the actual discharge from the surface potential before and after

breakdown and a measurement of the sample effective capacitance by the surface charge and voltage dependency during charging. They concluded that the "replacement" charge does not appear to compensate for all of the charge lost in the discharge. As noted in their work, however, edge effects are very important. The expected surface charge for their larger sample would be 66μC on the basis of the ideal capacitance and breakdown voltage (compared to 11.6μC for this work). However, the edge effects lowered the observed breakdown voltage to 12 kV from 17.5 kV and evidently increased the effective capacitance from 3.8 nF to a value between 4.2 and 5.0 nF. Since edge effects drastically lowered the breakdown potential, perhaps much of the missing charge was an edge breakdown.

A comparison of the maximum currents observed in this work and Reference 4 shows them to be approximately commensurate (250A vs. 100A, respectively). Even if a factor of 3 to 4 is applied to the previous work's result to predict an arc discharge of 300 to 400A, this conclusion is unchanged. Further, the pulse widths observed have a ratio of about 10 and the discharge charges about 5 (in the opposite sense). It appears that in the absence of edge effects, the total charge is observed and scales with area (a factor of 6). However, the pulse width also scales with the area (an RC constant), so that the peak current is not dependent on surface area. Edge discharging evidently causes part of the current not to be observed as "replacement" current and lengthens the duration of the "replacement" signal.

The magnetometer boom longeron section and cable braid test (Fig. 3) produced a very interesting result. During the exposure of this sample the charging of the fiberglass longeron caused a force which attracted the flexible cable braid. The braid was observed to bow out, contact the relatively stiff longeron, and occasionally remain in contact for periods up to fifteen minutes. The subsequent sudden release was always correlated with the observation of a discharge signal. After the test a direct measurement of the force required to produce this observation set the value at 0.11 N. A calculation of the force in terms of a uniform line of charge parallel to a cylindrical conductor leads to a total charge on the longeron of 8.8×10^{-9}C. In terms of capacitance and breakdown voltage, the 15-cm section corresponded to 8.6pF charged to -10.2kV. The maximum observed charge was 4×10^{-8}C on a 5A discharge event. The simplest explanation of the observation of only part of the possible total arc charge is that the discharge was partial due to the braid springing back and the limited region of original contact. In any event at least one half of the arc charge was observed in the "replacement" signal. Edge effects were also operative since the cable braid was mounted on the longeron by conductive "knuckles". Therefore any discharge from this spacecraft component is limited to that from a section between adjacent "knuckles".

The atypical pulses are the most difficult result to understand. On the basis of their appearance in the low resistivity samples only, the hypothesis of a burst of very small local discharges is attractive. The damping would then be due to mutual inductance of these several parallel breakdown paths. The resistively damped LRC oscillation interpretation is supported by the observed change in the appearance of the signals from the RTG case end dome when an external 47μH inductor was placed in parallel to the external

resistor (Figs. 7 and 8). The plume shield may have been an intermediate case with its thin oxide layer, i.e., some global discharges and some local discharges.

This picture is enhanced by an extra test conducted on a stainless steel sample of the size of the RTG case coating sample. During the first three hours, this dummy sample exhibited three atypical pulses similar to the RTG case coating results. Then no more events were observed. Apparently, there were some localized areas of surface contamination which cleaned up due to the vacuum and the electron beam.

CONCLUSIONS

Twelve material and component samples of the Voyager spacecraft have been evaluated in terms of their electrostatic discharge tendencies. As expected all of the test articles exhibited some discharge phenomena when exposed to an electron beam. An important unexpected result was the appearance of a damped oscillating discharge from the poor insulators in contrast to a simple pulse signal from the good insulators.

Of direct interest to the spacecraft ESD question is the demonstrated possibility of a global or complete discharge from a dielectric. The current pulse as measured represents a charge commensurate with the actual discharge (a factor of 0.5, say) provided that edge effects are absent or minimized. This can be accomplished by masking the edges of the sample from the beam. The peak current probably does not scale with surface area. Insulator thickness will affect the value through the breakdown voltage, however. The arc charge probably scales with capacitance, while the pulse width is likewise proportional to capacitance. The atypical discharges from the poor insulators appear to be a series of local discharges. As such, none of the parameters would scale with sample surface area.

Further systematic research would be desirable to place some of these tentative conclusions on a firmer basis, especially the "replacement" current/arc current and the scaling hypotheses. For analysis of circuit susceptibility to discharges in nearby insulators, an arc rise time model is required. Finally, the sense of the observed current, electrons flowing into the conductor from the external circuit, is difficult to explain with any simple discharge model. A good model would be indispensable in conjunction with research yet to be accomplished.

REFERENCES

1. Rosen, A. "Spacecraft Charging: Environment-Induced Anomalies", Journ. of Spacecraft and Rockets 13, No. 3 (1976).

2. Whittlesey, A.C., "Voyager Electrostatic Discharge Protection Program", 1978 IEEE International Symposium on Electromagnetic Compatibility, June 20-22, 1978, IEEE CH1304 (1978).

3. Sanders, N. L., Inouye, G.T., and Rosen, A., "Voyager Spacecraft Charging Immunization Support to JPL; TRW No. 31440-6002-RU-00, (1977).

4. Stevens, N. J., Berkopec, F.D., Staskus, J.V., Blech, R.A., and Narisco, S. J., "Testing of Typical Spacecraft Materials in a Simulated Substorm Environment", NASA TM X-73603 (1976) (also published in proceedings of the Conference on Spacecraft Charging Technology, October 27-29, 1976, NASA TM X-73537).

TABLE 1. - PHYSICAL PROPERTIES OF SAMPLES TESTED

TEST ARTICLE	DIELECTRIC SURFACE			CAPACITANCE (pF)
	COMPOSITION	THICKNESS (μm)	AREA (cm2)	
FEP TEFLON	FEP TEFLON	127	50	630
LONGERON/CABLE BRAID	FIBERGLASS	N/A	N/A	8.6
LONGERON/MAG CABLE	FIBERGLASS/TEFLON*	N/A	N/A	?
MAG CABLE	TEFLON*	63	45.6	?
BREWSTER PLATE	EPOXY	50	620	38,000
PLUME SHIELD	NICKEL OXIDE	?	50	?
HIGH GAIN ANTENNA	PV-100 PAINT	100 (NOM)	290	2500
FREQUENCY SELECTIVE SUBREFLECTOR	PV-100 PAINT	100 (NOM)	N/A	14 (EST)
SEPARATION CONNECTOR	PHENOLIC	N/A	N/A	150 (EST)
THERMAL BLANKET	SHELDAHL*	25 (NOM)	50	?
RTG CASE PIECE (END DOME)	IRON TITANATE BOROSILICATE MATRIX	50-75	25 [700]	3 [10,000]

* INTENDED TO BE CONDUCTIVE

TABLE 2. - SPACECRAFT MATERIALS DISCHARGE TEST RESULTS SUMMARY

TEST ARTICLE	TYPICAL MEASURED PULSE[a]		
	RISETIME (ns)	WIDTH (ns)	AMPLITUDE (A)
FEP TEFLON	30	50-300	20-250
LONGERON/CABLE BRAID	2	5	0.5-6
LONGERON/MAG CABLE	4-10 N/A	10-20 N/A	0.8-2 (BRAID) (0.08-0.8)[b] (WIRE)
MAG CABLE	N/A N/A	N/A N/A	0.5-5[b] (BRAID) (1V)[b] (WIRE)
BREWSTER PLATE	1.5-10	4-20	0.1-3
PLUME SHIELD	10-40	50-300	0.05-0.3
HIGH GAIN ANTENNA	2-10	8-20	0.1-0.4
FREQ SELECTIVE SUBREFLECTOR	2-8	8-80	0.1-8
SEPARATION CONNECTOR	10-20	15-30	0.2-18
THERMAL BLANKET	N/A	N/A	2-3[b]
RTG CASE PIECE	N/A	N/A	0.15-100[b]
RTG CASE END DOME	N/A	N/A	0.2-5.5[b]

[a]PULSE PARAMETERS, ESPECIALLY AMPLITUDE ARE ENERGY DEPENDENT

[b]ATYPICAL OSCILLATORY SIGNALS, NO PULSE-LIKE SIGNALS

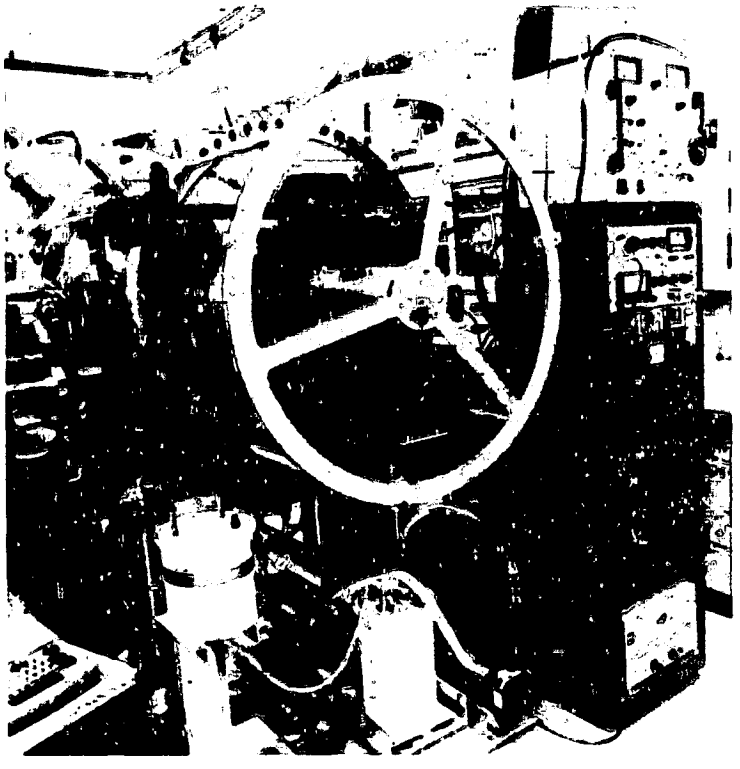

Figure 1. - Combined radiation effects test chamber (CRETC) system.

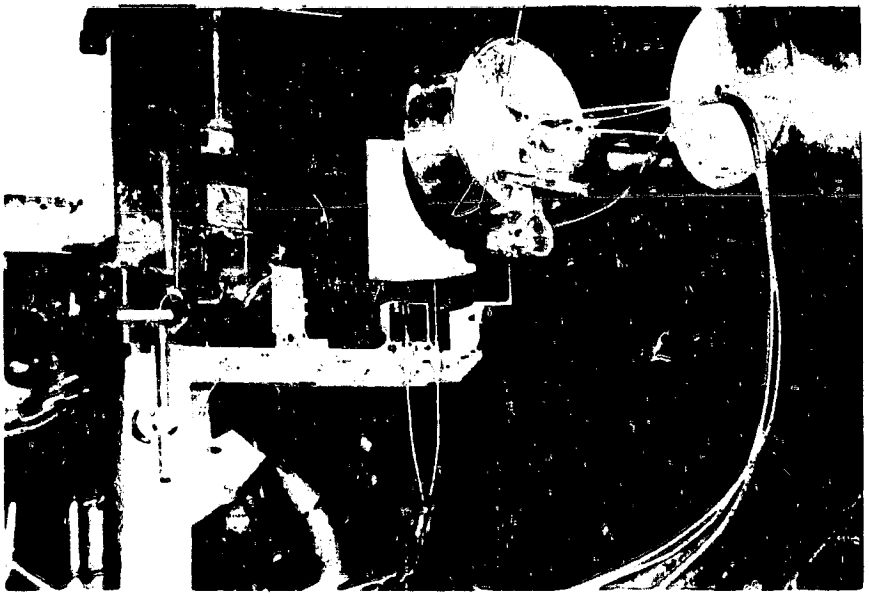

Figure 2. - Teflon test setup.

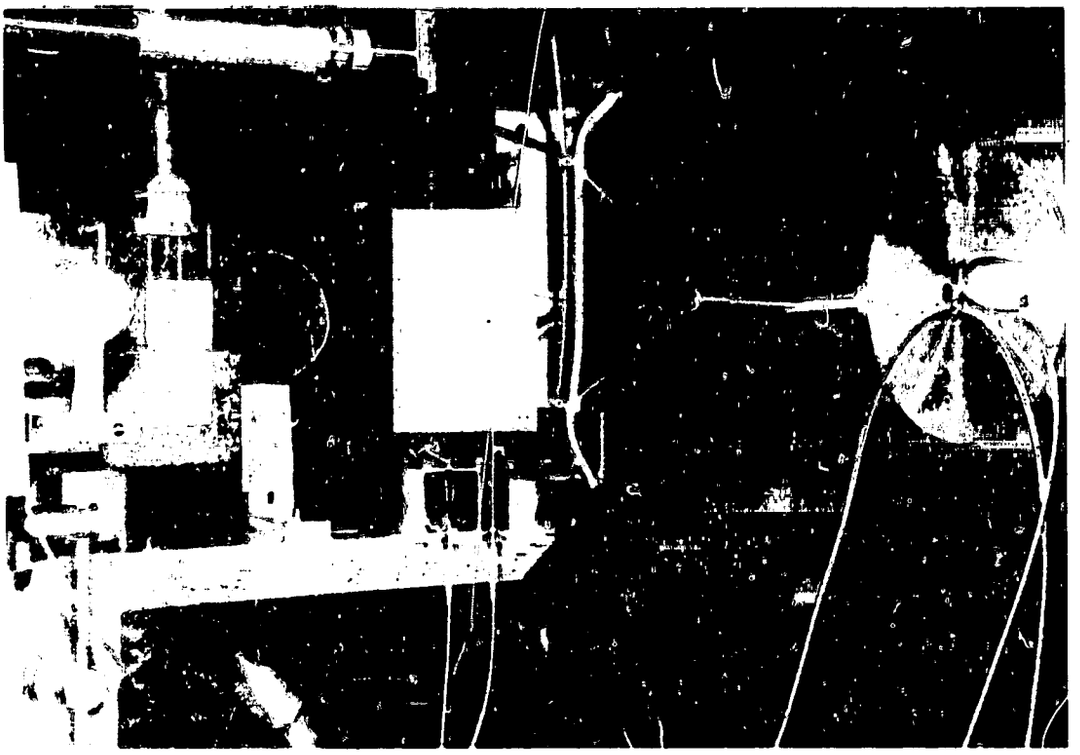

Figure 3. - Longeron and braic test setup.

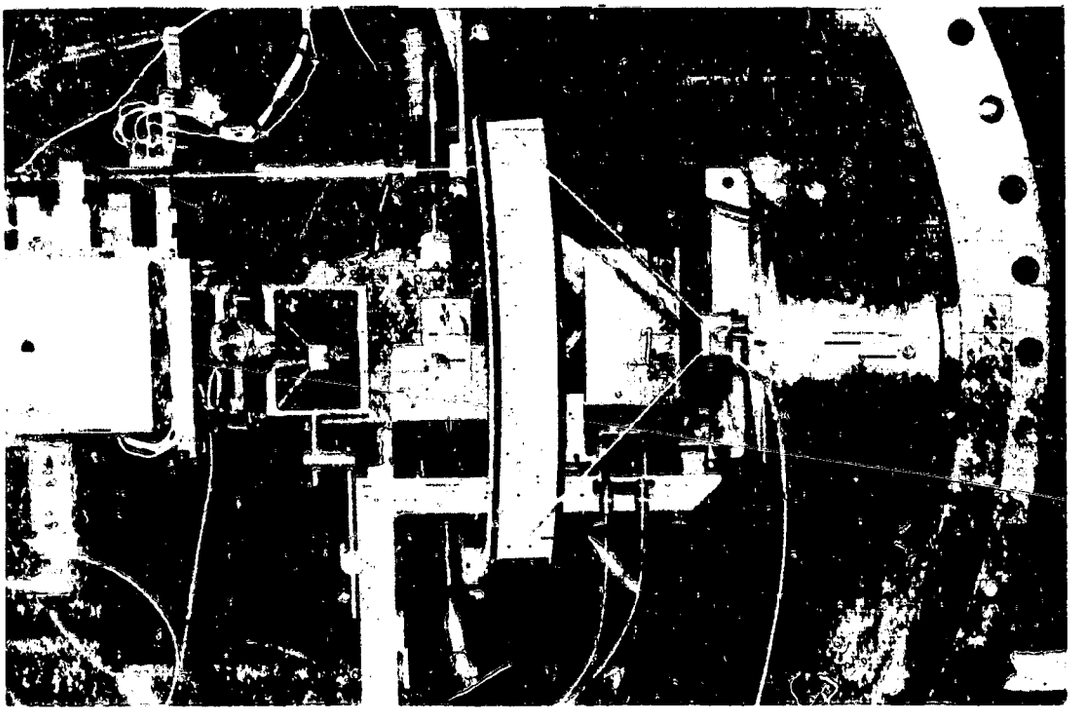

Figure 4. - Antenna section test setup.

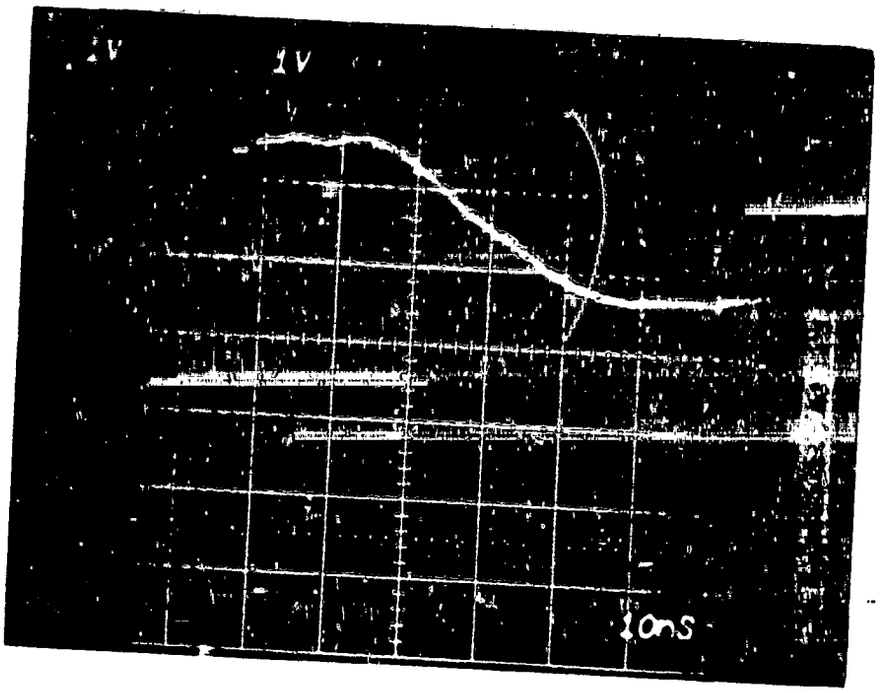

Figure 5. - Teflon loop antenna discharge pulse. Energy, 40 keV; 1 V/division; 100 A/division.

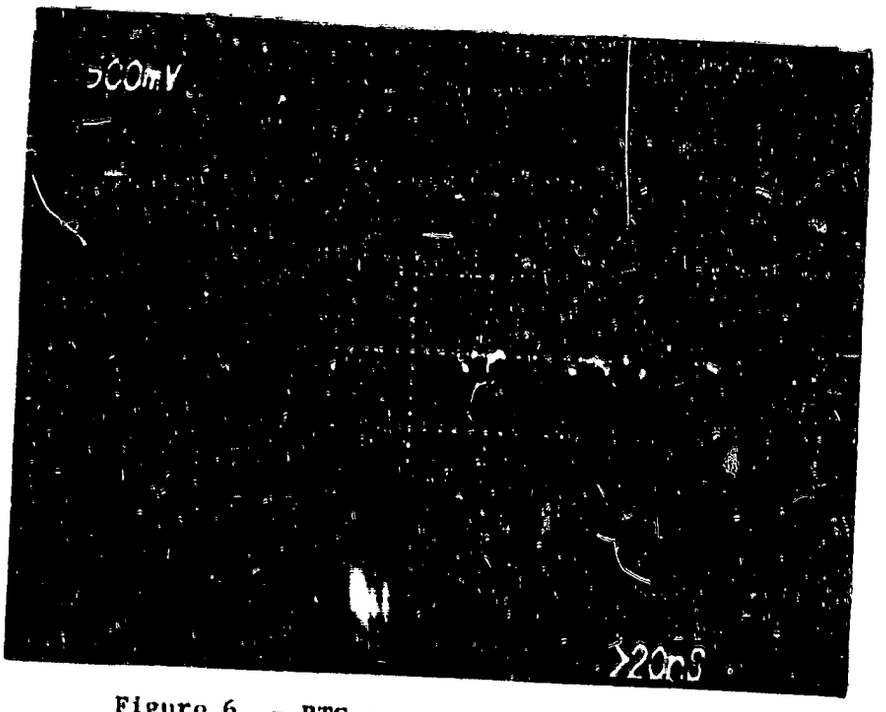

Figure 6. - RTG case strip pulse. Energy, 20 keV; 500 mV/division; 0.2 A/division.

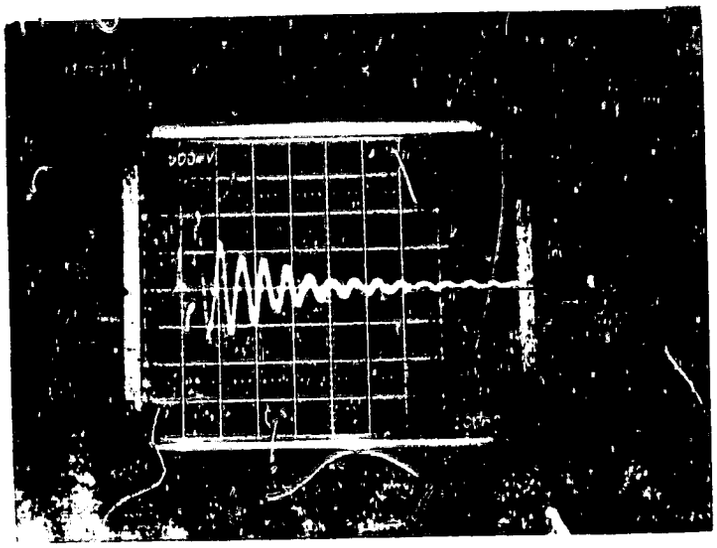

Figure 7. - RTG end dome pulse. Energy, 100 keV (room temperature); 500 mV/division; 1 A/division.

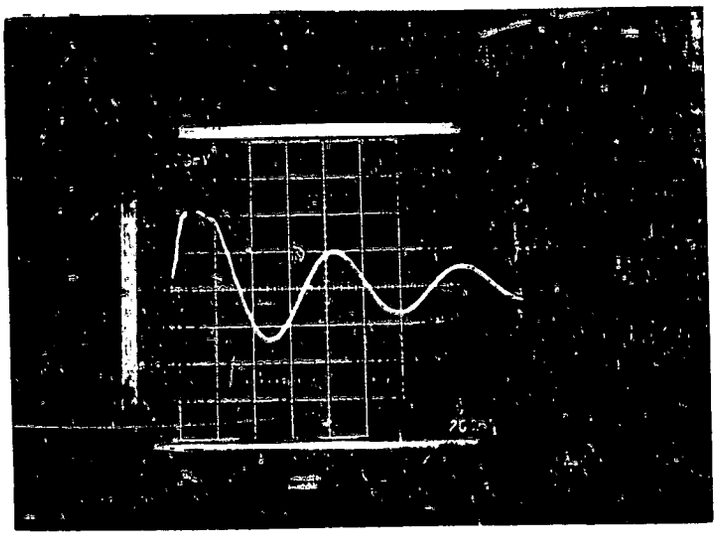

Figure 8. - RTG end dome pulse with 47-μH external inductor. Energy, 100 keV (room temperature), L = 47 μH); 100 mV/division; 0.04 A/division.

D39

N79-24040

CHARACTERIZATION OF ELECTRICAL DISCHARGES ON TEFLON DIELECTRICS USED AS SPACECRAFT THERMAL CONTROL SURFACES*

E. J. Yadlowsky, R. C. Hazelton and R. J. Churchill
Colorado State University†

SUMMARY

The dual effects of system degradation and reduced life of synchronous-orbit satellites as a result of differential spacecraft charging underscore the need for a clearer understanding of the prevailing electrical discharge phenomena.

In a laboratory simulation, measurements are made of electrical discharge current, surface voltage, emitted particle fluxes, and photo-emission associated with discharge events on electron beam irradiated silver-backed Teflon samples. Sample surface damage has been examined with optical and electron beam microscopes. The results are suggestive of a model in which the entire sample surface is discharged by lateral sub-surface currents flowing from a charge deposition layer through a localized discharge channel to the back surface of the sample. The associated return current pulse appears to have a duration which may be a signature by which different discharge processes may be characterized.

INTRODUCTION

In situ measurements on synchronous-orbit satellites during magnetic substorm activity have indicated that the associated electrical discharges result from differential charging of satellite surfaces by fluxes of high energy electrons (≳ 20 KeV). The task of ameliorating the effect of spacecraft charging on satellite performance requires a clear understanding of the charging and discharging phenomena. In particular, the system parameters which determine the electrical breakdown threshold, the particles emitted and electrical currents associated with the breakdown must be understood. This information would facilitate the development of techniques to alleviate electrical stresses on satellite components and of models to predict locations on the satellite of minimum electromagnetic interference where sensitive instrumentation could be located.

---

*Sponsored by NASA GRANT NSG-3145
†The authors are now at Kollmorgen Corporation, 501 First Street, Radford, Virginia

The research program described here deals with the characteristics of breakdown events on silver-backed Teflon samples irradiated by a monoenergetic beam of electrons under conditions where the sample edges have been shielded from direct irradiation by the electron beam. The dependence of the minimum breakdown voltage on sample thickness and irradiation history was determined. The additional evaluation included the dependence on sample area and breakdown voltage of the transient currents associated with the discharges, the energy and angular distribution of the particles emitted, and the temporal characteristics of the emitted light. Surface damage resulting from discharge events was studied using optical and scanning electron beam microscopes.

The results indicate that puncture breakdowns through the sample are prevalent, that the sample is discharged by lateral surface currents which flow beneath the sample surface, and that plasma effects are important in the discharge process. Further, the discharges are observed to fit two distinct groups with the time duration of the return current pulse being a convenient distinguishing characteristic.

In the remainder of the paper, the experimental system is discussed briefly. This is followed by a presentation of the experimental technique and the measurements obtained. A discussion of results and a conclusion section complete the paper.

EXPERIMENTAL SYSTEM

The spacecraft charging phenomenon is simulated in a vacuum chamber by irradiating a dielectric target with a high-energy electron beam. It is convenient to discuss the total system relative to the schematic diagram shown in figure 1.

The simulation chamber consists of a 30 cm diameter cylindrical glass tube about 1 meter in length. Four cylindrical ports 15 cm in diameter located at the central section of the tube provide outlets for vacuum ports, introduction of electrical and photographic measurement systems and the installation of target assemblies. The electron beam gun is located at one end of the 30 cm diameter cylinder and generates an axial electron beam to the centrally located target area. Base pressures of 10^{-7} Torr are possible using a 10 cm diameter oil diffusion pump system.

To simulate the spacecraft charging, the dielectric targets are bombarded with a mono-energetic divergent electron beam having an acceleration potential from 0 to 34 kV and a beam current density at the target location of 0-5 nA/cm^2. Uniformity of the electron beam over the target area is about 25% for a 10 cm diameter target located 50 cm from the electron beam gun.

The silver-backed dielectrics used in the irradiation process are mounted on various target assemblies at the center of the four-port region of the simulation chamber so as to have the dielectric front surface of the target at an angle of 50^o to the axis of the electron beam. The sample is

supported by an annular aluminum ring providing electrical contact to the silver-backed Teflon sample through conducting paint. The entire sample holder is placed within, but electrically insulated from, a grounded enclosure containing an aperture through which the sample is irradiated. By means of this arrangement, the sample edges are not irradiated directly by the electron beam thus facilitating breakdown studies not dominated by edge effects. The aperture opening can be varied from 2.5 cm to 8 cm dia. by controlling the opening of an adjustable iris mounted on the sample enclosure. The control linkage is brought through the vacuum wall to facilitate the study of discharge properties which depend on the surface area irradiated. The front surface of the sample is visible for inspection and photographic measurements.

The electron beam voltage required to initiate a breakdown is determined by irradiating the sample to nearly steady state conditions with successively larger accelerating beam voltages until a discharge occurs.

The transient current that flows to the silver backing on the sample during a discharge event is measured by a Tektronix CT-1 current probe clipped on the lead connecting the silver backing to ground potential.

A system of mirrors and viewing ports permits time-integrated photographs of the self-luminous electrical discharges to be taken. The resultant photographs of the discharge path along the sample surface and the central site of the discharge are correlated with scanning electron microscope studies of material damage.

Charged particle measurements are made using a biased Faraday cup and a retarding potential analyzer (RPA), both of which are illustrated in figure 2. The Faraday cup consists of a shielded collector which can be biased to collect either positive or negative particles through a grid aperture of 2.5 cm. The output current of the collector is shunted to ground through a 50 ohm load and the resulting voltage measured with a Tektronix 556 oscilloscope.

The retarding potential analyzer used for the measurement of emitted particles consists of a particle collector plate and two independently biasable grids enclosed in a grounded shield having an input aperture of 1.2 cm. For the measurement of positive particles the collector is biased at -9 V to capture the positive particles which pass through the grids. Grid G2, the suppressor grid, is biased at -800 V to prevent secondary electron emission from the collector surface which could be erroneously interpreted as positive particles. The first grid is then biased positively to define a threshold energy for the incoming particles. By varying the bias on the first grid the energy spectrum of the incoming ions can be measured.

The output of the collector is measured in a manner identical to that used with the Faraday cup. A temporally resolved particle flux is thereby derived and particle transit times and total particle emissions are determined. Similar measurements are made for negative particles with the collector biased to + 9 V, the second grid grounded, and the first grid biased negatively. In all cases the amplitudes of the incident particle fluxes are derived

by multiplying the measured signal by the weighting factor of 1.8 to account for grid attenuation. The distribution of particle energies is obtained from the measured dependence of collector current on retarding grid voltage by graphical differentiation.

For the angular measurements presented herein, the probes were positioned as shown in figure 3. The sample is tilted $\sim 40^{o}$ to the beam axis to allow observation of normally emitted particles free from detector interference with the beam. The Faraday cup is set at a fixed angle of 40^{o} below the horizontal plane, 9.5 cm from the sample surface. The RPA is located about 15 cm from the sample center and is free to pivot some 70^{o} about the sample center line. The entrance aperture of the RPA subtends an angle of 3^{o} with respect to a point on the target surface.

A high energy retarding potential analyzer (HERPA) was designed to provide a retarding potential of up to 11 kV. The HERPA is positioned 9.2 cm from the sample surface and has an aperture of 5.6 cm. Measurements are made in a fashion identical to those of the RPA.

The temporal characteristics of the light emitted during an electrical breakdown were recorded using an optical system consisting of an f/2 lens collection system, fiber optics to transmit the light signal through the wall of the vacuum chamber and a photomultiplier to detect the signal.

EXPERIMENTAL RESULTS

In order to provide a coherent and consistent picture of the electrical discharge process on the dielectric samples, measurements have been made of minimum breakdown voltage, material damage, return currents, particle emission and photo-emission from the sample surface.

Breakdown Voltage

The breakdown voltage was measured for previously unirradiated samples of thickness 25, 50, 75 and 125 μ (1,2,3 and 5 mil) silver-backed Teflon. Since a method of direct measurement of surface potential was unavailable, the surface potentials at breakdown were inferred from the measured electron beam voltage. Work by Stevens (private communication) indicates that the measured surface potential is 1.8 kV less than the beam voltage. The thresholds are plotted against sample thickness in figure 4 and demonstrate a reasonably linear correlation between thickness and breakdown voltage. The history of the breakdown occurring on a single 75 μ sample (fig. 5) demonstrates a wide variation in the breakdown voltage. For the particular example shown the initial breakdown voltage is 26 kV decreasing to 14 kV after 20 breakdowns. It is noteworthy that the breakdown voltage does not stabilize at any particular value.

Material Damage

Material damage on the irradiated dielectric surface following an electrical discharge has been studied using an optical microscope and a scanning electron beam microscope (SEM). The optical microscope reveals information about sub-surface damage as well as surface damage whereas the SEM is used for high resolution surface studies. The photographs in figure 6 reveal a hole through the dielectric material to the grounded silver backing resulting from the discharge current flow. In addition, this microscopic investigation reveals the existence of filamentary surface tracks which terminate at the holes as in figures 6a and 6b. These material damage tracks are similar in form and appearance to luminous Lichtenberg streamers observed on the surface during the discharge, although no direct comparison has been made. The tracks in the Teflon appear to be the results of currents which flow through the Teflon parallel to the surface during the discharge of the sample. Ionization and recombination in the current channels are accompanied by light emission which gives rise to the luminous Lichtenberg patterns. The process of discharging the sample by currents flowing underneath the sample surface is consistent with puncture sites where filamentary material damage has occurred as in figures 6a and 6b. In figure 6c, a current filament is seen to surface a number of times before reaching the main discharge channel.

The microphotographs of the discharge sites dramatically demonstrate the material damage resulting from the discharges on the sample. It is evident that the energy in the current channel is sufficient to rupture the channel as in figure 6b and to eject molten Teflon from the puncture site. In addition, there is appreciable silver loss from the grounded silver backing as seen in figure 6d as well as extensive melting and ejection of material from the discharge sites.

Return Current

Return currents to the sample were measured during a discharge with a Tektronix CT-1 current probe and a Tektronix oscilloscope. Since the probe was installed outside of the vacuum system, a shielded cable leading from the sample to the probe was terminated in its characteristic impedance (50 ohms) so as to minimize reflections.

From numerous observations of the return current associated with a breakdown, two distinct categories of pulses have been identified. The first is characterized by a long duration pulse of 200 to 400 ns, while the second is represented by a short pulse of 20 ns duration. These two time scales appear to relate to different discharge processes and are discussed in the next section.

In addition, the total charge in the return current pulses was determined by integrating the recorded current traces. Figure 7 illustrates the relationship between this charge and the irradiated area of the sample

surface. Although there are large shot-to-shot variations in total charge a generally linear relationship exists implying that the entire sample surface is discharged during a given event.

Particle Emission

Using the particle collecting probes (Faraday cup, RPA, HERPA), the charge, energy, and angular distribution of the particles emitted during a discharge were determined. Figure 8 shows two traces from the Faraday cup with the bias first set to collect negative particles (8a) and then to collect positive particles (8b). The time history of negative particles includes an early electron spike followed by a longer electron pulse. The early pulse is present in all breakdowns while the later pulse is intermittent.

The maximum retarding potential (3 kV) of the RPA was not sufficient to reduce significantly the amplitude of the early spike. Therefore, a high energy retarding potential analyzer (HERPA) was designed and tested to 11 kV. Using this probe the energy of the electrons in the early spike was found to be in the range of 5-7 keV.

The later pulse of electrons exhibited energies less than the threshold sensitivity of the RPA ($\simeq$1eV). Coincident with the late electron pulse is a pulse of positive particles as shown in figure 8b. Using the RPA, the particle flux was measured as a function of the retarding potential as shown in figure 9. From figure 9 the energy of the positive particles is estimated to be 70 eV. The total number of electrons and positive particles is of the same magnitude. The coincidence of arrival times, the equality of particle number and the relative energies of the positive and negative particles all imply that the late pulse leaving the sample constitutes a plasma.

Figure 10 shows the total number of early electrons as a function of the irradiated area of the sample. As with the return current, the number of emitted particles is linearly related to the area of the sample.

Light Emission

Light emission during electrical discharge was measured in conjunction with the return current pulse. The experimental data clearly shows that the emitted light signals follow closely upon the return current. It may also be observed that the emitted light persists for 100 ns beyond the point at which the return current pulse has decreased to zero. It should also be noted that the amplitude of the light emission during the short return current pulse is four times as large as that occurring during the long duration return current pulse.

DISCUSSION OF RESULTS

A consideration of the measurements presented provides a physical picture of the general process by which the sample surface is discharged. The interrelationship of these measurements leading to a cataloging of different discharge processes is presented in this section.

The dependence of the minimum breakdown voltage on the shielding of the sample edges, on sample thickness, and on the previous history of discharges on the sample provides insight into the material characteristics which govern the breakdown voltage.

The dramatic increase in the minimum breakdown voltage from 15 kV to 32 kV for a 125 μ (5 mil) sample when the sample edges are shielded from irradiation indicates that bulk properties of the sample control the breakdown threshold once surface effects associated with sample edges are eliminated. The slope of the straight line in figure 4 yields a breakdown strength for the bulk material of 2.6×10^6 V/cm (6.5 kV/mil) which is in good agreement with the manufacturers' value of 1.8×10^6 V/cm (ref. 1) for a 75 μ sample. Preexisting defects are expected to depress the breakdown voltage from the ideal value. This can be seen in figure 5 where the value for the first 20 discharges is decreasing on the average. The discharges can also alter the material properties to increase the breakdown voltage as seen by the non-monotonic variation.

The sub-surface crazing together with the surface cracks are similar in form to the luminous Lichtenberg patterns and are in close agreement with the observation of others (Crutcher, private communication). The fissures are evidence for current channels formed by vaporization and ionization of the dielectric material. They imply that the surface is discharged by lateral currents flowing beneath the surface and indicate the extent of the region discharged.

All of the return current pulses represent a unidirectional flow of electrons from ground to the silver backing on the sample, in agreement with the observation of Berkopec *et al.* (ref. 2) The majority of the return current pulses could be classified as short (≈ 20 ns half-width) or long (200-400 ns) with a few scattered values of 90-120 ns. The trend in figure 5 is for the short pulses to be associated with peak values in the breakdown voltage and long pulses to be associated with decreasing or minimum values in threshold voltage. The total charge in the pulse appears to depend on the irradiated area for the long pulse but not the short pulse. Although there is scatter in the data, the relatively straight line through the maximum values of charge flow for long pulses in figure 7 indicates that the entire sample surface irradiated is being discharged under the conditions studied. Stevens (private communication) has observed both partial and total discharges of the sample which could account for some of the scatter in the data. This classification of return current pulses as to short or long pulses provides a convenient method for distinguishing between different discharge phenomena.

The emission of particles from the surface was studied to determine the origin of the return current pulse. The initial burst of high energy electrons accounts for the polarity of the return current pulse. The energy of the particles is in the range of 5-7 keV for the duration of the pulse. Since the time of flight for these electrons (20 ns) is much less than the duration of emission, the pulse length of the high energy electron emission appears to be representative of the sample discharge time.

Both the short and the long duration emissions of high energy electrons occur simultaneously with the corresponding return current pulse. The two-fold difference in duration for the particle emission is a factor of 10 less than the difference in the return current case. The results tend to support the observations of Nanevicz and Adamo (ref. 3) and Gross *et al.* (ref. 4) that electrons are emitted during a discharge.

The later pulse consisting of positive ions and electrons was observed only when the return current pulse was short. The magnitude and duration of the positive and negative particle signals indicate that the particles are emitted as a near neutral plasma. An insight into the nature of the pulse is obtained from a consideration of the particle energies. The results shown in figure 9 indicate that the ions are emitted with a minimum energy of 30 eV. Another estimate of the particle energies can be obtained by determining the time of arrival of the particles at the collector from the temporal evolution of the collector signal. From the transit time and known sample-to-detector distance the velocity, and hence, kinetic energy can be determined. The results again show that all the particle energies exceed a minimum value. By equating the minimum energies, an estimate of the positive ion mass can be found if the ion is assumed to be singly ionized. The value of 13.3 amu so obtained is sufficiently close to the atomic weight of carbon 12 to encourage a tentative identification of the later positive ion peaks as due to singly ionized carbon, although the data is not sufficiently definitive to rule out fluorine.

An estimate of the currents flowing on the sample surface can be obtained by dividing the total charge of the 75 μ thick sample charged to 24 kV by the time given by the duration of the high energy electron burst. This value (300 A) can account for the vaporization and ionization required to produce a plasma. The presence of the plasma pulse in turn accounts for the light emission during the discharge as well as the sub-surface cracks and fissures on the sample.

CONCLUSION

The somewhat random variation in the measured parameters in this study indicates the complex and changing nature of the electrical discharges. Therefore, the need to develop a realistic model becomes readily evident.

The experiments indicate that puncture discharges occur when the Teflon sample edges are shielded from direct irradiation by the electron beam. Under

these conditions the surface voltage of an irradiated sample increases until the electric field strength within the sample, possibly at a material defect, exceeds the dielectric strength of the material, thereby initiating a breakdown through the sample with the grounded silver backing, serving as one electrode. Apparently the entire sample surface can be discharged by lateral currents flowing beneath the surface. Material damage in the form of fissures and cracks results from these currents. Correlation of light emission and return current measurements indicates plasma formation takes place during the initial stages of the breakdown process. The plasma formed provides the necessary conducting paths for discharging the sample. The burst of high energy electrons accounts for the polarity of the return current and provides a measure of the sample discharge time.

Another significant feature is the duration of the return current pulse which is an easily measured parameter to distinguish between two different discharge processes. When a long duration return current pulse is observed, the following discharge characteristics are also present: a) particle emission consists of a relatively long burst of high energy electrons, b) the total charge in the return current pulse is proportional to the irradiated area of the sample, and c) the light emission indicates a low-amplitude, long-duration pulse. For a short duration return current pulse the following discharge characteristics are observed: a) particle emission consists of a relatively short burst of high energy electrons followed by a later near-neutral pulse consisting of positive ions and electrons, b) the total charge in the return current pulse is independent of irradiated sample area, and c) the light emission is a large amplitude short pulse.

If the experimental results are sorted according to the time duration of the return current pulse, a meaningful identification of the discharge characteristics emerges. Correlation of experimental parameters thereby generates signatures useful in the delineation of the various discharge processes.

REFERENCES

1. DuPont Technical Information Bulletin T-4D

2. Berkopec, F. D.; Stevens, N. J.; and Sturman, J. C.: The LeRC Substorm Simulation Facility. USAF/NASA Spacecraft Charging Technology Conference, Colorado Springs, Oct. 27-29, 1976.

3. Nanevicz, N. E. and Adamo, R. C.: Malter Discharges as a Possible Mechanism Responsible for Noise Pulses Observed on Synchronous-Orbit Satellites. Progress in Astronautics and Aeronautics, vol. 47, A. Rosen, ed., Cambridge MIT Press, 1976, pp. 247-261.

4. Gross, B.; Sessler, G. M.; and West J. E.: Radiation Hardening and Pressure - Actuated Charge Release of Electron-Irradiated Teflon Electrets. App. Phys. Lett., vol. 24, no. 8, 1974, pp. 351-353.

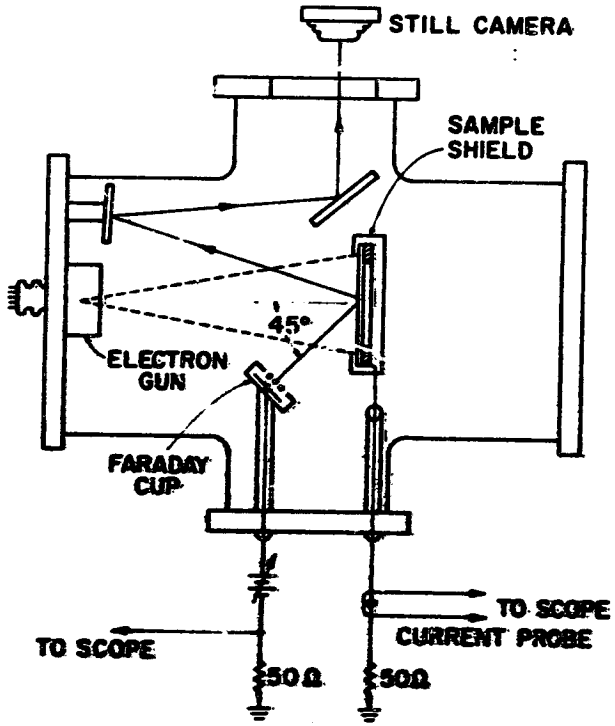

FIGURE 1. SPACECRAFT CHARGING SIMULATOR AND MEASUREMENT SYSTEM.

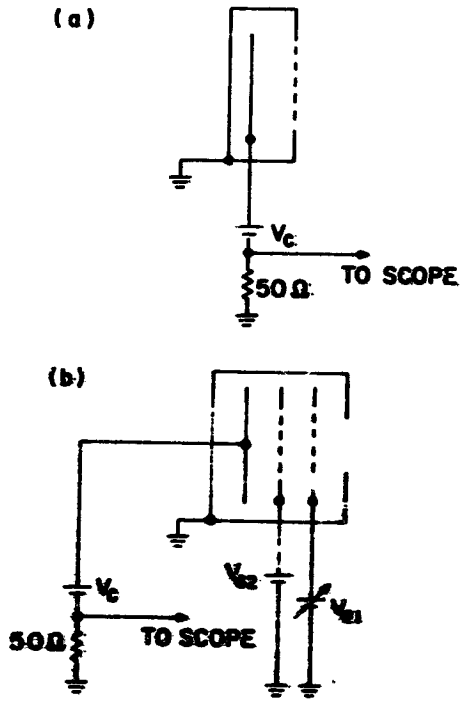

FIGURE 2. CHARGED PARTICLE DETECTORS:
(a) FARADAY CUP
(b) RETARDING POTENTIAL ANALYZER

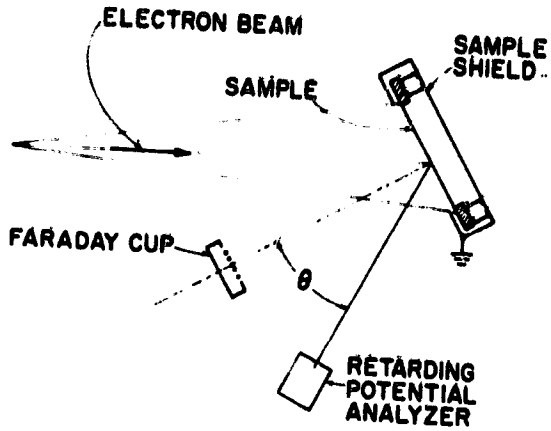

FIGURE 3. ANGULAR DISTRIBUTION MEASUREMENT SYSTEM (RELATIVE ORIENTATION OF DIELECTRIC SAMPLE, ELECTRON BEAM AND CHARGED PARTICLE DETECTORS).

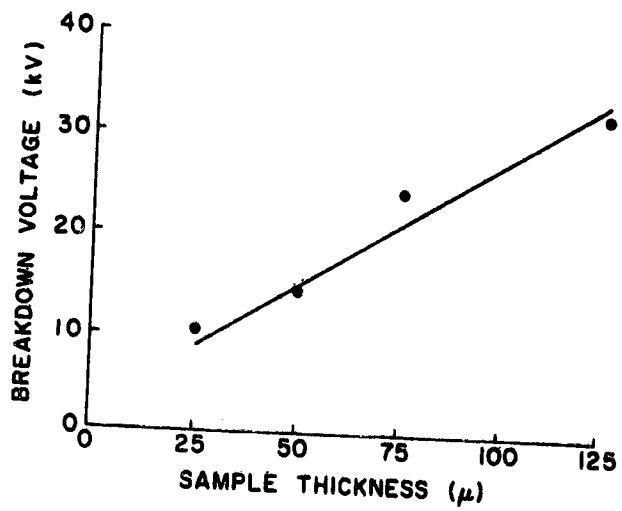

FIGURE 4. ELECTRICAL BREAKDOWN OF SILVER-BACKED TEFLON SAMPLES.

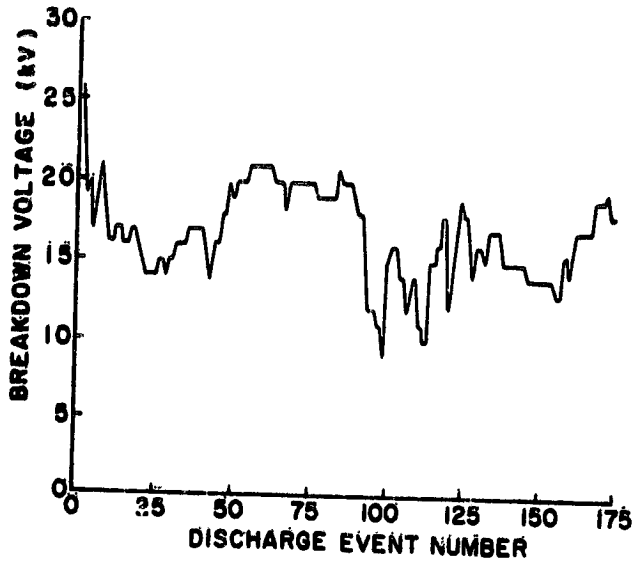

FIGURE 5. HISTORY OF BREAKDOWN VOLTAGE FOR 75μ SILVER-BACKED TEFLON SAMPLE.

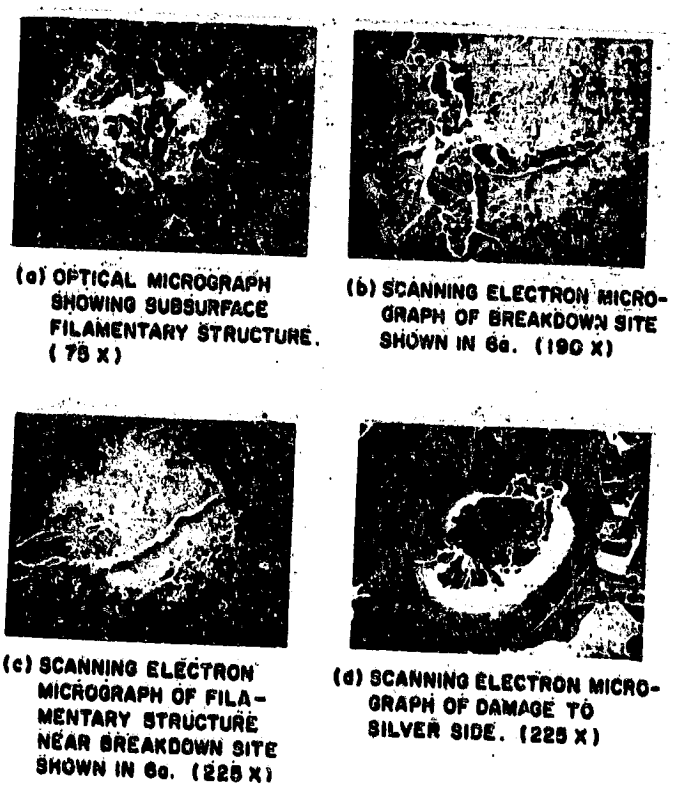

(a) OPTICAL MICROGRAPH SHOWING SUBSURFACE FILAMENTARY STRUCTURE. (75 X)

(b) SCANNING ELECTRON MICROGRAPH OF BREAKDOWN SITE SHOWN IN 6a. (190 X)

(c) SCANNING ELECTRON MICROGRAPH OF FILAMENTARY STRUCTURE NEAR BREAKDOWN SITE SHOWN IN 6a. (225 X)

(d) SCANNING ELECTRON MICROGRAPH OF DAMAGE TO SILVER SIDE. (225 X)

FIGURE 6. 75 μ SILVER-BACKED TEFLON SAMPLE IRRADIATED AT 26 kV WITH A BEAM CURRENT DENSITY OF ~ 1 nA/cm².

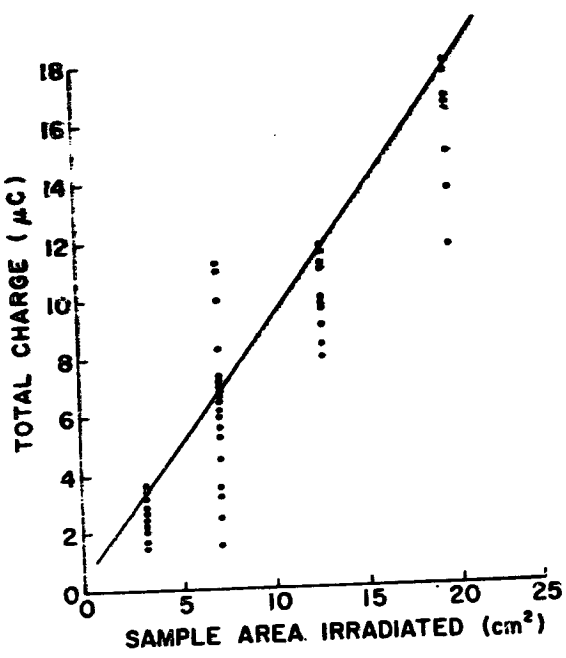

FIGURE 7. CHARGE CONTAINED IN RETURN CURRENT PULSE FOR VARIOUS SAMPLE AREAS IRRADIATED.

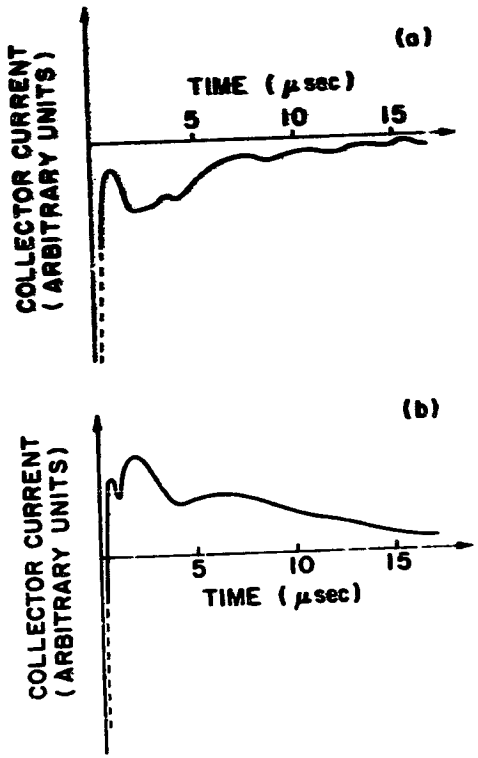

FIGURE 8. OSCILLOSCOPE TRACES OF FARADAY CUP CURRENT:
(a) FARADAY CUP BIASED TO COLLECT NEGATIVE PARTICLES
(b) FARADAY CUP BIASED TO COLLECT POSITIVE PARTICLES.

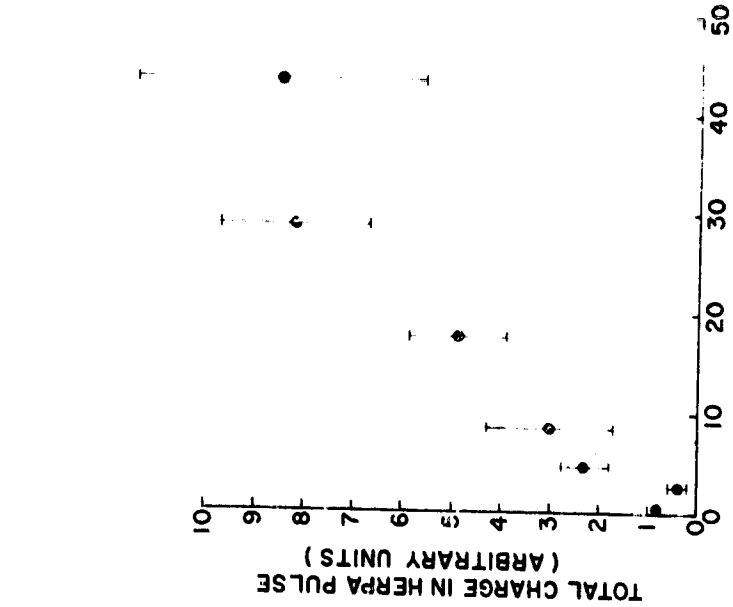

FIGURE 10. CHARGE CONTAINED IN EARLY ELECTRON PULSE FOR VARIOUS SAMPLE AREAS IRRADIATED.

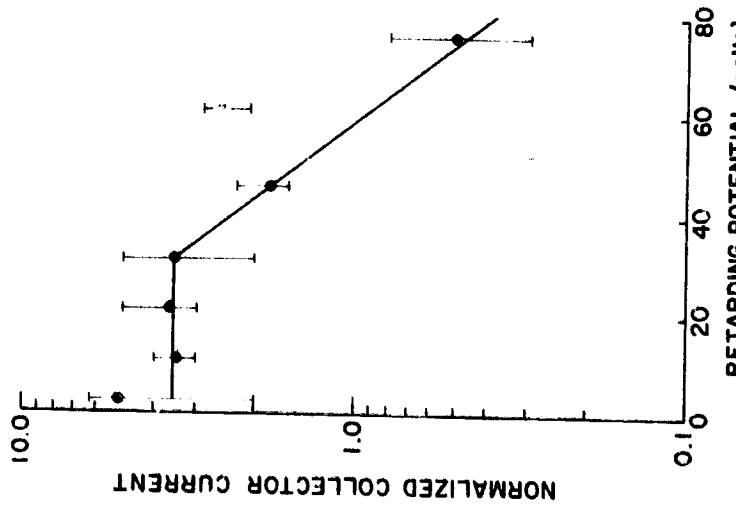

FIGURE 9. ENERGY DISTRIBUTION OF POSITIVE IONS MEASURED WITH THE RETARDING POTENTIAL ANALYZER.

D4°

N79-24041

SCALING LAWS AND EDGE EFFECTS FOR POLYMER SURFACE DISCHARGES*

Keith G. Balmain
University of Toronto

SUMMARY

Specimens of Mylar sheet were exposed to a 20 kV electron beam. The resulting surface discharge arcs were photographed and the discharge current into a metal backing plate measured as a function of time. The area of the Mylar sheet was defined by a round aperture in a close-fitting metal mask, and the current pulse characteristics were plotted against area on log-log paper. The plots appear as straight lines (due to power-law behavior) with slopes of 0.50 for the peak current, 1.00 for the charge released, 1.49 for the energy and 0.55 for the pulse duration. In addition, evidence is presented for the occurrence of banded charge distributions near grounded edges, on both Teflon and Mylar.

INTRODUCTION

Numerous extensive laboratory simulation studies on spacecraft dielectric charging and arc discharging have been reported in references 1, 2 and 3. Many such laboratory experiments involved dielectric areas much smaller than the exposed dielectric areas existing on operational synchronous-orbit satellites, and so the question of area scaling of charge/discharge phenomena arises naturally. Certainly it is easier and faster to carry out small-scale experiments, compared to large-scale experiments in vacuum chambers large enough to hold spacecraft components or even an entire spacecraft.

Experimental results reported in reference 4 showed that, for surface macrodischarges on metal-backed polymer dielectrics, the peak discharge current is proportional to the surface area raised to a power "p" lying between 0.5 and 0.8, for the range of areas lying between 0.2 cm^2 and 20 cm^2. The most consistent results were for Teflon with a value p = 0.575, giving a peak-current power law which extrapolated downward in area into close proximity with microdischarge measurements in the range of areas from 10^{-5} cm^2 to $10^{-3} cm^2$.

The above extrapolation would have produced a better fit if the value of p had been slightly lower. This observation raises the question of area definition, because in the macrodischarge case the charged area was defined by

*Research supported by the Natural Sciences and Engineering Research Council of Canada under Grant No. A-4140. The measurements reported here were carried out primarily by G.R. Dubois.

cutting the specimen to size, while in the microdischarge case the charged area was defined by the cross-sectional area of the incident electron beam as deduced from scanning-electron-microscope examination of deposited charge patterns. For the macrodischarges, cutting the specimen to size could stress or otherwise damage the specimen edge, and furthermore leaving this edge exposed could produce anomalous effects on charge penetration, charge accumulation, discharge initiation and discharge propagation.

A method of area definition which is precise and which does not involve cutting or edge exposure is to cover the specimen with a close-fitting metal mask and to use masks with various apertures in order to establish experimentally the area scaling laws. This paper describes such a masking technique and gives experimental results of discharge characteristics obtained using masked Mylar specimens.

If a metal mask avoids some types of edge effects, it is reasonable to wonder what edge effects remain. One type of masked-dielectric edge effect was noted by M. Cuchanski and first reported in reference 5. It involved exposure to an electron beam of a polymer sheet covered by a vacuum-deposited-aluminum mask with a circular aperture. This was followed first by exposure to air to neutralize surface charge and then by examination in a scanning electron microscope at low voltage to look for embedded charge made visible by its enhancement of secondary emission. Charged annular rings were observed, suggesting the existence of high-field regions near the mask edge. This work was later extended (ref. 6) and some of these latter results are included here.

EXPERIMENTAL ARRANGEMENT

The masked specimen and its backing plate are shown in figure 1 and are mounted on (and isolated from) a removable section of the vacuum chamber wall. A vacuum-sealed bulkhead receptacle carries the discharge pulse signal through the chamber wall to a 10-ohm termination and thence via attenuators to a 400-MHz oscilloscope.

The incident electron beam is deflected magnetically in order to permit photography of the surface arc discharge. The resultant current density at the specimen surface is of the order of 1 $\mu A/cm^2$ at a beam accelerating voltage of 20 kV. Precautions had to be taken to ensure adequate shielding of operating personnel from X-radiation.

A different Mylar specimen cut from the same sheet was used for each masked area to produce the results presented graphically in this paper.

DISCHARGE MEASUREMENTS

A typical photograph of a surface arc on Mylar is shown in figure 2. The arc concentration at several points around the mask edge is evident and is common to all arcs photographed. Also visible in most photographs (although

not strongly evident in this case) is the alignment of many of the interior arcs along a preferred direction dependent on specimen orientation.

Typical discharge current pulses are shown in figure 3. For smaller areas the pulses were more sharply peaked, and for the smallest areas tested the pulses were much shorter with some overshoot and ringing noticeable.

The variation of peak current I_m with specimen area is shown in figure 4, in which each point is the average from approximately ten pulses. The straight line drawn through the points has a slope of 0.50 indicating that the peak current is proportional to the area raised to the power 0.50. It is worth noting that this line extrapolates to I_m = 1000 A at an area of 1 m^2.

The charge Q passing through the measurement system is given by

$$Q = \int I \, dt$$

and this integration was carried out manually from oscilloscope photographs. The resulting graph of charge against area is shown in figure 5, in which each point is the average from approximately five pulses. The straight-line approximation has a slope of 1.00 and the fit to the straight line is good even for small areas.

The energy dissipated in the load resistor R is given by

$$E = R \int I^2 \, dt$$

The resulting graph of energy against area is shown in figure 6, in which each point is the average from approximately five pulses. The straight-line approximation has a slope of 1.49. It should be noted that the highest energies are of the order of a few millijoules, indicating that unsuitable load resistors or attenuators attached to the system could be burned out by the discharge pulses.

The pulse duration was calculated from the relation

$$T = \frac{1}{I_m} \int I \, dt$$

The resulting graph of duration against area is shown in figure 7. The points exhibit more scatter than in the other graphs, with the result that the straight-line approximation having a slope of 0.55 could almost as well have been drawn with slopes anywhere in the range from 0.50 to 0.58. Departure from the straight-line approximation is most noticeable for small areas and thus for short pulses, this departure taking the form of lowered amplitudes and extended pulse durations, accompanied by small-amplitude ringing for the smallest areas. The probable primary cause of this effect is the 400 MHz bandwidth of the oscilloscope, with a secondary cause being the overall dimensions of the specimen, mask, back-plate and distance to the load, all adding up to about a wavelength at 1000 MHz.

The penetration depth for 20 kV electrons in Mylar is estimated to be 8 μm (ref. 6), so presumably most of the embedded charge resides near this depth. If discharge arc propagation and subsequent damage are concentrated near the penetration depth as in the high-energy experiments of Gross (ref. 7),

then one might expect to see surface damage of about 8 μm depth. A Mylar specimen which had been used for many experiments was coated with vacuum-deposited gold and viewed in a scanning electron microscope, a typical result being shown in figure 8. The large depression is about 8 μm deep and presumably resulted from the blowoff of material during the propagation of an arc along the groove at the bottom of the depression. The groove has branches which seem to disappear into holes in the depression wall. The corresponding transmitted-light photograph of figure 9 indicates that the holes continue into the material, forming a network of damage tracks or tunnels of about 2 μm diameter at a depth of about 8 μm.

The propagation of a discharge along a well-defined path must of course take place at an equally well-defined velocity. This velocity can be estimated by noting from figure 7 that an aperture radius of 1 cm corresponds to a pulse duration of 33 ns, the ratio giving a velocity of 3×10^5 m/s. This is similar to the value of roughly 10^5 m/s which can be deduced by means of the same type of calculation from the results in references 5 and 6 for microdischarges.

The banded charge distributions near a metallization edge (as referred to in the Introduction) are shown in figure 10. The basic procedure used was first to irradiate the exposed dielectric in the aperture with a scanned 20 kV electron beam while viewing the secondary-electron image, in the usual scanning electron microscope (SEM) set-up. Then the specimen was exposed briefly to room air to neutralize most of the surface charge. The specimen was then returned to the SEM, scanned at 1 kV and its secondary-electron image photographed. Because embedded charge must increase secondary emission due to electrostatic repulsion, the area of embedded negative charge shows up as a lighter region in the photographs. In figure 10, the top row of photographs shows the annular-ring form of the charged bands on both Teflon and Mylar. In the middle row a discharge event is indicated by the white streak, which appears to have caused an indentation in the charged band. Perhaps the discharge was initiated in the charged band near the metallization edge. In the bottom row, notch-shaped and rectangular apertures were tried with similar results.

INTERPRETATION

The area-scaling graphs of I_m, Q and T are all approximately consistent with the notion of a discharge arc which propagates at a well-defined velocity. If the discharge originated from a point and expanded outward uniformly, then the current would be proportional to the length of the wavefront, and l_m would be proportional to its maximum length, a quantity related in turn to the linear dimensions of the specimen. A sequence of linear, branching discharge paths should produce the same result.

If the discharge initiates at the aperture edge and propagates inward, the replacement current into the metal base could arise in two ways. One way is for electrons to be ejected at or near the arc wavefront. The other is for the electrons to be propelled down the network of damage tunnels to the point of initiation where they are ejected, there giving rise to the replacement

current. In the latter case the relevant velocity would be the sum of the arc velocity and the electron expulsion velocity along the tunnels.

A vivid analogy is that of a "flash flood" caused by a rainstorm of specified area. If the water runoff velocity were constant then the peak runoff current flow would be proportional to the square root of the storm area.

Clearly the surface discharge is not at all similar to a capacitor discharge. Although the capacitor released charge is proportional to the capacitor plate area (as in fig. 5), its peak discharge current is also proportional to the plate area (in contrast to fig. 4).

CONCLUSIONS

Surface discharge arcs on metal-backed Mylar (and probably on a wide range of polymers) exhibit characteristics which scale with variations in specimen area according to very well defined power laws. The characteristics identified are peak current, released charge, released energy and pulse duration, and the respective powers are 0.50, 1.00, 1.49 and 0.55. The latter figure of 0.55 for pulse duration probably would become 0.50 with improved experimental technique, because it is determined pulse-by-pulse as the ratio of released charge to peak current. For small areas and thus for short pulses, departures from power-law behaviour are believed due to limited oscilloscope bandwidth.

The discharge arcs appear to propagate at about 3×10^5 m/s in hair-like, branching tunnels at the penetration depth, with occasional blowoffs of surface material. Probably these discharge tunnels are not re-used by subsequent discharges, because the appearance of discharge arcs always changes markedly from one arc to the next.

Specimen edges play a special role, with cut and exposed edges significantly affecting the area scaling laws. Charge accumulates with greatest density near an edge, usually in multiple bands parallel to the edge. Indications are that these charged bands offer preferential sites for discharge initiation.

REFERENCES

1. Rosen, A. (Ed.): Spacecraft Charging by Magnetospheric Plasmas. Progress in Astronautics and Aeronautics, vol. 47, 1976. (Pub. by AIAA and MIT Press).

2. Pike, C.P.; Lovell, R.R. (Eds.): Proceedings of the Spacecraft Charging Technology Conference. Report AFGL-TR-77-0051/NASA TMX-73537, 24 Feb. 1977.

3. Proceedings of the 1978 Symposium on the Effect of the Ionosphere on Space and Terrestrial Systems, Washington DC, sponsored by NRL/ONR.

4. Balmain, K.G.; Kremer, P.C.; Cuchanski, M.: Charged-Area Effects on Spacecraft Dielectric Arc Discharges. In reference 3.

5. Balmain, K.G.: Charge/Discharge and Electromagnetic Radiation Studies on Spacecraft Materials and Structures. Final report on DSS Contract No. OSU76-00064 prepared for the Department of Communications, Canada, April 1977.

6. Cuchanski, M.: Simulation Studies of Charging, Discharging and Discharge Pulse Propagation on Spacecraft Materials and Structures. M.A.Sc. Thesis, Department of Elect. Engrg., University of Toronto, 1978.

7. Gross, B.: Irradiation Effects in Plexiglas. J. Polymer Sci., vol. 27, 1958, pp. 135-143.

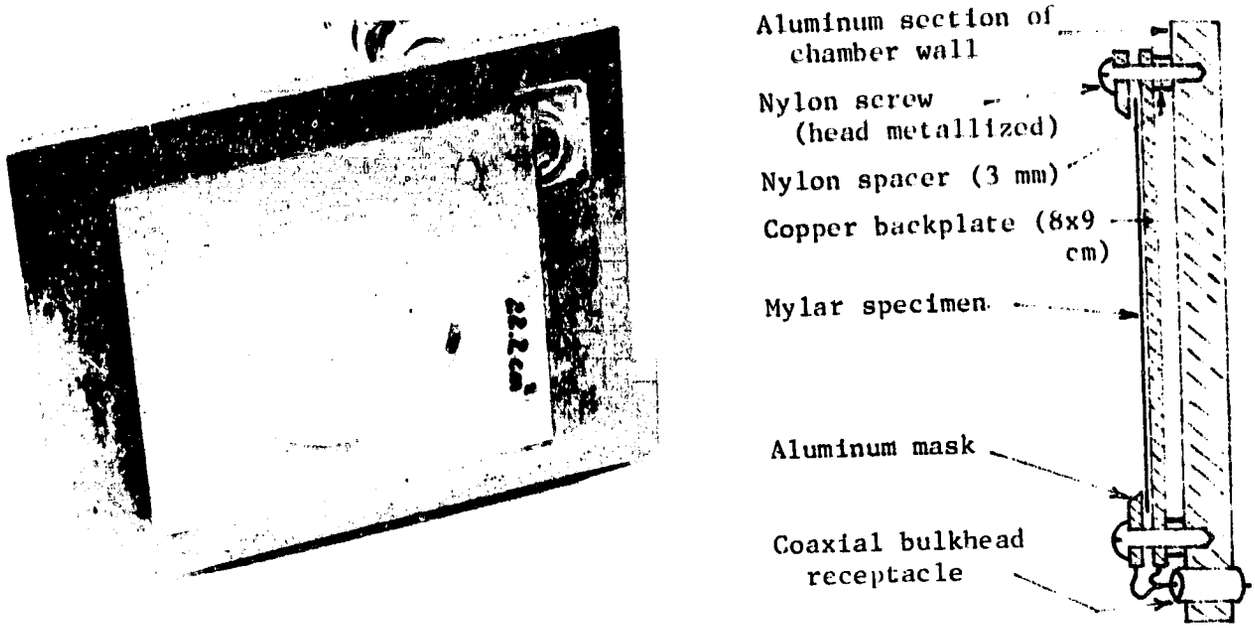

Figure 1. The specimen mounting assembly with circular-aperture aluminum mask. The specimens used in the experiments were Mylar sheets 120 μm thick.

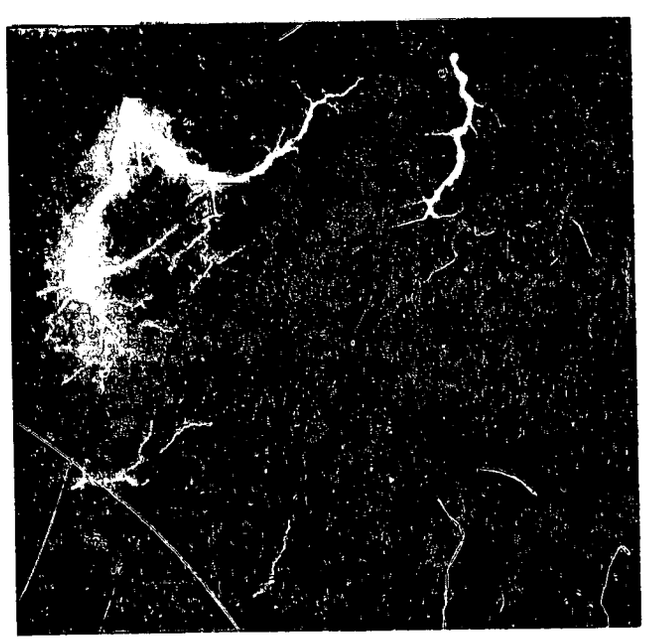

Figure 2. A typical arc discharge on a 47.6 cm^2 Mylar specimen.

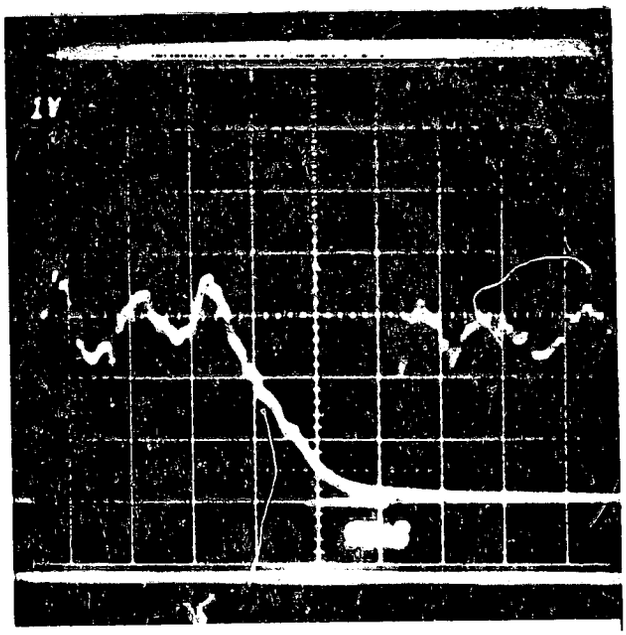

Figure 3. Two typical current pulses from a 22.2 cm^2 Mylar specimen. I_m=30.2A and 26.2A

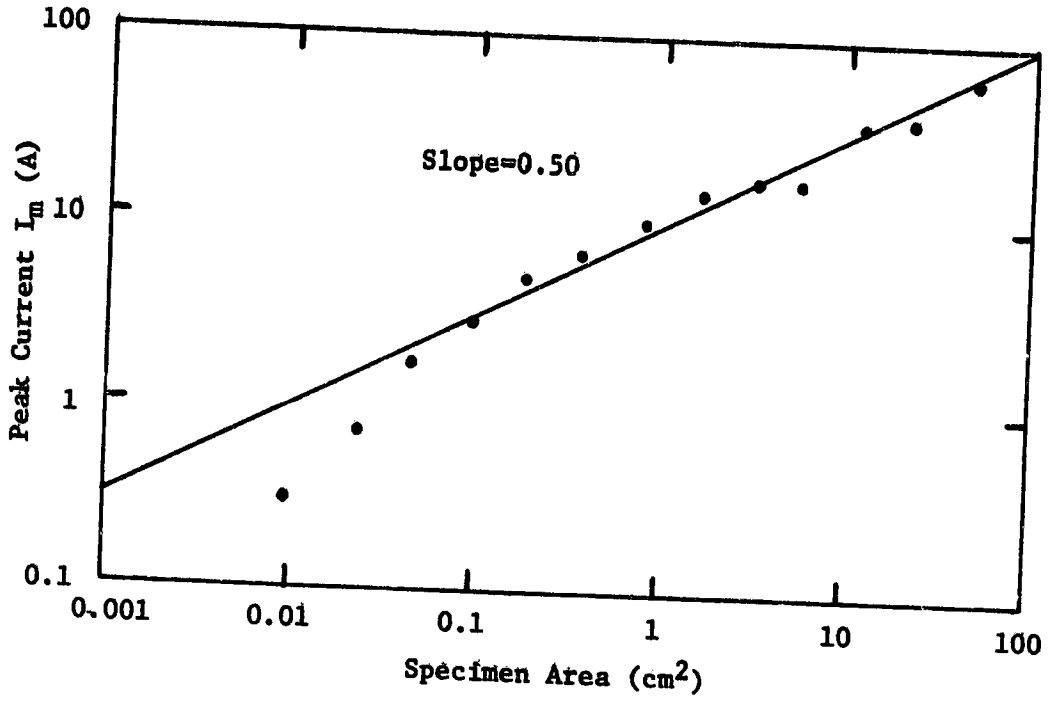

Figure 4. The variation of peak current I_m with Mylar specimen area.

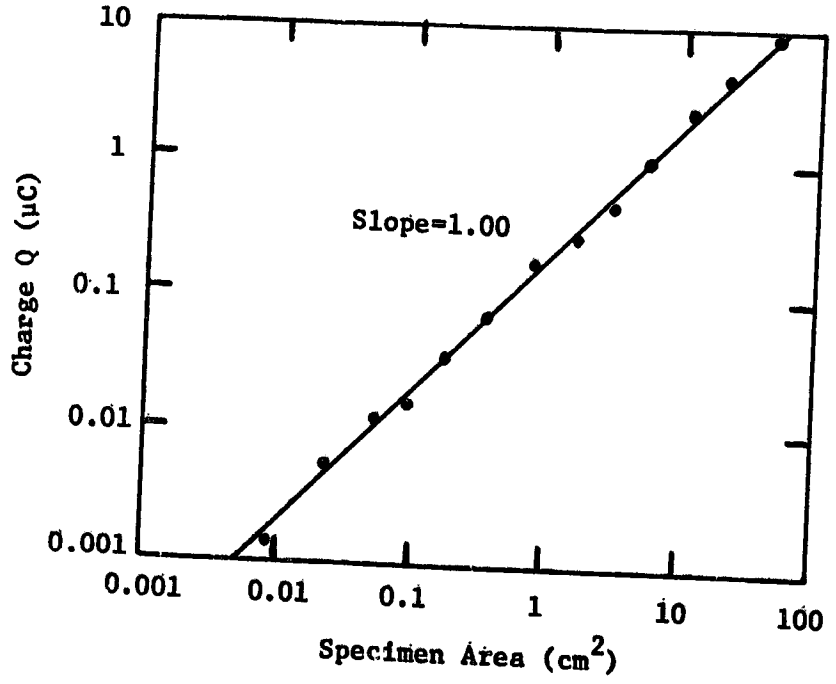

Figure 5. The variation of released charge $Q = \int I \, dt$ with Mylar specimen area.

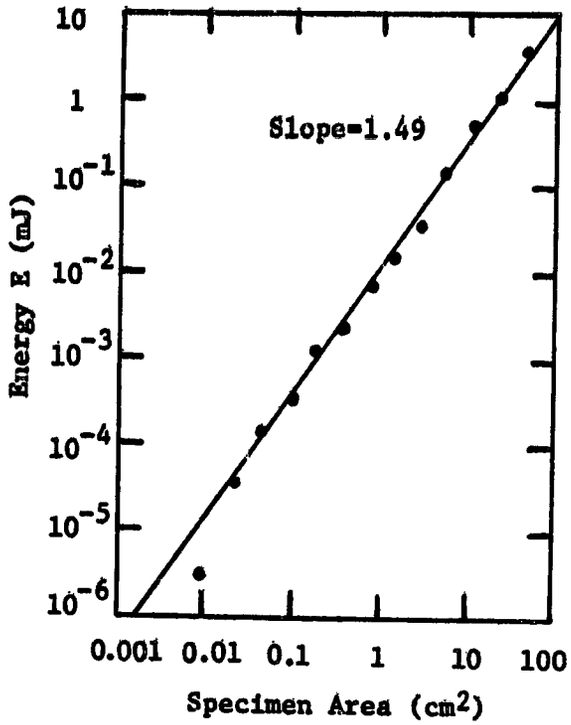

Figure 6. The variation of energy $E = R \int I^2 dt$ with Mylar specimen area. The energy is dissipated in a load resistor R=10 ohms.

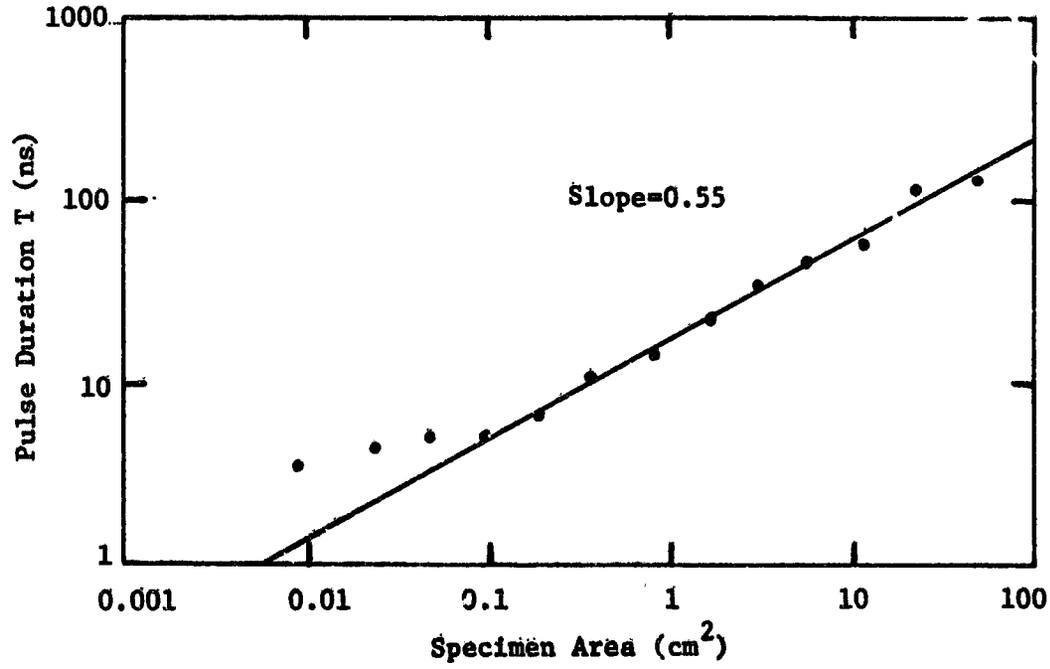

Figure 7. The variation of pulse duration $T = \frac{1}{I_m} \int I\, dt$ with Mylar specimen area.

Figure 8. Secondary electron image in a scanning electron microscope of a gold-coated, damaged Mylar specimen.

Figure 9. Transmitted-light microscope photograph of the specimen shown in figure 8.

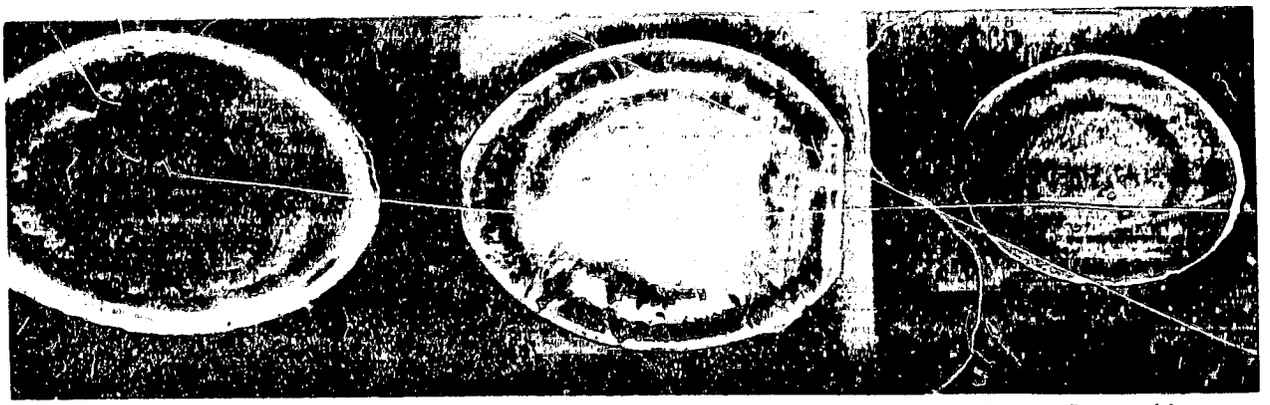

1 kV, 5 mm dia. 1 kV, 10 mm dia. 1 kV, 2.5 mm dia.

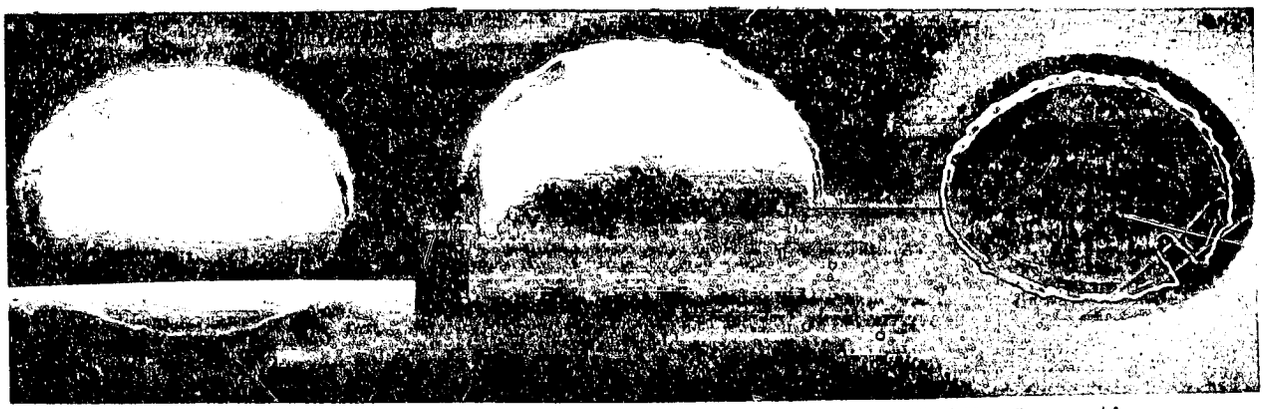

20 kV, 3 mm dia. 20 kV, 3 mm dia. 1 kV, 3 mm dia.

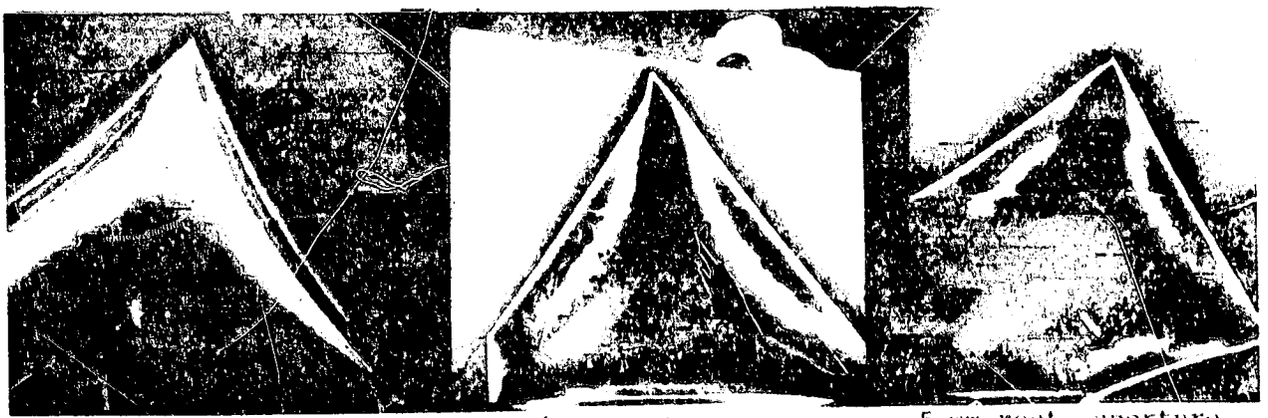

wedge aperture
20 kV

wedge aperture
1 kV

5 mm rect. aperture
1 kV

Figure 10. Charge accumulation on masked Teflon specimens as viewed by secondary-electron imaging in a scanning electron microscope (top right image is Mylar). All specimens have been charged by a 20 kV scanned beam. The apertures are in grounded aluminum metallization. The voltages given are those used for imaging.

D41

N79-24042

THERMAL BLANKET METALLIC FILM GROUNDSTRAP AND SECOND SURFACE MIRROR VULNERABILITY TO ARC DISCHARGES

G. T. Inouye, N. L. Sanders, G. K. Komatsu,
J. R. Valles, and J. M. Sellen, Jr.
TRW Defense and Space Systems Group

SUMMARY

This paper discusses tests on both thermal blanket metallic film groundstraps and second surface mirrors.

The grounding of the metallic vacuum deposited aluminum film on thermal blankets has been a recommended practice on spacecraft design for electromagnetic compatibility (EMC) purposes for a long time. With the recognition of the potential hazards due to spacecraft charging, the requirements on the survivability of these groundstraps have increased many fold because they now must conduct the many amperes of arc discharge current bursts.

The relative durability of a number of different groundstrap configurations to standardize pulses of 100 amperes peak and 1 microsecond decay time constant shows a wide variation, from less than 50 to greater than 10,000 pulses, before burnout. Available data on the geosynchronous orbit environment were used to estimate the number of arc discharges per year. An arc breakdown threshold electric field of 10^6 volts/cm was assumed, and dielectric resistivity and thickness parameters were varied. For a 2 mil thickness and 10^{18} ohm-cm resistivity the estimated number of arc discharges is 1324 per year. A series of electron swarm tunnel tests were undertaken to verify the validity of the 100 ampere, 1 microsecond test pulse parameters. The results of these tests are not definitive but do indicate that the actual pulses could be more benign.

In addition, electron swarm tunnel tests on second surface mirrors were performed. These tests were performed on mirrors with both quartz and glass (microsheet) windows. The results showed that the quartz mirrors arced at all temperatures from 20°C to 100°C at 10 na/cm^2 electron current. The glass windows did not arc at temperatures higher than 50°C.

INTRODUCTION

The grounding of the metallic film on thermal blankets, usually vacuum deposited aluminum (VDA), has been a recommended practice in spacecraft designs for EMC purposes for a long time. With the recognition of the potential hazards to spacecraft survival due to spacecraft charging, the requirements on the durability of these groundstraps have increased many fold. Where the previous re-

requirements were for radio frequency interference (RFI) shielding purposes, the groundstraps must now conduct the many amperes of arc discharge current bursts.

The relative durability of a number of different groundstrap configurations to standardize pulses of 100 amperes peak and 1 microsecond decay time constant shows a wide variation, from less than 50 to greater than 10,000 pulses, before burnout. Available data on the geosynchronous orbit environment were used to estimate the number of arc discharges per year. An arc breakdown threshold electric field of 10^6 volts/cm was assumed, and dielectric resistivity and thickness parameters were varied. For a 2 mil thickness and 10^{18} ohm-cm resistivity the estimated number of arc discharges is 1324 per year. A series of electron swarm tunnel tests were undertaken to verify the validity of the 100 ampere, 1 microsecond test pulse parameters. The results of these tests are not definitive but do indicate that the actual pulses could be more benign.

Second surface mirrors (SSM) constitute a significant portion of the total dielectric surface area of spacecraft. Because the windows of SSM are of good dielectric materials such as fused silica (quartz) or borosilicate glass, charging/discharging of SSM can be a hazard to spacecraft. The tests performed on SSM show that

- The surface of a quartz SSM may charge up as high as -12,000 volts and is likely to break down and constitute an EMI hazard. Raising the temperature to 100°C does not lower the resistivity sufficiently to prevent chargeup to breakdown potentials.

- If the SSM has a glass window arcing is less likely to occur. Leakage through the relatively low bulk resistivity of glass, $\rho < 10^{14}$ ohm-cm, limits the charge up voltage. If arcing does occur at room temperature due to edge effects, the resistivity should become sufficiently low at higher temperatures to prevent even this effect.

ENVIRONMENTAL MODEL FOR DEFINING GROUNDSTRAP REQUIREMENTS

An excellent data base on the geosynchronous orbit environment has been gathered by the University of California at San Diego (UCSD) plasma detector experiments on ATS-5 and ATS-6. Many research oriented papers have been published and a number of provisional specifications of the environment have been generated from this data base (refs. 1,2,3,4). However, further work needs to be done in the area of data reduction and analysis. Table 1 summarizes our characterization of the geosynchronous orbit environment for the purpose of defining requirements on the durability of groundstraps. The data available in the literature have been combined with some ATS-5 data for 1970 which had been analyzed at TRW on prior occasions.

In table 1, the entire year is subdivided into severe, moderate, mild, and quiet substorm days, with a maximum possible daily duration of 12 hours from pre-midnight to post-dawn. A four parameter Maxwellian characterization, electron and ion temperatures and current fluxes, are given for each class of substorm day. The four parameters are reduced to two by assuming charge neutrality,

electron current density = 43 • ion current density, and that

ion temperature = 2 • electron temperature.

Both assumptions are consistent with the data that we have examined. The ATS-5 data for the first three days of January 1970 are shown in fig. 1. Jan. 2nd fits in the severe category, Jan. 3rd in the moderate category, and Jan. 1st in the mild substorm day category.

Two recent papers, one by Garrett (ref. 5) of the Air Force Geophysical Laboratory and the other by Johnson, Quinn and DeForest (ref. 6) of UCSD provide a deeper insight into the statistical variations of the environmental parameters. Incorporation of these data would put the present analysis on a firmer basis. The dependence of these parameters on the eleven-year solar cycle, for example, has not been determined, and further data collection and analyses are required. Even in these papers, the amount of data analyzed covers only a period of a few months, and a much better statistical basis would be achieved if more data, already available, would be reduced and characterized.

COMPUTATION OF THE EXPECTED NUMBER OF ARC DISCHARGES PER YEAR

The expected number of arc discharges per year may be computed using the environmental model characterized in table 1. The charging time to an assumed arc breakdown threshold of 10^6 volts/cm is determined from the following equation for the total current density, J:

$$J = J_e - J_{se} - J_i - J_{se} - J_R - J_c$$

where

J_e = Electron current density

J_{se} = Secondary and backscattered current density

J_i = Ion current density

J_{si} = Secondary and backscattered current density

J_R = Resistive leakage current density

J_c = Capacitive displacement current density.

Each of the current density components of J depend on the surface potential as well as the various material parameters. The capacitive term defines the time dependence of voltage, V:

$$t = \frac{\varepsilon_o \varepsilon_r}{dJ_{oe}} \int_0^V \left[(1-S_e)\, e^{-V/T} - \frac{1+S_i}{43} \left(1 + \frac{V}{2T}\right) - \frac{V}{\rho d J_{oe}} \right]^{-1} dV$$

where

J_{oe} = Electron current density when V = 0

T = Electron temperature (actually T/e)

S_e = Secondary emission factor for electrons

S_i = Secondary emission factor for ions

d = Dielectric thickness

ε_r = Relative dielectric constant

ρ = Dielectric resistivity

Figure 2 shows the rise of voltage with time computed from the above equation for a 3 mil dielectric thickness. A non-linear resistivity of the form

$$\rho = \rho_o\, e^{-V/1.922}, \quad \text{(V in kilovolts)}$$

has been assumed for several values of ρ_o. Table 2 shows the number of arcs per year computed on the basis of the environment summarized in table 1. Experimental data on non-linear resistivity measured by Hoffmaster and Sellen (ref. 7) was re-evaluated and the value of $\rho_o = 2.66 \cdot 10^{18}$ ohm-cm was found to best approximate the observed data when secondary emission effects were taken into account (ref. 8). Further details of the computations for table 2 are also given in ref. 8.

THERMAL BLANKET CONFIGURATIONS AND ARCING MODES

Before the potential problems due to spacecraft charging were recognized, the exterior surface configuration was dictated mainly by thermal control considerations. Typically, except for the arrays of solar cells which are also covered with a thin quartz dielectric coverglass, well over 90% of the exterior surface is covered with thermal blankets and with second surface mirrors which are also used for thermal control purposes. Because these dielectric surfaces comprise a significant portion of the total exterior surface of spacecraft, they are also a major factor in determining the overall charging characteristic of spacecraft in orbit. In the current state-of-the-art of thermal control, generally, the outermost layer of thermal blankets is a sheet of a very good dielectric, typically kapton, mylar, or teflon, with thicknesses in the order of

a few (1 to 5) mils. The inner or backside is coated with a film of VDA. Occasionally, silver or inconel have been used instead of the aluminum.

A typical thermal blanket has an outer (exposed to the space environment) layer of 3 mil kapton and an inner layer of 2 mil kapton. In between, there are ten layers of 1/4 mil kapton which are intentionally "crinkled" to improve its thermal properties. The nominal thickness of the composite blanket is 100 mil. All layers have the VDA film on the inner side, and no attempt is made to change the VDA thickness with varying thicknesses of the dielectric sheets. The outer and inner layer VDA resistance is specified to be less than 1 ohm per square. These are spot checked as received and typically are measured to be about 1 ohm per square. The inner layers, because of the crinkling process, are typically 100 ohm per square even though the VDA thickness is nominally the same for all layers. Calculating the VDA thickness, t, on the basis of the bulk resistivity of aluminum ($\rho = 2.83 \cdot 10^{-6}$ ohm-cm) and the 1 ohm per square resistance gives

$$t = \rho/R = 2.83 \cdot 10^{-6} \text{ cm} = 283 \text{ Angstroms}$$

Because of the vacuum deposition method of putting the aluminum on the dielectric, the actual thickness of the VDA film is more nearly in the 1,000 Angstrom range.

Although it is not possible to "ground" the external dielectric surface, it has been recommended that the interior VDA film be connected electrically to the spacecraft structure. The reasoning behind this recommendation is that the effects of arcing from the metallic film would be far worse than from arcing of the dielectric surface. It was assumed that arcing from a metallic film would, because of its inherently greater conductivity, drain charge from a much larger area than would an arc from a dielectric surface. This reasoning has been shown to be not wholly confirmed by subsequent tests which indicate that a charge "wipeoff" effect exists at least for dielectric test sample areas of a few hundred to a few thousand square centimeters. Thus, even though the metallic film is grounded, arcs from the dielectric surfaces may cause current surges to flow through the groundstrap.

Figure 3 shows examples of some possible arcing configurations. Flashover or punch-through arcs (3a) from the dielectric surface to the metal film do not stress the groundstrap directly. A secondary effect exists in which the rate of change of surface potential and the capacitance to space causes a much smaller replacement current to flow through the groundstrap. Dielectric-to-metal and dielectric-to-dielectric arcs are shown in (3b) and (3c). Metal-to-dielectric and metal-to-metal arcs, which could occur if the metallic film is ungrounded, are shown in (3d) and (3e). Arcs to space, observed in laboratory tests as arcs to the tank walls, are shown in (3f).

The question of the grounding of the VDA on the many inner layers of thermal blankets has been posed frequently. Our view is that if the outermost layer is properly grounded, the problem vanishes. If it is not, then the outermost layer, usually being much thicker, presents the greatest hazard because its capacitance is less, the chargeup rate is fastest, and the breakdown threshold voltage is the highest. Although some groundstrapping techniques

attempt to ground the inner layers, their high ohms-per square resistivity is an indication that large portions of the film are already isolated and thus it is even more important that the outermost layer be well grounded.

ARC DISCHARGE CHARACTERISTICS

A series of electron swarm tunnel tests were undertaken to define the arc discharge breakdown thresholds and current waveforms. Unfortunately, as many problems were raised as were answered, and no definitive characterizations were possible. In regard to the breakdown thresholds, these were found to be very dependent on the sample configuration. By carefully folding over the edges of a 2 mil aluminized kapton sample so that only punch-through type arc breakdowns could occur, we observed no discharges with the maximum beam voltage of 20 kV. Allowing for a 2 kV differential between beam voltage and surface potential due to clamping at the secondary emission cross-over, an 18 kV stress gives a breakdown field greater than 9 kV/mil or $3.5 \cdot 10^6$ V/cm.

Removing the VDA at the corners of the test sample to provide points of enhanced field gradients resulted initially in arcs at the rate of a few times per minute. At a beam current density, J, of 10 na/cm^2 and a capacitance of 50 pf/cm^2 the chargeup rate may be calculated as

$$\frac{V}{t} = \frac{J}{C} = 200 \text{ volts/second} = 12 \text{ kV/minute}$$

For a 6 kV arcing voltage, the breakdown electric field is 3 kV/mil or $1.2 \cdot 10^6$ V/cm. After about 5 or 10 minutes however, the rate was found to decrease and eventually arcing ceased entirely. Examination of the sample out of the vacuum tank showed that the metallic VDA film had been eroded from the edge. Another test sample configuration in which the edges were simply cut with scissors and not folded over behaved similarly.

All of the test samples described thus far were mounted on a plastic frame and the VDA connection was brought out of the backside to the external grounding resistor and diagnostics. Another sample configuration tried was with the thermal blanket folded over the plastic frame, but with the entire unit mounted on an aluminum panel as shown in figure 4. The VDA was insulated from the panel and the connection was brought out through a hole in the panel and the connection to the panel was brought out of the vacuum tank as well as the VDA. With a 0.5 ohm terminating resistor, currents as large as 500 amperes with a 1.5 microsecond width were observed on a 14 x 28 cm sample. Figure 5a shows an example of the waveform. Visually, most of the arcs started at the edges and spread over the surface of the sample. Figures 5b and c show examples of currents on a 12 x 12 cm sample and an 8 x 8 cm sample which are 100 and 12 amperes, respectively. In addition to demonstrating an increase of peak current with sample area, it should be noted that the pulse width also increases from 0.5 μs to 1.0 μs as the sample area is increased. The smallest sample, 8 x 8 cm, also had a somewhat different configuration in that a 0.25" guard ring was

etched around its periphery. This may account for its inordinately small peak current magnitude.

Originally, traces were taken simultaneously on a dual beam oscilloscope. However, it was found that the two external signals were cross-coupling, so that these were subsequently taken individually. When the VDA return current was 500 amperes, 20% or 100 amperes was found to flow to the aluminum backing plate. Examination of the data indicated that the termination load resistance determined the relative as well as total amounts of currents flowing to the plate and to the tank walls. The decrease in peak current as the VDA load resistor was increased as shown below:

Load Resistance (ohms)	1	10	100	1000
Peak Current (amperes)	400	100	30	3

It should be noted that no attempt was made to minimize wiring inductances from the sample to the external load resistors. Thus, the sample voltage, especially with the smallest load resistances, could have been much larger because of the inductive reactance and therefore have been a limiting factor on the peak current.

GROUNDSTRAP DURABILITY TESTS

In view of the different groundstrapping techniques used for grounding the metallic film of thermal blankets on different spacecraft programs, tests were performed to compare their relative durability to large current pulses such as would result from arc discharges. For a standardized 100 ampere peak current from a .01 microfarad capacitor charged to 10 kV, a 1 microsecond time constant, the number of pulses survived before open circuiting varied from ∿50 to ∿1000 for the different groundstrapping techniques. An improved technique for grounding was also tested under the same conditions and was found to be far superior to any other, surviving more than 10,000 pulses with no indication of any deterioration.

From the previous discussions on thermal blanket arcing modes and arc discharge characterization it is clear that a typical arc discharge cannot be defined at this time with much confidence. In particular, arc breakdown threshold or triggering mechanisms, area of dielectric surface drainage, and effects of surface potential during discharge or replacement currents are not understood. Since pulse durations of less than 100 ns to greater than 10 μs have been observed, a 1 μs pulse width was assumed to be a reasonable compromise. Similarly, since arc breakdown voltages of 2 kV to greater than 20 kV have been observed, 10 kV was assumed to be a relatively high level. The capacitance, .01 μf, corresponds to that for 500 cm^2 of 2 mil kapton. Although larger areas, ∿4000 cm^2, have been observed to discharge in a single pulse, K. P. Bogus (ref. 9) of the European Space Agency has found that the peak current does not increase linearly, but rather more nearly as the square root. Furthermore, arc discharge modes and surface potential effects are expected to further reduce the magnitudes of peak currents flowing in the groundstrap.

TEST SETUP AND SAMPLE CONFIGURATIONS

The test setup is shown schematically in figure 6. A hydrogen thyratron is triggered from a pulser to energize the discharge circuit. An 8" x 6" sample of the thermal blanket is connected by a metal cross-bar over its entire width on one side and by the groundstrap on the other. A 100 ohm non-inductive resistor limits the peak current from the .01 μf capacitor to 100 amperes.

Drawings of the four groundstrap configurations are shown in figures 7a, 7b, 7c, and 7d.

TEST RESULTS AND DISCUSSION

The test results are shown in figures 8a, b, c and d as curves of groundstrap resistance vs the number of current bursts. The results are also summarized below, showing the number of pulses to burnout various groundstrap configurations:

DSP	20 to 60 Pulses
FSC	40 to 200 Pulses
DSCS II	600 to 1200 Pulses
MODIFIED	Greater than 10,000 Pulses

The wide variation in the number of pulses required to cause the groundstrap to open-circuit seems to depend on the peripheral length of the contact between the metallizing VDA film and the aluminum foil of the groundstrap itself. This is indicated by an examination of the contact configurations of the various samples and by the fact that it was observed that it is at these peripheries at which the VDA is burned off. In the case of the best sample, accelerated life testing at 500 amperes peak showed that VDA burnoff occurred at the metal cross-bar rather than at the groundstrap. In the case of the poorest configuration, significant increases in resistance are observable with each individual pulse. Figure 9 is a photograph showing small pucker mounds associated with each pulse.

SECOND SURFACE MIRROR CHARGING TESTS

Typical second surface mirrors consist of 6-8 mil thick and 2 to 2-1/2 inch squares of quartz or borosilicate glass windows. Window materials used on TRW programs were

Program	Window Material
DSCS II	Glass (Borosilicate)
FLTSATCOM	Quartz (Fused Silica)
DSP	Glass up to Serial #9, then Quartz
TDRSS	Quartz

The inner surface of the window is coated with vacuum deposited silver to a thickness of 500-1000 Å. The metallized layer is protected with a thin layer, 100-1000 Å, of ceramic. Until several years ago, a layer of inconel was used instead of the ceramic, but the ceramic was found to provide better protection. The second surface mirror is bonded to the spacecraft with a silicone adhesive, roughly 3 mils thick. Silicone adhesive is used to permit thermal compliance, i.e., permits relief of thermal stresses.

Second Surface Mirror Tests

The second surface mirror (SSM) tests were performed in the 2' diameter by 4' long vacuum tank with the test setup as shown is figure 10. An electron gun at one end of the tank is capable of providing an electron beam density of 100 na/cm^2 at 20 kV. The positive side of the acceleration power supply is grounded to the tank. A door is provided near the mid-section of the tank to permit the "substorm" to be turned on and off. Faraday cups are provided both in front of the door and in front of the test sample to calibrate the incident current density. Electrostatic voltage probes are provided on swinging arms to provide scans of surface potentials. During most of the SSM testing the electron current was set at 10 na/cm^2 with an accelerating potential of 20 kV.

Two test samples were used. Both samples consisted of six SSM's mounted on an aluminum substrate with roughly a 3 mil thickness of silicone adhesive. In one sample all the SSM's had quartz windows and in the other glass windows. In each case a heating pad was mounted on the side of the substrate opposite to the mirrors. The samples were also instrumented with thermocouples to determine the sample temperature. Several connections were brought out from the sample under test. These consisted of heater wires, thermocouple output wires and a single output current wire from the aluminum SSM substrate. This output was grounded through a 1-ohm resistor which fed the input to a strip chart recorder. Occasionally the same output was examined using a Tektronix 555 oscilloscope loaded with a 50 Ω resistor at its input.

Arcing occurred with the quartz SSM sample soon after the door was opened. The arcs could be observed visually by looking through a window in the tank. Most of the arcs appeared in the cracks between the mirrors but occasionally arcs appeared to flash across the mirror surface. An oscilloscope trace of a typical pulse associated with the arcs is shown in figure 11. The trace shows an approximately 40 ampere pulse of about one-third of a microsecond duration. Note that the polarity is positive, indicating that electrons are leaving the sample and (presumably) going to the vacuum tank walls, which are at zero (ground) potential. The electrical circuit is completed by electrons which flow from ground through the resistor to the sample. This is equivalent to positive charges flowing in the opposite direction, which is consistent with the observed signal polarity.

There should also be a displacement current component which flows due to the capacitance between the test sample and the vacuum tank walls. Assuming that this capacitance if 100 pf and that the sample surface represented by this capacitance goes from -11 kV to 0 V in .33 microseconds, the charge and voltage currents are

$$Q = CV = 1.1 \cdot 10^{-6} \text{ coulomb}; \quad I = Q/t = 3.3 \text{ amperes}$$

The displacement current would be in the opposite direction and smaller than the former current and would reduce the amplitude of the observed positive pulse.

Two different modes of arc discharging, to the tank walls and across the SSM window to the substrate can occur and are illustrated in figure 12. If the arc is to the tank wall as in figure 12a, both currents discussed in the previous paragraph will flow. Since the displacement current is smaller, a positive polarity pulse is anticipated. Note that if the arc is to the substrate (fig. 12b), the current pulse polarity is reversed and a negative polarity is predicted. This polarity has not been observed experimentally.

The potential on the SSM just before breakdown was measured using the capacitance probe and found it to be -11 kV. The capacitances of the six mirrors is approximately 3600 pf, therefore the total current that would appear in the pulse if all the charge went to the walls is given by

$$I = \frac{CV}{t} = \frac{3.6 \times 10^{-9} \times 11{,}000}{333 \times 10^{-9}} \text{ amperes} = 120 \text{ amperes}$$

Therefore the 40 amperes shown in the oscilloscope trace corresponds to only one-third of the total charge on the mirrors. The remainder of the charge either remains on the mirrors or "flashes over" to the grounded aluminum substrate effectively reducing the positive current pulse observed.

The rate at which arcing occurred was determined from the strip chart recording pulses. This data was taken as a function of temperature from 20°C to 100°C. An example of the strip chart recording is shown in figure 13. In the example shown, the chart is moving at a rate of 1 inch/minute and the sample is arcing at the rate of 7.8 arcs/minute. Note that the pulse heights vary significantly from pulse to pulse. No quantitative information on the amount of charge involved in the pulses can be obtained from these recordings because of the slow response of the strip chart recorder.

Results of the arc rate vs temperature test for the quartz SSM is shown in figure 14. It is clear from the data that the rate of arcing was not significantly affected by the temperature change. The leakage due to the resistivity of quartz apparently remains a small contribution to the current balance of the sample even when the temperature is as high as 100°C and arcing continues at all temperatures up to 100°C. When the incident electron current was reduced to 1 na/cm^2 from 10 na/cm^2, the arc rate decreased from about 7 arcs/minute to 0.7 arc/minute but did not cease.

The six glass window mirrors were placed in the chamber and irradiated with the same electron current (10 na/cm^2 at 20 kV) to which the quartz window mirrors were exposed. At room temperature arcs were observed both visually and on the chart recorder but at a lower rate than seen with a quartz window. When

the current was reduced to 1 na/cm^2 the arcing ceased. Figure 15 shows the results of the arc rate vs temperature test on glass SSM's with an incident current of 10 na/cm^2. In contrast to the quartz SSM results a definite temperature dependence is observed. The arc rate decreases monotonically with temperature and no arcing was observed at temperatures greater than 54°C.

SUMMARY AND CONCLUSIONS

Available data on the geosynchronous orbit energetic plasma environment has been examined, and a crude model generated to permit an estimation to be made of the number of arc discharges per year to which a thermal blanket groundstrap would be subjected. Laboratory experiments and a survey of the literature on arc discharge characteristics were performed to define typical and worst case arc discharge current waveforms. In-air tests of different groundstrap configurations to a standardized test pulse were performed and a wide variability of durability values were found. A new groundstrap technique, not used thus far, was found to be far superior than the others.

The estimation of the requirements on groundstrap durability discussed here need to be improved in many areas:

- Definition of the environment
  - in terms of statistical distributions
  - in terms of satellite longitude
  - in terms of the solar cycle
- Definition of the charging process
  - in terms of material parameters
  - in terms of specific spacecraft configurations
  - in terms of specific satellite orientations
- Definition of arc discharge characteristics
  - arc discharge breakdown thresholds
  - triggering mechanisms
  - areas and patterns of discharge
  - arc discharge current and voltage waveforms

Since groundstraps on the metallized film of thermal blankets cannot prevent arc discharges of the outer dielectric surface, it is important that further work be performed to characterize these dielectric surface discharges in terms of their potential hazard to spacecraft equipment, i.e., in terms of electromagnetic interference.

Whether the groundstrap techniques for a given spacecraft program needs to be improved cannot be answered definitively at the present time because of the lack of adequate data and knowledge about the charging process and about arc discharge characteristics as listed above. The greatest uncertainty in the

computed numbers of arcs per year in table 2 (500 to 2,000), are probably due to the lack of understanding of the arc breakdown process. Deficiencies in environmental and materials parameters characterizations are also major factors in the computational inaccuracy. Because many of these uncertainties have opposing influences on the discharge rate, e.g., lower breakdown threshold and lower resistivity, the upper range of 2,000 pulses per year is probably not too bad. The numbers of pulses to cause burnout, 20 to >10,000, are most likely too high by several orders of magnitude for the reason of the test load resistance effects summarized previously. The various arcing configuration effects are outlined in figure 3; whether or not the arc currents actually flow through the groundstrap has not been determined. Only direct arcs to the test chamber walls (to space) have been observed in most tests performed to date simply because the other arcing modes are difficult to detect and to quantify.

The results of the second surface mirror tests verify that quartz SSM's do pose an arc discharge hazard for spacecraft, but borosilicate glass, because of its poorer insulating property, does not. The trend, unfortunately, is towards greater use of quartz SSM's because of their superior thermal control properties. The partial cleanoff ($\sim$1/3 of the initial charge) of all of the SSM's (six) in the sample has been observed to occur in $\sim$1/4 microsecond. As with the thermal blanket discharge measurements, the peak currents observed, in the order of 40 amperes, was undoubtedly dependent on the diagnostic load impedance (1 ohm plus lead inductances).

REFERENCES

1. DeForest, S. E.; and Wilson, A. R.: A Preliminary Specification of the Geosynchronous Plasma Environment. Defense Nuclear Agency, 3951T, Sept. 1976.

2. Stevens, N. J.; Lovell, R. R.; and Purvis, C. K.: Provisional Specification for Satellite Time in a Geomagnetic Substorm Environment. NASA TMX-73446, Oct. 1976.

3. Su, S. Y.; and Konradi, A.: Description of the Plasma Environment at Geosynchronous Altitudes. NASA/Johnson Space Center Note P-10, March 22, 1977.

4. Inouye, G. T.: Spacecraft Potentials in a Substorm Environment. Progress in Astronautics and Aeronautics, Vol. 47, Spacecraft Charging by Magnetospheric Plasmas, Editor, A. Rosen, 1976.

5. Garrett, H. B.: Modeling of the Geosynchronous Orbit Plasma Environment - Part I. AFGL-TR-77-0288, 14 Dec. 1977.

6. Johnson, B. J. Quinn; and DeForest, S. E.: Spacecraft Charging on ATS-6. Proceedings of the 1978 Symposium on the Effect of the Ionosphere on Space and Terrestrial Systems, Jan. 25, 1978.

7. Hoffmaster, D.K.; and Sellen, Jr., J. M.: Spacecraft Material Response to Geosynchronous Substorm Conditions. Progress in Astronautics and Aero-

nautics, Vol. 47, Spacecraft Charging by Magnetospheric Plasmas, Editor, A. Rosen, 1976.

8. Inouye, G. T.; and Sanders, N. L.: Non-Linear Resistivity Effects in Spacecraft Charging. TRW Report 8800.3.1-78-11, 31 March 1978.

9. Bogus, K. P. of the European Space Agency, private communication dated 8 July 1977, published in the Proceedings of Spacecraft Materials Conference in Toulouse, 5 July 1977.

TABLE 1. SUBSTORM MAXWELLIAN PARAMETERS WITH DURATIONS FROM ATS-5 1970 DATA

	Severe			Moderate	Mild	Quiet
	Jan. 2	(Avg.)	Mar. 27	Jan. 3	Jan. 1	Feb. 6
Peak Electron Current Density, J_{oe} (na/cm^2)	0.84	(0.95)	1.05	0.35	0.14	0.054
Peak Electron Temperature, T_e (keV)	13.0	(7.5)	2.0	8.0	5.0	5.0
*Average, J_{oe} (1/2 Peak) (na/cm^2)	0.42	(0.48)	0.53	0.18	0.070	0.027
*Average, T_e (keV)	6.0	(6.0)**	1.5	5.0	3.0	3.5
*Average, J_{oi} (J_{oe} : 43) (na/cm^2)		0.011		0.0042	0.00163	0.00063
*Average, T_i (2 T_e) (keV)		7.6		10.0	6.0	7.0
Duration/Day (Hours)		12.0		9.6	2.4	12.0
Days/Year (Days)		36.5		29.2	43.8	255.5
Hours/Year (Hours)		438.0		280.0	105.0	3066.0

*Average during substorm.

**Use higher temperature for worst case.

TABLE 2. COMPUTATION OF THE NUMBER OF ARCS PER YEAR WITH RESISTIVITY DEPENDENCE

Type of Substorm	Severe	Moderate	Mild	Quiet	Total
J_{oc} (na/cm^2)	.48	.18	.07	.027	-
T_e (kilovolts)	6	8	3	3.5	-
Duration (hrs/year)	438	280	105	3066	-
Arcs Per Year with Non-Linear Resistivity					
$\rho_o = 10^{18}$ ohm-cm					
d = 1 mil	1500	292	8	23	1823
d = 2 mils	1083	184	0	0	1267
d = 3 mils	702	54	0	0	756
$\rho_o = 10^{17}$ ohm-cm					
d = 1 mil	1407	216	0	0	1623
d = 2 mils	1049	0	0	0	1049
d = 3 mils	467	0	0	0	467
$\rho_o = 2.66 \cdot 10^{16}$ ohm-cm					
d = 1 mil	1031	0	0	0	1031
$\rho_o = 10^{16}$ ohm-cm					
d = 1 mil	0	0	0	0	0
Arcs Per Year with Constant Resistivity					
$\rho = 10^{18}$ ohm-cm					
d = 1 mil	1500	295	13	230	2038
d = 2 mils	1090	191	0	0	1281
d = 3 mils	715	82	0	0	797
$\rho = 10^{17}$ ohm-cm					
d = 1 mil	1467	273	0	0	1740
d = 2 mils	1049	158	0	0	1207
d = 3 mils	657	0	0	0	657
$\rho = 2.66 \cdot 10^{16}$ ohm-cm					
d = 1 mil	1093	189	0	0	1282
$\rho = 10^{16}$ ohm-cm					
d = 1 mil	0	0	0	0	0

January 1, 1970

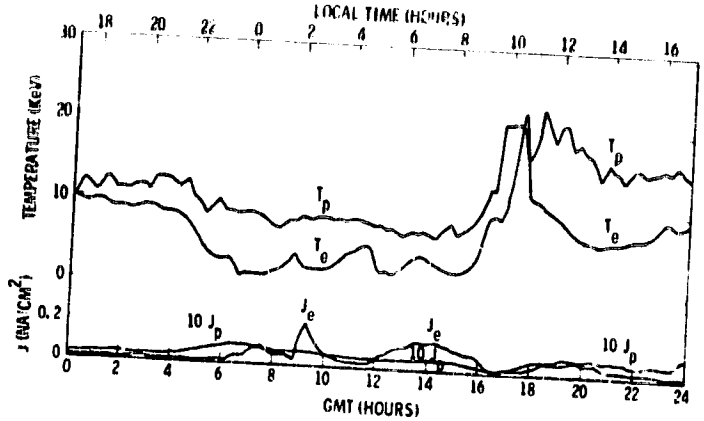

January 2, 1970

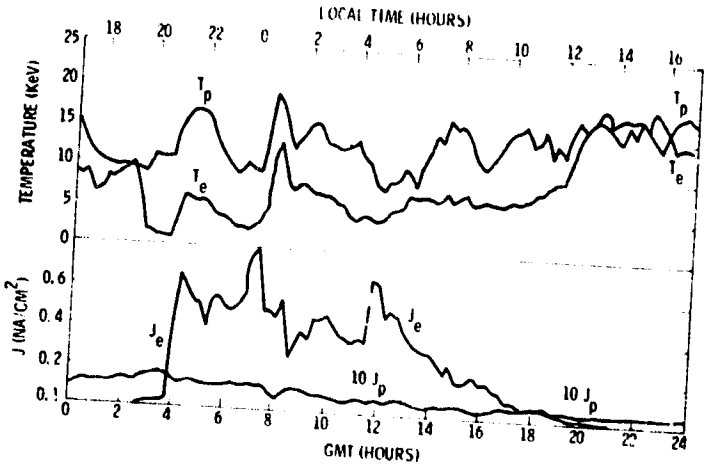

January 3, 1970

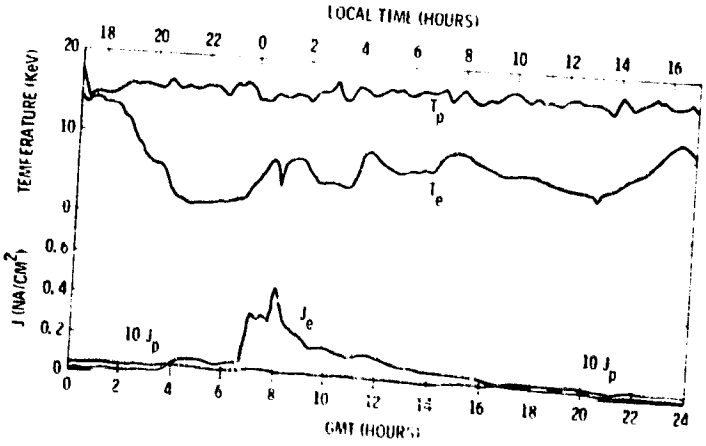

FIGURE 1. ATS-5 DATA FOR JAN. 1, 2, 3, 1970

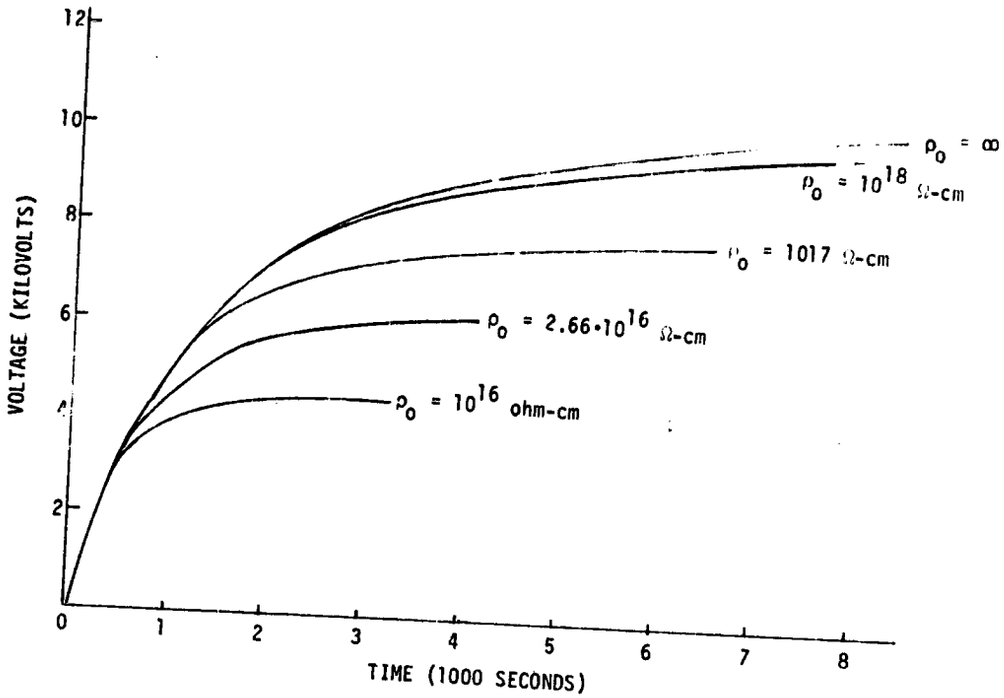

FIGURE 2. CHARGEUP CURVES FOR 3 MIL DIELECTRIC WITH NON-LINEAR RESISTIVITY IN A "SEVERE" SUBSTORM

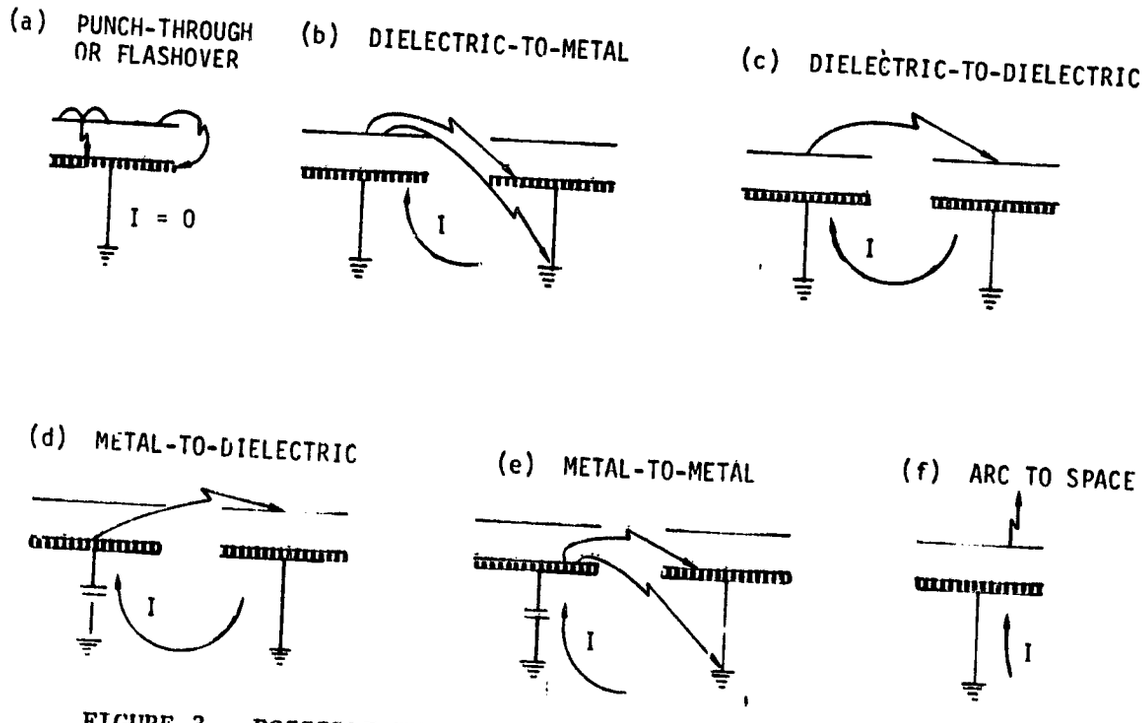

FIGURE 3. POSSIBLE THERMAL BLANKET ARCING CONFIGURATIONS

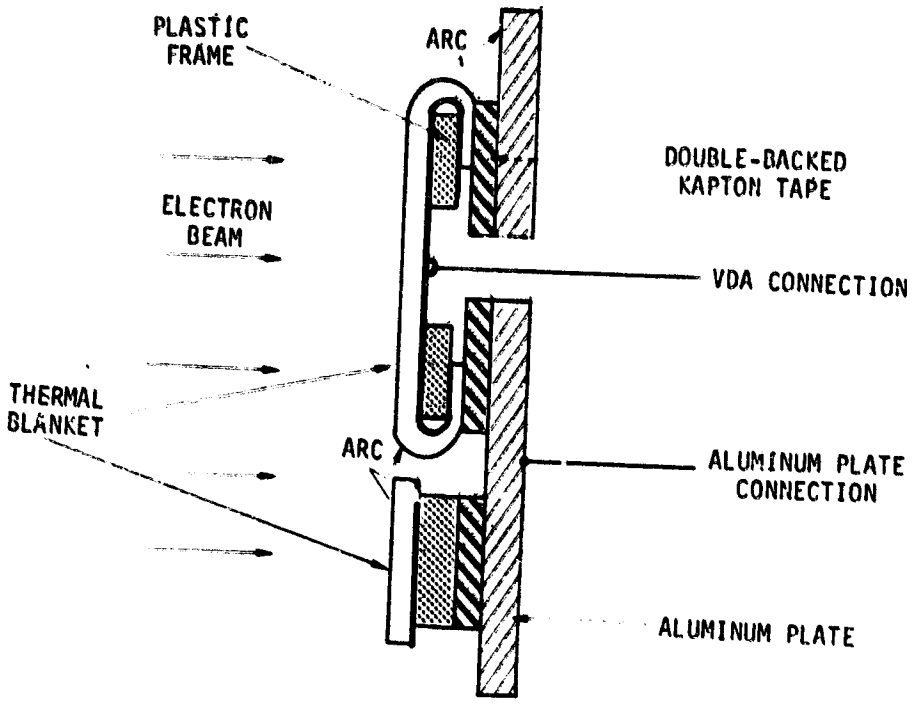

FIGURE 4. TRW TEST SAMPLE CONFIGURATION

(a)
14 x 28 cm SAMPLE
500 AMPERES PEAK
1.5 μs WIDE

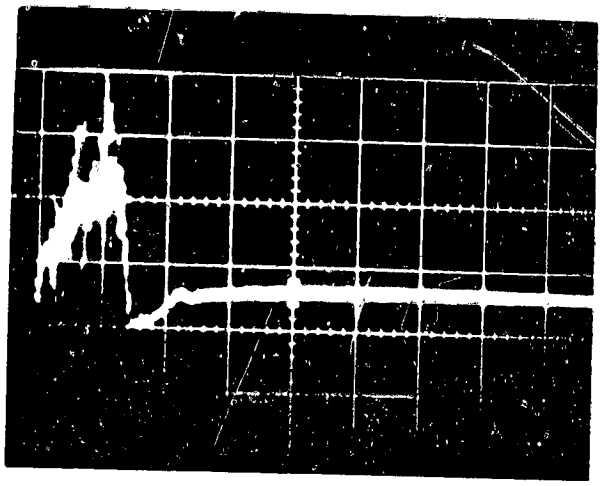

(b)
12 x 12 cm SAMPLE
100 AMPERES PEAK
1 μs WIDE

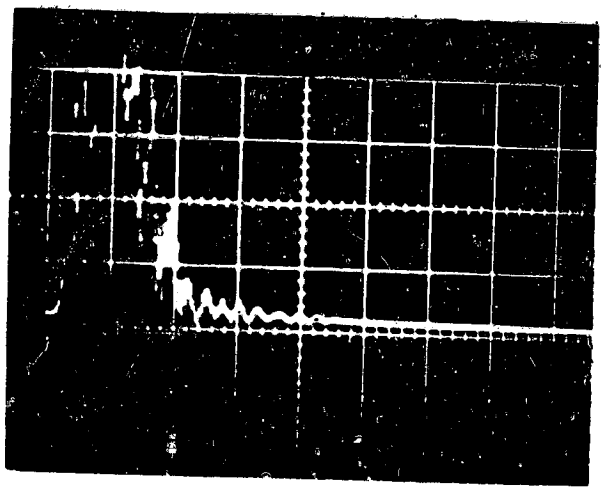

(c)
8 x 8 cm SAMPLE
12 AMPERES PEAK
0.5 μs WIDE

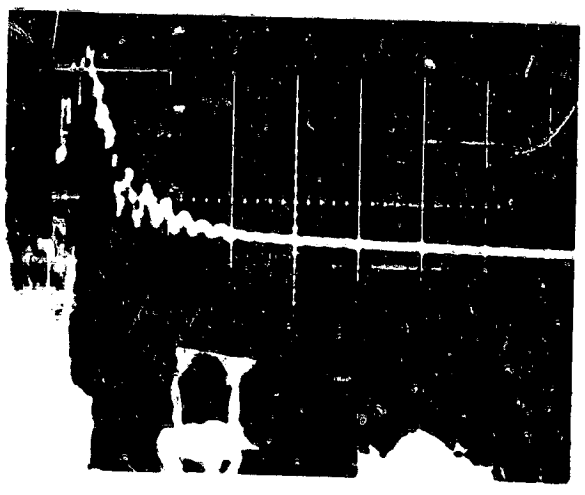

FIGURE 5. ARC DISCHARGE CURRENT WAVEFORMS

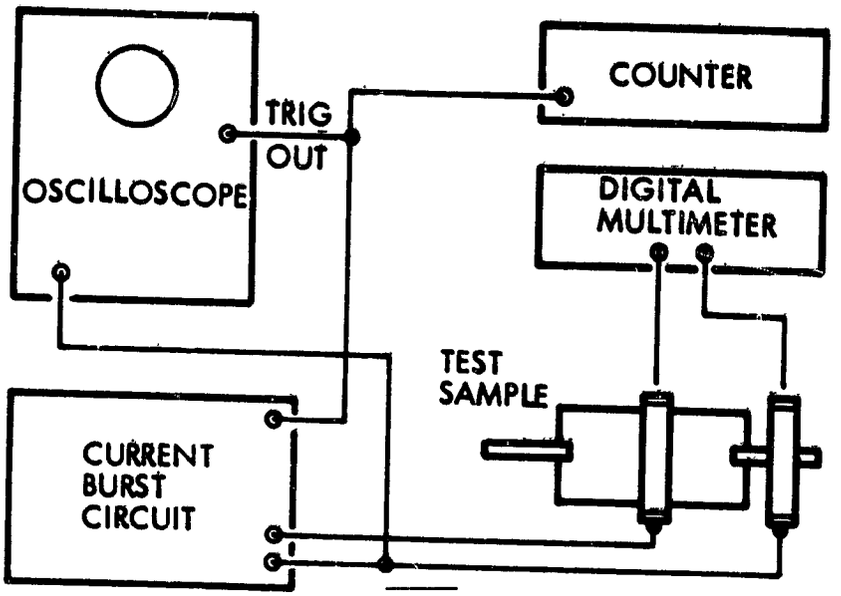

FIGURE 6. GROUNDSTRAP TEST SET.

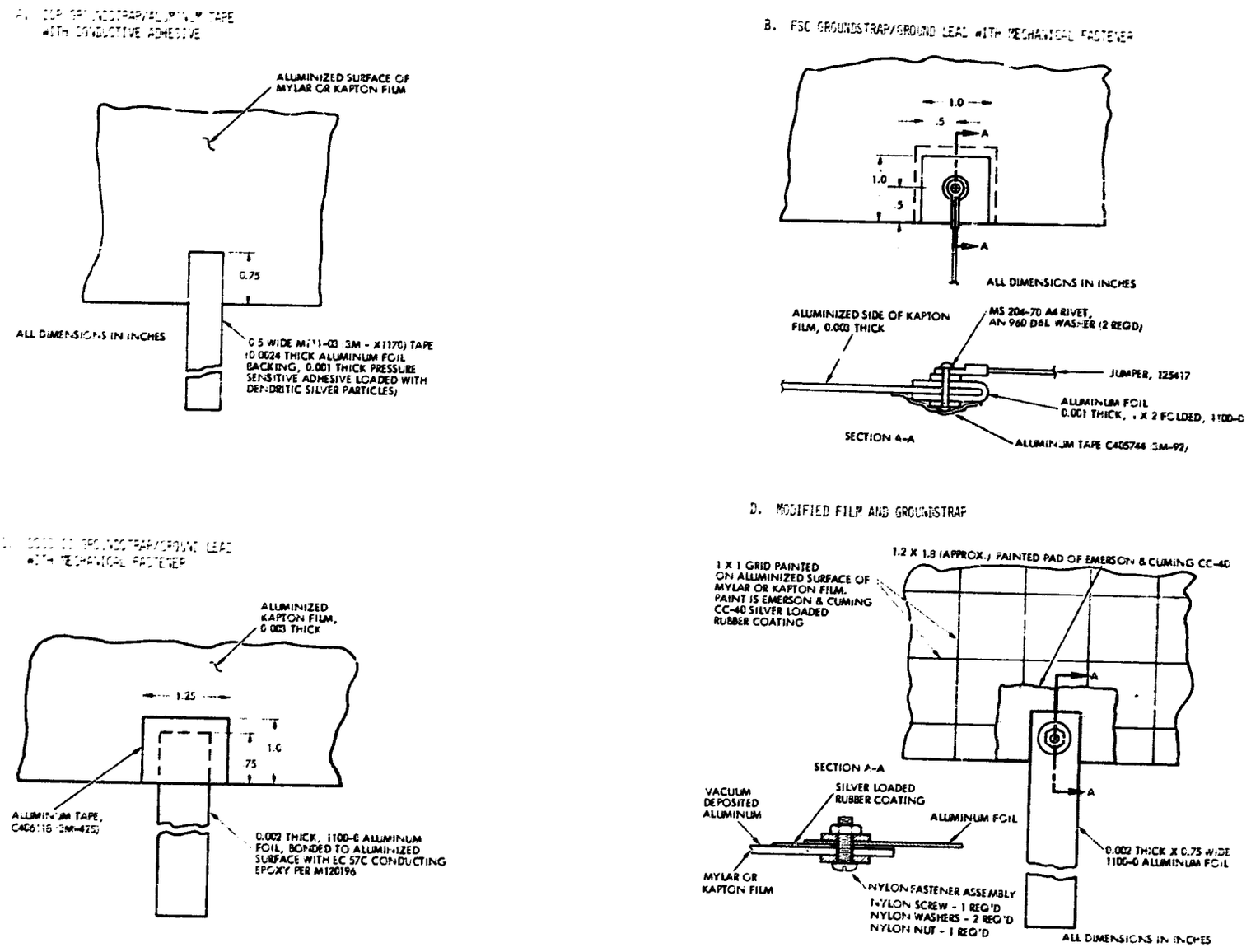

FIGURE 7. GROUNDSTRAP CONFIGURATIONS

A. MOD. 35 TYPE GROUNDSTRAP (0.75" WIDE STRAP)

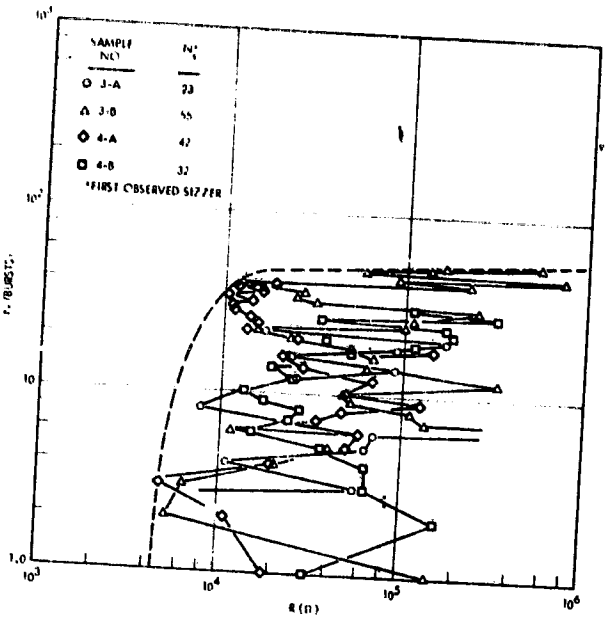

B. FSC GROUNDSTRAP

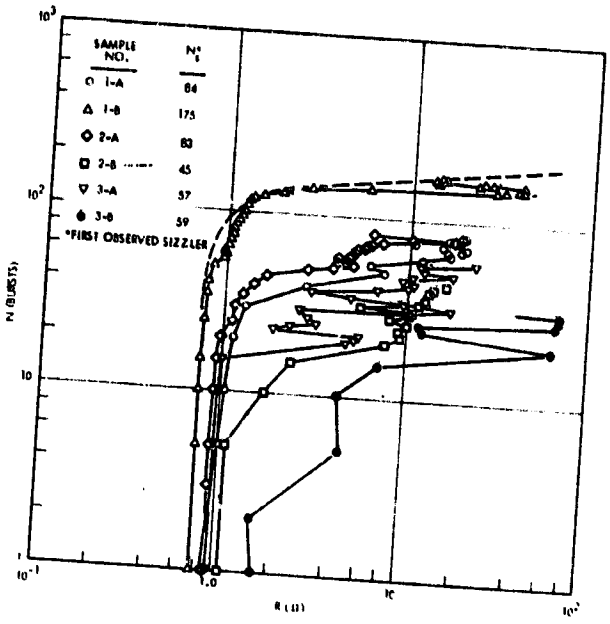

C. DSCS GROUNDSTRAP

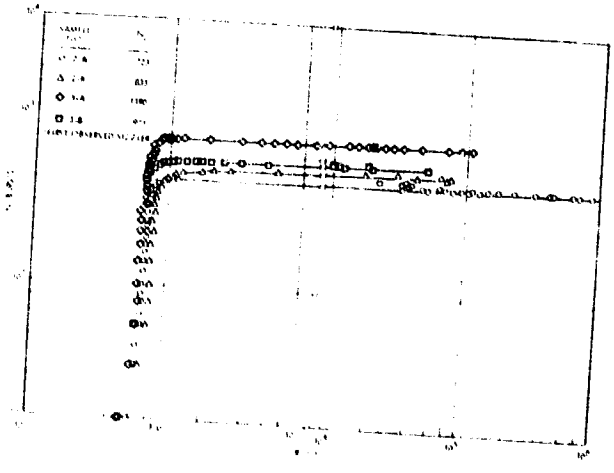

D. MODIFIED FILM/GROUNDSTRAP (SAMPLE 1-A)

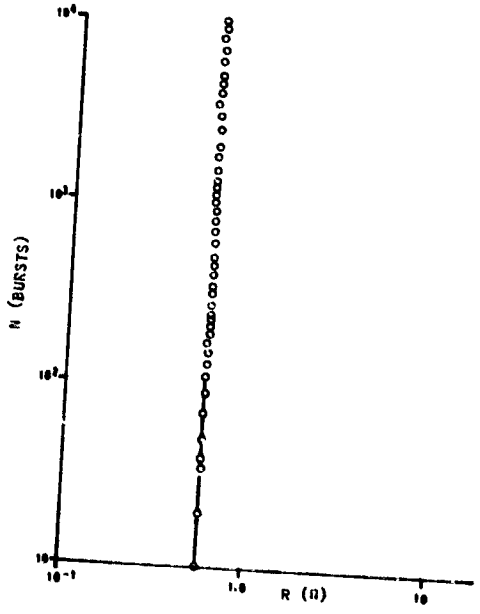

FIGURE 8. GROUNDSTRAP DURABILITY TEST RESULTS

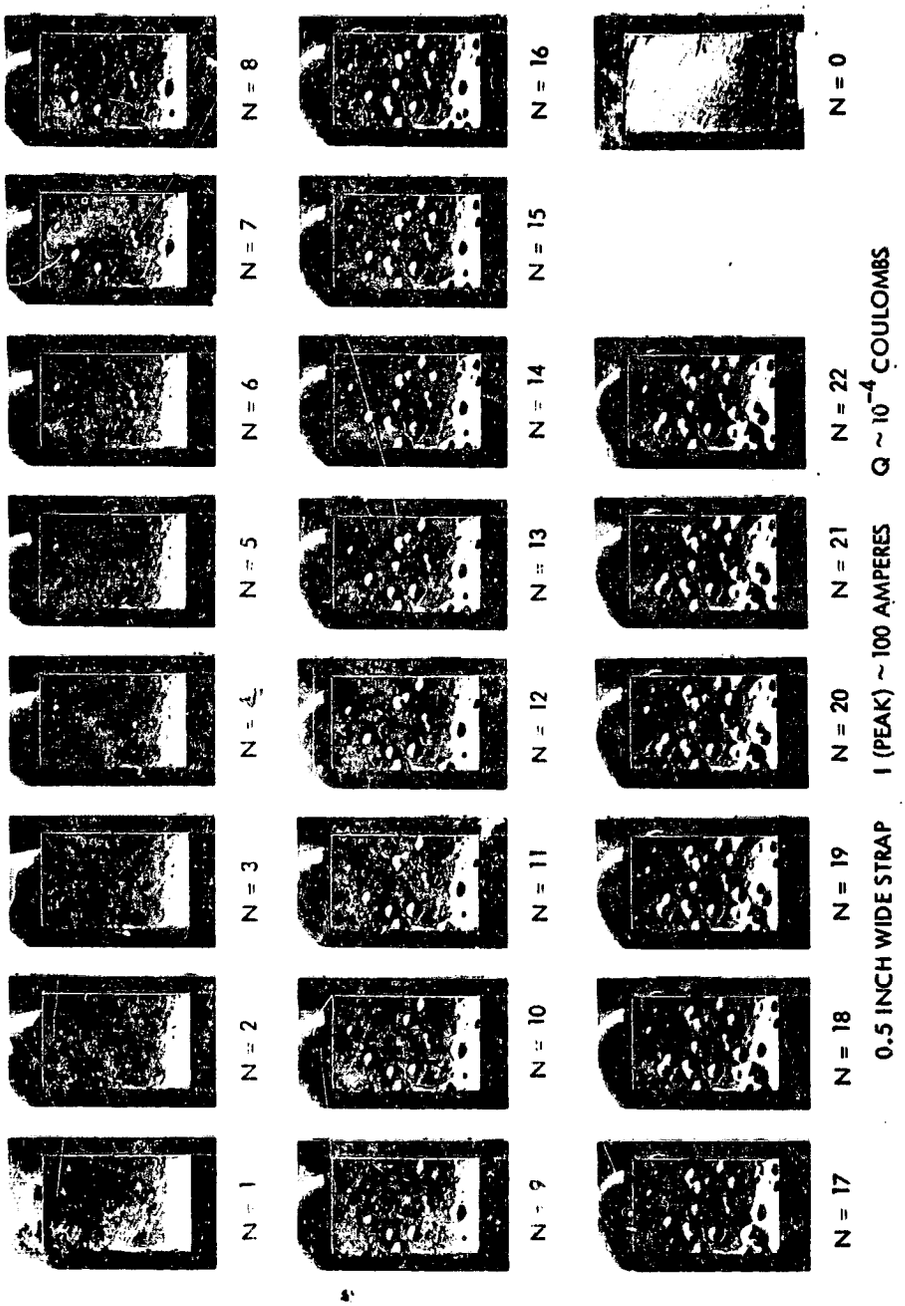

FIGURE 9. GROUNDSTRAP TEST

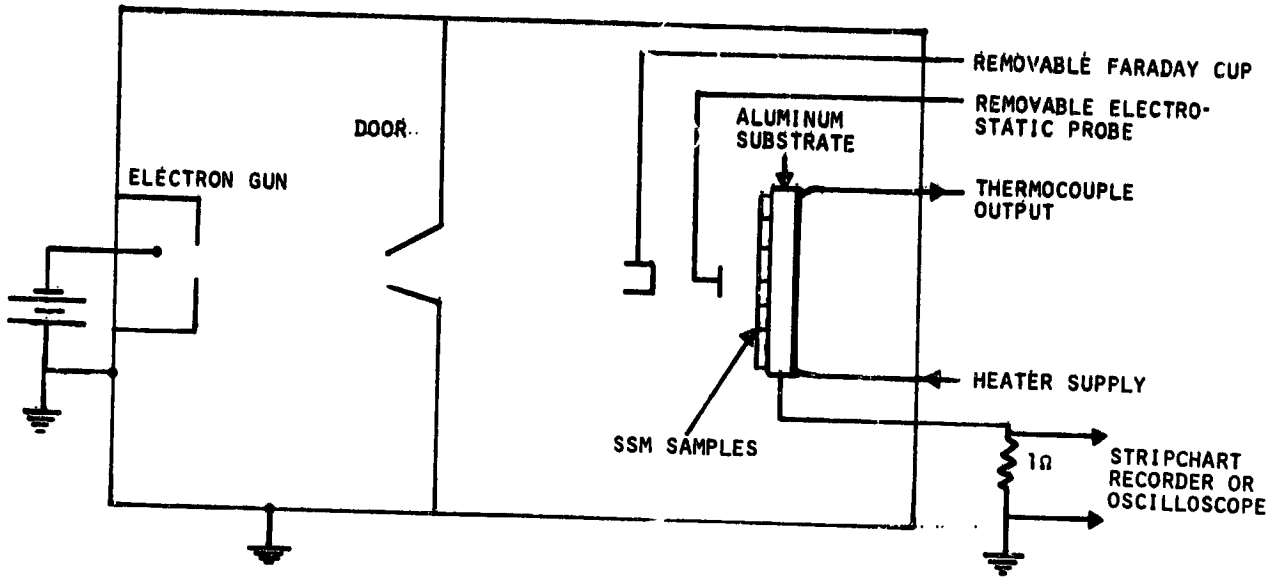

FIGURE 10. TEST CONFIGURATION

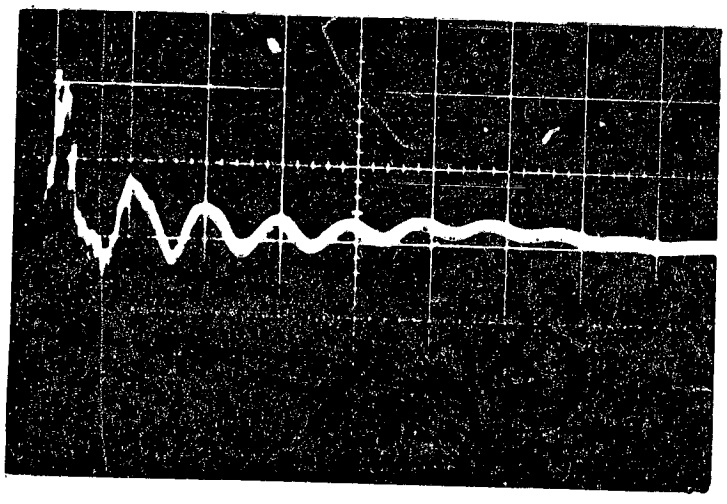

FIGURE 11. OSCILLOSCOPE TRACE OF TYPICAL PULSE ASSOCIATED WITH SSM ARCS. (ONE VERTICAL DIVISION = 20 AMPERES AND ONE HORIZONTAL DIVISION = 1 μSEC.)

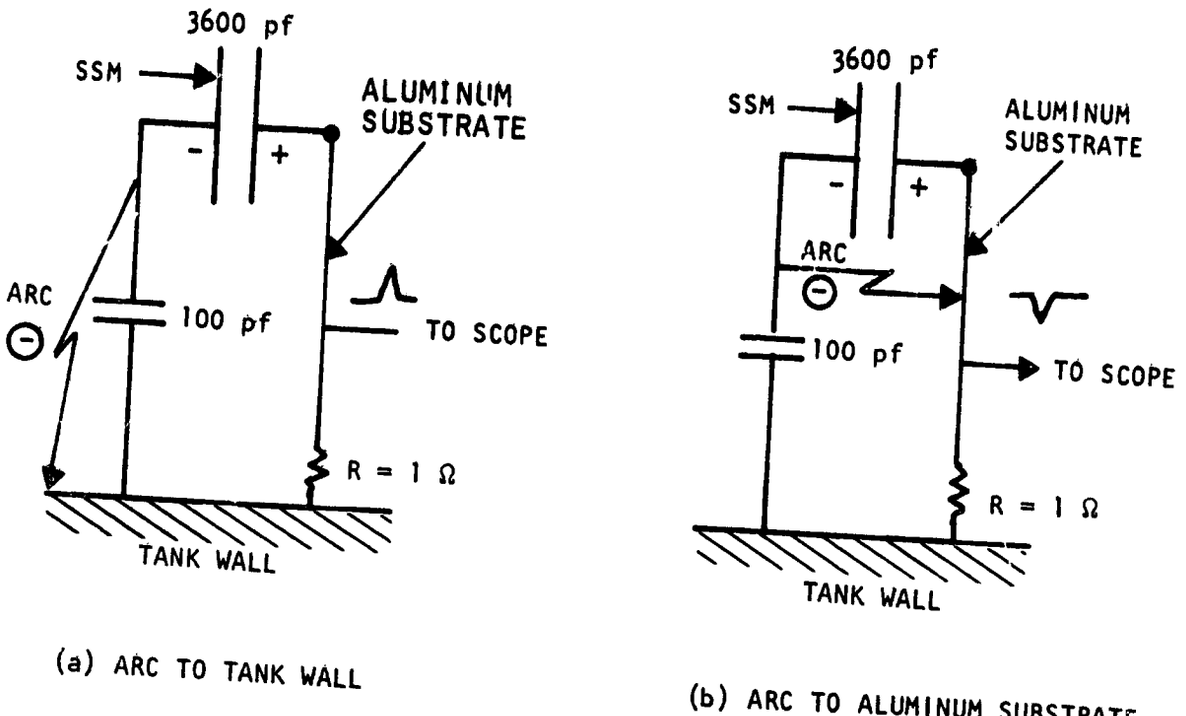

(a) ARC TO TANK WALL

(b) ARC TO ALUMINUM SUBSTRATE

FIGURE 12. ARC DISCHARGE MODES FROM SSM WINDOW

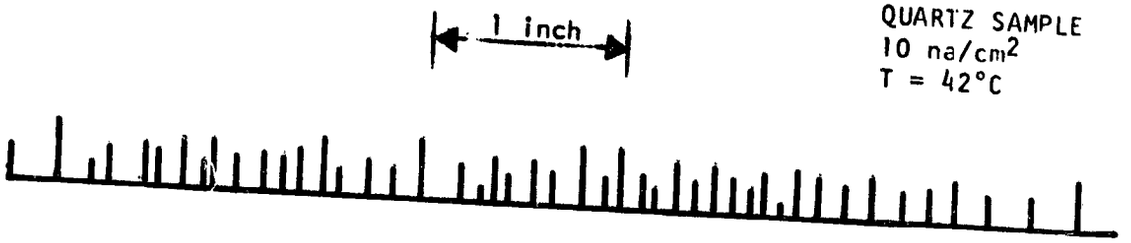

FIGURE 13. STRIP CHART RECORDING OF PULSES RESULTING FROM QUARTZ MIRROR ARCING CHART SPEED = 1 INCH/MINUTE (RATE = 7.8 ARCS/MINUTE)

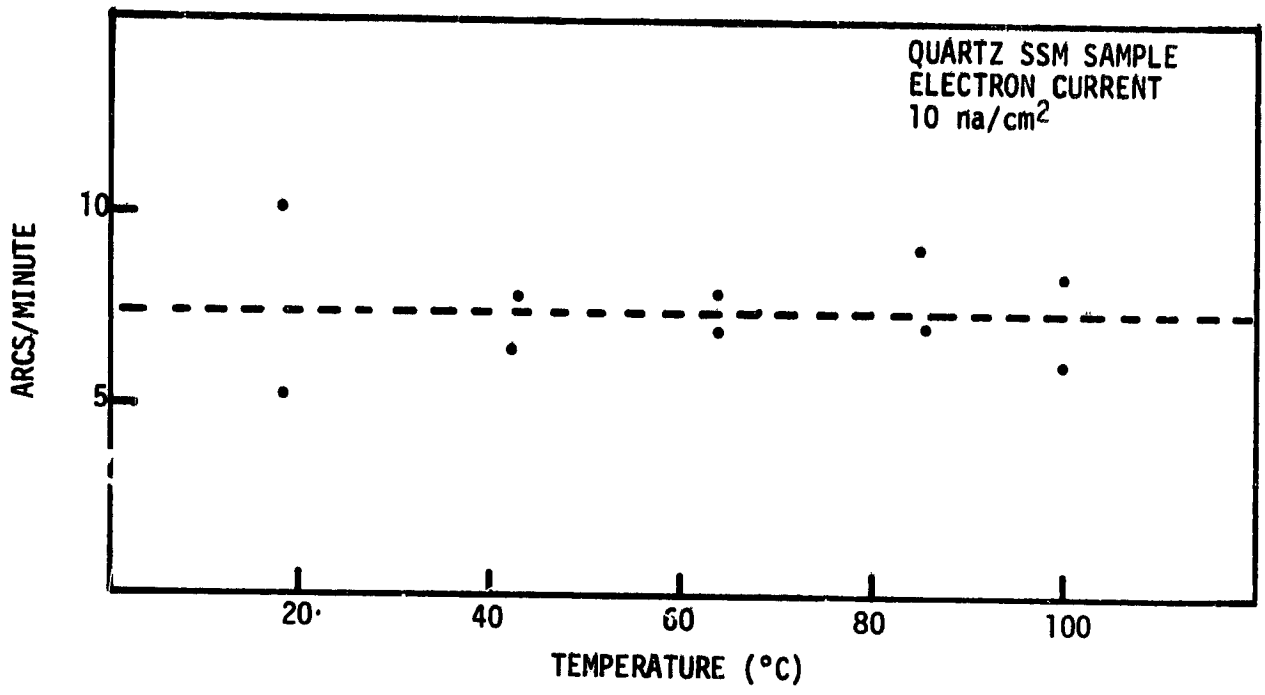

FIGURE 14. RATE OF ARCING OF QUARTZ SSM SAMPLE (LEAST SQUARE FIT SHOWN DOTTED) ..

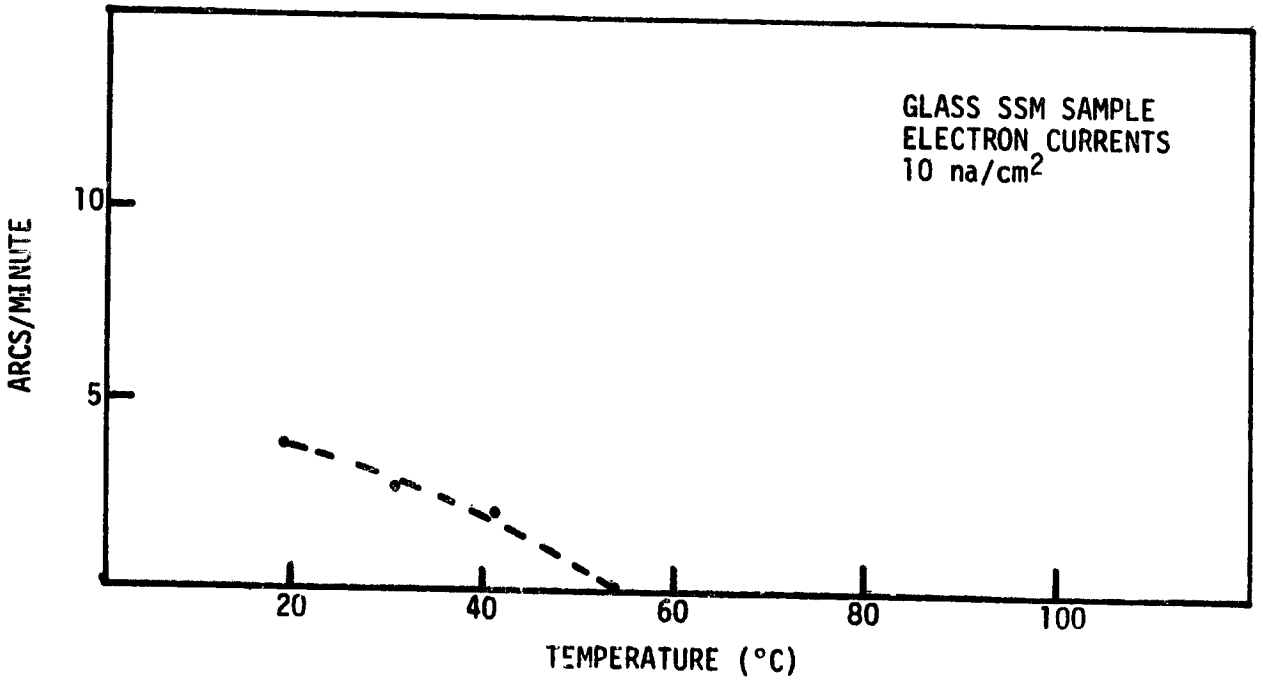

FIGURE 15. RATE OF ARCING GLASS SSM SAMPLE

D42

N79-24043

INVESTIGATION OF ELECTROSTATIC DISCHARGE PHENOMENA ON CONDUCTIVE AND NON-CONDUCTIVE OPTICAL SOLAR REFLECTORS

S. J. Bosma and C. F. Minier
European Space Research and Technology Centre

and

L. Levy
Département d'Etudes et de Recherches en Technologie Spatiale

INTRODUCTION

As part of a study of the effects of charge build-up on thermal control coating materials, a sample composed of non-conductive optical solar reflectors (OSR) was irradiated with low energy electrons at the DERTS facility in Toulouse (Ref. 1).

The degradation effects on this panel due to electrostatic discharges justified a follow-up investigation into possible alternatives to limit the amount of damage. This paper evaluates the following systems :

a) Non-conductive OSR - non-conductive adhesive
b) Non-conductive OSR - conductive adhesive
c) Conductive OSR - conductive adhesive (no interconnection of the OSR's)

TEST FACILITY

The tests were performed in an irradiation chamber (Fig. 1) at the DERTS Laboratories in Toulouse. The chamber consists of the following elements :

- A High Tension Feed-Through

This feed-through is connected to the conductive substrate on which the test sample is glued.

- A Diaphragm

To limit the incident beam on the test sample.

- Three Faraday Cups

To monitor the incident beam during irradiation.

- A Viewing Port

- An Electron Beam Diffusion Window

This window consists of a 2 micron thick aluminium sheet, which permits

the irradiation of large surfaces by diffusion of the initial mono-energetic beam. The obtained flux uniformity over the samples area is $\pm$ 40%.

MEASURED ELECTRICAL PARAMETERS

Leakage Current

The conductive substrate of the test sample is grounded through a series of resistances and a nanoampèremeter (Fig. 2), which measures the leakage current.

Discharge Pulse

An oscilloscope is connected to the resistances in a voltage divider mode (Fig. 2).

A discharge is characterised by comparing the voltage pulses measured over the divider (Figs. 3A and B).

Discharge Current

The substrate of the test sample is directly grounded. The discharge current is measured with a current probe and a fast storage oscilloscope. (Fig. 3C)

Surface Potential

If a test sample is submitted to an electron beam with an energy E_o and a current I_o, the actual current I reaching the surface of the test sample will depend on the potential V of this surface.

DERTS have determined the different relations I (V) for various electron beam currents I_o and energies E_o.

From these curves the surface potential (V) may be evaluated by measuring the corresponding current (I) at the time of the discharge.

TEST CONDITIONS

A vacuum of better than 10^{-5} torr was maintained during the irradiation.

All samples tested had dimensions of 65 x 65 mm. They were irradiated with electrons of increasing energy, starting from 5 KeV up to 30 KeV with current densities of 0.1 nA/cm^2 to 2 nA/cm^2 until discharges were observed.

When the conditions for electrostatic discharges are obtained, the sample remains irradiated and is allowed to discharge during 6 hours.

GENERAL BEHAVIOUR OF THE IRRADIATED SAMPLE

The impinging electrons on the sample surface cause a charge displacement in the conductive substrate which accounts for the initial high leakage current. This "displacement" current decays with time, because the incident electrons are partially retarded by a potential build-up on the sample surface.

There are two cases to be considered :

case A) (Fig. 4A) The potential build-up is sufficient to decrease the number of incident electrons to a value which can be removed by the leakage paths of the test sample. An equilibrium potential is obtained which is lower than the breakdown voltage of the di-electric.

case B) (Fig. 4B) The charge removal through the leakage paths is at all times smaller than the number of incident electrons. The test sample will charge to the breakdown voltage of the di-electric at which time an abrupt drop in surface potential occurs. It is assumed that this is caused by a discharge of a large surface area. After the discharge the leakage current jumps to a high value and starts to decay until a new discharge takes place.

The discharges described in case B are identified as "large", in contradiction to "small" discharges, which do not considerably modify the surface potential and are assumed to be "point" discharges. This latter type can occur in both cases A and B. These phenomena have been reported by other sources (Refs. 2 and 3).

SYSTEM (a): NON-CONDUCTIVE OSR - NON-CONDUCTIVE ADHESIVE

Test Sample

The sample tested was a panel composed of 9 OSR's manufactured by OCLI, bonded to a rigid plate using RTV 560 (manufacturer : General Electric, USA). This bonding has been done by ERNO, who apply the same procedure to the OTS project. The assembly was mounted onto the test plate at ESTEC, using a conductive adhesive developed by ESTEC which consists of RTV 566 (manufacturer: General Electric, USA) and metal powder 1029B from Chomerics.

Before mounting, the test plate was primed with Dow Corning silicone primer DC 1200. Figure 5 shows the composition of the test panel.

Test Results

A summary of the results obtained from testing the OSR panel is shown by Table I.

Table I

	original	long duration (6 hours)
Irradiation parameter	15 keV, 2 nA	30 keV, 2 nA
Surface potential	4 < U < 9 kV	4 < U < 9 kV
Electrical breakdown	"large and small"	65 large

Investigation of Degradation Effects

This investigation consisted of the following steps :

1) photographic examination of 16 pre-determined points (Figure 6); no degradation at first observation

2) cleaning with iso propyl alcohol and lens tissues. The sample was examined under grazing incidence. 14 degradation areas were observed with a total area of about 3 mm^2, i.e. 1.5% of the entire area (Figure 7).

All defects are close to or around defects in the adhesive which were already present before irradiation. It is clear that these points, where RTV is absent or thinner, were weak points because breakdown occurred due to lower insulation resistance.

3) Microscopic investigation.

A Reichert projection microscope was applied working as an interferometer using the Nomarski technique. This technique allows a better visualisation of the defect, but - due to the polarized light - the vertical defects are far more emphasized than the horizontal ones.

At this stage, it was observed that the degradation was a deposit on the surface of the OSR. (Figures 8 and 9)

4) Cleaning with iso propyl alcohol and normal wipe tissues

These tissues which are more abrasive than lens tissues removed the deposit. It should be noticed that the deposit is not soluble in either isopropyl alcohol or acetone but can be abraded or scratched. An investigation into the bottom layer of the quartz (the silver layer) showed that the silver had not been affected.

5) Reproduction of the defect

A highly powerful electrical breakdown was simulated to recreate the deposit. For this purpose, a "Tesla coil", manufactured by Edwards under the name "H.F. Tester" was used. This instrument supplies a high frequency voltage (0-20 kV) which creates a charge on dielectric material and a discharge through a conductive path mechanism. When such a discharge was applied to the OSR panel, the weak points could easily be seen as a preferred path for discharges.

A first intensive discharge created a deposit comparable to the one obtained in the DERTS test. The silver layer at the bottom was also damaged. (Figure 10)

A similar effect was created when the discharge was initiated in a break line of the OSR itself rather than in the RTV gap. A further analysis of a 15 kV discharge passed through an OSR defect for several seconds revealed a small hole in the top layer together with degradation of the silvered coating in the bottom layer. (Figures 11 and 12)

As only a small deposit on the top layer was observed, it was decided to create a weak discharge with the HF test, but for a longer period of time. A discharge of around 5 kV at a rate of 30 per minute, for 6 hours, was used in the same defect. Little change was observed in the defect in the silver layer, but the deposit on the top layer increased significantly.

6) Interpretation

It is probable that the accumulation of small discharges pyrolyses the silicone adhesive (RTV 560) and gives rise to a projection of silica particles which deposit on the top layer.

Summary

1) After irradiation at DERTS, no degradation of the silver layer had occurred;
2) At the weak points, with respect to breakdown resistance, a deposit is formed which is probably silica;
3) The changes in thermo-optical properties due to these deposits should be rather low (a few percent increase in α, but perhaps also in ε);
4) The amount of these deposits should increase with an increasing number of discharges;
5) If a large breakdown occurs, it will affect the bottom layer of silver, but the size of the defect will probably not increase with the number of discharges. Microscopic investigations show, however, that the aluminium layer of the substrate is more severely attacked;
6) It seems that any failure in the OSR is a privileged area as regards the likely occurrence of a discharge;
7) It seems reasonable to suppose that, with a conductive binder, this sort of defect will not appear.

SYSTEM (b): NON-CONDUCTIVE OSR - CONDUCTIVE ADHESIVE

Test Sample

In accordance with Point 7 of the summary of the previous test, DERTS have performed a second test on 9 OCLI OSR's bonded directly onto a test plate with a conductive adhesive developed by ESTEC Materials Section and consisting of RTV 566 with metal powder 1029B from Chomerics. (Ref. 4) Before mounting, the test plate was primed with Dow Corning silicone primer DC 1200.

Test Conditions

The test conditions were similar to those applied to the previous test. The sample was irradiated with electrons of increasing energy, starting from 15 KeV up to 30 KeV with current densities of 1 nA/cm^2 to 2 nA/cm^2.

Test Results

A summary of the results from testing the OSR panel is shown in Table II. The first discharges started at 20 KeV and 1 nA/cm^2, whereas in the previous test, the discharges commenced at 25KeV and 2nA/cm^2. This could be due to the fact that one of the OSR's was broken. A photographic investigation during the test showed that the crack was a preferential path, but not the only one. (Figure 13).

Furthermore the breakdown limit of the sample appeared to decrease after longer irradiation periods. At the beginning of the test, there were no discharges at 15 KeV electron irradiation, but at the end of the test sequence, there were 2 "large" discharges at this level. If the irradiation time had been extended, more discharges would have occurred. The sample was however constrained to the same irradiation time as the previous sample for comparison.

Investigation of Degradation Effects

Prior to cleaning the panel the surfaces of the OSR have been examined, using the same technique with the Reichert microscope.

- The observation shows that, on the front layer, there is a faint deposit of microscopic particles; again projection of silica, but a smaller amount than previously observed.

- The bottom layer of the OSR (the silver layer) is more severely damaged along the border line. Cracks in the silver layer appear which are in the order of 0.2 mm diameter. (Figure 14).

- In addition, a lot of micro spots (0.02 mm in diameter) of burnt silver in the middle of the OSR itself were visible.

- In another place, these micro spots have generated a blistering effect on the silver layer in a larger area (0.1 mm diameter). In this case, the front layer shows no defect at all.

On the previously cracked OSR, holes have been created between the front layer and the bottom layer, with demetallisation. This phenomenon had been predicted and analysed in the previous test. (Figure 15)

Interpretation

It was difficult to find a plausible explanation for the unexpected behaviour of the non-conductive OSR with conductive adhesive. Instead of diminishing the degradation effects of the OSR, increased damage in the silver layer was introduced. The missing link was found when information was received that the OCLI OSR's have a non-conductive layer (silicium-oxide and an organic finish) on the backside. A electrical resistance check with an Ohm-meter showed that the backside was indeed non-conductive.

The following discharge mechanisms could be adapted after this new development was introduced. (Figure 16).

In the case of a conductive adhesive a leakage current will flow from the front face to the metal layer on the back of the OSR due to the conductivity of the adhesive. A differential voltage will appear between the silver layer and the non-conductive silicium-oxide layer. A discharge from the silver layer will occur when the breakdown voltage of the silicium-oxide layer is exceeded. This will cause fusing and vapourisation of micro spots of silver.

The question arises : "Why this phenomenon does not appear when the non-conductive adhesive is used?" A possible answer is that, as shown in the previous test, a breakdown was created preferably at a defect in the adhesive layer. In this case, the silver is not a preferential path because it is completely insulated by a non-conductive layer on either side.

Summary

- After irradiation at DERTS, the silver layer was seen to be damaged (edges and micro spots).

- There was little or no deposit of silica on the front layer.

- The degradations of the silvered layer are small in area and at this point cannot change significantly the thermo-optical properties of the OSR, but they would be cumulative during life.

- As previously observed, cracks in the OSR are preferential areas of degradation and shall not be tolerated in spacecraft design.

INTERMEDIATE REVIEW

With the introduction of a new dimension due to the non-conductive backlayer of the OCLI OSR's, the range of three types of systems has been extended to four types (see Figure 17).

a) OSR non-conductive front layer / non-conductive back layer - non conductive adhesive

b) OSR non-conductive front layer / non-conductive back layer - conductive adhesive

c) OSR conductive front layer / conductive back layer - conductive adhesive

d) OSR non-conductive front layer / conductive back layer - conductive adhesive

SYSTEM (c) : - BOTH SIDES CONDUCTIVE OSR - CONDUCTIVE ADHESIVE

(no interconnection on the front face)

Test Sample

A third test was performed on 4 PPE OSR's with the conductive adhesive described in the previous test. The top surface of the OSR is coated with indium-oxide which is a conductive medium. Moreover, the rear side of the

PPE OSR is not coated with a non-conductive layer.

The sample was composed of three mirrors of 40 x 20 mm and one mirror of 40 x 15, which was intentionally broken. (Figure 18) The dimensions of the substrate were again 65 x 65 mm.

Test Conditions

The test conditions were similar to those used for the two previous tests. The sample was irradiated with electrons of increasing energy, starting from 20 KeV up to 30 KeV with current densities of 1 nA/cm^2 to 10 nA/cm^2.

Test Results

A summary of the results of the test on the OSR panel is given in Table III.

The surface potential of the sample was low, which indicates a high leakage current. No discharges were noticed below incident electrons of 30 KeV energy.

When the flux was increased to 2 nA/cm^2, very small discharges appeared at the beginning of the irradiation, but their number decreased during irradiation.

At a flux of 4 nA/cm^2, the same phenomenon was noticed, but the number of discharges did not decrease as rapidly as at the 2 nA/cm^2 flux level.

At a flux level of 10 nA/cm^2, there were a number of small discharges at the start of irradiation, but after 24 hours they had disappeared. A fluorescence effect was observed on the OSR during electron impact, however, this effect disappeared as soon as the electron beam was interrupted.

Investigation into Degradation Effects

Prior to cleaning the panel, we have examined the surfaces of the OSR, using the same technique as before with the Reichert microscope. No degradation was observed either as projection of silica or damage in the silver layer. The cracks which had been caused before the irradiation test showed no degradation effects.

The conductive backside of the PPE OSR brings about that the silver layer does not not accumulate charge while the indium-oxide achieves the same effect for the top layer.

In how far the indium-oxide layer is necessary will be investigated in a fourth test planned in the future on the system :

OSR non-conductive front layer
conductive back layer - conductive adhesive

The effects may be less serious than expected. As was indicated by the second test with the OCLI OSR and conductive adhesive, the most severe degradation occurred in the silver layer which was caused by the non-conductive layer on the backside of the OSR. This would not be the case with PPE OSR's which have a conductive backside.

CONCLUSION

The implications of this paper are very important. It has been proven that a combination of a both sides conductive OSR with a conductive adhesive shows no visible degradation during the irradiation tests performed.

In contradiction, a non-conductive OSR with a conductive or non-conductive adhesive shows degradation effects which could accumulate to hazardous proportions during life.

In particular, the non-conductive backside of the OCLI OSR causes defects in the intermediate silver layer in combination with a conductive adhesive.

Apart from the electrostatic charging advantages of the conductive OSR with conductive adhesive, the application and financial aspects should not be underestimated. In combination with a conductive adhesive, interconnecting pads between the conductive OSR's individually and to ground would not be necessary. These pads are very fragile and tend to break easily. In the past, they have given rise to many problems. OSR's with conductive pads are considerably more expensive than standard types.

Additionally, a great many man-hours, now required for very delicate interconnection work, may be saved.

REFERENCES

1. Irradiation par Electrons de Revêtement de Contrôle Technique. Report on work performed by DERTS under ESA contract No. 2638/76.

2. Stevens, N.J., Lovell, R.R. and Gore, V : Spacecraft Charging Investigation for the CTS Project. NASA TMX-71795, June 1975.

3. Pike, L.P. and Lovell, R.R. : Proceedings of the Spacecraft Charging Technology Conference. NASA TMX-73577, February 1977.

4. Froggatt, M. and Gourmelon, G. : Evaluation of Three Conductive Adhesives for Use on ECS. ESA E.W.P. 1010, May 1976.

TABLE II

Electron Energy	Electron Flux	Irradiation time	Discharge		Discharge Rate	Surface Potential at Time of Discharge	Number of Discharges over 6 hours	Remarks
			Small	Large				
15 keV	1 nA/cm^2	30 min						No discharging surface potential 5.5 kV
20 keV	1 nA/cm^2	80 min	Yes	Yes	5min to 7min	6 kV*	60	
25 keV	1 nA/cm^2	36 min	Yes	Yes	4min	5.4 kV*	90	Irradiation stopped after ½ hr. due to instability. Irradiation continued with lower energies
20 keV	1 nA/cm^2	86 min	Yes	Yes	3½min to 4¼ min	4.5 kV*	90	
25 keV	1 nA/cm^2	25 min	Yes	Yes	3½min	4.4 kV*	100	
25 keV	2 nA/cm^2	21 min	Yes	Yes	1½min	4 kV*	240	
30 keV	1 nA/cm^2	44 min	Yes	Yes	3min	4.7 kV*	120	Time between two irradiations: 15hrs.
30 keV	2 nA/cm^2	40 H	Yes	Yes	1½min to 2 min	4.6 kV*	200	
15 keV	1 nA/cm^2	45 min	Yes	Yes	15 to 20min	7.5 kV	20	Measurements are based on two discharges

* Values are based on a large number of discharges.

TABLE III

Electron Energy	Electron Flux	Irradiation Time	Observations
20 keV	1 nA/cm^2	20 min	None
30 keV	1 nA/cm^2	20 min	None
30 keV	2 nA/cm^2	25 min	Numerous small discharges during the first 5 minutes
30 keV	4 nA/cm^2	8 hours	Numerous small discharges during the first hours (several discharges per minute). Still some discharging at the end of the irradiation
30 keV	10 nA/cm^2	24 hours	Very small discharges at the start of the irradiation - no discharging at the end.

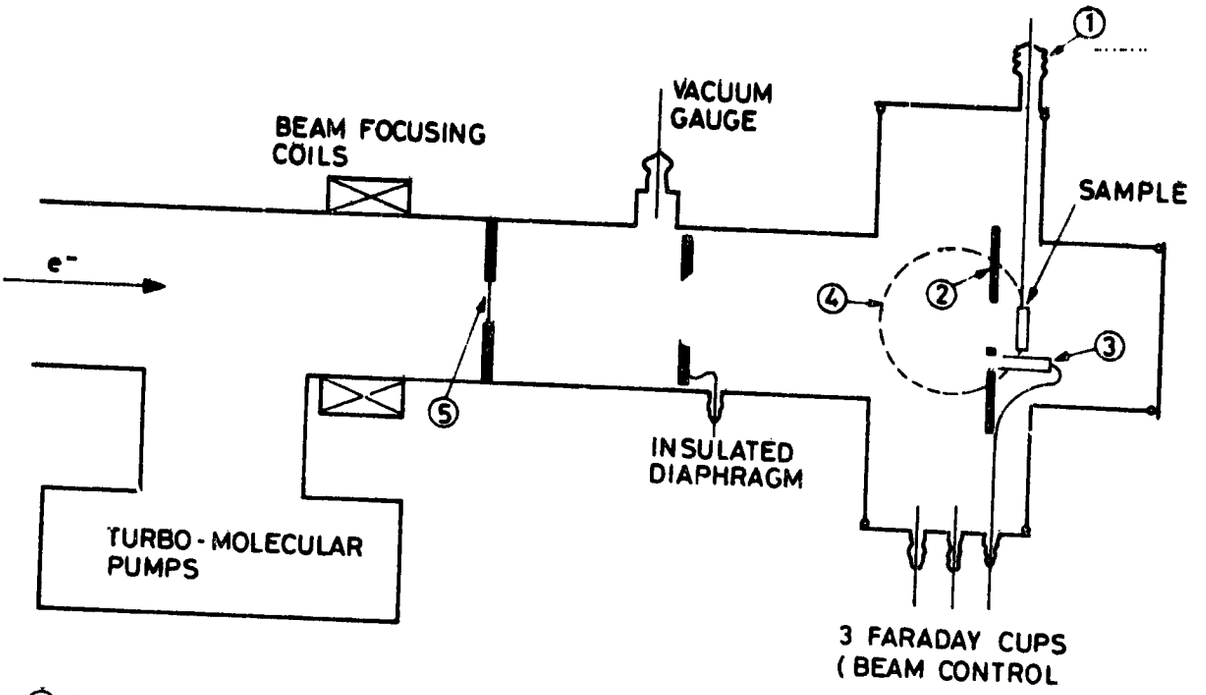

FIG. 1 EXPERIMENTAL SET-UP

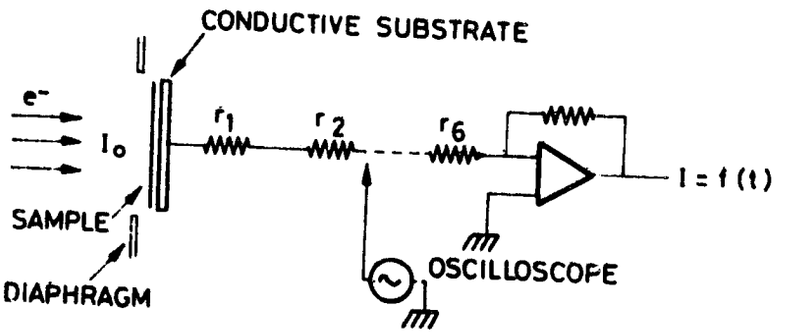

FIG. 2 MEASUREMENT SYSTEM

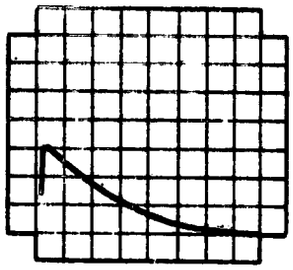

AFTER 21H
IRRADIATION

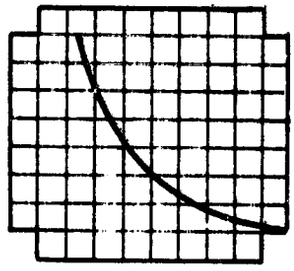

AFTER 26H
IRRADIATION

OSR
MIRRORS 20 x 20 (9)
30 keV - 2 nA/cm^2
50 V/cm , 100 µs/cm
$R = \frac{110}{11000}$

FIG.3 A AND B TYPICAL VOLTAGE PULSES

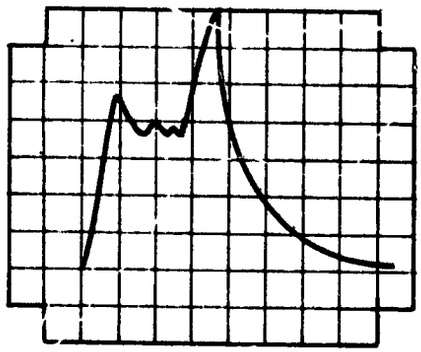

OSR
MIRRORS 20x20 (9)
30 keV - 2 nA/cm^2
5 A / DIV.
50ns / DIV.

FIG.3 C A TYPICAL DISCHARGE CURRENT PULSE

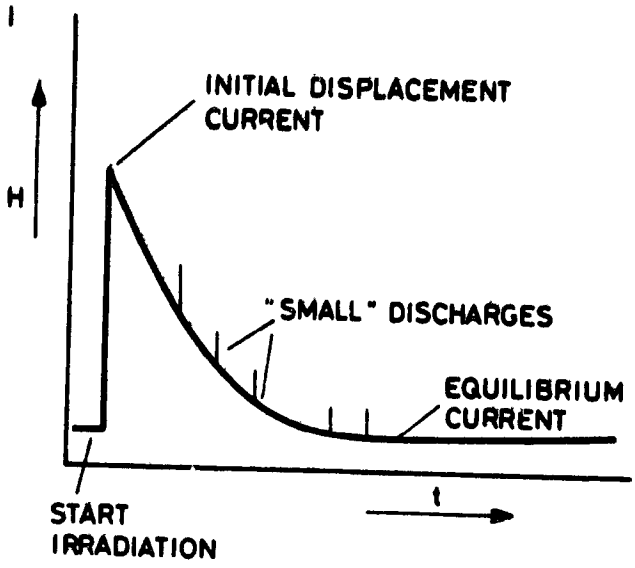

FIG. 4A CASE A

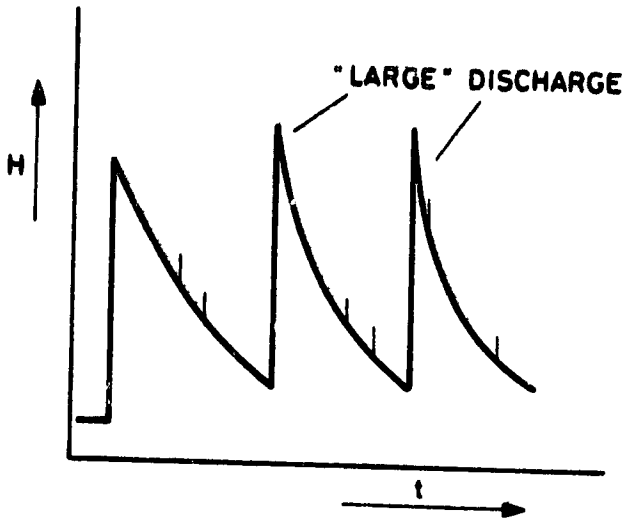

FIG. 4B CASE B

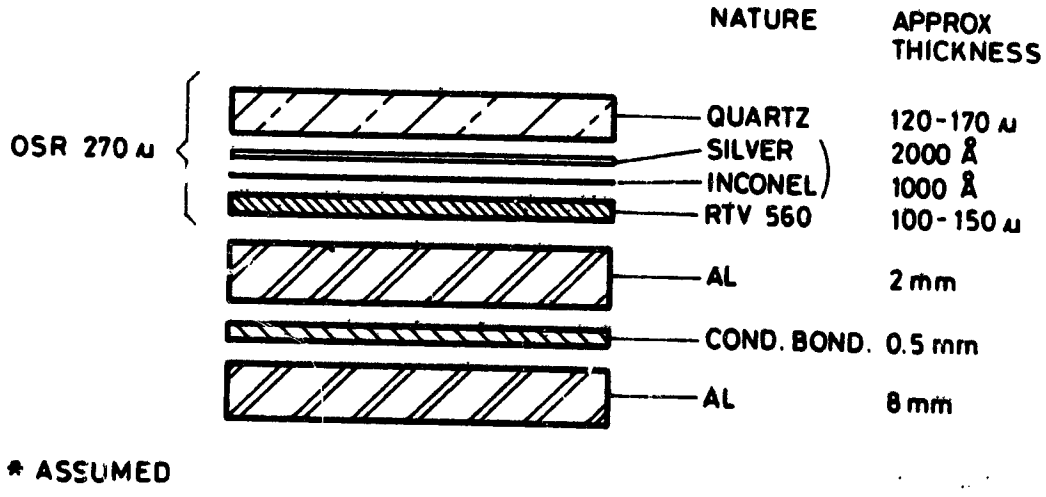

FIG. 5 NON-CONDUCTIVE OSR - NON-CONDUCTIVE ADHESIVE

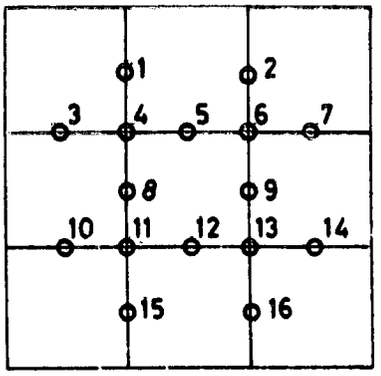

FIG.6 PRE-DETERMINED EXAMINATION POINTS

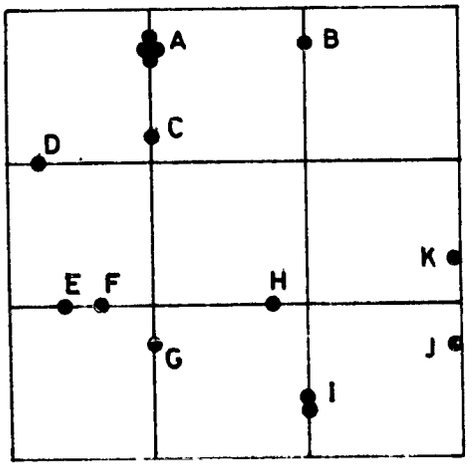

FIG.7 DEGRADED AREAS

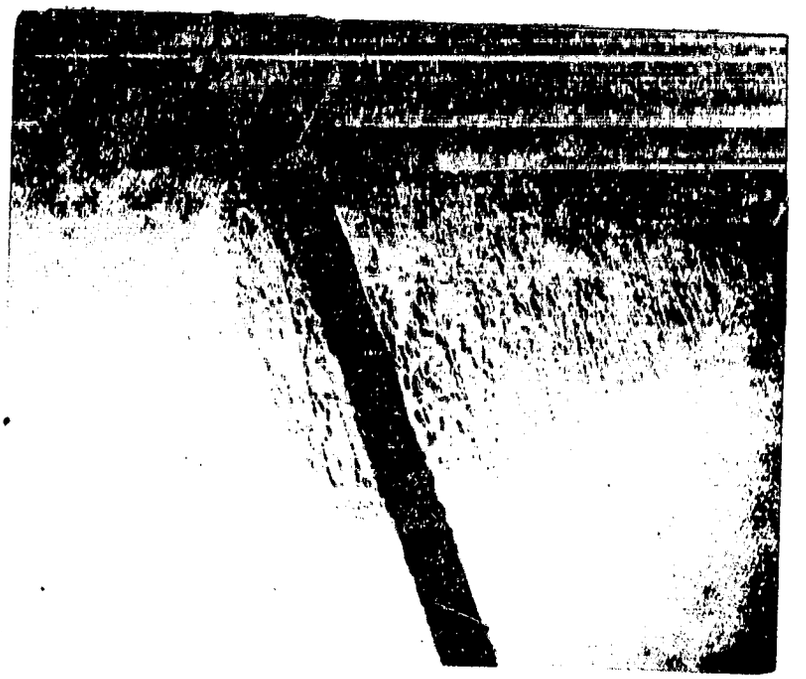

FIG.8 DEFECT AT POINT H (x30)

FIG.9 SAME DEFECT AS IN FIG.8 BUT AT HIGHER MAGNIFICATION (x 300)

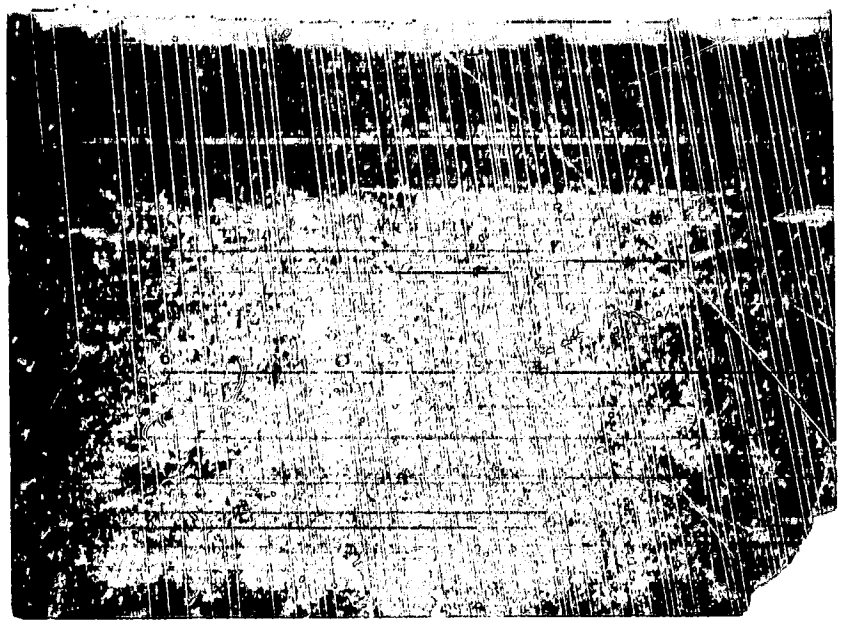

FIG.10 BREAKDOWN CREATED BY HF CHANGE IN SILVER LAYER

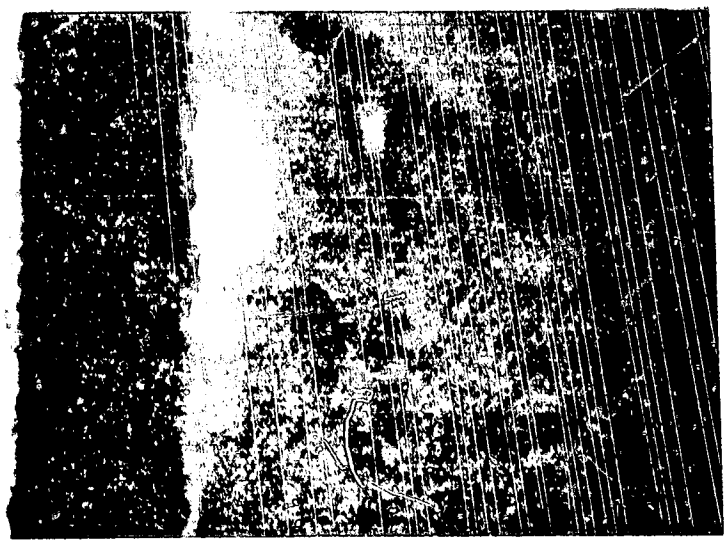

FIG.11 BREAKDOWN IN THE QUARTZ ITSELF TOP LAYER

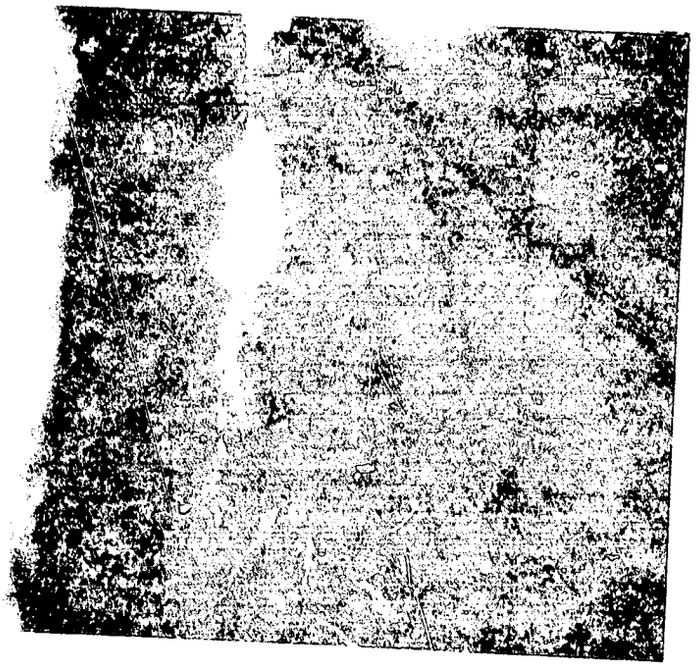

FIG.12 AS FIG.11 BUT SHOWING BOTTOM LAYER

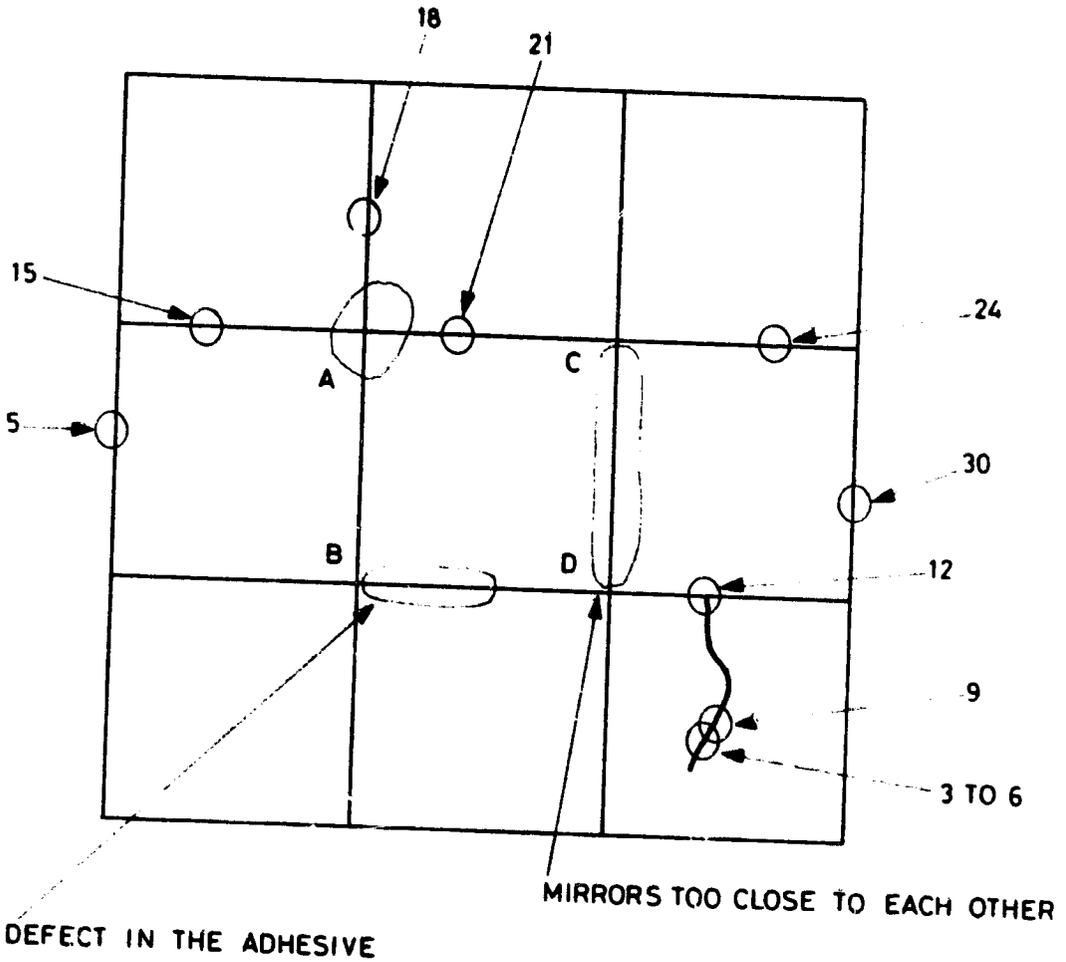

FIG. 13 DEGRADED AREAS ON OCLI OSR'S WITH CONDUCTIVE ADHESIVE

FIG.14 DEFECT IN THE SILVER LAYER (x125)

FIG.15 DEFECT IN PREVIOUSLY CRACKED OSR

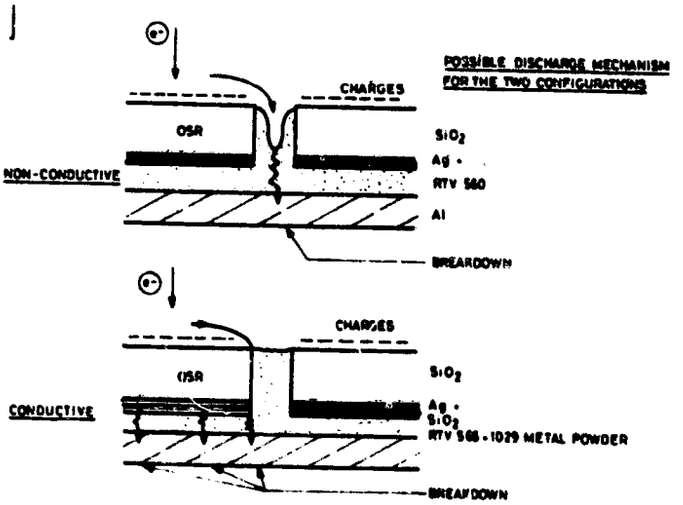

FIG.16 POSSIBLE DISCHARGE MECHANISMS IN OSR'S

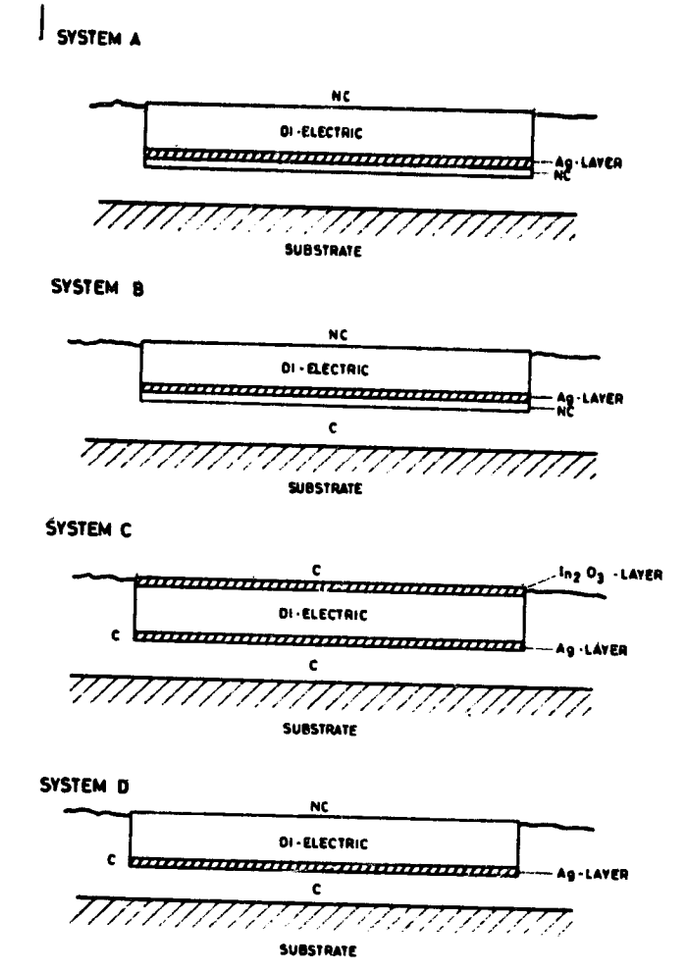

FIG. 17 TESTED SYSTEMS

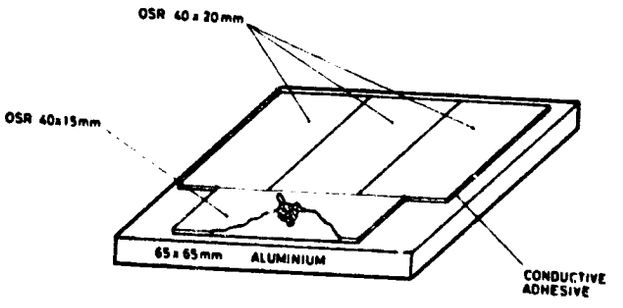

FIG. 18 CONDUCTIVE PPE OSR WITH CONDUCTIVE ADHESIVE

D43

N79-24044

MODEL FOR BREAKDOWN PROCESS IN DIELECTRIC DISCHARGES*

Roland Leadon
JAYCOR

Jason Wilkenfeld
IRT Corporation

ABSTRACT

A heuristic model is presented to explain the blowoff of charge during an electron-induced dielectric discharge. It is proposed that blowoff of charge is not an independent breakdown mechanism but is a consequence of a breakdown initiated by a punchthrough or a flashover. As the trapped charge funnels toward the punchthrough or flashover point, the $\tilde{v} \times \tilde{B}$ force on the moving electrons and the local electric field between the trapped charge and the free surface of the dielectric force electrons outward. Part of the moving charge goes directly to the substrate but the remainder breaks through the surface of the dielectric near the breakdown point, which is weakened by I^2R heating, and escapes from the dielectric. The discharge time is assumed to be governed by an LC time constant where L is the inductance of the electrons flowing in the branches of the Lichtenberg figures at an electron range below the irradiated surface and C is the capacitance between the trapped electrons and the substrate for the discharged area. Experiments are proposed to verify that blowoff is a consequence of punchthrough or flashover and to test the assumed relation for the discharge time.

INTRODUCTION

During the discharge of a thin dielectric over a grounded conducting substrate, it has been noted that the current through the ground lead during the discharge corresponds to electrons flowing from ground to the substrate (references 1,2,3,4,5). This sign of the return current is consistent with electrons being blown off the dielectric surface during the discharge. This outward emission of electrons, and possibly even ions, during discharges has also been observed directly (references 2,5). The amount of charge that is emitted outward in a typical discharge has been measured to be about 50 percent of the trapped charge that is lost in the discharge, as measured by the change in the surface potential (references 1,5). The experimental evidence also indicates that breakdowns appear to start at localized points on the dielectric, and the trapped charge at an electron range below the irradiated surface flows toward the breakdown point in Lichtenberg trees that form in the plane of the trapped charge (reference 5).

In order to understand the existing data, to plan additional logical experiments, and to make reasonable predictions of the coupling of discharges into

* Work sponsored by Defense Nuclear Agency and Space and Missile Systems Organization.

satellite systems, it is necessary to have a reasonably accurate model of the discharge process. Some of the features that a complete discharge model should contain are the discharge mode (punchthrough, flashover, blowoff); the initiation, spreading, and quenching mechanisms for the discharge current distribution; the total charge released, pulse width, and peak current as a function of the discharge area; and the effect of sample material, size, and boundaries in determining the details of the discharge.

Thusfar there has been relatively little published work which attempts to model the breakdown process for spacecraft charging conditions. At a previous Spacecraft Charging Conference, Meulenberg presented a model for the blowoff of charge during a discharge which relied on a high electric field between the trapped electrons and the surface of the dielectric, which was assumed to have a thin layer of positive charge due to the high surface rate of secondary emission (reference 4). Unfortunately this model is basically one-dimensional and does not seem to be consistent with the observation that at least part of the breakdown process involves charge funneling toward one discharge point. More recently, Sellen and Inouye have proposed a mechanism for the initiation and propagation of a dielectric surface discharge based on a propagating surface wave and secondary electron multiplication on the surface of the dielectric (reference 6). Other attempts to characterize the discharge parameters have been mainly empirical curve fitting of experimental peak currents and pulse widths versus discharge area (reference 7). While such empirical relations can be useful for some engineering applications, they usually give little information on the basic physical processes in the discharge and can even lead to serious errors if extrapolations are attempted well beyond the range of the experimental parameters and/or if data from different experimental conditions or materials are indiscriminantly mixed together.

In the present paper, a model is proposed which postulates mechanisms for the initiation and the spreading of the discharge, the blowoff of charge, the maximum charge release per unit area, and the variation of pulse width with sample area and thickness. It does not contain specific details on the effects of sample boundaries or the discharge quenching (area limiting) mechanisms, but it probably contains the ingredients for the area-limiting mechanism if the basic physical parameters could be accurately determined. Experiments are proposed which would verify that blowoff is a consequence of punchthrough or flashover and which would measure the punchthrough current and the variation of discharge time with the sample area and thickness.

PROPOSED MODEL

In many of the discussions of dielectric discharge, three different independent breakdown mechanisms are assumed or implied — punchthrough, flashover, and blowoff. The main thrust of the present paper is that blowoff is not an independent breakdown mechanism but is a consequence of a breakdown that is initiated either by a punchthrough or a flashover. It is proposed that all breakdowns on thin dielectrics with conducting substrates are initiated either by punchthrough of the trapped electrons through the bulk of the dielectric or by flashover of the trapped electrons to a conducting contact on or near the boundaries of the dielectric.

When a punchthrough or flashover process is initiated, the high conductivity region near the breakdown point causes the ground potential of the conductor to be extended to a local point in the plane of the trapped electrons inside the dielectric. Positive image charge accumulates at this point and causes a large electric field in the plane of the trapped electrons which pulls the trapped electrons from their traps. These previously trapped electrons then flow in the trapping plane toward the breakdown point, and the discharge area spreads out as more and more of the trapped charge moves toward the discharge point. The exact mechanism for spreading of the discharge area is not clear, but perhaps the position of the ground potential moves outward from the breakdown point in the plane of the trapped charge and is always close to the electrons that are still trapped.

Initially, the trapped charge that moves toward the discharge point goes directly to the substrate, either via the punchthrough path or by flashover to a ground contact that is connected to the substrate. Because the samples of interest are very thin, this initial flow of charge directly to the substrate causes negligible return current in the ground lead. As the electrons in the trapped layer and the positive image charges in the substrate move toward the breakdown point, a magnetic field is created between the moving electrons in the dielectric and the substrate. The resulting $\tilde{v} \times \tilde{B}$ force on the electrons is in the direction to force the electrons toward the surface of the dielectric. The geometry of the situation before and during a bulk punchthrough is illustrated in figure 1. The magnitude of the $\tilde{v} \times \tilde{B}$ force in a typical discharge can be estimated by the following calculation. Assume that a uniformly charged circular sample with the radius of 10 cm breaks down at the center of the sample when the trapped charge has a density of $\sigma = 2 \times 10^{-7}$ coul/cm^2. ($E \simeq 2 \times 10^6$ V/cm through the sample, which is typical of the breakdown strength of spacecraft dielectrics.) If the total trapped charge ($Q = \pi r^2 \sigma = 628 \times 10^{-7}$ coul) is released in 10 ns, the peak current is about I = 6280 A. At a distance of 0.1 cm from the punchthrough point, the magnetic field due to the current I is

$$H = \frac{I}{2\pi(0.001\ \text{m})} = 10^6\ \text{A/m}$$

Using an electron velocity of $\tilde{v}$ = 10 cm/10 ns = 10^9 cm/sec, the equivalent electric field due to the $\tilde{v} \times \tilde{B}$ force is

$$E = \mu_o\, v \times H = 4\pi \times 10^{-7}(\text{h/m})(10^7 \text{m/sec})(10^6\ \text{A/m})(10^{-2}\ \text{m/cm})$$

$$\simeq 1.2 \times 10^5\ \text{V/cm}$$

The electric field from the trapped charge to the surface of the dielectric due to the Meulenberg effect also forces the electrons toward the surface of the dielectric. The magnitude of this field has not been measured and its theoretical magnitude is uncertain due to uncertainties in the amount of radiation-induced conductivity. In the region of the breakdown, the high current density increases the I^2R heating and weakens the dielectric sufficiently so that the $\tilde{v} \times \tilde{B}$ force, which is maximum close to the punchthrough point, and the Meulenberg electric field can force some of the electrons through the surface of the dielectric. Once the electrons break through the surface, the

negative surface potential, which usually exists on an electron-irradiated dielectric, forces the emitted electrons further away from the dielectric. The net result is blowoff of electrons shortly after the initiation of the punch-through or flashover breakdown. This blowoff of charges causes an approximately equal return current in the ground lead, in contrast to the negligible return current due to the direct punchthrough or flashover currents. The maximum amount of charge that can be released in one discharge is the amount of charge required to produce the initial breakdown field, which is determined by the breakdown strength of the material or the flashover voltage, which is geometry dependent.

It is also proposed that the duration of the discharge pulse is governed by an LC time constant where L is the inductance of the electrons flowing in the Lichtenberg figures in the plane of the trapped electrons toward the breakdown point and C is the capacitance between the trapped electrons and the substrate for the discharge area, A. The inductance of the Lichtenberg trees is estimated to be considerably larger than the inductance of a uniform sheet of charge moving toward one punchthrough point. Since C is proportional to A, and L probably varies as a power of A less than 0.5, the discharge pulse width should go as A to a power somewhat greater than 0.5. Moreover, since C depends inversely on the thickness of a dielectric and L has only a logarithmic dependence on the distance from the Lichtenberg trees to their images in the substrate, the discharge pulse width should vary approximately as the dielectric thickness to the power (-0.5).

POSSIBLE VERIFICATION EXPERIMENTS

The following proposed experiments should clearly demonstrate whether or not blowoff of charge is a consequence of punchthrough or flashover and also provide repeatable data to verify the variation of pulse width with sample area and thickness. The experimental setup is illustrated in figure 2. A thin dielectric with a grounded conducting substrate is irradiated as in most discharge experiments with low energy electrons (≈20 keV), which typifies the surface charging component of the space electron environment. The edges of the sample would be shielded to prevent edge breakdown or the electron beam could be rastered to cover only the central portion of the sample. The difference between the present and previous discharge experiments is that a small area of the substrate is removed and a conducting stylus is inserted a slight ways into the backside of the dielectric through the area where the substrate was removed. The stylus is connected to the substrate by a lead with minimum inductance that is instrumented to measure transient currents. This lead has a switch that can be remotely controlled.

In the first experiments, the switch between the stylus and the substrate would be closed, and the sample would be irradiated with electrons until a spontaneous breakdown occurred. Presumably this breakdown would be a punch-through from the trapped electrons to the stylus due to the enhanced electric fields around the point of the stylus when it is grounded. It is recognized that the threshold potential for this breakdown should be less than the potential for bulk punchthrough without the stylus. However, once the punch-through discharge is initiated, it is felt that the dynamics of the discharge should be similar with and without the stylus. In this experiment, the punch-

through current time history will be measured directly through the stylus lead. Also, the occurrence of blowoff can be inferred from the current through the ground lead and by direct measurements with one or more fast Faraday cups and possibly a charged particle analyser. If the present model is correct, a blowoff of charge should occur more-or-less simultaneously with the measured punchthrough. The sum of the punchthrough charge and the blowoff charge (as measured most accurately by the current through the ground lead) should agree with the total charge lost in the discharge, as measured by the change in the sample surface potential.

Even if a blowoff of charge is observed with every punchthrough, it could be argued that this was just coincidence and that blowoff was still an independent discharge mechanism. To investigate this possibility further, the experiments would be repeated, except that the switch from the stylus to the substrate would be open while the sample was irradiated to a slightly larger fluence than was required above to cause discharge with the switch closed during the irradiation. Since electric field lines do not concentrate around the stylus with the switch open, the sample will presumably not break down by punchthrough at this fluence with the switch open. Also, presumably a blowoff discharge will not occur. When the desired fluence has been delivered to the sample, the electron beam would be turned off and then the switch from the stylus would be closed. If the deposited fluence was somewhat greater than the fluence which caused a punchthrough with the stylus closed during the irradiation, closing the switch should induce a punchthrough. Also, if the present model is correct, a blowoff of charge should also occur almost simultaneously with the punchthrough. This sequence of events would demonstrate conclusively that the blowoff followed as a result of the punchthrough. It would also show that the electron plasma from the electron gun and the secondary emission was not essential to a blowoff discharge. Experiments of this kind are presently being designed, but results are not available as yet.

Another advantage of the stylus-stimulated discharges is that it should be possible to obtain more consistent and repeatable data and thus to determine more accurately the variation of discharge time and peak current with sample parameters, such as area and thickness. In these experiments, the location of the discharge point will be controlled relative to the nearest boundaries of the sample. Without the stylus, the discharges can occur randomly over the surface of the sample, depending on where the discharge channels are initiated, so the distance to the sample edges will vary from discharge to discharge, which could noticeably affect the discharge characteristics. In order to check the predicted (-0.5) power dependence of discharge time on sample thickness, one has to be able to distinguish factors-of-2 differences in discharge time for a realistic four-fold variation in sample thickness.

Another prediction of the model is that the ratio of blowoff charge to total charge lost during a discharge could vary with the energy of the electron beam. This result would occur if the probability that the total Lorentz force $e(\vec{E} + \vec{v} \times \vec{B})$ can force the electrons through the surface depends on the depth of the trapped electrons below the surface. For example, for higher energy electrons which are trapped closer to the substrate than the irradiated surface, most of the discharge would probably go directly to the substrate and very little would be blown off. Since the return charge from ground is essentially

proportional to the blowoff charge, changing the fraction of the blowoff could affect the interpretation of peak return currents as a function of sample area when data for different beam energies are compared. Thus, until this dependence is determined, caution should be used when comparing data for different beam energies.

A final advantage of the stylus-stimulated discharges is that the "true" discharge time would be measured directly. The pulse width of the return current from ground, which is the basis for the previous estimates of the discharge time, is always the slower of three characteristic blowoff discharge times — the time for the charge to just escape from the dielectric surface, the transit time for the blowoff electrons to reach the walls of the test chamber, and the circuit time constant of the sample, ground lead, and measuring system. The last two times are dependent on the experimental setup and chamber geometry and are not representative of the basic discharge process. Moreover, the transit time should be essentially independent of sample size. Thus, if any measured ground-lead currents are limited by transit time, it is misleading to draw a single curve through such data points and other data points where the discharge time varies significantly with area.

SUMMARY

It is proposed that blowoff of charge from electron-charged dielectric is a consequence of a punchthrough or flashover discharge. According to the model, the physical process which forces the electrons outward through the dielectric surface is the $\tilde{v} \times \tilde{B}$ and electric field forces on the electrons. The model predicts a variation of discharge time on the sample area and thickness and a possible dependence of the return current from ground during a discharge on the energy of the electron beam. Stylus-stimulated discharges would provide a direct measurement of the punchthrough current time history and would verify whether or not blowoff occurs only as a result of punchthrough or flashover.

REFERENCES

1. N. J. Stevens, R. R. Lovell, and V. Gore, "Spacecraft-Charging Investigation for the CTS Project," Progress in Astronautics and Aeronautics, Vol. 47, 1976, pg 263.

2. R. C. Adams and J. E. Nanevicz, "Spacecraft-Charging Studies of Voltage Breakdown Processes on Spacecraft Thermal Control Mirrors," Progress in Astronautics and Aeronautics, Vol. 47, 1976, pg 225.

3. K. G. Balmain, M. Orszag, and P. Kremer, "Surface Discharges on Spacecraft Dielectrics in a Scanning Electron Microscope," Progress in Astronautics and Aeronautics, Vol. 47, 1976, pg 213.

4. A. Meulenberg, Jr., "Evidence for a New Discharge Mechanism for Dielectrics in a Plasma," Progress in Astronautics and Aeronautics, Vol. 47, 1976, pg 287.

5. E. J. Yadlowsky, "Laboratory Simulation of Irradiation-Induced Dielectric Breakdown in Spacecraft Charging," Annual Status Report under NASA Research Grant No. NSG-3145, with Colorado State University, May 10, 1978.

6. G. T. Inouye and J. M. Sellen, Jr., "A Proposed Mechanism for the Initiation and Propagation of Dielectric Surface Discharges," Proc. of 1978 IES Symposium on the Effects of the Ionosphere on Space and Terrestrial Systems.

7. K. G Balmain, P. C. Kremer, and M. Cuchanski, "Charged-Area Effects on Spacecraft Dielectric Arc Discharges," Proc. of 1978 IES Symposium on the Effect of the Ionosphere on Space and Terrestrial Systems.

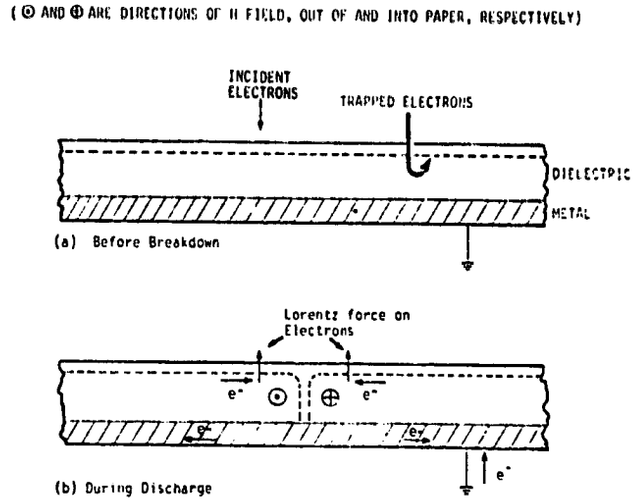

FIGURE 1. ILLUSTRATION OF BREAKDOWN MECHANISM

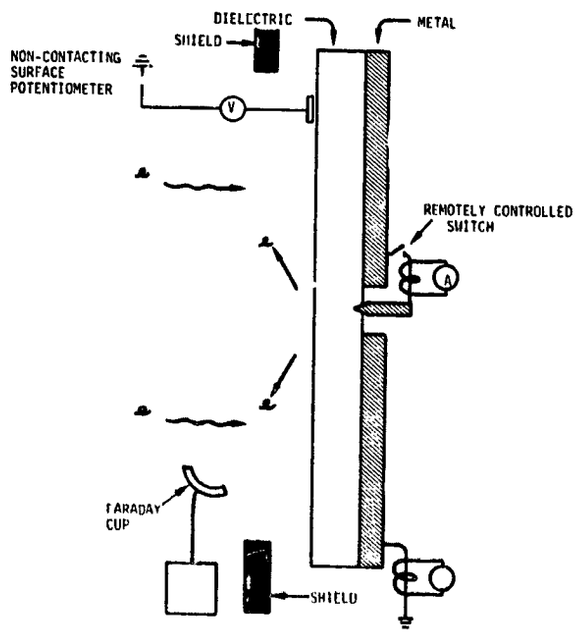

FIGURE 2. EXPERIMENTAL SETUP FOR STYLUS – STIMULATED DISCHARGES

N79-24045

PARAMETER DEPENDENCE OF EQUILIBRIUM CHARGING POTENTIALS

Paul K. Suh and Michael C. Stauber

Grumman Aerospace Corporation

ABSTRACT

Equilibrium surface potentials for slab configurations (representative e.g. of a large solar power satellite) are determined under extensive parametric variations of material, solar exposure and substorm characteristics. The results can guide the material selection and design of large space systems to minimize dielectric breakdowns and reduce parasitic leakage currents on SPS.

INTRODUCTION

Future large space systems, such as a photovoltaic solar power system or a deployable antenna, will be of low-density construction ($\sim 10^{-5}$ g/cm^3), employing various light-weight materials. Among the candidate materials being discussed the emphasis is on polymeric materials (Kapton, Teflon, etc) and composites (glass or graphite fibers in an epoxy matrix). Such dielectric materials may be expected to undergo a substantial evolution in their physical properties, including electrical characteristics, as a result of prolonged space environmental exposure. The electrical properties, in particular, may be strongly sensitive to environmental conditions (e.g. temperature), even at the outset, and in some cases (e.g. for composites) remain to be more fully characterized.

This uncertainty and variability in relevant material responses is a major complicating factor in the prediction of spacecraft charging effects for an energetic substorm environment, and provides the major impetus for this paper. Namely, the intent is to explore the consequences for the attained equilibrium charging potentials of systematic variations in such material and exposure related quantities as photoelectric current, electron backscattering yield, secondary electron yield from proton and electron bombardment, material resistivity, and substorm plasma temperature. To identify the impact of such variations in their full context, the analyses include both primary electron and proton currents, together with all their secondary currents, as well as the resistivity-dependent bulk leakage current. The importance of considering resistivity variations can be gauged, for example, from Table 1, in which the bulk resistivity of Kapton and several glasses is seen to change by 4-5 orders of magnitude in traversing the temperature range 25 to 200°C.

The method of analysis utilizes (one-dimensional) Langmuir probe theory, applied to the self-consistent search for the equilibrated surface potential. The geometry employed generally is that of a flat slab, although some exploration is also made of a spherical or cylindrical collection surface. The slab configuration, in particular, is examined under conditions of both single and double sided exposure to the plasma charging currents, with one-sided solar

exposure in some cases. For single-sided plasma exposure, the unexposed side is held uniformly at a reference potential. The case, where the shielded side carries an impressed potential gradient and floats to yield a zero net current to the exposed surface, corresponds to the inner cover slide surface of a solar array and is examined in a companion paper (Paper III-7, this conference).

It is noted that the shadowed slab side exposed to a substorm plasma can develop high negative potentials (tens of kilovolts) that may easily exceed the dielectric breakdown strength of thin sheets (see Table 1). The analyses seek to identify possible adjustments in materials parameters that may prevent such exceedances.

It is also realized that the analysis approach employed has limited validity; in particular it is not adequate for describing conditions near spacecraft edges, nor does it consider the perturbation of particle trajectories that may lead to differential charging. Nonetheless, it is felt that these shortcomings do not seriously distort the influence of the various material responses on the charging process that is explored in this work.

PLASMA ORIGINATED CURRENTS

The large spacecraft is approximated by an extended slab, and a one-dimensional Maxwell velocity distribution

$$f(v) = \sqrt{\frac{m}{2\pi kT}} \exp\left(-\frac{mv^2}{2kT}\right) \tag{1}$$

is assumed for the substorm plasma particles. The spacecraft surface potential V_s modifies the impinging charged particle distribution.

The incident plasma electron current is thus approximated (Ref. 1) by

$$\begin{aligned} J_e &= J_o \exp\left(-\frac{\varepsilon_s}{kT}\right) \text{ for } V_s < 0 \\ &= J_o\left(1 + \frac{\varepsilon_s}{kT}\right)^g \text{ for } V_s > 0 \end{aligned} \tag{2}$$

where the experimental values for the J_o corresponding to $\sqrt{\frac{kT}{2\pi m}}\, N e$ will be used. Here, $\varepsilon_s = e\,|\,V_s|$, and N and e are, respectively, the electron density and charge. All other notations follow the conventional representation.

The exponential geometric parameter g ranges from 0 for the flat configuration discussed in this paper to 1 for a spherical configuration. Due to the comparatively large Debye length coupled with possible edge effects, the effective g may have a nonvanishing value. Note, however, that the geometric effect can in general be appreciable when $|eV_s|/kT \gtrsim 1$.

For the incident plasma proton current $J_p = \xi J_o$, the experimental value of $\xi \approx 1/40$ is adopted. The J_p augmented by the effect of its secondary electron current $J_{ps} = \phi J_p$ (where $\phi \approx 2.5$ for $V_s < 0$) can become the dominant charging current when the surface potential becomes highly negative. The effect of the surface potential polarity for J_p is opposite to that for electrons as given in Eq. (2).

Adopting the impact yield parameter (Ref. 2) for electrons of energy $\varepsilon_1 = \frac{mV^2}{2}$, i.e.,

$$\delta = \frac{7.4\ \delta_m}{\varepsilon_m} (\varepsilon_1 + eV_s) \exp\left[-2\sqrt{\frac{\varepsilon_1 + eV_s}{\varepsilon_m}}\right] \tag{3}$$

that gives the maximum yield δ_m at energy ε_m, the secondary electron current is approximated by

$$J_s = 2 J_1 J_o F \tag{4}$$

where $$J_1 = 7.4\ \delta_m \frac{kT}{\varepsilon_m} \exp\left(\frac{eV_s}{kT} + \frac{kT}{\varepsilon_m}\right)$$

Values of $\delta_m \approx 3$ and $\varepsilon_m \approx 0.3$ KeV are adopted (Ref. 3) and

$$F = 3!i^3 \sqrt{\frac{\pi}{2}}\, \mathrm{erfc}(y_1) \text{ for } V_s < 0$$

$$= (3!i^3 + (3y_2)2!i^2 + (3y_2^2)i + y_2^3) \sqrt{\frac{\pi}{2}}\, \mathrm{erfc}(y_5) \text{ for } V_s > 0$$

where $y_1 = \sqrt{\frac{kT}{\varepsilon_m}}$, $y_2 = \sqrt{\frac{\varepsilon_s}{kT}}$, and $y_5 = y_1 + y_2$

The backscattered electrons, on the other hand, constitute the high energy portion of the scattered electron spectrum. Since available data here are scant, the following simple approximation, using the backscattering yield parameter β, is adopted:

$$J_{bs} = \beta J_o \exp\left(-\frac{\varepsilon_s}{kT}\right) \text{ for } V_s < 0$$

$$= \beta J_o \left(1 + \frac{\varepsilon_s}{kT}\right)^6 \exp\left(-\frac{\varepsilon_s}{kT}\right) \text{ for } V_s > 0 \tag{5}$$

This expression often permits separating the backscattering effect out in the analysis, so that a straightforward reassessment of its contribution can be made as more data become available.

The leakage current is approximated by

$$J_\ell = \Delta V_s / R \tag{6}$$

where $R = \rho \ell$ with ρ and ℓ representing, respectively the volume resistivity and the slab width. Currents as well as all associated quantities here are given per unit area (cm^2).

PHOTOELECTRON YIELDS IN THE SPACE ENVIRONMENT

The photoelectron yield depends on the material work function and the width and peak of its energy distribution on the solar photon energy spectrum. Spacecraft surfaces in the space environment are, however, quickly contaminated and the surface contamination tends to cause inelastic scattering of the photo-excited electrons (Ref. 4).

The photelectron spectrum from such metals as gold, aluminium, and stainless steel in the space environment was observed to have an energy distribution similar to that for many nonmetals (for example graphite). The photoelectron energy distribution in general has a Gaussian form, peaking at 1~2 eV and tapering off rapidly toward higher energies.

In the absence of a comprehensive theory, on the basis of observed data the photoelectron energy E distribution (normalized to 1) produced by a photon of energy ω is determined by

$$N(E, \omega) = \frac{2h(\omega)\, E}{1-\exp\left[-h(\omega)(\omega - \varphi)^2\right]} \exp\left[-h(\omega)E^2\right] \tag{7}$$

where φ is the work function.

Here $h(\omega) = \dfrac{1}{2E_m^2(\omega)}$, with the approximation

$$E_m(\omega) = E_1 \left[1 - \exp\left(\sum_{n=1}^{4} \sigma_n \omega^n\right)\right] \tag{8}$$

for the range of $4.5 < \omega \lesssim 30$ eV. The $E_m(\omega) \to E_1$ toward the upper ω domain and represents the energy E at which $N(E, \omega)$ peaks.

Values for σ_n and E_1, derived from empirical data, are

	Aluminium	Steel	Nonmetal
σ_1	2.84367×10^{-2}	1.45236×10^{-2}	0.292431
σ_2	-1.12782×10^{-2}	2.59762×10^{-3}	-8.82673×10^{-2}
σ_3	1.32354×10^{-3}	-1.45428×10^{-3}	6.29027×10^{-3}
σ_4	-7.03183×10^{-5}	3.56235×10^{-5}	-1.59182×10^{-4}
E_1 (eV)	5	2	3

The photoelectron yield per incident photon of energy ω is approximated by

$$Y(\omega) = k\omega^p \exp\left(\sum_{n=0}^{4} k_n \omega^n\right) \quad \text{for } 5 \lesssim \omega < 17 \text{ eV}$$

$$= 0.193 \quad \text{for } \omega \gtrsim 17 \text{ eV} \tag{9}$$

where

$k = 2.456 \times 10^6$ $\quad p = -249.874$

$k_1 = 104.388$ $\quad k_2 = -7.20837$

$k_3 = 0.276707$ $\quad k_4 = -4.30132 \times 10^{-3}$

Since the shape of the yields is similar for most of the metal as well as nonmetal cases, as discussed above, any desired adjustment can be made by modifying the parameter k. The photoelectron yield energy distribution is now determined by

$$Y(E, \omega) = Y(\omega)\, N(E,\omega) \tag{10}$$

The continuous and discrete solar photon intensity distributions (in photons/cm^2·sec·eV) are approximated by

$$I_{cont}(\omega) = 1.3 \times 10^{19} \exp(-1.985\,\omega) \quad \text{for } 4 < \omega \lesssim 11 \text{ eV}$$

$$= 8 \times 10^9 \quad \text{for } 11 \lesssim \omega \lesssim 15 \text{ eV} \tag{11}$$

$$= 1.2 \times 10^{9} \qquad \text{for } 15 \lesssim \omega < 30 \text{ eV}$$

$$I_{disc} = 2 \times 10^{11} \qquad \text{at } \omega \approx 10.2 \text{ eV}$$

The total photoelectron energy distribution in $(cm^2 \text{ sec eV})^{-1}$ then is

$$Y(E) = \int_{E+\phi}^{\infty} I(\omega)Y(\omega)N(E,\omega)\, d\omega \tag{12}$$

When the spacecraft surface potential V_s is positive, photoelectrons require an energy $E > eV_s$ to overcome the potential barrier. The photoelectron current $\hat{J}_{pe}$ as a function of V_s and with a cut-off at $E \approx 30$ eV, i.e.,

$$\hat{J}_{pe}(V_s) \approx \int_{eV_s}^{30} eY(E)\, dE \tag{13}$$

$$\approx \int eI(\omega)Y(\omega)\, \frac{\exp[-h(eV_s)^2] - \exp[-h(30-\phi)^2]}{1 - \exp[-h(\omega - \phi)^2]}\, d\omega$$

is shown in Fig. 1. The $\hat{J}_{pe}$ is nearly constant up to 1 eV, beyond which it rapidly becomes negligible as the positive surface potential increases to a few eV.

MODIFIED SECONDARY ELECTRON YIELD

The emission mechanism for secondary electrons by electron bombardment is similar to the case of photoelectrons. The shapes of the electron energy spectra in both cases are comparable with more than 80% of the secondaries emitted at energies below 20 eV (Ref. 5). As the surface potential turns positive, the secondary electron current thus becomes sensitively dependent on the energy distribution, due to the potential barrier.

Therefore, from Eq. (4), the following simple approximation is adopted for the electron-induced secondary electron energy spectrum,

$$J_{es}(\varepsilon, E) \approx 2J_1 J_o F\, b^2 E \exp(-bE) \tag{14}$$

where $b \approx 0.3\ (eV)^{-1}$ and $\varepsilon = kT$. The integrated secondary electron current modified by positive surface potential V_s is

$$\hat{J}_s(\varepsilon, V_s) \approx 2J_1 J_o F \int_{eV_s}^{\varepsilon} b^2 E \exp(-bE)dE \approx J_o \hat{J}_{sec} \quad (15)$$

where, because of $be \gg 1$,

$$\hat{J}_{sec} \approx 2J_1 F(1 + beV_s)\exp(-beV_s)$$

SURFACE POTENTIAL IN THE DARK

As shown in Fig. 2, a spacecraft in the dark is exposed to a substorm, while its inner surface is maintained at the reference potential zero. The exposed surface in the dark becomes negatively charged, with currents being balanced by

$$J_e = J_p + J_{es} + J_{bs} + J_{ps} + J_\ell \quad (16)$$

Here, as modified by the equilibrium surface potential V_s,

$$J_e = J_o \exp\left[-\frac{e|V_s|}{kT}\right] \quad \text{(electron current)}$$

$$J_p = \xi J_o \left[\cdot + \frac{e|V_s|}{kT}\right]g \quad \text{(proton current)}$$

$$J_{bs} = \beta J_e \quad \text{(backscattering current)}$$

$$J_{es} = J_{so} J_e \quad \text{(electron-induced secondary electron current)}$$

$$J_\ell = \frac{|V_s|}{R} \quad \text{(leakage current)}$$

$$J_{ps} = \phi J_p \quad \text{(proton-induced secondary electron current)}$$

where

$$J_{so} = 7.4\,\delta_m \frac{kT}{\varepsilon_m} \exp\left(\frac{kT}{\varepsilon_m}\right)\sqrt{\pi}3!i^3\mathrm{erfc}\left[\sqrt{\frac{kT}{\varepsilon_m}}\right]$$

and $\phi = 1.5$ is adopted for $V_s < 0$.

Observation indicates that, while the energies of the substorm plasma particles are higher than in quiet periods, their currents are reduced. The substorm electron current (in nA/cm^2) adopted in the analysis is approximated (Ref. 6) by

$$J_o = \sum_{n=0}^{4} A_n \varepsilon^n \qquad \text{for } 2 < \varepsilon \lesssim 12 \text{ KeV}$$

$$= 0.5 \qquad \text{for } 12 \text{ Kev} < \varepsilon \tag{17}$$

where $A_o = 2.30725$ $\quad A_1 = -0.255535$

$A_2 = -2.34739 \times 10^{-3}$, $\quad A_3 = 1.79609 \times 10^{-3}$

$A_4 = -7.26494 \times 10^{-5}$, $\quad \varepsilon = kT$

Eq. (16) gives

$$\beta = 1 - J_{so} - \left[\xi^*\left(1 + \frac{e|V_s|}{kT}\right)^g + \frac{1}{J_o}\frac{|V_s|}{R} \right] \exp\left(\frac{e|V_s|}{kT}\right) \tag{18}$$

where $\xi^* = \xi(1 + \phi)$. In Fig. 3 A and B, respectively for the cases of $g = 0$ and 1, V_s is shown as function of surface potential β at various values of electron temperature $\varepsilon = kT$ and resistance R.

At $g = 0$, with a backscattering parameter $\beta = 0.2$, for example $V_s \approx$ (-55, -36, -14, -2) KV at $\varepsilon = 25$ KeV, and $V_s \approx$ (-17, -13, -7, -1.2) KV at $\varepsilon = 10$ KeV, respectively for $R = (\infty, 10^{15}, 10^{14}, 10^{13})$ Ω. The corresponding surface potentials V_s at $g = 1$ with the same backscattering parameter $\beta = 0.2$ are V_s = (-33, -27, -13, -2) KV at $\varepsilon = 25$ KeV and V_s = (-10, -9, -6, -1) KV at ε = 10 KeV, respectively, for $R = (\infty, 10^{15}, 10^{14}, 10^{13})$ Ω.

At high values of R, there is a large difference in V_s between the cases $g = 0$ and 1, indicating the possible extent of the geometric dependence of V_s. For the case of $g = \frac{1}{2}$, the corresponding V_s lies close to the midpoint between the values for $g = 0$ and 1. The high energy tail in the plasma electron distribution helps at high R values to support surface voltages considerably higher than the incident electron temperature (especially in the $g = 0$ case).

The relative magnitude of the various currents (in unit of J_e, i.e., $J_i = J_i/J_e$) in the approach to equilibrium is compared in Fig. 4, for example, for the case of $R = 10^{15}$ Ω and $\varepsilon = 15$ KeV. Note that at further higher V_s, the initially insignificant J_p and J_{ps} become increasingly important (especially at $g = 1$), eventually overtaking the other J_i.

The equilibrium reached at $\Sigma J_i = 1$ for $R = (10^{14}, 10^{15})$ Ω, respectively, yields

$$V_s = (-8.6, -15.5)\ \text{KV} \qquad \text{for } g = 1$$

$$V_s = (-9.7, -22)\ \text{KV} \qquad \text{for } g = 0$$

showing an appreciable dependence of V_s on R and g. The strong dependence of V_s on the resistivity is quite significant in view of the fact that R is a sensitive function of temperature (see Table 1) and the surface temperature can undergo large variations.

Also the equilibrium surface potential V_s, if it appears across a thin but high resistance material, may become sufficiently high to exceed the dielectric strengths shown in the Table 1. At low R, where the dielectric acts more like a conductor, the leakage current depresses the surface voltage.

Introducing a multiplier I for the plasma electron current

$$J = I\, J_o \tag{19}$$

the effect of current variation on V_s at $R = 10^{15}$ Ω is shown in Fig. 5 for the case of $g = 0$. At low energy, the effect of varying I is small but becomes important at high energies.

SPACECRAFT POTENTIAL IN THE SUN

As shown in Fig. 6, the spacecraft is exposed to a substorm on the sun illuminated side, while the shadowed side is shielded and held at a reference potential zero. The effective solar intensity is a function of the sun angle θ, causing at large θ a slight modification to the case of spacecraft in the dark discussed previously. The sun exposure at small θ, however, becomes sufficiently strong that the surface potential may become positive.

The low energy electrons (emitted with insufficient vertical velocity) are trapped by the positive potential barrier. Because most of the secondary and photoelectrons are of low energies, a very sensitive balance is established between the surface potential and the currents. The determination of the effective currents ther requires a knowledge of the electron energy distributions.

First, consider the case of $V_s \leq 0$. The surface potential V_s is determined by $J_o - J_{os} - J_p - J_s - J_{pe} - J_{bs} - J_{ps} = 0$, yielding

$$\beta \approx 1 - J_{so} - \left[\xi^* \left(1 + \frac{e\,V_s}{kT}\right)g + \frac{1}{J_o}\frac{|V_s|}{R} + \frac{J_{pe}}{J_o}\right] \exp\left(\frac{e|V_s|}{kT}\right) \qquad (20)$$

For $V_s = 0$, Eq. (20) is reduced, with $\Sigma = 1 - J_{so} - \xi^*$, to

$$\Sigma - \left(\beta + \frac{J_{pe}}{J_o}\right) = 0 \qquad (21)$$

requiring $\Sigma - (\beta + J_{pe}/J_o) \gtrless 0$ for $V_s \lessgtr 0$. Since the Σ (shown in Fig. 7) is independent of J_o, g and R, Eq. (21) itself is independent of g and R.

Since $\Sigma \approx 0.74$ at $\varepsilon = 25$ KeV and 0.49, at $\varepsilon = 10$ KeV, for example (with the backscattering parameter $\beta = 0.2$)

$$J_{pe}/J_o \lesssim 0.54 \text{ at } \varepsilon = 25 \text{ KeV}$$

$$\lesssim 0.29 \text{ at } \varepsilon = 10 \text{ KeV}$$

are required for $V_s \lesssim 0$. With substorm currents $J_o \approx 0.5$ and 0.58 nA/cm^2, respectively, at $\varepsilon = 25$ and 10 KeV,

$$J_{pe} > 0.27 \text{ nA/cm}^2 \text{ at } \varepsilon = 25 \text{ KeV}$$

$$> 0.17 \text{ nA/cm}^2 \text{ at } \varepsilon = 10 \text{ KeV}$$

to charge the spacecraft surface positive.

For the case of $V_s < 0$, the equilibrium surface potential V_s at $R = 10^{15}$ Ω is plotted in Figs. 8A and B as a function of backscattering yield β for $\varepsilon = 25$ and 15 KeV, by varying J_{pe} (in nA/cm^2 at $V_s = 0$). The solid lines here are for the substorm currents J_o of Eq. (17), while the dashed lines are for the doubled substorm current $2J_o$ case [see Eq. (9)].

For $R = 10^{15}$ Ω, there is an appreciable shift in the $\beta - V_s$ curves in going from $g = 1$ to $g = 0$ (i.e., from a sphere to an infinite plane), both at $\varepsilon = 25$ KeV (Fig. 8A) and 15 KeV (Fig. 8B). At $\varepsilon \lesssim 5$ KeV for $R = 10^{15}$ Ω, as well as at $R \lesssim 10^{14}$ for all electron temperatures, however, the shift generally becomes

negligible. For $R \lesssim 10^{11}$ Ω, the surface potential V_s readily turns positive.

For a given R, the effective β as function of V_s gradually becomes smaller as ε is reduced. For small J_{pe} ($\lesssim 0.1$ nA/cm^2), there is substantial latitude for β to keep V_s negative, especially when ε is high. As J_{pe} increases beyond a few tenths of nA/cm^2, however, V_s is likely to turn positive. The $\beta - V_s$ curves rapidly reach a plateau as $|V_s|$ decreases, making the determination of the surface potential as function of β there delicate.

Relative strength of the currents at ε = 15 KeV and $J_{pe} = 0.01$ nA/cm^2 in units of $J_e = J_o \exp(-e|V_s|/kT)$, i.e.,

$$j_i = J_i/J_e$$

are shown in Figs. 9A and B, respectively, for $R = 10^{15}$ and 10^{13} Ω. Note that, especially at $R = 10^{15}$ Ω, all currents are in the same order of magnitude near equilibrium [By coincidence, $j_{pe} \approx j_p(g = 0)$ here].

The shifts in $j_p(g)$ and $j_{ps}(g)$ between the g = 1 and 0 cases are appreciable for $R \gtrsim 10^{15}$ Ω. For $R \lesssim 10^{13}$, the difference in the currents between the g = 1 and 0 cases is small and thus ignored in the diagram.

For $R \gtrsim R_c = O(10^{17}$ Ω), the effect of J_ℓ is negligible and the material behaves as a perfect insulator (i.e., R = ∞). For $R < R_c$, J_ℓ increases steeply toward the equilibrium V_s, and, especially when β is low, J_ℓ becomes significant even at relatively high R. For $R < O(10^9$ Ω), the material practically behaves as a conductor.

When $V_s > 0$, while the primary plasma electrons are accelerated toward the spacecraft, the emitted electrons are retarded by the potential barrier. Because of the low energy of the secondary and photoelectrons, the balancing of the various currents for the positive V_s by

$$J_e + J_\ell - \hat{J}_{pe} - \hat{J}_{es} - J_p - \hat{J}_{bs} - \hat{J}_{ps} = 0 \qquad (22)$$

becomes delicate. Here, $\hat{J}_{pe}$ and $\hat{J}_s$ are given, respectively, in Eqs. (13) and (15), and $\hat{J}_{ps}$ corresponds to $\hat{J}_{es}$ (and $\hat{J}_{bs}$).

Solar incidence here is assumed to be nearly vertical, and the photoelectric current is normalized to approximately 1.5 nA/cm^2 at zero surface potential.

Reduction of the solar intensity with an increased sun-angle may cause the spacecraft to become negatively charged, as discussed above. Because of $|eV_s|/kT \ll 1$ here, possible geometric effects in the electron attraction to the surface are negligible.

For $R = 10^9$ Ω, the J_ℓ becomes significant and increases rapidly with V_s. The equilibrium surface potentials are thus small (V_s = 0.92 V and 0.8 V at KT = 15 KeV, respectively, for the I = 1 and 2 cases), and, in approaching equilibrium, the currents other than J_ℓ are nearly constant.

At low R, the J_ℓ thus becomes the controlling factor in the determination of V_s. The effective V_s as a function of ε and R are shown in Fig. 10, again with $\beta = 0.2$ and $J_{pe}(V_s = 0) = 1.5$ nA/cm^2 (the solid and dotted lines are, respectively, for the I = 1 and 2).

The V_s is not much affected by the variation of R from 10^{11} to 10^{15} Ω. Below 10^{10} Ω, however, decreases in R give rise to a progressively stronger reduction in the effective V_s. Note also that as expected, the V_s for a given R is a decreasing function of average plasma electron energy ε, although the dependence is relatively weak.

SPACECRAFT TOTALLY IMMERSED IN A SUBSTORM

The case of a slab configuration spacecraft totally immersed in a substorm environment in the earth's shadow is similar to that of a spacecraft slab of infinite resistance unilaterally exposed to the substorm in the dark. With sun exposure on one side (see Fig. 11), however, a potential difference develops between the two surfaces.

If the incident solar intensity is weak, due to a large sun angle θ, the two surface potentials V_1 and V_2 remain negative. When the solar exposure becomes sufficiently strong, the illuminated side potential V_1 turns positive, while the dark side potential V_2 remains negative at large values of the bulk resistance R but eventually may turn positive for small R. The potential difference between the two surfaces induces a leakage current J_ℓ.

First, consider the case of $V_{1,2} \leq 0$, by writing

$$M_{1,2} = - V_{1,2} \tag{23}$$

The explicit current balance equations to be simultaneously solved are

$$\frac{M_1 - M_2}{RJ_o} + \left[\eta \exp\left(-\frac{eM_2}{kT}\right) - \xi^*\left(1 + \frac{eM_2}{kT}\right)^g \right] = 0 \tag{24}$$

$$\frac{J_{pe}}{J_o} + \xi^* \left[\left(1 + \frac{eM_1}{kT}\right)^g + \left(1 + \frac{eM_2}{kT}\right)^g \right] - \eta \left[\exp\left(-\frac{eM_1}{kT}\right) + \exp\left(-\frac{eM_2}{kT}\right)\right] = 0$$

where $\eta = 1 - \beta - J_{so}$, $\xi^* = \xi(1 + \phi)$, and g is the geometric configuration parameter.

For the case of $M_1 = 0$, the above relations are simplified to

$$\frac{M_2}{R} = J_o \left[\eta \exp\left(-\frac{eM_2}{kT}\right) - \xi^*\left(1 + \frac{eM_2}{kT}\right)^g \right] \tag{25A}$$

$$(J_{pe})_c = \frac{M_2}{R} + J_o(\eta - \xi^*) \tag{25B}$$

Note that $(J_{pe})_c$ is the value of J_{pe} needed to raise the surface potential V_1 to zero.

The M_2 is determined by solving Eq. (25A) as function of $\epsilon = kT$, and the results are shown in Fig. 12 for the cases of various values of R and $\beta = 0.2$. The corresponding critical photoelectric current $(J_{pe})_c$ is in turn determined by Eq. (25B) as shown in Fig. 13. The impact of the geometric parameter variation from $g_2 = 1$ to 0 is generally negligible with low R but becomes noticable for $R \gtrsim 10^{15}$ Ω as shown in Fig 13 and especially in Fig. 12.

When $eM_2/kT \ll 1$, Eq. (25A) is reduced to

$$M_2 \approx (\eta - \xi^*) / \left[\frac{1}{RJ_o} + e(\eta + g\xi^*)/kT \right] \tag{26}$$

The relation is further simplified for $(RJ_o)^{-1} \gg e(\eta + \xi^*)/kT$ to

$$M_1 \approx RJ_o(\eta - \xi^*) \tag{27}$$

where M_1 now becomes proportional to R.

The η is independent of R but is a function of ε and approaches $\xi^* \approx 0.07$ toward $\varepsilon \approx 5.3$ KeV. Therefore, M_o in Fig. 12 vanishes rapidly as ε decreases toward 5.3 KeV. In Fig. 13, $(J_{pe})_c$ is seen to approach rapidly a limiting value as R decreases to the order of 10^{11} Ω (where the approximation (27) becomes good) and also to decrease steeply toward $\varepsilon \approx 5.3$ KeV. This characteristic is expected, because the $(J_{pe})_c$ determined there by Eq. (25B) becomes (in conjunction with (27)) proportional to $\eta - \xi^*$ and independent of R.

As the unmodified J_{pe} exceeds $(J_{pe})_c$, the sun exposed side becomes positive. The low energy electrons in the secondary and particularly in the photoelectric currents on this side are then trapped by the potential barrier as discussed previously.

While $V_{1,2} < 0$, the Eqs. (24) are solved for the surface potential $M_{1,2} = -V_{1,2}$, with its corresponding leakage current $J_\ell = (M_2 - M_1)/R$. When the sun exposed side becomes positively charged (i.e., $V_1 = M_1 > 0$), while the shadowed side remains negatively charged, (i.e., $V_2 = -M_2 < 0$), the corresponding equations become

$$\frac{M_1 + M_2}{R} = \hat{J}_{pe} + \hat{J}_{es} + \hat{J}_{bs} + J_o\left[\xi^* \exp\left(-\frac{eM_1}{2kT}\right) - \left(1 + \frac{eM_1}{kT}\right)\xi\right]$$
$$= J_o\left[\eta \exp\left(-\frac{eM_2}{kT}\right) - \xi^*\left(1 + \frac{eM_2}{kT}\right)\xi\right] \tag{28}$$

Here, because of the relative smallness of J_p on the sun exposed side (which is at a very low positive surface potential), a simple approximation of $\xi \approx \phi$ is adopted. The integrated $\hat{J}_{pe}$ and $\hat{J}_{es}$ are given, respectively, in Eqs. (14) and (15).

The $V_{1,2}$ as function of $J_{pe}(V_s = 0)$ are shown in Figs. 14A and B, respectively, for the cases of $R = 10^{15}$ and 10^{10} Ω, with $\beta = 0.2$. For $R \leq 10^{11}$ Ω, $V_1 \approx V_2$ in the domain of $J_{pe}(V_s = 0)$ where $V_1 < 0$.

The effect of changing the geometric parameter g from 1 to 0 is apparent only when $|eV_s|/kT$ is comparatively large, as seen from the figures. Note, however, that as V_1 rapidly turns positive while leaving the magnitude of the negative V_2 large, the resulting large potential difference between the two surfaces produces a correspondingly large leakage current J_ℓ. This large J_ℓ then negates the relative importance of the effect of the shifts in J_p and J_{ps} due to the variation in g, even if $|eV_s|/kT$ is not small.

For $J_{pe} = 0$, $V_1 = V_2 < 0$, which, as stated above, corresponds to the surface potential of an isolated (i.e., $R \to \infty$) spacecraft slab unilaterally exposed to the substorm in the dark (see previous section and Figs. 3A and B). As J_{pe} increases, V_1 rises rapidly to become positive at $(J_{pe})_c$ (see Fig. 14) and quickly reaches a plateau value of a few to several volts.

This is due to the low energy of the secondary and especially photoelectrons, resulting in a rapid increase in the current attenuation when the surface potential turns positive and begins to rise.

The value of the bulk resistance R primarily affects V_2. For $R = 10^{15}$ Ω, because the leakage current J_ℓ is relatively small, V_2 remains essentially the same throughout the variation of $J_{pe}(V_s = 0)$, while V_1 increases rapidly and turns to stabilize at a small positive value.

When R is reduced to 10^{10} Ω, because of the large leakage current J_ℓ, V_1 increases and turns positive at relatively slower rate than for $R = 10^{15}$ Ω, while V_2 keeps increasing and may change sign to become positive, especially in the low ε domain.

For a given $J_{pe}(V_s = 0)$, V_1 and V_2 are, respectively, an increasing and decreasing function of R, while both $V_{1,2}$ are decreasing functions of J_o. In a typical substorm environment, the sun exposure may turn both $V_{1,2}$ positive for $\varepsilon < 5.3$ KeV and (in general) $R < 10^{10}$ Ω. The positive excursion of V_1 and V_2 is restricted to a few volts.

SUMMARY AND CONCLUSIONS

The primary objective of this paper has been to describe the dependence of the charging process for dielectric surfaces on the various material response characteristics. This was done with the intent of exhibiting the ranges of magnitudes over which certain materials parameters either have a significant influence on the charging process or contribute only weakly to the charging levels attained. For this purpose it was important to include in the analysis all the currents involved in the equilibration of the charging potential. Where possible the material dependence of these currents was described by variables to facilitate parametric excursions. The main areas treated in the analyses and the chief conclusions derivable from the results are as follows:

The influence of bulk resistance on the charging potential was analyzed parametrically for $R \gtrsim 10^{10}$. The results show that for the lowest part of this resistance range the leakage current becomes a dominant factor in the equilibration process. For high resistance values the shadowed side of a dielectric slab in a substorm environment can develop a large negative potential. In this case the otherwise relatively insignificant plasma proton current and its secondary electron current may assume a dominant role in preventing further growth of the negative potential. In view of the conspicuous dependence of equilibrium potentials on dielectric resistivities, the large variability of resistivity values for important candidate materials makes the prediction of charging potentials problematic. Also, for dielectric materials of a few mils thickness, such as Kapton sheets, the potential differences developed are frequently sufficient to produce dielectric breakdown. Repeated breakdown in turn may lead to progressive changes in resistivity.

For a sheet of dielectric material the equilibrium potential V_s on the sun-illuminated side tends to saturate for $J_{pe} \sim 1$ nA/cm^2. The saturation V_s is a few volts positive and depends only weakly on kT. The largest effect on V_s is in the range 0 - 0.5 nA/cm^2, where V_s moves from large negative (kV) values to small positive values. This dynamic behavior is important in sun-angle variations and terminator crossings. If the bulk resistance of the sheet is large, the shadowed side potential settles at a large negative value; however, for a sufficiently low resistance ($\sim 10^{10}$ ohm-cm^2) both sides may become positive.

An analysis of the sensitivity of the charging process to the value of the backscattering yield β shows the following trend: If β is significantly larger than 0.2, then at lower substorm plasma temperatures (e.g. $kT \lesssim 5$ keV), even a shadowed surface may turn positive. However, for large kT (> 10 keV) the influence of β on the attained surface potential V_s becomes progressively weaker.

REFERENCES

1. Langmuir, I. and Mott-Smith, H. M. (1920), Phys. Rev., vol. 28, no. 717.

2. Sternglass, E.J., Phys. Rev., vol. 80, p. 925, 1950.

3. Willis, R.F. and Skinner, D.K., Solid State Communications, vol. 13, p. 685, 1973.

4. Feuerbacher, B. and Fitton, B (1972), J. Appl. Phys. vol. 43, no 15, p. 15, 1972.

5. Grad, R.J.L, Knott, K, and Pedersen, A., Photon and Particle Interactions with Surfaces in Space, D. Reidel Pub. Co., Dordrecht-Holland; 1972.

6. Stevens, N.J., Lovell, R.R., and Purvis, C.K., Proc. of the Spacecraft Charging Technology Conf., vol. 735, 1977.

Table 1 Electrical Characteristics of Selected Dielectrics

	VOLUME RESISTIVITY (Ω-CM)	DIELECTRIC STRENGTH (VOLTS/MIL)
TEFLON FEP	10^{18} (25-175°C)	$8 \cdot 10^3$ (0.5 MIL) – $4 \cdot 10^3$ (4 MIL)
KAPTON	10^{18} (25°C) – 10^{14} (200°C)	$7 \cdot 10^3$ (1 MIL) – $4.6 \cdot 10^3$ (3 MIL)
BOROSILICATE GLASS	$5 \cdot 10^{13}$ (25°C) – $5 \cdot 10^9$ (200°C)	$1 \cdot 10^4$ – $2 \cdot 10^4$
FUSED SILICA	10^{18} (25°C) – $5 \cdot 10^{13}$ (200°C)	$1 \cdot 10^4$ – $2 \cdot 10^4$
SODA LIME GLASS	10^{11} (25°C) – $5 \cdot 10^7$ (200°C)	$1 \cdot 10^4$ – $2 \cdot 10^4$

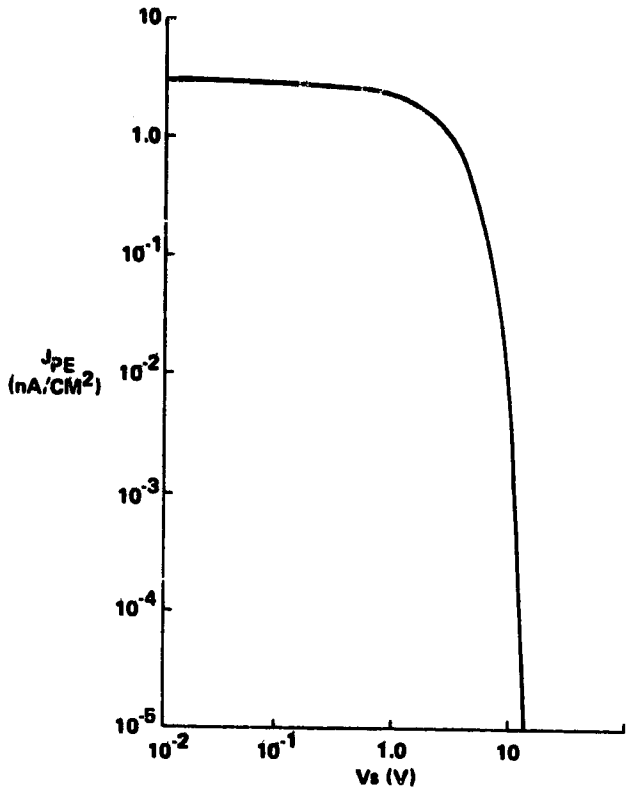

1003-78/82-1

Fig. 1 Attenuation of Integrated Photoelectric Current by Positive Surface Potential Barrier V_S

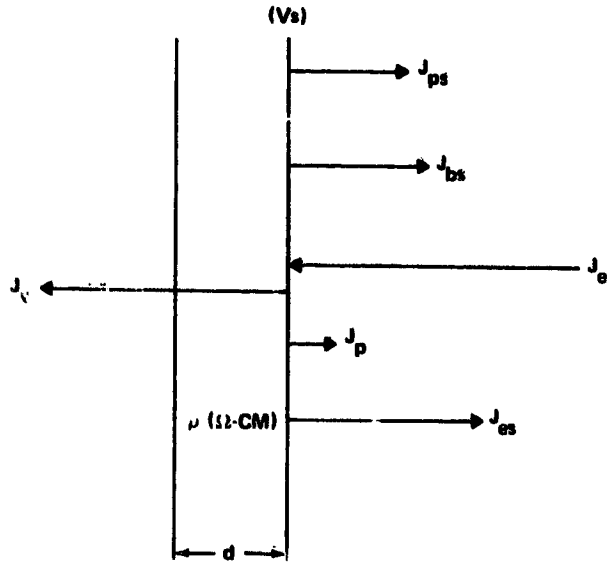

Fig. 2 Substorm Plasma Generated Charging Currents Under Eclipse Conditions

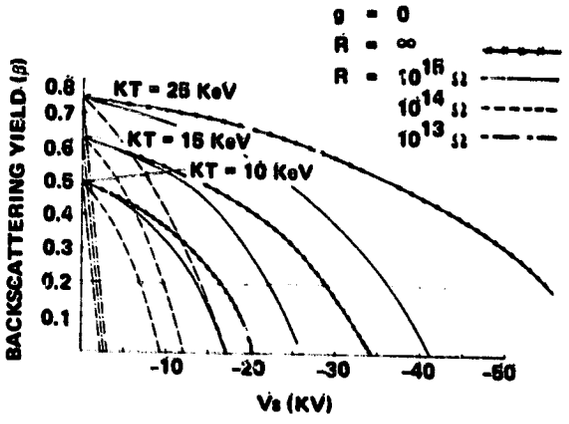

Fig. 3A Effect of Backscattering Yield and Leakage Currents on Equilibrium Surface Charging Potential for Infinite Flat Surface (Typical Substorm Currents in Eclipse)

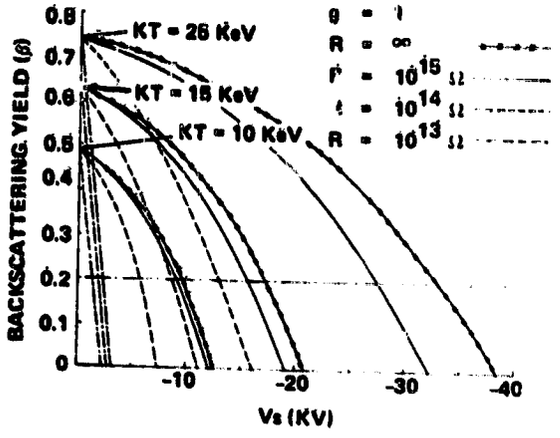

Fig. 3B Effect of Backscattering Yield and Leakage Currents on Equilibrium Charging Potential for Spherical Surface (Typical Substorm Currents in Eclipse)

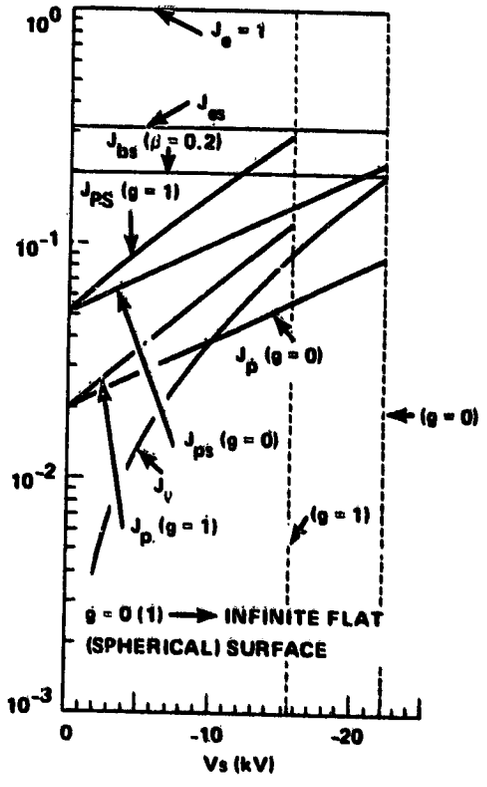

Fig. 4 Surface Potential Dependence of Various Charging Currents in the Dark (Relative to je = 1) in Approach to Equilibrium ($R = 10^{15}$ Ω, kT = 15 KeV)

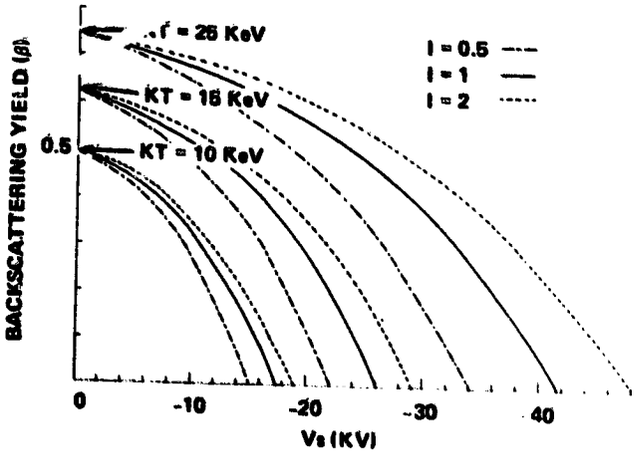

Fig. 5 The Equilibrium Surface Potential Vs as Function of the Backscattering Yield β for Various Current Multiplyer I and Electron Temperature kT (g = 0 Case at $R = 10^{15}$ Ω)

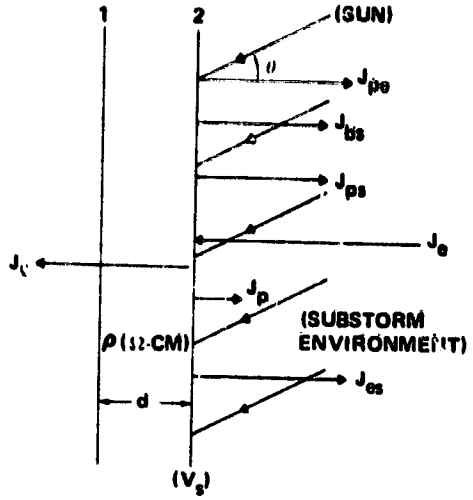

Fig. 6 Plasma Charging Current and Secondary Currents on a Sun-Illuminated Surface (2) (Interior Surface (1) at Reference Potential)

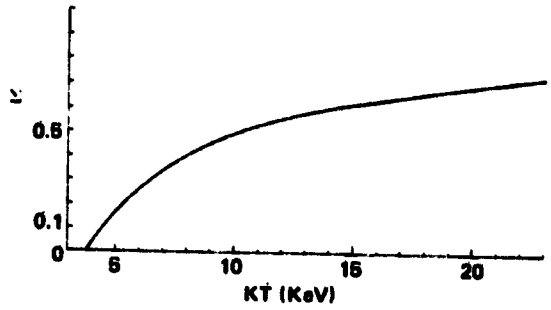

Fig. 7 Effect of Combined Backscattering/Photo-Electric Current at Zero Surface Potential on Polarity of Equilibrium Charging Potential ($\Sigma - (\beta + J_{pe}(0)/J_e(0)) \gtrless 0 \rightarrow V_s \lesssim 0$)

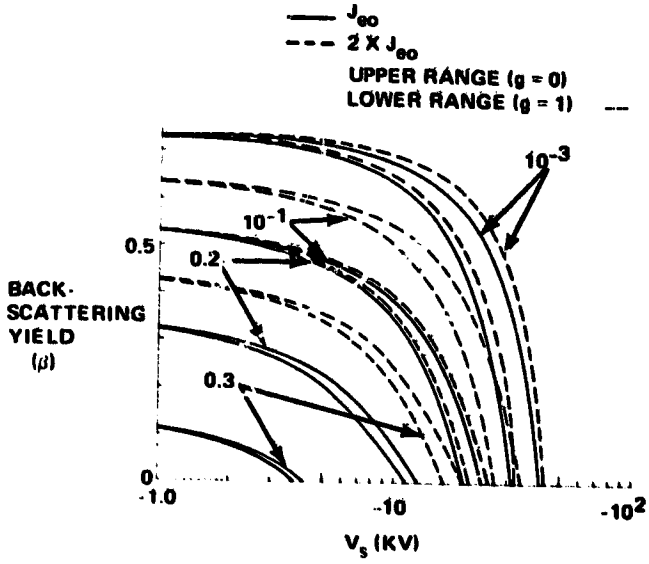

Fig. 8A Surface Charging Potential as Function of Backscattering Yield β for Various J_{pe} (V_s = 0) Values Appropriate to Large Sun Angles (kT = 25 keV; R = 10^{15} Ω)

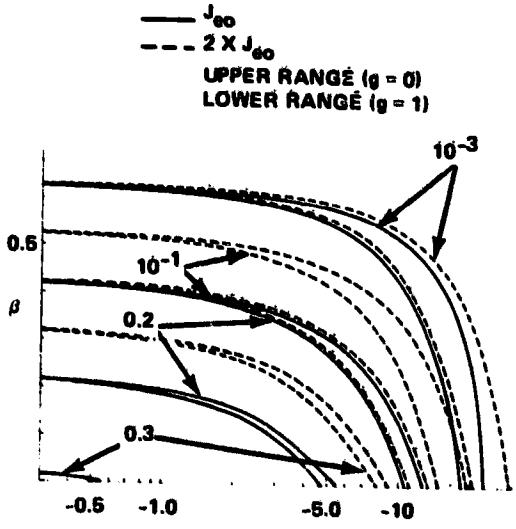

Fig. 8B Surface Charging Potential as Function of Backscattering Yield β for Various J_{pe} (V_s = 0) Values Appropriate to Large Sun Angles (kT = 15 keV; R = 10^{15} Ω)

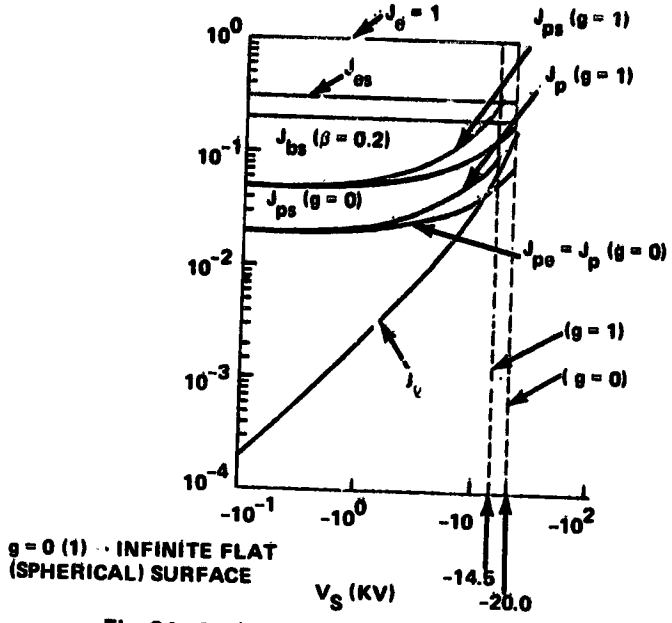

Fig. 9A Surface Potential Dependence of Various Charging Currents (Relative to $J_e = 1$) in Approach to Equilibrium ($R = 10^{15}\ \Omega$; kT = 15 KeV; $\beta = 0.2$; J_{pe} ($V_s = 0$) = 0.01 nA/cm^2)

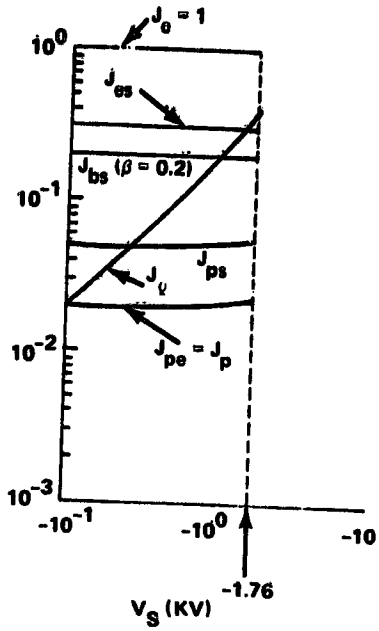

Fig. 9B Surface Potential Dependence of Various Charging Currents (Relative to $J_e = 1$) in Approach to Equilibrium ($R = 10^{13}\ \Omega$; kT = 15 KeV; $\beta = 0.2$; J_{pe} ($V_s = 0$) = 0.01 nA/cm^2)

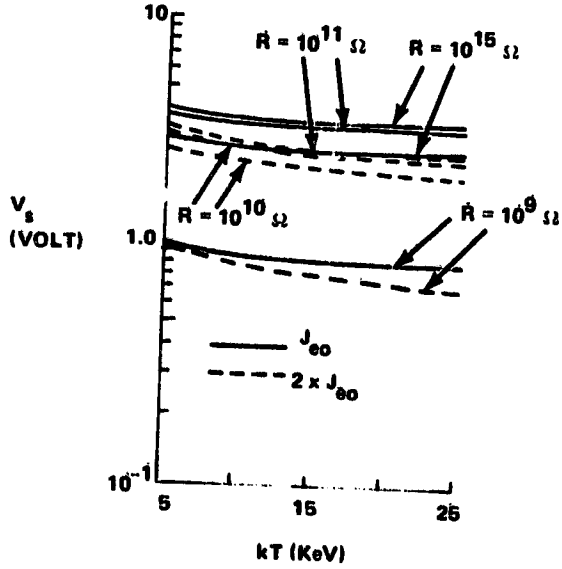

Fig. 10 Positive Surface Potential V_s As Function of Average Plasma Electron Energy kT and Resistance R. (J_{pe} ($V_s = 0$) = 1.5 nA/cm^2)

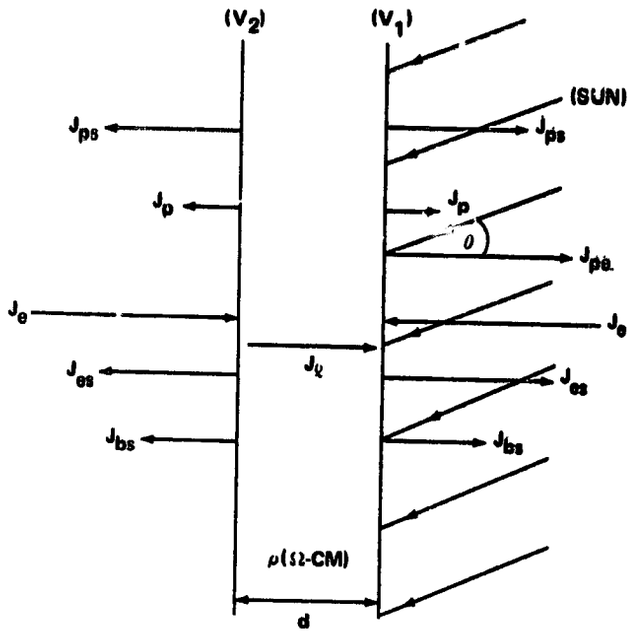

Fig. 11 Plasma Charging Currents and Secondary Currents on Substorm Environment Immersed Slab (One Side Sun-Illuminated)

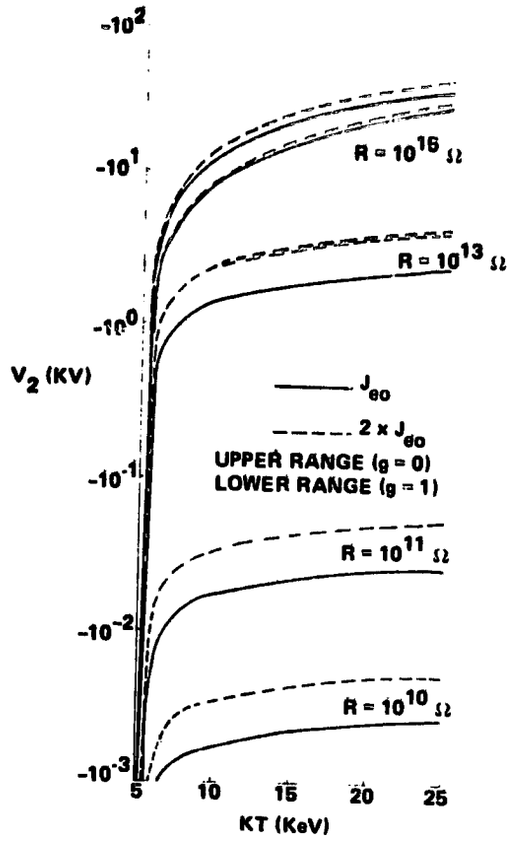

Fig. 12 Shadowed Side Surface Potential V_2 for Sun-Illuminated Side Potential $V_1 = 0$, as Function of Resistance and Electron Temperature (Backscattering Yield $\beta = 0.2$)

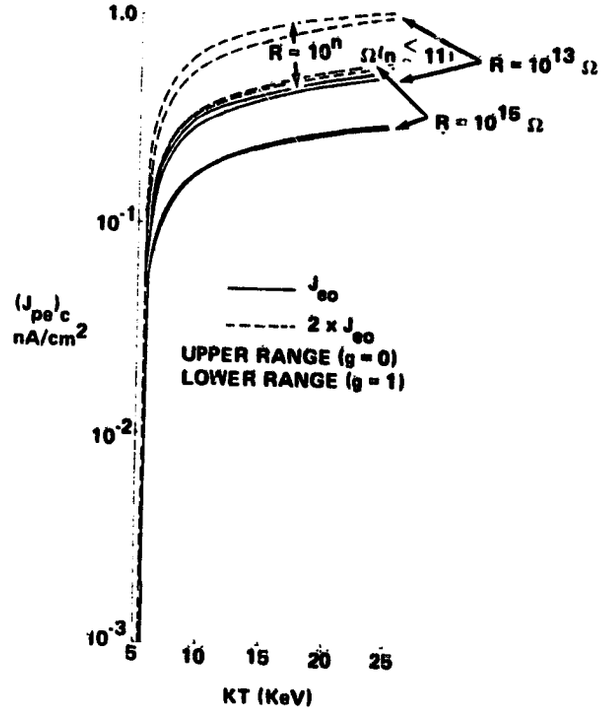

Fig. 13 The Critical Photoelectric Current $(J_{pe})_c$ for Sun-Illuminated Side Potential $V_1 = 0$, as Function of Resistance and Electron Temperature (Backscattering Yield $\beta = 0.2$)

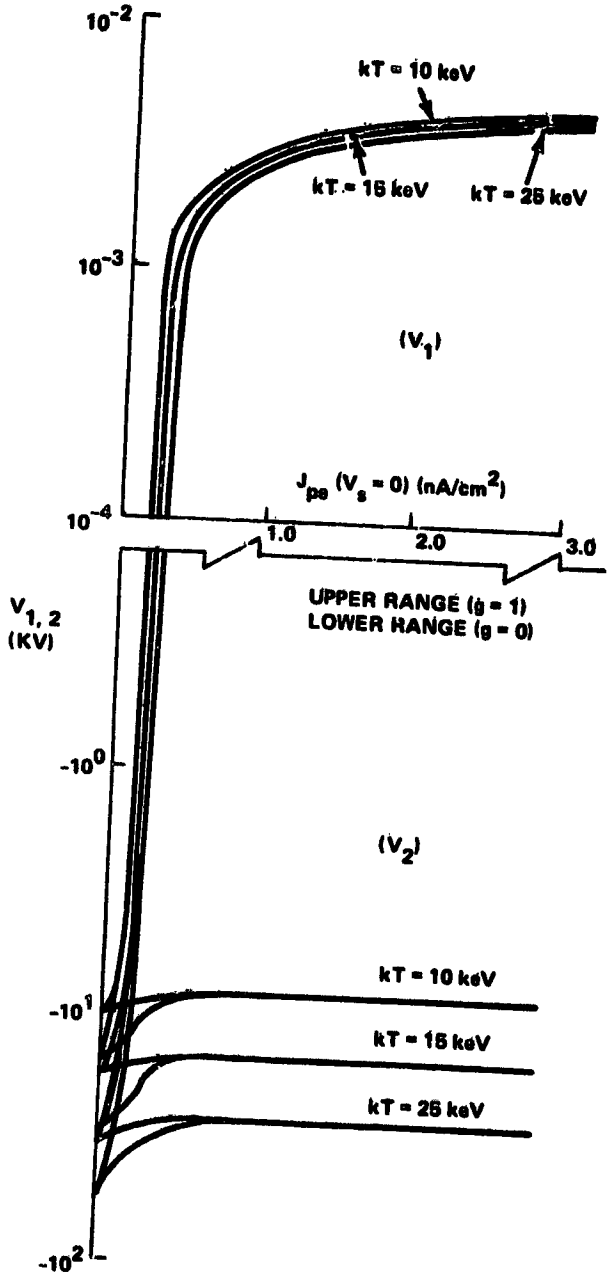

Fig. 14A Equilibrium Charging Potentials on Slab Immersed in Substorm Environment (One Side Sun-Illuminated) as Function of J_{pe} (V_S = 0) (R = 10^{15} Ω; β = 0.2)

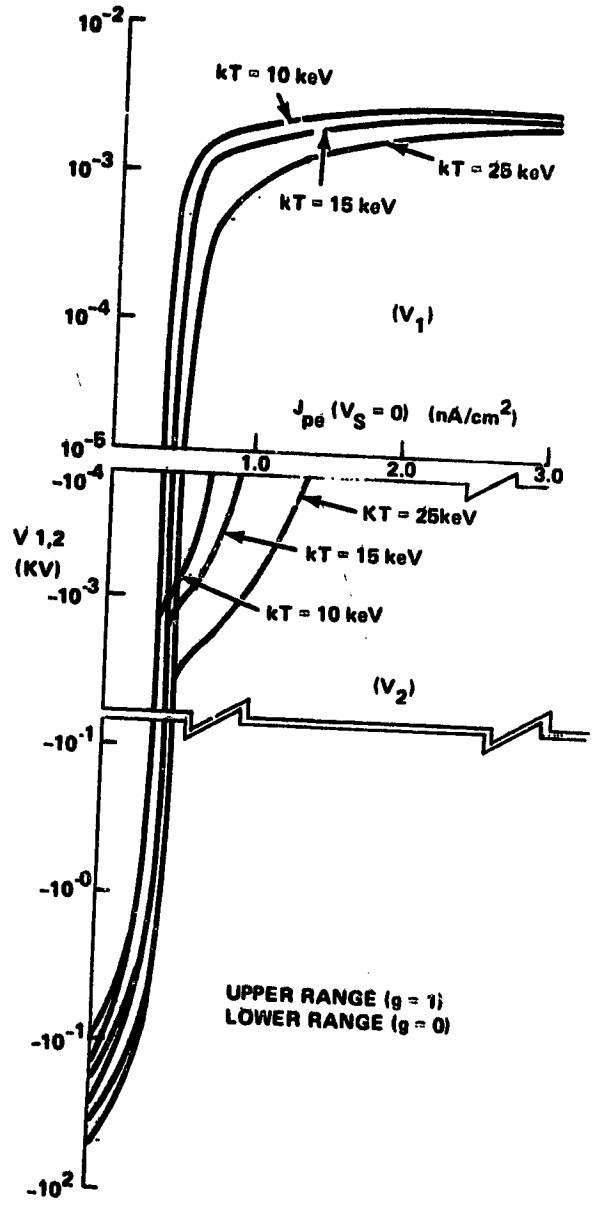

Fig. 14B Equilibrium Charging Potentials on Slab Immersed in Substorm Environment (One Side Sun-Illuminated) as Function of J_{pe} (V_S = 0) (R = 10^{10} Ω; β = 0.2)

D45

N79-24046

STABLE DIELECTRIC CHARGE DISTRIBUTIONS FROM FIELD ENHANCEMENT OF SECONDARY EMISSION*

James W. Robinson
The Pennsylvania State University

SUMMARY

The emission of secondary electrons from dielectrics is subject to numerous effects of electric field which are experimentally difficult to control. Measurements have been reported using pulse techniques such that local fields do not build to significant levels, but measurements with fields present are also of interest. This paper describes a specific series of measurements under controlled conditions and examines their implications in terms of fields, magnitude and angle, near the dielectric surface. The measurements were made for a charged fluorinated-ethylene-propylene surface near a grounded aluminum half-round resting on the surface. The geometry produced a stable surface-charge gradient being controlled by a strongly enhanced secondary emission for which a model is constructed. Observations of surface flashovers under various conditions confirm the predictions of some scaling exercises.

INTRODUCTION

When a dielectric-metal interface is exposed to an electron beam, the dielectric surface becomes negatively charged (at least if the beam energy exceeds a few kilovolts) and potential gradients are established near the interface which is held at ground potential. Previous studies of the charge distribution and the associated potential contours are reported in reference 1 which describes the method of measuring the charge distribution and some typical results. Some distributions are more stable than others with stability expressed in term of the probability of flashover, a transient discharge where the accumulated charge is cleared from the dielectric surface. This paper examines the charge transfer processes near an interface so as to identify characteristics of a stable distribution of charge. The dielectric is a 0.127-mm (5-mil) sheet of fluorinated-ethylene-propylene with a metal backing.

The importance of secondary emission was emphasized in reference 1, yet at the time of that writing, pertinent data had not been attained. Summarized in figure 1 is a series of measurements (ref. 2) of secondary emission in the

*This work was supported by the National Aeronautics and Space Administration under grant NSG-3097.

presence of a normal field. These show that emission differs from the conventional, zero-field, characteristic (ref. 3). The field increases the critical potential (upper unity-crossing point) and thus reduces the steady state surface potential in a monoenergetic electron beam. This trend is consistent with the lowering which is observed near an interface but the observed lowering exceeds that attributable to normal electric fields. In the vicinity of the interface are found tangential as well as normal field components and, though the effect of tangential fields has not been measured, it is surmised that they account for the discrepancy.

A particular measured charge distribution is chosen as a reference data set and from this the equipotential lines and fields near the interface are calculated. Effects of perturbing or scaling this reference data set are examined and the critical potential for secondary emission is related to surface fields. From observations that microscopic structures trigger flashovers, one confirms the scaling predictions.

CALCULATING POTENTIAL PROFILES

From a measured distribution of potential on the surface of the dielectric, the equipotential curves and fields were calculated above the surface. The calculation depended of course on the nature of the interface which, for this discussion, is formed by placement of a half-round grounded aluminum strip on the surface of the dielectric sheet as shown in figure 2. As a first step in the calculation, the geometry was transformed by the conformal mapping $W = Z + 1/Z$ such that the surface became a plane. A Green's integral (ref. 4) was employed to generate values of potential and field above the plane and then the results were mapped back to the original geometry for display. This process, as described in reference 2, was implemented by representing the potential on the dielectric surface with an easily integrated piecewise-linear function. Because of this approximation, some irregularities in field data were observed, especially near the vertices of the piecewise-linear function. Also the influence of a ground plane placed several centimeters above the specimen was ignored. The calculational procedures were organized in two ways, one being to generate displays of equipotential contours and the other to tabulate surface fields at the midpoints between vertices. The latter output was used by an iterative program which sought to find a surface potential distribution that satisfied some criterion placed on the surface fields.

SURFACE MODELS

Charge does not reside precisely at the surface of the dielectric but rather in layers slightly below the surface. Katz et al (ref. 5) describe a buried electron layer and an electron depletion layer close to the surface. The electrons are buried, because of their impact energy, at several hundred angstroms yet secondaries escape from nearer the surface. Field patterns may be represented crudely by assuming discrete charge layers as shown in figure 3.

The weakest fields are those outside the dielectric yet they aid secondary emission as do the fields just below the surface. However should the external fields be reversed in direction, though weak they would stifle emission of secondaries. This is because secondaries are emitted with low kinetic energies, their range in dielectric being at most a few angstroms. Fields tangential to the surface will be the same on either side of the surface and they will often exceed the normal external field component. While realizing that the internal fields are perhaps 10 times as large we find that external normal fields 3 kV/mm significantly influence secondary emission. Because of the equality of tangential fields, the aiding sense of the internal normal field, and the dominance of the external field, the dielectric is modelled simply as a surface charge sheet.

Near interfaces, equipotential lines are nearly normal to the surface such that electrons are accelerated nearly parallel to the surface. An emitted secondary may, in traveling a few micrometers, gain enough energy to cause additional secondary emission. If it strikes the surface with a grazing angle it is an efficient producer of secondaries. When field lines are nearly parallel to the surface we thus find an efficient mechanism for electron emission. A quantitative description of how tangential fields affect secondary production is not available but nevertheless certain aspects of the phenomenum are indicated in the analyses which follow. The term, secondary emission, is used here to include the effects of avalanching so that a given primary may have a widespread effect on charge distribution. Regardless of the process, a steady state is gained when at all points charges emitted balance charges received.

STABLE CHARGE DISTRIBUTION

Shown in figure 4 is a piecewise linear representation of experimental data for a half-round radius of 1.2 mm. Experimental resolution was no better than 0.5 mm so that some liberty has been taken to form this representation. Data has been smoothed. When this data set is used in the routine which generates equipotential lines, results are as shown in figure 5. The figure is taken as a reference for later simulations and it represents a stable interface configuration. Several features are noteworthy. As surface potential approaches zero the equipotentials become more nearly normal to the surface such that secondary emission increases. More specifically we would say that the critical point shifts to higher voltages, approaching 20 kV at the interface. Furthermore the equipotentials become more closely spaced; tangential fields approach 50 kV/mm such that bulk conduction may be significant. If the inclination angle θ is defined as the angle between the surface and the equipotentials, then its variation with potential (fig. 6) summarizes the surface conditions.

SIMULATIONS

Although experimental data are crucial for explaining interface phenomena, they are obtained only with a substantial time investment and resolution is limited. The calculational routines permit a simulation of conditions not measured as well as hypothetical conditions not experimentally obtainable. Several important features have evolved from the simulations conducted.

One of the easiest exercises was to assume the same surface potential distribution in the presence of smaller half-rounds. Results for a 0.24-mm radius are compared with the reference condition in figure 6. With the same distribution and a smaller half-round the angles are greater and the distribution of charge is not expected to be in steady state. Rather the charge distribution will shift toward a new equilibrium in a manner to be determined.

Whereas figure 6 was drawn for a given surface potential near different sizes of half-round, it may just as well represent scaled surface potentials near half-rounds of the same size. When such an interpretation is used we conclude that a steeper gradient corresponds to lesser angles. If now we reconsider our reference distribution near a half-round of reduced size, we expect the potential gradient to increase and the angles to relax toward the reference case.

Assuming that, when the half-round is made smaller, the charge distribution becomes steeper, we may anticipate a high-field limit where stable conditions no longer exist. This may also be argued another way. The equipotential lines of figure 5 may be scaled along with the half-round and no changes in potential or angle will be perceived though electric fields will change inversely with dimensions. Expermentally we have tested two configurations that by this scaling procedure would produce fields much higher than the reference case. For one of the tests, a .25-mm (10-mil) wire was laid across the surface of an otherwise stable system. For the other a slit was cut in the dielectric and conductive epoxy was forced from the underside through the slit to form a bead somewhat resembling a half-round. We have found that neither configuration allows formation of a stable charge. Flashovers occur at relatively low voltages during the charging process and full charge at 20 kV is never reached. It is significant to note that when epoxy was applied and hardened before the slit was cut, the distribution near the slit was stable.

One might argue that if secondary emission is a highly sensitive function of θ near $\theta = 90°$ then for a stable configuration θ will be within perhaps a few degrees of 90 for most of the range of potentials. On this basis one could let θ be 90° as a first approximation and calculate what the charge distribution must be for this condition to hold. Possibly figure 6 is very sensitive to experimental errors and should be discounted. This possibility was tested by programming an iterative routine which shifted the data points of figure 4 until all points (but one) of figure 6 were within 4 degrees of 90. The potential distribution attained in this way is compared with the reference distribution in figure 4. The discrepancy between the

curves is several times what can be attributed to experimental errors and thus the assumption $\theta = 90°$ is not a good one. Another trial requiring that $\theta = 80°$ led to similar results. The angle θ is not constant but decreases as surface potential increases.

Equipotential curves are shown in figure 7 for the assumed condition that fields will be tangential to the surface. The somewhat plausible argument in support of tangential fields is rebuffed by comparison with the experimental data represented in figure 5. In figure 7, the curve for -1 kV is not normal as are the others. Though an attempt was made to force conformity, the iterative computation became unstable and the effort was abandoned.

PHYSICAL IMPLICATIONS

From the preceding material, a model of the secondary emission characteristics emerges. Assumptions are made that the steady state potential corresponds to the condition of a unity secondary emission coefficient, that the secondary critical voltage is a unique function of field strength and angle, and equivalently that secondary avalanches are relatively insignificant. All illustrations are based on 20-kV electron fluxes so that, in a steady state, surface voltage V_s and critical voltage V_c are related by $V_c - V_s = 20$. In a transient situation the equality is violated yet it is assumed nevertheless that

$$V_c = f\ (E, \theta)$$

where the function of field strength E and θ is still considered to exist. If $20 + V_s$ is less than V_c, electrons will arrive with some energy less than the critical value and the surface will lose charge until a steady state is attained. If $20 + V_s$ is higher, charge will accumulate. From an assumed perturbation in a potential distribution changes in E and θ can be found. For stability the corresponding change in V_c must be of the proper polarity and thus constraints are placed on f.

Perturbations are represented as lateral displacements of the reference data points shown in figure 4. Each point is thus identified with a given V_s and a variable coordinate. The perturbation illustrated here consists of expanding the reference distribution by 25 percent while holding the half-round constant. Using changes in E and θ we may calculate ΔV_c in terms of the partial derivatives f_E and f_θ:

$$\Delta V_c = f_E\, \Delta E + f_\theta\, \Delta\theta$$

For restoration of the reference distribution, charge must accumulate on the surface and consequently the following condition must be met:

$$V_c - V_s < 20 \text{ or } \Delta V_c < 0$$

Anticipating that both f_E and f_θ are positive, we require that $f_E \Delta E$ be the dominant term.

A possible function $f(E,\theta)$ is shown in figure 8 along with the reference data from figure 6. It is drawn so that the partial derivatives are positive and so that it conforms to the reference distribution. It is notable that the slope of the constant-E lines must be less than the slope of the reference curve if f_E is to be positive. Otherwise the slope is not clearly specified. The function is shown to decrease as θ increases beyond 90° because the normal field component opposes secondary emission. Focusing our attention on the point at $V_s = -7$, we may estimate partial derivatives to be

$$f_\theta = 0.06 \text{ kV}$$

$$f_E = 0.14 \text{ mm}$$

At this point the perturbation produces changes of $\Delta E = -3.37$ kV/mm and $\Delta\theta = 1.19°$. The change ΔV_c then has the value -0.4 kV which is of the desired polarity. For the function illustrated in figure 8, the values of ΔV_c are all negative and the assumed perturbation should relax toward the reference condition. Details are shown in Table I. This function cannot be used as a quantitative representative of secondary emission characteristics because it is not sufficiently supported by data. Rather it is a qualitative model which suggests how a greater data base might be used in developing an accurate description.

When θ is near 90°, the occurrence of avalanches may disallow the use of $f(E,\theta)$ as a representative of critical voltage. The size (< 0.1 mm) of this region precludes using the experimental procedures of reference 1 to attain more detailed information. Consequently any use of the model near 90° is highly speculative. However for lesser angles, secondary electrons have little probability of returning to the dielectric surface and the concept of critical voltage is justifiable. Further experimentation should provide a detailed description of $f(E,\theta)$.

EXPERIMENTAL DETAILS

In all cases where flashover probability was high, the cause of flashover could be ascribed to some fine detail in the interface. When care was taken to avoid or remove the causative feature, then surface charge distributions stablized. Several examples are described in this section.

A stable distribution was attained by covering the dielectric sheet with a metal aperture plate having a thickness of 1 to 1.5 mm. Occasional flashovers were accompanied by light flashes on the edge of the hole cut in the plate. As time passed, flashovers became less frequent because, it is presumed, the rough spots on the edge were eroded. After extensive exposure

to beams of high flux, the dielectric surfaces were found to be coated near the interface with a nonconductive-whitish substance thought to be aluminum oxide. Figure 9 is a microphotograph illustrating the deposit.

When an aperture plate was cut in half and assembled by butting edges, flashover probability was high unless care was taken to align the joints properly. When assembly was sloppy, light flashes at the joint accompanied the flashovers.

Half-rounds were inserted and clamped between the halves of split aperture plates. The charge distributions were stable except for possible joint effects. However when a fine wire was used instead of a half-round, the wire became the cause of flashovers.

Several specimens were prepared with slits or punctures which exposed the underlying ground plane through the dielectric sheet. When the underlying conductive coating was bonded with conductive epoxy to a rigid metal substrate, the cutting of slits or holes did not, at first, cause flashover rates to become high. Yet as these specimens aged, flashovers became more frequent. Light flashes concentrated on specific spots along the slits, the repetitive discharges eroded dielectric, and the spots became trigger points for discharges. One such spot formed at the end of a slit as illustrated in figure 10.

When a slit was cut before the epoxy and backing plate were applied, the epoxy oozed through the slit and formed a bead on the exposed surface of the epoxy. This configuration was unstable from the beginning.

CONCLUDING REMARKS

Measured surface potentials near dielectric-metal interfaces provide a basis for the modelling of secondary emission phenomena reported here. Measurements of secondary emission from the dielectric show that normal electric fields increase the critical voltage, that point where the emission coefficient is unity. Assuming that, for steady state, the coefficient is unity under all field conditions we then calculated the critical voltages at the various values of field magnitude and angle represented by the measured distribution. A model, based on this limited data, shows that critical voltage increases with both the field magnitude and the angle between the surface and equipotential lines. Scaling exercises predict increasing field strengths as the size of a ground strip is reduced. Corresponding experiments show that surface charge distributions become less stable.

REFERENCES

1. Robinson, J. W.: Charge Distributions Near Metal-Dielectric Interfaces Before and After Dielectric Surface Flashover. Proceedings of the Spacecraft Charging Technology Conference, pp. 503-515, 24 February 1977.

2. Quoc-Nguyen, N.: Secondary Electron Emission from a Dielectric Film Subjected to an Electric Field. NASA CR-155231, Nov. 1977.

3. Willis, R. F. and Skinner, D. K.: Secondary Electron Emission Yield Behavior of Polymers. Solid State Communications 13, pp. 685-688, 1973.

4. Jackson, J. D.: Classical Electrodynamics, 2nd ed. Wiley, pp. 40-44, 1975.

5. Katz, D. E. et al.: A Three Dimensional Dynamic Study of Electrostatic Charging in Materials, NASA CR-135256, August 1977.

TABLE I - THE CHANGE ΔV_c CORRESPONDING TO AN ASSUMED PERTURBATION

Potential	Reference		Change				
	E	θ	ΔE	Δθ	f_E	f_θ	ΔV_c
kV	kV/mm	degrees	kV/mm	degrees	mm	kV	kV
- 1	48.17	105.44	-9.67	0.26	--	--	--
- 3	32.73	81.13	-6.63	0.55	0.11	0.06	-0.70
- 5	26.71	64.47	-5.50	0.76	0.11	0.06	-0.56
- 7	15.69	50.44	-3.37	1.19	0.14	0.06	-0.40
- 9	9.01	45.25	-2.06	1.91	0.3	0.06	-0.50
-11	5.68	45.55	-1.35	2.73	0.6	0.06	-0.65

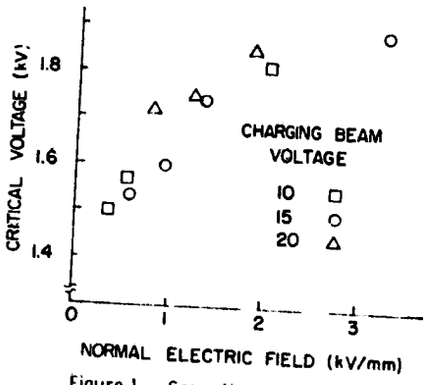

Figure 1. - Secondary emission critical voltage as function of normal field outside surface.

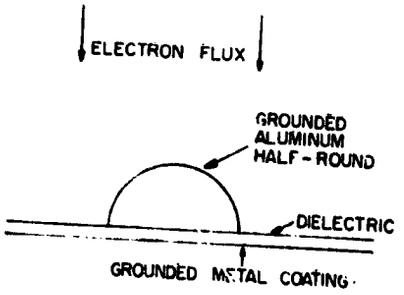

Figure 2. - Configuration used for experiment and simulation.

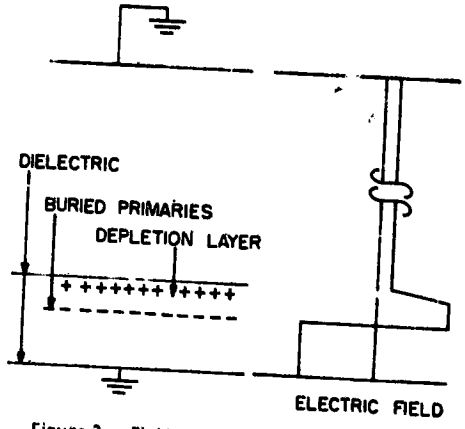

Figure 3. - Field configuration near dielectric surface.

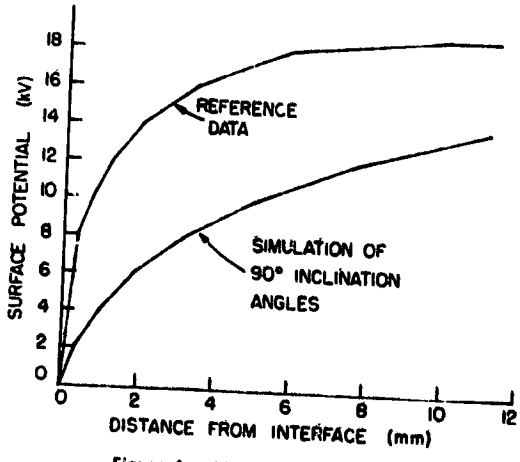

Figure 4. - Dielectric surface potential.

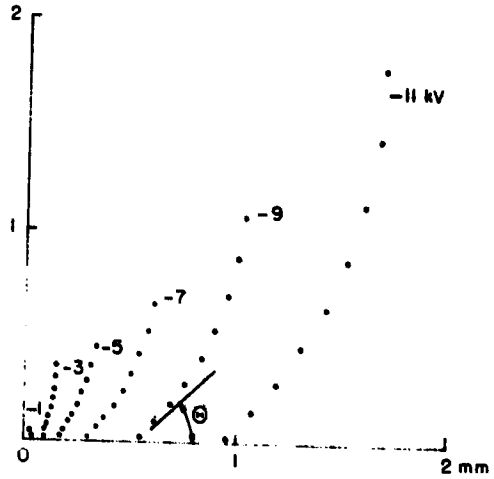

Figure 5. - Equipotential contours for reference distribution near half-round.

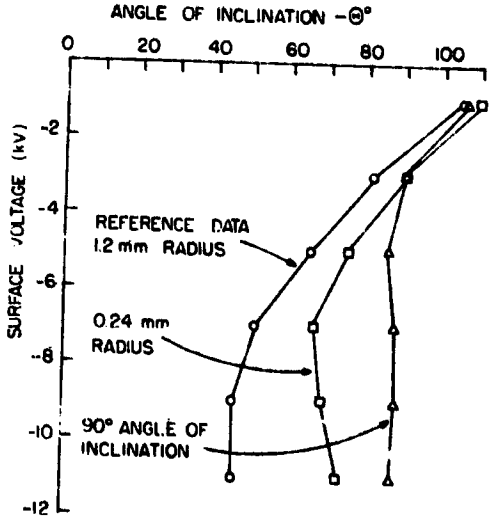

Figure 6. - Summary of surface conditions.

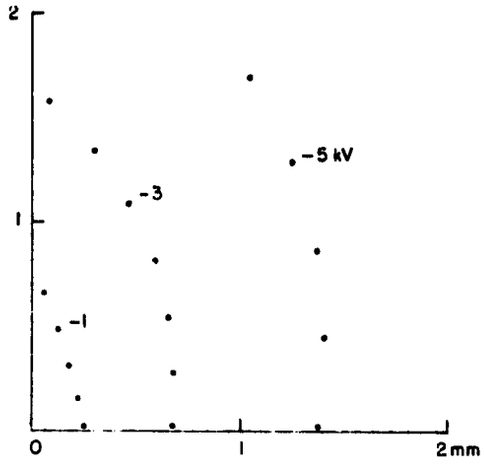

Figure 7. - Equipotential contours with 90° angles of inclination.

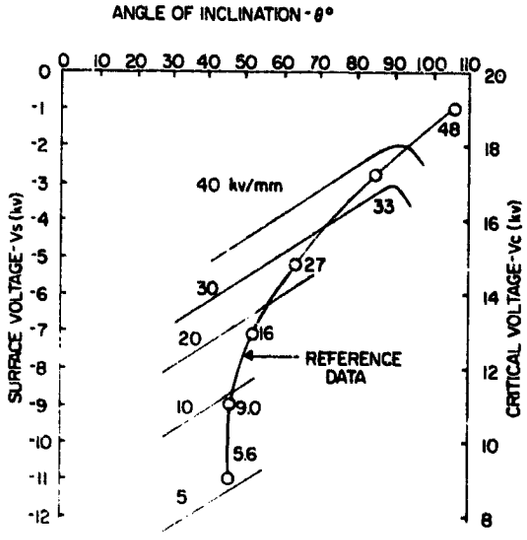

Figure 8. - Critical voltage function conforming with reference data.

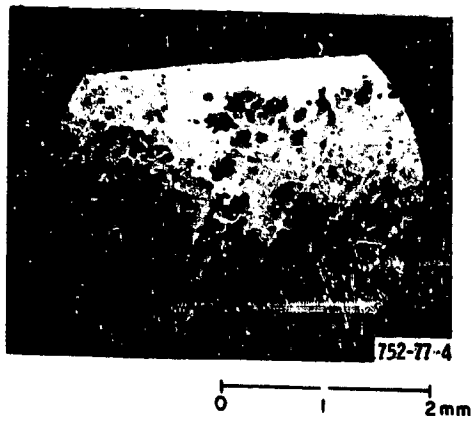

Figure 9. - Coating near edge of aperture plate.

Figure 10. - Erosion pit at end of slit.

D46

N79-24047

SECONDARY EMISSION EFFECTS ON SPACECRAFT CHARGING: ENERGY DISTRIBUTION CONSIDERATIONS

N. L. Sanders and G. T. Inouye
TRW Defense and Space Systems Group

SUMMARY

Calculations of the floating potential V of a spacecraft in geosynchronous orbits often lead to multiple voltage root solutions to the current balance equation ($J_i(V) - J_e(V) + J_s(V) + J_{scat}(V) = 0$) for the ion, electron, secondary emission and backscattered currents. The multi-valued solutions result from the double-valued nature of the incident electron energy when expressed as a function of secondary electron yield.

We have examined the conditions under which multiple valued solutions occur by computing the floating potential of an isolated eclipsed surface on a geosynchronous orbit spacecraft. Two different surface materials were considered, aluminum with an oxide coating and BeCu (activated). Several different approximations for the electron spectra during a geomagnetic substorm were used.

The result of the study indicates that if the incident electron flux has a Maxwellian energy distribution, the ratio of the secondary emitted current to the incident electron current is independent of the spacecraft potential. In this case a single valued solution to the current equation occurs. However, if the electron spectra can be described by the sum of two Maxwellian energy distributions then either multiple potentials or a single small positive or a single large negative potential can occur. Under certain conditions the nature of the solution can change from positive to negative to multiple by making relatively small changes in the incident electron spectrum shape. In this case of variable spectral shape large temporal changes in potential of a spacecraft surface in eclipse could occur during a geomagnetic substorm.

INTRODUCTION

In the early 1970's, plasma clouds containing kilovolt electrons were observed in the magnetosphere at synchronous latitudes (ref. 1) resulting in the chargeup of spacecraft to thousands of volts potential. Since then numerous calculations of the floating and differential potential of a spacecraft in geosynchronous orbit (refs. 2, 3, 4, 5) and in the Jupiter environment (refs. 6 and 7) have been performed. More recently it has been shown that the spacecraft current balance equation can have multiple solutions yielding two stable and one unstable solution for the floating potential of the charged up spacecraft (ref. 4). Multiple roots are a consequence of secondary emission from the surface. They can occur when the maximum value of the secondary electron fractional yield δ_{max} is greater than one.

In this paper we have examined some of the conditions under which multiple solutions to the current balance equation can occur. We have assumed that the spacecraft surface in question is in eclipse and is spherically symmetrical and that the spectrum of the ambient electron flux could be described by one or two Maxwellian energy distributions.

COMPUTATIONS

To determine the current-voltage characteristics one must balance the current to the spacecraft. If J_{net} is the net current to the spacecraft, then in the steady state

$$J_{net} = J_e(V) - J_i(V) - J_s(V) - J_{scat}(V) = 0 \tag{1}$$

where the J's are the voltage dependent current densities for electrons, ions, secondary electrons and back scattered electrons, respectively. The current density for electrons that can be described by a single Maxwellian energy distribution is given by $J_e(V) = J_{oe} \exp [eV/kT]$ for electrons incident on a negatively charged surface.

In the case of ions, we have used the same assumptions as Prokopenko and Laframboise (ref. 4), i.e., that the ion flux is Maxwellian with an ion temperature of one kilovolt and that the ratio of ambient ion to electron current densities $J_{oi}/J_{oe} = 0.025$. With these assumptions the ion current density in the attractive case (i.e., positive ions incident on a negatively charged surface) becomes

$$J_i = .025\ J_{oe}\ (1-V) \tag{2}$$

where V is in kilovolts.

In order to compute the secondary electron current it was assumed that the fractional yield, $\delta(E)$, as described by Sternglass (ref. 8) could be approximated by the difference of two exponentials, i.e.,

$$\delta(E) = c(e^{-E/a} - e^{-E/b}) \tag{3}$$

To compute the constants a, b and c, equation (3) was compared to the Sternglass relation for the fractional yield

$$\delta(E) = 7.4\ \delta_{max}(E/E_{max})\ e^{-2(E/E_{max})^{1/2}} \tag{4}$$

The values of δ_{max} and E_{max} for the materials used in the study were taken from the table in reference 4. A comparison of the $\delta(E)$ obtained from the two relations for an aluminum surface is shown in figure 1. In the case of aluminum the Sternglass expression can be fit to the difference of two exponentials fortuitously well.

Incident Maxwellian Electron Flux

If the incident electron flux is Maxwellian then the current continuity equation has at most one root, $J_{net}(V) = 0$. This can be seen by computing the secondary emission current density from

$$J_s = J_{oe} \int_{eV}^{\infty} \delta(E+eV)\ e^{\frac{eV}{kT}} \left(1 + \frac{eV}{E}\right) dE \tag{5}$$

Using equation (3) for $\delta(E)$ one finds

$$J_s = cJ_{oe}\ e^{\frac{eV}{kT}} \left\{ \frac{1}{\left(1 + \frac{kT}{a}\right)^2} - \frac{1}{\left(1 + \frac{kT}{b}\right)^2} \right\} \equiv \left(J_{oe}\ e^{\frac{eV}{kT}} \right) \cdot S$$

so that the secondary emission factor S defined by

$$J_s / J_e \equiv S = c \left\{ \frac{1}{\left(1 + \frac{kT}{a}\right)^2} - \frac{1}{\left(1 + \frac{kT}{b}\right)^2} \right\} \tag{6}$$

is independent of V. Therefore the current continuity equation can be written as

$$J_i(V) - J_e(V)\ (1-S) = 0 \qquad \text{or}$$

$$.025\ J_{oe}\ (1-V) - J_{oe}\ e^{eV/kT}\ (1-S) = 0$$

for a negatively charged surface. Since S is a constant, equation (5) has only one root.

Incident Electron Flux Described by Two Maxwellians

The synchronous orbit electron flux during a substorm is not always well described by a single Maxwellian. We have therefore also examined the multi-root nature of the current continuity equation in the case where the incident electron flux is more appropriately described by two Maxwellian energy distributions. In this case the current continuity equation can be written as

$$J_{net} = J_i(V) - J_{e_1}(V)\ (1-S_1) - J_{e_2}(V)\ (1-S_2) = 0 \tag{8}$$

This equation has more than one root only if $(1-S_1)$ and $(1-S_2)$ have opposite polarities. The conditions on J_{net}, S_1 and S_2 for a single positive, single negative or multiple roots are shown in table 1.

SYNCHRONOUS ORBIT STORM SPECTRA

As an application of the above we have computed the current-voltage characteristics for two different surface materials exposed to the storm electron spectra for synchronous orbit described by Knott (ref. 2). This spectrum is based on ATS-5 data (ref. 1). We have approximated the Knott spectrum by three approximations, each of which consisted of two Maxwellians. Each approximation to the electron spectrum had a differential flux given by

$$\frac{d\phi}{dE} = 10^8\ E\ e^{-\frac{E}{4}} + 10^9\ E\ e^{-\frac{E}{kT_2}} \tag{9}$$

The three different approximations were generated by selecting different values of kT_2, i.e., $kT_2 = 0.4$, 0.5 and 1.0 keV. These approximations and the Knott spectra are shown in figure 2. Also shown in the figure are the in-orbit data points obtained by DeForest.

Roots for a BeCu (Activated) Surface

Using the spectrum described, the floating potential of an activated BeCu surface in eclipse was computed. This material was selected because of the large number of secondary electrons released by it per incident electron. For BeCu (activated) $\delta_{max} = 5.00$ and $E_{max} = 0.4$ keV yields

$$\delta(E) = 6.3\left(e^{-\frac{E}{1.9}} - e^{-\frac{E}{0.1}}\right)$$

for our approximation to the Sternglass equation.

The net flux (J_{net}/e) vs potential of the surface is shown in figure 3 for each of the three spectra used. Note that even though the three spectra differ only slightly from each other, the nature of the three solutions are dramatically different. The solution for the spectra with $kT_2 = 1$ keV has only one positive root. In the case of $kT_2 = 0.4$ keV there is only one negative root, whereas if $kT_2 = 0.5$ keV three roots are found. In this case the middle root is unstable (ref. 4).

In figure 4 we show the nature of the floating potential solutions for an eclipsed BeCu (activated) surface in an ambient electron flux given by

$$\frac{d\phi}{dE} = 10^8 E e^{-\frac{E}{4}} + A_2 E e^{-\frac{E}{kT_2}}$$

We notice from the figure that the spectra selected for this study had values of A_2 and kT_2 near the boundaries in the figure separating the different kinds of solutions. As a result small changes in kT_2 or A_2 can produce significantly different solutions to the current continuity equation.

Voltage Solutions for an Aluminum Surface with Oxide Coating

A similar calculation was performed for an oxide coated aluminum surface in eclipse. In this case $\delta_{max} = 2.6$ and E_{max} 0.3 keV resulting in a = 1.33, b = 0.115 and c = 3.6.

A kind of voltage solution of the current continuity equation obtained are depicted in figure 5. We notice that in this case, all three spectra used to fit the Knott storm spectrum result in single negative solutions to $J_{net}(V) = 0$.

CONCLUSIONS

The possibility of the occurrence of multiple solutions for the floating potential of a body in eclipse has been studied particularly for the case where the electron flux is described by two Maxwellian energy distributions. In this case mutliple solutions can be obtained. In some instances, particularly if the material in question has a large fractional secondary emission yield (such as activated BeCu), the nature of the solutions can be sensitive to small changes in the spectrum. For example, for activated BeCu, a change in the flux of the incident electrons of about a factor of three at the spectral peak can change the solution for the floating potential from a large negative potential of over 3.5 kilovolts to a small positive potential of less than a kilovolt. This mechanism can result in large rapid changes in the floating potential of a body in eclipse during a substorm without requiring that the body move into sunlight.

REFERENCES

1. DeForest, S.E.; and McIlwain, C.E.: Plasma Clouds in the Magnetosphere. J. Geophys. Resh., vol. 76, 1971, pp. 3587-3611.

2. Knott, K.: The Equilibrium Potential of a Magnetospheric Satellite in an Eclipse Situation. Planet. Space Sci., vol. 20, 1972, pp. 1137-1146.

3. Inouye, G. T.: Spacecraft Charging Model. J. Spacecraft and Rockets, vol. 12, no. 10, 1975, pp. 613-620.

4. Prokopenko, S.: and Laframboise, J.G.: Prediction of Large Negative Shade-side Spacecraft Potentials. Proc. Spacecraft Charging Technology Conference, C. P. Pike and R. R. Lovell, Editors, AFGL-TR-77-0051 and NASA TMX-73537, Feb. 24, 1977, pp. 369-387.

5. Parker, L. W.: Differential Charging of Nonconducting Spacecraft. Proc. 1978 Symposium on the Effect of the Ionosphere on Space and Terrestrial Systems. Sponsored by ONR and NRL, Session IV, Jan. 25, 1978.

6. Goldstein, R.; and Devine, N.: Plasma Distribution and Spacecraft Charging Modeling Near Jupiter. Proc. of the Spacecraft Charging Technology Conference, C. P. Pike and R. R. Lovell, Editors, AFGL-TR-77-0051 and NASA TMX-73537, Feb. 24, 1977, pp. 131-141.

7. Sanders, N. L.; and Inouye, G. T.: Voyager Spacecraft Charging Model Calculations. Proc. 1978 Symposium on the Effect of the Ionosphere on Space and Terrestrial Systems. Sponsored by ONR and NRL, Session IV, Jan. 25, 1978.

TABLE I. VOLTAGE SOLUTIONS TO $J_{NET}(V) = 0$ USING A TWO MAXWELLIAN SPECTRA

ONE POSITIVE	ONE NEGATIVE	ONE POSITIVE & TWO NEGATIVE
$S_1 < 1$, $S_2 < 1$ and $J_{net} > 0$ at $V = 0$	$J_{net} < 0$ at $V = 0$	$(1-S_2) < 0$, $(1-S_1) > 0$ and $J_{net} > 0$ at $V = 0$ and $J_{net} < 0$ for some $V < 0$
or $S_1 > 1$, $S_2 > 1$		
or $(1-S_2) < 0$, $(1-S_1) > 0$ and $J_{net} > 0$ for all $V < 0$		

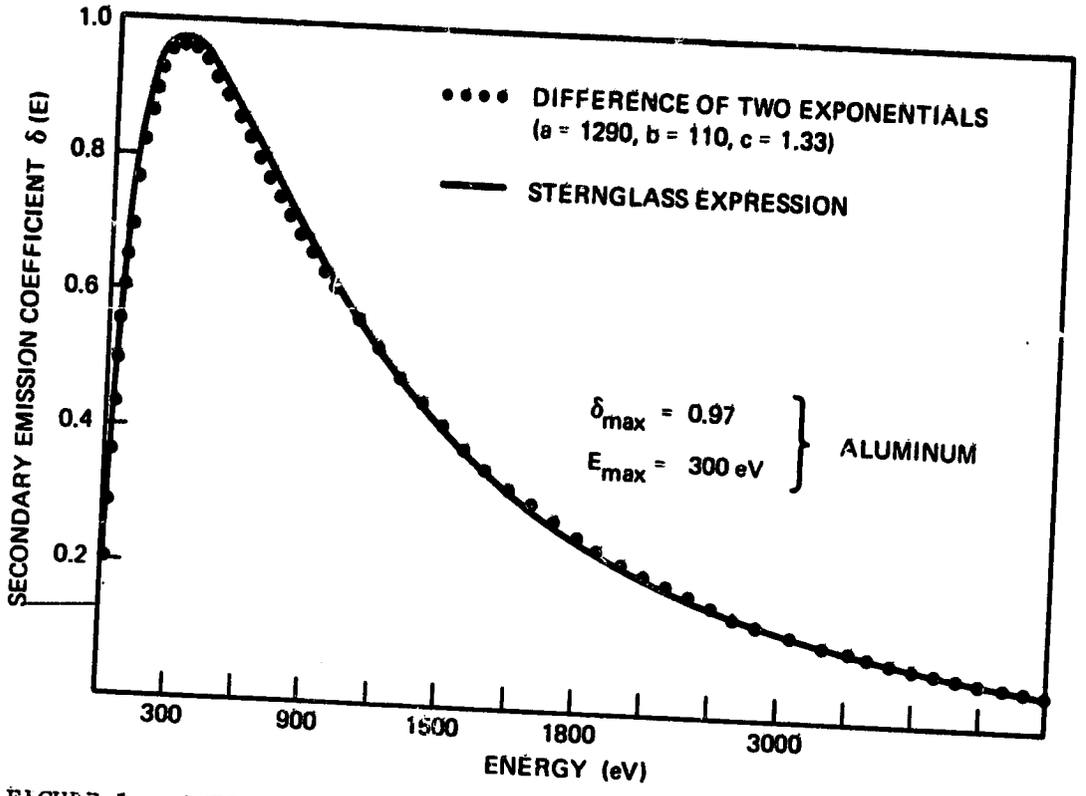

FIGURE 1. APPROXIMATION TO SECONDARY EMISSION COEFFICIENT, δ(E), FOR ALUMINUM USING THE DIFFERENCE OF TWO EXPONENTIALS.

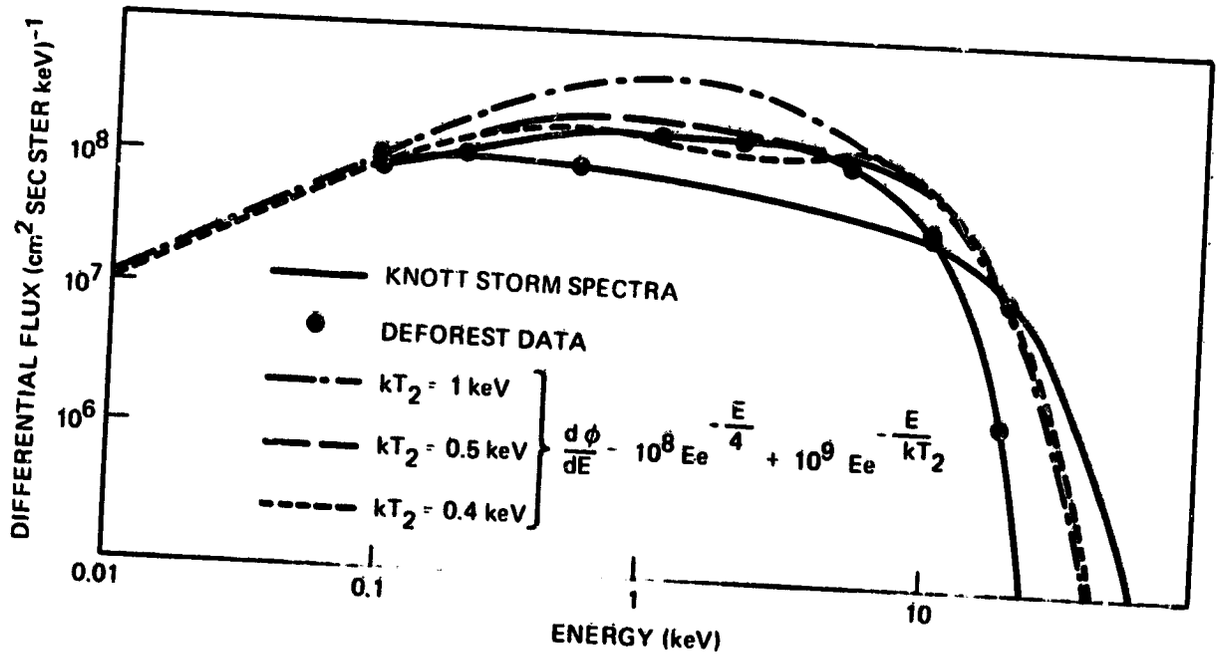

FIGURE 2. STORM SPECTRA USED IN STUDY

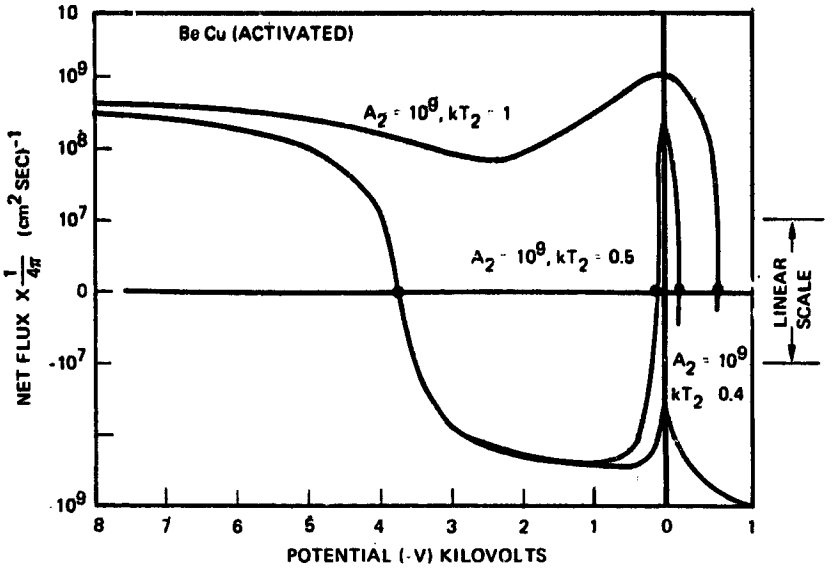

FIGURE 3. NET FLUX TO SPACECRAFT VS FLOATING POTENTIAL FOR THREE DIFFERENT STORM SPECTRA DESCRIBED BY

$$\left(\frac{d\phi}{dE} = 10^8 E e^{-E/4} + A_2 E e^{-E/kT_2}\right)$$

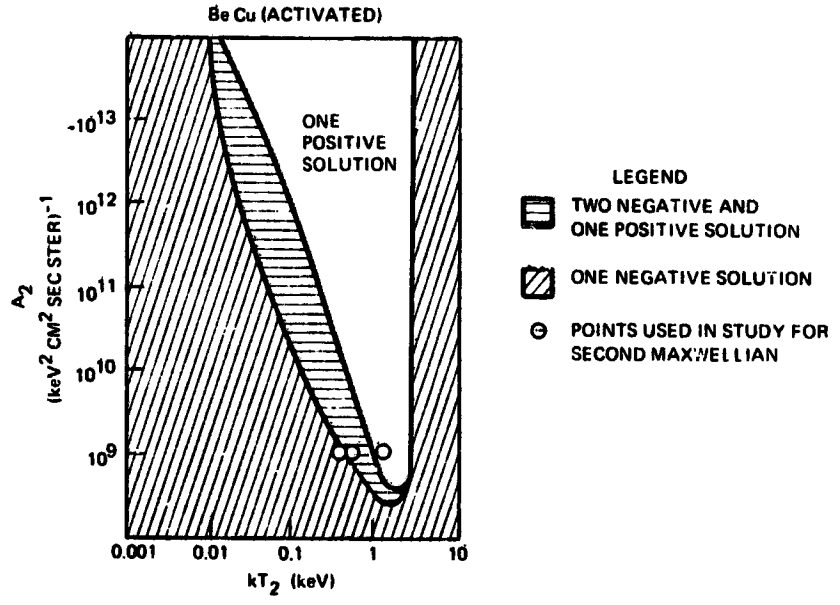

FIGURE 4. NATURE OF FLOATING POTENTIAL SOLUTIONS FOR BeCu (ACTIVATED) USING A TWO MAXWELLIAN SPECTRAL FIT

$$\left(\frac{d\phi}{dE} = 10^8 E e^{-E/4} + A_2 E e^{-E/kT_2}\right)$$

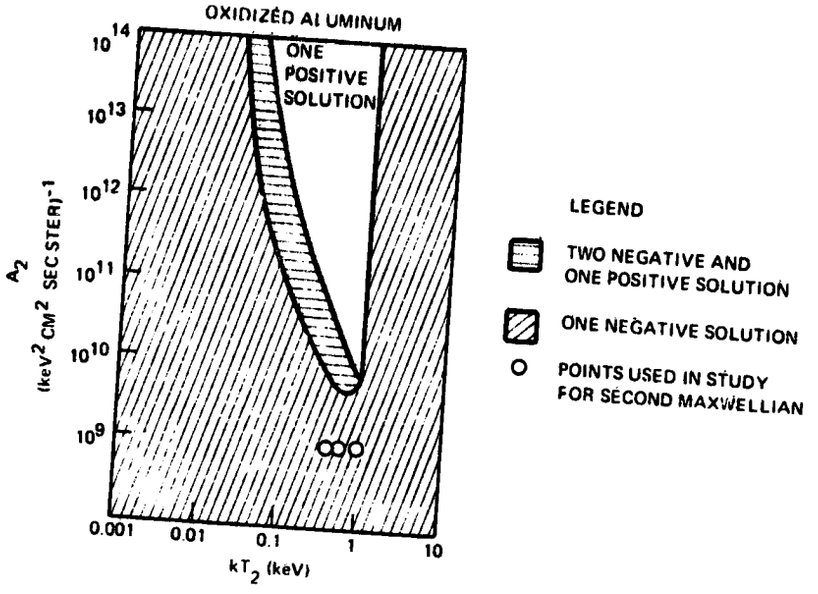

FIGURE 5. NATURE OF FLOATING POTENTIAL SOLUTIONS FOR OXIDE COATED ALUMINUM USING A TWO MAXWELLIAN SPECTRAL FIT

$$\left(\frac{d\phi}{dE} = 10^8 \, E \, e^{-E/4} + A_2 \, E \, e^{E/kT_2}\right)$$

D47

N79-24048

SECONDARY ELECTRON EFFECTS ON SPACECRAFT CHARGING

J. W. Haffner
Rockwell International Corporation

SUMMARY

Calculations have been carried out to determine the effects of electron-produced secondary electrons on the net charging current and the equilibrium voltage of spacecraft surfaces immersed in hot (keV) plasmas. The ratio of secondary to primary electrons as functions of the primary electron energy, E, was fit by expressions of the form $A(e^{-aE} - e^{-bE})$ where A, a, and b were material-dependent parameters. Materials evaluated were aluminum, Mylar, Teflon, and Kapton.

The energy, E, at which the secondary/primary electron ratio has a maximum was in the 0.1- to 1-keV region. Assuming a Maxwellian primary electron energy distribution, the secondary electrons were found to limit equilibrium spacecraft voltage only for plasma temperatures $\leq$3 keV. The charging rate was reduced for higher-temperature plasmas, but only until spacecraft voltages reached ~10 keV. The limited effectiveness of the secondary electrons in limiting spacecraft charging parameters (voltage, current) was due to the low primary electron energies at which they were produced.

INTRODUCTION

In an electrically neutral plasma there will be equal densities of negative and positive charges. (If the plasma is not fully ionized there will be neutral particles as well. These will be ignored in this discussion.) Usually the negative charges are electrons. Near geosynchronous orbit the positive charges are mostly protons, and the small neutral component is largely made up of hydrogen atoms.

Because of collisions, both the negative component (electrons) and the positive component (mostly protons) of the geosynchronous orbit plasma have quasi-Maxwellian energy distributions with comparable (within a factor of 2) average energies. Since neither the electrons nor the protons are relativistic (velocities ~0.01 c), the electrons have $\sqrt{1836} = 42.85$ times the average velocity of the protons. Therefore, the electrons will impact any surface within the plasma (e.g., a spacecraft skin) much more often than the protons will. Assuming that comparable fractions of the impacting electrons and protons stick, the surface will acquire a negative charge. As the surface acquires a negative charge the rate at which electrons impact it will decrease while the proton impact rate will increase. When the rate at which the net charge transfers to the surface equals zero, charging stops and the surface will have an equilibrium potential (voltage).

While there are other charge transfer mechanisms to and from the surface beside the impacts of primary electrons and protons (such as secondary electrons and photoelectrons leaving the surface), only the impacts of these primary particles will be considered in this section. The rate of the electron impacts will decrease exponentially as the spacecraft surface acquires a negative voltage because the electrons in the plasma are subsonic (the directed component of their velocity is less than the thermal velocity component). Thus

$$J_e(V) = J_o \, e^{-V/V_o}$$

where

$J_e(V)$ = current density of electrons of energy (voltage) V

V_o = average energy (voltage) of the electrons (it is also a measure of the plasma temperature)

J_o = $N \, q \, \bar{v}$

N = density of electrons in the plasma

q = charge/electron

$\bar{v}$ = average electron velocity

For the purposes of this discussion, V_o will be considered to remain constant.

The total primary electron current density consists of all electrons able to reach the spacecraft surface — i.e., those with energies > V. Thus

$$J_e(>V) = \int_V^\infty J_e(V) \, dV = J_o \, V_o \, e^{-V/V_o}$$

This expression shows that the total primary electron current density increases with V_o (which is a measure of plasma temperature) and that the larger V_o is, the more slowly the current density decreases with spacecraft voltage (V).

The primary positive current density when the spacecraft is uncharged will be approximately

$$J_p(V) \approx \frac{J_o}{42.85}$$

However, as the spacecraft surface acquires a negative voltage the primary positive current only increases linearly because the protons are supersonic (their directed velocities exceed their thermal velocities). Thus the total primary proton current density as a function of spacecraft voltage is

$$J_p(>V) = \int_{-V}^{\infty} J_p(V)\, dV = \frac{J \cdot V_o}{42.85}\left(\frac{V}{V_o} + 1\right)$$

The equilibrium voltage (if no secondary effects are operating) occurs when

$$\frac{1}{42.85}\left(\frac{V}{V_o} + 1\right) = e^{-V/V_o}$$

As can be seen from Figure 1, this occurs when $V/V_o \approx 2.5$. This figure also shows two other crossover points — one at $V/V_o \sim 2.7$ (if the proton integral current is proportional to V/V_o instead of $V/V_o + 1$) and the other at $V/V_o \sim 3.75$ (if the proton current does not increase as V increases). These other values of V/V_o at equilibrium are sometimes quoted in the literature, but $V/V_o \sim 2.5$ is correct for the primary currents (secondary electron and photoelectron emission will reduce this value).

As V_o (the average energy of the particles in the plasma) increases, the magnitudes of the primary currents and the equilibrium voltage also increase (see Figure 2). Thus the time to reach equilibrium is essentially independent of V_o. This time is a function of the capacitance unit area and typically is on the order of a few minutes.

SECONDARY ELECTRONS

When charged particles impinge upon matter they will displace electrons in that matter from their equilibrium positions. Some of these electrons may acquire sufficient energy in the backward direction to escape from the matter completely. These are called secondary electrons, as contrasted to backscattered electrons. Backscattered electrons result when the incident charged particles are electrons and some of them are reflected in the backward direction. Thus if the incident particles are not electrons, no backscattered electrons can be produced (but secondary electrons can be produced). If the incident particles are electrons, both backscattered electrons and secondary electrons can be produced. The backscattered electrons usually have energies which are a considerable fraction of the incident electrons' energies, while the secondary electrons will have lower energies — typically <1 keV — and while the ratio of backscattered electrons to incident electrons will always be ≤1, the ratio of secondary electrons to incident particles (electrons or anything else) is often >1.

Both backscattered electrons and secondary electrons are important in spacecraft charging. They affect the rate at which the spacecraft will acquire charge (and hence voltage) and also (assuming there is no electrical breakdown) the equilibrium voltage to which the spacecraft will charge. This is due to the fact that every electron which leaves the spacecraft cancels the charging effects of every electron which impacts the spacecraft. When the number of electrons leaving minus the number of electrons arriving equals the

number of positive charges arriving, an equilibrium is achieved and the spacecraft no longer acquires additional charge.

There have been measurements of both backscattered and/or secondary electrons from many materials. Often little or no attempt has been made to separate these two types of electrons, so the results are presented as the ratio of emergent/incident electrons as a function of incident electron energy. Typical of such measurements is that for aluminum (Reference 1), shown in Figure 3. This figure shows that the measured ratio (secondary electron current/primary electron current) has a maximum of ~1.1 at an incident electron energy of ~0.4 keV. Attempts to fit this ratio by an analytical function which could be multiplied by an exponential and integrated led to the calculated curve, viz.,

$$\frac{J_e'(V)}{J_e(V)} = 1.1 \left(e^{-0.1\ V} - e^{-10\ V} \right)$$

where

$J_e(V)$ = primary electron current density (amp/cm^2)

$J_e'(V)$ = secondary electron current density (amp/cm^2)

V = energy of primary electrons (keV)

The primary electron current density as a function of electron energy (V) is

$$J_e(V) = J_e\ e^{-V/V_o}$$

where V_o is the hot plasma temperature (keV). The current density due to electrons with energies >V is

$$J_e(>V) = J_e \int_V^\infty e^{-V/V_o}\, dV = J_e\ V_o\ e^{-V/V_o}$$

Thus, if the spacecraft voltage is V, which means that only electrons with energies >V will be able to reach it, the primary electron current will be exponentially decreased from the primary electron current able to reach an uncharged spacecraft.

If the ratio of secondary electron current to primary electron current is given by the expression

$$\frac{J_e'(V)}{J_e(V)} = K \left(e^{-aV} - e^{-bV} \right)$$

the secondary electron current will be

$$J_e'(V) = J_e\, e^{-V/V_o}\, K \left(e^{-aV} - e^{-bV}\right)$$

$$= J_e\, K \left[e^{-\left(a + \frac{1}{V_o}\right)V} - e^{-\left(b + \frac{1}{V_o}\right)V} \right]$$

In these expressions K, a, and b are parameters which depend upon the spacecraft surface material. Integrating this expression to obtain the net electron current on a spacecraft surface of voltage, V, yields ...

$$J_e'(>V) = \int_V^\infty J_e'(V)\, dV$$

$$= J_e\, K \left[\frac{e^{-\left(a + \frac{1}{V_o}\right)V}}{a + \frac{1}{V_o}} - \frac{e^{-\left(b + \frac{1}{V_o}\right)V}}{b + \frac{1}{V_o}} \right]$$

For aluminum K = 1.1, a = 0.1, and b = 10. This function (for $J_e = 1$) is shown graphically in Figure 4. It shows that for V = 0 (an uncharged spacecraft) the secondary current is approximately proportional to V_o (the plasma temperature). However, as the spacecraft becomes charged (V/V_o increases) the secondary electron current decreases, and that decrease is more rapid if the plasma has a high temperature (large V_o) than if it has a low temperature. This is to be expected since for a large V_o the importance of the 0.1 - 10 keV region (where secondary electrons are important in aluminum) is less than it is for a small V_o.

By noting the intersections of the curves in Figure 2 (the net primary current) with the corresponding curves in Figure 4 (the secondary electron current) it is possible to obtain the equilibrium voltage to which aluminum will charge in the absence of sunlight. The results of such a graphical solution are listed in Table 1.

The effects of sunlight are to increase the secondary electron current by ~0.5 nanoamps/cm^2. If the primary electron current (when the spacecraft is uncharged) is 1 nA/cm^2, the total secondary electron current is obtained by increasing the ordinates of the curves in Figure 4 by 0.5. This has been done to obtain the curves shown in Figure 5. While the effects of the photoelectrons are relatively small at V = 0, as V (the spacecraft potential) increases the photoelectrons dominate the secondary electron current. This accounts for the asymptotes at ~0.5 of the curves in Figure 5. By overlaying Figure 5 with Figure 2, the equilibrium voltages may be obtained from the intersections of the corresponding curves, as before. After multiplying by V_o, the results are listed in Table 1.

If the primary electron current density is 10 nA/cm^2, the curves of Figure 4 are increased by 0.05, yielding the curves of Figure 6. Proceeding as before yields the equilibrium potentials listed in the last column of

Table 1. As expected, if the initial (V = 0) primary electron current density is small (e.g., 1 nA/cm^2), the equilibrium voltage is fairly low because the secondary electrons only have to approach half of this amount (the photoelectrons accounting for the remainder). However, if the initial primary electron current density is large (e.g., 10 nA/cm^2) the effect of sunlight is small, leading to an equilibrium voltage little different from that in the absence of sunlight. The effects of the photoelectrons, unlike those of the secondary electrons, do not depend upon the value of V_o (the temperature of the plasma).

The ratios of secondary electron current to primary electron current for three common plastics (Mylar, TFE Teflon, and Kapton) are shown in Figure 7 (References 2, 3, and 4). Since these curves exhibit the same general peaked behavior as a function of primary electron energy as aluminum, the same type of analytical expression was used to approximate this behavior. Proceeding as for aluminum, the secondary electron currents for these three plastics are

Mylar $K = 9 \quad a = 3 \quad b = 15$

$$J_e' = 9\, J_e \left[\frac{e^{-\left(3 + \frac{1}{V_o}\right)V}}{3 + \frac{1}{V_o}} - \frac{e^{-\left(15 + \frac{1}{V_o}\right)V}}{15 + \frac{1}{V_o}} \right],$$

TFE Teflon $K = 5.8 \quad a = 1 \quad b = 5$

$$J_e' = 5.8\, J_e \left[\frac{e^{-\left(1 + \frac{1}{V_o}\right)V}}{1 + \frac{1}{V_o}} - \frac{e^{-\left(5 + \frac{1}{V_o}\right)V}}{5 + \frac{1}{V_o}} \right]$$

Kapton $K = 3.5 \quad a = 2 \quad b = 15$

$$J_e' = 3.5\, J_e \left[\frac{e^{-\left(2 + \frac{1}{V_o}\right)V}}{2 + \frac{1}{V_o}} - \frac{e^{-\left(15 + \frac{1}{V_o}\right)V}}{15 + \frac{1}{V_o}} \right]$$

Proceeding as for aluminum, the secondary currents as functions of plasma temperature (V_o) and the mechanisms acting (secondary electrons, photoelectrons) have been calculated from these equations (the photoelectron current was taken as 0.5 nA/cm^2 for all cases). By overlaying these secondary current curves with the net primary current, curves of Figure 2 yielded the equilibrium voltages listed in Table 2.

It is seen that the secondary electron emission for Mylar and Kapton is too small to effectively limit the equilibrium potentials for most of the plasma temperatures considered (2 to 10 keV). If sunlight is present, the photoelectrons limit the equilibrium potentials if the plasma temperature (V_o) is not too high and if the primary electron current initially present (J_e) is not too high. The secondary electron emission for TFE Teflon limits the equilibrium potentials for low plasma temperatures ($V_o = 3$ keV) even in the

absence of sunlight and helps prevent charging in the presence of sunlight until plasma temperatures exceed a few kilovolts.

Examining Figure 7 with these results in mind shows that it is the energy region over which the secondary electron emission is active that determines its effectiveness for the plasma temperatures considered. For incident (primary) electron energies ≥1 keV, only Teflon has much secondary electron emission. Comparing the effects of secondary electron emission from aluminum (Figure 3 and Table 1) with those from the plastics (Figure 7 and Table 2) shows that the higher the incident electron energies as which secondary electrons are emitted, the more effective the secondary electrons are at limiting the equilibrium potentials — especially at high plasma temperatures. Considerable effort is being expended in trying to develop such materials (Reference 5) as well as in looking for conductive coatings with desirable thermophysical properties (Reference 6).

The effects of secondary electrons upon the spacecraft voltage as a function of time may be calculated by obtaining the average current as a function of V/V_o and summing the inverses of these currents for convenient-sized voltage steps. For example, in the absence of secondary electrons, the net primary current is 1 if $V/V_o = 0$, 0.75 if $V/V_o = 0.25$, 0.56 if $V/V_o = 0.50$, etc. The average time to charge from $V/V_o = 0$ to $V/V_o = 0.25$ will be ~1/0.875 or 1.14 units, while the average time to charge from $V/V_o = 0.25$ to $V/V_o = 0.50$ will be ~1/0.655 or 1.53 units, etc. The time to charge from 0 to $V/V_o = 0.25$ is thus 1.14 units, while the time to charge from 0 to $V/V_o = 0.50$ is 2.67 units, etc. By proceeding in this manner, the curves shown in Figure 8 were generated for aluminum in the absence of sunlight. It is seen that the secondary electrons slow down the charging process even in those situations in which they have a negligible effect upon the equilibrium potential as $t \to \infty$. Thus if there are electrical breakdowns which prevent the equilibrium potential from being reached, the secondary electrons (and the photoelectrons as well, if sunlight is present) act to reduce the frequency of such breakdowns.

Many plastic materials have a dielectric strength of ~500 volts/mil of thickness. While handbook values of this quantity vary or show ranges of values, 500 volts/mil is a good average for the three plastics considered here (Teflon, Mylar, and Kapton). Based upon this dielectric strength, it is possible to calculate the minimum thickness necessary to prevent electrical breakdown in plasma of a given temperature (V_o). If $V_o = 10$ keV (a reasonable upper limit, since the maximum measured spacecraft potential due to hot plasma has been ~19 keV) plastic surfaces should be ~50 mils thick unless they will be continually exposed to sunlight (in which case some reduction can be made for synchronous orbits).

CONCLUSIONS

The equilibrium voltage attained in a hot plasma due to primary protons and primary electrons only is shown to be ~2.5 V_o (the electron thermal

energy). The effects of secondary electrons produced by the primary plasma electrons were examined for aluminum and three common plastics (Teflon, Mylar, and Kapton). One result of this investigation was that it is the primary electron energy region over which the secondary electrons are emitted (rather than the ratio of secondary to primary electrons) which determines the effectiveness of the secondary electrons in limiting the net charging current. Thus aluminum (which has a maximum secondary electron/primary electron ratio of ~1.1 at ~0.4 keV) is more effective in this regard than any of the plastics (even though the plastics have maximum secondary electron/primary electron ratios up to 4.8). This is due to the fact that the plastics have these ratios at 0.1 to 0.3 keV. A second result is that while the electron-produced secondary electrons decreased the charging current, they had little effect upon the equilibrium voltages attained. This is due to the fact that as the spacecraft voltage becomes high (≥10 kilovolts negative) the only primary electrons able to reach it are too energetic to produce a significant number of secondary electrons. Under these conditions only the photoelectron current (which is ~ constant, independent of negative spacecraft voltages) acts to decrease the equilibrium voltage.

REFERENCES

1. Whipple, E. C.: The Equilibrium Electric Potential of a Body in the Upper Atmosphere and in Interplanetary Space. Report X-615-65-296, NASA Goddard Space Flight Center (June 1965).

2. Darlington, E. H. and Cosslett, V. E.: Backscattering of 0.5-10 keV Electrons from Thick Targets. Journal of Physics D, Applied Physics 5, 1969-1981 (1972).

3. Willis, R. F. and Skinner, D. K.: Secondary Electron Emission Yield Behavior of Polymers. Solid State Communications 13, 685-688 (1973).

4. Darlington, E. H.: Backscattering of 10-100 keV Electrons from Thick Targets. Journal of Physics D, Applied Physics 8, 85-93 (1975).

5. Frey, G. C.: AF/NASA (OAST) Space Technology Group Meeting on Spacecraft Charging. Internal Letter to L. L. Bissing, Rockwell International, Space Division (4-19-77).

6. Eagles, A. E. and Belanger, V. J.: Conductive Coatings for Satellites. Report AFML-TR-76-233, General Electric Space Division (December 1976).

Table 1. Equilibrium Voltages for Aluminum Spacecraft Surfaces in Hot Plasma (Temperature V_o)

V_o (keV)	Equilibrium V(keV) No Secondary e⁻ No Sunlight	Equilibrium V(keV) Secondary e⁻ No Sunlight	Equilibrium V (keV) Secondary e⁻ Sunlight	
			$J_e = 1 \frac{nA}{cm^2}$	$J_e = 10 \frac{nA}{cm}$
1	2.5	0.6	~0	0.2
2	5.0	3.5	~0	1.5
3	7.5	6.3	~0	4.2
5	12.5	11.5	~0	9.25
10	25.0	24.5	~0	20.5

Table 2. Equilibrium Voltages for Various Plastic Spacecraft Surfaces

Material	V_o (keV)	Equilibrium V(keV) No Secondary e⁻ No Sunlight	Equilibrium V(keV) Secondary e⁻ No Sunlight	Equilibrium V (keV) Secondary e⁻ Sunlight	
				$J_e = 1 \frac{nA}{cm^2}$	$J_e = 10 \frac{nA}{cm^2}$
Mylar	1	2.5	~ 0	~0	~ 0
	2	5.0	~ 5.0	~0	~ 0
	3	7.5	~ 7.5	~0	~ 6.3
	5	12.5	~12.5	~3.0	~10.5
	10	25.0	~25.0	~6.0	~21.0
Kapton	1	2.5	~ 2.5	~0	~ 2.1
	2	5.0	~ 5.0	~0.4	~ 4.2
	3	7.5	~ 7.5	~1.8	~ 6.3
	5	12.5	~12.5	~3.0	~10.5
	10	25.0	~25.0	~5.0	~21.0
Teflon	1	2.5	~ 0	~0	~ 0
	2	5.0	~ 0	~0	~ 0
	3	7.5	~ 0	~0	~ 0
	5	12.5	~12.5	~0	~10.5
	10	25.0	~25.0	~6.0	~21.0

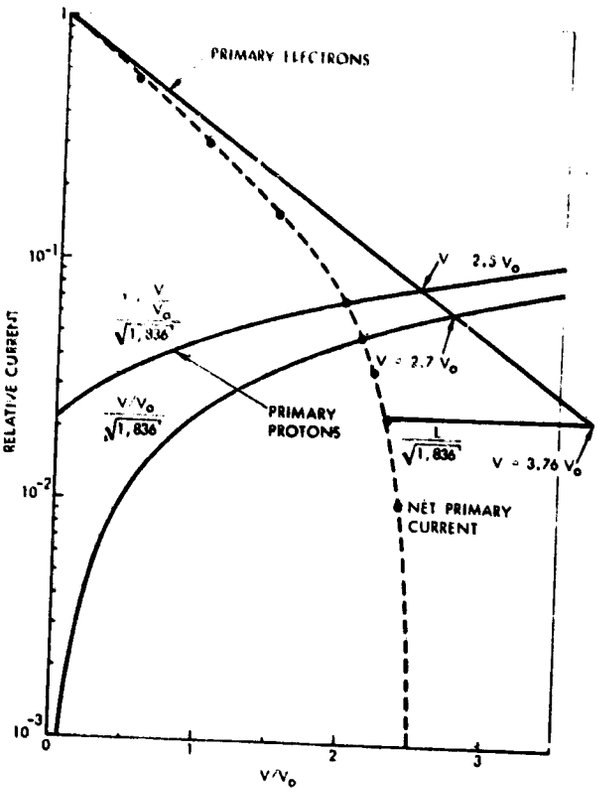

Figure 1. Net Primary Current as a Function of Spacecraft Voltage/ Plasma Temperature Ratio

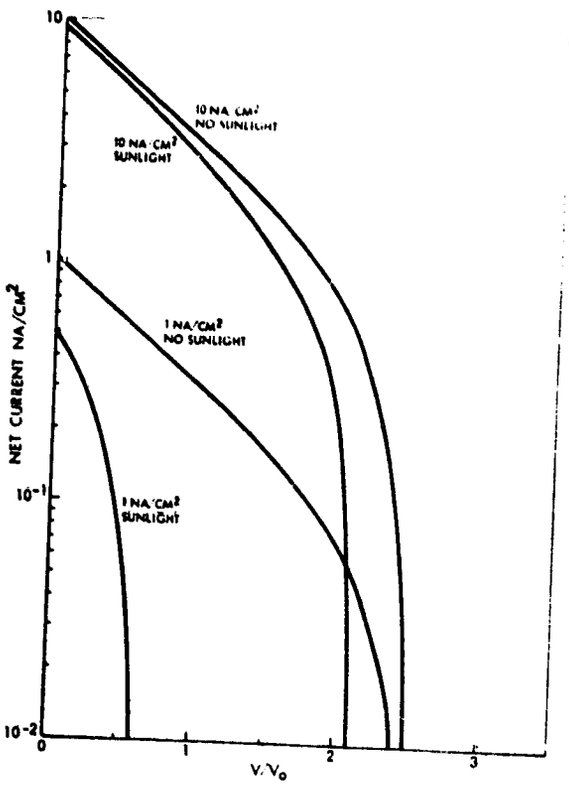

Figure 2. Net Primary Current With and Without Sunlight

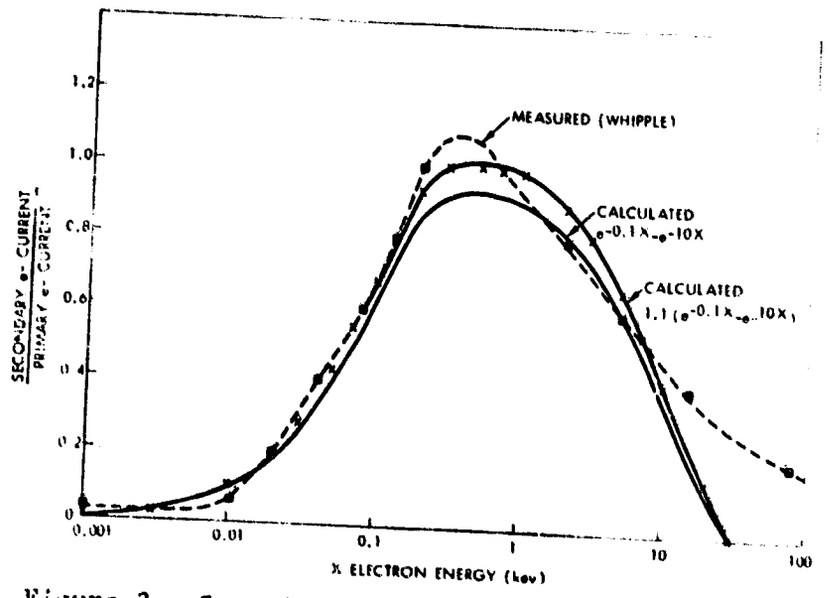

Figure 3. Secondary Electron Emission Due to Primary Electrons on Aluminum

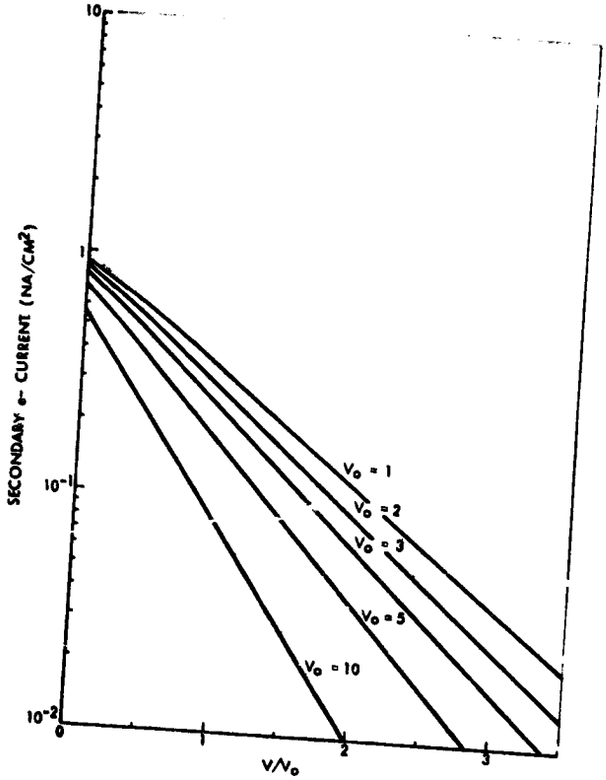

Figure 4. Secondary Electron Current from Aluminum Due to 1 Na/cm^2 Primary Electron Current, No Sunlight

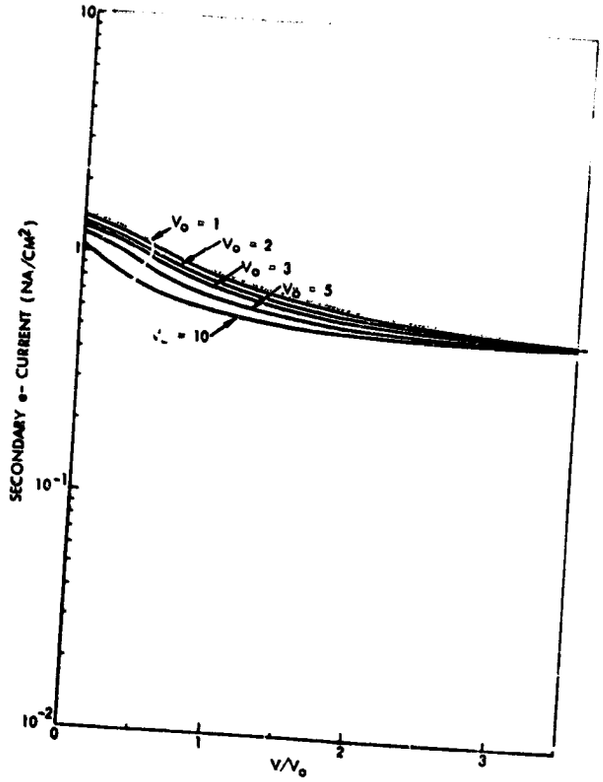

Figure 5. Secondary Electron Current from Aluminum Due to 1 Na/cm^2 Primary Electron Current, in Sunlight

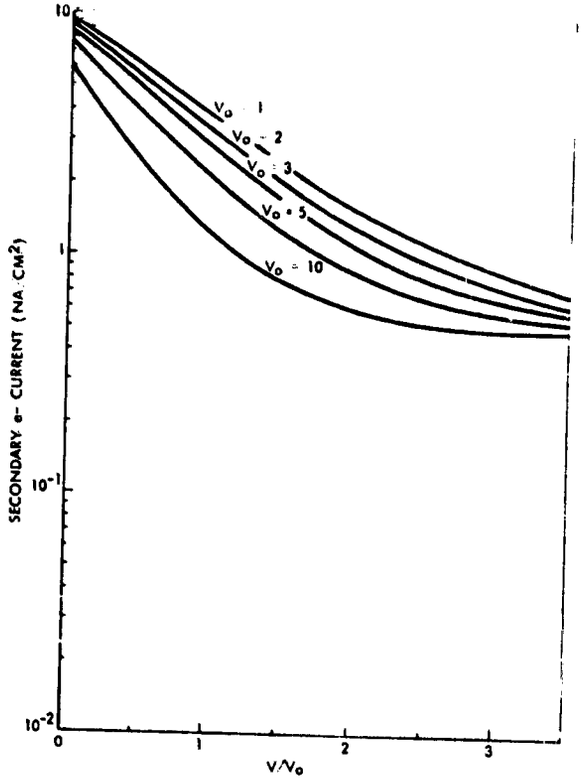

Figure 6. Secondary Electron Current from Aluminum Due to 10 Na/cm^2 Primary Electron Current, in Sunlight

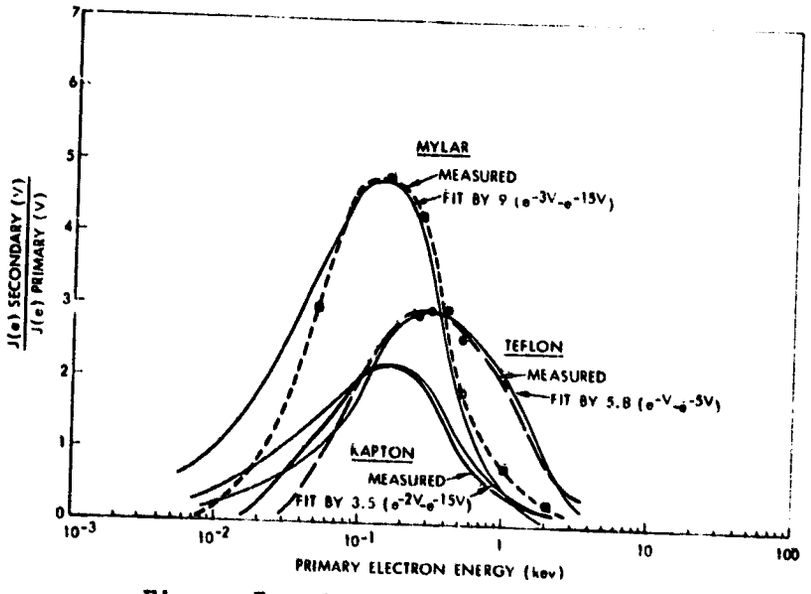

Figure 7. Secondary Electron Emission Due to Primary Electrons on Mylar, Teflon, and Kapton

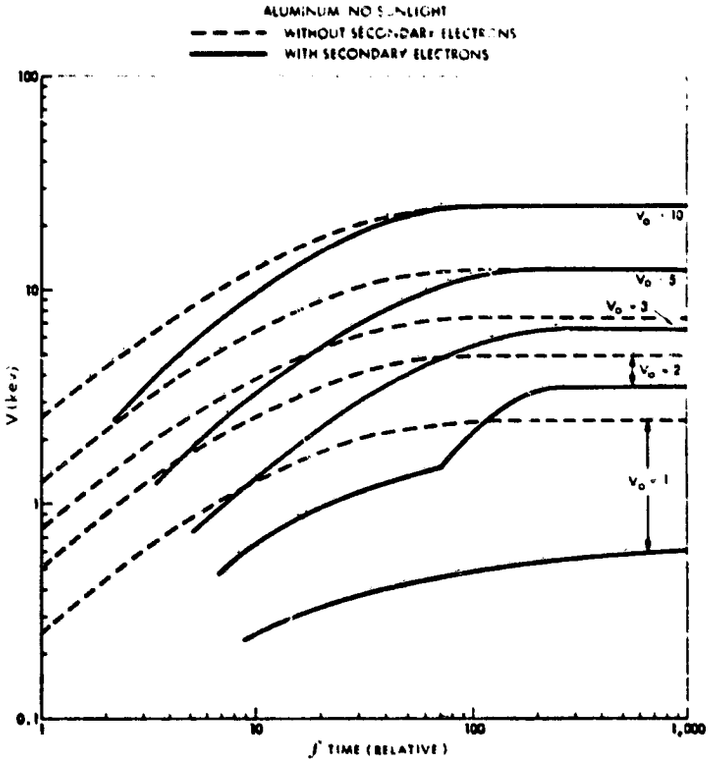

Figure 8. Effect of Secondary Electrons on the Charging Rates Due to Hot Plasma on Aluminum

GEOSYNCHRONOUS SATELLITE OPERATING ANOMALIES CAUSED BY INTERACTION WITH THE LOCAL SPACECRAFT ENVIRONMENT*

Michael A. Grajek
Hiram College

Donald A. McPherson
Science Applications, Inc.

ABSTRACT

It is now apparent that a significant number of satellite operating anomalies are due to differential charging of spacecraft surfaces and resultant discharges. Recent satellite anomaly investigations generally support this conclusion. However, these investigations provide only limited information about the nature of charging/discharging mechanisms and, collectively, they support conflicting opinions on the importance of some environmental effects. This is due in part to limitations of the available data and in part to non-analytical visual inspection procedures that are frequently used to scrutinize and interpret the data. Examples illustrate how such procedures might lead to faulty conclusions. Further examples demonstrate quantitative statistical analysis procedures that can be used to strengthen the data handling, especially attempts to correlate spacecraft anomalies with geophysical parameters. As data from the SCATHA mission becomes available, it should be possible to carry out a very detailed statistical analysis of satellite operating anomalies because of certain key features of the SCATHA Data Analysis Plan.

STATE-OF-THE-ART ANOMALY INVESTIGATIONS

As table I illustrates, hundreds of geosynchronous satellite operating anomalies have been observed, recorded and subjected to analysis (ref. 1 through ref. 7). Most of these events have had little impact on the spacecraft mission, but they have been as serious as total failure of the power system. An examination of these investigations reveals the following general characteristics:

- A relation between actual anomalous behavior and spacecraft charging has been established. The most substantial evidence for this seems to be the highly significant statistical correlation between implied surface discharges and faulty

* Work supported in part through contract NAS3-21048 with NASA/LeRC and F04701 - 77 - C - 0166 with SAMSO.

responses and circuit resets (ref. 6).

- Conclusions have usually been based on a "pattern recognition" approach. The calculation of meaningful statistical correlations has been severely hampered by a lack of high time resolution data regarding the spacecraft local environment. Nearly all studies have called for routine inclusion of monitoring devices on board future flights.

- Various "correlations" of anomalous behavior with environmental and other effects have been observed. These include

  -local time dependence
  -seasonal dependence
  -geomagnetic activity dependence
  -day-of-the-week dependence
  -long-term decrease

Not all of these dependences are reported in every study, and the statistical basis for the dependences that appear to exist varies greatly. Moreover, there are some discrepancies between studies in the ways that certain correlations are supported:

- local time dependence: this is reported in about half of the flights. The transient events reported in reference 6 show a skewed distribution favoring local midnight to dawn that is statistically highly significant. On the other hand, the anomalous switching events reported in reference 4 are distributed more uniformly. This has led to the proposal of charge storage theories or theories involving discharges occurring at varying thresholds.

- geomagnetic activity dependence: this is said to be apparent in about half of the studies. However, this discrepancy is not considered important because of the limited information contained in the various ground-based geomagnetic activity indices used in the investigation.

- day-of-the-week dependence: this is noted in reference 1. The anomalous events appear to significantly favor the weekend. A similar trend can be found in the reference 6 data, but here the favored days are Friday and Tuesday. A further discussion of this peculiarity will follow.

- a seasonal dependence: an increased likelihood of anomalous behavior during eclipse seasons--and a long term decrease in the rate of anomaly occurrences are noted in most investigations. The latter trend has been theorized to be due to materials degradation effects.

In reference 8, a more detailed discussion of state-of-the-art anomaly investigations, through early 1978, is included.

NEED FOR QUANTITATIVE ANALYSIS

Reliable information regarding the previously outlined interactions of a satellite with its local environment is needed in the following efforts:

- Development of the Spacecraft Charging Standard
- Design Guidelines Update
- Validation and Development of various models including predictive equations for satellite behavior

(These projects are discussed in detail in other papers in these conference proceedings.) The following examples illustrate potential pitfalls of not using proper statistical procedures in these efforts.

Example: Misleading Data Patterns

Table II presents hypothetical data for the local time of sixty observed satellite upsets. In figure 1, this data is depicted in the usual manner in a polar representation with time as the angular coordinate and frequency as the radial coordinate. The data *appears* to support a theory suggesting that upsets are most likely to occur in the midnight to dawn quadrant. Rather than stop at a visual inspection, the *strength* of the support can be quantified by calculating the chi-square (χ^2) statistic using

$$\chi^2 = \sum \frac{(O_i - E_i)^2}{E_i}$$

This statistic measures the deviations of observed frequencies (O_i) in each data subdivision from what they would be expected to be (E_i) if the phenomenon producing the data is purely random. Then chi-square tables can be used to associate a probability value with the calculated chi-square value. (See reference 9, pp.274-278, for a detailed explanation.)

In the example, there are four data subdivisions (time quadrants) and since there are sixty data points altogether, each E_i is 15. The calculated chi-square value is 4.13 and the associated probability value is .7522 (ref. 9, table E). The interpretation is that a purely random phenomenon would produce data as unevenly distributed in the four time quadrants as ours with a probability of .2478; in other words, there is nearly a twenty-five percent chance that we would be mistaken if we claimed that the data was *not* due to random phenomenon. Thus, in spite of the visual appeal, it would seem risky to use this data to support a theory suggesting that upsets favor the midnight to dawn quadrant.

Example: Which Hypothesis to Choose?

Similar to figure 1, figure 2 illustrates hypothetical data for satellite upsets. The total number is one hundred. The data appears skewed, but it supports various theories of non-randomness with quite different strengths.

Theory A: upsets favor certain one-hour time periods over others. In this case, 24 data subdivisions are used, and we obtain

$$\chi^2 = 28.14$$

probability = .7893

Theory A has only minimal support.

Theory B: upsets favor the midnight-dawn quadrant. Here there are four data subdivisions yielding

$$\chi^2 = 5.28$$

Probability = .8476

Thus, theory B receives mild support.

Theory C: upsets favor the 0300-0600 and 0600-0900 sectors. This time there are eight data subdivisions and we obtain

$$\chi^2 = 17.12$$

Probability = .9834

Theory C seems well-supported by this data.

Obviously, there should be good reasons for choosing theory C (for example, the possible existence of a "charge buildup" mechanism) aside from its statistical superiority. It is an extremely important principle of inferential statistics that hypotheses should be formulated before data is examined. Nearly all data will support, at least weakly, *some* theory of non-randomness. The problem of examining complicated data sets in search of patterns or clusters is discussed at length in reference 10.

STATISTICAL VERIFICATION OF SPACECRAFT ANOMALY-ENVIRONMENT RELATIONSHIPS

In the anomaly investigations discussed in the first section, and in other studies, correlation analysis frequently consists of plotting the anomaly data versus the appropriate geophysical parameter and attempting to judge the degree of correlation by visual inspection. Unfortunately, this does not generate quantitative, probabilistic statements about the strength of the relationship; as noted in the previous section, it can be misleading, and furthermore, such a non-analytical approach can overlook subtle or weak correlations that may be real and identified with a high degree of confidence

provided that a large amount of data are available.

The most common correlation measure is the (Pearson) product-moment correlation coefficient. It is calculated by dividing the covariance of two sets of data by the product of the standard deviations of each set (ref.9, ch. 12). Unity correlation coefficient corresponds to perfect correlation whereas 0 and -1 correspond to no correlation and perfect anticorrelation respectively. The square of the correlation coefficient may be interpreted as that proportion of the variation of one variable that can be explained by variation of the other variable. Thus, if the coefficient is r = .9, then only nineteen percent of the variation of one variable cannot be explained by its relationship to the other variable.

If the correlation between two variables is zero (no relationship) and the correlation obtained from the data is r, then the variable

$$t = r[(n-2)/(1-r^2)]^{\frac{1}{2}}$$

has a probability function given by

$$f(t) = \frac{\Gamma\left(\frac{\nu+1}{2}\right)}{\sqrt{\pi\nu}\,\Gamma\left(\frac{\nu}{2}\right)}\left(1+\frac{t^2}{\nu}\right)^{-(\nu+1)/2}$$

where the number of degrees of freedom, ν, is given by n-2 with n being the number of data points (ref.11, ch.10 and ch. 17). Then this function can be integrated from negative infinity to t and the result subtracted from 1 to obtain P, which can be interpreted as the probability of error in reporting a relationship if there is none. The analysis can be continued (ref.11, ch.17) to obtain a confidence interval, centered at r, for the true correlation between the variables. Thus r is a measure of the potential strength of the relationship between two variables while P and the confidence interval together give a measure of the reliability of the suggested relationship.

P and the confidence interval depend on r as well as the number of data points. For r = .50, table III shows values of P for various data-base sizes. Note that P decreases, and therefore reliability increases, as the number of data points increases.

In the examples that follow, the correlation coefficient r, the chi-square statistic, and the Kolmogorov-Smirnov test will be illustrated as methods for quantifying the relationship between two variables. Of course, many other statistical correlation techniques exist. Reference 12, appendix A contains a brief overview. Excellent in-depth presentations can be found in references 9, 10, and 11.

Example: Large Data Base Correlation

Nanevicz, Adamo, and Shaw (ref.13) show that a certain optical sensor exhibits an increase in temperature at a rate dependent upon geomagnetic activity. Visual examination of the data in Figure 9 of their report does

not show any obvious relationship, but a statistical analysis yields a weak correlation with a high degree of confidence ($P < .001$) because there are so many data points available.

Example: Correlation of Anomalies with Geomagnetic Activity

Table IV presents data for anomaly occurrences versus geomagnetic activity for a satellite discussed in references 3 and 13.

The geomagnetic activity is expressed in terms of the index D_{ST} that is designed to measure the equatorial magnetic disturbance produced by magnetic storms, with diurnal and local-time effects removed. Increasing negative D_{ST} implies a more active field. The basis for comparison is the relative cumulative frequency of occurrence of the two variables. Note that about half of the time, the geomagnetic activity corresponds to a $D_{ST} > -15$. Therefore on the average, the anomalies occur during times when the field is more active than normal. One possible statistical test would be to test the hypothesis that the means of two distributions in Table IV are the same. But to do this requires that the theoretical distribution functions for the two variables be known (ref. 11, ch. 10).

It is recommended instead that a distribution-free test be used to test whether the distribution of anomalies is the same as the distribution of D_{ST}. If the two distributions were the same, then there would be no reason to believe that the anomalies depend upon geomagnetic activity. The Kolmogorov-Smirnov test will be used since fewer than 30 data points are available (ref. 9, pp.281-283). Otherwise a chi-square test would be appropriate.

To perform the test, the largest difference between the relative cumulative frequencies (Table IV, middle column) is noted. This value, .44, is compared to tabled values of the Kolmogorov-Smirnov statistic for its significance. The result is that a value this great would be obtained by chance with probability less than .00003.

Conclusion: with 99.997% confidence, occurrence of the anomalies is dependent upon geomagnetic activity as measured by D_{ST}.

Example: Correlation of Anomalies with Local Time

As was noted in the first section of this paper, a common practice for testing correlation of anomalies or events with local time is to plot the time of occurrence on a polar representation of local time. If the data are grouped at any particular time period then the data are judged to be "correlated". If the data are distributed over all local times, then quite often it is concluded that there is no correlation.

More properly, the distribution of the anomaly data should be tested relative to a uniform distribution over local time. If the number of points is less than 30, then the Kolmogorov-Smirnov approach can be used. Otherwise use a chi-square test.

A test has been made of the hypothesis that the Transient Events Counter data in reference 6 are uniformly distributed (occur randomly) in local time. For the three-month period February through April 1976, there were 21 events and the Kolmogorov-Smirnov distribution was used to perform the test. The probability of obtaining a distribution with greater variance, than measured, from uniform was 15%. The conclusion, based on this limited data, is that the events could be uniform in local time. However, as more events are added in for the next nine months, a chi-square test shows that random phenomena would produce such a skewed local time distribution only 0.037% of the time.

Conclusion: with 99.963% confidence, the events are not distributed uniformly in local time.

Example: Correlation of Charging Voltages between Two Satellites

Bartlett, DeForest, and Goldstein (ref.14) have given measurements of charging voltages on two spacecraft when the vehicles were eclipsed simultaneously. For the data presented in Table V, the two satellites were separated by 11 degrees in longitude (over 8000 Km).

The correlation coefficient of these two sets of data is r = 0.84. The corresponding value of P is .0003.

Conclusion: with 99.97% confidence, there is a relationship between the charging voltages on the two spacecraft during eclipse. (Note that we do not suggest a dependency; the existence of a significant correlation does not imply a causal relationship.)

Example: Correlation of Anomalies with Day-of-the-Week

In the first section of this paper it was noted that the spacecraft anomalies of reference 1 appear to significantly favor the weekend. A day-of-the-week dependence is also suggested by the data in reference 6, but here the favored days are Friday and Tuesday. However, in both of these studies, if second and subsequent events on multiple event days are ignored, the day-of-the-week correlation disappears. Moreover, the distribution of multiple event days does not deviate from randomness in a statistically significant manner [for the reference 1 data, $\chi^2 = 8.62$, Probability = .8039].

Conclusion: It would seem that a day-of-the-week dependence is not supported.

STATISTICAL ANALYSIS OF THE SCATHA MISSION DATA

The data ambiguity of the last example of the previous section might not have occurred if it had been possible to accurately measure the magnitude, as well as merely count, discharge events. Then several relatively small discharges occurring over a short time interval would not receive the same status as several larger events spread out over several days. Magnitude is

one example of what is called a blocking variable: a variable that defines a category within which the experimenter can restrict the observation of other variables. The reliability and sophistication of a statistical analysis is directly proportional to the number of blocking variables included in the collection of experimental data.

In the preparation of the P78-2 Data Analysis Plan (reference 12) the importance of proper selection of blocking variables was noted in the design of one of the key features of the Plan: the Mission Data Time Line. This concept begins with an enumeration of important spacecraft operating condition categories:

SPACE PLASMA ENVIRONMENT
- -Quiet
- -Mild Substorm
- -Moderate Substorm
- -Severe Substorm
- -Transient Period (specify kind)

ECLIPSE
- -yes
- -no

MAGNETOSHEATH CROSSING
- -Region 1
- -Region 2
- -Transient Crossing Period

CONTROLLED EXPERIMENTS/OPERATIONS
- -None on
- -SC4 Guns on (specify kind)
- -Thruster Operations

Then the Mission Data Time Line consists of a chart indicating which of the 90 (5x2x3x3) mathematically possible unique categories the spacecraft is in at any time.

The information contained in the Time Line will be used in two major ways. First, it will be, itself, an important contribution to an understanding of the local environment of a geosynchronous satellite. Second, it will provide important additional blocking variables to be used in the statistieal analysis of the various on-board experiments. Thus, for example, internal transient count rates may be compared across different levels of substorm activity; or, it may be possible to develop a regression equation (ref.11, ch.17) that will provide a good, in the sense of statistical significance, formula for the active control of charging effects with gun operations under various spacecraft operating conditions.

CONCLUDING REMARKS

In conclusion, the dependence of a spacecraft anomaly or event upon geophysical parameters should be established on the basis of statistical analysis and the results should be expressed numerically. Examples have been provided for establishing relationships between events and parameters such as geomagnetic activity, local time, and events on other spacecraft. Other examples have illustrated the potential dangers of not using quantitative statistical techniques. As was noted in the last section, the data collection planning and statistical analysis planning should be done together.

It may be noted that most of the examples given demonstrate a high correlation between the events and the geophysical parameter being investigated. These examples have been drawn from data which may have been published because of the highly visible correlation that exists. It is likely that there are data sets that have not been published because the correlation with geophysical parameters is not obvious, but it may well exist if analyzed properly.

REFERENCES

1. Inouye, G.T.: Spacecraft Charging Anomalies on the DSCS II, Launch 2 Satellites. NASA TM X-73537, 1977.

2. McPherson, D.A.; et al.: Spacecraft Charging at High Altitudes - the SCATHA Satellite Program. AIAA paper 75-92, January 1975.

3. Naneviez, J.E.; and Adamo, R.C.: Transient Response Measurement On a Satellite System. NASA TM X-73537, 1977.

4. Robbins, A.; and Short, C.D.: Space Environmental Effects on the SKYNET 2B Spacecraft. NASA TM X-73537, 1977.

5. Rosen, A.: Spacecraft Charging by Magnetospheric Plasmas. IEEE Transactions on Nuclear Science, Vol. NS - 23, No. 6, December 1976.

6. Stevens, N.J.; et al.: Summary of the CTS Transient Event Counter Data After One Year of Operation. NASA TM-73710, 1977.

7. Fennell, J.F.: Nato - III ESA Anomalies. Aerospace Technical Memorandum ATM - 78 (3872-01)-3, October 1977.

8. Kamen, R.F.; et al.: Design Guidelines for Spacecraft Charging. Science Applications, Inc., March 1978.

9. Johnson, N.L.; and Leone, F.C.: Statistics and Experimental Design in Engineering and the Physical Sciences, vol.1, 2nd. ed. John Wiley and Sons, 1977.

10. Anderberg, M.R.: Cluster Analysis for Applications. Academic Press, 1973.

11. Chou, Ya-Lun: Statistical Analysis, 2nd ed. Holt, Rinehart and Winston, 1975.

12. Fong, J.C.; et al.: P78-2 Data Analysis Plan. Science Applications, Inc., CDRL 008AZ, August 1978.

13. Nanevicz, J.E.; Adamo, R.C.; and Shaw, R.R.: Electrical Discharges Caused by Satellite Charging at Synchronous Orbit Altitudes. Stanford Research Institute, September 1975.

14. Bartlett, R.O.; DeForest, S.E.; and Goldstein, R.: Spacecraft Charging Control Demonstration at Geosynchronous Altitude. AIAA Paper 75-359, AIAA 11th Electric Propulsion Conference, March 1975.

Table I. Summary of State-of-the-Art Anomaly Investigations

REFERENCE	NATURE OF ANOMALY	DATA BASE SIZE	ANALYSIS PROCEDURES	COMMENTS
1	Six types, primarily logic upsets and switching events	101	Distribution of anomalies presented in various histograms and graphs. No statistical correlation calculations reported.	33 months of data on two flights. Reported day-of-the week correlation probably artificial.
3	Faulty detector responses; uncommanded circuit resets surface discharges	41	41 actual anomalies correlated with detected surface discharges. Probability calculations.	Correlations are claimed between time of anomaly occurrence and both substorm activity and spacecraft surface discharges. Presents the most substantial evidence of relation between actual anomalous behavior and sheath environment.
4	Anomalous telemetry events	300+	Distribution of anomalies presented in several histograms. No statistical correlation calculations reported.	No local time correlation report. Two years of data; Precautions t[illegible] to insure data reliability; Vehic[illegible] contains unusually large number of switching devices. Reports anomalies correlate well with eclipse season and geomagnetic activity.
6	Transients in wiring harnesses	215	Distribution of anomalies presented in various histograms and scatter diagrams. No reported correlation calculations.	1 year of data. Rough correlation with eclipse season noted. Discussion relates transient events to charging and discharging models and lab experiments.
2 & 5	Various performance abberations	200+	Distribution of anomalies presented in various graphs and histograms. Some probability claculations.	Group anomaly data from seven different flights. Correlations reported do not always apply to individual flights.
7	Switching Events	13	K and Af index readings at times of events compared to the overall distribution of K and Af. Results of 8 events would occur by chance less than 20% of the time.	Small data base. Exact time of events unknown; some of time estimates could be off by over 24 hours. Interesting probability approach.

Table II. Number of Upsets Occurring in Local Time Segments (Hypothetical Data)

Mid-0100	3	0900-Noon	5
0100-0200	3	Noon-1500	7
0200-0300	4	1500-1800	5
0300-0400	4	1800-2100	6
0400-0500	3	2100-Mid	5
0500-0600	4		
0600-0700	4	N=60	
0700-0800	4		
0800-0900	3		

TABLE III. Effect of Data Base Size on the Reliability of the Correlation Coefficient (r = .50)

N	P
5	.196
10	.071
15	.029
20	.012
25	.005
30	.002

Table IV. Spacecraft Anomaly Occurrence Versus Geomagnetic Activity

D_{ST}	Relative Cumulative Frequency of D_{ST} or greater value	Difference (col.4-col.2)	Relative Cumulative Frequency of Anomaly Occurrences	Number of Anomaly Occurrences
-65	.02	.07	.09	2
-55	.04	.14	.18	2
-45	.08	.24	.32	3
-35	.18	.37	.55	5
-25	.29	.44	.73	4
-15	.48	.38	.86	3
-5	.73	.22	.95	2
+5	.93	.07	1.00	1
+15	.97	.03	1.00	0
+25	.99	.01	1.00	0
+35	1.00	.0	1.00	0

Table V. Charging Voltages on Two Spacecraft When Eclipsed

Vehicle 1	Vehicle 2
0	0
-4000	-3000
0	0
0	0
-1500	-1400
-9000	-11000
-1000	-1400
-6000	-800
-6000	-6000
-1000	-1000
-1600	-3200
-1100	-800

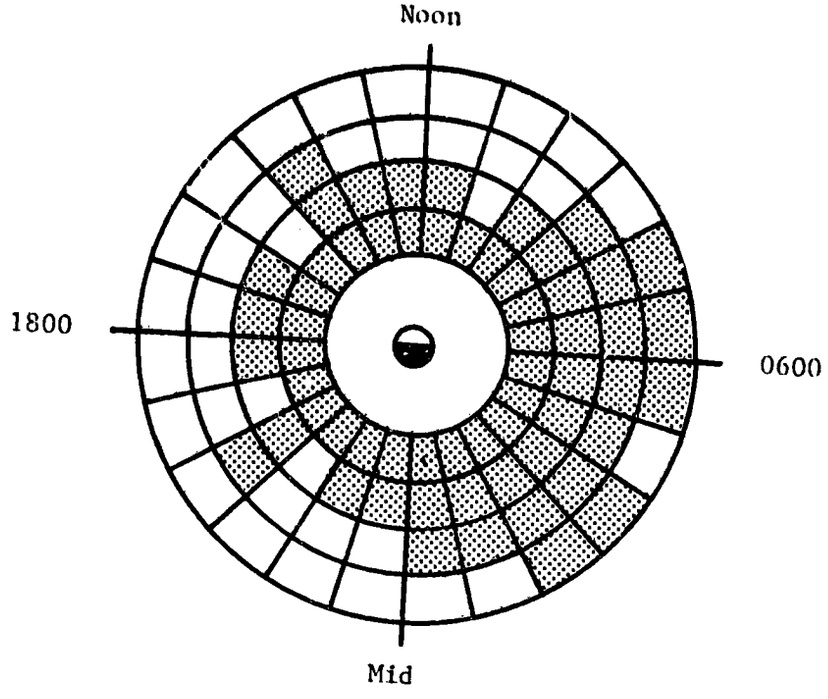

Figure 1. Polar Representation of Local Time of Sixty Upsets (Hypothetical Data).

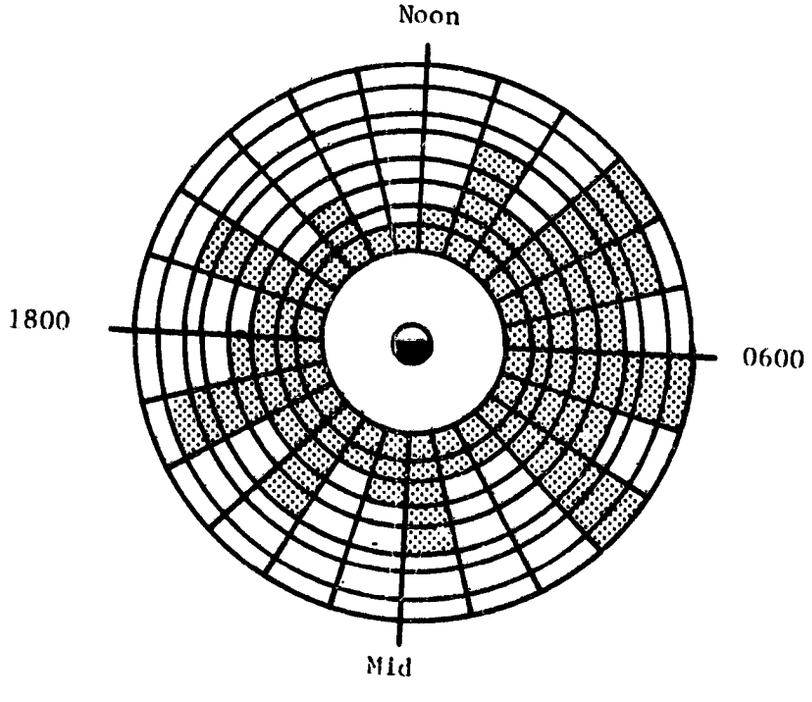

Figure 2. Polar Representation of Local Time of One Hundred Upsets (Hypothetical Data).

SPACECRAFT CHARGING STANDARD*

Alan B. Holman
Science Applications, Inc.

Maurice H. Bunn
Space and Missile Systems Organization

SUMMARY

A preliminary Spacecraft Charging Standard has been generated as one of the key activities in the cooperative NASA/AF Spacecraft Charging Investigation. The document was initially generated as a "baseline specification" and has undergone careful review by the spacecraft charging community including the Air Force, NASA, private industry, government labs, universities, and other agencies. The document will be formalized into a Military Standard for Spacecraft Charging when updated to include SCATHA spaceflight data.

The format of this paper is identical to that of the Spacecraft Charging Standard except that Appendix A: Spacecraft Charging Phenomenon Background has been omitted in order to limit the length of the paper. The complete text, including the appendix is available through the authors. Comments on this document would be appreciated and may be sent directly to Dr. A. B. Holman at SAI. Pertinent information will be incorporated directly into the next update of the standard.

1.0 SCOPE

1.1 This standard establishes the spacecraft charging (SCC) protection requirements for space vehicles which are to operate in the magnetospheric plasma environment.

1.2 The environment can cause differential charging of space vehicle elements which can result in discharges, with resultant propagation of electromagnetic interference (EMI), material degradations, and enhanced contamination effects.

2.0 REFERENCED DOCUMENTS

2.1 Issues of Documents

The following documents of the issue in effect on date of invitation for bids or request for proposal, form a part of this standard to the extent specified herein:

---

* Work supported through contract F04701-77-C-0166 with SAMSO.

STANDARDS

Military

MIL-STD-1541 (USAF) Electromagnetic Compatibility Requirements for Space Systems

2.2 Other Publications

The following documents form a part of this standard to the extent specified herein. Unless otherwise indicated, the issue in effect on date of invitation for bids or request for proposal shall apply.

NASA TM X-73446 - Provisional Specification for Satellite Time in a Geomagnetic Substorm Environment

AFML-TR-76-233 - Conductive Coatings for Satellites

AFGL-TR-77-0288 - Modeling of the Geosynchronous Orbit Plasma Environment - Part 1

NASA (To be Published) - Design Guidelines for Spacecraft Charging Monograph

NASA CR-135259 - NASCAP User's Manual

3.0 DEFINITIONS

3.1 Definitions that Apply to this Standard

The terms used in this standard are either defined in MIL-STD-1541 or listed in the following paragraphs.

3.1.1 Backscattering

The deflection of particles or radiation by scattering processes through an angle greater than 95^0 with respect to the original direction of motion.

3.1.2 Dielectric-To-Metal Spark

A spark discharge between two electrodes, one of which is a dielectric charge retaining surface and the other is a conductive (metal) electrode in the vicinity of the dielectric. A dielectric material will typically accumulate charge when irradiated by electrons or ions or under certain conditions when placed in a plasma environment.

3.1.3 Differential Charging

The act of charging neighboring space vehicle surfaces to differing potentials by the combined effects of space plasma charging, photoemission, secondary emission and backscatter.

3.1.4 Faraday Cage

An electromagnetically shielded enclosure. The term generally refers to a conductive metallic structur , package, or mesh which attenuates electromagnetic interference to specified levels on the interior.

3.1.5 Flash-Over Spark

A spark characterized by a current path that travels along the surface of the material and generally around an edge to close the path to the other electrode.

3.1.6 Geomagnetic Substorm Activity

The conditions near geosynchronous altitude during the injection of solar storm particles into the earth's magnetic field, including disturbances in the dipole field and increased plasma energies and current densities.

3.1.7 Magnetospheric Plasma

The space plasma environment constituent in the magnetosphere. This is an electrically neutral collection of electrons and positive ions (primarily protons) with densities near geosynchronous altitude on the order of one particle/cm^3.

3.1.8 Maxwellian Energy Distribution

An energy distribution based on Maxwell-Boltzmann statistics and applicable in a general form to the space plasma environment. The energy distribution has the integral form

$$\phi\ (>E) = N\sqrt{\frac{8kT}{\pi m}}\left(1 + \frac{E}{kT}\right)\exp(-\ E/kT)$$

where

$\phi\ (>E)$ = integral flux at energies greater than E (particles/cm^2 sec)

E = energy (keV)

N = total number density (particles/cm^3)

k = Boltzmann constant = 8.6×10^{-8} keV/^{0}K

T = plasma temperature (^{0}K)

m = particle mass (g)

It is interesting to note that $\sqrt{8kT/\pi m}$ is the average speed of the particles, so that the flux of all particles (setting E = 0) is found by multiplying the density by the average speed.

3.1.9 Metal-To-Metal Spark

A spark discharge between two electrodes both of which are conducting.

3.1.10 Photoemission

An effect whereby radiation of sufficiently short wavelength impinging on substances causes bound electrons to be given off with a maximum energy that varies linearly with the frequency of the radiation.

3.1.11 Primary Radiated Spark Fields

The electric and magnetic fields radiated from the spark gap.

3.1.12 Punch-Through Spark

A spark discharge through the bulk of a dielectric material. It is a bulk breakdown of the insulating strength of a dielectric separating two electrodes. The current path is through the bulk of the material, with surfaces above and below the dielectric acting as electrodes. The punch-through spark may occur in vacuum or in air.

3.1.13 Replacement Current

Current, excluding the spark gap current, in the region of the spark gap and within the material surrounding the spark gap due to the rearrangement of charge following the spark discharge.

3.1.14 Secondary Emission

An effect whereby electrons or ions, called secondary electrons or ions, are emitted from a material as a result of the collision of higher energy electrons or ions with the material. The ratio of secondary particles to incident particles can be greater than unity.

3.1.15 Space Emission Spark

A vacuum spark characterized by the ejection of current into the space surrounding an electrode. To produce a space emission spark, the electric field must be sufficiently high to ionize and vaporize the charge retaining material.

3.1.16 Spacecraft Charging (SCC)

The phenomenon where space vehicle elements and surfaces can become differentially charged to a level sufficient to cause discharges and resulting EMI. The primary effects of SCC are electrical transients and upsets, material degradation and enhanced contamination.

3.1.17 Spark Discharge

A sudden breakdown of the insulating strength of the dielectric separating two electrodes, due to the formation of ions by an intense electric field, accompanied by a pulse of electricity across the spark gap and a flash of light indicating very high temperature. In contrast to the arc discharge or glow

discharge, the spark is of very short duration. It may be oscillatory, or intermittent, with several discharges taking place in quick succession.

3.1.18 Spark Discharge Current

The total current within the spark gap.

3.1.19 Spark Lag

The interval between the attainment of the sparking threshold potential and the initiation of the spark.

3.1.20 Sparking Threshold Potential

If the voltage across a spark gap is progressively raised, a spark passes when the voltage level has become sufficiently high. The lowest voltage at which the initial spark will pass is the sparking threshold potential. Note that the voltage may be increased considerably above this value without producing a spark. After one spark has passed others may follow, at different sparking potentials.

3.1.21 Vacuum Spark Discharge

A spark discharge taking place in a vacuum region with high potential gradients. The electric field may exist within a dielectric or in the vacuum region surrounding the charge retaining material. In the latter case the gradients are between the electrode and either the vacuum chamber walls or an equivalent space charge surrounding the electrode. In these cases the potential gradients must be sufficiently high to ionize and vaporize the charge retaining material. There are different types of vacuum sparks that are of considerable importance, each classified by the configuration of the electrodes or the characteristics of the current path of the spark gap. These are the dielectric-to-metal spark and the metal-to-metal spark, each with a spark gap path that is classified as a punch-through spark, a flash-over spark or a space emission spark.

4.0 GENERAL REQUIREMENTS

4.1 Spacecraft Charging Protection Program

The contractor shall (a) conduct a spacecraft charging protection program, (b) prepare and maintain an analytical plan and (c) prepare and maintain a test plan. The intent of the program shall be to assure that the space vehicle is capable of operating in a space plasma charging environment without degradation of the specified space vehicle capability and without changes in operational modes, location or orientation. This performance must be accomplished without the benefit of external control such as commands from a ground station. The spacecraft charging protection program, the analytical plan and the test plan shall be approved by the procuring agency.

4.1.1 Performance

4.1.1.1 Electrical Systems

The contractor shall assure through analysis and/or test that all space vehicle electrical systems perform to specified capabilities when operating in a space plasma charging environment.

4.1.1.2 Materials

The contractor shall assure through analysis and/or test that all space vehicle materials which may be exposed to a space plasma charging environment will retain specified capabilities.

4.1.1.3 Contamination

The contractor shall assure through analysis and/or test that any contamination effects due to electrostatics induced by a space plasma charging environment will not degrade the performance of space vehicle surfaces or elements below specified capabilities.

4.1.2 Design

4.1.2.1 Electrical Systems

The contractor shall design all space vehicle electrical systems to perform to specified capabilities in a space plasma charging environment. This may include protective design measures compatible with MIL-STD-1541 (USAF).

4.1.2.2 Materials

The contractor shall use materials in the space vehicle design that will perform to specified capabilities in a space plasma charging environment. Any protection features incorporated to reduce material damage must not reduce material performance below specified levels.

4.1.2.3 Contamination

The contractor shall design the space vehicle to minimize the effects of contamination enhanced by a space plasma charging environment. Any contamination present must not reduce performance of space vehicle systems below specified capabilities.

5.0 DETAILED REQUIREMENTS

5.1 Performance

5.1.1 Electrical Systems

Space vehicle electrical system outage is permissible during a discharge if operation returns to normal within a telemetry main frame period after onset

of the discharge. A command to the space vehicle from an external source such as a ground station is not required to be completed if a discharge occurs during transmission of the command, provided that an unintended action does not result and provided that the space vehicle is capable of receiving and executing subsequent commands and meeting specified performance. Space plasma induced electrical transients shall not affect on board digital data beyond the specified design limits. Conditions outside of specified limits for electronic equipment due to space plasma induced electrical transients shall be prohibited.

5.1.2 Materials

Thermal control surfaces, second surface mirrors, and solar cell coverslides shall not degrade in thermal or optical properties or structural integrity in a space plasma charging environment below the level required to perform to specified capabilities. Space vehicle structural elements shall not be permitted to degrade in mechanical properties in a space plasma charging environment below the level required to perform to specified capabilities.

5.1.3 Contamination

Contamination of thermal and optical space vehicle elements due to space plasma charging effects shall not degrade performance below the specified capabilities. Contamination of any other space vehicle elements or subsystems shall not reduce the operational performance of the space vehicle below its specified limits.

5.2 Design

5.2.1 Electrical Systems

Space vehicle electrical systems shall be designed such that transients induced by space plasma associated discharges do not interfere with space vehicle performance. Where practical this shall be accomplished by pulse duration discrimination. Where this is not practical, other design techniques shall be utilized such as filtering and RF shielding of selected wiring harnesses. The following design techniques shall be incorporated and made compatible to MIL-STD-1541 (USAF) specifications.

(1) All electronic boxes should consist of solid metal enclosures with no openings which permit the penetration of significant EMI.

(2) All metallic structural elements and other conductors shall incorporate sufficient common grounding to prevent metal to metal discharges.

(3) All metallized surfaces on thermal blankets shall incorporate multiple grounds to the space vehicle conducting structure.

(4) The space vehicle structure should provide a "Faraday Cage" design with a minimum of openings to prevent radiated EMI generated on the space vehicle exterior from propagating to internal locations. This may not be necessary if it can be shown by analysis and test that the "Faraday Cage" is not required.

5.2.1.1 Design Guidelines

The design guidelines present design features which will reduce the levels of discharging on the space vehicle and the effects of SCC on electrical systems. The design guidelines as presented in the "Design Guidelines for Spacecraft Charging Monograph" (NASA document to be published) should be followed wherever applicable. The monograph provides further detail on the design techniques given in Section 5.2.1.

5.2.2 Materials

Materials used in the space vehicle design shall be selected to minimize differential charging and discharge effects from a space plasma charging environment while maintaining specified performance capabilities. All dielectric materials used on exposed surfaces should be tested or analyzed to determine their discharge characteristics in a space plasma charging environment. Surfaces located internal to the outer space vehicle structure should be shielded from the space plasma environment by eliminating openings in the structure. Design guidelines as presented in the "Design Guidelines for Spacecraft Charging Monograph" (NASA document to be published) should be followed for materials applications.

5.2.3 Contamination

Space vehicle design shall incorporate techniques which minimize outgassing and other sources of contamination. Exposed surfaces which are most susceptible to effects of enhanced contamination due to space plasma charging shall be identified and protected where necessary.

6.0 SYSTEM ANALYSIS REQUIREMENTS

6.1 Spacecraft Charging Analysis Plan

The contractor shall prepare and maintain an analytical plan for SCC. The plan shall be subject to approval by the procuring agency. The contractor shall implement the plan to analyze the space vehicle for the effects of SCC. The analysis plan should complement the test plan and the analysis should generate data useful to identifying susceptible design areas and quantifying representative test levels. Analysis procedures as presented in the "Design Guidelines for Spacecraft Charging Monograph" (NASA document to be published) should be followed where applicable.

6.2 Analysis Concepts

Analysis of the SCC phenomena is based on four primary modeling areas:

(1) Space plasma environment modeling

(2) Sheath/charging modeling

(3) Discharge modeling

(4) EMI/coupling modeling

Models are being developed and will be available for use in analytical treatments of SCC effects on space vehicles. The contractor shall utilize these models or others suitable to the procuring agency in analyzing the space vehicle performance susceptibility to electrical effects, material degradations, and contamination effects due to SCC.

6.2.1 Space Plasma Environment Models

Space plasma environment models (see Appendix A) shall be used to determine the plasma environment at the space vehicle. This includes estimating frequencies of occurrence and duration of exposure of all space vehicle surfaces to the various environment constituents and estimating the energy levels and current densities of the constituents.

6.2.2 Sheath/Charging Models

Sheath/charging models (see Appendix A) shall be used to determine the extremes of differential charging levels for space vehicle elements and exposed surfaces. This requires input from the environment models and application to the specific space vehicle geometries (including illumination effects), with the incorporation of the characteristic material properties.

6.2.3 Discharge Models

Discharge models shall be applied for the extremes in differential charging levels as calculated from the sheath/charging models for representative space vehicle geometries. Estimates of extremes of radiated EMI (external and internal to the space vehicle) and structural current levels shall be generated by the analysis.

6.2.4 EMI/Coupling Models

EMI/coupling models shall be applied for the extremes in radiated EMI and structural current as calculated from the discharge model for representative space vehicle geometries. Estimates of extremes of characteristics of electrical transients shall be generated by the analysis.

6.3 Analysis Procedures

Analysis shall be performed to determine extremes of SCC effects in the area of electrical transients. In addition, models should be applied where applicable to determine material degradation and contamination effects. In general the SCC phenomena models shall be utilized to estimate worst case extremes of effects on the specific space vehicle. If these extremes present conditions which would result in degraded space vehicle performance (below specified levels), then more detailed use of the phenomena models should be performed as a second iteration of the analysis. This less conservative approach will provide more realistic estimates of SCC effects than the worst case extremes, but at the added expense of the more detailed analytical modeling treatment.

6.3.1 Electrical Transients

The procedure for analyzing the space vehicle for electrical transients induced by SCC follows.

(1) Determine the frequency of occurrence and duration of periods of space plasma charging using the environment models for the particular orbit and mission of the space vehicle. Generate environment inputs for (2).

(2) Determine extremes of differential charging levels for the space vehicle elements and surfaces based on sheath/charging model analysis. Determine capacitance of the space vehicle material configurations and for locations susceptible to charging (including capacitances within thermal blankets and between thermal blankets and other structural surfaces). Determine the charge and voltage levels of the capacitors.

(3) Determine extremes in amplitudes, frequencies and general characteristics of discharges on the space vehicle based on discharge model analyses and material test results. Determine most likely discharge locations.

(4) Determine extremes in radiated EMI and current injection into the space vehicle structure for the expected discharges.

(5) Use a coupling model in detail to determine the frequency of occurrence and characteristics of induced transients in all space vehicle electrical systems, including wiring harnesses, circuits, and components.

(6) Determine the effect of these electrical transients on space vehicle performance.

6.3.2 Material Degradation

The procedure for analyzing the space vehicle for material degradations caused by electrostatic discharge follows. This should be followed where applicable.

(1) Determine the frequency of occurrence and duration of space plasma charging using the environment models for the particular orbit and mission of the space vehicle. Generate environment inputs for (2).

(2) Determine extremes of differential charging levels for exposed space vehicle surfaces based on sheath/charging model analysis.

(3) Determine the locations, frequencies and energy content of discharges from these surfaces based on the discharge model analysis.

(4) Determine the mission integrated effect of these discharges on the thermal, optical, and mechanical properties of the exposed materials.

(5) Determine the effect of degradation in any of the material properties on space vehicle performance.

6.3.3 Contamination

The procedure for analyzing the space vehicle for effects of contamination caused by SCC follows. This should be followed where applicable.

(1) Determine the frequency of occurrence and duration of space plasma charging using the environment models for the particular orbit and mission of the space vehicle. Generate environment inputs for (2).

(2) Determine characteristic profiles of fields and potential distributions exterior to the space vehicle and surface charge distributions on the space vehicle from the sheath/charging model analysis.

(3) Estimate the characteristics of the outgassing products, propulsion system gases, and discharge sputtered material from the space vehicle.

(4) Determine extremes in radiated EMI and current injection into the space vehicle structure for the expected discharges.

(5) Determine the effect on space vehicle performance of thermal or optical degradation of the material surface properties due to this contamination (including degradation of this contamination).

7.0 SYSTEM TEST REQUIREMENTS

7.1 Spacecraft Charging Test Plan

The contractor shall prepare and maintain a test plan for SCC. The plan shall be subject to approval by the procuring agency. This plan shall include but not be limited to the following:

(a) Measurement instruments and test equipment

(b) Test conditions

(c) Test methods

(d) Test analysis and verification

The test plan should be complementary to the SCC analysis plan (see Section 6.1). The contractor shall implement the plan to test the space vehicle susceptibility to the effects of SCC. Test procedures as presented in the "Design Guidelines for Spacecraft Charging Monograph" (NASA document to be published) should be followed where applicable.

7.2 Measurement and Test Instruments

7.2.1 Measurement Instruments

The equipment used to monitor space vehicle susceptibility to SCC caused transients shall be capable of measuring signals with adequate accuracy to a level of 6 dB below the unit, subsystem, or system requirements. These instru-

ments should provide adequate bandwidth and proper time response to meet the test measurement requirements.

Measured signals shall be permanently recorded for later analysis as needed. Use shall be made of wideband oscilloscopes, spectrum analyzers, wideband transient detectors, circuit monitors, recorders, current meters and probes, wideband RF detectors and/or other instrumentation capable of monitoring unit, subsystem or system performance. The equipment used in this testing shall have the approval of the procuring agency and be fully described in the applicable test plan.

Measuring techniques and instrumentation accuracies shall be discussed in the test plan. Any peculiarities in operation, performance, or output in the measuring instruments shall be also discussed in the test plan.

All space vehicle telemetry equipment, aerospace ground equipment, and EMC test equipment (see MIL-STD-1541 (USAF)) used in these tests shall be described in the test plan. Any specially designed SCC measuring equipment shall also be described in the test plan.

7.2.2 Test Equipment

Special equipment used to simulate SCC effects on units, subsystems, or systems shall be described in the test plan. They should be calibrated within specified limits. This test equipment should include devices to

(1) Induce charge density levels of up to 10^{-3} coulombs/m^2 on the exposed surfaces of the space vehicle structure

(2) Insulate the space vehicle from all surrounding grounds during periods of testing

(3) Directly inject currents of up to 300 amperes into the space vehicle structure at selected critical test points. Lower levels may be shown adequate through analysis

(4) Generate EMI with specified intensity and characteristics at selected critical test points external to the space vehicle

(5) Deliver an electrical pulse of specified energy at selected critical test points

This equipment, its operation and its use for SCC testing shall be approved by the procuring agency before any testing of the space vehicle is started.

7.3 Test [illegible] tions

7.3.1 [illegible]/Subsystem Test Conditions

The test conditions for units and subsystems should follow the procedure outlined in "Design Guidelines for Spacecraft Charging Monograph" (NASA docu-

ment to be published). Test conditions must be tailored to each individual unit or subsystem.

7.3.2 System Test Conditions

System level ambient environment testing shall be performed on a qualification model vehicle, if available, or on a flight model vehicle, if a qualification model is not available. System level testing shall be conducted in a manner that will minimize risk to the space vehicle. System level tests shall simulate, to the extent possible, the conditions expected in space. Currents and voltages induced in space vehicle structural elements and electrical systems shall not exceed by more than a factor of 2 the extremes expected in space.

7.4 Test Methods

7.4.1 Unit/Subsystem Test Method

Each unit and subsystem shall be tested for spacecraft charging susceptibility. As a minimum testing shall be performed for radiated EMI. Each unit and subsystem shall perform within specified levels during and after the testing.

7.4.2 System Test Method

System level testing shall consist of monitoring selected circuits and general space vehicle health signals while conducting the following tests:

(1) Inject current into the space vehicle structure at selected critical test points. Test levels should be determined by analysis.

(2) Induce charge flow in the space vehicle by using the space vehicle structure as one plate of a capacitor and charging and discharging the other plate of the capacitor (a test plate mounted at selected critical test points). Test levels should be determined by analysis.

(3) Create radiated EMI in the same manner as that for the unit/subsystem tests.

Critical test points shall be chosen by analysis as those locations most likely to experience discharges in space. The magnitude of the discharge should be less than double but at least equal to the expected levels estimated by the analysis. Engineering model or qualification model systems should be subjected to this full level testing. To avoid electrical stressing of flight equipment, flight vehicle systems may be subjected to lower level (1% to 10%) testing if supportive analysis is performed to assure system performance to specified capabilities in the SCC 100% threat environment.

The magnitudes of the capacitance for (2) above and the voltages at discharge shall be representative of levels estimated in the analysis.

7.5 Test Analysis and Verification

The measurements recorded during the SCC tests shall be analyzed and used to verify that the space vehicle performs to specified levels. Transients shall be shown to be below upset levels for all critical circuits and components in electrical systems. Thresholds for upsets of space vehicle critical circuits and components may be measured at the unit level or calculated analytically. The method chosen is subject to approval by the procuring agency. Protective features shall be incorporated for all electrical systems to correct any performance below specified levels. The effectiveness of the protective features shall be demonstrated by further test and analysis.

7.6 Material Degradation Tests

All materials used on exposed surfaces in the space vehicle design should be characterized for their performance in a space plasma charging environment. This information may be obtained from the literature, e.g. the "Design Guidelines for Spacecraft Charging Monograph" (to be published by NASA) or from material tests for new materials. Life cycle testing should be incorporated where applicable and where considered necessary. All materials are subject to approval by the procuring agency.

APPENDIX A: SPACECRAFT CHARGING PHENOMENON BACKGROUND (Available upon request).

D50

N79-24051

SPACECRAFT CHARGING MODELING DEVELOPMENT AND VALIDATION STUDY*

E. E. O'Donnell
Science Applications, Inc.

SUMMARY

Prediction of the effects of spacecraft charging requires validated analytical models of the magnetospheric environment, the charging interaction between the spacecraft and the plasma sheath, the discharge phenomena, electromagnetic coupling from the discharge to spacecraft components, and of material damage. This paper reviews the analytical models now available and describes the use of SCATHA data and ground tests to validate the models.

INTRODUCTION

One of the objectives of the cooperative NASA/Air Force Spacecraft Charging Investigation is to ensure that validated analytical models are developed which are capable of predicting the interaction of spacecraft with the environment. Historically, modeling activity has been divided into four regions:

- The undisturbed environment
- The plasma sheath surrounding the spacecraft
- The spacecraft surface
- The spacecraft interior

Models must be capable of predicting the degradation of the spacecraft due to its interaction with the environment. This degradation can fall into two categories: (1) anomalies, which are interruptions in service due to electromagnetic coupling of static discharges into sensitive electronic circuits, and (2) materials degradation, such as changes in thermal absorption and emission coefficients. Anomalies can be temporary, such as the upset of a digital logic circuit, which is restorable by ground command, or permanent damage due to burnout of semiconductor elements.

Emphasis to date has been put on solving the anomaly problem, but with long mission life requirements expected for space systems, material degradation may become extremely important.

---

* *Work supported through Contract F04701-77-C-0166 with SAMSO and Contract NAS3-21048 with NASA/LeRC.*

ANALYTICAL MODELS

Environmental Models

The environmental model describes the magnetospheric substorm in terms of electron and ion concentrations, particle energies, and probability of occurrence. A comprehensive model should include

- Electric and magnetic fields
- Plasma particle identities and number densities
- Particle fluxes and current densities
- Particle energy spectra
- Particle angular distributions (isotropy, field alignment, etc.)
- Temporal variations of plasma parameters
- K_p, A_p dependence of plasma parameters
- Spatial dependences
- Probabilities of occurrence of various severities of substorm activity

Table 1 lists the environmental models available and in use today. The AFGL model, usually known as the Environmental Atlas (Ref. 1), when updated with data from the SCATHA satellite, will be issued in CY 1980 and will serve as the standard reference for magnetospheric environments. Haffner (Ref 5) has computed substorm conditions and probabilities of occurrence for subsynchronous orbits.

Sheath/Charging Models

The sheath/charging model determines the spacecraft charging condition, the electromagnetic fields in the plasma sheath surrounding the spacecraft and the particle trajectories and fluxes in the sheath region. For engineering purposes, it is sufficient to determine the charging condition: potential distributions on the spacecraft surface; but for scientific payloads, the sheath fields, particle trajectories, and particle fluxes may be of extreme importance.

Engineering models, such as those used by design organizations, usually are of the equivalent circuit type, described by Inouye (Ref 8) and Massaro (Ref. 9). More sophisticated treatments needed for scientific purposes require

iterative solutions of the Poisson and Vlasov equations with the approach dependent upon the geometry involved. Table 2 lists the models used for sheath/charging analyses.

The most ambitious model to date is the NASCAP code developed by Systems, Science, and Software for NASA (Ref. 14).

Discharge Models

As the charge accumulates on a spacecraft dielectric surface, the probability increases that the surface will discharge to spacecraft ground or another surface of lower potential. Discharges fall into three categories:

- Punchthrough - dielectric breakdown from the front to back surfaces of a material
- Flashover - dielectric breakdown along a surface or between two adjacent surfaces
- Blowoff - the expulsion of charge to free space

It has been observed that all three types of discharges will result in charge expulsion, and it is the time dependence of the effluent charge that is the single most important parameter in modeling discharges.

The discharge models must describe the discharge current amplitude and pulse shape, the energy released ejecta material species and time history, the current paths, and the dependence of these upon the following variables:

- Surface area
- Dielectric properties (Teflon, Kapton, etc.)
- Material juxtaposition
- Environmental conditions (electron and ion spectra, photo illumination, etc.)

Discharge models fall into three categories: (1) phenomenological, which are simply aggregations of data tied together with empirical relationships; (2) qualitative models, which postulate a physical process but do not attempt mathematical formulations; and (3) physical models, which attempt to formulate a fundamental physics approach to explaining discharge phenomena. At present no suitable models of any category exist. Table 3 describes the models now existing and those in development.

Coupling/EMI Models

The Coupling/EMI models are used to predict the electromagnetic interference (EMI) at sensitive electronics packages due to the dielectric discharge. This can be done in one or two steps, depending upon the analyst.

In the one-step approach, as was used by Inouye, et. al, (Ref. 19) an EMI model of the spacecraft is devised and a standard EMI computer code such as IEMCAP or SEMCAP is used to predict interface transients. In the two-step approach, a time-domain electromagnetic analysis is performed to predict spacecraft structural currents and internal fields. Then, using a transient circuit analysis code such as SYSCAP, the transient interface and voltages and currents are predicted.

Table 4 lists the codes available for Coupling/EMI analyses.

Buried Component and Cable Models

High energy electrons (trapped radiation) will penetrate spacecraft surfaces and deposit charges at depth in the spacecraft. It has been shown by Beers (unpublished) and Wenaas (Ref. 20) that spacecraft cables can accumulate sufficient charge to approach breakdown conditions in the cable dielectric. It is expected that other buried dielectrics, such as capacitor dielectrics, printed circuit boards, etc., could also experience breakdown.

Of the buried components, only the cables have been treated analytically, and these analyses are not adequate to predict the spacecraft performance. It should be noted that in the event of an exoatmospheric nuclear explosion, trapping of fusion product beta radiation could lead to severe high energy electron environments, in which the buried component discharge phenomena could well dominate magnetospheric plasma effects.

Materials Damage Models

A materials damage model would relate important materials properties (emission, absorption, electrical and thermal conductivity, etc.) to sample charging and discharging history. Though some data exist, no attempt has been made to formulate even a phenomenological model.

MODEL VALIDATION ACTIVITIES

The previous section has shown that a variety of analytical models have been developed or are being developed for spacecraft charging analyses. This section describes the ground and space programs which will be used to validate the models.

SCATHA Model Validation

Table 5 lists the SCATHA experiments and describes how the data will be used for model validation. As this table is summary in nature, it will be useful to describe in detail the process by which SCATHA data will be used. Two examples will be given:

- SC1-1,2,3 validation of NASCAP
- SC1-8B validation of discharge, coupling, and EMI models

NASCAP Validation

The Satellite Surface Potential Monitors (SSPMs) are material samples specially instrumented to measure the sample potential relative to spacecraft ground, the leakage and displacement currents. A SCATHA version of NASCAP has already been developed by Systems, Science, and Software (S^3) and sample runs have been made. Once SCATHA is in orbit and data have been telemetered to ground, the environmental conditions at the spacecraft will be determined from other SCATHA experiments (SC2, SC3, SC5, SC6, SC7, SC8, SC9), and this environment will be used as NASCAP imput, which will predict SSPM parameters. The comparison of predicton with data provided by SC1, 1, 2, and 3, will validate NASCAP.

Further validation of NASCAP will come from monitoring the SSPM readings during SC4 (electron and ion gun) operation. Predictions will be made of the SSPM potential as a function of time during gun operation. If NASCAP is capable of predicting the potentials correctly, then the code is assumed to be valid.

Discharge, Coupling, and EMI Model Validation

Data from the Narrowband Pulse Analyzer can be used to validate coupling/EMI and discharge models as follows:

- From the NASCAP charging analysis, it will be possible to select likely discharge positions. Those positions will be the source locations for a time-domain coupling analysis. The driving function (current density vs time) will be provided by the discharge model.
- The coupling calculations will predict SCATHA structural currents and near fields as functions of time.

- The field excitation of the dipole antenna will be computed for each of the discharge sources. These results will be compared with SCI-8B measurements. The source terms will be iterated until agreement is satisfactory.

- Coupling calculations will also provide internal fields. Cable harness transients will be predicted using standard circuit analysis routines and the results compared with the incernal monopole and loop antenna results.

The above process can be simplified considerably if the discharge location can be identified uniquely. For example, if the SSPM measurements indicated that one of the material samples discharged at time t_o, and the SCI-8B detailed a transient at the same time, then the SSPM single could be assumed to be the source of the discharge.

GROUND TEST PROGRAMS

As can be seen from Table 5, the primary purpose of SCATHA is to provide data for the environmental and sheath/charging models. Thus the bulk of the data for validation of discharge, coupling, EMI, and material damage models must be obtained via ground tests. Table 6 is a compilation of ground tests and other validation activities that are planned, in progress, or have recently been completed. Comments on selected efforts follow.

Validation of NASCAP will come primarily from material sample exposures at NASA LeRC, and a number of these tests have been conducted. A comparison of NASCAP with the Laframboise code will be initiated soon and should determine the effect of the corners in the NASCAP geometry. The Laframboise technique assumes an infinite cylindrical geometry; analysis of long cylinders should provide good comparisons for the purpose of code validation.

The discharge data of Balmain, at the University of Toronto, indicate strong functional dependence of discharge return current amplitude, charge, and energy upon sample area. Peak amplitude appears proportional to the half power of area, total charge is proportional to area, and energy is proportional to the three-halves power of area. The pulse duration, which data have more scatter, seem to vary roughly as area to the 0.55 power.

At present, the only program involving physical discharge modeling with experimental confirmation is a joint effort by SAI and SRI with SAMSO funding. This program should provide the first quantitative definition of the discharge source for use in coupling calculations.

A scale model of SCATHA has been constructed for coupling model validation and for EMI testing at IRT. Using this test vehicle, IRT has developed a set of preliminary test procedures that should serve as the basis for test standardization. Also, using a capacitive drive technique that best represents the discharge mechanism, IRT is developing empirical transfer functions that will simplify the interpretation of SCATHA data.

RECOMMENDATIONS

Most of the modeling activity to date has been concentrated in the areas of the free-field environments and the plasma-sheath region, and likewise, most of the SCATHA instrumentation is designed to validate these models. It is apparent that the cooperative NASA/Air Force Spacecraft Charging Investigation Program will provide at the minimum validated environment and sheath/charging models.

Coupling and EMI models can borrow from the technology developed for nuclear weapons effects phenomena. With only modest modifications, a number of computer codes developed for analysis of system-generated electromagnetic pulse (SGEMP) effects can be used for studies of electromagnetic coupling from discharges.

It is ironic that the earliest recognized electrical phenomenon, the electrostatic discharge, remains one of the most poorly understood. And it is important to realize that until the physics of the discharge phenomenon are understood, both qualitatively and quantitatively, there will be very little confidence in scaling laws or "worst-case" specifications that are imposed as design criteria.

What is needed is a thorough program to characterize discharges in physical terms. This program should have both analytical and experimental elements, interactive in the sense that analytical results are used to define experimental goals and experimental results are used to guide analytical directions.

Another program need is the development of a materials damage model. This model could be empirical, or semiempirical, but should make use of the data provided by the discharge model development.

To date, no one has extended the buried component and cable charging effects analyses past infancy. JAYCOR, with AFWL funding, is initiating a program that includes these effects, and these efforts should be included in an overall system assessment.

Finally, a system level combined effects test (simulating plasma, solar photons, and trapped radiation) should be planned. This test would validate (as well as possible in a ground test) the charging, discharge, coupling, and EMI analyses, as well as system level current injection (proof) tests.

REFERENCES

1. Garrett, Capt. H. B.: Modeling of the Geosynchronous Orbit Plasma Environment, Part I. AFGL, December 1977.

2. LaQuey, R.: A Preliminary Specification of the Environment at Geosynchronous Altitude. Maya Dev. Corp., August 1976.

3. Stevens, N. J.; et al: Provisional Specification for Satellite Time In a Geomagnetic Substorm Environment. NASA TM X-73446, October 1976.

4. Vogel, J. L.; et al: Substorm Induced S/C Charging Currents from Field-Aligned and Omnidirectional Particles. From Spacecraft Charging by Magnetospheric Plasmas, A. Rosen, 1976.

5. Haffner, J. W.: Spacecraft Charging Probabilities as a Function of Altitude; Presented at the IEEE Conference on Nuclear and Space Radiation Effects. Albuquerque, NM, July 1978.

6. Pavel, Capt. A. L.: Plasma Environment of a Synchronous Orbit Satellite. AFGL-TR-76-0028, February 1976.

7. Garrett, H. B.; et al: Rapid Variations in S/C Potential. AFGL-TR-77-0132, June 1977.

8. Inouye, G. T.: Spacecraft Charging Models, AIAA 13th Aerospace Sciences Meeting, January 1975.

9. Massaro, M. J.; Green; and Ling: A Charging Model of Three-Axis Stabilizer Spacecraft, Proceedings Spacecraft Charging Technology Conference, October 1976.

10. Beers, B. L., and Pine, V. W.: Electron Transport Model of Dielectric Charging, Proceedings Spacecraft Charging Technology Conference, November 1978.

11. Parker, L. W.: Differential Charging of Nonconducting Spacecraft. Presented at the 1978 Symposium on the Effect of the Ionosphere on Space and Terrestrial Systems, January 1978.

12. Rothwell, P. L.; Rubin, and Yates: A Simulation Model of Time-Dependent Plasma-Spacecraft Interactions.

13. Laframboise, J. G, and Prokopenko: Numerical Simulation of Spacecraft Charging Phenomena. Proceedings Spacecraft Charging Technology Conference, October 1976.

14. Katz, I.; Parks; Mandell; Harvey; Brownell; and Rotenberg: A Three-Dimensional Dynamic Study of Electrostatic Charging in Materials. NASA CR-135256, August 1977.

15. Bower, S.: Spacecraft Charging Characteristics and Protection. Presented at 1977 IEEE Conference on Nuclear and Space Radiation Effects, Williamsburg, VA.

16. Wilkenfeld, J., et al: Electrostatic Discharge Modeling, Testing, and Analysis for SCATHA. IRT Corp. Monthly Progress Report No. 8161-005.

17. Muehlenberg, A.: Evidence for a New Discharge Mechanism for Dielectrics in a Plasma. Progress in Astronautics and Aeronautics, Vol. 47, 1975.

18. Inouye, G. T. and Sellen, J. M.: A Proposed Mechanism for the Initiation and Propagation of Dielectric Surface Discharges. Proceedings 1978 Symposium on the Effect of Ionosphere on Space and Terrestrial Systems.

19. Inouye, G. T., Whittlesey, Ponamgi, Cooperstein, and Thomas: Vogager Spacecraft Electrostatic Discharge Immunity Verification Tests; Proceedings of the 1978 Symposium on the Effects of the Ionosphere on Space and Terrestrial Systems, January 1978.

20. Wenaas, E. P.: Spacecraft Charging Effects by the High-Energy Natural Environment; IEEE Transactions on Nuclear Science. Vol NS-27, No. 6, December 1977.

TABLE 1. - ENVIRONMENTAL REFERENCE SUMMARY

SOURCE	DESCRIPTION	THEORY, DATA BEHIND APPROACH
AFGL (Garrett) (Reference 1)	Elec. & mag. fields, particle distribution fcts., isotropy, maxwell vel. dist. K_p, A_p dependence, 3 hr. time resolution, local time variations incl.	Based on ATS-5, ATS-6 data. 4 plasma moments calculated for 10 days of data, 3 hour a_p dependence of predicted environment.
MAYA Dev. Corp. (LaQuey) (Reference 2)	24 hr. spectrograms, particle distribution fcts., 6 spectra output each 24 hour period, isotropy assumed.	Samples of ATS-5 and ATS-6 data for typical variety of conditions (6 days), 2.3 to 6.8 minute avgs., no theoretical treatment.
NASA/LeRC (Stevens, et.al.) (Reference 3)	Preliminary guide for environmental spec isotropy assumed, estimates for particle energies, spectra current densities, estimates of S/C - environment encounter times.	3 months of ATS-5 and ATS-6 data, mild, moderate, severe substorms defined, probability of occurrence estimated.
TRW & UCSD (Vogl & DeForest) (Reference 4)	Provides estimates of importance of field-aligned components.	Based on ATS-5 and ATS-6 data (20 field aligned components in 6 months data)
Rockwell (Haffner) (Reference 5)	Provides some spatial and altitude dependence of environment.	Combination of theory and empirical information, reasonable treatments.
AFGL (Reference 6,7)	Statistical representation of substorm fluxes, rapid time variations of potentials.	Pre-1975 data.

TABLE 2. - SHEATH/CHARGING MODEL SUMMARY

SOURCE	DESCRIPTION	PURPOSE
Equivalent Circuit Models (Reference 8,9)	Lumped element model of spacecraft with plasma currents as current sources.	Engineering estimates of spacecraft surface potentials.
Beers and Pine (Reference 10)	Monte Carlo calculation of electron transport in planar samples.	Charge distribution and internal fields as a function of time.
Lee Parker (Reference 11)	Numerical solution of Poisson and Vlasov equations. No azimuthal variations allowed. Uses "inside out" method of particle tracking.	Scientific studies of plasma sheath.
Rothwell, et al (Reference 12)	Monte Carlo simulation for spherically symmetric bodies.	Design studies; effect of material conductivity on spacecraft potential.
Laframboise (Reference 13)	Poisson-Vlasov iteration in infinite cylinder geometry.	Useful for studies of non-azimuthally symmetric bodies.
System, Science, and Software NASCAP (Reference 14)	Poisson-Vlasov iteration in three dimensions. Geometric building blocks are cubic grids and diagonal sections.	Particle trajectories, surface potentials, charging rates. Useful for engineering & scientific applications.

TABLE 3. - DISCHARGE MODELING ACTIVITY

SOURCE	DESCRIPTION OF ACTIVITY AND KEY RESULTS
Bower (Reference 15)	Worst-case specification for spacecraft. Assumes pulse duration proportional to area.
Wilkenfeld, et al (Reference 16)	Input to coupling analyses. Assumes charge transferred dependency on Area of the form. $Q = \frac{dQ}{dA} A_o (1 - \exp). [-A/A_o])$
Muehlenberg (Reference 17)	Postulates blowoff charge is caused by surface bilayer.
Brushfire I & II Sellen (Reference 18)	Qualitative model of surface discharge propagation. Postulates that high field gradients near discharge point cause secondary electron acceleration and multiplication. Brushfire II extends model to depth in dielectric material.
Beers	Monte Carlo modeling of discharge propagation. Field gradients caused by bulk breakdown cause free charge acceleration in dielectric. Electron motion heats a material, increasing conductivity, allowing greater mobility and discharge spreads, causing "tree" effect.
Balmain	Empirical relationships between discharge current amplitude, charge removed, and pulse widths as functions of sample area.
Leadon	Mechanism similar to Beers. Postulates that magnetic fields caused by discharge current expel charge.

TABLE 4. - COUPLING/CMI CODE SUMMARY

CODE TYPE	APPLICATION	COMMENTS
Transient Circuit Analysis Codes (SYSCAP, ISPICE, SCEPTRE, etc.)	ISPICE used by Hughes for PIONEER charging, coupling, and EMI analyses. Can be used for black box analysis given internal fields.	Widely available and used. Lumped element model definition of spacecraft not unique. May have problems with multiwire effects.
Frequency Domain EMI Codes (SEMCAP, TEMCAP)	Used by JPL/TRW for Viking Coupling and EMI study.	Not designed for transient analyses. Accuracy can be improved by iterating test and analytical model results.
Three Dimensional Maxwell Equation Solvers (SABER, SEMP, FAT, etc.)	Time domain coupling given discharge current as driver. Computes structural currents fields. SABER used by IRT for SCATHA modeling.	Developed for SGEMP analyses. Well suited for spacecraft charging coupling analysis.
Transmission Line Analytical Models	Multiwire transmission line analyses. May be applicable to EMI analyses at spacecraft harnesses.	Developed for aircraft EMP studies. Development not complete.

TABLE 5. - SCATHA DATA UTILIZATION FOR MODEL VALIDATION

EXPERIMENTAL	DESCRIPTION	MEASURED QUANTITIES	DERIVED QUANTITIES	VALIDATION USE
SCI Engineering Experiments SC1-1	Satellite surface potential monitor (SSPM) 4 small samples, side mounted	Back surface E-field, leakage current, displacement current	Surface potential, material conductivity charging current, breakdown threshold, time of breakdown	NASCAP Discharge models (if samples discharge) Evaluate conductive coatings Materials properties
SC1-2	SSPM Large Kepton sample, side mounted reference band	Same as SC1-1	Same as SC1-1	Same as SC1-1
SC1-3	SSPM 4 small samples, end mounted	Same as SC1-1	Same as SC1-1	Same as SC1-1
SC1-4	External loop antenna External dipole antenna	Electromagnetic fields external to spacecraft	Discharge moments Spacecraft structural currents	Discharge models Coupling models
SC1-5	Internal loop antenna	Electromagnetic fields interior to spacecraft	Interior fields, structural currents	Same as SC1-4
SC1-7	RF analyzer	External EMI spectrum	EMI waveforms, discharge moments, structural currents	Discharge models Coupling model EMI model
SC1-8A	VLF narrowband analyzer			Not applicable for model validation
SC1-8B	Narrowband pulse analyzer with internal monopole antenna	Time domain waveforms detected by SC1-4,5 and internal monopole		Discharge models Coupling models EMI models

TABLE 5. - Continued.

EXPERIMENTAL	DESCRIPTION	MEASURED QUANTITIES	DERIVED QUANTITIES	VALIDATION USE
SC2 Sheath Electric Fields and Energetic Proton Detector SC2-1 SC2-2	Electrostatic analyzers (ESA) Spherical probes 3 meters from spacecraft surface, commendable bias voltage	Probe potential relative to S/C ground proton & electron energy spectra 1 eV - 20 KeV	Particle trajectories electron emission coefficients (correlate with SC-9)	NASCAP Materials properties Environmental atlas
SC2-3	Body mounted ESA and light sensor	Low energy proton & electron spectra (1 eV & 20 KeV)	Same as SC2-1,2	Same as SC2-1,2
SC2-3B	Ion background detector	Low energy low concentrations		Discharge model environmental atlas
SC2-6	Energetic proto telescope	Proton flux from 20-1000 KeV 20 Kev - 25 MeV		
SC3 High Energy Particle Spectrometer	Particle telescope with solid state radiation sensors	Electron spectra from 50 KeV to 10 MeV, proton spectra from 1 MeV to 100 MeV, alpha particle spectra from 6 MeV to 60 MeV	Absorbed dose as a function of shielding thickness	Environmental atlas

TABLE 5. - Continued.

EXPERIMENTAL	DESCRIPTION	MEASURED QUANTITIES	DERIVED QUANTITIES	VALIDATION USE
SC4 Particle Guns SC4-1	Electron emission gun 6 voltage steps from .05 to 3 Kv 6 current steps from .001 to 13 mA	Beam current, accelerating voltage	Beam particle trajectories, vehicle discharge rates spacecraft potentials	NASCAP discharge models Active potential control
SC4-2	Positive ion emitter can emit positive ions and/or electrons	Beam current, accelerating voltage	Same as SC4-1	Same as SC4-1
SC5 Rapid Scan Particle Detector	Electrostatic analyzers and solid state spectrometers. High time resolution capability	Differential energy analysis for electrons (50 eV to 1.2 MeV) and protons (50 eV to 35 MeV)	Sheath geometries particles trajectories spacecraft potential	Environmental atlas NASCAP
SC6 Thermal Electron Measurements	Body mounted and boom mounted gridded probes	Photoelectron, secondary electron and ion densities and energies from 1 to 100 eV	Emission rates	Materials data NASCAP Discharge model Environmental atlas
SC7 Light Ion Mass Spectrometer	Potential analyzer, mass spectrometer, and ion detector	Ion densities and species 1 - 100 eV		Environmental atlas Discharge model

TABLE 5. - Concluded.

EXPERIMENTAL	DESCRIPTION	MEASURED QUANTITIES	DERIVED QUANTITIES	VALIDATION USE
SC8 Lockheed Energetic Ion Spectrometer	Electrostatic analyzer and velocity filter	Ion energy spectra from 100 eV to 20 KeV		Environmental atlas
SC9 UCSD Particle Detectors	Electrostatic analyzers, electrostatic lens, and particle counter	Electron and proton fluxes from 1 eV to 80 KeV (63 energy groups)	Spacecraft potentials sheath geometries and particle trajectories	Environmental atlas NASCAP
SC10 Electric Field Detector	100 meter electric dipole	AC fields $3H_z$ to 10 KH 1 - 100μV/M, DC fields from 0.1 to 20 mV/M	Spacecraft potential and near fields	NASCAP Discharge Coupling
SC11 Magnetic Field Monitor	3-axis magnetometer	Magnetic field density in the range ± 5 milligauss		Environmental atlas
ML12 Thermal Control & Contamination	Quartz crystal microbalance retarding potential analyzer thermal control coatings	Contamination mass flux temperature changes	Temperature dependence of contamination adsorption and desorption Ion gun return flux hemispherical absorptivity	Material damage NASCAP Discharge
Transient Pulse Monitor	Pulse detector and counter detector are low and high impedence cable bundle antennas, current probes on power reference ground and solar array input	Total transients, positive and negative peak amplitude, positive and negative pulse integrals	Cable bundle peak currents, internal fields, structural currents	Discharge models Coupling models EMI models

TABLE 6. - GROUND TESTS AND OTHER MODEL VALIDATION ACTIVITIES

MODELS	DESCRIPTION OF VALIDATION EFFORT	ORGANIZATION	COMMENTS
Sheath/ Charging	Exposure of material samples to monoenergetic electrons and monitoring surface potentials.	NASA LeRC	Good agreement with NASCAP for Teflon & Kapton; quartz and aluminum show disagreement.
	Analytical comparisons between Laframboise and NASCAP models for long cylinder.	York University, [illegible]	Scheduled to begin late CY1978.
	Experimental validation of calculations of pre-charging condition in planar Kapton sample.		Not yet awarded. Will be funded by Comsat Corp.
Discharge	Electron spraying of planar Teflon samples. Measuring discharge return current. Faraday cup measures effluent charge.	Colorado State University	Provides valuable scaling data & understanding of effluent. SEM photos indicate discharge paths.
	Electron spraying of planar mylar samples, measuring discharge return current.	University of Toronto	Provides area scaling data over several orders of magnitude. SEM photos of discharge tracks.
	Electromagnetic characterization of discharges in planar samples. Sprayed with electrons.	SRI International	Transient electromagnetic fields essential to coupling models.
	Electron spraying of planar Teflon samples, attempting to correlate electron beam voltage with discharge frequency, optical radiation amplitude, & radiated RF.	Communication Research Centre of Canada	Has seen discharges on floating samples.
	Dielectric breakdown studies of irradiated planar samples.	SRI International	Goal is to develop discharge-resistant materials.

TABLE 6. - Continued.

MODELS	DISCRIPTION OF VALIDATION EFFORT	ORGANIZATION	COMMENTS
Discharge (con't)	Electron spraying of planar Teflon samples, measuring discharge return current.	NASA LeRC	Capable of large (=200 in^2) samples. Teflon tape used.
	Electron spraying of samples.	TRW	Provide scaling data.
	Electron spraying of samples.	Boeing	Also provide data for materials damage models.
	Conductivity measurements of irradiated planar samples. Characterization of secondary electrons and effluent.	IRT	Also provides data for use in charging models.
	Electron spraying of small & large planar samples, measuring return current and electromagnetic characteristics of discharge. Segmented backplate will localize discharge; uses rastered electron beam.	MRC	Also includes x-ray exposure to investigate SGEMP-charging synergisms. DNA program will start CY1978.
	Irradiation of planar samples & subsystem components with high and low energy electrons. Electromagnetic measurements & Faraday cup will characterize discharge phenomena. Attempt to measure punch thru current directly	JAYCOR	AFWL funding. Program will begin CY1978. Provides information for internal component discharge models.

TABLE 6. - Concluded.

MODELS	DESCRIPTION OF VALIDATION EFFORT	ORGANIZATION	COMMENTS
EMI/ Coupling	Capacitive and arc discharge drive of SCATHA scale model. Measures structural & cable currents. Comparisons made with SABER coupling code.	IRT	Defined EMI test procedures. Data will be used for SCATHA interpretation.
	Electron spraying of SKYNET satellite. Measured structural & power line currents induced by discharges.	MRC	Observed x-ray triggering of discharge.
	Voyager EMI tests.	TRW/JPL	Compared SEMCAP calculations with EMI measurements during arc discharges.
Material Damage	Electron spraying of small material samples & characterization of thermal property degradation.	GE	Also evaluating effectiveness of conductive coatings.

N79-24052

DESIGN GUIDELINES FOR THE CONTROL OF SPACECRAFT CHARGING*

R.E. Kamen and A.B. Holman
Science Applications, Inc.

N.J. Stevens and F.D. Berkopec
NASA Lewis Research Center

A nationwide, state-of-the-art technology survey has been completed that has led to the development of a list of guidelines that can be used by spacecraft design and program technical management personnel faced with the task of hardening their satellite against the effects of spacecraft charging.

The technology survey included a literature search and interviews with government, university and aerospace industry people knowledgeable of spacecraft charging. Information was collected in the areas of 1) spacecraft history, anomalies, designs, testing, specifications, experiments, 2) substorm environment and spacecraft analytical modeling, and 3) materials development and characterization. The information was summarized, compared, evaluated, and compiled in an unpublished dossier. The dossier includes discussions of the state-of-the-art, conflicting opinions, current recommendations and future plans for 19 technology sub-areas in addition to a bibliography with abstracts, raw interview reports and some general background and explanatory information.

The dossier was finalized and reorganized into a monograph titled "Design Guidelines for Spacecraft Charging" which will be published and available from NASA LeRC. The monograph provides DESIGN GUIDELINES in the areas of 1) filtering, 2) spacecraft system design, 3) spacecraft subsystem design, 4) spacecraft analysis and 5) spacecraft testing. The monograph contains a total of 55 design guidelines, organized as shown in Table I. The guidelines state specific requirements for successful design of spacecraft systems; each guideline is supported by a discussion of recommended practices that will assure successful implementation of the guideline. The monograph also includes background information, a summary of the present state of spacecraft charging knowledge, a bibliography, appendices and an index designed to facilitate the use of the document by spacecraft design and technical management personnel.

This paper introduces the DESIGN GUIDELINES Monograph and calls attention to the availability of additional backup information at NASA LeRC. This initial version of the monograph addresses the near-term goal of avoiding spacecraft anomalies. As more information becomes available (e.g., SCATHA flight data), the monograph will be updated and will address the far-term goal of avoiding spacecraft differential charging.

---

*Work supported through contract NAS3-21048 with NASA/LeRC

In conclusion, we wish to thank the following organizations for their contributions to the technology survey: Air Force Materials Laboratory, Communications Satellite Corp., Ford Aerospace, General Electric, Hughes Aircraft, IRT Corp., Jet Propulsion Lab, NASA Goddard Space Flight Center, Naval Research Laboratory, Mission Research Corp., Rockwell International, and Space and Missile Systems Organization.

TABLE I. - ORGANIZATION OF GUIDELINES LISTED IN MONOGRAPH

I.	Filtering (for the elimination of electronic anomalies)
II.	Spacecraft System Design
	A. Grounding
	B. Shielding
	C. EMC Practices
	D. Handling/Assembly/Inspection
	E. Spacecraft Charging Phenomena Monitors
	F. Spacecraft Charging Control
III.	Subsystem Design
	A. Electronics
	B. Power Systems
	C. Mechanical and Structure
	D. Thermal Control
	E. Communications Systems
	F. Attitude Control
	G. Other Payloads
IV.	Spacecraft Analysis
	A. System Analysis
	B. Design Trade Studies
V.	Spacecraft Testing
	A. Components, Units and Subsystems
	B. Flight Systems and Qualifications Models

THE QUALIFICATION OF A LARGE ELECTRON IRRADIATION FACILITY FOR TELECOMMUNICATION SATELLITE DIFFERENTIAL CHARGING SIMULATION

B.E.H. Serene and J. Reddy
European Space Agency

INTRODUCTION

The European Communication Satellite network will comprise a series of three axis stabilised satellites in geostationary orbit. The extensive use of insulating materials for thermal control suggests that there is a serious risk of surface potential build-up with correlated effects due to discharges: materials degradation and electro-magnetic interference.

Consequently the concept of system level simulation of the electron environment during normal thermal vacuum/solar simulation testing is being actively persued by the European Space Agency. We believe that the method of charge build-up by electron bombardment of the entire satellite is the most representative test that can be performed to evaluate the impact of differential charging on system performance.

To achieve such large test set-up it was necessary to define, procure and qualify all the critical items and a programme was established, sub-contracting procurement and test activities to CNES/SOPEMEA under ESA technical and financial management.

DEFINITION AND PROCUREMENT PROGRAMME

Electron Source

For the electron source the basic requirements were
- electron potential: variable up to 30 kev
- electron flux: variable up to 1 $\mu A cm^{-2}$
- illuminating cone solid angle: $\pi/3$
- homogeneity: better than 30%

Three approaches were considered (presented below) of which only the last one was followed in view of the schedule, reliability and cost.

Triode System

The electron beam was derived by heating up tungsten wires in vacuum and then accelerating the electrons produced by the heated wire in an electric field (Ref.1). The tungsten wires are installed in a large copper frame closed on the

back and the electric field is created between the frame and a large mesh. These two parts have to be hung in the chamber and well isolated from it. The advantages of such a system are low price and a large quasi-parallel and homogeneous electron beam. On the other hand this source is difficult to implement safely, introduces uncertainties and risks during space simulation testing and finally cannot be repaired without opening the chamber.

Electron Gun with Defocalization Lenses

Most of the electron guns provide a very focalised beam and with the addition of one or two electrostatic lenses it is possible to adjust the beam divergence according to the size of the sample and the type of vacuum chamber used. Unfortunately such electrostatic lenses can be manufactured only by a long process (handmade modification and test) which introduces a high price for an uncertain result.

Electron Gun with Scattering Foil

In this case we use a conventional electron gun with a scattering foil instead of a lens to achieve a large divergent homogeneous beam. This introduces a new constraint with regard to the fusion property of the scattering foil receiving electrons with an energy up to 30 kev.

In consequence we have recommended the purchase of an existing electron gun manufactured by SAMES (Grenoble - France) shown on figure 1. This gun is equipped with four filaments which are interchangeable under vacuum, can provide an electron flux of 8 mA cm^{-2} (by adjustment of the filament current up to 20A) with an energy adjustable from 0 to 30 kev and an illuminating cone solid angle of $\pi/20$. The first part of the test programme was concerned with defining the characteristics of the beam.

Scattering Foil

Such a method has been used successfully by other laboratories (Ref. 2). The homogeneity of the electron beam in the test plane is achieved by using a thin aluminium scattering foil (2μ), which is mounted at a distance of 52 cm in front of the anode of the electron gun. The primary beam impinges on the 2 μm thick foil, pressed into a 8 cm diameter aperture of a diaphragm made of aluminium sheets, with locally different intensity (figure 2).
After inelastic scattering, a sufficiently large portion of the electrons leaves the foil with random distribution, for which a cos-law distribution is to be expected as a first approximation. If the foil is considered to be a secondary electron source, it can be regarded, in spite of its finite extent, as sufficiently point-like in comparison with the large distance to the test plane, so that a dependence according to $1/r^2$ is to be expected for the electron current density at the location of the test object. The use of the electron scattering aluminium foil has both advantages and disadvantages. In addition to the fact that mounting the foil is the simplest method to achieve a large-area homogeneous irradiation, the previously lineshaped monoenergetic distribution of the electron energy, after passing through the foil, represents a continuum which rises from a low intensity at low energy to a maximum at

about 0.8 of the primary energy and subsequently decays abruptly (Ref. 3). The continuous energy spectrum occurring after scattering means a better simulation of the electron energy distribution during magnetic substorm in geostationary orbit. A disadvantage is, however, that due to the physical laws governing the electrons' passing through the Al-foil, a very high minimum acceleration voltage is required to achieve a sufficient electron current density. In this way, compared with the monoenergetic irradiation, an important parameter is lost for the investigation of the test objects, which otherwise can be varied by increasing the acceleration voltage in defined steps. Such increase also has an upper limit due to the high amount of thermal energy which has to be radiated by the aluminium foil or conducted by the diaphragm plate (Ref. 4) and which approaches in some spots the melting temperature of the foil.

Consequently the establishment of the fusion limit of the 2 µm aluminium scattering foil under 10, 20 and 30 kev was the second point of the test programme.

Measurement and Monitoring Equipment

Faraday Cups

The flux measurement was made using faraday cups of 10 cm^2 collecting area, connected to a nanoammeter.

The test set-up used for the characteristics determination of the electron gun and the fusion point of the scattering foil is shown in figure 3 with a distance between the electron gun and faraday cup of 57 cm.

For the determination of the flux distribution of the large divergence electron beam a total of 50 faraday cups was used:
- 47 of them were installed on an aluminium plate of 3 meter diameter covered with a fluorescent paint (see figures 4 and 5).
- 3 of them, as "pilots", were installed on a ring of 2.10 meter diameter at a distance of 1.70 meter from the scattering foil (see figure 5).

The drawing giving the exact location of all of them is given in figure 6.

Discharges Detection and Amplitude Measurements

Two current probes were used on the leads connecting the ground plane to the grounding point. In addition, a calibrated current probe was connected to a memory scope to measure amplitude and duration of discharges.

Vacuum Chambers

Three different vacuum chambers needed to be used during this programme:
- a small chamber of 250 liters for the characteristics determination of the electron gun
- a medium size chamber of 27 m^3 for the fusion test and a short ageing test on the scattering foil
- Simdia chamber of 30 m^3 for the determination of the flux distribution and the irradiation test of the two superisolation panels

THE QUALIFICATION PROGRAMME

Determination of the Electron-Gun Characteristics

This test was performed in a small vacuum chamber of 250 liter with a faraday cup mounted 57 cm from the filament. The flux values were recorded as a function of the filament current for electron accelerations of 10, 20 and 30 kev as shown in figure 7 with a vacuum of 2×10^{-5} torr. The measured beam divergence was greater than expected. Instead of $\pi/20$ we obtained $\pi/18$.

Fusion Limit of the Scattering Foil

The vacuum chamber used for this test was the HEURTEY chamber with 27 m^3 volume, 3.5 meter long, vacuum of 2×10^{-6} torr and a window for visual examination of the scattering foil under irradiation. Figure 3 shows the test set-up used. In this condition for electron energy of 30 kev the curve

$$\phi = f \text{ (I filament)}$$

was plotted and gave a linear function

$$\phi \text{ (} \mu A \text{ } cm^{-2}) = k \text{ I (} \mu A)$$

with $k = 5.10^{-3}$ cm^{-2} indicating that the maximum beam current incident on the foil was 600 µA after which the foil was punctured (figures 8 and 9). The flux was 3 µA cm^{-2} at 5 cm distance just before fusion of the foil was observed. During irradiation, large deformation of the scattering foil was observed. This deformation was complicated by the radial mechanical constraints centered around hot points. In consequence a short ageing test was performed on an Al foil of 2 µm with

vacuum : 2×10^{-5} torr
electron energy : 30 kev
filament current : 500 µA
duration : 1h 30 min

without any degradation.
The flux value at 3 meters from the scattering foil was 2 nA cm^{-2}.

Mapping of Electron Beam Homogeneity

The mapping of the electron beam was performed in a plane normal to the electron beam over a diameter of three meters at distances 2.0, 2.5 and 3.0 meters from the diffusion window (see figure 10). Measurements were made at a single energy of 30 kev and at three different intensities (nominally 1 nA cm^{-2} and 3 nA cm^{-2}). The vacuum chamber used was Simdia (30 m^3) with a vacuum of 10^{-6} torr. The position of the 50 faraday cups used for flux measurements is shown on figure 6. For each distance the 3 monitoring cups (P1, P2 and P3) and the 47 measurement cups were recorded.

Table I shows
- the values measured by P1, P2 and P3
- the maximum, the minimum and the average of the values recorded on the 47 other cups corrected by a factor $K = 1/\cos \alpha$ (α is the angle between the axis of the faraday cup and the electron trajectory). This approximation is valid in regard of the small faraday cup aperture compared with the distance from the source.

The results indicated that at all distances a mean homogeneity of between 25% and 30% was obtainable at current densities in the range 1 nA cm^{-2} – 3 nA cm^{-2}.

The beam center was slightly deflected from the center of the target due to local magnetic field effects.

Thermal Blanket Irradiations

In view of the good homogeneity of the beam in the large chamber it was decided to perform irradiations of two samples of blanket simultaneously:
- 60 x 80 cm^2 of OTS VHF Shield Assembly as described in reference 4
- 60 x 80 cm^2 of ECS laminated foils of 3 mil Kapton with 1 mil Aluminium

Both samples were mounted on frames with the aluminium side grounded (Figs. 11 and 12). They were irradiated simultaneously for one hour after which time the samples were inspected for damage and photographed. There then followed a second period of irradiation at the same level but for three hours. At the end of this period the samples were removed, inspected and photographed.

The test conditions were

Incident electron energy	: 30 kev
Filament current	: 560 µA
Distance samples/Diffusion window	: 2.5 m
Flux on P1	: 2.75 nA cm^{-2}
P2	: 2.51 nA cm^{-2}
P3	: 2.64 nA cm^{-2}
Vacuum	: 5.10^{-6} torr

During the irradiations measurements were made of the discharge currents in both samples and the number and rate of discharges (Figure 13). The following observations were made:

a) number of discharges per hour

Sample \ hour	First	Second	Third
OTS	74	57	45
ECS	85	68	42

b) Two types of discharge observed on each sample - a small localised discharge and a large surface discharge

c) Amplitudes and duration of discharges different for each sample generally longer slower discharges for O.T.S.
Sample typically >150 A - 30 µsecs for O.T.S.
>200 A - 5 µsecs for E.C.S.

d) Degradation of aluminisation of Kapton foil on OTS sample particularly around rivets (Figure 14) and edges. Effects on E.C.S. samples were impossible to evaluate after 4 hours irradiation.

e) No degradation for both samples of the ratio α/ε

Discharge influence over a complete temperature measurement chain.

During the irradiation of the two large samples thermocouples were installed in the chamber behind and inside the samples. Negative pulses were recorded at the time of electrostatic discharges. However, their rate and amplitude were not destructive to the equipment and not considered as an error source in the thermal data.

CONCLUSION

As a result of the programme we feel that we have successfully qualified a large irradiation source which will be suitable for magnetic substorm environment simulation during normal satellite thermal vacuum testing.

The combination of cannon and diffusion window gives a widely divergent beam which allows irradiation of large systems with only a small separation between source and system.

The characteristics of the beam itself are well defined within the limitations of maximum flux and minimum energy.

Further development is planned to improve the source with respect to these limits of flux and also to allow irradiation at low energies. In addition a system which will permit the centering of the electron beam in the place of the test object is presently being developed and tested.

We consider also that future "space-simulation" tests will include plasma sources which will eventually allow an accurate assessment of the differential charging performance of all European satellites during ground based testing.

REFERENCES

1. Gustafsson, N.: Electrostatic charge/discharge test set-up for large samples. ESTEC Working Paper 1055, January 1977.

2. Feibig, W.; Görler, G. P.; Klein, G.: Electron irradiation experiments on two types of surface blankets of the satellite O.T.S. - DFVLR final report IB 353 - 77/14

3. Bourrieau, J.: CERT - DERT, Toulouse Private Communication.

4. Reddy, J.; Serene, B. E. H.: Effects of electron irradiation on large insulating surfaces used for European Communications Satellites - Spacecraft Charging Conference. Colorado Spring 1978.

TABLE 1: MAPPING OF THE ELECTRON GUN HOMOGENEITY

DISTANCE (m)	FILAMENT CURRENT (μA)	P1 nA/cm^2	P2 nA/cm^2	P3 nA/cm^2	ϕ MAX nA/cm^2	ϕ MIN nA/cm^2	$\bar{\phi}$ nA/cm^2
3	500	3,5	3,3	2,4	3,3	1,2	2,3
2,5	560	3,5	3,6	2,6	3,4	1,5	2,5
2	510	3,5	3,5	2,5	5,4	1,5	3,5
3	340	2,7	2,4	1,8	2,4	0,9	1,7
2,5	390	2,7	2,7	1,9	2,6	1,1	1,9
2	360	2,7	2,8	1,9	3,8	1,1	2,5
3	180	1,5	1,2	0,9	1,3	0,5	0,9
2	190	1,5	1,5	1	2,1	0,5	1,3

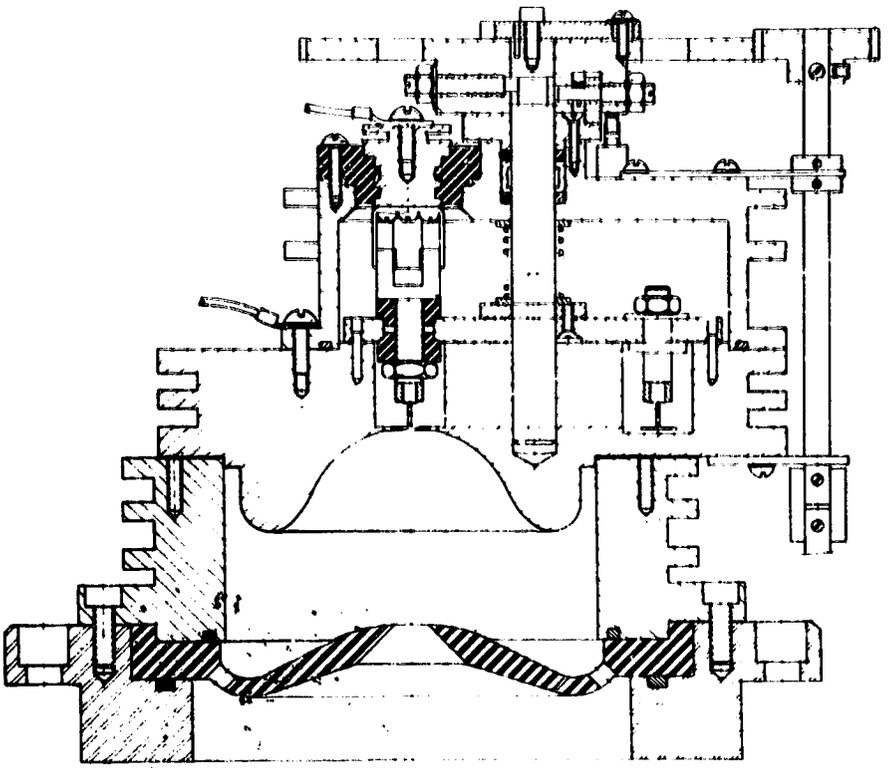

FIGURE 1: ELECTRON GUN CROSS SECTION

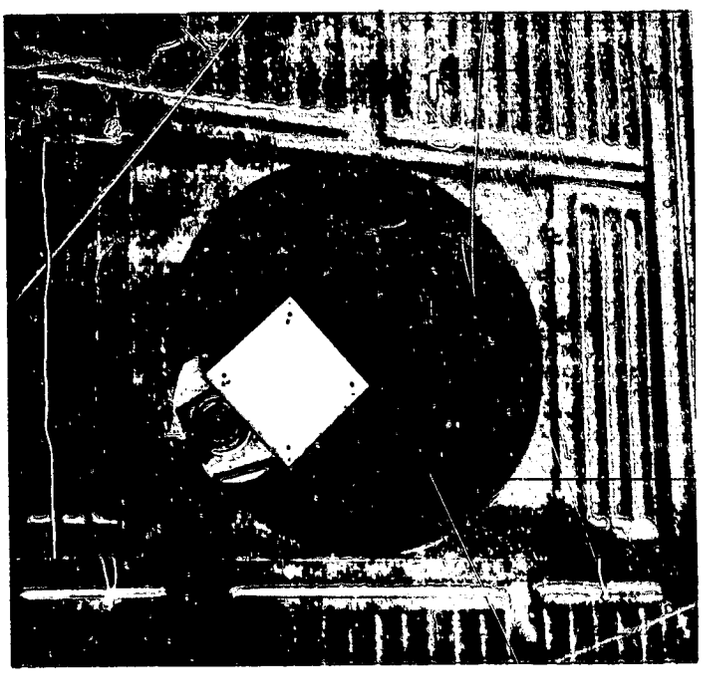

FIGURE 2: SCATTERING FOIL, DIAPHRAGM AND ELECTRON GUN

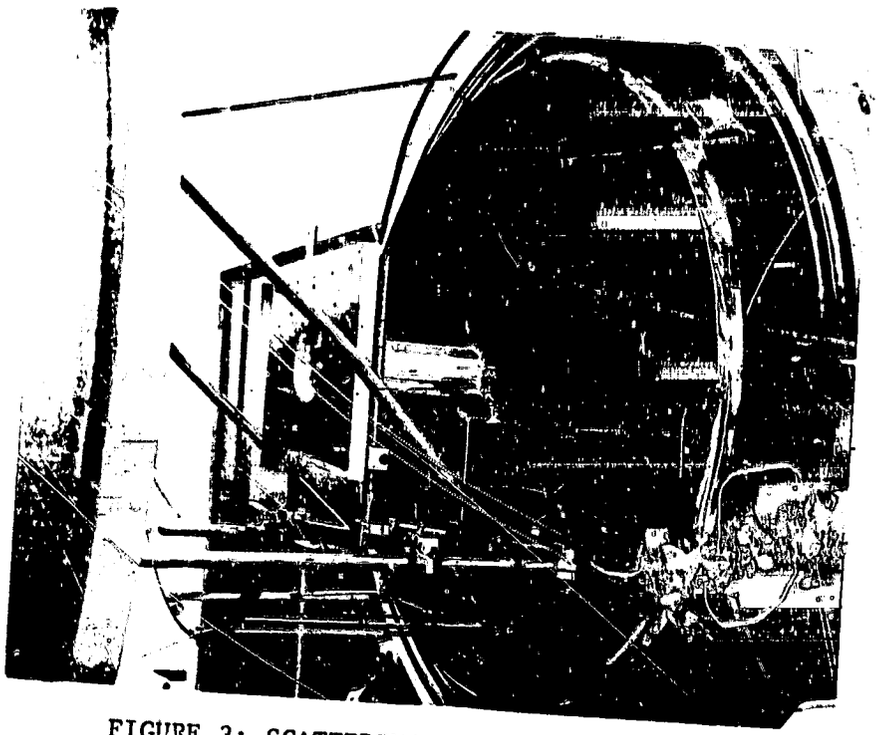

FIGURE 3: SCATTERING FOIL AND FARADAY CUP

FIGURE 4:
POSITION OF THE 47 FARADAY CUPS

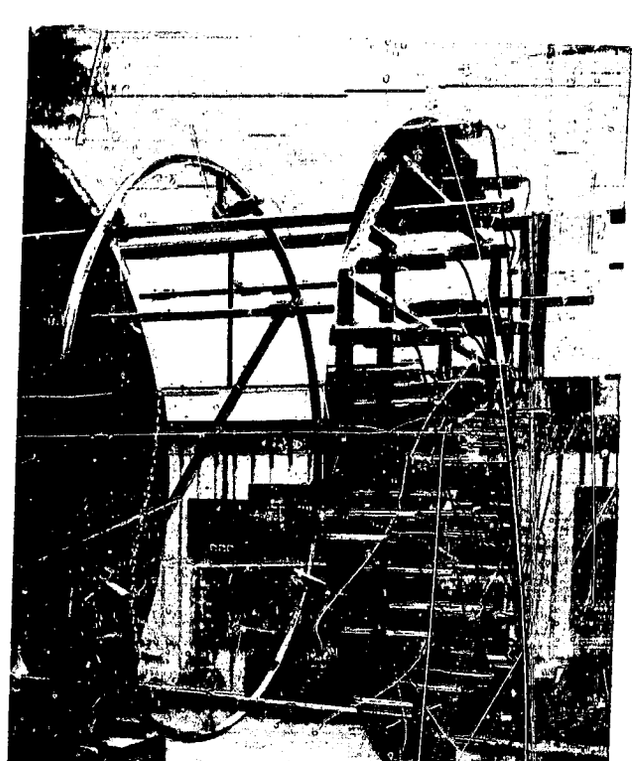

FIGURE 5:

FARADAY CUPS AND THE THREE "PILOTS"

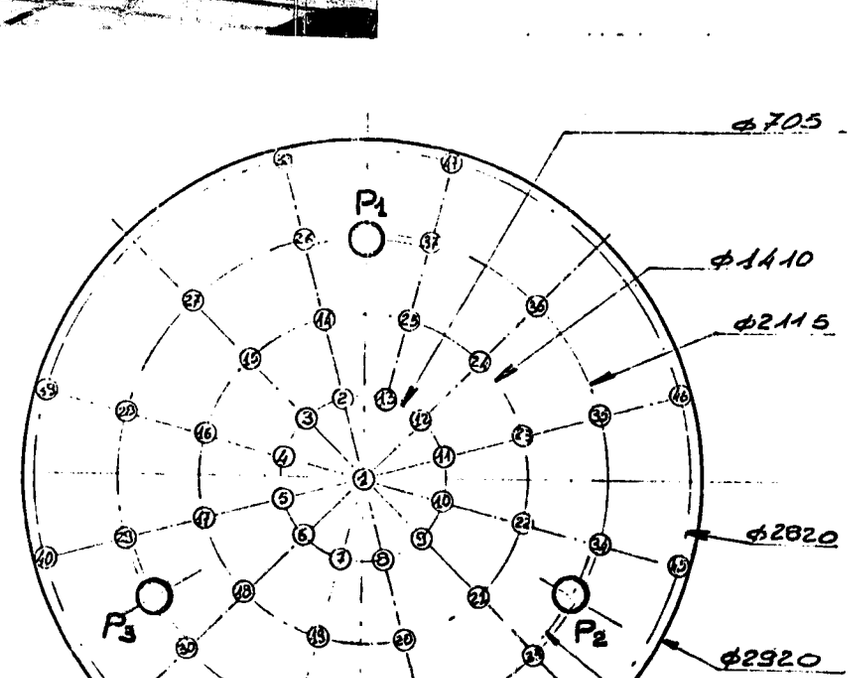

FIGURE 6:

POSITION OF THE 50 FARADAY CUPS

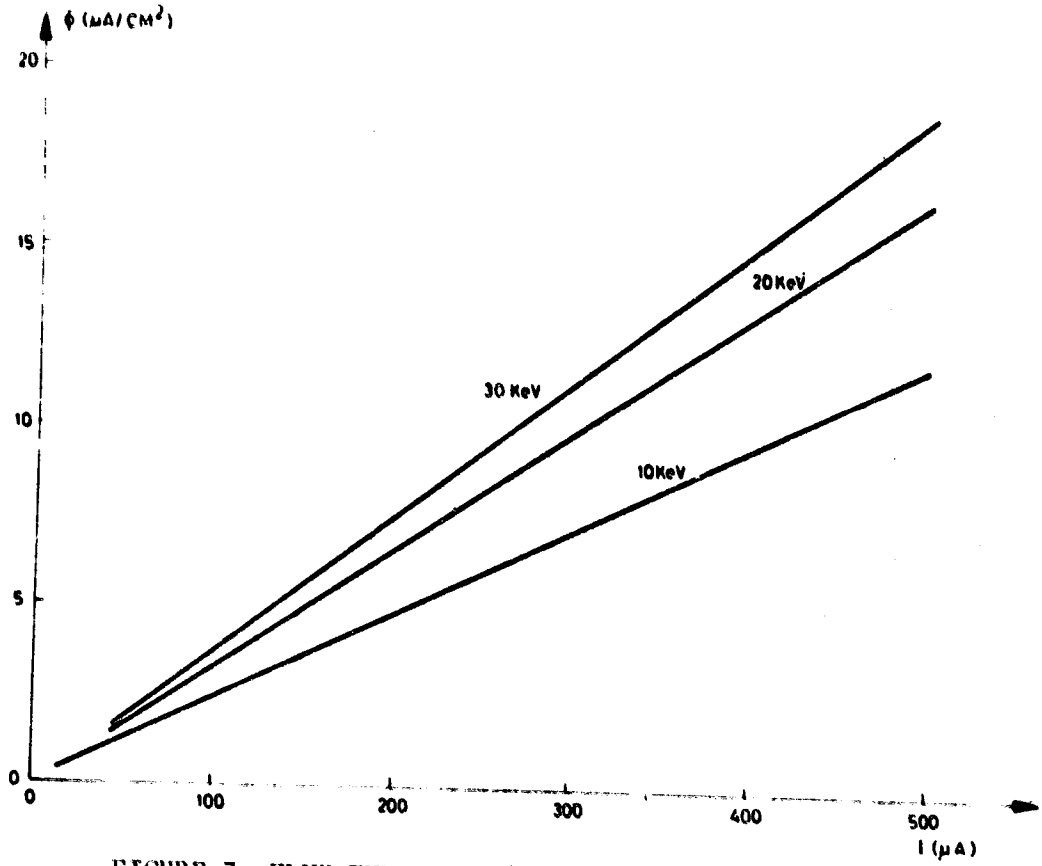

FIGURE 7: FLUX FUNCTION OF THE FILAMENT CURRENT

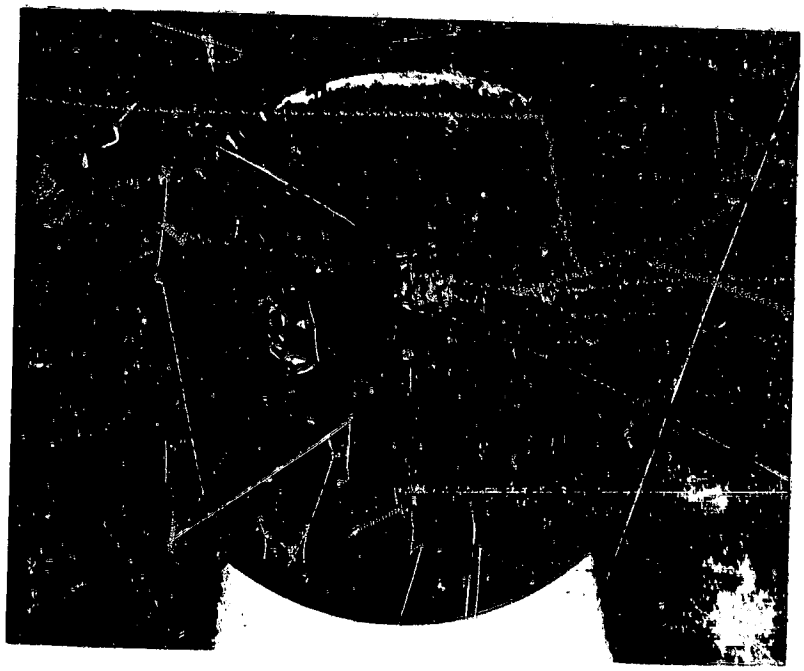

FIGURE 8: PUNCTURED AL-FOIL

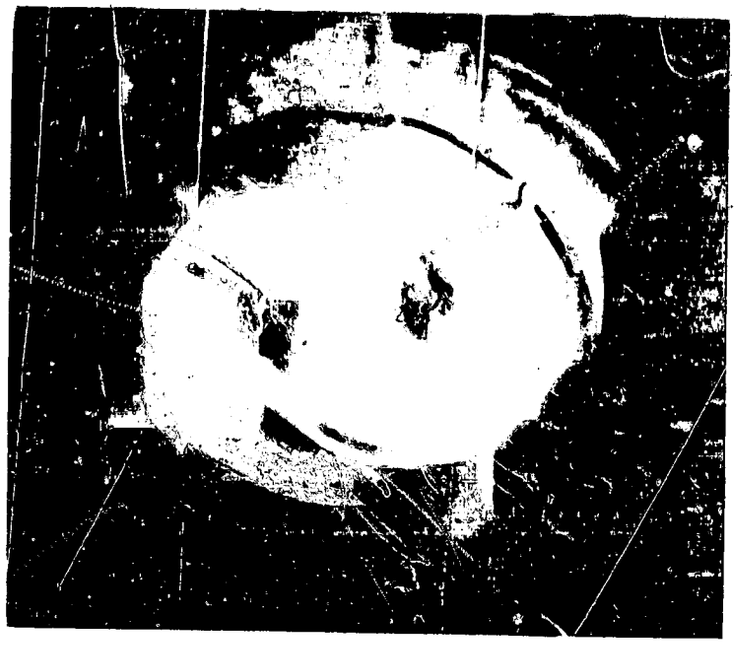

FIGURE 9: FUSION OF THE SCATTERING FOIL

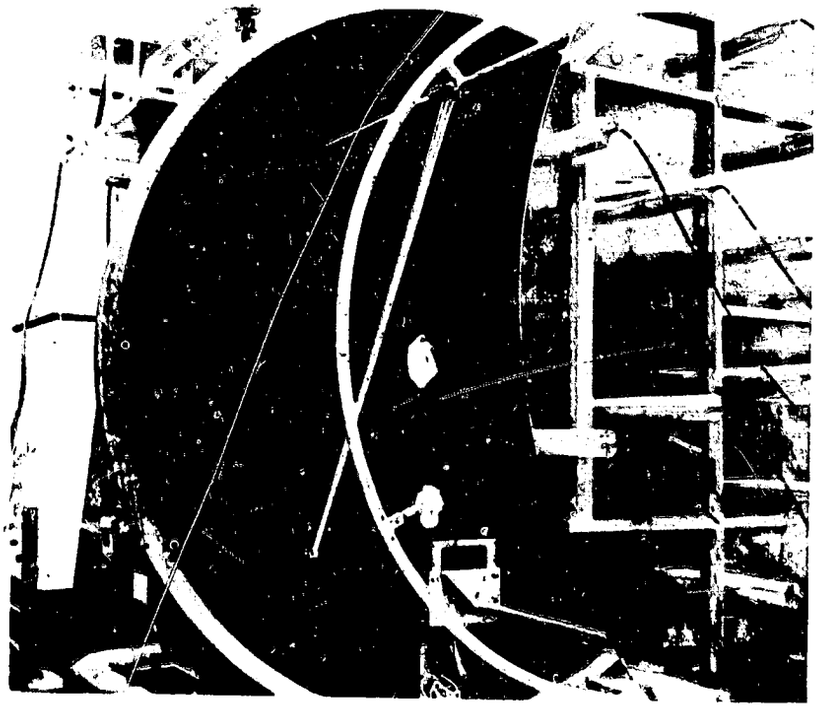

FIGURE 10: TEST SET-UP FOR LARGE ELECTRON BEAM MAPPING

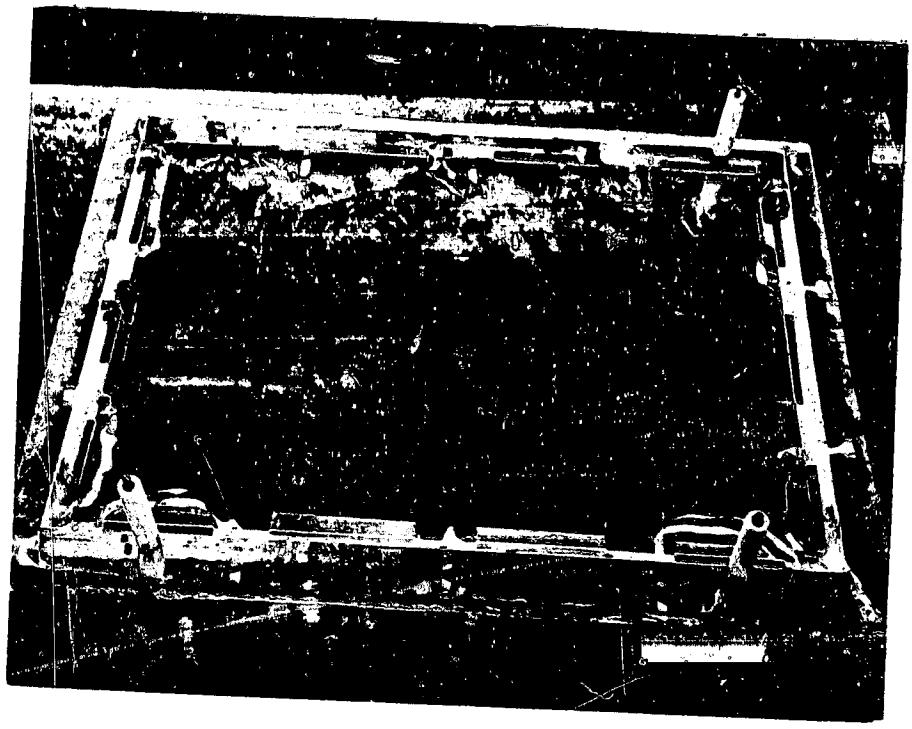

FIGURE 11:

SAMPLE ON THE MOUNTING FRAME

FIGURE 12:

POSITION OF THE SAMPLES IN THE CHAMBER

FIGURE 13: SAMPLES UNDER IRRADIATION

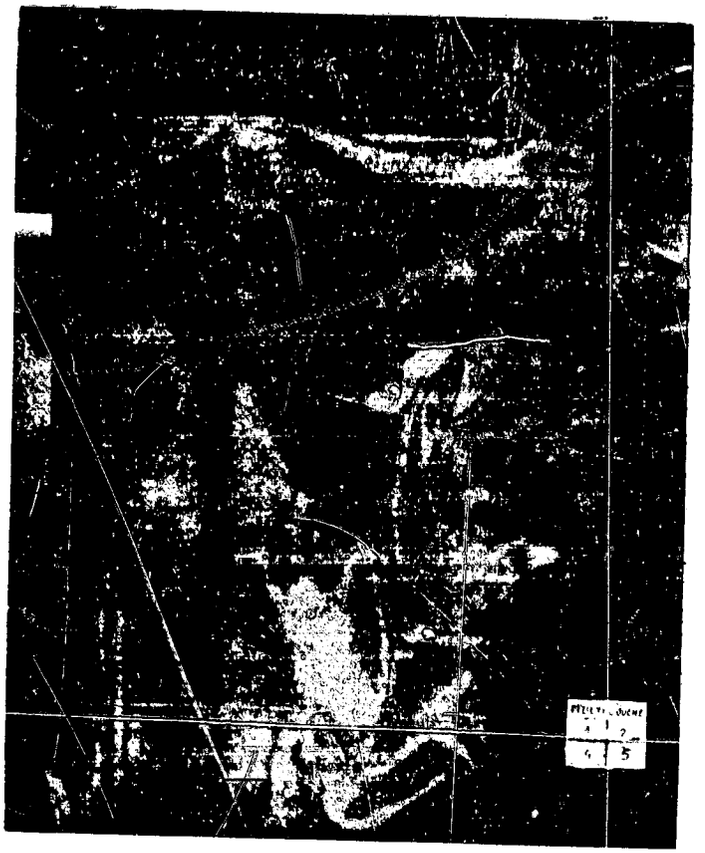

FIGURE 14: DAMAGES AROUND THE RIVET OF THE O.T.S. SAMPLE

N79-24053

TDRSS SOLAR ARRAY ARC DISCHARGE TESTS*

G. T. Inouye and J. M. Sellen, Jr.
TRW Defense and Space Systems Group

SUMMARY

The Communications Technology Satellite (CTS) experienced a fifteen percent power loss, possibly due to spacecraft charging and consequent arc discharge. This paper covers tests that were performed to develop design guidelines and recommended practices for use in the design of solar arrays of similar construction such as that for the Tracking and Data Relay Satellite (TDRSS) spacecraft.

The most interesting results were obtained with the solar array test samples irradiated with electrons on the backside and with ultraviolet on the solar cell side. The test sample was isolated from ground (tank walls) with a 25,000 megohm resistor so that the sample potentials were determined predominantly by the "environmental" fluxes of electrons and UV, with only a minor influence from external diagnostics. An enhanced photo-induced emission of electrons from the solar cell side due to UV irradiation was observed in the preferred test sample configuration in which the backside is coated with a conducting paint. This effect leads to the elimination of a major part of the charge buildup and energy storage which is the source of potentially hazardous arc discharges.

INTRODUCTION

The current state-of-the-art in designing satellites to be immune to the geomagnetic substorm environment at synchronous orbit altitudes is not a matured engineering discipline. Many geosynchronous and other satellites have experienced anomalous events which have been attributed to the spacecraft charging phenomenon (ref. 1). On CTS, arc discharges resulting from environmental charging are surmised to have caused a partial loss of solar array power (ref. 2). Our main interest from the viewpoint of spacecraft charging is that both TDRSS and CTS solar arrays are deployed with a fixed solar pointing attitude. Both, therefore, have large areas of excellent dielectric (kapton) material exposed only to the ambient energetic plasma, and not to sunlight, on the backside of the solar arrays. Figure 1 shows the configuration of the original TDRSS solar array. The darkside kapton, if unexposed

*This work performed under Contract No. 76159 with Western Union.

to solar UV, constitutes a large capacitor of about 2 microfarads per array. If charged to -10 kV, for example, the stored energy, 1/2 CV^2, is 100 joules. Coating this surface with a conducting paint and grounding it to the aluminum honeycomb core of the substrate eliminates the possibility of charging this capacitor. The tests described in this paper confirm the necessity for the conducting backside but also indicate that an additional effect exists which also reduces the stored energy in the large capacitance formed by the solar cell coverglasses on the sunlit side of the solar array.

TEST APPROACH

Most previous vacuum chamber tests on solar arrays have been performed by irradiating the solar cell side from an electron gun and grounding the solar cells and other metallic portions of the test sample (ref. 3). Typically, the electron source is a hot tungsten wire with an acceleration voltage of 20 kV, the positive terminal of the high voltage power supply being grounded to the tank wall. This grounding scheme simplifies the problem of diagnostic implementation in that the metallic parts are at ground potential. However, the polarity of the charge on the irradiated dielectric surfaces can then only be negative relative to the metallic parts. In the case of solar arrays, particularly for those which are 3-axis stabilized to always point toward the sun, the surfaces of the solar cell coverglasses are "clamped" to zero potential by photoemission of electrons. Thus the polarity of stress due to environmental charging can only be such that the dielectric surfaces are positive with respect to the solar cell itself. That is, the potential of the metallic parts of the spacecraft, including the solar cells, are at a negative potential relative to the far plasma potential (and to the coverglass surface).

The test approach, then, was to simulate this in orbit charging situation of positive polarity and to test various samples to define an acceptable configuration. The samples were subjected to impinging electrons on the backside and to UV on the solar cell side. The metallic portions were all tied together and allowed to "float" by grounding via a 25,000 megohm resistor. Tests performed at the European Space Agency (ref. 4) on CTS-type solar array samples were somewhat similar in that electrons were irradiated on the backside and a solar simulator irradiated the solar cell side. The differences with our approach were that no attempt was made to isolate the metallic parts from the walls of the chamber and that no precautions were taken to assure the UV content of the solar simulator. The solar simulator was included in the European Space Agency tests mainly to investigate thermal effects on the conductivity of the kapton substrate.

Test Setup

The test setup in the 2' diameter by 4' long vacuum tank is shown in figure 2. The electron gun at one end is capable of providing an electron beam density of 100 na/cm^2 at 20 kV. The positive side of the acceleration power supply is grounded to the tank. Since the maximum current density observed in a 3-month period on ATS-5 was 8 na/cm^2 with "average" densities of the order

of 0.2 na/cm^2, the operating current was normally set at 10 na/cm^2. A door is provided near the mid-section of the tank to permit the "substorm" to be turned on and off. Faraday cups are provided both in front of the door and in front of the test sample to calibrate the incident current density. Electrostatic voltage probes are provided on swinging arms to provide scans of surface potentials. Various connections to the test sample, the solar cells and substrate core were brought out. In general, however, all of the wires were tied together and treated as a single connection. In figure 2 we show this connection brought out to a 25,000 megohm to 1 megohm voltage divider. In some tests the connection was grounded through a 5-ohm. or .1 megohm, resistor to determine arc discharge pulse waveforms. For the paper chart records shown here, the 25000:1 voltage divider output was fed to an X-Y plotter which generated the X(time) scale of 20 sec/cm internally.

Test Samples

The following solar array samples were tested:

1. All-metal substrate.
   Substrate: 11.25" x 14"; 48 cells, 6 strings of 8 cells (2 cm x 4 cm cells). Coated with 1.2 to 1.5 mil of catalac black paint on backside.

2. Lightweight substrate with no paint on backside perforated kapton.
   Substrate: 7.25" x 9"; 20 cells, 2 strings of 10 cells (2 cm x 4 cm cells).

2a. Lightweight substrate with 0.5 mil Bostik-Finch 463-6-14 (epoxy) on backside perforated kapton.
   Substrate: 7.25" x 9"; 20 cells, 2 strings of 10 cells (2 cm x 4 cm cells).

3. Aluminum Panel: 11.25" x 14" x .125".

Tests with the All-Metal Substrate Sample (1)

The test configuration was that shown in figure 2 in which the backside is irradiated with electrons and the solar cell side with UV. The load resistance was 25,000 megohms with a 1-megohm resistor added in series to provide a voltage-divided monitoring point.

Prior to the tests with this sample (1), sample (3), an aluminum plate (11.25" x 14"), the same size as the substrate for sample (1), was put into the chamber to check the level of UV intensity available. The dimensions of the setup are shown in figure 3. The lamps are Pen Ray Model 11-SC-1C units. The result of this test with sample (3) was that a current of 180 na was photoemitted. Assuming that the area illuminated is 7" x 14", or 632 cm^2, the current density is .28 na/cm^2, or 9.5% of 3 na/cm^2, a commonly used value for photoemission. It takes 30 to 60 seconds for the UV lamps to "warm up" to full intensity, especially the first time they are turned on. A limit of about 5 to

10 minutes operation exists because of lamp heating and the resulting loss of vacuum. Further details of the sample (3) tests are given in a later section of this paper.

The result of the tests with sample (1) was surprising in that turn on of the UV lamps caused the sample potential to drop from -15 kV to about -1 kV. Figure 4 shows a typical trace obtained at the voltage divider monitor point. At -15 kV with no UV there are occasional discharges to the wall. At -1 kV, the signal is somewhat erratic as though a corona-like discharge were occurring.

This result was surprising in that

- The incident current at 10 na/cm^2 and 1016 cm^2 (11.25" x 14") is 10.2 μa.
- By Ohm's law, 0.6 μa is drained by the 25,000 megohm load resistor at 15 kV.
- The photoemission current measured previously (on the same sized aluminum plate) was 0.18 μa.
- The photo-induced current must be greater than 0.6 μa and must approach a significant fraction of 10.2 μa.

On the assumption that a 7" x 14" area (632 cm^2) of the solar cells is photo-emitting, the photoemission current densities are .95 na/cm^2 (for .6 μa), and 16.13 na/cm^2 (for 10.2 μa). Recalling that the current density observed in the aluminum plate test was .28 na/cm^2, the above values are 3.4 times (for .95 na/cm^2) and 57.6 times (for 16.13 na/cm^2) greater than might be expected, if the front surface were of aluminum. In fact, the photoemitting surface on the solar cell side consists only of the exposed metallic interconnects which comprise only about 5% of the solar cell coverglass surface area. In the steady state, the leakage of the coverglass is so low that all of the photoemission must initiate from the interconnects. The photoemission from this reduced area is effectively 20 times larger, giving current density values 68 to 1152 times greater than those observed on the aluminum plate.

A final test performed on sample (1) was to connect a negative variable power supply directly to the sample rather than to charge it with the electron gun. With the UV lamps on, a corona-like discharge was observed starting at around -500 volts and arcs were observed at -1 kV. We use the term "corona" only because of the similarity of effects, the enhanced current emission and the consequent lowering of voltage, which are observed in conjunction with real coronas. In our case, we hypothesize that there is no real gas discharge involved, but rather, an enhanced emission of high-field induced electrons with, perhaps, secondary electron emission effects involved. Increasing the voltage up to -1.5 kV increased corona current and the frequency of arcs to several per minute. This was the largest negative voltage applied. Although no photo-induced current measurements were made on this sample, such data were taken on sample (2a) with the power supply and are described in a subsequent section.

The tests and results on the all-metal substrate sample (1) are summarized in table 1. The test results with the UV lamps on, the reduction of the sample voltage from -16 kV to -1 kV, was unexpected. However, this result is very significant in that such an effect would reduce electrostatic stresses across the solar cell cover glass by a factor of 16. The energy involved would be reduced by a factor of 256. Furthermore, if the test level of UV irradiation is extrapolated to the one-sun level, the charging problem essentially disappears as far as the solar array is concerned, since the metallic backside is at the same low potential as the substrate and the solar cells (within 28 or 32 volts). We have tentatively called this photo-induced current multiplication phenomenon a "zenering action." The fact that this zenering action continued, once initiated, even after the UV lamps were turned off is a commonly observed characteristic of coronas and arc discharges.

Tests with Lightweight Substrate with No Conducting Paint on Backside, Sample (2)

This sample had 20 of the TDRSS type solar cells, two strings of 10 cells, on a 7.25" x 9" lightweight substrate. These cells had ceria glass coverglasses as compared to the fused silica on sample (1), and the interconnect design was also different. Note also that the sample size as well as its illuminated area is less than for sample (1). The backside was uncoated for these tests, and was subsequently spray coated with 0.5 mil of Bostik-Finch 463-6-14 epoxy paint to become sample (2a) which is discussed after this section.

The test configuration was as shown in figures 2 and 3. In figure 3, the outline of the sample (2a) substrate is shown in broken lines on the frontal view. Note that the UV lamp coverage is not the same as for sample (1). Irradiation with the 20 kV 10 na/cm^2 electron beam caused the sample voltage to go to about -15 kV as detected on the 25,000:1 voltage divider. Occasional arcs were observed. Turning the UV lamps on and off had no effect. Figure 5 shows a typical monitor trace of the 25,000:1 voltage divider output for this sample.

The test results obtained with sample (2) are summarized in table 2. The observed result of metallic portions of the sample at -15 kV with no "zenering action" from UV irradiation was again surprising in view of the results obtained from the all-metal sample (1). Particularly since the metallic parts were at -15 kV. One possible explanation is that the negative charges embedded on the backside dielectric are immobile and inhibit the flow of electrons in the metallic substrate towards the UV-exposed metallic solar cell interconnects which are "trying" to "corona" to the solar cell coverglass surface. The fact that the metallic portions get to -15 kV rapidly is not surprising, since the backside kapton is 51% open with holes which expose the underlying aluminum honeycomb material.

The implications of the observed -15 kV metallic portion voltage are serious in that these large stresses and stored energy in the coverglass might prove to be damaging to diodes on the solar array. Repeating of this test and further investigation of this configuration is required. This is particularly the case if a requirement to make the backside conductive causes the thermal design to necessitate a drastic redesign of the entire array.

Tests with the Lightweight Substrate with Conductive Coating on the Backside, Sample (2a)

This sample (2a) is sample (2) with the 0.5 mil Bostik-Finch 463-6-14 epoxy paint sprayed on the backside kapton. The test configuration as shown in figures 2 and 3 has the electron beam irradiating the backside and the UV shining on the solar cell side.

As with sample (2), with the UV lamps off, the metallic portions went to -15 kV with the 20 kV 10 na/cm^2 electron beam. Initially after turning on the UV lamps, this sample behaved as sample (2), arcing occasionally and remaining at -15 kV. After a few tens of minutes of UV irradiation, however, it began to behave more like sample (1) in that the sample potential reduced to a few kV negative. Figure 6 shows the initial behavior of this sample. Turning on the UV lamp caused the arcing frequency to increase, with very few arcs occurring when the lamps were turned off. Occasionally, the sample would "try" to zener as is seen in figure 6. On some occasions the zenering continued after the lamps were turned off as with sample (1). Reducing the electron beam current slightly by lowering the electron gun filament voltage from 60 volts to 55 volts caused the sample to behave more nearly as the all-metal sample (1). Figure 7 shows the result of a more careful calibration of the electron beam current flux at the sample as a function of the electron gun filament voltage. At the normal 60 volts, the current density is more nearly 30 na/cm^2 than 10 na/cm^2, and at 55 volts, about 6 na/cm^2. Figure 8 shows some of the traces at the voltage monitor point for this sample. Note that the "zenering" is more gradual and that turning off of the UV lamps allows the potential to gradually rise back to the -15 kV level. Extrapolation of the UV effect observed in this test to the one-sun level would indicate that this sample (2a) configuration is acceptable from the viewpoint of spacecraft charging. The test and results with sample (2a) are summarized in table 3.

Further Tests with Sample (2a)

The preliminary TDRSS design guidelines were established on the basis of the foregoing test results. The following tests were performed subsequently on sample (2a) to obtain a better understanding of the phenomena observed. As noted earlier, additional tests should be performed on the sample (2) configuration also. A verification test on the final TDRSS solar array design is also required.

The following test was run on sample (2a) to define the photo-induced current as a function of the potential of the metallic portions of the sample. A variable 250 V to 15 kV supply was used to bias the sample as shown in figure 9. As the lamps were turned on, an initially large capacitive charging current is seen as in figure 10. When this current reached a steady state value, the lamps were turned off, and this change constituted a measure of the photo-induced current. The results, as shown in figure 11, indicate an initially linear 8 na/volt increase of current with bias voltage. Near -1 kV arc discharges begin to occur, and the curve begins to flatten.

Figure 11 is a plot of the steady state photoemission and does not include the transient displacement current which charges up the coverglass capacitance. If one assumes that the interconnects comprise 5% of the coverglass area, the current from the interconnects would be much smaller than any of the measured currents shown in figure 11:

$$I = (.05 \cdot 160\ cm^2) \cdot (.28\ na/cm^2) = 2.24\ na$$

The currents of the order of 100 na shown in figure 11, on the other hand, would not account for the dramatic decrease of potential observed with sample (2a) or sample (1) where currents of 1-10 μa would be required. The current required for "zenering" is affected by the displacement or capacitive charging currents of the solar cell coverglass. Figure 10 indicates that these currents may be in the microampere range. These currents will flow away (electrons leaving) from the sample if the capacitance is discharged by arc breakdown. These arc discharges are observed when the power supply voltage is in the order of -1 kV. Measurements of the coverglass surface potential after turning off the negative power supply show voltages in the order of 500 volts. This also is an indication that voltage stresses of greater than 500 to 1000 volts cannot be maintained with this polarity.

Figure 12 shows discharge oscilloscope traces taken across the capacitivity coupled 5 ohm resistor shown in figure 9. The peak discharge currents range from 0.6 to 3.6 amperes as the sample voltage is raised from -1750 volts to -15 kV, and the widths were in the order of 2 to 4 microseconds. The peak pulse current does not appear to be linearly related to sample voltage. Peak pulse current vs sample voltage is shown below:

Sample Voltage (kV)	1.75	2.0	2.5	5.0	10.0	15.0
Peak Current (amps)	0.6	0.8	0.9	1.6	2.8	3.6

Test with Aluminum Plate Sample (3)

The aluminum plate (11.25" x 14"), used to obtain a measure of the photoemission level from the UV lamps as described in the tests on the all-metal substrate (1), was tested to determine whether enhanced photo-induced currents would be obtained at high negative potentials. The initial photoemission tests on this sample were made with a -22 volt bias.

With the 20 kV 10 na/cm^2 electron beam, the sample (3) potential went to about the same -15 kV as the other solar array samples. No arcs were observed whether the UV lamps were turned on or not. The voltage traces for this test are shown in figure 13. Note that the UV effects are barely perceptible. Summary of tests and results on aluminum plate sample (3) are listed below:

- Electron bombardment on one side and UV irradiation on the other side. 20 kV 10 na/cm^2 beam; ~9.5% of one-sun UV.

- Sample potential went to ∿ -15 kV.
- No arc discharges with or without UV.

The fact that this sample (3, did not exhibit the enhanced photo-induced emission current observed with all-metal sample (1) and the conductivity coated backside lightweight sample (2a) is an indication that some process involving dielectrics on the UV irradiated side is a necessary condition for enhanced emissions to occur.

The test results with sample (2) which had solar cells on it, but no conductive coating on the backside, indicate that a conductive backside tied to the metallic parts of the array is a necessary part of the acceptable array design. The test on the sample (2) substrate without the solar cells on it also indicate that a conducting backside is necessary.

SUMMARY AND CONCLUSIONS

The tests and results performed to develop TDRSS solar array design guidelines for immunity to the geomagnetic substorm environment at geosynchronous altitudes are summarized in each section. The preliminary design guidelines and recommended practices based on these test results are given table 4. The guidelines and recommendations are consistent with a survey of our inhouse experience with spacecraft charging effects and with information exchanges with outside institutions such as NASA, European Space Agency and Canadian Research Centre. The tests described here provide data which back up these recommendations and our experience, both analytical and experimental, indicate that these guidelines are reasonable. Being a relatively recently discovered (or acknowledged) phenomenon and a field of active research, it is impossible to write a definitive design guideline document for immunizing against geomagnetic substorm charging effects. Much work is being performed at the present time on the engineering as well as scientific aspects of the spacecraft charging phenomenon at many organizations. Specific design and immunity verification problems on each spacecraft program will have to be solved on an individual basis until the technology has matured to an adequate level.

REFERENCES

1. Rosen, Alan: Spacecraft Charging: Environment Induced Anomalies, AIAA Paper 75-91, presented at AIAA 13th Aerospace Sciences Meeting, Pasadena, CA. Jan. 20-22, 1975.

2. Gore, J. V.: Design, Construction and Testing of the Communications Technology Satellite - Protection Against Spacecraft Charging, Proc. Spacecraft Charging Technology Conference, editors C. P. Pike and R. R. Lovell, AFGL-TR-77-0051 and NASA TMX-73537, 24 Feb. 1977.

3. Stevens, N. J.; Berkopec, F. D.; Staskus, J. V.; Blech, R. A.; and Narisco, S. J.: Testing of Typical Spacecraft Materials in a Simulated Substorm Environment, Proc. Spacecraft Charging Technology Conference, editors C. P. Pike and R. R. Lovell, AFGL-TR-77-0051 and NASA TMX-73537, 24 Feb. 1977.

4. Bogus, K. P.: Investigation of a CTS Solar Cell Test Patch Under Simulated Geomagnetic Substorm Charging Conditions, Proc. Spacecraft Charging Technology Conference, editors C. P. Pike and R. R. Lovell, AFGL-TR-77-0051 and NASA TMX-73537, 24 Feb. 1977.

TABLE 1. SUMMARY OF TESTS AND RESULTS ON ALL-METAL SUBSTRATE SAMPLE (1)

- Electron bombardment of backside, UV on solar cell side. -20 kV, 10 na/cm^2 beam; ∿9.5% of one-sun UV.
- Sample metallic portions brought out of tank and grounded through 25,000 megohms ($2.5 \cdot 10^{10}$ ohms).
- Sample voltage was ∿ -16 kV, occasional arcs with no UV.
- Voltage dropped to ∿ -1 kV with UV; noisy.
- Voltage remained low when UV was turned off.
- Preceeding sequence starting with high negative voltages may be repeated by closing doors and stopping the electron beam.
- Power supply directly on sample, no electron beam, shows "corona" starting at -500 volts, arcing at -1 kV. Increased arcing frequency and increased "corona" current at -1.5 kV.
- Aluminum plate the same size as all-metal substrate (11.25" x 14.25") showed 0.8 μa photoemission current with -22.5 volt bias. Photoemission current density calculated to be .28 na/cm^2, or about 9.5% of that expected in orbit (one-sun).
- Photo-induced currents are 68 to 1152 (or even larger) times greater than might be expected from aluminum plate test (interconnect area only).
- For one-sun conditions this extrapolates to 35 to 580 times or 10.2 na/cm^2 to 173 na/cm^2 (on an overall area basis including coverglass area).

TABLE 2. SUMMARY OF TESTS AND RESULTS ON UNPAINTED LIGHTWEIGHT SUBSTRATE SAMPLE (2)

- Electron bombardment and UV irradiation as for sample (1): 20 kV 10 na/cm^2 beam; ∿.95% of one-sun UV.
- Sample(2) is smaller (7.25" x 9" substrate, 20 cells) than sample (1).
- Sample metallic portion at ∿ -15 kV; occasional arc discharges.
- Turning on UV lamps has no noticeable effect.
- Essentially the same results were obtained with the substrate for sample (2) with no solar cells put on it.

TABLE 3. SUMMARY OF TESTS AND RESULTS ON LIGHTWEIGHT SUBSTRATE WITH CONDUCTIVE COATING ON BACKSIDE, SAMPLE (2a)

- Electron bombardment and UV irradiation as for samples (1) and (2); 20 kV 10 na/cm^2 beam; $\sim$ 9.5% of one-sun UV.
- This sample (2), 7.25" x 9" substrate with 20 cells, but with backside spray coated with .5 mil of Bostik-Finch 463-6-14 epoxy paint.
- The resistance measured with 1" diameter discs laid on the paint measured $\sim 10^5$ ohms.
- To the substrate from one of the discs, the resistance was measured to be 0.5 to 1 times 10^4 ohms.
- The enhanced photo-induced electron emission was observed as for sample (1) but was not as pronounced.
- The incident electron beam was recalibrated and this showed that with 10 na/cm^2 and a one-sun UV irradiation, this configuration would result in a low stress design for the TDRSS solar array.

TABLE 4. PRELIMINARY DESIGN GUIDELINES AND RECOMMENDED PRACTICES

1. The back surfaces of the solar array panels must be conductive.
2. The conductive back surface must be connected to structure.
3. The aluminum honeycomb core must be grounded to structure.
4. The solar panel edges must be covered with conductive tape and grounded.
5. The solar cell coverglass may be fused silica or ceria glass.
6. The solar array wiring may be on the frontside or the backside—the backside is preferred.
7. The blocking and shunt diodes may be located on the frontside or the backside—the backside is preferred.
8. The blocking and shunt diodes should have the largest possible forward current ratings.
9. Design verification tests must be performed.

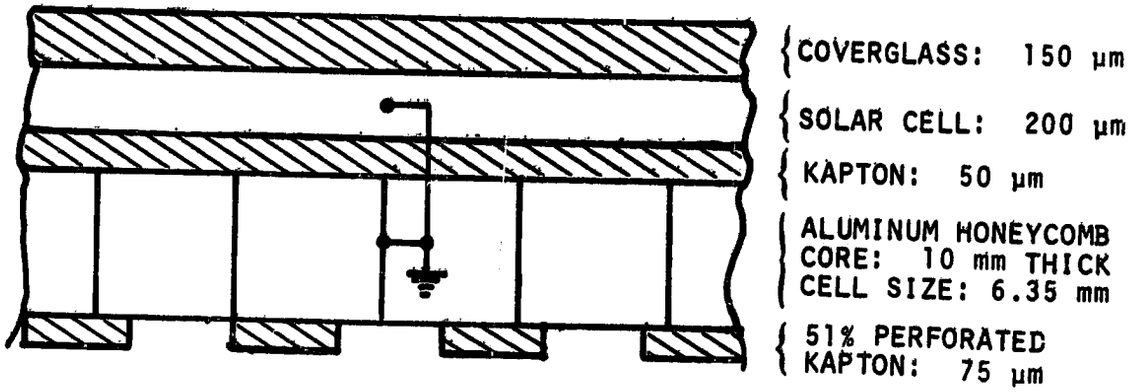

Figure 1. TDRSS SOLAR ARRAY CONFIGURATION

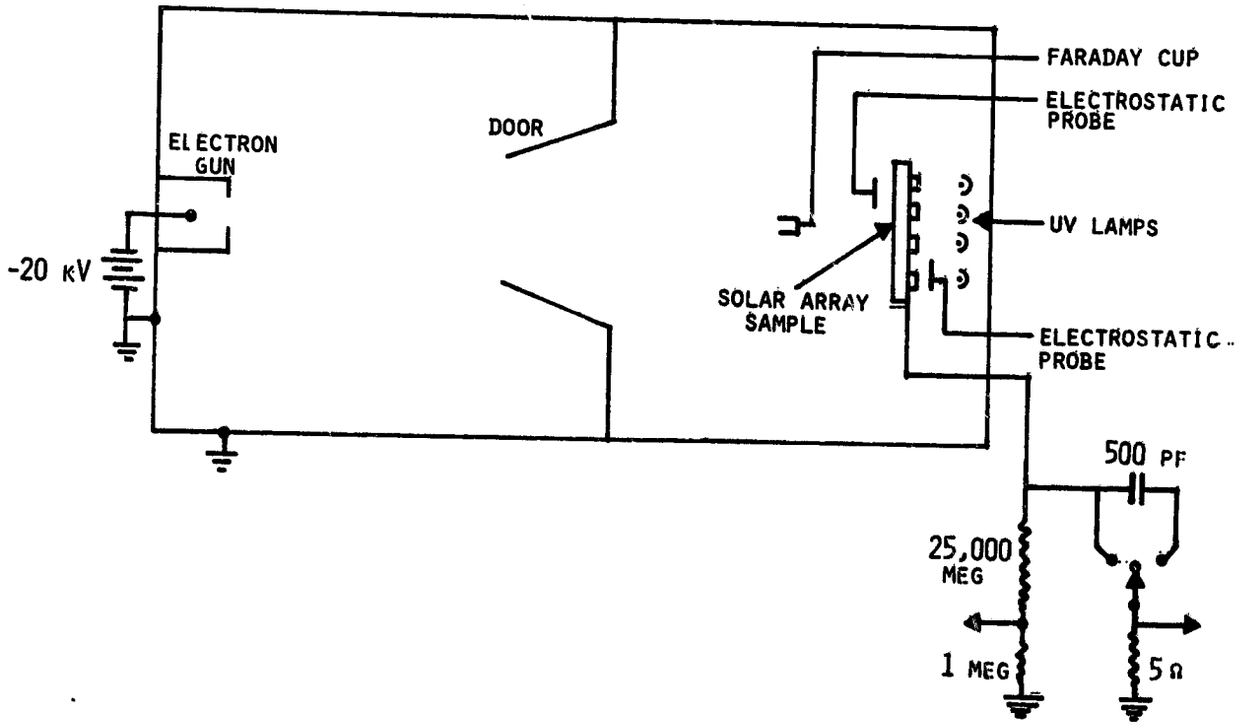

Figure 2. TEST SETUP IN 2' x 4' VACUUM TANK

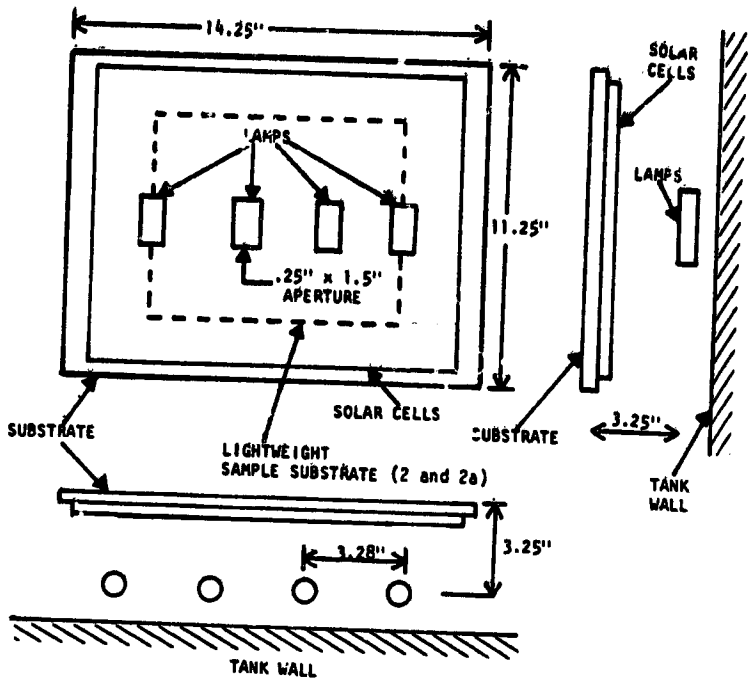

FIGURE 3. ALL-METAL SAMPLE (1) TEST CONFIGURATION SHOWING UV LAMP GEOMETRY

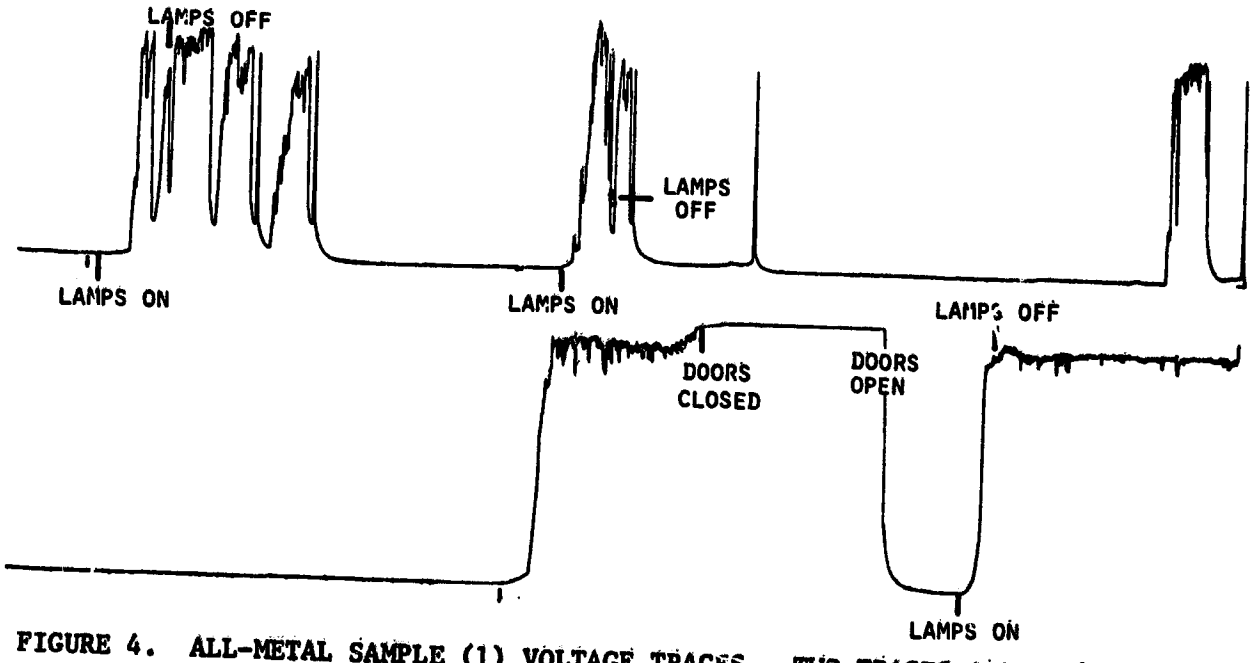

FIGURE 4. ALL-METAL SAMPLE (1) VOLTAGE TRACES. TWO TRACES ARE SHOWN. THE LOWEST PORTION OF EACH TRACE CORRESPONDS TO ∿ -15 kV. THE HIGHEST PORTIONS OF THE TRACES ARE ∿ -1 kV. THE HORIZONTAL PERIOD IS ABOUT 10 MINUTES PER TRACE.

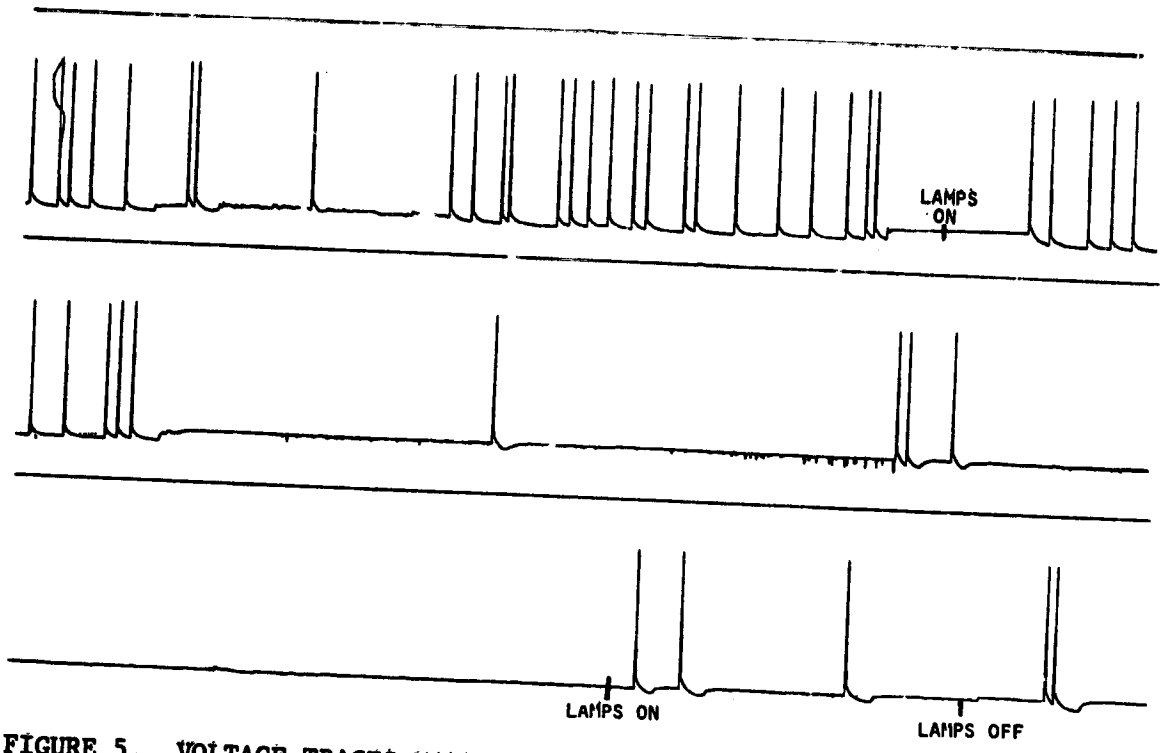

FIGURE 5. VOLTAGE TRACES WITH LIGHTWEIGHT SUBSTRATE SAMPLE (2) (NO CONDUCTIVE COATING ON BACKSIDE). VOLTAGE TRACES SHOW THAT UV LAMPS DO NOT CAUSE "ZENERING" ACTION.

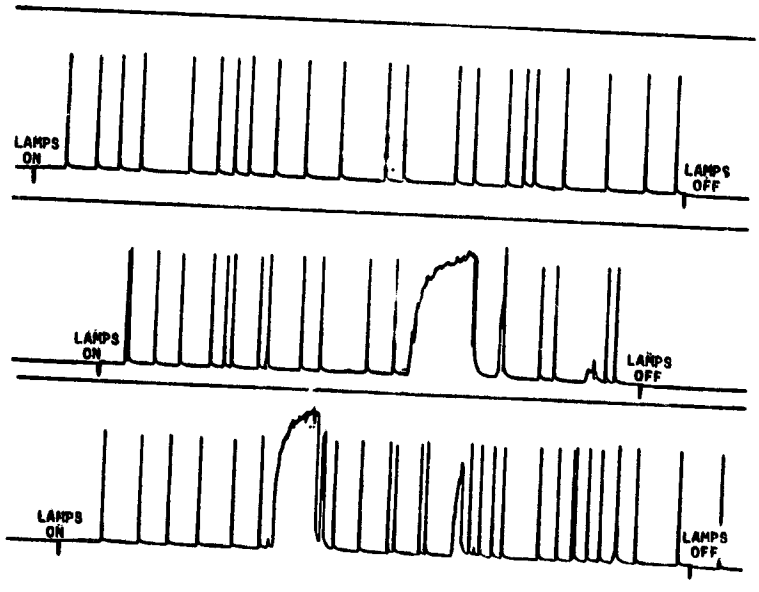

FIGURE 6. INITIAL VOLTAGE TRACES OBTAINED WITH SAMPLE (2a). NOTE THAT TURNING ON THE UV LAMPS INCREASES THE OCCURRENCE OF ARC DISCHARGES AND OCCASIONALLY SHOWS A TENDENCY OF ZENERING.

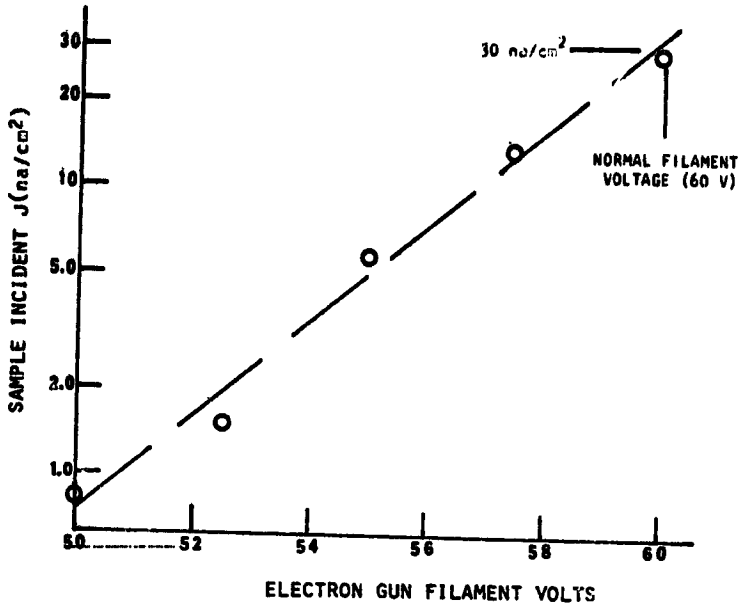

FIGURE 7. SAMPLE INCIDENT CURRENT DENSITY VS ELECTRON GUN FILAMENT VOLTAGE.

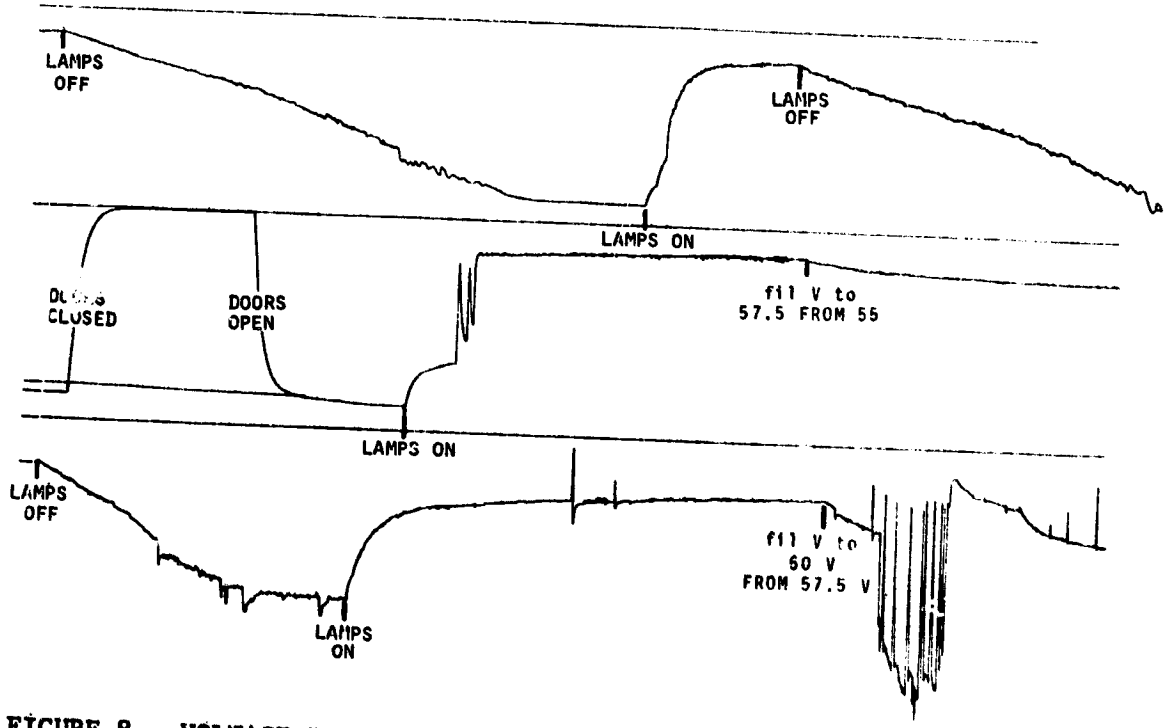

FIGURE 8. VOLTAGE TRACES WITH SAMPLE (2a) (LIGHTWEIGHT SUBSTRATE WITH CONDUCTIVE COATING ON BACKSIDE). VARIABLE ELECTRON BEAM CURRENT DENSITY FROM 6 TO 30 na/cm^2.

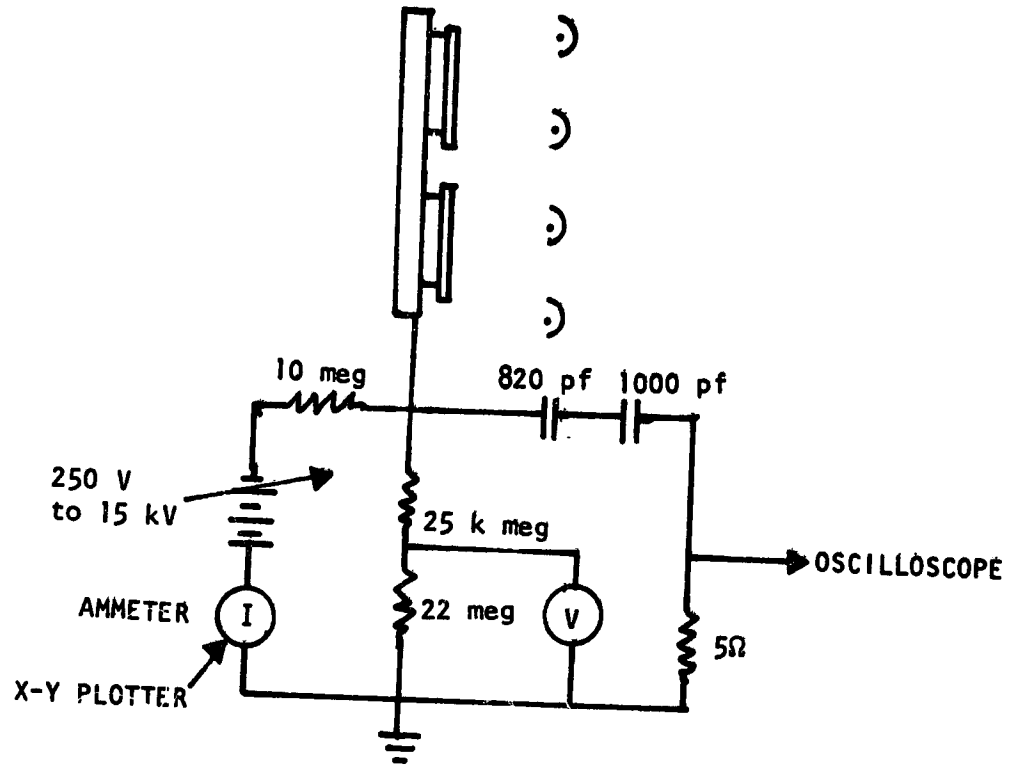

FIGURE 9. CIRCUITS TO MEASURE PHOTO-INDUCED CURRENT VS POTENTIAL.

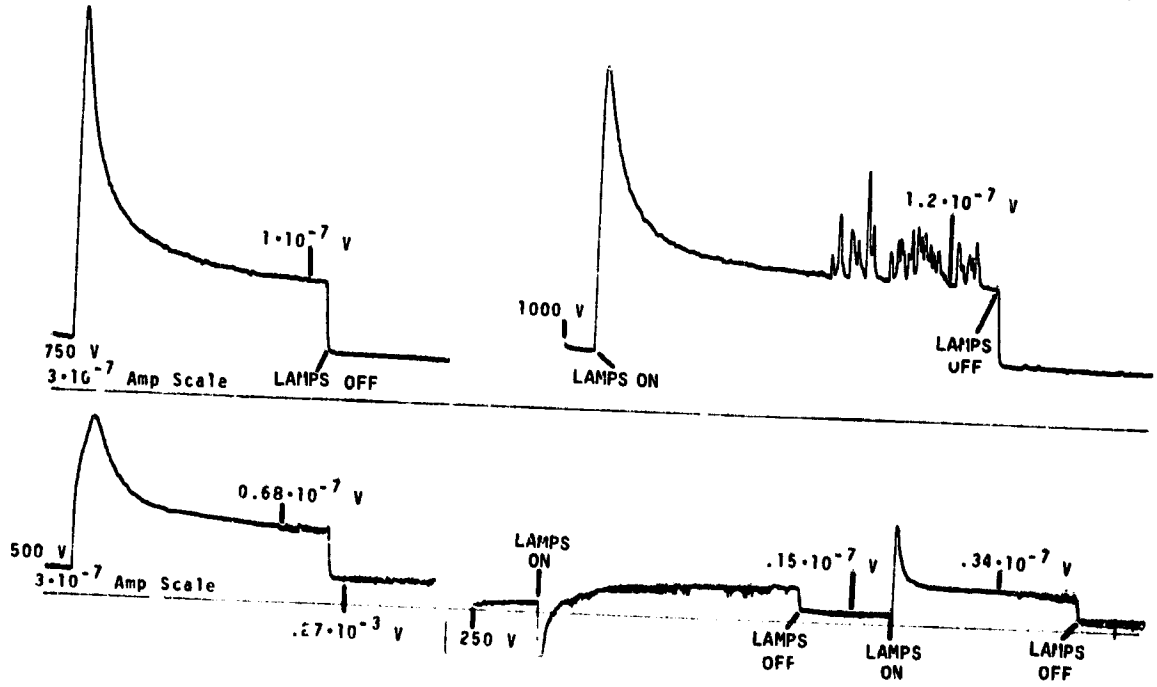

FIGURE 10. PHOTO-INDUCED CURRENTS FROM SAMPLE (2a) VS SAMPLE VOLTAGE.

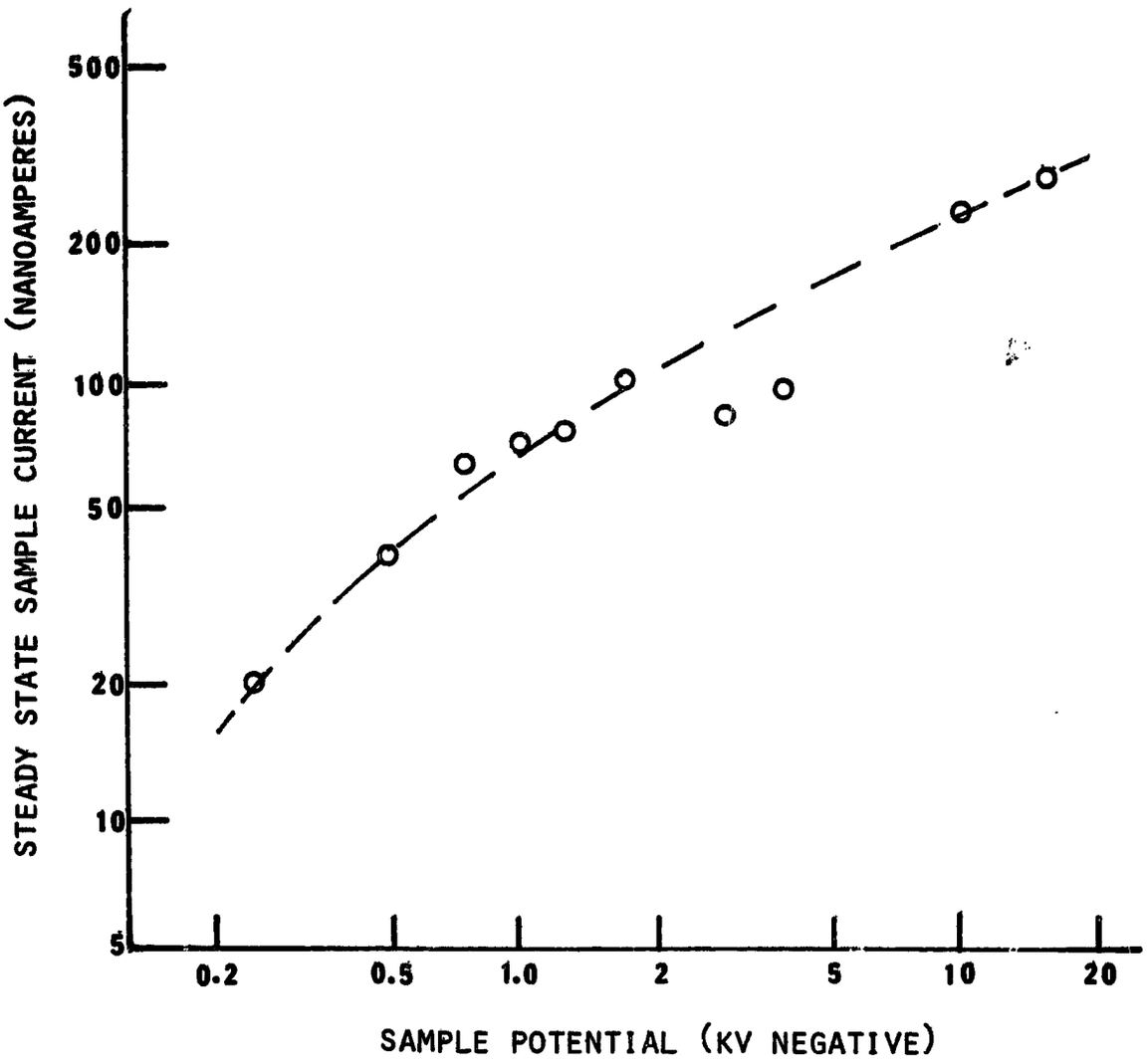

FIGURE 11. STEADY STATE SAMPLE (2a) PHOTO-INDUCED CURRENT VS POTENTIAL

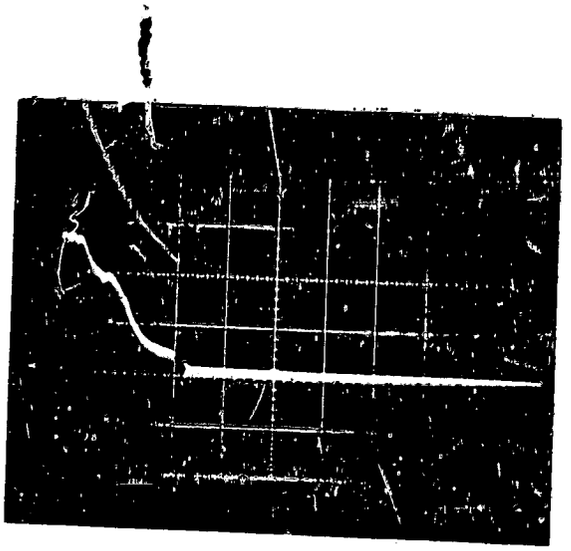

A

V = -1750 Volts
R = 5 ohms
.2 amp/cm Vertical
1 μs/cm Horizontal

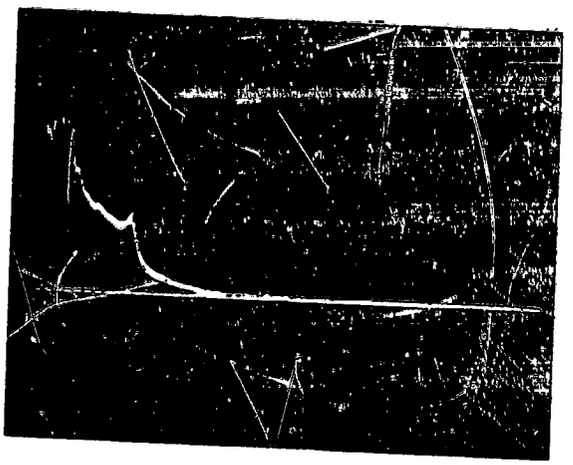

B

V = 5000 Volts
R = .5 ohms
.4 amp/cm Vertical
1 μs/cm Horizontal

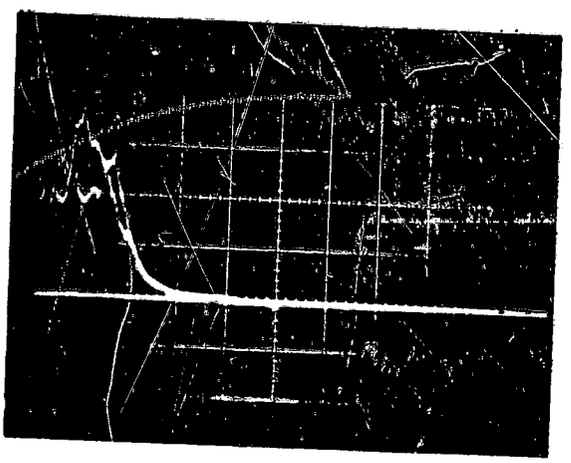

C

V = -15 kilovolts
R = 5 ohms
1 amp/cm Vertical
1 μs/cm Horizontal

FIGURE 12. ARC DISCHARGE WAVEFORMS OBTAINED WITH SAMPLE (2a).

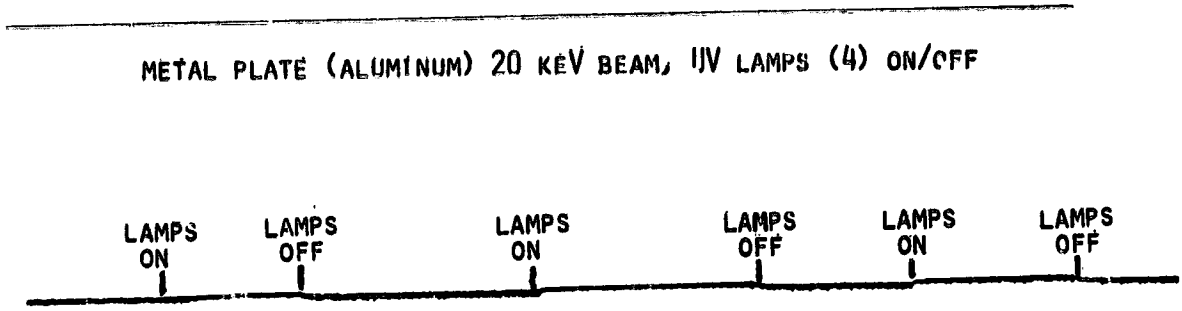

FIGURE 13. VOLTAGE TRACES WITH AN ALUMINUM PLATE SAMPLE (3)

The following papers were not presented at the conference but are included here for additional information.

D53

N79-24054

A COMBINED SPACECRAFT CHARGING AND PULSED X-RAY SIMULATION FACILITY*

Steven H. Face, Michael J. Nowlan,
William R. Neal, and William A. Seidler+
Spire Corporation

SUMMARY

A spacecraft charging simulation facility has been constructed to investigate the response of satellite materials in a typical geomagnetic substorm environment. The conditions simulated include vacuum, solar radiation, and substorm electrons; in addition, a nuclear threat environment simulation using a flash x-ray generator is combined with the spacecraft charging facility. Results obtained on a solar cell array segment used for a preliminary facility demonstration are presented with a description of the facility.

INTRODUCTION

Recently, much interest has been shown in the subject of anomalous behavior of electrical systems deployed in satellites in geosynchronous orbit (refs. 1-4). This behavior is now being investigated extensively in the belief that it is caused by electrostatic charging of dielectric surfaces due to the space environment (refs. 5-8). The electrical discharges associated with spacecraft charging result in electromagnetic interference which can couple into the spacecraft harness. In addition, the dielectric surface becomes contaminated with surface tracks which may lead to device failure or poor performance (ref. 9).

An electron charging facility was constructed at Spire for the simulation of the low-energy plasma environment encountered in geosynchonous orbit. A flash x-ray generator was combined with the charging facility to simulate the effects of a nuclear threat environment. In this facility the response of satellite materials can be determined for any combination of x-ray, surface charging, or simulated solar radiation, taken either separately or simultaneously. Although there have been earlier studies of spacecraft charging under a variety of conditions (refs. 10-12), the simultaneous exposure of satellite dielectrics to flash x-rays and electron surface charging has not been previously reported. Figure 1 is a schematic of the major elements of the combined facility.

*This work was supported by the Defense Nuclear Agency.
+Presently at Jaycor

This paper describes the combined x-ray and electrostatic charging facility and summarizes the preliminary results obtained during irradiation of solar cell array segments deployed on Skynet satellites.

FACILITY DESCRIPTION

Flash X-Ray Source

The x-radiation used for assessing the survivability/vulnerability of solar cells and other electrical devices is produced by the SPI-PULSE™ 6000 pulsed-power electron generator operating in the bremsstrahlung mode. The anode of the field emission tube used in these experiments is a high-Z target for the conversion of electron energy to bremsstrahlung. The diode of the field emission tube consists of a 6.4-cm diameter cathode and a 7.6-cm diameter tantalum foil anode. An 8-mm diode gap spacing provides a nominal 5- to 10-ohm load impedance for the 1.5-ohm energy store. This overmatched impedance results in the diode voltage being a significant fraction of the store voltage. Since the x-ray conversion efficiency increases with electron energy, x-ray production is increased with high-impedance loads, and depending on the charge level of the energy store, photon energies of up to 280 keV can be produced.

Diode operation is monitored by recording the voltage and current produced during discharge of the energy store. Voltage on the inner conductor of the field emission tube is measured with a capacitive divider and current is determined from a resistive shunt. The voltage and current reproducibility of the diode discharge is better than ±5 percent.

The electron beam power pulse generated by this diode configuration has a nominal width of 150 ns FWHM. The x-ray pulse produced has a width of 100 ns FWHM due to the decrease of bremsstrahlung production efficiency for low-energy electrons at the pulse. Measurement of the x-ray time history is made with a scintillator-photodiode, consisting of an EG&G SGD-100A photodiode and a Pilot B plastic scintillator rod. A gold foil calorimeter is used to measure the x-ray fluence, which, at the center of the sample mount of the charging facility, is given by

$$\phi = 2.9 \times 10^{-12} (V_o)^{4.25} \qquad (1)$$

where ϕ is the fluence in millicalories per square centimeter and V_o is the charging voltage of the pulser in kilovolts.

The x-ray fluence at the upper and lower ends of the 45° sample mount were measured as 60 percent and 170 percent, respectively, of the central fluence.

Electron Charging Source

The electron charging facility was designed to simulate the monoenergetic electron fluxes encountered in a geomagnetic substorm environment. The electron beam is produced by a standard cathode-ray tube flood gun with a maximum thermionic current output of 1 mA. The size and intensity of the electron beam is controlled by biased grids in the gun and by the three-element cylindrical lens system shown in figure 1. The electron energy in the lens is only a few hundred volts, so that shielding from stray magnetic fields is required. The electron source and lens system is raised to accelerating potentials up to 20 kV; a copper mesh is used for the electrostatic shielding of the lens region.

A parallel-mesh acceleration field region at the exit of the lens system provides the high voltage acceleration for the electrons. Components of electron velocity perpendicular to the accelerating field are negligible compared with the velocity through the exit mesh, so that beam divergence is minimal.

The test volume consists of an aluminum vacuum chamber, 20 cm in diameter by 18 cm in length, which attaches to the diode flange of the SPI-PULSE 6000 for the combined x-ray and electron irradiations. Access to the target region is facilitated by four circumferential chamber ports.

Electron intensity and uniformity are measured with a spatially resolving Faraday collector array placed at the specimen position. The collector plate is 10 cm in diameter and contains twenty 0.8-cm-by-0.45-cm collectors across a diameter. The remainder of the collector assembly is coated with cathode-ray-tube phosphor for visual observation of the electron beam while adjusting the focus.

The orientation of the current collector array in the test chamber is controlled externally by rotation of the sample-mount rod. The current collector array may be rotated 360^{o} to sample the entire electron beam. A representative map of the initial beam uniformity obtained for a 1-nA/cm^2 peak current density is shown in figure 2 with a solar array segment. Superimposed bremsstrahlung fluence intensities, for a representative test configuration, are also shown in the figure.

During testing, electron intensity is maintained constant by monitoring the current density with four stationary current collectors near the circumference of the beam at the entrance to the test chamber and adjusting the filament current accordingly.

Measurements of the current density made at various distances from the beam entrance aperture indicate no beam divergence or convergence within the test volume. Differences in beam current density at the top and bottom of the chamber are less than 3 percent. Current density is variable up to 30 nA/cm^2 for an 8 cm diameter beam. Higher intensities are attainable with smaller diameter beams.

Specimens are mounted on a dielectric or conductive support in the center of the test chamber. The panel is mounted at a 45° angle to expose equal areas to radiation from the electron source and x-ray source. Light from a spectrally calibrated tungsten lamp is introduced through a quartz window in the back plate of the chamber. A mirror mounted on the front plate reflects the light onto the specimen surface. Light intensity is adjusted to provide 140 mW/cm^2 incident to simulate air-mass-zero solar intensity. The quartz window is also used for viewing the sample during electron charging.

Prior to specimen irradiation, the uniformity and intensity of the electron beam are measured. The test specimen is then positioned in the chamber, while the test volume is evacuated to a pressure of less than 5×10^{-5} torr. Total pump-down time is about 15 minutes.

The electron gun filament current is adjusted to provide the intensity of interest as determined by the current measured with the four Faraday collectors at the beam periphery. During the irradiation, a TREK Model 340 HV noncontacting voltage probe is used to measure the surface electrostatic potential on test specimens. This unit has a voltage resolution of 0.1 percent, with measurements relatively independent of probe-to-surface spacing. The time-response of the probe is less than 2 ms. The potential of the probe floats to that of the surface being measured, minimizing its effect upon the test environment. The probe may be manipulated from outside the test chamber using a set of external controlling rods. Position over the test surface is indicated by an x-y plotter connected to the rods. When not in use the probe is retracted into a side chamber.

FACILITY DEMONSTRATIONS

Description of Solar Cell Array

The solar cell panels used for facility demonstration testing consisted of nine 2-cm-by-2-cm cells configured in a three-by-three array. This configuration was chosen as the smallest array which might represent an actual satellite deployment geometry (i.e., the central cell is completely surrounded by other cells). The electrical circuit of the central cell was independent of the outer cells to facilitate measurement of the cell response to various environments, although it was recognized as not being a realistic configuration.

Four solar arrays, designated 4057-1, 4057-2, 4057-3, and 4057-4, were provided by Ford Aerospace and Communications Corp. from Skynet satellites. Details of the solar cell geometry are shown in figure 3. The solar cells were n-on-p silicon fabricated from 5- to 14-ohm-cm material with junction depths of 0.25 to 0.30 micrometer. Two of the test panels, arrays 4057-3 and 4057-4, had interconnected conductive coverslip coatings of indium oxide.

The four solar cell arrays were irradiated with x-rays, electrons, and solar spectrum photons. Initially, each array was irradiated with x-rays with and without incident solar light. Array 4057-2 was pulsed more than the others to observe any

cumulative effects. Each array was charged with electrons at a nominal 1-nA/cm^2 flux level. During charging, the arrays were exposed alternately to light and darkness to simulate day-night conditions. Finally, simultaneous x-ray, electron charging, and incident light exposures were provided to assess the combined effects upon cell array performance.

At the conclusion of each phase of testing, the I-V characteristics of the central cell were measured with a Spectrosun Model X25 MKII AM0 solar simulator. In addition, the solar cells were examined for signs of physical degradation after each exposure.

Solar Cell Response to X-Rays

The solar cell arrays were subjected to x-ray fluence levels of 0.07, 0.2, and 0.45 mcal/cm^2 incident upon the central cell. These levels correspond to SPI-PULSE 6000 charging voltages of 150, 200, and 250 kV and a source-to-target distance of 9 cm. The total x-ray dose delivered was 3, 4, and 6 rads (Si) at the front surface.

The ambient temperature of the test volume was recorded for each pulse. A chromel-alumel thermocouple attached to the backside of the central cell was calibrated and monitored. Output of the thermocouple indicated a maximum temperature rise of less than 1°C at the highest x-ray fluence level. This corresponds to a 0.5 percent decrease in V_{oc} and 0.1 percent increase in cell current.

A typical cell response is shown in figure 4. The x-ray energy deposition in the solar cell saturates the junction region due to creation of electron-hole pairs. The pulsewidth of the cell output is dependent on the injection level, carrier drift velocity, carrier recombination time, and load circuit. No difference was seen in the output signal when the coverslips of arrays 4057-3 and 4057-4 were grounded.

A transient I-V curve generated from the x-ray response for panel 4057-2 is compared to the AM0 curve in figure 5. No transient response was observed during simulation of daylight conditions. Heating of the test volume with the tungsten lamp produced a slight voltage decrease. No permanently adverse effects on cell performance occurred from the x-ray exposures.

Solar Cell Response to Electron Charging

The solar cell arrays were irradiated with electrons to simulate the environment encountered in a geosynchronous orbit. The nominal flux density of the electron beam was maintained at 1 nA/cm^2, while the electron energy was varied from 2 to 20 keV.

The TREK electrostatic voltage probe recorded the potentials built up on the array surface and the fiberglass substrate. Generally, the potential of the solar cell coverslips reached one-fourth to one-third of the incident electron energy, while the

fiberglass substrate at the periphery of the array charged from one-half to two-thirds of the electron energy. A typical voltage profile across the surface is shown in figure 6.

Differences in potential on the cell surfaces also caused discharges to occur among the cell coverslips or between a cell and the fiberglass substrate. For some of the testing the front contact of the center cell was grounded. In this case, potential differences between cells due to electron charging resulted in electrical discharges from the peripheral cell coverslips to the grounded contact.

The surface discharge rate and associated potential drop were recorded with the TREK probe. A discharge over the cell surface caused the potential to drop below 1 kV. Discharges to the fiberglass substrate were generally only partial, resulting in a potential drop of 2 to 3 kV. A time history of the potential over the cell surface and substrate exposed to the electron irradiation is shown in figure 7.

Not all the electrical discharges appeared in the load circuit. If the front contact of the cell was grounded, few signals were observed in the load, since the discharge could go directly to ground. For most of the testing, the cell back contact was grounded so that discharges to the front contact would appear across the load. In this mode of operation, there was generally a coincidence in the drop in potential recorded by the TREK probe and the signal recorded in the load circuit. To obtain a signal of reasonable amplitude, a 1-MΩ preamplifier was used as a load to the solar cell.

Signals of tens of millivolts were recorded during the electrical discharges. These signals reached their peak in a few milliseconds, then decayed exponentially in about 10 ms. The charge contained in the discharge signals amounted to a few tenths of a microcoulomb. This quantity represents the charge lost in a 3-kV potential drop on the cell surface, using the calculated capacitance of a cell coverslip. The corresponding energy lost in a discharge was about 1 mJ. The electrical discharge signals were of both positive and negative polarity, and, in general, were very reproducible for fixed experimental conditions.

Photographic observation of the cell electrical discharge activity was recorded with a Polaroid camera. Open shutter photographs of 5- to 10-min exposure were taken using the chamber quartz window as a view port. Evidence of electrical discharges was observed with beam voltages from 2 to 20 kV at 1 nA/cm^2 for times of several minutes. An example of the electrical discharging is shown in figure 8.

Most of the electrical arcs occurred around the central cell whose front contact was connected to ground through the load circuit. Some discharging is evident among the outer cells. The number of visible electrical arcs increases with the surface potential of the cells.

A reduced level of discharging was observed for the conductive coverslip cell arrays. The potential of the fiberglass substrate around the cells was observed to be lower by 10 to 30 percent when the coverslips were grounded.

With the tungsten lamp turned on, the electrical discharging ceased immediately for all arrays, as determined from monitoring the cell load circuit. The potential on the fiberglass substrate decayed to a few hundred volts in minutes. No evidence of electrical discharge was recorded over the substrate.

After multiple discharges, measurement of the I-V characteristics showed that panels 4057-1 and 4057-2 experienced a loss in maximum operating power of 12 percent. Panels 4057-3 and 4057-4 incurred no effective power loss as a result of charging and discharging. The I-V curves for panels 4057-1 and 4057-4 are shown in figures 9 and 10.

Two of the solar arrays were physically damaged by the electrical discharging. The central cells of panels 4057-1 and 4057-3 each had a crack develop in the coverslip. The position of the crack on both cells coincided with an observed electrical arc. These panels were irradiated for a total time of 8h and 5h, respectively, at electron energies of up to 20 keV. The other two panels, irradiated for less than 4h each, did not develop similar coverslip cracks.

Solar Cell Response to Combined Environment Exposure

All the panels were subjected to x-ray exposure during electron irradiation. Each panel was charged with a 16-kV, 1-nA/cm^2 electron beam for 1h in the dark. The panels were then pulsed with x-rays at test levels of 3, 4, and 6 rads (Si). The conductive coverslip cells were pulsed with and without the coverslips grounded.

None of the cells exhibited anomalous behavior during the x-ray pulse. The x-ray response signals were the same as observed without electron charging. There was no potential drop observed, within the time-response of the TREK probe, either on the fiberglass substrate or over the cell surface during the x-ray pulse. It is possible that there may have been a late time response or a low-amplitude response that could not be recorded with the instrumentation available.

CONCLUDING REMARKS

The spacecraft charging facility developed at Spire represents an economical and reliable simulation device. Results obtained using a three-by-three solar cell array are in general agreement with previously published results at other facilities (refs. 13 and 14). These results demonstrate the utility of using small-area samples to simulate larger area behavior.

REFERENCES

1. Fredericks, R.W.; and Scarf, F.L.: (1973) Observations of Spacecraft Charging Effects in Energetic Plasma Regions. Photon and Particle Interactions with Surfaces in Space, R.J. Grard, ed., D. Reidel Publishing Co., Dordrecht, Holland, pp. 277-308.

2. McPherson, D.A.; Cauffman, D.P.; and Schober, W.: (1976) Spacecraft Charging at High Altitudes: The Scatha Satellite Program. Spacecraft Charging by Magnetospheric Plasmas. Progress in Astronautics and Aeronautics, Vol. 47, A. Rosen, ed.. AIAA, MIT Press, 1976, pp. 15-30.

3. Inouye, G.T.: Spacecraft Charging Anomalies on the DSCS 11, Launch 2 Satellites. Proceedings of the Spacecraft Charging Technology Conference, NASA TMX-73537, 1976, pp. 829-852.

4. Robbins, A.; and Short, C.D : Space Environmental Effects on the SKYNET 2B Spacecraft. Proceedings of the Spacecraft Charging Technology Conference, NASA TMX-73537, 1976, pp. 853-863.

5. Whipple, E.C.: Modelling of Spacecraft Charging. Proceedings of the Spacecraft Charging Technology Conference, NASA TMX-73537, 1976, pp. 225-235.

6. Rosen, A.: (1975) Spacecraft Charging - Environment Induced Anomalies. AIAA paper 75-91, AIAA 13th Aerospace Sciences Meeting, Pasadena, California.

7. Katz, I.; Parks, D.E.; Wang, S.; and Wilson, A.: Dynamic Modelling of Spacecraft in a Collisionless Plasma. Proceedings of the Spacecraft Charging Technology Conference, NASA TMX-73537, 1976, pp. 319-330.

8. Pike, C.P.: (1975) A Correlation Study Relating Spacecraft Anomalies to Environmental Data. Spacecraft Charging by Magnetospheric Plasmas. Progress in Astronautics and Aeronautics, Vol. 47, A. Rosen, ed., AIAA, MIT Press, 1976, pp. 45-60.

9. Stevens, N.J.; Lovell, R.R.; and Gore, V.: (1975) Spacecraft Charging Investigations for the CTS Project. NASA TMX-71795.

10. Keyser, R.; and Swift, O.: Analysis and Tests of a Satellite Model in a Photon Environment. IEEE Transactions on Nuclear Science NS-24, No. 6, 1977, pp. 2440-2444.

11. Luft, W.: Radiation Effects on High Efficiency Silicon Solar Cells. IEEE Transactions on Nuclear Science NS-23, No. 6, 1976, pp. 1795-1802.

12. Kalma, A.H.; and Fischer, C.J.: 4 Space Radiation of Solar Cells. IEEE Transactions on Nuclear Science NS-23, No. 6, 1976, pp. 1789-1794.

13. Stevens, N.J.; Berkopec, F.D.; Staskus, J.V.; Blech, R.A.; and Narciso, S.J.: Testing of Typical Spacecraft Materials in a Simulated Substorm Environment. Proceedings of the Spacecraft Charging Technology Conference, NASA TMX-73537, 1976, pp. 431-457.

14. Bogus, K.P.: Investigation of a CTS Solar Cell Test Patch Under Simulated Geomagnetic Substorm Charging Conditions. Proceedings of the Spacecraft Charging Technology Conference, NASA TMX-73537, 1976, pp. 487-501.

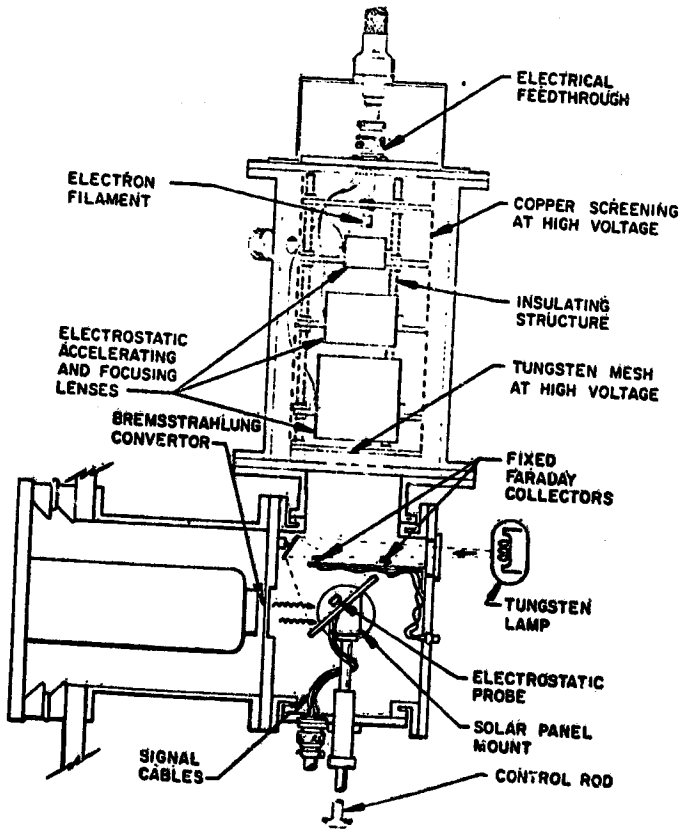

Figure 1. - Schematic of electron charging source.

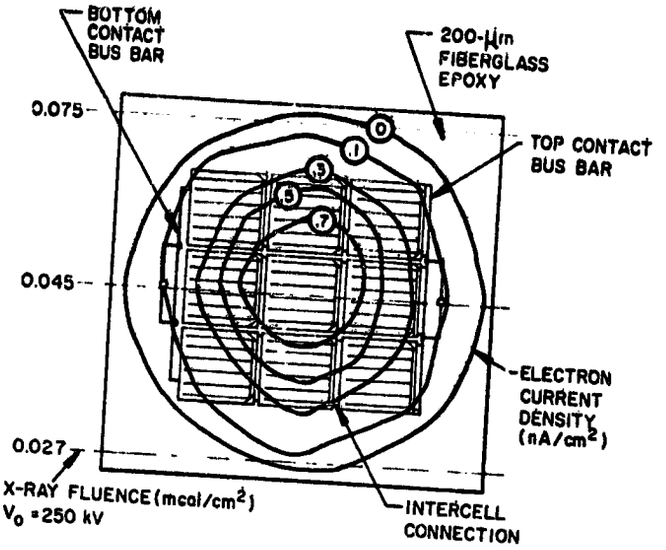

Figure 2. - Electron beam uniformity over three-by-three solar cell array.

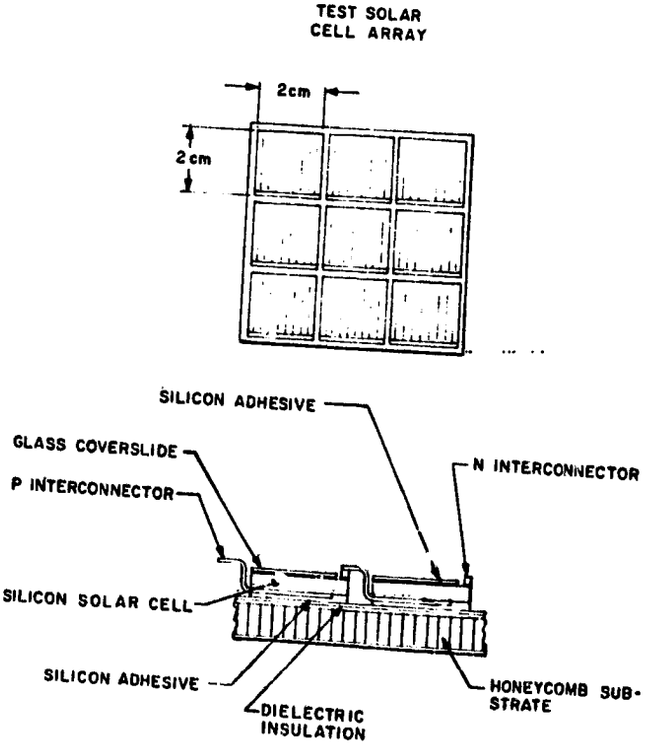

Figure 3. - Schematic of solar cell array with aluminum honeycomb substrate.

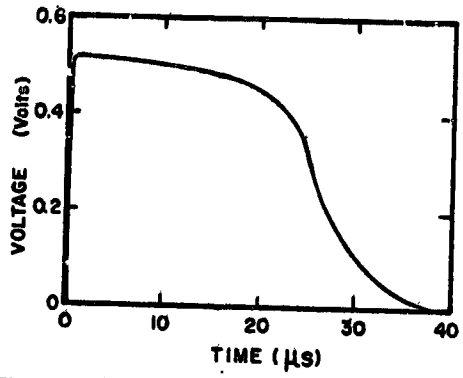

Figure 4. - Representative transient response of central cell of solar array 4057-2 to X-ray irradiation (V_0 = 200 keV).

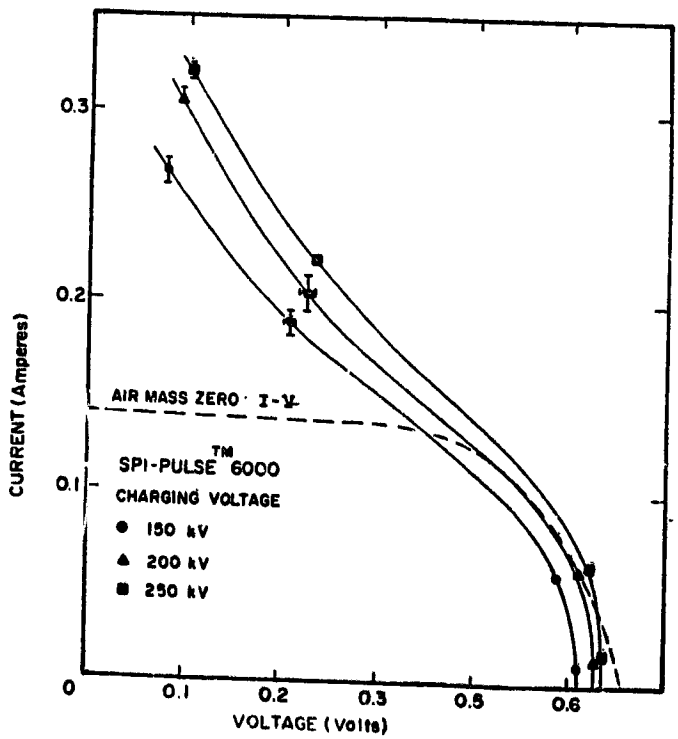

Figure 5. - Transient current-voltage characteristics of central cell of solar array 4057-2 under X-ray irradiation.

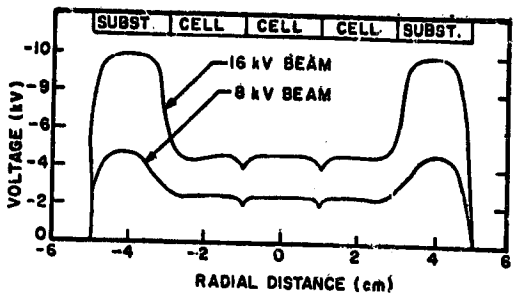

Figure 6. - Surface potential of solar array 4057-4 due to electron irradiation.

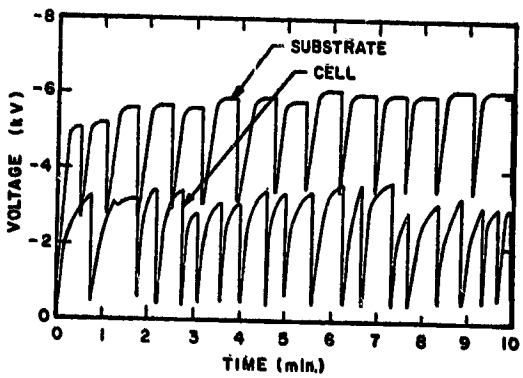

Figure 7. - Time history of surface potential of solar array 4057-4 for 16-keV electron irradiation, coverslips grounded through 1 MΩ.

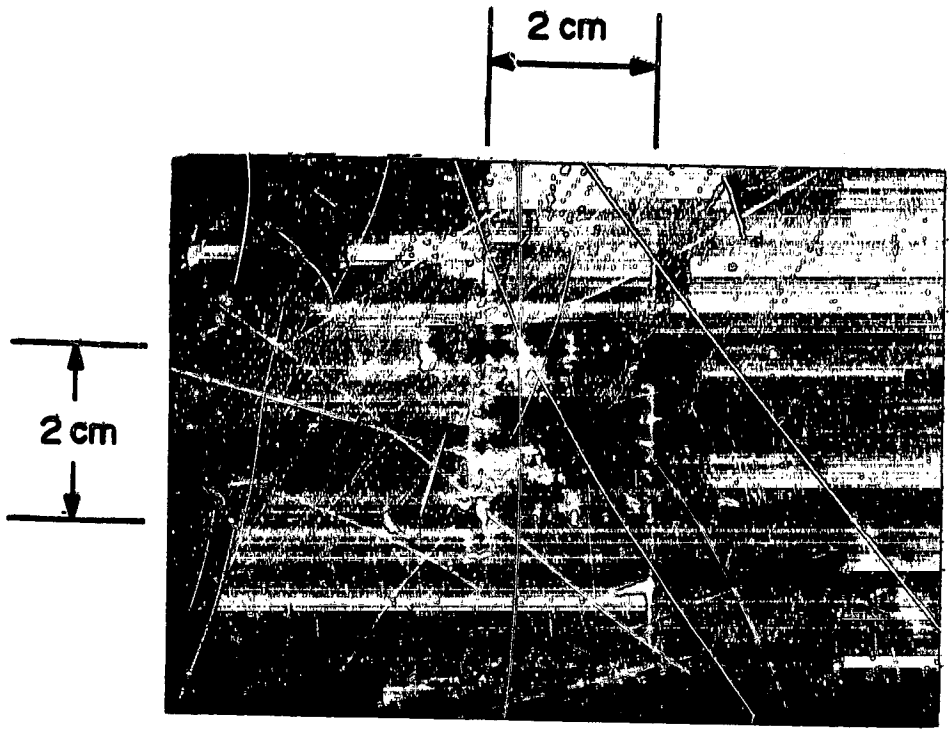

Figure 8. - Open-shutter photograph of electrical discharging of solar cell array.

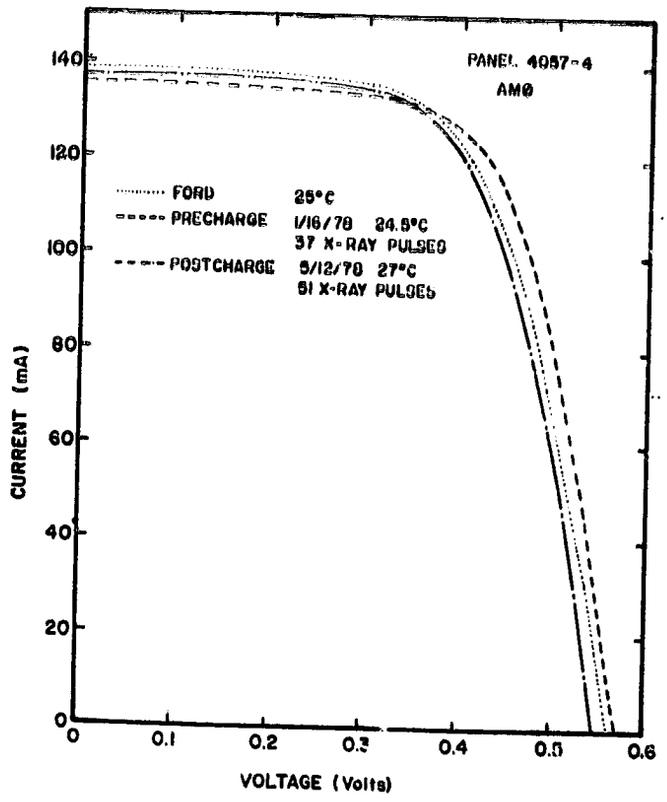

Figure 9. - Current-voltage curves for central cell of solar array 4057-4.

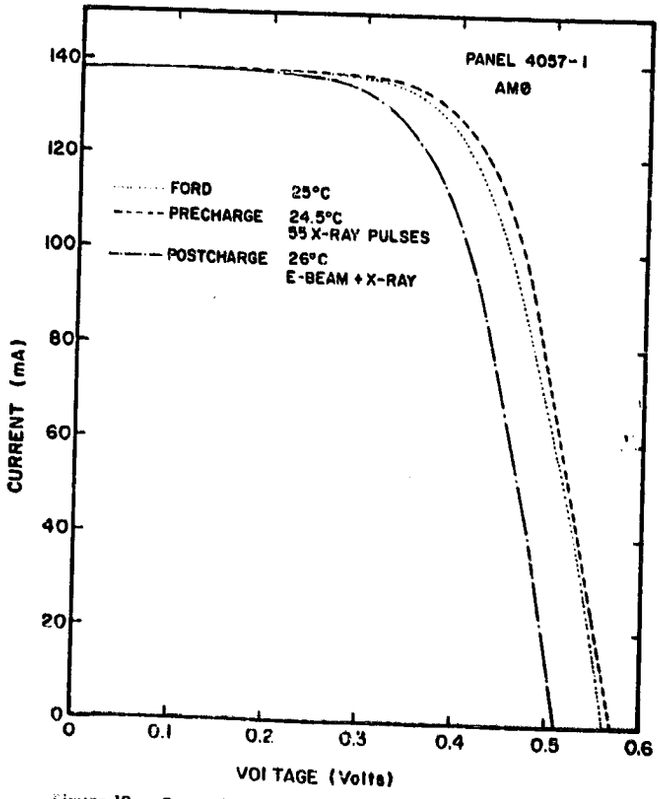

Figure 10. - Current-voltage curves for central cell of solar array 4057-1.

D64

N79-24055

CHARACTERIZATION OF ELECTROMAGNETIC SIGNALS GENERATED BY ELECTRICAL BREAKDOWN OF SPACECRAFT INSULATING MATERIALS*

J. E. Nanevicz and R. C. Adamo
SRI International

B. L. Beers
Science Applications, Inc.

BACKGROUND

As part of a program to develop an understanding of the behavior of typical spacecraft insulating materials under exoatmospheric charging conditions, a series of exploratory measurements of the external transient electric and magnetic fields produced by electrical breakdown of materials was performed. Although the metal test chamber used for these early measurements was not ideally suited for detailed electromagnetic transient studies, the magnitudes of the observed fields were sufficiently large that the need for a concentrated effort to determine the true electromagnetic nature of discharge generated transients was recognized. A program was therefore initiated to conduct discharge characterization tests in an electromagnetically "clean" and clearly defined structure, in order that the data obtained be free of artifacts associated with the measurement setup.

The data presented in this paper were generated as part of a series of quick look experiments intended to verify the functioning of the experimental setup and to provide preliminary inputs for the development of analytical models of the discharge process. Thus, although it is planned that additional measurements will be made to carry out the complete program, it is felt that the results to date are significant in that they provide information on source characteristics in a form useful to the electromagnetic compatibility engineer.

EXPERIMENTAL SETUP

For the electromagnetic breakdown studies, the test samples were mounted in the middle of a ground plane within an electromagnetically transparent vacuum chamber in the general manner illustrated in figure 1. This arrangement simulates a region of charged dielectric mounted on the skin of a satellite. The electron gun is of a special type designed at SRI and uses a multipactor electron source to provide a large-area uniform beam over a wide range of energies and current densities as discussed in a companion paper.**

*The work reported here was supported by the U.S. Air Force under contracts F49620-77-C-0113 and ~~SAI-77-C-0166~~.

**J. E. Nanevicz and R. C. Adamo, "Further Development of the Multipactor Discharge Electron Source."

The electron-gun circuitry includes a feedback system to maintain the electron-beam current density at a preset level over long periods of time.

This setup produces an environment similar to that existing on a satellite when breakdowns occur. These discharges on the outer surface generate transient electric fields above the skin and transient currents on the skin. The electric fields induce signals in wiring on the exterior of the satellite while both electric fields and skin currents excite apertures in the skin which excite wiring on the interior of the satellite. Thus an EMC engineer requires information about the time structure and spatial variation of the surface electric fields and skin currents generated by electrical discharges on the surface of the satellite. (It is worth noting that in this case, the electric field (E) and the magnetic field (H) are not generally related by the free-space impedance of 377 ohms as they would be in free space, so that it is necessary to measure both E and H.)

Measurements of E and H (H is equivalent to skin current) are being made using simple antennas located at varying distances from the discharge test panel as suggested in figure 1. The antennas being used are small electric dipoles and half loops. The electric dipole sensors measure E while the loop antennas respond to the H field. Although figure 1 shows E-field sensors and a signal from the target-material base as providing the outputs to an oscilloscope, other combinations of antennas are also being used.

Transient data generated to date were recorded using a Tektronix Model 7844 dual-beam oscilloscope equipped with 7A19 preamplifiers, providing a system bandwidth of 400 MHz. For future measurements, a Biomation Model 6500 waveform recorder will also be used. This system has a bandwidth of 100 MHz and allows the rapid digitization and storage of data for computer processing.

EXPERIMENTAL RESULTS

In generating the records presented here, the instrumentation system shown in figure 1 was configured so that target-material base current was displayed on one channel of the oscilloscope. The second oscilloscope channel was connected to a small E-field sensor located 30 cm from the center of the bell jar. All of the records presented here were generated by discharges that covered a large part of the dielectric surface and extended to the edge of the test sample. They generally are a representative sample of the higher amplitude signals generated for each particular material sample.

As the quick-look experiments progressed, various experimental shortcomings were uncovered, and appropriate improvements and modifications were systematically incorporated into the test setup. For example, it was found that the bell jar material was sufficiently insulating that the electron beam could deposit substantial charge on its inside surface. Charged particles generated by test sample breakdown neutralized this charge on the bell jar and produced a large change in dc field at the E-field sensor. Bell jar charging was eliminated by covering the inside of the bell jar with a high-resistance conductive coating which bleeds away dc charge but does not attenuate the

high-frequency signals generated by the discharge. When the systematic data-gathering phase of this program begins, all of the measurements will be made with the conductive coating installed. Presently, however, data from many of the interesting test samples were obtained with the insulating bell jar, and certain precautions must be observed in using the results. It is felt that the waveforms and magnitudes of the signals generated by breakdown of the samples are of sufficient interest that the results should be presented at this time in spite of their imperfections. In particular the data in figure 2 were obtained with the conductively coated bell jar, while the rest of the records were obtained with an insulating bell jar.

Figure 2 shows a record generated by the breakdown of a second-surface quartz optical solar reflector (OSR) panel. A positive unipolar pulse is generated in the test sample base replacement-current circuit indicating that negative charge is driven away from the sample by the breakdown process. The current reaches its peak value of 1.7 A in roughly 100 ns and then decays monotonically. The behavior of the E-field can be explained by the following argument. The negative excursion, which is roughly a mirror image of the current waveform, is caused by the electrons generated in the breakdown plasma being driven upward from the surface, thereby increasing their dipole moment. A simple back-of-the-envelope calculation quickly verifies that the magnitude of the field change observed can be produced by the quantity of charge involved. In the first 100 ns, the average blow-off current is 0.87 A; thus the charge removed from the surface is 87×10^{-9} coul. If it is assumed that this charge is contained in a column extending to a height of 30 cm from the ground plane, the electric field at a point on the ground plane 30 cm from the dipole axis will be 7 kV/m which is consistent with the measured peak field excursion of 6 kV/m.

Figure 3 shows an early record generated by the breakdown of an OSR panel in the insulating bell jar. The positive unipolar replacement current pulse indicates that negative charge is driven away from the sample. The current reaches its peak value of 0.68 A in roughly 300 ns and then monotonically decays until, at roughly 1400 ns after the beginning of the discharge, another breakdown process occurs.

As before, the initial behavior of the E-field can be explained by the fact that the dipole moment of electrons driven upward by the discharge is greatly increased. In the first 100 ns, the average blow-off current is 0.25 A so that the charge removed from the surface is 25×10^{-9} coul. Thus we would expect an E-field change at the measurement point of 2.03 kV/m which is consistent with the measured peak negative field excursion of 2.8 kV/m.

As the breakdown proceeds, the negatively charged particles driven away from the sample surface arrive at the multipactor electron gun where they are collected so that they no longer contribute to the electric field at the ground plane. Removal of negatively charged particles from the plasma region leaves an expanding volume of positive charge which moves out and neutralizes the negative charges on the bell jar wall, so that after the first 100 ns, a positive-going field change is produced. The E-field at the sensor continues to become more positive until, at the end of the record, a total field change

of 7.5 kV/m has been produced. This positive-going field change is an artifact of the early experimental setup and should be ignored.

To indicate the occurrence of bell jar wall effects, the E-field records in figure 3 and succeeding records have been shown dashed in the late-time regions where these effects become pronounced.

A record showing the signals generated by a discharge on a 10 cm by 15 cm (6" x 4") aluminized-Kapton test sample is presented in figure 4. The general form of the signals is the same as for the OSR panel of figure 3, but both the replacement current and the E-field-change magnitudes are an order of magnitude or more higher in figure 4. The replacement current to the base of the test sample reaches a peak magnitude of 65 A in 400 ns.

Again, the field change is initially negative in response to the blow-off of negative charge. The field reaches a negative peak of 9 kV/m in roughly 60 ns. Since the average replacement current during the first 60 ns is roughly 2.5 A, this means that the charge blown away is 100×10^{-9} coul. Thus we should expect a peak negative field change 4 times that observed with the OSR panel of figure 3, or the field change would be expected to be $4 \times 2.03 = 8.12$ kV/m in excellent agreement with the measured value.

It should be noted that 9 kV/m is a very substantial field change. Thus it is not surprising that spacecraft charging can cause transient-upset-level signals to be induced in spacecraft electronic systems.

Figure 5 shows another breakdown of the 10 cm by 15 cm (6" x 4") aluminized-Kapton sample in which three individual discharges separated by 400 ns in time occurred. Each of the individual discharges produced a current change of roughly 10 A and generated a burst of blow-off charge that drove the field roughly 7 to 8 kV/m more negative.

To investigate the importance of sample size in determining discharge characteristics, breakdown experiments were conducted using a 5 cm by 7.5 cm (2" x 3") aluminized-Kapton test sample. The signals generated by a discharge of this sample are shown in figure 6. Comparing figure 6 with figures 4 and 5 indicates that the duration of replacement current flow is roughly 1/2 as long with the half-size sample.

Again, the E-field signal is initially negative going, in response to the blow-off of charged material, reaching a negative peak of 15 kV/m in roughly 160 ns. Since the average current flowing in this period is 15 A, the charge blown off is 240×10^{-9} coul. Thus we would expect the field change to be $240/25 = 9.6$ times that observed with the OSR of figure 3 or $\Delta E = 9.6 \times 2.03 = 19.5$ kV/m. This is in reasonable agreement with the measured negative field change.

CONCLUSIONS

The breakdown characterization studies conducted thus far indicate that the electromagnetic signatures generated are highly material sensitive. For a given material, current-pulse length increases with sample size.

The absolute magnitudes of the signals generated are highly significant. Transient field changes of tens of kV/m occurring in a period of $\approx$ 200 ns have been measured with the sensor roughly 30 cm from the center of the test sample. Such transient fields are comparable to those normally associated with nuclear EMP events or nearby lightning. It has long been recognized that lightning and EMP can seriously affect unprotected electronic systems and that deliberate measures must be taken to harden systems against these electromagnetic threats. Since the transient noise signals generated as the result of satellite charging appear to be of comparable magnitude, it is important that this source be more completely characterized to allow the intelligent development of new or modified materials and design techniques having the necessary discharge immunity to ensure the required high reliability and long lifetime of future space systems.

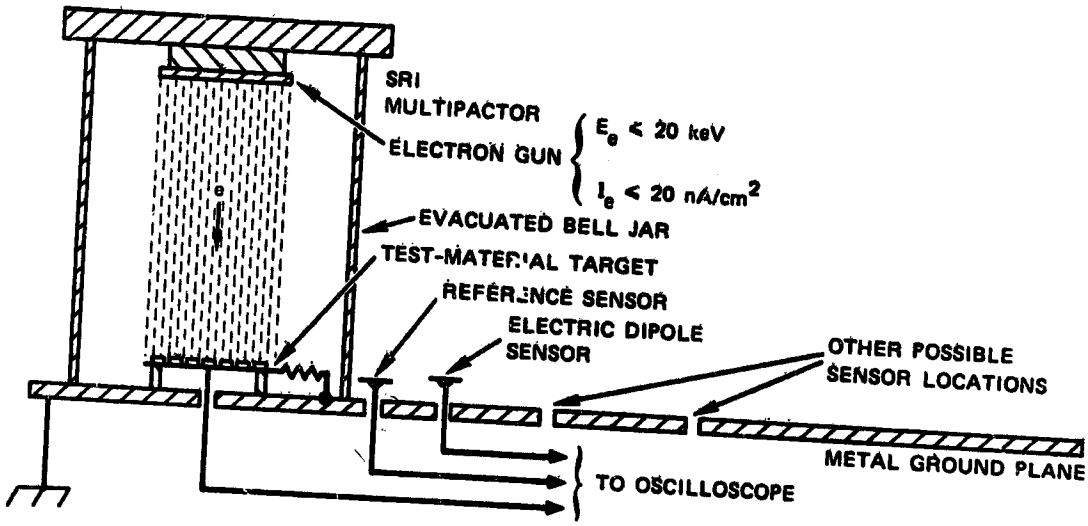

FIGURE 1 EXPERIMENTAL SETUP FOR BREAKDOWN PULSE CHARACTERIZATION

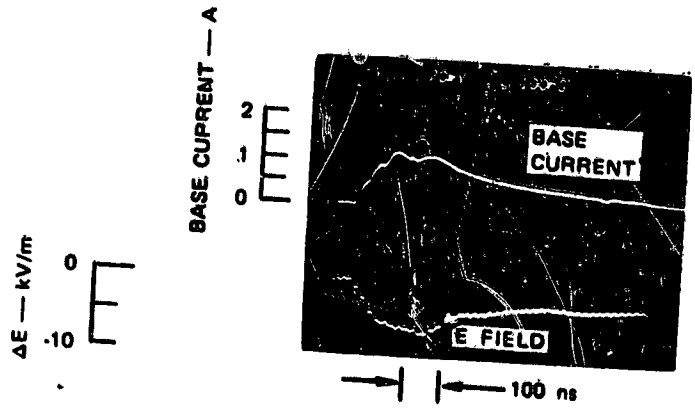

FIGURE 2 SIGNALS GENERATED BY OSR PANEL BREAKDOWN (CONDUCTING BELL JAR)

12 in. x 12 in. OSR PANEL
10-keV BEAM
CURRENT DENSITY = 10 nA/cm^2

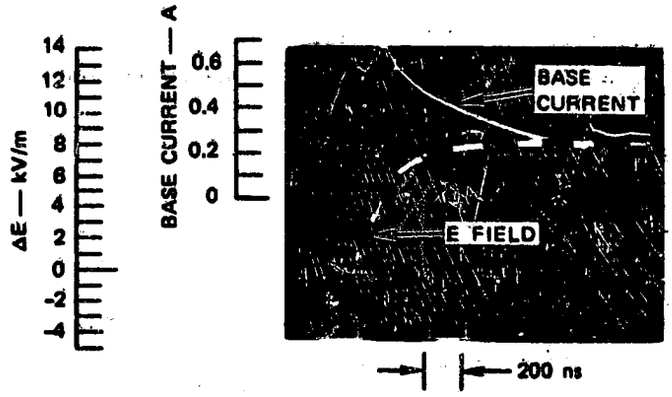

FIGURE 3 SIGNALS GENERATED BY OSR PANEL BREAKDOWN (INSULATING BELL JAR)

4 in. x 6 in. SILVERED KAPTON — 0.002 in. THICK
20-keV BEAM
CURRENT DENSITY = 10 nA/cm^2

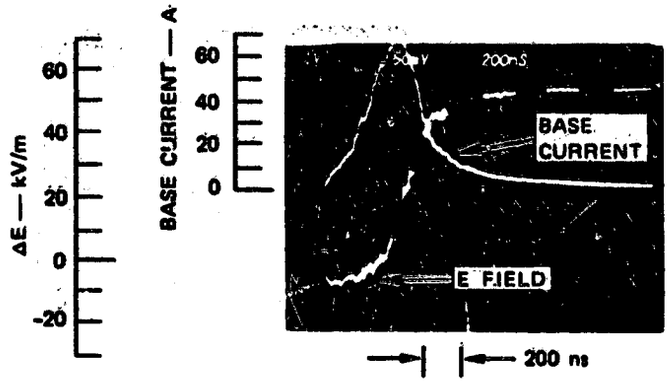

FIGURE 4 SIGNALS GENERATED BY BREAKDOWN OF 4 in. x 6 in. ALUMINIZED KAPTON SAMPLE (INSULATING BELL JAR)

4 in. x 6 in. SILVERED KAPTON — 0.002 in. THICK
20-keV BEAM
CURRENT DENSITY = 10 nA/cm^2

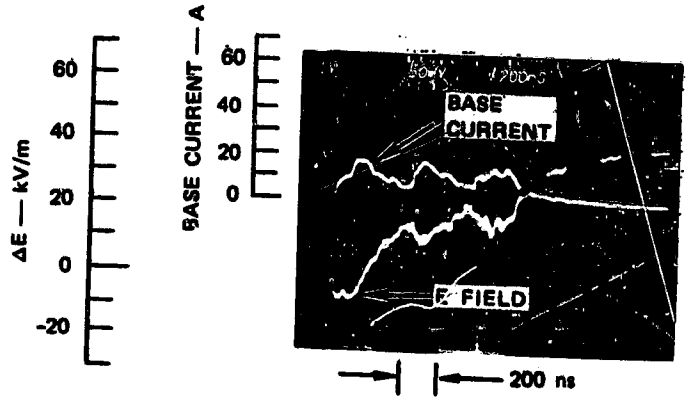

FIGURE 5 MULTIPLE BREAKDOWN OF ALUMINIZED KAPTON (INSULATING BELL JAR)

2 in. x 3 in. SILVERED KAPTON — 0.002 in. THICK
20-keV BEAM
CURRENT DENSITY = 10 nA/cm^2

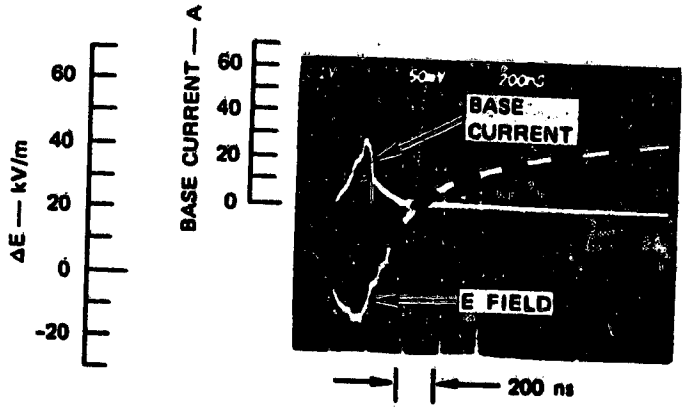

FIGURE 6 SIGNALS GENERATED BY BREAKDOWN OF 2 in. x 3 in. ALUMINIZED KAPTON SAMPLE (INSULATING BELL JAR)

D55

N79-24053

DEVELOPMENT OF THE TRANSIENT PULSE MONITOR (TPM) FOR SCATHA/P78-2

R. C. Adamo, J. E. Nanevicz, G. R. Hilbers
SRI International

INTRODUCTION

The Transient Pulse Monitor (TPM) discussed at the 1976 Spacecraft Charging Conference* has been assembled, tested and installed on the P78-2 spacecraft. This instrumentation system was developed to meet the need for a compact, lightweight piggy-back package for the detection of electrical transients on space vehicles.

The primary objective of the Transient Pulse Monitor on P78-2 is to obtain a quantitative description of the electromagnetic pulse environment on a spacecraft at synchronous altitude. Relative frequency of occurrence of pulses as a function of amplitude and duration, when obtained, will permit design of command/control logic which is relatively immune to spurious signals on typical spacecraft. A secondary objective is the characterization of signals produced by arcing between differentially charged elements on the spacecraft. Additionally, data from known discharge events, identified by data from the Spacecraft Surface Potential Monitor on P78-2 can be used quantitatively and qualitatively in the validation of electromagnetic pulse coupling models.

TPM DESCRIPTION

Although the basic TPM system can be used to characterize electrical transients occurring on the outside surface or internal to a spacecraft, the P78-2 TPM will be used entirely with internal sensors since the electromagnetic signatures of breakdown pulses on the exterior of the satellite will be characterized by portions of the onboard SC1 payload.

The TPM, as configured for the P78-2 spacecraft, consists of an electronic processor (shown in figure 1) and four electrical transient sensors. As shown in figure 2, two of the TPM sensors are passive current probes and two are long wire antennas. One current probe is located on one of the two wires that connect the upper solar array to the Power Conditioning Unit (PCU). The other current sensor is located on one of seven ground wires between the PCU and the vehicle frame. Both current sensors have sensitivities of 1 mV/mA.

---

*J. E. Nanevicz and R. C. Adamo, "Transient Response Measurements on a Satellite System," Proceedings of the Spacecraft Charging Technology Conference, U.S. Air Force Academy, Colorado, 27-29 October 1976.

The long wire antennas each consist of unshielded insulated wires tied to the outside of the foil wrap of the main vehicle wiring harness. The two wires run parallel to each other and extend half way around the inside of the vehicle center tube. These antennas differ only in the magnitudes of their termination impedances. As shown in figure 2, the low-impedance antenna is connected directly to the vehicle frame at the far end and is terminated in 50 Ω within the TPM processor housing. The high-impedance antenna is connected to the vehicle frame through a 100 K Ω resistor at the far end. At the TPM end of the high-impedance antenna there is a 10 K Ω resistor in series with the 50 Ω TPM input impedance.

Figure 2 also shows the 20 db attenuators that were installed in the low-impedance antenna and solar array sensor input channels to reduce the TPM sensitivity to internal low-level background noise observed during P78-2 system tests.

The TPM electronic processor continuously monitors electrical signals from each of the four sensors simultaneously and provides the following information for each sensor once per second, as is illustrated in figure 3.

- Positive peak amplitude
- Negative peak amplitude
- Total pulse count
- Positive integral
- Negative integral

The TPM has two modes of operation: the continuous mode (mode Ø) which is expected to be the normal mode of operation and the single-pulse mode (mode 1) which will be used only in cases of high rate of occurrence of detected transients.

The TPM also has four commandable gain (or threshold) settings that affect the sensitivities of the pulse count and pulse integral channels. The TPM continuously supplies a mode status indication bit to two gain level status indication bits to the space vehicle telemetry system.

A clock signal is supplied by the vehicle telemetry system to the TPM once per second. Upon receipt of this signal, data acquired during the previous one-second period are transferred to the outputs of the TPM. Therefore, data supplied by the TPM during any one-second period represent information gathered during the previous one-second period.

The two peak amplitude channels associated with each sensor indicate the maximum positive and negative excursions of the input signals during each timing window. In the continuous mode (mode Ø), the timing window is the entire one-second frame. In the single-pulse mode (mode 1), the inputs to the peak amplitude channels from any sensor are disabled approximately 10 mS after the occurrence of any transient that exceeds the threshold of the pulse counter channel associated with that sensor. The peak amplitude channels are not affected by changes in gain setting.

The dynamic range of the peak amplitude channels is 2 mV to 24 V for the high-impedance antenna, 20 mV to 240 V for the low-impedance antenna, 4 mA to 48 A for the solar array sensor, and 140 mA to 1700 A for the power distribution unit sensor. These ranges include the effects of 20 db attenuators in the inputs to the low-impedance and PCU sensors and also the fact that only one of seven identical power leads is monitored by the PCU sensor and one of two identical input leads is monitored by the solar array sensor.

The pulse count channel associated with each sensor indicates the total number of times that the magnitude of the input signal exceeds a set threshold during each one-second telemetry window. However, if the input signal exceeds the set threshold more than once during any 1 ms period, it is counted only once. The pulse counters acquire data throughout each one-second telemetry frame regardless of the TPM mode setting. The dynamic range of the pulse count channels is from 0 to 100 pulses per second.

The two pulse integral channels associated with each sensor indicate the total positive and negative integral of the input signals during each timing window. However, the portions of the input signal that do not exceed the lower amplitude threshold, as shown in figure 3, are not included in the integral measurement. In the continuous mode (mode Ø), the timing window is the entire one-second telemetry frame. In the single-pulse mode (mode 1), the inputs to the pulse integral channels from any sensor are disabled approximately 10 ms after the occurrence of any transient that exceeds the threshold of the pulse counter channel associated with that sensor.

The P78-2 TPM provides 20 continuous analog outputs (5 for each sensor) as described above.

The electronic processor shown in figure 1 consumes 6.8 watts and has dimensions of 20 cm x 21.3 cm x 9.65 cm. The entire system including sensors weighs 2.7 kg.

It is planned that the TPM will be turned on and checked out early during P78-2 transfer orbit and will remain on to continuously acquire data throughout the mission.

It is hoped that the TPM on P78-2 will provide a substantial supplement to the limited data presently available on the actual electromagnetic pulse environment on orbital spacecraft and if successful will serve as a model for similar systems for inclusion on other spacecraft.

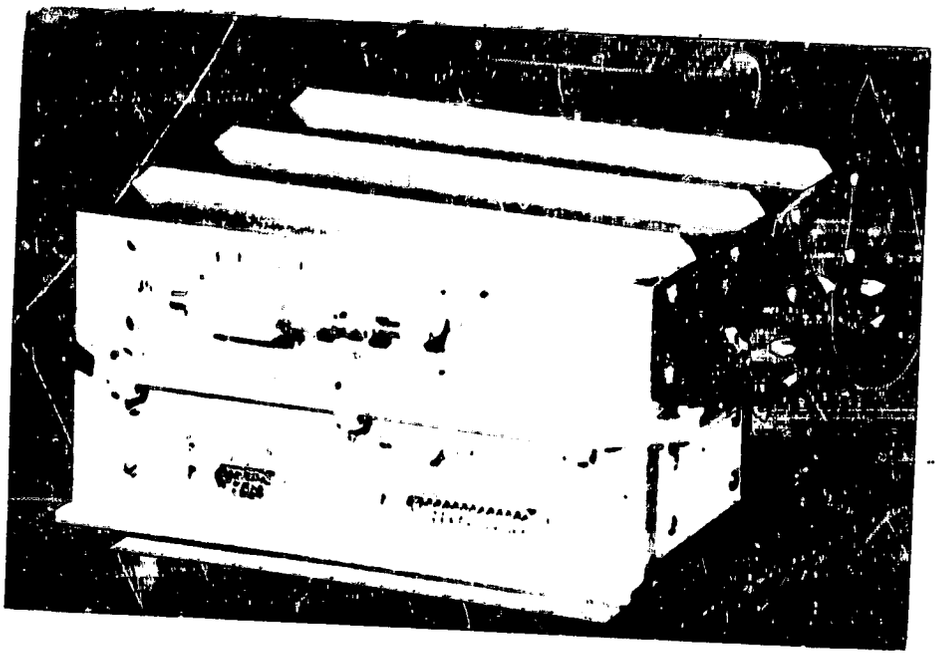

FIGURE 1 TRANSIENT PULSE MONITOR (TPM) ELECTRONIC PROCESSOR

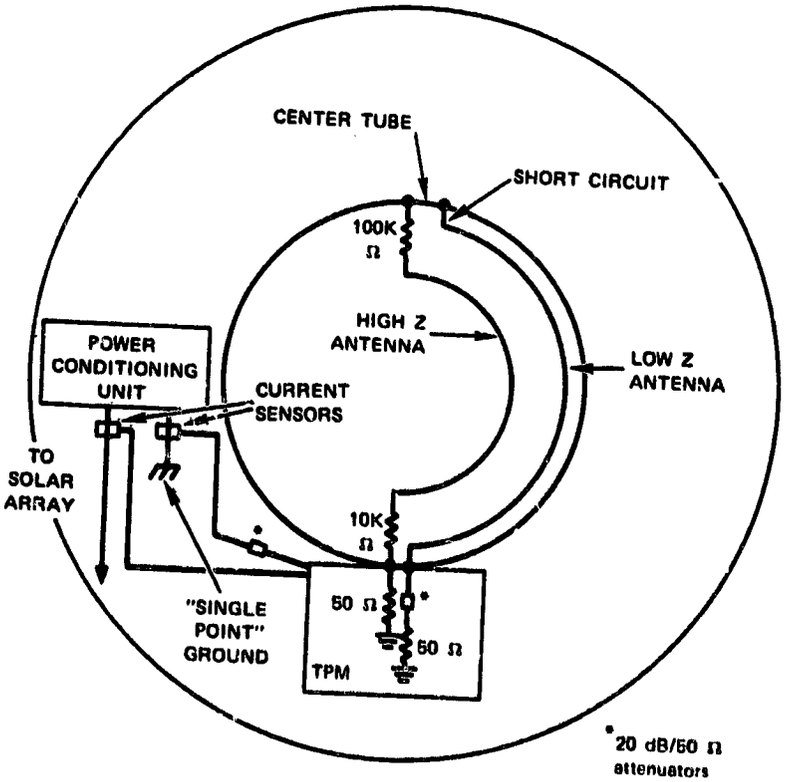

FIGURE 2 TPM SENSOR LOCATIONS ON P78-2

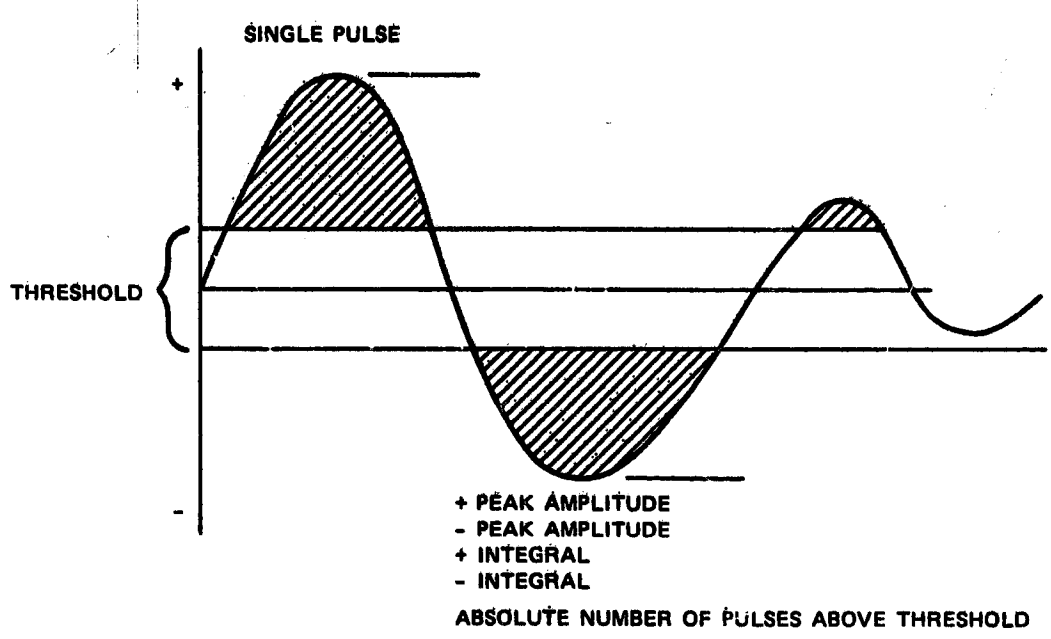

FIGURE 3 DATA DERIVED FROM TRANSIENT-PULSE MONITOR

N79-24057

FURTHER DEVELOPMENT OF THE MULTIPACTOR DISCHARGE ELECTRON SOURCE

J. E. Nanevicz and R. C. Adamo
SRI International

BACKGROUND

At the last spacecraft charging conference, we described a rugged electron gun developed for use in the study of the behavior of spacecraft insulating materials (ref. 1). In this system, electrons are generated using a multipactor discharge between a pair of plates with a diameter equal to the desired target diameter so that a uniform, collimated, large-area electron beam is produced. Multipactor discharge occurs when two electrodes in vacuum are driven with an RF source of the proper frequency. An initial electron occurring near the first electrode will be accelerated across the gap, strike the second electrode and generate one or more secondary electrons just as the field changes polarity. The secondary electrons, in turn, are accelerated across the gap and generate additional secondaries when they strike the first electrode. In this way the number of electrons in the breakdown cascades until various loss mechanisms come into play and limit further growth in the number of electrons participating in the breakdown. Thus, the multipactor breakdown may be thought of as a sheet of electrons oscillating between a pair of electrodes in synchronism with the applied RF field. The desirable features of the multipactor electron source include high immunity to degradation from contamination and virtually no dependence of beam size and uniformity on accelerating voltage.

The original multipactor electron gun setup shown in figure 1 included a control grid to adjust beam current, but the beam accelerating voltage was applied between the electron source and the target. The multipactor electron source has since been modified to include the electron accelerating system within the source. As a result, the region between the source and the target is free of fields produced by the source electrodes. This arrangement is more suitable for the simulation of spacecraft charging conditions.

In addition, a beam current feedback control system has been incorporated to maintain a constant source current density over a wide range of beam accelerating voltages.

MODIFIED MULTIPACTOR SOURCE

A photograph of one of the multipactor electron sources presently in use is shown in figure 2. The one shown generates a beam 10 inches in diameter.

A second unit, currently being used in discharge characterization, generates a beam 12 inches in diameter.

All of the surfaces visible in figure 2, including the grid through which the beam is emitted, are at ground potential. The electron source is supported via mounting fixtures on the back surface of the assembly. RF and dc voltages are supplied to the source via connectors also located on the back surface of the assembly.

A schematic of the new source design is shown in figure 3. The multipactor discharge region is essentially the same as it was in the earlier system. The lower plate is perforated to allow the escape of electrons to form the beam. It may be considered to constitute the "cathode" of the electron gun. The control grid, located below the perforated multipactor plate, has been modified by the addition of a solid skirt which extends up to cover the entire multipactor gap. This modification was found to be necessary to allow complete cutoff of the electron beam. Without the skirt, electrons diffusing radially from the discharge regions are not cutoff by the control grid.

In the present design, an accelerating grid has been added below the control grid. A skirt on the accelerating grid extends upward past the upper multipactor plate. The skirt is capped with a solid metal sheet at its upper periphery. Thus, the accelerator grid and its associated structure completely enclose the electron gun system.

The accelerating grid structure is connected to system ground. Electrons are accelerated by biasing the multipactor cathode negative with respect to the accelerating grid. With this arrangement, both RF and dc fields are completely contained within the outer shell of the gun.

To simplify the problem of providing high-voltage-dc isolation of the RF source, the multipactor discharge is driven using transformer coupling between a pair of coils. The primary and secondary windings of the transformer are located one on the inside and one on the outside of a Teflon cylinder. Practical considerations of circuit values associated with the transformer coupling scheme caused the operating frequency to be reduced from 150 MHz to 50 MHz.

BEAM CURRENT CONTROLLER

Although the basic multipactor source is basically stable and provides a reasonably constant beam current over periods of the order of minutes, certain applications require that the tests continue unattended for periods of 24 hours and more. Over this length of time, it was found that unacceptable changes in beam current could occur. Also, in working with the multipactor electron source, it was found that there was some interaction between beam current and beam accelerating voltage. To avoid these drawbacks of the multipactor electron gun, a feedback system for controlling beam current was developed.

The beam-current-control system is shown as a box in figure 3. Essentially, it maintains the total return current to the electron source constant. This approach was chosen as being most representative or orbital conditions in which a large-scale ambient current density illuminates the vehicle as a whole, while local current densities are determined by local conditions such as surface charge on insulating materials.

Essentially, the system senses the return current and generates an appropriate ac signal which is fed through a high-voltage isolation system to a grid voltage power supply controller maintained at "cathode" potential. The grid-to-cathode voltage is adjusted in this way to establish the required return current.

TESTS OF THE MULTIPACTOR SOURCE

Beam Uniformity

The uniformity of the electron beam generated by the electron source was investigated in a vacuum chamber equipped with a Faraday cup mounted on a movable arm to permit it to be swept through the beam. Measured results indicate that, over the diameter of the source, the current density is uniform to within 30%.

Arrangements were made to rotate the source in increments of 45° to make certain that there were no nonuniformities anywhere within the beam.

Further checks of beam uniformity were carried out by using the beam to illuminate a metal sheet coated with cathode-ray-tube phosphor. A highly uniform glow was observed.

Current Controller Functioning

The beam current controller was tested by setting it at a given current and monitoring the return current periodically for roughly 24 hours. It was found that the beam current was maintained within $\pm$ 5% over this period.

In a second test, the return current was set at a predetermined value within the range 1 to 10 nA/cm^2 and the beam energy was varied from 5 to 15 KeV. The beam return current was maintained constant to within 5%.

APPLICATION OF MULTIPACTOR GUN

The new multipactor electron source has been used for several months now in various experiments involving spacecraft charging simulation. These have involved frequent opening of the vacuum system to install new test samples and to adjust instrumentation. Aside from occasional cleaning of the multipactor electrodes, no maintenance has been necessary. Reliable operation has

been obtained with a minimum of time for adjustment of either RF or dc systems. It is felt that the additional complexity of the present multipactor electron gun is more than offset by the increased capability and operating convenience.

REFERENCE

1. Nanevicz, J. E. and Adamo, R. C., "A Rugged Electron/Ion Source for Spacecraft Charging Experiments," Proceedings of the Spacecraft Charging Technology Conference, U.S. Air Force Academy, Colorado Springs, Colorado, 27-29 October 1976.

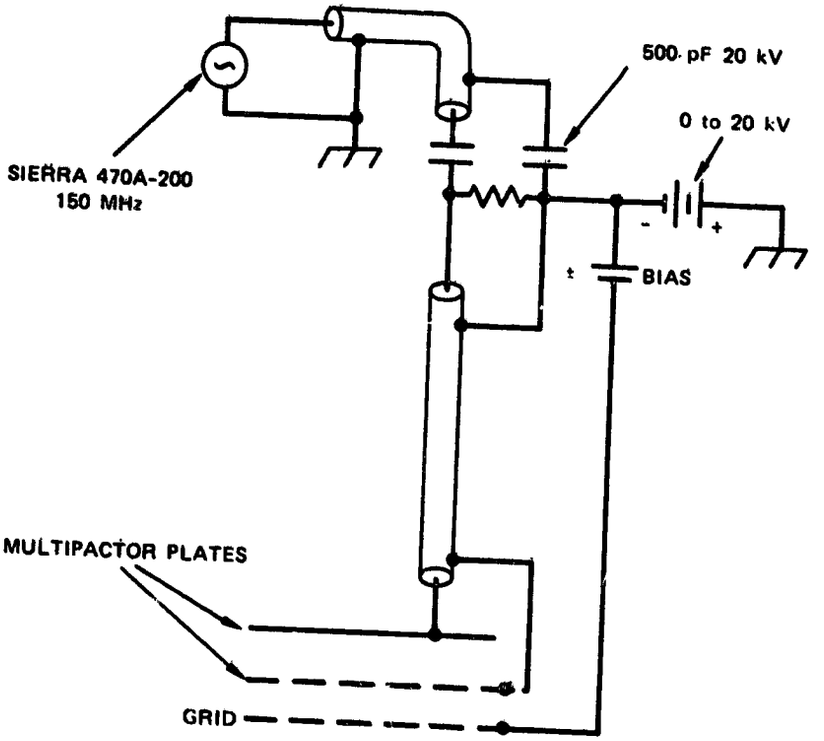

SOURCE DIAMETER = 8 in.
MAXIMUM ELECTRON CURRENT DENSITY = 5 $\mu A/cm^2$

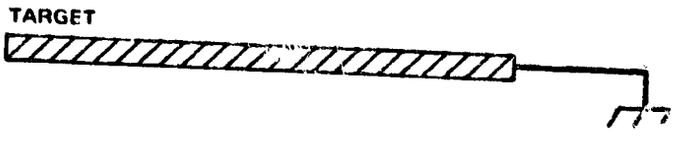

FIGURE 1 SCHEMATIC OF ORIGINAL MULTIPACTOR ELECTRON SOURCE

FIGURE 2 PRESENT MULTIPACTOR ELECTRON SOURCE

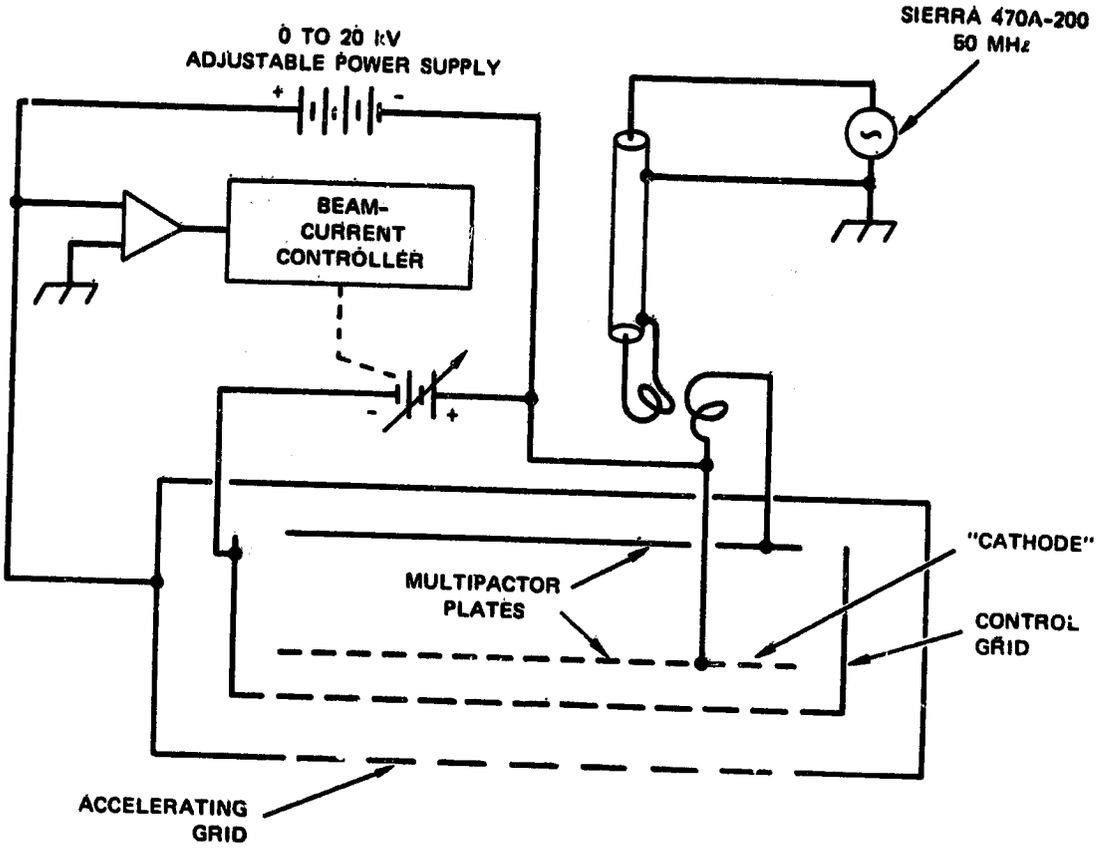

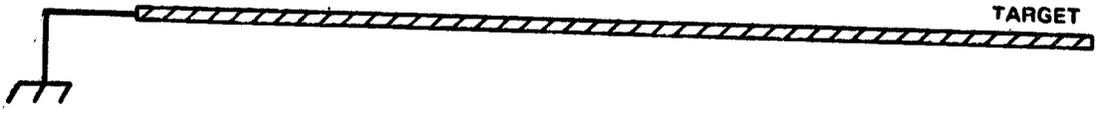

FIGURE 3 SCHEMATIC OF PRESENT MULTIPACTOR ELECTRON SOURCE

SUMMARY OF PANEL DISCUSSION

Chairman: Alan Rosen
TRW

A. Rosen: Our topic is the spacecraft charging hazard to space systems and the credibility of that hazard to managers and systems designers who are charged with the task of doing something about it and also what constitutes a reasonable response to this perceived hazard. The panel members are a distinguished group and represent organizations that are concerned with the hazard. They may be regarded as technical spokesmen for their organizations and have the responsibility to do something about the perceived hazard. To many of us, they represent funding agencies, agencies that support much of our work. But, it is important to realize that they, themselves, are constrained to address what constitutes the "real" hazard rather than some imagined hazard.

The panel members are Major George Kuck, representing SAMSO; Robert Finke, from the NASA Lewis Research Center; Michael Massaro, from General Electric; William Lehn, from the Air Force Materials Laboratory; John Darrah, from the Air Force Weapons Laboratory; and Charles Pike, representing the Air Force Geophysics Laboratory.

Because of the late hour, our agenda and format for this discussion are aimed at giving each panel member an opportunity to respond to the key issues. I will open the discussion with some definitions and clarification of the topic problem. Each panel member will then respond, for about 5 minutes, to the problem. Then the session will be opened to general discussion.

If we could identify a well-defined threat to space systems, all tasks aimed at alleviating or eliminating that threat would be funded. Project managers and other people who are involved in the space program do respond to a threat that they perceive. The question is, can we put the spacecraft charging hazard in some sort of perspective on a scale of 0 to 10, where 0 is no hazard, 1 is a nuisance or outage of a second or less, 5 is an outage of a few hours, and 10 is some sort of catastrophe? At this time, we have failed to establish in a quantitative manner where the spacecraft charging hazard falls on this scale.

The elements that go into a quantitative definition of the hazard are the environment, the interaction of a spacecraft with the environment (the charging model and the arc discharge characterization or the frequency-amplitude domain) where the charge goes (a crucial element in determining the hazard to space systems), and the coupling analysis. What happens to the rest of a system during a discharge and what damage may occur seem to be unclear. Key members of the spacecraft design community cannot answer these questions. We have done quite a bit in describing the spacecraft charging environment and in defining a charging model. But we have failed in the area of discharges and coupling analysis and in doing the necessary work to define the hazard. Is it a valid hazard and what should be done about it?

G. Kuck: My introduction to the spacecraft charging problem was about 6 months ago when I was made project officer on the SCATHA program. Thus, I am the most junior member of this group. Although I was warned not to get involved with the SCATHA program and told it is a boondoggle, a WPA project for geophysicists, I do not hold this view. I believe it to be an important program and I think this is the perception of a large number of people. However, project personnel do not seem to consider spacecraft charging to be a hazard, and therefore nobody from the SAMSO Systems Program Offices attended this conference.

R. Finke: NASA has very little involvement with geosynchronous spacecraft. Although NASA is synonymous with spacecraft, we do not build and operate many geosynchronous spacecraft. We provide launch services. We did build the Applications Technology Satellite (ATS) spacecraft and were co-experimenters on the Communications Technology Satellite (CTS). And we are now taking part in the Tracking and Data Relay Satellite System (TDRSS) which is a big project involving a series of geosynchronous spacecraft.

So what is NASA doing in a spacecraft charging program? Well, we are technologists, and some of the early ATS data taken by Goddard indicated that there was a charging phenomenon. The particle detector on the ATS spacecraft indicated that in the geosynchronous environment spacecraft charged up. It is an interesting phenomenon. Others began reporting anomalies in their geosynchronous spacecraft, primarily the military communications spacecraft. Some of the commercial spacecraft people began talking about anomalies - switching of logic circuits, and so forth. We started looking at what might be the cause of this and suggested the charging-discharging phenomenon. It became apparent that there was a problem with spacecraft - a relatively serious problem. So as technologists we perceived that there was a technological need.

NASA had for years worked on high-voltage systems in vacuum, and some of us were familiar with the space sciences, instrumentation, and so forth. We felt that, with our background and experience, we could make a contribution. So, NASA decided to get involved in this activity. Eventually, we evolved the present intercenter spacecraft charging program and developed an interdependent cooperative effort with the Air Force.

We tried to use our ground-based facilities to simulate the space environment for testing. We demonstrated that, after a solar array was charged differentially, it arced and discharged. Kapton blankets, if not properly grounded, also exhibited arcing effects. We turned the electron beam in the vacuum system on to the Global Positioning Satellite (GPS) louvers and saw them arc, discharge, and flutter (the louvers opening and closing very rapidly).

From the ground test data, in this particular environment, it appeared that anomalies (arcing and sparking that would couple into the spacecraft system) could happen. So we began a modeling program and did more testing on the ATS-5 and ATS-6. We also developed an on-board monitor, a detector system, and put it on CTS. There were 215 transient events on CTS during a year in

orbit. A transient event in this case is up to 60 spikes on the power bus. Fifteen percent of the solar-array power bus was lost after a particularly active flurry of transient events. So, again a problem seemed to exist that needed attention. We installed the same kind of monitor on the Orbital Test Satellite (OTS), and it is detecting transient events. The data have not yet been analyzed.

So, to address the question of credibility and hazards, we feel, from ground tests and analyses and our knowledge of the spacecraft charging environment, that there is a potential hazard but that it depends on the configuration and the spacecraft design. Transients can cause switching anomalies. We are trying to develop techniques to prevent these anomalies. As discussed in the papers given at this conference, NASA is publishing design guidelines and test data, but the acceptance of this technology by the user is highly dependent on our education of that user.

Think of this program as an R&QA function. If a user does not want to use qualified parts on his spacecraft but wants to risk using parts he can buy from Radio Shack, nobody can stop him except his sponsor or his boss. There is, perhaps, an unquantifiable risk - a risk that is going to vary a lot with the spacecraft, its design life, and its components. We may never be able to pin down exactly what the hazard is. But not looking at the charging criteria may be a lot like not using R&QA.

M. Massaro: I agree with most of Dr. Rosen's assessment. Whether a spacecraft charging hazard can be rated from 0 to 10 will depend on the spacecraft design. That is, you can probably have the full range of events, anywhere from 0 to 10, when an electrostatic discharge occurs, depending on the particular payload or spacecraft design.

Through internally funded research, government research contracts, and space hardware development contracts, GE has made some progress toward quantitatively assessing the effects of electrostatic discharges (ESD). At the systems level, we have analyzed ESD-produced structural currents and estimated their amplitude and wave shapes. We have measured the shielding effectiveness of our Faraday cage design to both radiated and conducted fields in order to determine the effects of electromagnetic-interference (EMI)-produced ESD on components and systems. Again, at the systems level, we have performed ESD radiated-spray testing on telemetry and command systems and on communications payloads while monitoring system performance. At the component level, we have performed current-injection tests of blanket bonding and grounding techniques to determine degradation of electrical grounds. We have performed electron bombardment tests of materials to determine optical and thermal degradation and discharge characteristics. We have measured spectrum signatures of materials that produced ESD. That is, we have measured the magnitude of the radiated-field spectrum produced by ESD in electron bombardment tests. Future approaches to quantitatively assessing the effects of ESD are as follows: large-scale environmental testing of systems while monitoring system performance parameters, as discussed by members of the European space community; development of combined-effects facilities to more accurately simulate the space environment for monitoring of materials responses and parameters.

In response to the question whether the hazards of spacecraft charging have been overestimated, the scientific community's reaction to most new phenomena that pose a threat to system performance tends to be very conservative. This results in excessive design and test requirements in an effort to control the problem. As the spacecraft charging phenomenon becomes better understood, more realistic design and test requirements will emerge. But the threat posed by spacecraft charging and discharging is real and dangerous, as pointed out in the last two conference papers. For example, it can lead to thermal degradation of materials, communications performance degradation, logic upsets, sensor degradation, and even spacecraft failure.

However, we may be erring in attributing most spacecraft anomalies to charging. Some of the occurrences may be attributable to poor design. Currently, there is no system to identify the exact source of anomalies. We also do not know enough about the effects of ESD. That is, exactly what happens when there is a breakdown, what are the coupling mechanisms, what are the systems interactions, how does ESD couple into spacecraft systems? In short, there is a credibility gap in perceiving the actual hazard.

Government agencies should continue to fund basic research into modeling and testing efforts that will help our understanding of the charging-discharging phenomenon; sponsor large-scale system-level test efforts; develop and recommend definitive, unambiguous, cost-effective design procedures that can control the effects of ESD; make design guidelines a contractual requirement but allow the design procedures to be tailored to the specific mission and payload; sponsor development of a standard, practical, ESD monitoring system that can become available as government-furnished equipment to spacecraft manufacturers and provide its interface requirements. Private industry should use good guidelines that are presently in practice, for example, EMI shielding of critical signal lines; use engineering spacecraft charging models; apply systems-level analysis to validate designs; apply recognized, standardized test procedures to ensure good design.

W. Lehn: As evidenced by this conference and the previous one, the spacecraft charging-discharging phenomenon exists. It is now recognized as a phenomenon that is encountered by satellites and other space systems, particularly those that operate in the geosynchronous environment. Recognition of the phenomenon and proper consideration of it in spacecraft design can reduce its potential effect from a hazard to a cause of disruptions or anomalies or can eliminate it completely, as evidenced by the experience with GEOS. GEOS was designed to be 96 percent conductive and has reported no instances of any disruptions or anomalies that could be attributed to spacecraft charging. On the other hand, Meteosat-1 is reported to be performing extremely well in spite of occasional (about 1 per week) status changes. These changes are attributed to surface discharges (spacecraft charging) resulting from the presently rather high solar activity. A recent anomaly in the on-board satellite clock system of an operational satellite has been attributed to spacecraft charging, but the event has not been duplicated in the laboratory. Spacecraft charging is often offered as the cause of certain satellite anomalies without any real direct supporting evidence. There is only one reported case in which spacecraft charg- was established as the cause of the catastrophic failure of a satellite - a DSCS power system.

It is my opinion that spacecraft charging is not really a hazard but a problem that must be treated early in the design of a satellite. By incorporating the proper standards and guidelines it can be designed out of a satellite. As reported earlier, an electrostatic discharge (ESD) control program has been incorporated into the design, development, and testing of the DSCS III satellite and promises to minimize or eliminate the effects of spacecraft charging ESD. The preliminary spacecraft charging standard and the design guidelines for the control of spacecraft charging reported in be previous session are two of the key activities in the cooperative NASA-AF spacecraft charging investigation. When updated to include SCATHA spaceflight data and formalized, these documents will provide the basis for the design of charging-free operational satellites. Certain scientific satellites whose mission includes measurements of very low-energy radiation and charge buildup present special problems that must be handled on an individual satellite-by-satellite basis.

The many papers presented at this conference are ample evidence of the progress that has been made in qualitatively and quantitatively assessing the overall phenomenon and its potential for causing problems with various spacecraft systems and subsystems. SCATHA will add greater insight into the overall problem and provide the data needed to further define the dynamic, often very rapidly changing, geosynchronous radiation environment. The SCI and ML12 experiments will provide valuable materials performance and response data and relate spacecraft charging with contamination. A thorough understanding of spacecraft charging and related modeling activities is expected to take many years, but the standards and design guidelines to build satellites essentially free from any major hazards or anomalies should be available within the next 2 to 3 years.

Is the Air Force response to spacecraft charging reasonable? Spacecraft charging is only one factor that must be considered in the development and application of new satellite thermal-control coatings and materials. Table 1 shows these factors.

TABLE 1. - PROTECTIVE THERMAL-CONTROL COATINGS AND MATERIALS

FOR EXTENDED-LIFE SURVIVABLE SATELLITES

- Tailored optical properties
  α_s, E

- Space stable 7-10 years (UV, e⁻s, P+)
- Low contamination
- Reduced space charging

YOUR

FAVORITE

SATELLITE

- Hardened for nuclear and laser effects
- Low-intrinsic-signature materials (visible, IR, radar)
- Shroud and decoy materials

First and foremost, the new materials must have the required thermo-optical properties to function as thermal-control coatings. These materials must be stable to the natural space environment for the life of the particular mission and, depending on the specific mission (communications, surveillance, etc.), be very low-contamination sources and/or be able to control spacecraft charging. In addition to natural-environment survivability, design of Air Force operational satellites must also consider the vulnerability factors in the right-hand column of table 1. Certain of these factors were in the realm of science fiction not too many years ago. A space-stable, low-contamination, reduced-space-charging material that is suited for a commercial satellite might be totally unsatisfactory for an Air Force satellite because of deficiencies in hardness properties.

In summary, spacecraft charging is only one factor that must be considered in the design, development, and testing of spacecraft. Proper application of the spacecraft charging standard and the design guidelines for the control of spacecraft charging from the Air Force - NASA cooperative effort should reduce or essentially eliminate spacecraft charging as a major concern in future satellites. Very large space structures represent a special case, and further effort and analysis will be required. There is a definite lack of secondary emission, radiation-induced surface and bulk conductivity, photoconductivity, and other classical materials data needed to support the spacecraft-charging modeling activities and to form the basis for developing new and improved thermal-control coating materials. Responsibility for developing such data within the AF-NASA spacecraft-charging working group has not been determined.

J. Darrah: At the Air Force Weapons Laboratory, we are principally concerned with nuclear warfare and the survivability of spacecraft. There is thus less ability, through normal experience in peacetime, to check potential spacecraft performance. The performance of spacecraft in ambient and enhanced electron environments (e.g., solar substorms) by no means explains what would happen in a nuclear explosion. Here we have not only the electron environment, but also the effects of gamma rays (which cause a number of charges to move in a spacecraft, potentials to develop, currents to flow, and the conductivity of materials to change), as well as X-rays and photoelectric phenomena (one principal mechanism called the system-generated electromagnetic pulse (SGEMP) effect). And in some cases there may be synergistic effects, depending on the state of the charge, between the electrons and the gamma rays or X-rays. The current in the spacecraft can be significantly higher, particularly in the high-energy portion, during a nuclear explosion than during a solar substorm. Consequently, problems that might not be experienced during spacecraft operation in the natural space environment may become problems in the nuclear environment. Essentially, the time to accumulate enough charge to cause discharges and difficulties could be very long in the natural environment but could be a few orders of magnitude shorter in the nuclear environment. So this is a different problem and cannot be evaluated well from peacetime experience.

Nuclear tests above the atmosphere have started with the Starfish test, which is the first of the Fishbowl series of high-latitude tests. There are not a lot of data from these tests. However, there has been some review of the data, and some spacecraft anomalies do not seem to be attributable simply to total dose effects, for example, solar-cell degradation and prompt TREE effects,

which clearly lead to eventual spacecraft failure. So some nuclear anomalies may be related to spacecraft charging. The problems are clearly not catastrophic (e.g., burnout of most of the major electronics) or there would be a lot of panic.

The best data available clearly come from space tests rather than from laboratory tests. Unfortunately, there seems to be a lack of cooperation between the spacecraft designers and operators and the spacecraft-charging community. So there is no clearinghouse where incidents of anomalies are reported and the seriousness of the problem is investigated systematically.

Progress will never be made on the total engineering problem down to the interface level without laboratory experiments on the full systems level. Basic modeling phenomenology physics by itself will not do very much. The solution to this problem is not going to come from first-principle physics and it is not going to come from small-sample and limited-geometry tests. First-principle calculations for the nuclear case, including synergisms, produce results that are not real. If they were real, total burnout of spacecraft electronics would have occurred in many cases. The problem of how dangerous spacecraft charging is will be resolved by large-scale laboratory experiments backed up by a reasonably prudent amount of even larger scale laboratory experiments and theory.

Although spacecraft charging is obviously a hazard to some as yet undetermined degree, some operational problems mentioned by the panel members are simply a matter of design. So anomalies cannot be used as proof of how important a problem charging is.

No one, neither systems house nor government agency, is capable of determining the effect of a nuclear explosion on spacecraft charging. This effect could become of prime importance during wartime and is a present concern of the systems houses. Even the effect of a peacetime explosion causes concern.

In conclusion, the Air Force Weapons Laboratory is going to try, within the limits of our understanding, to reproduce the spacecraft charging phenomenon in the laboratory. We will also try to conduct systems-level experiments with reasonable phenomenology across the whole spectrum of electron energies.

C. Pike: The reliability and survivability of military mission spacecraft is of paramount consideration. In this program, technology dollars must compete with systems dollars, which are certainly far more significant. A technology base must be developed and transferred to the users. Fortunately, the hazard of spacecraft charging was recognized many years ago by Air Force Headquarters. The Air Force then established an interdependent technology program with NASA. As this program has progressed, the list of operating anomalies from military and civilian spacecraft has grown and provides a very strong justification for pursuing our program. Indeed, there is a problem, although what is perceived by one program manager as an anomaly of great concern to his program would be merely a nuisance to another program manager. This is a subjective area where candor is often lacking. It is very difficult to assess what, from an operations and reliability viewpoint, is a hazard.

Some significant results of the Air Force - NASA program were presented at this conference. Very significant also is the presence at the conference of the aerospace industry, especially the large corporations who are the contractors for the mission programs. They will implement the technology we develop and are strong spokesmen for this technology.

MIL standard 1541, which is a charging-related test standard, has had a significant impact on satellite development. The only satellite development program using this standard is DSCS III. This satellite is being developed in the context of the AF-NASA technology program. The growing list of anomalies have occurred on satellites that were designed many years ago and have had band-aid fixes to them. The technology that we have been developing in the past 2 to 3 years is being incorporated in the DSCS III program. Dr. Massaro's paper on charging calculations on DSCS III shows that indeed the satellites will see high voltages and that in some cases steps have been taken to mitigate that voltage buildup. Gil Condon's paper shows the design and test program that General Electric is pursuing.

The DSCS III program is developing our next generation of communications satellites, a significant payoff from the AF-NASA technology program. The spacecraft charging hazard has been recognized, a technology base has been developed, and it is being implemented. The Air Force Geophysics Laboratory has been successful in defining the spacecraft charging environment and we know where the technology gaps are - in the field-alined fluxes and ionic composition. SCATHA will certainly provide needed information. In conclusion, there has been strong progress in the technology program. Technology transfer has been proceeding very smoothly. These conferences are a very important part of the transfer process. Technological development generally requires at least 10 years, and we have only been involved in it for 2 or 3 years. Only in 1972 to 1974 did spacecraft charging come to the forefront. In a very short time a lot of progress has been made, and the technology is being applied in our next generation of communications satellites.

A. Rosen: There is one person that hasn't been represented - the person who is responsible for assuring that a system that is about to be launched survives. That person generally needs a measured response to many, many hazardous situations. He really doesn't know whether to immerse the spacecraft in a gigantic swarm tunnel and subject it to electrons and ions or merely to do an air test with simulated arcs. He does not even know what sort of arcs to use. Subjecting the spacecraft to unknown arcs that may not be representative of the in-orbit condition could be a greater hazard than not testing it at all. Should he do a coupling analysis program, which could be very expensive? Or a charging analysis? If he grounds some of the thermal blankets, does he need a verification program to ensure that everything is grounded? These questions haven't really been addressed. He would like to have a measured response to what he considers to be the hazard, but he doesn't know what a good measured response is. This is why some quantitative assessment of the spacecraft charging hazard must be made.

Are there any questions of the panelists among each other? Then, the discussion is open to the audience.

J. Napoli: I am with RCA American Communications. At the conference 2 years ago there was a similar panel discussion, but the theme was a little different. The panel members planned to tell industry - all users, systems designers, and manufacturers - that they wanted to plot orbitial arcing to see what the environment is like. They were going to supply sensors to industry. Unfortunetely, no action was taken. I think for that very reason there is a credibility gap.

Three of the five commercial users of satellites attended the last conference. At this conference, I am the only commercial representative. The five commercial users have 18 satellites in geosynchronous orbits. If there wasn't a credibility gap, these users would be represented here. In the next couple of years, there will be two more commercial users. They are not represented at this conference either. Unless it can be demonstrated that electrostatic discharging (ESD) will either curtail an 8-year mission and thus cause a loss of potential profit and earnings on a commercial satellite, there is going to be a credibility gap with the commercial users. That is one of the problems.

As far as incorporating sensors on the spacecraft, I tried to bring the message to my management but was met with the credibility gap. They said sensors would be nice to have if the procurement and installation were free. The procurement from NASA was free. The installation by the contractor was not. My management wanted to know what government agencies that have launched satellites in the last 2 years have these sensors on their own satellites. That is a hard question to answer and is one that I would like to put to the panel.

Mike Massaro from GE would like to see many test programs conducted. If all these test programs are sponsored by the government, fine. Would GE run an internally funded program to test spacecraft in plasma tanks to show that there is a hazard or that there is a solution to the hazard? I think that, if GE wasn't funded by the Air Force and NASA, that the position wouldn't be taken. I feel that I'm being a realist here and I have one more question. Is DSCS III going to have any sensors on board?

R. Finke: All government-sponsored spacecraft put into geosynchronous orbit have had sensors. The Canadian government put a sensor on CTS. ESA put a sensor on OTS. Both were simple sensors that counted transient events. But both these government-sponsored spacecraft have them. Again, NASA has not sponsored or built spacecraft, with the exception of TDRSS. Ms. Bever represents the Goddard Space Flight Center and TDRSS. The Director of Goddard, Dr. Cooper, has requested the support of the Lewis Research Center in investigating charging problems and design criteria for TDRSS. We are supporting that project. NASA, again, just is not in the geosynchronous spacecraft business. But we do take spacecraft charging seriously.

G. Kuck: Something like a Transient Pulse Monitor (TPM) was installed on an operational Air Force satellite many years ago. But the present spacecraft charging program is more expensive than just a single instrument. The P78-2 satellite alone costs over $45 million. The SCATHA portion is just over $5 million. So the Air Force has invested over $50 million in trying to identify and solve the spacecraft charging problem. I have seen evidence at this conference that GE is working on the problem. So, the existence of the problem is

recognized. Now, if we do our job right, the problem will no longer exist in 2 years for the types of spacecraft being built now or to 1980 or 1985. Except for kilometer-size structures, the problem will be solved.

M. Massaro: In response to the question about ESD monitors, SAMSO in their original contract did not request a monitor system on DSCS. Actually, General Electric proposed it in our response to the proposal. However, later, because of budgetary constraints and mainly because we don't think ESD will be a problem on DSCS because of the materials being used and the special precautions being taken, GE decided not to install an ESD monitor. However, the Japanese (our customer) during their contract with us requested that we "ESD proof" their Broadcast Satellite Experimental System. They, as a user, were concerned about it.

In response to the question about spacecraft outage, the domestic common-carrier satellite companies who lease transponders on the Domsats are terribly concerned about outages due to solar activity or any other cause. We may not be too aware of what the outages are, as pointed out by another panel member. A lot of spacecraft manufacturers and operators do not want to discuss the problems they have had with their systems. Some representatives from Comsat Laboratories are present and they may want to discuss the outages on the Intelsats because they do seem concerned about the problem.

S. Bosma: Mr. Darrah said that a small-scale test would not be relevant for engineering problems on a spacecraft. However, if you take any material, you start with what its basic behavior will be. You establish its outgassing properties, its thermo-optical properties, etc., with small-scale laboratory tests. You also want to determine its electrical properties. It would be quite normal to apply a screening test method on the electrostatic properties of materials. In a sense this is already taking place. Furthermore, Mr. Darrah said that there are no solutions for electrostatic problems. I think that Dr. Lehn will agree that most of the thermal-control coatings have conductive alternatives. There are conductive black paints, conductive optical solar reflectors (OSR's), and metal surfaces that are themselves conductive. Only the problem of a conductive flexible solar reflector has yet to be solved. In 2 or 3 years solving the electrostatic problem will be standard practice.

J. Darrah: Although the materials tests mentioned by Mr. Bosma are of use, they have limitations that severely affect the original question of the credibility of spacecraft charging as a hazard. From a small area of material it is difficult to establish, even from a basic physics standpoint, the area of thermal blanket or the area of solar cells that contributes to an arc. That is, as material is added to the spacecraft, on the outside and the inside, how large an area contributes to a discharge current at what time? Small-scale experiments do not even establish the boundaries of the problem. So you don't know how much increasing the area to more of a systems level might contribute to an arc. So there is not a bound on current, localization, or time history from small-scale experiments. That is why larger-scale experiments are required. The whole spectrum hasn't been treated, particularly the nuclear case. It isn't clear that results from thermal blankets and external coating tests can be used to evaluate the potential of discharges in printed-circuit boards, in cables, and in other dielectrics in the interior of the spacecraft during nuclear war-

fare. The coupling problem of arcs in many of these latter cases is a much more complicated problem than the insight into the physics that comes from the small-scale samples. The small-scale experiment results on coupling depend very much on the design.

W. Lehn: A lot of progress has been made in the materials charging aspect, in trying to modify FEP Teflon or Kapton to be conductive. But that is only part of the problem. The right side of the table I presented earlier shows the more severe problem, which hasn't been broached at this meeting. Peacetime use, as indicated, is not a problem. In another situation, some of the best materials for solving the charging problem have been totally inadequate for those problems listed on the right. We have some solutions, but we don't have the solution that will fill all the Air Force requirements. We have some materials, data, and approaches but also many questions. The question of in-depth charging is still open. The need for bulk conductivity of materials has not been determined. There is no good, adequate approach to provide a substitute material for any current material that has all the optical properties, long lifetime, and high bulk conductivity and that can be substituted directly.

G. Kuck: The question of the level to which you test is one with which you are always faced. No matter what type of environment is involved, you must decide whether you want to simulate the environment or the effects of the environment. You have to differentiate between verifying that the system will be able to operate in that environment and making a system that operates reliably in the effects of that environment. All satellites that are hardened for SGEMP and for some of the nuclear effects are not tested in underground nuclear tests. We try to test the systems some other way. We specify to the contractor what type of test the Air Force or the customer requires so that the operational spacecraft will be proved reliable, without costing a percentage of the gross national product. One of the approaches taken in the SCATHA program is to try to fill that gap between the environment and the effects of the environment. The P78-2 satellite will check what the EMI and RFI environments are in space. A laboratory scale model will be tested, possibly including a spray test, to see what its EMI-RFI environment is. The laboratory environment can then be related to what we see in space. We will then try to relate the laboratory environment to the results of small-sample tests in order to complete this logic loop. Relatively inexpensive tests that model all those effects will be levied on the contractor. It is a money and resources problem.

Earlier I was remiss in not saying what I think the government's responsibility is. The government's responsibility is to make sure that we get the tests and procedures that the contractor can adapt to the system he is building. In final analysis, we need a combination of analysis, testing, and whatever so that we can assure the satellite sponsor that the satellite will operate reliably when we launch it. If there is an anomaly, it will not be anywhere on the scale between 1 and 10, but will be about 0.5. To gain an extra 0.1 percent in reliability would cost too much. The question is how to tie together the small-scale test, the larger scale test, and the actual operation in the space environment. Then, how does one model the effects and define the appropriate, affordable, systems-level test that gives you confidence before a launch. You have to look at the whole system.

Member of audience: Would the panel comment on the launch time of SCATHA relative to the 11-year solar sunspot cycle?

C. Pike: In the past 6 or 9 months, solar activity has gone up very dramatically and, more recently, it appears to be plateauing. SCATHA will be orbiting and collecting data near the sunspot maximum, a very disturbed time.

E. Whipple: When Dr. Rosen formulated his point on a credibility gap, he put it in terms of questions to modelers: Have they really done their job? Have the environmental modelers really done things properly? Have the sheath modelers done their job? Have the discharge modelers really modeled that properly? That seems to be putting the burden on the theoretical side. I'm enough of a theoretician to know you never trust a theoretical answer but you should look to the data. I'm disappointed, in a way, that the people who have flown spacecraft, that is, the spacecraft designers and builders, have not found the causes for these anomalies. Why aren't they more interested? Is there a conflict of interest, perhaps, in that the designer doesn't want to admit that his design didn't take care of this particular problem? Why hasn't there been more work? We need to know more about the anomalies that have already occurred.

A. Rosen: I didn't put the whole burden on the theoretician for solving or not solving the important problems. I did put some of the burden on them; but also some on the experimentalists for not tackling the right problems; and also some on the project managers, who are responsible for disseminating funds, for not seeing to it that the right problems were tackled. And, I'll accept the responsibility myself for being blind 2 years ago to what the real problems were. So the theoreticians are not being blamed for everything. The anomalies are an exercise in frustration for most project managers. It is almost impossible to reconstruct events as they occur on a spacecraft. Large sums of money - about $10 million in half a dozen cases - and quite a bit of effort have gone into this. The results have been inconclusive in the cases I have been involved with. So, we are really chasing our tails. On the one hand the spacecraft designer refuses to put diagnostics (transient monitors) on the spacecraft because monitors are not going to fix anything for him. On the other hand, when he does get into trouble, he is in a dilemma and can't determine what the source of the problem is.

E. Whipple: Why hasn't there been a strong emphasis on diagnostics? A small TPM monitor is not expensive.

A. Rosen: The people who are responsible for operational spacecraft generally don't want to undertake a research and development program by using diagnostics monitors.

G. Kuck: Elden, it's money.

J. Napoli: One of the real reasons is that the level of problems has been about 0.5 on a scale of 0 to 10 - problems that have not caused any outages, at least none that we can attribute to spacecraft charging. In my 3 years of satellite operational experience - that 3 years is a total of 6 if you take the two satellites - we have not had any problems or any outages that we can

attribute to spacecraft charging. That is true, in general, with all the commercial satellite programs. Without an outage caused by some unknown, you can't justify the cost of sensors.

S. Deforest: That statement doesn't make sense unless we add the qualification that all anomalies have been tracked down to a source without these diagnostics being made.

J. Napoli: The anomalies we haven't been able to track down are so insignificant that they are not of any major concern.

A. Rosen: There was one anomaly that was a 10 on a scale of 0 to 10 and it was tracked down very vigorously. This total failure and loss of a space system was attributed to a charging phenomenon. There was no other cause for that failure that was as credible as a charging and discharging event. Although we cannot say that it definitely was the cause.

M. Massaro: Maybe the design features of the RCA satellites precluded any problems with ESD. In other words, ESD did not affect the components because of the design procedures RCA had used for these two spacecraft. In other words, it is fortunate that you didn't have any problems.

J. Napoli: Let me give you a little background on that. About 3½ or 4 years ago myself, as a user, and our contractor, RCA Astroelectronics of Princeton, toured the country after we had read the report about that particular catastrophic problem that Dr. Rosen made reference to. We were in the design phase at that time so we were concerned. That is the very reason why I'm here and have followed this subject for the last 4 years. We tried to find out what the problems were and what to do to avoid them. Then we went through all the ramifications and reviewed all the test data we had picked up by contacting people in the optical coating industry, in the other contracting industries, at SAMSO, and in various other places. We looked at our basic design, but even so we made no changes other than those we had originally planned to make anyway.

A. Rosen: At this point I would like to close the session.